



AFRL-RB-WP-TR-2009-3109

SURFACE EXCRESCENCE TRANSITION STUDY
Delivery Order 0053

Aaron Drake and Anne Bender

Northrop Grumman Aerospace Systems

APRIL 2009
Final Report

Approved for public release; distribution unlimited.

See additional restrictions described on inside pages

STINFO COPY

AIR FORCE RESEARCH LABORATORY
AIR VEHICLES DIRECTORATE
WRIGHT-PATTERSON AIR FORCE BASE, OH 45433-7542
AIR FORCE MATERIEL COMMAND
UNITED STATES AIR FORCE

NOTICE AND SIGNATURE PAGE

Using Government drawings, specifications, or other data included in this document for any purpose other than Government procurement does not in any way obligate the U.S. Government. The fact that the Government formulated or supplied the drawings, specifications, or other data does not license the holder or any other person or corporation; or convey any rights or permission to manufacture, use, or sell any patented invention that may relate to them.

This report was cleared for public release by the USAF 88th Air Base Wing (88 ABW) Public Affairs Office (PAO) and is available to the general public, including foreign nationals. Copies may be obtained from the Defense Technical Information Center (DTIC) (<http://www.dtic.mil>).

AFRL-RB-WP-TR-2009-3109 HAS BEEN REVIEWED AND IS APPROVED FOR PUBLICATION IN ACCORDANCE WITH ASSIGNED DISTRIBUTION STATEMENT.

*//Signature//

Capt. WAYNE ROHE
Project Engineer
Aerodynamic Configuration Branch
Aeronautical Sciences Division

//Signature//

CHRISTOPHER P. GREEK
Chief
Aerodynamic Configuration Branch
Aeronautical Sciences Division

//Signature//

CARL TILMANN
Technical Advisor
Aerodynamic Configuration Branch
Aeronautical Sciences Division

This report is published in the interest of scientific and technical information exchange, and its publication does not constitute the Government's approval or disapproval of its ideas or findings.

*Disseminated copies will show “//Signature//” stamped or typed above the signature blocks.

REPORT DOCUMENTATION PAGE				Form Approved OMB No. 0704-0188	
<p>The public reporting burden for this collection of information is estimated to average 1 hour per response, including the time for reviewing instructions, searching existing data sources, gathering and maintaining the data needed, and completing and reviewing the collection of information. Send comments regarding this burden estimate or any other aspect of this collection of information, including suggestions for reducing this burden, to Department of Defense, Washington Headquarters Services, Directorate for Information Operations and Reports (0704-0188), 1215 Jefferson Davis Highway, Suite 1204, Arlington, VA 22202-4302. Respondents should be aware that notwithstanding any other provision of law, no person shall be subject to any penalty for failing to comply with a collection of information if it does not display a currently valid OMB control number. PLEASE DO NOT RETURN YOUR FORM TO THE ABOVE ADDRESS.</p>					
1. REPORT DATE (DD-MM-YY) April 2009		2. REPORT TYPE Final		3. DATES COVERED (From - To) 01 September 2007 – 17 April 2009	
4. TITLE AND SUBTITLE SURFACE EXCRESCENCE TRANSITION STUDY Delivery Order 0053				5a. CONTRACT NUMBER F33615-00-D-3054-0053	
				5b. GRANT NUMBER	
				5c. PROGRAM ELEMENT NUMBER 0602201	
6. AUTHOR(S) Aaron Drake and Anne Bender				5d. PROJECT NUMBER A071	
				5e. TASK NUMBER	
				5f. WORK UNIT NUMBER 0B	
7. PERFORMING ORGANIZATION NAME(S) AND ADDRESS(ES) Northrop Grumman Aerospace Systems Strike and Surveillance Systems Division One Hornet Way El Segundo, CA 90245				8. PERFORMING ORGANIZATION REPORT NUMBER	
9. SPONSORING/MONITORING AGENCY NAME(S) AND ADDRESS(ES) Air Force Research Laboratory Air Vehicles Directorate Wright-Patterson Air Force Base, OH 45433-7542 Air Force Materiel Command United States Air Force				10. SPONSORING/MONITORING AGENCY ACRONYM(S) AFRL/RBAA	
				11. SPONSORING/MONITORING AGENCY REPORT NUMBER(S) AFRL-RB-WP-TR-2009-3109	
12. DISTRIBUTION/AVAILABILITY STATEMENT Approved for public release; distribution unlimited.					
13. SUPPLEMENTARY NOTES PAO Case Number: 88ABW 2009-2370, 02 Jun 2009. Report contains color.					
14. ABSTRACT An examination of the effects of surface excrescences on boundary layer transition has been performed, using a unique experimental facility. The experimental study focused on stagnation-line starting condition boundary layers in incompressible flow without sweep effects. The study was performed at flight-representative Reynolds numbers—equivalent to chord Reynolds numbers of 4 to 8 million—and included the effects of favorable pressure gradients. The results for both forward and aft-facing steps indicate a substantial stabilizing effect of favorable pressure gradient on excrescence-induced boundary layer transition. These findings suggest that manufacturing tolerances for laminar flow aircraft could be loosened in areas where even mild favorable pressure gradients exist.					
15. SUBJECT TERMS boundary layer transition, excrescence, manufacturing tolerances, laminar flow					
16. SECURITY CLASSIFICATION OF:			17. LIMITATION OF ABSTRACT: SAR	18. NUMBER OF PAGES 584	19a. NAME OF RESPONSIBLE PERSON (Monitor) Capt. Wayne Rohe 19b. TELEPHONE NUMBER (Include Area Code) N/A
a. REPORT Unclassified	b. ABSTRACT Unclassified	c. THIS PAGE Unclassified			

TABLE OF CONTENTS

Section	Page
LIST OF FIGURES	v
LIST OF TABLES	xxi
ACKNOWLEDGEMENTS	xxii
NOMENCLATURE	xxiii
1.0 SUMMARY	1
2.0 INTRODUCTION	2
3.0 BACKGROUND	5
4.0 MODEL DESCRIPTION	18
4.1 Model Aerodynamic Design	18
4.1.1 Design and Analysis Using Computational Fluid Dynamics	18
4.1.2 Modeling of Wind Tunnel Installation Effects	26
4.1.3 Modeling of Unsteady Effects	30
4.2 Model-Integrated Instrumentation.....	33
4.3 Model Construction.....	35
4.4 Predicted Skin Friction Coefficients	43
5.0 SHAKEDOWN TEST	47
5.1 Objective	47
5.2 Shakedown Test Facility Description	47
5.3 Shakedown Test Results.....	49
6.0 TOWING WIND TUNNEL FACILITY	52
6.1 Model Installation	55
7.0 MEASUREMENT METHODS	63
7.1 Pressure Distributions	63
7.1.1 Pressure System	63
7.2 Measured Pressure Distributions.....	64
7.3 Boundary Layer Probe Traversing System	93
7.3.1 Boundary Layer Probe Traversing System Design.....	93
7.3.2 Boundary Layer Probe Traversing System Application	93
7.3.3 Boundary Layer Probe Velocity Profile Results.....	95
7.4 Preston Tubes	98
7.4.1 Preston Tube Design	98
7.4.2 Preston Tube Application	99
7.4.3 Preston Tube Results.....	100
7.5 Hotwire Anemometry.....	191
7.5.1 Hotwire Anemometry Setup	191
7.5.2 Hot wire Repair Station	198
7.5.3 Vibration Measurements.....	199
7.5.4 Temperature Control.....	200
7.5.5 Data Acquisition System.....	202
7.5.6 Review of Linear Stability Theory	204
7.5.7 Hot-wire Anemometry Results	208
7.5.7.1 Velocity Time Series and Spectra	208
7.5.7.2 Selected Comparison of Spectra	320

7.5.7.3	Velocity Root Mean Square (RMS)	337
7.5.7.4	Traversing Data	349
7.5.7.5	Supplementary data: flow uniformity	354
7.5.7.6	Supplementary data: accelerometer results	384
7.5.7.7	Flow characterization	452
7.5.8	Comparison with Stability Analysis	464
7.5.9	Comparison with Skin Friction Measurements.....	478
8.0	EXCRESCENCE RELATIONS	488
9.0	CONCLUSIONS.....	503
10.0	RECOMMENDATIONS.....	506
	REFERENCES	507
	APPENDIX A.....	509
	APPENDIX B	509
	APPENDIX C	528
	APPENDIX D.....	537
	APPENDIX E	548
	APPENDIX F.....	551
	APPENDIX G.....	552

LIST OF FIGURES

Figure	Title	Page
Figure 1:	RQ-4 Global Hawk Block 10.	2
Figure 2:	Northrop Grumman SensorCraft concept designed for laminar flow.....	3
Figure 3:	Three hurdles to laminar flow.	3
Figure 4:	Transition Reynolds number comparison for a laminar flow wing.	4
Figure 5:	Test section with upper wall deflected to provide a favorable pressure gradient on the flat plate model.	6
Figure 6:	MEATLOAF Task 1 model geometry.	6
Figure 7:	Task 1 forward-facing step locations.	7
Figure 8:	Task 1 aft-facing step locations.....	7
Figure 9:	Task 1 test plate upper surface with forward-facing step in position D.	8
Figure 10:	Task 1 tested static pressure distributions.	9
Figure 11:	Task 1 Transition Trend, Aft Steps, $K = -5.2E-7$	10
Figure 12:	Task 1 Transition Trend, Fwd Steps, $K=-5.2E-7$	11
Figure 13:	Task 1 Transition Trend, Aft Steps, $K=-2.9E-7$	11
Figure 14:	Task 1 Transition Trend, Fwd Steps, $K=-2.9E-7$	12
Figure 15:	Task 1 Transition Trend, Aft Steps, $K=0.5E-7$	12
Figure 16:	Task 1 Transition Trend, Fwd Steps, $K=0.5E-7$	13
Figure 17:	Task 1 Transition Trend, Aft Steps, $K=3.2E-7$	13
Figure 18:	Task 1 Transition Trend, Fwd Steps, $K=3.2E-7$	14
Figure 19:	Task 1 Transition Trend, Aft Steps, $K=6.1E-7$	14
Figure 20:	Task 1 Transition Trend, Fwd Steps, $K=6.1E-7$	15
Figure 21:	Task 1 Transition Trend, Aft Steps, $K=9.4E-7$	15
Figure 22:	Task 1 Transition Trend, Fwd Steps, $K=9.4E-7$	16
Figure 23:	Pressure distribution and K for Gradient-Zero model.	19
Figure 24:	Pressure distribution and K for Gradient-A model.....	20
Figure 25:	Pressure distribution and K for Gradient-B model.	21
Figure 26:	Top view of Gradient-Zero model showing splitter plate (dimensions in inches).	22
Figure 27:	Top view of Gradient-A model showing splitter plate (dimensions in inches).	22
Figure 28:	Top view of Gradient-B model showing splitter plate (dimensions in inches).	23
Figure 29:	Gradient-A C_p distributions at various span stations.	23
Figure 30:	Gradient-B C_p distributions at various span stations.	24
Figure 31:	Gradient-A spanwise percent deviation from target K values.	25
Figure 32:	Gradient-B spanwise percent deviation from target K values.	26
Figure 33:	Gradient-A pressure distributions with and without tunnel walls.	27
Figure 34:	Gradient-B pressure distributions with and without tunnel walls.	27
Figure 35:	Gradient-A change in nondimensional pressure gradient.....	28
Figure 36:	Gradient-B change in nondimensional pressure gradient.	29
Figure 37:	Gradient-A pressure distribution comparison with corrections applied.	30
Figure 38:	Gradient-B time-accurate gridding scheme.....	31
Figure 39:	Comparison of shedding vortices for the Gradient-A and Gradient-B models.	31
Figure 40:	Temporal lift distribution for the Gradient-B model.....	32
Figure 41:	Gradient-B with an aft extension.....	32
Figure 42:	Gradient-B stagnation point travel.	33
Figure 43:	Model shapes and static pressure tap locations.	34
Figure 44:	Coordinate system for SETS models.....	34
Figure 45:	Gradient-Zero model exploded assembly drawing.....	35
Figure 46:	Gradient-Zero model forward subassembly drawing.	36
Figure 47:	Gradient-Zero leading edge (non-measurement side) in CNC machine.....	37
Figure 48:	Gradient-Zero leading edge piece (measurement side) before handwork	37
Figure 49:	Gradient-A leading edge (non-measurement side).....	38
Figure 50:	Gradient-A composite skin under vacuum.	39
Figure 51:	Backbone structure being attached to Gradient-A skin.	39
Figure 52:	Gradient-Zero leading edge and midsection inspection results, measurement side.	40

Figure 53: Gradient-A leading edge and midsection inspection results, measurement side.	41
Figure 54: Gradient-A fiberglass panel inspection results, measurement side.	41
Figure 55: Gradient-B assembly inspection results, measurement side.	42
Figure 56: Gradient-Zero predicted skin friction coefficient distribution.	43
Figure 57: Gradient-A predicted skin friction coefficient distribution.	44
Figure 58: Gradient-B predicted skin friction coefficient distribution.	44
Figure 59: Gradient-Zero predicted boundary layer thickness.	45
Figure 60: Gradient-A predicted boundary layer thickness.	45
Figure 61: Gradient-B predicted boundary layer thickness.	46
Figure 62: Northrop Grumman 7x10-ft wind tunnel schematic and characteristics.	48
Figure 63: Tufts used on Gradient-A aft pressure recovery region.	49
Figure 64: Smoke wand used on Gradient-A.	50
Figure 65: Smoke wand at model leading edge.	50
Figure 66: Smoke wand used on Gradient-A upper splitter plate.	51
Figure 67: Towing Wind Tunnel track diagram (not to scale).	52
Figure 68: Guideway cross-section showing test section hood (right).	53
Figure 69: HART carrier vehicle.	53
Figure 70: HART vehicle inside test section.	54
Figure 81: DSM3400 and 4 ZOC22/TCU units make up the pressure recording system.	64
Figure 82: Gradient-Zero C_p distribution data (Run 38), $U=15$ m/s (nominal).	65
Figure 83: Gradient-Zero average C_p distribution, $U=15$ m/s (nominal).	66
Figure 84: Gradient-Zero C_p distribution data (Run 36), $U=20$ m/s (nominal).	66
Figure 85: Gradient-Zero C_p distribution data (Run 32), $U=20$ m/s (nominal).	67
Figure 86: Gradient-Zero average C_p distribution, $U=20$ m/s (nominal).	67
Figure 87: Gradient-Zero C_p distribution data (Run 37), $U=25$ m/s (nominal).	68
Figure 88: Gradient-Zero average C_p distribution, $U=25$ m/s (nominal).	68
Figure 89: Gradient-Zero C_p distribution data (Run 35), $U=30$ m/s (nominal).	69
Figure 90: Gradient-Zero C_p distribution data (Run 74), $U=30$ m/s (nominal).	69
Figure 91: Gradient-Zero C_p distribution data (Run 33), $U=30$ m/s (nominal).	70
Figure 92: Gradient-Zero average C_p distribution, $U=30$ m/s (nominal).	70
Figure 93: Comparison of Gradient-Zero average C_p distribution.	71
Figure 94: Gradient-Zero speed averaged C_p distribution.	71
Figure 95: Comparison of Gradient-Zero average K distribution.	72
Figure 96: Gradient-Zero speed averaged K distribution.	72
Figure 97: Gradient-A C_p distribution data (Run 163), $U=15$ m/s (nominal).	73
Figure 98: Gradient-A C_p distribution data (Run 165), $U=15$ m/s (nominal).	73
Figure 99: Gradient-A average C_p distribution, $U=15$ m/s (nominal).	74
Figure 100: Gradient-A C_p distribution data (Run 161), $U=20$ m/s (nominal).	74
Figure 101: Gradient-A C_p distribution data (Run 166), $U=20$ m/s (nominal).	75
Figure 102: Gradient-A average C_p distribution, $U=20$ m/s (nominal).	75
Figure 103: Gradient-A C_p distribution data (Run 164), $U=25$ m/s (nominal).	76
Figure 104: Gradient-A C_p distribution data (Run 169), $U=25$ m/s (nominal).	76
Figure 105: Gradient-A average C_p distribution, $U=25$ m/s (nominal).	77
Figure 106: Gradient-A C_p distribution data (Run 162), $U=30$ m/s (nominal).	77
Figure 107: Gradient-A C_p distribution data (Run 170), $U=30$ m/s (nominal).	78
Figure 108: Gradient-A average C_p distribution, $U=30$ m/s (nominal).	78
Figure 109: Comparison of Gradient-A average C_p distribution.	79
Figure 110: Gradient-A speed averaged C_p distribution.	79
Figure 111: Comparison of Gradient-A average K distribution.	80
Figure 112: Gradient-A speed averaged K distribution.	80
Figure 113: Gradient-B C_p distribution data (Run 310), $U=15$ m/s (nominal).	81
Figure 114: Gradient-B C_p distribution data (Run 310), $U=15$ m/s (nominal).	81
Figure 115: Gradient-B C_p distribution data (Run 392), $U=15$ m/s (nominal).	82
Figure 116: Gradient-B average C_p distribution, $U=15$ m/s (nominal).	82
Figure 117: Gradient-B C_p distribution data (Run 305), $U=20$ m/s (nominal).	83
Figure 118: Gradient-B C_p distribution data (Run 393), $U=20$ m/s (nominal).	83

Figure 119: Gradient-B average C_p distribution, $U=20$ m/s (nominal).....	84
Figure 120: Gradient-B C_p distribution data (Run 306), $U=25$ m/s (nominal).....	84
Figure 121: Gradient-B C_p distribution data (Run 394), $U=25$ m/s (nominal).....	85
Figure 122: Gradient-B average C_p distribution, $U=25$ m/s (nominal).....	85
Figure 123: Gradient-B C_p distribution data (Run 308), $U=30$ m/s (nominal).....	86
Figure 124: Gradient-B C_p distribution data (Run 395), $U=30$ m/s (nominal).....	86
Figure 125: Gradient-B average C_p distribution, $U=30$ m/s (nominal).....	87
Figure 126: Comparison of Gradient-B average C_p distribution.....	87
Figure 127: Gradient-B speed averaged C_p distribution.....	88
Figure 128: Comparison of Gradient-B average K distribution.....	88
Figure 129: Gradient-B speed averaged K distribution.....	89
Figure 130: Model comparison of average C_p distribution, $U=15$ m/s (nominal).....	90
Figure 131: Model comparison of average C_p distribution, $U=20$ m/s (nominal).....	90
Figure 132: Model comparison of average C_p distribution, $U=25$ m/s (nominal).....	91
Figure 133: Model comparison of average C_p distribution, $U=30$ m/s (nominal).....	91
Figure 134: Model comparison of speed averaged C_p distribution.....	92
Figure 135: Model comparison of speed averaged C_p distribution.....	92
Figure 136: Boundary layer traverse used to measure velocity profiles and to traverse hot wire.....	93
Figure 137: Illustration of velocity profile and u_k	94
Figure 138: Light trigger connected to BLDS.....	95
Figure 139: Gradient-Zero boundary layer velocity profile summary.....	96
Figure 140: Gradient-A boundary layer velocity profile summary.....	97
Figure 141: Gradient-B boundary layer velocity profile summary.....	97
Figure 142: Preston tube.....	99
Figure 143: Preston tubes arranged on the Gradient-Zero model.....	100
Figure 144: Gradient-Zero, $k=0$ -in, $U=13.73$ m/s skin-friction distribution.....	101
Figure 145: Gradient-Zero, $k=0$ -in, $U=17.9$ m/s skin-friction distribution.....	101
Figure 146: Gradient-Zero, $k=0$ -in, $U=23.11$ m/s skin-friction distribution.....	102
Figure 147: Gradient-Zero, $k=0$ -in, $U=29.61$ m/s skin-friction distribution.....	102
Figure 148: Gradient-Zero, $k=0.03$ -in forward step, $U=19.19$ m/s skin-friction distribution.....	103
Figure 149: Gradient-Zero, $k=0.03$ -in forward step, $U=24.37$ m/s skin-friction distribution.....	103
Figure 150: Gradient-Zero, $k=0.03$ -in forward step, $U=29.05$ m/s skin-friction distribution.....	104
Figure 151: Gradient-Zero, $k=0.035$ -in forward step, $U=18.7$ m/s skin-friction distribution.....	104
Figure 152: Gradient-Zero, $k=0.035$ -in forward step, $U=23.53$ m/s skin-friction distribution.....	105
Figure 153: Gradient-Zero, $k=0.035$ -in forward step, $U=26.53$ m/s skin-friction distribution.....	105
Figure 154: Gradient-Zero, $k=0.035$ -in forward step, $U=28.39$ m/s skin-friction distribution.....	106
Figure 155: Gradient-Zero, $k=0.04$ -in forward step, $U=13.69$ m/s skin-friction distribution.....	106
Figure 156: Gradient-Zero, $k=0.04$ -in forward step, $U=17.81$ m/s skin-friction distribution.....	107
Figure 157: Gradient-Zero, $k=0.04$ -in forward step, $U=20.88$ m/s skin-friction distribution.....	107
Figure 158: Gradient-Zero, $k=0.04$ -in forward step, $U=22.79$ m/s skin-friction distribution.....	108
Figure 159: Gradient-Zero, $k=0.04$ -in forward step, $U=27.61$ m/s skin-friction distribution.....	108
Figure 160: Gradient-Zero, $k=0.045$ -in forward step, $U=19.4$ m/s skin-friction distribution.....	109
Figure 161: Gradient-Zero, $k=0.045$ -in forward step, $U=21.56$ m/s skin-friction distribution.....	109
Figure 162: Gradient-Zero, $k=0.045$ -in forward step, $U=24.14$ m/s skin-friction distribution.....	110
Figure 163: Gradient-Zero, $k=0.045$ -in forward step, $U=26.7$ m/s skin-friction distribution.....	110
Figure 164: Gradient-Zero, $k=0.045$ -in forward step, $U=29.19$ m/s skin-friction distribution.....	111
Figure 165: Gradient-Zero, $k=0.05$ -in forward step, $U=13.29$ m/s skin-friction distribution.....	111
Figure 166: Gradient-Zero, $k=0.05$ -in forward step, $U=17.89$ m/s skin-friction distribution.....	112
Figure 167: Gradient-Zero, $k=0.05$ -in forward step, $U=20.16$ m/s skin-friction distribution.....	112
Figure 168: Gradient-Zero, $k=0.05$ -in forward step, $U=22.75$ m/s skin-friction distribution.....	113
Figure 169: Gradient-Zero, $k=0.055$ -in forward step, $U=13.76$ m/s skin-friction distribution.....	113
Figure 170: Gradient-Zero, $k=0.055$ -in forward step, $U=16.55$ m/s skin-friction distribution.....	114
Figure 171: Gradient-Zero, $k=0.055$ -in forward step, $U=18.8$ m/s skin-friction distribution.....	114
Figure 172: Gradient-Zero, $k=0.055$ -in forward step, $U=21.67$ m/s skin-friction distribution.....	115
Figure 173: Gradient-Zero, $k=0.06$ -in forward step, $U=14.2$ m/s skin-friction distribution.....	115
Figure 174: Gradient-Zero, $k=0.06$ -in forward step, $U=16.75$ m/s skin-friction distribution.....	116

Figure 175: Gradient-Zero, $k=0.06$ -in forward step, $U=19.29$ m/s skin-friction distribution.....	116
Figure 176: Gradient-Zero, $k=0.02$ -in aft step, $U=19.41$ m/s skin-friction distribution.	117
Figure 177: Gradient-Zero, $k=0.02$ -in aft step, $U=23.37$ m/s skin-friction distribution.	117
Figure 178: Gradient-Zero, $k=0.02$ -in aft step, $U=26.39$ m/s skin-friction distribution.	118
Figure 179: Gradient-Zero, $k=0.02$ -in aft step, $U=28.51$ m/s skin-friction distribution.	118
Figure 180: Gradient-Zero, $k=0.025$ -in aft step, $U=19.55$ m/s skin-friction distribution.	119
Figure 181: Gradient-Zero, $k=0.025$ -in aft step, $U=21.88$ m/s skin-friction distribution.	119
Figure 182: Gradient-Zero, $k=0.025$ -in aft step, $U=24.27$ m/s skin-friction distribution.	120
Figure 183: Gradient-Zero, $k=0.025$ -in aft step, $U=26.75$ m/s skin-friction distribution.	120
Figure 184: Gradient-Zero, $k=0.025$ -in aft step, $U=28.89$ m/s skin-friction distribution.	121
Figure 185: Gradient-Zero, $k=0.03$ -in aft step, $U=15.23$ m/s skin-friction distribution.	121
Figure 186: Gradient-Zero, $k=0.03$ -in aft step, $U=20.37$ m/s skin-friction distribution.	122
Figure 187: Gradient-Zero, $k=0.03$ -in aft step, $U=22.31$ m/s skin-friction distribution.	122
Figure 188: Gradient-Zero, $k=0.03$ -in aft step, $U=25.24$ m/s skin-friction distribution.	123
Figure 189: Gradient-Zero, $k=0.03$ -in aft step, $U=29.54$ m/s skin-friction distribution.	123
Figure 190: Gradient-Zero, $k=0.035$ -in aft step, $U=15.5$ m/s skin-friction distribution.	124
Figure 191: Gradient-Zero, $k=0.035$ -in aft step, $U=17.68$ m/s skin-friction distribution.	124
Figure 192: Gradient-Zero, $k=0.035$ -in aft step, $U=20.44$ m/s skin-friction distribution.	125
Figure 193: Gradient-Zero, $k=0.035$ -in aft step, $U=22.46$ m/s skin-friction distribution.	125
Figure 194: Gradient-Zero, $k=0.035$ -in aft step, $U=25.2$ m/s skin-friction distribution.	126
Figure 195: Gradient-Zero, $k=0.04$ -in aft step, $U=14.67$ m/s skin-friction distribution.	126
Figure 196: Gradient-Zero, $k=0.04$ -in aft step, $U=16.99$ m/s skin-friction distribution.	127
Figure 197: Gradient-Zero, $k=0.04$ -in aft step, $U=19.07$ m/s skin-friction distribution.	127
Figure 198: Gradient-Zero, $k=0.04$ -in aft step, $U=20.99$ m/s skin-friction distribution.	128
Figure 199: Gradient-Zero, $k=0.04$ -in aft step, $U=23.46$ m/s skin-friction distribution.	128
Figure 200: Gradient-A, $k=0$ -in, $U=14.19$ m/s skin-friction distribution.	129
Figure 201: Gradient-A, $k=0$ -in, $U=18.33$ m/s skin-friction distribution.	129
Figure 202: Gradient-A, $k=0$ -in, $U=23.25$ m/s skin-friction distribution.	130
Figure 203: Gradient-A, $k=0$ -in, $U=28.04$ m/s skin-friction distribution.	130
Figure 204: Gradient-A, $k=0.055$ -in forward step, $U=18.69$ m/s skin-friction distribution.	131
Figure 205: Gradient-A, $k=0.055$ -in forward step, $U=23.58$ m/s skin-friction distribution.	131
Figure 206: Gradient-A, $k=0.055$ -in forward step, $U=28.33$ m/s skin-friction distribution.	132
Figure 207: Gradient-A, $k=0.065$ -in forward step, $U=12.4$ m/s skin-friction distribution.	132
Figure 208: Gradient-A, $k=0.065$ -in forward step, $U=16.87$ m/s skin-friction distribution.	133
Figure 209: Gradient-A, $k=0.065$ -in forward step, $U=20.97$ m/s skin-friction distribution.	133
Figure 210: Gradient-A, $k=0.065$ -in forward step, $U=22.09$ m/s skin-friction distribution.	134
Figure 211: Gradient-A, $k=0.065$ -in forward step, $U=25.65$ m/s skin-friction distribution.	134
Figure 212: Gradient-A, $k=0.068$ -in forward step, $U=12.58$ m/s skin-friction distribution.	135
Figure 213: Gradient-A, $k=0.068$ -in forward step, $U=16.43$ m/s skin-friction distribution.	135
Figure 214: Gradient-A, $k=0.068$ -in forward step, $U=22.2$ m/s skin-friction distribution.	136
Figure 215: Gradient-A, $k=0.068$ -in forward step, $U=26.17$ m/s skin-friction distribution.	136
Figure 216: Gradient-A, $k=0.07$ -in forward step, $U=16.09$ m/s skin-friction distribution.	137
Figure 217: Gradient-A, $k=0.07$ -in forward step, $U=16.38$ m/s skin-friction distribution.	137
Figure 218: Gradient-A, $k=0.07$ -in forward step, $U=21.02$ m/s skin-friction distribution.	138
Figure 219: Gradient-A, $k=0.07$ -in forward step, $U=25.48$ m/s skin-friction distribution.	138
Figure 220: Gradient-A, $k=0.073$ -in forward step, $U=13.12$ m/s skin-friction distribution.	139
Figure 221: Gradient-A, $k=0.073$ -in forward step, $U=13.15$ m/s skin-friction distribution.	139
Figure 222: Gradient-A, $k=0.073$ -in forward step, $U=22.86$ m/s skin-friction distribution.	140
Figure 223: Gradient-A, $k=0.073$ -in forward step, $U=28.43$ m/s skin-friction distribution.	140
Figure 224: Gradient-A, $k=0.08$ -in forward step, $U=13.32$ m/s skin-friction distribution.	141
Figure 225: Gradient-A, $k=0.08$ -in forward step, $U=17.8$ m/s skin-friction distribution.	141
Figure 226: Gradient-A, $k=0.08$ -in forward step, $U=22.61$ m/s skin-friction distribution.	142
Figure 227: Gradient-A, $k=0.085$ -in forward step, $U=11.84$ m/s skin-friction distribution.	142
Figure 228: Gradient-A, $k=0.085$ -in forward step, $U=16.73$ m/s skin-friction distribution.	143
Figure 229: Gradient-A, $k=0.09$ -in forward step, $U=12.09$ m/s skin-friction distribution.	143
Figure 230: Gradient-A, $k=0.09$ -in forward step, $U=16.99$ m/s skin-friction distribution.	144

Figure 231: Gradient-A, $k=0.025$ -in aft step, $U=28.06$ m/s skin-friction distribution.....	144
Figure 232: Gradient-A, $k=0.03$ -in aft step, $U=22.33$ m/s skin-friction distribution.....	145
Figure 233: Gradient-A, $k=0.03$ -in aft step, $U=27.06$ m/s skin-friction distribution.....	145
Figure 234: Gradient-A, $k=0.035$ -in aft step, $U=17.53$ m/s skin-friction distribution.....	146
Figure 235: Gradient-A, $k=0.035$ -in aft step, $U=22.01$ m/s skin-friction distribution.....	146
Figure 236: Gradient-A, $k=0.035$ -in aft step, $U=27.59$ m/s skin-friction distribution.....	147
Figure 237: Gradient-A, $k=0.04$ -in aft step, $U=13.03$ m/s skin-friction distribution.....	147
Figure 238: Gradient-A, $k=0.04$ -in aft step, $U=13.55$ m/s skin-friction distribution.....	148
Figure 239: Gradient-A, $k=0.04$ -in aft step, $U=17.33$ m/s skin-friction distribution.....	148
Figure 240: Gradient-A, $k=0.04$ -in aft step, $U=20.19$ m/s skin-friction distribution.....	149
Figure 241: Gradient-A, $k=0.04$ -in aft step, $U=21.37$ m/s skin-friction distribution.....	149
Figure 242: Gradient-A, $k=0.04$ -in aft step, $U=22.85$ m/s skin-friction distribution.....	150
Figure 243: Gradient-A, $k=0.04$ -in aft step, $U=28.1$ m/s skin-friction distribution.....	150
Figure 244: Gradient-A, $k=0.045$ -in aft step, $U=12.14$ m/s skin-friction distribution.....	151
Figure 245: Gradient-A, $k=0.045$ -in aft step, $U=17.02$ m/s skin-friction distribution.....	151
Figure 246: Gradient-A, $k=0.045$ -in aft step, $U=21.51$ m/s skin-friction distribution.....	152
Figure 247: Gradient-A, $k=0.05$ -in aft step, $U=12.78$ m/s skin-friction distribution.....	152
Figure 248: Gradient-A, $k=0.05$ -in aft step, $U=17.05$ m/s skin-friction distribution.....	153
Figure 249: Gradient-A, $k=0.055$ -in aft step, $U=12.73$ m/s skin-friction distribution.....	153
Figure 250: Gradient-A, $k=0.055$ -in aft step, $U=17.7$ m/s skin-friction distribution.....	154
Figure 251: Gradient-B, $k=0$ -in, $U=12.44$ m/s skin-friction distribution.	154
Figure 252: Gradient-B, $k=0$ -in, $U=13.11$ m/s skin-friction distribution.	155
Figure 253: Gradient-B, $k=0$ -in, $U=17.13$ m/s skin-friction distribution.	155
Figure 254: Gradient-B, $k=0$ -in, $U=17.52$ m/s skin-friction distribution.	156
Figure 255: Gradient-B, $k=0$ -in, $U=17.81$ m/s skin-friction distribution.	156
Figure 256: Gradient-B, $k=0$ -in, $U=19.92$ m/s skin-friction distribution.	157
Figure 257: Gradient-B, $k=0$ -in, $U=21.52$ m/s skin-friction distribution.	157
Figure 258: Gradient-B, $k=0$ -in, $U=21.98$ m/s skin-friction distribution.	158
Figure 259: Gradient-B, $k=0$ -in, $U=22.71$ m/s skin-friction distribution.	158
Figure 260: Gradient-B, $k=0$ -in, $U=23.98$ m/s skin-friction distribution.	159
Figure 261: Gradient-B, $k=0$ -in, $U=25.47$ m/s skin-friction distribution.	159
Figure 262: Gradient-B, $k=0$ -in, $U=26.13$ m/s skin-friction distribution.	160
Figure 263: Gradient-B, $k=0$ -in, $U=27.74$ m/s skin-friction distribution.	160
Figure 264: Gradient-B, $k=0.035$ -in forward step, $U=21.82$ m/s skin-friction distribution.....	161
Figure 265: Gradient-B, $k=0.035$ -in forward step, $U=26.75$ m/s skin-friction distribution.....	161
Figure 266: Gradient-B, $k=0.04$ -in forward step, $U=24.98$ m/s skin-friction distribution.....	162
Figure 267: Gradient-B, $k=0.04$ -in forward step, $U=27.49$ m/s skin-friction distribution.....	162
Figure 268: Gradient-B, $k=0.045$ -in forward step, $U=17.14$ m/s skin-friction distribution.....	163
Figure 269: Gradient-B, $k=0.045$ -in forward step, $U=22.7$ m/s skin-friction distribution.....	163
Figure 270: Gradient-B, $k=0.045$ -in forward step, $U=24.35$ m/s skin-friction distribution.....	164
Figure 271: Gradient-B, $k=0.045$ -in forward step, $U=25.81$ m/s skin-friction distribution.....	164
Figure 272: Gradient-B, $k=0.05$ -in forward step, $U=18.14$ m/s skin-friction distribution.....	165
Figure 273: Gradient-B, $k=0.05$ -in forward step, $U=23.42$ m/s skin-friction distribution.....	165
Figure 274: Gradient-B, $k=0.05$ -in forward step, $U=25.23$ m/s skin-friction distribution.....	166
Figure 275: Gradient-B, $k=0.05$ -in forward step, $U=27.49$ m/s skin-friction distribution.....	166
Figure 276: Gradient-B, $k=0.055$ -in forward step, $U=14.18$ m/s skin-friction distribution.....	167
Figure 277: Gradient-B, $k=0.055$ -in forward step, $U=14.65$ m/s skin-friction distribution.....	167
Figure 278: Gradient-B, $k=0.055$ -in forward step, $U=18.61$ m/s skin-friction distribution.....	168
Figure 279: Gradient-B, $k=0.055$ -in forward step, $U=18.86$ m/s skin-friction distribution.....	168
Figure 280: Gradient-B, $k=0.055$ -in forward step, $U=19.19$ m/s skin-friction distribution.....	169
Figure 281: Gradient-B, $k=0.055$ -in forward step, $U=21.06$ m/s skin-friction distribution.....	169
Figure 282: Gradient-B, $k=0.055$ -in forward step, $U=23.53$ m/s skin-friction distribution.....	170
Figure 283: Gradient-B, $k=0.055$ -in forward step, $U=23.62$ m/s skin-friction distribution.....	170
Figure 284: Gradient-B, $k=0.06$ -in forward step, $U=14.08$ m/s skin-friction distribution.....	171
Figure 285: Gradient-B, $k=0.06$ -in forward step, $U=18.28$ m/s skin-friction distribution.....	171
Figure 286: Gradient-B, $k=0.06$ -in forward step, $U=19.34$ m/s skin-friction distribution.....	172

Figure 287: Gradient-B, $k=0.06$ -in forward step, $U=23.36$ m/s skin-friction distribution.....	172
Figure 288: Gradient-B, $k=0.065$ -in forward step, $U=13.52$ m/s skin-friction distribution.....	173
Figure 289: Gradient-B, $k=0.065$ -in forward step, $U=18.45$ m/s skin-friction distribution.....	173
Figure 290: Gradient-B, $k=0.065$ -in forward step, $U=22.59$ m/s skin-friction distribution.....	174
Figure 291: Gradient-B, $k=0.07$ -in forward step, $U=14.29$ m/s skin-friction distribution.....	174
Figure 292: Gradient-B, $k=0.07$ -in forward step, $U=19.45$ m/s skin-friction distribution.....	175
Figure 293: Gradient-B, $k=0.07$ -in forward step, $U=24.4$ m/s skin-friction distribution.....	175
Figure 294: Gradient-B, $k=0.09$ -in forward step, $U=14.18$ m/s skin-friction distribution.....	176
Figure 295: Gradient-B, $k=0.09$ -in forward step, $U=23.61$ m/s skin-friction distribution.....	176
Figure 296: Gradient-B, $k=0.01$ -in aft step, $U=18.4$ m/s skin-friction distribution.....	177
Figure 297: Gradient-B, $k=0.01$ -in aft step, $U=23.33$ m/s skin-friction distribution.....	177
Figure 298: Gradient-B, $k=0.01$ -in aft step, $U=27.65$ m/s skin-friction distribution.....	178
Figure 299: Gradient-B, $k=0.015$ -in aft step, $U=12.74$ m/s skin-friction distribution.....	178
Figure 300: Gradient-B, $k=0.015$ -in aft step, $U=14.44$ m/s skin-friction distribution.....	179
Figure 301: Gradient-B, $k=0.015$ -in aft step, $U=16.4$ m/s skin-friction distribution.....	179
Figure 302: Gradient-B, $k=0.015$ -in aft step, $U=19.09$ m/s skin-friction distribution.....	180
Figure 303: Gradient-B, $k=0.015$ -in aft step, $U=22.12$ m/s skin-friction distribution.....	180
Figure 304: Gradient-B, $k=0.015$ -in aft step, $U=26.65$ m/s skin-friction distribution.....	181
Figure 305: Gradient-B, $k=0.02$ -in aft step, $U=9.51$ m/s skin-friction distribution.....	181
Figure 306: Gradient-B, $k=0.02$ -in aft step, $U=12.2$ m/s skin-friction distribution.....	182
Figure 307: Gradient-B, $k=0.02$ -in aft step, $U=13.56$ m/s skin-friction distribution.....	182
Figure 308: Gradient-B, $k=0.02$ -in aft step, $U=18.61$ m/s skin-friction distribution.....	183
Figure 309: Gradient-B, $k=0.02$ -in aft step, $U=23.55$ m/s skin-friction distribution.....	183
Figure 310: Gradient-B, $k=0.02$ -in aft step, $U=28.58$ m/s skin-friction distribution.....	184
Figure 311: Gradient-B, $k=0.03$ -in aft step, $U=8.07$ m/s skin-friction distribution.....	184
Figure 312: Gradient-B, $k=0.03$ -in aft step, $U=12.77$ m/s skin-friction distribution.....	185
Figure 313: Gradient-B, $k=0.035$ -in aft step, $U=12.03$ m/s skin-friction distribution.....	185
Figure 314: Gradient-B, $k=0.035$ -in aft step, $U=12.74$ m/s skin-friction distribution.....	186
Figure 315: Gradient-B, $k=0.035$ -in aft step, $U=17.3$ m/s skin-friction distribution.....	186
Figure 316: Gradient-B, $k=0.035$ -in aft step, $U=17.54$ m/s skin-friction distribution.....	187
Figure 317: Gradient-B, $k=0.04$ -in aft step, $U=12.74$ m/s skin-friction distribution.....	187
Figure 318: Gradient-B, $k=0.04$ -in aft step, $U=13.54$ m/s skin-friction distribution.....	188
Figure 319: Gradient-B, $k=0.04$ -in aft step, $U=17.02$ m/s skin-friction distribution.....	188
Figure 320: Gradient-B, $k=0.04$ -in aft step, $U=18.67$ m/s skin-friction distribution.....	189
Figure 321: Gradient-B, $k=0.04$ -in aft step, $U=21.71$ m/s skin-friction distribution.....	189
Figure 322: Gradient-B, $k=0.04$ -in aft step, $U=22.88$ m/s skin-friction distribution.....	190
Figure 323: Gradient-B, $k=0.04$ -in aft step, $U=27.61$ m/s skin-friction distribution.....	190
Figure 324: AA Lab Systems Hot-wire anemometer AN-1005.....	192
Figure 325: Dantec boundary layer hot-wire probe (top) and probe support (bottom), dimensions in mm.	193
Figure 326: Calibrator, air filter and pressure regulator (left), Pitot tube and hot-wire probe support in the calibrator holder (right)	196
Figure 327: Pressure transducer and its power supply.....	196
Figure 328: Calibration of the MKS 223BD pressure transducer.....	197
Figure 329: Microscope and micro manipulation stages.	198
Figure 330: Accelerometer (right) and its power supply/amplifier (left).....	199
Figure 331: One accelerometer is glued to testing side of the model to measure k -component of vibrations; second accelerometer is glued to L-bracket to measure s -component.	200
Figure 332: Thermocouple (left) and its controller (right)	201
Figure 333: Calibration of thermocouple (TC).....	201
Figure 334: Laptop (left) and Data Acquisition card (right).....	202
Figure 335: LogBook: front view (left) and rear view (right).	203
Figure 336: Uninterrupted Power Supply (UPS).	203
Figure 337: Interpretation of β parameter for a similar wedge flow.	205
Figure 338: Stability diagram for Blasius non-parallel and parallel flows.	206
Figure 339: Stability diagram for different pressure gradients.	207
Figure 340: Velocity power spectrum for zero flow in calm environment (lab test).....	213

Figure 341: Comparison of fluctuating velocity time series for all wires, Run 118. Note that the traces for HWs 2-4 are offset by -0.5 from the previous wires for clarity.	214
Figure 342: Measured power spectra.	215
Figure 343: Measured velocity time history.	215
Figure 344: Measured power spectra.	216
Figure 345: Measured velocity time history.	216
Figure 346: Measured power spectra.	217
Figure 347: Measure velocity time history.	217
Figure 348: Measured power spectra.	218
Figure 349: Measured velocity time history.	218
Figure 350: Measured power spectra.	219
Figure 351: Measured velocity time history.	219
Figure 352: Measured power spectra.	220
Figure 353: Measured velocity time history.	220
Figure 354: Measured power spectra.	221
Figure 355: Measured velocity time history.	221
Figure 356: Measured power spectra.	222
Figure 357: Measured velocity time history.	222
Figure 358: Measured power spectra.	223
Figure 359: Measured velocity time history.	223
Figure 360: Measured power spectra.	224
Figure 361: Measured velocity time history.	224
Figure 362: Measured power spectra.	225
Figure 363: Measured velocity time history.	225
Figure 364: Measured power spectra.	226
Figure 365: Measured velocity time history.	226
Figure 366: Measured power spectra.	227
Figure 367: Measured velocity time history.	227
Figure 368: Measured power spectra.	228
Figure 369: Measured velocity time history.	228
Figure 370: Measured power spectra.	229
Figure 371: Measured velocity time history.	229
Figure 372: Measured power spectra.	230
Figure 373: Measured velocity time history.	230
Figure 374: Measured power spectra.	231
Figure 375: Measured velocity time history.	231
Figure 376: Measured power spectra.	232
Figure 377: Measured velocity time history.	232
Figure 378: Measured power spectra.	233
Figure 379: Measured velocity time history.	233
Figure 380: Measured power spectra.	234
Figure 381: Measured velocity time history.	234
Figure 382: Measured power spectra.	235
Figure 383: Measured velocity time history.	235
Figure 384: Measured power spectra.	236
Figure 385: Measured velocity time history.	236
Figure 386: Measured power spectra.	237
Figure 387: Measured velocity time history.	237
Figure 388: Measured power spectra.	238
Figure 389: Measured velocity time history.	238
Figure 390: Measured power spectra.	239
Figure 391: Measured velocity time history.	239
Figure 392: Measured power spectra.	240
Figure 393: Measured velocity time history.	240
Figure 394: Measured power spectra.	241
Figure 395: Measured velocity time history.	241

Figure 396: Measured power spectra.....	242
Figure 397: Measured velocity time history.....	242
Figure 398: Measured power spectra.....	243
Figure 399: Measured velocity time history.....	243
Figure 400: Measured power spectra.....	244
Figure 401: Measured velocity time history.....	244
Figure 402: Measured power spectra.....	250
Figure 403: Measured velocity time history.....	250
Figure 404: Measured power spectra.....	251
Figure 405: Measured velocity time history.....	251
Figure 406: Measured power spectra.....	252
Figure 407: Measured velocity time history.....	252
Figure 408: Measured power spectra.....	253
Figure 409: Measured velocity time history.....	253
Figure 410: Measured power spectra.....	254
Figure 411: Measured velocity time history.....	254
Figure 412: Measured power spectra.....	255
Figure 413: Measured velocity time history.....	255
Figure 414: Measured power spectra.....	256
Figure 415: Measured velocity time history.....	256
Figure 416: Measured power spectra.....	257
Figure 417: Measured velocity time history.....	257
Figure 418: Measured power spectra.....	258
Figure 419: Measured velocity time history.....	258
Figure 420: Measured power spectra.....	259
Figure 421: Measured velocity time history.....	259
Figure 422: Measured power spectra.....	260
Figure 423: Measured velocity time history.....	260
Figure 424: Measured power spectra.....	261
Figure 425: Measured velocity time history.....	261
Figure 426: Measured power spectra.....	262
Figure 427: Measured velocity time history.....	262
Figure 428: Measured power spectra.....	263
Figure 429: Measured velocity time history.....	263
Figure 430: Measured power spectra.....	264
Figure 431: Measured velocity time history.....	264
Figure 432: Measured power spectra.....	265
Figure 433: Measured velocity time history.....	265
Figure 434: Measured power spectra.....	266
Figure 435: Measured velocity time history.....	266
Figure 436: Measured power spectra.....	267
Figure 437: Measured velocity time history.....	267
Figure 438: Measured power spectra.....	268
Figure 439: Measured velocity time history.....	268
Figure 440: Measured power spectra.....	269
Figure 441: Measured velocity time history.....	269
Figure 442: Measured power spectra.....	270
Figure 443: Measured velocity time history.....	270
Figure 444: Measured power spectra.....	271
Figure 445: Measured velocity time history.....	271
Figure 446: Measured power spectra.....	272
Figure 447: Measured velocity time history.....	272
Figure 448: Measured power spectra.....	279
Figure 449: Measured velocity time history.....	279
Figure 450: Measured power spectra.....	280
Figure 451: Measured velocity time history.....	280

Figure 452: Measured power spectra.....	281
Figure 453: Measured velocity time history.....	281
Figure 454: Measured power spectra.....	282
Figure 455: Measured velocity time history.....	282
Figure 456: Measured power spectra.....	283
Figure 457: Measured velocity time history.....	283
Figure 458: Measured power spectra.....	284
Figure 459: Measured velocity time history.....	284
Figure 460: Measured power spectra.....	285
Figure 461: Measured velocity time history.....	285
Figure 462: Measured power spectra.....	286
Figure 463: Measured velocity time history.....	286
Figure 464: Measured power spectra.....	287
Figure 465: Measured velocity time history.....	287
Figure 466: Measured power spectra.....	288
Figure 467: Measured velocity time history.....	288
Figure 468: Measured power spectra.....	289
Figure 469: Measured velocity time history.....	289
Figure 470: Measured power spectra.....	290
Figure 471: Measured velocity time history.....	290
Figure 472: Measured power spectra.....	291
Figure 473: Measured velocity time history.....	291
Figure 474: Measured power spectra.....	292
Figure 475: Measured velocity time history.....	292
Figure 476: Measured power spectra.....	293
Figure 477: Measured velocity time history.....	293
Figure 478: Measured power spectra.....	294
Figure 479: Measured velocity time history.....	294
Figure 480: Measured power spectra.....	295
Figure 481: Measured velocity time history.....	295
Figure 482: Measured power spectra.....	296
Figure 483: Measured velocity time history.....	296
Figure 484: Measured power spectra.....	297
Figure 485: Measured velocity time history.....	297
Figure 486: Measured power spectra.....	298
Figure 487: Measured velocity time history.....	298
Figure 488: Measured power spectra.....	299
Figure 489: Measured velocity time history.....	299
Figure 490: Measured power spectra.....	300
Figure 491: Measured velocity time history.....	300
Figure 492: Measured power spectra.....	301
Figure 493: Measured velocity time history.....	301
Figure 494: Measured power spectra.....	302
Figure 495: Measured velocity time history.....	302
Figure 496: Measured power spectra.....	303
Figure 497: Measured velocity time history.....	303
Figure 498: Measured power spectra.....	304
Figure 499: Measured velocity time history.....	7304
Figure 500: Measured power spectra.....	305
Figure 501: Measured velocity time history.....	305
Figure 502: Measured power spectra.....	306
Figure 503: Measured velocity time history.....	306
Figure 504: Measured power spectra.....	307
Figure 505: Measured velocity time history.....	307
Figure 506: Measured power spectra.....	308
Figure 507: Measured velocity time history.....	308

Figure 508: Measured power spectra.....	309
Figure 509: Measured velocity time history.....	309
Figure 510: Measured power spectra.....	310
Figure 511: Measured velocity time history.....	310
Figure 512: Measured power spectra.....	311
Figure 513: Measured velocity time history.....	311
Figure 514: Measured power spectra.....	312
Figure 515: Measured velocity time history.....	312
Figure 516: Measured power spectra.....	313
Figure 517: Measured velocity time history.....	313
Figure 518: Measured power spectra.....	314
Figure 519: Measured velocity time history.....	314
Figure 520: Measured power spectra.....	316
Figure 521: Measured velocity time history.....	316
Figure 522: Measured power spectra.....	317
Figure 523: Measured velocity time history.....	317
Figure 524: Measured power spectra.....	318
Figure 525: Measured velocity time history.....	318
Figure 526: Measured power spectra.....	319
Figure 527: Measured velocity time history.....	319
Figure 528: Measured power spectra.....	320
Figure 529: Measured power spectra.....	321
Figure 530: Measured power spectra.....	321
Figure 531: Measured power spectra.....	322
Figure 532: Measured power spectra.....	323
Figure 533: Measured power spectra.....	324
Figure 534: Measured power spectra.....	324
Figure 535: Measured power spectra.....	325
Figure 536: Measured power spectra.....	326
Figure 537: Measured power spectra.....	326
Figure 538: Measured power spectra.....	327
Figure 539: Measured power spectra.....	328
Figure 540: Measured power spectra.....	328
Figure 541: Measured power spectra.....	329
Figure 542: Measured power spectra.....	330
Figure 543: Measured power spectra.....	330
Figure 544: Measured power spectra.....	331
Figure 545: Measured power spectra.....	331
Figure 546: Measured power spectra.....	332
Figure 547: Measured power spectra.....	332
Figure 548: Measured power spectra.....	333
Figure 549: Measured power spectra.....	334
Figure 550: Measured power spectra.....	334
Figure 551: Measured power spectra.....	335
Figure 552: Measured power spectra.....	335
Figure 553: Measured power spectra.....	336
Figure 554: Measured power spectra.....	336
Figure 555: Stream-wise RMS velocity.....	337
Figure 556: Stream-wise RMS velocity.....	338
Figure 557: Stream-wise RMS velocity.....	338
Figure 558: Stream-wise RMS velocity.....	339
Figure 559: Stream-wise RMS velocity.....	339
Figure 560: Stream-wise RMS velocity.....	340
Figure 561: Stream-wise RMS velocity.....	340
Figure 562: Stream-wise RMS velocity.....	341
Figure 563: Stream-wise RMS velocity.....	342

Figure 564: Stream-wise RMS velocity.....	342
Figure 565: Stream-wise RMS velocity.....	343
Figure 566: Stream-wise RMS velocity.....	344
Figure 567: Stream-wise RMS velocity.....	345
Figure 568: Stream-wise RMS velocity.....	345
Figure 569: Stream-wise RMS velocity.....	346
Figure 570: Stream-wise RMS velocity.....	346
Figure 571: Stream-wise RMS velocity.....	347
Figure 572: Stream-wise RMS velocity.....	347
Figure 573: Stream-wise RMS velocity.....	348
Figure 574: Mean velocity profile (left) and RMS velocity (right), as a function of distance from the surface.....	349
Figure 575: Mean velocity profile (left) and RMS velocity (right), as a function of distance from the surface.....	350
Figure 576: Mean velocity profile (left) and RMS velocity (right), as a function of distance from the surface.....	350
Figure 577: Mean velocity profile (left) and RMS velocity (right), as a function of distance from the surface.....	351
Figure 578: Mean velocity profile (left) and RMS velocity (right), as a function of distance from the surface.....	352
Figure 579: Mean velocity profile (left) and RMS velocity (right), as a function of distance from the surface.....	352
Figure 580: Mean velocity profile (left) and RMS velocity (right), as a function of distance from the surface.....	353
Figure 581: Mean velocity profile (left) and RMS velocity (right), as a function of distance from the surface.....	353
Figure 582: Power spectra.	355
Figure 583: Velocity time series.	355
Figure 584: Power spectra.	356
Figure 585: Velocity time series.	356
Figure 586: Turbulence intensity.	357
Figure 587: Turbulence intensity.	357
Figure 588: Power spectra.	358
Figure 589: Velocity time series.	358
Figure 590: Power spectra.	359
Figure 591: Velocity time series.	359
Figure 592: Turbulence intensity.	360
Figure 593: Turbulence intensity.	360
Figure 594: Power spectra.	361
Figure 595: Velocity time series.	361
Figure 596: Power spectra.	362
Figure 597: Velocity time series.	362
Figure 598: Turbulence intensity.	363
Figure 599: Turbulence intensity.	363
Figure 600: Power spectra.	365
Figure 601: Velocity time series.	365
Figure 602: Power spectra.	366
Figure 603: Velocity time series.	366
Figure 604: Turbulence intensity.	367
Figure 605: Turbulence intensity.	367
Figure 606: Power spectra.	368
Figure 607: Velocity time series.	368
Figure 608: Power spectra.	369
Figure 609: Velocity time series.	369
Figure 610: Turbulence intensity.	370
Figure 611: Turbulence intensity.	370
Figure 612: Power spectra.	371
Figure 613: Velocity time series.	371
Figure 614: Power spectra.	372
Figure 615: Velocity time series.	372
Figure 616: Turbulence intensity.	373
Figure 617: Turbulence intensity.	373
Figure 618: Power spectra.	374
Figure 619: Velocity time series.	374

Figure 620: Power spectra	375
Figure 621: Velocity time series	375
Figure 622: Turbulence intensity	376
Figure 623: Turbulence intensity	376
Figure 624: Power spectra	377
Figure 625: Velocity time series	377
Figure 626: Power spectra	378
Figure 627: Velocity time series	378
Figure 628: Turbulence intensity	379
Figure 629: Turbulence intensity	379
Figure 630: Power spectra	381
Figure 631: Velocity time series	381
Figure 632: Power spectra	382
Figure 633: Velocity time series	382
Figure 634: Turbulence intensity	383
Figure 635: Turbulence intensity	383
Figure 636: Power spectra in test section.	385
Figure 637: Voltage for full run.....	385
Figure 638: Power spectra in test section.	386
Figure 639: Voltage for full run.....	386
Figure 640: Power spectra in test section.	387
Figure 641: Voltage for full run.....	387
Figure 642: Power spectra in test section.	388
Figure 643: Voltage for full run.....	388
Figure 644: Power spectra in test section.	389
Figure 645: Voltage for full run.....	389
Figure 646: Power spectra in test section.	390
Figure 647: Voltage for full run.....	390
Figure 648: Power spectra in test section.	391
Figure 649: Voltage for full run.....	391
Figure 650: Power spectra in test section.	392
Figure 651: Voltage for full run.....	392
Figure 652: Power spectra in test section.	393
Figure 653: Voltage for full run.....	393
Figure 654: Power spectra in test section.	394
Figure 655: Voltage for full run.....	394
Figure 656: Power spectra in test section.	395
Figure 657: Voltage for full run.....	395
Figure 658: Power spectra in test section.	396
Figure 659: Voltage for full run.....	396
Figure 660: Power spectra in test section.	397
Figure 661: Voltage for full run.....	397
Figure 662: Power spectra in test section.	398
Figure 663: Voltage for full run.....	398
Figure 664: Power spectra in test section.	399
Figure 665: Voltage for full run.....	399
Figure 666: Power spectra in test section.	400
Figure 667: Voltage for full run.....	400
Figure 668: Power spectra in test section.	401
Figure 669: Voltage for full run.....	401
Figure 670: Power spectra in test section.	402
Figure 671: Voltage for full run.....	402
Figure 672: Power spectra in test section.	403
Figure 673: Voltage for full run.....	403
Figure 674: Power spectra in test section.	404
Figure 675: Voltage for full run.....	404

Figure 676: Power spectra in test section.	405
Figure 677: Voltage for full run.....	405
Figure 678: Power spectra in test section.	406
Figure 679: Voltage for full run.....	406
Figure 680: Power spectra in test section.	407
Figure 681: Voltage for full run.....	407
Figure 682: Power spectra in test section.	408
Figure 683: Voltage for full run.....	408
Figure 684: Power spectra in test section.	409
Figure 685: Voltage for full run.....	409
Figure 686: Power spectra in test section.	410
Figure 687: Voltage for full run.....	410
Figure 688: Power spectra in test section.	411
Figure 689: Voltage for full run.....	411
Figure 690: Power spectra in test section.	412
Figure 691: Voltage for full run.....	412
Figure 692: Power spectra in test section.	414
Figure 693: Voltage for full run.....	414
Figure 694: Power spectra in test section.	415
Figure 695: Voltage for full run.....	415
Figure 696: Power spectra in test section.	416
Figure 697: Voltage for full run.....	416
Figure 698: Power spectra in test section.	417
Figure 699: Voltage for full run.....	417
Figure 700: Power spectra in test section.	418
Figure 701: Voltage for full run.....	418
Figure 702: Power spectra in test section.	419
Figure 703: Voltage for full run.....	419
Figure 704: Power spectra in test section.	420
Figure 705: Voltage for full run.....	420
Figure 706: Power spectra in test section.	421
Figure 707: Voltage for full run.....	421
Figure 708: Power spectra in test section.	422
Figure 709: Voltage for full run.....	422
Figure 710: Power spectra in test section.	423
Figure 711: Voltage for full run.....	423
Figure 712: Power spectra in test section.	424
Figure 713: Voltage for full run.....	424
Figure 714: Power spectra in test section.	425
Figure 715: Voltage for full run.....	425
Figure 716: Power spectra in test section.	426
Figure 717: Voltage for full run.....	426
Figure 718: Power spectra in test section.	428
Figure 719: Voltage for full run.....	428
Figure 720: Power spectra in test section.	429
Figure 721: Voltage for full run.....	429
Figure 722: Power spectra in test section.	430
Figure 723: Voltage for full run.....	430
Figure 724: Power spectra in test section.	431
Figure 725: Voltage for full run.....	431
Figure 726: Power spectra in test section.	432
Figure 727: Voltage for full run.....	432
Figure 728: Power spectra in test section.	433
Figure 729: Voltage for full run.....	433
Figure 730: Power spectra in test section.	434
Figure 731: Voltage for full run.....	434

Figure 732: Power spectra in test section.	435
Figure 733: Voltage for full run.....	435
Figure 734: Power spectra in test section.	436
Figure 735: Voltage for full run.....	436
Figure 736: Power spectra in test section.	437
Figure 737: Voltage for full run.....	437
Figure 738: Power spectra in test section.	438
Figure 739: Voltage for full run.....	438
Figure 740: Power spectra in test section.	439
Figure 741: Voltage for full run.....	439
Figure 742: Power spectra in test section.	440
Figure 743: Voltage for full run.....	440
Figure 744: Power spectra in test section.	441
Figure 745: Voltage for full run.....	441
Figure 746: Power spectra in test section.	442
Figure 747: Voltage for full run.....	442
Figure 748: Power spectra in test section.	443
Figure 749: Voltage for full run.....	443
Figure 750: Power spectra in test section.	444
Figure 751: Voltage for full run.....	444
Figure 752: Power spectra in test section.	445
Figure 753: Voltage for full run.....	445
Figure 754: Power spectra in test section.	446
Figure 755: Voltage for full run.....	446
Figure 756: Power spectra in test section.	447
Figure 757: Voltage for full run.....	447
Figure 758: Power spectra in test section.	448
Figure 759: Voltage for full run.....	448
Figure 760: Power spectra in test section.	449
Figure 761: Voltage for full run.....	449
Figure 762: Power spectra in test section.	450
Figure 763: Voltage for full run.....	450
Figure 764: Power spectra in test section.	451
Figure 765: Voltage for full run.....	451
Figure 766: Local freestream speed.....	453
Figure 767: Displacement thickness.....	453
Figure 768: Coefficient of pressure.....	454
Figure 769: Nondimensional pressure gradient.....	454
Figure 770: Shape factor.....	455
Figure 771: Pressure parameter versus shape factor.....	455
Figure 772: Pressure parameter.....	456
Figure 773: Local freestream speed.....	457
Figure 774: Displacement thickness.....	457
Figure 775: Coefficient of pressure.....	458
Figure 776: Nondimensional pressure gradient.....	458
Figure 777: Shape factor.....	459
Figure 778: Pressure parameter.....	459
Figure 779: Local freestream speed.....	460
Figure 780: Displacement thickness.....	460
Figure 781: Coefficient of pressure.....	461
Figure 782: Nondimensional pressure gradient.....	461
Figure 783: Shape factor.....	462
Figure 784: Pressure parameter.....	462
Figure 785: Shape factor.....	463
Figure 786: Pressure parameter.....	463
Figure 787: T-S wave normalized amplitudes.....	465

Figure 788: T-S wave normalized amplitudes.....	465
Figure 789: T-S wave normalized amplitudes.....	466
Figure 790: T-S wave normalized amplitudes.....	466
Figure 791: T-S wave normalized amplitudes.....	467
Figure 792: T-S wave normalized amplitudes.....	467
Figure 793: T-S wave normalized N-factors.....	468
Figure 794: T-S wave normalized N-factors.....	468
Figure 795: T-S wave normalized N-factors.....	469
Figure 796: T-S wave normalized N-factors.....	469
Figure 797: Stability diagram.....	470
Figure 798: N-factors (comparison with simulation).....	471
Figure 799: N-factors (comparison with simulation).....	472
Figure 800: N-factors (comparison with simulation).....	472
Figure 801: N-factors (comparison with simulation).....	473
Figure 802: T-S wave normalized amplitudes.....	474
Figure 803: T-S wave normalized amplitudes.....	475
Figure 804: T-S wave normalized amplitudes.....	475
Figure 805: T-S wave normalized N-factors.....	476
Figure 806: Stability diagram.....	477
Figure 807: Velocity RMS.....	479
Figure 808: Cf distribution.....	479
Figure 809: Velocity RMS.....	480
Figure 810: Velocity (left) and RMS (right) profiles.....	480
Figure 811: Cf distribution.....	481
Figure 812: Velocity RMS.....	481
Figure 813: Velocity (left) and RMS (right) profiles.....	482
Figure 814: Cf distribution.....	482
Figure 815: Velocity RMS.....	483
Figure 816: Cf distribution.....	484
Figure 817: Velocity RMS.....	484
Figure 818: Velocity (left) and RMS (right) profiles.....	485
Figure 819: Cf distribution.....	485
Figure 820: Velocity RMS.....	486
Figure 821: Velocity (left) and RMS (right) profiles.....	486
Figure 822: Cf distribution.....	487
Figure 823: Transition location for aft-facing steps on Gradient-Zero model.....	489
Figure 824: Transition location for aft-facing steps on Gradient-Zero model.....	490
Figure 825: Transition location for forward-facing steps on Gradient-Zero model.....	491
Figure 826: Transition location for forward-facing steps on Gradient-Zero model.....	492
Figure 827: Transition location for aft-facing steps on Gradient-A model.....	493
Figure 828: Transition location for aft-facing steps on Gradient-A model.....	494
Figure 829: Transition location for forward-facing steps on Gradient-A model.....	495
Figure 830: Transition location for forward-facing steps on Gradient-A model.....	496
Figure 831: Transition location for aft-facing steps on Gradient-B model.....	497
Figure 832: Transition location for aft-facing steps on Gradient-B model.....	498
Figure 833: Transition location for forward-facing steps on Gradient-B model.....	499
Figure 834: Transition location for forward-facing steps on Gradient-B model.....	500
Figure 835: Aft-facing step transition locations.....	501
Figure 836: Aft-facing step transition locations.....	502
Figure 837: Model installation support for SETS models in NGC 7x10-ft wind tunnel.....	528
Figure 838: Common frame installed on support structure in NGC 7x10-ft wind tunnel.....	529
Figure 839: Leading edge (background) and measurement-side skin installed on frame.....	530
Figure 840: Upper and lower splitter plates installed; pressure routing complete.....	531
Figure 841: Non-measurement side skin being installed.....	532
Figure 842: Gradient-Zero installed in NGC 7x10-ft wind tunnel (leading edge view).....	533
Figure 843: Gradient-A installed in NGC 7x10-ft wind tunnel (leading edge view).....	534

Figure 844: Gradient-A installed in NGC 7x10-ft wind tunnel (flow is right-to-left)	535
Figure 845: Hot wire instrumentation installed underneath model during shakedown test.	535
Figure 846: Pressure instrumentation installed underneath lower splitter plate during shakedown test.....	536
Figure 847: Laptop, accelerometers, and NI DAQ installed at aft end of model during shakedown test	536
Figure 848: Gradient-Zero boundary layer velocity profile, U=15 m/s (nominal).	537
Figure 849: Gradient-Zero boundary layer velocity profile, U=20 m/s (nominal).	538
Figure 850: Gradient-Zero boundary layer velocity profile, U=25 m/s (nominal).	538
Figure 851: Gradient-Zero boundary layer velocity profile, U=30 m/s (nominal).	539
Figure 852: Gradient-A boundary layer velocity profile, U=15 m/s (nominal).....	539
Figure 853: Gradient-A boundary layer velocity profile, U=15 m/s (nominal).....	540
Figure 854: Gradient-A boundary layer velocity profile, U=15 m/s (nominal).....	540
Figure 855: Gradient-A boundary layer velocity profile, U=15 m/s (nominal).....	541
Figure 856: Gradient-A boundary layer velocity profile, U=20 m/s (nominal).....	541
Figure 857: Gradient-A boundary layer velocity profile, U=20 m/s (nominal).....	542
Figure 858: Gradient-A boundary layer velocity profile, U=20 m/s (nominal).....	542
Figure 859: Gradient-A boundary layer velocity profile, U=25 m/s (nominal).....	543
Figure 860: Gradient-A boundary layer velocity profile, U=25 m/s (nominal).....	543
Figure 861: Gradient-A boundary layer velocity profile, U=25 m/s (nominal).....	544
Figure 862: Gradient-A boundary layer velocity profile, U=30 m/s (nominal).....	544
Figure 863: Gradient-A boundary layer velocity profile, U=30 m/s (nominal).....	545
Figure 864: Gradient-A boundary layer velocity profile, U=30 m/s (nominal).....	545
Figure 865: Gradient-B boundary layer velocity profile, U=15 m/s (nominal).	546
Figure 866: Gradient-B boundary layer velocity profile, U=20 m/s (nominal).	546
Figure 867: Gradient-B boundary layer velocity profile, U=25 m/s (nominal).	547
Figure 868: Gradient-B boundary layer velocity profile, U=30 m/s (nominal).	547
Figure 869: Typical calibration curve for hot-wire.....	550
Figure 870: Hot-wire probe attached to a surface of the model with L-bracket. Height adjuster is used to adjust distance of hot-wire from surface.....	553
Figure 871: Hot-wire height adjuster.....	553
Figure 872: Distance measurement between a hot-wire probe and model surface.	554
Figure 873: Hot-wire probe typical configuration on the model for stream wise flow measurements.	554
Figure 874: Hot-wire typical configuration on the model for span wise flow uniformity measurements.	555

LIST OF TABLES

Table	Title	Page
Table 1:	Task 1 excrescence locations.....	8
Table 2:	Task 1 excrescence piece sizes	8
Table 3:	Task 1 nondimensional pressure gradient values	9
Table 4:	Turbulence levels in 7- x 10-ft wind tunnel.....	48
Table 5:	Anemometer Specifications.....	192
Table 6:	Nikon Camera Specifications	193
Table 7:	Hot-wire Calibrator and Pressure Transducer Specifications	197
Table 8:	Hot-wire Repair Station.....	198
Table 9:	Accelerometer Specifications	200
Table 10:	Thermocouple Specifications	202
Table 11:	Data Acquisition Specifications	204
Table 12:	Parameters used in Table 13	209
Table 13:	Gradient-Zero hot-wire matrix	210
Table 14:	Gradient-Zero hot-wire transition locations	212
Table 245		
Table 15:	Parameters used in Table 16	245
Table 16:	Gradient-A hot-wire matrix	246
Table 17:	Gradient-A hot-wire transition locations	248
Table 273		
Table 18:	Parameters used in Table 19	273
Table 19:	Gradient-B hot-wire matrix	274
Table 20:	Gradient-B hot-wire transition locations	277

ACKNOWLEDGEMENTS

The authors would like to thank Capt. Wayne Rohe and Mr. Gary Dale for their support of this work.

The authors would like to thank Prof. Mike Gaster for the use of the Rapid-N code.

The authors would like to thank Dr. Bill Saric for his input on the turbulence intensity measurements.

NOMENCLATURE

α	angle of attack
ρ	density
U_e	edge velocity
U_∞, U	freestream velocity
C_p	coefficient of pressure
ν	kinematic viscosity
ν_k	kinematic viscosity at height k
t	thickness
c	chord
s	streamwise distance along surface, measured from leading edge
x	chordwise distance
k	excrescence height
u_k	velocity in boundary layer profile at height k
Re_k	excrescence height Reynolds number
Re_{xk}	excrescence location Reynolds number
Re_{tr}	transition Reynolds number
K	nondimensional pressure gradient
d_o	outer diameter
τ_w	shear stress evaluated at wall
C_f	skin friction coefficient
δ^*_k	displacement thickness at step location
A	power of T-S wave
A	amplitude of T-S wave
DC	direct current
f	frequency (with index for T-S wave, without index – current)
H	shape factor
hw	hot-wire
k/δ^*_k	step height normalized with displacement thickness at step location
N	N-factor of T-S wave
$Re_{\delta^*,k}$	Reynolds number based on displacement thickness
RMS	root-mean-square of stream-wise velocity component
TI	turbulence intensity
T-S	Tollmien-Schlichting wave
u	Fourier coefficient of disturbance velocity
U	upstream freestream speed
U_{car}	car speed
β	pressure parameter for Falkner-Skan flows
δ^*	displacement thickness
δ^*_k	displacement thickness at step location
Δf	half width of T-S wave frequency peak at its half height

1.0 SUMMARY

An examination of the effects of surface excrescences on boundary layer transition has been performed, using a unique experimental facility. The experimental study focused on stagnation-line starting condition boundary layers in incompressible flow without sweep effects. The study was performed at flight-representative Reynolds numbers—equivalent to chord Reynolds numbers of 4×10^6 to 8×10^6 —and included the effects of favorable pressure gradients. The results for both forward and aft-facing steps indicate a substantial stabilizing effect of favorable pressure gradient on excrescence-induced boundary layer transition. These findings suggest that manufacturing tolerances for laminar flow aircraft could be loosened in areas where even mild favorable pressure gradients exist.

2.0 INTRODUCTION

Drag reduction on aircraft brings a myriad of benefits and is given substantial attention in the design process for new long-range or long-endurance Intelligence, Surveillance, and Reconnaissance (ISR) aircraft, such as the RQ-4 Global Hawk (see Figure 1) or the SensorCraft concept (see Figure 2) where efficient flight is a high priority. For many aircraft designs skin friction drag is a substantial source of overall drag. Designing aircraft surfaces—in particular, wings—to have lower skin friction drag through the control of the boundary layer transition location has been pursued for many decades. The resulting drag reductions possible with such a “laminar flow aircraft” are often projected to be substantial. However, potential disadvantages associated with incorporating laminar flow wings have prevented the widespread use of this technology to improve aircraft performance, except in a few specialized cases.



Figure 1: RQ-4 Global Hawk Block 10.

Taking advantage of laminar flow on an actual operational aircraft requires overcoming the three hurdles of laminar flow illustrated in Figure 3: (1) design of the outer mold line (OML)—or, vehicle surface shape—to achieve delayed transition; (2) manufacturing quality of the vehicle surfaces; and (3) operational environment effects. The design of the OML must consider not only the control of boundary layer disturbances to prevent transition from occurring prematurely, but also the impact on the overall vehicle forces and moments. It is not unusual to encounter lower maximum lift coefficients with laminar flow wings, leading to fundamental sizing and design impacts for the overall vehicle. Of concern particularly for tailless aircraft, the pitching moment can be significantly constrained by the design requirements for laminar flow. Once the OML has been designed, actually building the aircraft can be difficult. The required manufacturing tolerances in regions where laminar flow is expected can be significantly tighter than conventional aircraft. However, this is further complicated by the fact that the tolerances needed for laminar flow aircraft are poorly understood. For research or prototype aircraft this can be overcome, but the potential cost impacts in a production program can be prohibitive. Lastly, once a laminar flow aircraft is built, effects of the operating environment, such as surface contamination or maintenance effects, can impede actual realization of the laminar flow benefits.



Figure 2: Northrop Grumman SensorCraft concept designed for laminar flow.

The Surface Excrescence Transition Study (SETS) addresses the second hurdle, manufacturability. An optimal balance of tight tolerances for laminar flow and loose tolerances for cost-efficient manufacturing can only be obtained by detailed understanding of the effects of surface excrescences on boundary layer transition in pressure gradients representative of laminar flow wings. Existing literature on laminar flow does not provide sufficient criteria on manufacturing tolerances for a surface in a pressure gradient. Therefore, the required tolerances must be determined from conducting a test specific to the geometry of interest, or they must be extrapolated from the existing literature on flow effects in the absence of a pressure gradient. The former method is inefficient, laborious and untimely. The later method is also highly undesirable as the pressure gradient can be expected to have a profound effect on boundary layer transition.

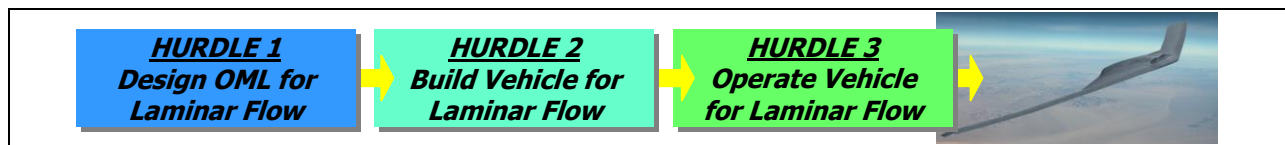


Figure 3: Three hurdles to laminar flow.

Generally-applicable, manufacturing tolerance criteria that is a function of pressure distribution—as well as other wing geometry parameters—is necessary for wings designed for laminar flow to be built to achieve those benefits in practice. Building on experimental and computational work performed as part of the Manufacturing Tolerances for Laminar Flow (MEATLOAF) study^{1,2} the current study developed general criteria for manufacturing tolerances for steps using a unique experimental facility. Thus the results are applicable to a broad range of future operational vehicle designs.

Testing for the effects of boundary layer transition is specifically being done using models designed to provide idealized growth of the boundary layer for the purpose of developing clear relations between excrescence size and transition. For this reason, the models were designed with favorable, but linear pressure gradients. The models were designed to be symmetric for use

in the test facility (to avoid inducing sideloads on the model support system). Additionally, the models focused on the region that would examine a laminar boundary layer, like that that would exist in the forward portion of a laminar flow wing, by making these regions as large as possible. Because of this, the transition Reynolds number (Re_{tr}) occurs at a higher percentage of the model chord than would be expected on a flight vehicle. Figure 4 shows a comparison of the test approach with a typical laminar flow wing. In this example, since the laminar flow wing is designed for 45% chord laminar flow, the transition Reynolds number is 3.2×10^6 for flight conditions that provide a chord Reynolds number of 7.1×10^6 . Since the SETS models are designed to devote as much of the chord to laminar flow as possible, that 3.2×10^6 transition Reynolds number is achievable on a model with a chord Reynolds number of just 3.8×10^6 . As such, the chord Reynolds number for wings to which these results are directly applicable needs to be determined from the expected length of the laminar region, not the geometric chord. This results in a broader range of applicability for the SETS results than might be indicated by merely examining the model chord Reynolds numbers.

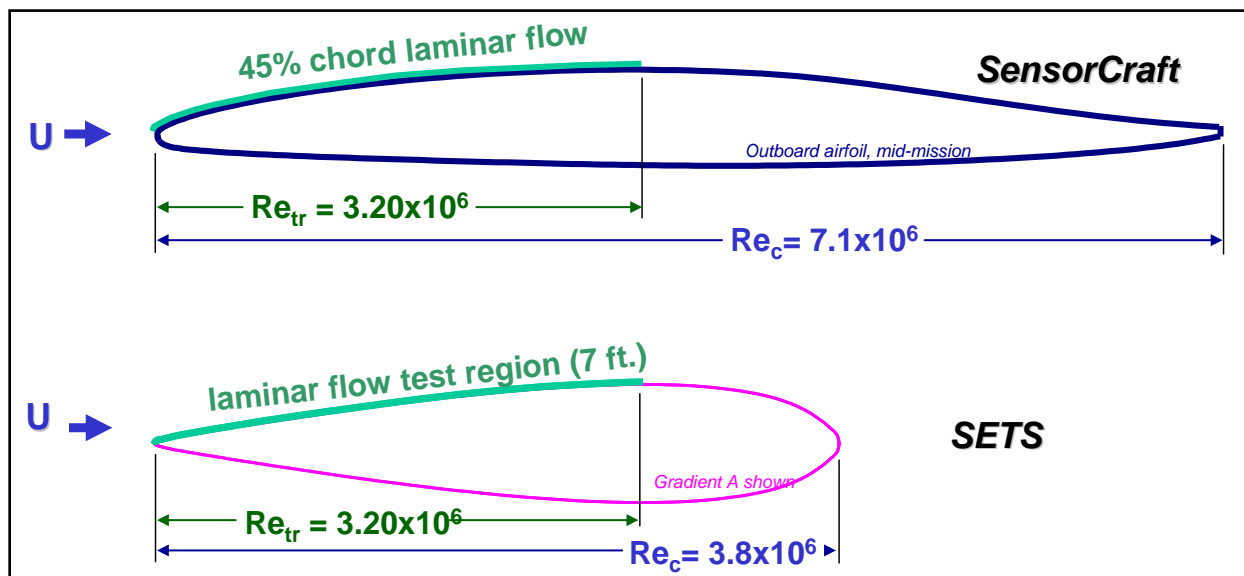


Figure 4: Transition Reynolds number comparison for a laminar flow wing.

The testing conducted for the SETS program was designed around the capabilities of a unique facility, the Towing Wind Tunnel (TWT) in Hyuga, Japan (for more details, see Section 6.0). Testing at this facility as part of MEATLOAF Task 6 indicated a substantial benefit from the very low disturbance environment for this study. To maximize the capabilities of this tunnel, three new models were designed and tested for SETS. These models, and their associated instrumentation, were based on the test approaches successfully employed in the MEATLOAF program, but optimized for the TWT. As a result, the high Reynolds number capability was successfully exploited to extend the relations developed for transition Reynolds number as a function of excrescence height Reynolds number (Re_k) from a maximum of 1×10^6 in the MEATLOAF study to over 4×10^6 in SETS.

3.0 BACKGROUND

In 2004, Northrop Grumman began examining the manufacturability concerns associated with designing and building a laminar flow aircraft. These investigations began with the Prediction of Manufacturing Tolerances for Laminar Flow (MEATLOAF) study, which examined the effect of pressure gradient on the allowable excrescence height. The MEATLOAF study was primarily an experimentally-based study and used a test model in a small low-speed wind tunnel. The MEATLOAF study was limited to low chord and transition Reynolds numbers (< 1 million) by the constraints of the wind tunnel facility. The results of the MEATLOAF study were promising – indicating that pressure gradient had a significant effect on the allowable height of an excrescence and offered the potential for loosening of tolerances. However, at such low Reynolds numbers, the results of the MEATLOAF study were not directly applicable to actual aircraft. The objective of SETS was to extend the results of the previous MEATLOAF studies to higher transition Reynolds numbers so that the results would be directly applicable to real systems of interest such as Global Hawk or SensorCraft.

The original MEATLOAF study was successfully completed in June 2005. The focus of the original study was an experimentally-based low-speed unswept parametric investigation of excrescence effects, which was called Task 1. The objective was to build a database of surface excrescence effects on boundary layer transition in the presence of a pressure gradient.

Task 1 used a special flat plate model that was mounted in a wind tunnel with a movable upper wall. The positioning of the upper wall determined the static pressure variation over the test plate. The test plate itself had provisions for excrescence inserts that allowed various step and wave geometries to be tested. A single chordwise row of 40 pressure taps, 2.5 inches from the centerline of the model, allowed measurement of the static pressure distribution on the plate. A movable Preston tube was used to measure the chordwise distribution of skin friction and to determine the transition location.

The Task 1 experimental work was conducted at the Washington State University, Tri-Cities Low Speed Contractionless Wind Tunnel in Richland, WA. The wind tunnel was designed and constructed especially for boundary layer research. The tunnel features a filter box to remove particulates in the air and the flow passes through a two-stage settling duct, a diffuser, several grids, honeycomb, and a series of screens, before entering the test section. The Washington State University tunnel's blower-type design positions the 2- by 2-ft cross-section, six-foot-long test section as the downstream-most component. Unit Reynolds numbers from zero to 0.2×10^6 per foot can be achieved.

The upper wall of the Washington State University tunnel is easily adjustable to allow the imposing of pressure gradients throughout the test section. Figure 5 shows the tunnel with the upper wall deflected to impose a favorable pressure gradient on the flat plate model.

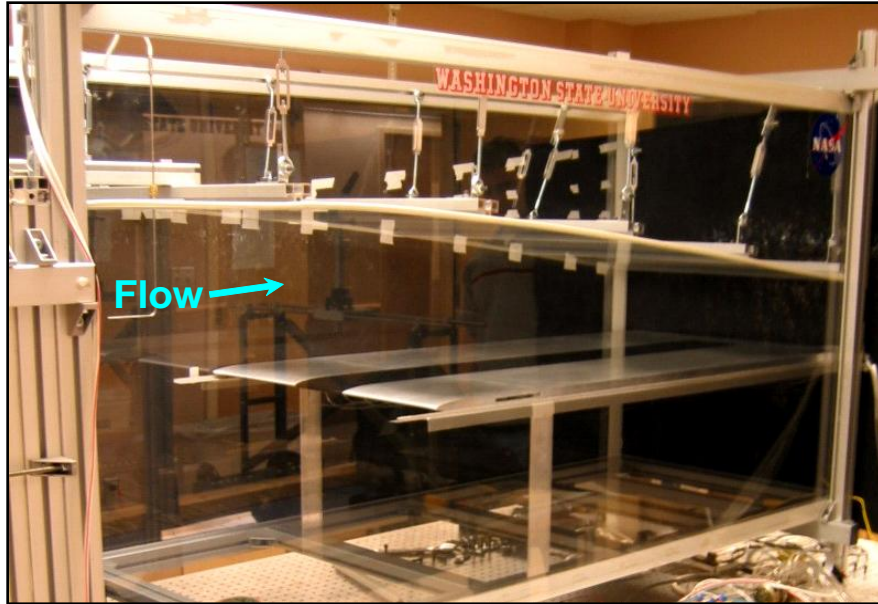


Figure 5: Test section with upper wall deflected to provide a favorable pressure gradient on the flat plate model.

The leading edge of the Task 1 model was a super ellipse, which has a second derivative that goes to zero at the minor axes. The span of the model was 23.5 inches to allow a clean fit in the 2-ft wide test section. The upper surface of the model had a 12-inch long full-span cavity milled in it to accept excrescence inserts (see Figures 6-9). Each insert was three inches in chord and could be positioned at any of four locations (denoted A, B, C, and D). The remaining three locations were fitted with filler pieces. The filler pieces were designed to provide a level surface and were each equipped with a single static pressure tap. The Task 1 excrescence locations and excrescence sizes are shown in Tables 1 and 2.

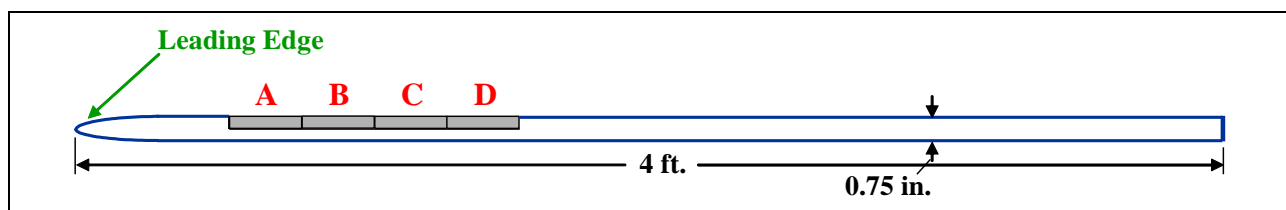


Figure 6: MEATLOAF Task 1 model geometry.

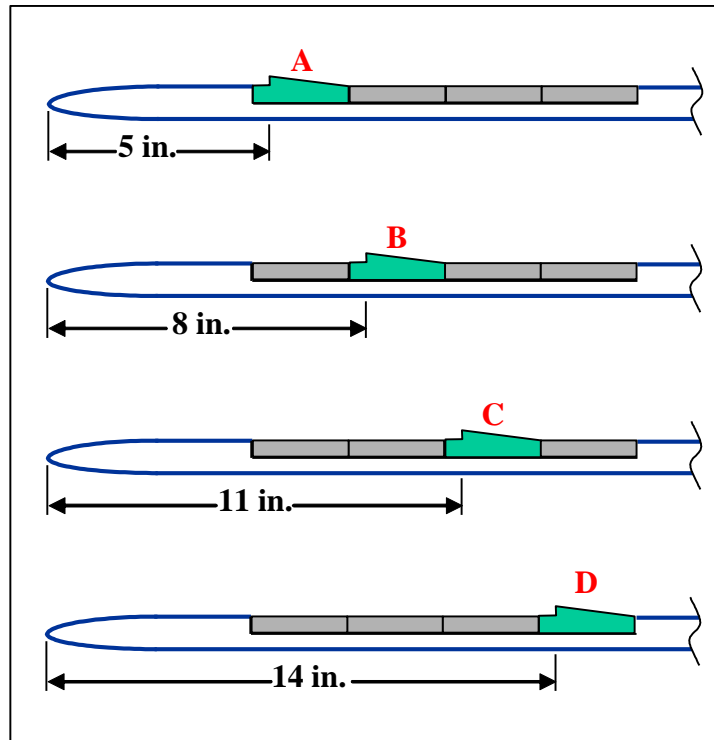


Figure 7: Task 1 forward-facing step locations.

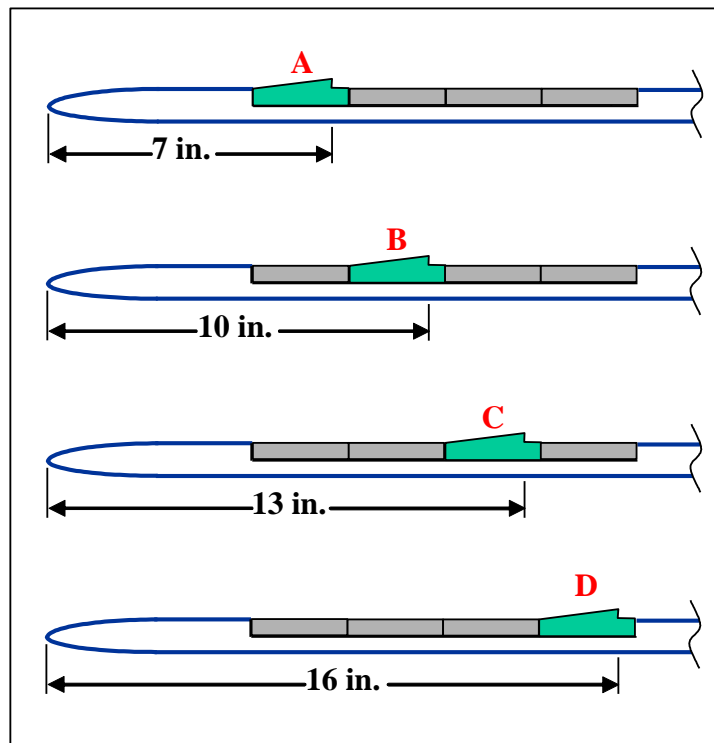


Figure 8: Task 1 aft-facing step locations.

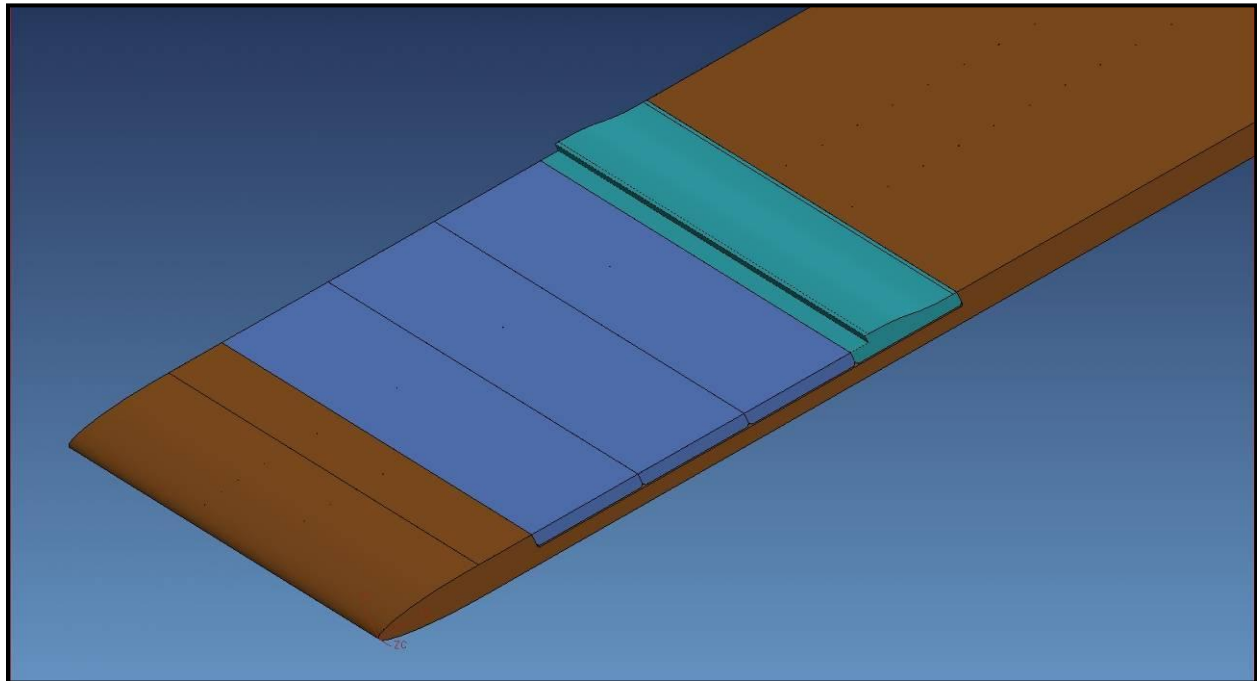


Figure 9: Task 1 test plate upper surface with forward-facing step in position D.

Table 1: Task 1 excrescence locations

Excrescence Type	A	B	C	D
Forward-Facing Step	5 in	8 in	11 in	14 in
Aft-Facing Step	7 in	10 in	13 in	16 in

Table 2: Task 1 excrescence piece sizes

Step Height [in]
0.100
0.090
0.080
0.070
0.055
0.035
Adjust-a-Step

Pressure measurements were made using a single pressure transducer connected to a mechanical multiplexer. The pressure gradients measured during Task 1 ranged from very adverse to very favorable and are shown in Figure 10. The corresponding nondimensional pressure gradient parameter K for each of the tested pressure distributions in Task 1 is shown in Table 3.

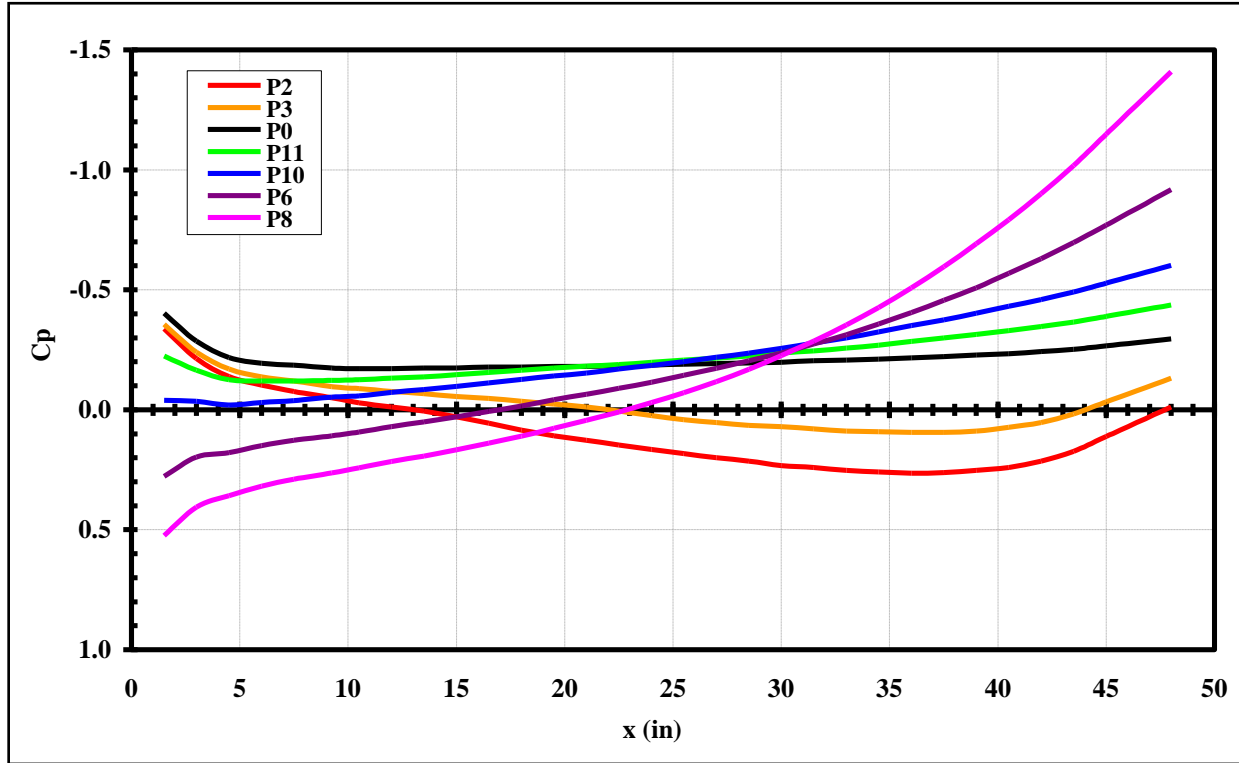


Figure 10: Task 1 tested static pressure distributions.

Table 3: Task 1 nondimensional pressure gradient values

Setting	K	Re _{xi}
P2	-5.25×10^{-7}	149,000
P3	-2.93×10^{-7}	275,000
P0	0.50×10^{-7}	745,000
P11	1.85×10^{-7}	728,000
P10	3.21×10^{-7}	744,000
P6	6.11×10^{-7}	717,000
P8	9.41×10^{-7}	677,000

In order to determine the excrescence height Reynolds number (Re_k), the boundary layer velocity profile was measured at each excrescence location for each pressure gradient. The boundary layer velocity profiles were measured with a total pressure tube mounted on an automated traverse.

Skin friction distributions were measured using a Preston tube. The Preston tube measurements were made with a 0.042 inch outside diameter hypodermic needle protruding

forward from a long rod. The probe tip was angled downward so that the opening would always rest touching the surface. The probe and rod assembly allowed the probe to be positioned anywhere on the test plate; the required local surface static pressure for each location was obtained by interpolating the surface pressure distribution. The resulting pressure differences were converted to skin friction coefficients using Patel's calibration for turbulent boundary layers and Poll's calibration for laminar boundary layers.

The results from Task 1 are the following boundary layer transition trend plots that show the transition trends for a family of Re_{xk} values for the given excrescence type and pressure gradient. Data points shown are transition locations from the skin friction distribution plots. The transition location criteria is defined as the location where the skin friction coefficient was greater than 1.5 times the measured clean plate skin friction coefficient. The data points were curve-fit as shown in the plots (Figures 11-22). In the figures, the closed symbols represent measured transition locations whereas the open symbols represent transition off the end of the model (e.g. the end of the plate was reached with no transition). The y-axis, Re_k , represents the nondimensional excrescence height while Re_{tr} , on the x-axis represents the transition location, expressed as a Reynolds number. There are different trendlines for different nondimensional excrescence locations (Re_{xk}). There is a separate plot for each nondimensional pressure gradient (K) and excrescence geometry (e.g. forward- or aft-facing step). The charts show the effect of pressure gradient and step geometry on the allowable height of an excrescence to prevent premature transition.

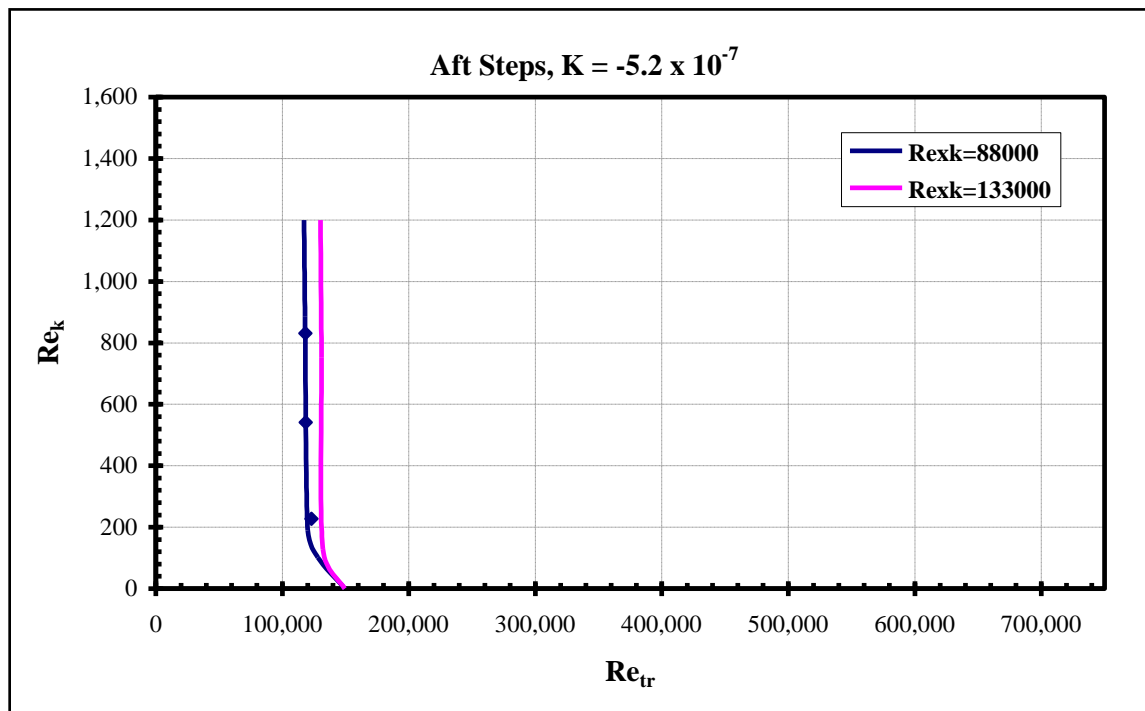


Figure 11: Task 1 Transition Trend, Aft Steps, $K = -5.2E-7$.

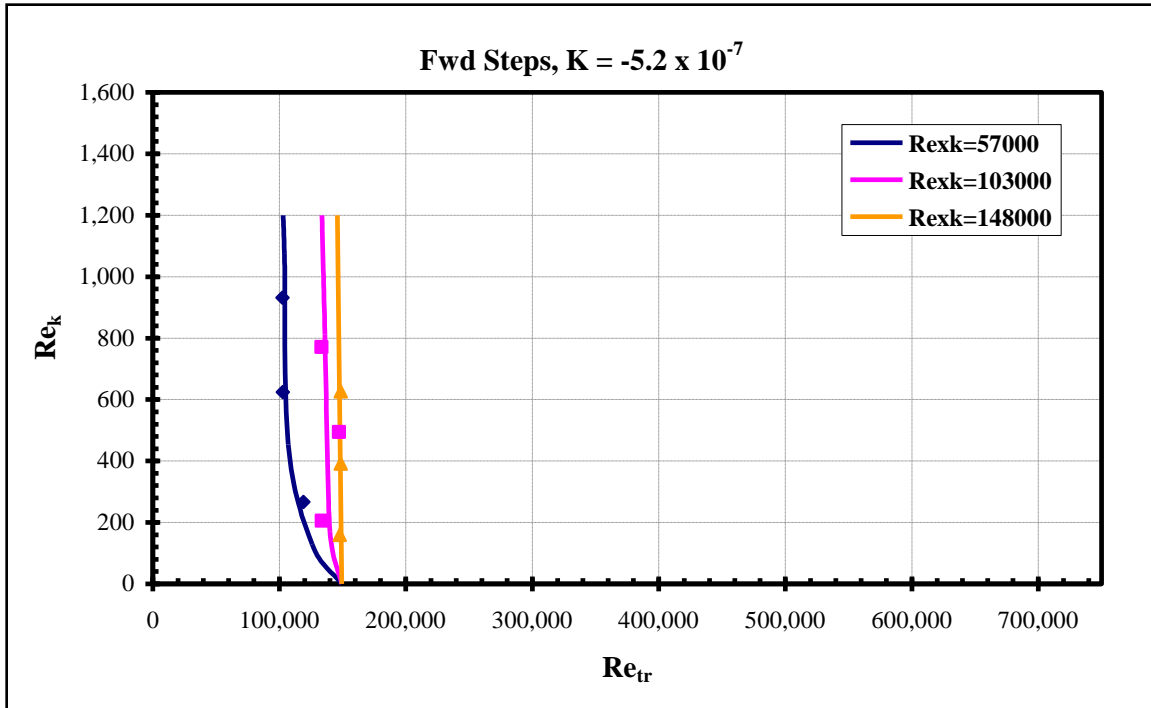


Figure 12: Task 1 Transition Trend, Fwd Steps, $K=-5.2E-7$.

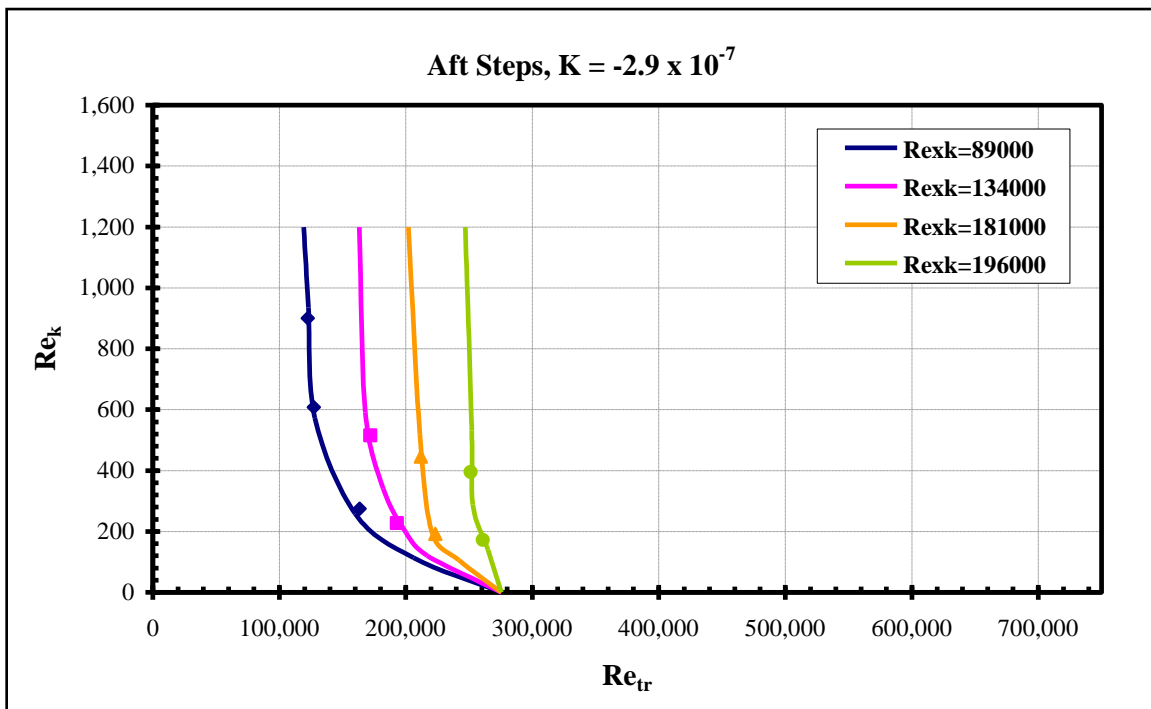


Figure 13: Task 1 Transition Trend, Aft Steps, $K=-2.9E-7$.

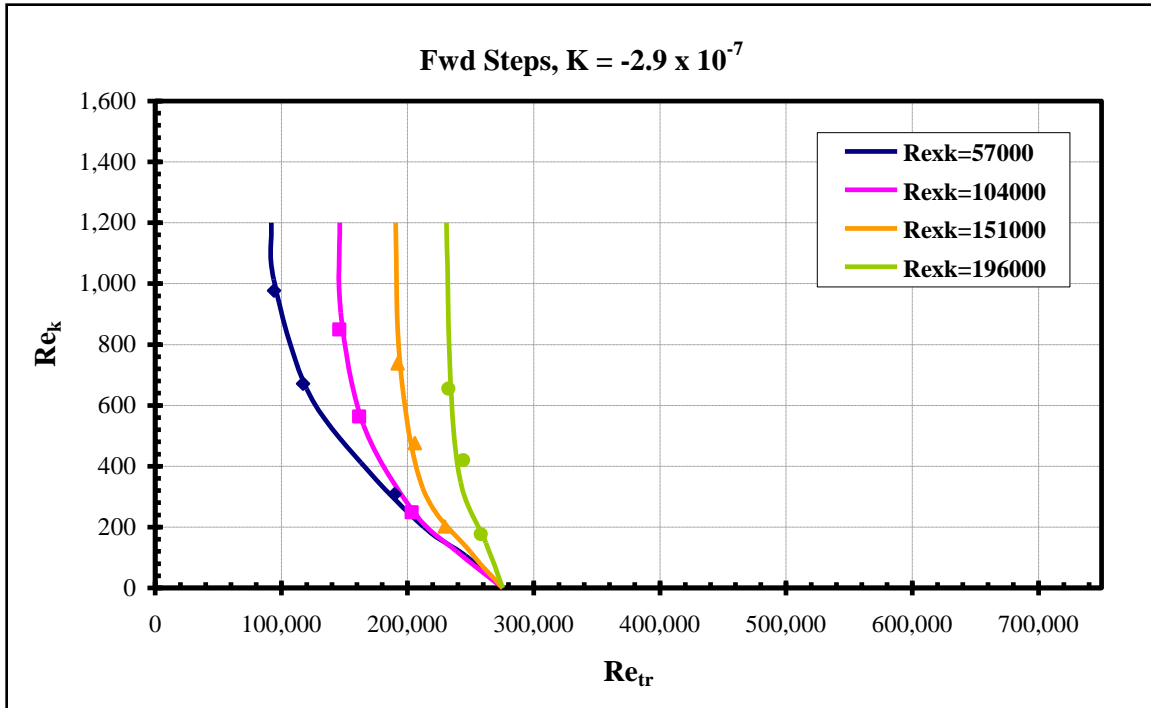


Figure 14: Task 1 Transition Trend, Fwd Steps, $K=-2.9E-7$.

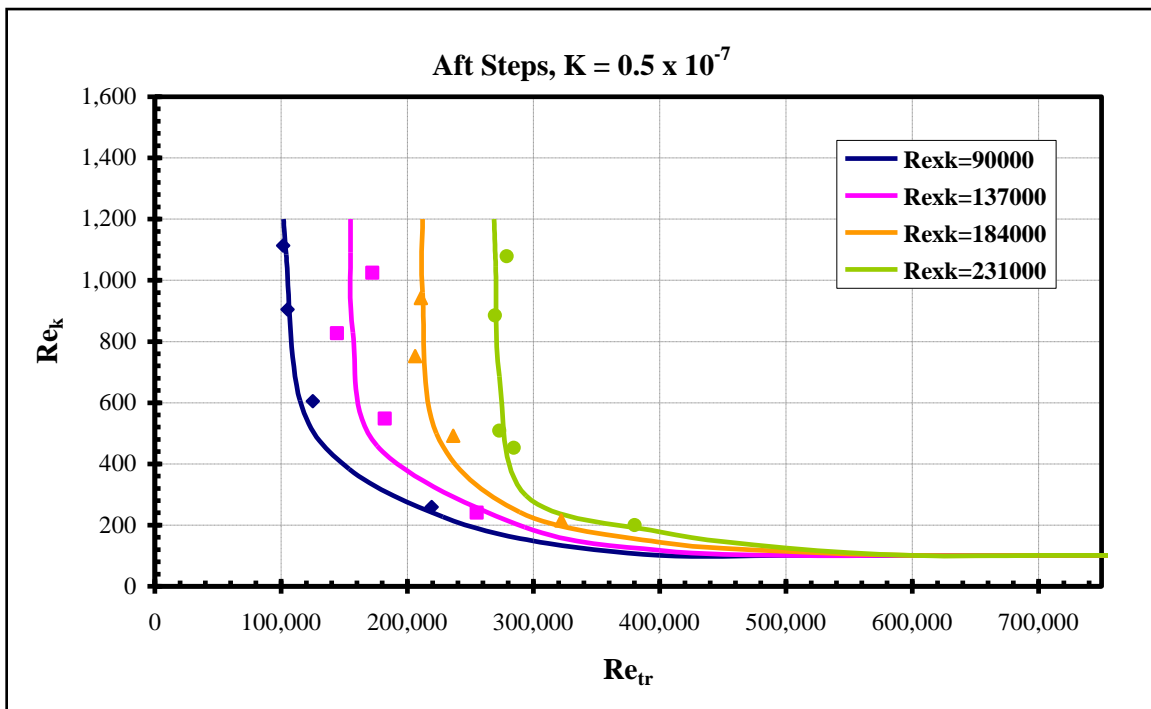


Figure 15: Task 1 Transition Trend, Aft Steps, $K=0.5E-7$.

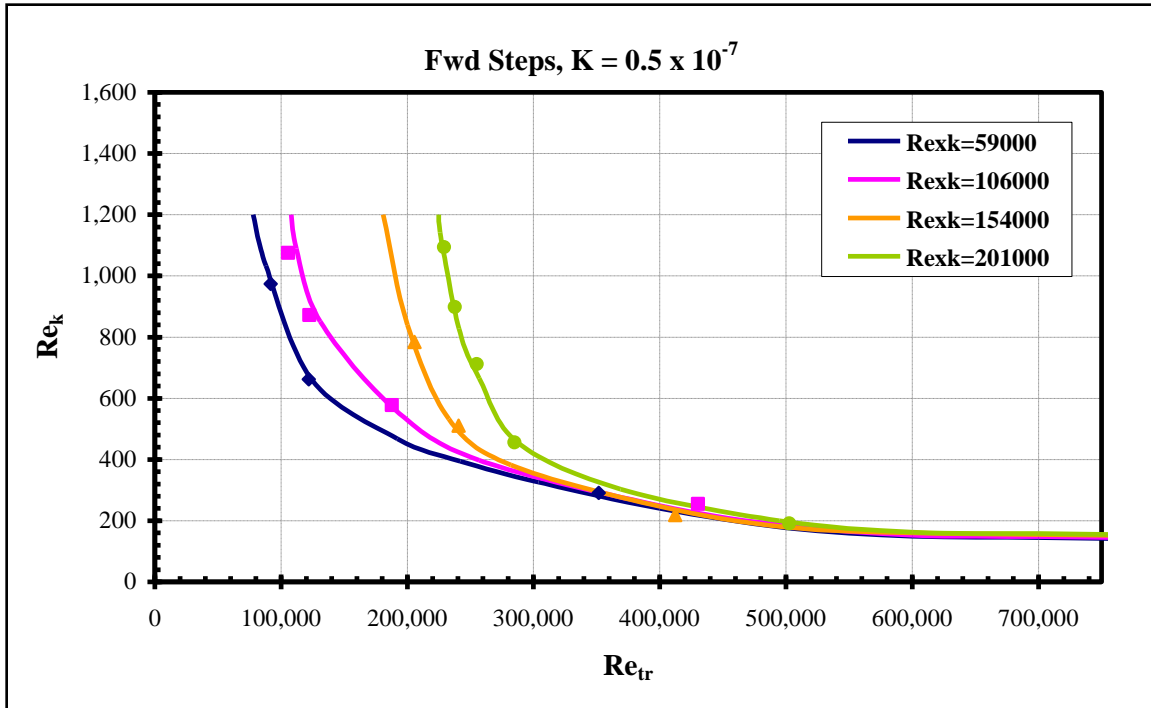


Figure 16: Task 1 Transition Trend, Fwd Steps, $K=0.5E-7$.

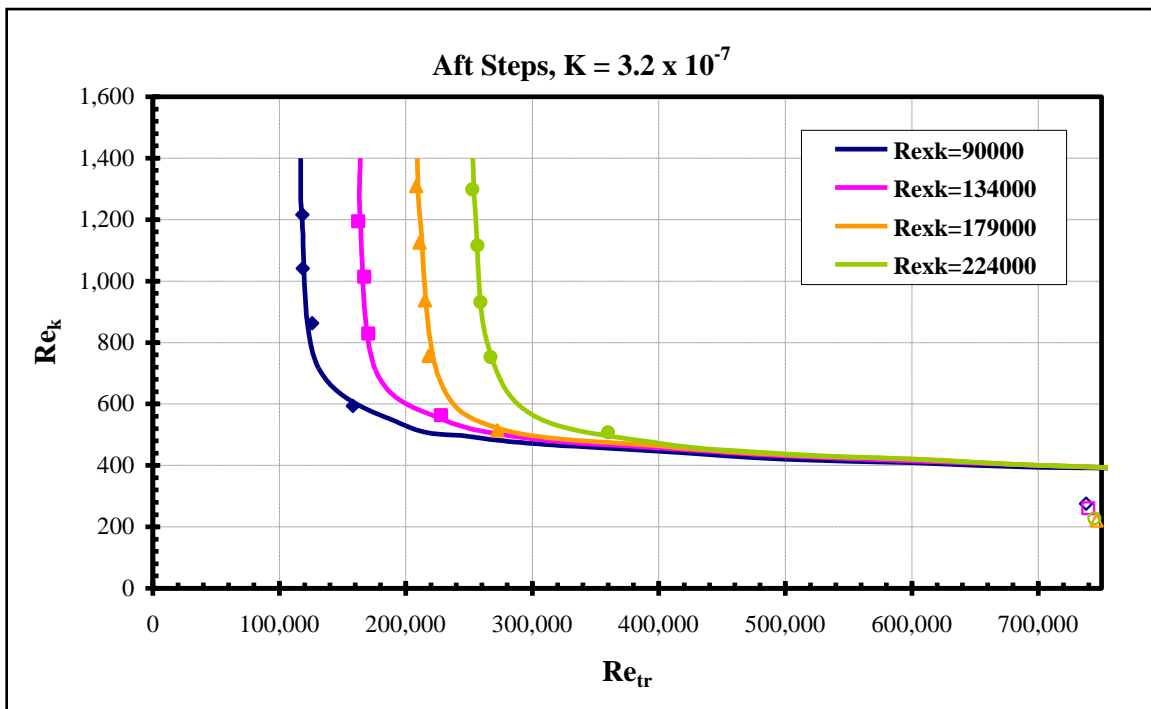


Figure 17: Task 1 Transition Trend, Aft Steps, $K=3.2E-7$.

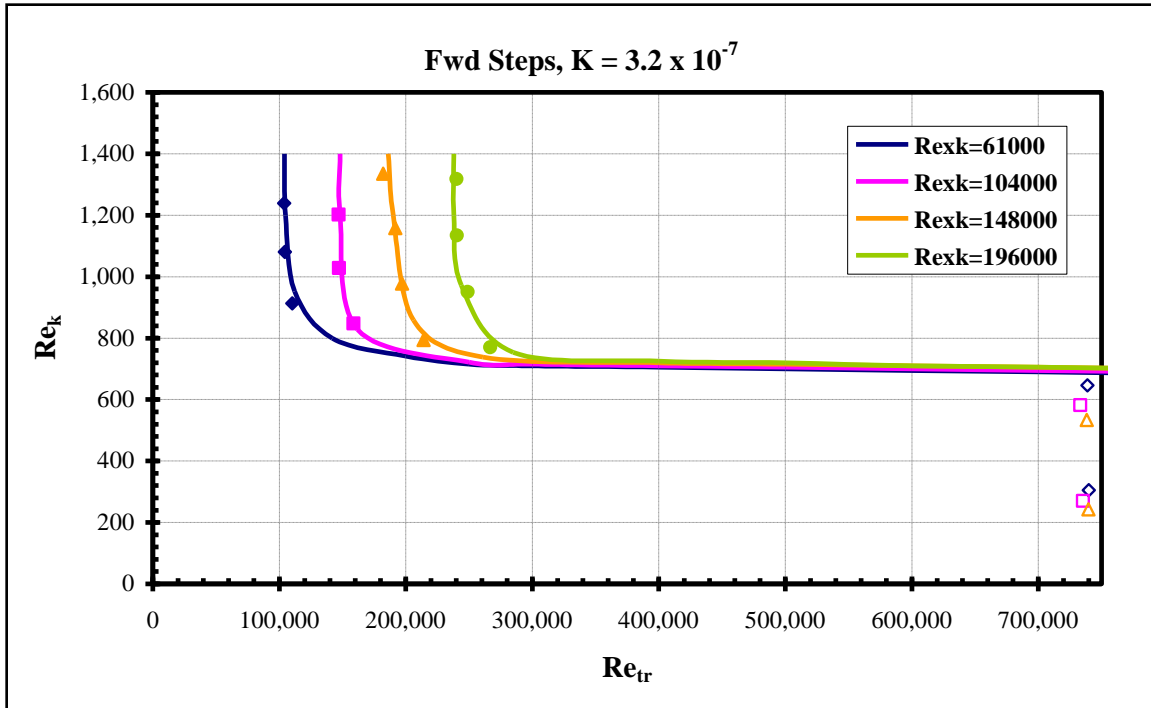


Figure 18: Task 1 Transition Trend, Fwd Steps, $K=3.2E-7$.

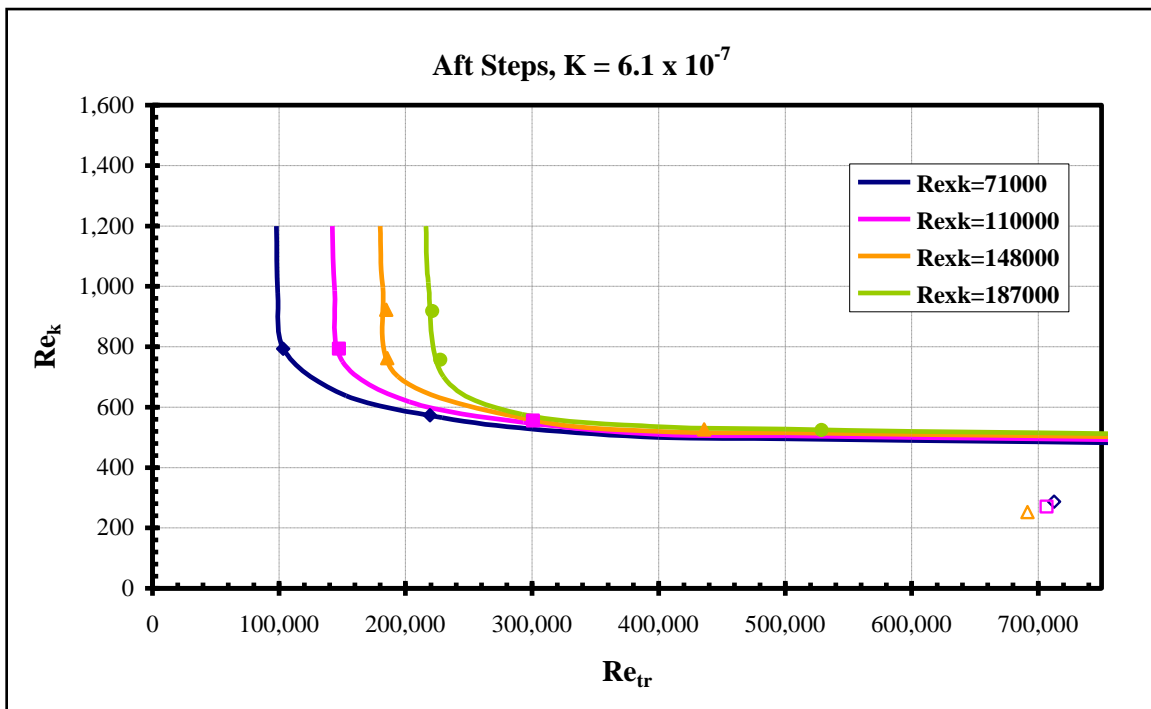


Figure 19: Task 1 Transition Trend, Aft Steps, $K=6.1E-7$.

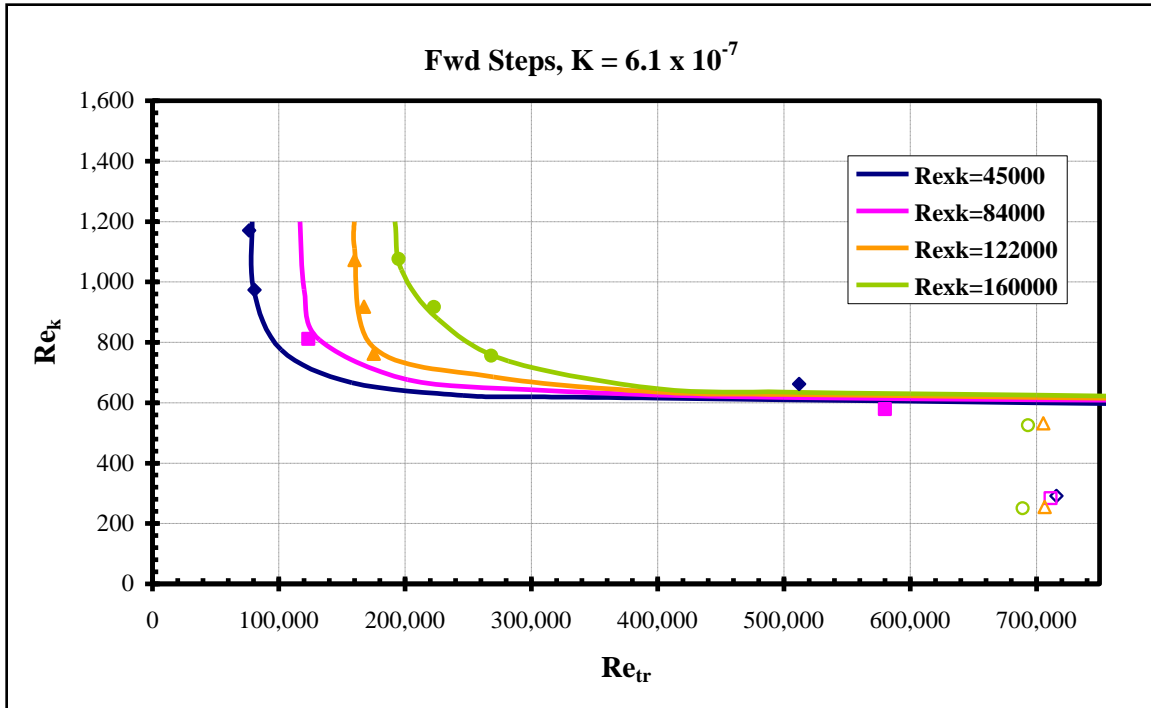


Figure 20: Task 1 Transition Trend, Fwd Steps, $K=6.1E-7$.

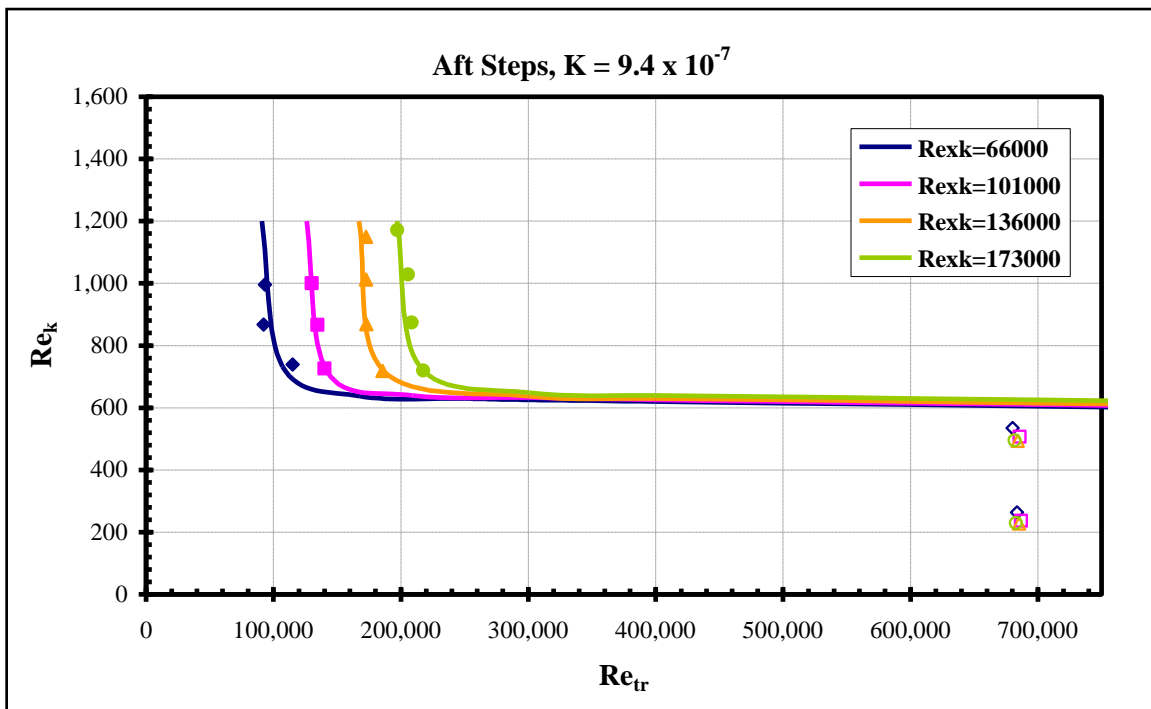


Figure 21: Task 1 Transition Trend, Aft Steps, $K=9.4E-7$.

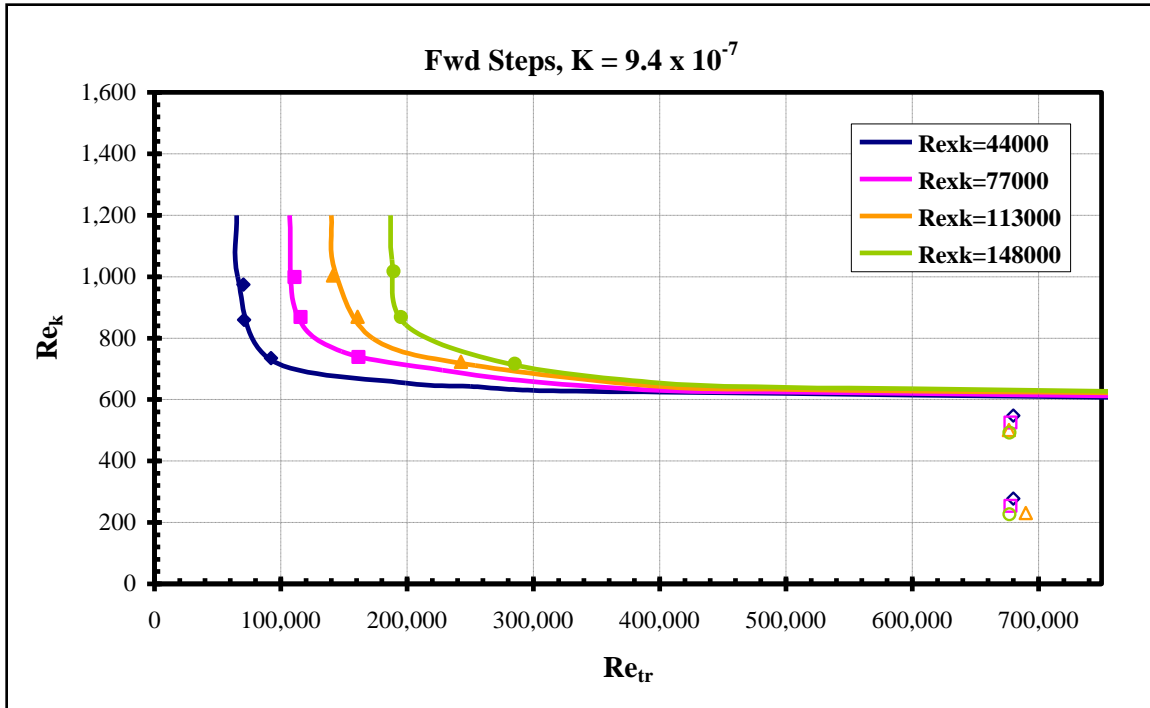


Figure 22: Task 1 Transition Trend, Fwd Steps, $K=9.4E-7$.

The Task 1 study showed that there is a pronounced effect of pressure gradient on boundary layer transition induced by surface excrescences. The effect of favorable pressure gradient was, as expected, beneficial in that the allowable height of the surface excrescence can be larger than a zero-pressure gradient case without inducing early transition. The effects of adverse gradient were observed to increase the susceptibility of the boundary layer to surface excrescences. This result was expected, though it is of less practical importance to the aerodynamic designer since it is often assumed that the boundary layer will transition once the pressure gradient becomes adverse, irrespective of surface excrescences.

The results from Task 1 covered the full applicable K (pressure gradient) range for real systems but fell short—in some cases, significantly—of full-scale transition Reynolds numbers. It was concluded that for decisions on allowable manufacturing tolerances to be made with confidence, further work must be done to increase the Reynolds number range.

The objective of SETS was to extend the results of the previous MEATLOAF studies to higher transition Reynolds numbers.

A database of effects of pressure distribution on boundary layer transition due to step excrescences was created as part of the SETS program. This database extends the current understanding of the required manufacturing tolerances for laminar flow into the specific flow regime of interest for aircraft such as Global Hawk and SensorCraft.

The SETS study was also an experimentally-based investigation. Detailed measurements of the flow and boundary layer development were taken as part of the study. These measurements included wing pressure coefficient distributions, boundary layer velocity profiles, skin friction coefficient distributions, and disturbance levels. A variety of measurement methods were used and included static pressure taps, a traversing total pressure tube, Preston tubes, hot wire anemometry, and accelerometers. These multiple measurements methods served to firmly establish the physical basis of the resulting tolerance requirements and allow their application to flight vehicles with confidence.

The SETS program used a novel low disturbance test facility, the Towing Wind Tunnel (TWT), to extend the results of the previous MEATLOAF wind tunnel studies to transition Reynolds numbers as high as 4-5 million. The Towing Wind Tunnel is located in Hyuga, Japan, and is operated by the Institute of Fluid Science at Tohoku University. The Towing Wind Tunnel uses an electrically-powered carrier vehicle to move a test model along a two-kilometer long track at speeds up to 30 meters/second. By moving the model through the air, some of the freestream disturbance problems that limit the use of conventional wind tunnels for laminar flow testing can be avoided.

Three models were constructed for the SETS testing. One model was a flat-plate model with a nominally zero pressure gradient, called Gradient-Zero. The other two models were favorable pressure gradient models called Gradient-A (favorable) and Gradient-B (more favorable). The models were each designed to hold a nominally constant pressure gradient over the length of their measurement regions. Each model had a continuously-adjustable two-dimensional step excrescence located 19 inches along the surface from the leading edge. The step could be adjusted to either a forward-facing or aft-facing step of any height between +0.25 and -0.25 inches.

Three test entries were conducted at the Towing Wind Tunnel from October 14-30 2008, November 3-30 2008, and January 13-30 2009. Prior to the test entries at the Towing Wind Tunnel, two shakedown wind tunnel test entries were conducted at the Northrop Grumman 7x10 Low Speed Wind Tunnel in Hawthorne, California, in August and September 2008.

4.0 MODEL DESCRIPTION

4.1 Model Aerodynamic Design

4.1.1 Design and Analysis Using Computational Fluid Dynamics

The objective of the model aerodynamic design was to create models that preserved near-constant chordwise and spanwise dimensionless pressure gradient (K) distributions. For the favorable pressure gradient models, the nominal target K-values were $K_A=0.5 \times 10^{-7}$ and $K_B=1 \times 10^{-7}$, for the Gradient-A and Gradient-B models, respectively. For Gradient-Zero, the nominal target K-value was $K_0=0$. These values of K were chosen after examining the nondimensional pressure gradients of long-endurance, laminar flow ISR aircraft, such as the RQ-4 Global Hawk and the SensorCraft concept. The chosen values of K bracket the most-applicable range of pressure gradient values for relevant aircraft at these Reynolds numbers. The models were designed to attain their respective K values before or at the step location, 19 inches aft of the leading edge, measured along the surface. Dimensionless pressure gradient K is given by the following formula of equation 1.

$$K = \frac{v}{U_e^2} \left(\frac{dU_e}{dx} \right) \quad (1)$$

Because the model was tested in an incompressible regime, Bernoulli's formula was used to manipulate equation (1) in order to obtain the pressure gradient as a function of C_p , as shown in equation 2. The design tools used in this work were more conveniently employed with a output targets expressed in C_p than edge velocity.

$$K = \frac{-v}{2U_\infty (1 - C_p)^{3/2}} \frac{dC_p}{dx} \quad (2)$$

The models were designed to maintain laminar flow throughout the test portion of the model in the absence of any excrescence. The approach taken with Gradient-Zero—a flat plate—resulted in the primary design task being that of the leading edge. In order to maintain laminar flow on the flat plate the leading edge needed to be designed such that the curvature maintained continuity in the second derivative at the junction of the leading edge and the flat plate. This was done by using a superellipse with a semi-diameter ratio of 1/6 and $n = 2.2$, as shown in equation 3.

$$y = \left\{ \left(\frac{t}{2} \right)^2 - \left(\frac{t}{2} \right)^2 \left(\frac{c-x}{c} \right)^{2+\left(\frac{x}{c}\right)^2} \right\}^{1/2} \quad (3)$$

The initial design for both of the favorable pressure gradient models (Gradient-A and Gradient-B) was done using XFLR5, a panel-code coupled with a two-equation lagged

dissipation integral boundary layer formulation. While this method is relatively inaccurate, it provided a way to quickly manipulate the geometry and make rapid C_p calculations in order to acquire a rough outer mold line (OML) shape for both models. The OML was then used to create a 2-D Navier-Stokes model using GRIDGEN. This grid was then run through a 2-D/3-D RANS flow solver called CFL3D³. Based upon the CFD results the curvature of the OML was further manipulated using a NURBS modeling package called Rhino. This process was repeated for each model until an OML that provided the desired pressure distribution was found.

The final design C_p and K distributions shown in Figures 23, 24 and 25.

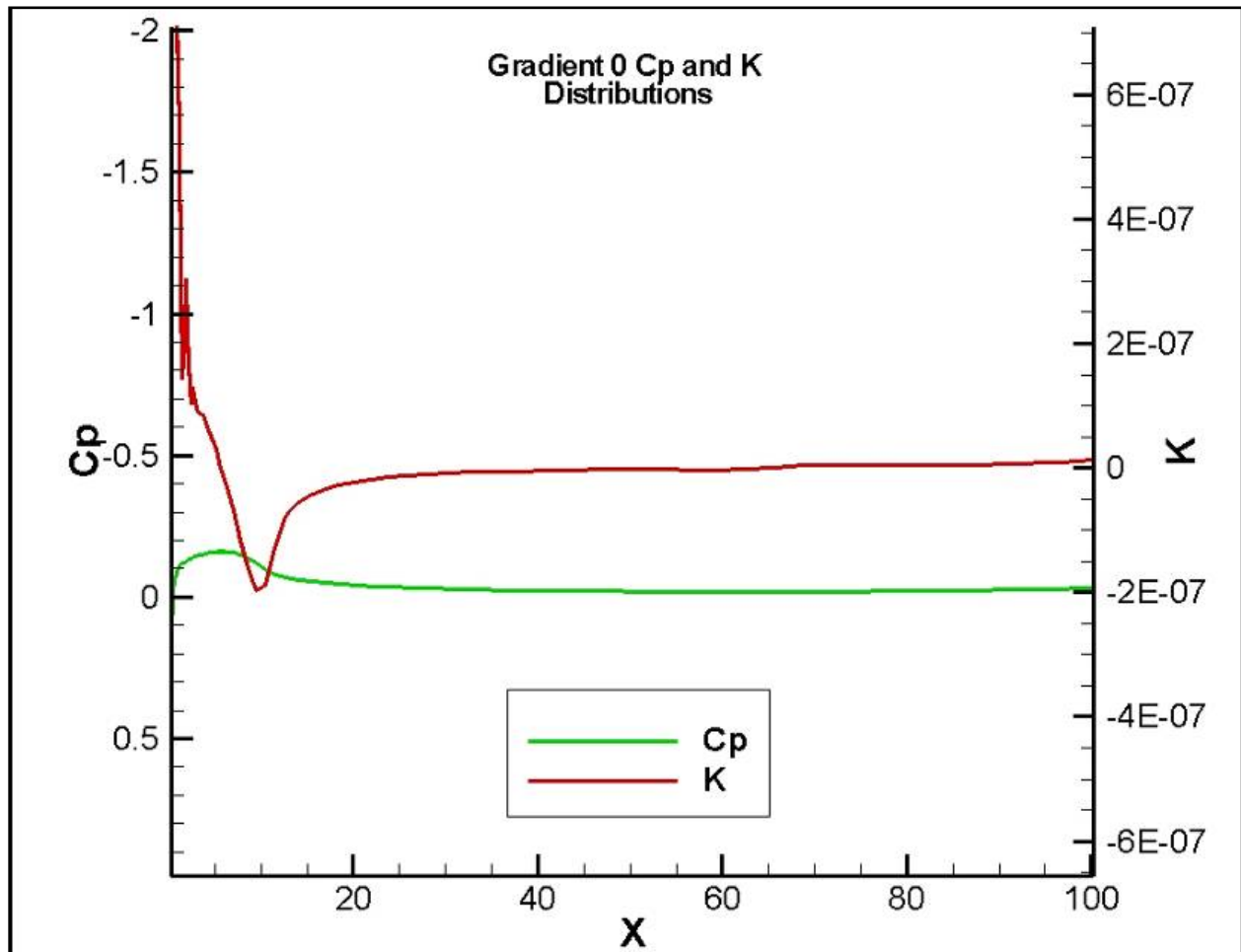


Figure 23: Pressure distribution and K for Gradient-Zero model.

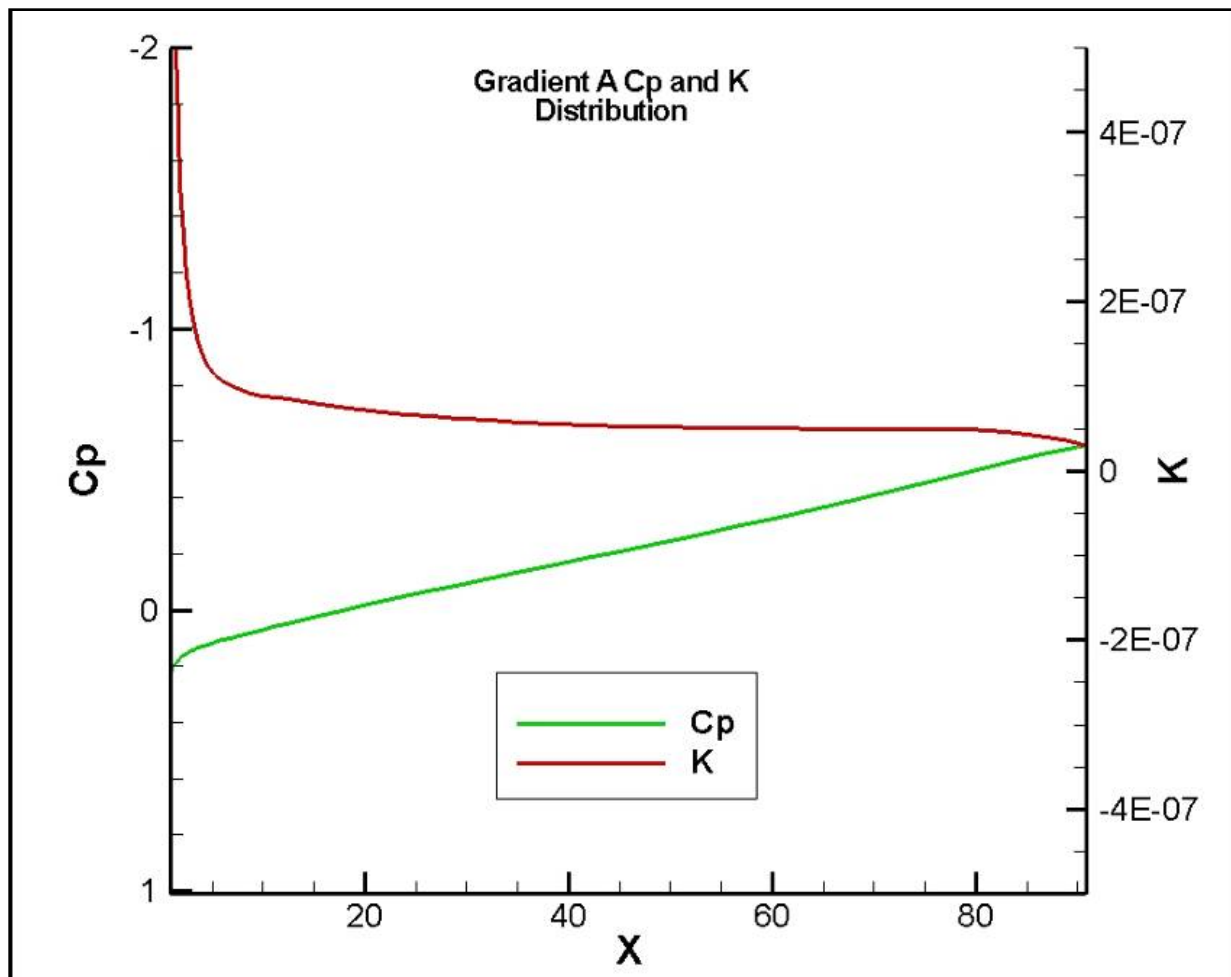


Figure 24: Pressure distribution and K for Gradient-A model.

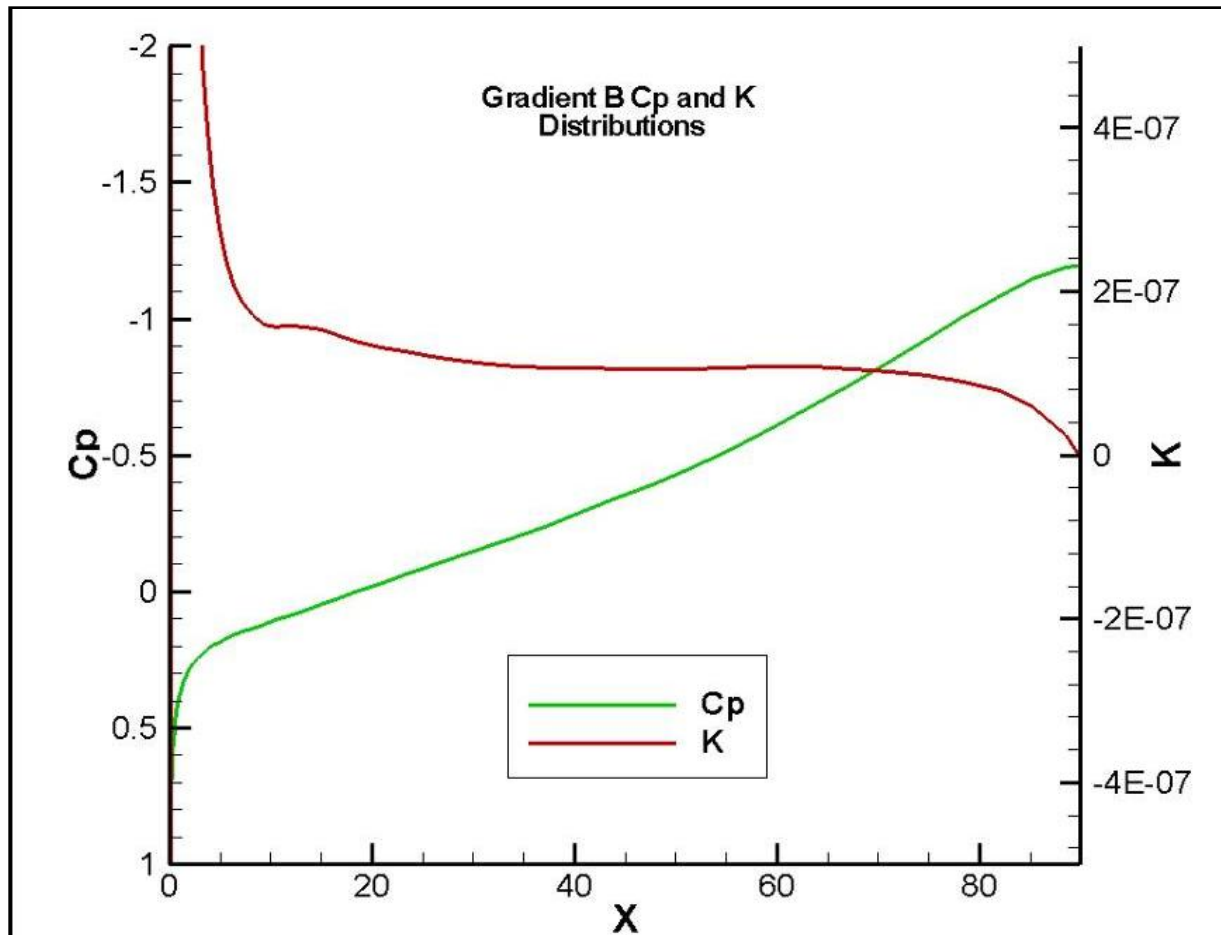


Figure 25: Pressure distribution and K for Gradient-B model.

Because of the low aspect ratio of the model (resulting from the large chord in order to take advantage of the large size of the carrier vehicle to increase the Reynolds number), splitter plates were used to maximize the two-dimensional character of the flow. Figures 26, 27 and 28 show the OML lines for all three models, as well as the planform of the splitter plates. To size the splitter plates a 3-D Navier-Stokes model was created in Gridgen and analyzed with CFL3D. An iterative process was used to size the splitter plates, increasing the lateral extent of these surfaces progressively until the spanwise uniformity of the pressure was achieved within 5%.

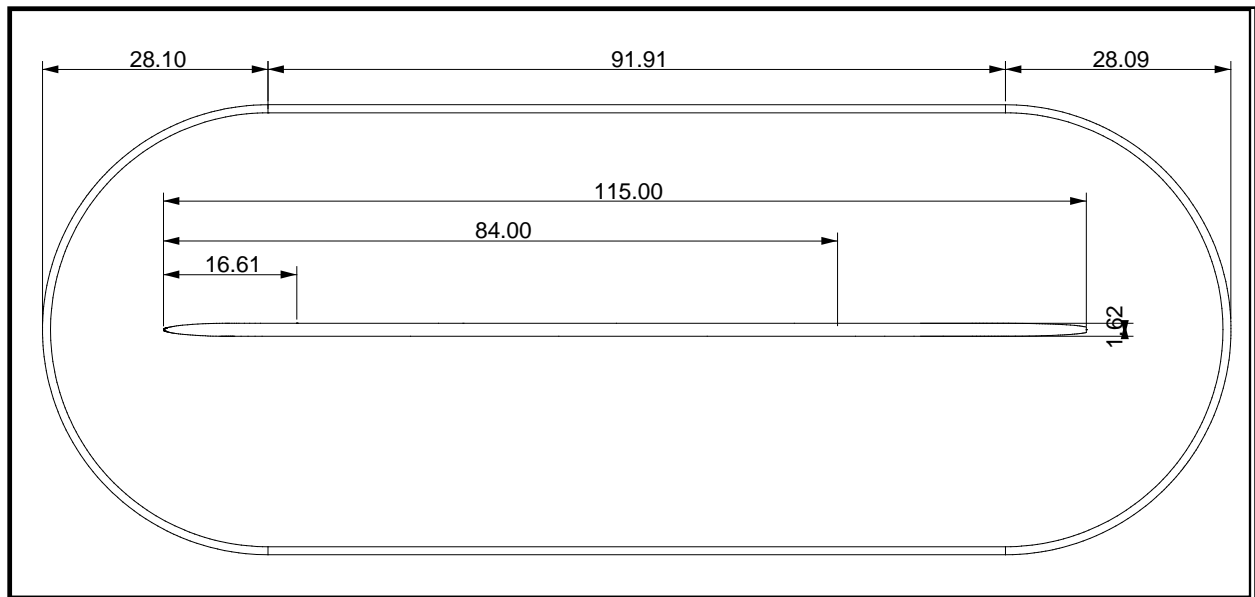


Figure 26: Top view of Gradient-Zero model showing splitter plate (dimensions in inches).

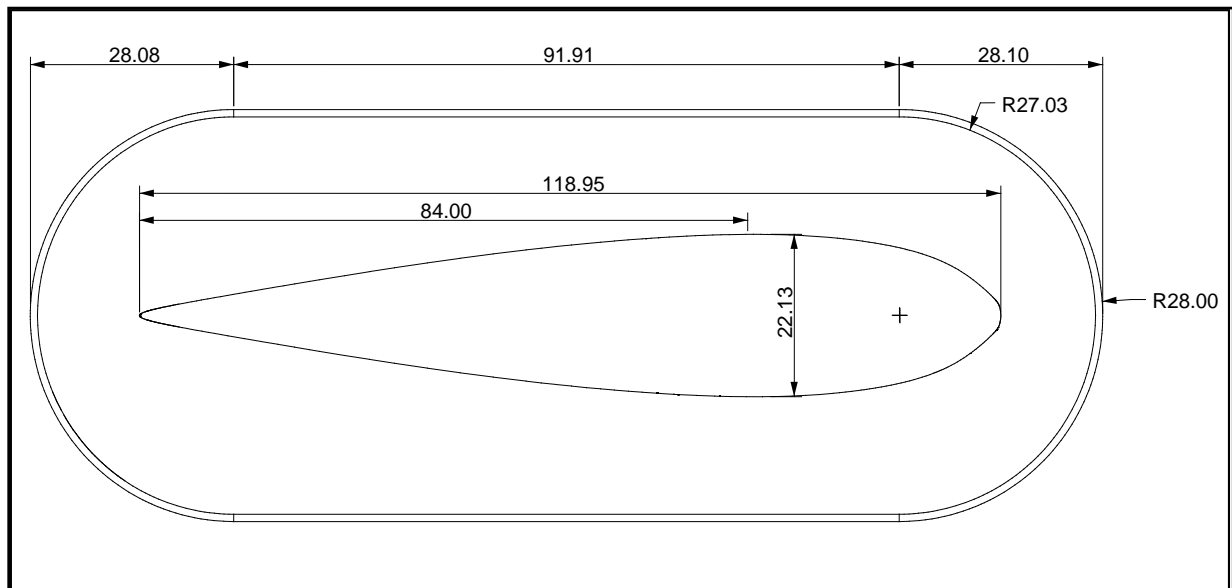


Figure 27: Top view of Gradient-A model showing splitter plate (dimensions in inches).

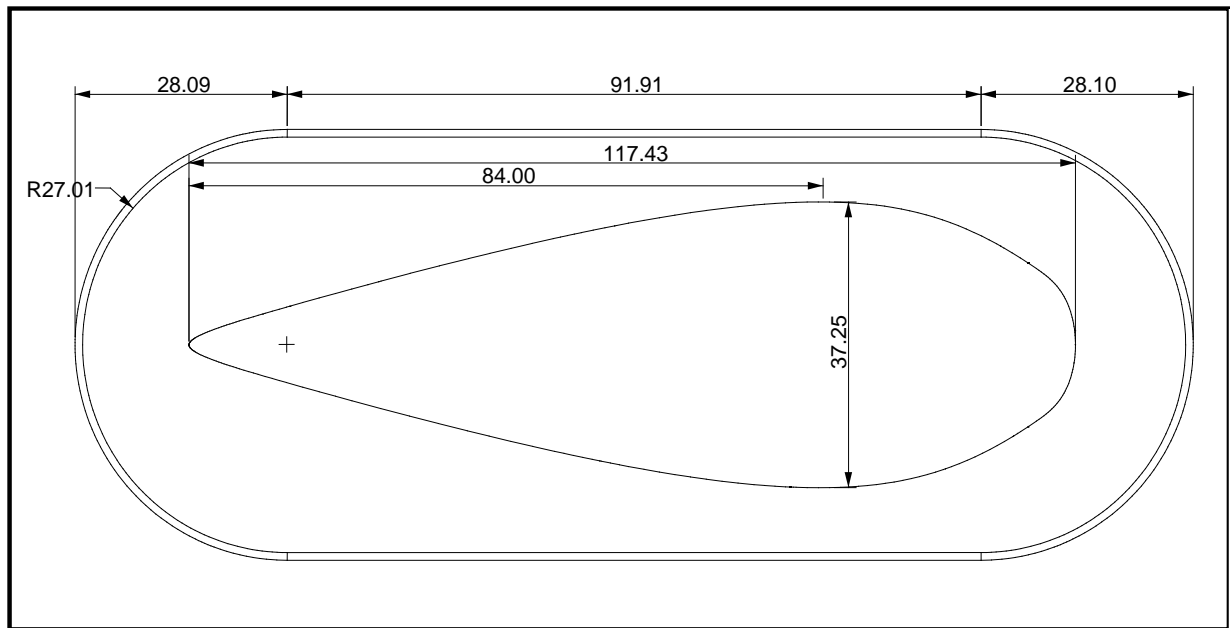


Figure 28: Top view of Gradient-B model showing splitter plate (dimensions in inches).

Figures 29 and 30 display the C_p distribution at various span stations for the A and B models respectively. Note that the model maintains 2-D flow through the central 80% of the span.

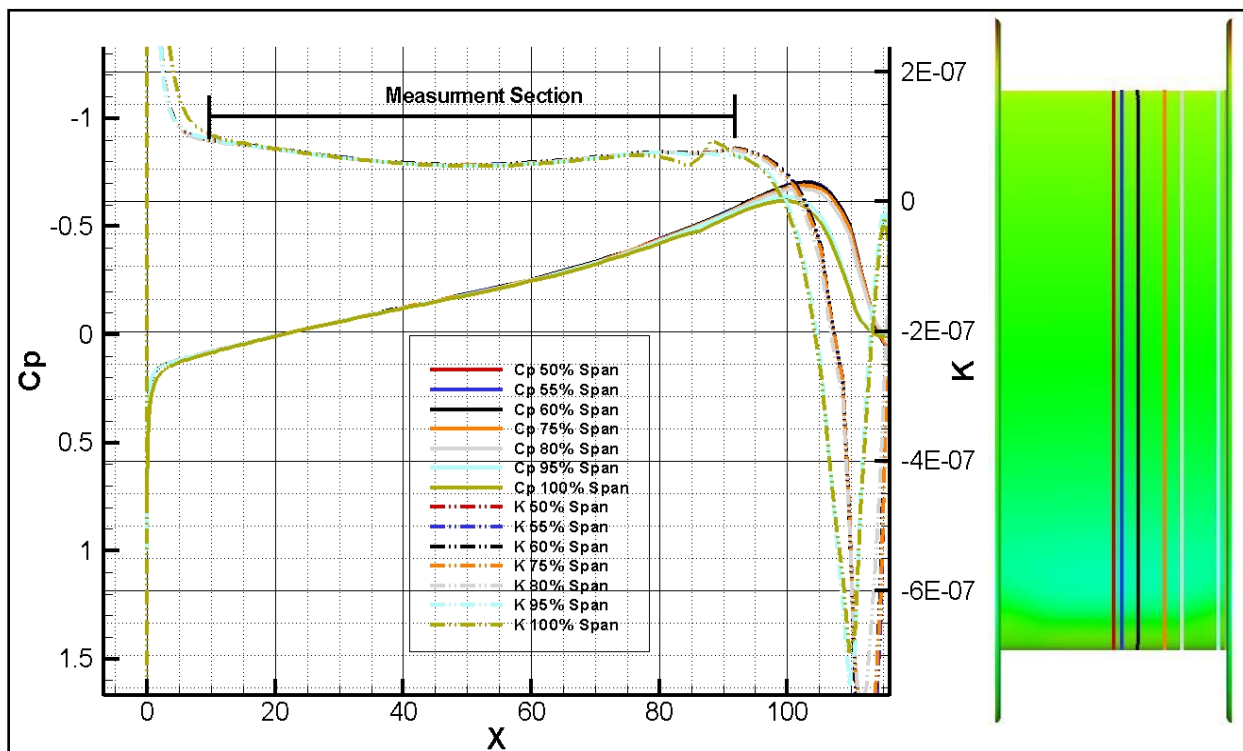


Figure 29: Gradient-A C_p distributions at various span stations.

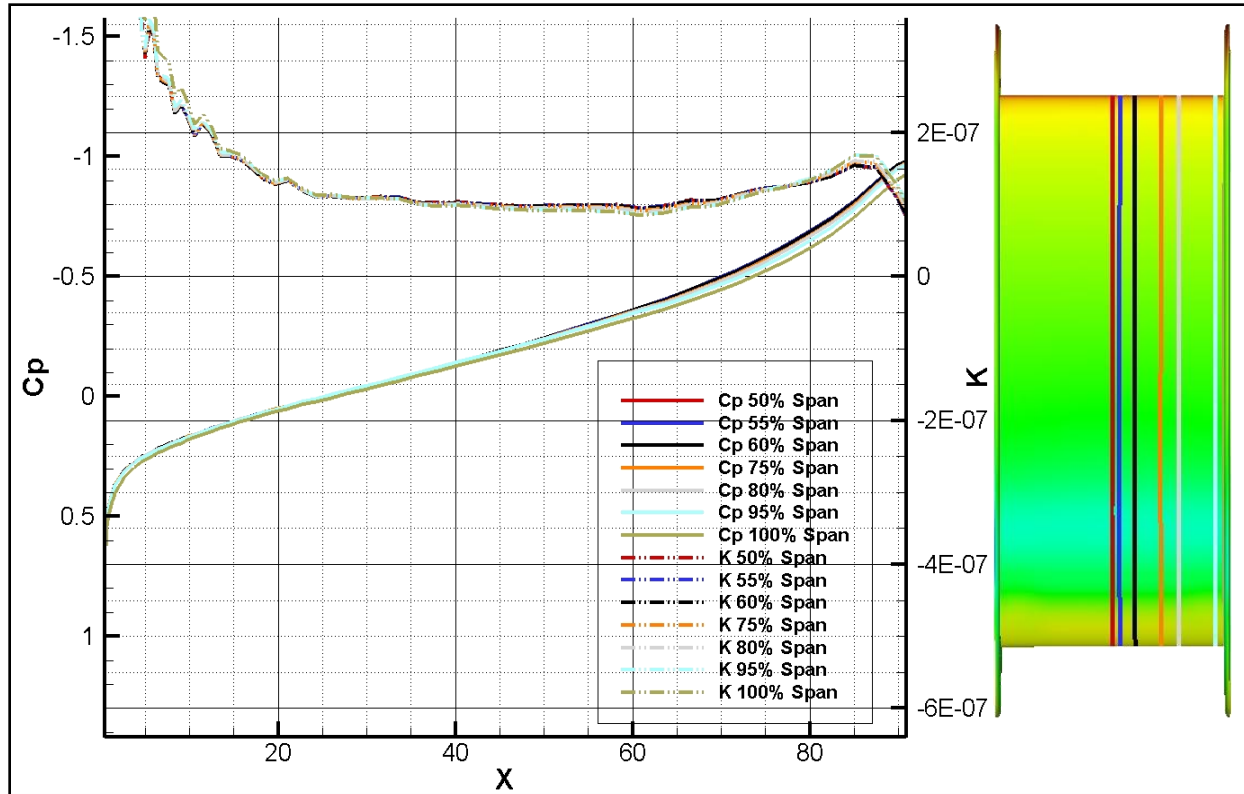


Figure 30: Gradient-B Cp distributions at various span stations.

Figures 31 and 32 illustrate the K distribution in span at chordwise locations (denoted in inches as XS) on the Gradient-A and Gradient-B models. The off-target K values in the leading edge region seen in the Cp plots, which result from the required leading edge shape, are readily apparent in the spanwise K distribution charts. However, even in this leading edge region where the pressure gradient is steeper than the target, the spanwise uniformity remains high.

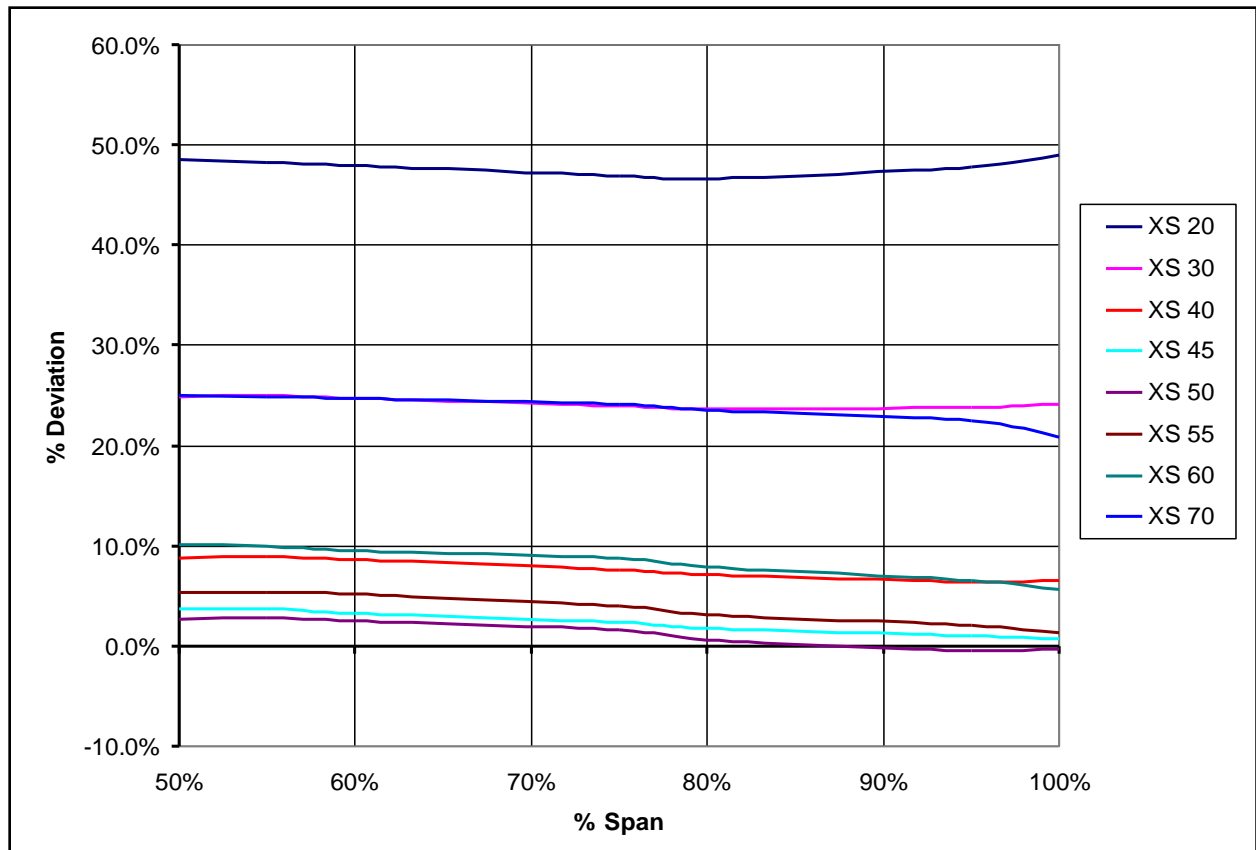


Figure 31: Gradient-A spanwise percent deviation from target K values.

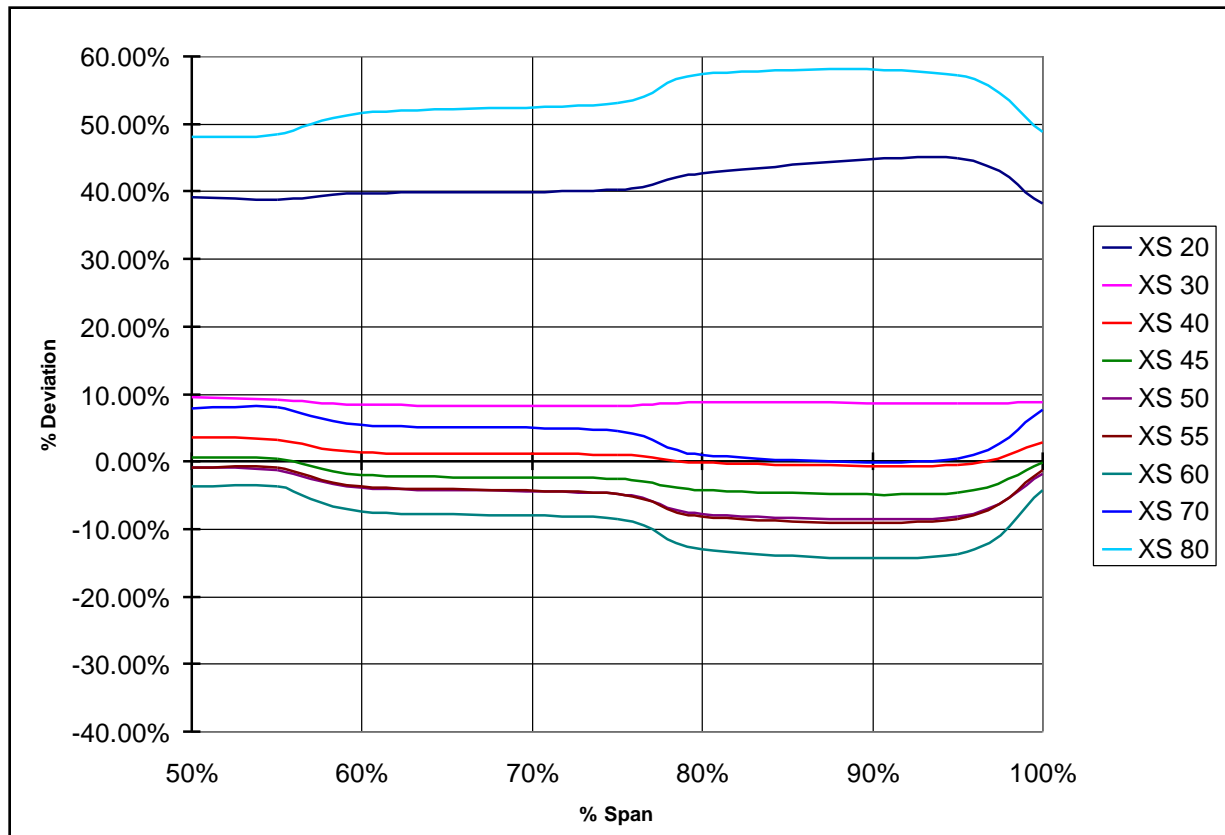


Figure 32: Gradient-B spanwise percent deviation from target K values.

4.1.2 Modeling of Wind Tunnel Installation Effects

Data obtained during the initial shakedown test indicated that there was a small discrepancy between the CFD predicted surface pressures and the measured data. After some investigation it was determined that the model-mounted Pitot probe was close enough to the model itself to be influenced. This Pitot probe provides the reference pressures for the test measurements and any difference in its values from the freestream would be readily apparent in a comparison of the CFD and measured pressures. Looking at the 3-D CFD results it was clear that at the location of the Pitot-probe the pressure coefficient was roughly .045, not zero. While this small difference had little effect on the data, it explained the noted discrepancy between the CFD results and the test data, thus increasing the confidence in the CFD calculations.

CFD analysis was also conducted with wind tunnel walls included in the model. Due to modeling limitations, these walls were idealizations of those in place in for the shakedown test and the testing in the TWT. The effects of the walls resulted in a significant change in the pressure distribution for both the Gradient-A and Gradient-B models (see Figures 33 and 34). As shown in these figures, the effect of modeling the wall or modeling open air has a significant effect on the predicted pressure gradient for both Gradient-A and Gradient-B models.

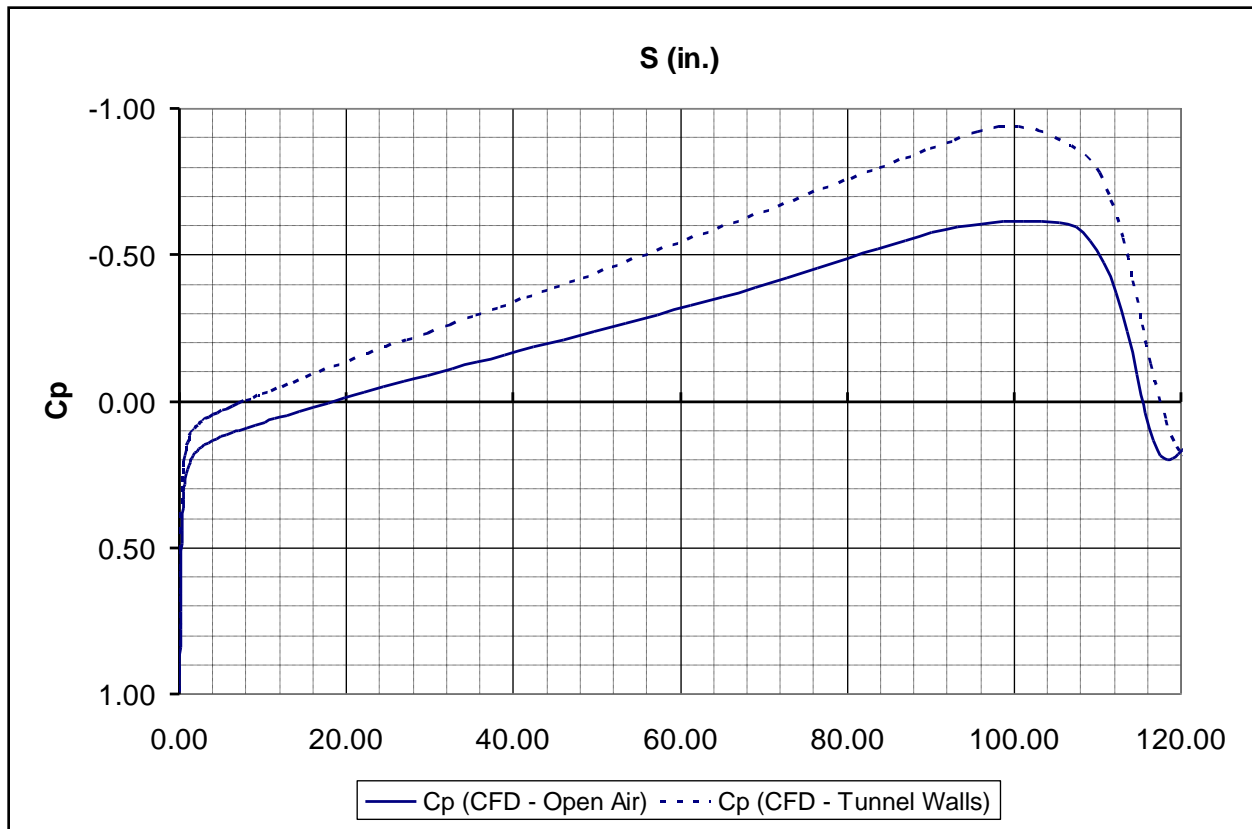


Figure 33: Gradient-A pressure distributions with and without tunnel walls.

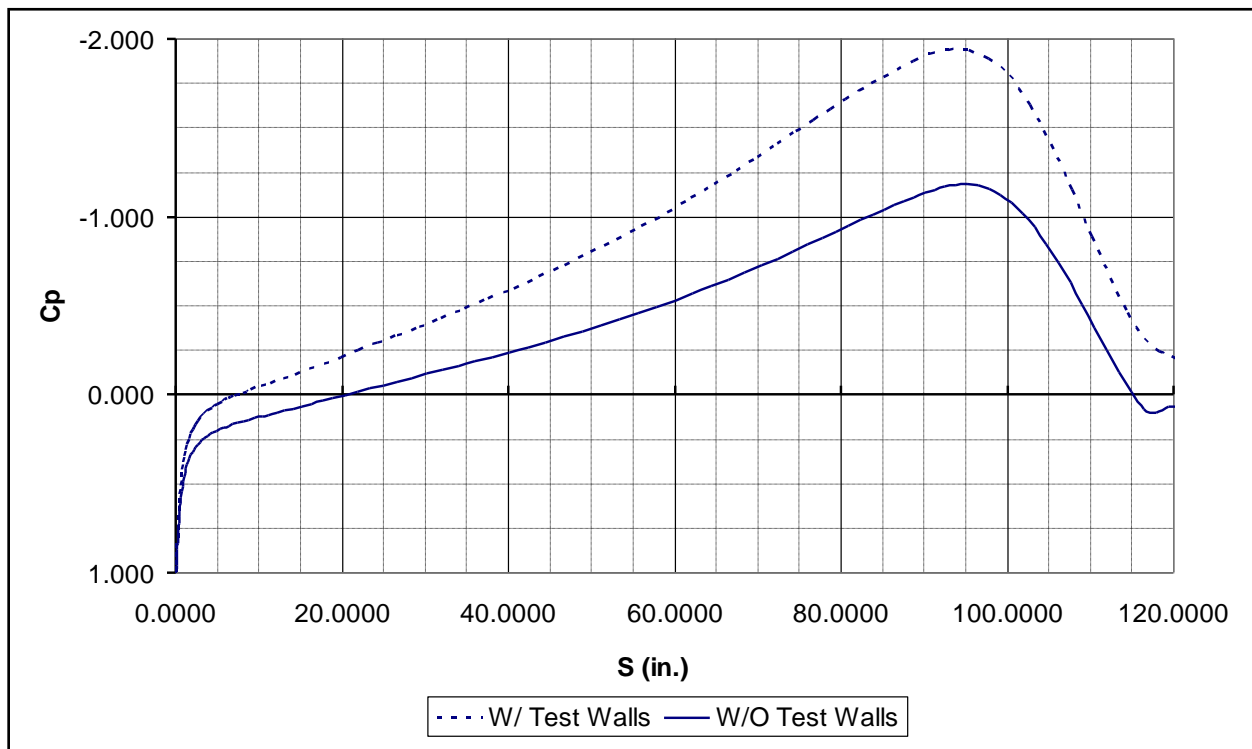


Figure 34: Gradient-B pressure distributions with and without tunnel walls.

The effect on the non-dimensional pressure gradient parameter, K , is shown in Figures 35 and 36.

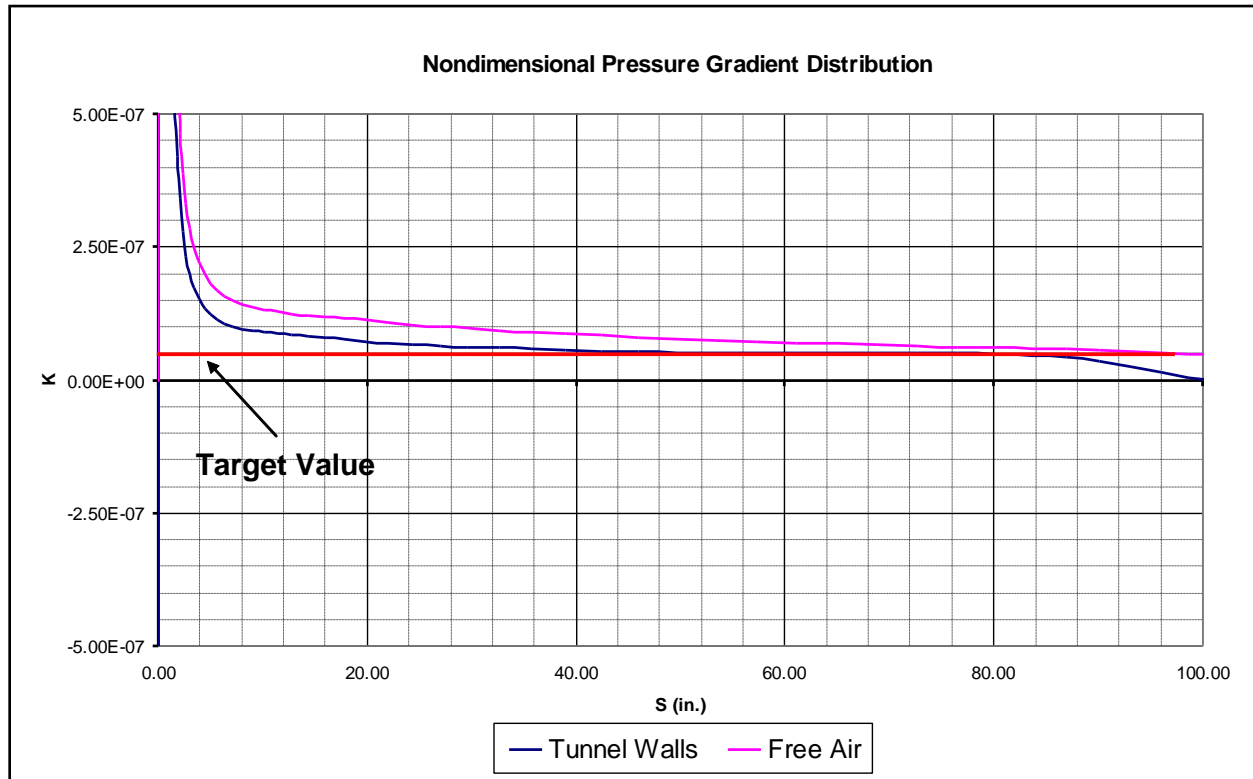


Figure 35: Gradient-A change in nondimensional pressure gradient.

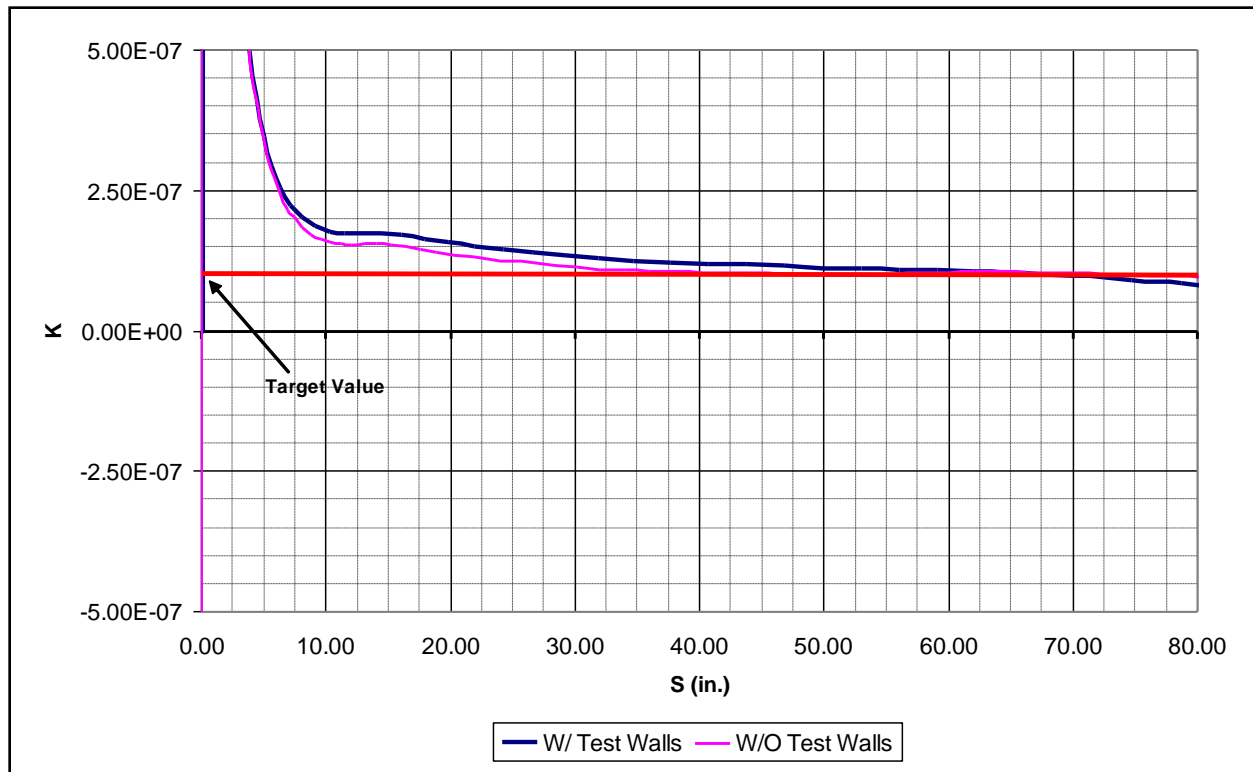


Figure 36: Gradient-B change in nondimensional pressure gradient.

Figure 37 shows a comparison of the pressure gradient for the Gradient-A model with the wind tunnel wall and Pitot probe corrections applied. The blue solid and dashed lines in Figure X are the same CFD results from Figure X, with open air and wind tunnel walls, respectively. Also plotted on this figure are the instantaneous experimental results (pink squares) and the experimental results after the aforementioned Pitot probe correction was applied (red diamonds). As can be seen in the figure, after the CFD correction for the wind tunnel walls and the analytical correction for the Pitot tube has been applied, the experimental results (red diamonds) closely match the CFD prediction (blue dashed line).

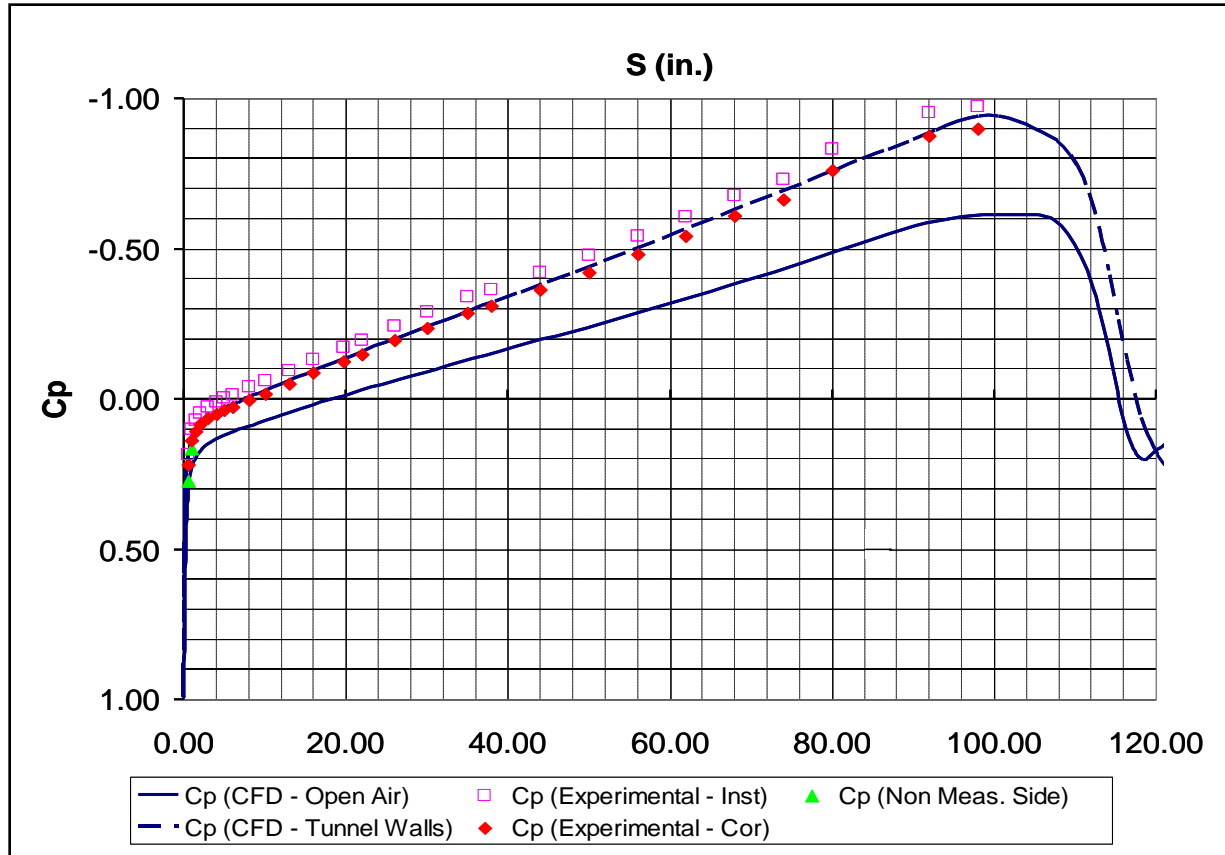


Figure 37: Gradient-A pressure distribution comparison with corrections applied.

4.1.3 Modeling of Unsteady Effects

Early in the model design it was evident that to attain the desired pressure distributions the Gradient-A and Gradient-B models would have a very broad aft end, creating a bluff body shape. Because the testing was to take place at such low dynamic pressures, concerns arose regarding the stability of the flow separating off the aft end of each model. In order to investigate whether the models exhibited significant vortex shedding 2-D time-accurate models for both the Gradient-A and Gradient-B models were created. Figure 38 illustrates the gridding technique that was used for the time-accurate cases.

This gridding scheme was employed to facilitate unsteady flow while running the time-accurate flow solver, CFL3D. In order to minimize analysis time and computational resources, the unsteady analysis was performed in 2-D. The 2-D analysis uses a Detached Eddy Simulation (DES) coupled with a Spalart-Allmaras (SA) turbulence model. This 2-D unsteady analysis is very conservative. It is shown in Figure 39 that the Gradient-B model is the limiting case because its shedding vortices are much stronger than that of the Gradient-A model. Therefore, only the Gradient-B analysis is presented.

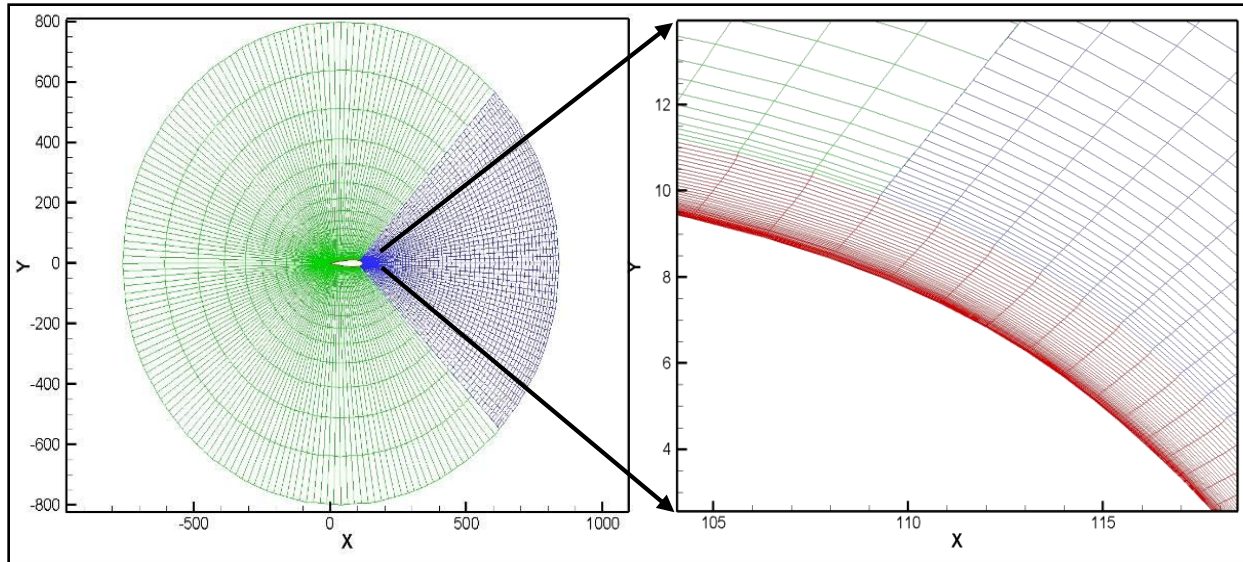


Figure 38: Gradient-B time-accurate gridding scheme.

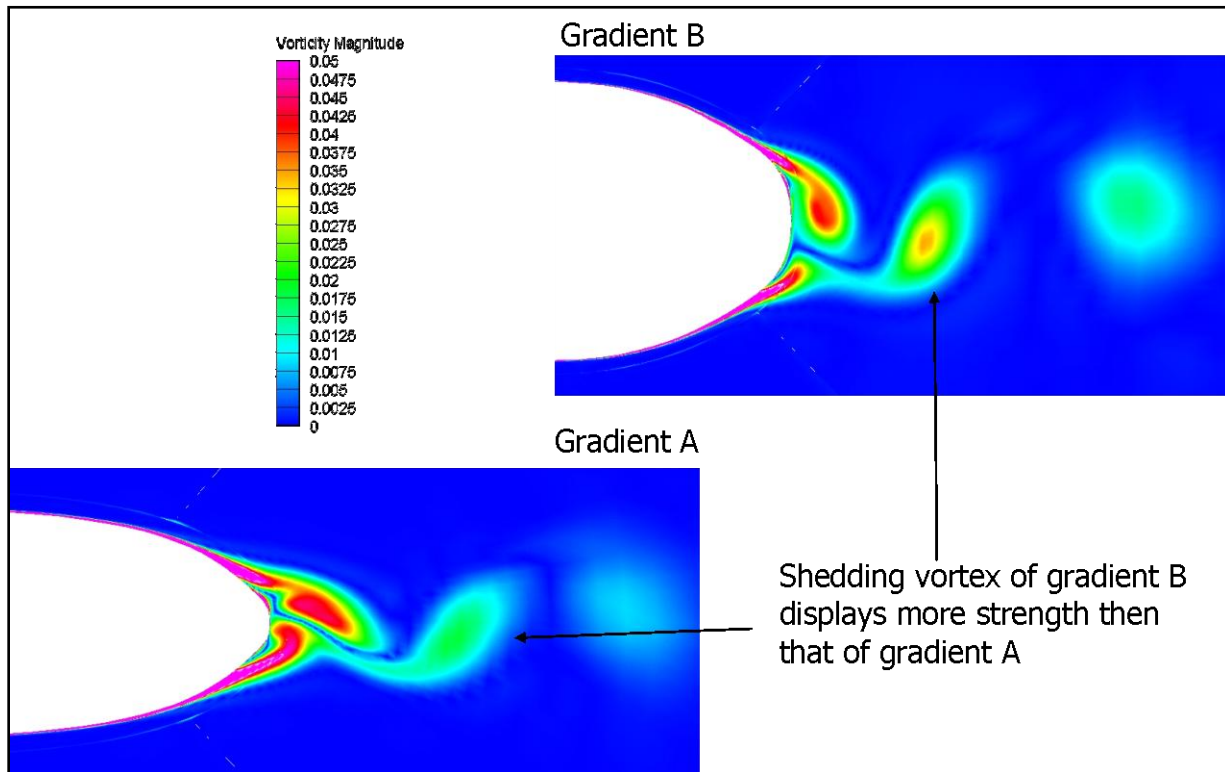


Figure 39: Comparison of shedding vortices for the Gradient-A and Gradient-B models.

Figure 40 displays the temporal lift variation with and without an extension (see Figure 41) that was used to mitigate vortex shedding. The frequency of the vortex shedding was found to be less than that of the Tollmien-Schlichting waves and therefore will not induce early transition. Also, because the model does exhibit low frequency vortex shedding, it was necessary to analyze how much the stagnation point moved and if this would also effect the transition location of the model.

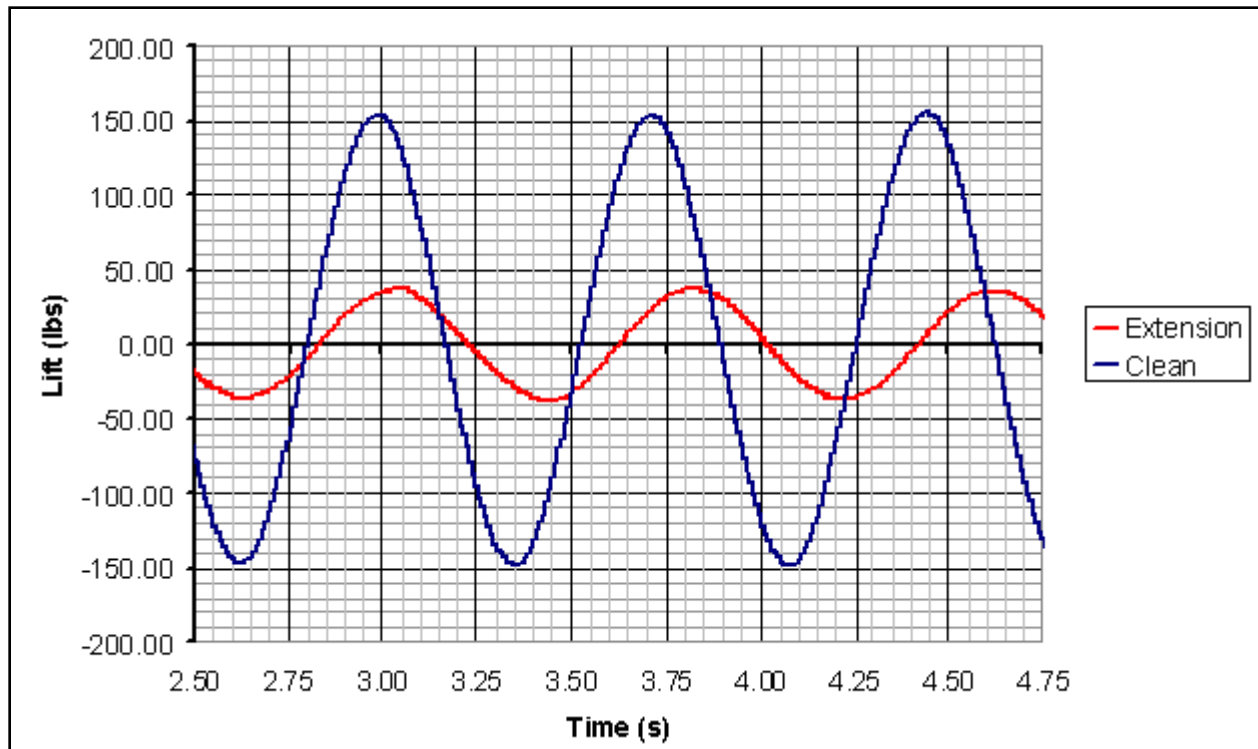


Figure 40: Temporal lift distribution for the Gradient-B model.

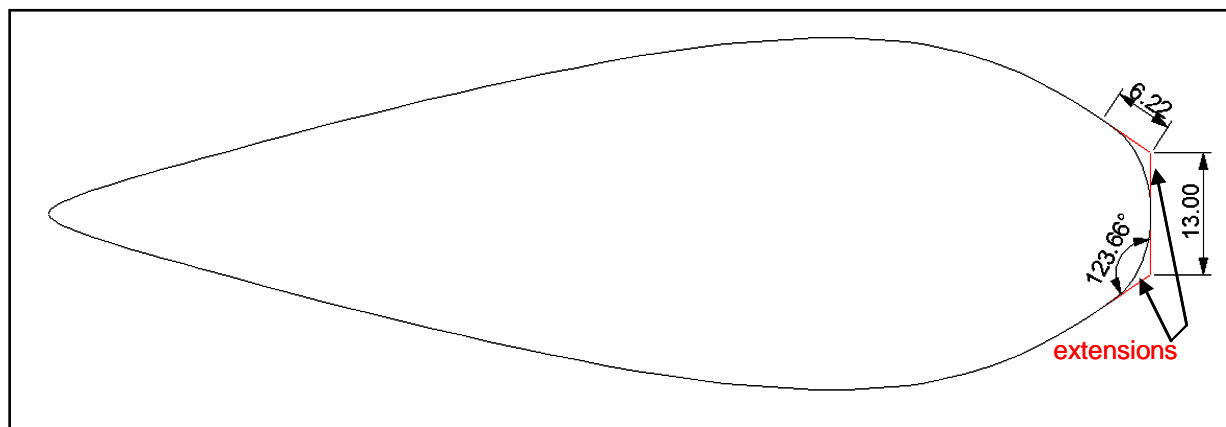


Figure 41: Gradient-B with an aft extension.

Figure 42 displays the center of the stagnation point and maximum stagnation point travel due to the vortex shedding. It was seen the stagnation point travel due to the vortex shedding is acceptable and will not induce early separation. A similar analysis was performed for the Gradient-A model with comparable results. It was then concluded that the vortex shedding had negligible effect upon the models and therefore no further action was required. No modification was made to Gradient-B for the testing at the Towing Wind Tunnel.

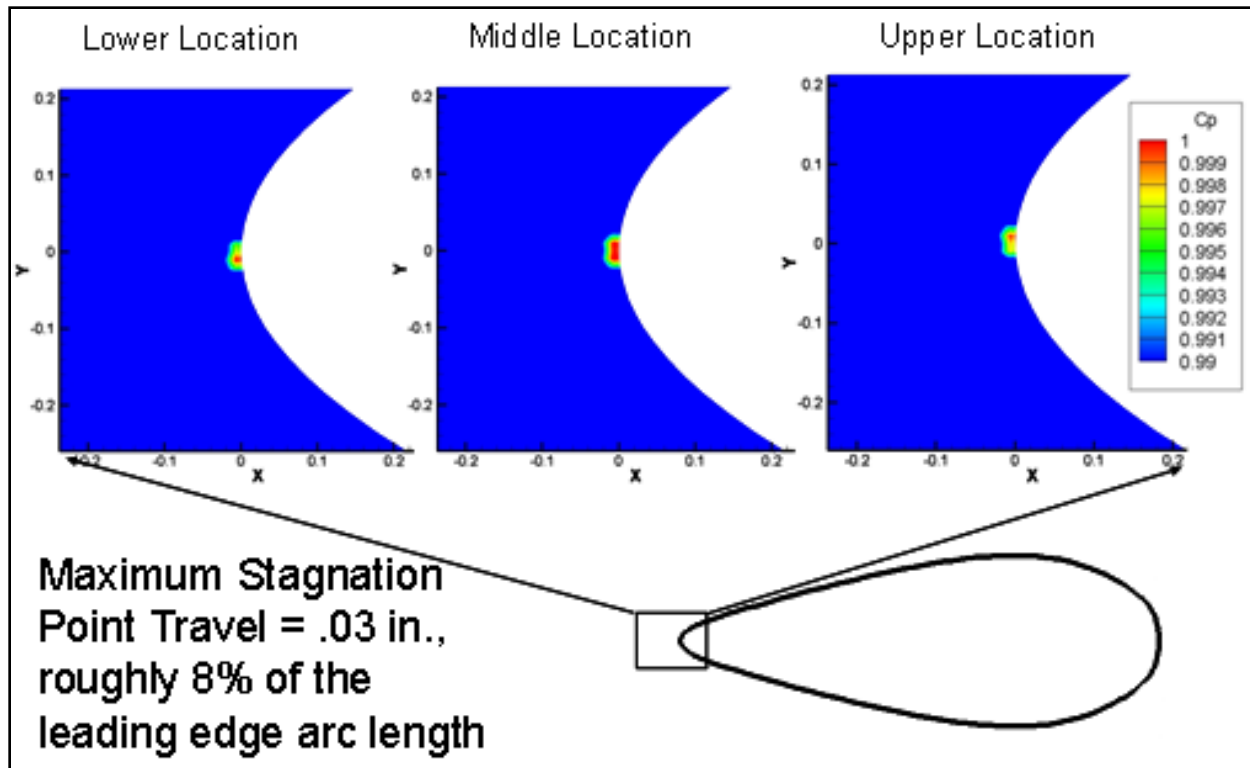


Figure 42: Gradient-B stagnation point travel.

4.2 Model-Integrated Instrumentation

Two chordwise rows of static pressure taps and one row of spanwise taps were installed on the models to measure the pressure distributions. The chordwise static pressure tap distribution was denser near the leading edge and spaced more coarsely towards the aft end of the models (see Figure 43). Two pressure taps per chordwise row were located on the non-measurement (or “reference”) side of the model, in order to help assess the location of the stagnation point. A detailed list of each pressure tap number and its corresponding percent chord location can be found in Appendix A. The coordinate system used for the models is shown in Figure 44.

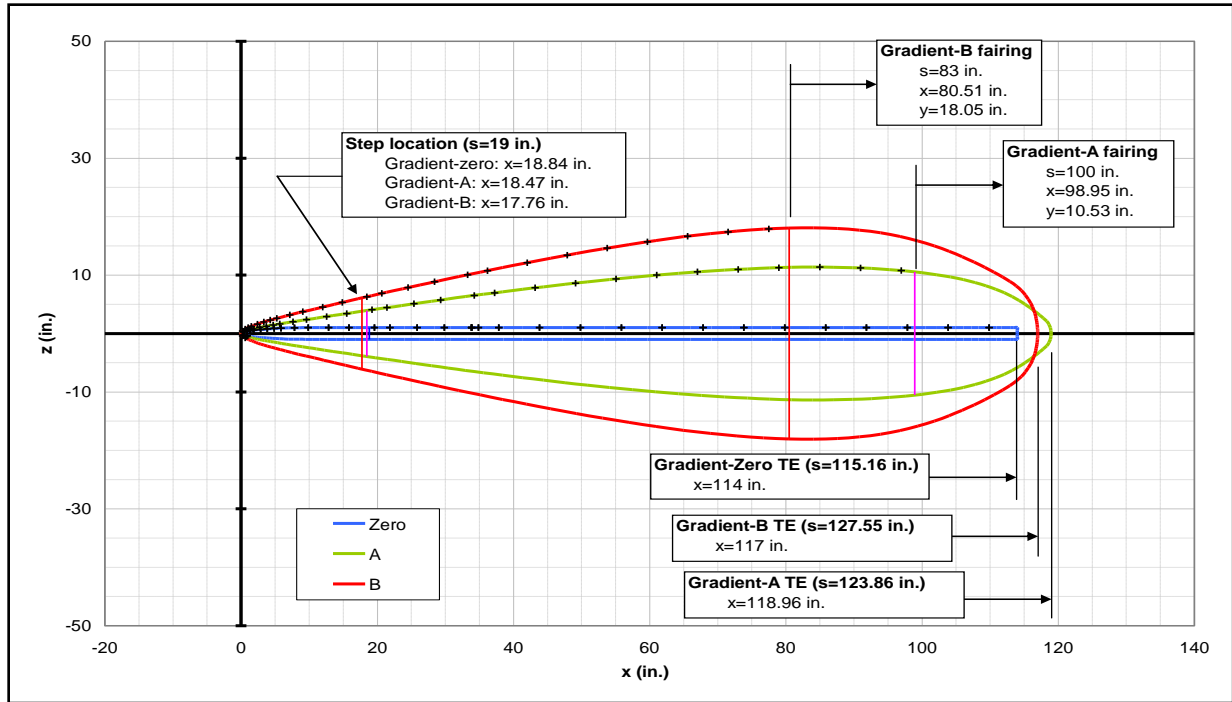


Figure 43: Model shapes and static pressure tap locations.

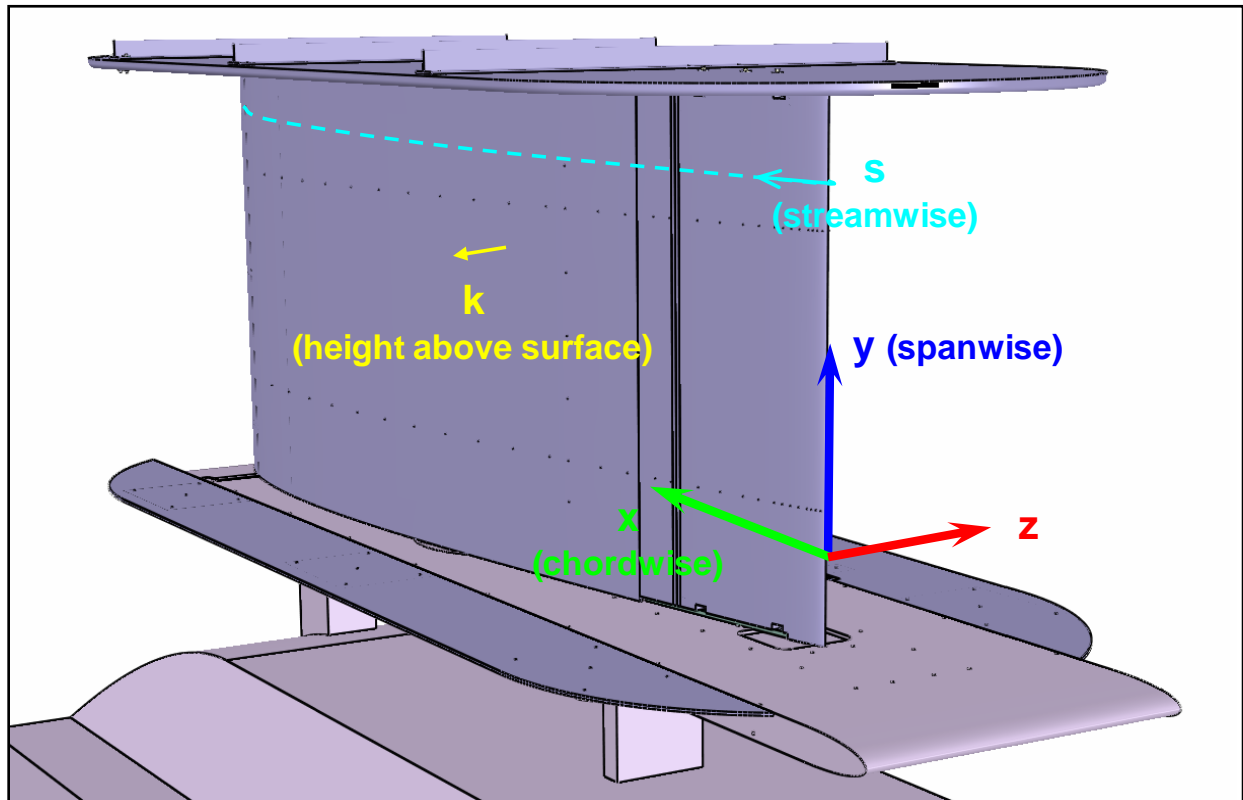


Figure 44: Coordinate system for SETS models.

4.3 Model Construction

The models are constructed from 6 major components including an aluminum frame, a forward (leading edge) assembly, the measurement surface panel, the non-measurement (reference) surface panel, and the upper and lower splitter plates. The aluminum frame and splitter plates are common to all 3 models. The surface panels and leading edge assemblies are specific to each of the 3 models. An exploded view of the model assembly with Gradient-Zero is shown in Figure 45 and the forward sub assembly of Gradient-Zero is shown in Figure 46.

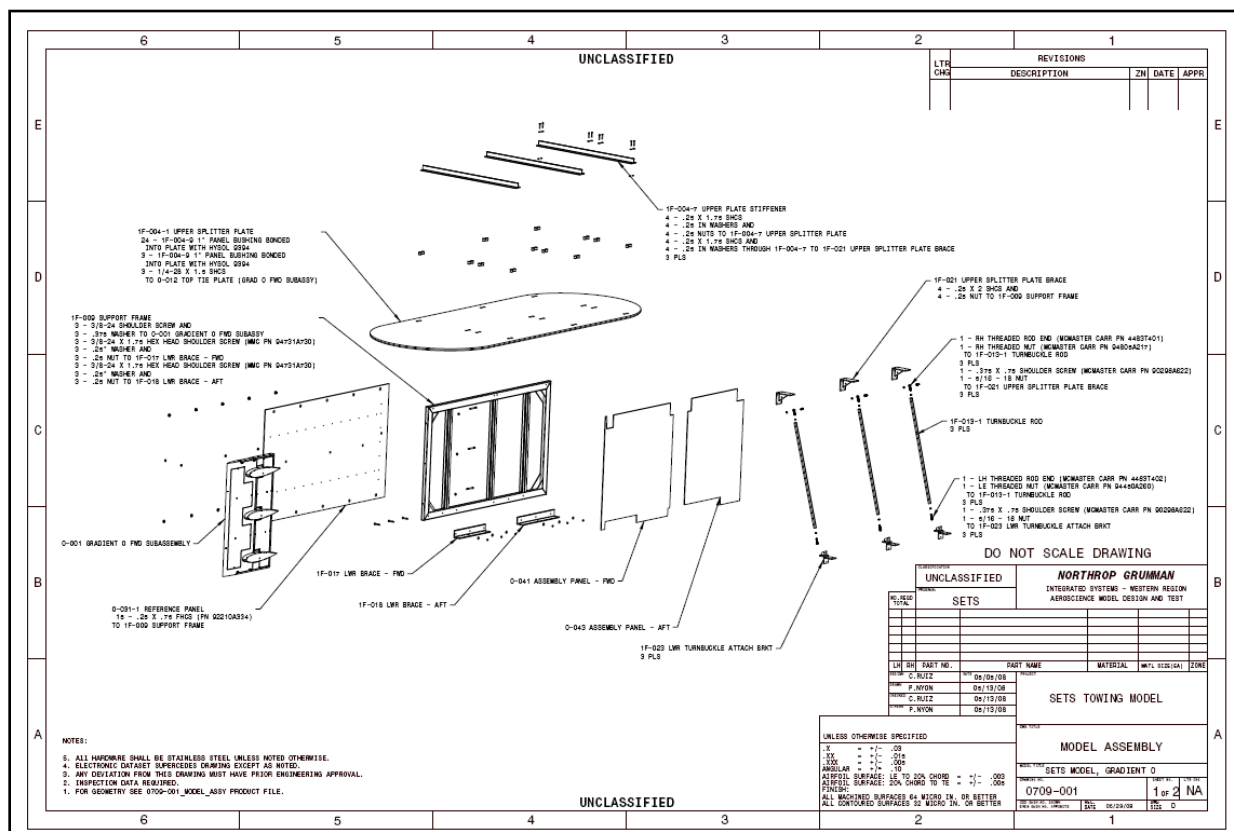


Figure 45: Gradient-Zero model exploded assembly drawing.

The forward subassembly includes the leading edge assembly and the midsection assembly. The leading edge assembly incorporates an assembly to move it laterally such that 0.001" incremental step heights can be created. The step that is created is the same for the entire vertical length of the leading edge assembly. The leading edge assembly is not allowed to "rack" relative to the rest of the model. Aft of the leading edge assembly there is a midsection assembly. This is the section of the model that the leading edge moves relative to. Aft of the midsection is the remaining OML of the model. There is also an upper and lower splitter plate. The lower splitter plate serves as the interface between the model and the mounting hardware on the HART carrier vehicle. The models were designed to tie-in to existing holes on the HART vehicle's existing lower splitter plate. Turnbuckles and struts were used to stabilize the upper and lower splitter plates.

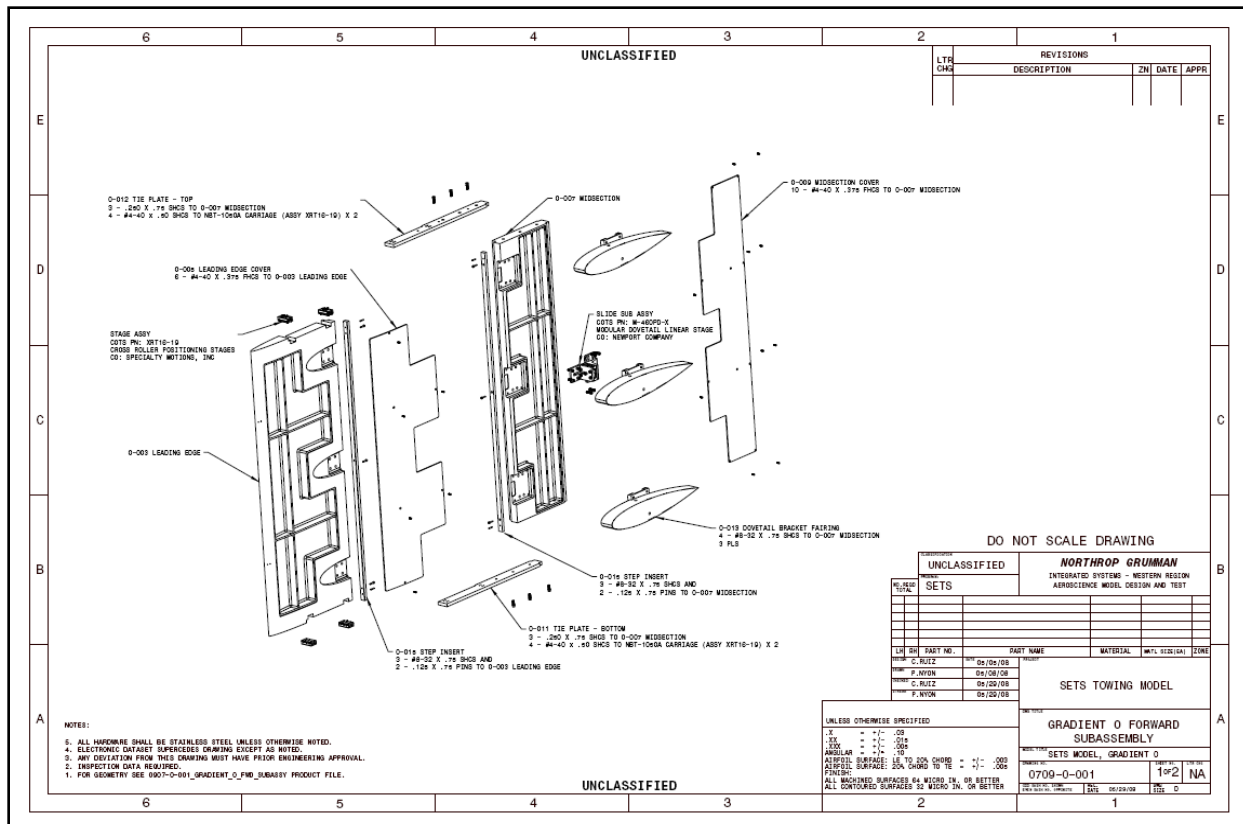


Figure 46: Gradient-Zero model forward subassembly drawing.

The majority of model components were CNC machined from CAD models. The leading edge and midsection assemblies were made from aluminum-6061. The leading edge pieces of the Gradient-Zero (see Figures 47 and 48) and Gradient-A (see Figure 49) models were manufactured from a single solid aluminum billet. The Gradient-B leading edge, because of its size and billet availability, was not cut from a single piece of aluminum, but the Gradient-B leading edge, as with the Gradient-Zero and Gradient-A models, had no split lines on the OML. Instead, the interface was located on the non-measurement side of the model, underneath the cover.

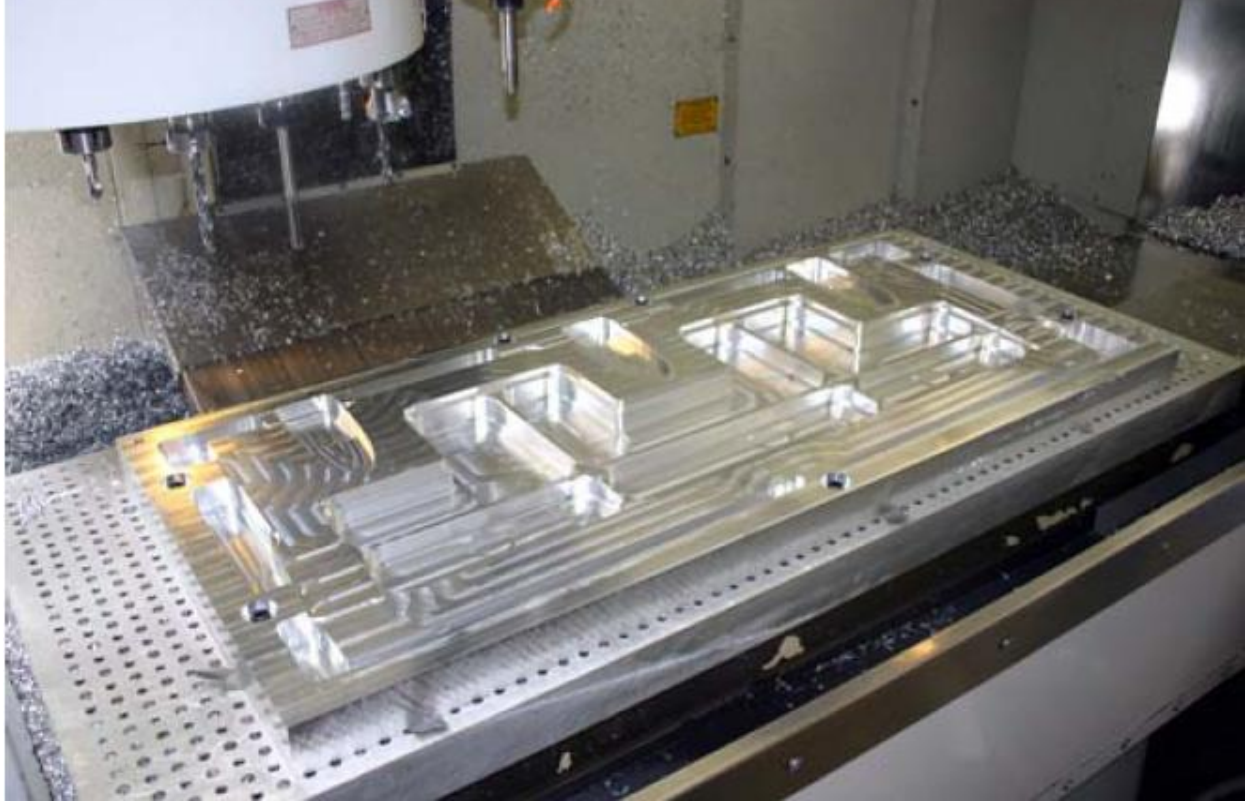


Figure 47: Gradient-Zero leading edge (non-measurement side) in CNC machine

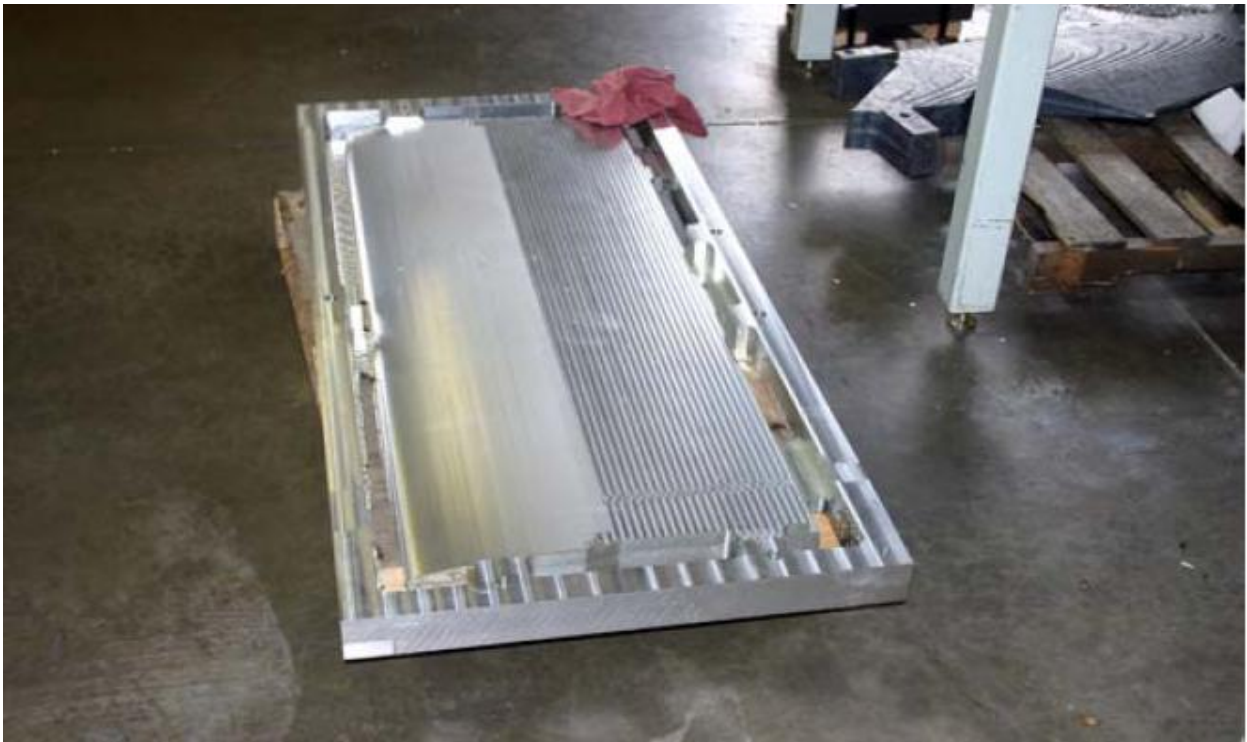


Figure 48: Gradient-Zero leading edge piece (measurement side) before handwork



Figure 49: Gradient-A leading edge (non-measurement side)

The area surrounding the step location was stainless steel, to ensure the tolerance, perpendicularity, and rigidity of the step excrescence. The side tie plates, which support the weight of the model as steps are dialed in, are also stainless steel.

The measurement side and non-measurement side skins are a fiberglass layup. The skins on the non-measurement side include access panels for instrumentation and step adjustment. The measurement side skins have no access panels so as not to disturb the boundary layer being measured. A master skin panel model was fabricated to serve as a lay up mold to produce the skins as well as the access panels. This master model was made from General Plastic's 4530 foam. The actual model skins were fabricated using Advanced Composites Group LTM 12 GFO 100 face plies and GFO 700 bulk plies (see Figure 50). The back structure was made from $\frac{1}{4}$ " thick solid laminate (see Figure 51). The skins and access panels were painted with gray Durra Build primer. An inspection of the master skin was done with a Laser Tracker. The inspection results for the fiberglass skin panels are shown in Figures 52-55. A Laser Tracker inspection of the fiberglass skin panels showed the worst-case OML variation was less than 0.010 inches. The maximum OML variation was seen at the edges of the model at the interface of the splitter plate, which is outside the measurement region. Significantly tighter tolerances were held throughout the measurement region.



Figure 50: Gradient-A composite skin under vacuum.



Figure 51: Backbone structure being attached to Gradient-A skin.

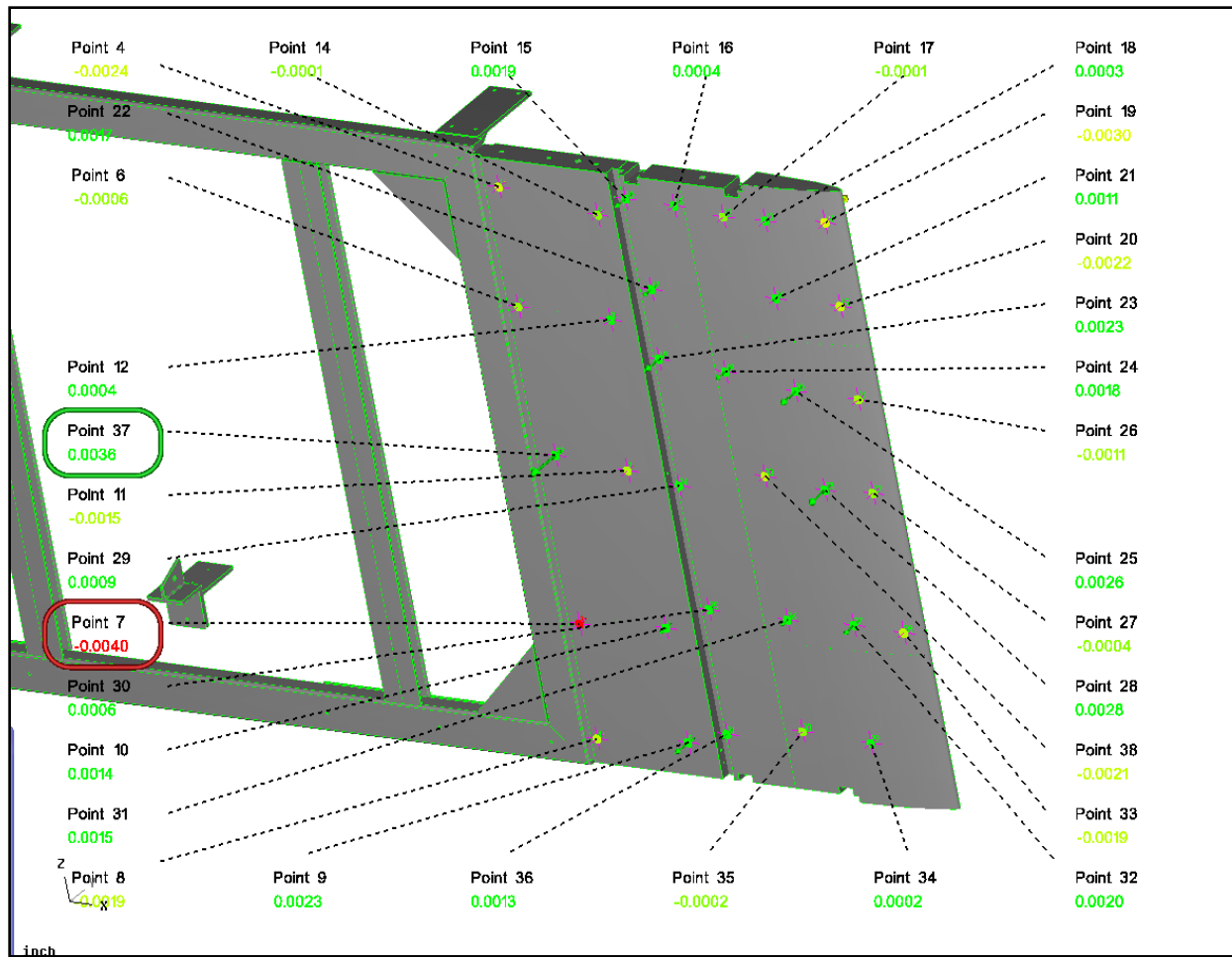


Figure 52: Gradient-Zero leading edge and midsection inspection results, measurement side.

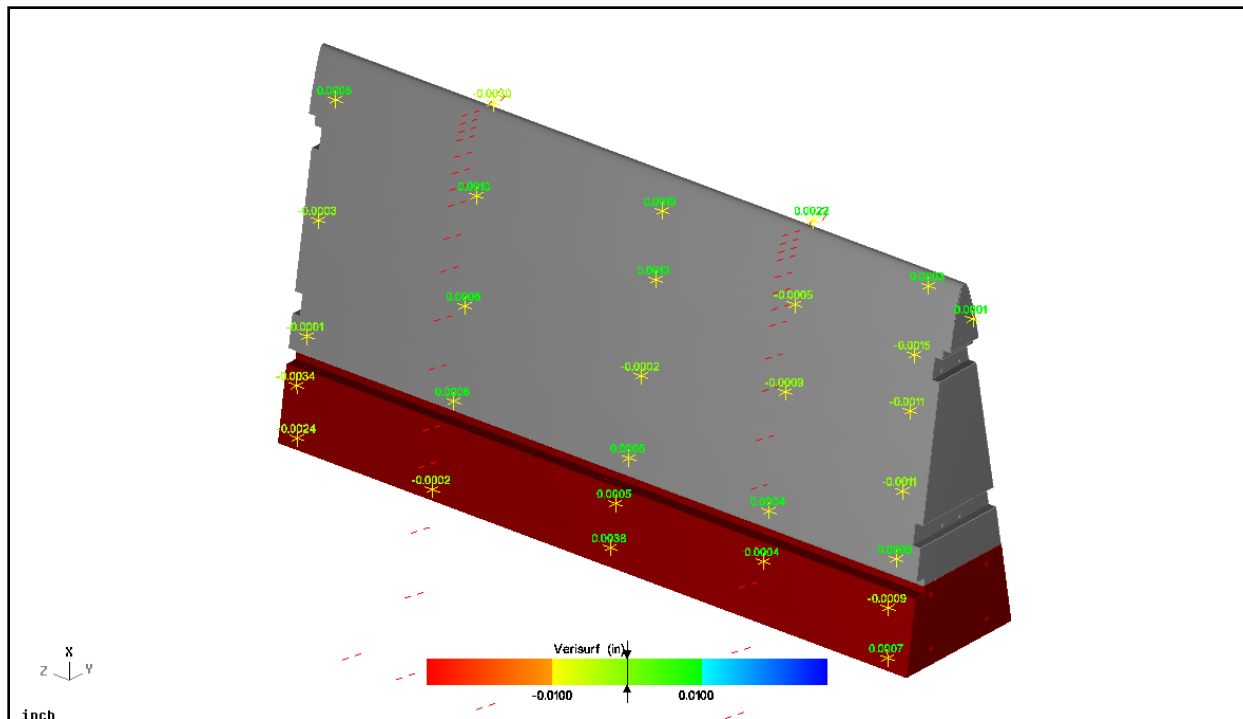


Figure 53: Gradient-A leading edge and midsection inspection results, measurement side.

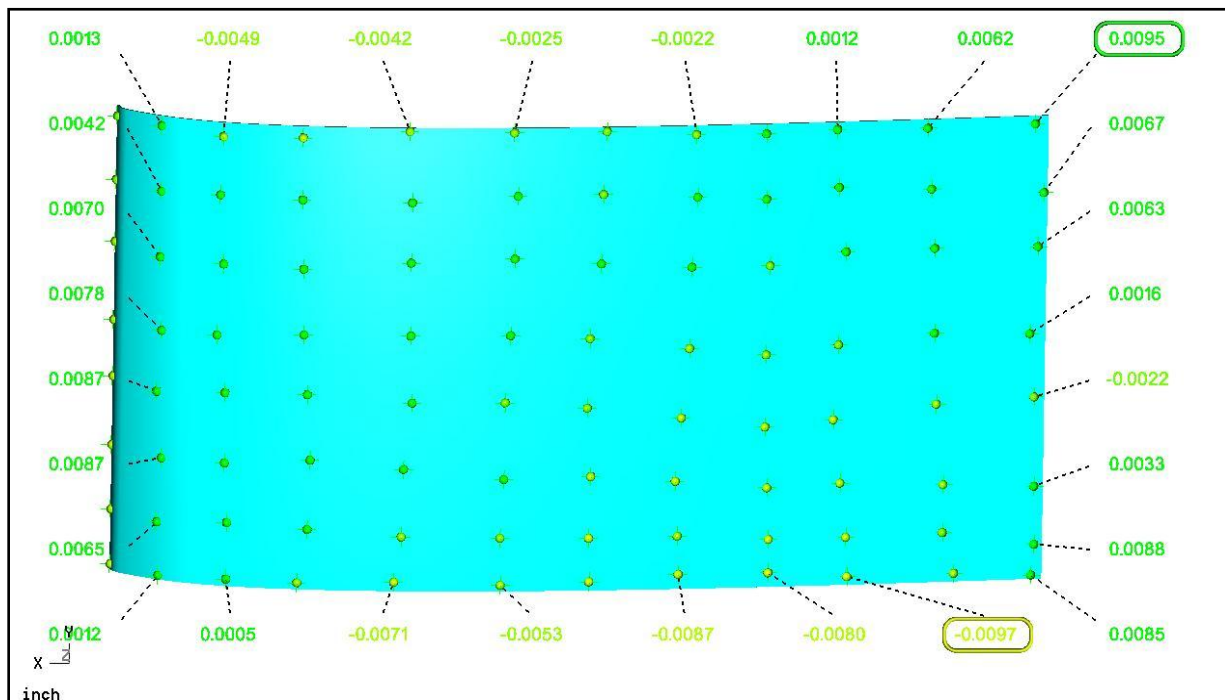


Figure 54: Gradient-A fiberglass panel inspection results, measurement side.

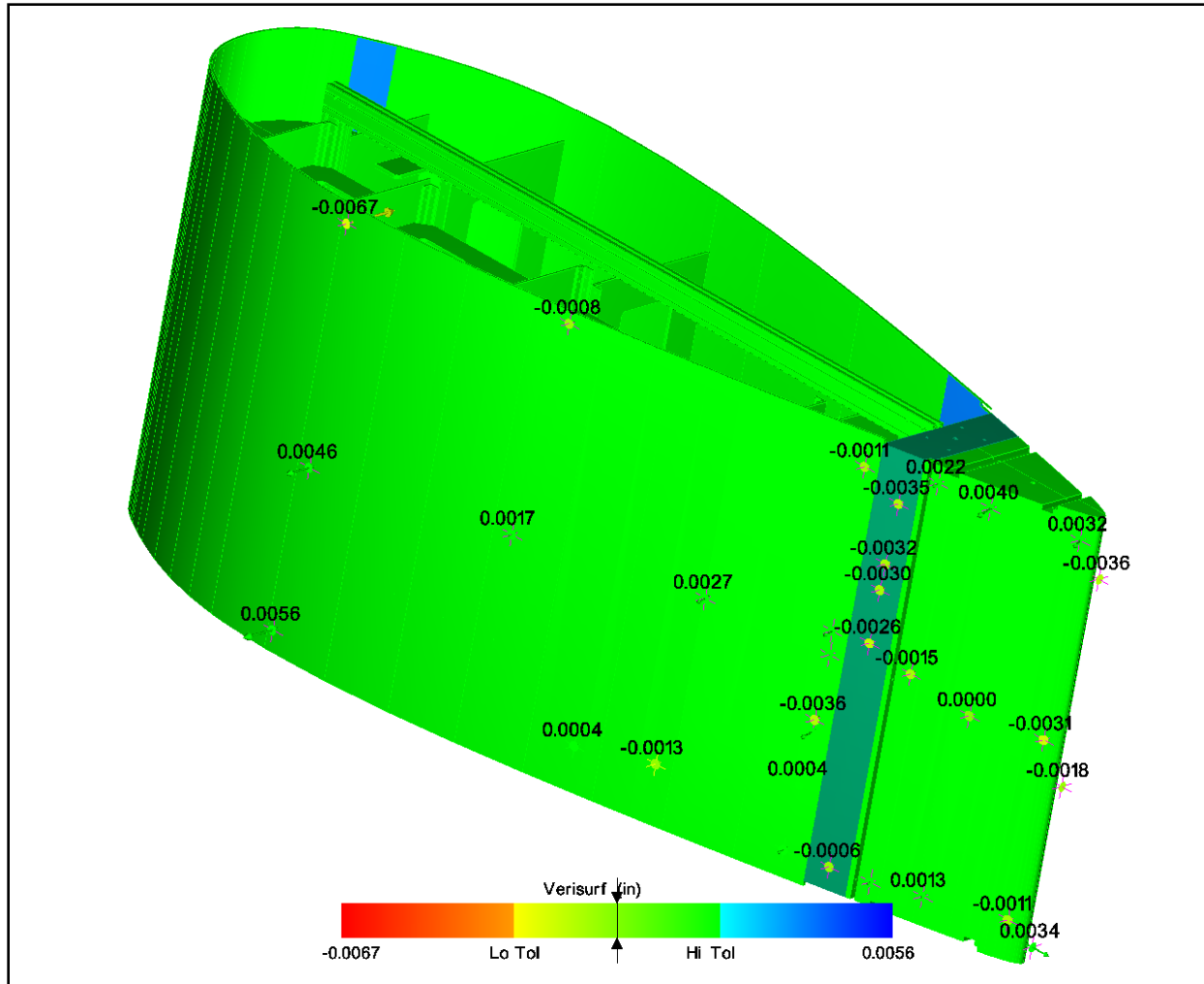


Figure 55: Gradient-B assembly inspection results, measurement side.

Additionally, a stress report was produced that covered all 3 models in the 7x10 Wind Tunnel and at the Towing Wind Tunnel. The factory of safety was deemed satisfactory for all applications. For details, see Appendix B

Static pressure taps were installed in each of the three models. The pressure taps were 0.063" stainless steel hard lines, extending a minimum of 4 inches from the port or location where the hard line exits the model structure. The termination of all pressure tubes was accessible from the non-measurement side of the model. At the termination of the hard-lines, Tygon tubing was connected and routed inside the model. This tubing exits the model at the aft end of the non-measurement side of the model. The Tygon tubing was sufficient length to reach the pressure transducer modules without requiring any tubing splices.

4.4 Predicted Skin Friction Coefficients

A 2-D boundary layer code called IBL⁴ was used to predict the skin friction coefficient distributions on the models. IBL computes 2D laminar, transitional, or turbulent boundary layers with or without prescribed arbitrary distributions of surface pressure, heat transfer, and/or mass transfer. Input into the code was the CFD predicted pressure distributions and nominal flow conditions. The resultant skin friction coefficient distributions, assuming both fully laminar flow and flow that is turbulent starting at the step location, are shown in Figures 56 through 58 for each of the models. The predicted skin friction distributions based on predicted pressure distributions were not used in the final analysis of the data. For the final data analysis, the actual measured pressure distributions were used exclusively since these are the conditions under which the boundary layer developed.

IBL also outputs boundary layer properties such as the displacement thickness, momentum thickness, boundary layer thickness, and velocity profiles, as a function of x . The IBL results were used to help set expectations of relative skin friction levels and to help size the instrumentation such as the Preston tubes. The IBL-predicted boundary layer thickness for each of each of the three models is shown in Figures 59-61.

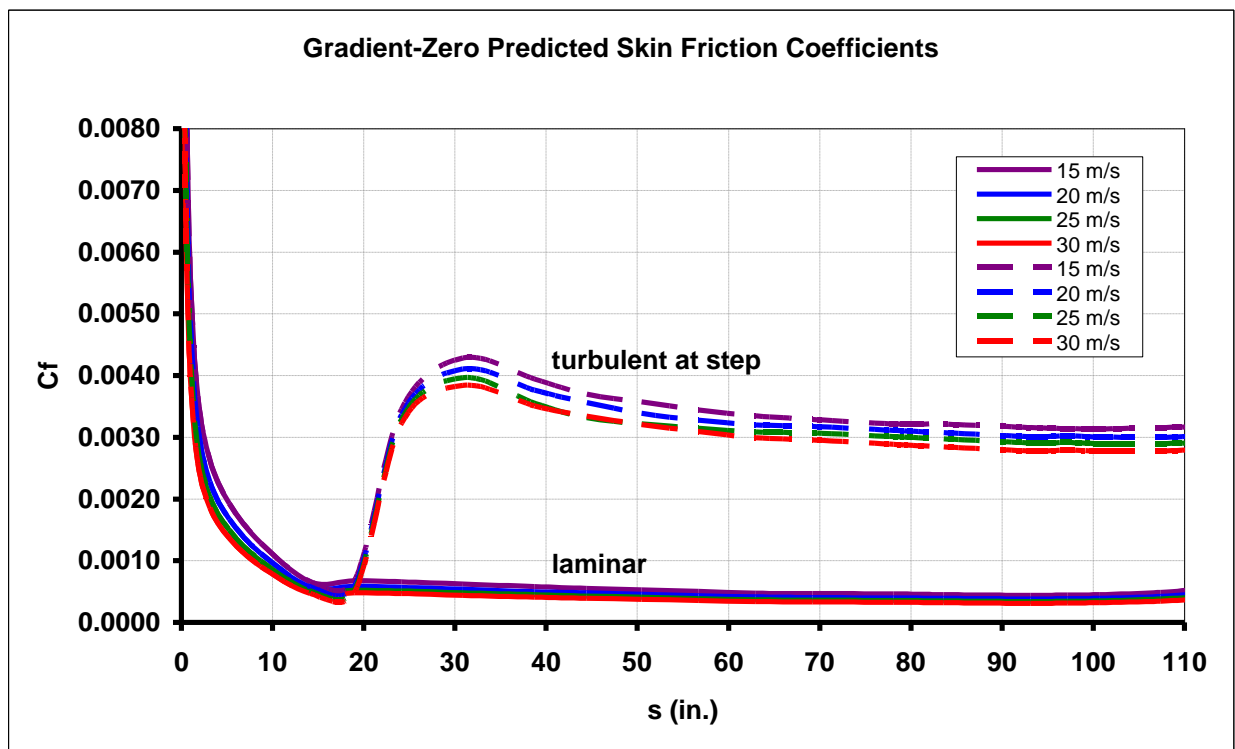


Figure 56: Gradient-Zero predicted skin friction coefficient distribution.

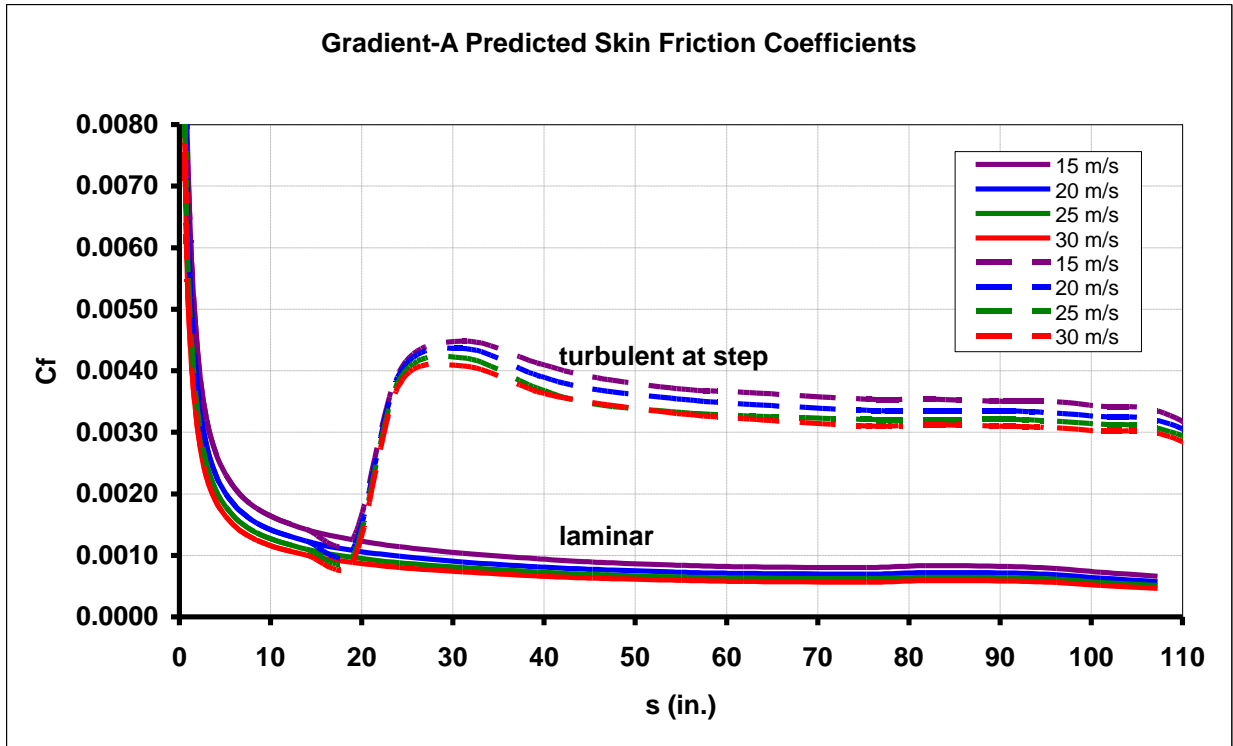


Figure 57: Gradient-A predicted skin friction coefficient distribution.

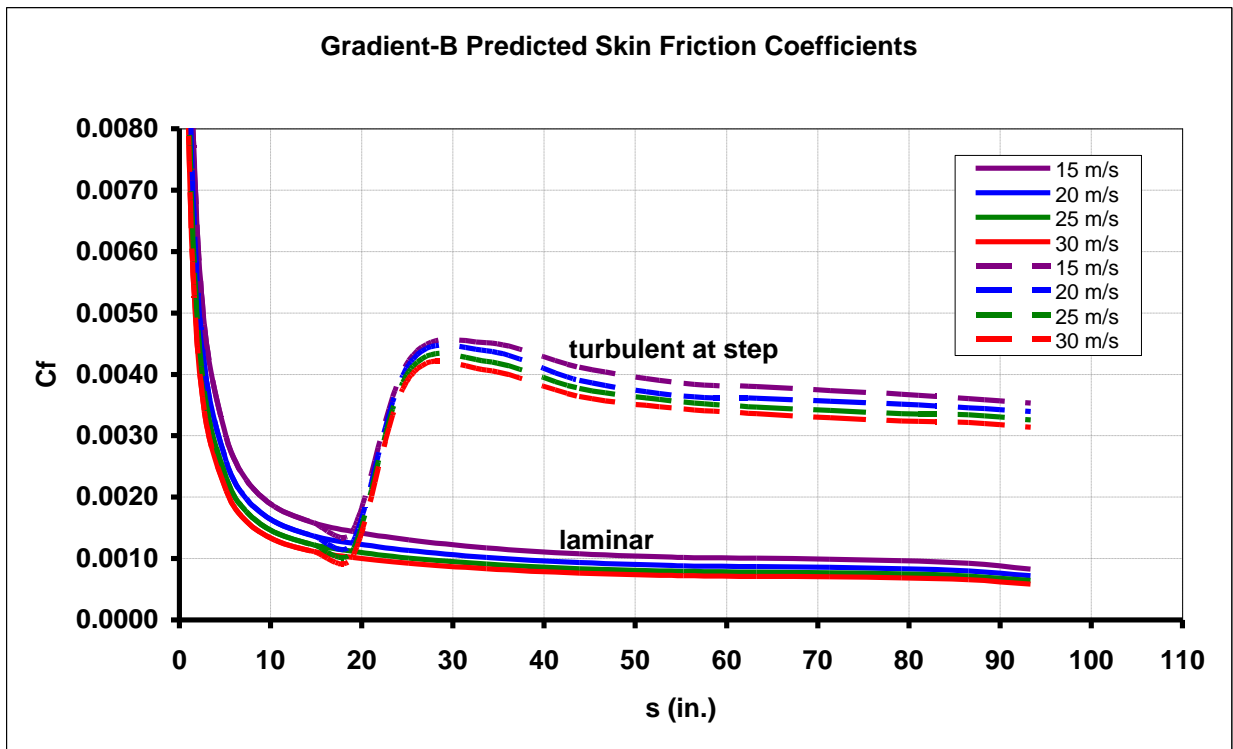


Figure 58: Gradient-B predicted skin friction coefficient distribution.

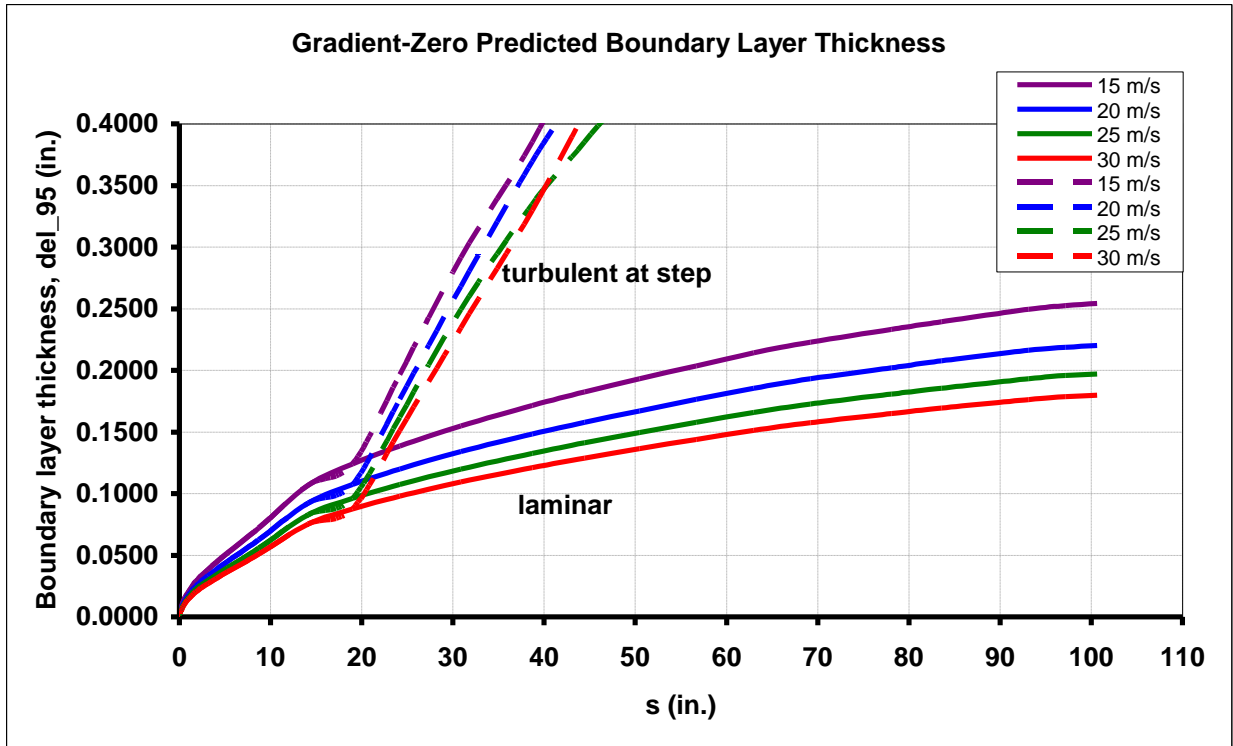


Figure 59: Gradient-Zero predicted boundary layer thickness.

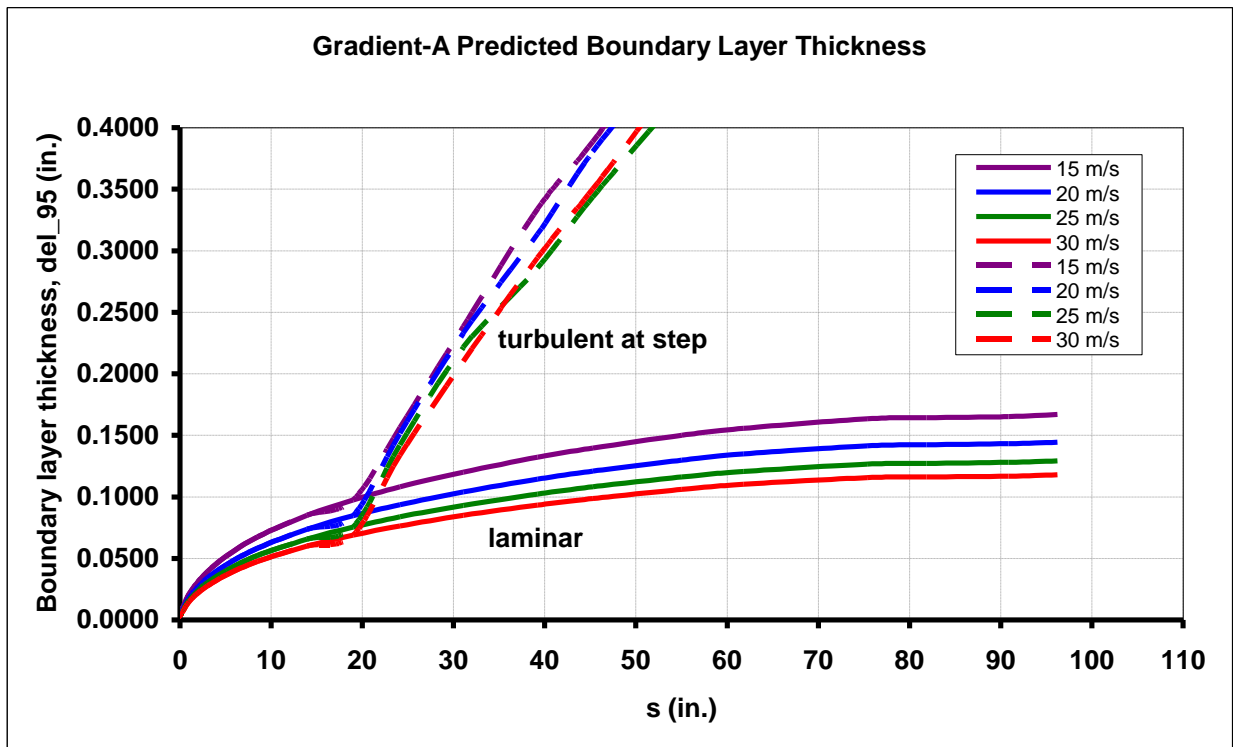


Figure 60: Gradient-A predicted boundary layer thickness.

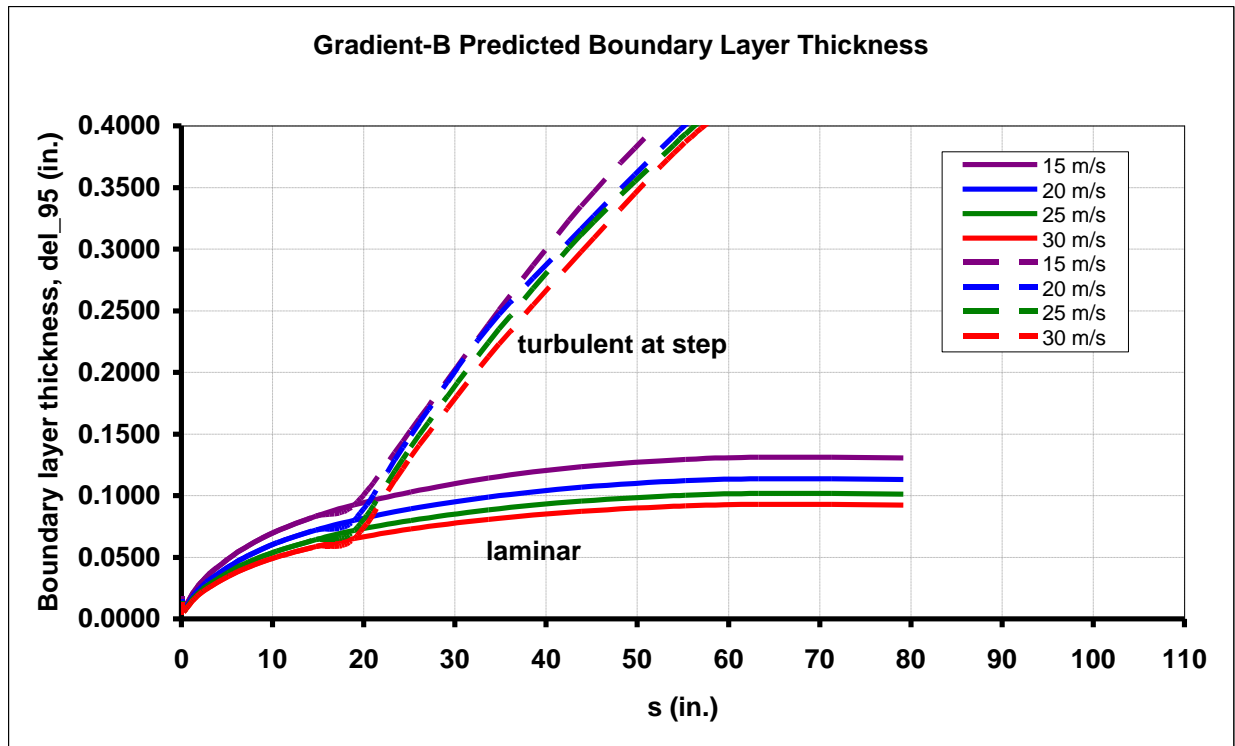


Figure 61: Gradient-B predicted boundary layer thickness.

5.0 SHAKEDOWN TEST

The facility used for the SETS testing—the Towing Wind Tunnel (TWT) in Hyuga, Japan—was fairly remote from the established model and test support resources of NGC. For this reason, it was deemed necessary to perform extensive checkout of the model and systems prior to shipping these components to the test facility. To accomplish this, shakedown testing was conducted in the NGC 7-x10-ft Wind Tunnel. Two one-week shakedown wind tunnel test entries were conducted, the first shakedown test was August 11-15, 2008 and the second shakedown test was September 8-12, 2008.

5.1 Objective

The primary objective of the shakedown tests was to provide an end-to-end check of the instrumentation and data acquisition systems and their integration with the models. This primary objective also included providing the test crew with the necessary model assembly experience, providing successful team coordination, determining the model hardware and tool requirements prior to shipment to the test site in Japan, and identifying any model design features or flaws that could impact test results in Japan. The shakedown test was divided into two separate entries to allow any modifications or procedural updates initially identified to be incorporated and tested.

The first shakedown test entry was focused on the following objectives and tasks:

- Assemble both models and identify manufacturing deficiencies;
- Identify possible efficiencies in model assembly sequence;
- Modify models to correct deficiencies and implement improvements;
- Validate correct installation of pressure and hot wire instrumentation; and
- Run models at actual test speeds to get an initial look at model characteristics.

The second shakedown test entry was focused on the following objectives and tasks:

- Assemble both models to validate repeatability of assembly;
- Validate instrumentation performance and further interrogate model characteristics with testing at conditions matched to those planned for the TWT; and
- Operate in simulated test facility environment to develop and refine test procedures.

Data obtained during the shakedown test was used to examine the performance of the model and instrumentation systems. However, obtaining boundary layer transition data in the 7-x10-wind tunnel was not a primary objective of the shakedown testing and was not pursued beyond what was necessary to accomplish the primary objectives.

5.2 Shakedown Test Facility Description

The facility used for the shakedown testing was the Northrop Grumman 7-x10- ft Wind Tunnel in Hawthorne, CA. This low-speed wind tunnel was originally designed for the X-21 Laminar Flow Research program, and was built for the purpose of conducting low-speed laminar flow testing. The tunnel was built in the 1950s and Northrop Grumman has extensively and continuously used the tunnel for five decades on all major programs. The facility is a closed circuit tunnel providing test section Reynolds numbers up to 2.4 million per foot. Clear tunnel dynamic pressure ranges from 0 to 200 pounds per square foot. Functioning at ambient

temperature and atmospheric pressure, the tunnel provides a continuously variable airspeed up to 440 feet per second (Mach 0.37). The layout and operating envelope of the wind tunnel is shown in Figure 62.

The flow quality was last formally assessed in June 2002. Table 4 shows the results obtained by the team from Arizona State University that used hotwire anemometry to assess freestream turbulence levels in the test section.

Table 4: Turbulence levels in 7- x 10-ft wind tunnel

Nominal Dynamic Pressure (lb/ft ²)	Speed (m/s)	Turbulence Intensity (% Freestream Velocity)	Bandpass Filter
2.9	15.88	0.122%	1 Hz – 2.0 kHz
5.1	21.12	0.094%	1 Hz – 2.0 kHz
8.1	26.71	0.084%	1 Hz – 2.0 kHz
11.5	31.73	0.088%	1 Hz – 2.0 kHz
15.6	36.96	0.095%	1 Hz – 2.0 kHz
15.6	37.08	0.071%	10 Hz – 9.5 kHz
20.4	41.10	0.063%	1 Hz – 9.5 kHz
32.0	54.49	0.045%	1 Hz – 9.5 kHz
46.0	65.38	0.047%	1 Hz – 9.5 kHz
62.5	75.53	0.060%	1 Hz – 9.5 kHz
82.0	85.97	0.072%	1 Hz – 9.5 kHz
100.0	94.43	0.107%	1 Hz – 9.5 kHz

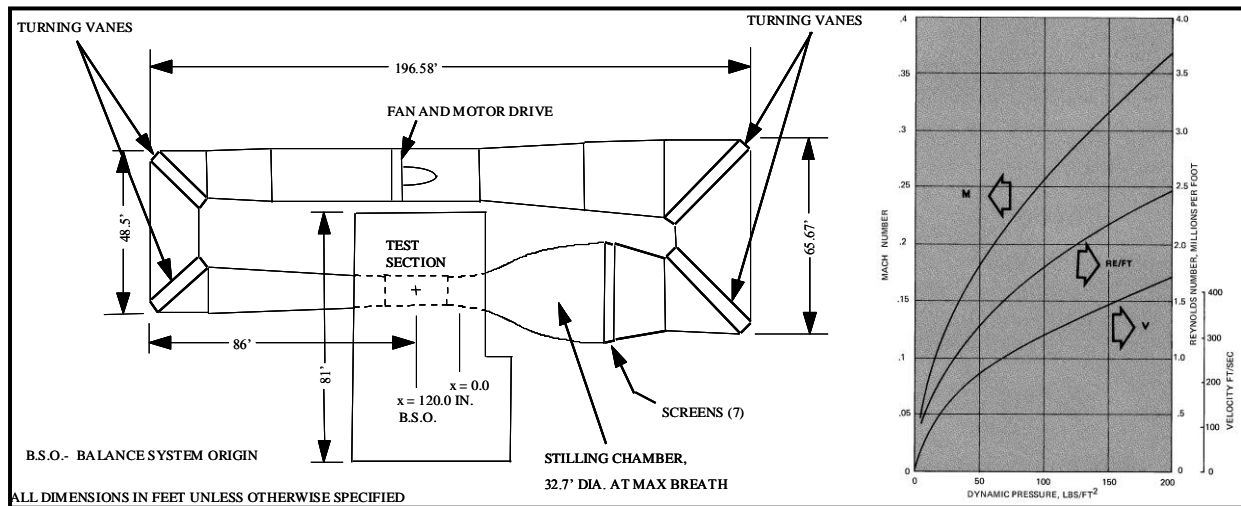


Figure 62: Northrop Grumman 7x10-ft wind tunnel schematic and characteristics.

The models were installed in the 7x10-ft wind tunnel as described in Appendix C.

5.3 Shakedown Test Results

The shakedown testing allowed successful verification of the correct function of the models and instrumentation systems. In the course of conducting the shakedown testing, numerous minor model modifications were made, including additional surface finish work to provide a very smooth surface on the measurement side, and the re-drilling and replacement of some fastener holes. The models proved to be generally well constructed and durable.

The data obtained during this testing proved invaluable to developing and refining data acquisition and reduction procedures. However, analysis of the data has shown that its utility for understanding transition behavior is limited, primarily owing to the test matrix being built around the objective of conducting system checkouts for the instrumentation, rather than a systematic examination of the boundary layer.

To examine whether the separated region on the aft closeout of the models induced any unsteady effects, tufts were installed on the Gradient-A model (see Figure 63). These tufts allowed determination of the location of the separated region and qualitative assessment of the unsteady effects. To further investigate this, a smoke wand (see Figure 64) was used to examine the flowfield at the leading edge (see Figure 65) as well as the splitter plate (see Figure 66). This assessment indicated that the unsteady effects of the separated region were sufficiently small to not interfere with the boundary layer.

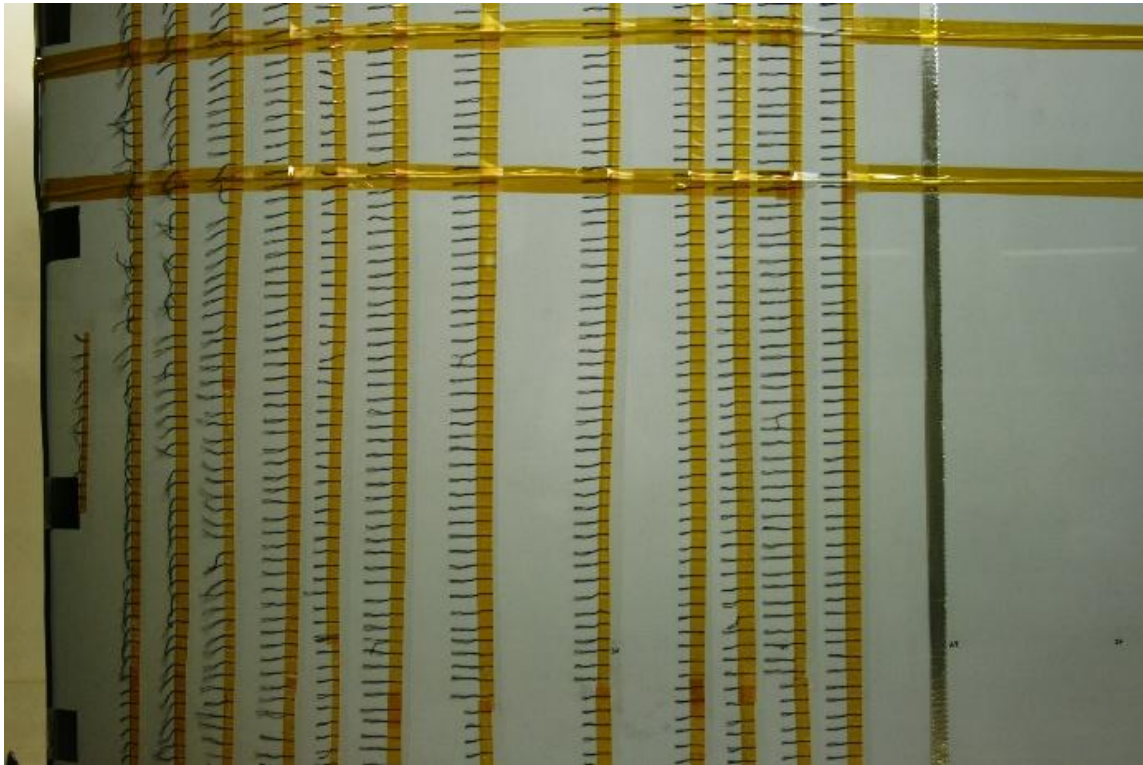


Figure 63: Tufts used on Gradient-A aft pressure recovery region.



Figure 64: Smoke wand used on Gradient-A.

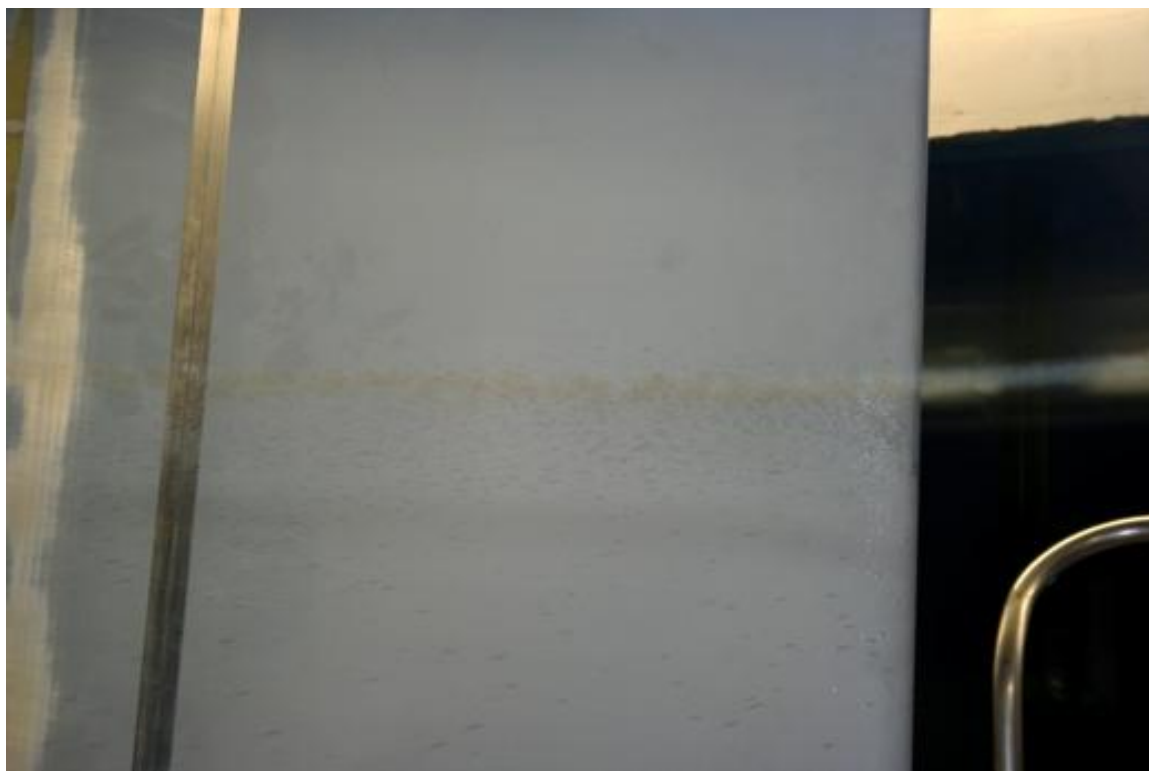


Figure 65: Smoke wand at model leading edge.



Figure 66: Smoke wand used on Gradient-A upper splitter plate.

6.0 TOWING WIND TUNNEL FACILITY

The Towing Wind Tunnel facility⁵ was built in 2003 and is owned and operated by Tohoku University. The facility is located in Hyuga, Miyazaki Prefecture, Japan. This newly developed facility consists of a carrier vehicle called the "HART vehicle" on which test article is placed, a guideway in which the HART vehicle runs, and a control system (the name "HART vehicle" comes from Hyuga Aerodynamic Research facility by Towing, the facility is located near the town of Hyuga). The facility was constructed on a former MAGLEV testing track owned by Railway Technical Research Institute of Japan⁶.

The track is 3.46m wide and 6.9 km long. However, only the first 1900m of the total 6.9km length track is currently used by the Towing Wind Tunnel. A diagram of the facility is shown in Figure 67. The first 910 m of the track is the acceleration section, the next 515 m is the test section and the final 475 m is the deceleration section. The entire test section is covered by a hood, but in Figure 67, for visual aid, the hood that covers the second half of this test section is not shown.

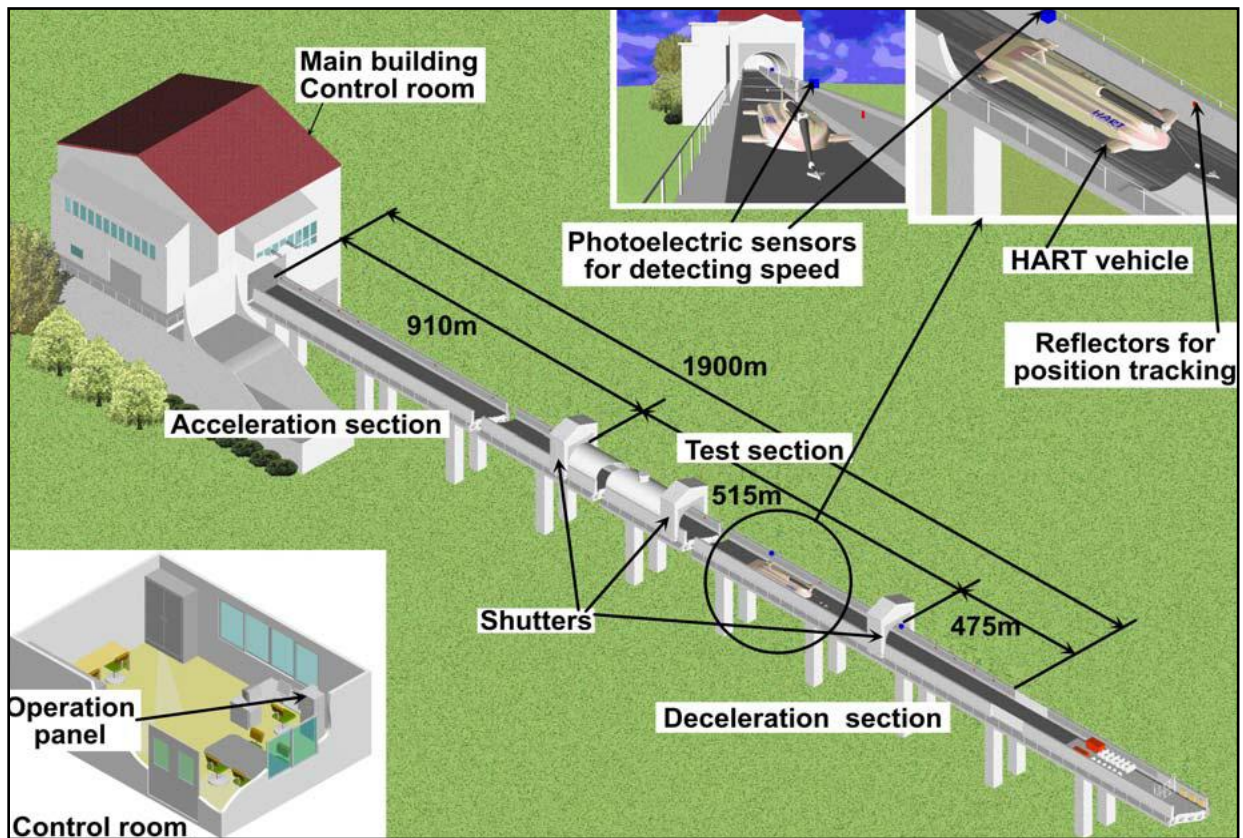


Figure 67: Towing Wind Tunnel track diagram (not to scale).

Figure 68 shows a schematic of the cross section of the guideway. The bottom surface of this guideway is paved asphalt. On both sides of the guideway are vertical guide walls. The test section is covered by a FRP hood which contains insulating material to minimize sound reflection and heat convection. Ventilators and lighting facilities are set up in the hood. There

are rolling door shutters installed at entrance, middle and exit of this hooded section to close the test section when this facility is not in use.

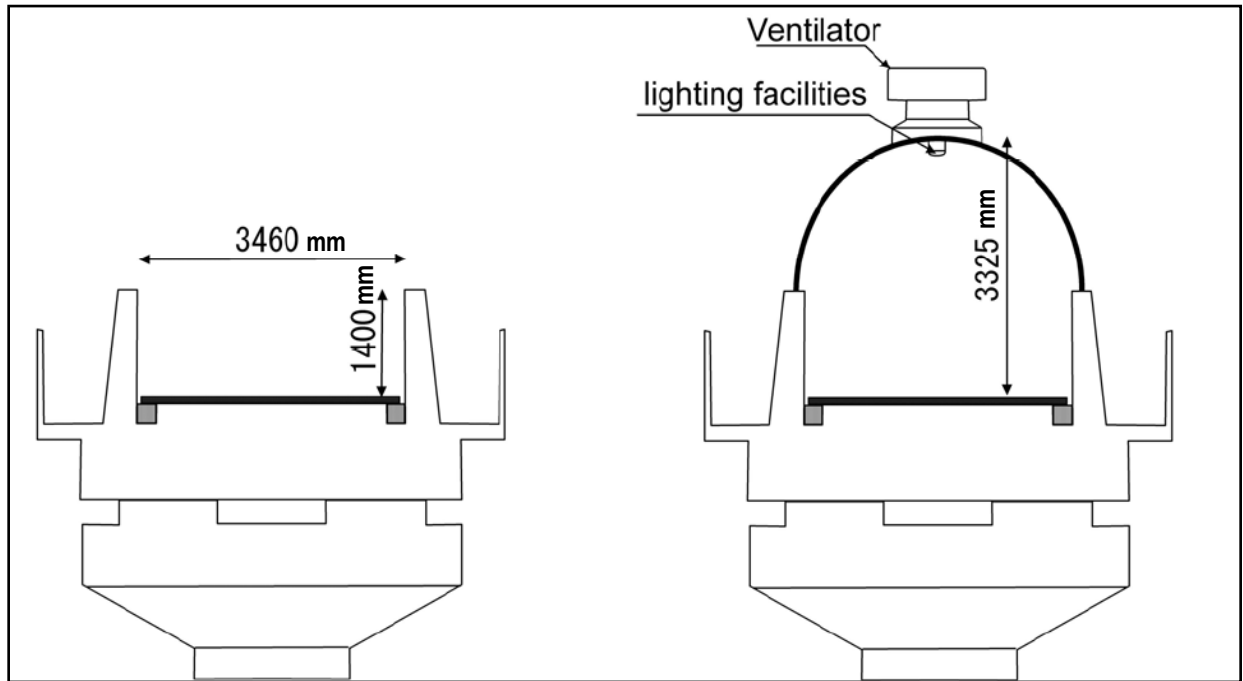


Figure 68: Guideway cross-section showing test section hood (right).

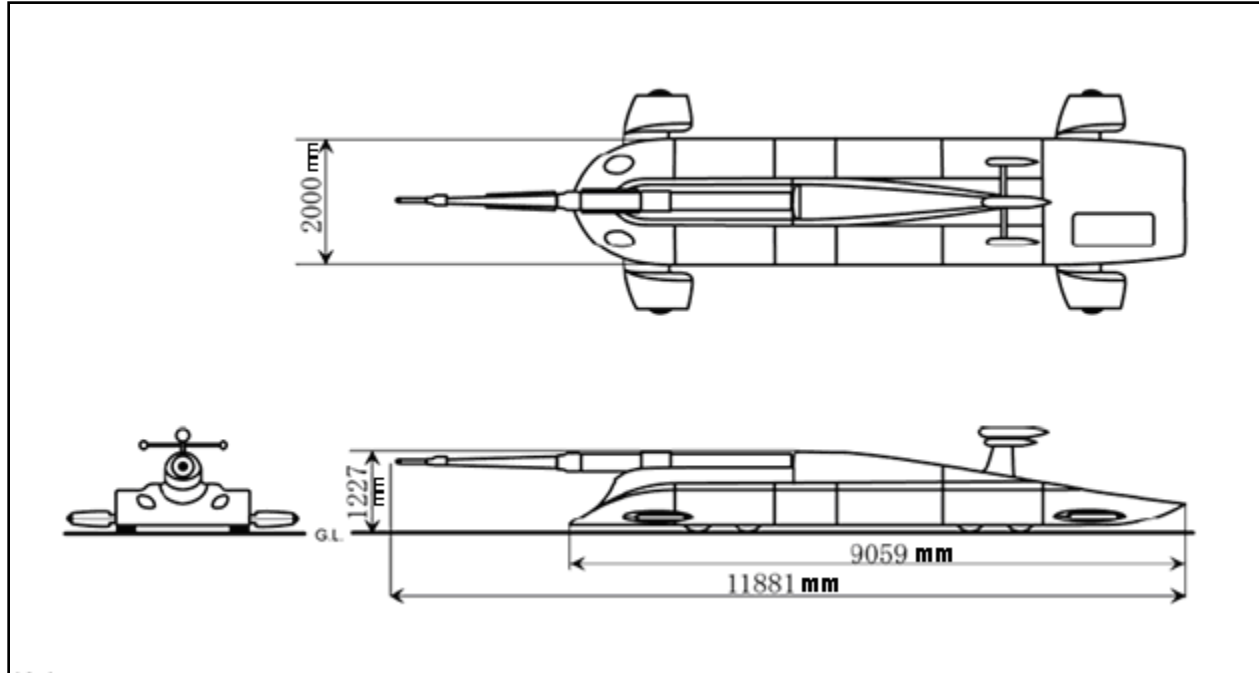


Figure 69: HART carrier vehicle.

The HART vehicle has eight tires underneath its body and four tires along its side. Four out of the eight underbody tires are driven by in-wheel 55kW electric motors. Electricity is supplied

from an onboard Lithium-ion battery. The side tires are forced to touch guide walls by springs so that the HART vehicle keeps its position in center of the track (Figure 70).



Figure 70: HART vehicle inside test section.

The HART vehicle is equipped with a hydraulically-actuated support arm to minimize vibrations experienced by the models. The maximum speed of the HART vehicle is 30 m/s during manned operation and 50 m/s during unmanned operation (clear tunnel, meaning without a model installed). Currently, the only mode of operation of the HART vehicle is manned operation. The acceleration and deceleration of the HART vehicle are 0.15g and -0.45g, respectively.

The HART vehicle is controlled by setting its ground speed. It is found that the air speed is slightly slower as compared with the ground speed because the HART vehicle entrains flow as it moves through the test section. At the end of the test section the air speed is slower than the ground speed by roughly 10%. Experiments were conducted by the Towing Wind Tunnel that monitored the wind speed at the exit of the test section as a function of time and the location of the HART vehicle as it moved through the test section. Those experiments verified that the HART vehicle's entrance into the test section is the reason for the observed difference between the ground speed and the air speed. This difference could be minimized in the future by accelerating the HART vehicle, though this not modification is not available at this time. However, this variation of airspeed did not adversely affect the SETS experiments because the SETS data is analyzed over a small subset of the time that the HART vehicle is in the test section. During this short period of time, the conditions can be considered to be constant. The

pressure signal in the Preston tubes and other pressure-based instrumentation settles in approximately 1-2 seconds, while the hot wire data is instantaneous. For the present experiments, the data from the entire time the HART vehicle is in the test section is analyzed and checked for constancy of results, however, only a subset of that data is used in the final processing of the results. Thus, the slow decay of airspeed is not a factor and the speed of the run is taken to be the speed at the subset of time that the data was analyzed.

6.1 Model Installation

The models were designed to fit onto the existing HART vehicle lower splitter plate. A hydraulically actuated support arm connects the splitter plate to the HART vehicle itself. Drawings of the HART vehicle lower splitter plate were provided by the facility and the SETS models were designed to attach using existing holes in the splitter plate. To install the SETS models, L-brackets were first attached to existing holes in the HART vehicle lower splitter plate (Figure 71) and then the common frame was attached (Figure 72). The leading edge assembly as a single piece was then lowered onto the lower splitter plate and attached to the frame. The entire leading edge assembly was moved as one piece to avoid having to disassemble the critical step mechanism. Once the leading edge assembly was attached, the pressure tubing from the leading edge piece was routed through the holes in the frame (Figure 73).



Figure 71: HART vehicle and existing lower splitter plate.



Figure 72: Common frame installed on HART vehicle.



Figure 73: Gradient-Zero leading edge installed on common frame.

After the leading edge assembly was installed, the next piece to be attached was the reference-side skin (Figure 74). The pressure tubing from the skin piece was then routed out through the back of the frame. The upper splitter plate was then lowered onto the assembly via the overhead crane (Figure 75). The lower splitter plate extensions were attached and the pressure instrumentation was mounted to the underside of the lower splitter plate extensions, which was also done during the shakedown wind tunnel tests. Aerodynamic fairings were placed over the three step adjustment mechanisms on the non-reference side of the model and the edges of the model (where the model connects to the splitter plates) were sealed with tape to ensure that no flow seepage occurred (Figure 76).



Figure 74: Gradient-Zero measurement side skin installed.



Figure 75: Upper splitter plate being installed.



Figure 76: Fairings installed over step adjustment mechanisms.

The completed Gradient-Zero installation is shown in Figure 77, showing the non-reference side of the model. Once the model assembly was complete, the HART vehicle was moved the short distance from the high bay to the beginning of the test track, directly outside (Figure 78). The measurement side of the model is shown in Figure 79, at the beginning of the test track. In this case, the model was instrumented with a full array of Preston tubes in order to measure the clean-plate boundary layer state. Figure 80 shows the HART vehicle and Gradient-Zero at the end of the test track, after a separate run.



Figure 77: Gradient-Zero assembled on HART vehicle.



Figure 78: HART vehicle with Gradient-Zero at beginning of test track.



Figure 79: Measurement side of Gradient-Zero at beginning of test track.



Figure 80: HART vehicle with Gradient-Zero at end of test track.

7.0 MEASUREMENT METHODS

Multiple measurement methods were used in order to provide redundancy, comparison and confidence, as well as to add to the physical foundation of the results. The parameters measured during the test included pressure coefficient distributions, skin friction coefficients, boundary layer velocity profiles and disturbance frequency distributions.

The static pressure taps were used to measure the pressure coefficient distributions on the models. A boundary layer traverse was used to measure boundary layer velocity profiles at the step location in order to reduce step heights to dimensionless Re_k values. Preston tubes were used to measure skin friction distributions. Hot wire anemometry and accelerometers were used to measure the dynamic flow environment. Each of the measurement methods is addressed in its own subsection.

7.1 Pressure Distributions

7.1.1 Pressure System

A pressure system was designed and procured for the SETS testing. Because the facility is a propelled-model facility, the pressure instrumentation needed to be self-contained such that it could ride along on the carrier vehicle. The pressure system needed to record pressures from the 60+ static pressure taps and up to 18 Preston tubes simultaneously, in addition to the Pitot probe.

The pressure system was designed by Prof. Westphal at Washington State University. The components of the pressure system included a Scanivalve DSM 3400 and four ZOC22/TCU units. During the test, three ZOCs were installed on the carrier vehicle and the remaining ZOC was treated as a spare. The range of the transducers was ± 10 in H₂O and the DSM 3400 logged 2 scans/second on all 96 channels simultaneously.

The pressure system was run off two 12-volt motorcycle batteries connected in series to provide 24-volts.



Figure 81: DSM3400 and 4 ZOC22/TCU units make up the pressure recording system.

7.2 Measured Pressure Distributions

The models were mounted vertically on the HART carrier vehicle. During the initial setup, the pressure distributions were checked to ensure that the model was aligned correctly and modifications to the alignment were made, if necessary. During the test runs, the pressure distributions are used to check the consistency of the data (e.g. to check if the model has become misaligned or otherwise modified), to check the uniformity of the flow between inboard and outboard taps, and, most importantly, to reduce and correlate the other data. Static pressure readings from the same chordwise position are required in order to reduce the data from each Preston tube. Recording and reporting the static pressure distributions measured during the testing is necessary because these are the conditions under which the boundary layer develops and thus the results are specific to those conditions.

The clean plate static pressure distribution was measured at various speeds for each model (Figures 82– 129). For each model, clean plate pressure distributions are shown for each speed. Some speeds have repeat runs. An average pressure distribution is also shown for each speed, which is the average of the inboard and outboard rows and any repeat runs, if applicable.

As can be seen from the plots, the spanwise uniformity indicated by the pressure distributions is good.

Summary plots are shown at the end of each model section. The first summary plot shows the average pressure distribution for the given model at every speed. As can be seen from the plots, there is little variation of pressure gradient with speed. The second summary plot shows the speed averaged pressure distribution, which is an average of the pressure distributions at each speed. The nondimensionalized pressure gradient parameter K is shown for each speed in the third summary plot. The fourth and final summary plot shows the speed averaged K for the given model. Since K is derived from the pressure gradient, it follows that K also does not vary significantly with speed, which is reflected in the plots. The excrescence relations results (see Section 8.0) are reported with the speed averaged K value for each model. However, naturally, the data from each individual run was reduced and analyzed using the pressure distribution measured during that run.

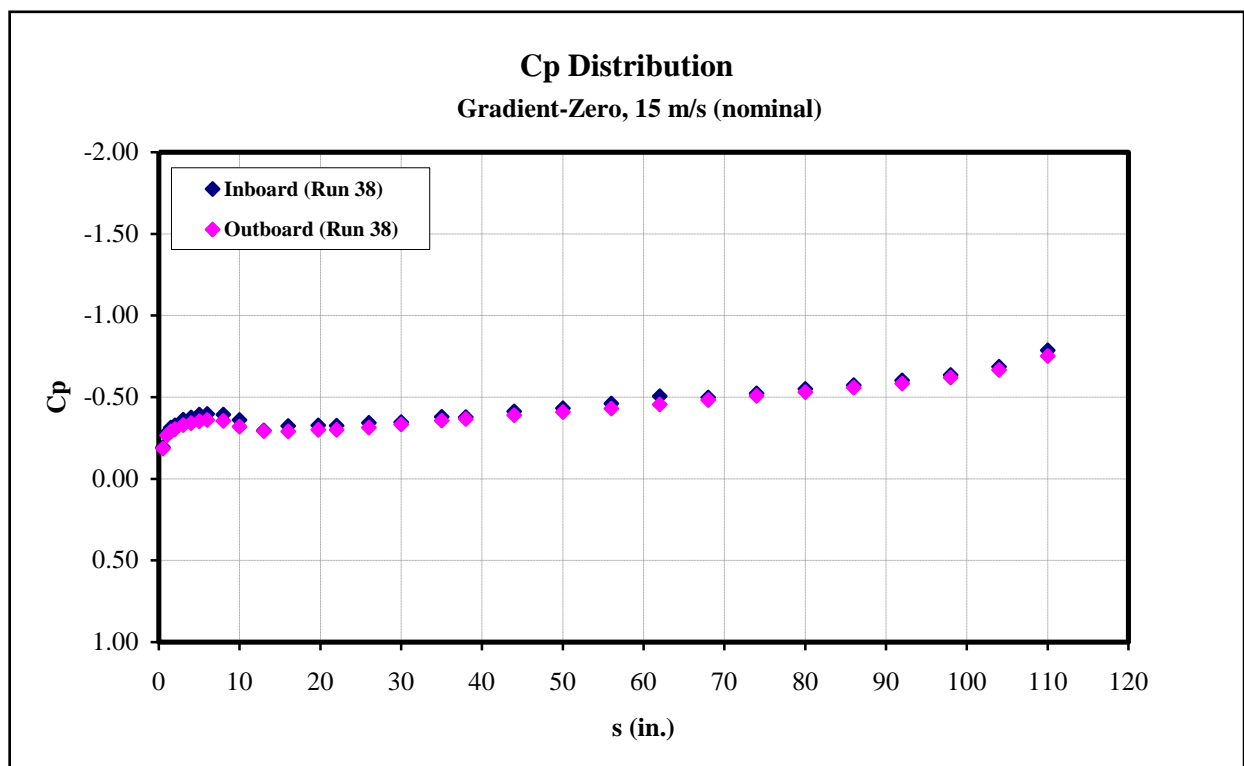


Figure 82: Gradient-Zero C_p distribution data (Run 38), $U=15$ m/s (nominal).

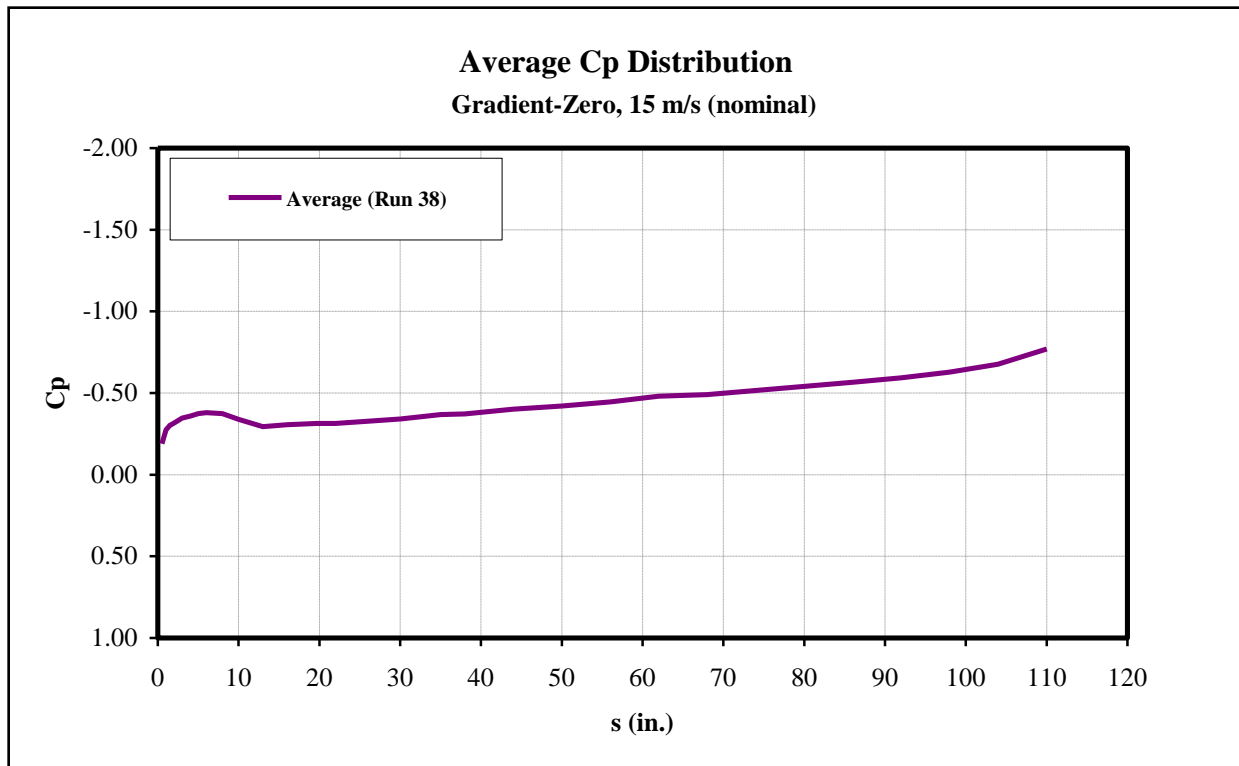


Figure 83: Gradient-Zero average Cp distribution, U=15 m/s (nominal).

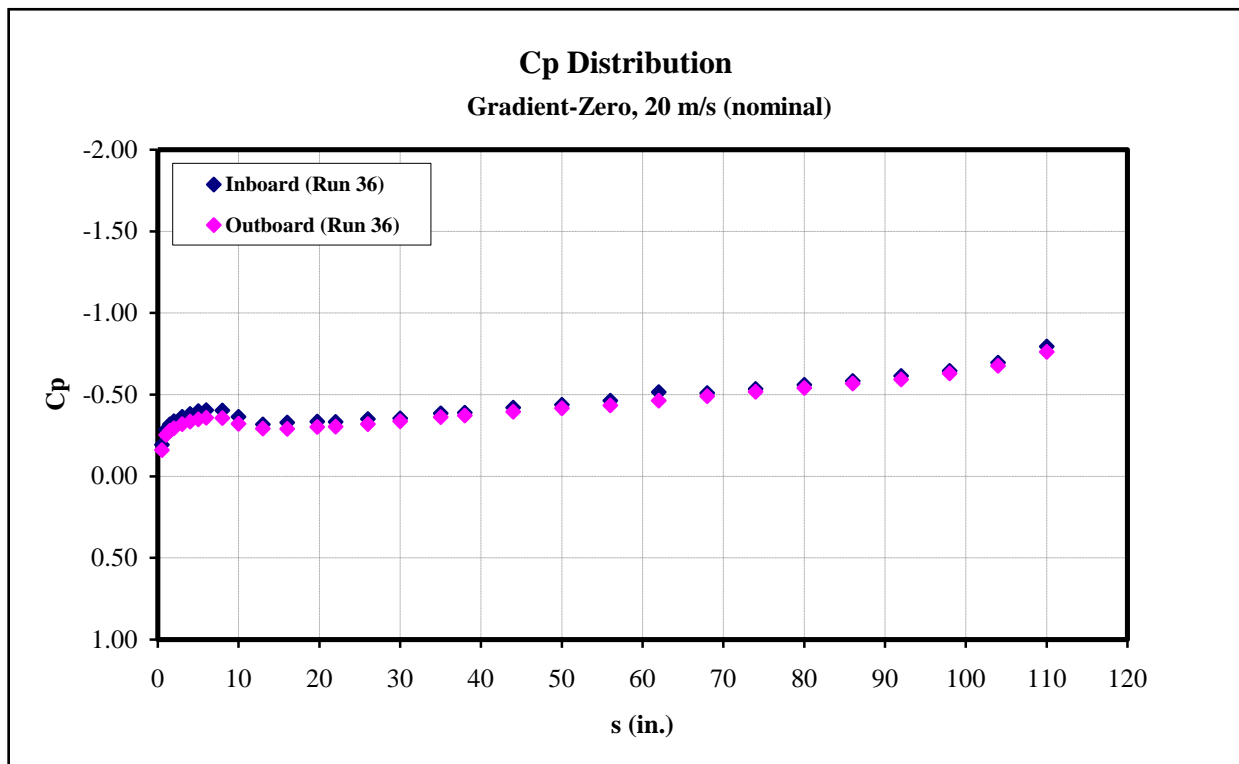


Figure 84: Gradient-Zero Cp distribution data (Run 36), U=20 m/s (nominal).

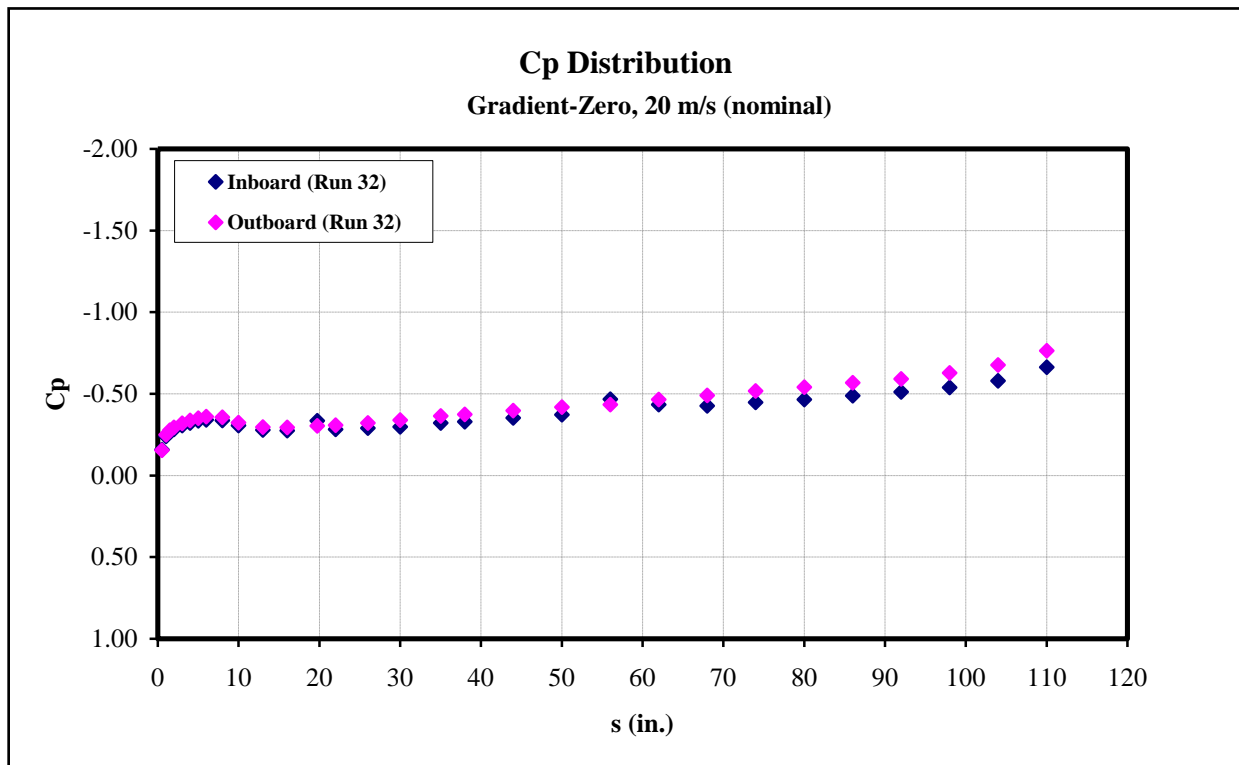


Figure 85: Gradient-Zero Cp distribution data (Run 32), U=20 m/s (nominal).

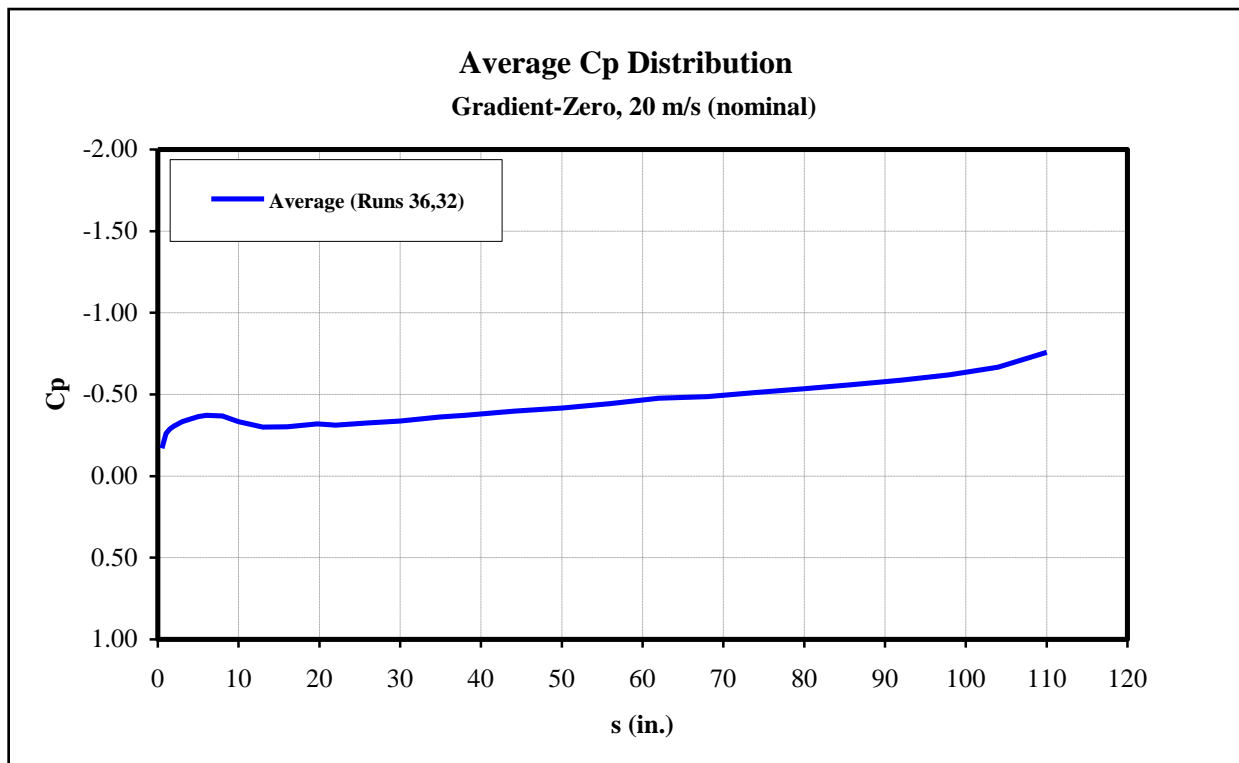


Figure 86: Gradient-Zero average Cp distribution, U=20 m/s (nominal).

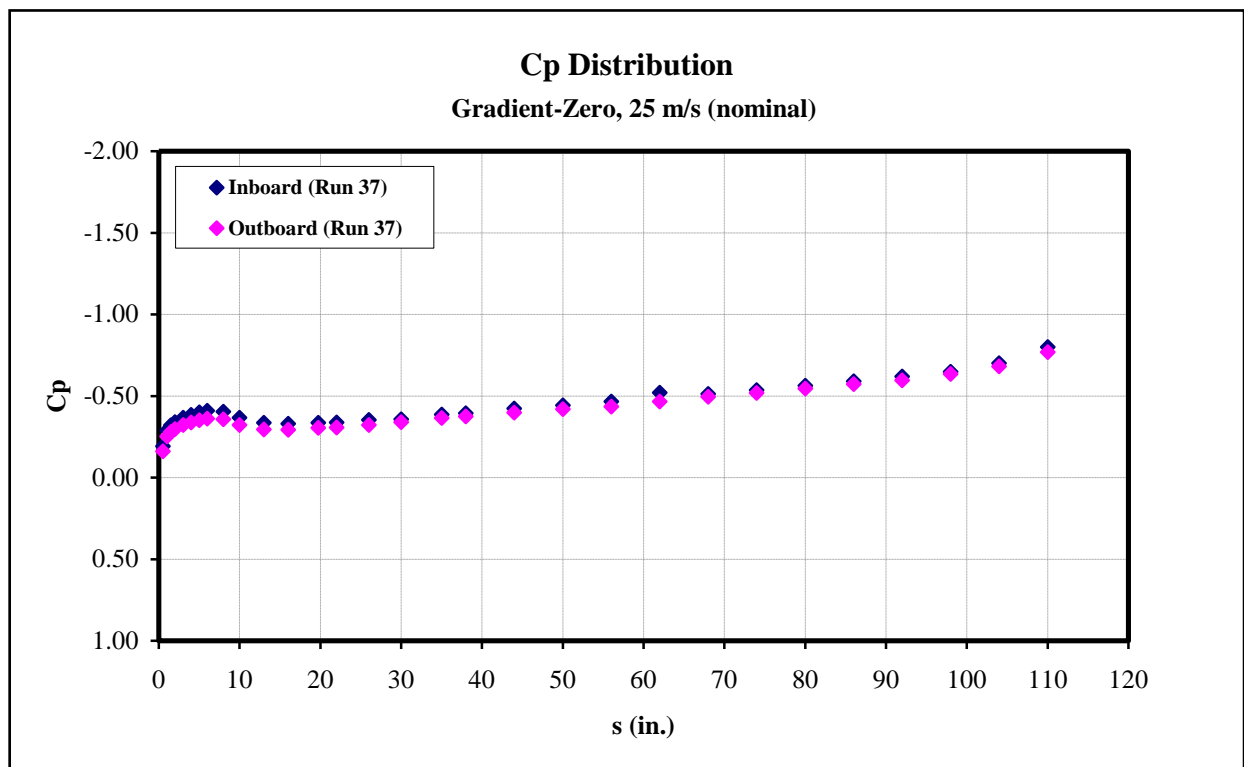


Figure 87: Gradient-Zero Cp distribution data (Run 37), U=25 m/s (nominal).

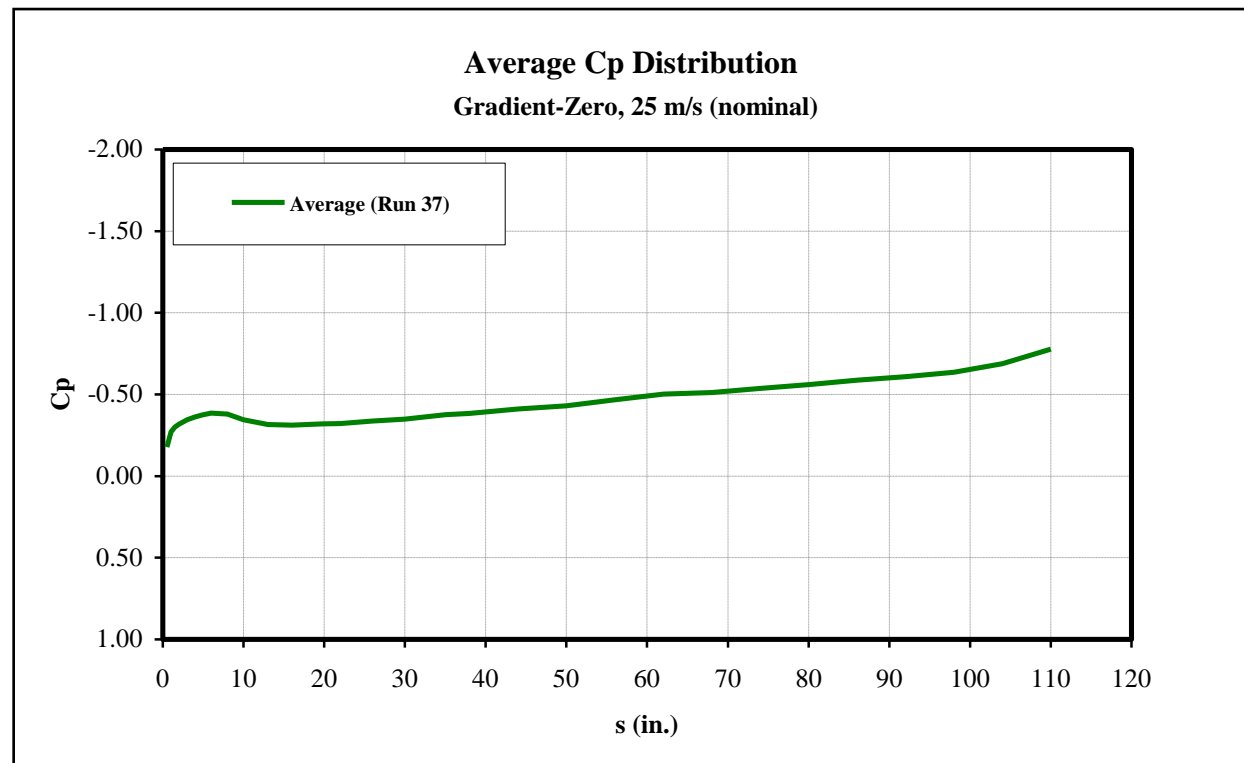


Figure 88: Gradient-Zero average Cp distribution, U=25 m/s (nominal).

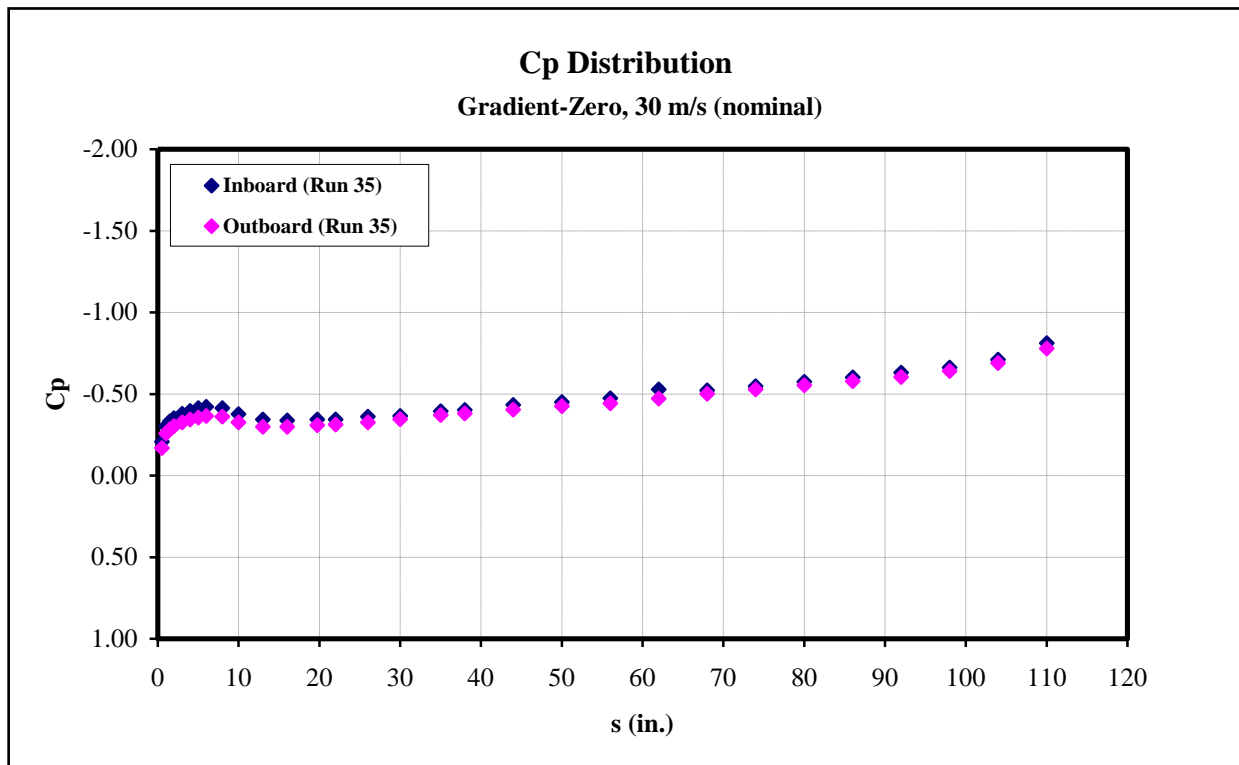


Figure 89: Gradient-Zero C_p distribution data (Run 35), $U=30$ m/s (nominal).

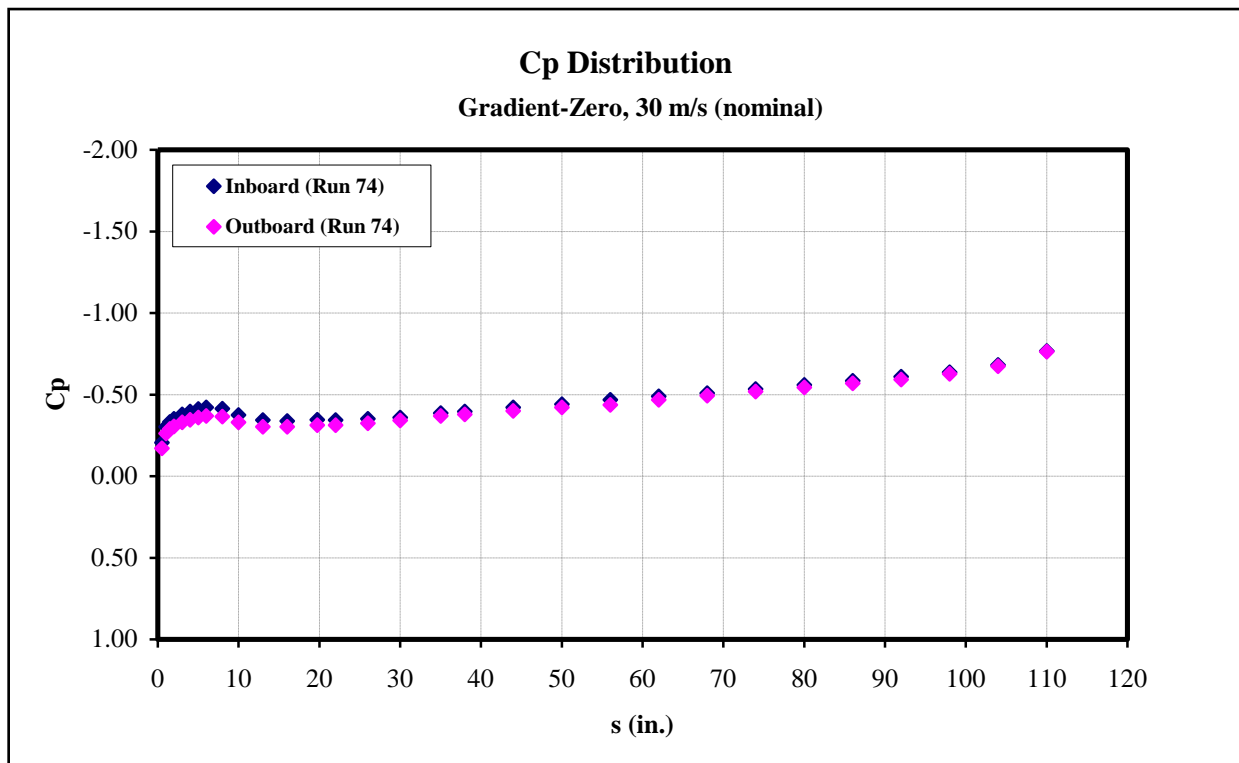


Figure 90: Gradient-Zero C_p distribution data (Run 74), $U=30$ m/s (nominal).

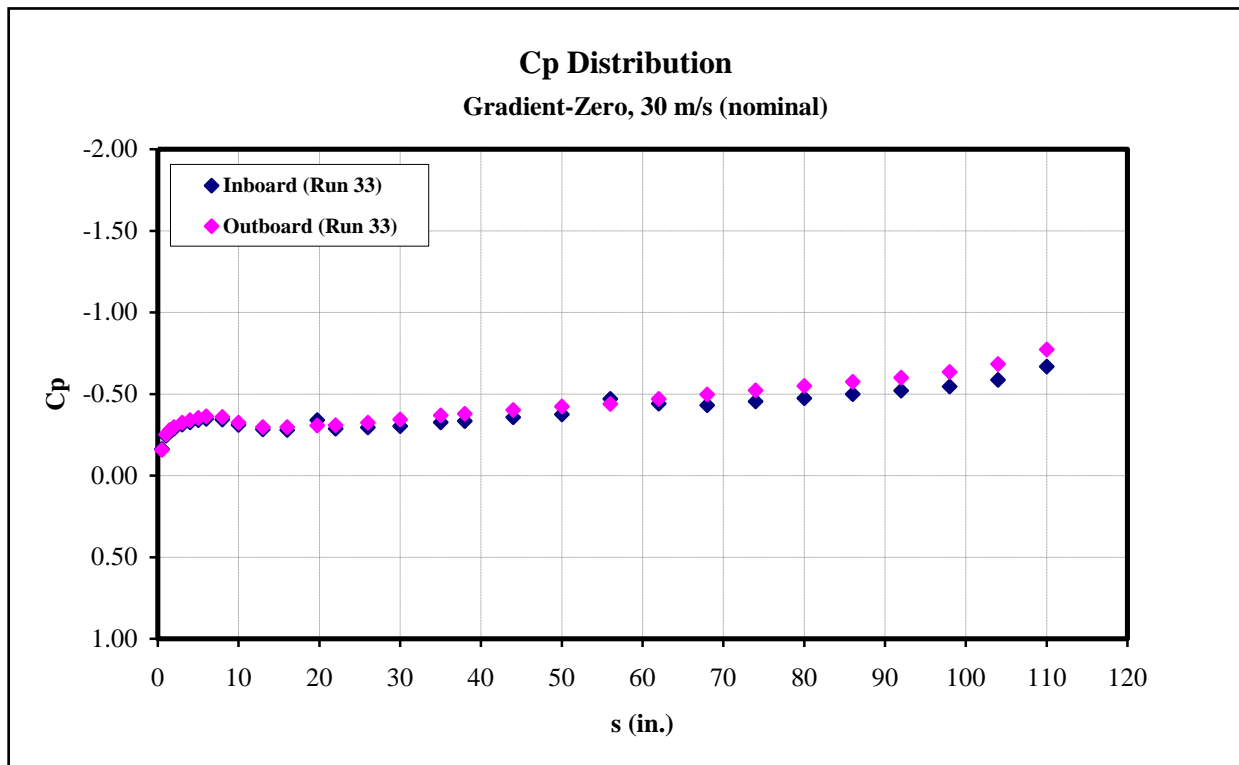


Figure 91: Gradient-Zero Cp distribution data (Run 33), U=30 m/s (nominal).

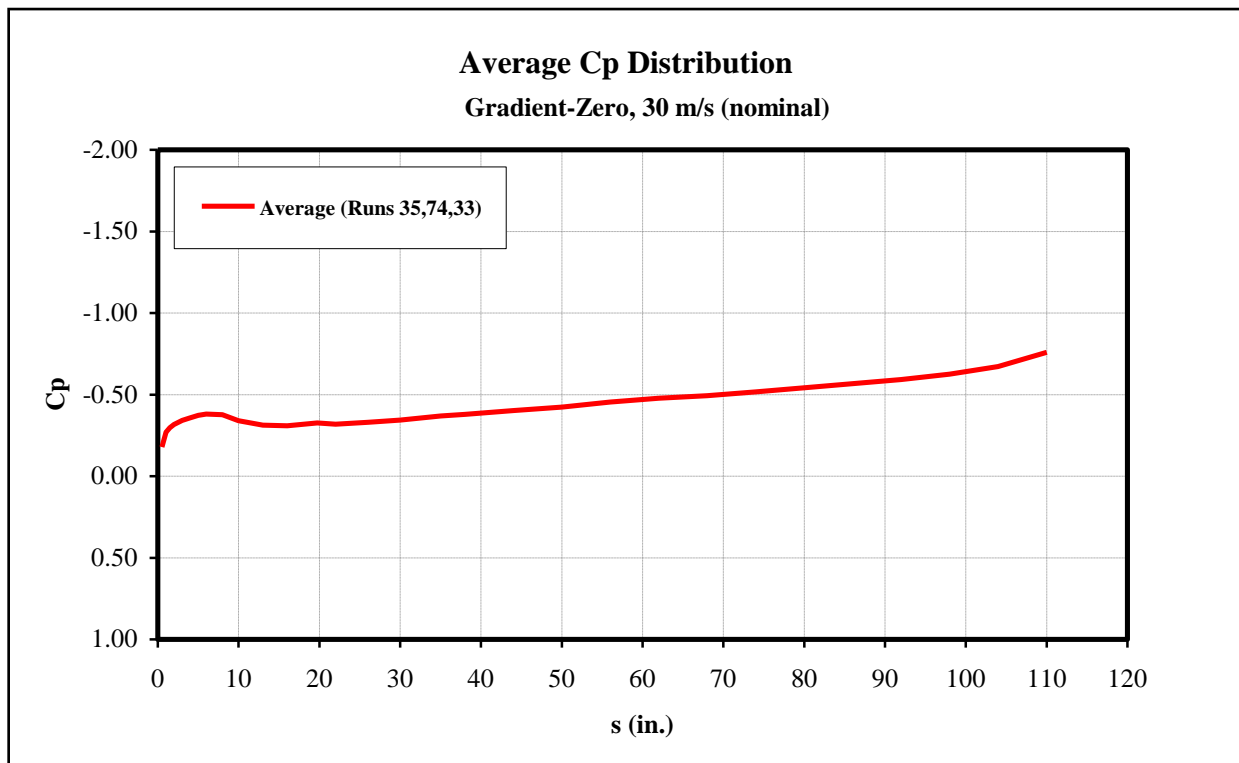


Figure 92: Gradient-Zero average Cp distribution, U=30 m/s (nominal).

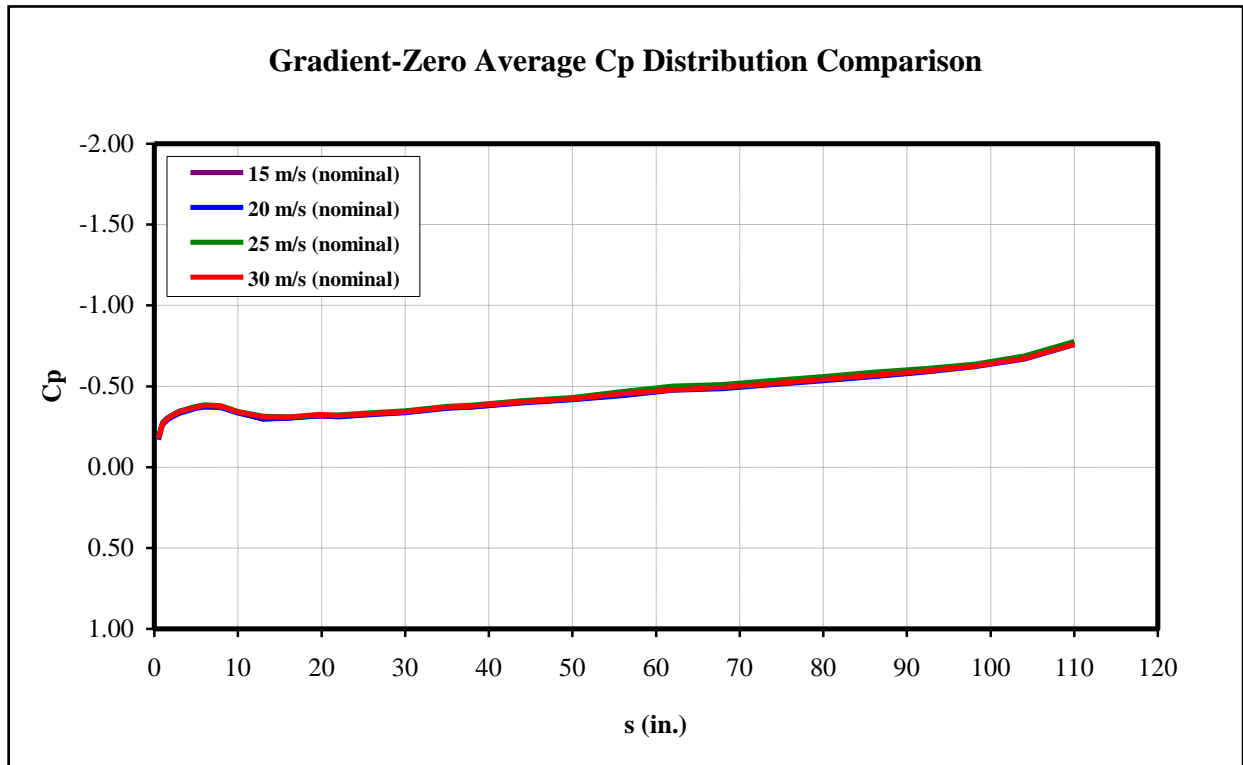


Figure 93: Comparison of Gradient-Zero average Cp distribution.

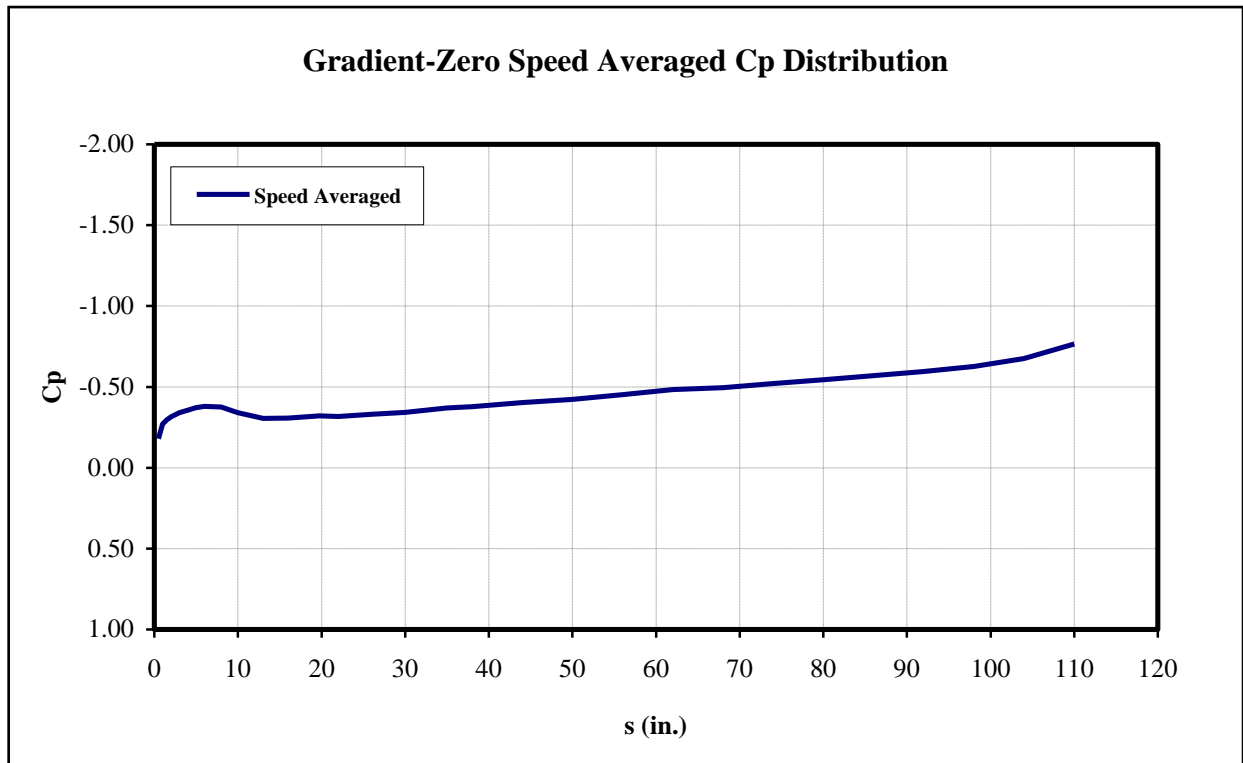


Figure 94: Gradient-Zero speed averaged Cp distribution.

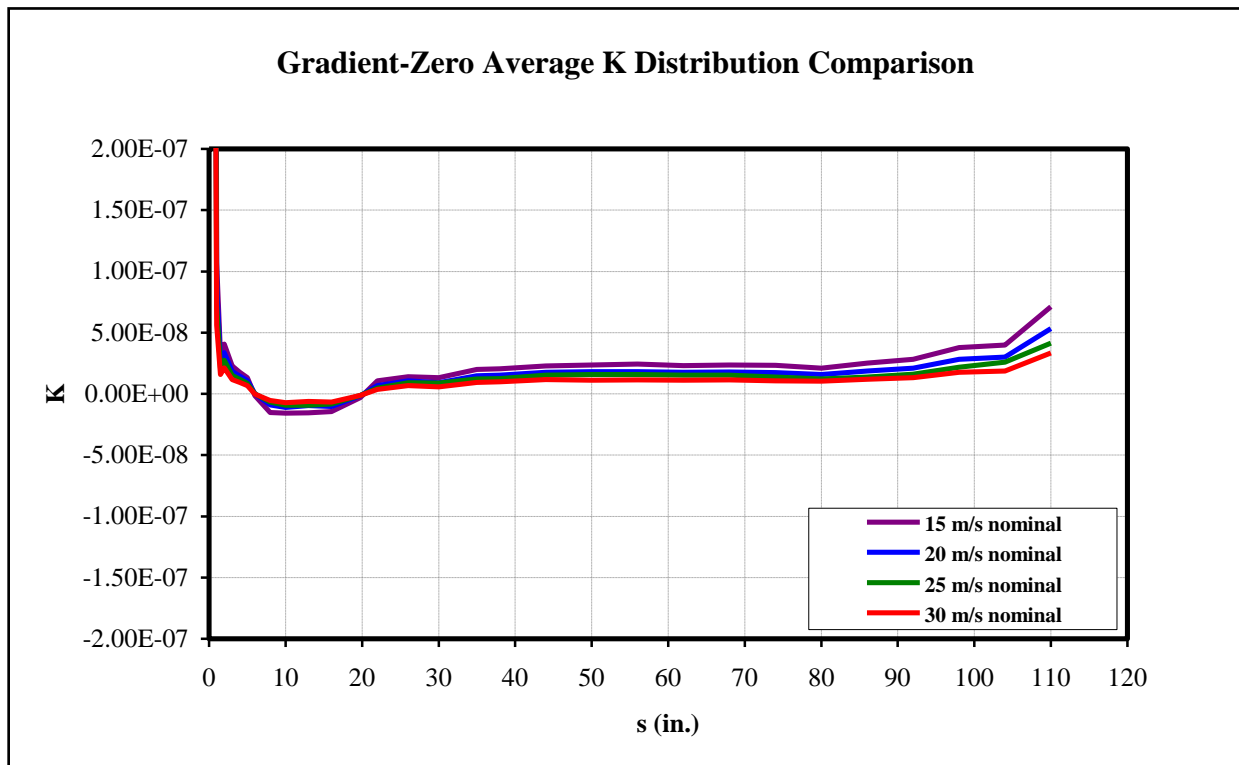


Figure 95: Comparison of Gradient-Zero average K distribution.

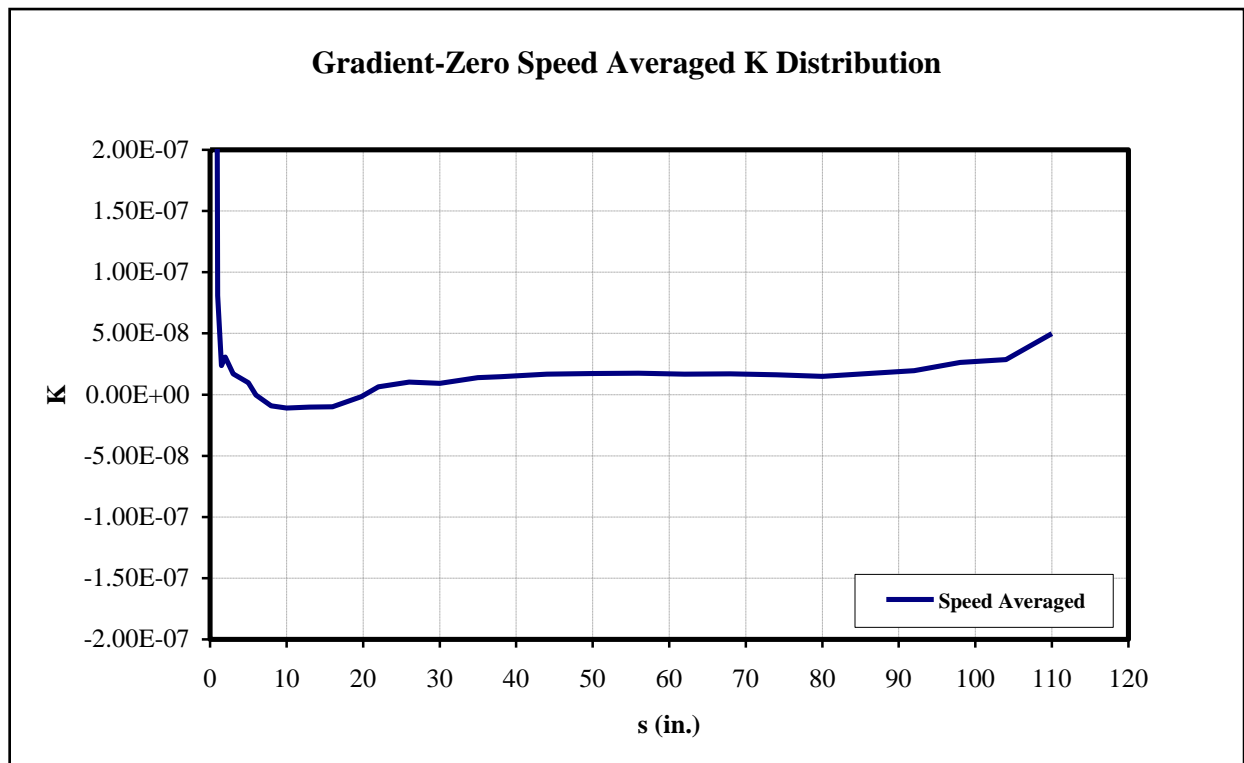


Figure 96: Gradient-Zero speed averaged K distribution.

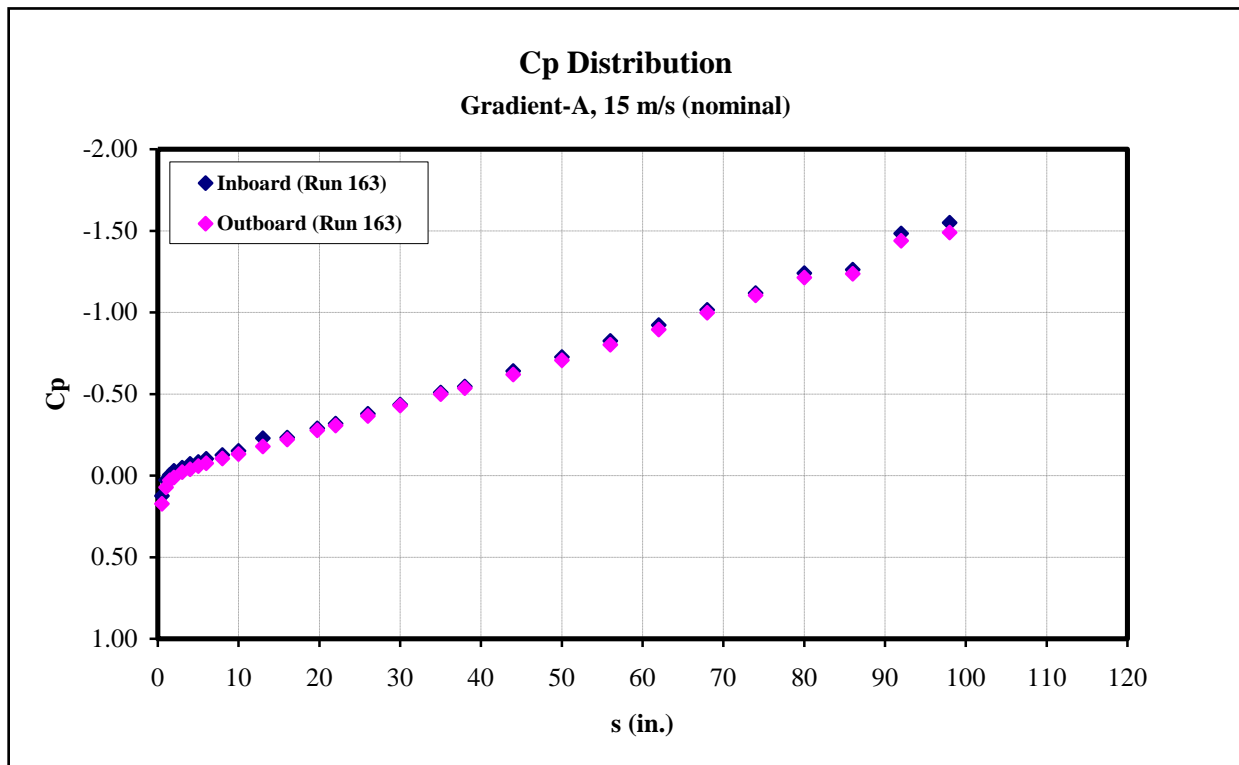


Figure 97: Gradient-A Cp distribution data (Run 163), U=15 m/s (nominal).

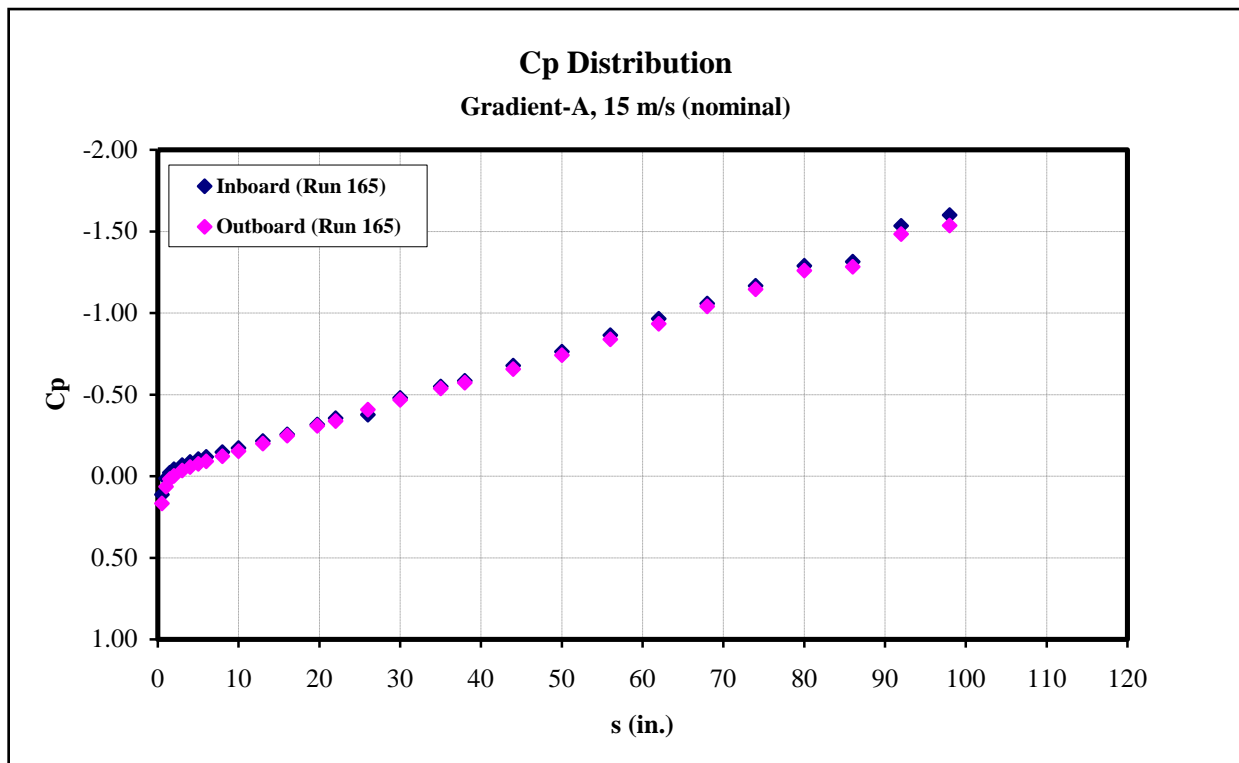


Figure 98: Gradient-A Cp distribution data (Run 165), U=15 m/s (nominal).

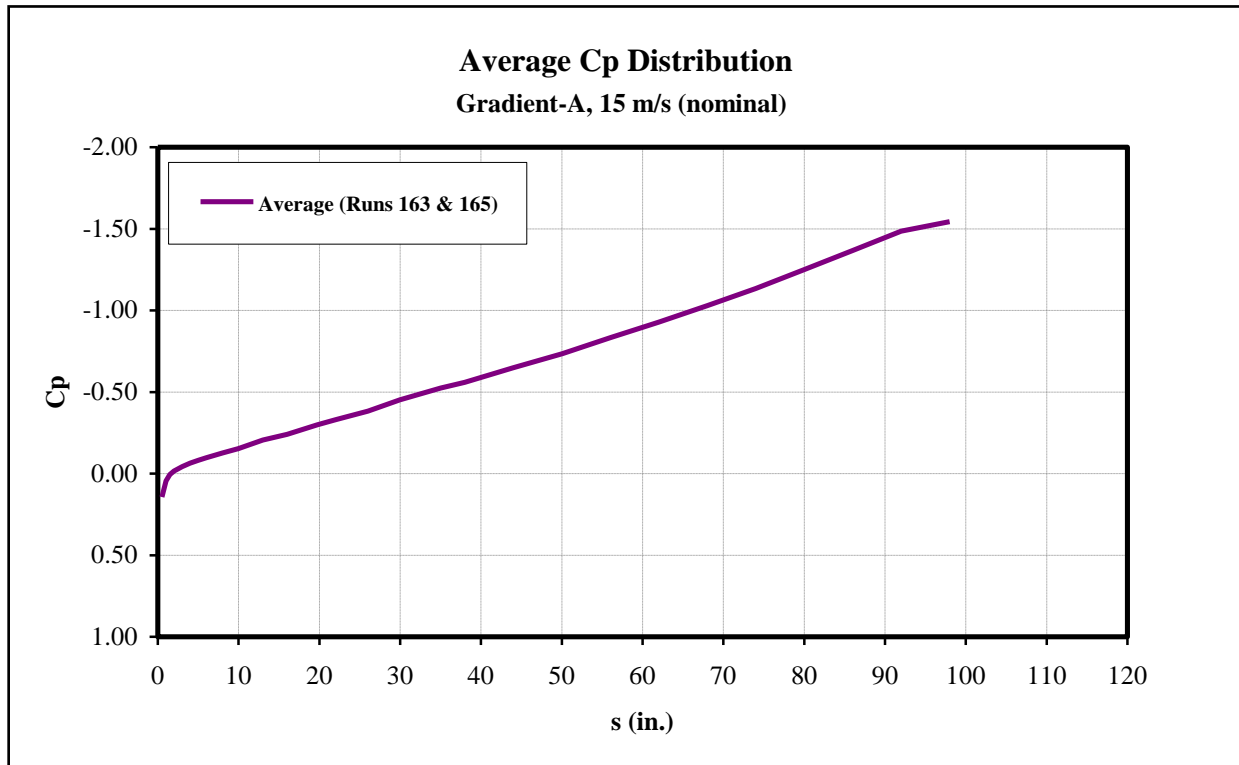


Figure 99: Gradient-A average Cp distribution, U=15 m/s (nominal).

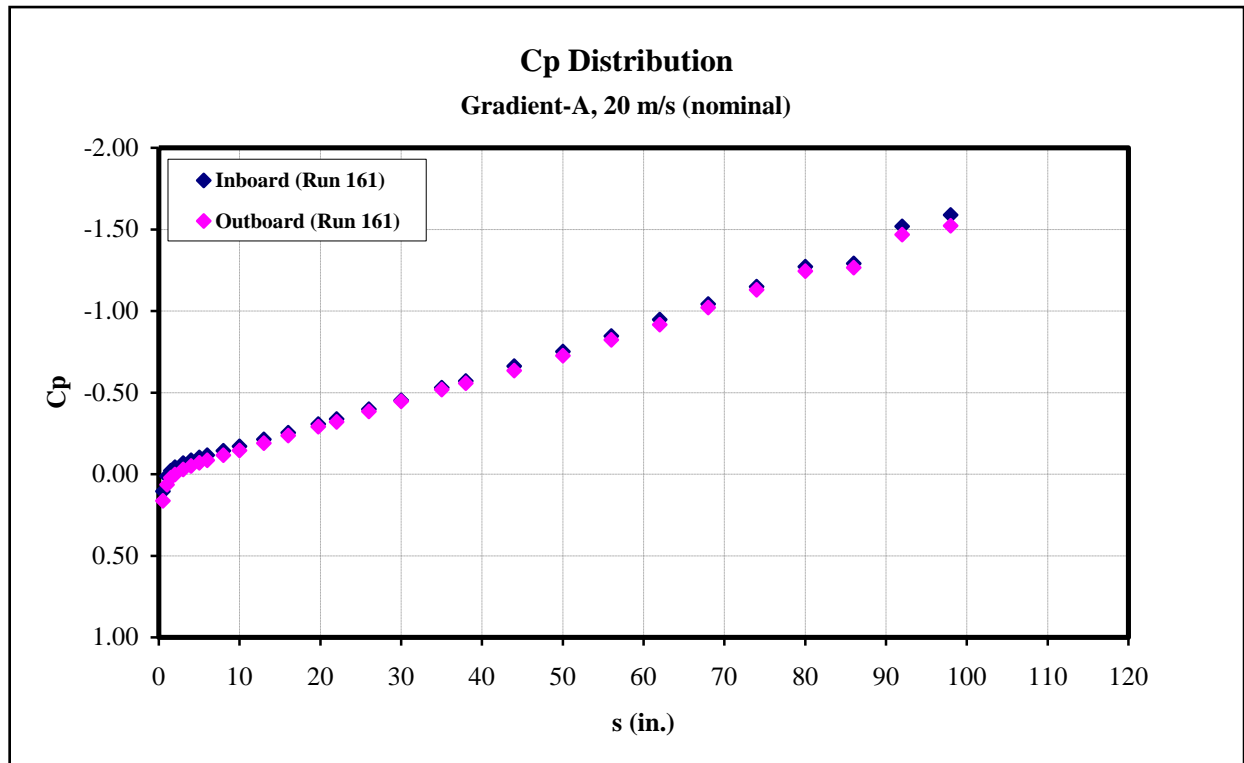


Figure 100: Gradient-A Cp distribution data (Run 161), U=20 m/s (nominal).

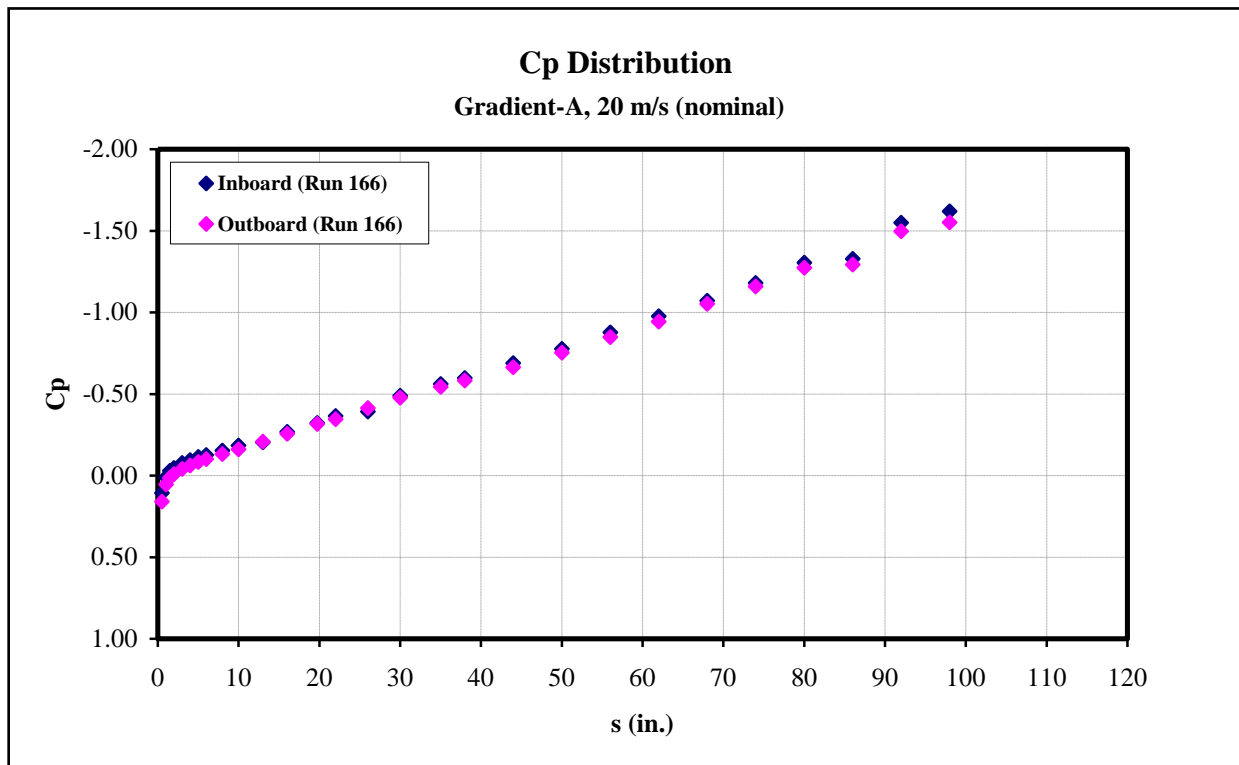


Figure 101: Gradient-A Cp distribution data (Run 166), U=20 m/s (nominal).

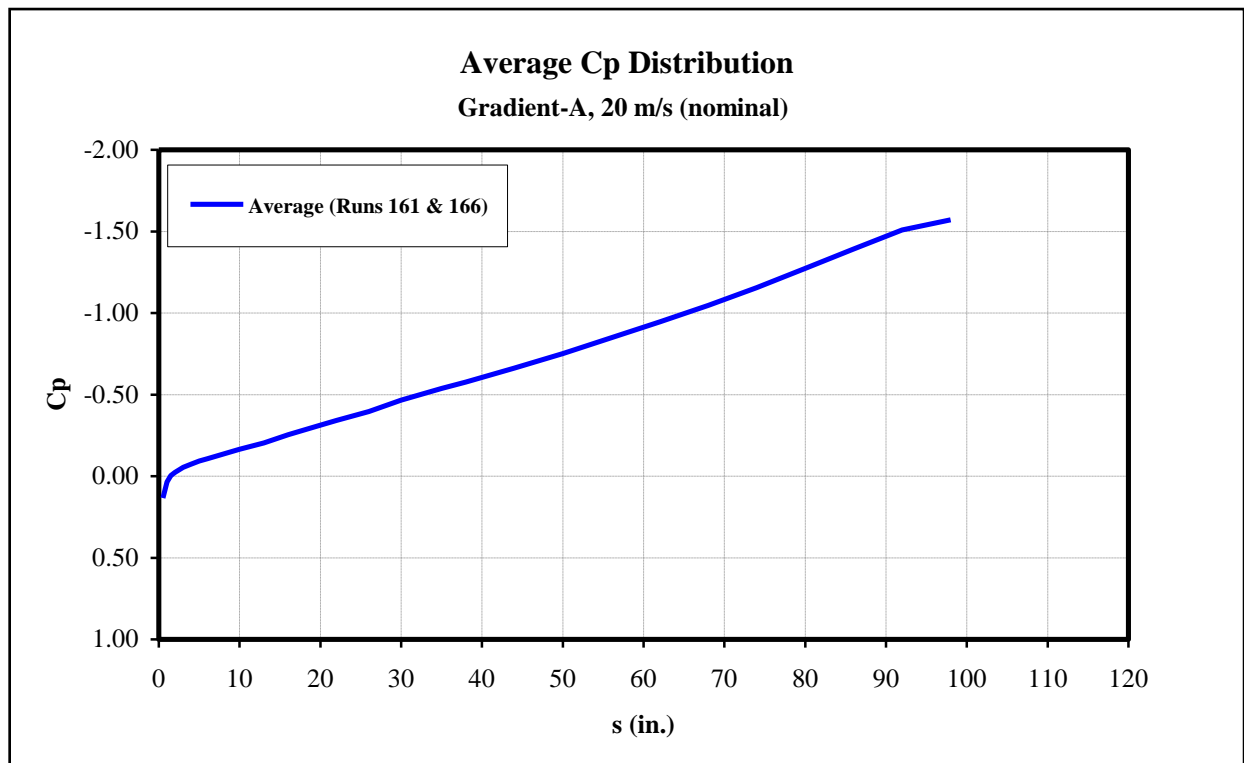


Figure 102: Gradient-A average Cp distribution, U=20 m/s (nominal).

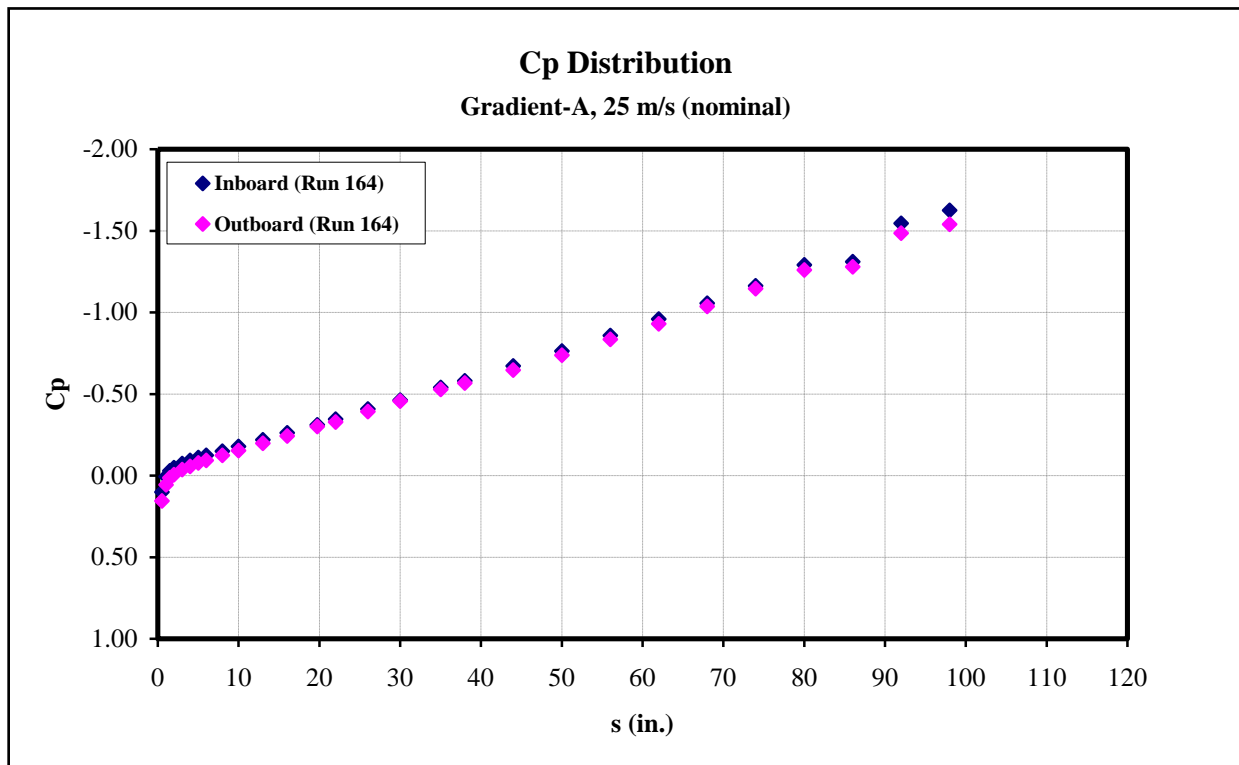


Figure 103: Gradient-A Cp distribution data (Run 164), U=25 m/s (nominal).

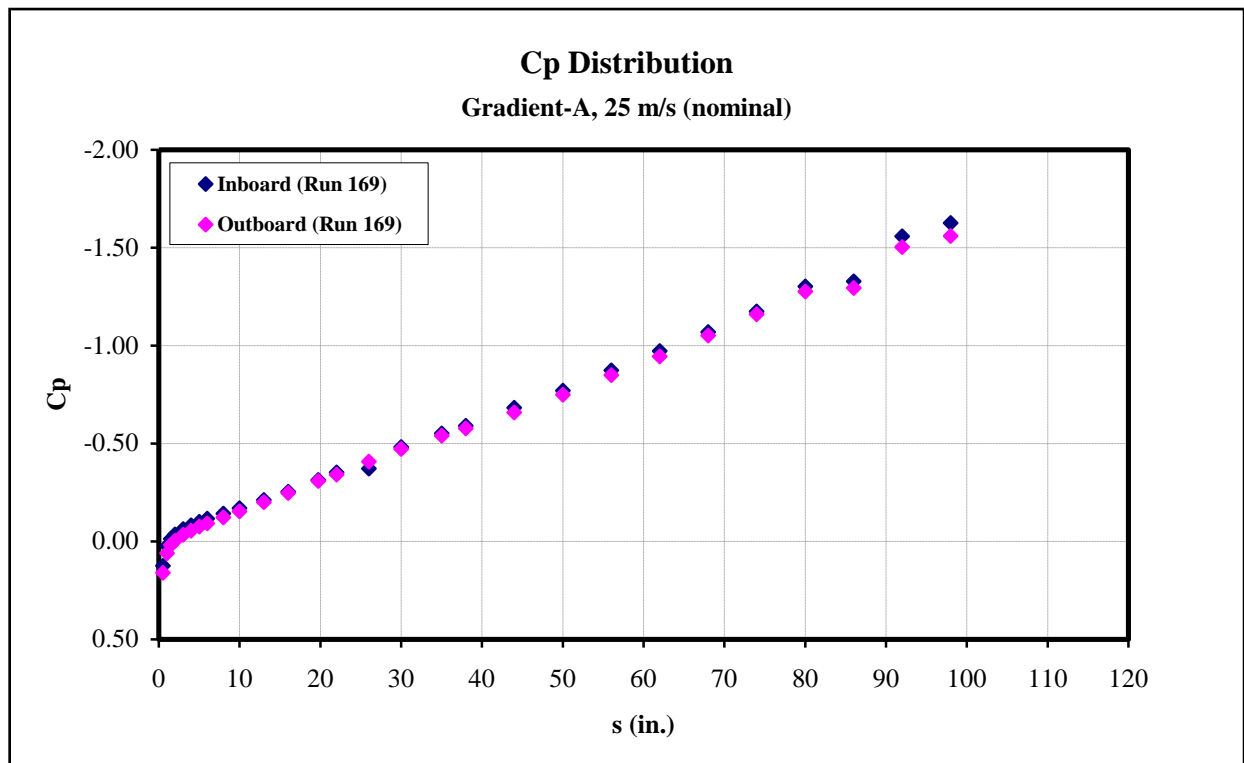


Figure 104: Gradient-A Cp distribution data (Run 169), U=25 m/s (nominal).

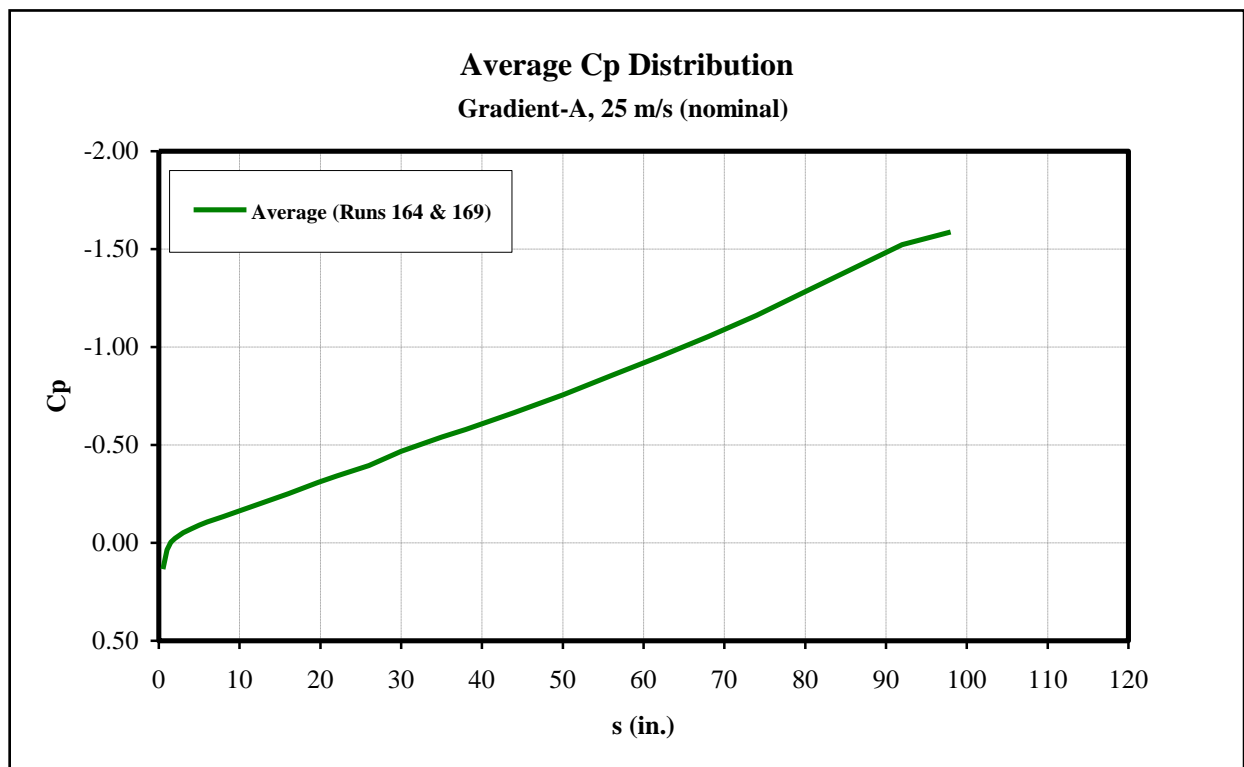


Figure 105: Gradient-A average Cp distribution, U=25 m/s (nominal).

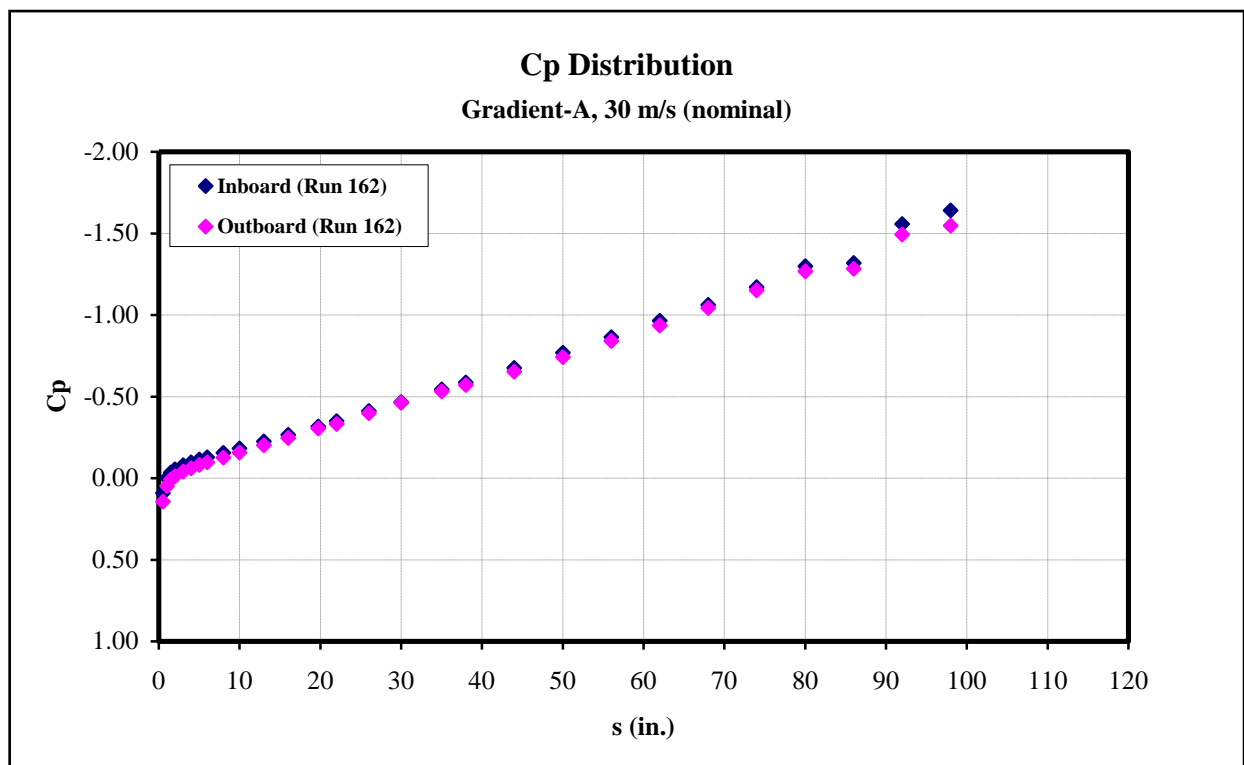


Figure 106: Gradient-A Cp distribution data (Run 162), U=30 m/s (nominal).

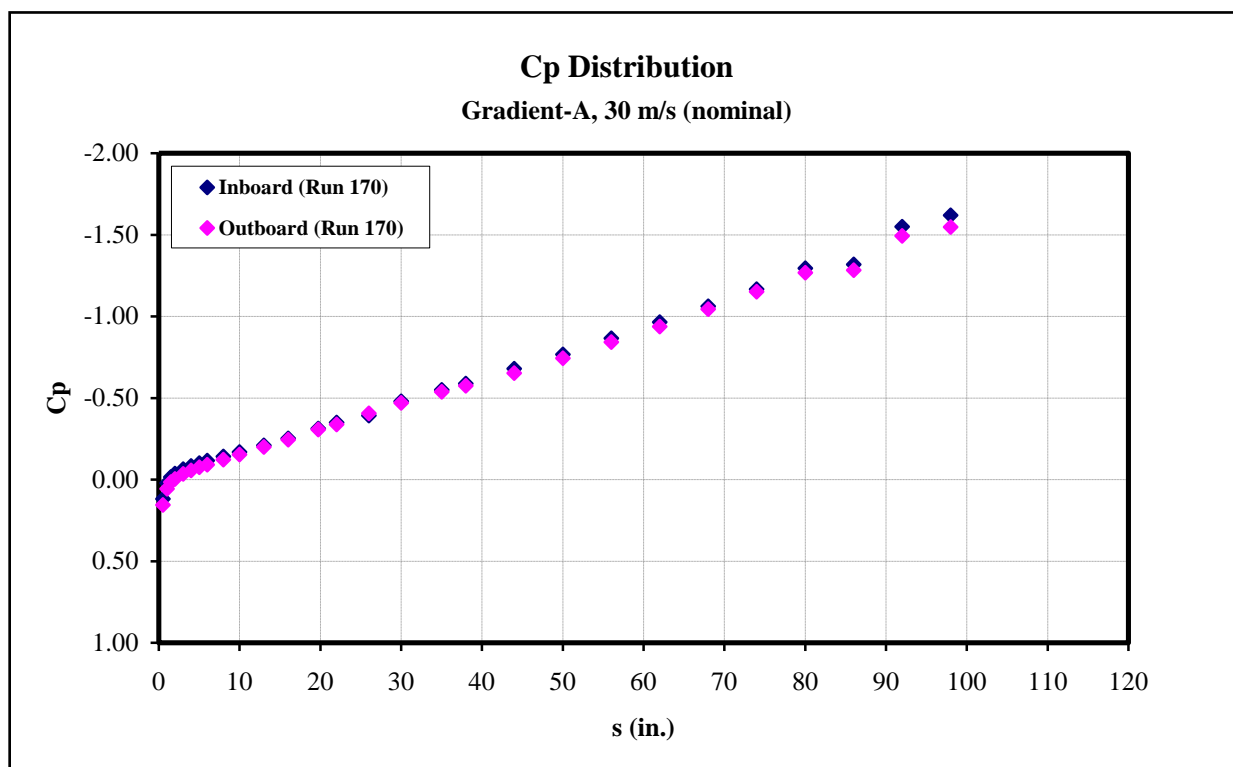


Figure 107: Gradient-A Cp distribution data (Run 170), U=30 m/s (nominal).

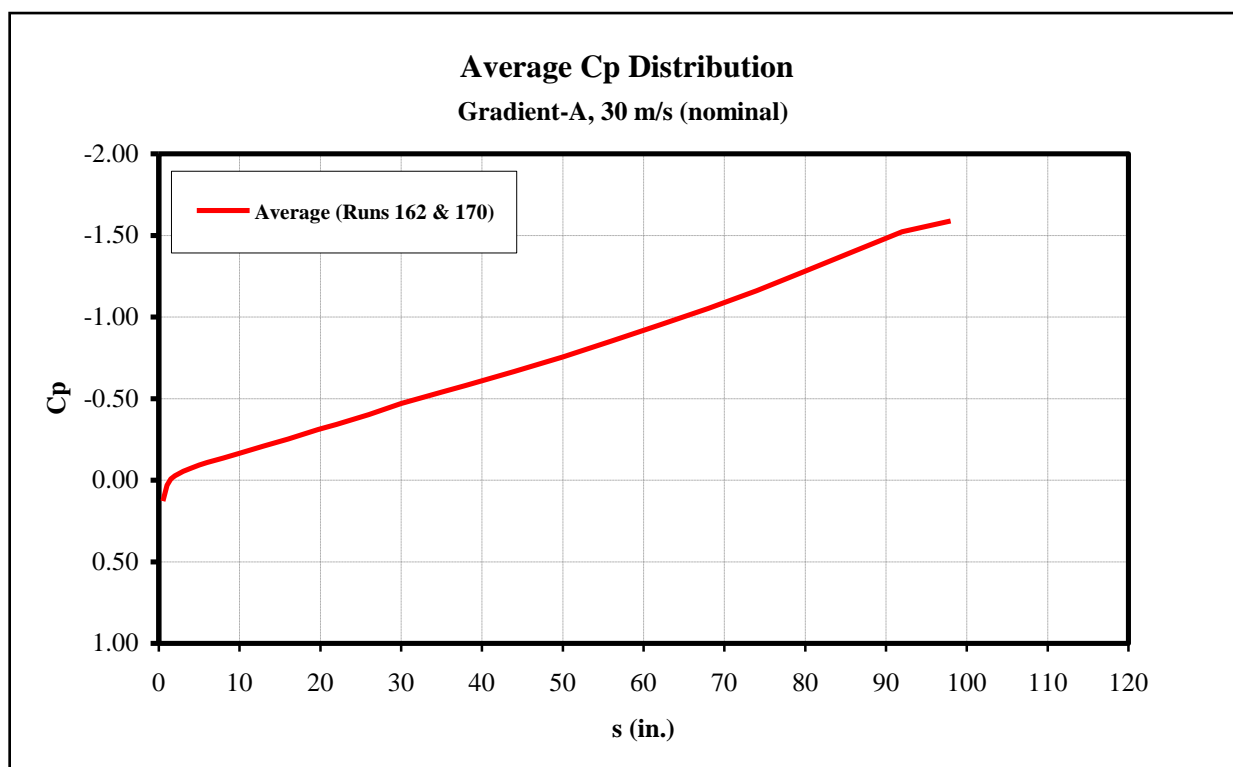


Figure 108: Gradient-A average Cp distribution, U=30 m/s (nominal).

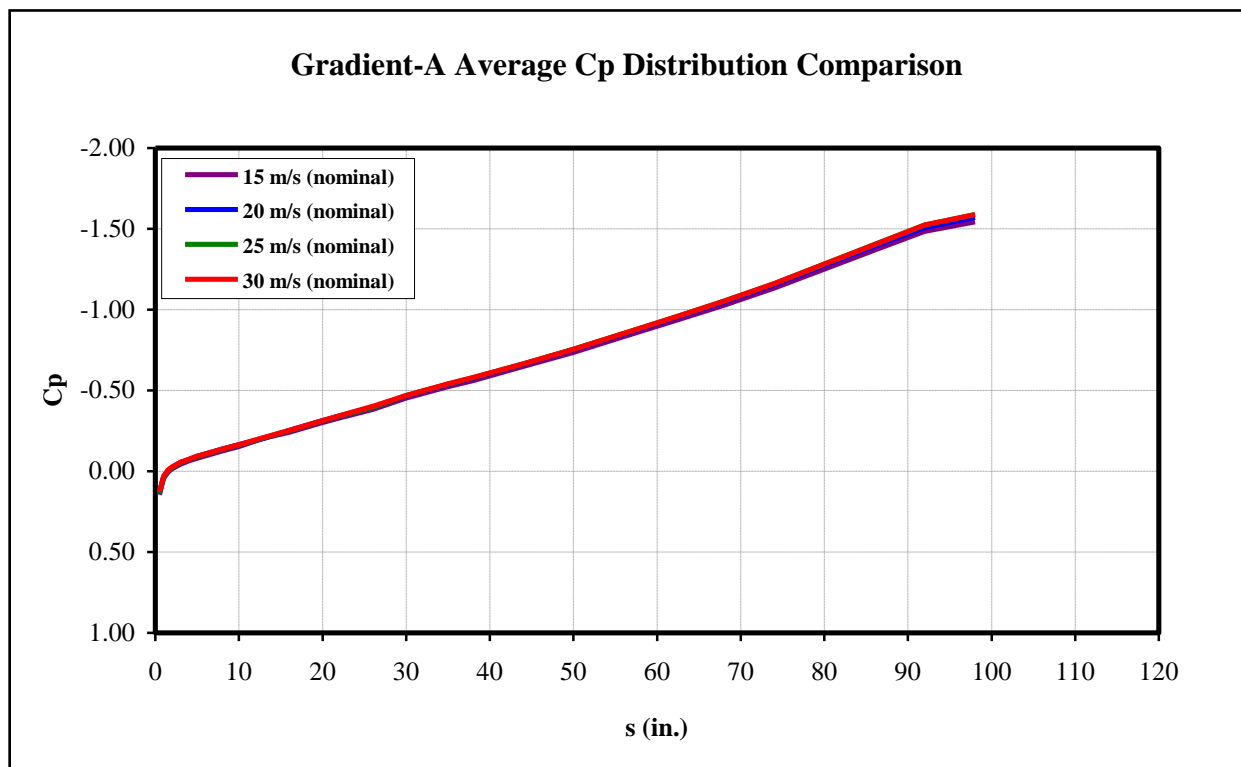


Figure 109: Comparison of Gradient-A average Cp distribution.

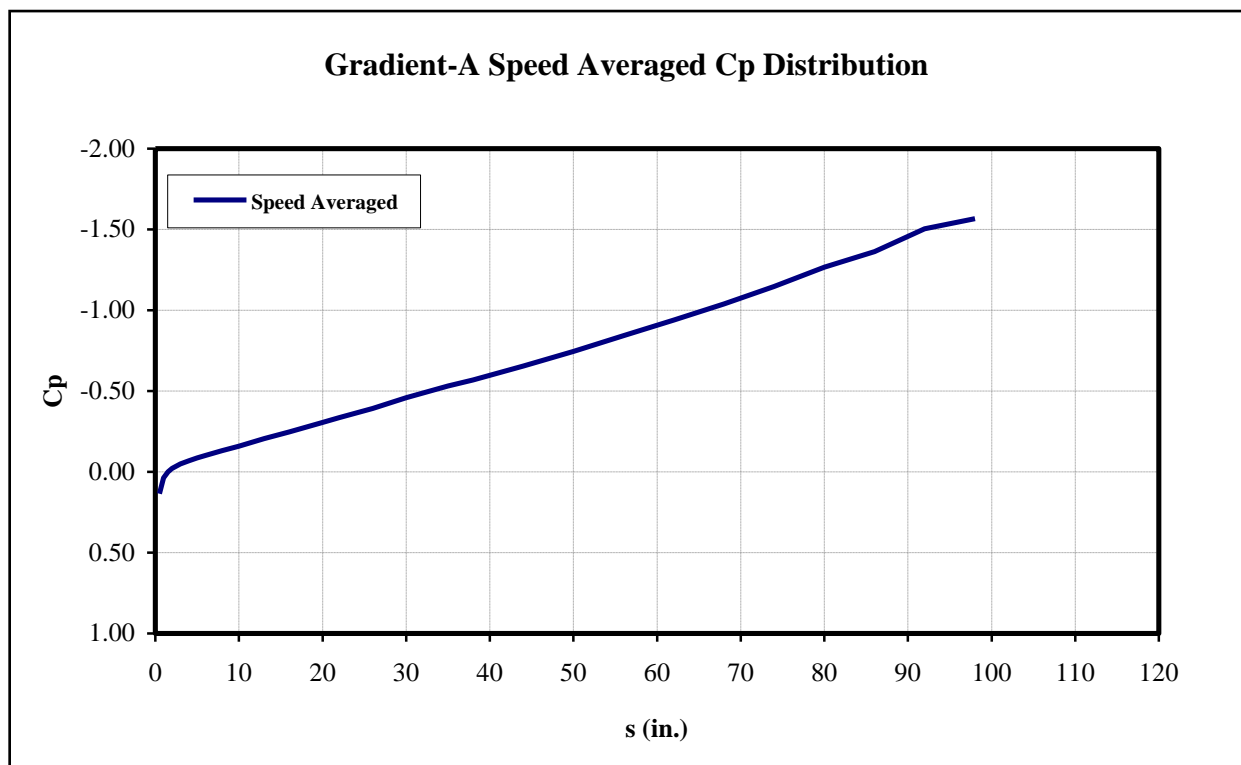


Figure 110: Gradient-A speed averaged Cp distribution.

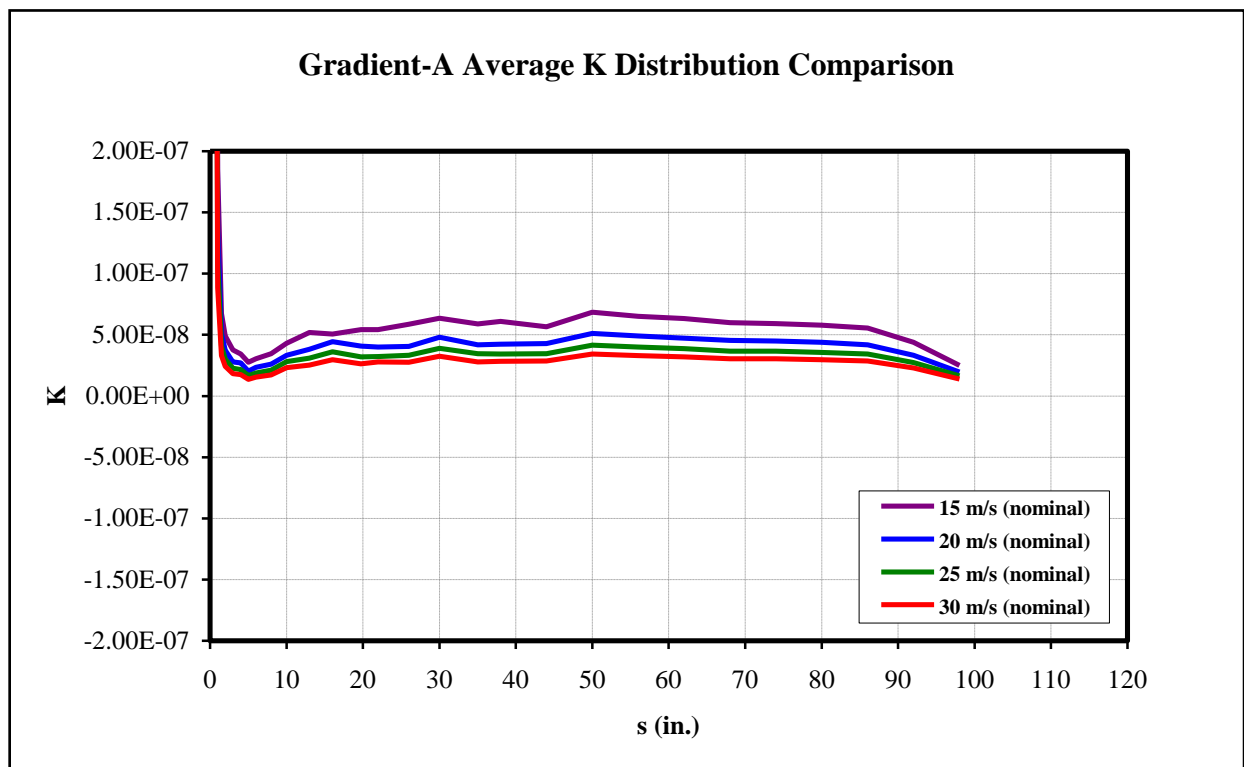


Figure 111: Comparison of Gradient-A average K distribution.

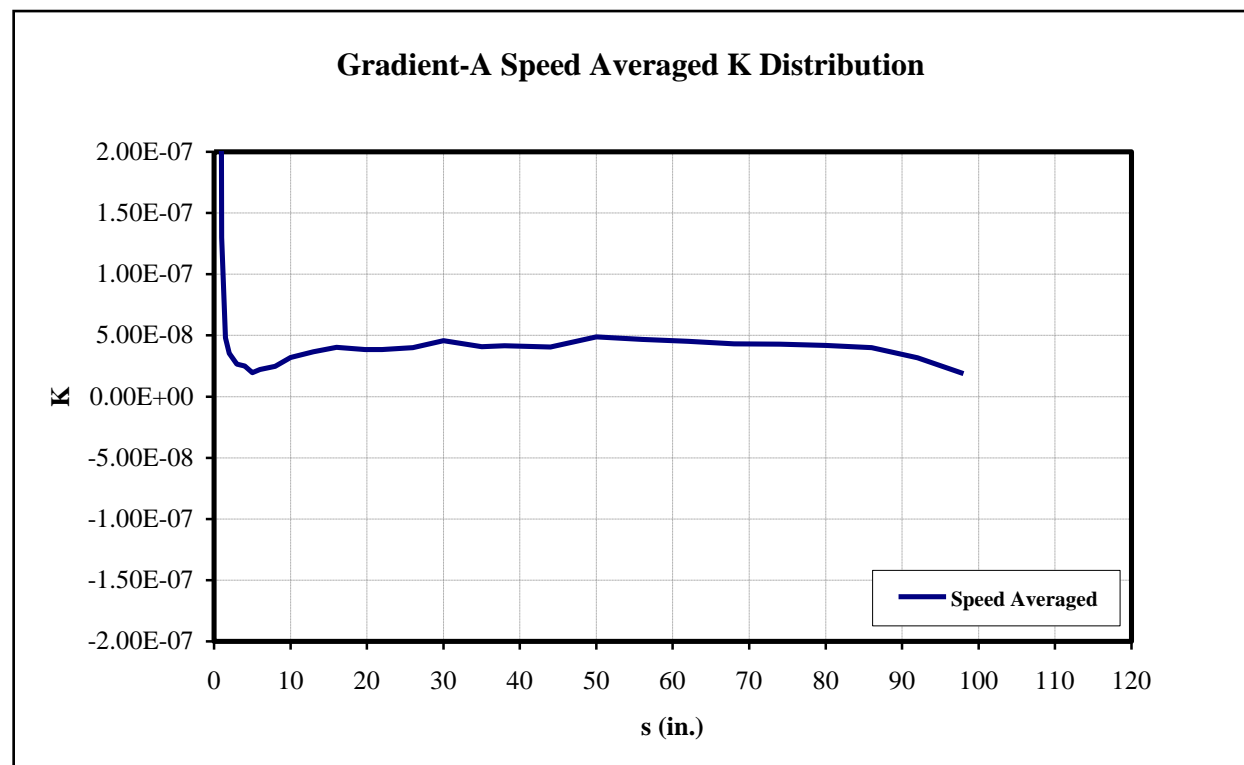


Figure 112: Gradient-A speed averaged K distribution.

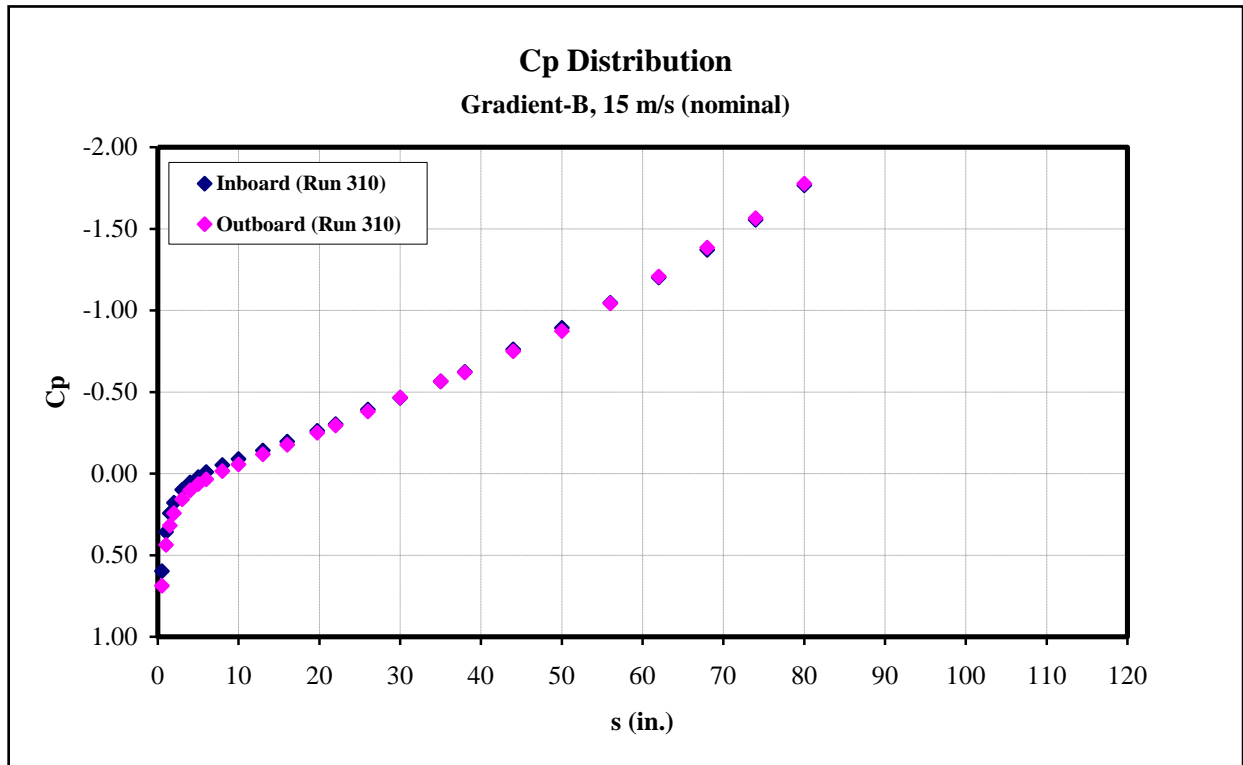


Figure 113: Gradient-B Cp distribution data (Run 310), U=15 m/s (nominal).

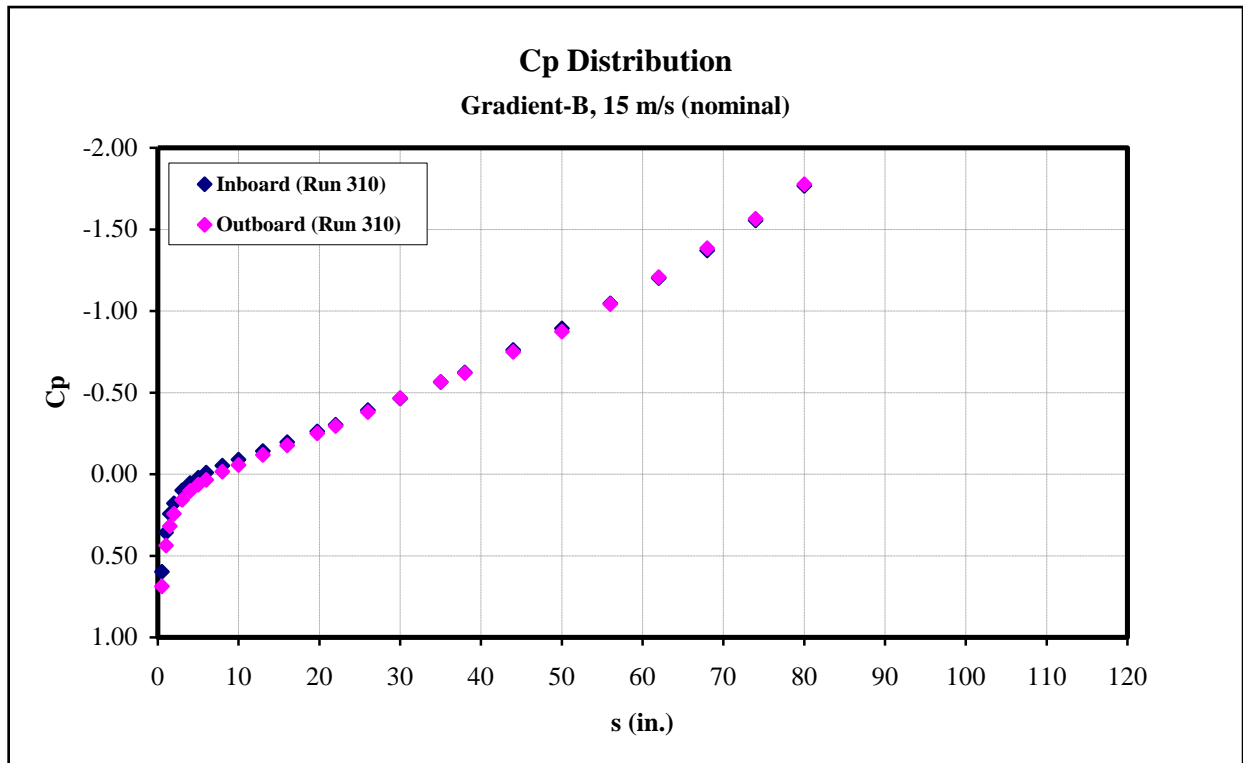


Figure 114: Gradient-B Cp distribution data (Run 310), U=15 m/s (nominal).

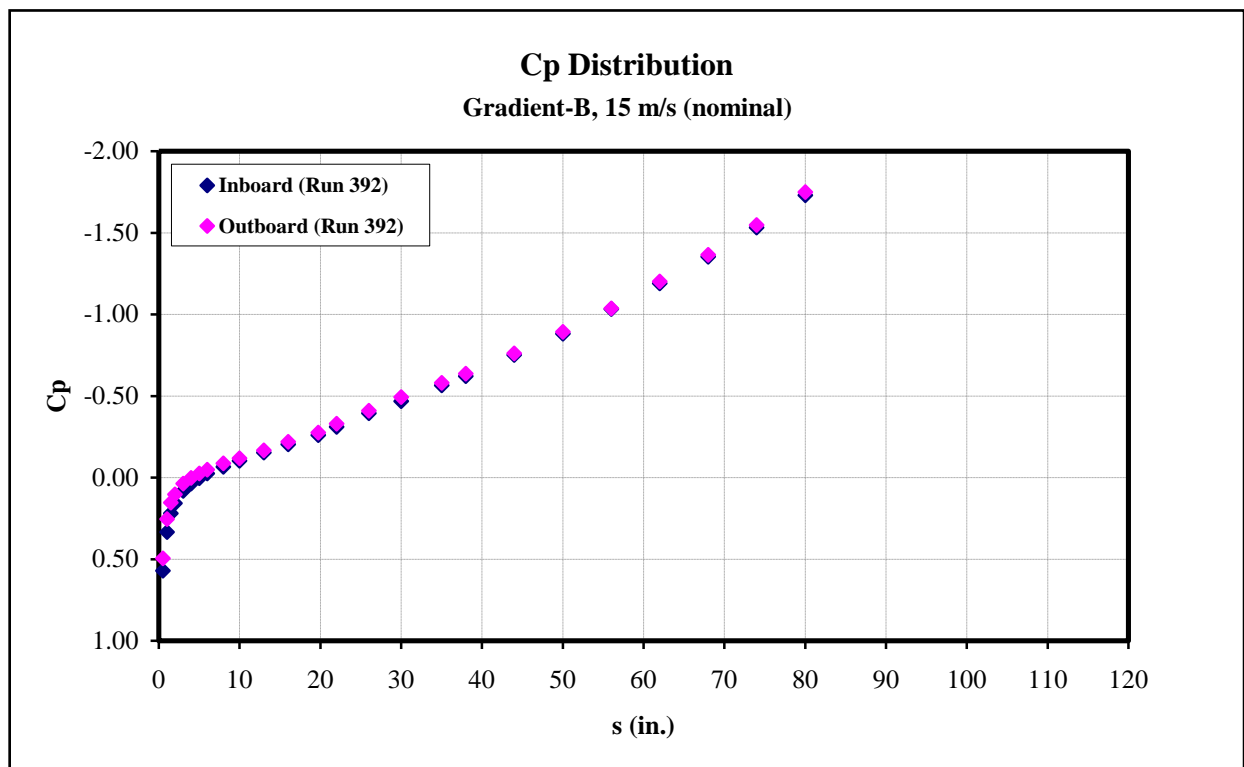


Figure 115: Gradient-B Cp distribution data (Run 392), U=15 m/s (nominal).

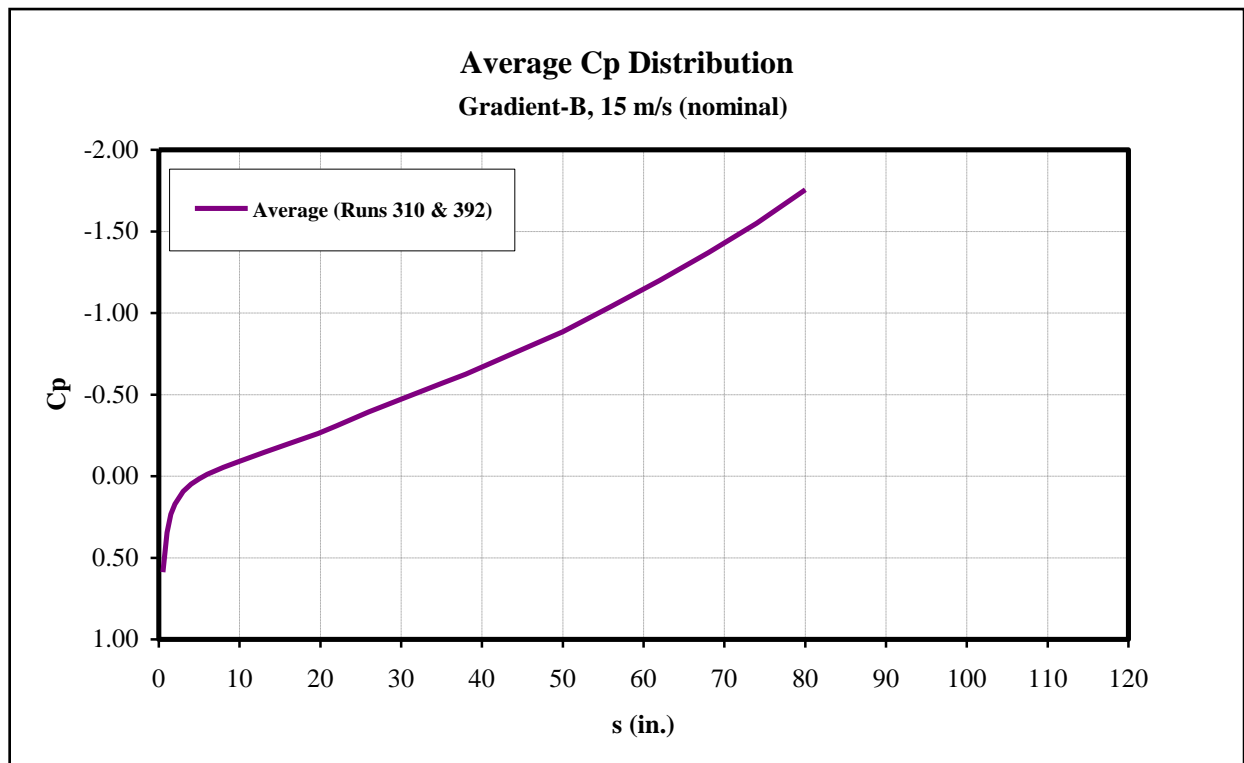


Figure 116: Gradient-B average Cp distribution, U=15 m/s (nominal).

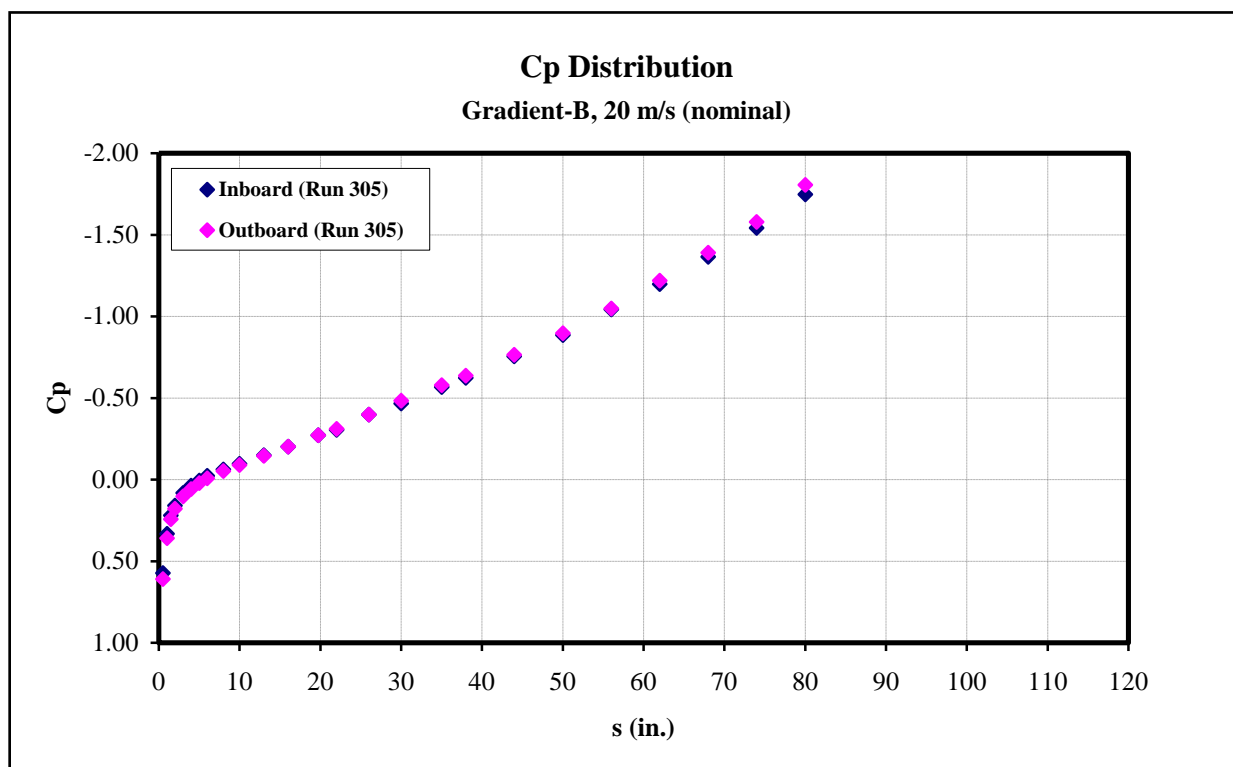


Figure 117: Gradient-B Cp distribution data (Run 305), U=20 m/s (nominal).

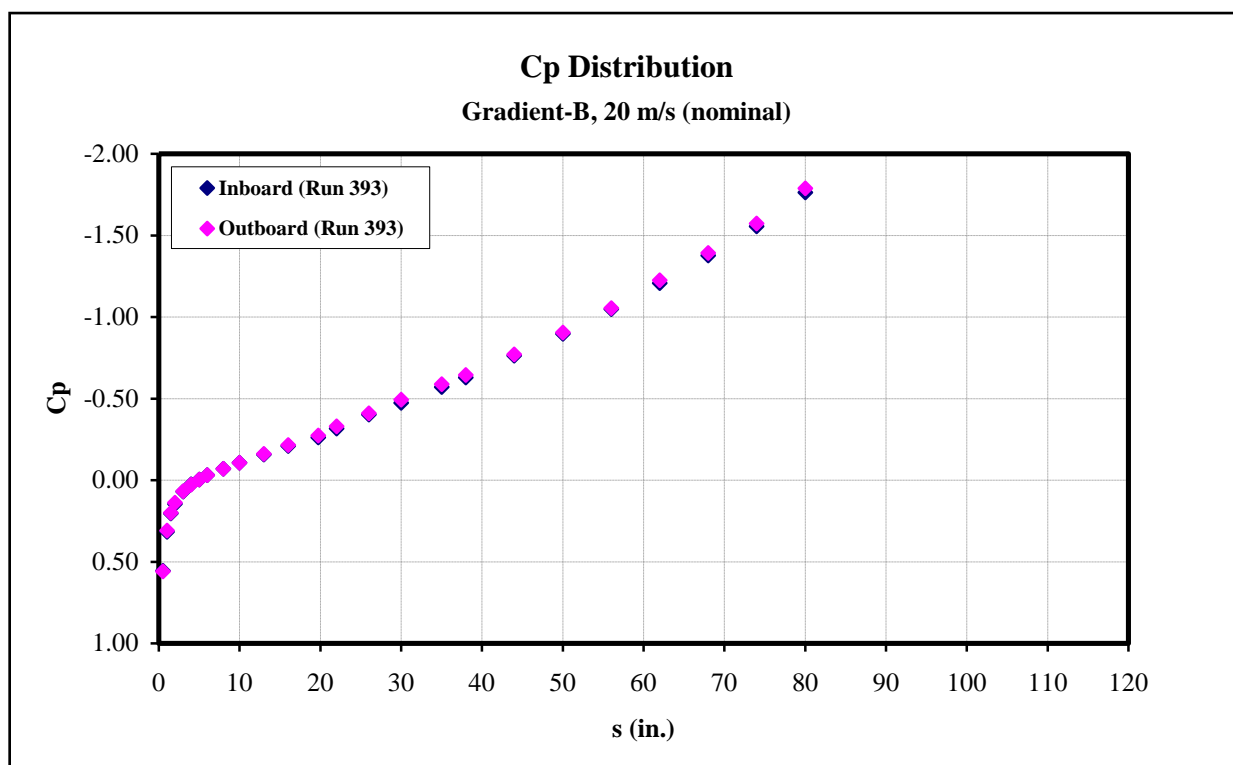


Figure 118: Gradient-B Cp distribution data (Run 393), U=20 m/s (nominal).

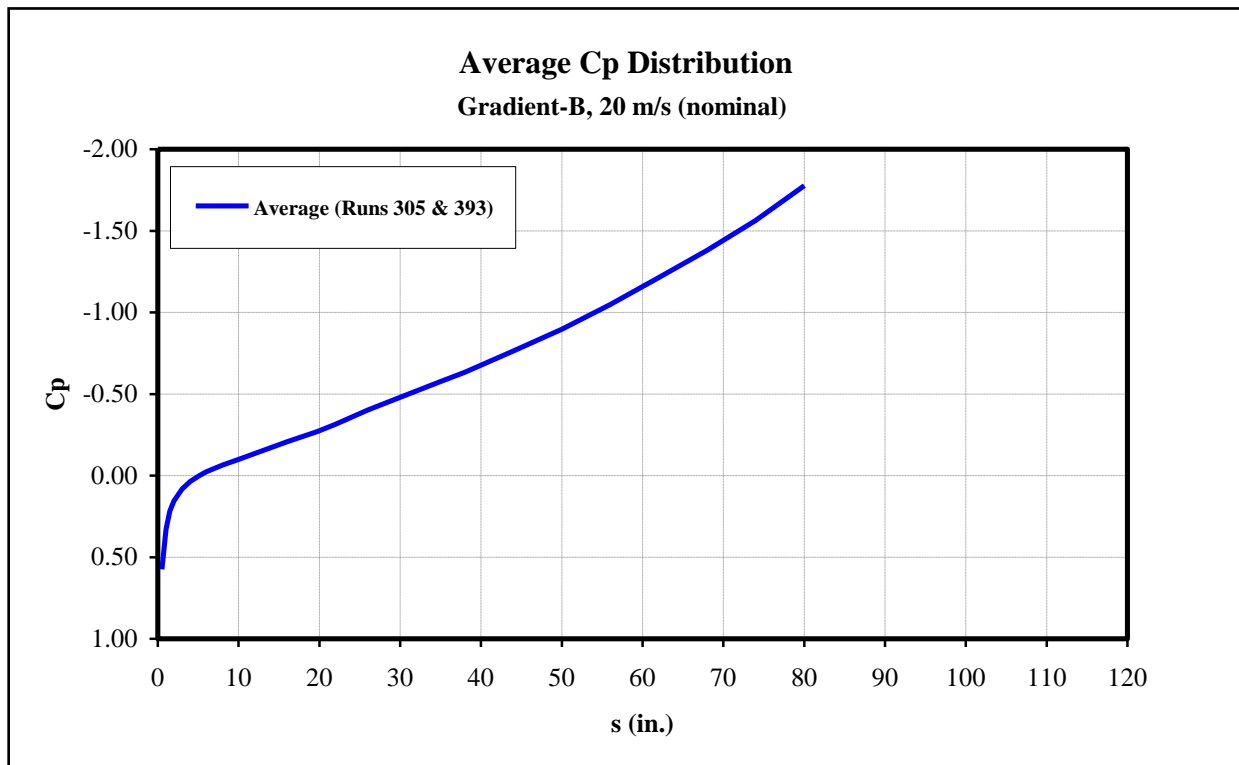


Figure 119: Gradient-B average Cp distribution, U=20 m/s (nominal).

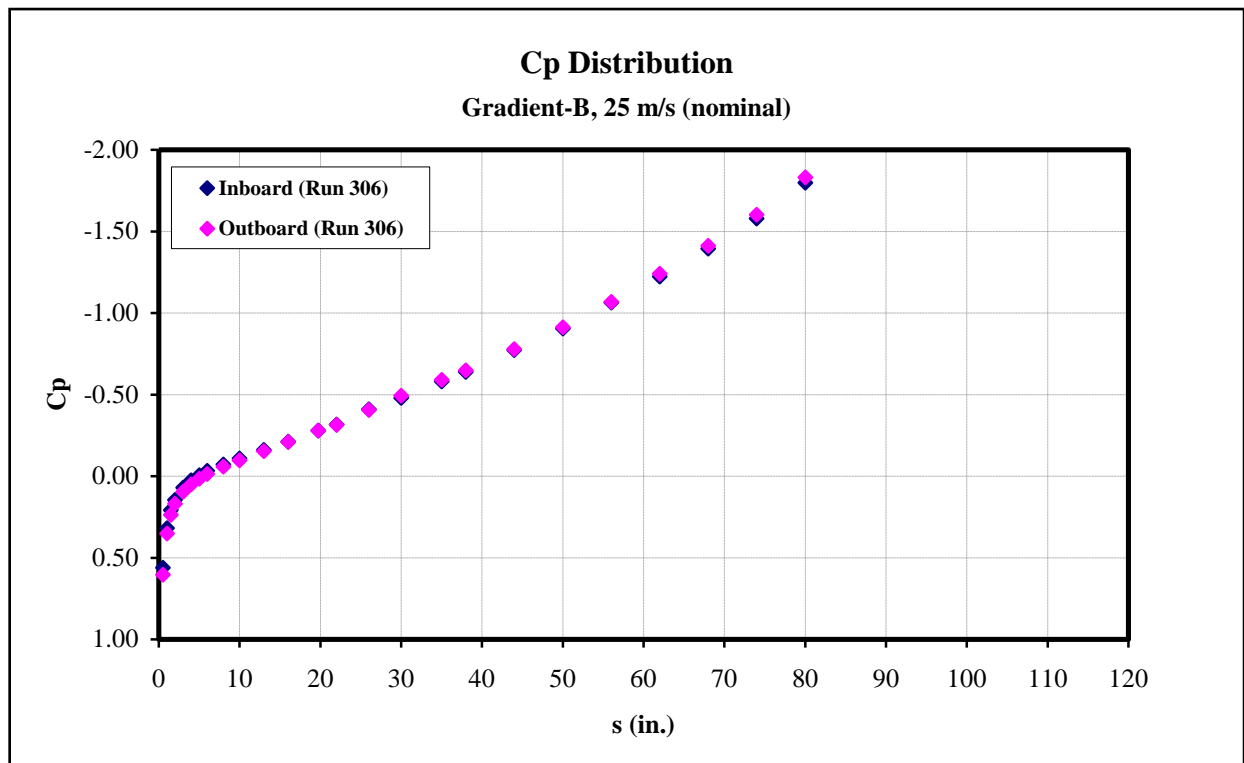


Figure 120: Gradient-B Cp distribution data (Run 306), U=25 m/s (nominal).

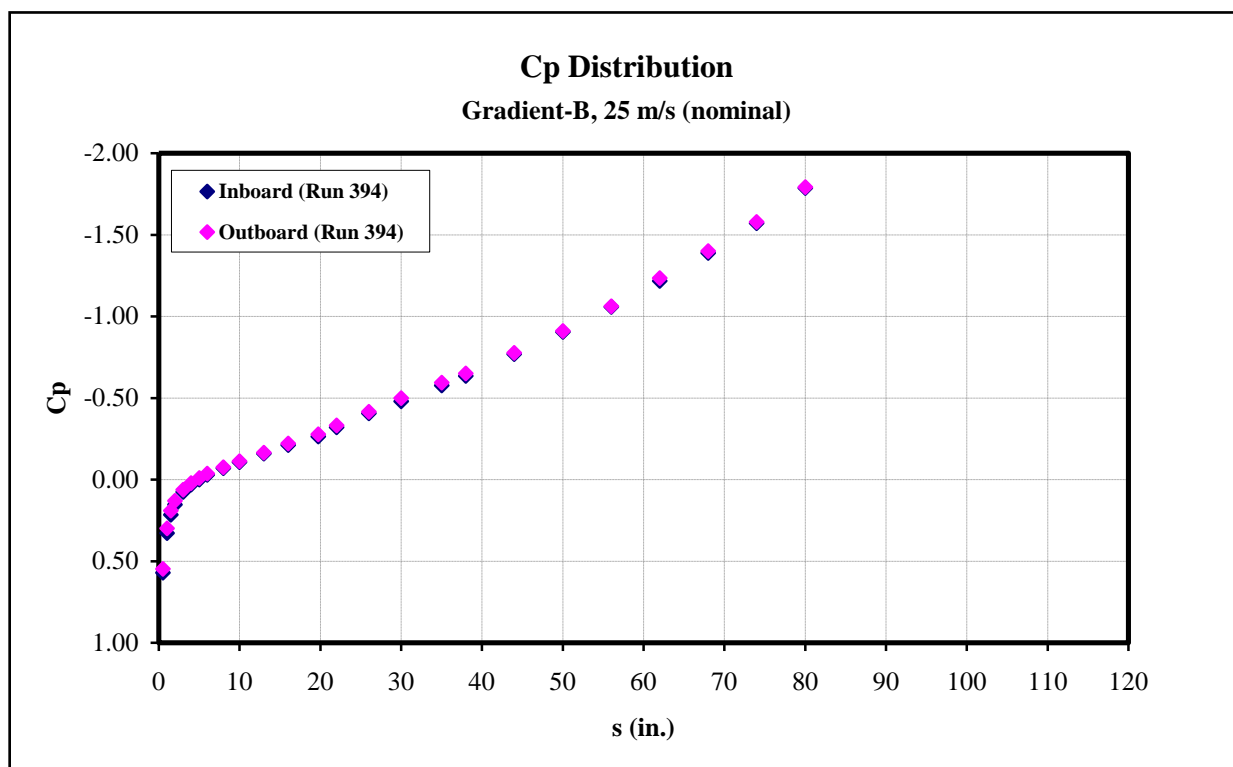


Figure 121: Gradient-B Cp distribution data (Run 394), U=25 m/s (nominal).

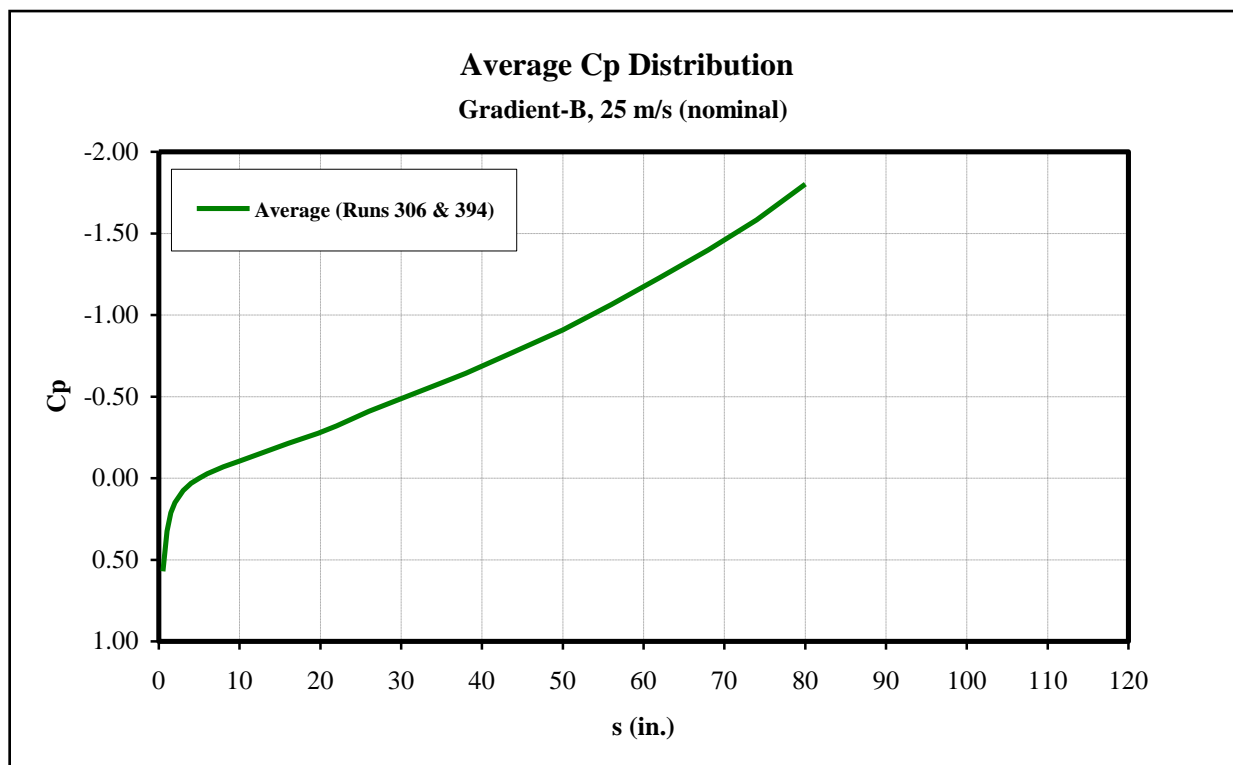


Figure 122: Gradient-B average Cp distribution, U=25 m/s (nominal).

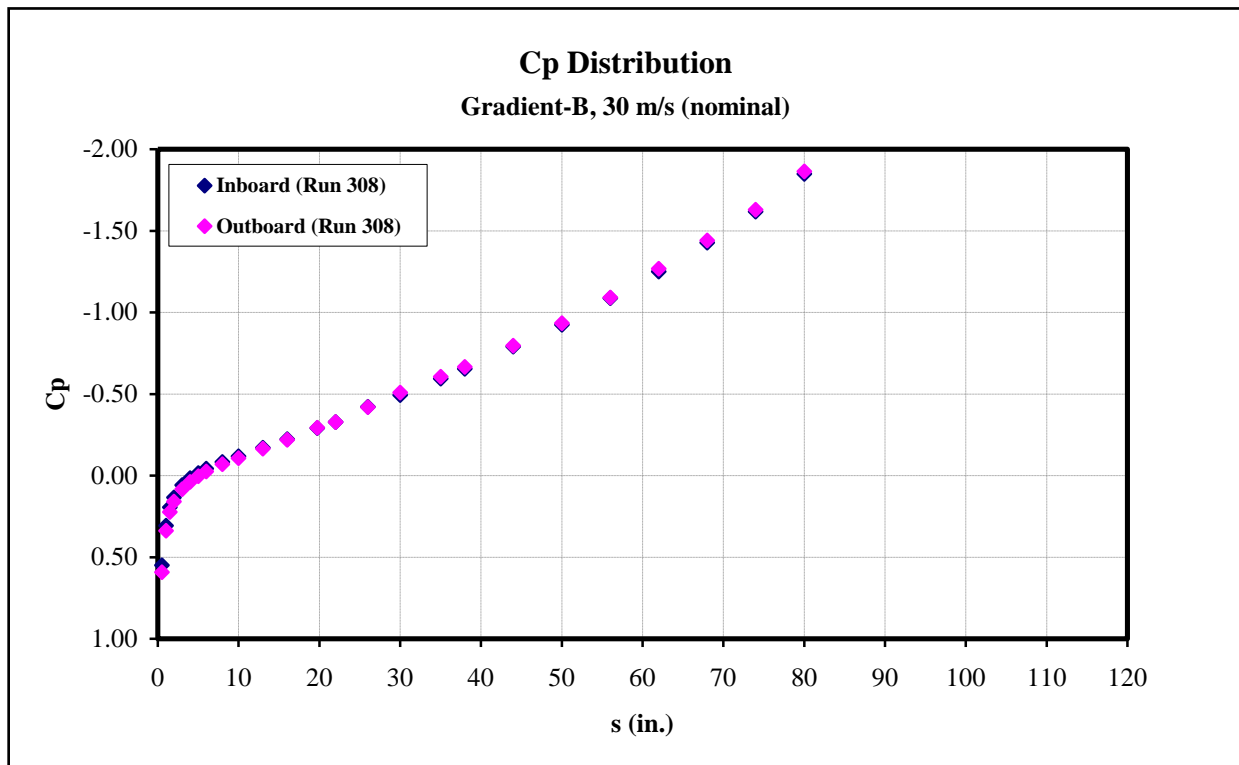


Figure 123: Gradient-B Cp distribution data (Run 308), U=30 m/s (nominal).

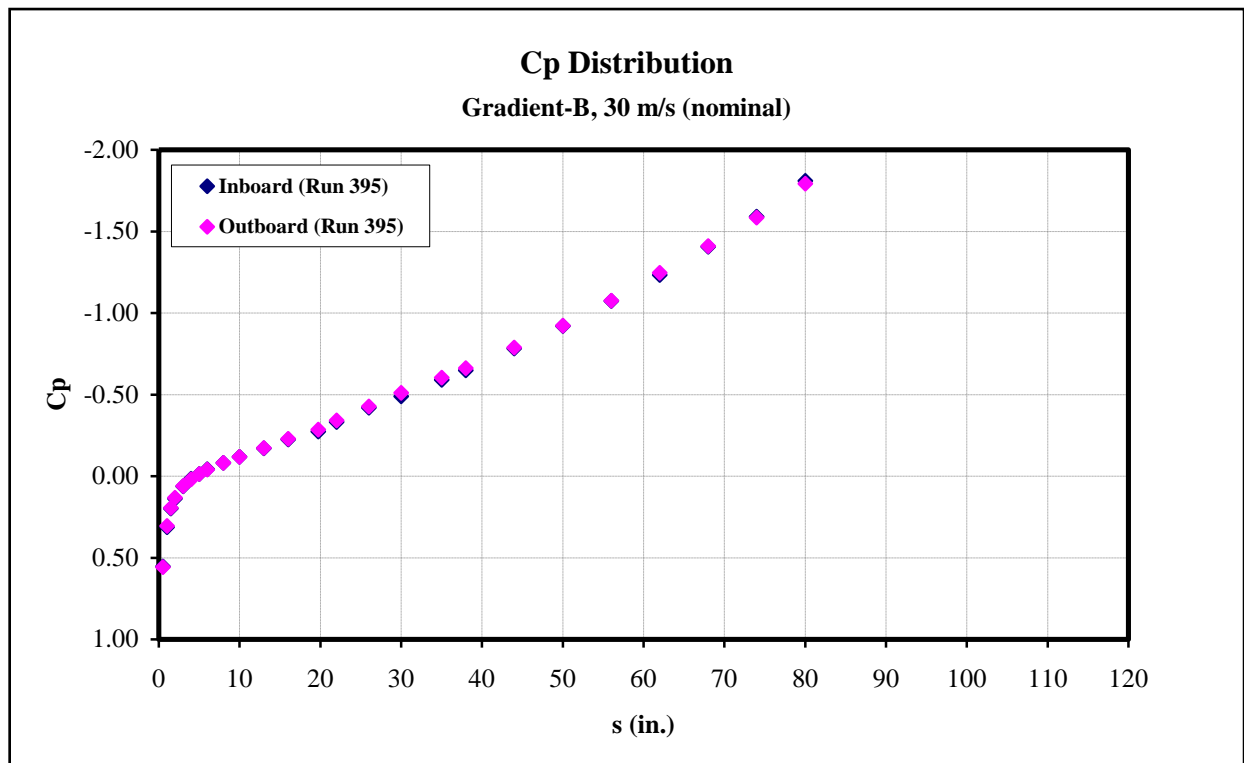


Figure 124: Gradient-B Cp distribution data (Run 395), U=30 m/s (nominal).

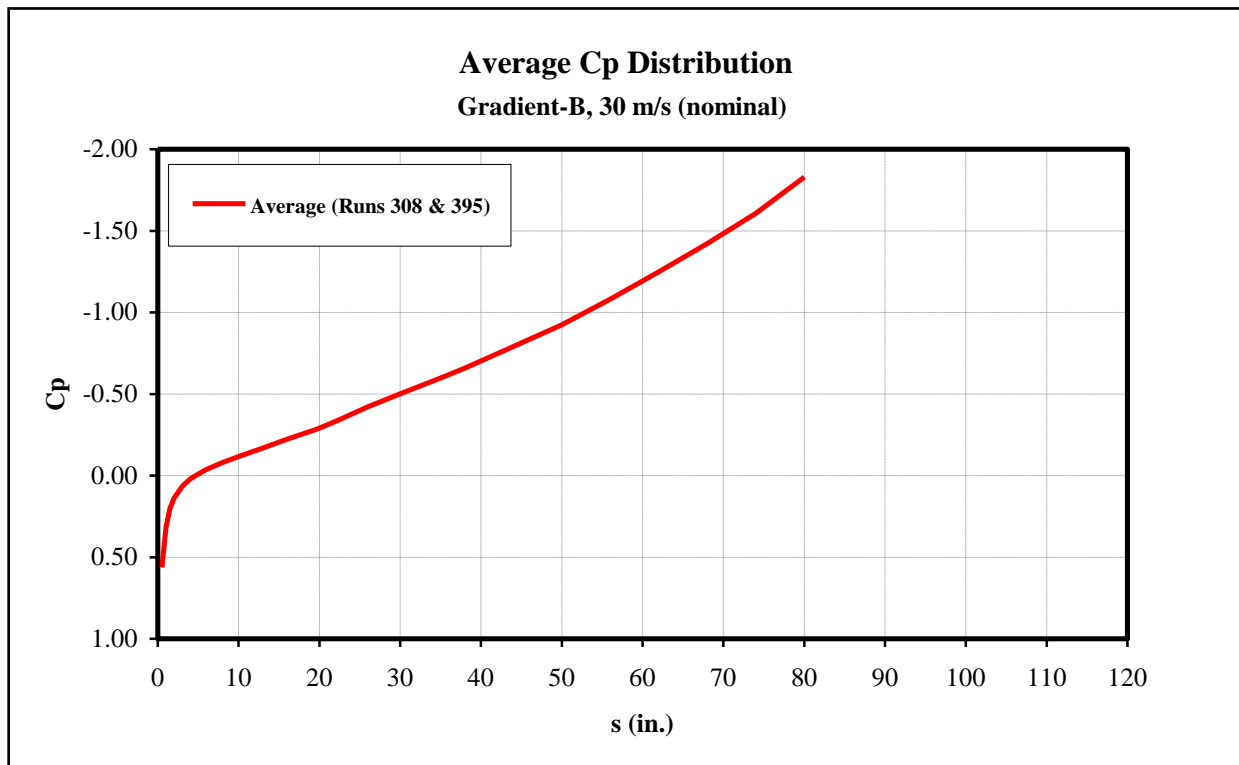


Figure 125: Gradient-B average C_p distribution, $U=30$ m/s (nominal).

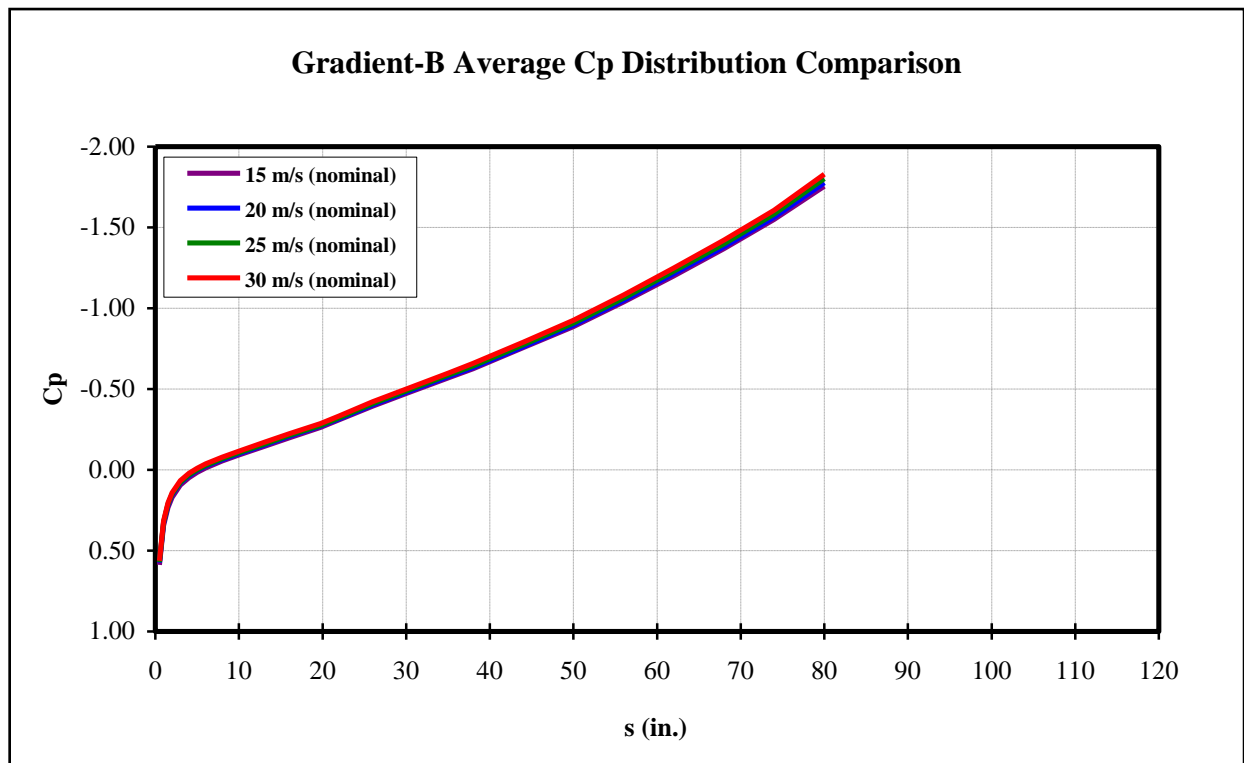


Figure 126: Comparison of Gradient-B average C_p distribution.

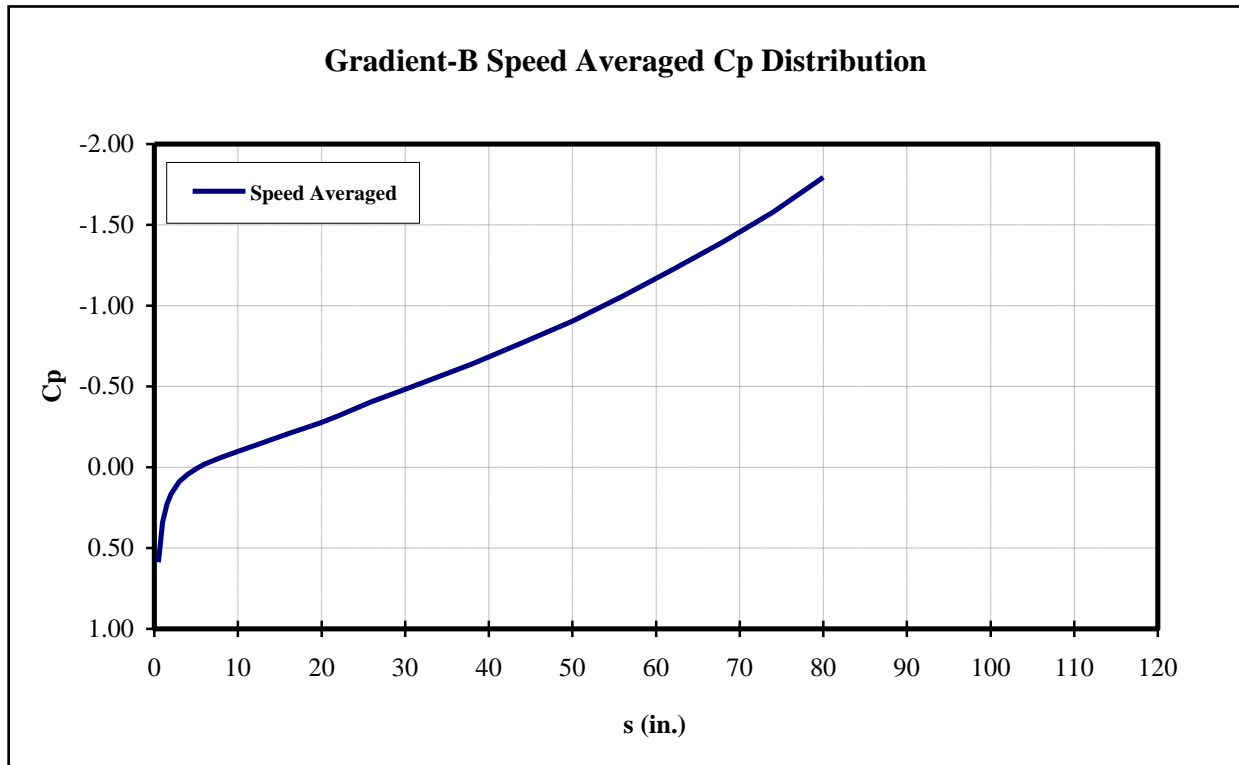


Figure 127: Gradient-B speed averaged Cp distribution.

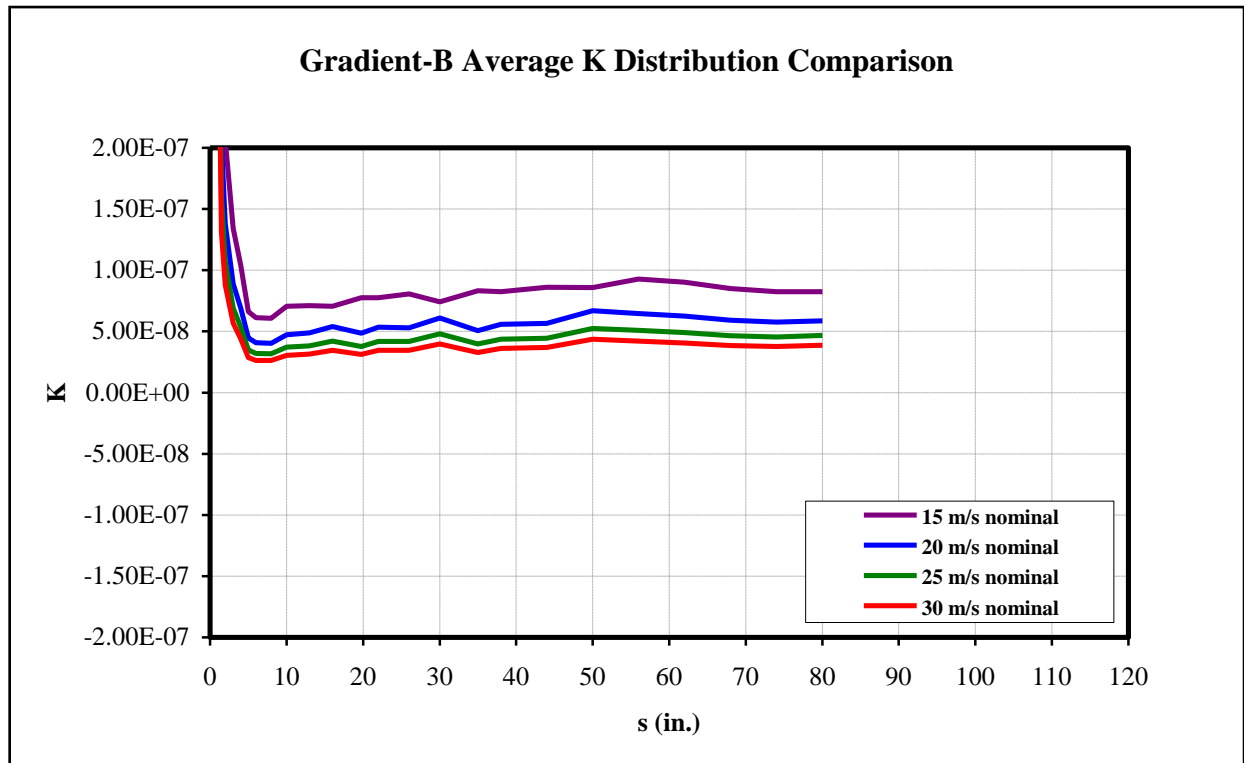


Figure 128: Comparison of Gradient-B average K distribution.

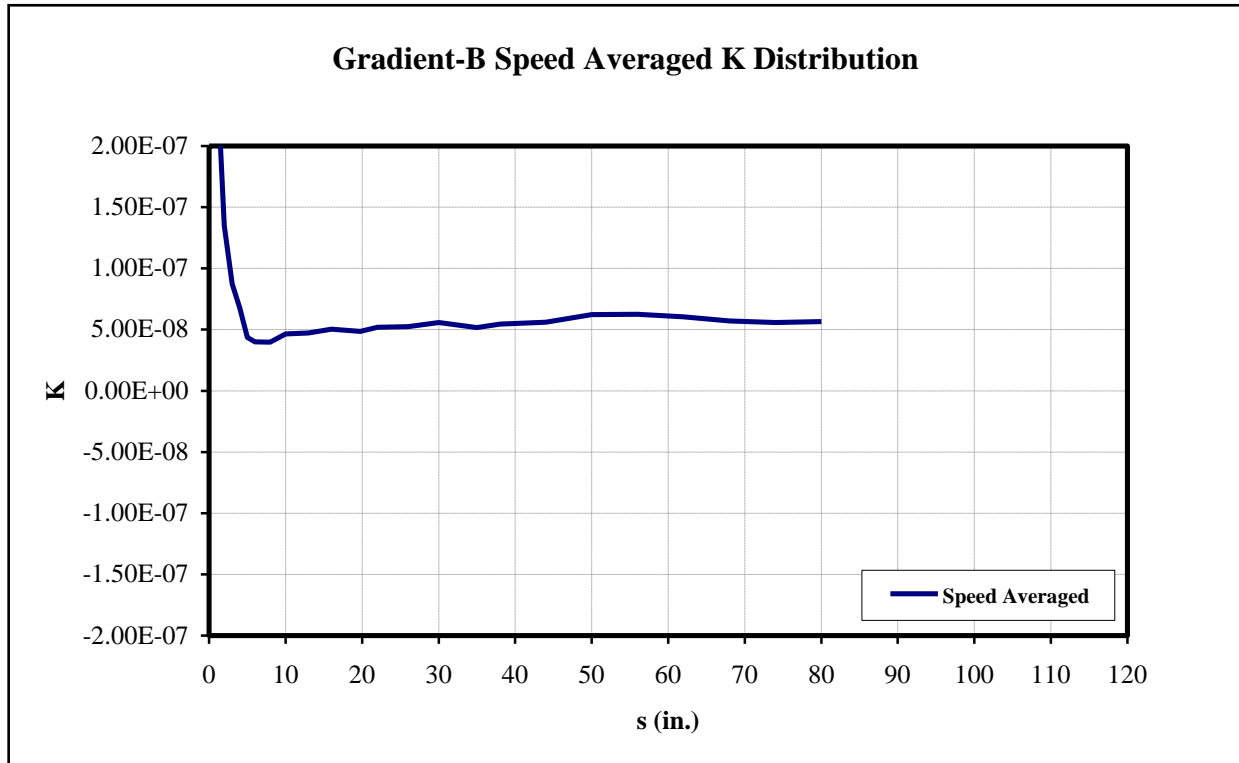


Figure 129: Gradient-B speed averaged K distribution.

A comparison between the three models' pressure distributions at various speeds is shown in Figures 130-133. The speed averaged comparison for the three models are shown in Figures 134-135. These plots show a comparison of pressure gradient (both dimensional and nondimensional) produced by the models.

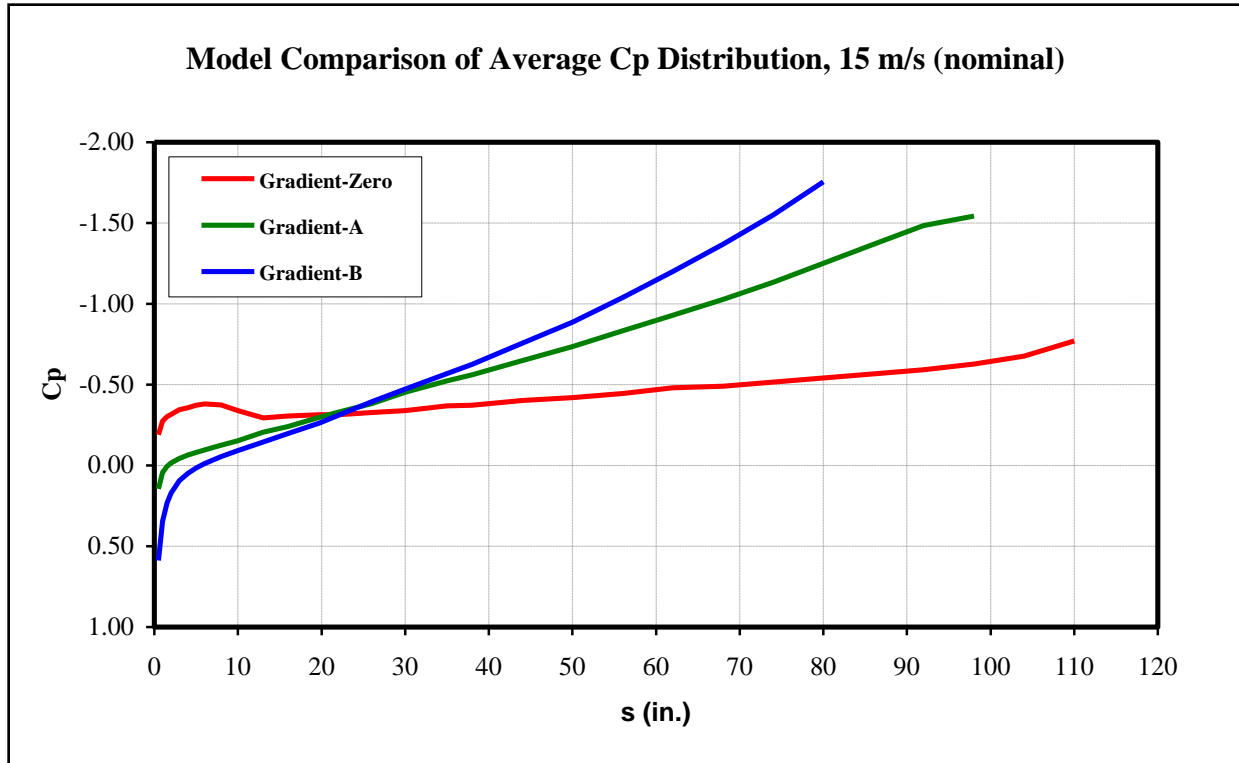


Figure 130: Model comparison of average Cp distribution, U=15 m/s (nominal).

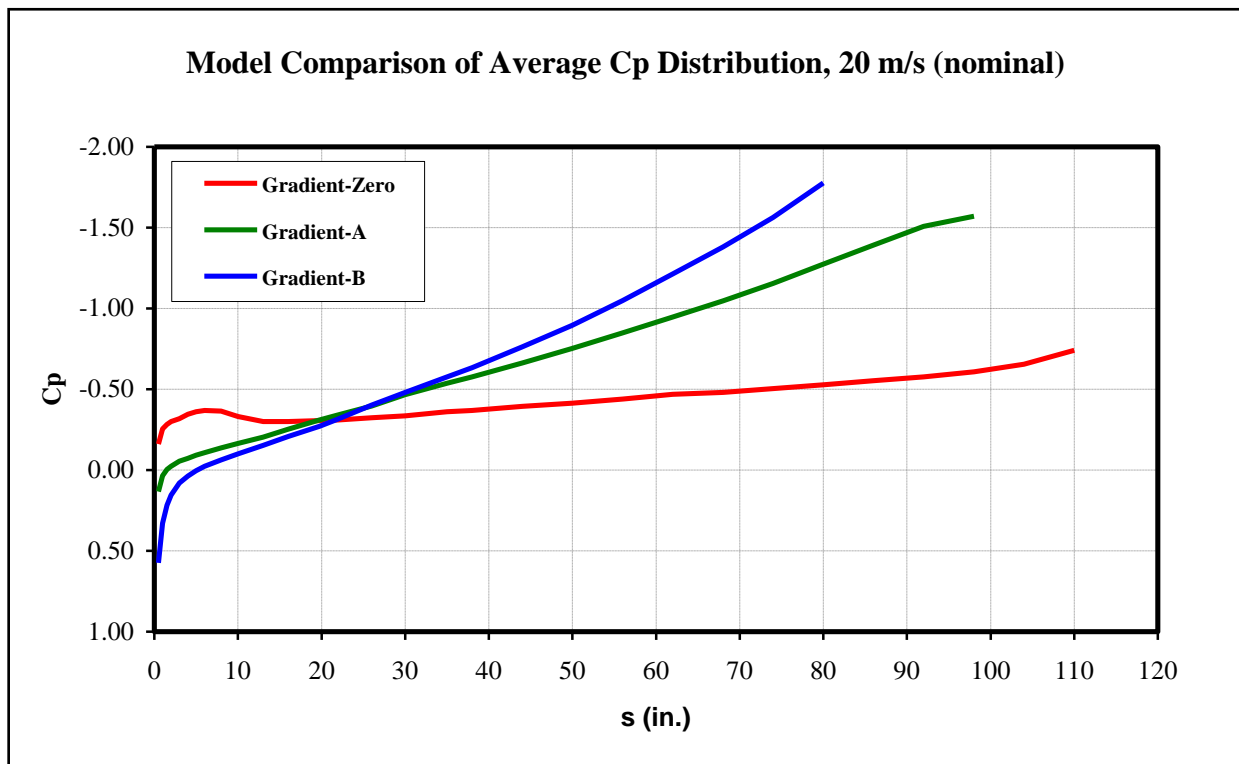


Figure 131: Model comparison of average Cp distribution, U=20 m/s (nominal).

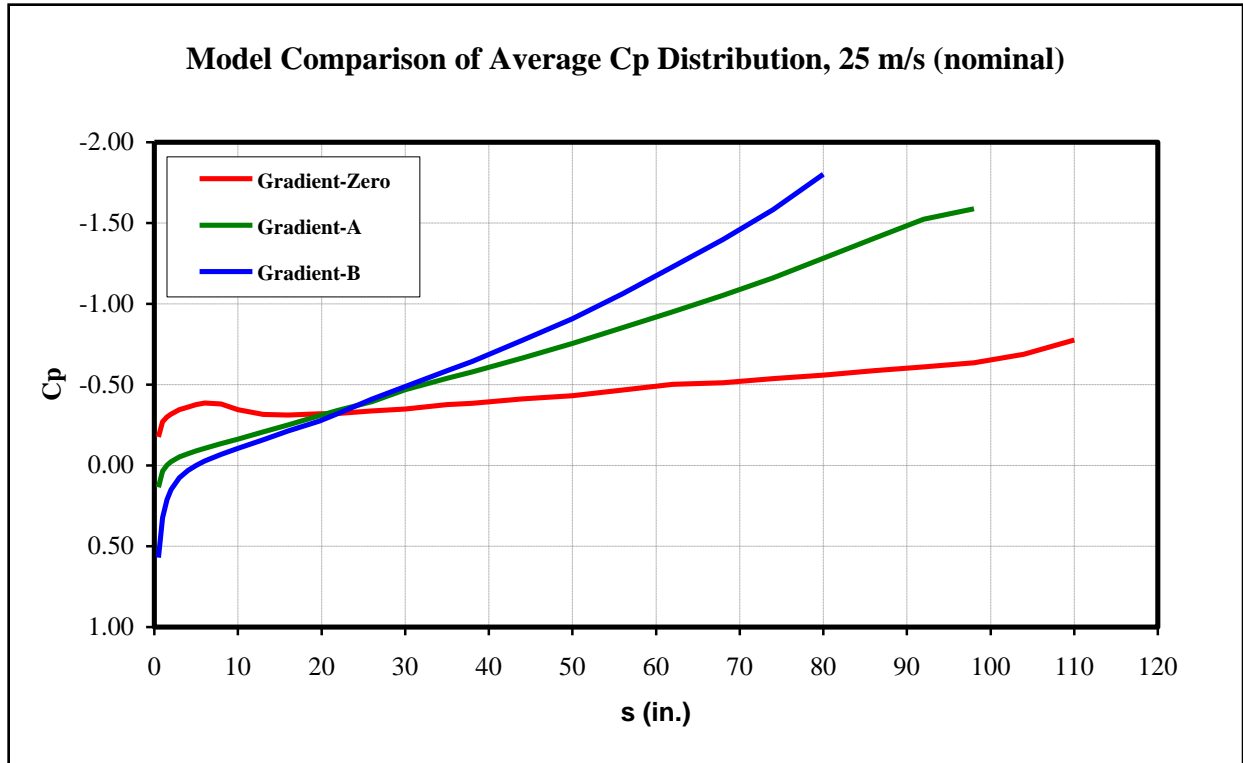


Figure 132: Model comparison of average C_p distribution, $U=25$ m/s (nominal).

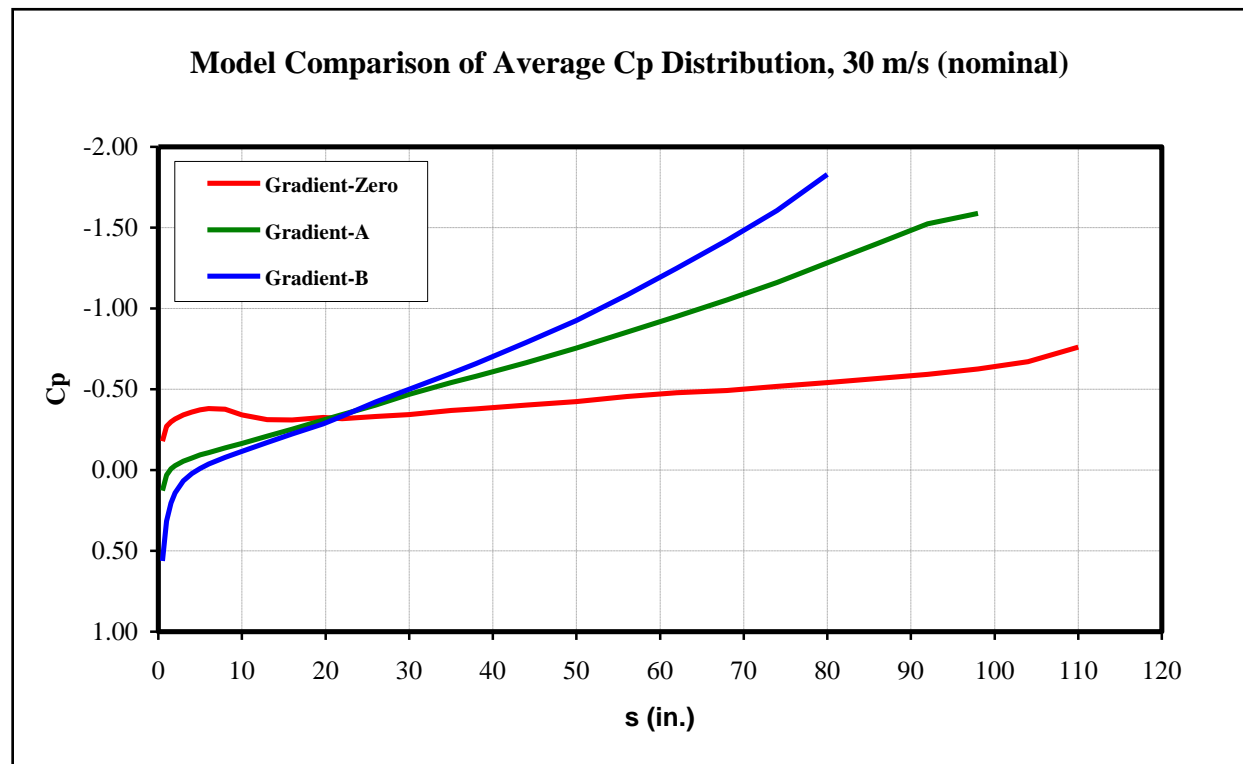


Figure 133: Model comparison of average C_p distribution, $U=30$ m/s (nominal).

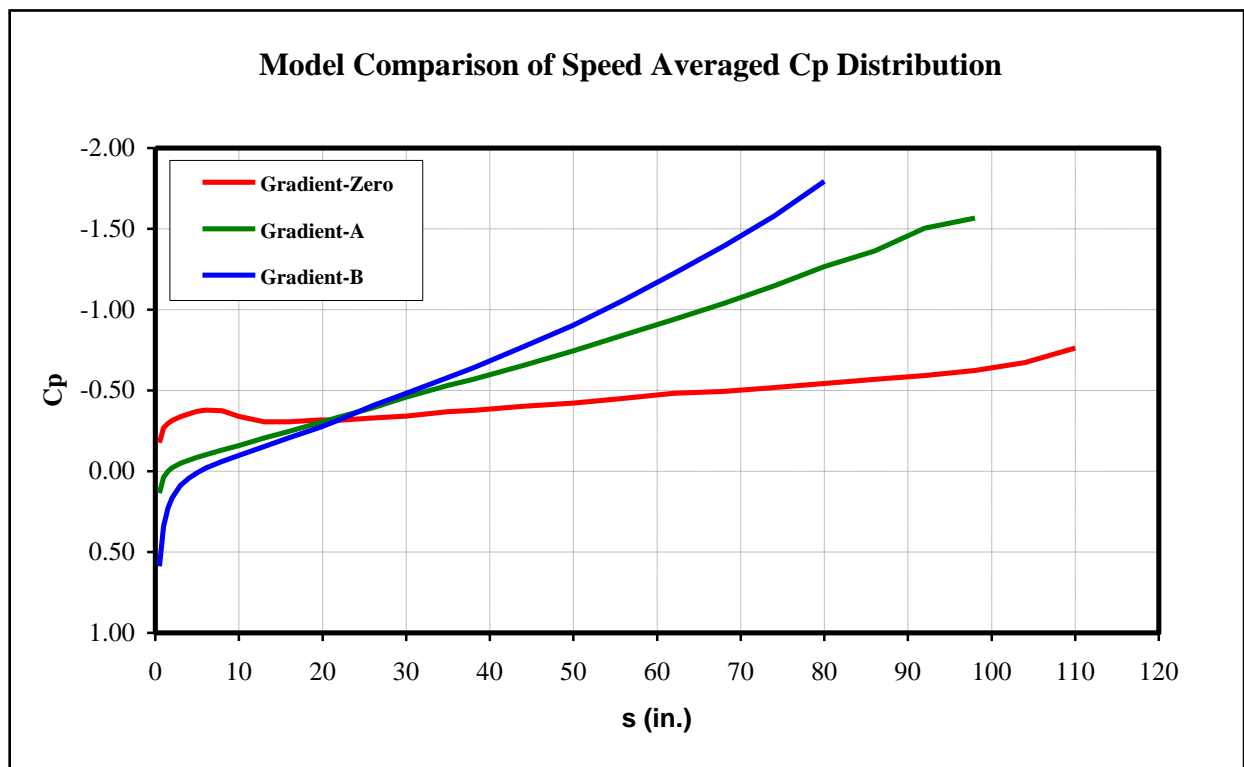


Figure 134: Model comparison of speed averaged C_p distribution.

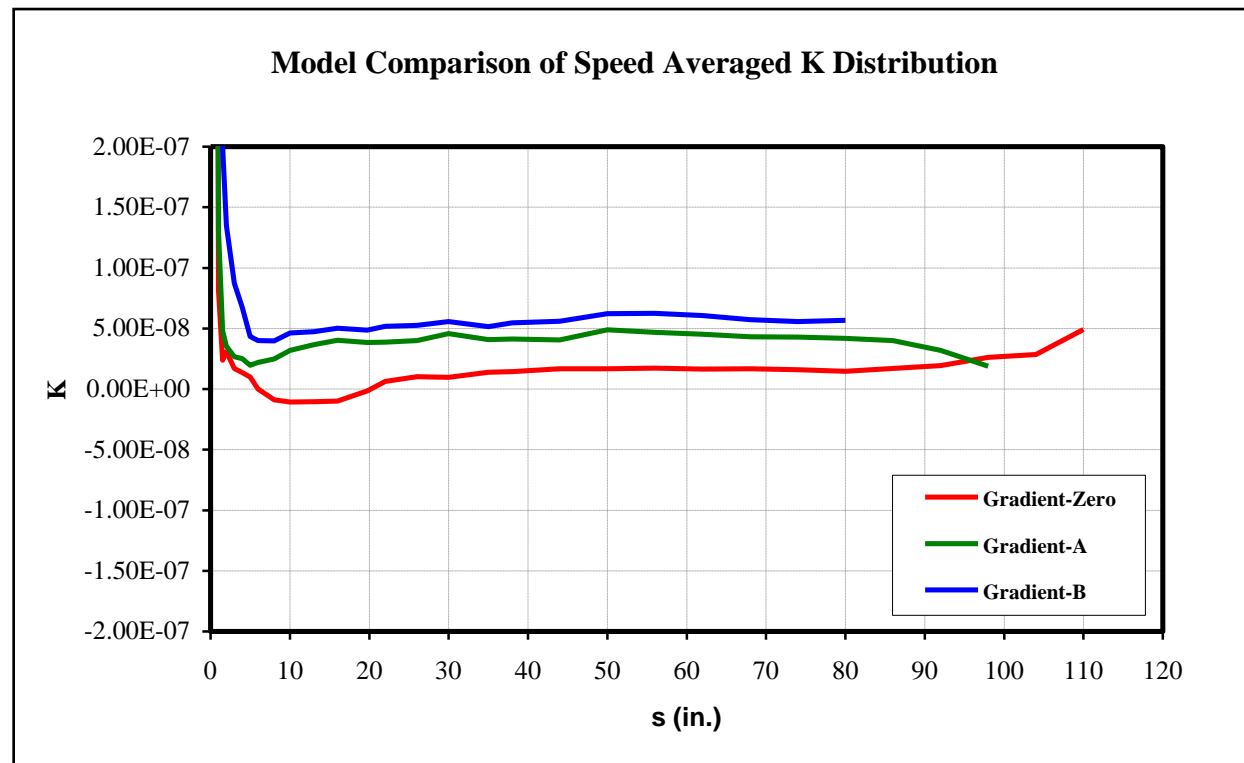


Figure 135: Model comparison of speed averaged C_p distribution.

7.3 Boundary Layer Probe Traversing System

7.3.1 Boundary Layer Probe Traversing System Design

A traverse was designed that would be capable of traversing both total pressure tube and a hot wire probe through the boundary layer (Figure 136). The traversing system, called Boundary Layer Data System (BLDS), is a fully self-contained device with internal power and memory. The BLDS device weighs 0.75 lb. and runs off a lithium-polymer (or, alternatively, a 9V) battery. The BLDS device provides precise position for either the hotwire or the total pressure probe. It records time-stamped position, local dynamic pressure, static pressure and temperature data at each point. The BLDS device can either be light-triggered, manually triggered, or set to record data after a given time delay. The BLDS attaches to the models with double-sided structural adhesive tape, and thus can be placed at any position on the models. The BLDS used by the SETS program is similar in concept to in-flight boundary layer velocity profile measurement devices that have been developed previously^{7,8}.

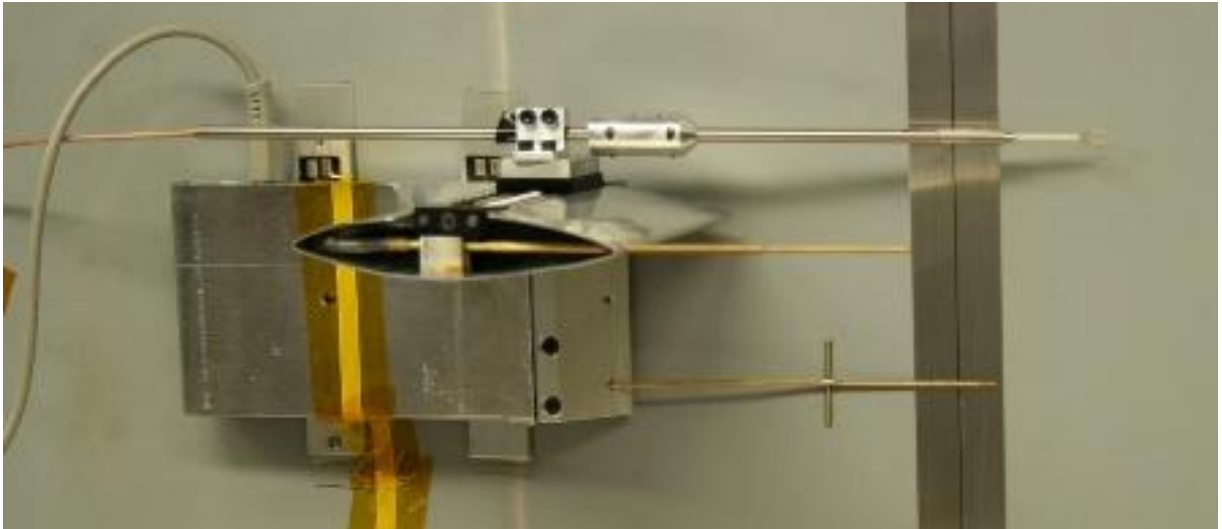


Figure 136: Boundary layer traverse used to measure velocity profiles and to traverse hot wire.

7.3.2 Boundary Layer Probe Traversing System Application

The BLDS device was used to measure local velocity profiles at the step location on each of the models. The local velocity profiles are needed in order to reduce the dimensioned step heights into dimensionless Re_k values (see Figure 137 and equation 4).

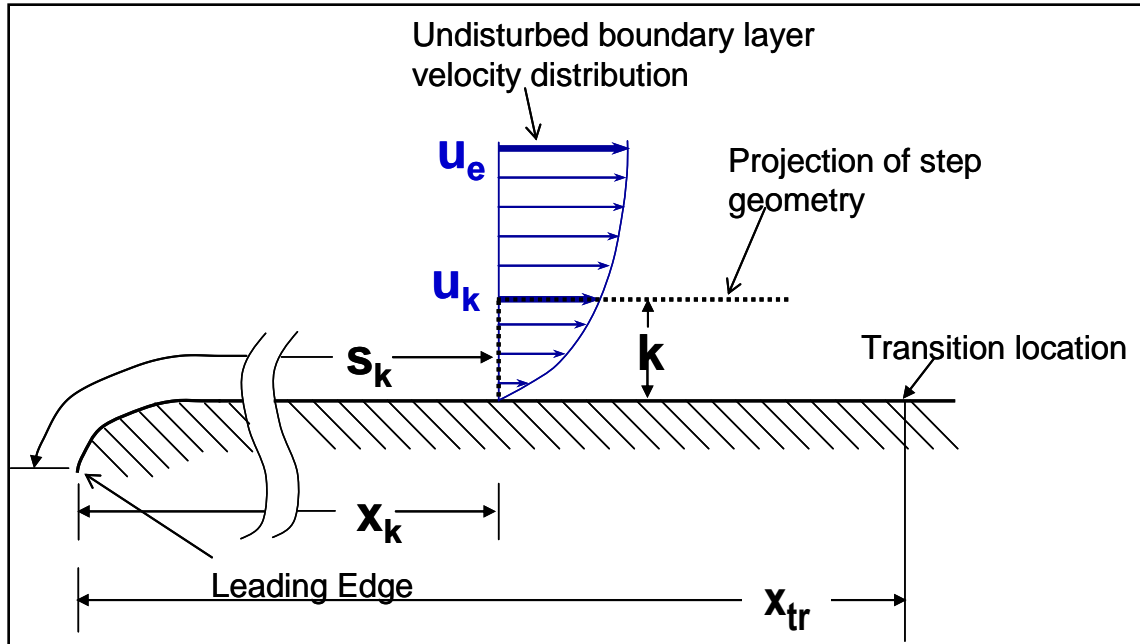


Figure 137: Illustration of velocity profile and u_k .

$$Re_k = \frac{u_k k}{\nu_k} \quad (4)$$

A light trigger (see Figure 138) was designed to start the data collection on the BLDS device once the HART vehicle moved into the test section. The test section is covered by a hood and thus the ambient light transitions from outside, ambient light to relative darkness (shadow), once the HART vehicle enters the hooded test section. The light trigger uses a photoresistor (CdS) and provides analog light level and digital trigger signals.



Figure 138: Light trigger connected to BLDS.

The data is stored onboard the BLDS in non-volatile memory until it is downloaded onto a laptop computer for viewing and analysis. The data is downloaded through a serial jack connection to a laptop running the BLDS software. The BLDS does not have to be removed from the model in order to download the data file after a run.

7.3.3 Boundary Layer Probe Velocity Profile Results

The file downloaded from the BLDS contains tab data of the following parameters, varying with time: date, time, the voltage of each of the three pressure probes (the out-of-the-boundary layer total pressure, the surface static pressure, and the moving total pressure), the temperature, voltage of the battery, encoder counts, and the analog and digital light signal in volts, if the light trigger is being used.

From the total encoder counts, a raw height above the surface, k , can be calculated. This raw value of k represents the total number of encoder counts the stage actually moved, however, it does not necessarily represent the total vertical distance that the total pressure probe moved. The

total pressure probe's starting position is set to be in-contact with the surface of the model, with the total pressure probe slightly deformed from the contact with the surface. Thus, when the profile is initially begun, the probe is still in-contact with the surface of the model, becoming less and less deformed until the probe lifts-off from the model surface. Therefore, the raw value of k must be corrected for this difference – essentially, the raw k value must be zeroed by the total number of encoder counts accrued when the probe lifted off the model surface.

This liftoff correction is determined by analyzing the pressure measured by the moving total pressure probe. If the stage is moving, but the pressure reading remains unchanged, this indicates that the total pressure probe has not moved off the model surface. Once the pressure read by the changes, it indicates that the total pressure probe has lifted off the model surface. After the liftoff correction is applied, the stage movement will corresponds to the movement of the total pressure probe.

The velocity component of the profile is calculated by converting the moving pressure probe and out-of-the-boundary layer total pressure probe readings into u/u_e by simple division. Because the primary end-use of the velocity profiles is the calculation of Re_k , the velocity profiles are then redimensioned with the average u_e from the profile. The final form of the velocity profiles is k in inches and U in meters per second. Thus, the necessary parameter for the Re_k calculation, namely u_k , can be easily extracted.

The measured velocity profiles for Gradient-Zero, Gradient-A, and Gradient-B are shown in Appendix D. A summary of velocity profiles for each model is shown in Figures 139 – Figures 141 below.

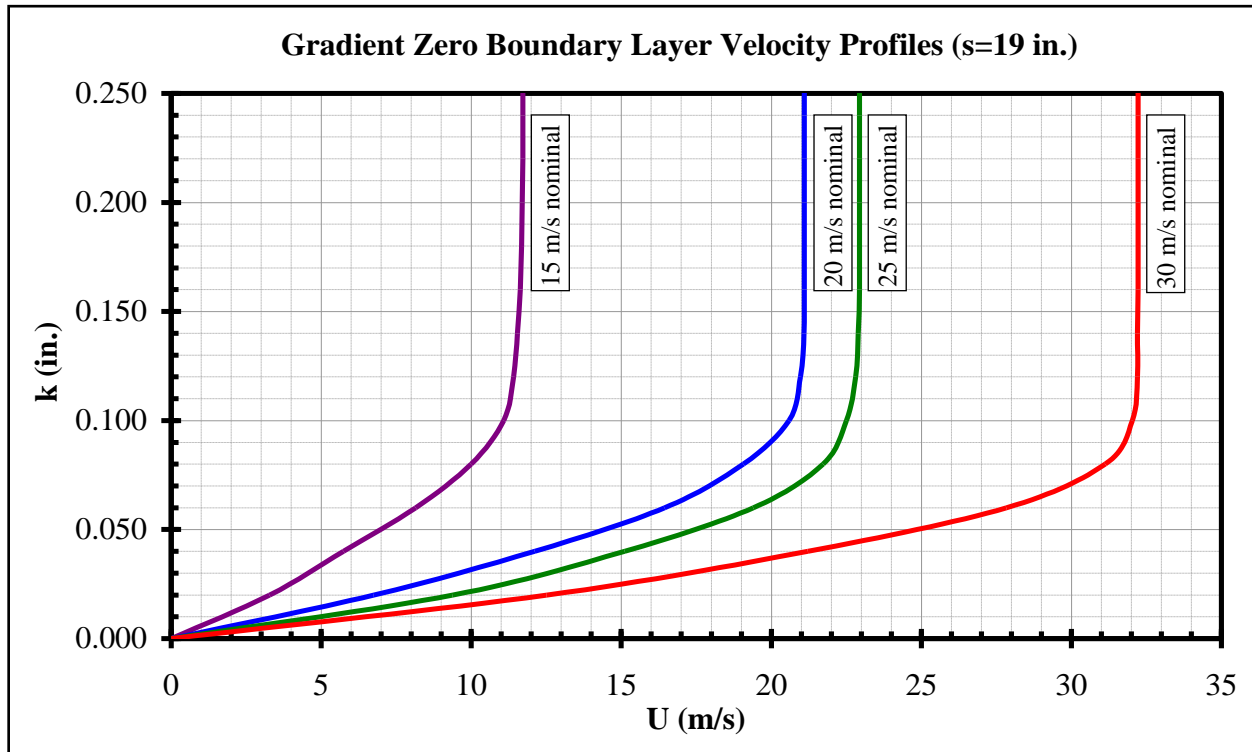


Figure 139: Gradient-Zero boundary layer velocity profile summary.

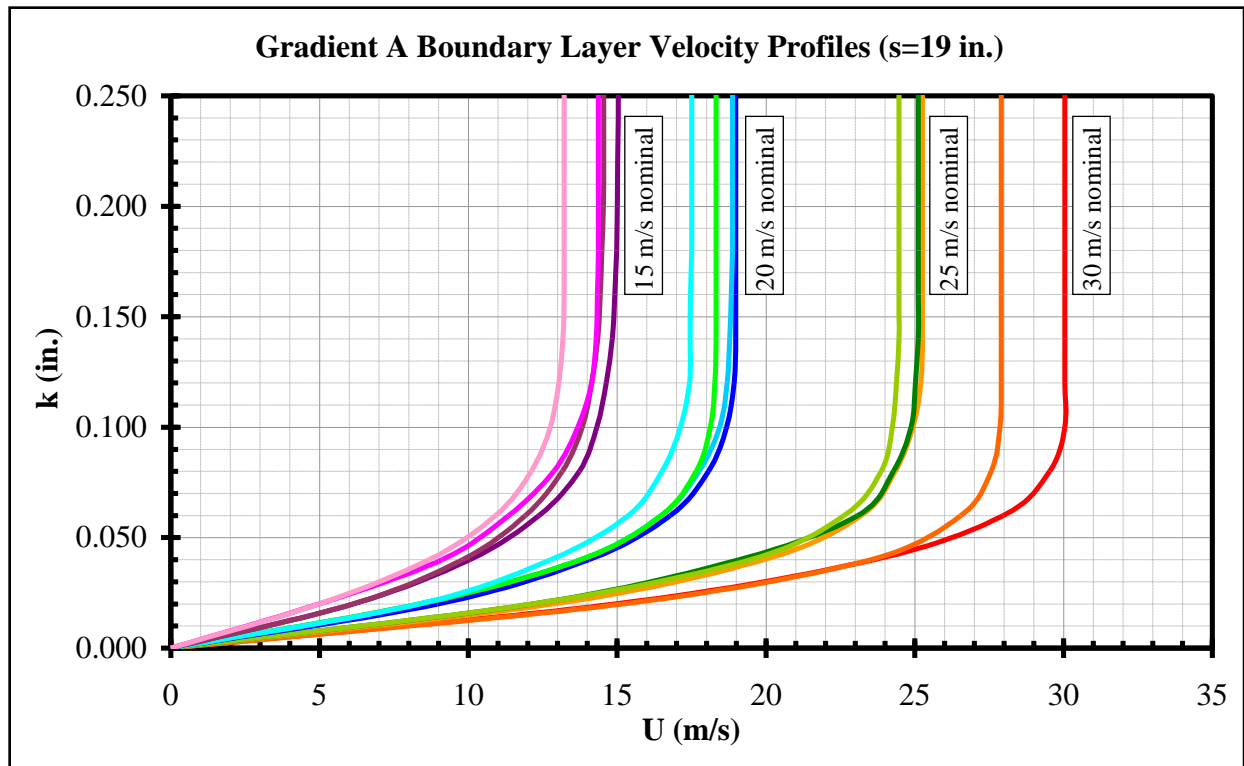


Figure 140: Gradient-A boundary layer velocity profile summary.

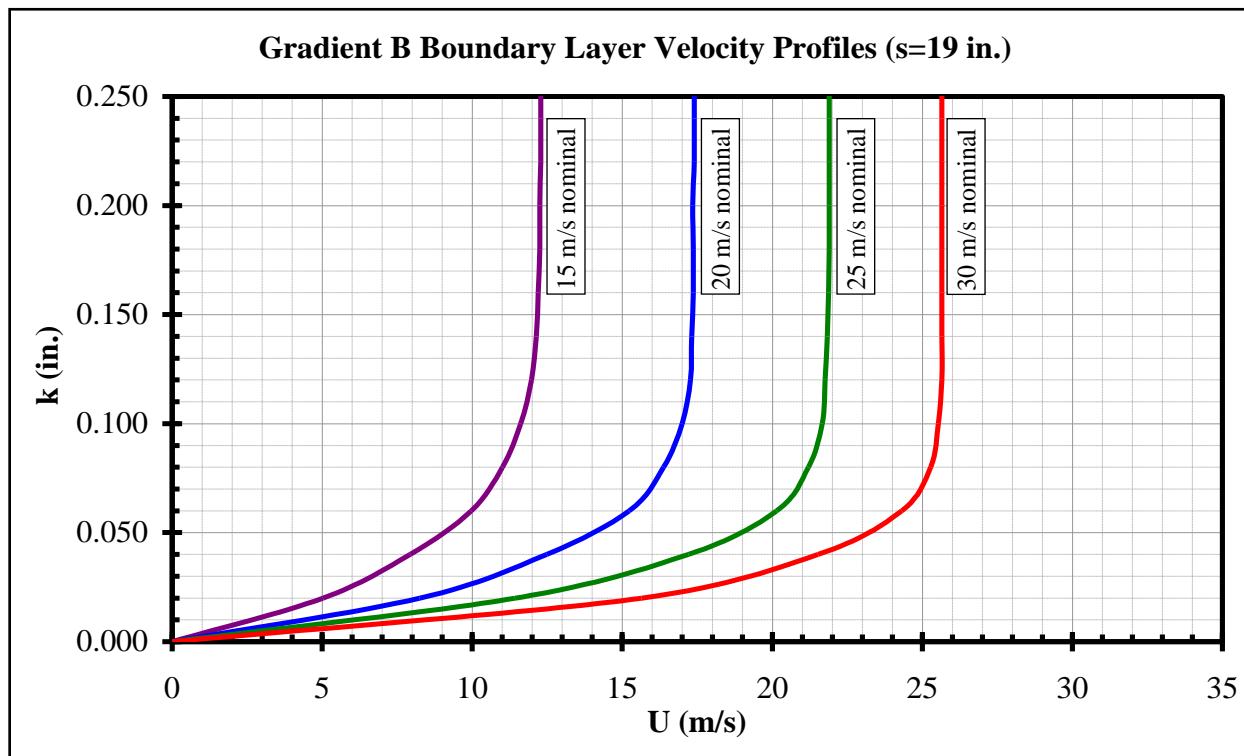


Figure 141: Gradient-B boundary layer velocity profile summary.

7.4 Preston Tubes

Preston tubes were used to measure skin friction distributions on the models. Preston tubes measure the stagnation pressure inside the boundary layer, close to the model surface. By calculating a pressure differential between the stagnation and local static pressure at the same chordwise location, wall sheer stresses can be calculated.

7.4.1 Preston Tube Design

A Preston tube is essentially a total pressure tube laid on the model surface. Six Preston tubes each of three different sizes were used: 0.020", 0.025" and 0.032". The ratio of inner diameter to outer diameter of each was 0.6. The appropriate tube diameter is dependent on the flow conditions, most importantly, the boundary layer thickness.

There are different calibrations to calculate skin friction coefficient and which calibration to use is dependent on the boundary layer state. Poll's calibration⁹ was used for laminar flow and Patel's calibration¹⁰ was used for turbulent flow.

Poll's calibration is as follows, and is valid for $120 < \bar{x} < 0.033(dU_e/v)^2$.

$$\bar{X} = \frac{\Delta P d_o^2}{4\rho v^2} \quad (5)$$

$$\bar{Y} = \frac{\tau_w d_o^2}{4\rho v^2} \quad (6)$$

$$\bar{Y} = 1.104\sqrt{\bar{X}} - \frac{18.96}{\sqrt{\bar{X}}} \quad (7)$$

Patel's calibration is as follows, assuming $3.5 < y^* < 5.3$.

$$x^* = \log_{10} \left(\frac{\Delta P_p d_o^2}{4\rho v^2} \right) \quad (8)$$

$$y^* = \log_{10} \left(\frac{\tau_w d_o^2}{4\rho v^2} \right) \quad (9)$$

$$x^* = y^* + 2\log_{10}(1.95 y^* + 4.10) \quad (10)$$

A Preston tube mounted on the model is shown in Figure 142. The Preston tubes were attached with the same double-sided structural adhesive that was used to attach the BLDS traverse.

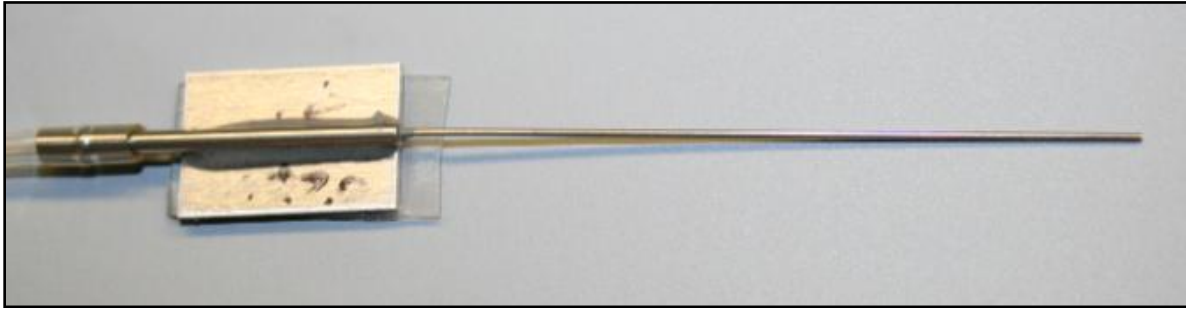


Figure 142: Preston tube.

7.4.2 Preston Tube Application

Preston tubes were mounted on the models nominally along a 15-degree half-angle line extending from the point where the leading edge meets the splitter plate, both upper and lower surface (see Figure 143). This configuration of Preston tubes was the standard configuration used, though other arrangements were sometimes used. Thus there were typically two spanwise and chordwise varying rows of Preston tubes, with 7 Preston tubes each (the last centerline Preston tube being shared by both rows). The two rows were designated as inboard and outboard, with the inboard row being the row closest to the lower splitter plate. On the skin friction distribution plots in the next section, data from both the inboard and outboard row of Preston tubes is shown. For the skin friction calibration, the static pressure was interpolated for the chordwise position from the nearby row of static pressure taps. The Preston tubes were attached to the model surface with double-sided structural adhesive tape, as was the case with the BLDS.



Figure 143: Preston tubes arranged on the Gradient-Zero model.

7.4.3 Preston Tube Results

The skin friction distributions and correlating transition locations derived from the Preston tube data are presented in Figures 144 – 323 for each of the three models. Results are presented first for Gradient-Zero, then Gradient-A, and finally Gradient-B. The results for forward-facing steps are presented before the aft-facing steps for each model. The results for a given model and step geometry are presented in order of increasing Re_k .

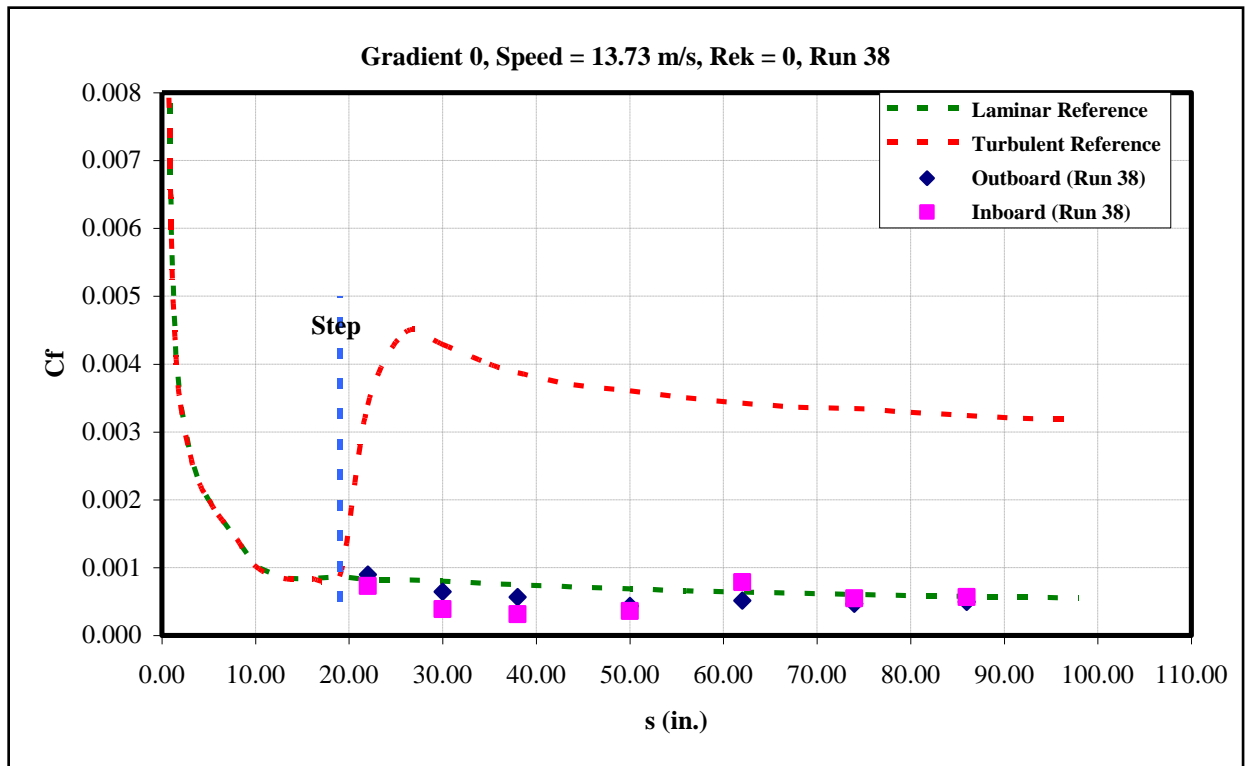


Figure 144: Gradient-Zero, $k=0$ -in, $U=13.73$ m/s skin-friction distribution.

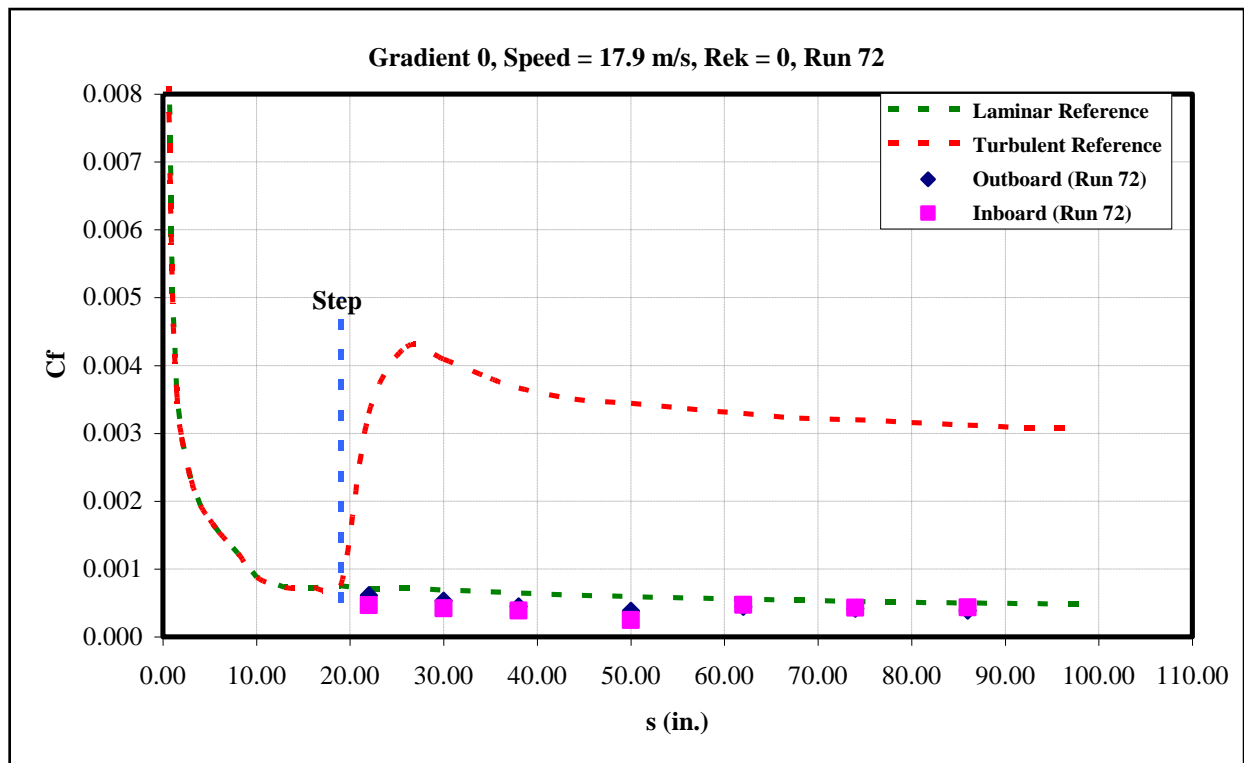


Figure 145: Gradient-Zero, $k=0$ -in, $U=17.9$ m/s skin-friction distribution.

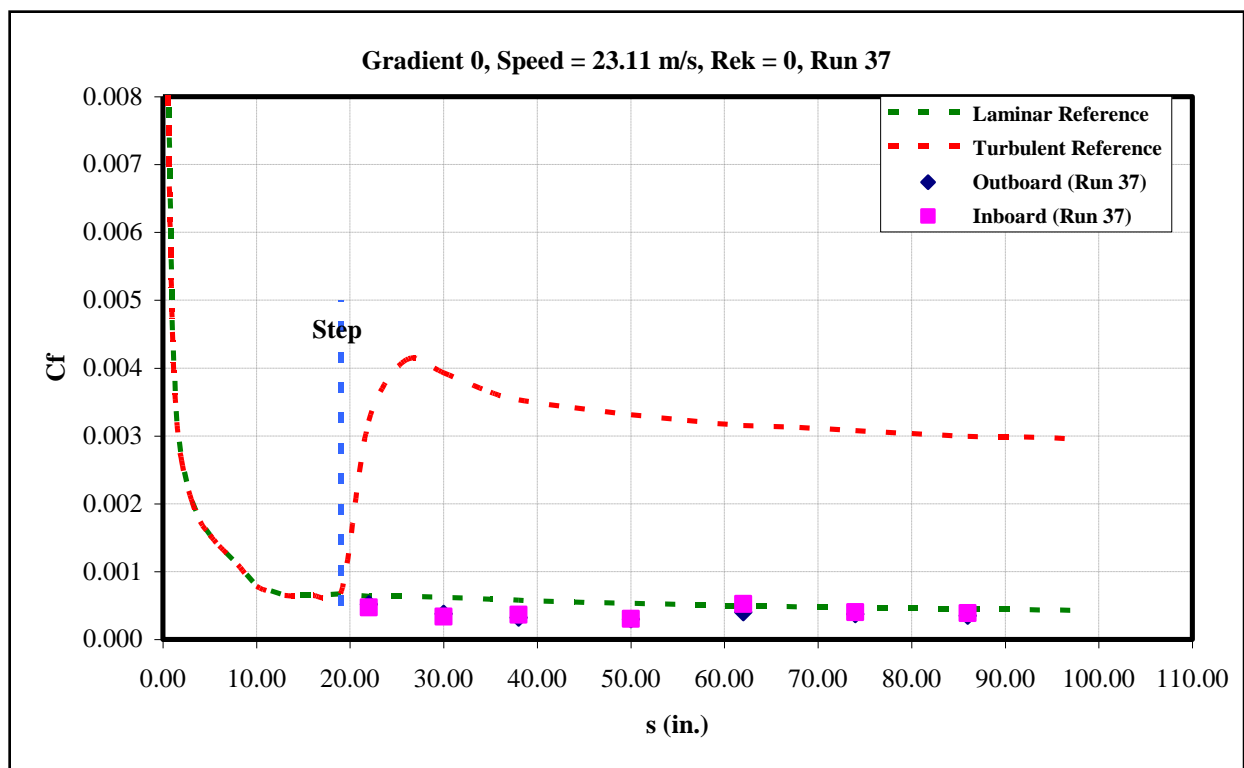


Figure 146: Gradient-Zero, $k=0$ -in, $U=23.11$ m/s skin-friction distribution.

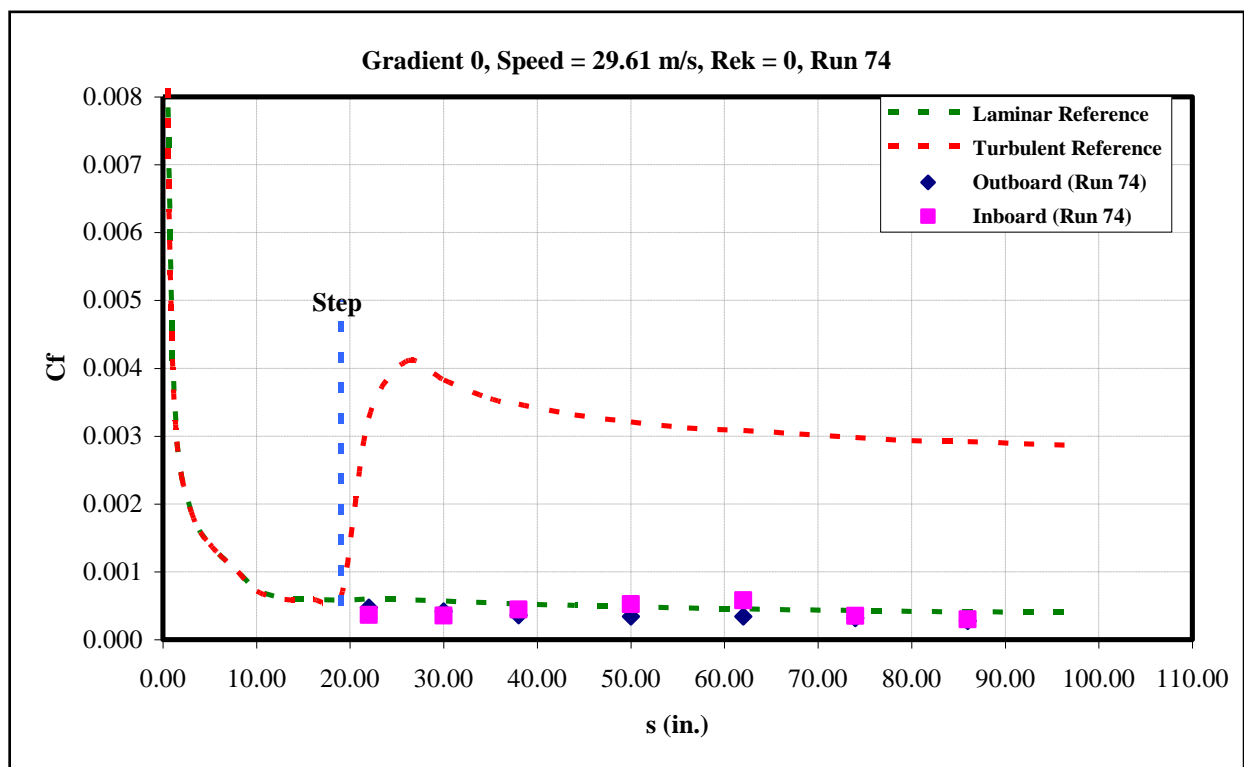


Figure 147: Gradient-Zero, $k=0$ -in, $U=29.61$ m/s skin-friction distribution.

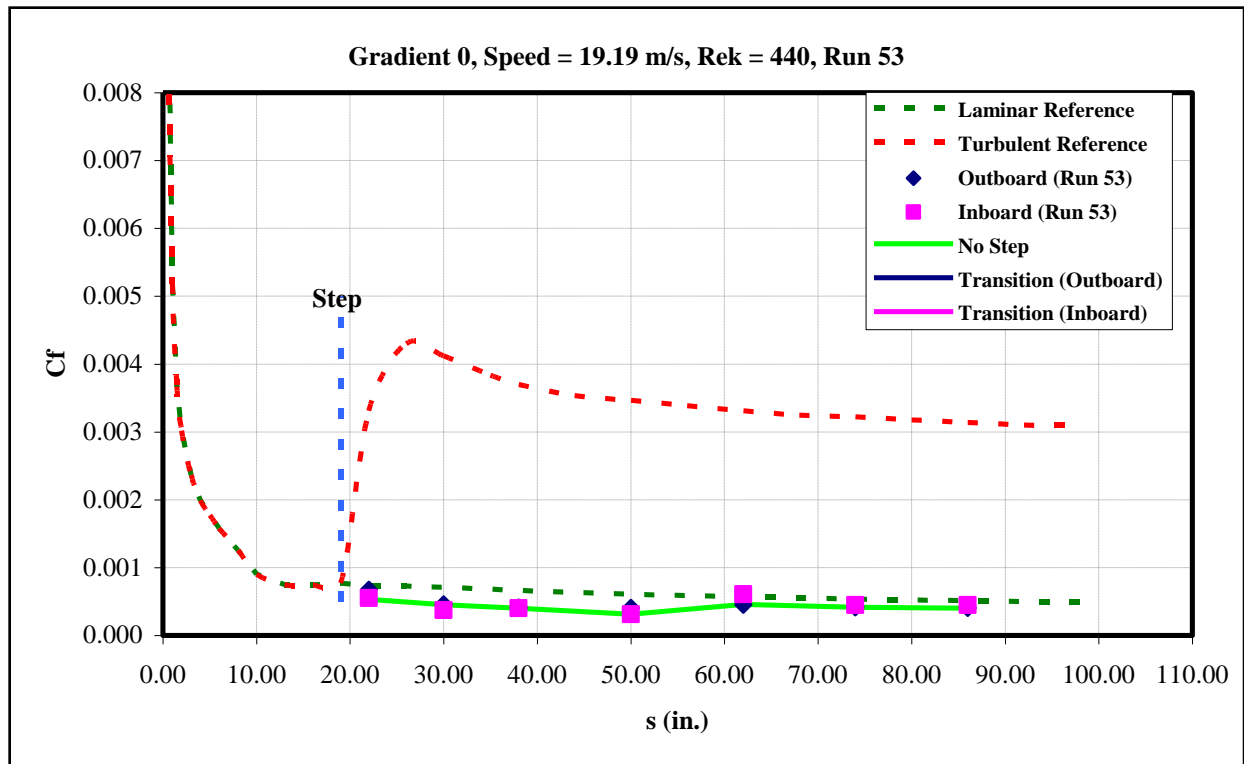


Figure 148: Gradient-Zero, $k=0.03$ -in forward step, $U=19.19$ m/s skin-friction distribution.

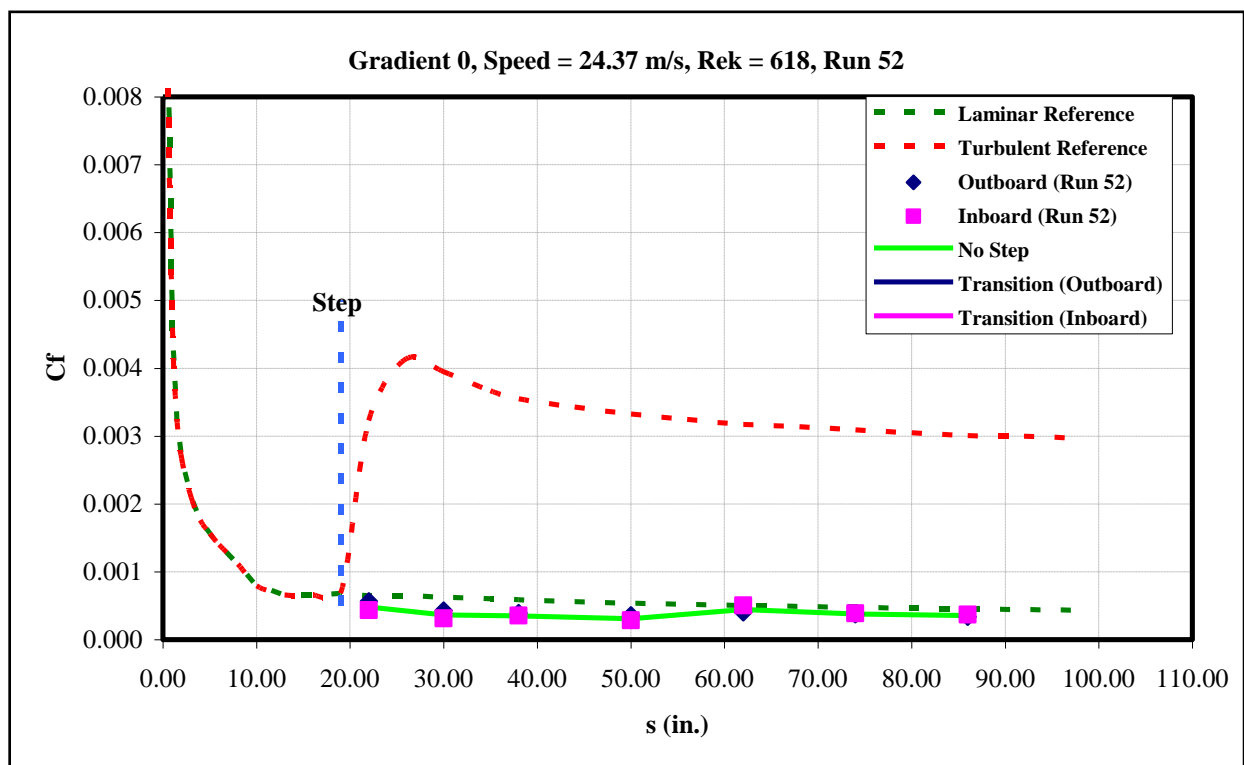


Figure 149: Gradient-Zero, $k=0.03$ -in forward step, $U=24.37$ m/s skin-friction distribution.

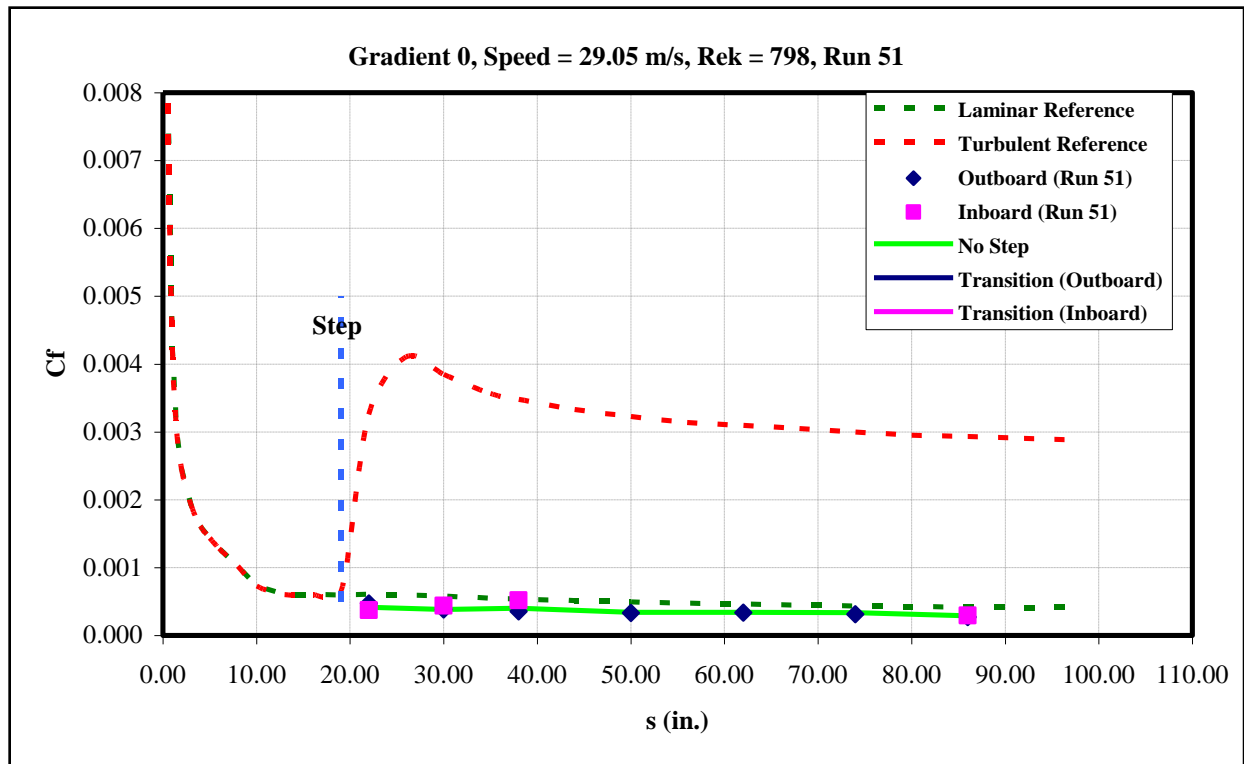


Figure 150: Gradient-Zero, $k=0.03$ -in forward step, $U=29.05$ m/s skin-friction distribution.

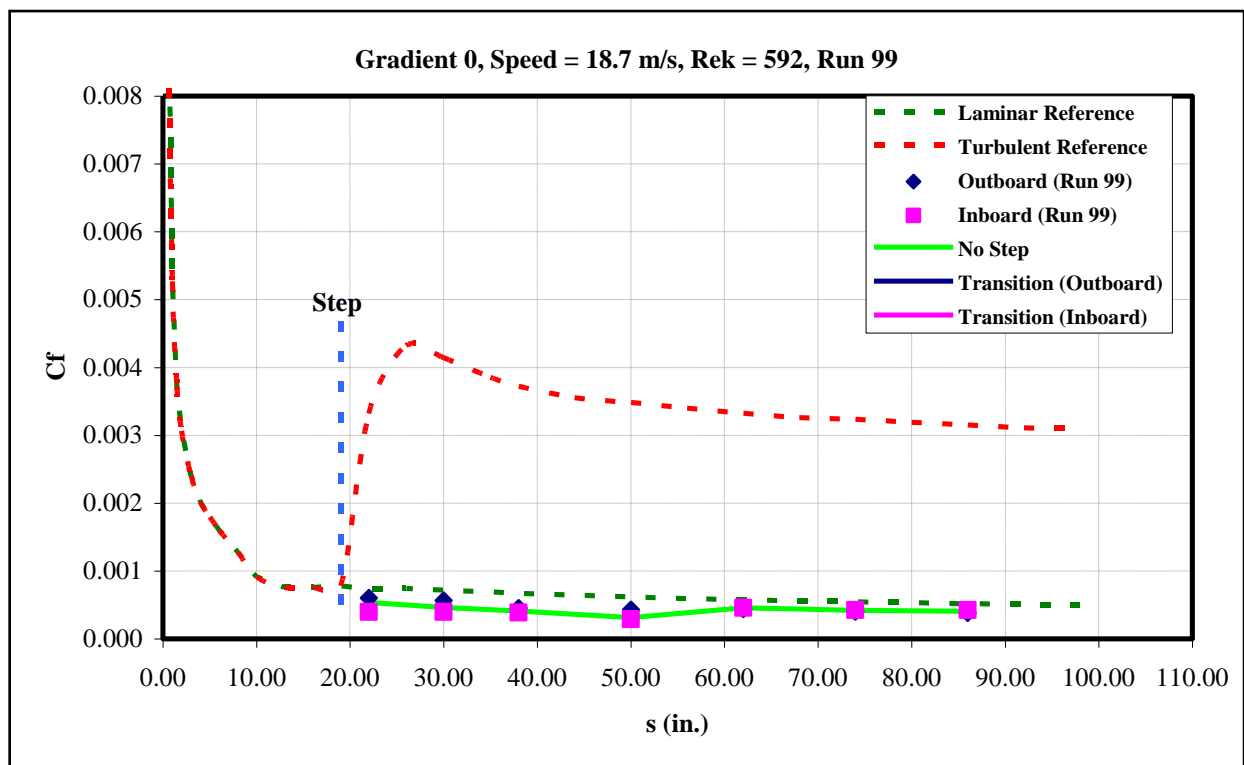


Figure 151: Gradient-Zero, $k=0.035$ -in forward step, $U=18.7$ m/s skin-friction distribution.

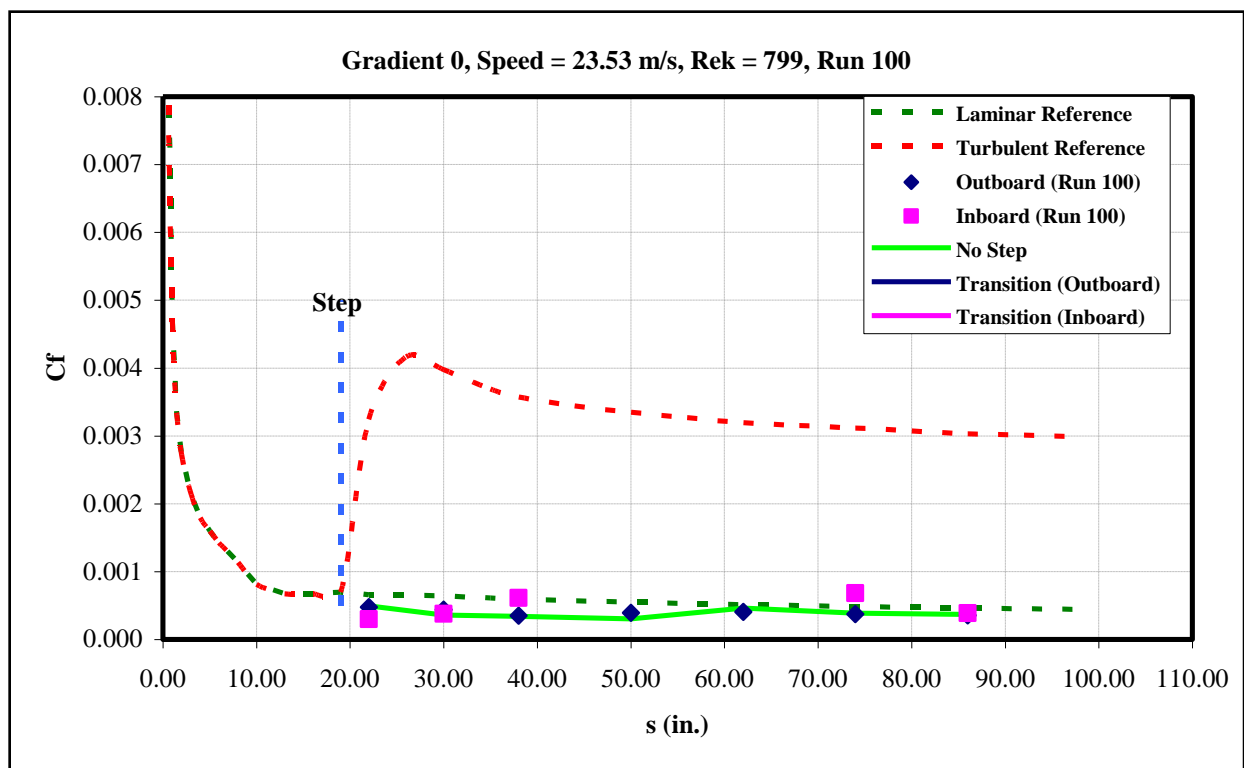


Figure 152: Gradient-Zero, $k=0.035$ -in forward step, $U=23.53$ m/s skin-friction distribution.

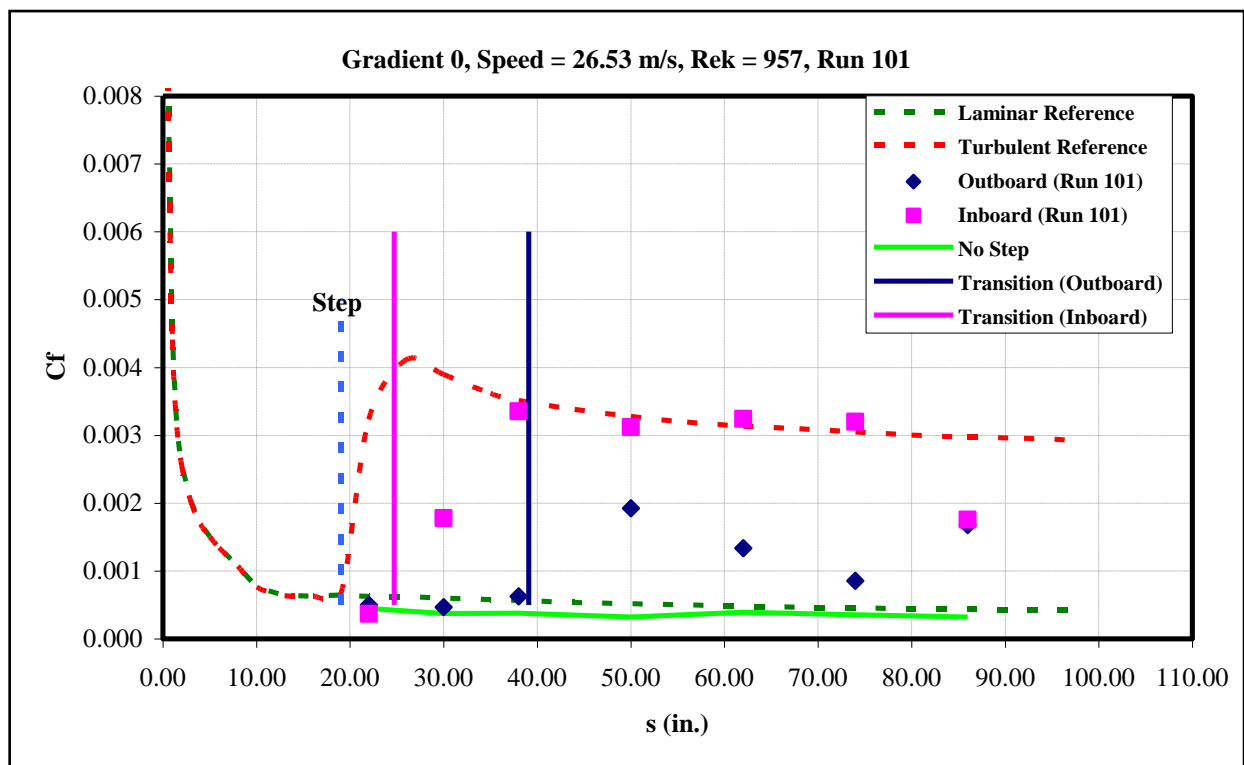


Figure 153: Gradient-Zero, $k=0.035$ -in forward step, $U=26.53$ m/s skin-friction distribution.

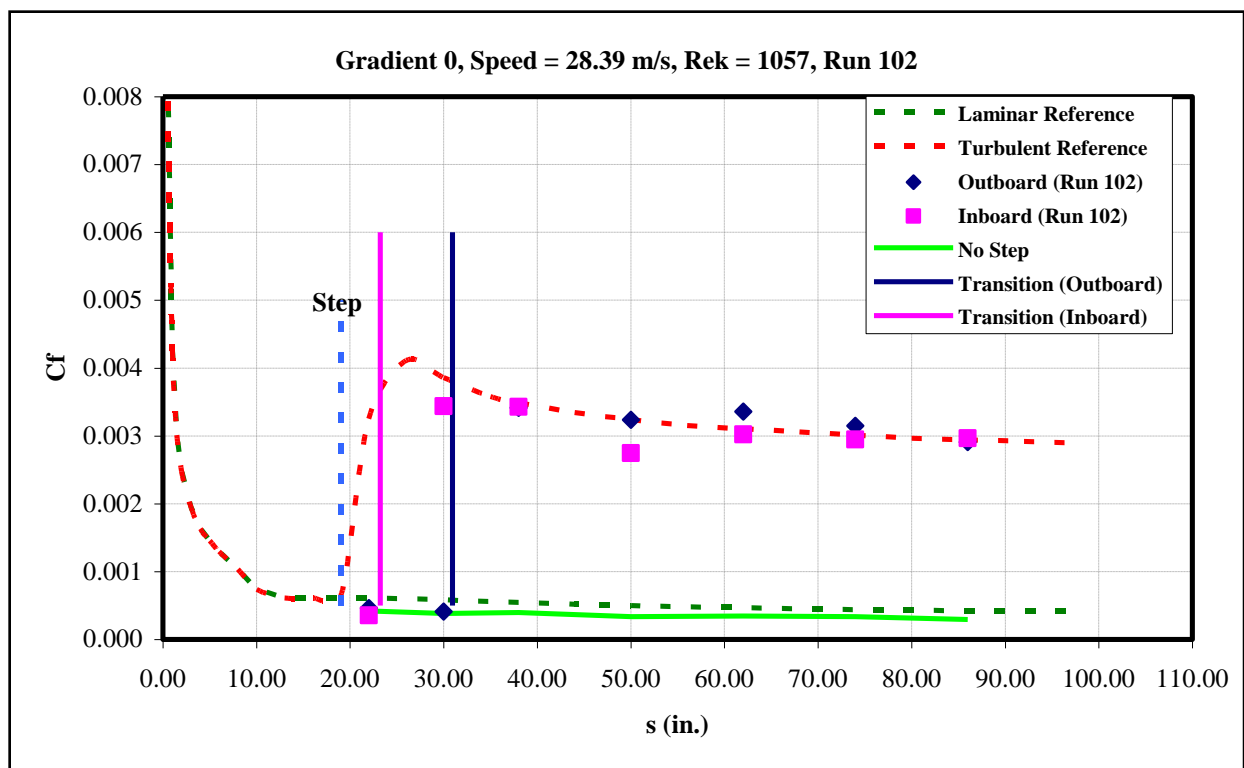


Figure 154: Gradient-Zero, $k=0.035$ -in forward step, $U=28.39$ m/s skin-friction distribution.

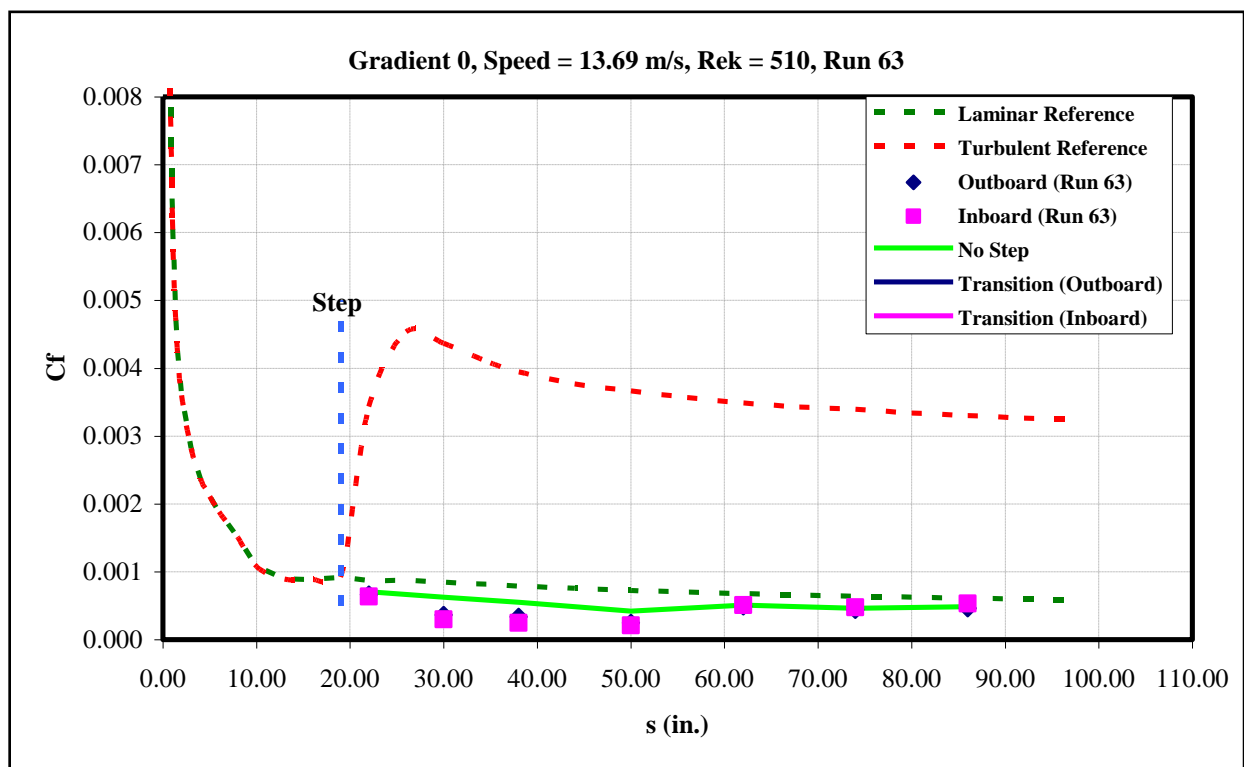


Figure 155: Gradient-Zero, $k=0.04$ -in forward step, $U=13.69$ m/s skin-friction distribution.

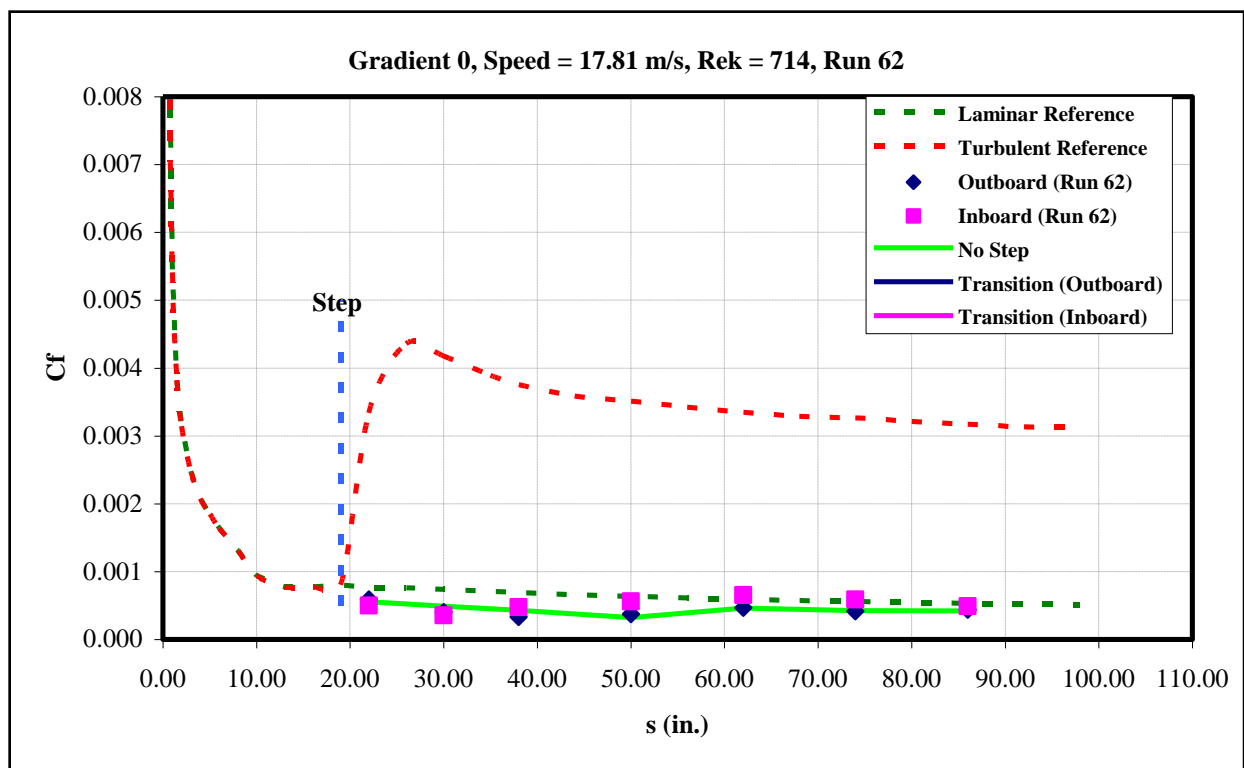


Figure 156: Gradient-Zero, $k=0.04$ -in forward step, $U=17.81$ m/s skin-friction distribution.

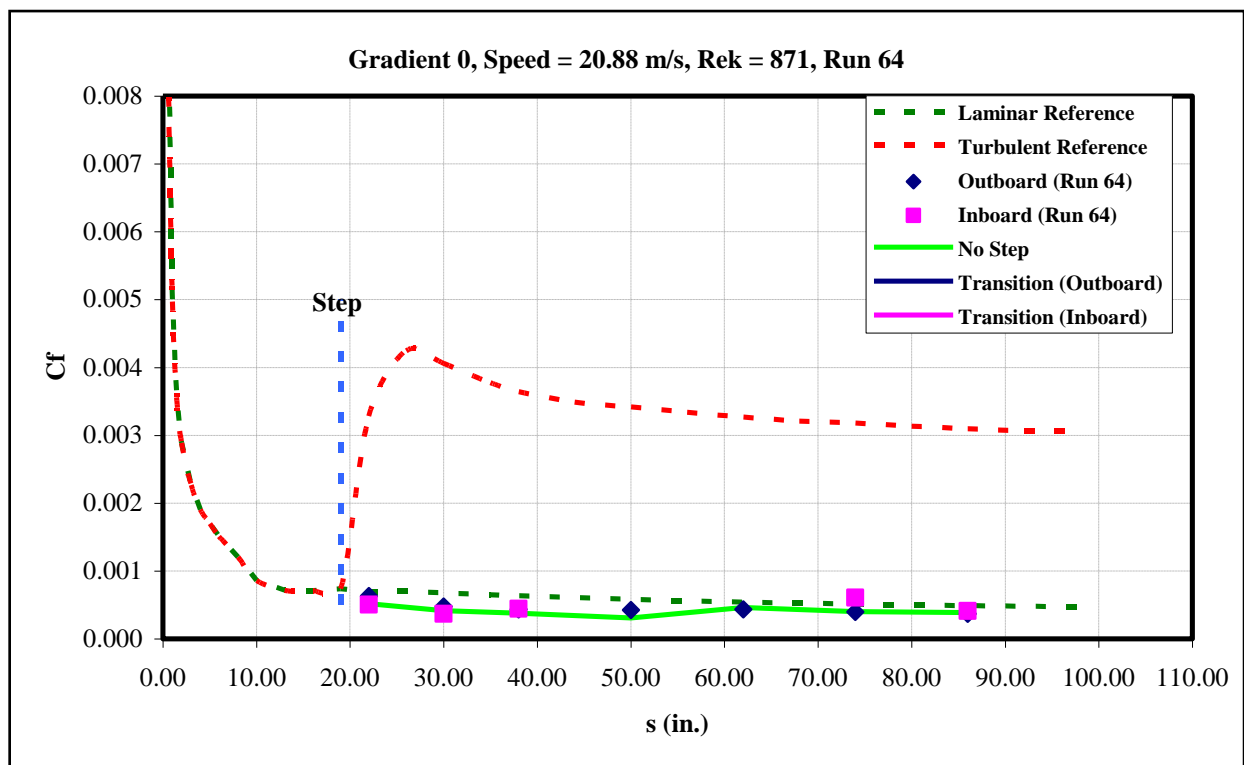


Figure 157: Gradient-Zero, $k=0.04$ -in forward step, $U=20.88$ m/s skin-friction distribution.

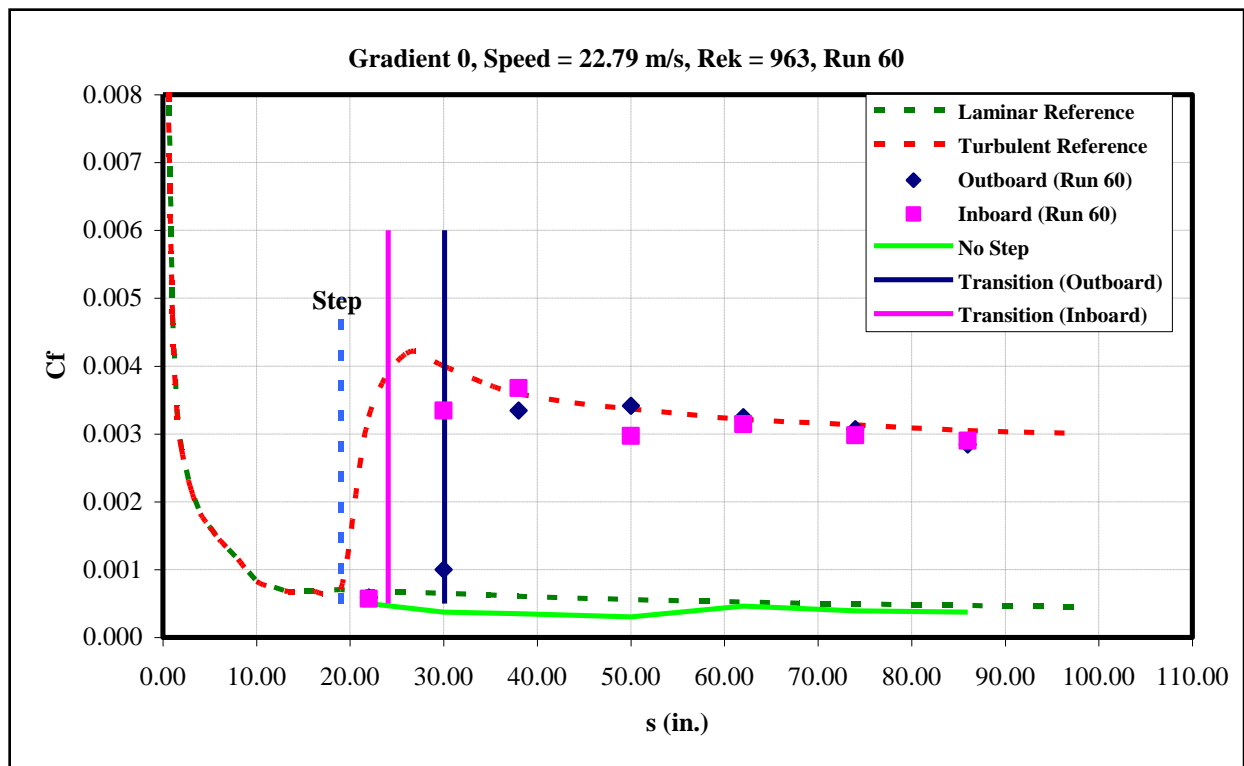


Figure 158: Gradient-Zero, $k=0.04$ -in forward step, $U=22.79$ m/s skin-friction distribution.

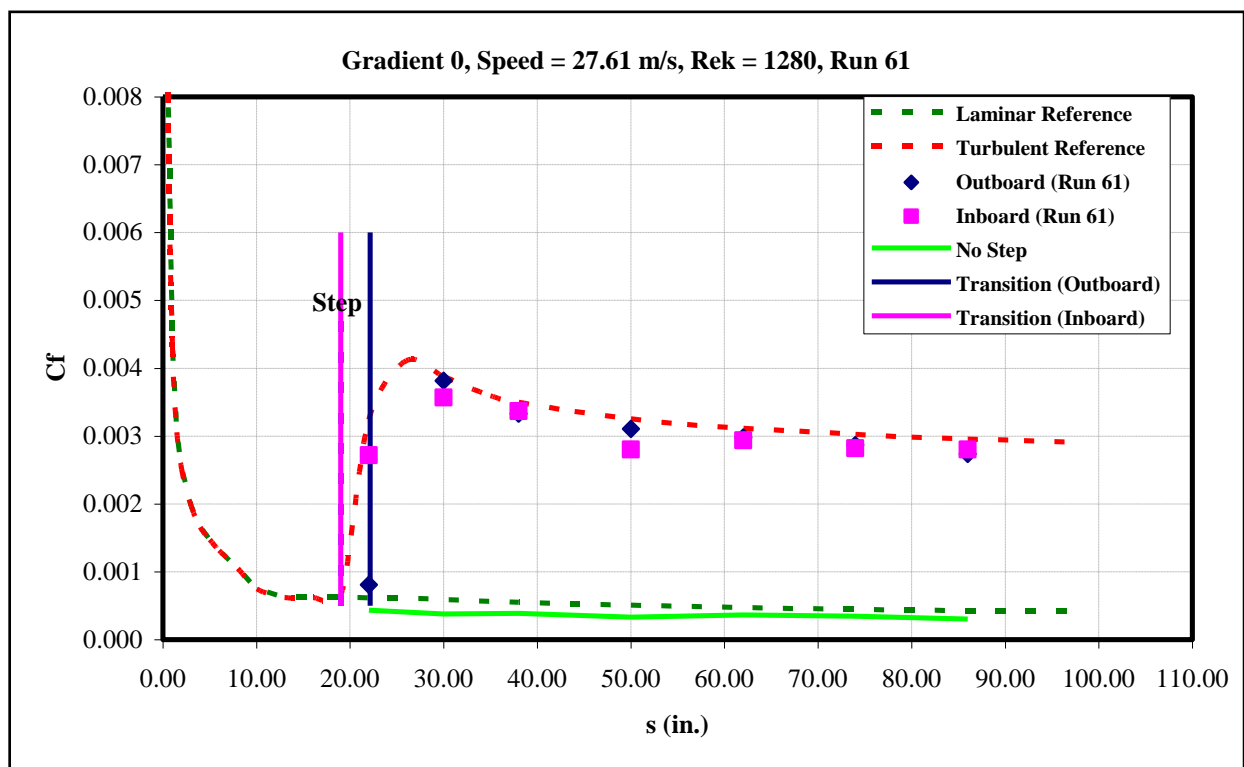


Figure 159: Gradient-Zero, $k=0.04$ -in forward step, $U=27.61$ m/s skin-friction distribution.

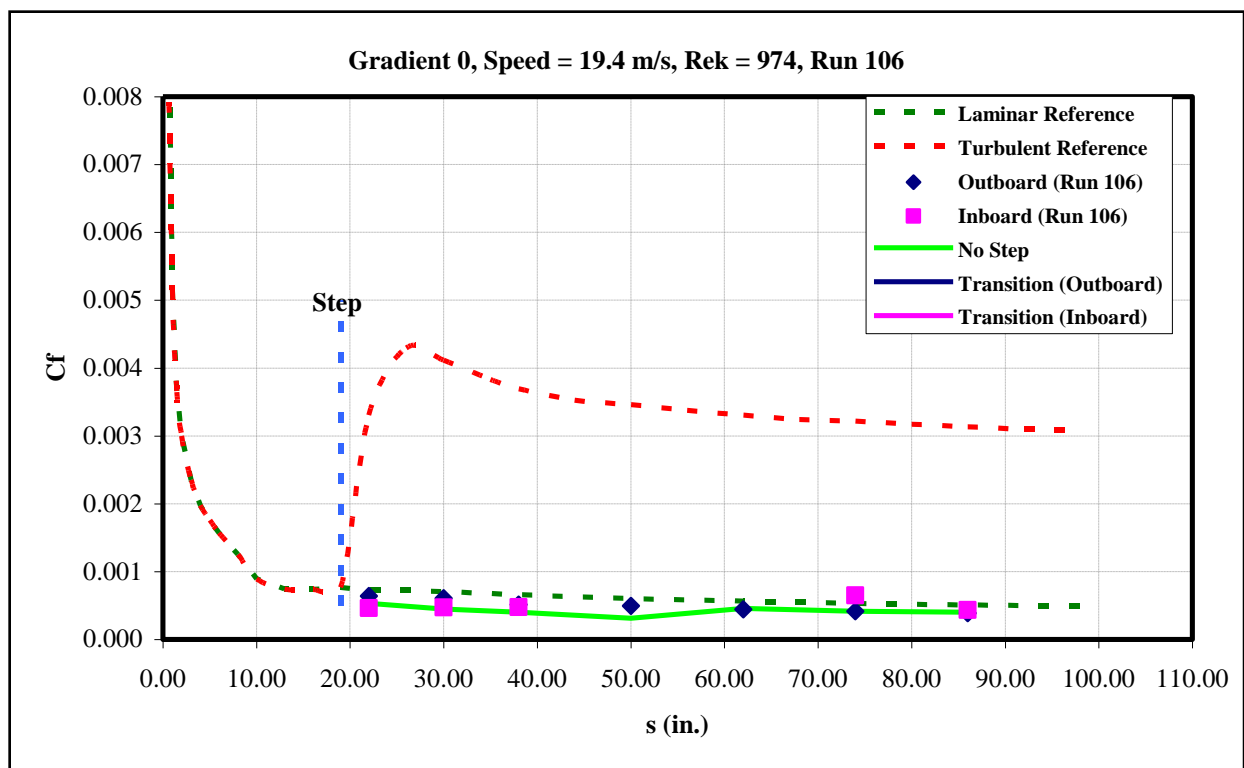


Figure 160: Gradient-Zero, $k=0.045$ -in forward step, $U=19.4$ m/s skin-friction distribution.

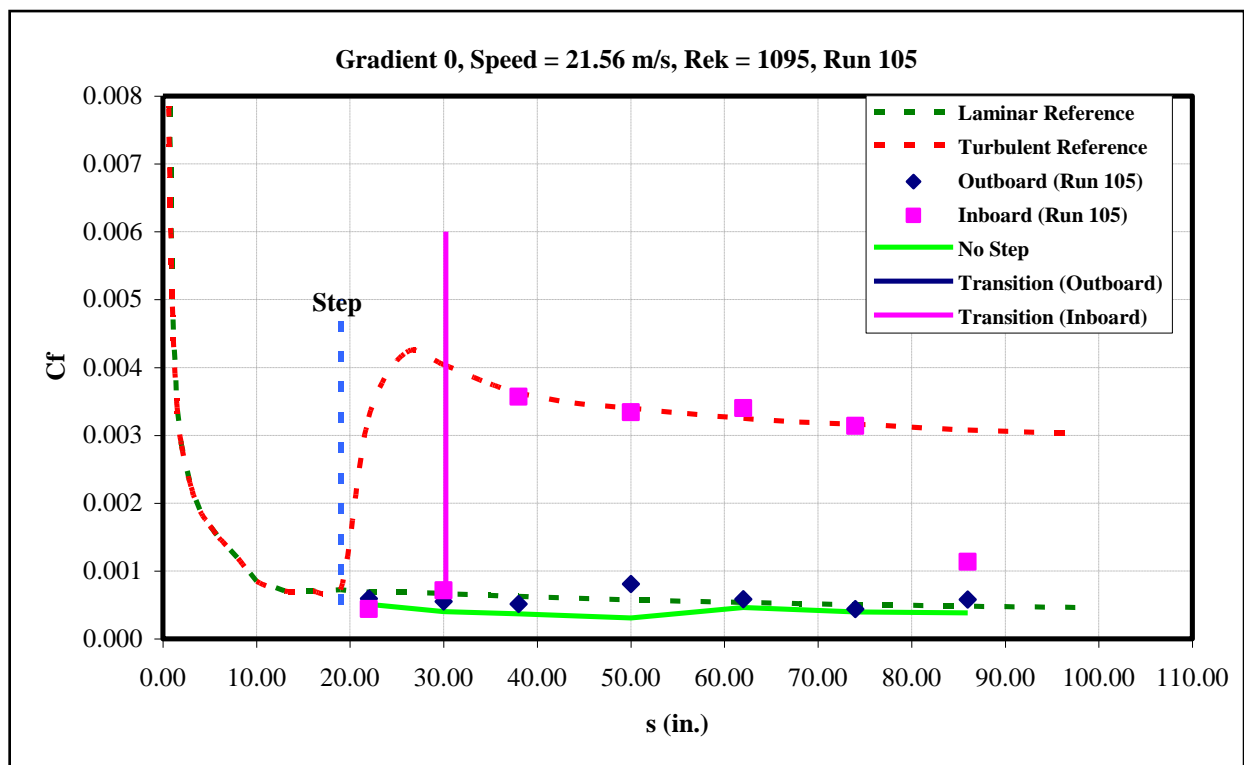


Figure 161: Gradient-Zero, $k=0.045$ -in forward step, $U=21.56$ m/s skin-friction distribution.

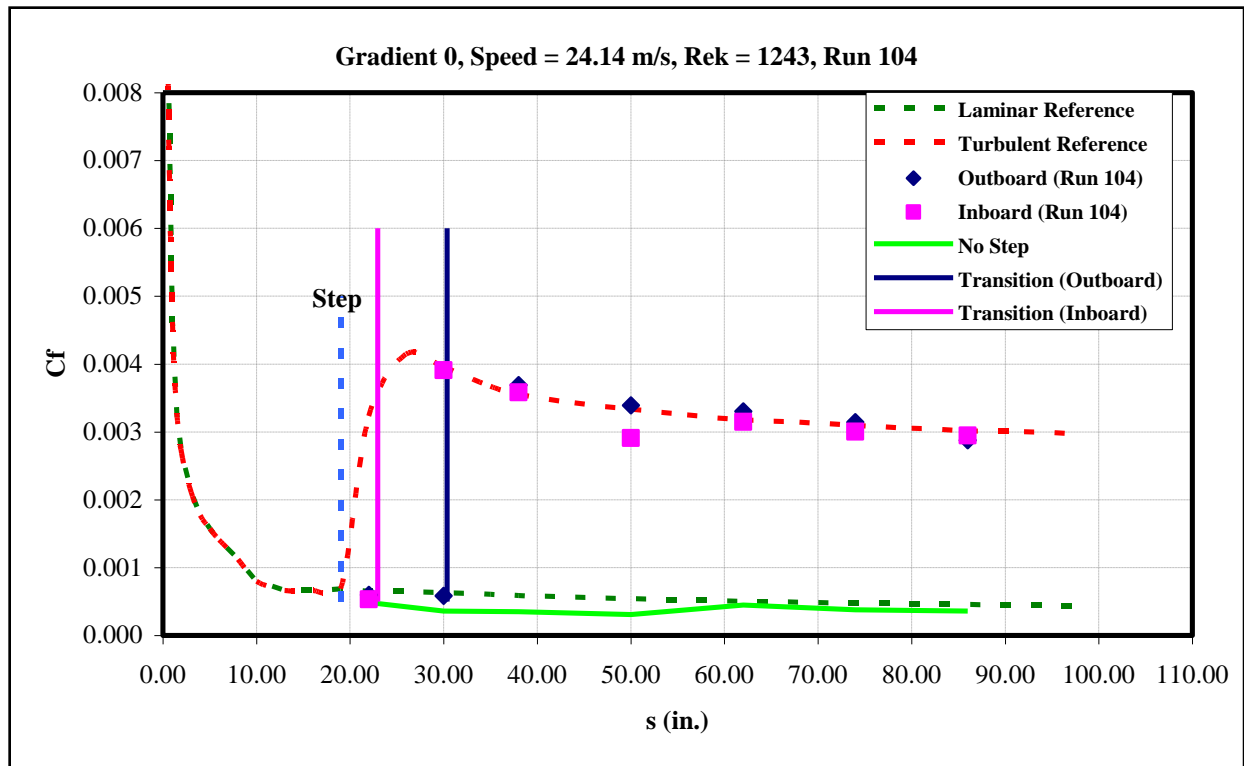


Figure 162: Gradient-Zero, $k=0.045$ -in forward step, $U=24.14$ m/s skin-friction distribution.

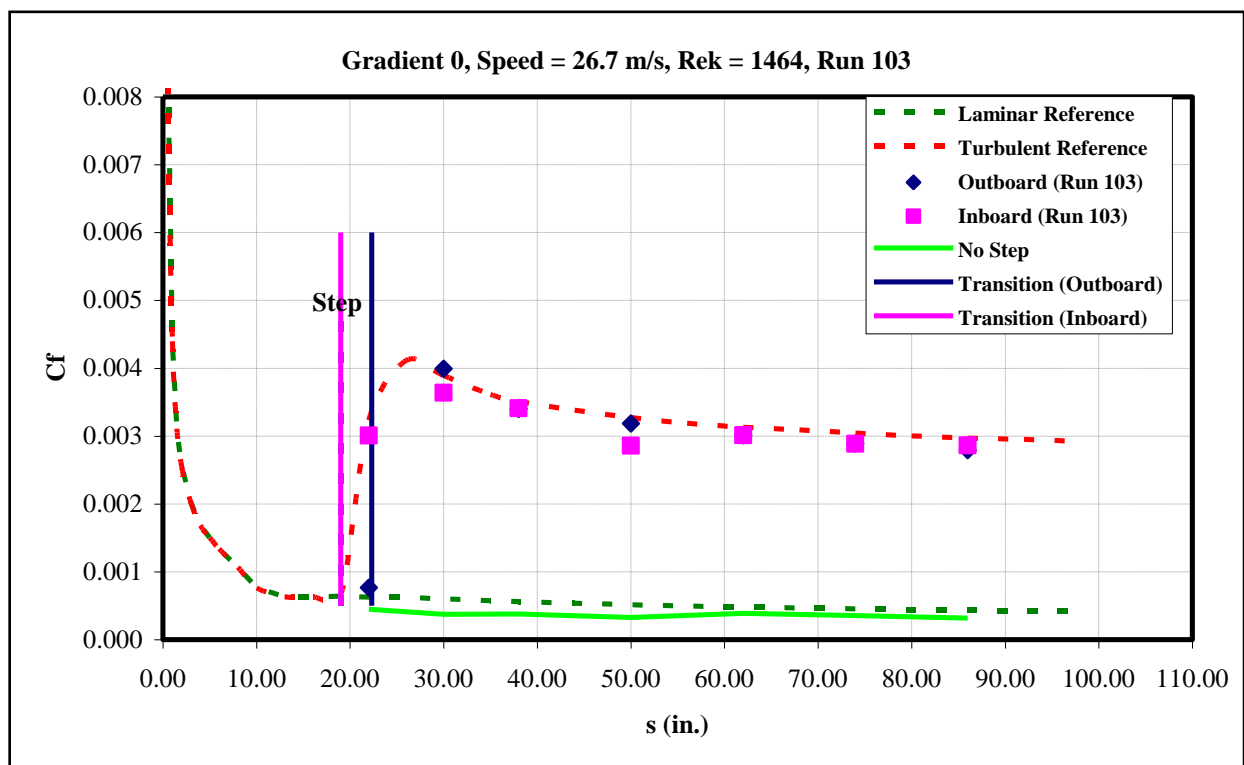


Figure 163: Gradient-Zero, $k=0.045$ -in forward step, $U=26.7$ m/s skin-friction distribution.

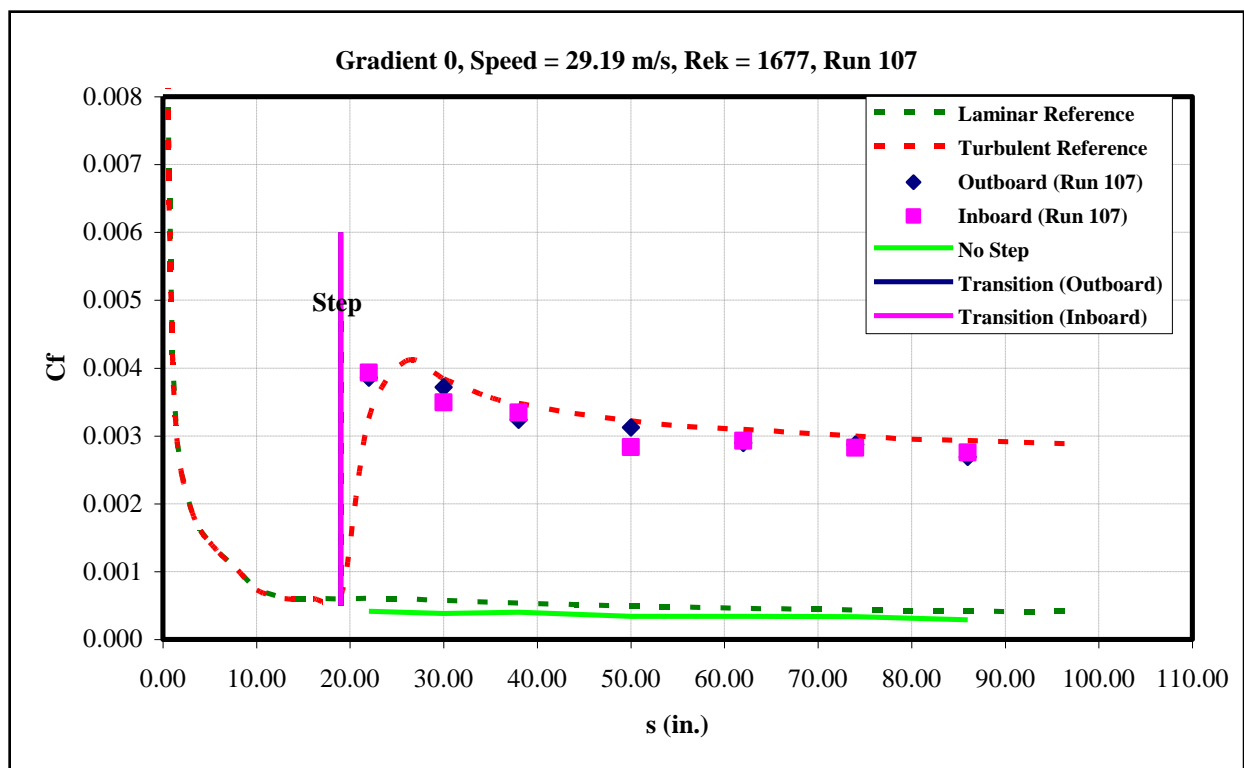


Figure 164: Gradient-Zero, $k=0.045$ -in forward step, $U=29.19$ m/s skin-friction distribution.

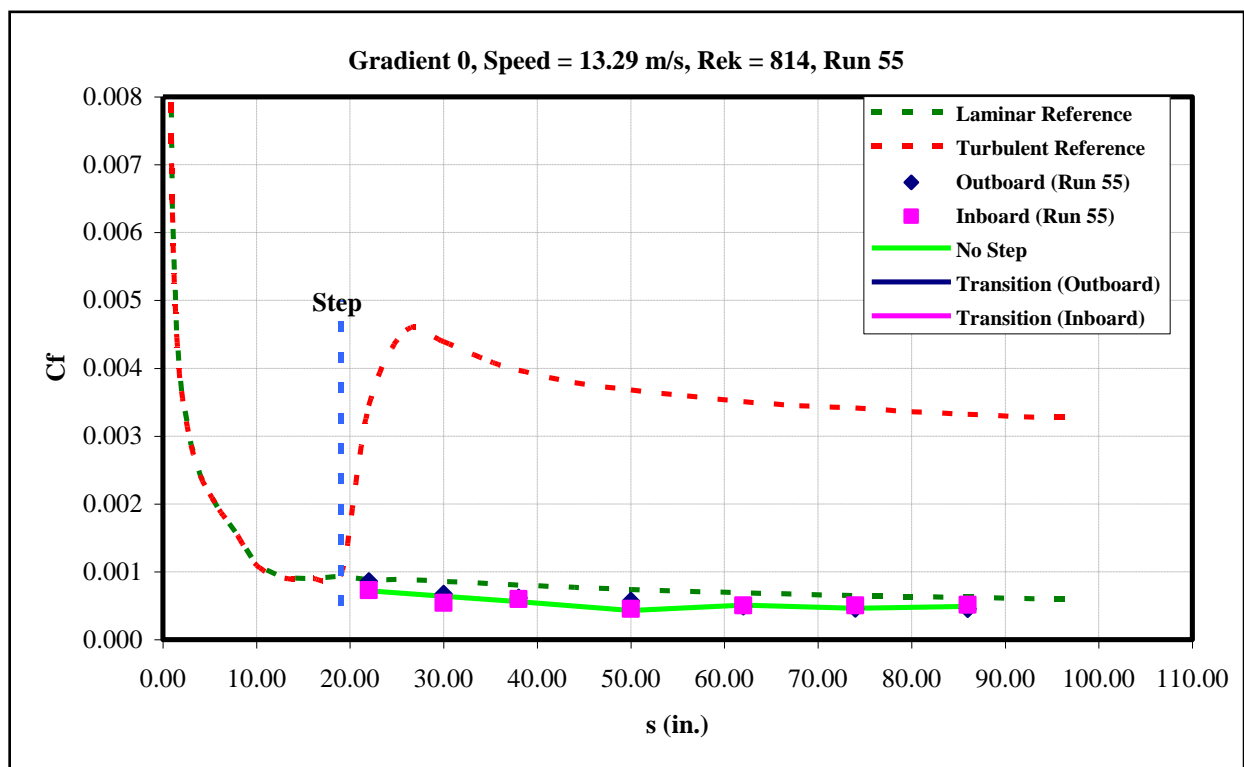


Figure 165: Gradient-Zero, $k=0.05$ -in forward step, $U=13.29$ m/s skin-friction distribution.

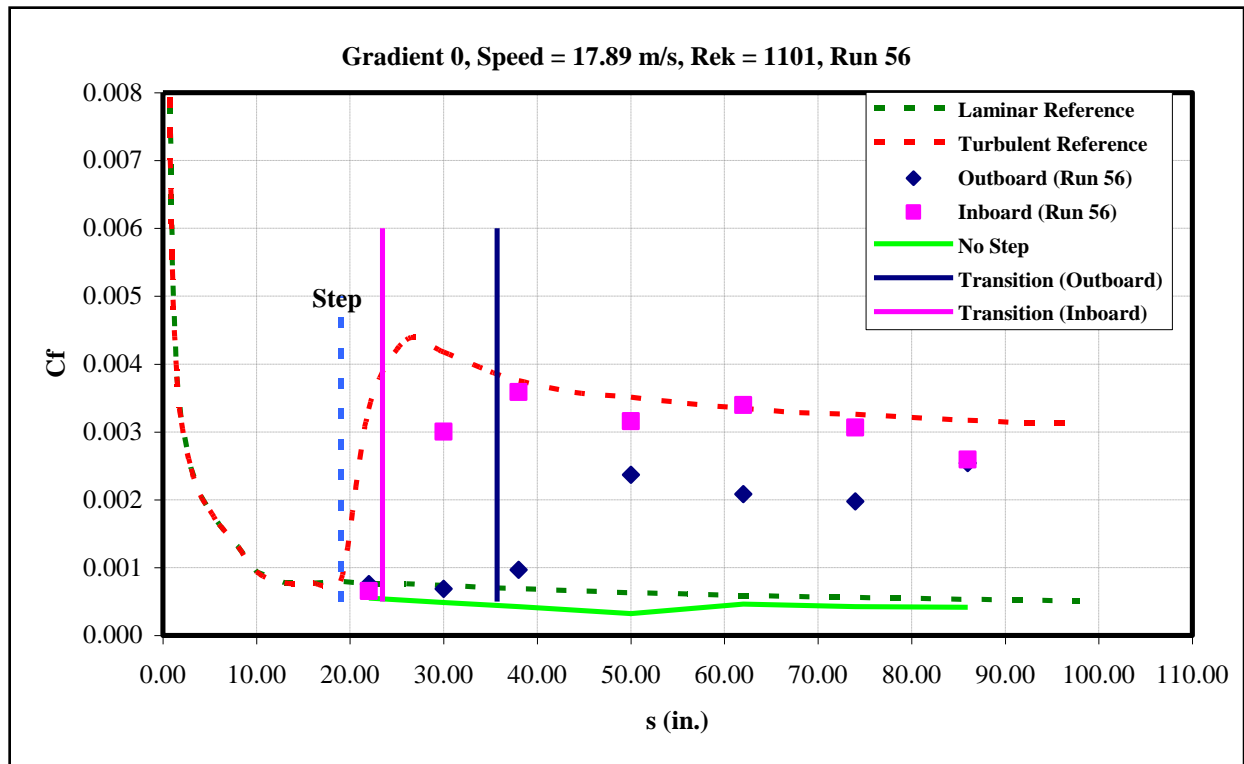


Figure 166: Gradient-Zero, $k=0.05$ -in forward step, $U=17.89$ m/s skin-friction distribution.

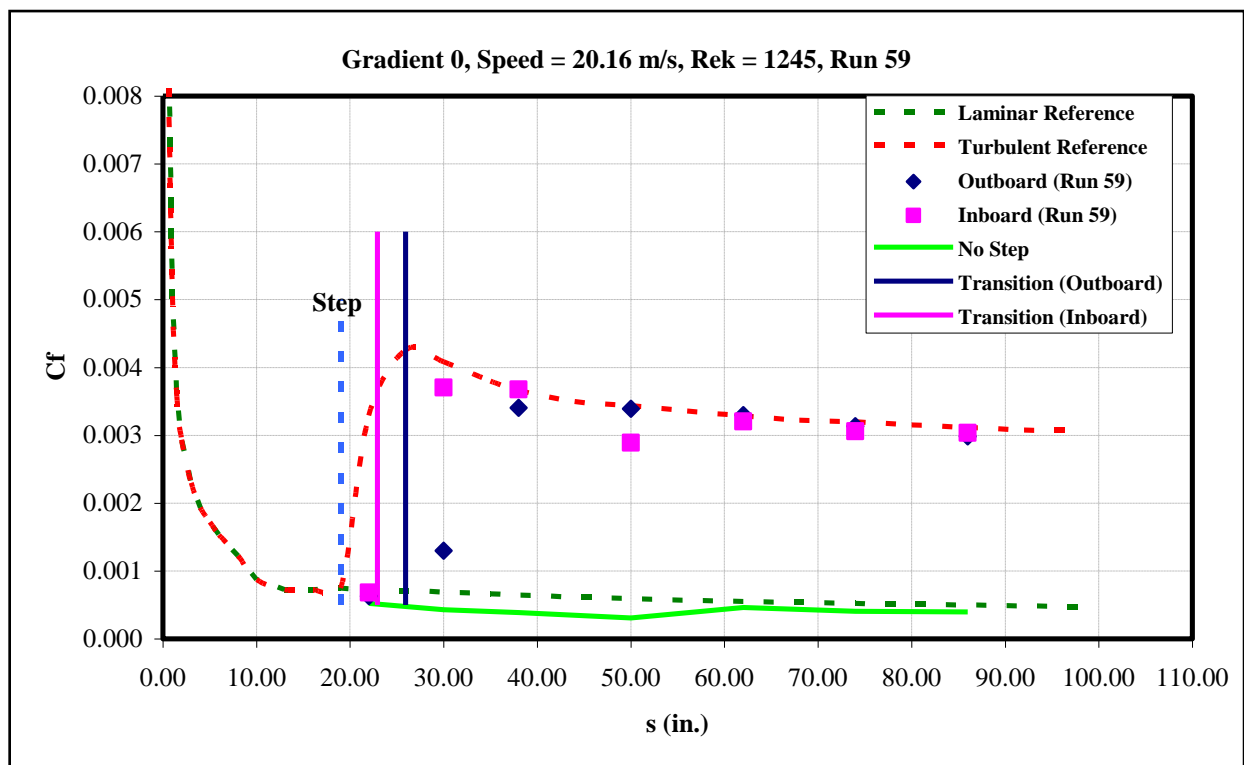


Figure 167: Gradient-Zero, $k=0.05$ -in forward step, $U=20.16$ m/s skin-friction distribution.

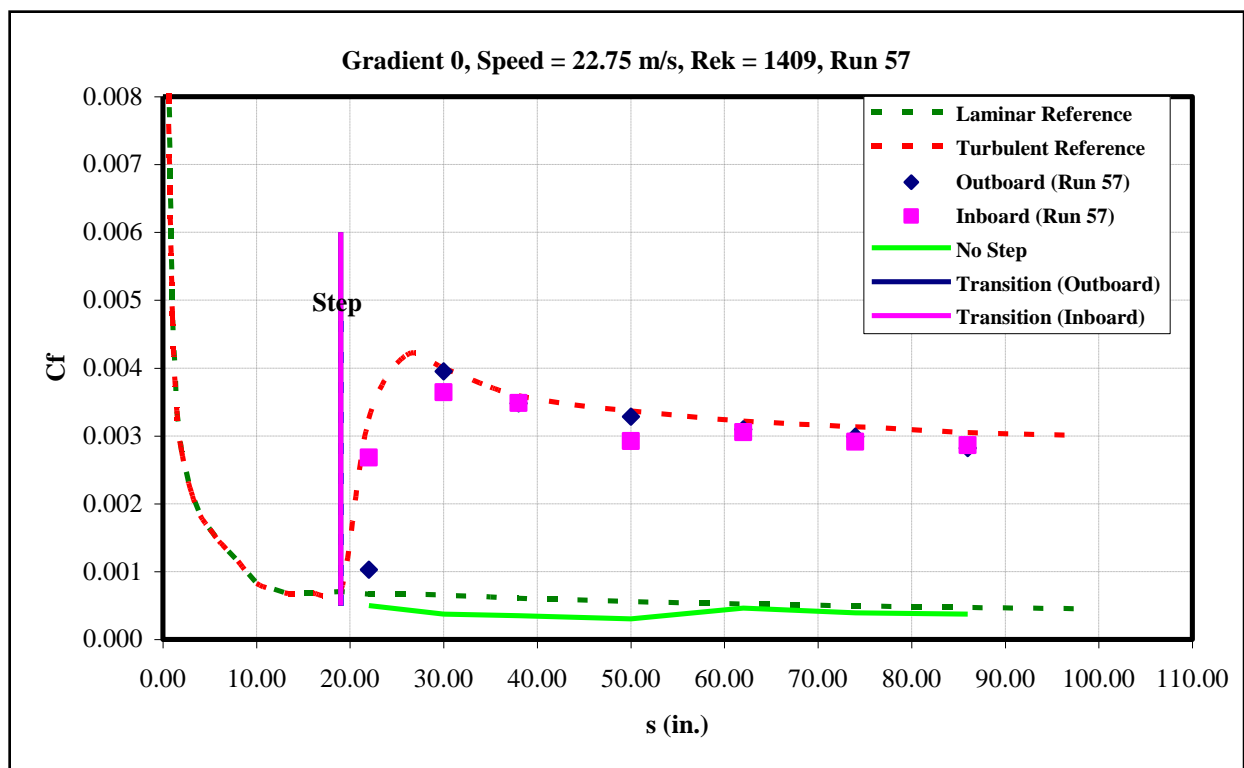


Figure 168: Gradient-Zero, $k=0.05$ -in forward step, $U=22.75$ m/s skin-friction distribution.

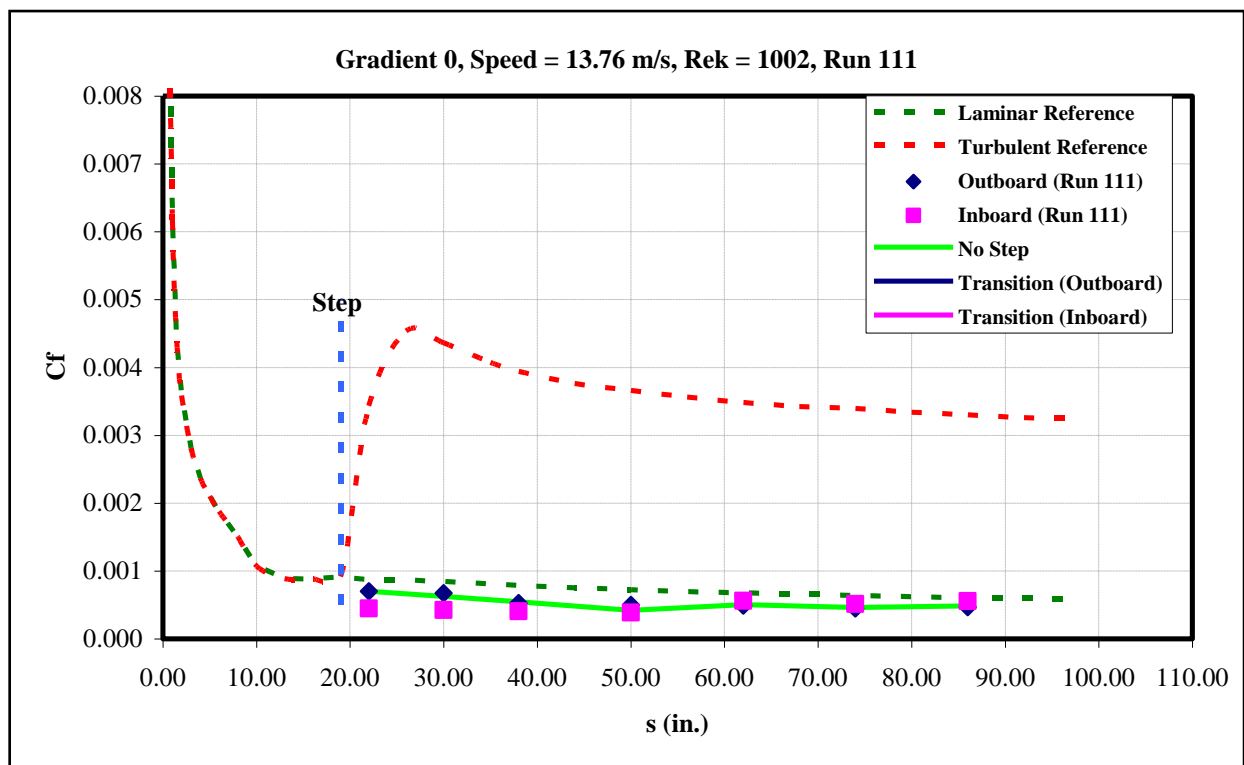


Figure 169: Gradient-Zero, $k=0.055$ -in forward step, $U=13.76$ m/s skin-friction distribution.

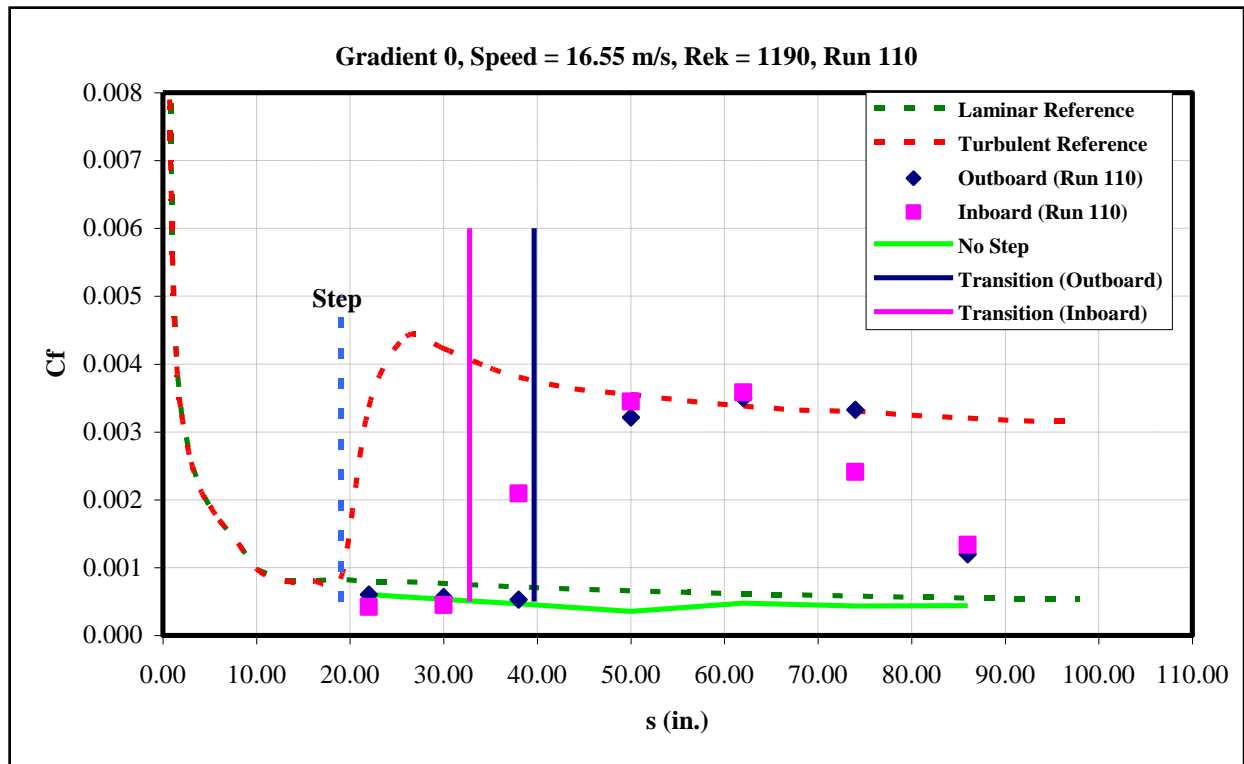


Figure 170: Gradient-Zero, $k=0.055$ -in forward step, $U=16.55$ m/s skin-friction distribution.

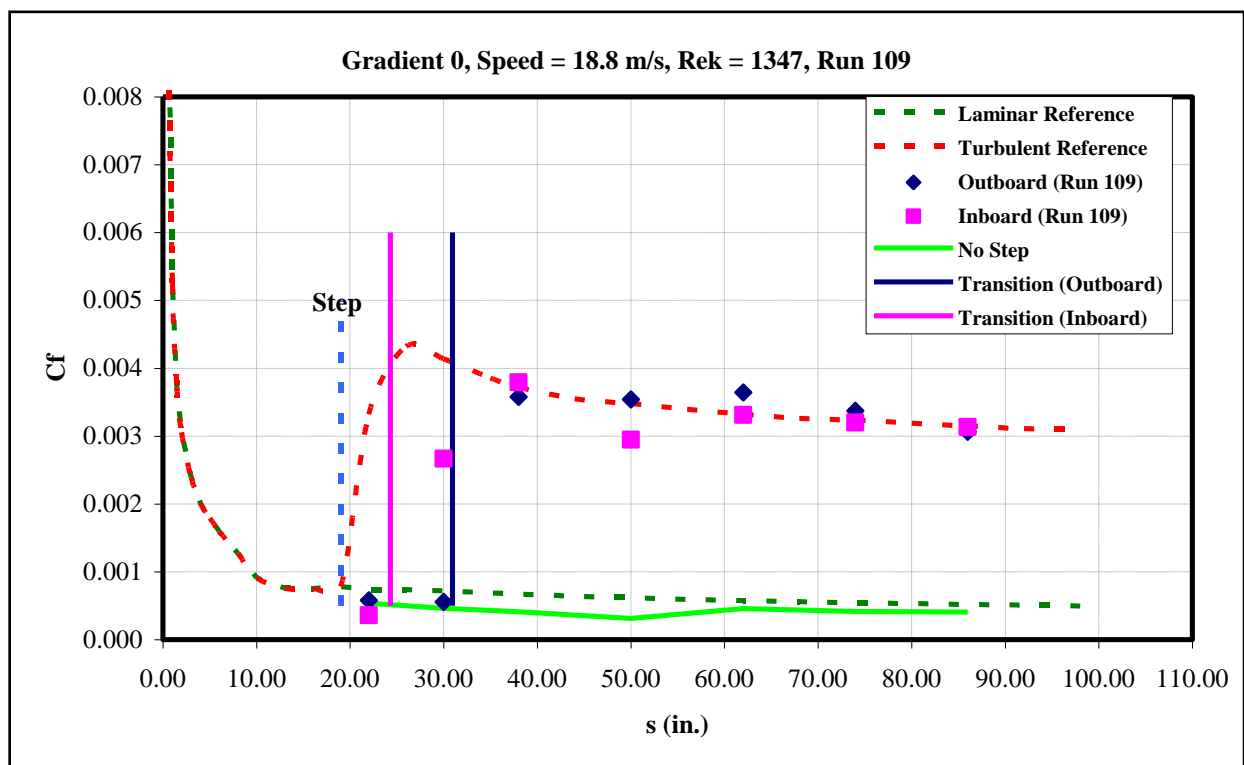


Figure 171: Gradient-Zero, $k=0.055$ -in forward step, $U=18.8$ m/s skin-friction distribution.

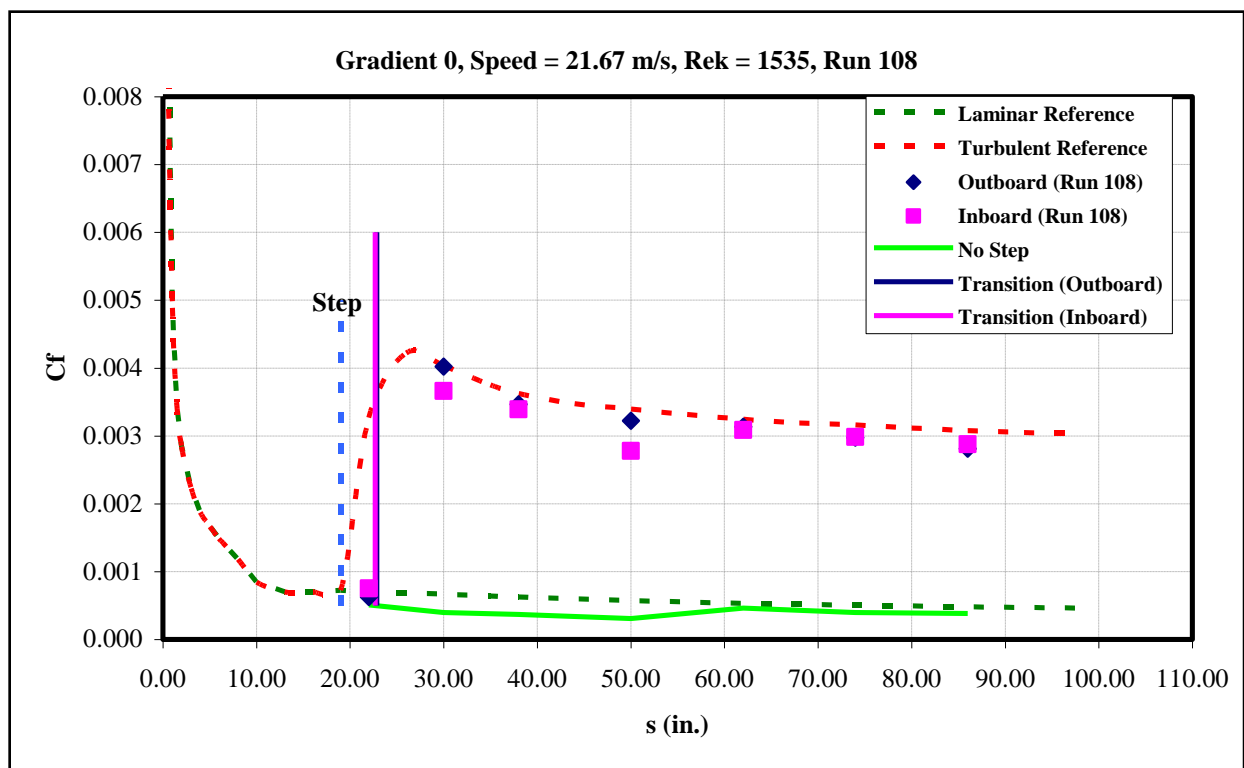


Figure 172: Gradient-Zero, $k=0.055$ -in forward step, $U=21.67$ m/s skin-friction distribution.

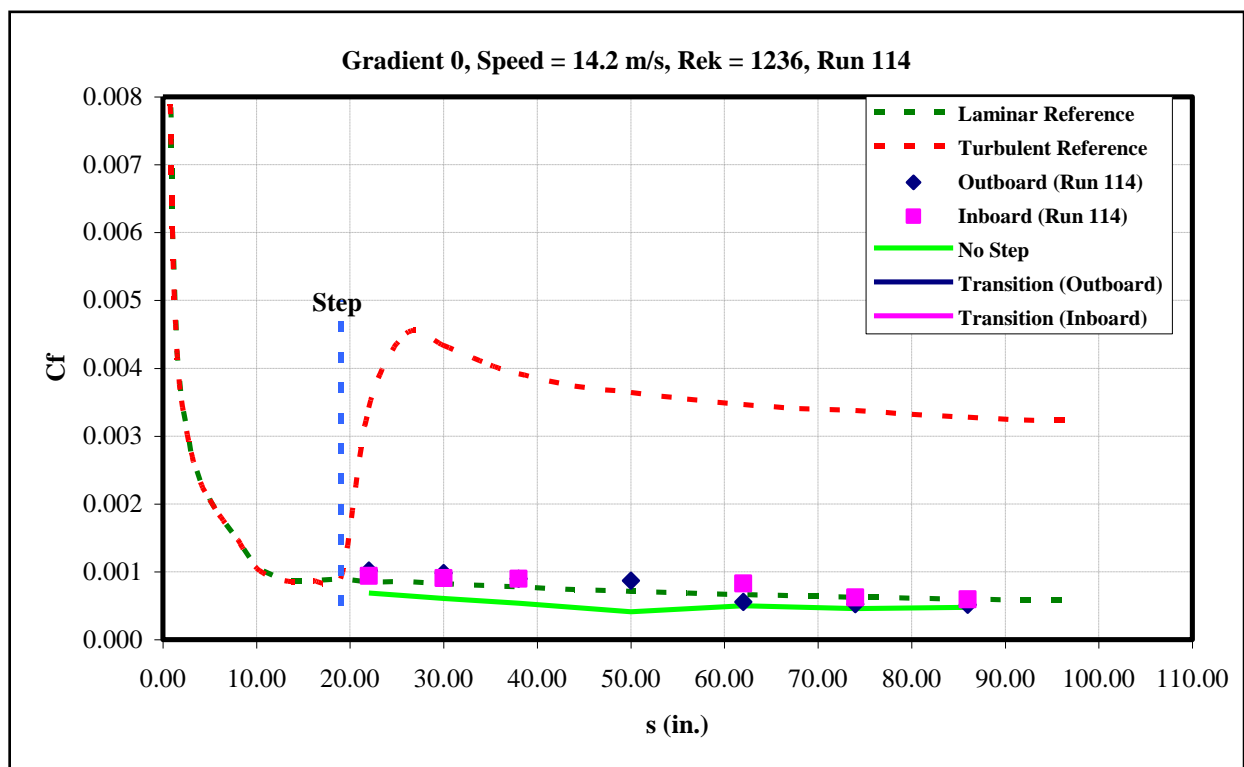


Figure 173: Gradient-Zero, $k=0.06$ -in forward step, $U=14.2$ m/s skin-friction distribution.

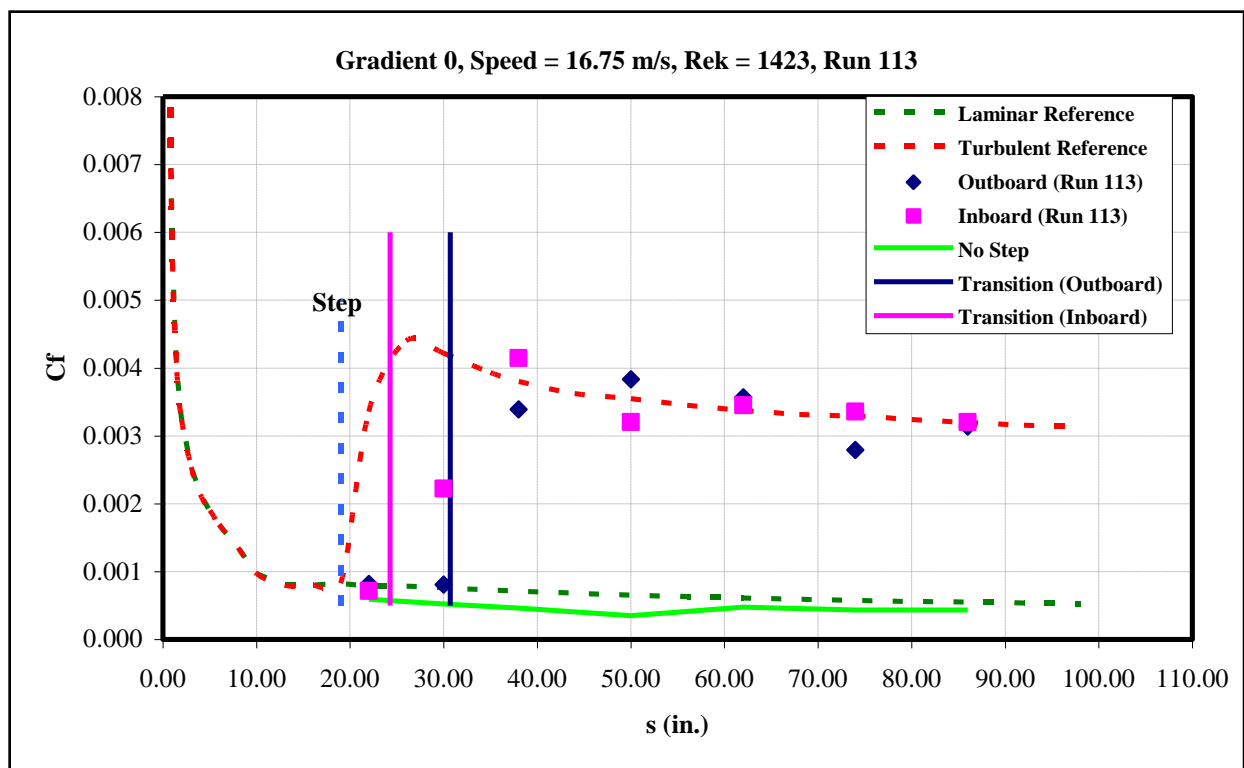


Figure 174: Gradient-Zero, $k=0.06$ -in forward step, $U=16.75$ m/s skin-friction distribution.

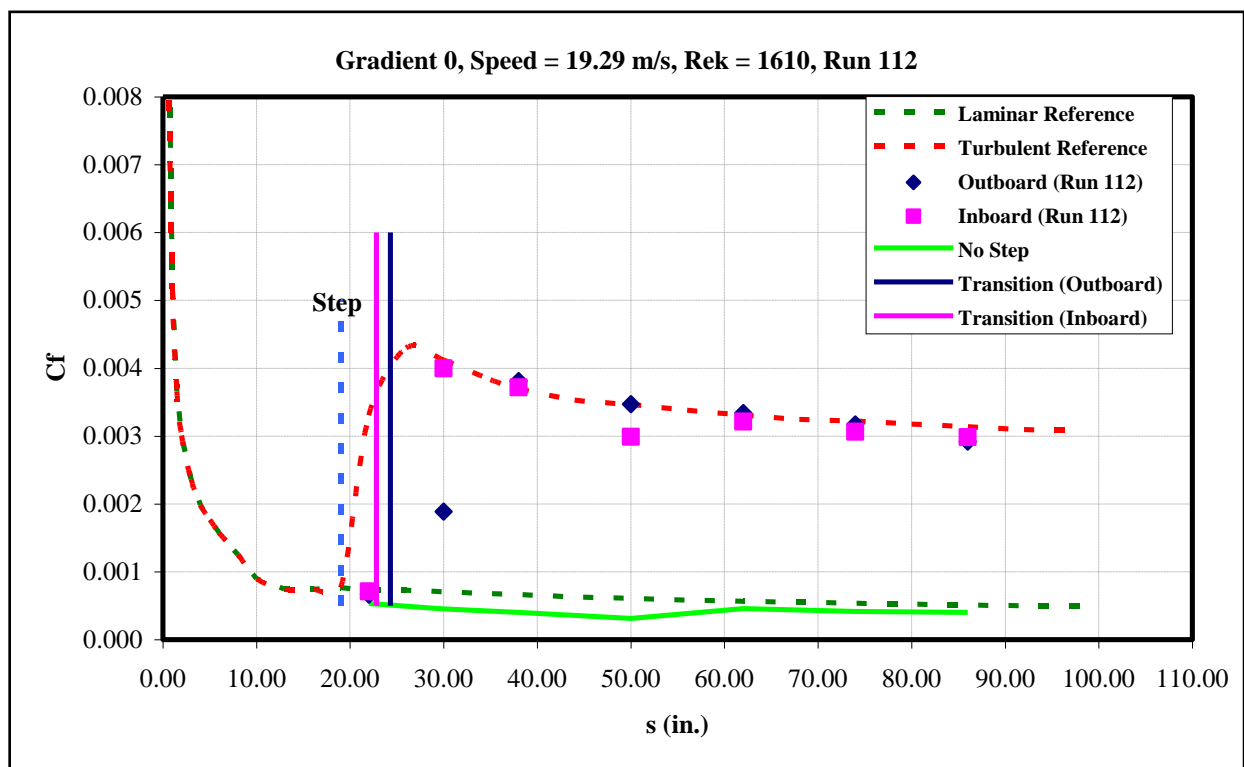


Figure 175: Gradient-Zero, $k=0.06$ -in forward step, $U=19.29$ m/s skin-friction distribution.

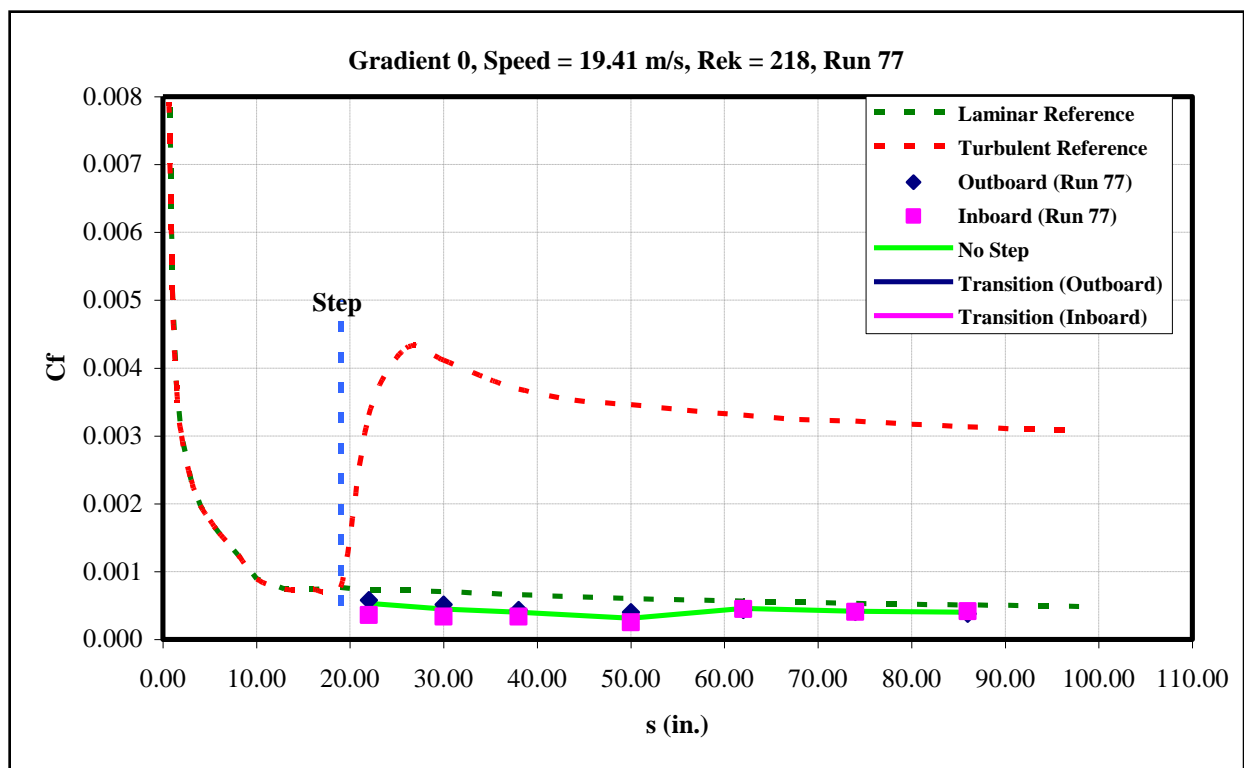


Figure 176: Gradient-Zero, $k=0.02$ -in aft step, $U=19.41$ m/s skin-friction distribution.

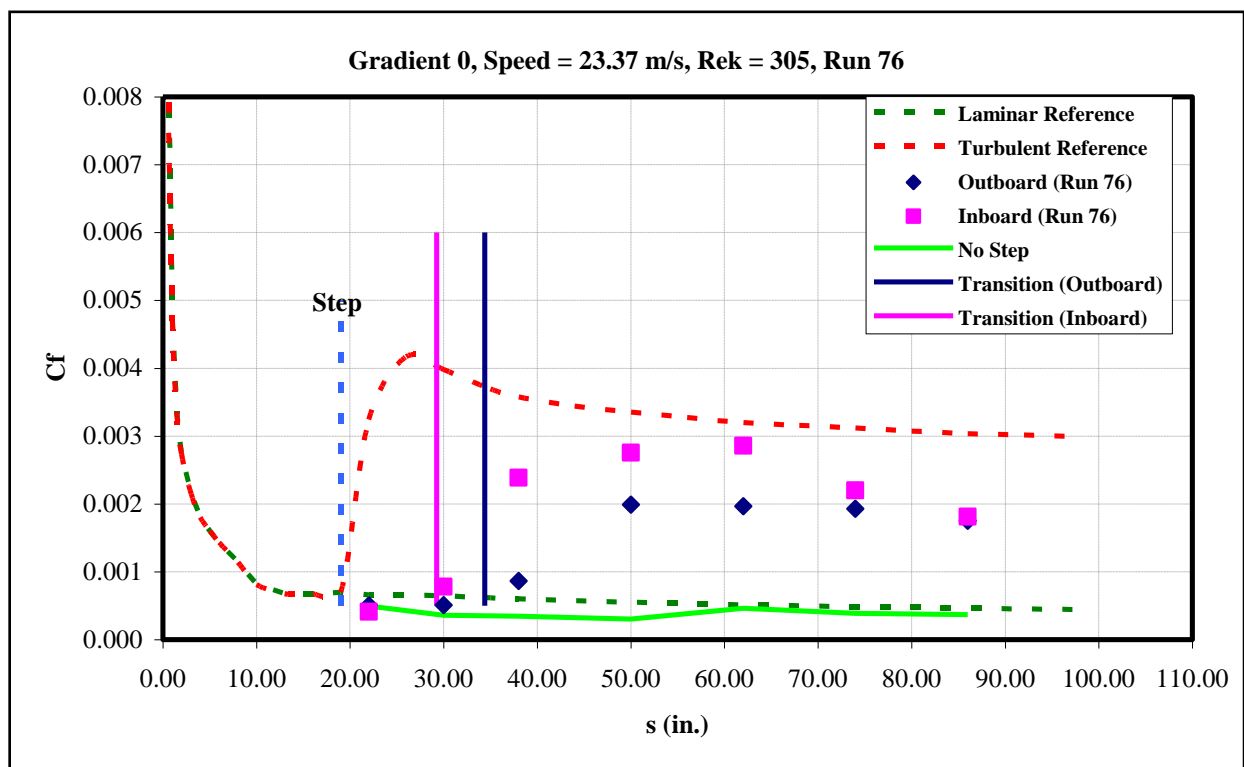


Figure 177: Gradient-Zero, $k=0.02$ -in aft step, $U=23.37$ m/s skin-friction distribution.

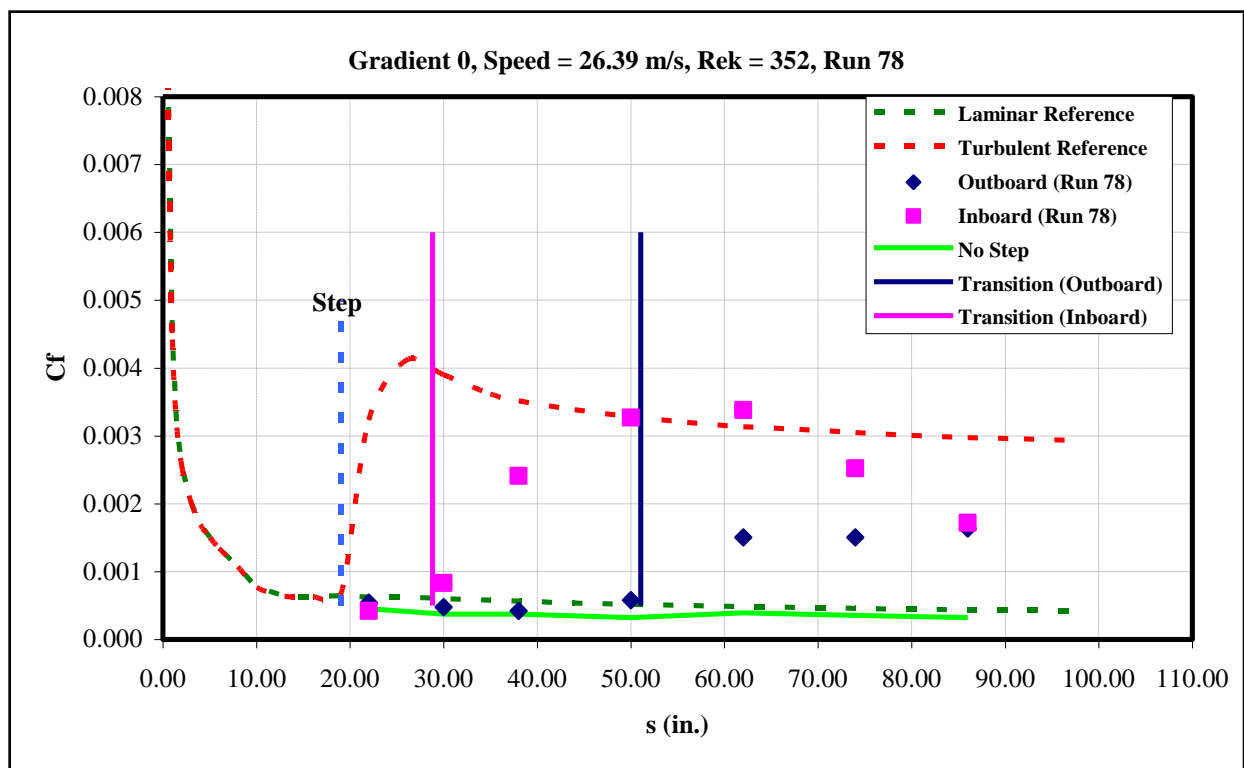


Figure 178: Gradient-Zero, $k=0.02$ -in aft step, $U=26.39$ m/s skin-friction distribution.

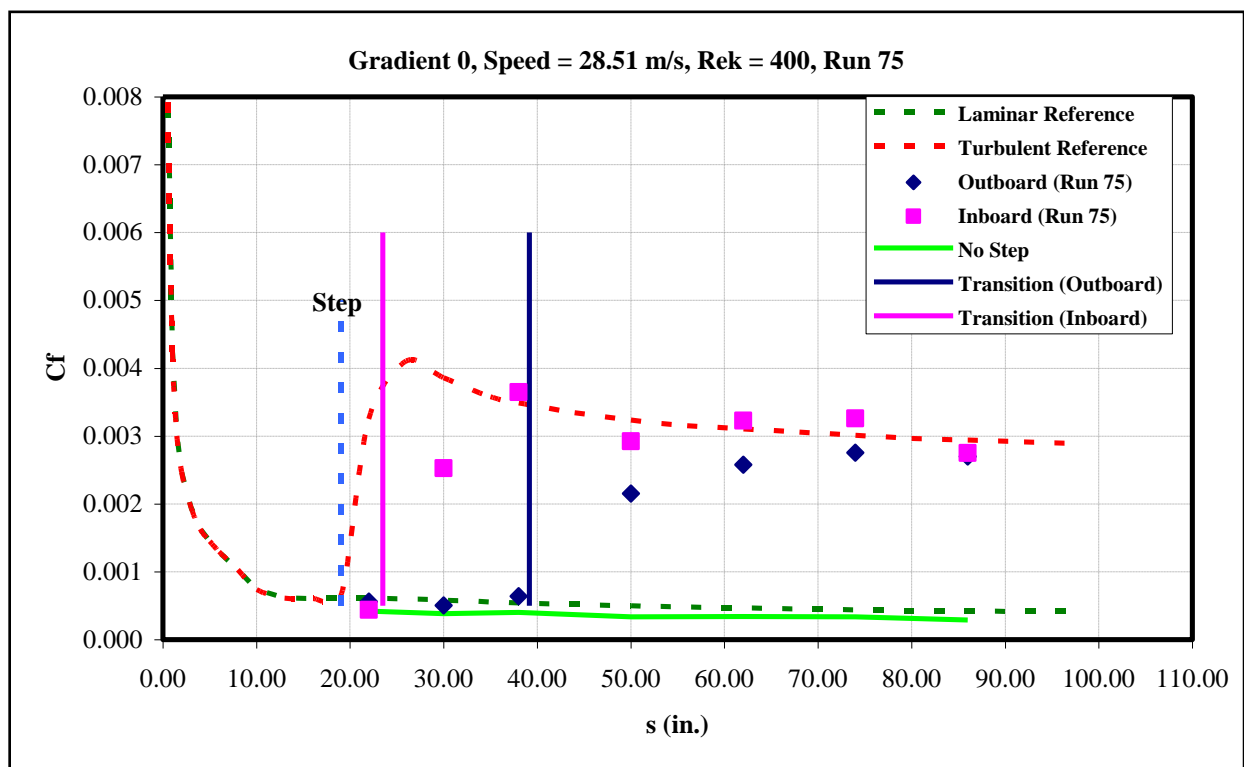


Figure 179: Gradient-Zero, $k=0.02$ -in aft step, $U=28.51$ m/s skin-friction distribution.

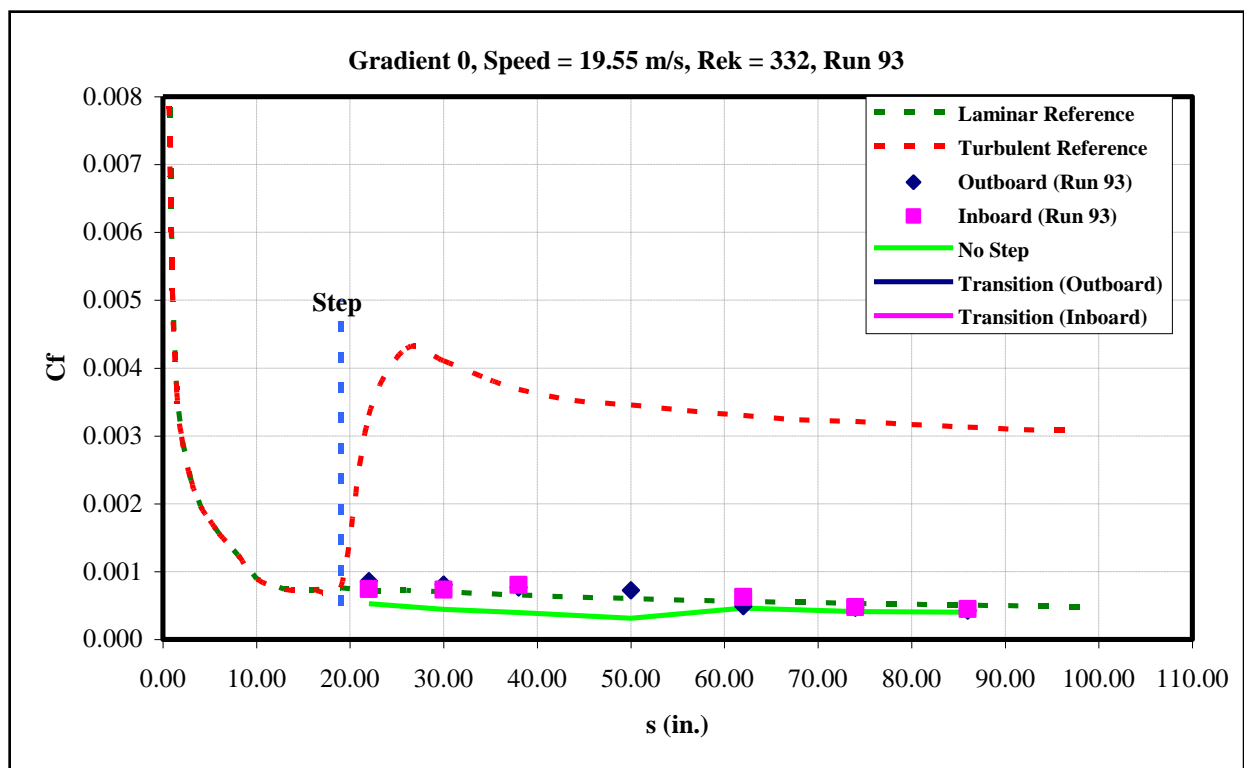


Figure 180: Gradient-Zero, $k=0.025$ -in aft step, $U=19.55$ m/s skin-friction distribution.

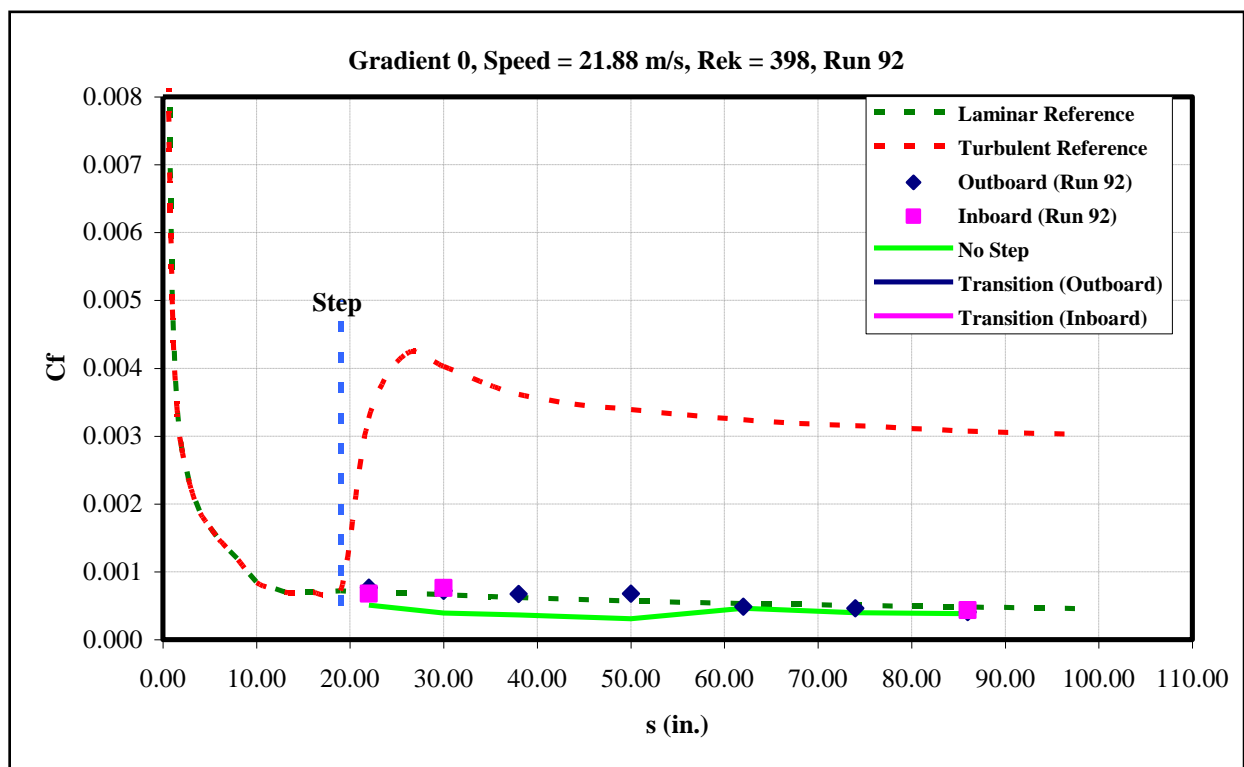


Figure 181: Gradient-Zero, $k=0.025$ -in aft step, $U=21.88$ m/s skin-friction distribution.

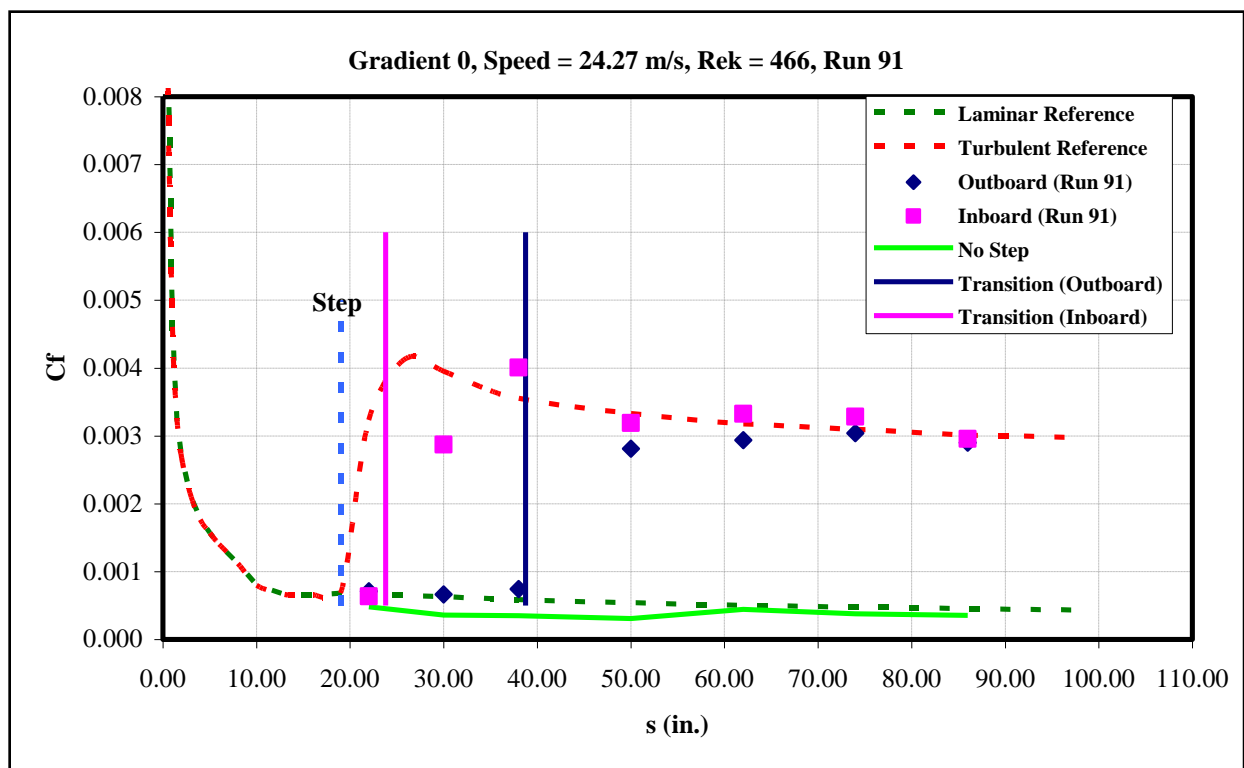


Figure 182: Gradient-Zero, $k=0.025$ -in aft step, $U=24.27$ m/s skin-friction distribution.

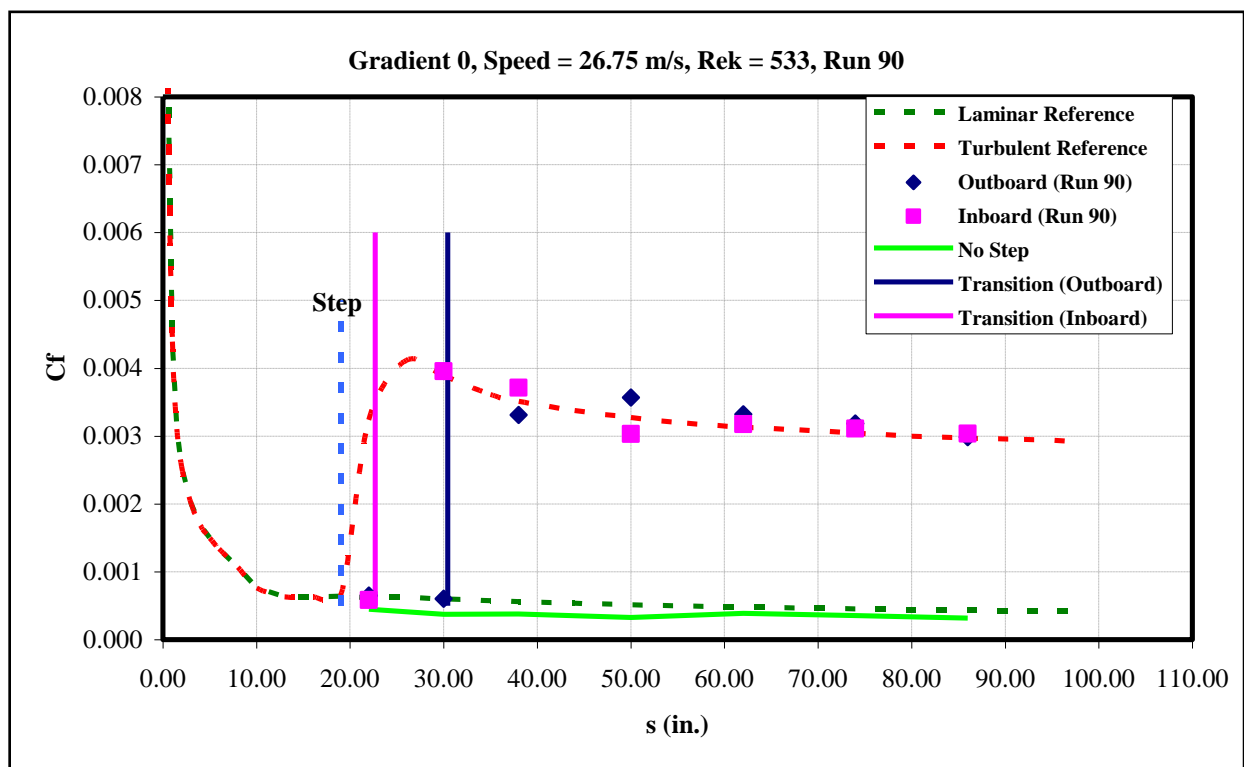


Figure 183: Gradient-Zero, $k=0.025$ -in aft step, $U=26.75$ m/s skin-friction distribution.

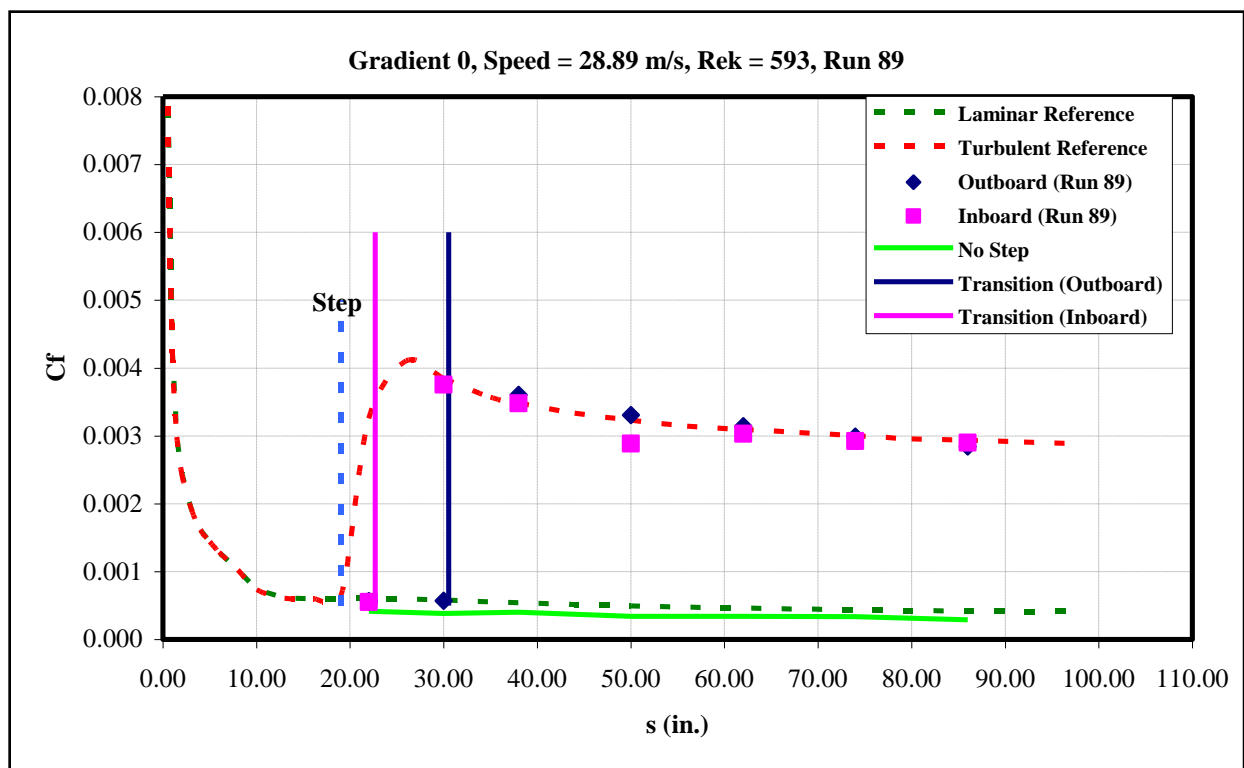


Figure 184: Gradient-Zero, $k=0.025$ -in aft step, $U=28.89$ m/s skin-friction distribution.

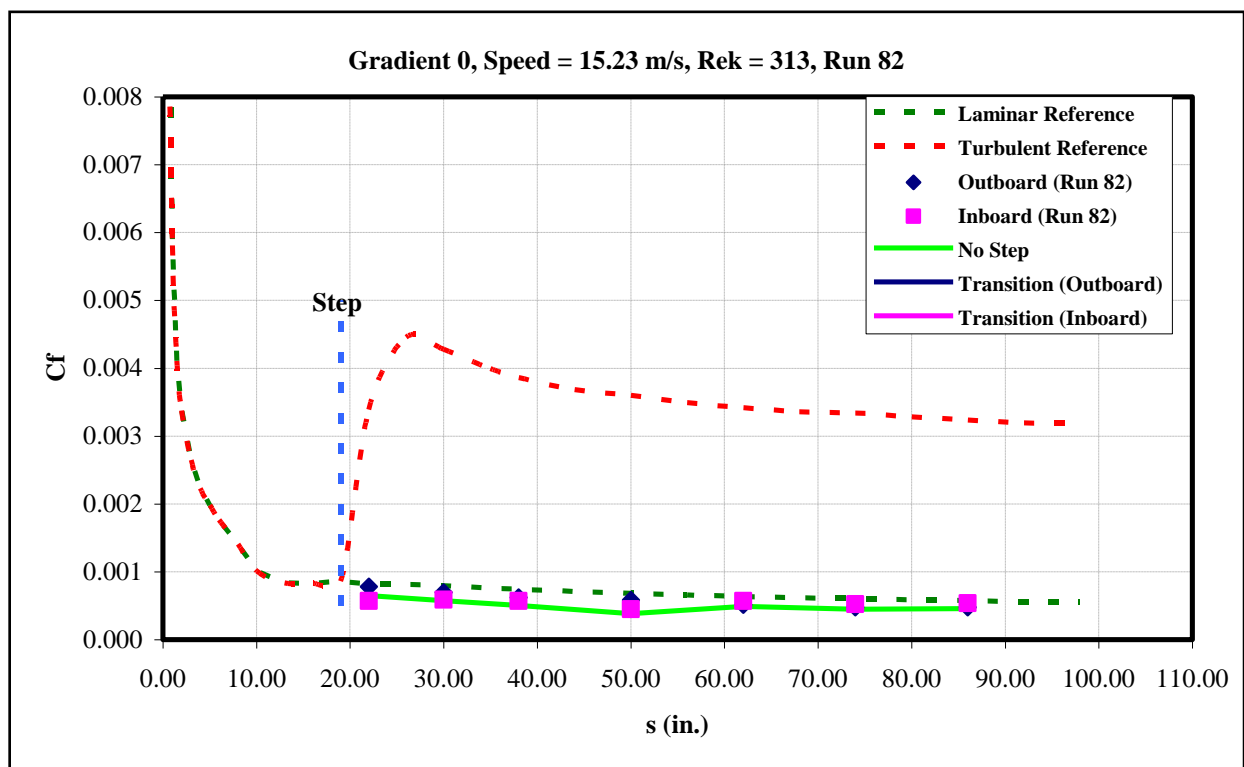


Figure 185: Gradient-Zero, $k=0.03$ -in aft step, $U=15.23$ m/s skin-friction distribution.

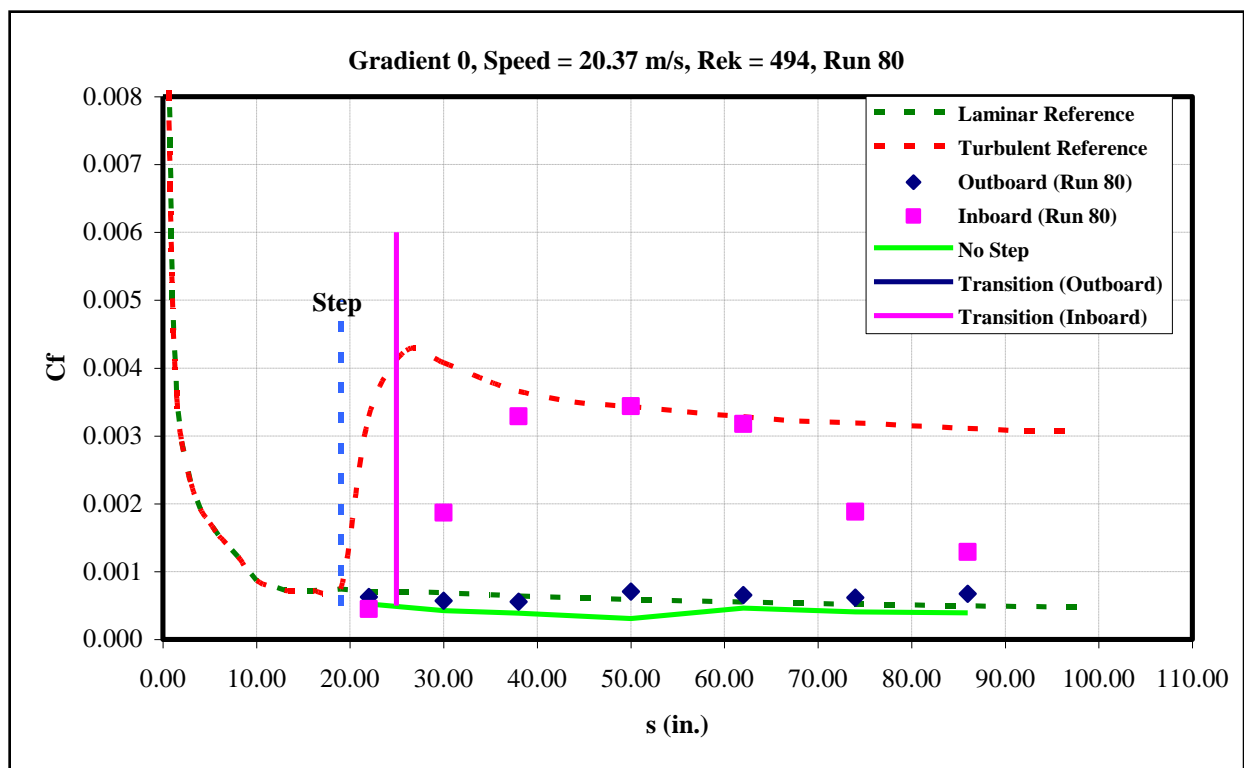


Figure 186: Gradient-Zero, $k=0.03$ -in aft step, $U=20.37$ m/s skin-friction distribution.

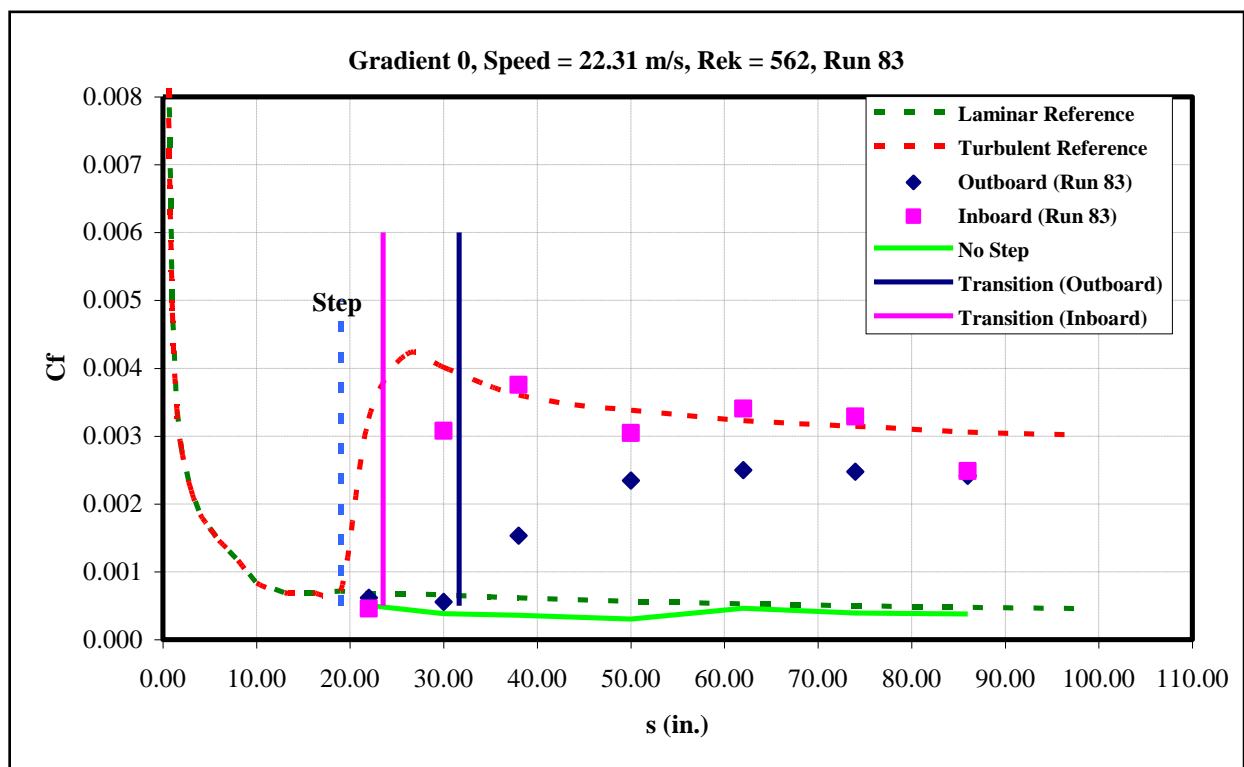


Figure 187: Gradient-Zero, $k=0.03$ -in aft step, $U=22.31$ m/s skin-friction distribution.

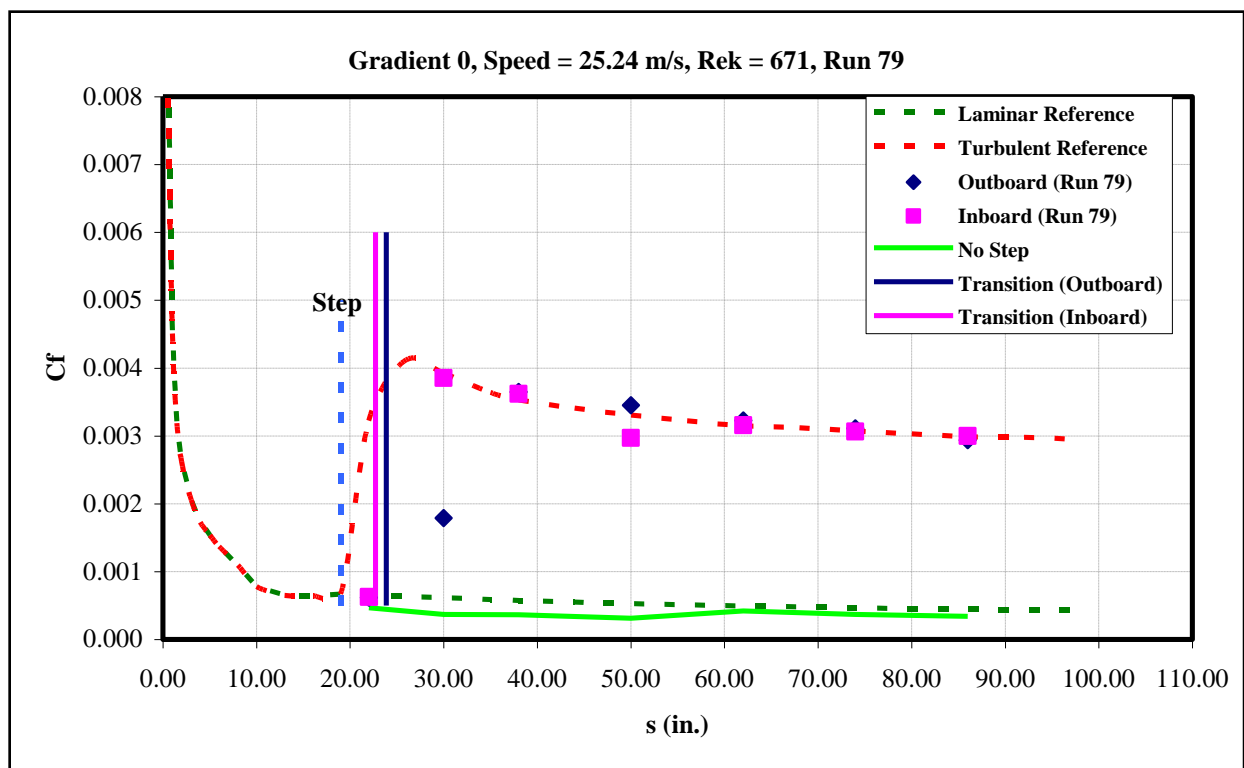


Figure 188: Gradient-Zero, $k=0.03$ -in aft step, $U=25.24$ m/s skin-friction distribution.

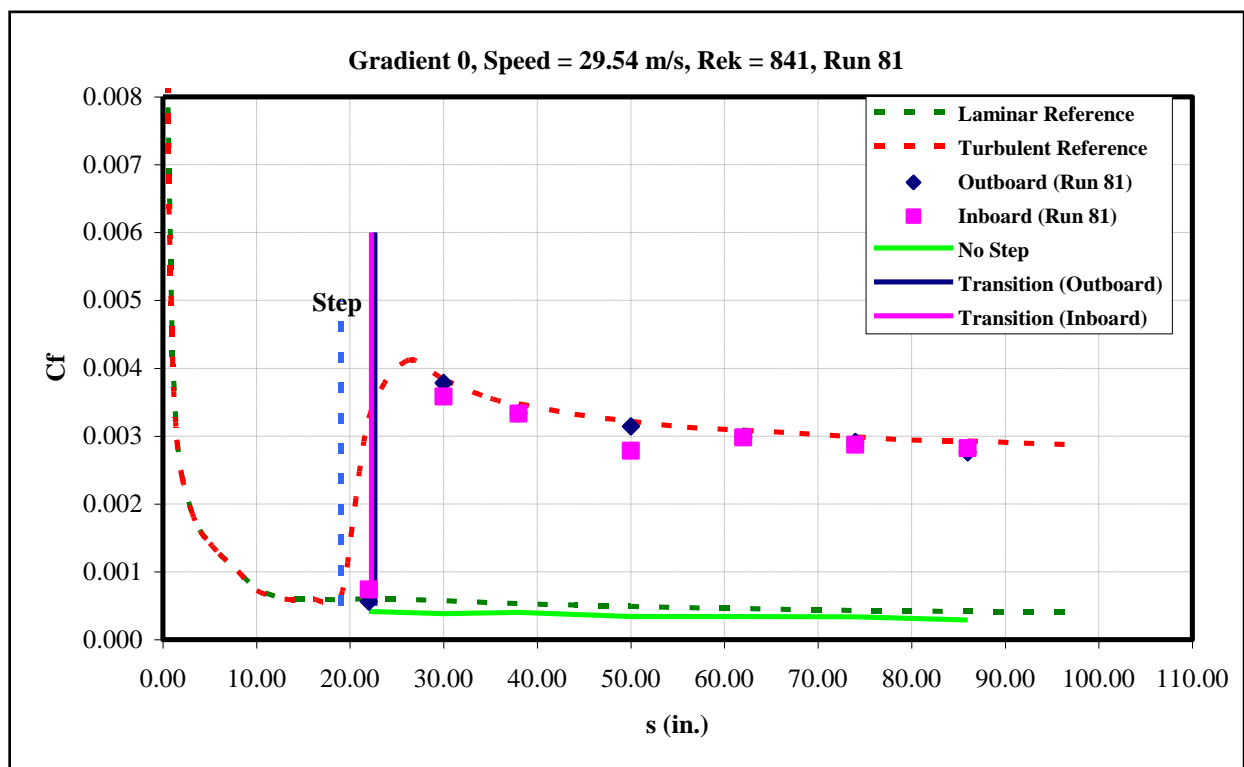


Figure 189: Gradient-Zero, $k=0.03$ -in aft step, $U=29.54$ m/s skin-friction distribution.

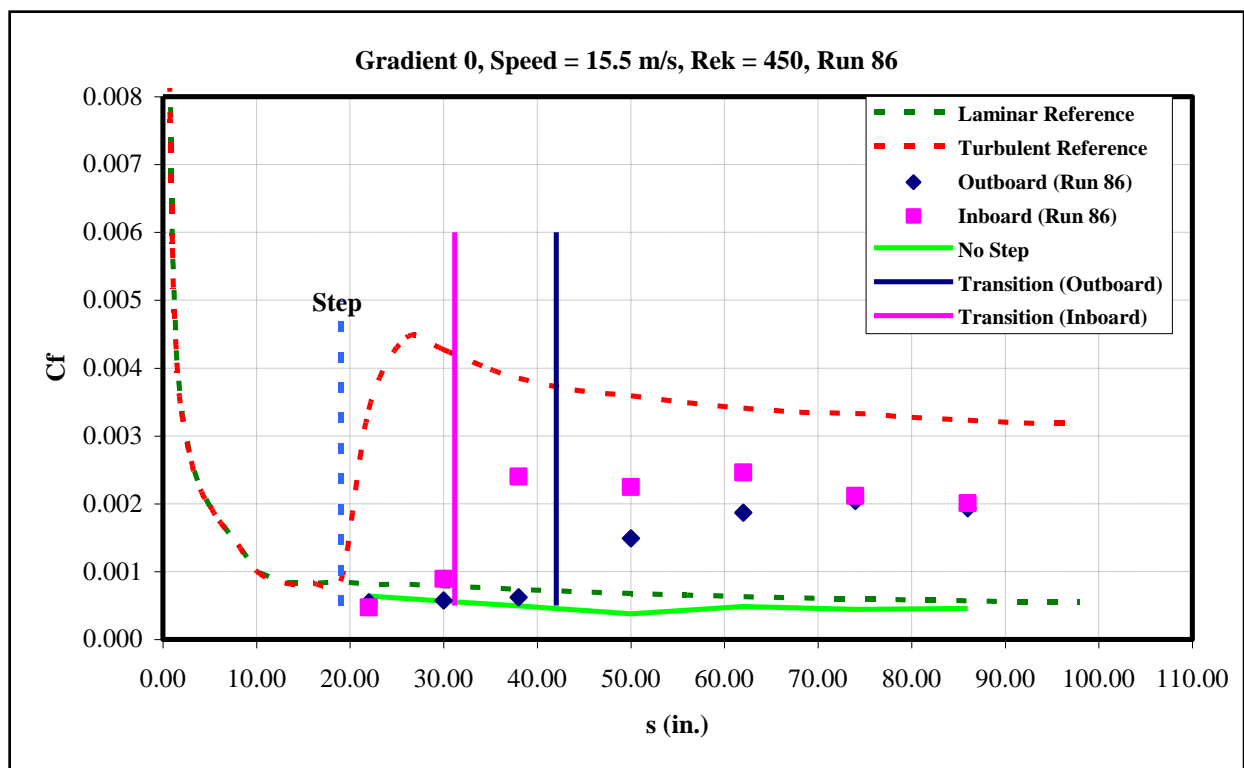


Figure 190: Gradient-Zero, $k=0.035$ -in aft step, $U=15.5$ m/s skin-friction distribution.

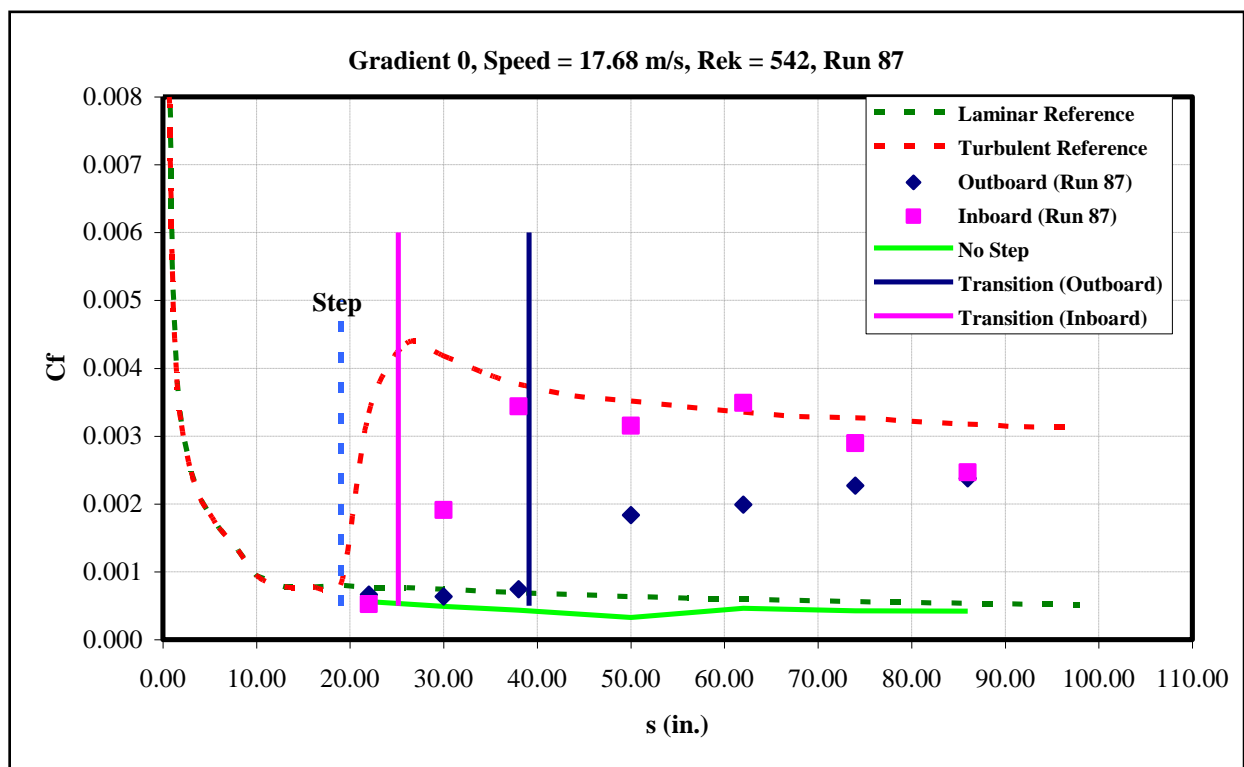


Figure 191: Gradient-Zero, $k=0.035$ -in aft step, $U=17.68$ m/s skin-friction distribution.

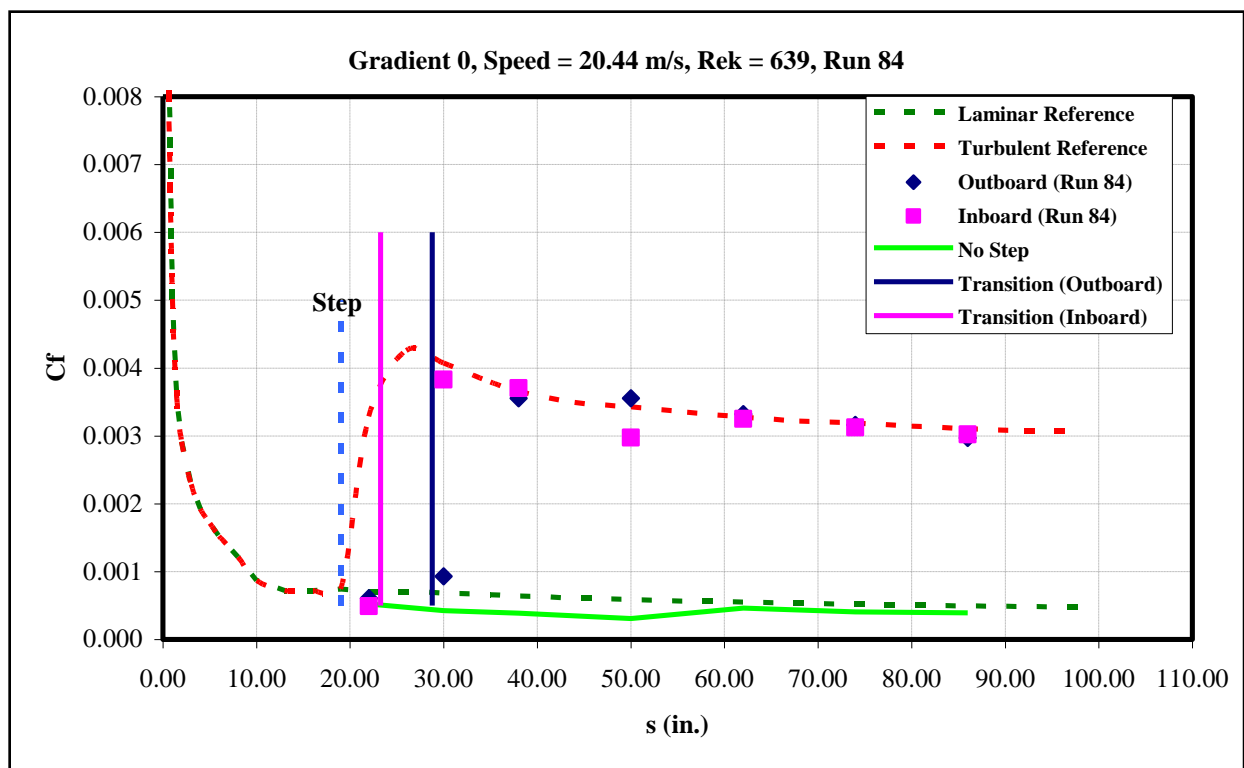


Figure 192: Gradient-Zero, $k=0.035$ -in aft step, $U=20.44$ m/s skin-friction distribution.

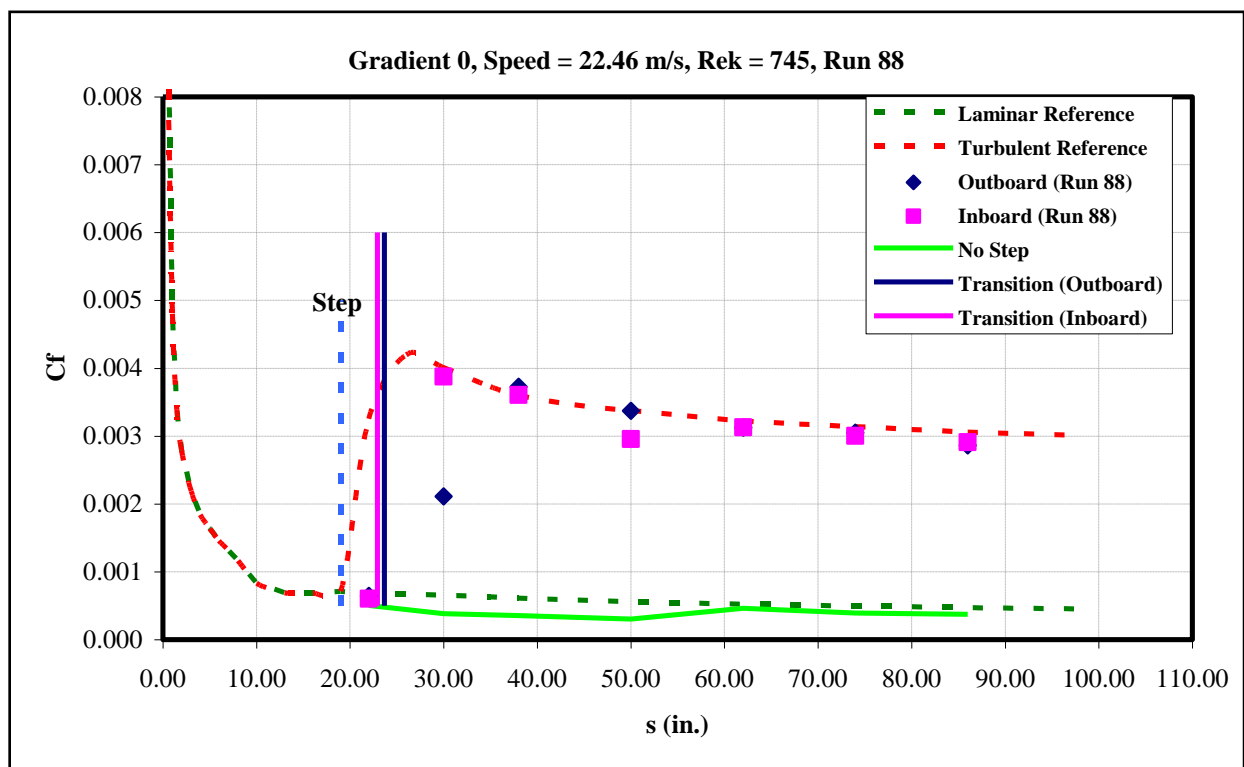


Figure 193: Gradient-Zero, $k=0.035$ -in aft step, $U=22.46$ m/s skin-friction distribution.

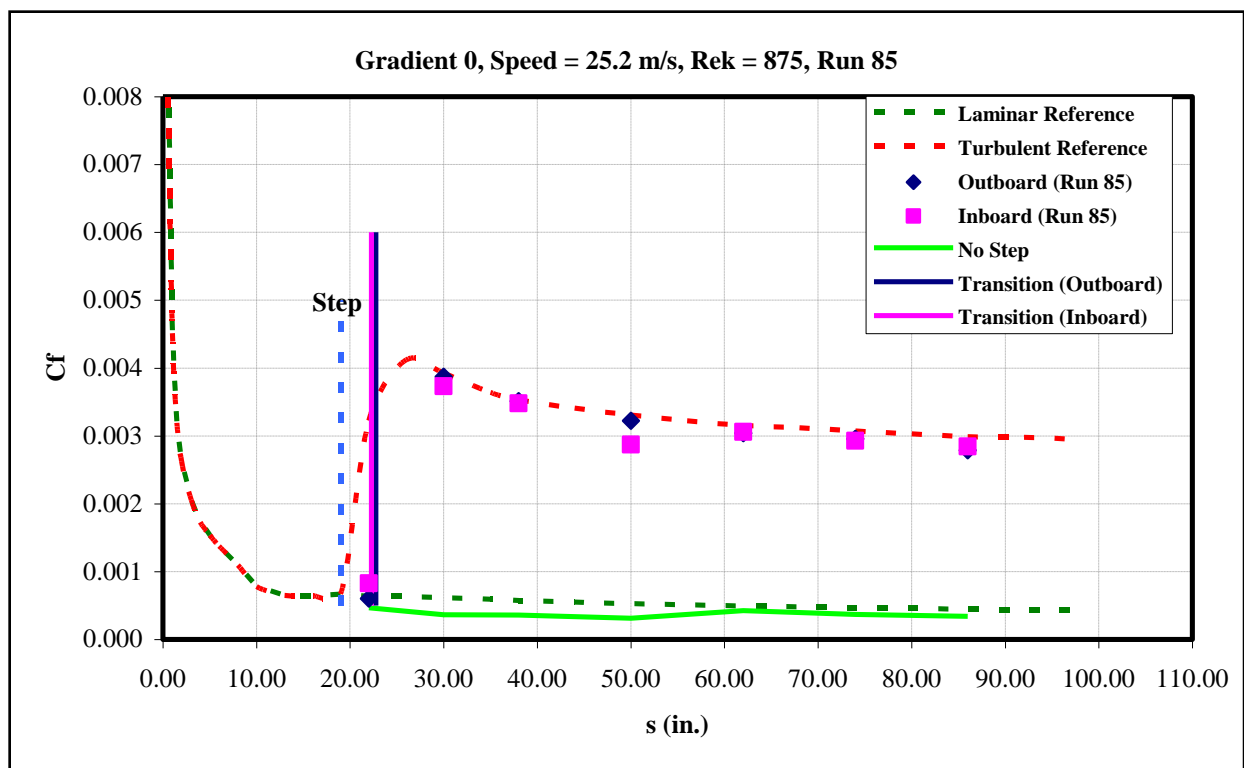


Figure 194: Gradient-Zero, $k=0.035$ -in aft step, $U=25.2$ m/s skin-friction distribution.

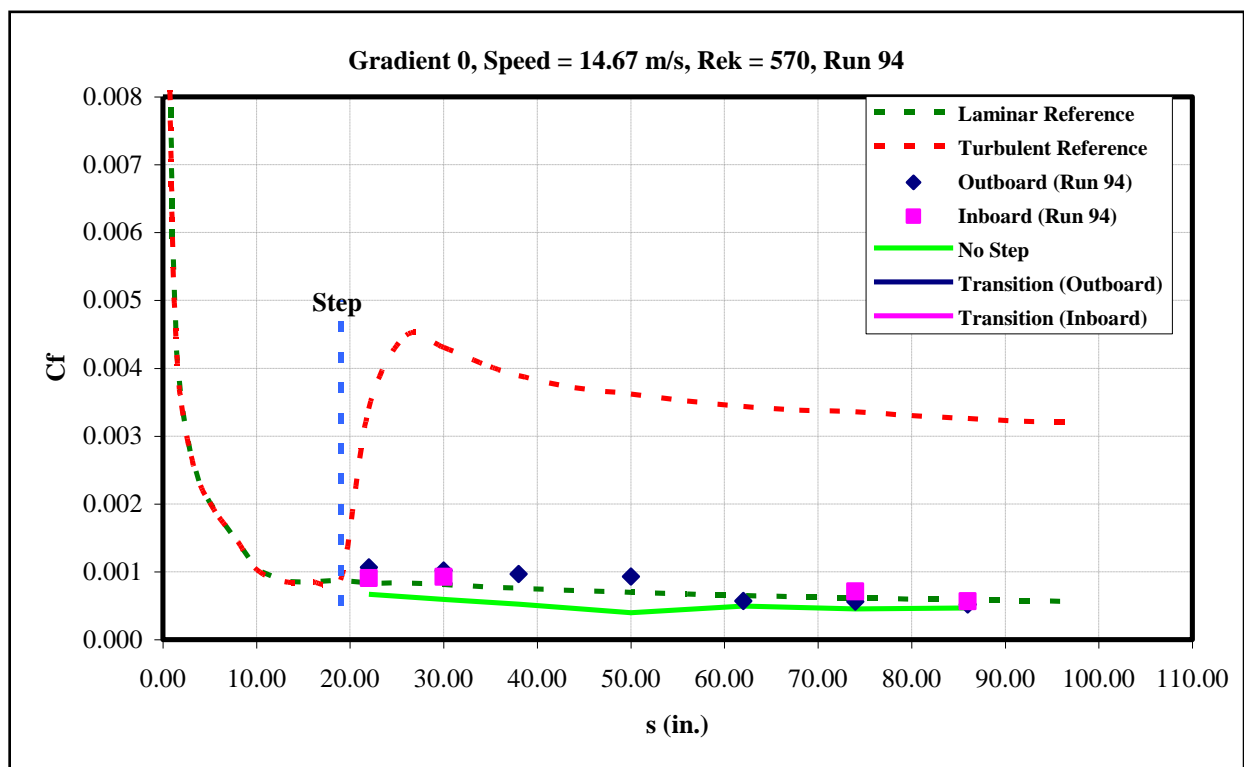


Figure 195: Gradient-Zero, $k=0.04$ -in aft step, $U=14.67$ m/s skin-friction distribution.

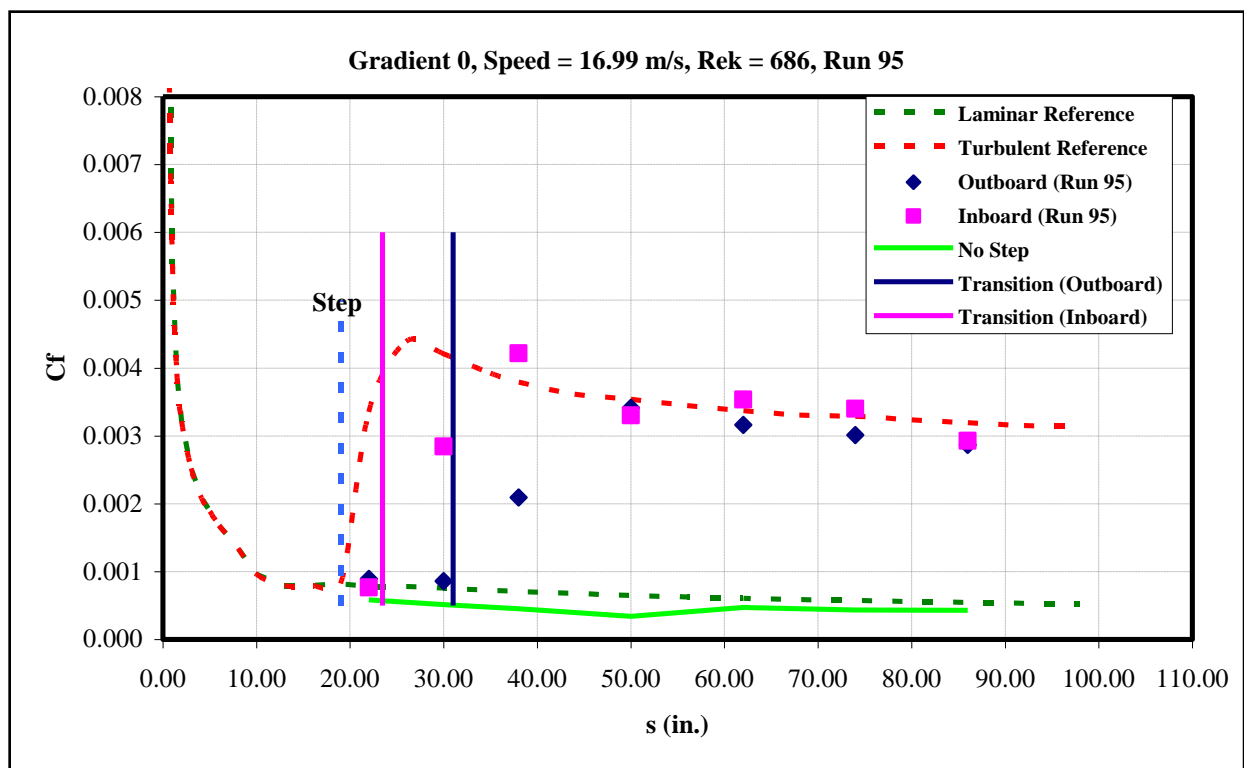


Figure 196: Gradient-Zero, $k=0.04$ -in aft step, $U=16.99$ m/s skin-friction distribution.

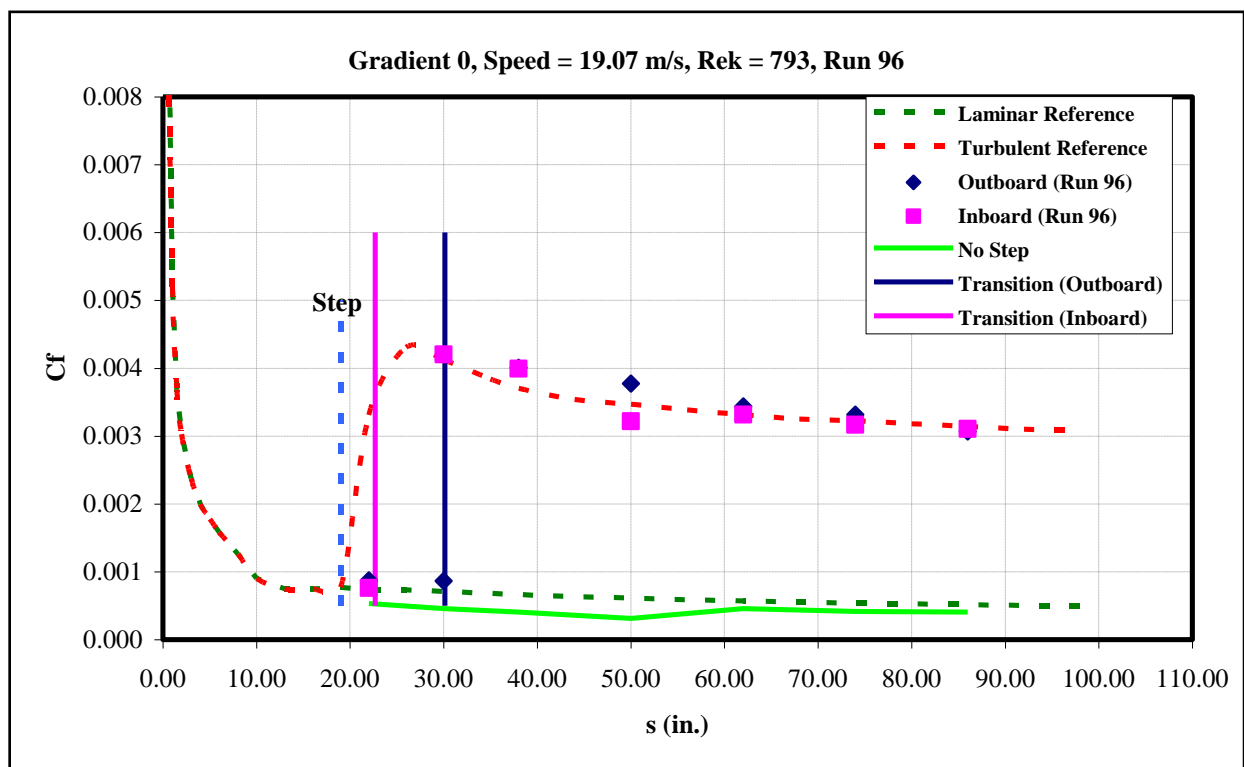


Figure 197: Gradient-Zero, $k=0.04$ -in aft step, $U=19.07$ m/s skin-friction distribution.

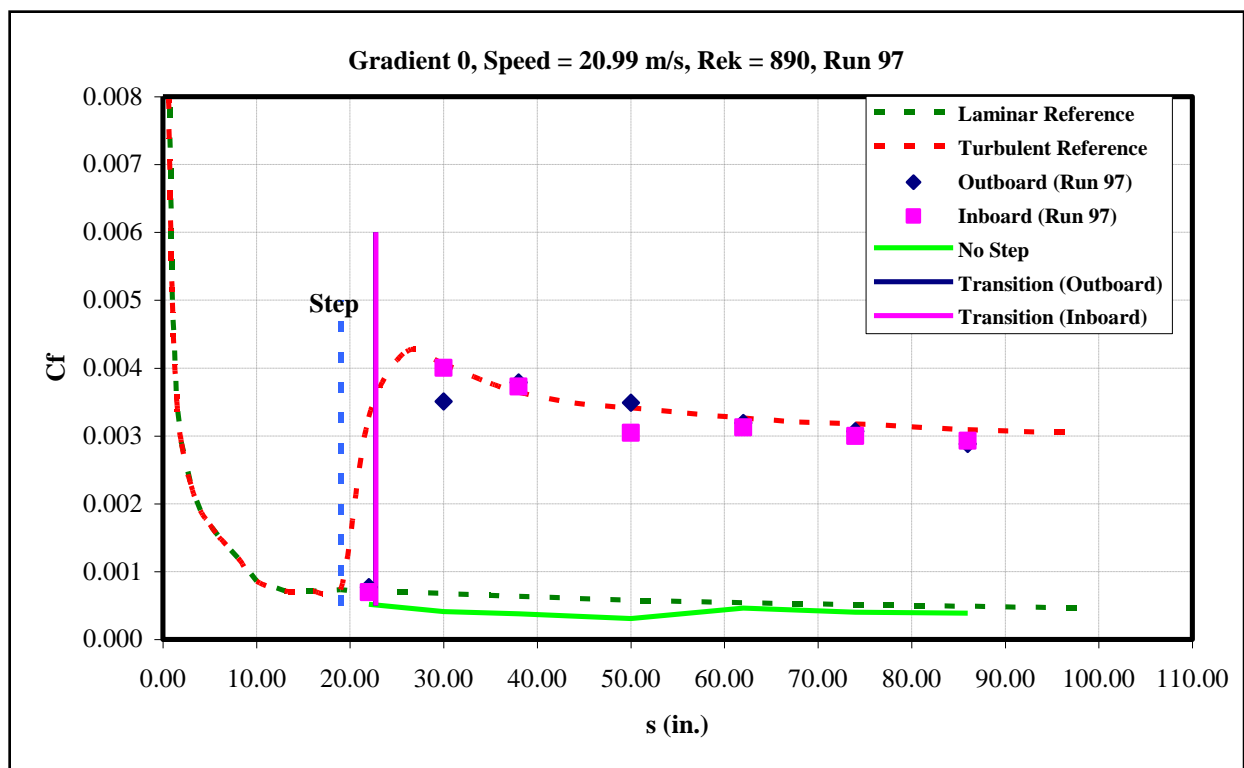


Figure 198: Gradient-Zero, $k=0.04$ -in aft step, $U=20.99$ m/s skin-friction distribution.

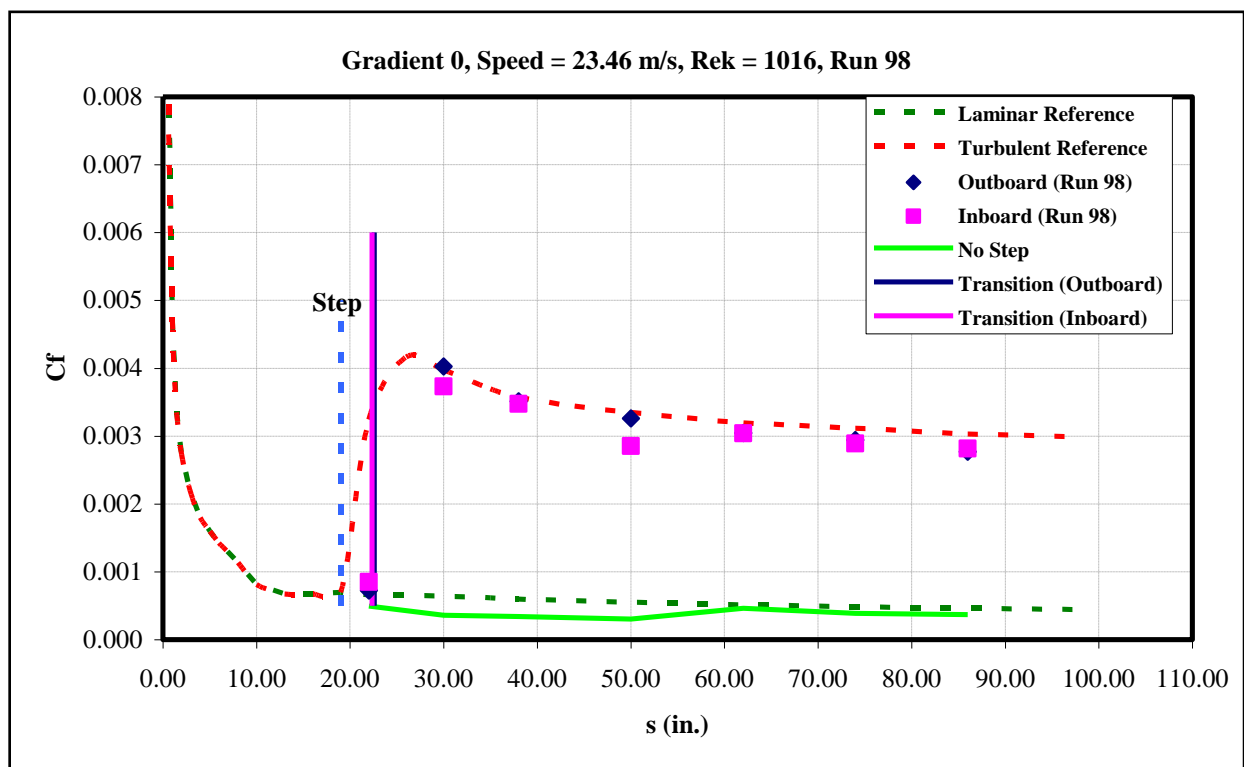


Figure 199: Gradient-Zero, $k=0.04$ -in aft step, $U=23.46$ m/s skin-friction distribution.

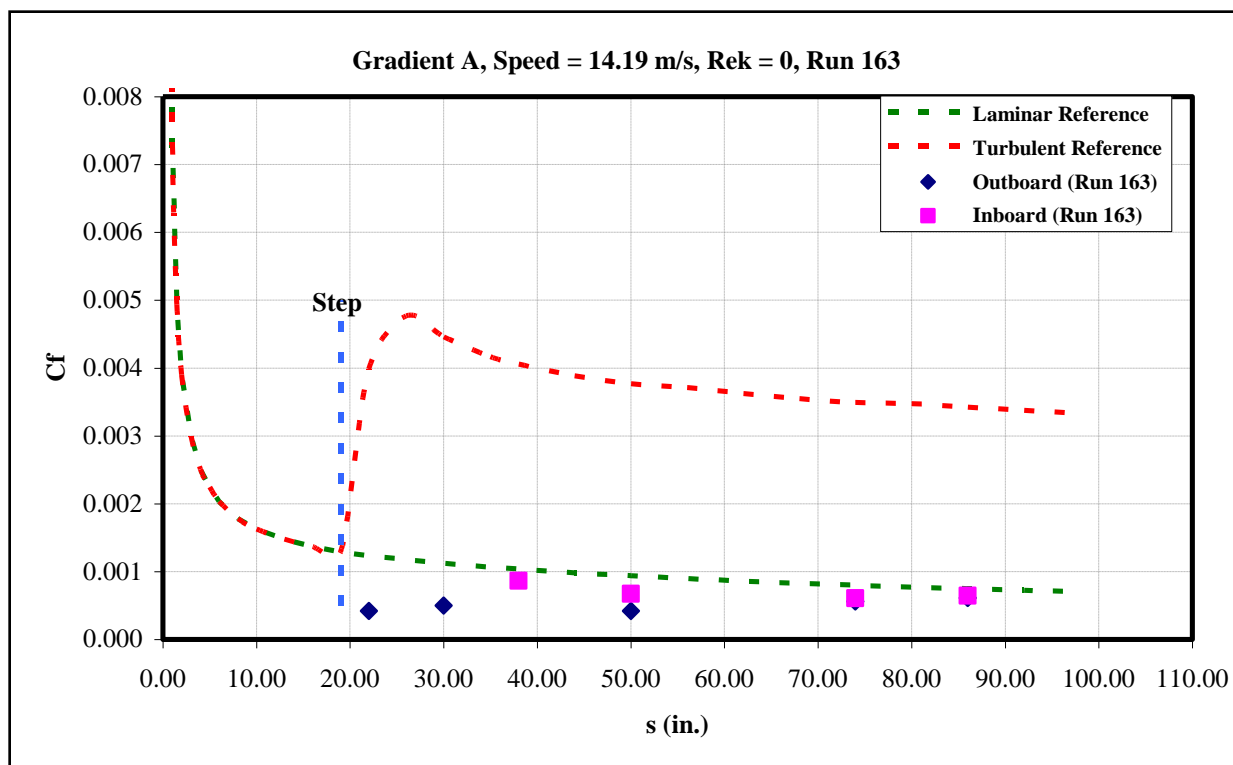


Figure 200: Gradient-A, $k=0$ -in, $U=14.19$ m/s skin-friction distribution.

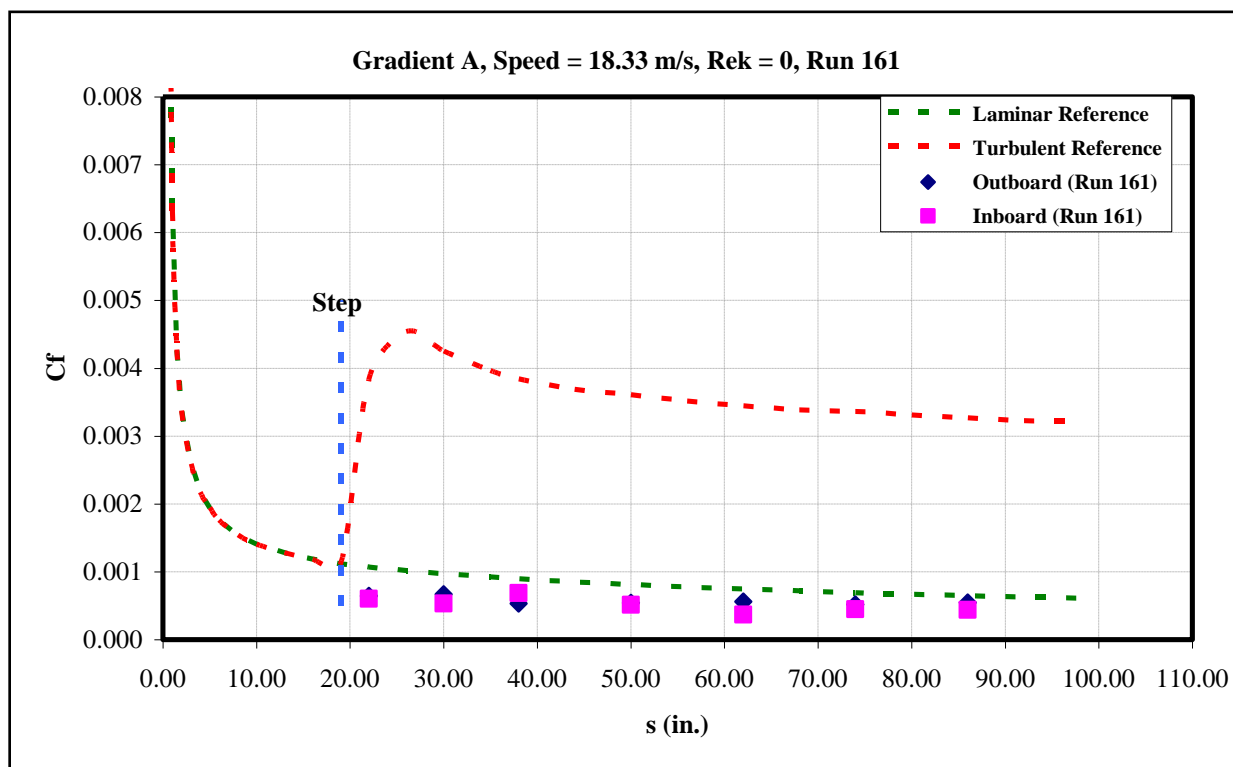


Figure 201: Gradient-A, $k=0$ -in, $U=18.33$ m/s skin-friction distribution.

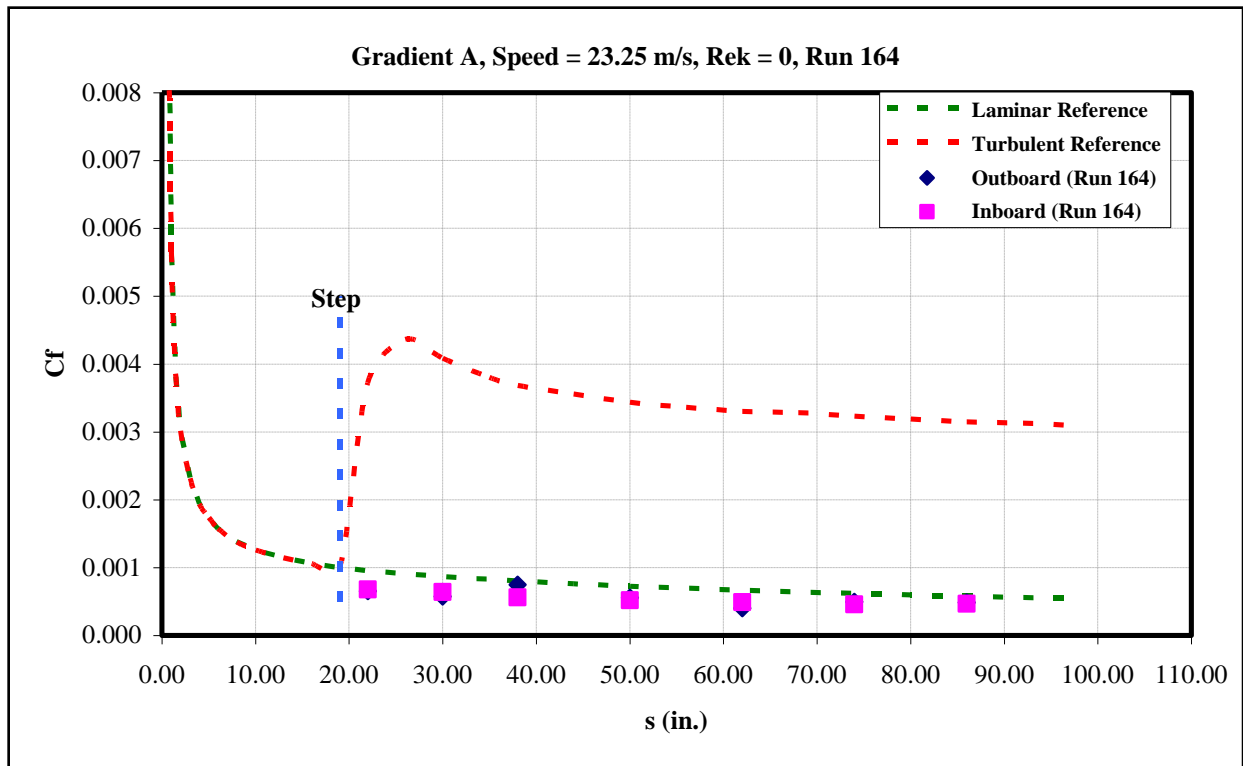


Figure 202: Gradient-A, $k=0$ -in, $U=23.25$ m/s skin-friction distribution.

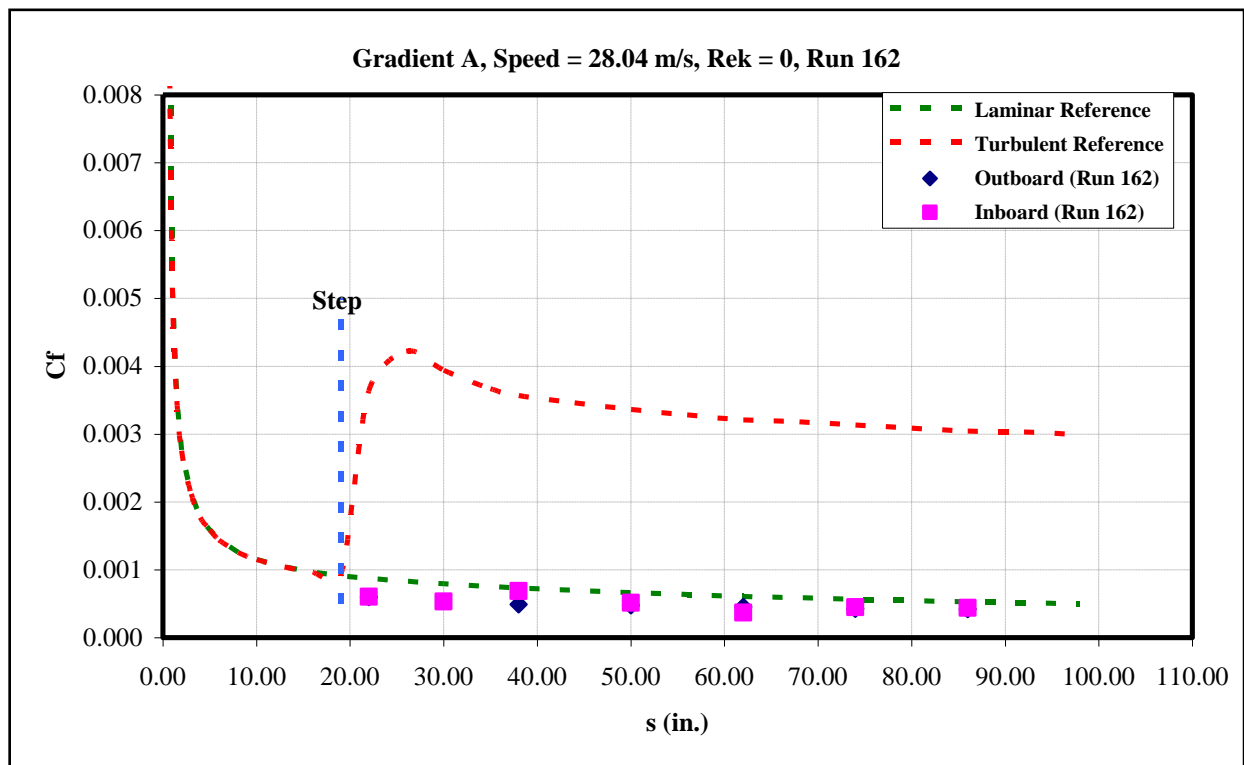


Figure 203: Gradient-A, $k=0$ -in, $U=28.04$ m/s skin-friction distribution.

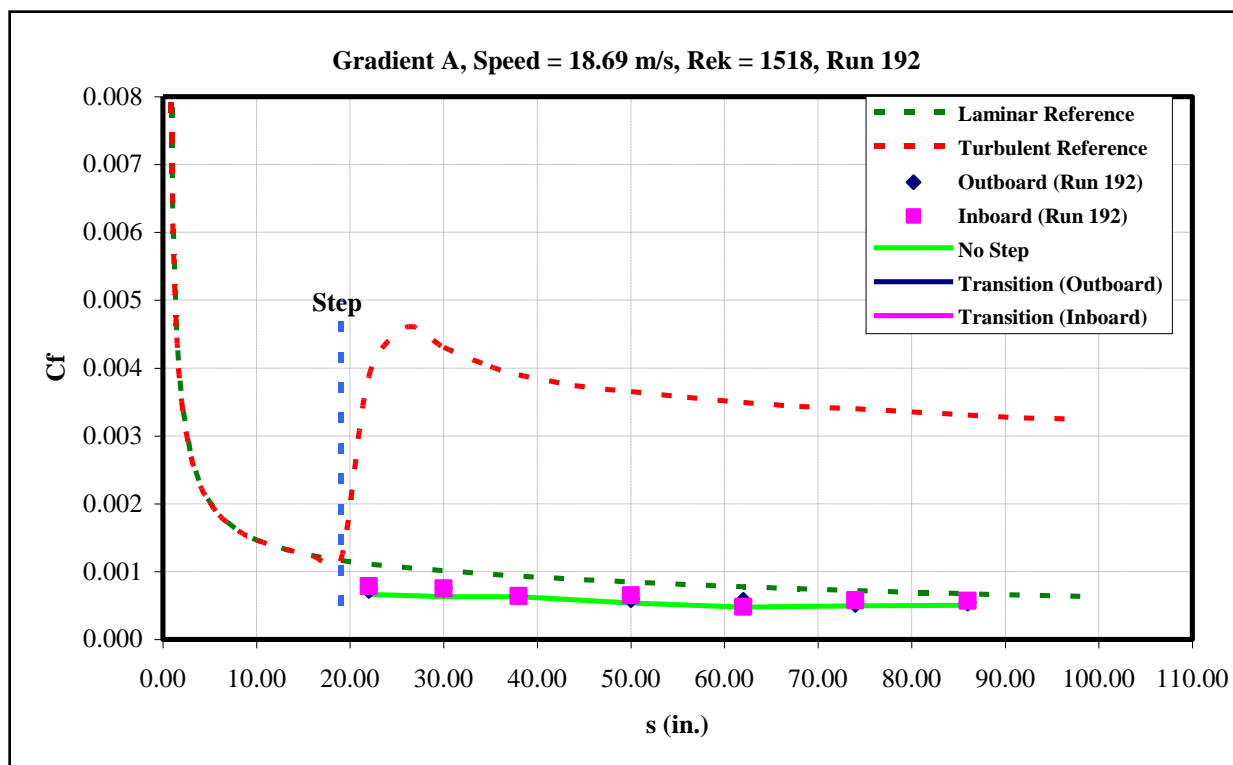


Figure 204: Gradient-A, $k=0.055$ -in forward step, $U=18.69$ m/s skin-friction distribution.

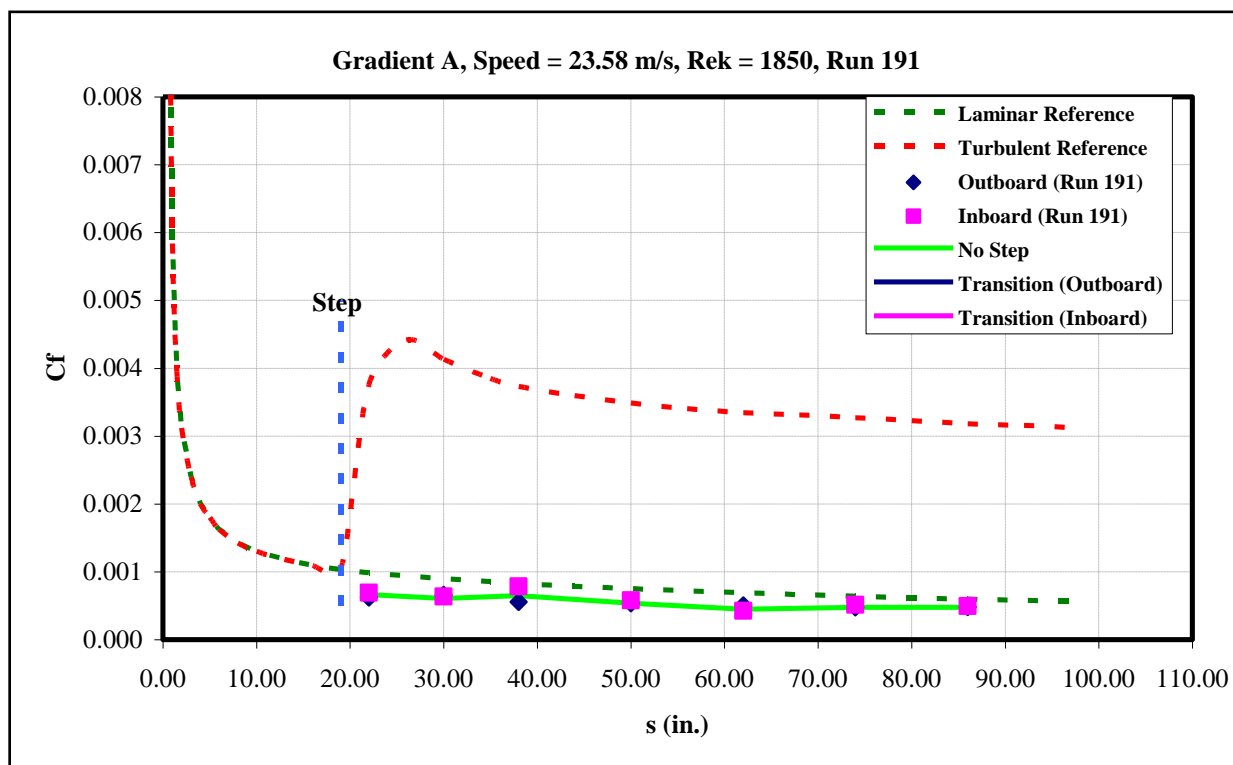


Figure 205: Gradient-A, $k=0.055$ -in forward step, $U=23.58$ m/s skin-friction distribution.

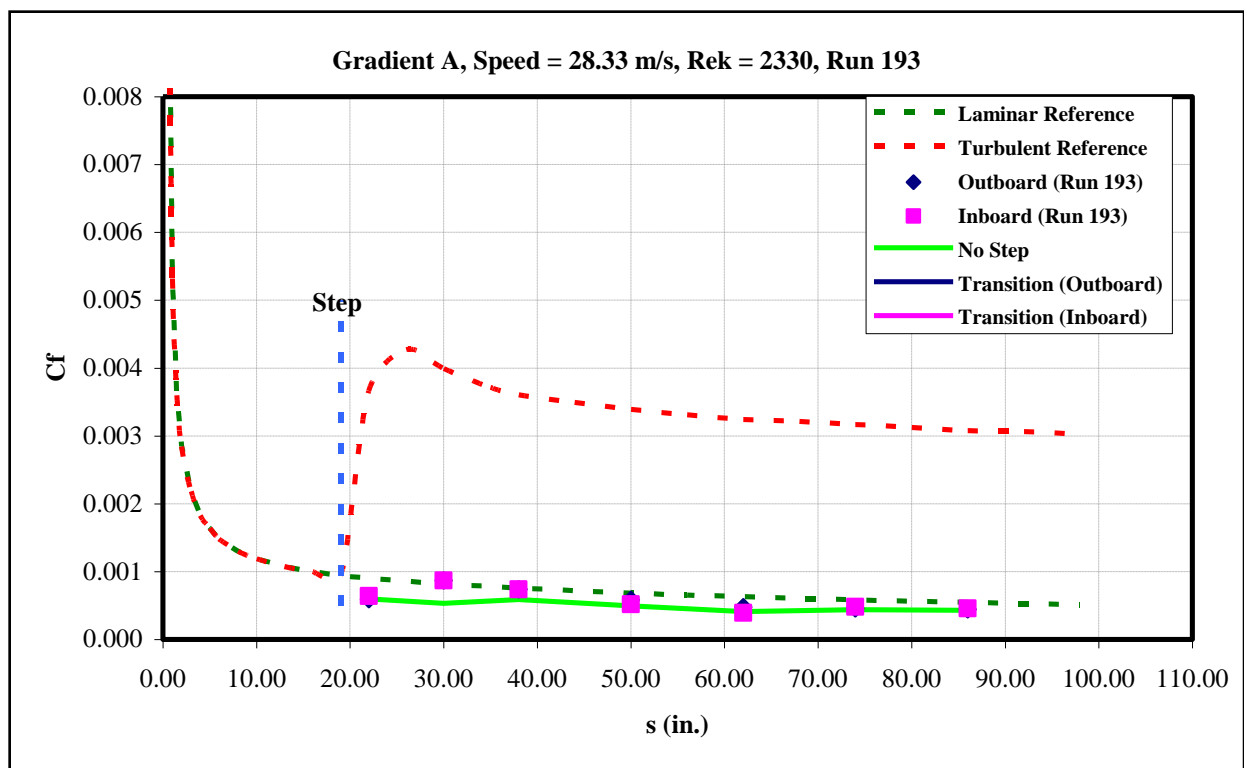


Figure 206: Gradient-A, $k=0.055$ -in forward step, $U=28.33$ m/s skin-friction distribution.

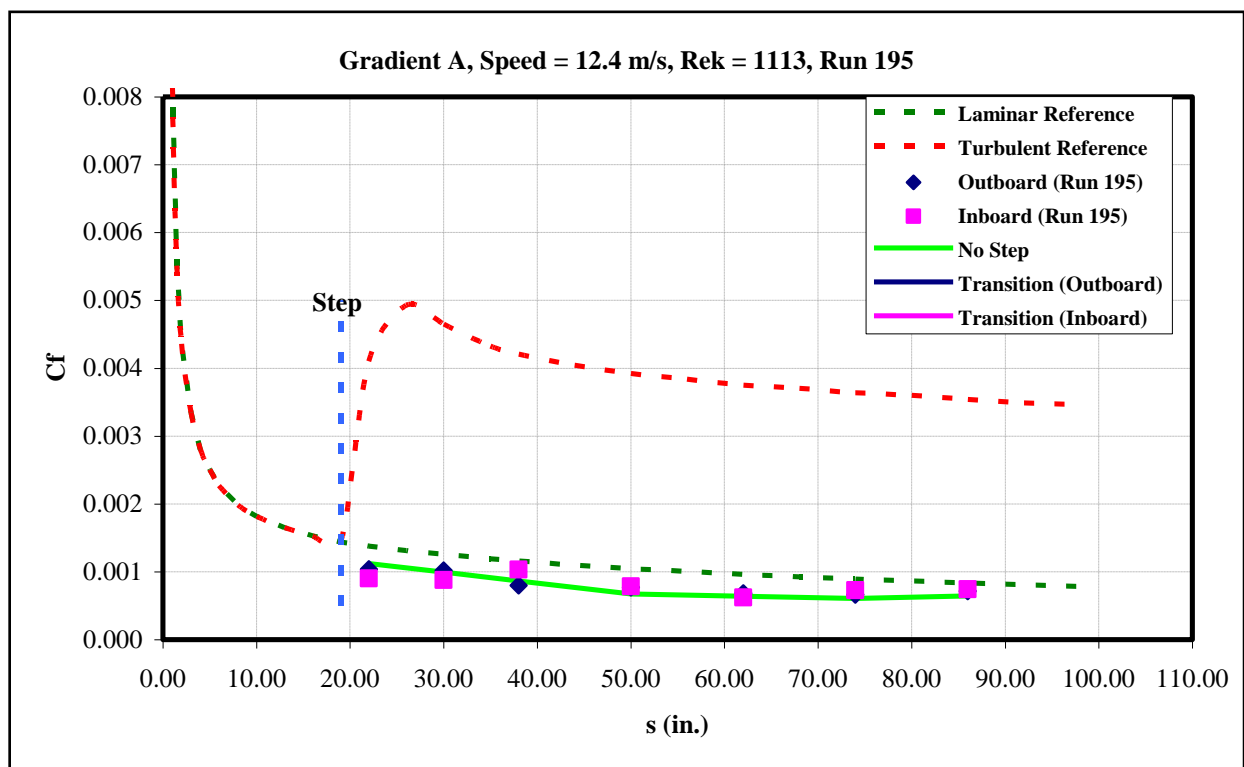


Figure 207: Gradient-A, $k=0.065$ -in forward step, $U=12.4$ m/s skin-friction distribution.

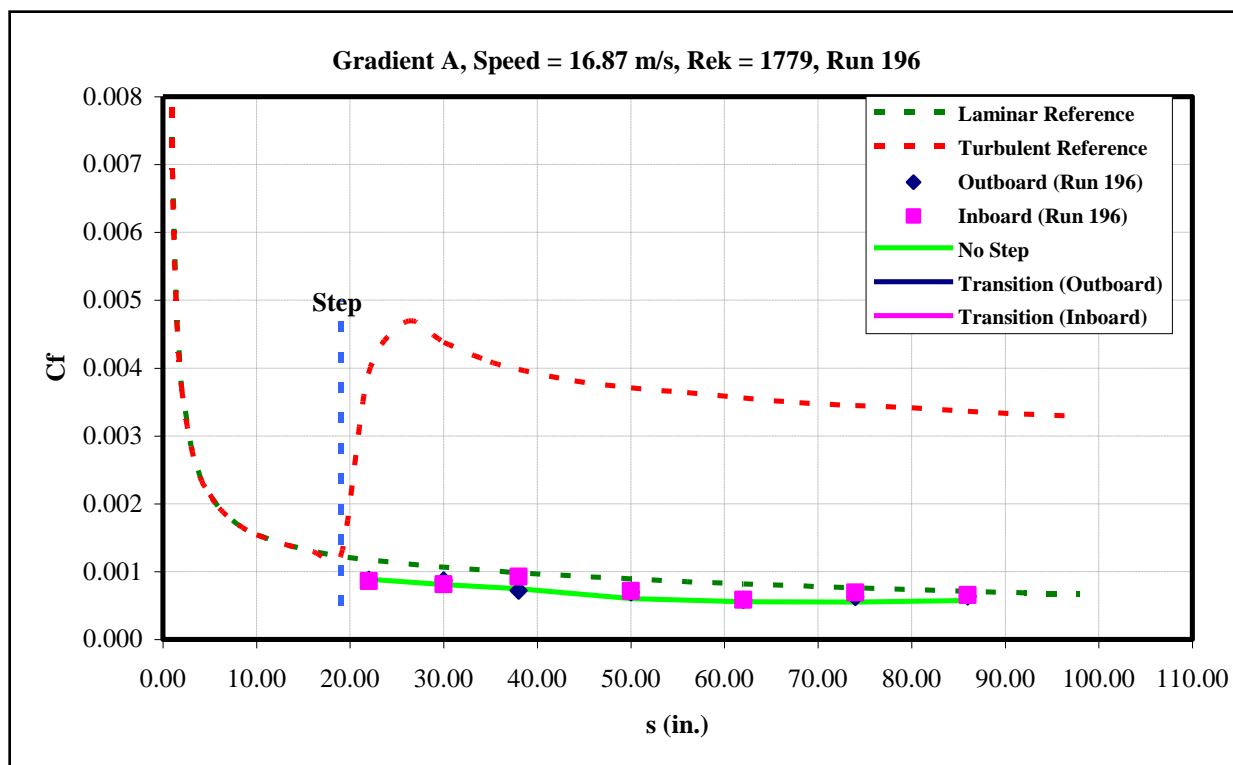


Figure 208: Gradient-A, $k=0.065$ -in forward step, $U=16.87$ m/s skin-friction distribution.

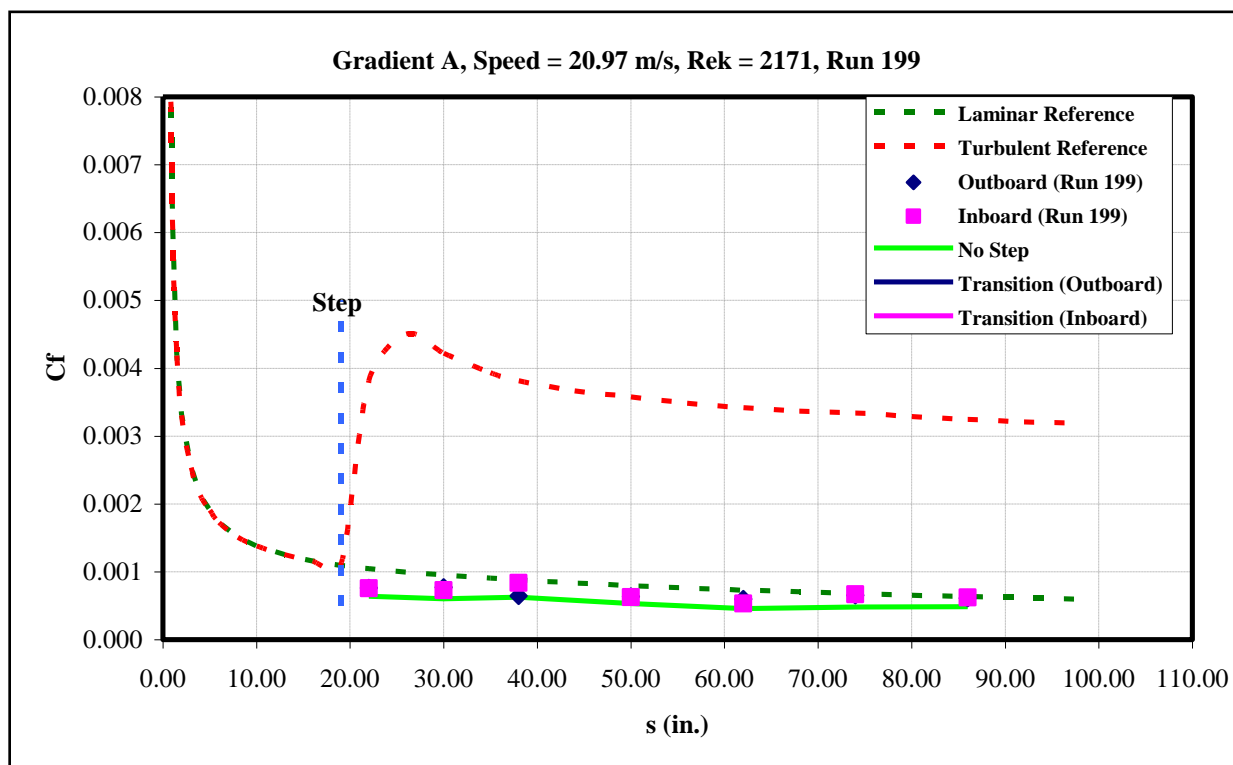


Figure 209: Gradient-A, $k=0.065$ -in forward step, $U=20.97$ m/s skin-friction distribution.

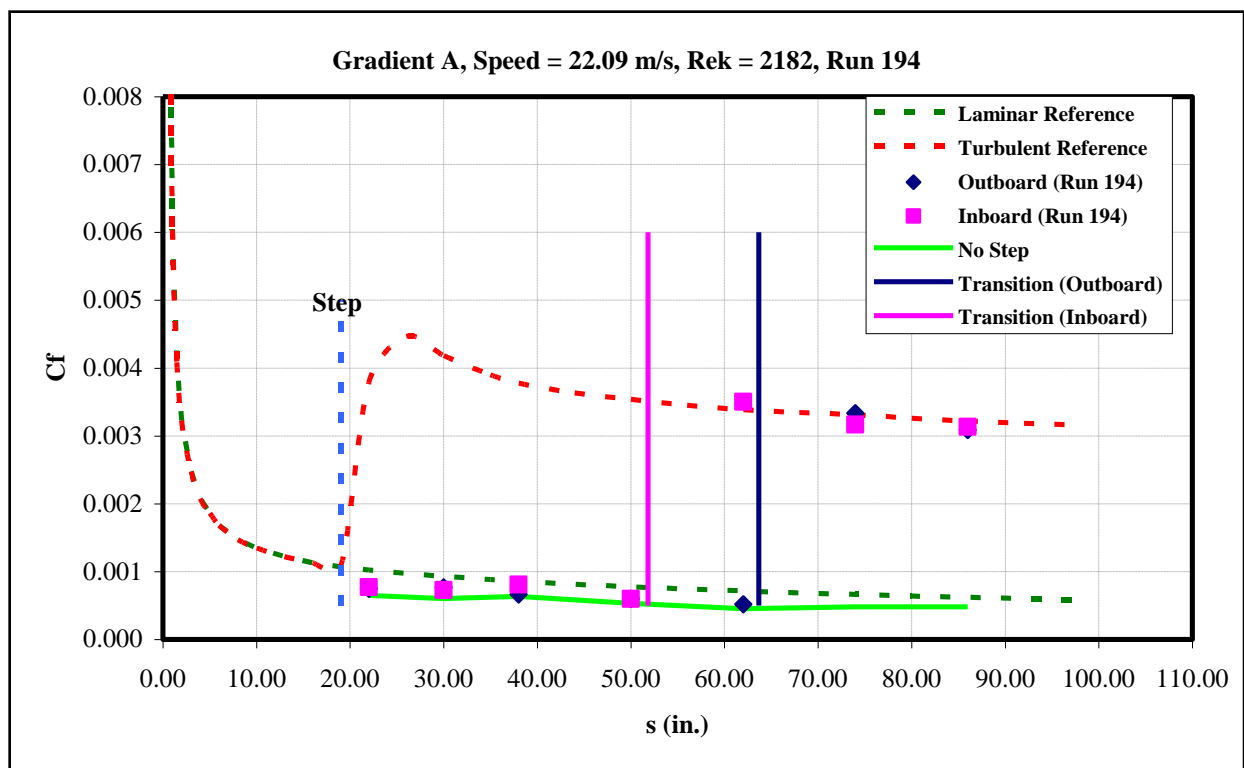


Figure 210: Gradient-A, $k=0.065$ -in forward step, $U=22.09$ m/s skin-friction distribution.

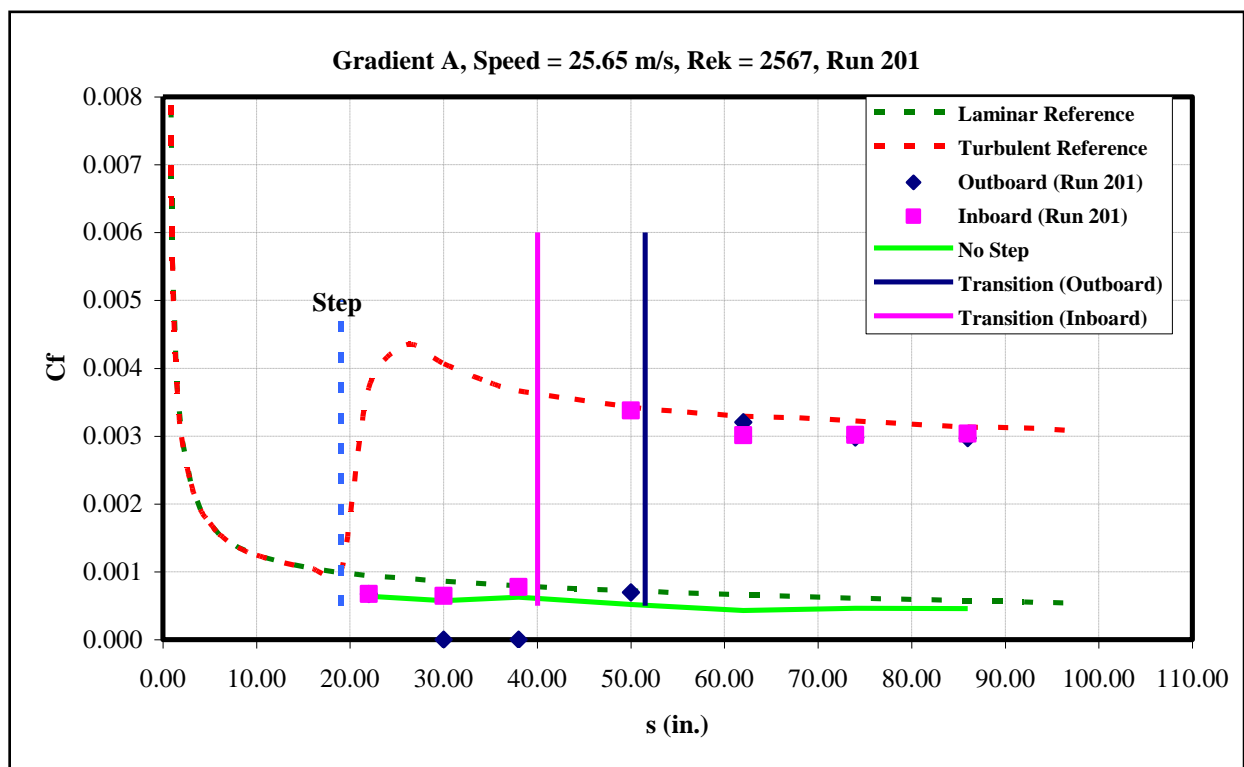


Figure 211: Gradient-A, $k=0.065$ -in forward step, $U=25.65$ m/s skin-friction distribution.

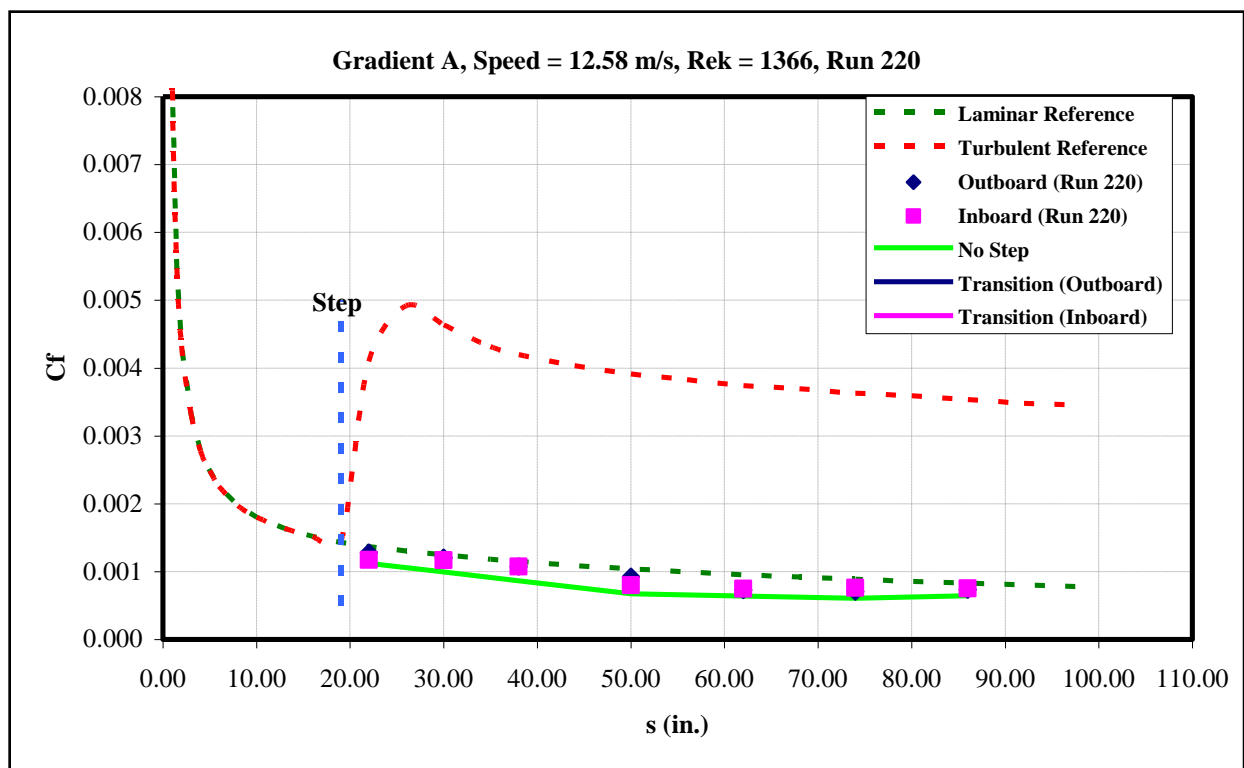


Figure 212: Gradient-A, k=0.068-in forward step, U=12.58 m/s skin-friction distribution.

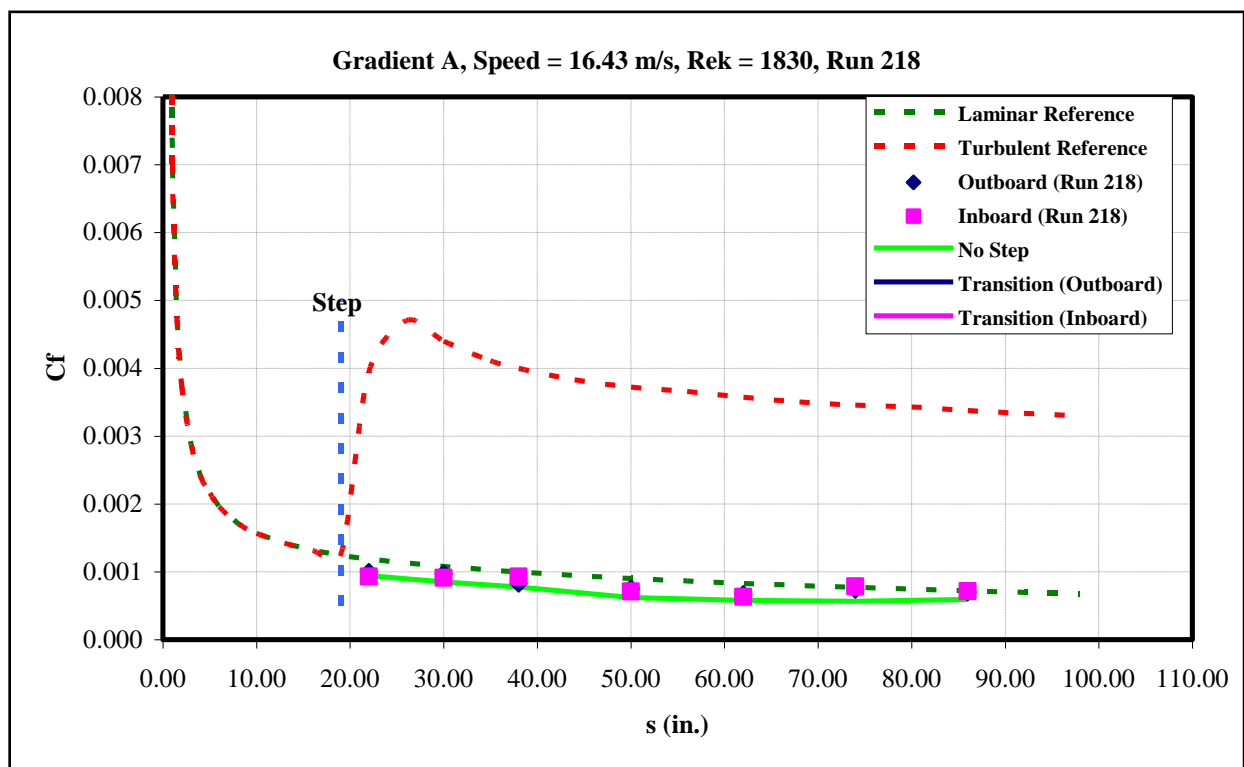


Figure 213: Gradient-A, k=0.068-in forward step, U=16.43 m/s skin-friction distribution.

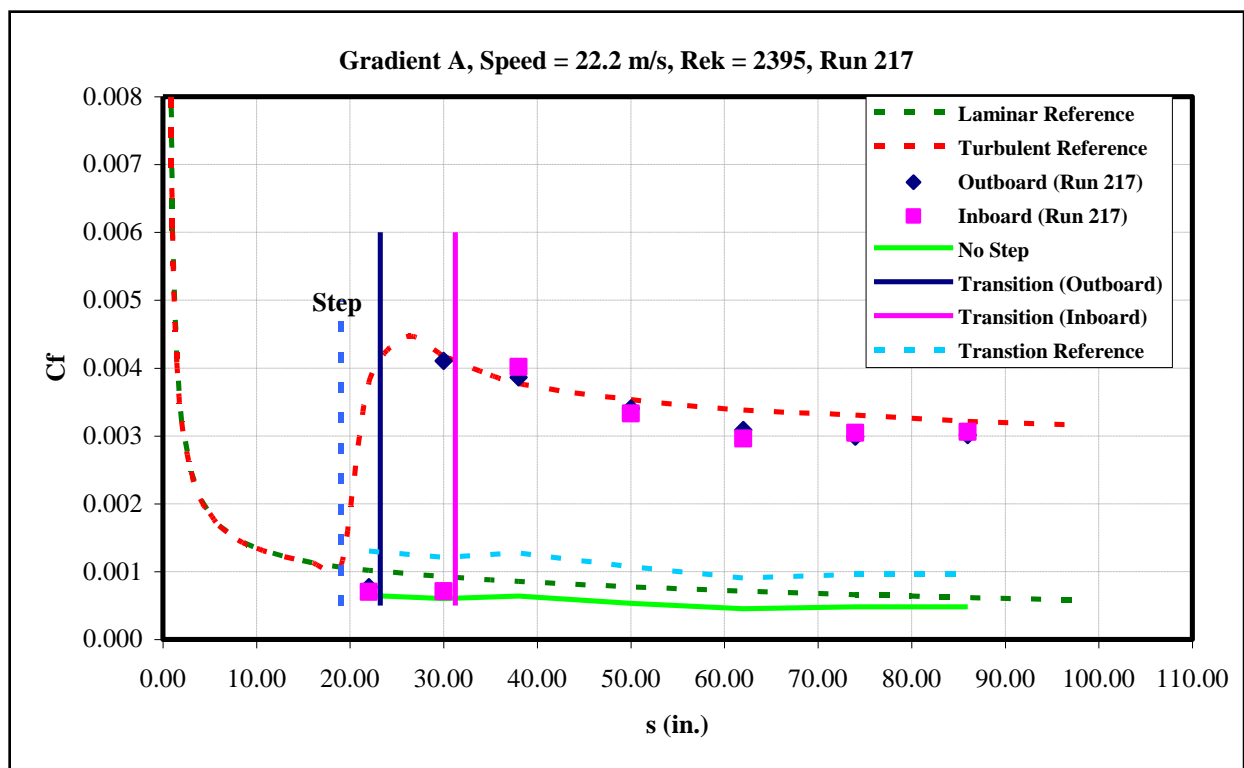


Figure 214: Gradient-A, $k=0.068$ -in forward step, $U=22.2$ m/s skin-friction distribution.

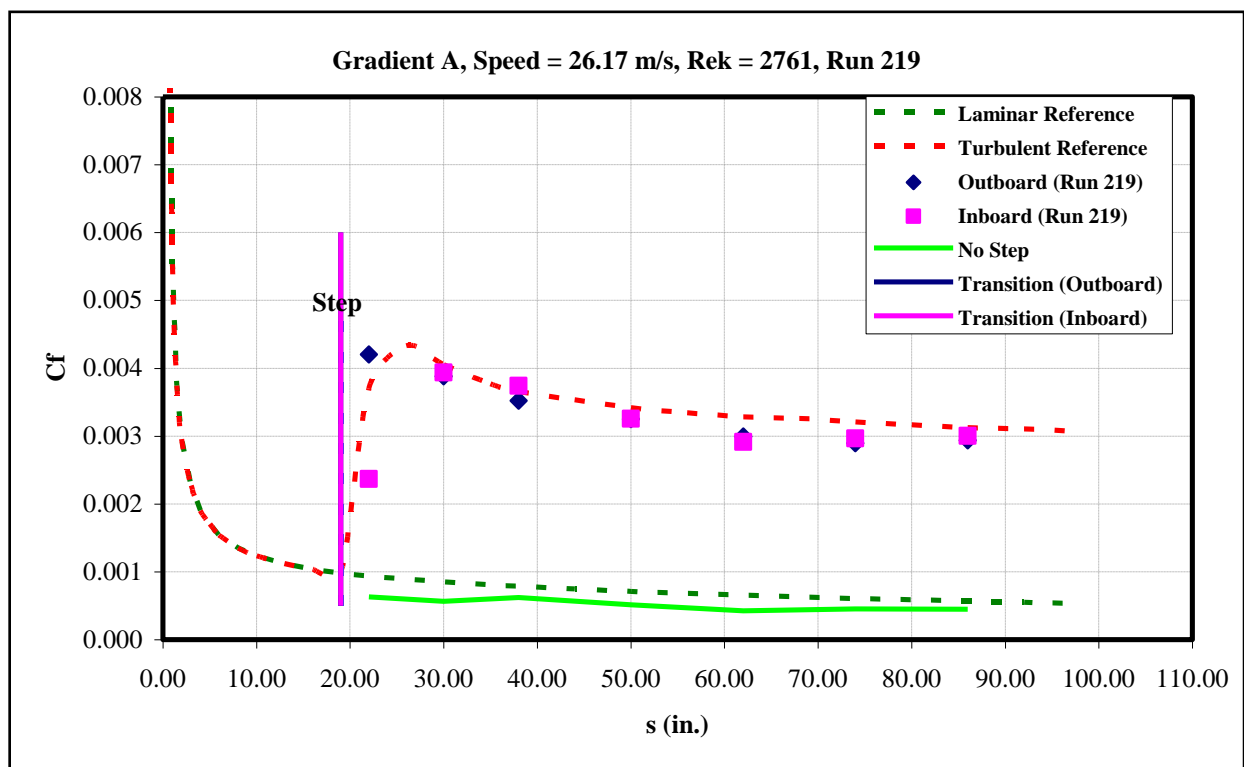


Figure 215: Gradient-A, $k=0.068$ -in forward step, $U=26.17$ m/s skin-friction distribution.

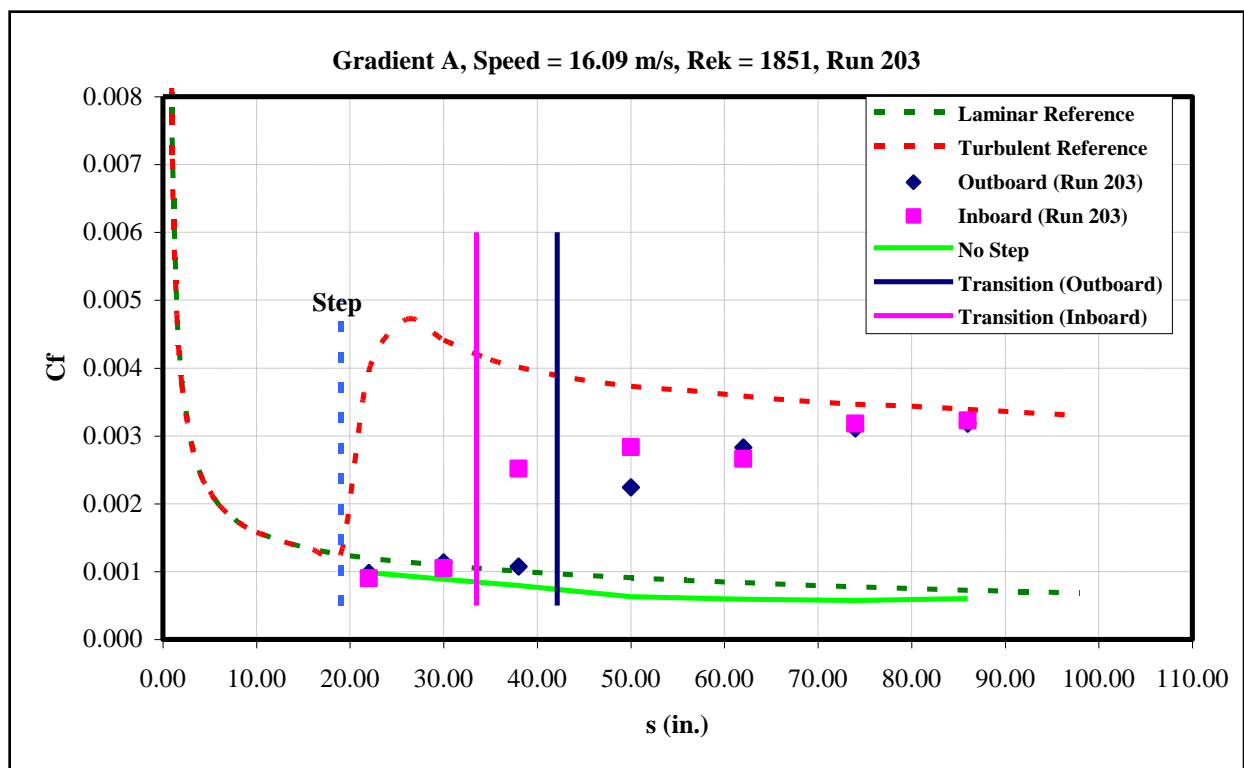


Figure 216: Gradient-A, $k=0.07$ -in forward step, $U=16.09$ m/s skin-friction distribution.

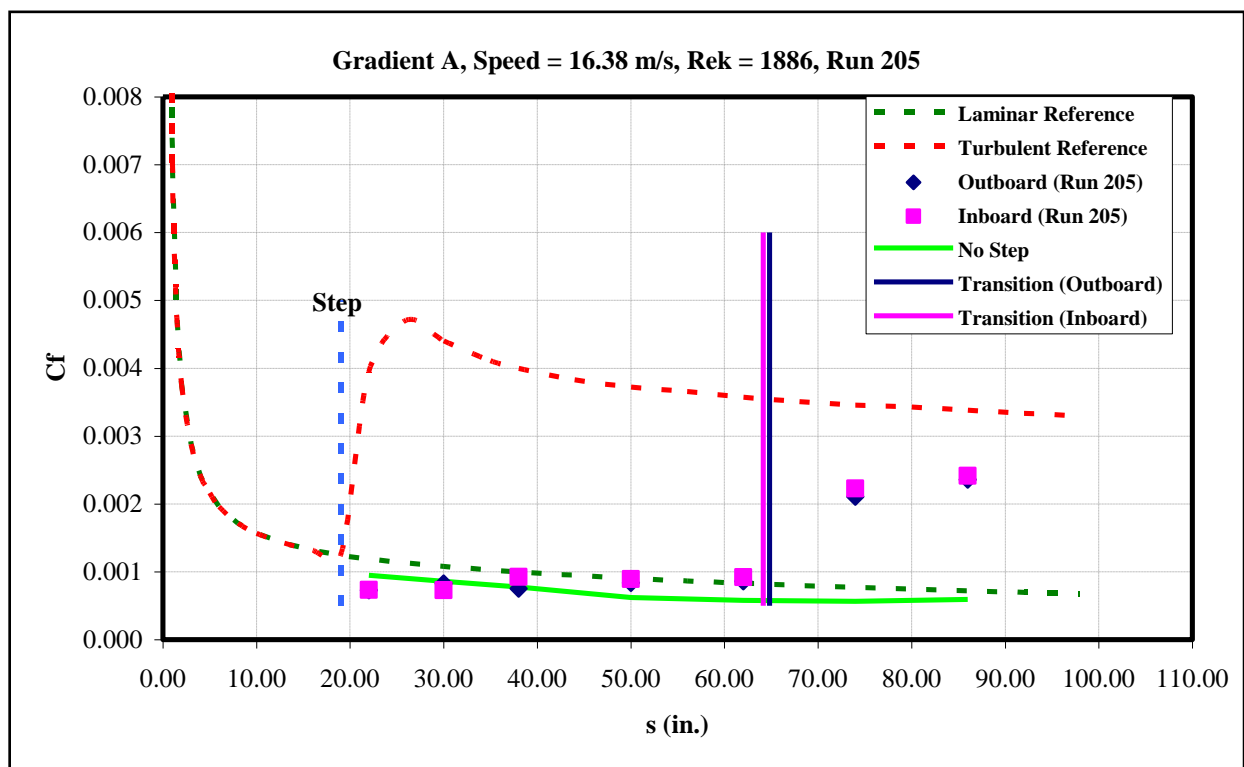


Figure 217: Gradient-A, $k=0.07$ -in forward step, $U=16.38$ m/s skin-friction distribution.

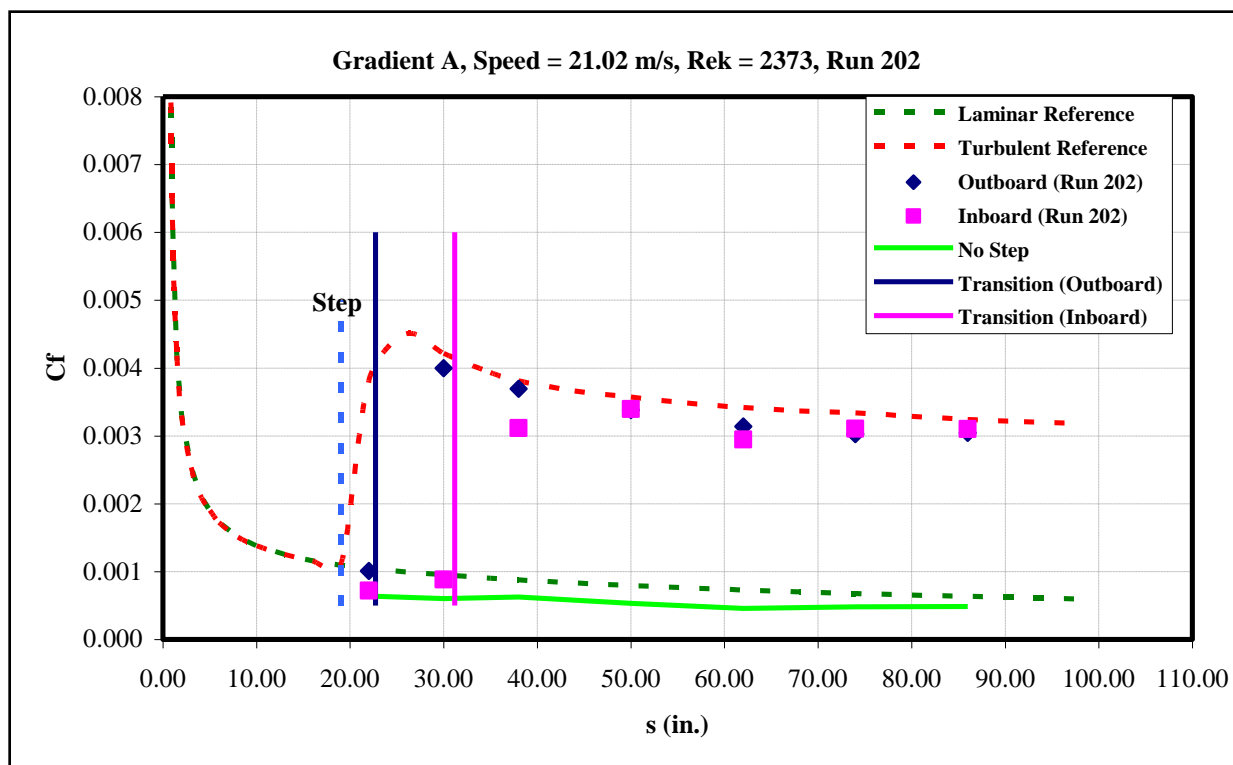


Figure 218: Gradient-A, $k=0.07$ -in forward step, $U=21.02$ m/s skin-friction distribution.

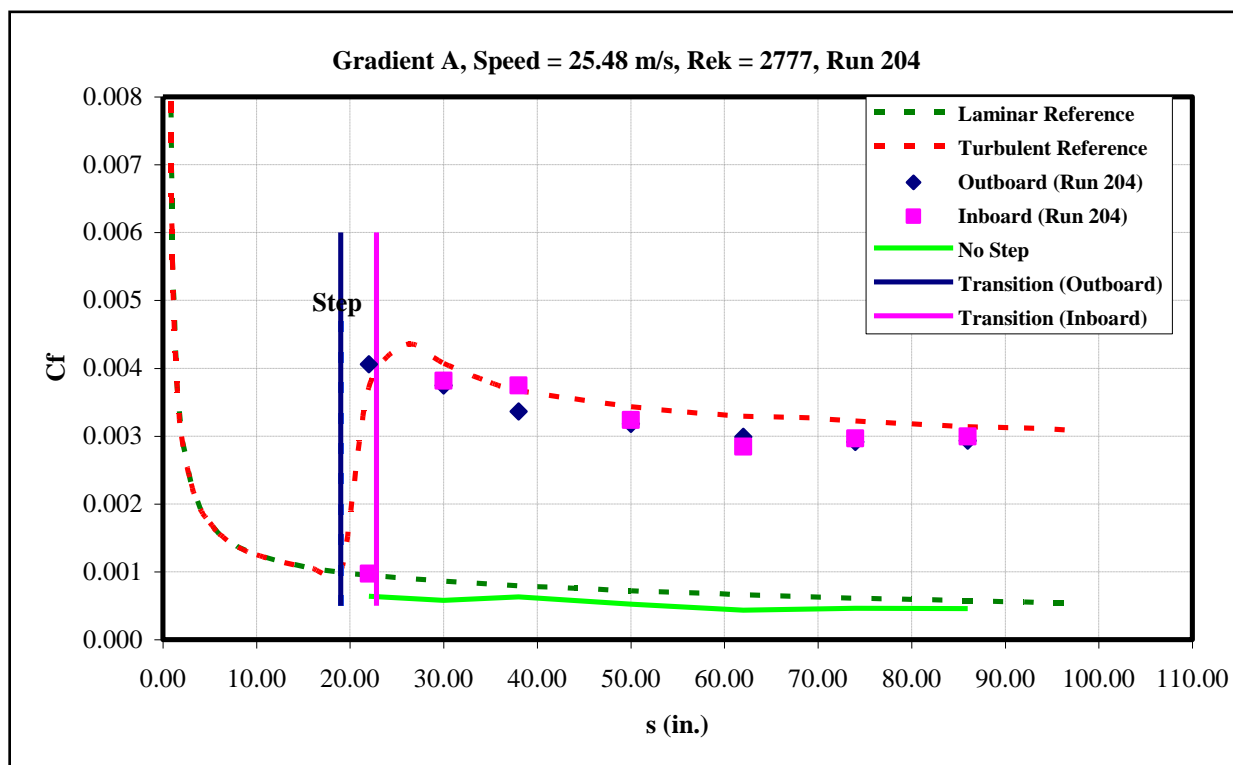


Figure 219: Gradient-A, $k=0.07$ -in forward step, $U=25.48$ m/s skin-friction distribution.

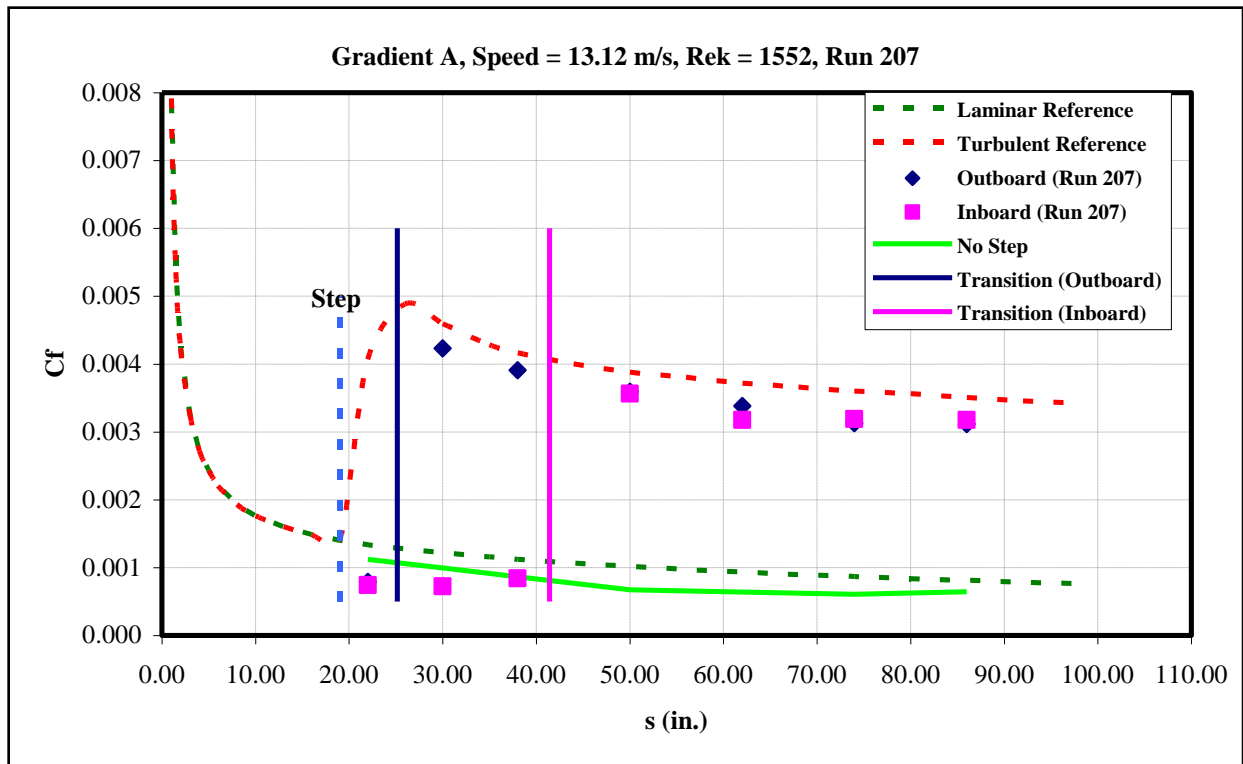


Figure 220: Gradient-A, $k=0.073$ -in forward step, $U=13.12$ m/s skin-friction distribution.

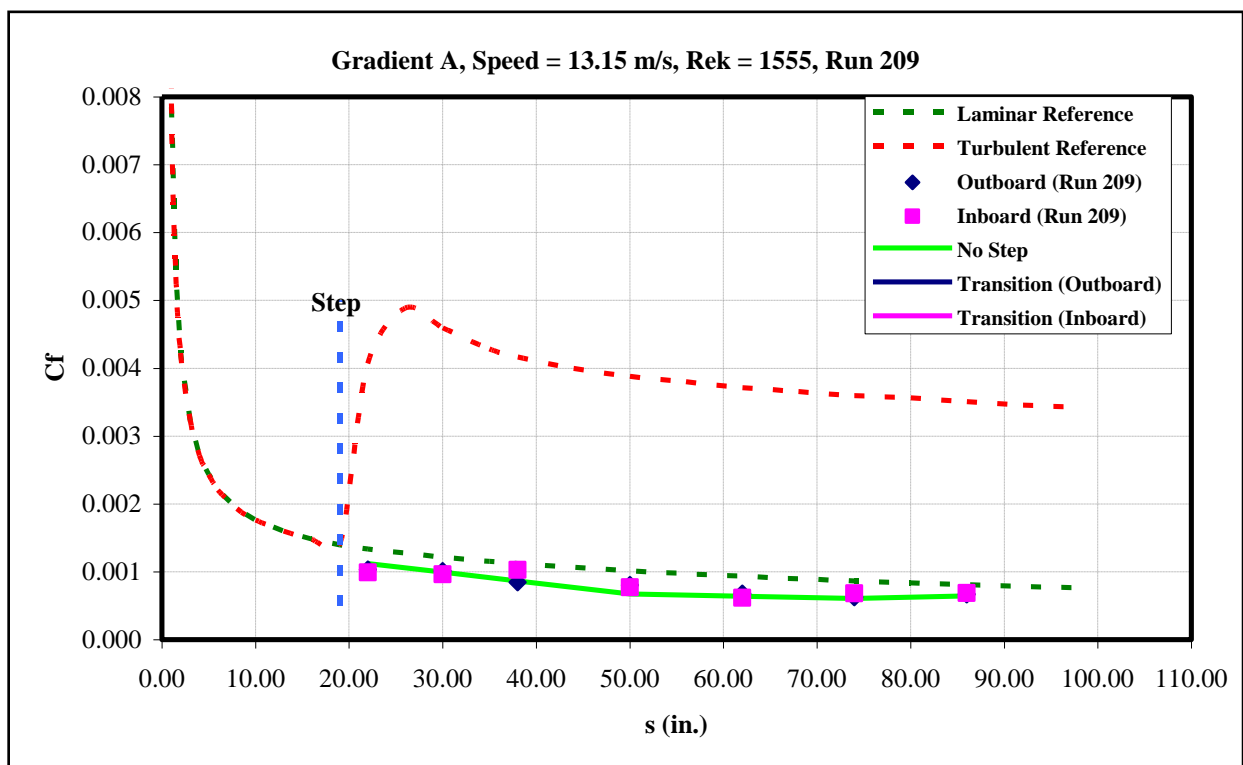


Figure 221: Gradient-A, $k=0.073$ -in forward step, $U=13.15$ m/s skin-friction distribution.

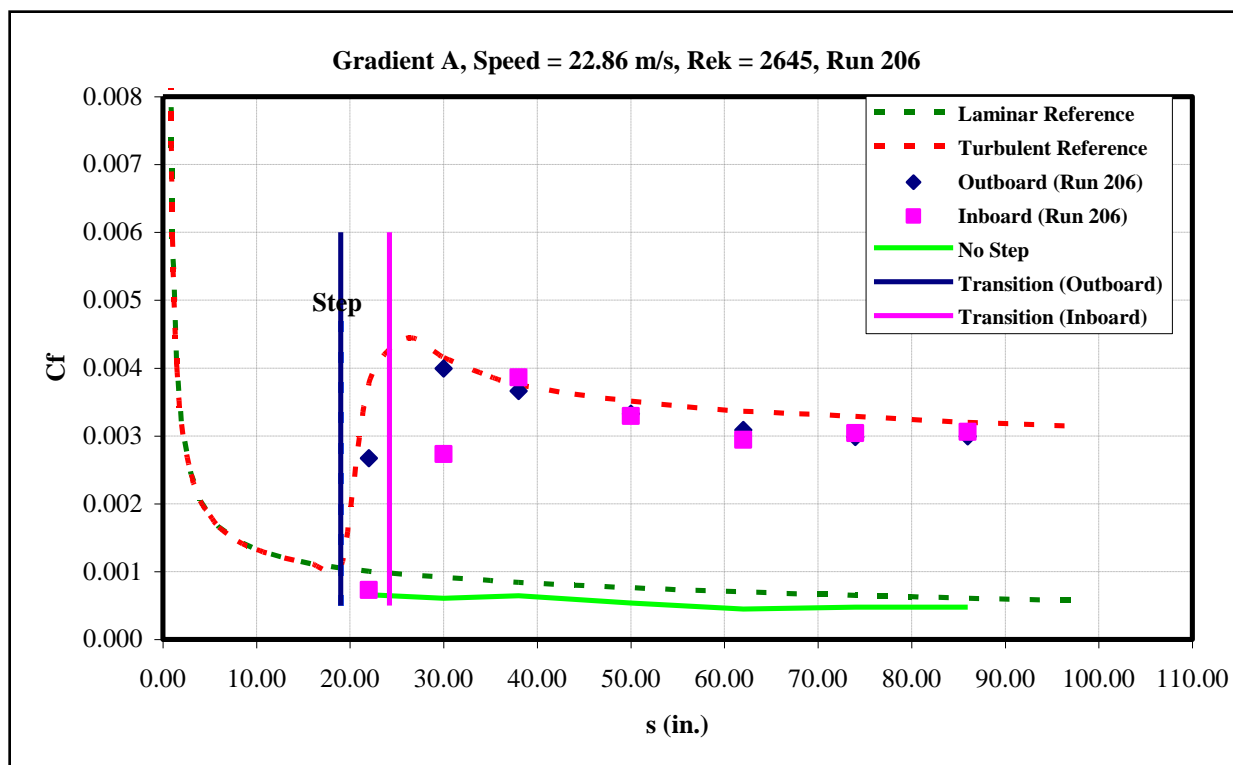


Figure 222: Gradient-A, $k=0.073$ -in forward step, $U=22.86$ m/s skin-friction distribution.

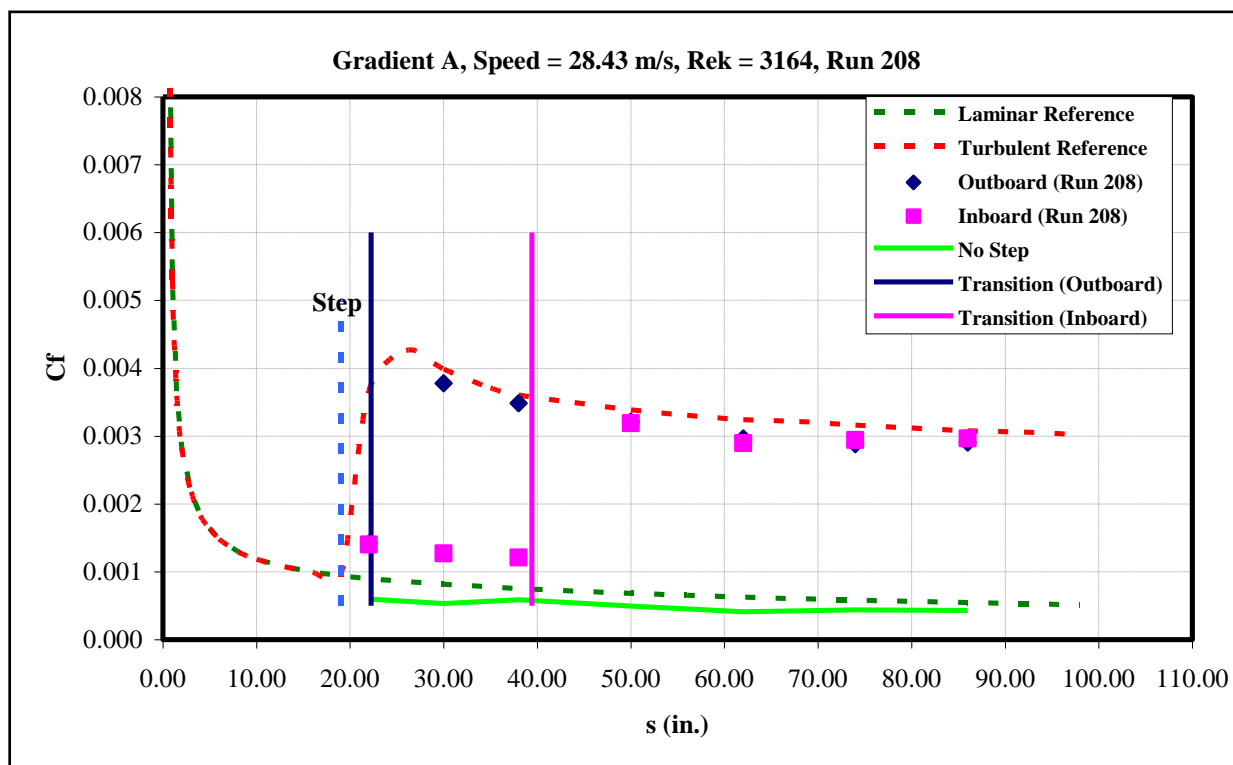


Figure 223: Gradient-A, $k=0.073$ -in forward step, $U=28.43$ m/s skin-friction distribution.

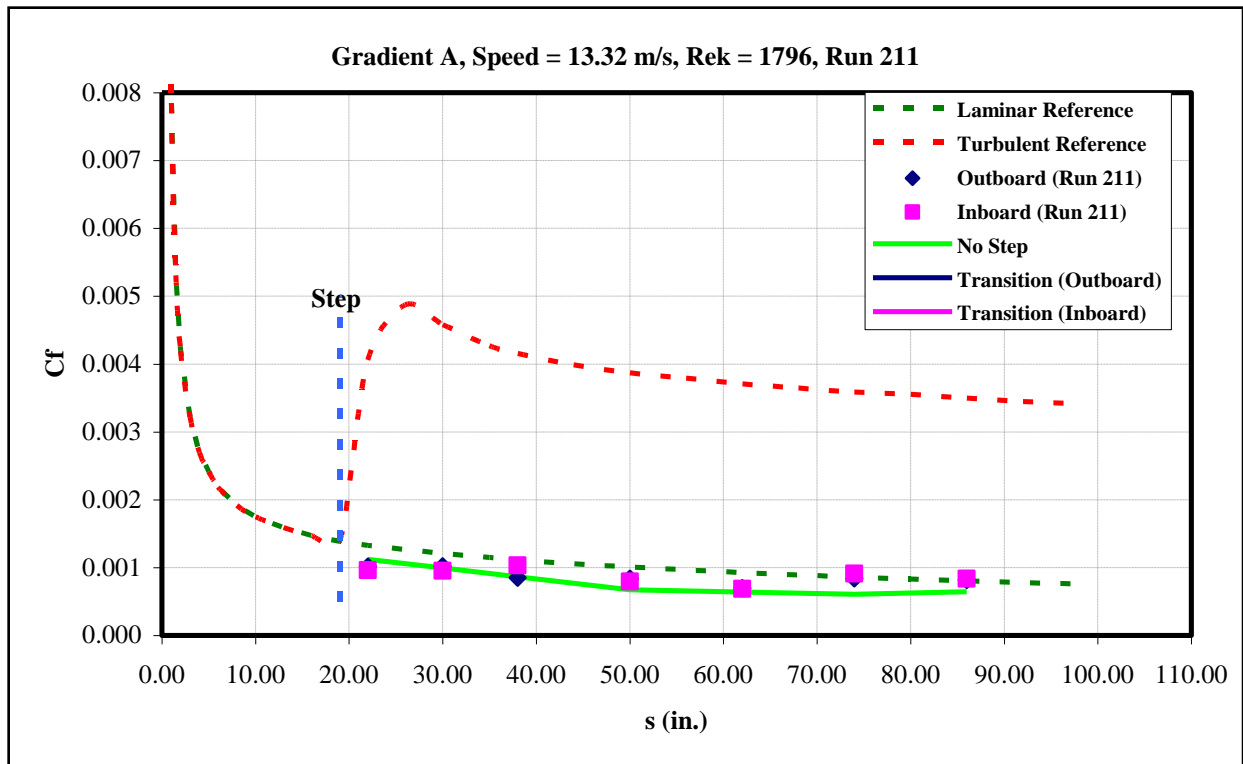


Figure 224: Gradient-A, $k=0.08$ -in forward step, $U=13.32$ m/s skin-friction distribution.

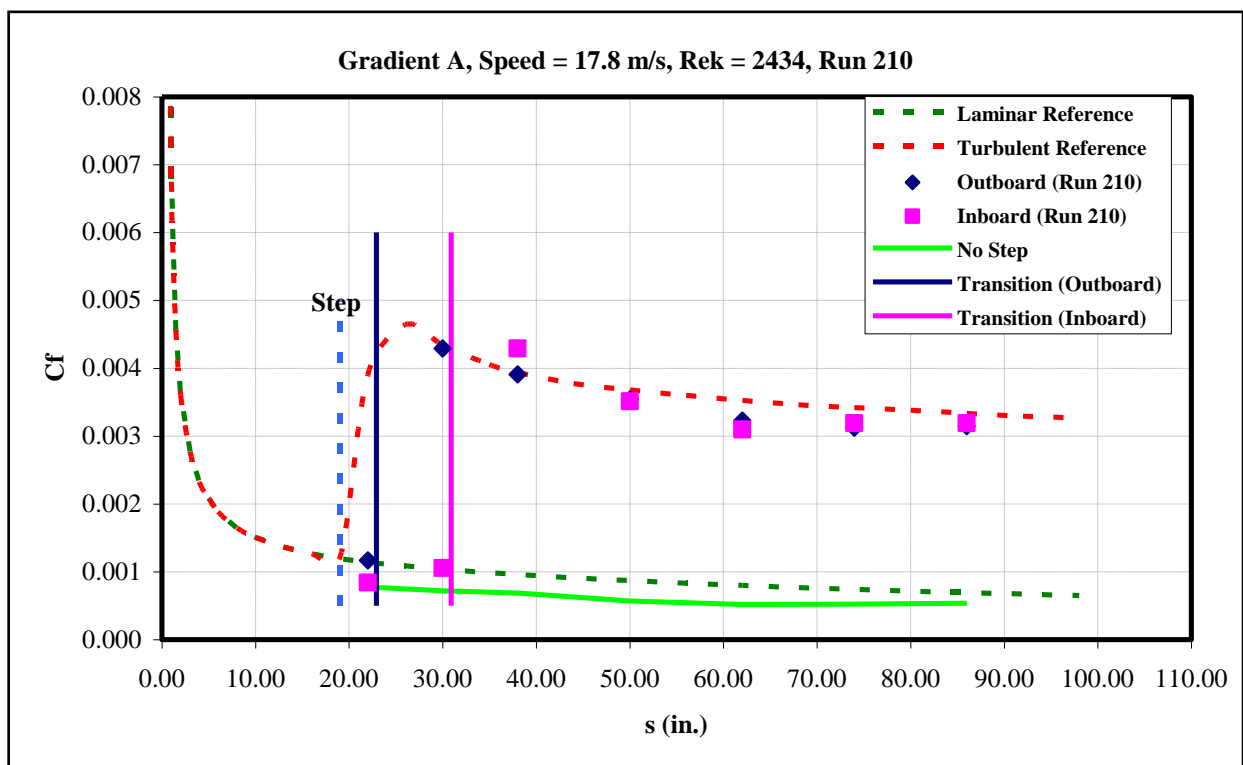


Figure 225: Gradient-A, $k=0.08$ -in forward step, $U=17.8$ m/s skin-friction distribution.

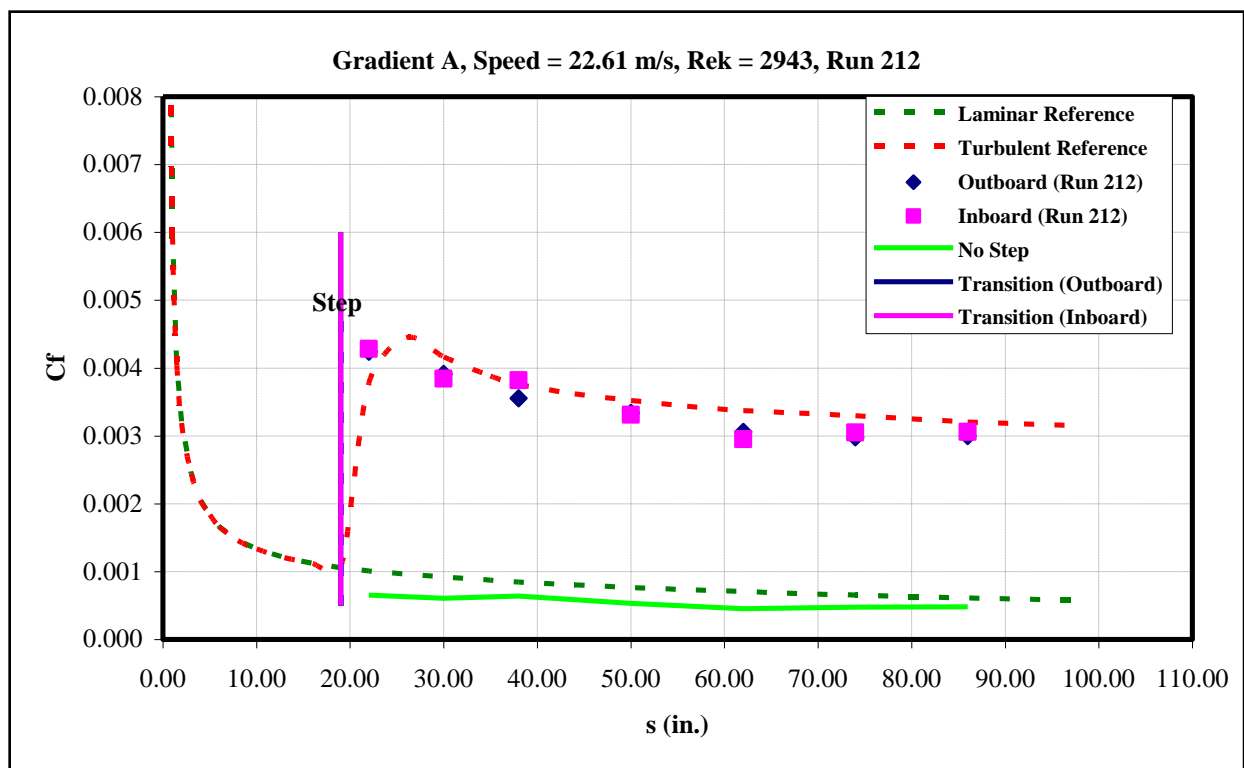


Figure 226: Gradient-A, $k=0.08$ -in forward step, $U=22.61$ m/s skin-friction distribution.

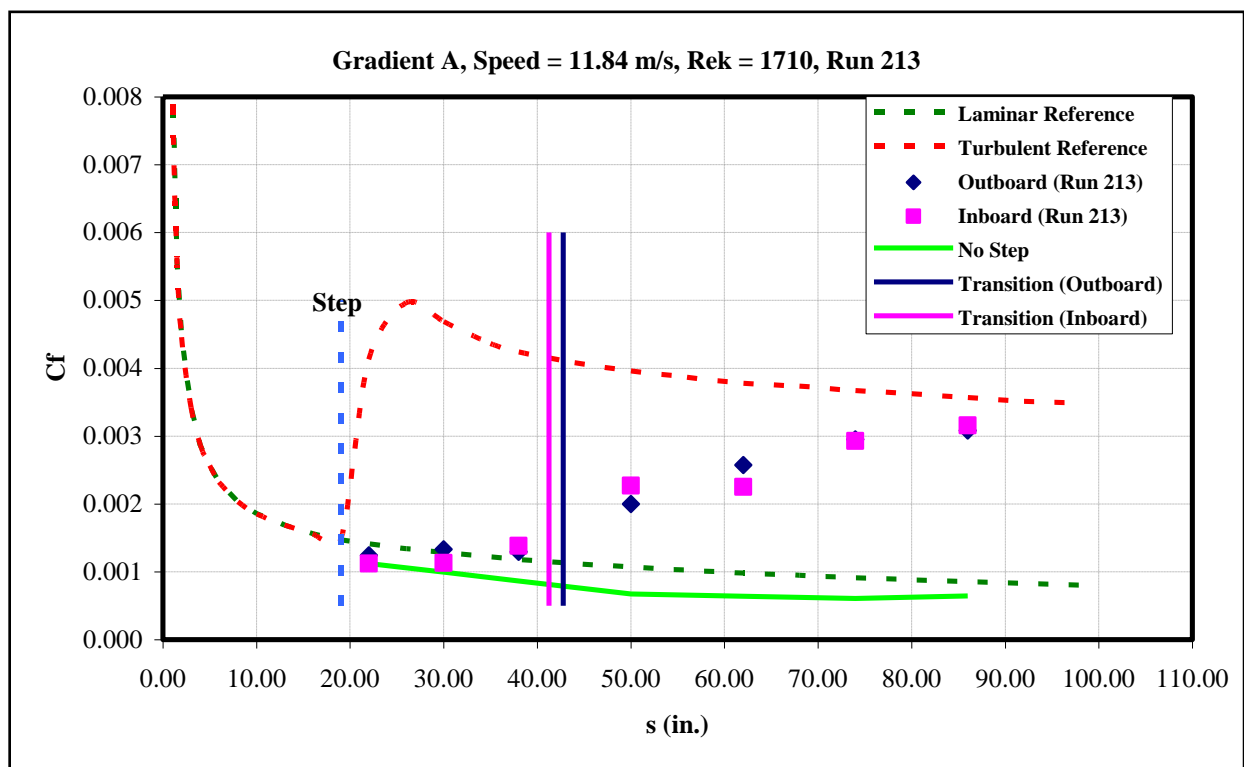


Figure 227: Gradient-A, $k=0.085$ -in forward step, $U=11.84$ m/s skin-friction distribution.

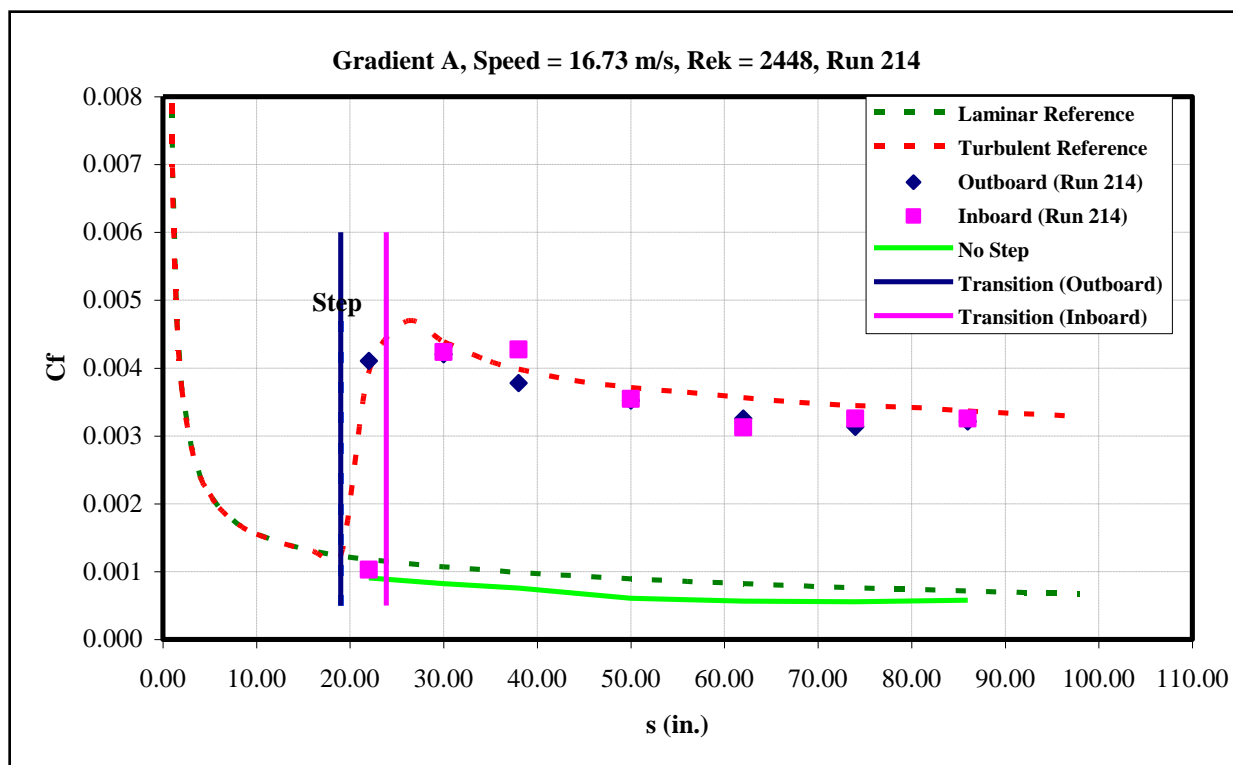


Figure 228: Gradient-A, $k=0.085$ -in forward step, $U=16.73$ m/s skin-friction distribution.

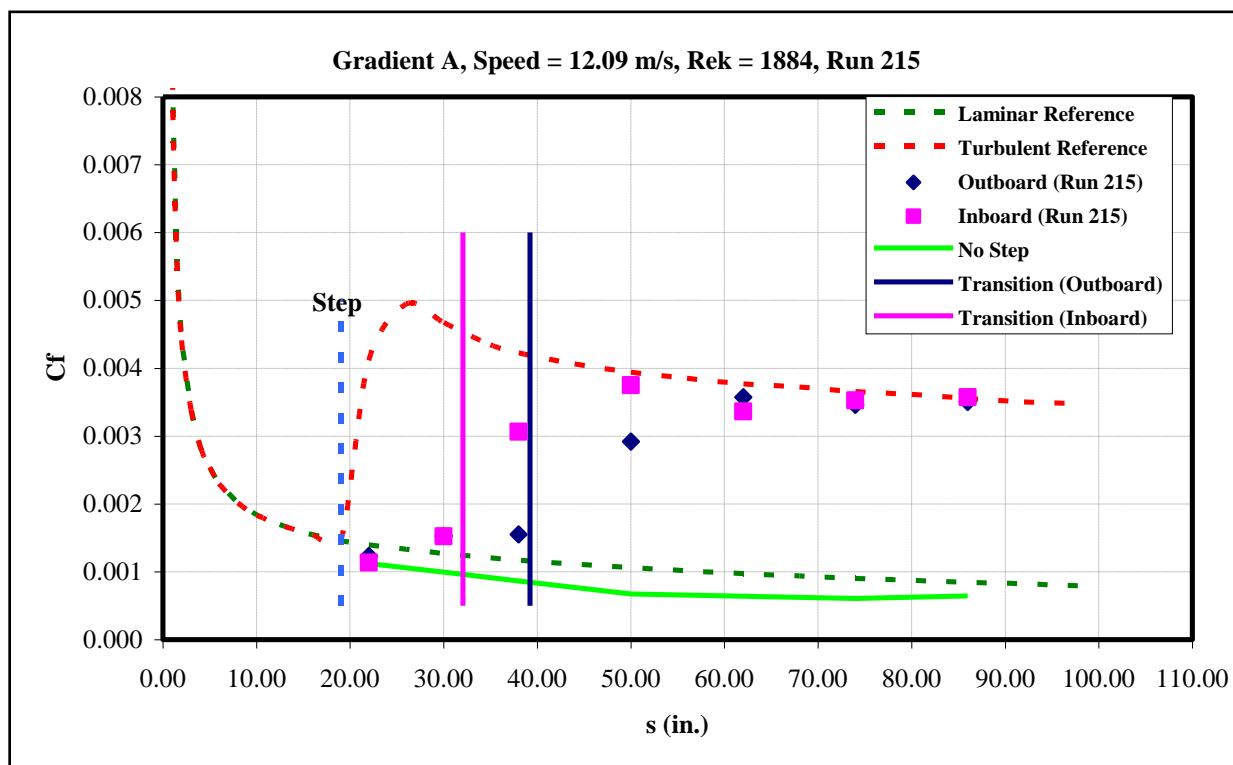


Figure 229: Gradient-A, $k=0.09$ -in forward step, $U=12.09$ m/s skin-friction distribution.

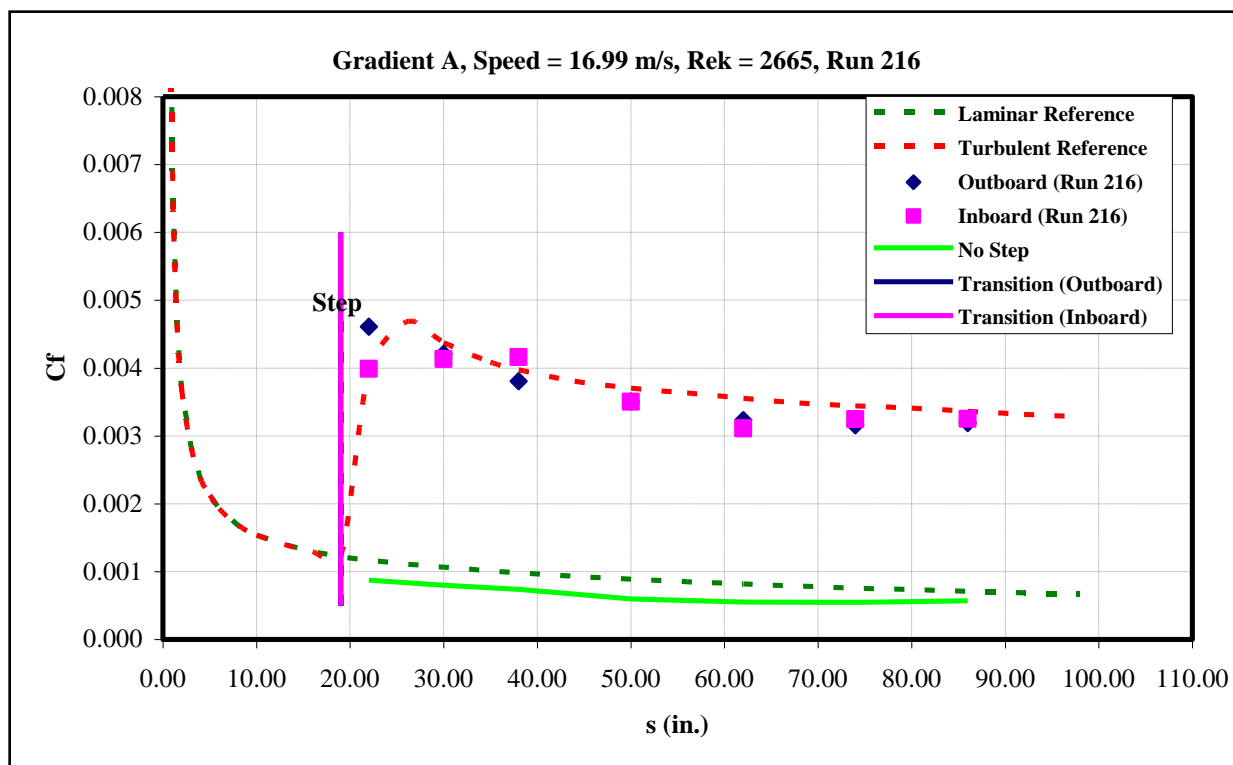


Figure 230: Gradient-A, $k=0.09$ -in forward step, $U=16.99$ m/s skin-friction distribution.

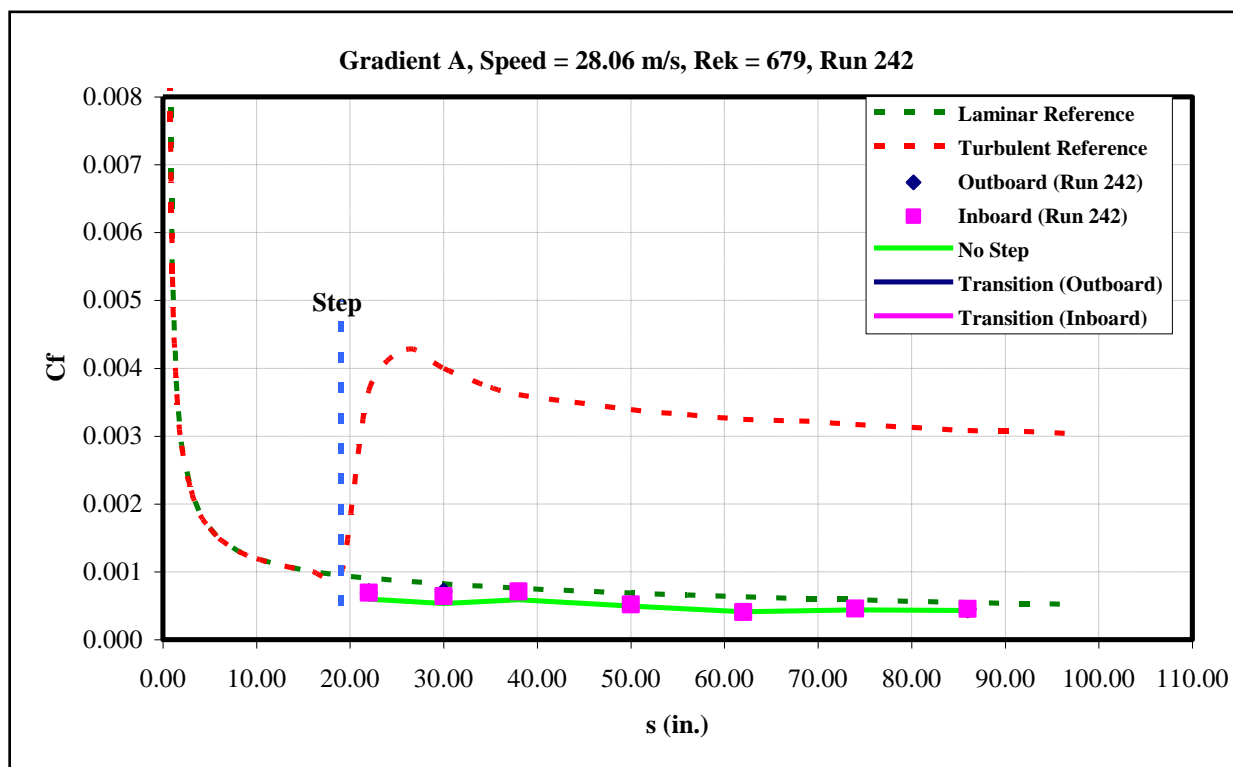


Figure 231: Gradient-A, $k=0.025$ -in aft step, $U=28.06$ m/s skin-friction distribution.

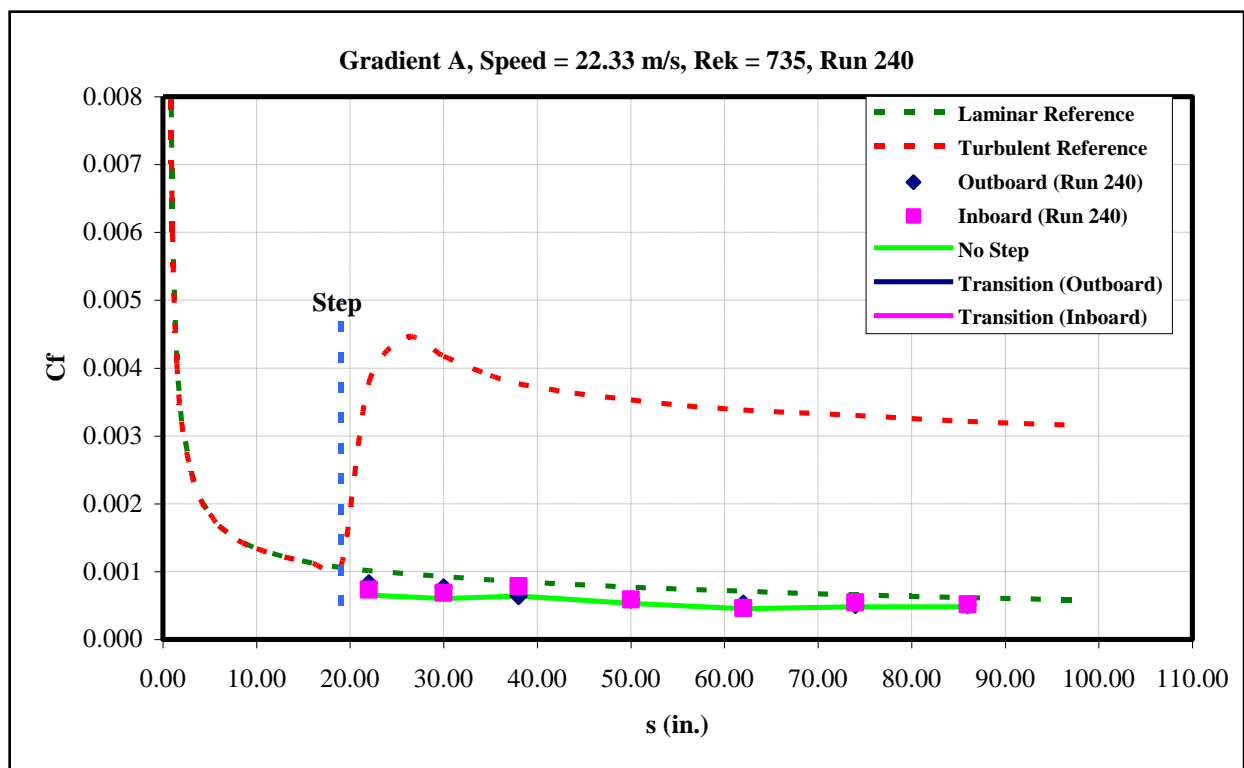


Figure 232: Gradient-A, $k=0.03$ -in aft step, $U=22.33$ m/s skin-friction distribution.

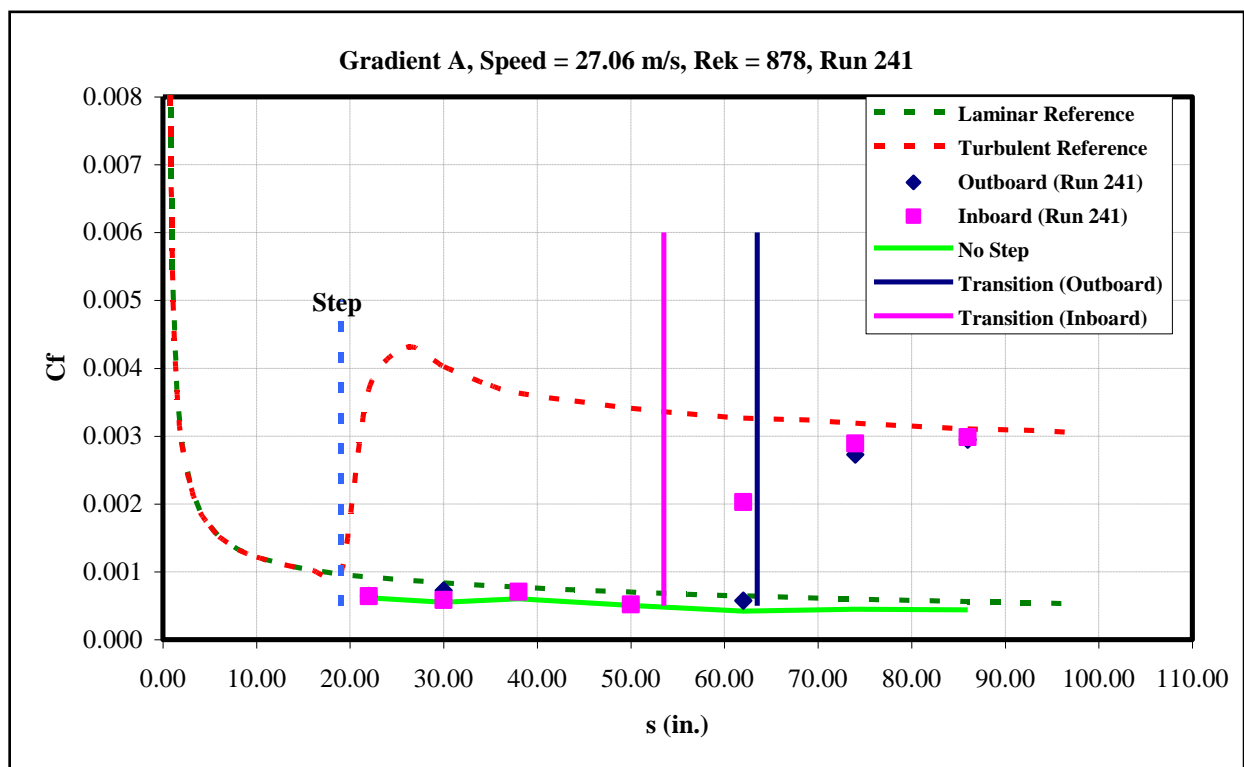


Figure 233: Gradient-A, $k=0.03$ -in aft step, $U=27.06$ m/s skin-friction distribution.

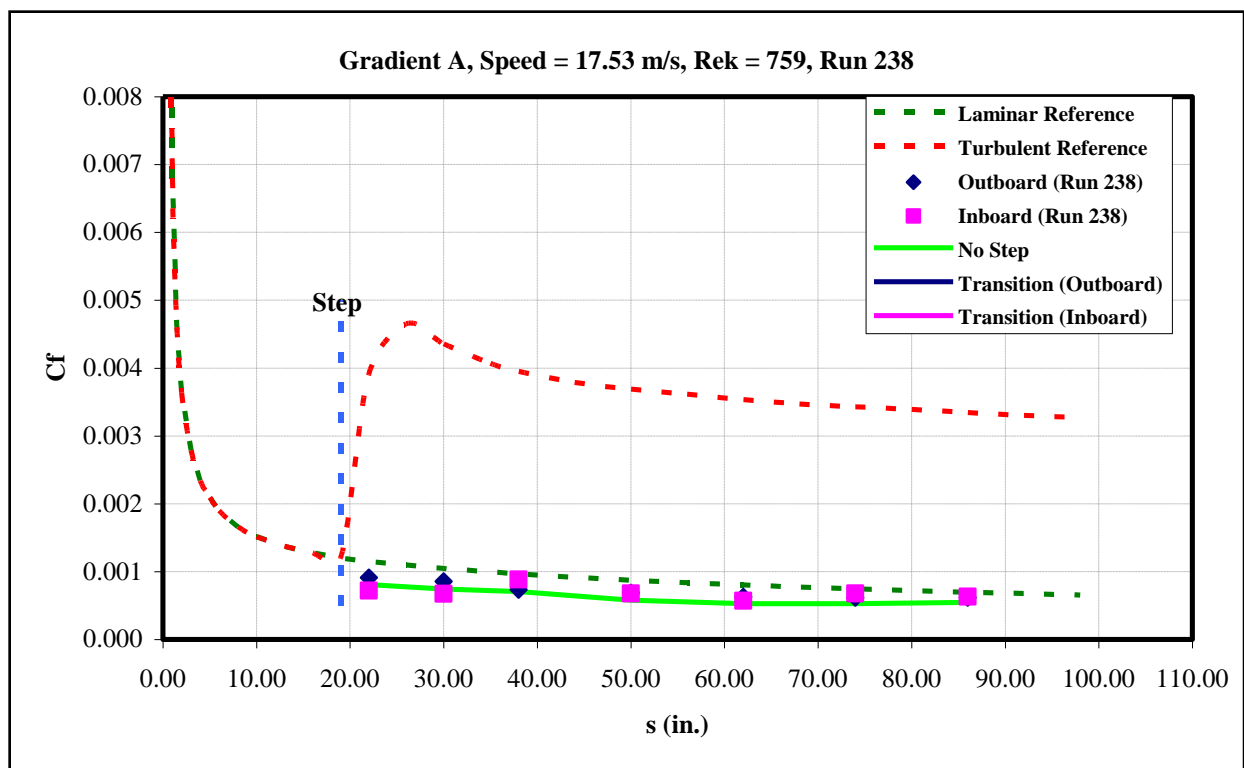


Figure 234: Gradient-A, $k=0.035$ -in aft step, $U=17.53$ m/s skin-friction distribution.

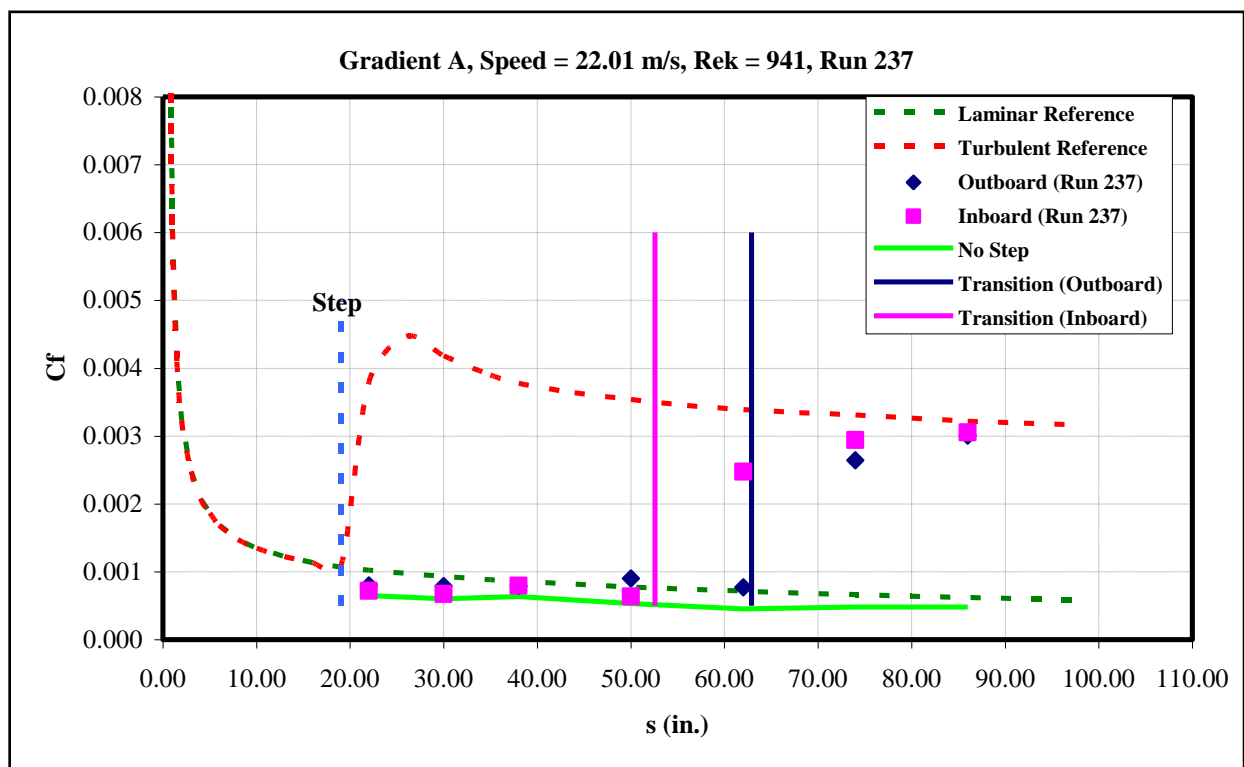


Figure 235: Gradient-A, $k=0.035$ -in aft step, $U=22.01$ m/s skin-friction distribution.

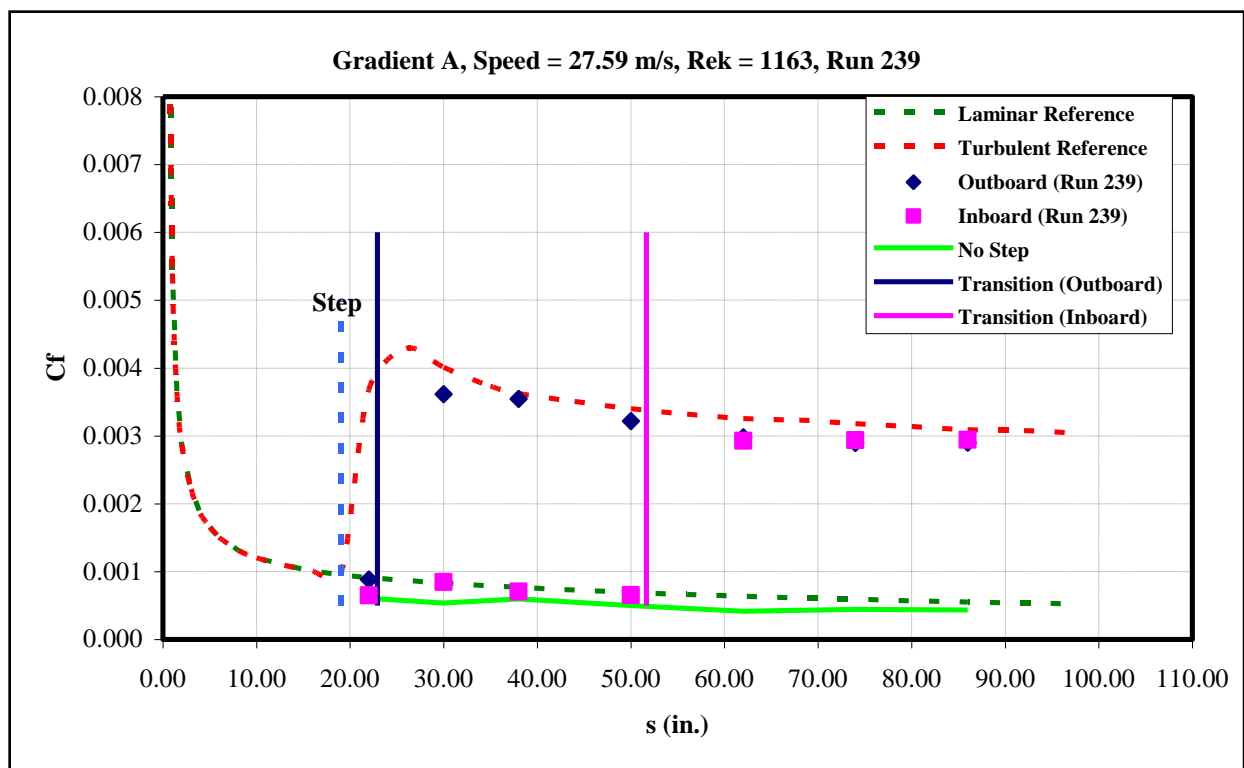


Figure 236: Gradient-A, $k=0.035$ -in aft step, $U=27.59$ m/s skin-friction distribution.

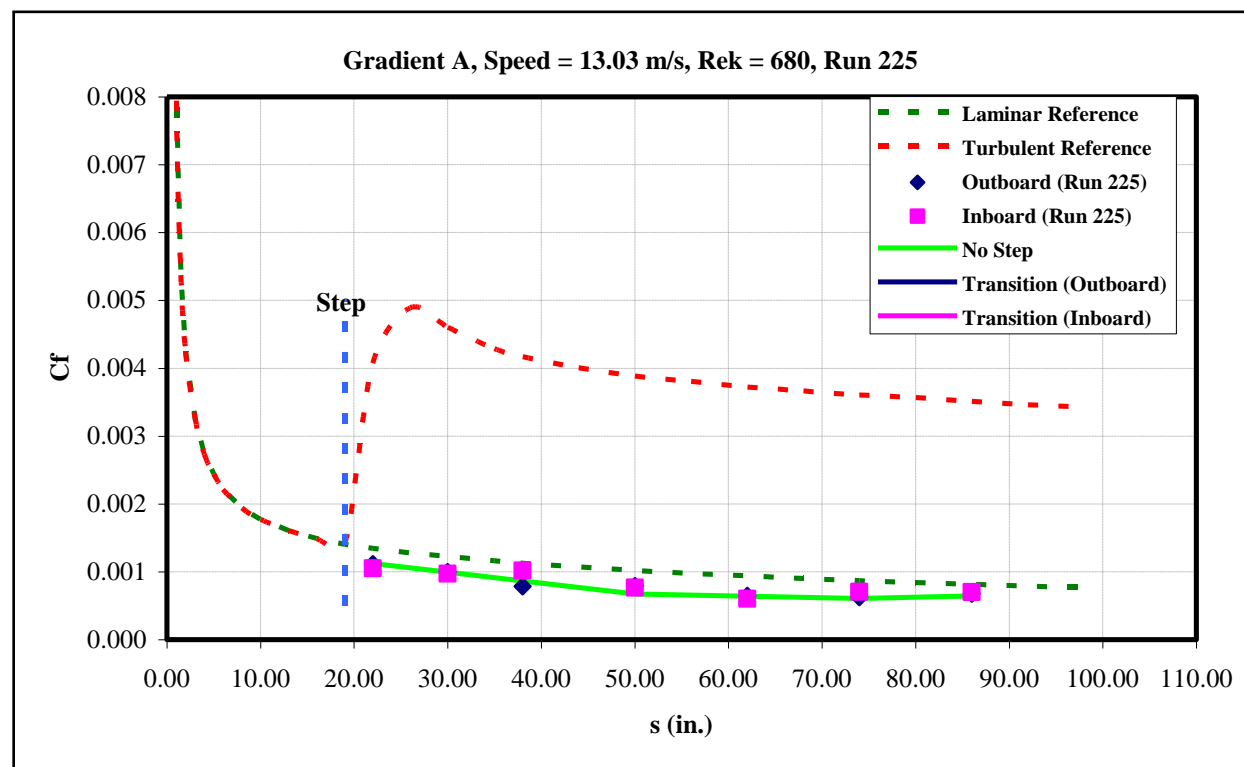


Figure 237: Gradient-A, $k=0.04$ -in aft step, $U=13.03$ m/s skin-friction distribution.

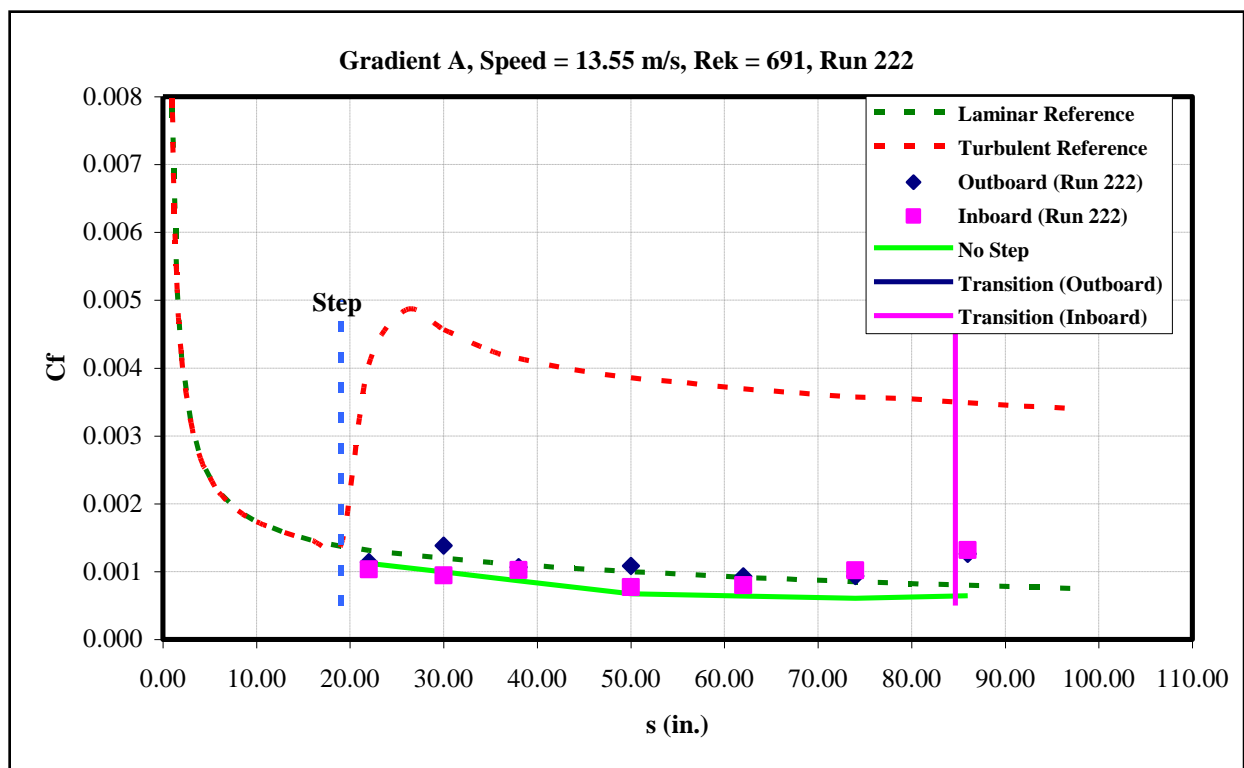


Figure 238: Gradient-A, $k=0.04$ -in aft step, $U=13.55$ m/s skin-friction distribution.

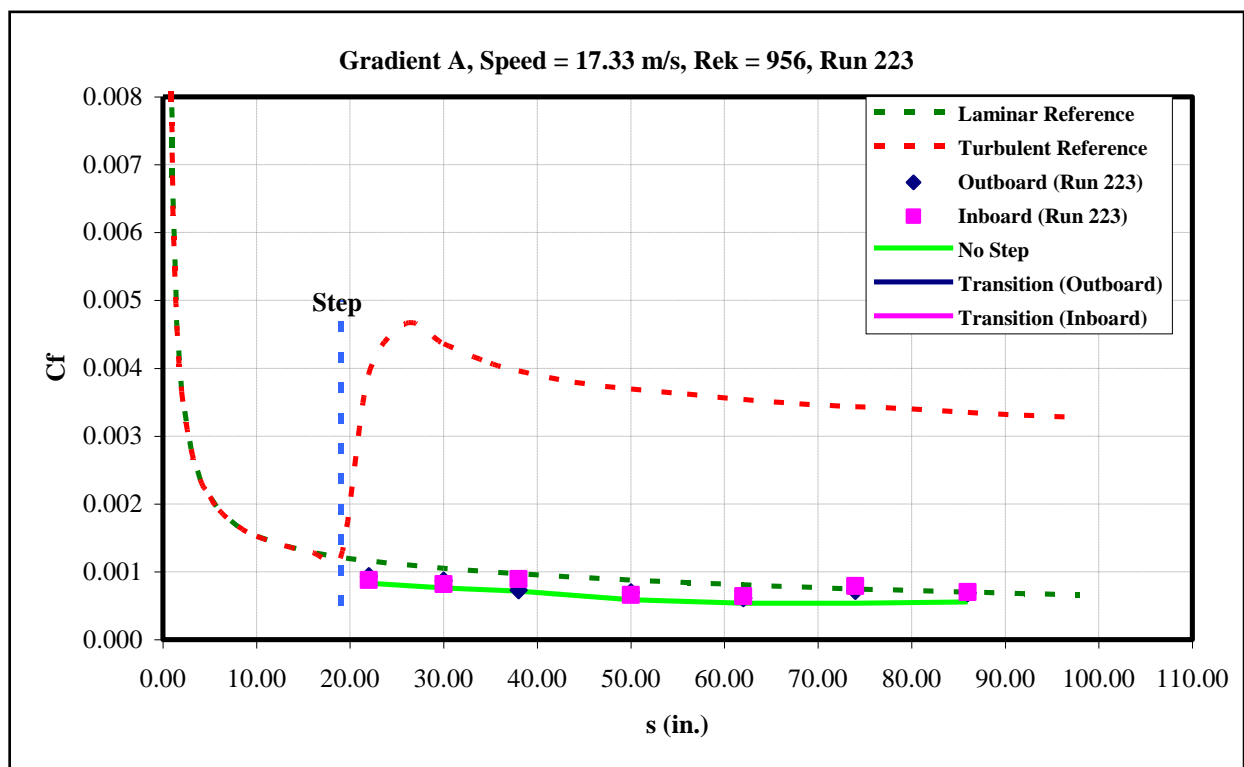


Figure 239: Gradient-A, $k=0.04$ -in aft step, $U=17.33$ m/s skin-friction distribution.

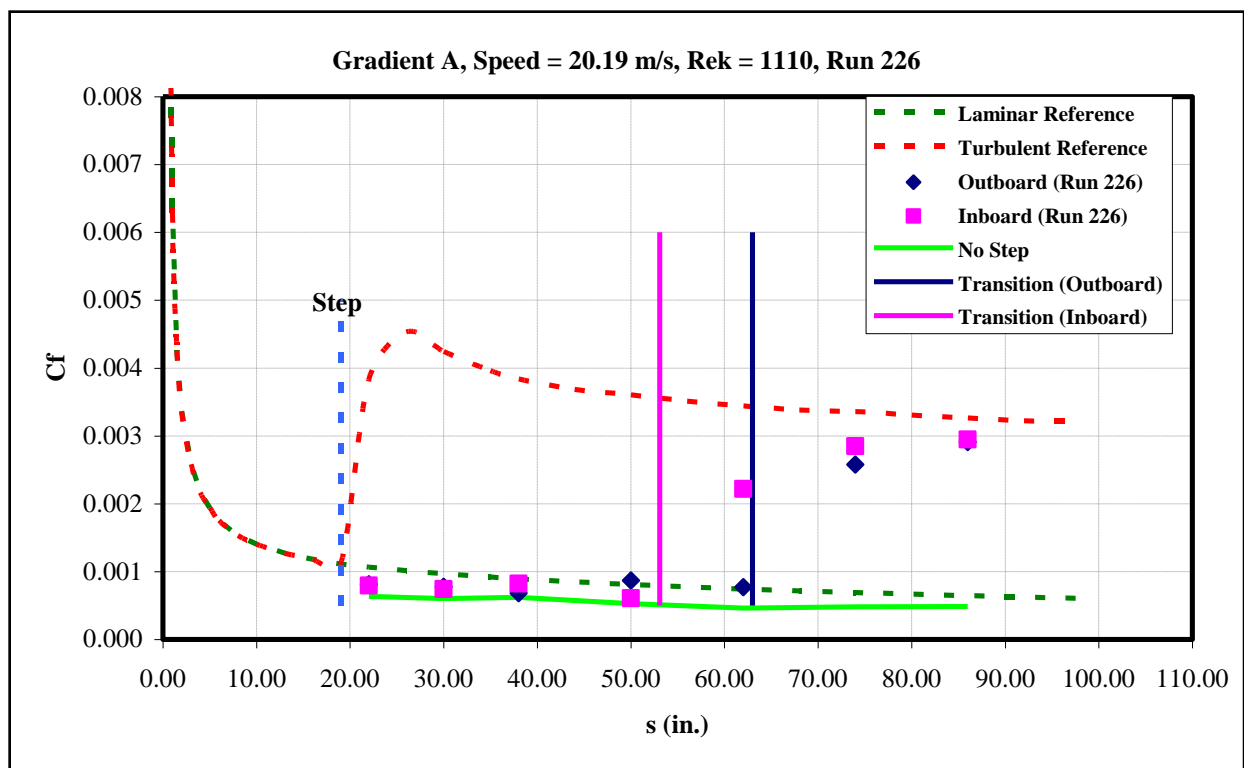


Figure 240: Gradient-A, $k=0.04$ -in aft step, $U=20.19$ m/s skin-friction distribution.

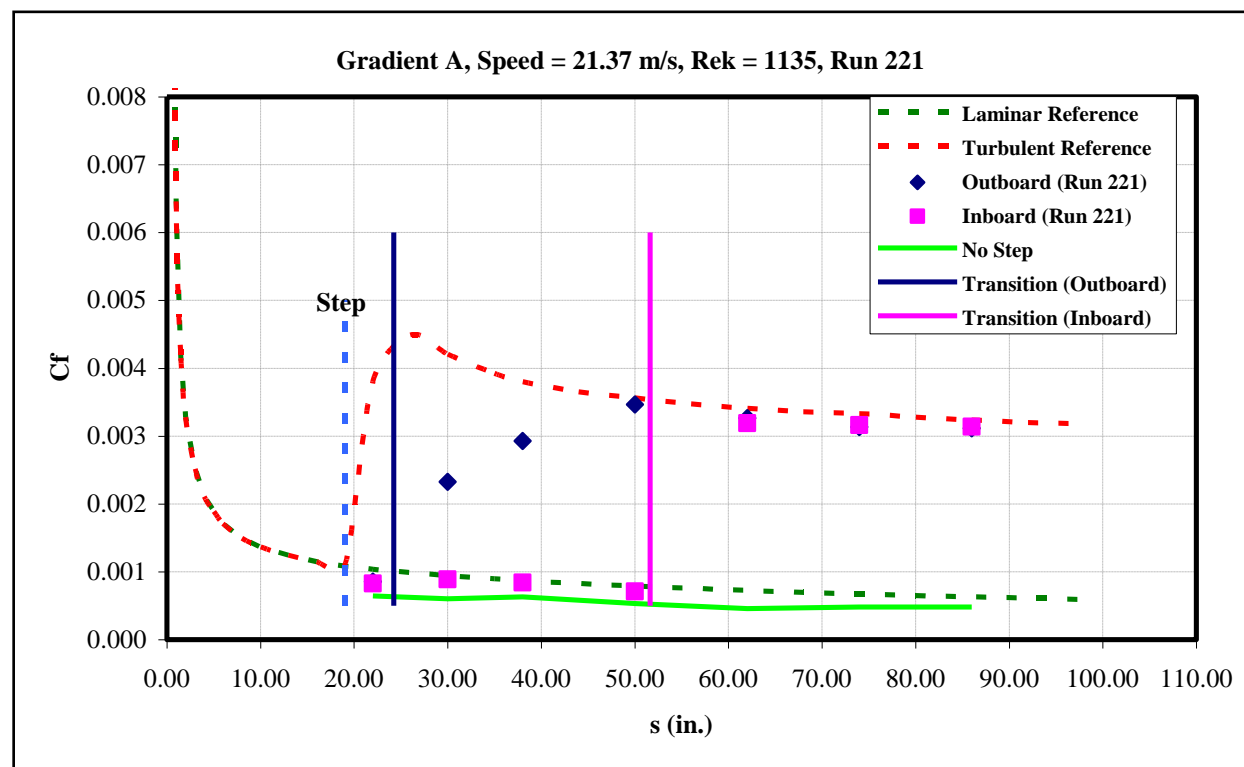


Figure 241: Gradient-A, $k=0.04$ -in aft step, $U=21.37$ m/s skin-friction distribution.

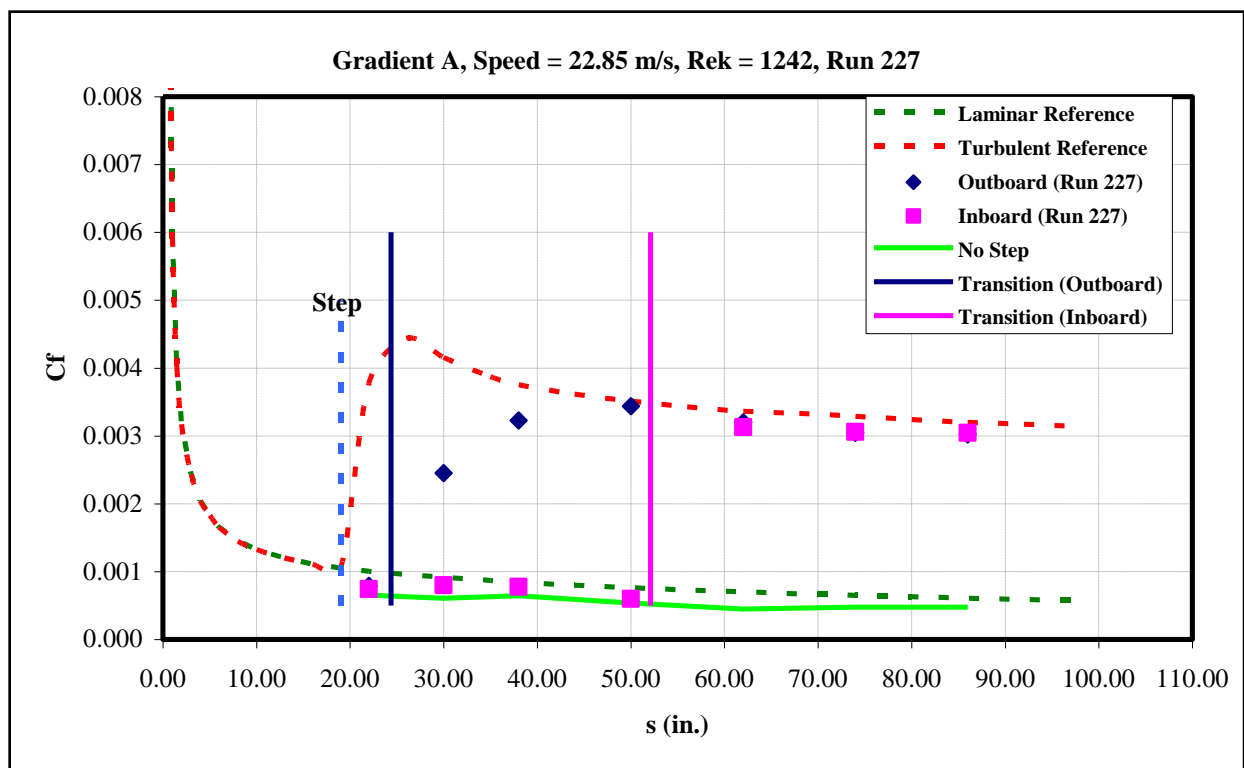


Figure 242: Gradient-A, $k=0.04$ -in aft step, $U=22.85$ m/s skin-friction distribution.

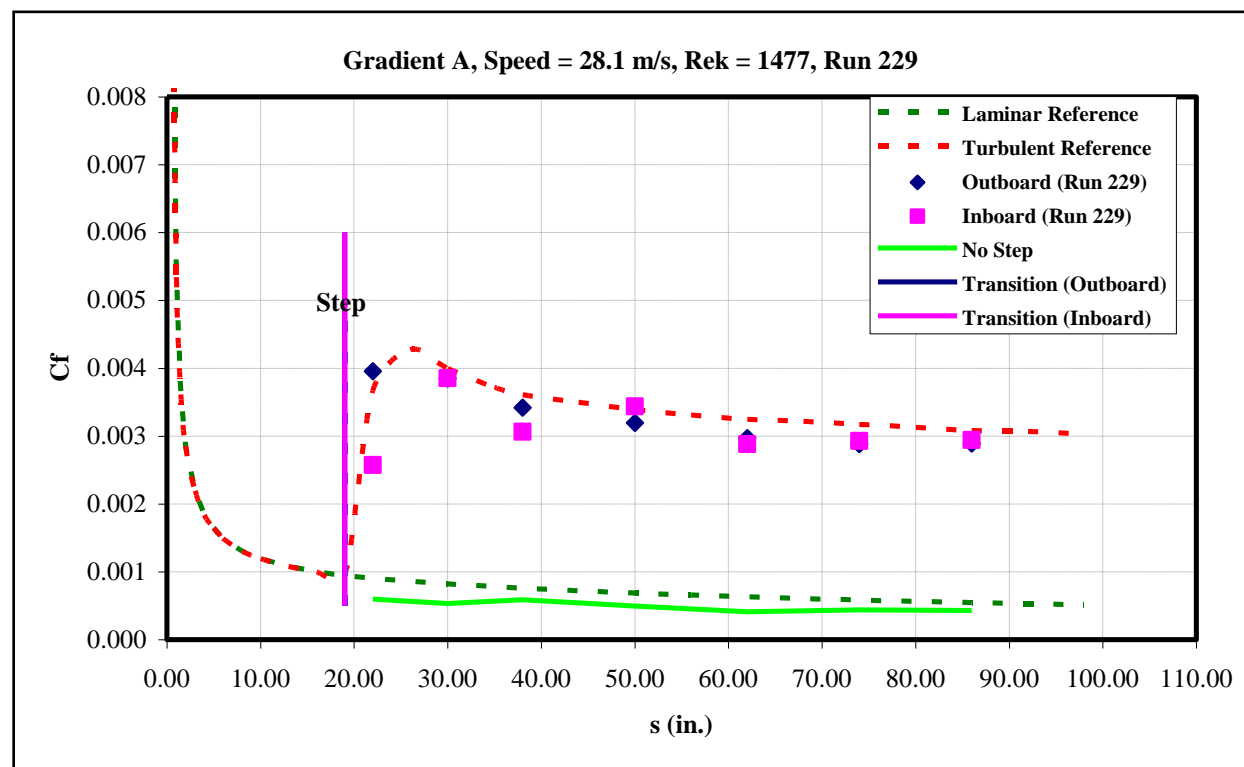


Figure 243: Gradient-A, $k=0.04$ -in aft step, $U=28.1$ m/s skin-friction distribution.

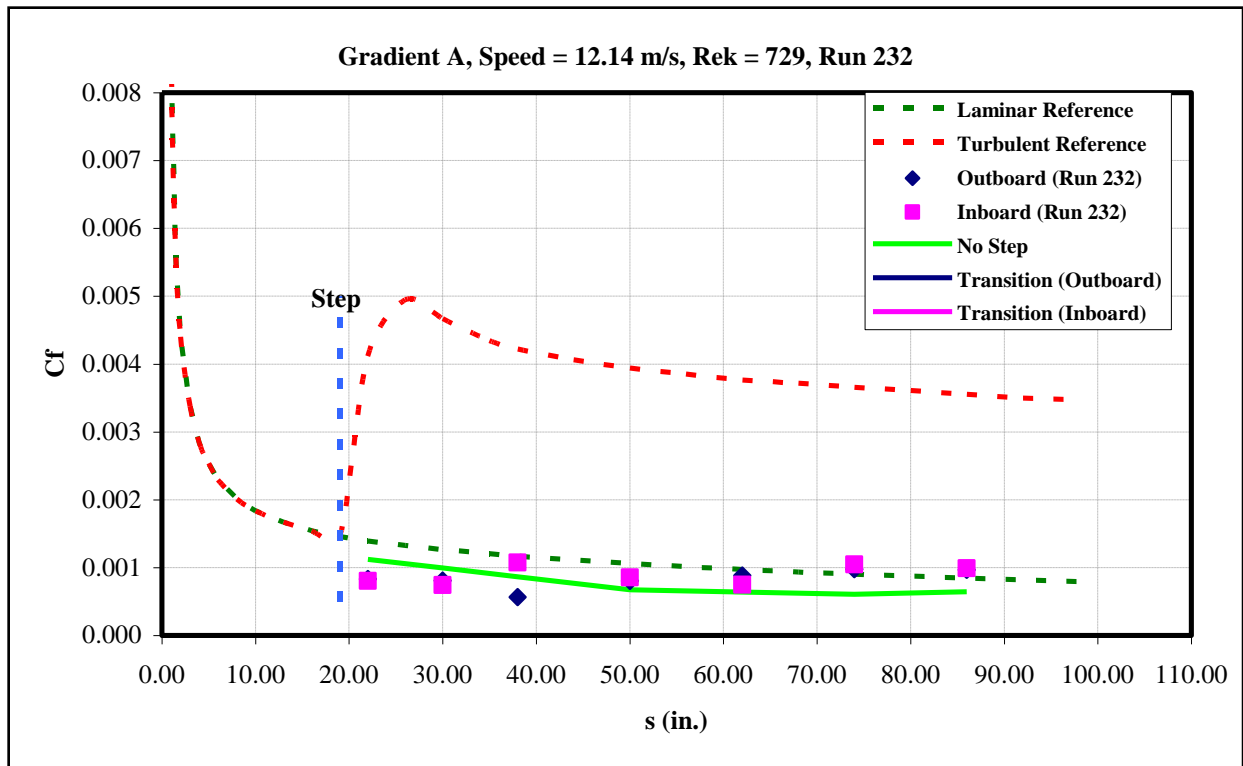


Figure 244: Gradient-A, $k=0.045$ -in aft step, $U=12.14$ m/s skin-friction distribution.

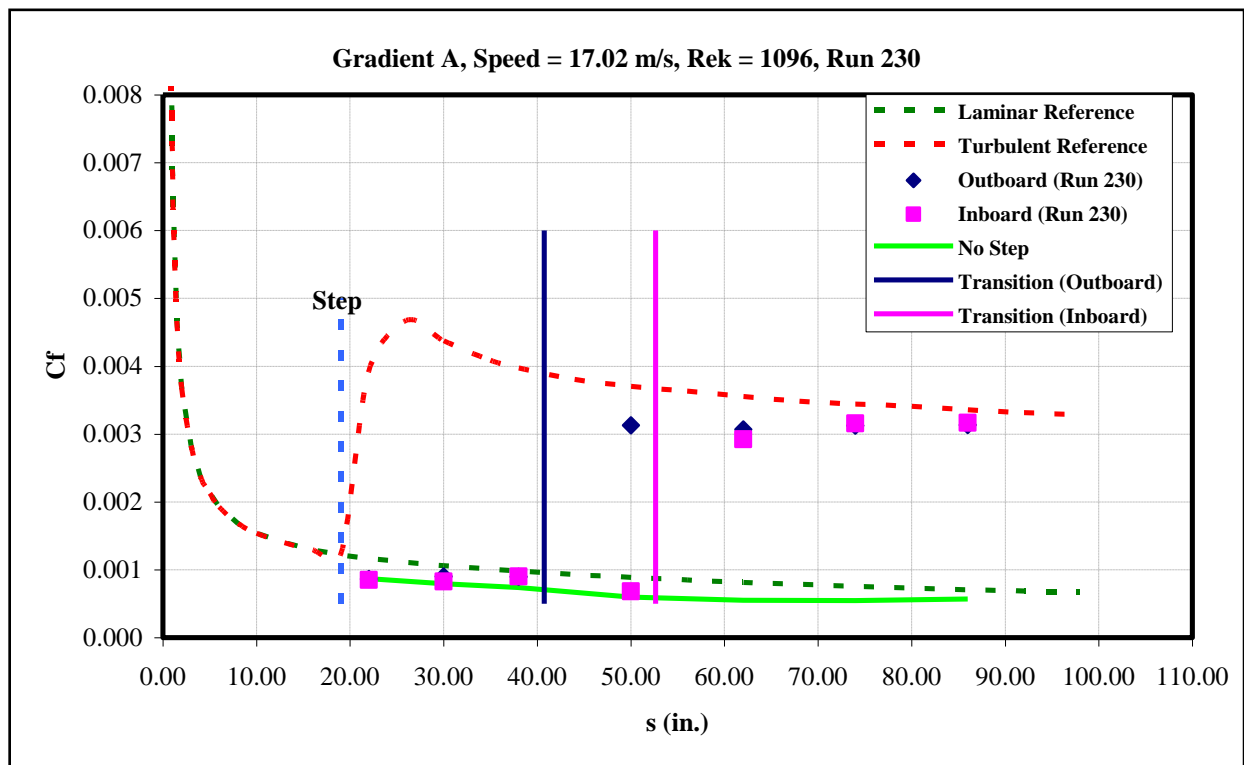


Figure 245: Gradient-A, $k=0.045$ -in aft step, $U=17.02$ m/s skin-friction distribution.

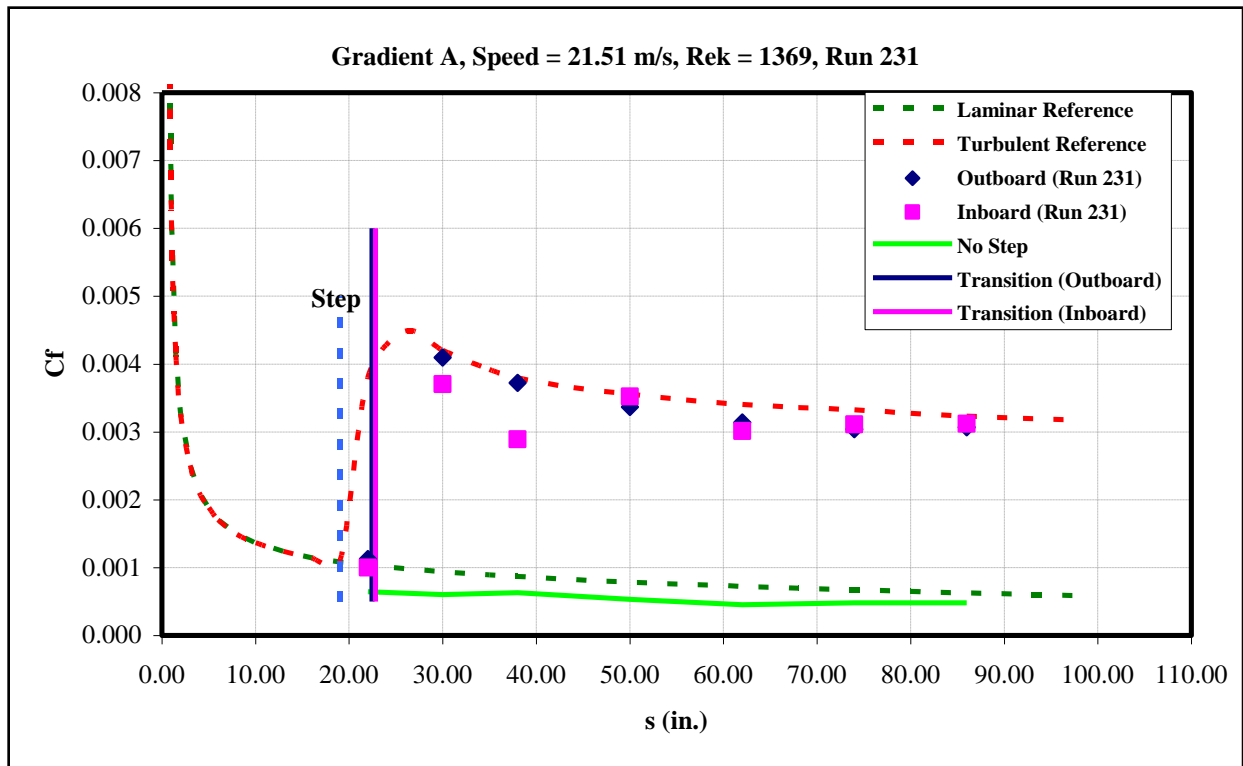


Figure 246: Gradient-A, $k=0.045$ -in aft step, $U=21.51$ m/s skin-friction distribution.

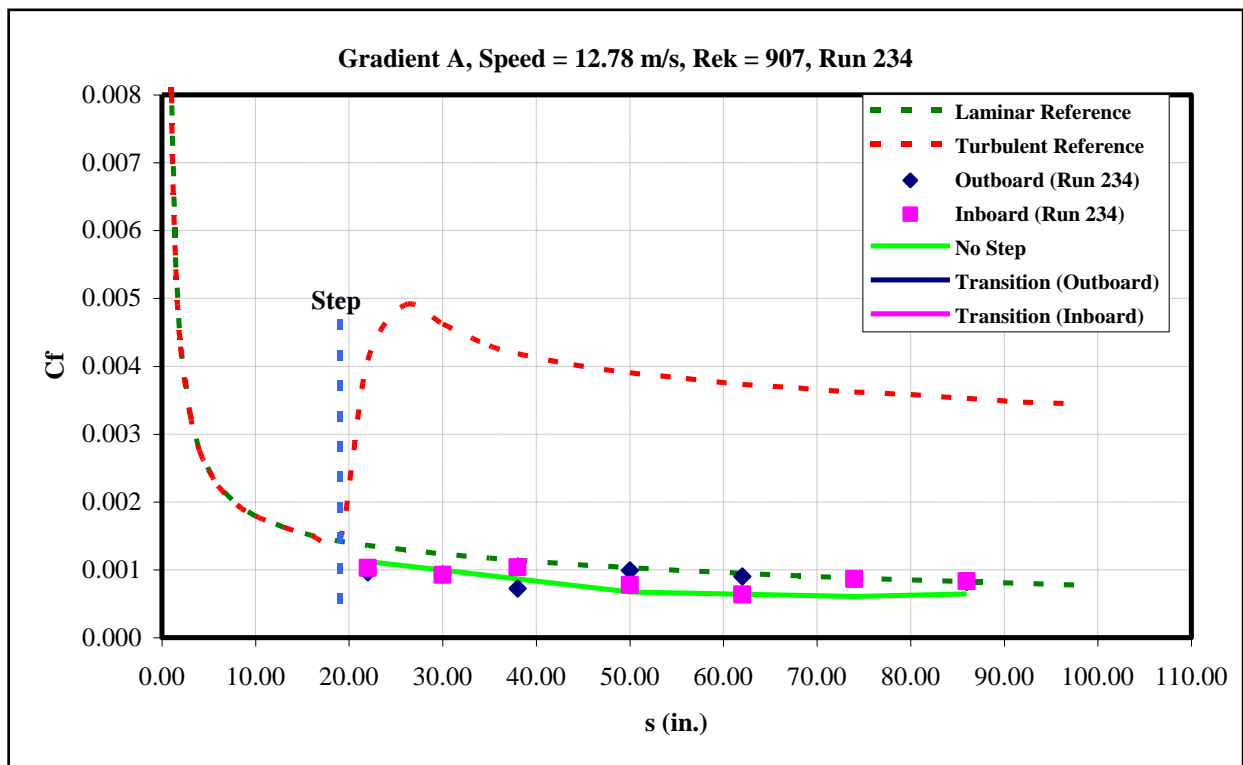


Figure 247: Gradient-A, $k=0.05$ -in aft step, $U=12.78$ m/s skin-friction distribution.

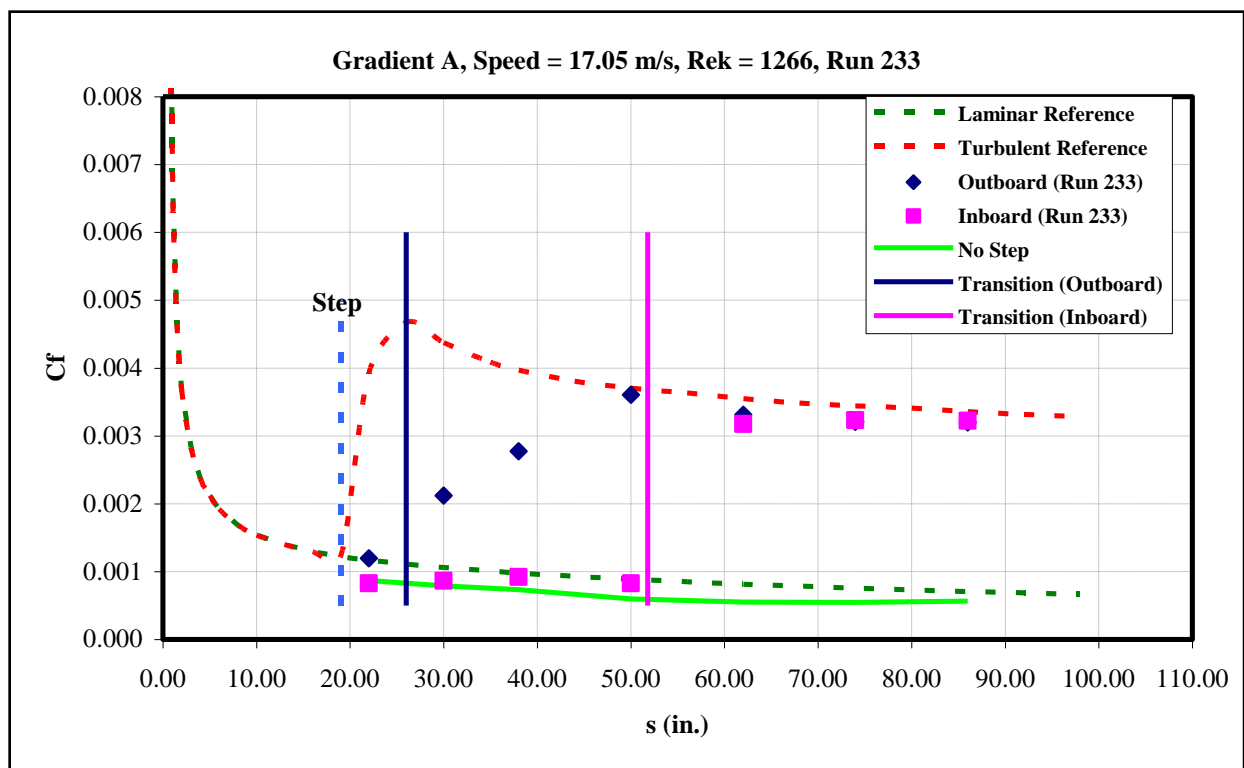


Figure 248: Gradient-A, $k=0.05$ -in aft step, $U=17.05$ m/s skin-friction distribution.

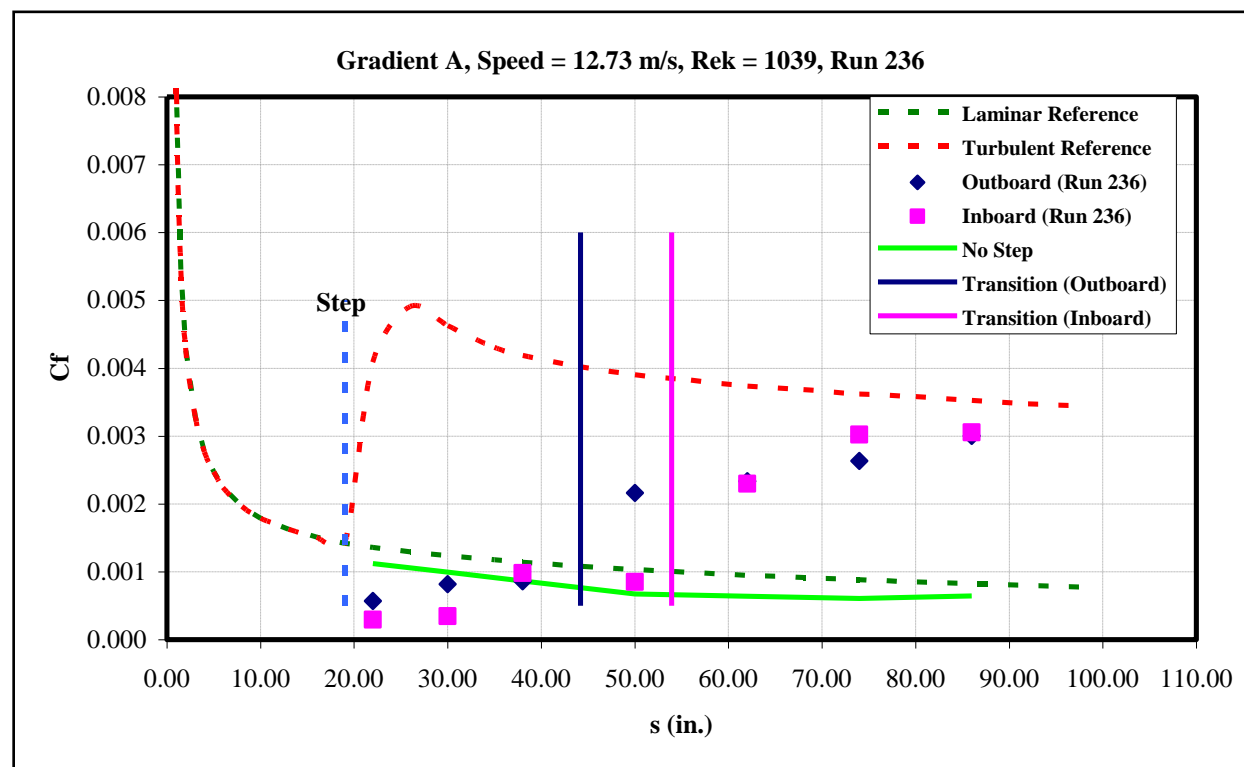


Figure 249: Gradient-A, $k=0.055$ -in aft step, $U=12.73$ m/s skin-friction distribution.

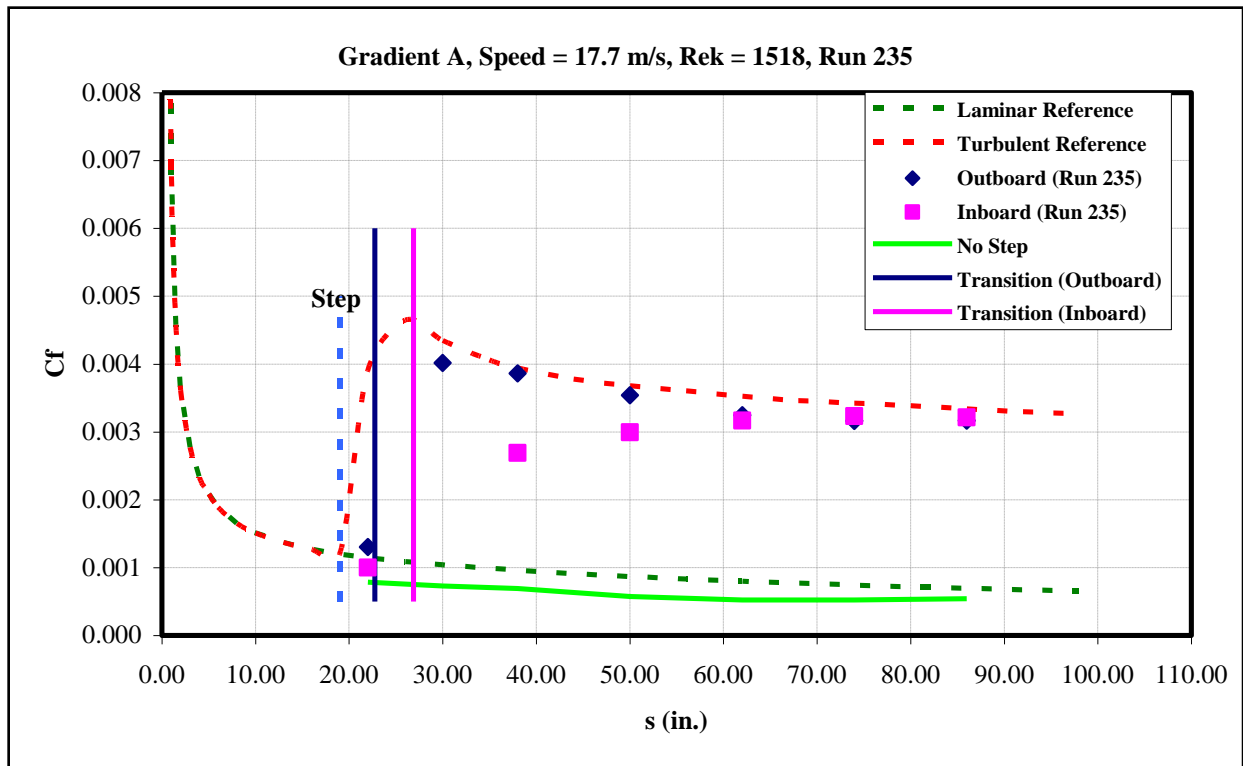


Figure 250: Gradient-A, $k=0.055$ -in aft step, $U=17.7$ m/s skin-friction distribution.

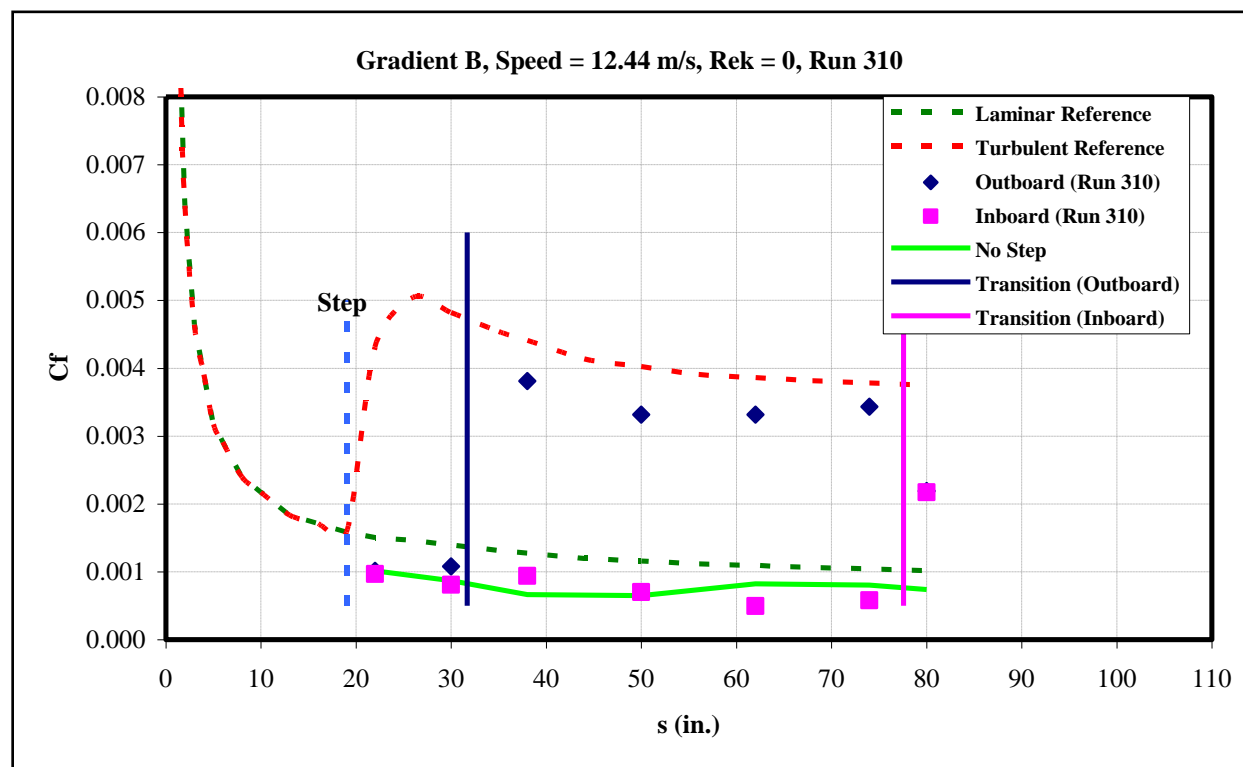


Figure 251: Gradient-B, $k=0$ -in, $U=12.44$ m/s skin-friction distribution.

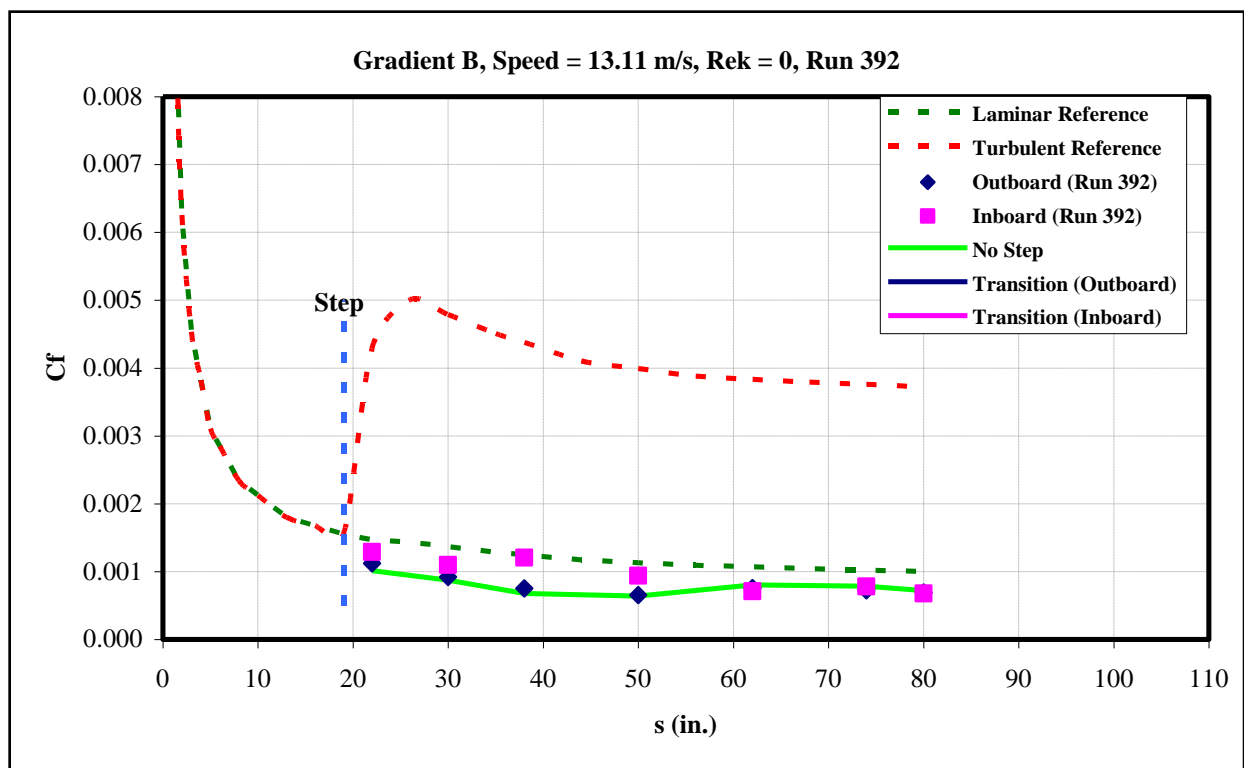


Figure 252: Gradient-B, $k=0$ -in, $U=13.11$ m/s skin-friction distribution.

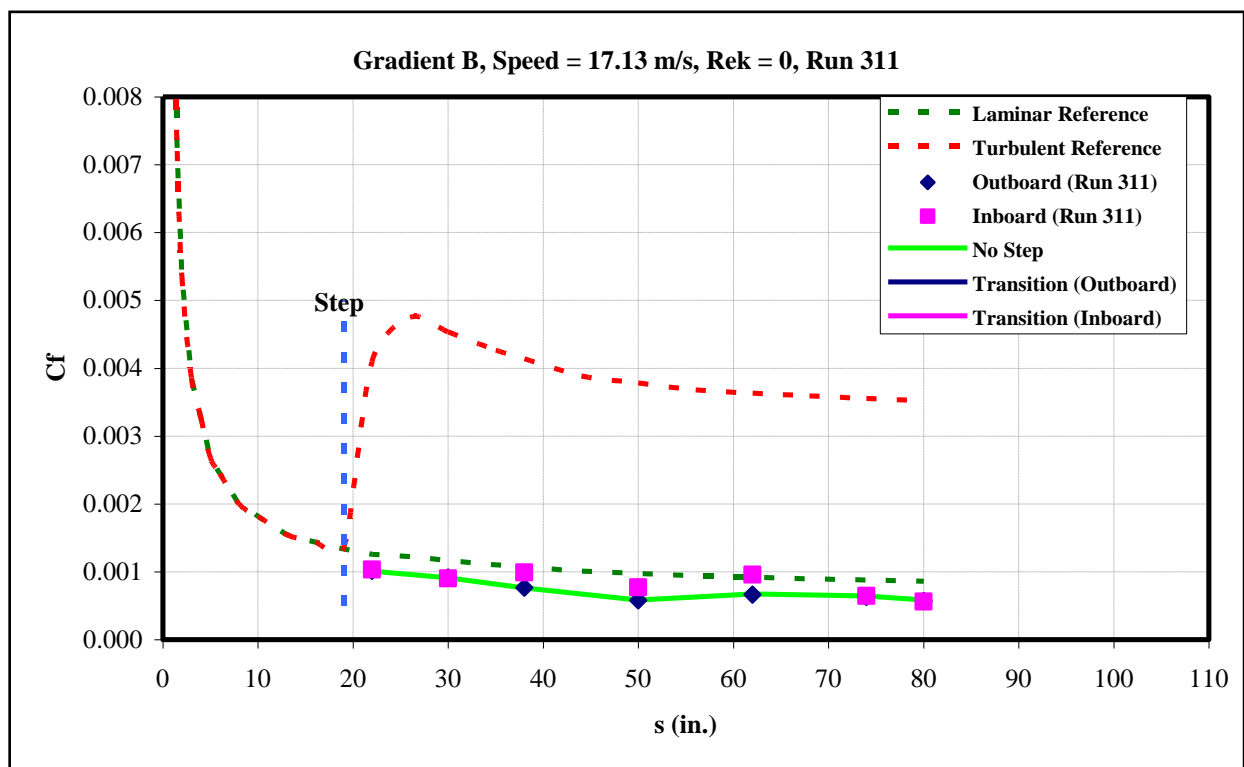


Figure 253: Gradient-B, $k=0$ -in, $U=17.13$ m/s skin-friction distribution.

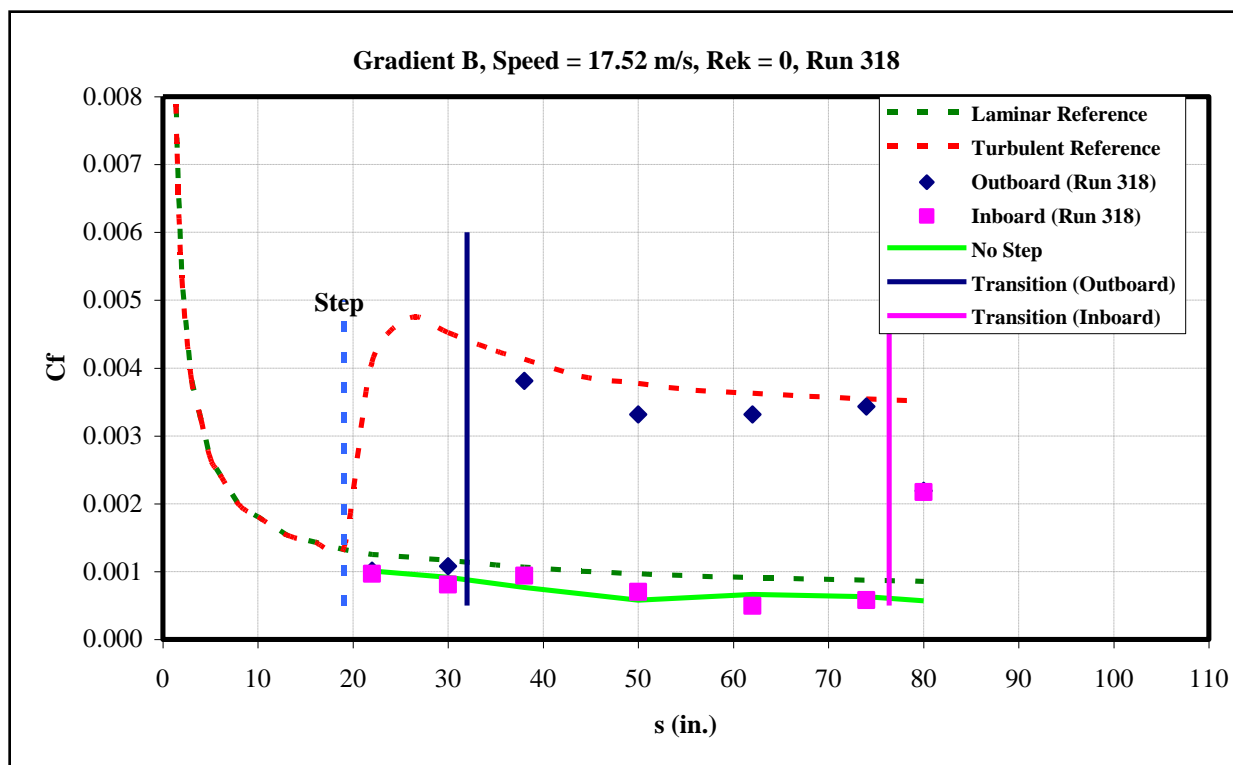


Figure 254: Gradient-B, $k=0$ -in, $U=17.52$ m/s skin-friction distribution.

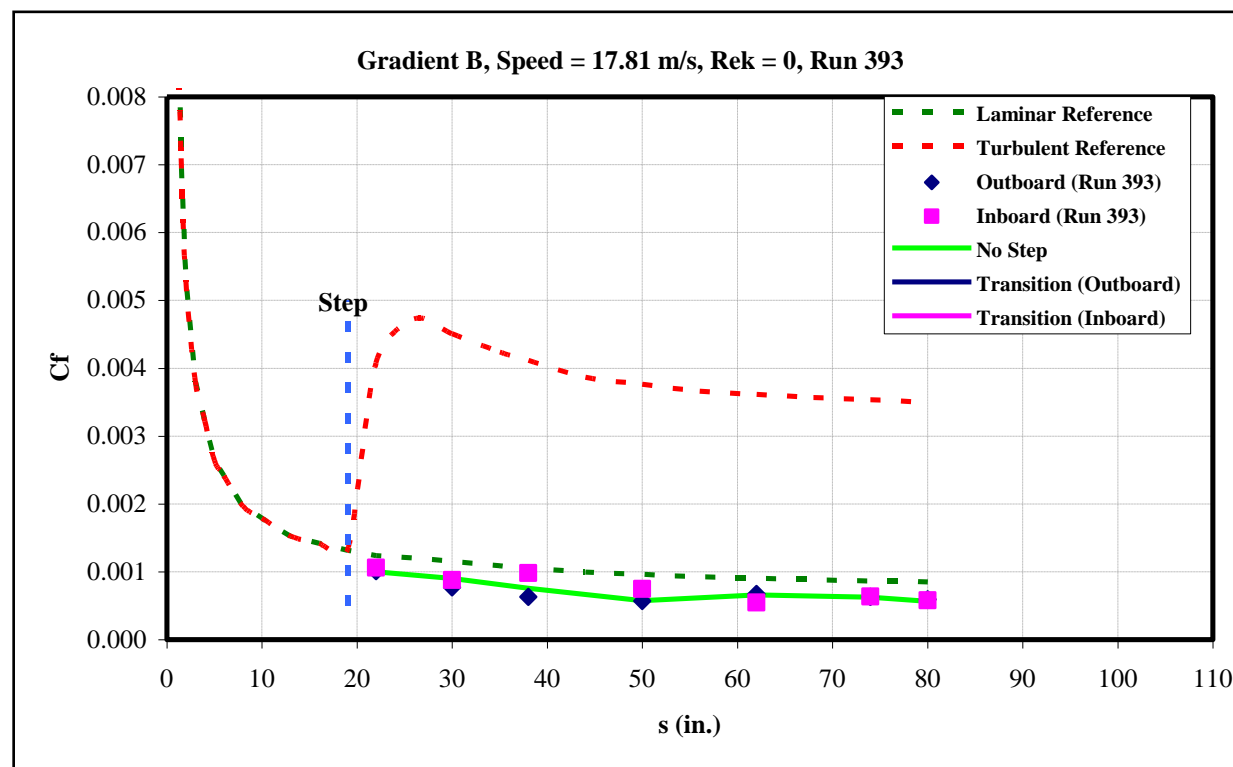


Figure 255: Gradient-B, $k=0$ -in, $U=17.81$ m/s skin-friction distribution.

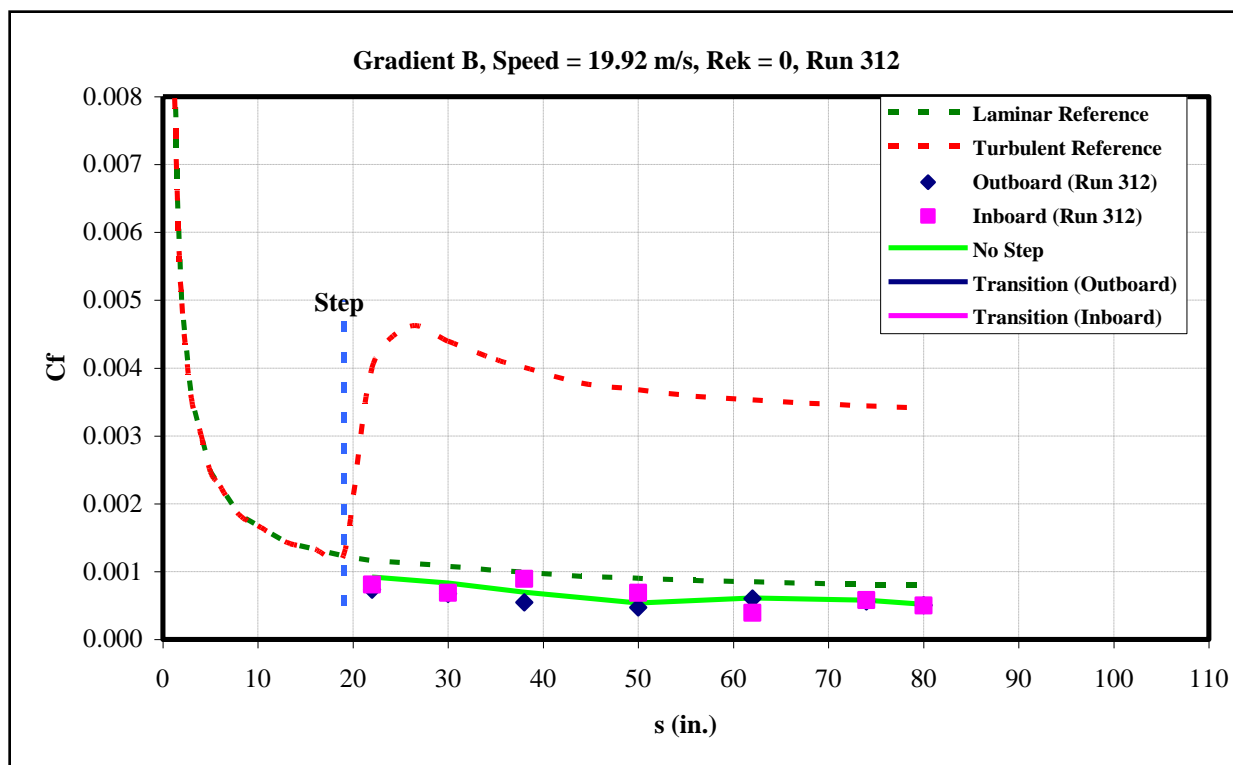


Figure 256: Gradient-B, $k=0$ -in, $U=19.92$ m/s skin-friction distribution.

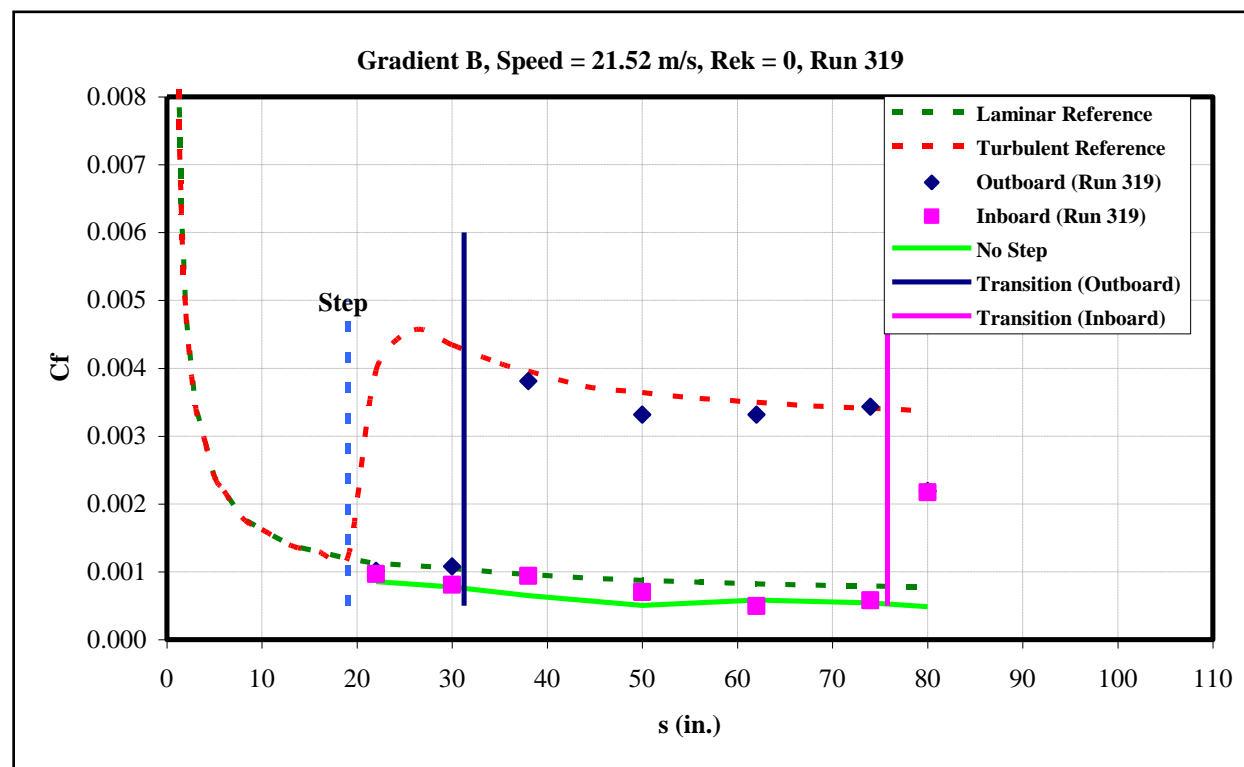


Figure 257: Gradient-B, $k=0$ -in, $U=21.52$ m/s skin-friction distribution.

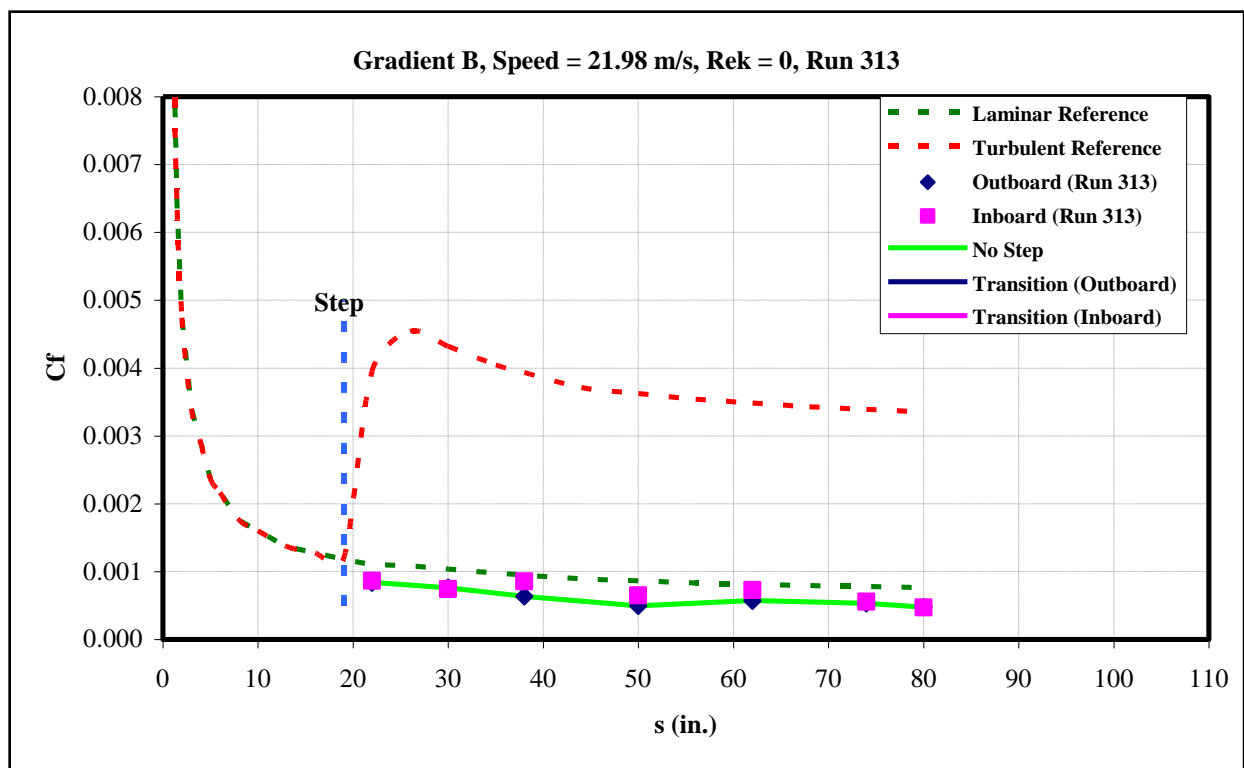


Figure 258: Gradient-B, $k=0$ -in, $U=21.98$ m/s skin-friction distribution.

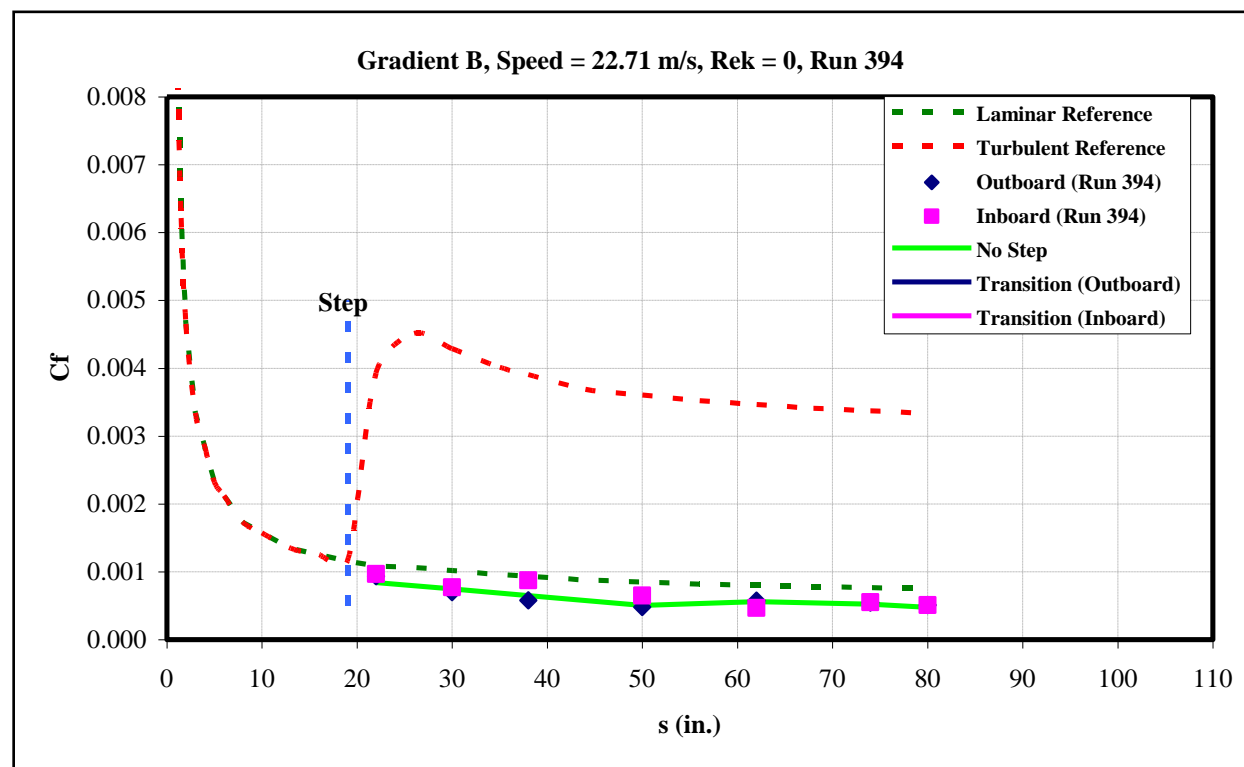


Figure 259: Gradient-B, $k=0$ -in, $U=22.71$ m/s skin-friction distribution.

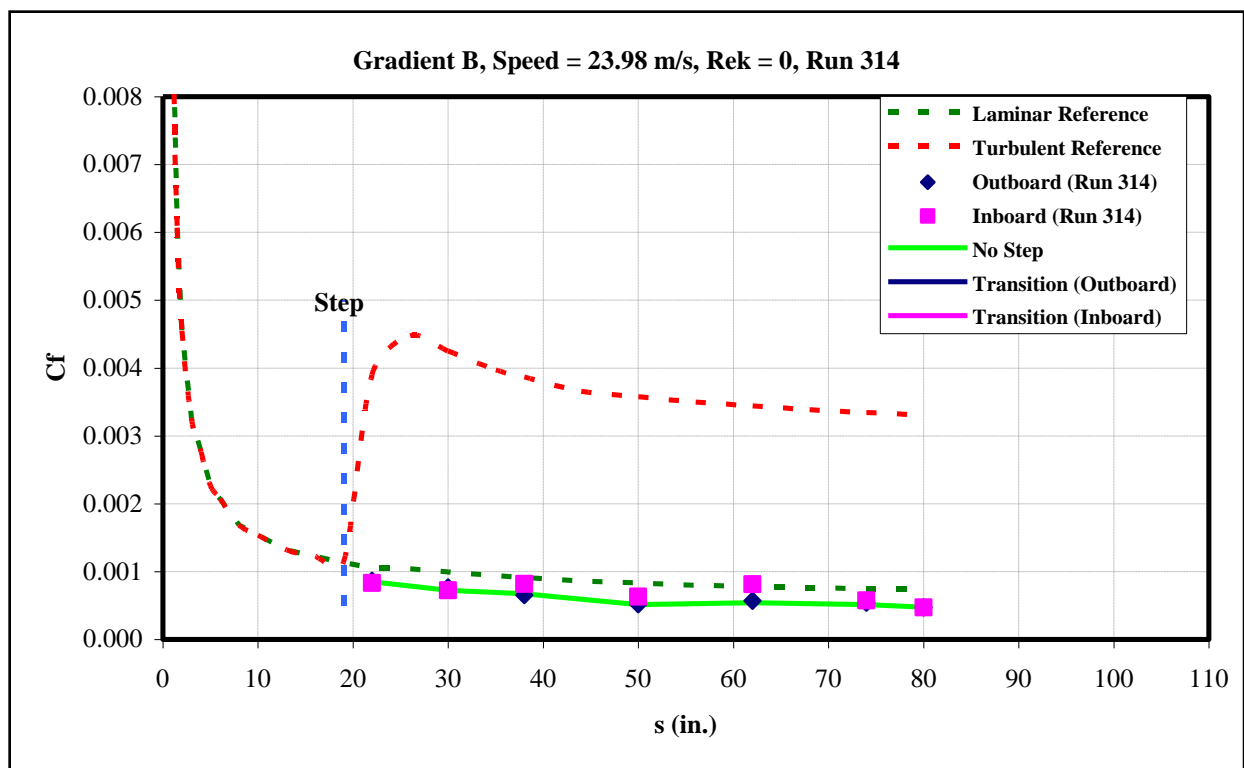


Figure 260: Gradient-B, $k=0$ -in, $U=23.98$ m/s skin-friction distribution.

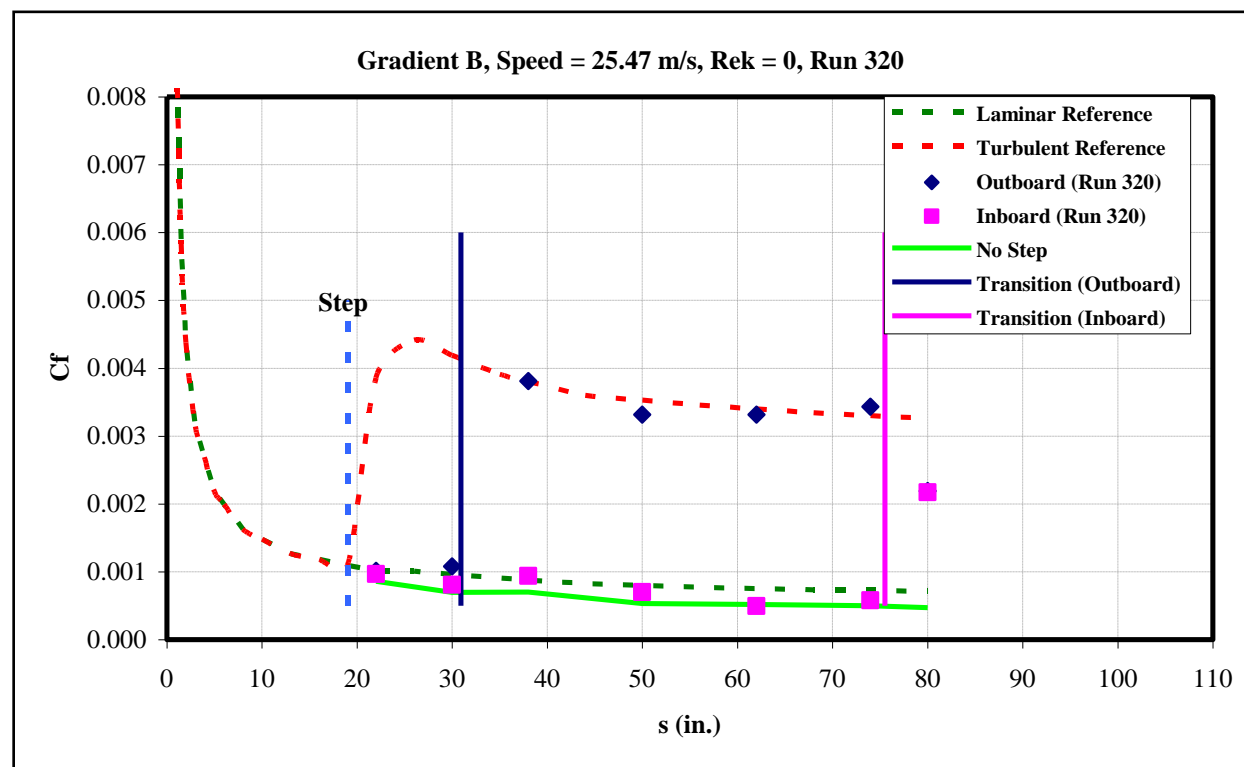


Figure 261: Gradient-B, $k=0$ -in, $U=25.47$ m/s skin-friction distribution.

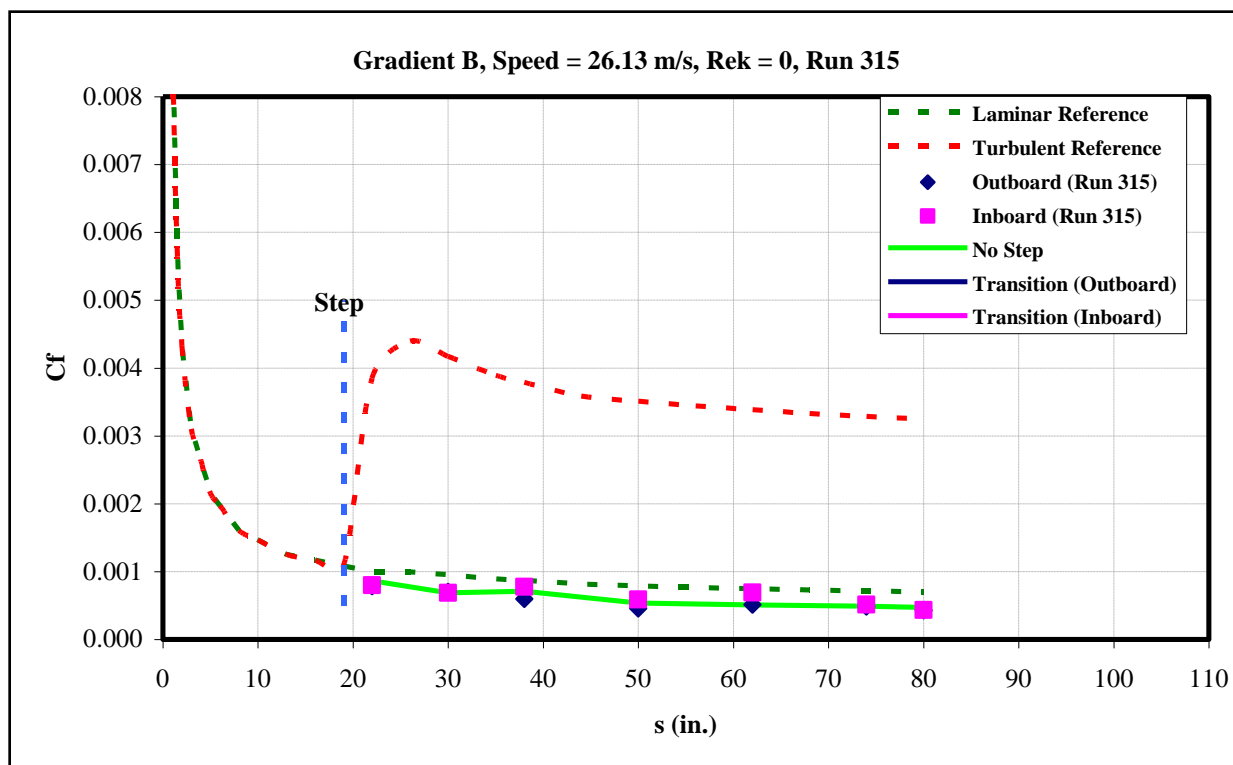


Figure 262: Gradient-B, $k=0$ -in, $U=26.13$ m/s skin-friction distribution.

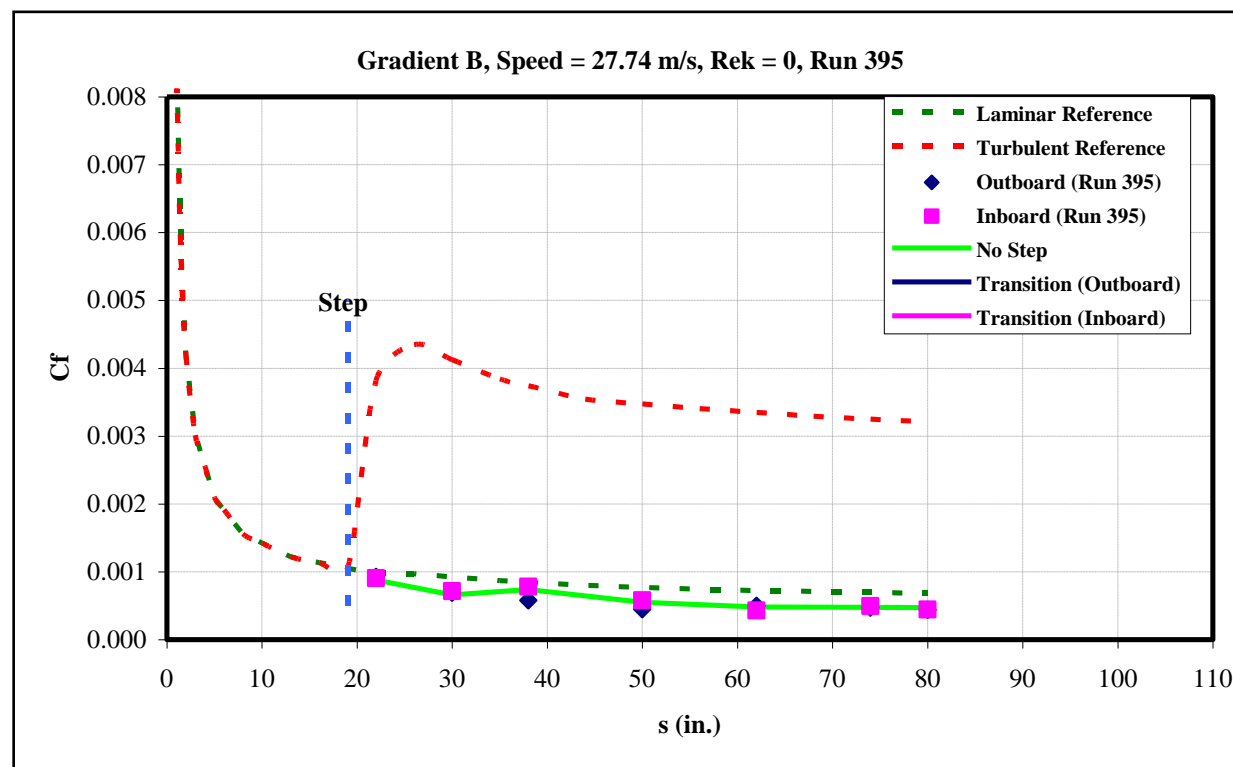


Figure 263: Gradient-B, $k=0$ -in, $U=27.74$ m/s skin-friction distribution.

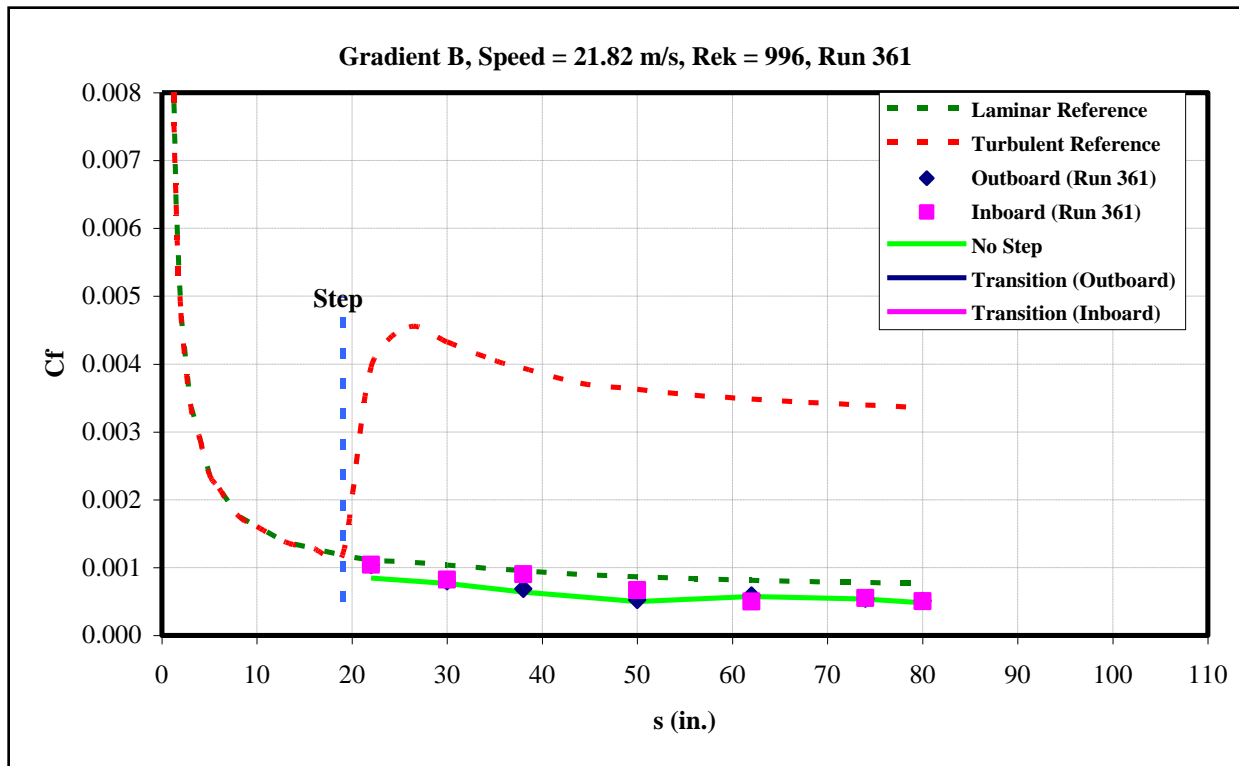


Figure 264: Gradient-B, $k=0.035$ -in forward step, $U=21.82$ m/s skin-friction distribution.

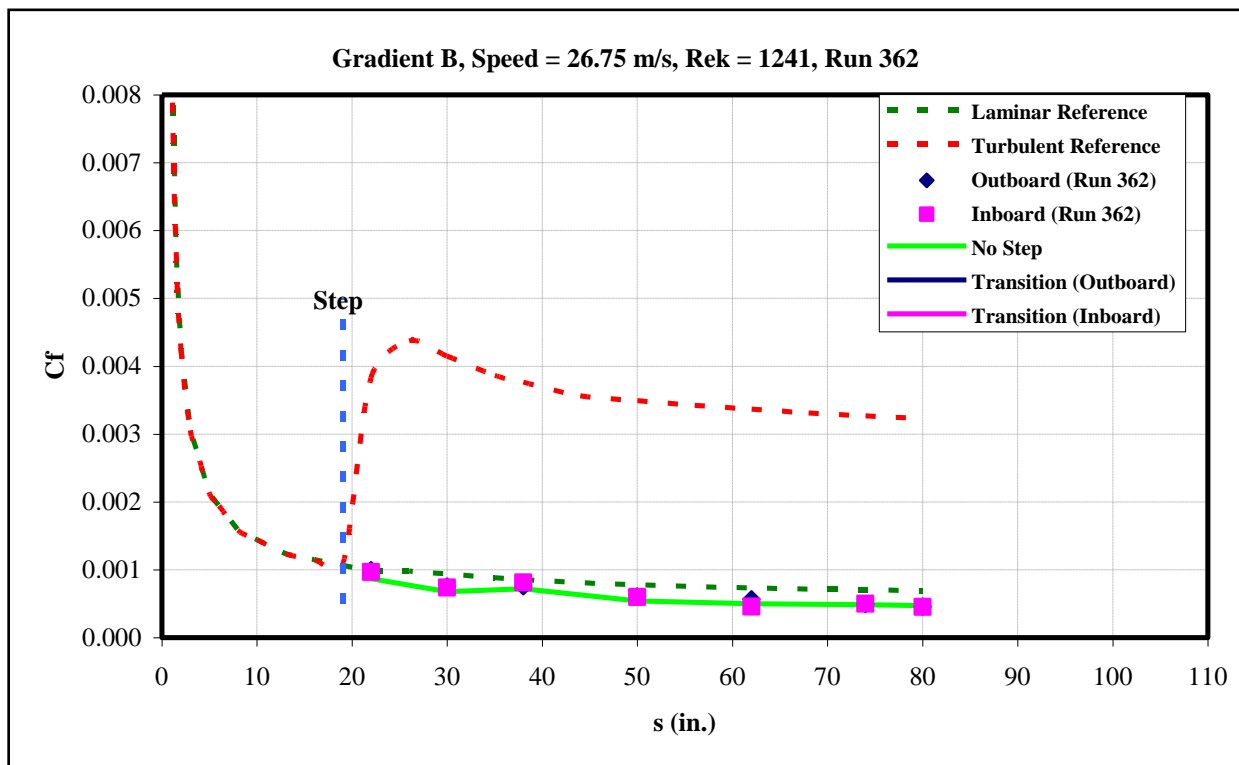


Figure 265: Gradient-B, $k=0.035$ -in forward step, $U=26.75$ m/s skin-friction distribution.

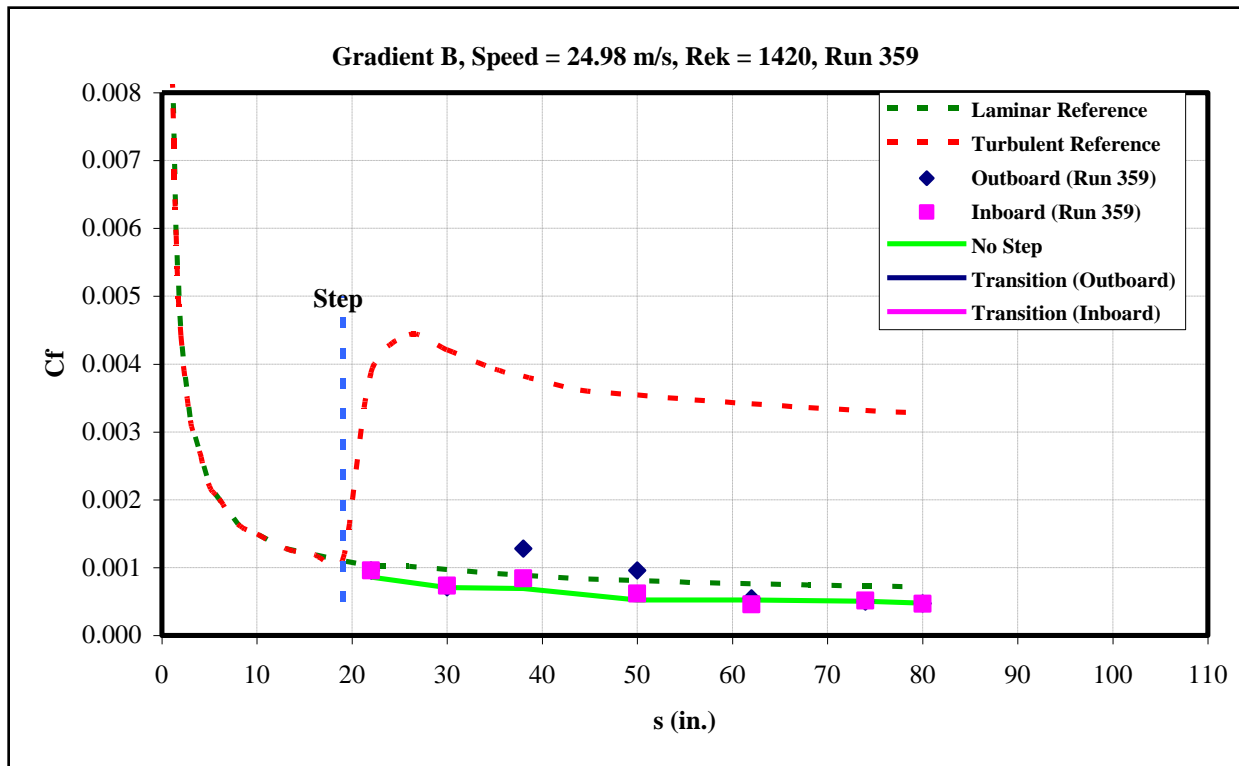


Figure 266: Gradient-B, $k=0.04$ -in forward step, $U=24.98$ m/s skin-friction distribution.

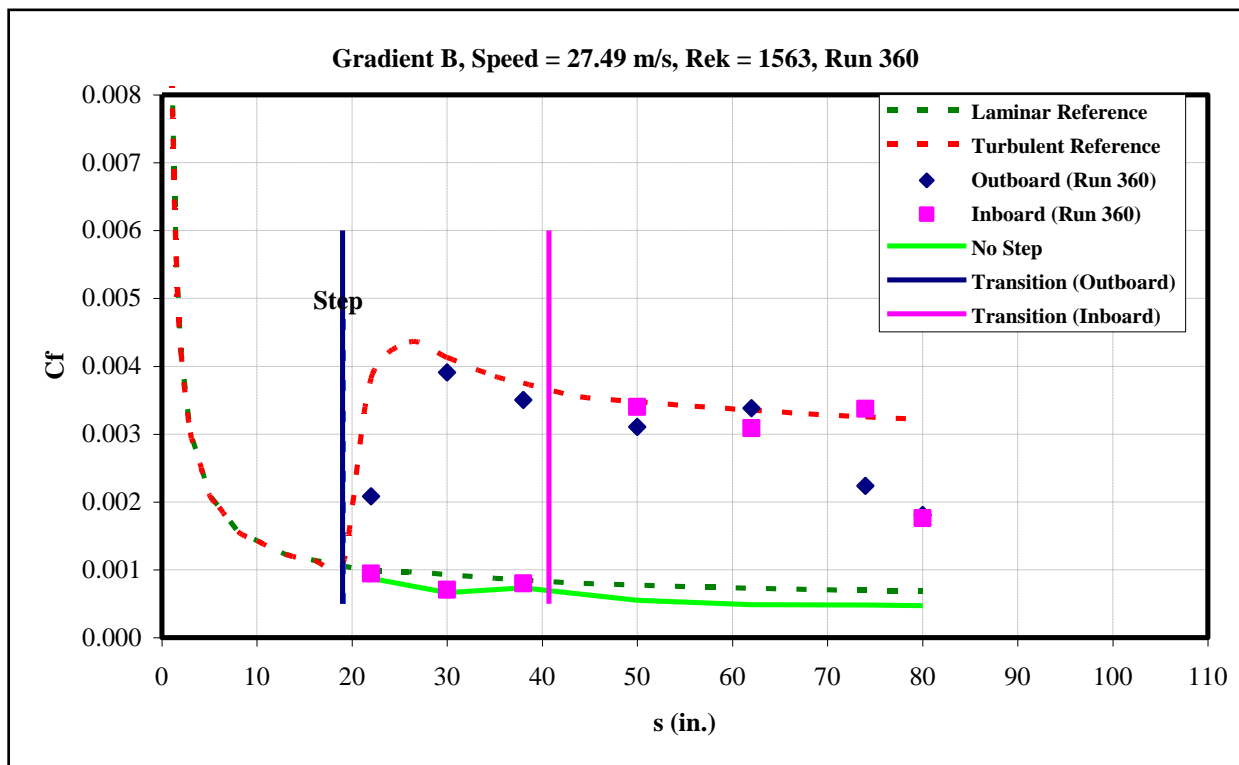


Figure 267: Gradient-B, $k=0.04$ -in forward step, $U=27.49$ m/s skin-friction distribution.

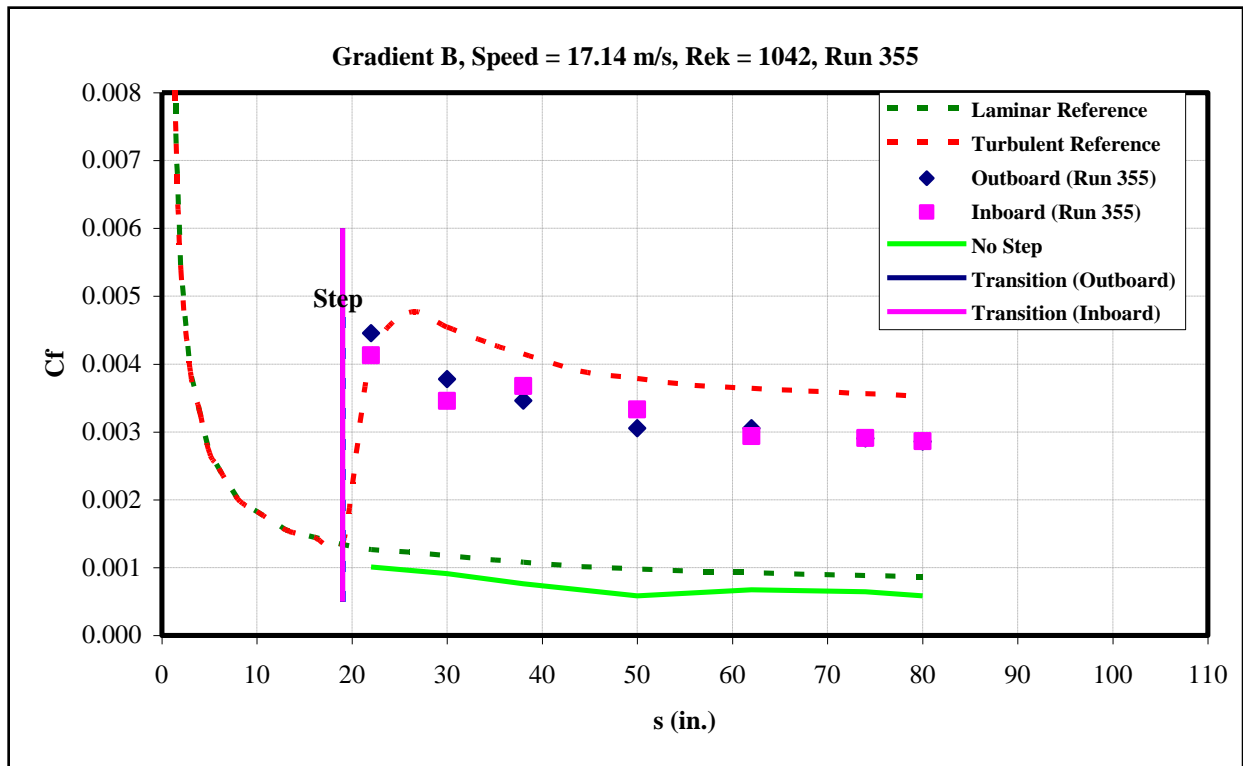


Figure 268: Gradient-B, $k=0.045$ -in forward step, $U=17.14$ m/s skin-friction distribution.

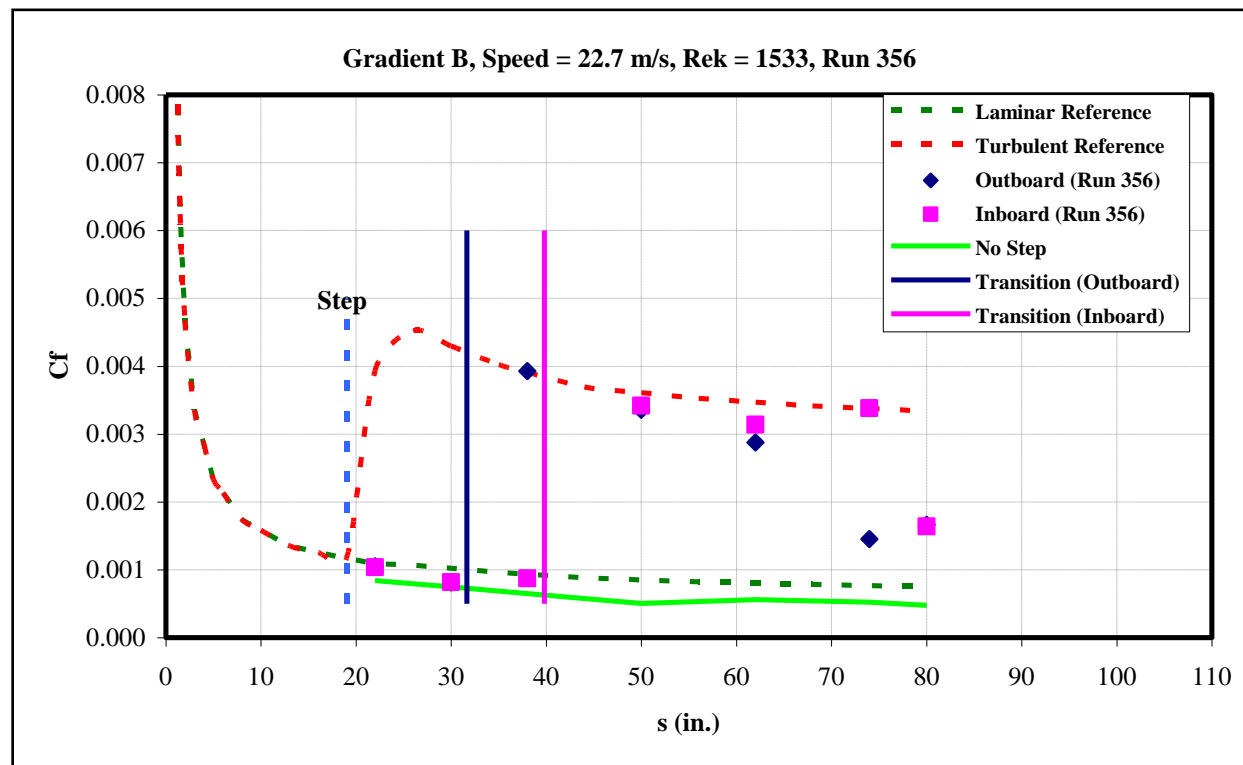


Figure 269: Gradient-B, $k=0.045$ -in forward step, $U=22.7$ m/s skin-friction distribution.

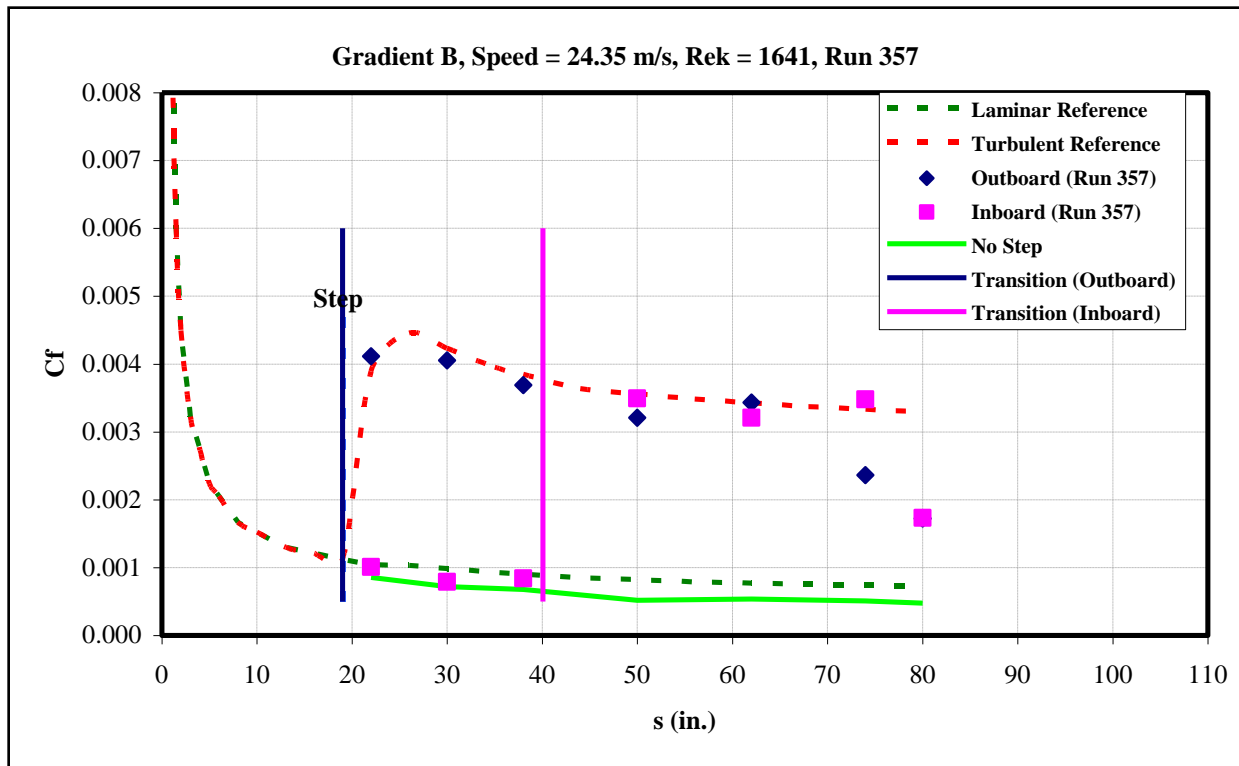


Figure 270: Gradient-B, $k=0.045$ -in forward step, $U=24.35$ m/s skin-friction distribution.

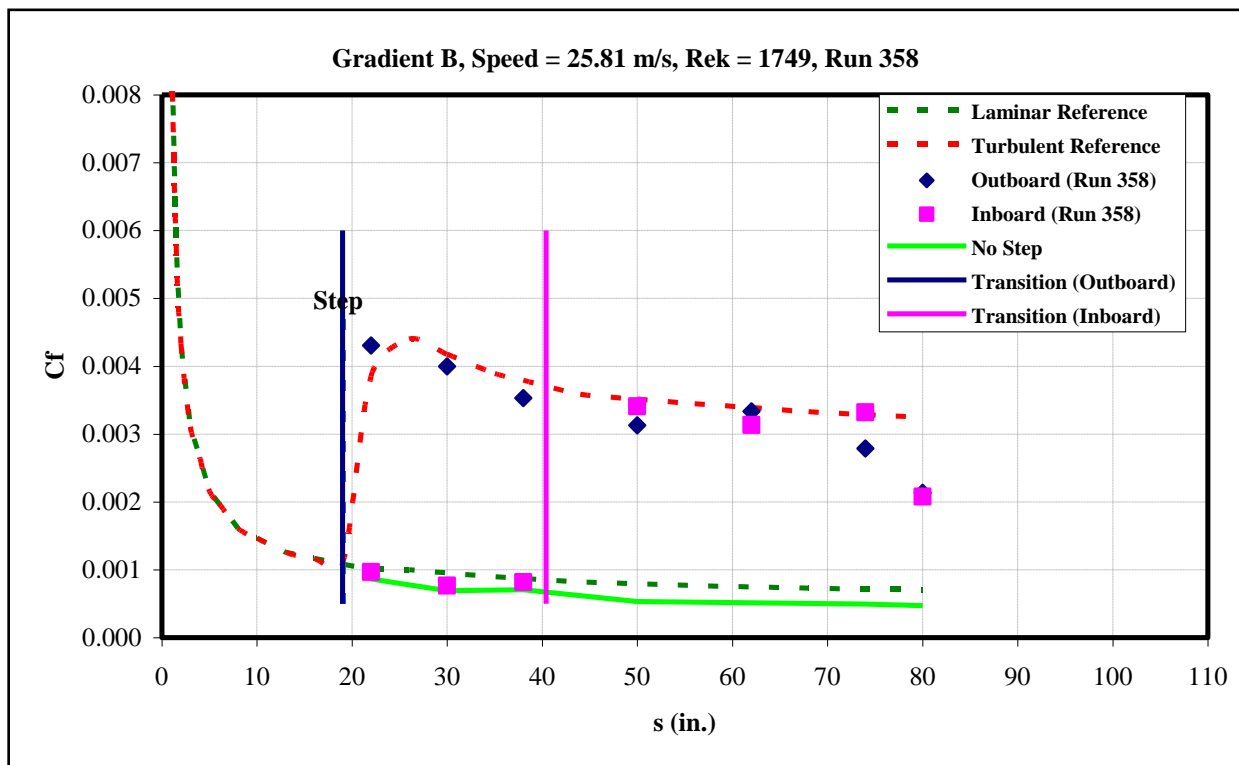


Figure 271: Gradient-B, $k=0.045$ -in forward step, $U=25.81$ m/s skin-friction distribution.

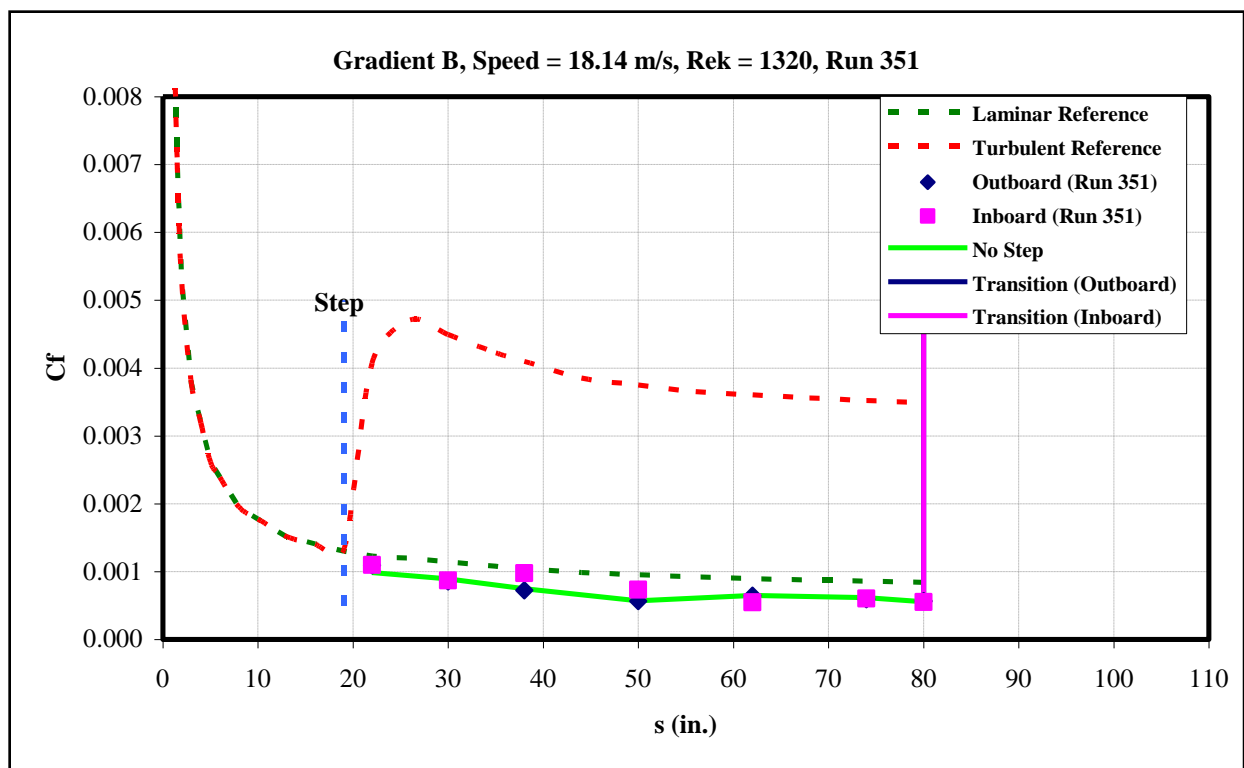


Figure 272: Gradient-B, $k=0.05$ -in forward step, $U=18.14$ m/s skin-friction distribution.

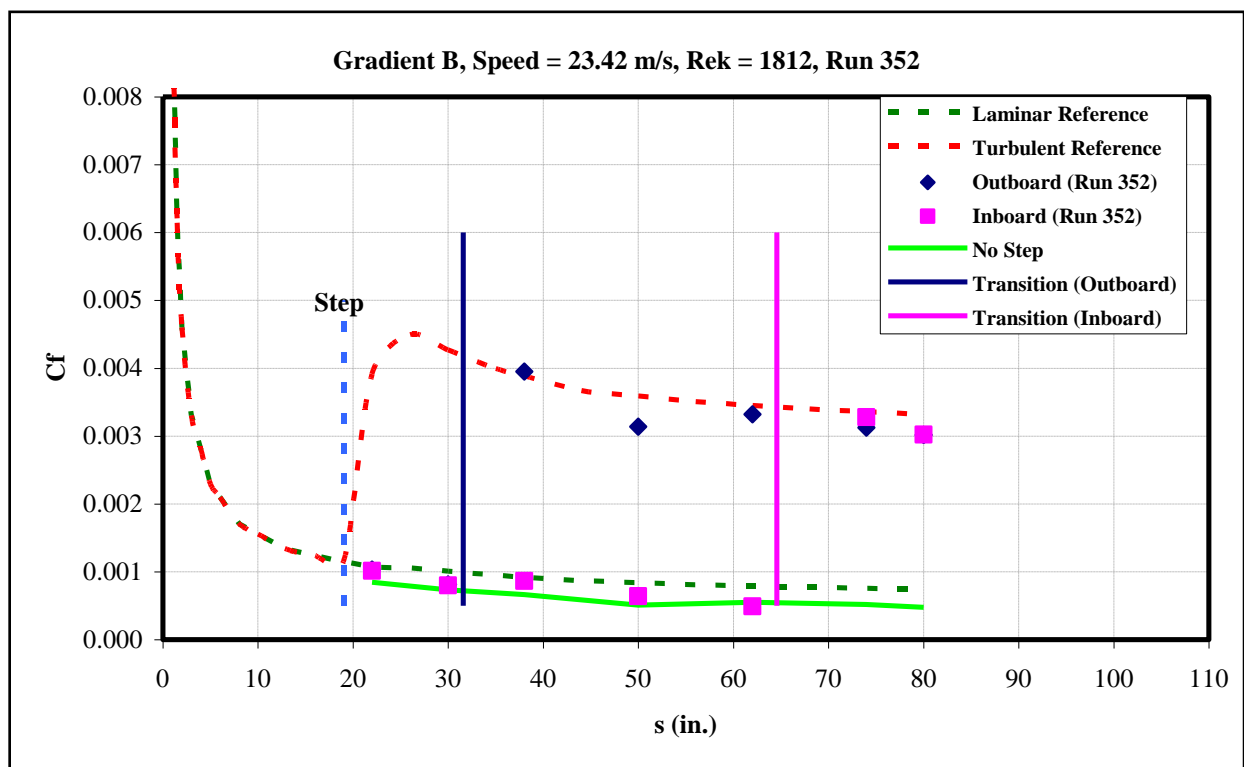


Figure 273: Gradient-B, $k=0.05$ -in forward step, $U=23.42$ m/s skin-friction distribution.

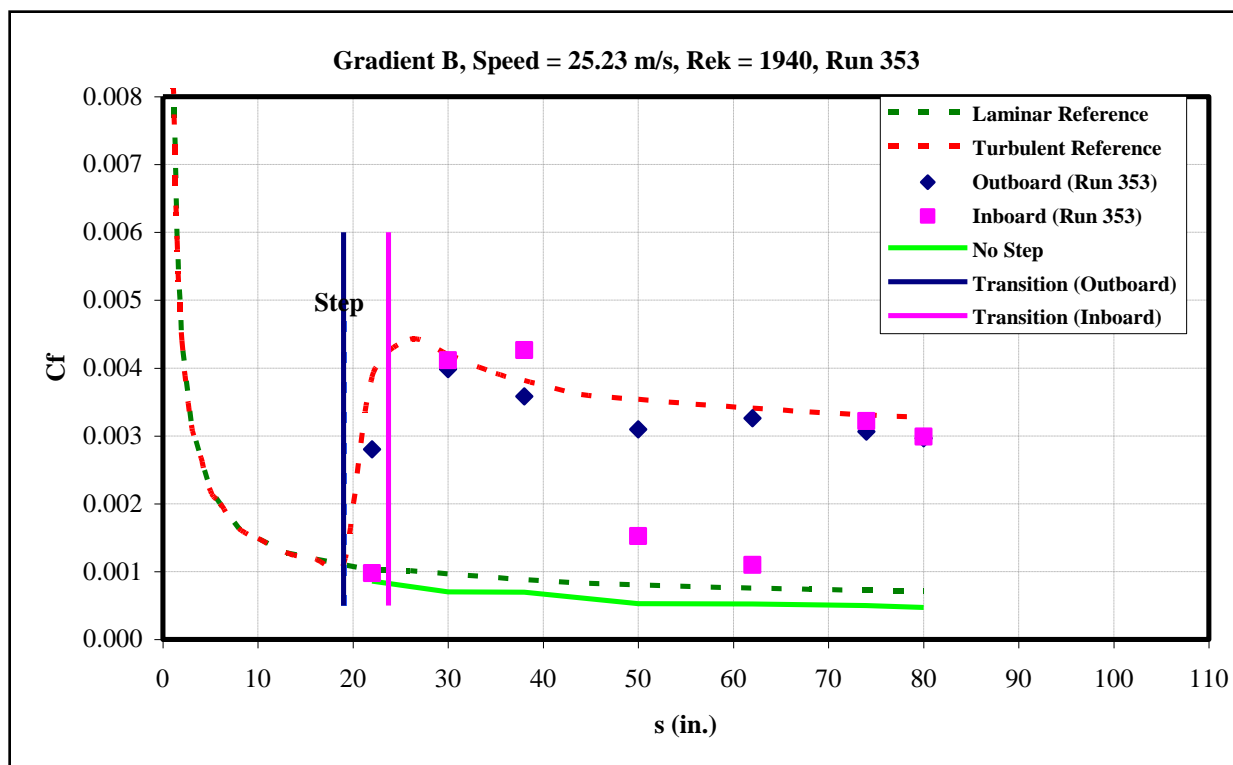


Figure 274: Gradient-B, $k=0.05$ -in forward step, $U=25.23$ m/s skin-friction distribution.

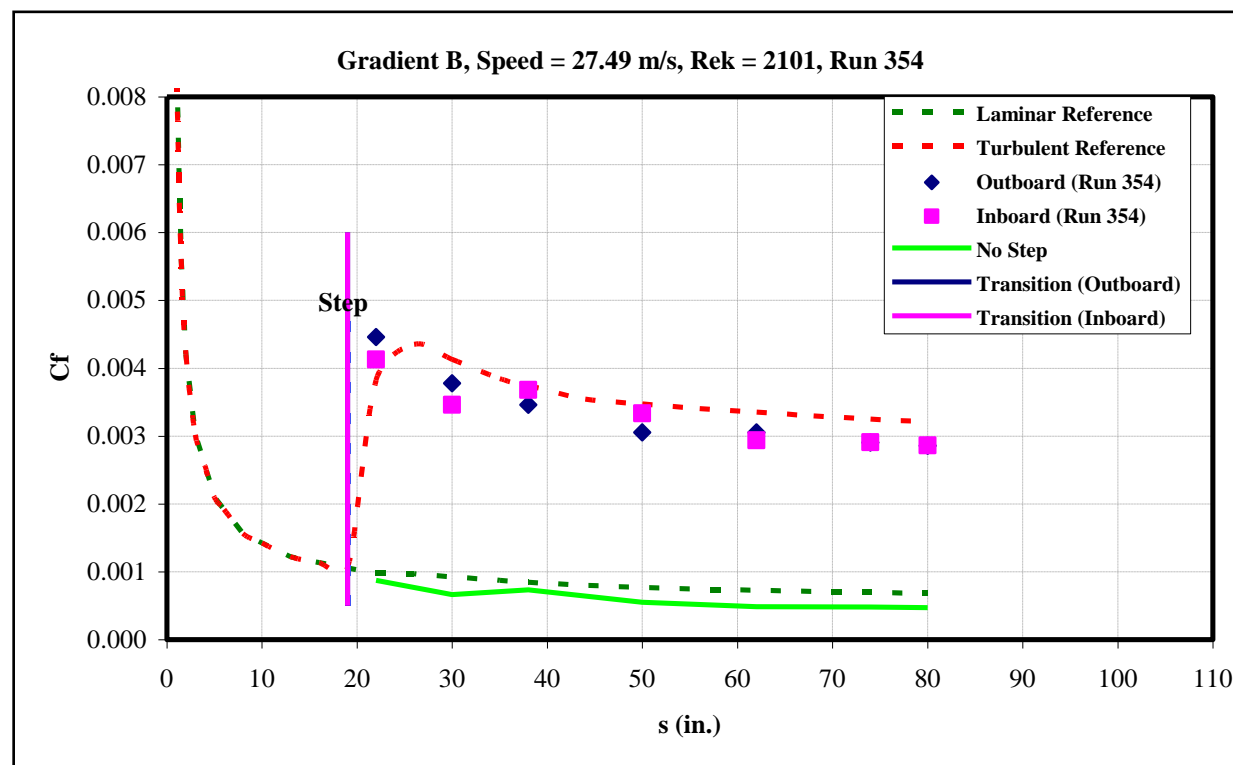


Figure 275: Gradient-B, $k=0.05$ -in forward step, $U=27.49$ m/s skin-friction distribution.

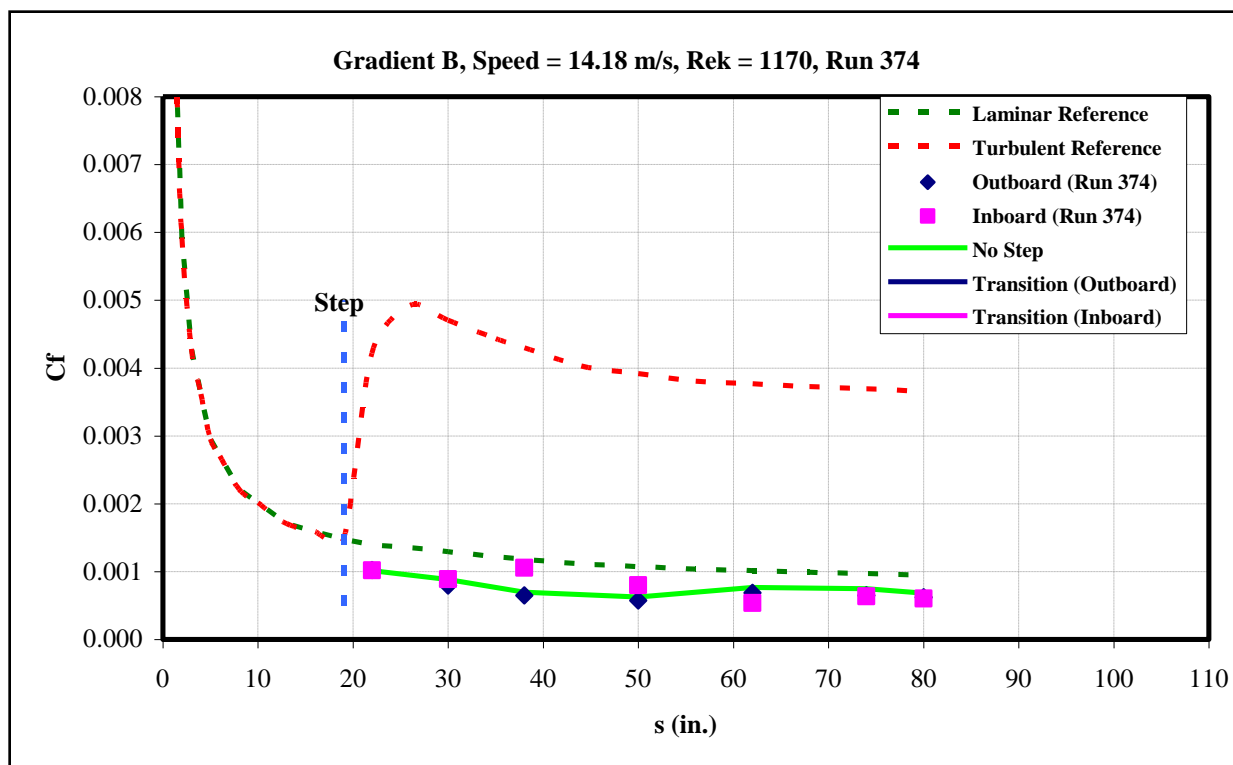


Figure 276: Gradient-B, $k=0.055$ -in forward step, $U=14.18$ m/s skin-friction distribution.

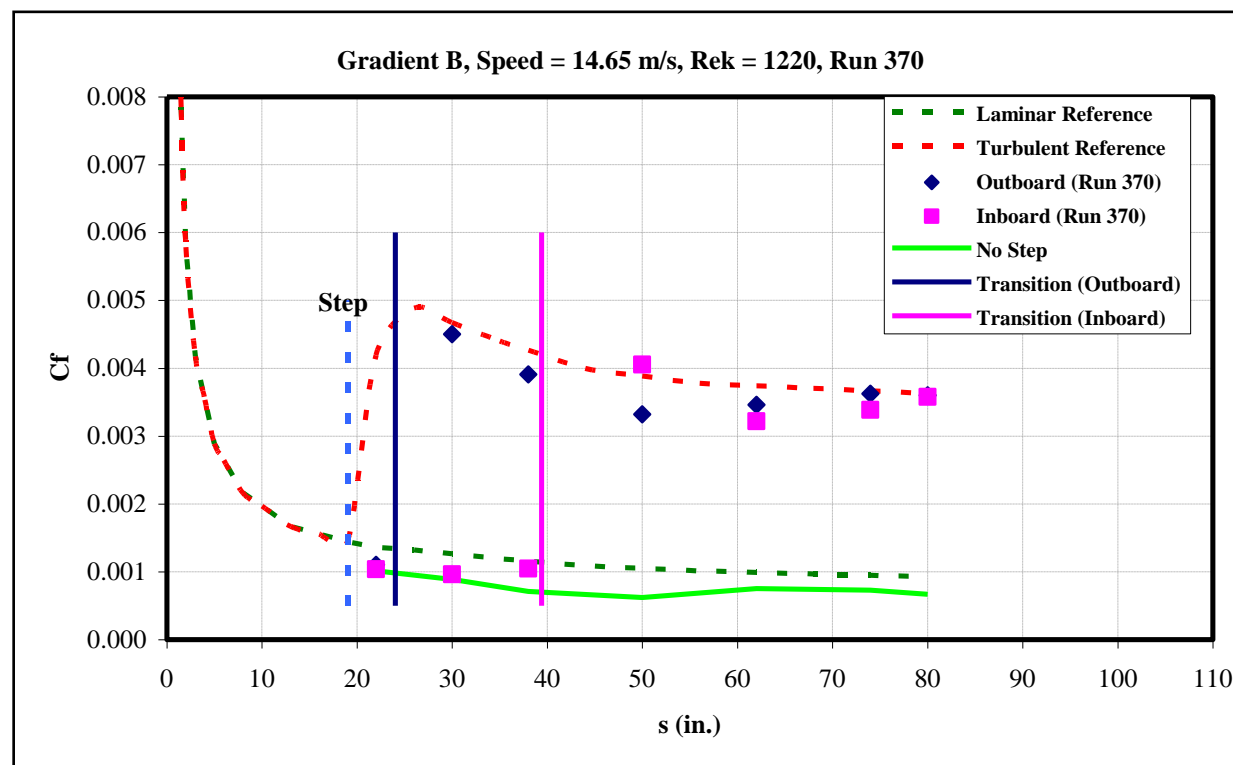


Figure 277: Gradient-B, $k=0.055$ -in forward step, $U=14.65$ m/s skin-friction distribution.

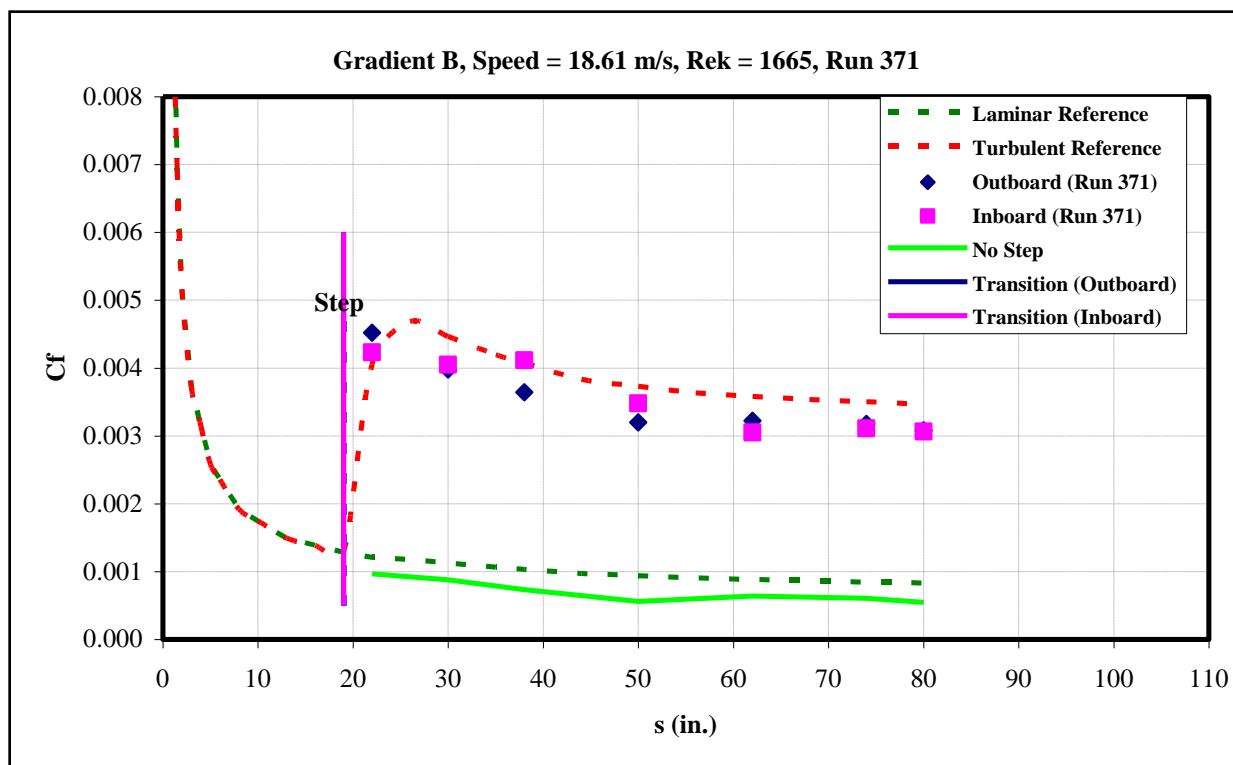


Figure 278: Gradient-B, $k=0.055$ -in forward step, $U=18.61$ m/s skin-friction distribution.

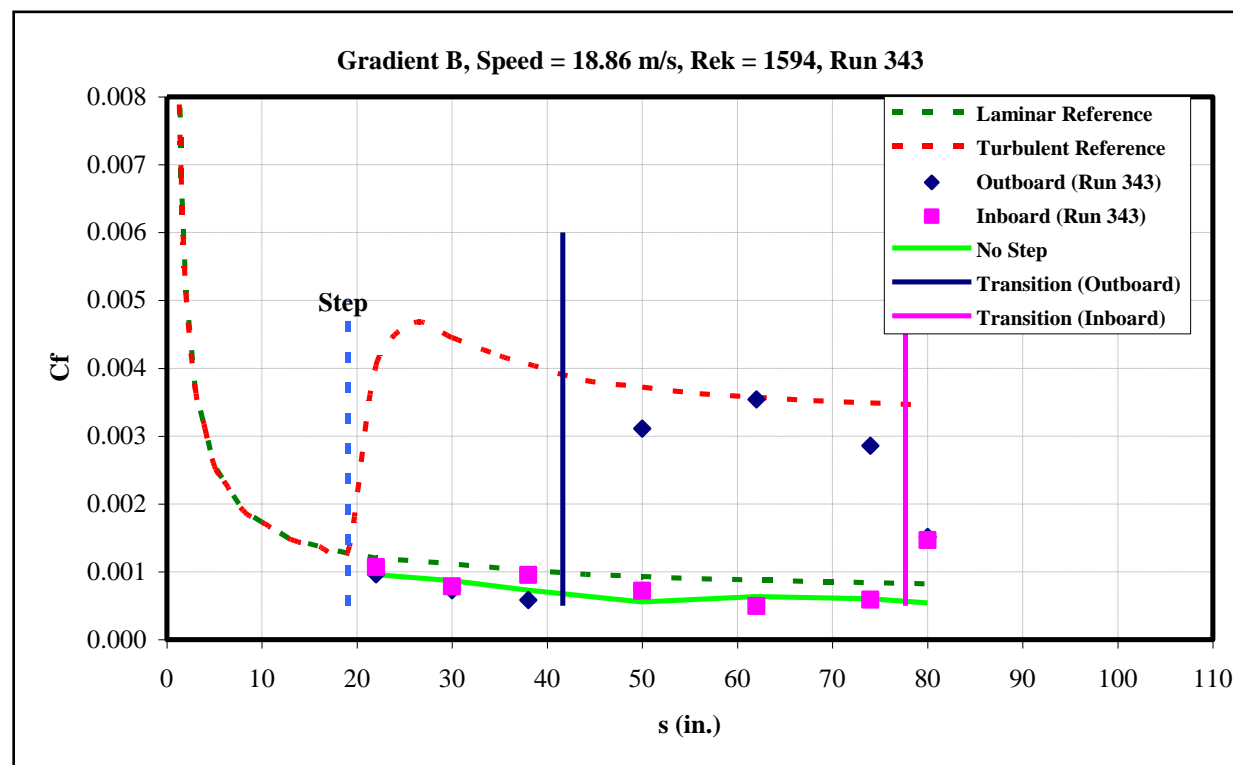


Figure 279: Gradient-B, $k=0.055$ -in forward step, $U=18.86$ m/s skin-friction distribution.

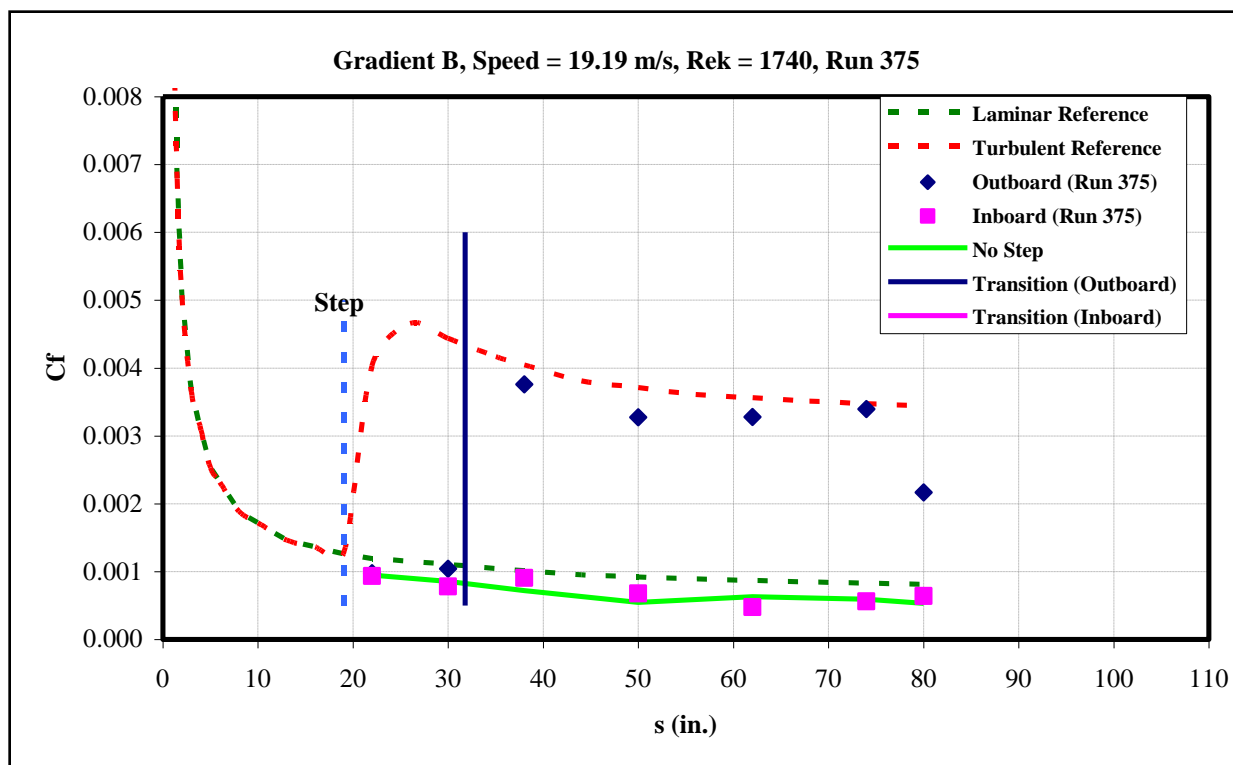


Figure 280: Gradient-B, $k=0.055$ -in forward step, $U=19.19$ m/s skin-friction distribution.

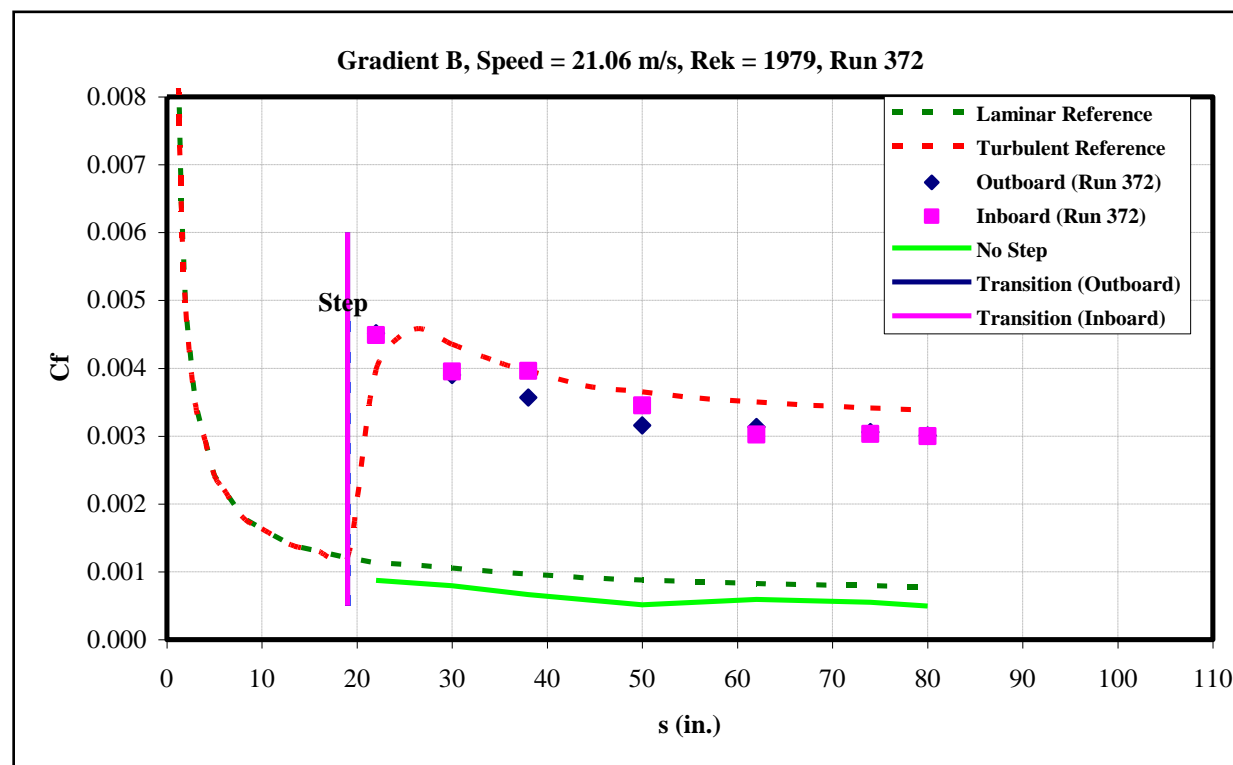


Figure 281: Gradient-B, $k=0.055$ -in forward step, $U=21.06$ m/s skin-friction distribution.

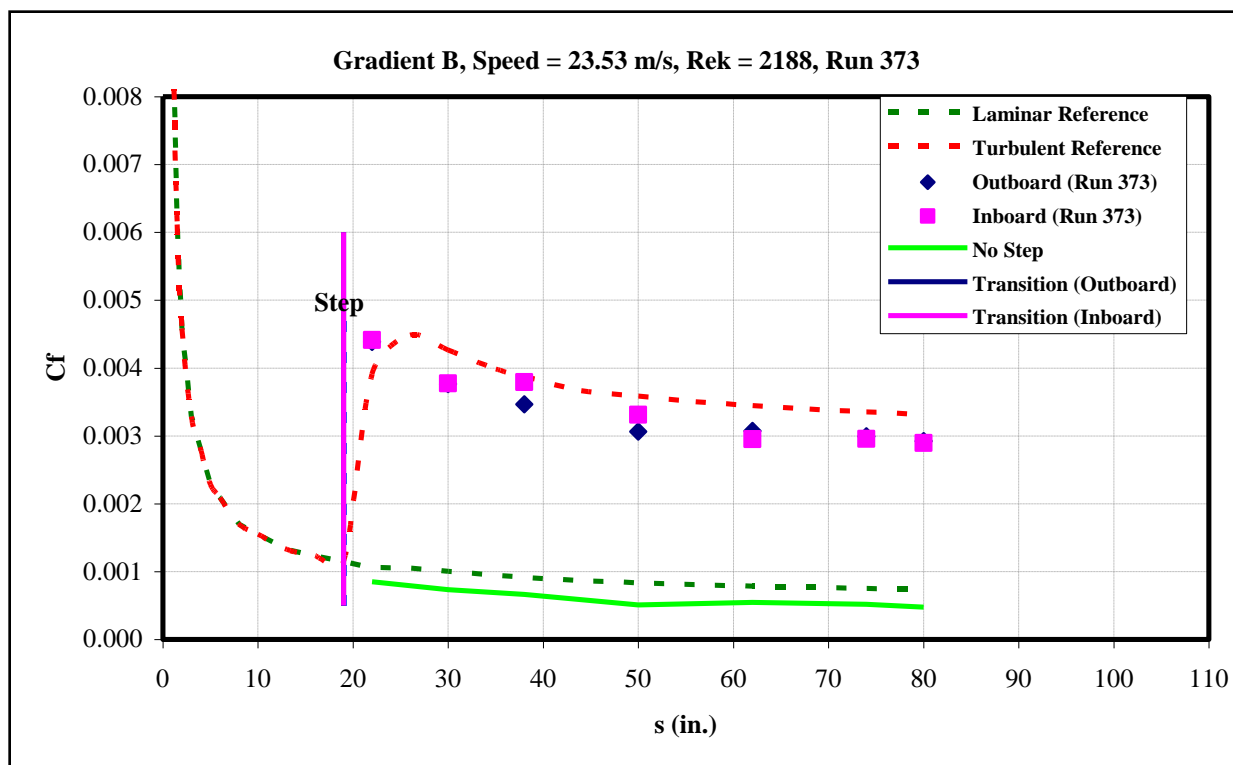


Figure 282: Gradient-B, $k=0.055$ -in forward step, $U=23.53$ m/s skin-friction distribution.

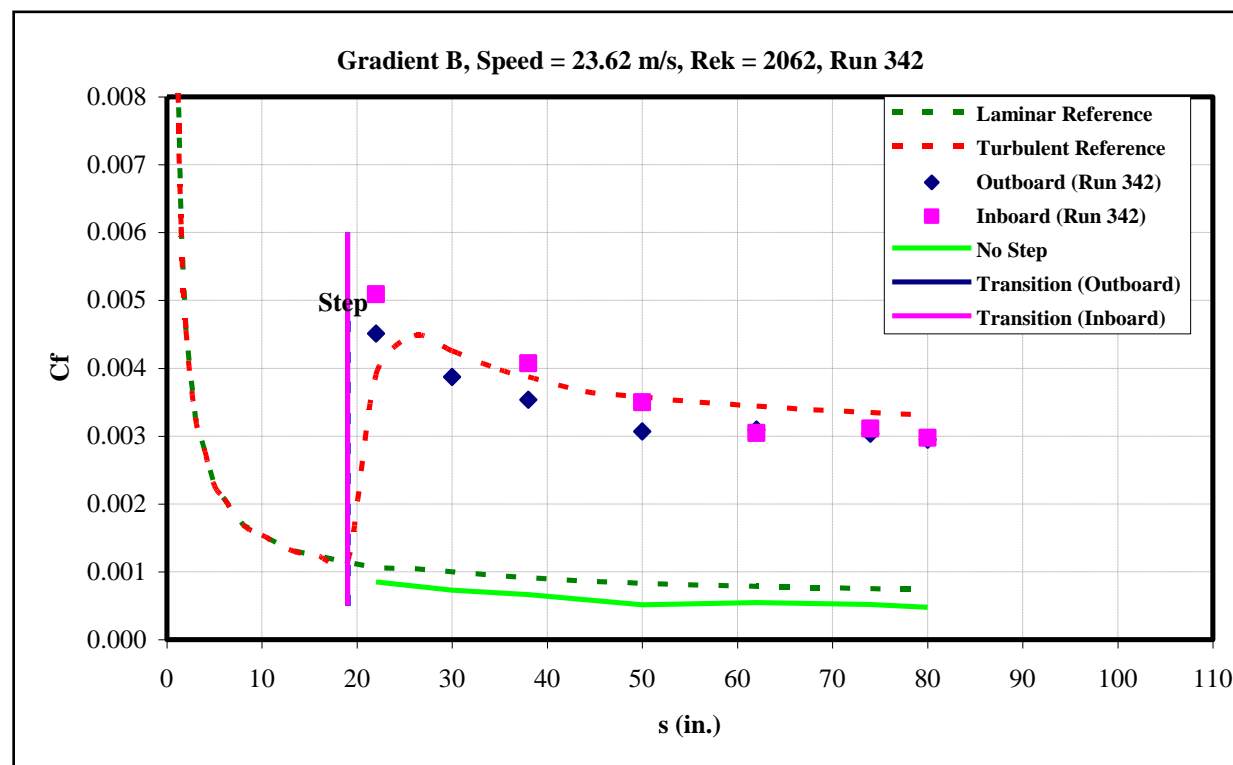


Figure 283: Gradient-B, $k=0.055$ -in forward step, $U=23.62$ m/s skin-friction distribution.

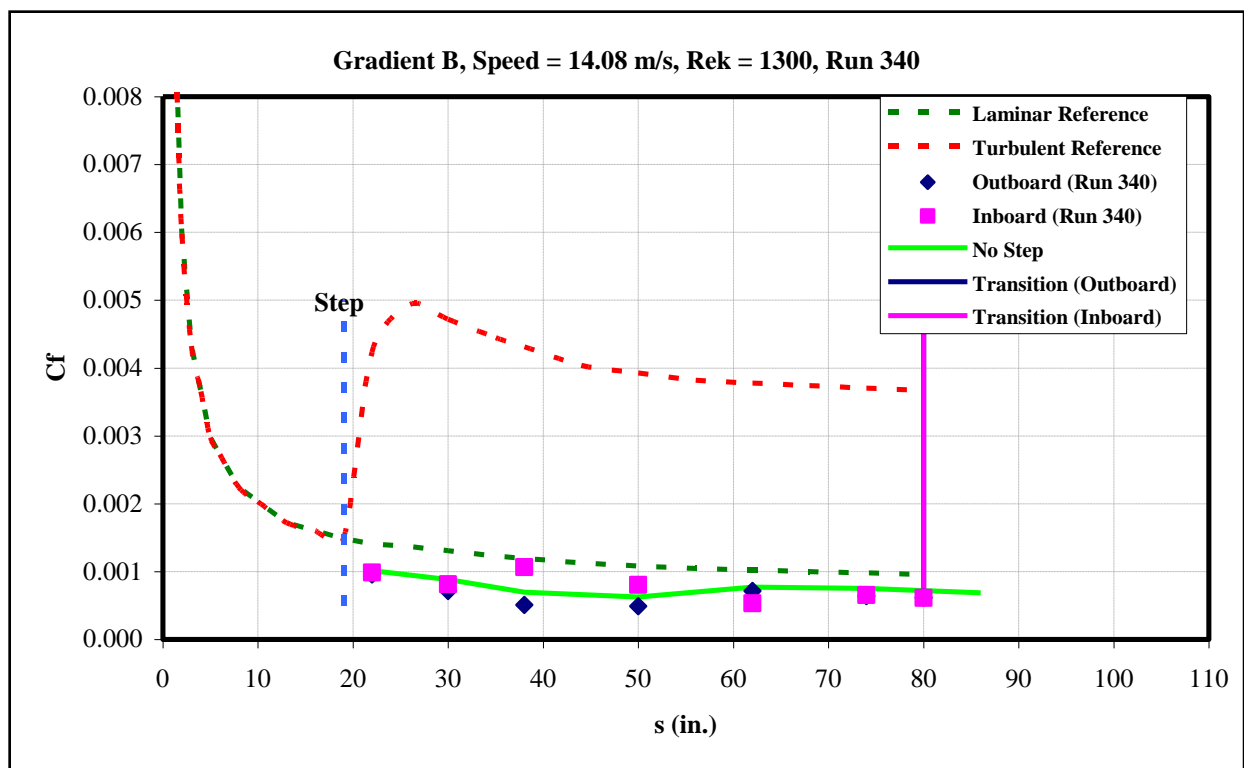


Figure 284: Gradient-B, $k=0.06$ -in forward step, $U=14.08$ m/s skin-friction distribution.

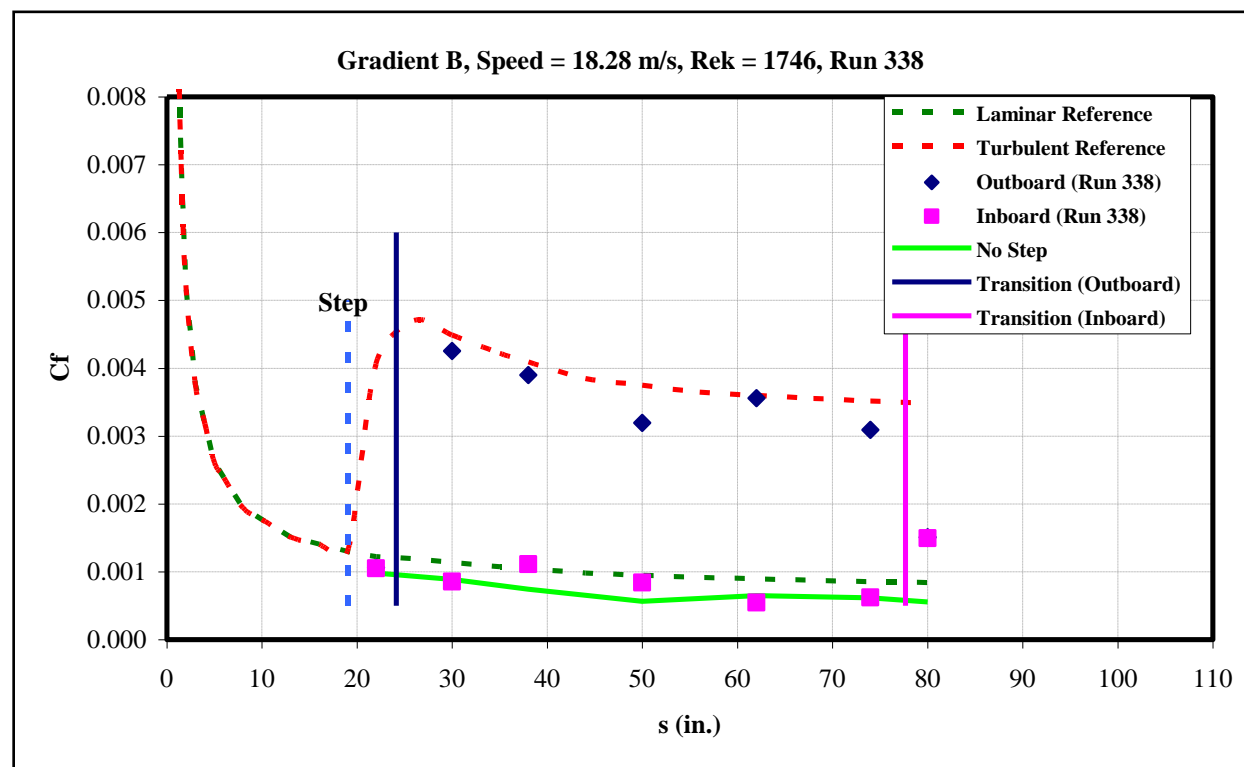


Figure 285: Gradient-B, $k=0.06$ -in forward step, $U=18.28$ m/s skin-friction distribution.

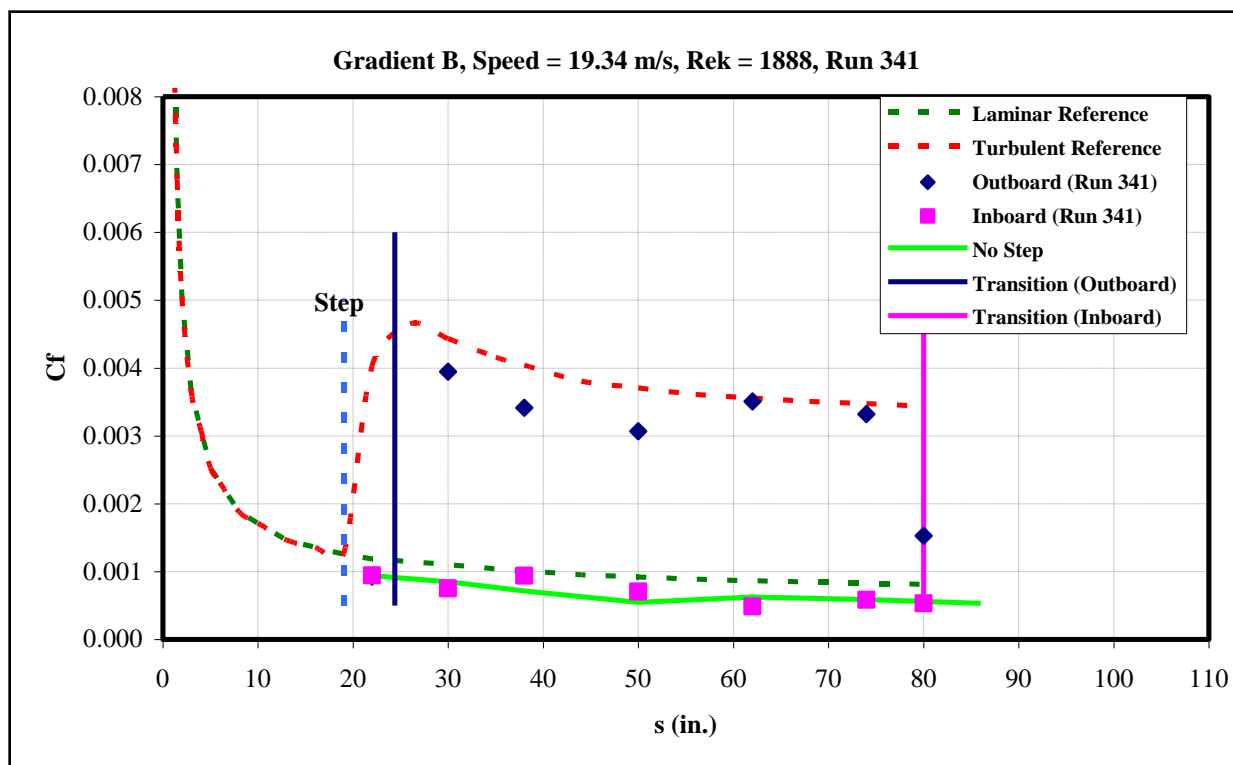


Figure 286: Gradient-B, $k=0.06$ -in forward step, $U=19.34$ m/s skin-friction distribution.

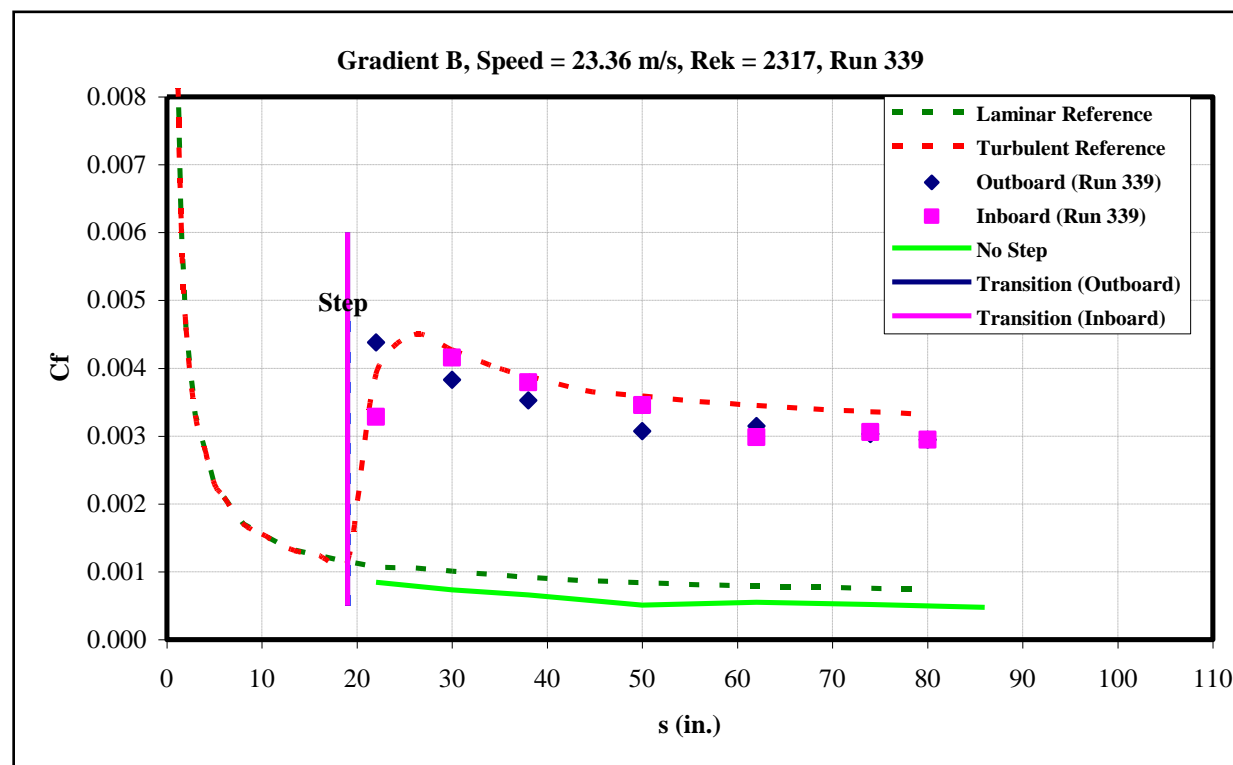


Figure 287: Gradient-B, $k=0.06$ -in forward step, $U=23.36$ m/s skin-friction distribution.

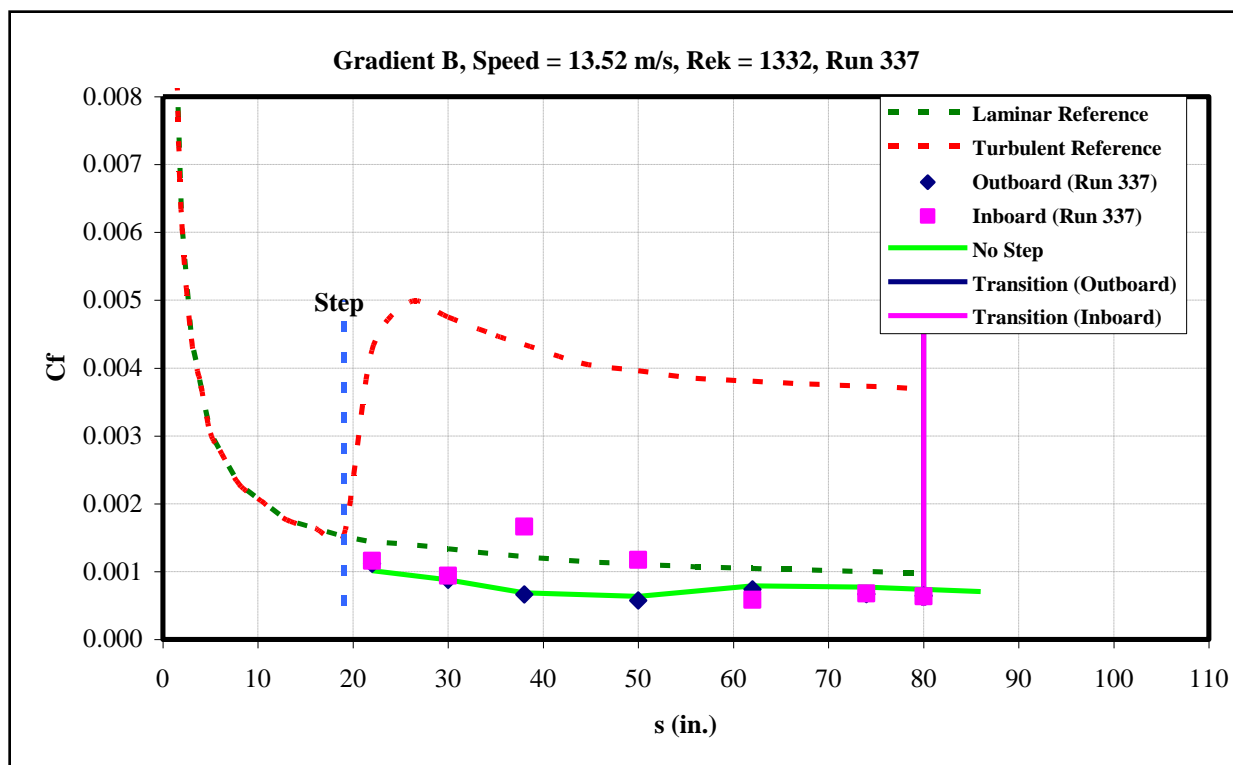


Figure 288: Gradient-B, $k=0.065$ -in forward step, $U=13.52$ m/s skin-friction distribution.

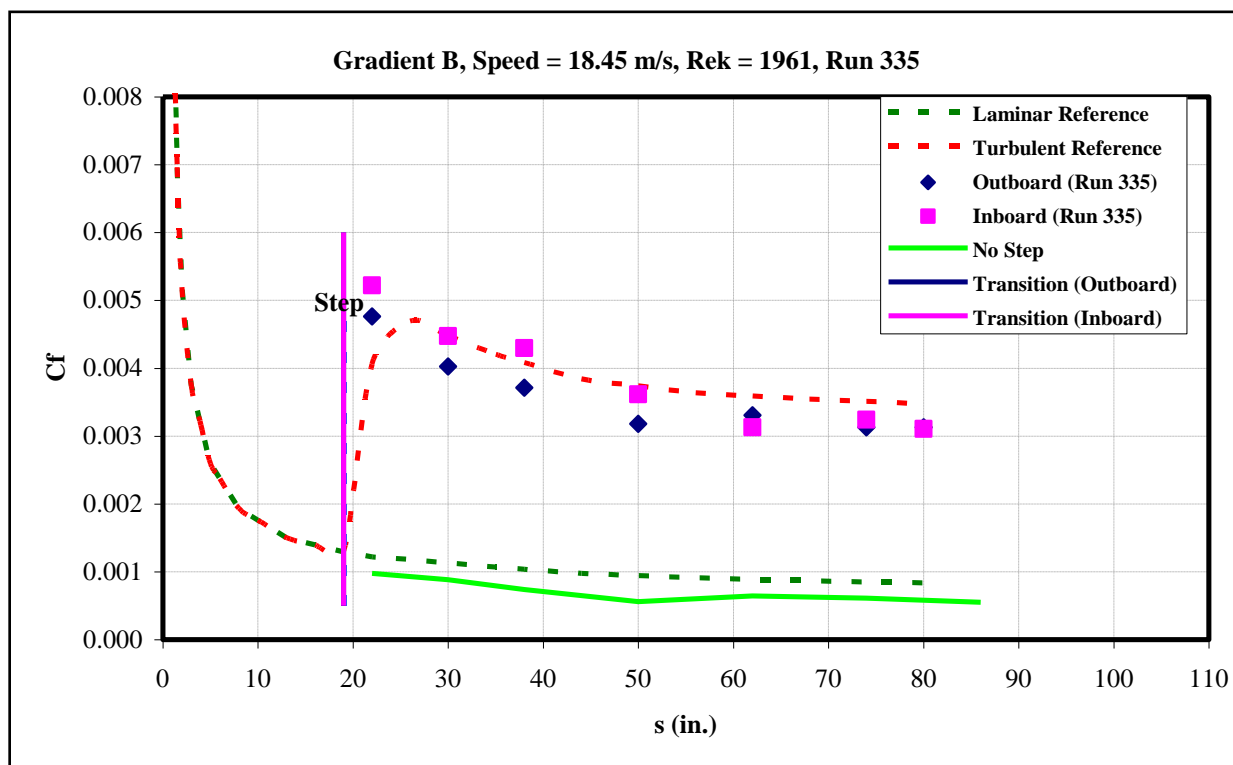


Figure 289: Gradient-B, $k=0.065$ -in forward step, $U=18.45$ m/s skin-friction distribution.

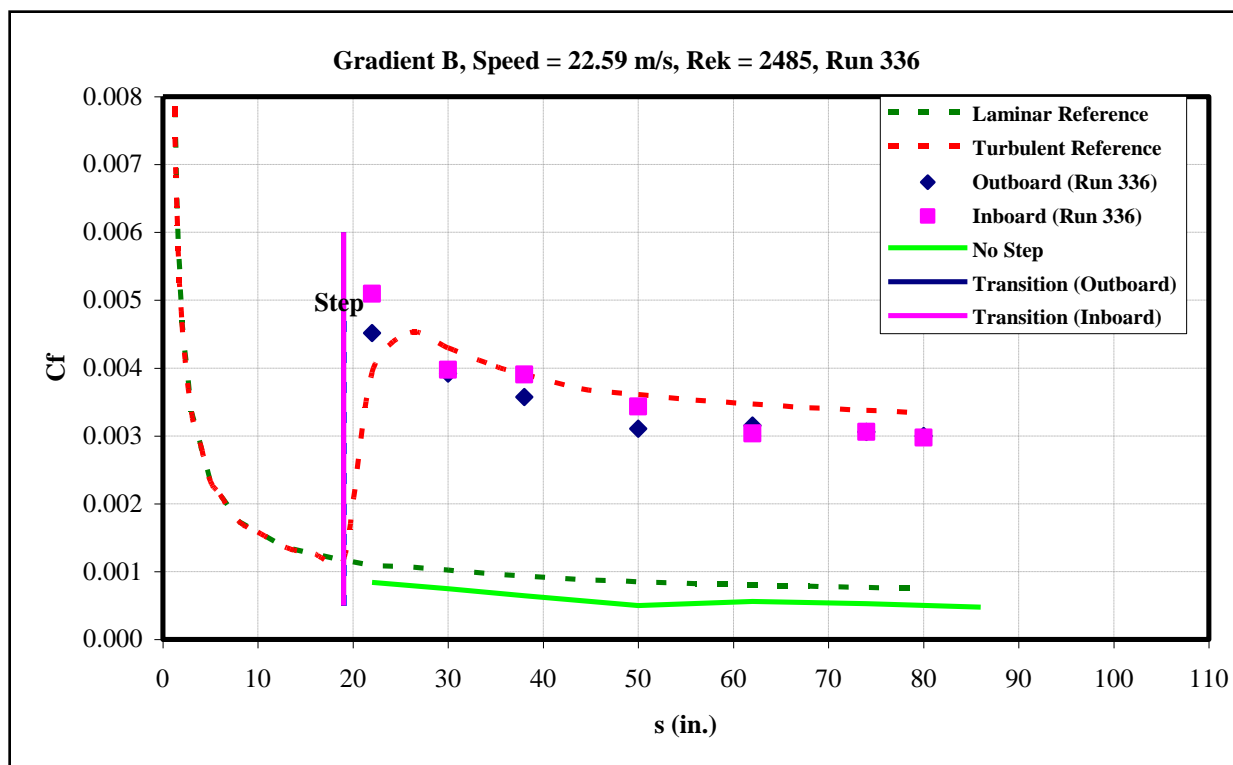


Figure 290: Gradient-B, $k=0.065$ -in forward step, $U=22.59$ m/s skin-friction distribution.

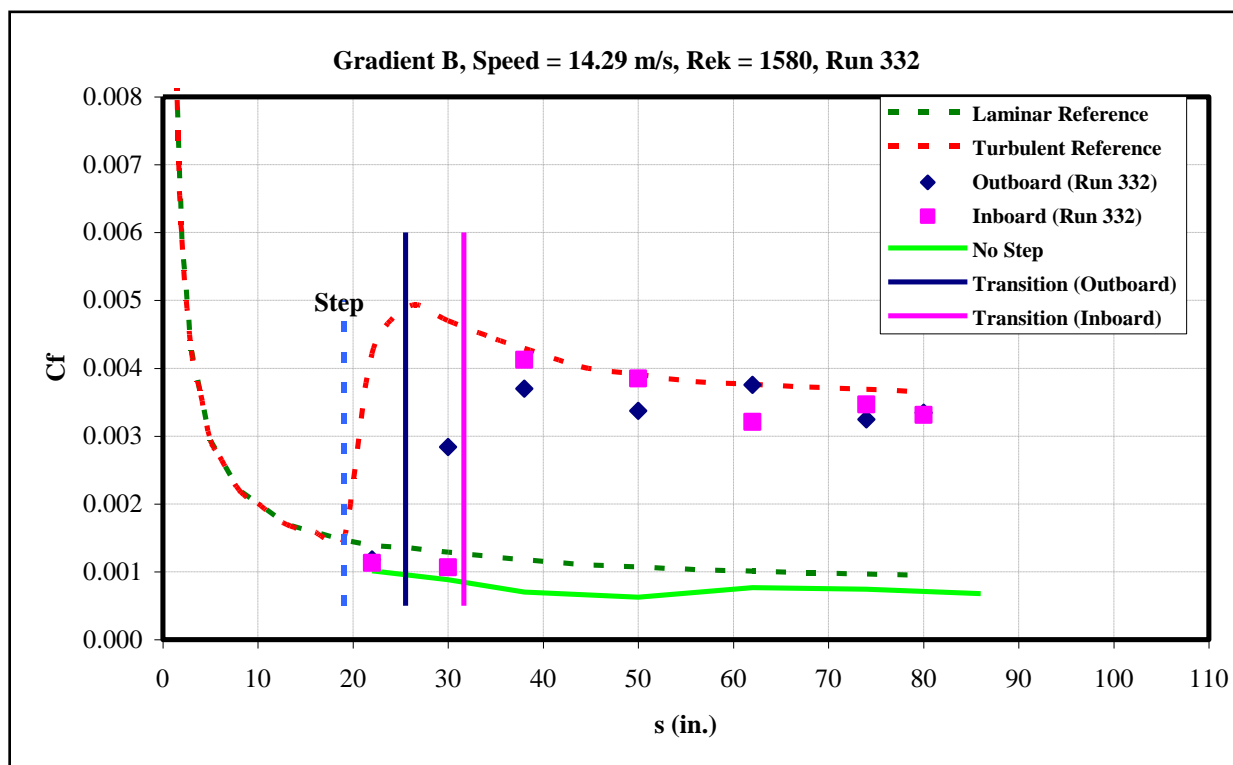


Figure 291: Gradient-B, $k=0.07$ -in forward step, $U=14.29$ m/s skin-friction distribution.

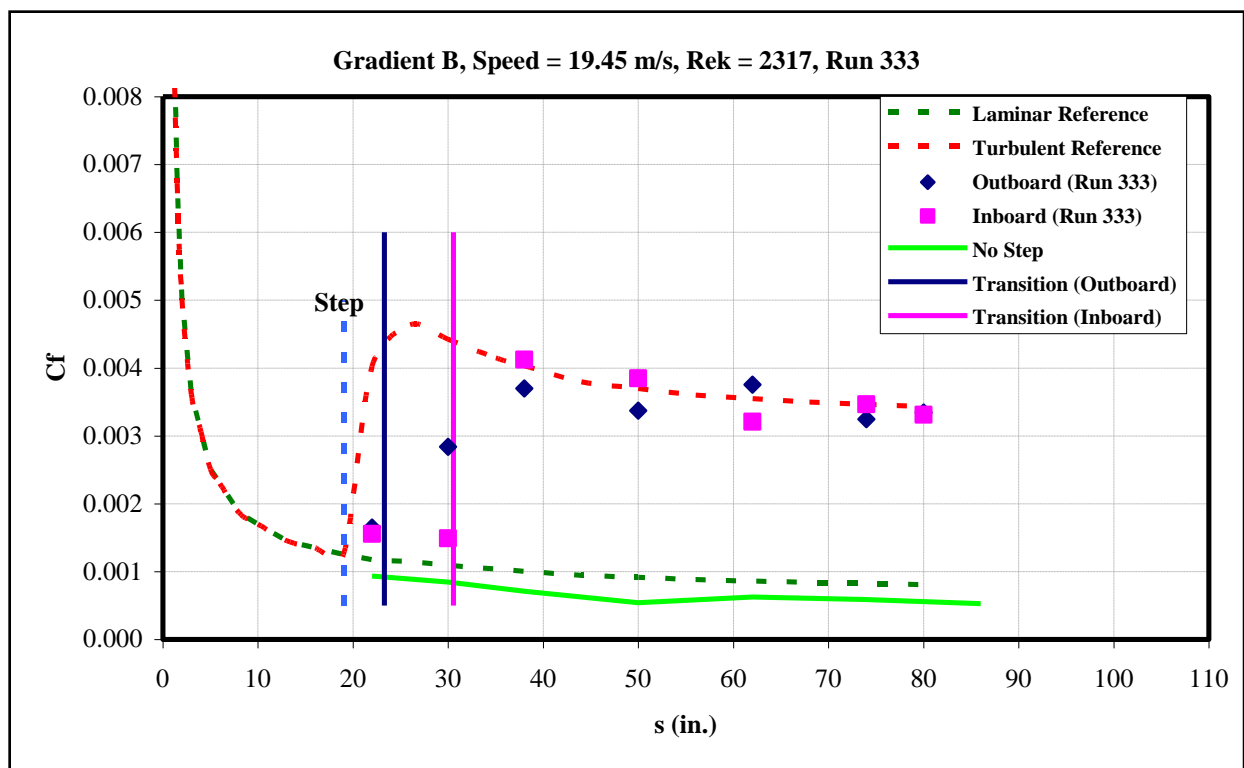


Figure 292: Gradient-B, $k=0.07$ -in forward step, $U=19.45$ m/s skin-friction distribution.

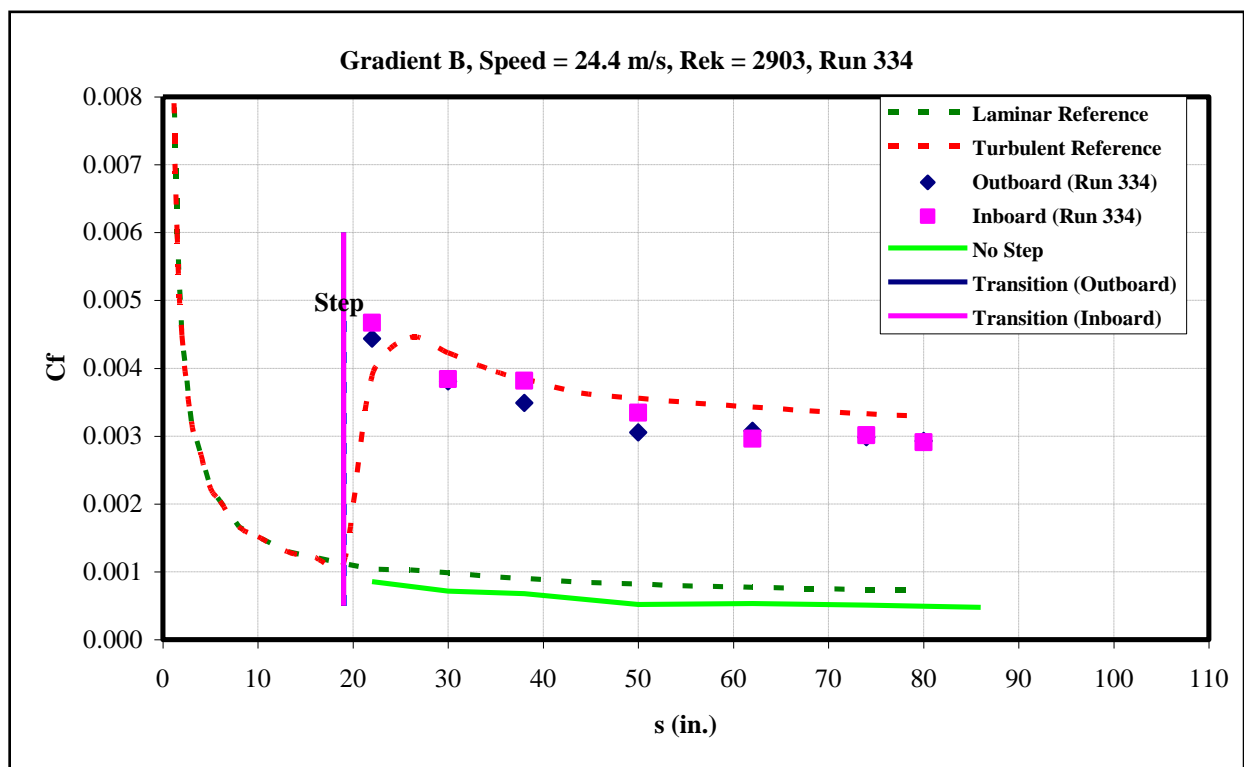


Figure 293: Gradient-B, $k=0.07$ -in forward step, $U=24.4$ m/s skin-friction distribution.

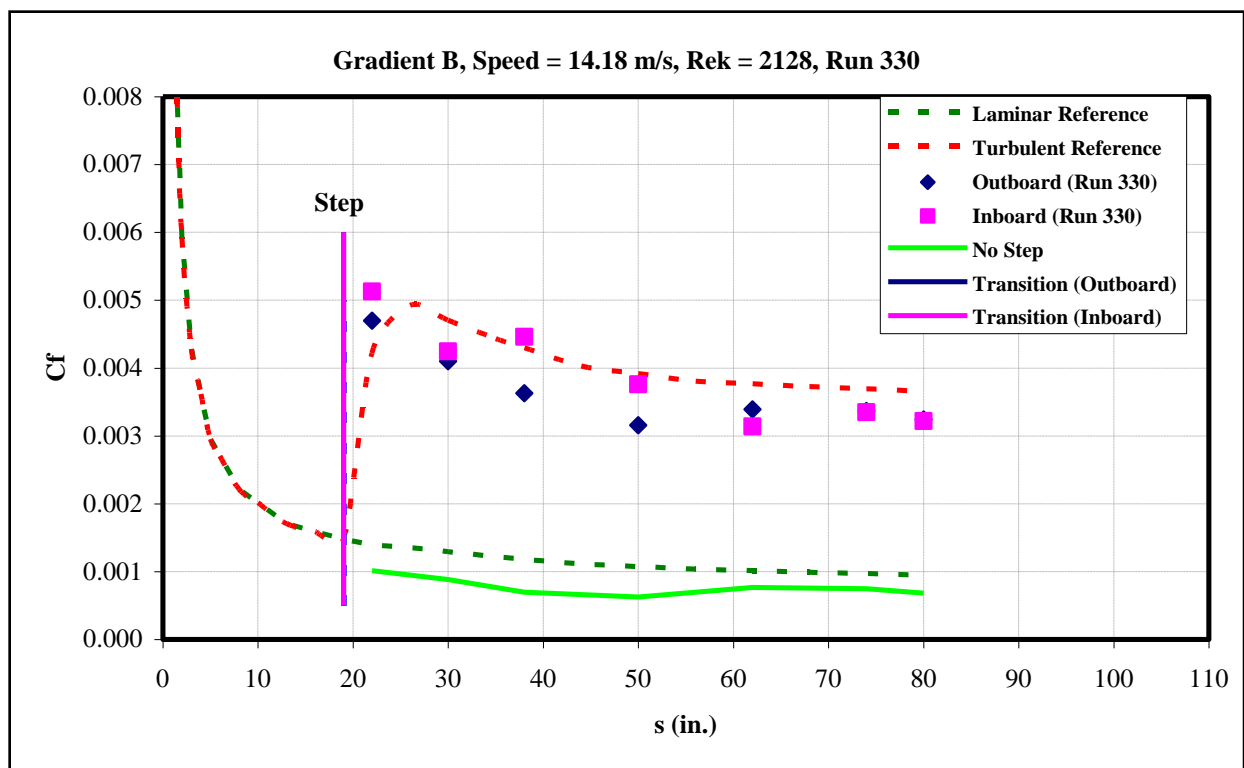


Figure 294: Gradient-B, $k=0.09$ -in forward step, $U=14.18$ m/s skin-friction distribution.

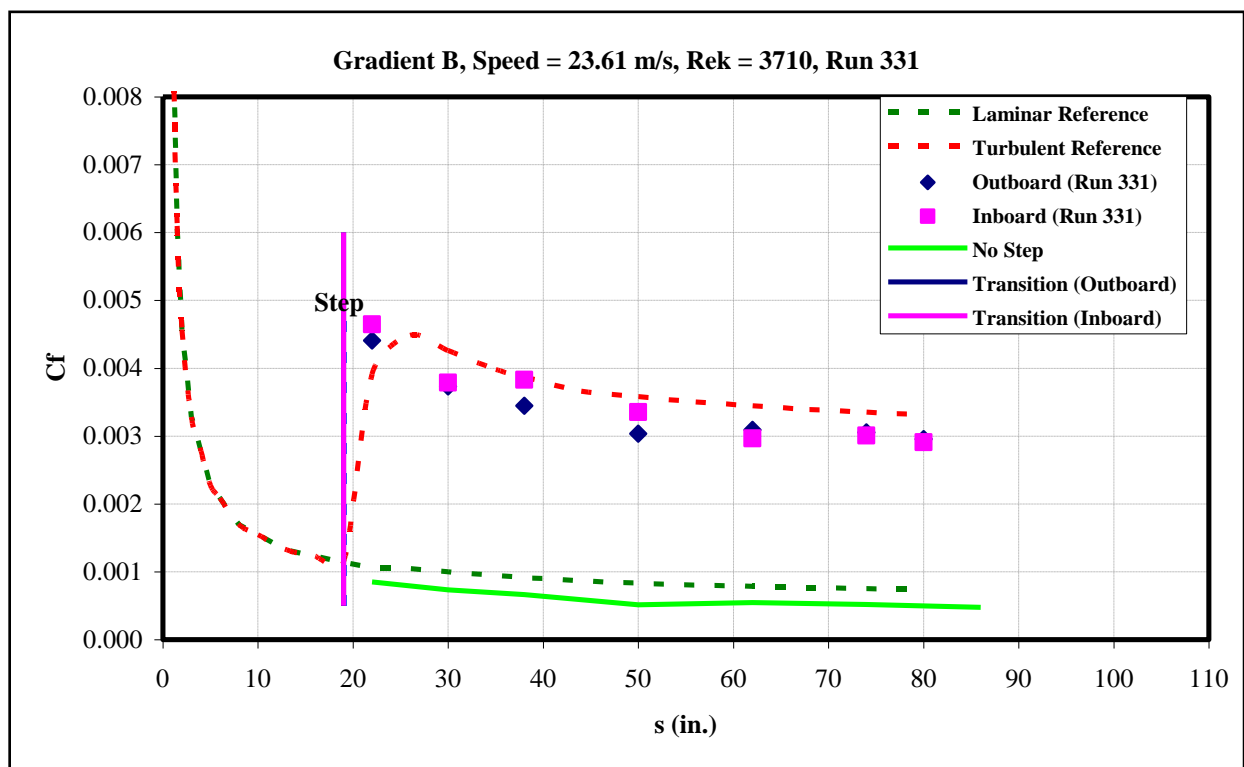


Figure 295: Gradient-B, $k=0.09$ -in forward step, $U=23.61$ m/s skin-friction distribution.

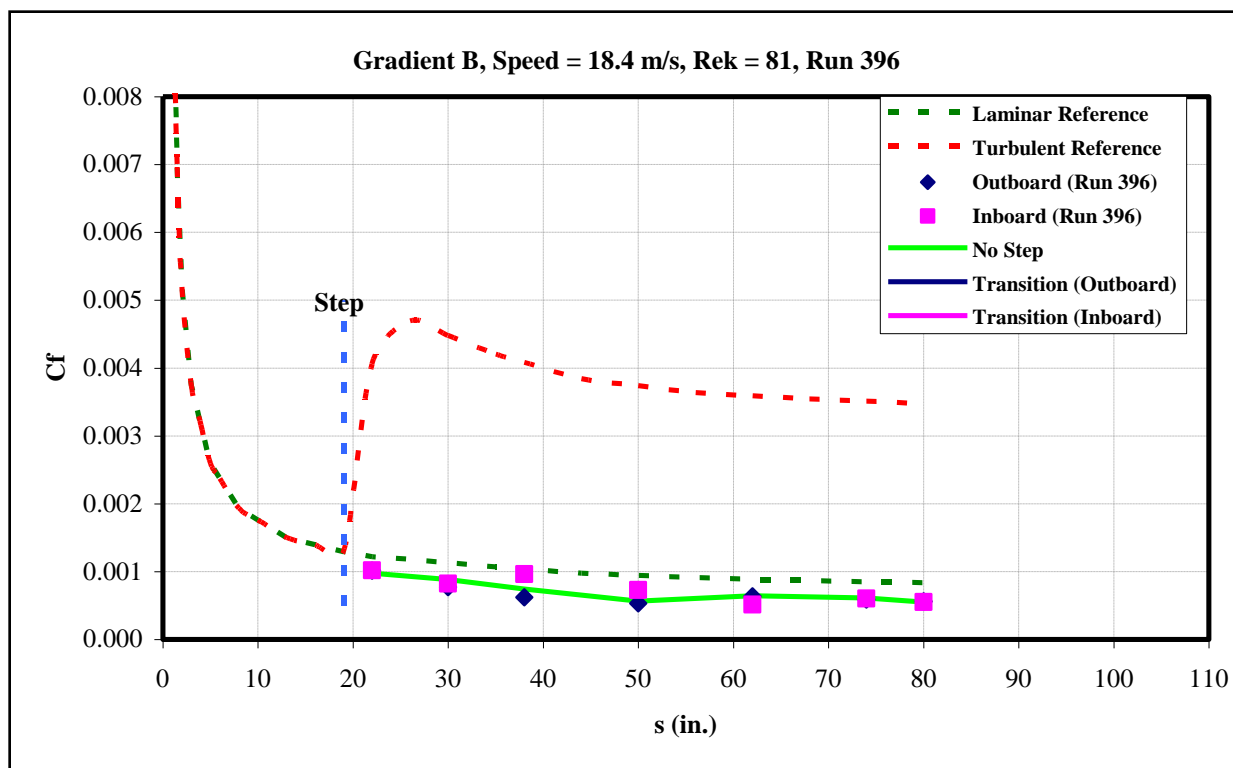


Figure 296: Gradient-B, $k=0.01$ -in aft step, $U=18.4$ m/s skin-friction distribution.

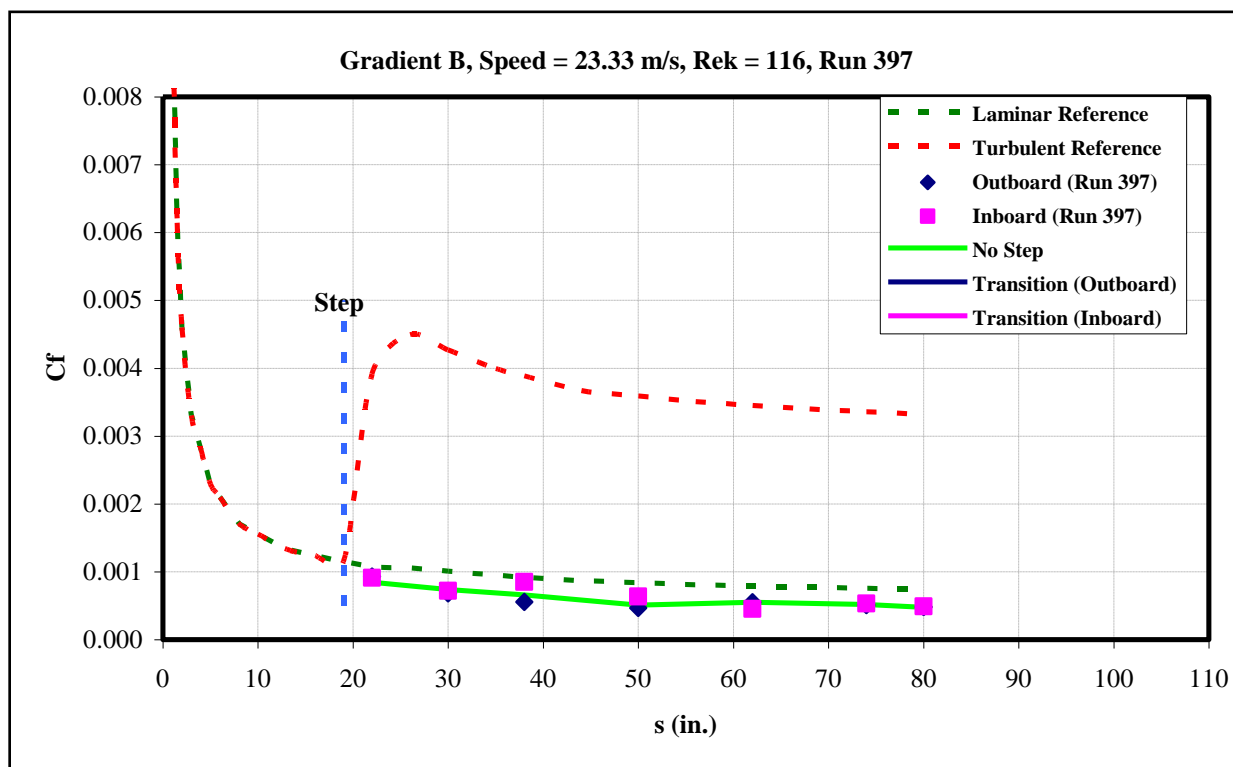


Figure 297: Gradient-B, $k=0.01$ -in aft step, $U=23.33$ m/s skin-friction distribution.

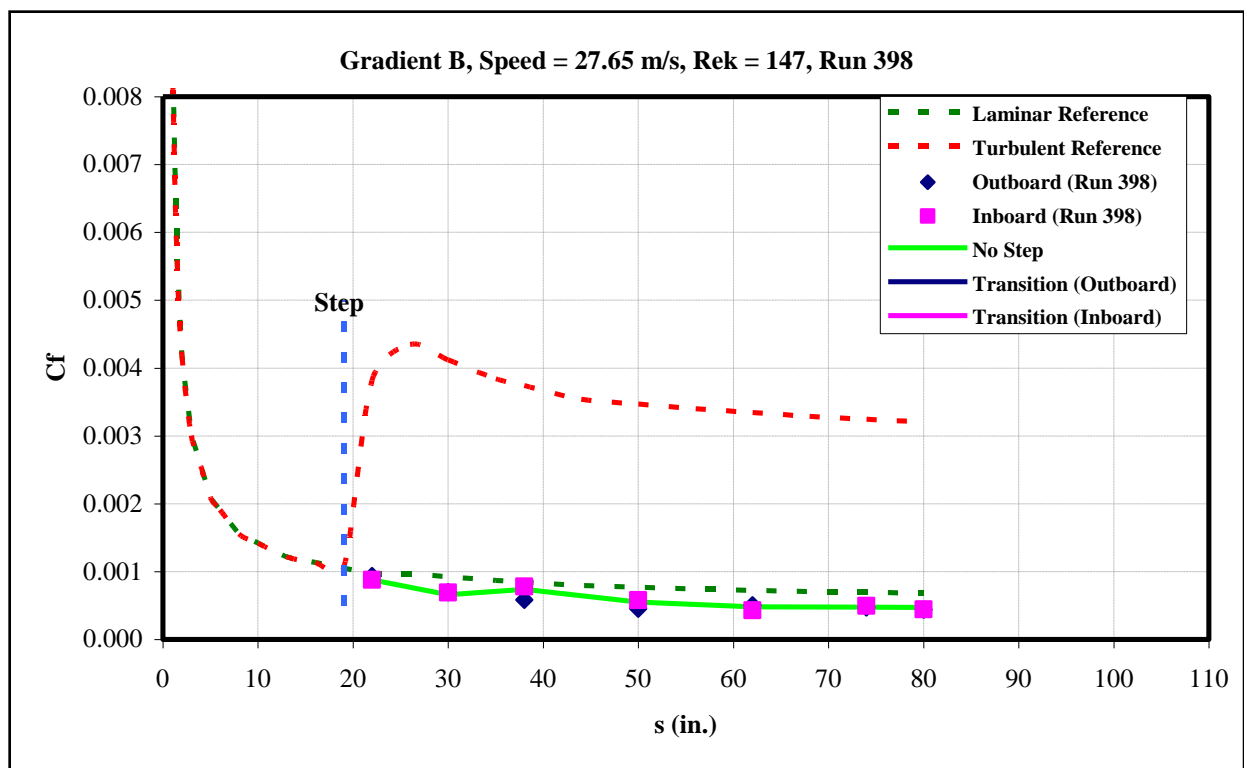


Figure 298: Gradient-B, $k=0.01$ -in aft step, $U=27.65$ m/s skin-friction distribution.

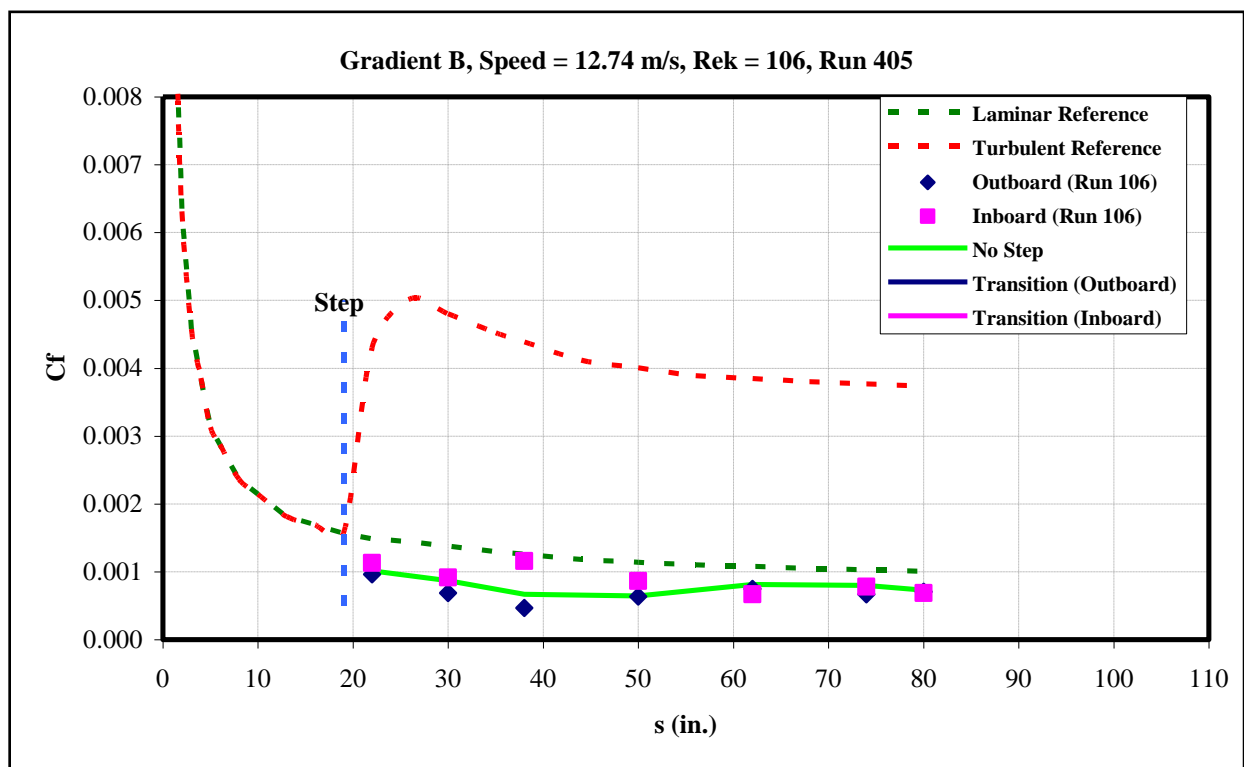


Figure 299: Gradient-B, $k=0.015$ -in aft step, $U=12.74$ m/s skin-friction distribution.

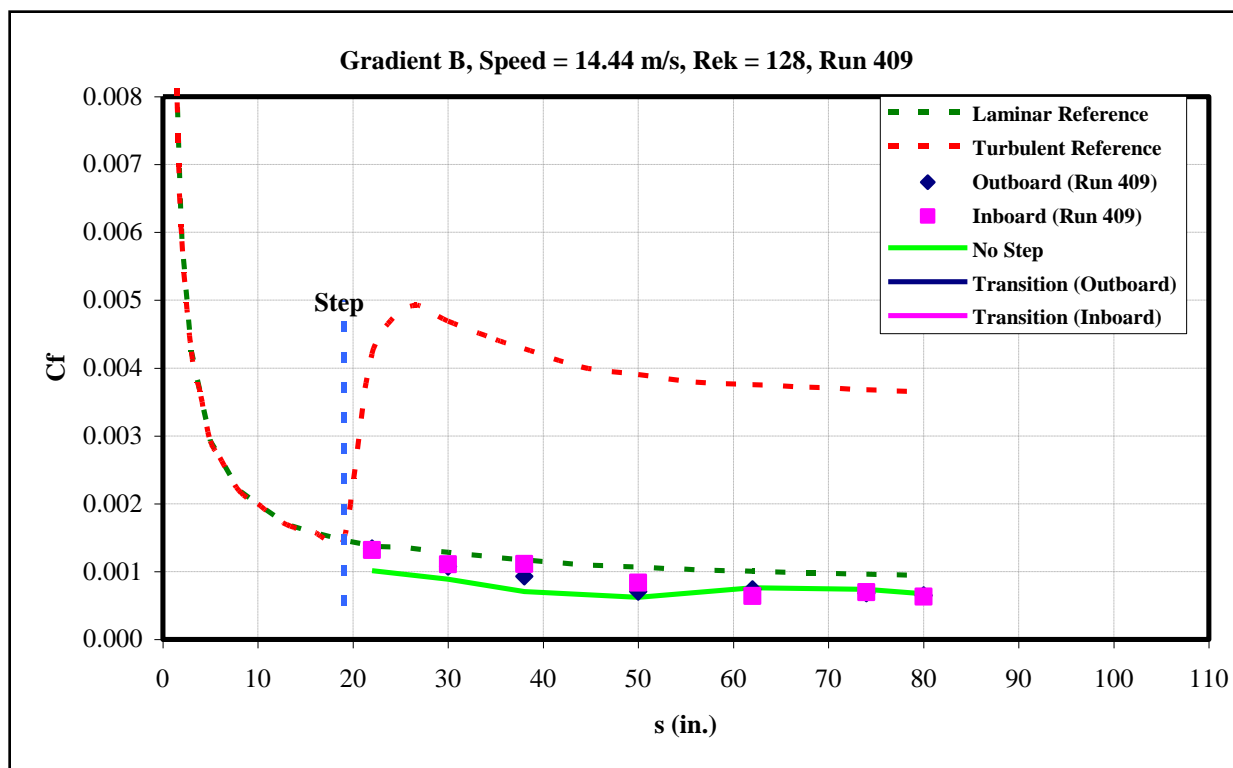


Figure 300: Gradient-B, $k=0.015$ -in aft step, $U=14.44$ m/s skin-friction distribution.

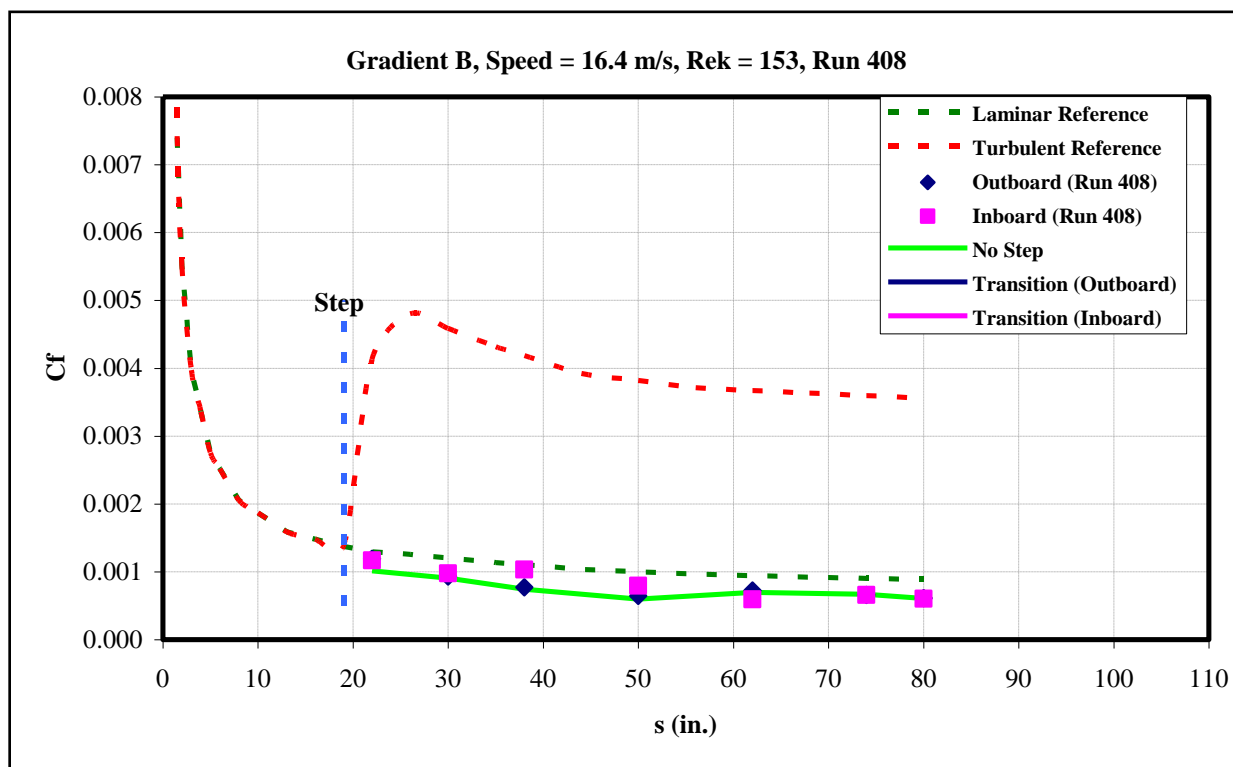


Figure 301: Gradient-B, $k=0.015$ -in aft step, $U=16.4$ m/s skin-friction distribution.

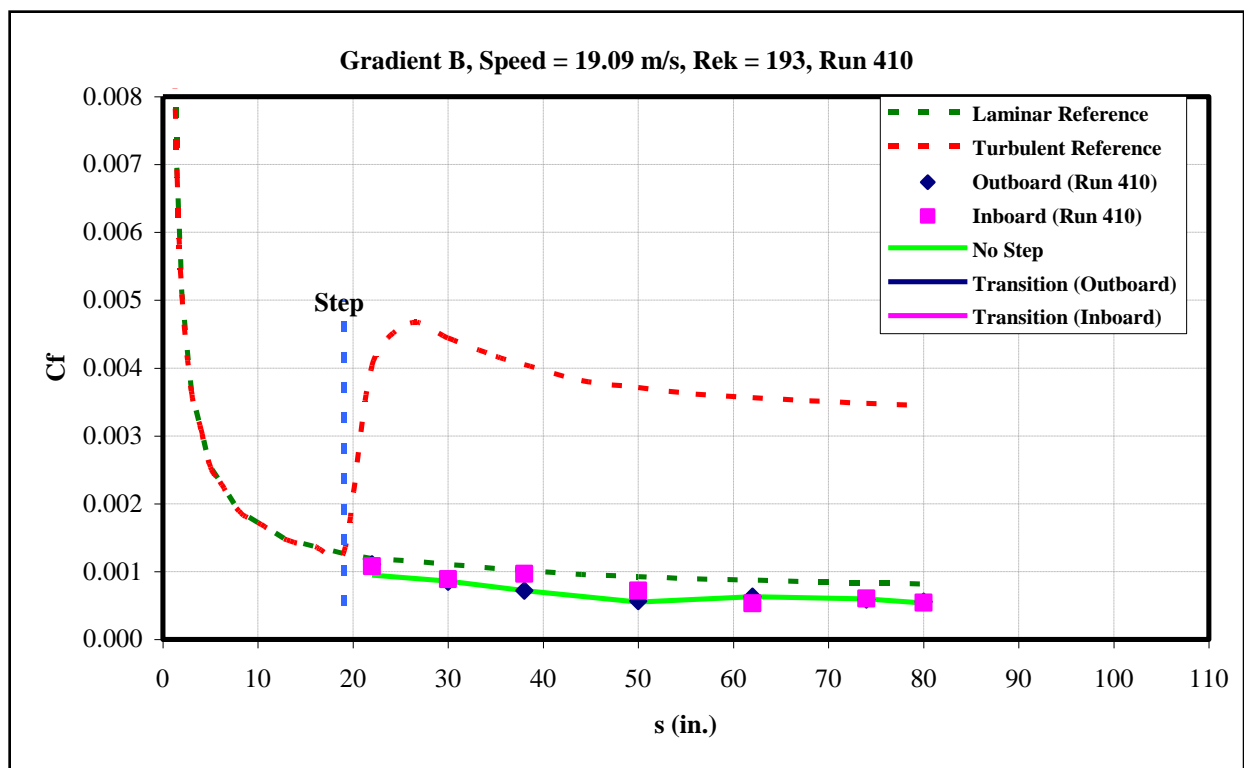


Figure 302: Gradient-B, $k=0.015$ -in aft step, $U=19.09$ m/s skin-friction distribution.

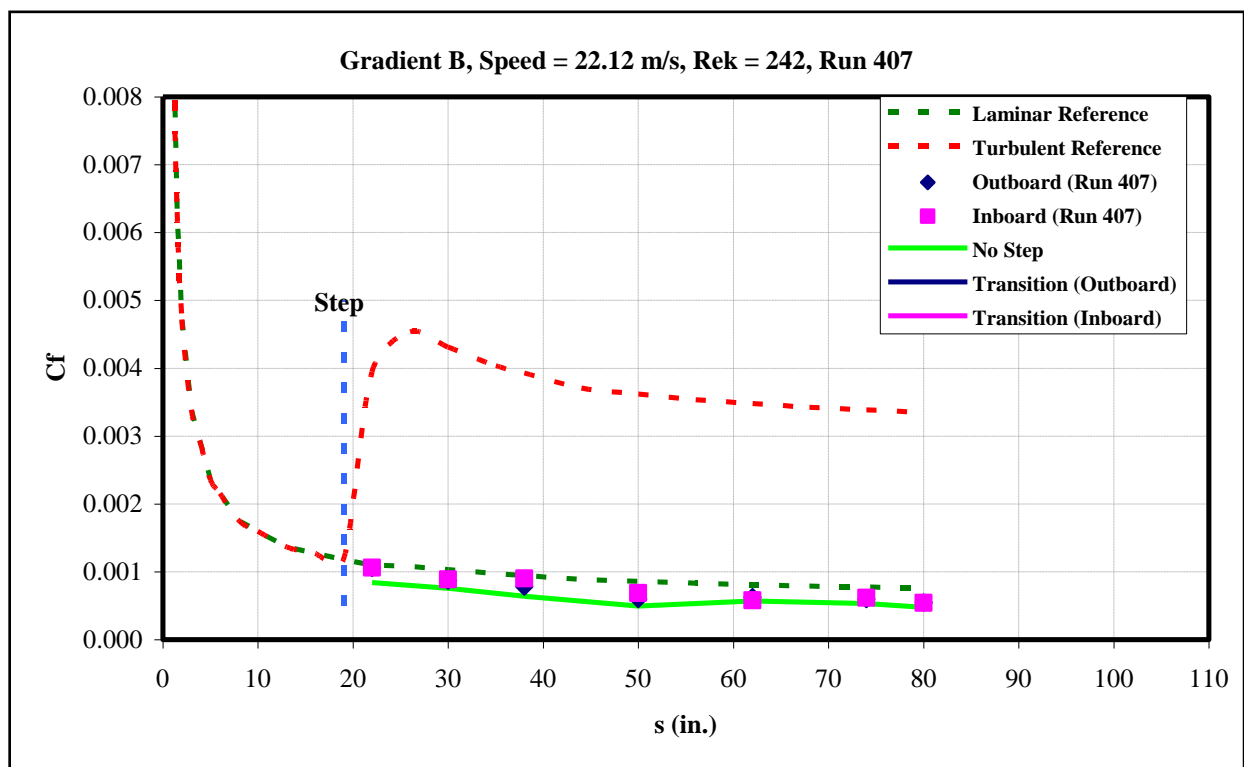


Figure 303: Gradient-B, $k=0.015$ -in aft step, $U=22.12$ m/s skin-friction distribution.

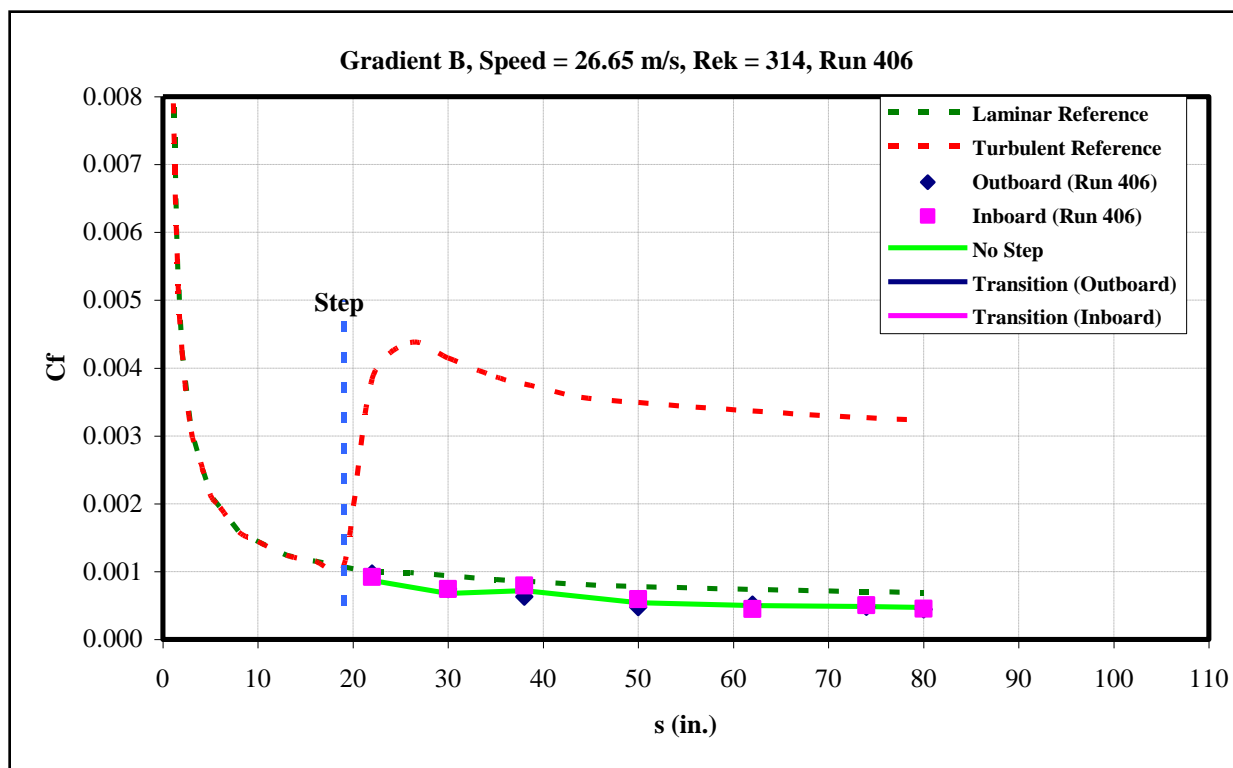


Figure 304: Gradient-B, $k=0.015$ -in aft step, $U=26.65$ m/s skin-friction distribution.

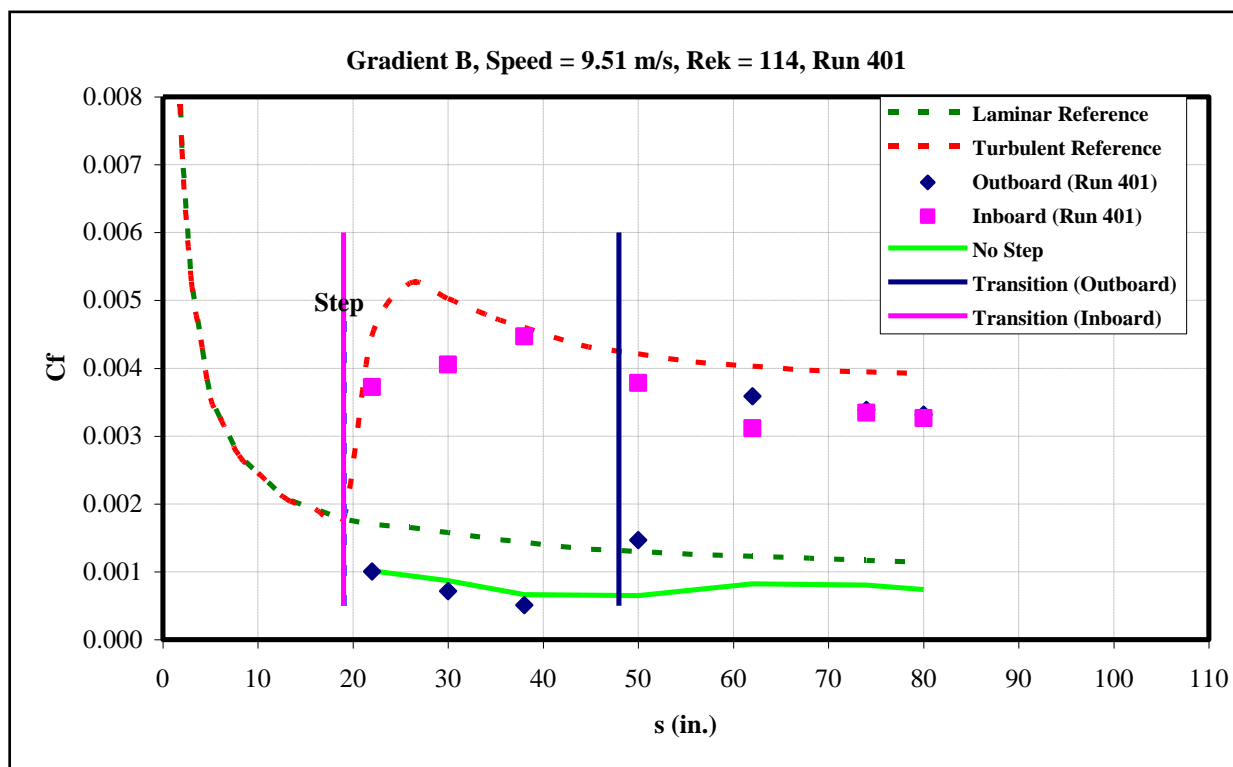


Figure 305: Gradient-B, $k=0.02$ -in aft step, $U=9.51$ m/s skin-friction distribution.

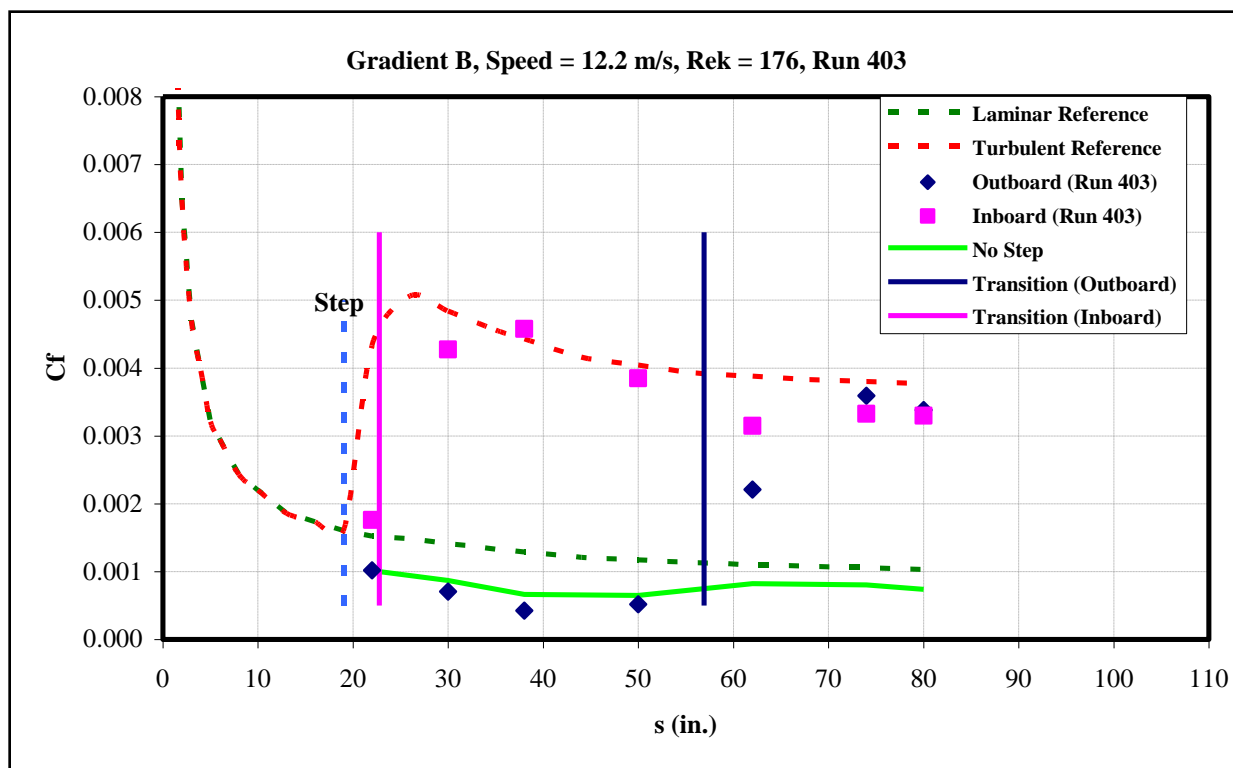


Figure 306: Gradient-B, $k=0.02$ -in aft step, $U=12.2$ m/s skin-friction distribution.

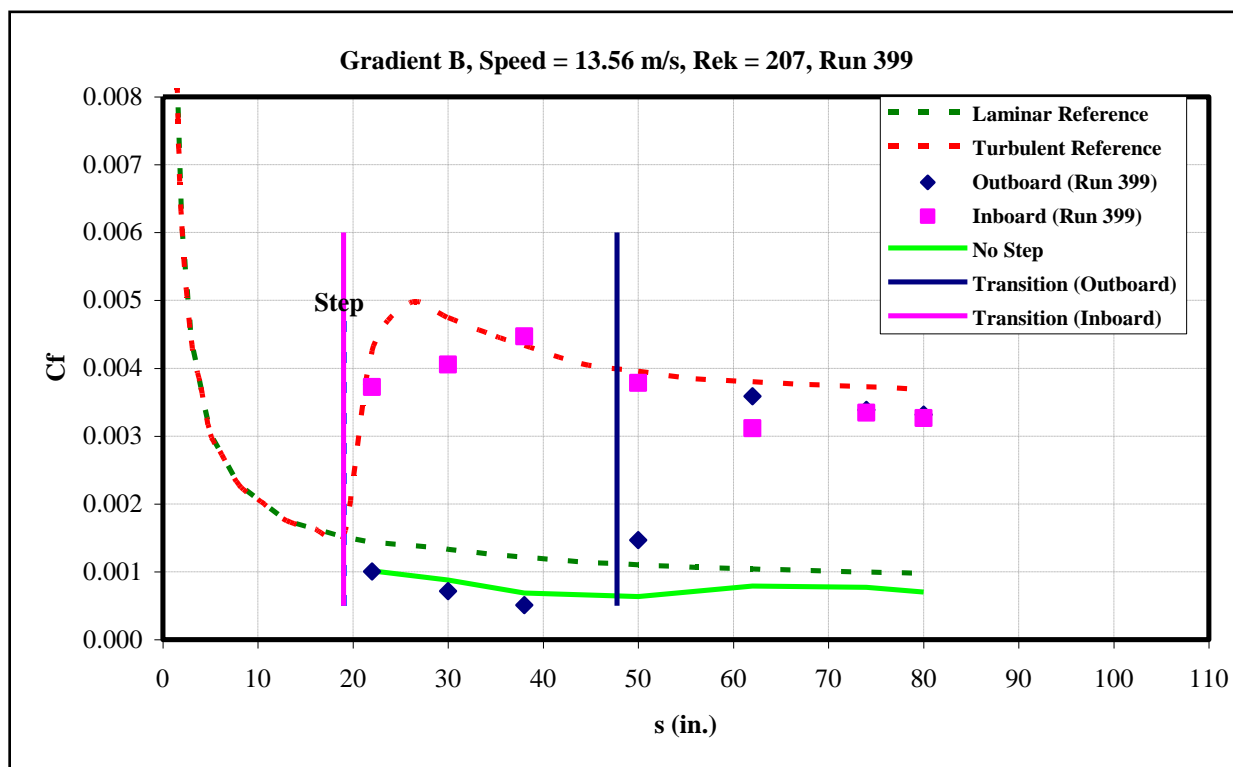


Figure 307: Gradient-B, $k=0.02$ -in aft step, $U=13.56$ m/s skin-friction distribution.

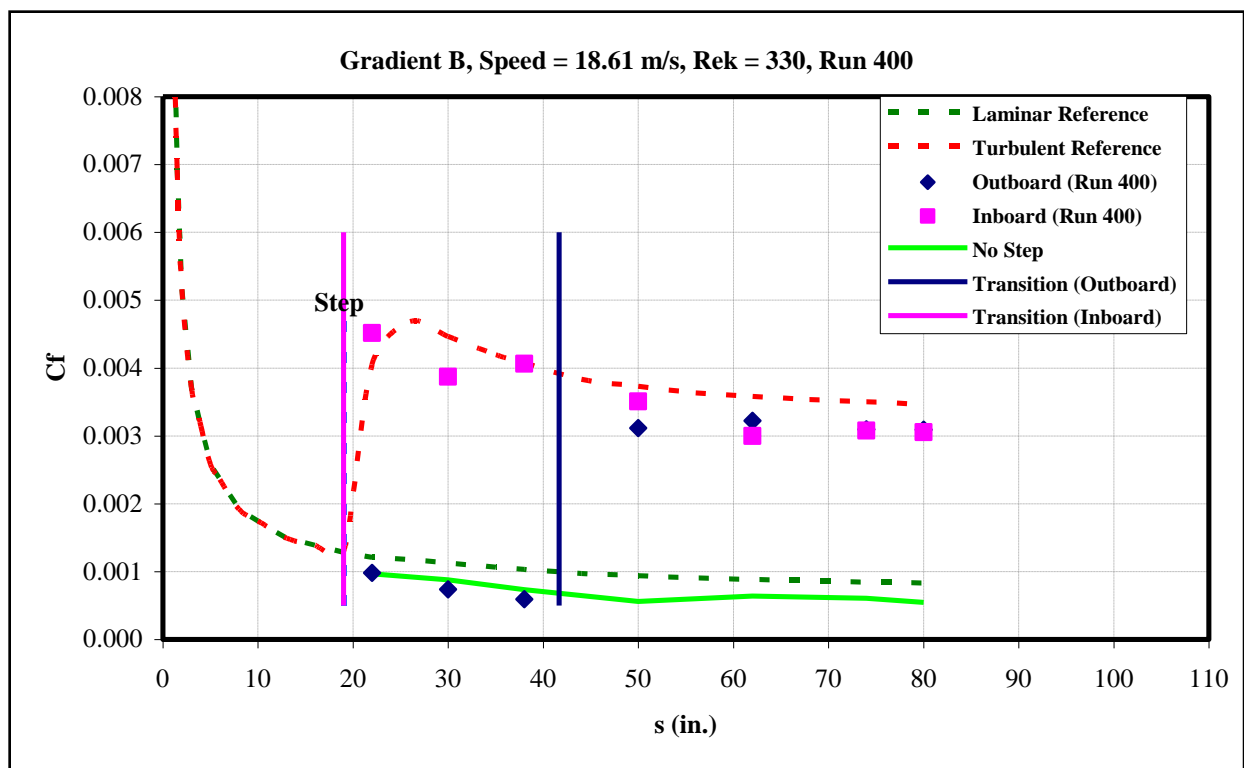


Figure 308: Gradient-B, $k=0.02$ -in aft step, $U=18.61$ m/s skin-friction distribution.

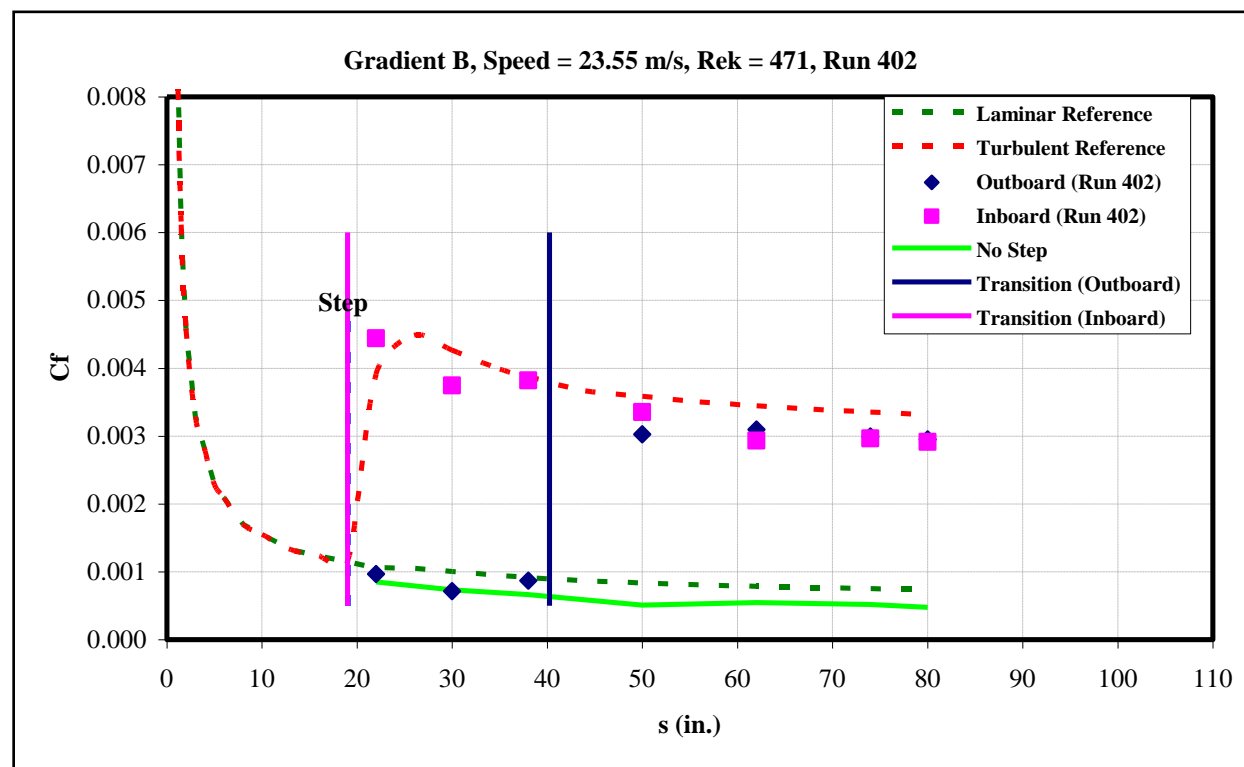


Figure 309: Gradient-B, $k=0.02$ -in aft step, $U=23.55$ m/s skin-friction distribution.

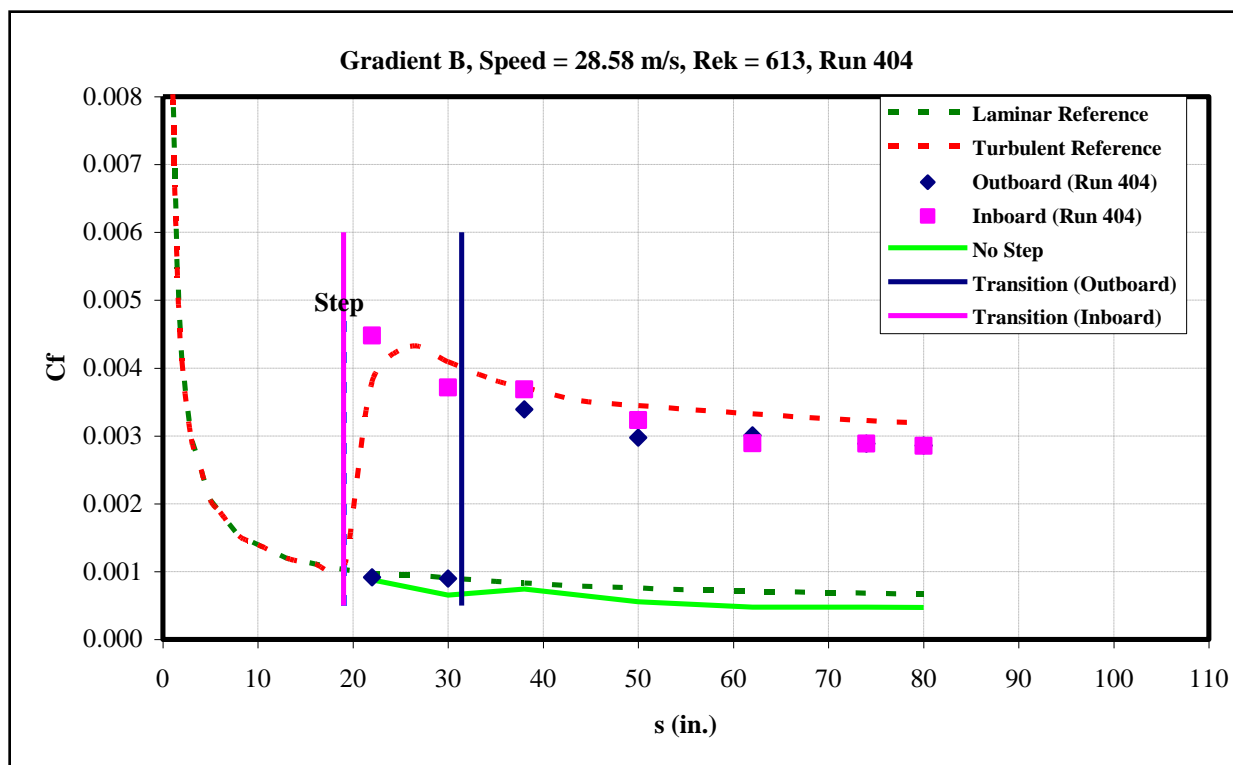


Figure 310: Gradient-B, $k=0.02$ -in aft step, $U=28.58$ m/s skin-friction distribution.

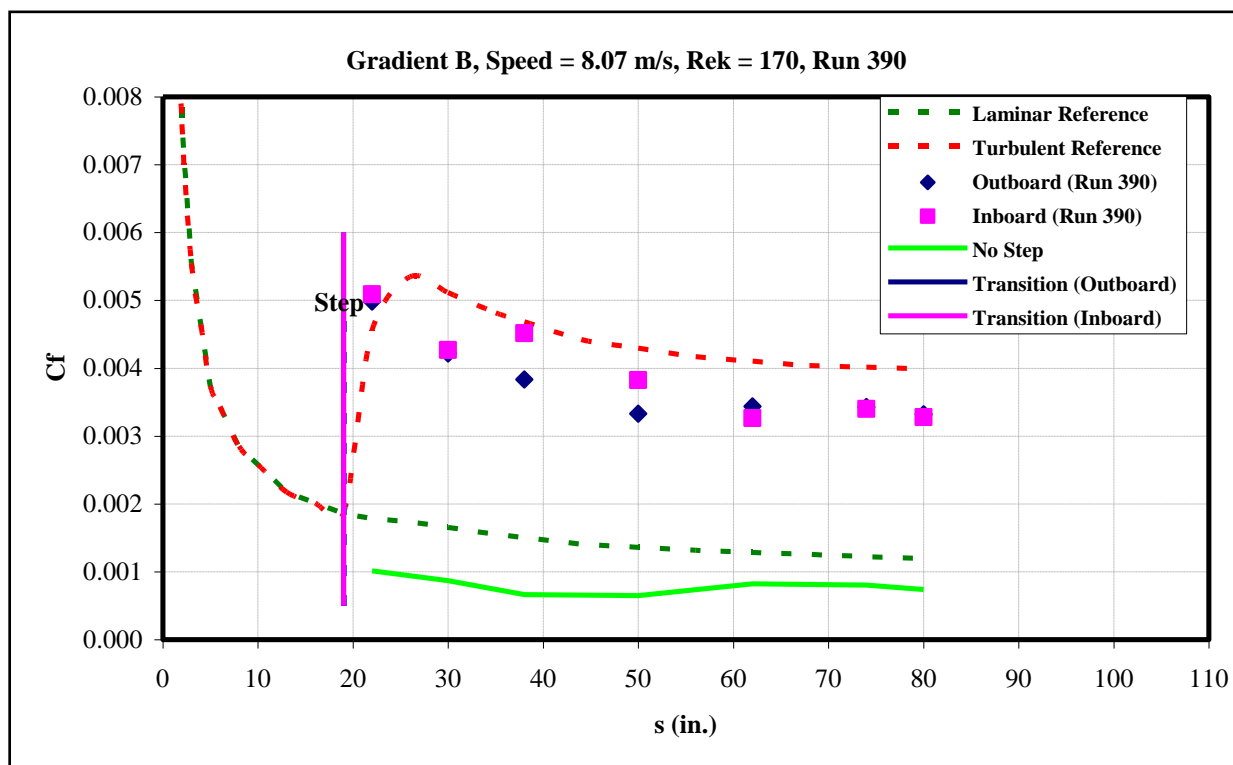


Figure 311: Gradient-B, $k=0.03$ -in aft step, $U=8.07$ m/s skin-friction distribution.

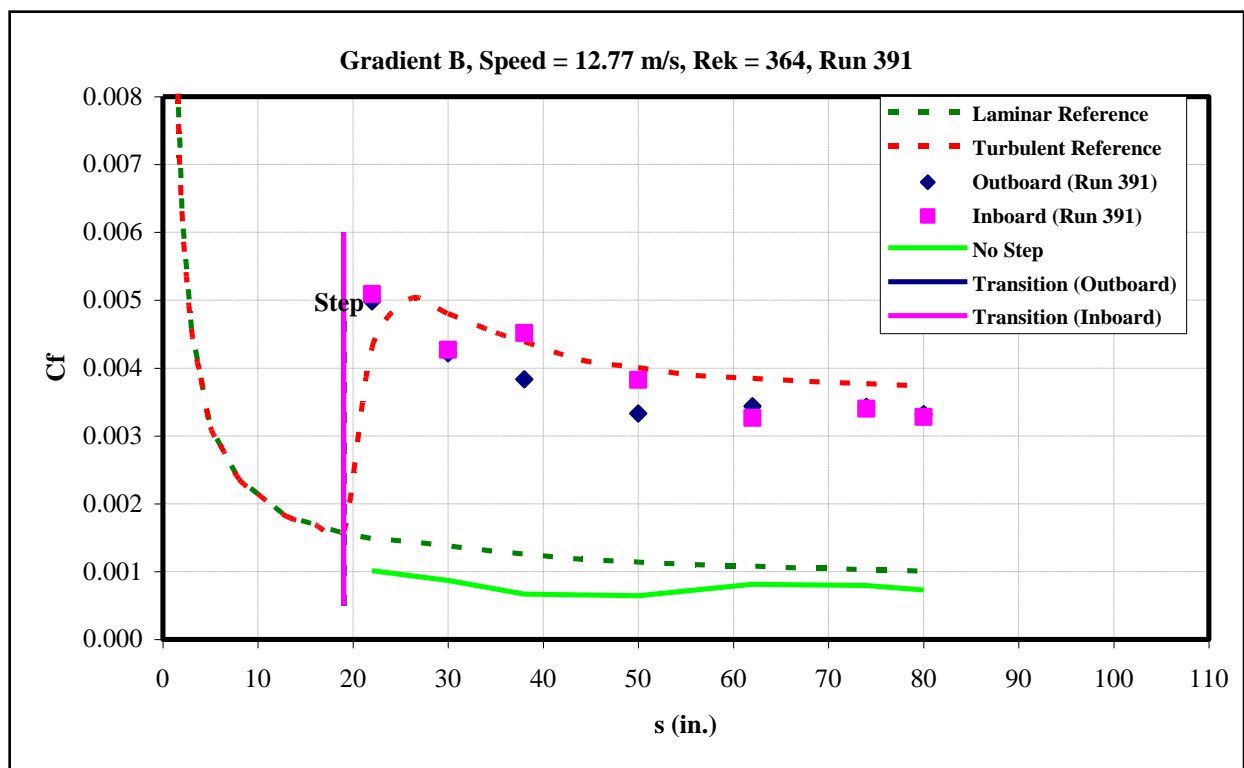


Figure 312: Gradient-B, $k=0.03$ -in aft step, $U=12.77$ m/s skin-friction distribution.

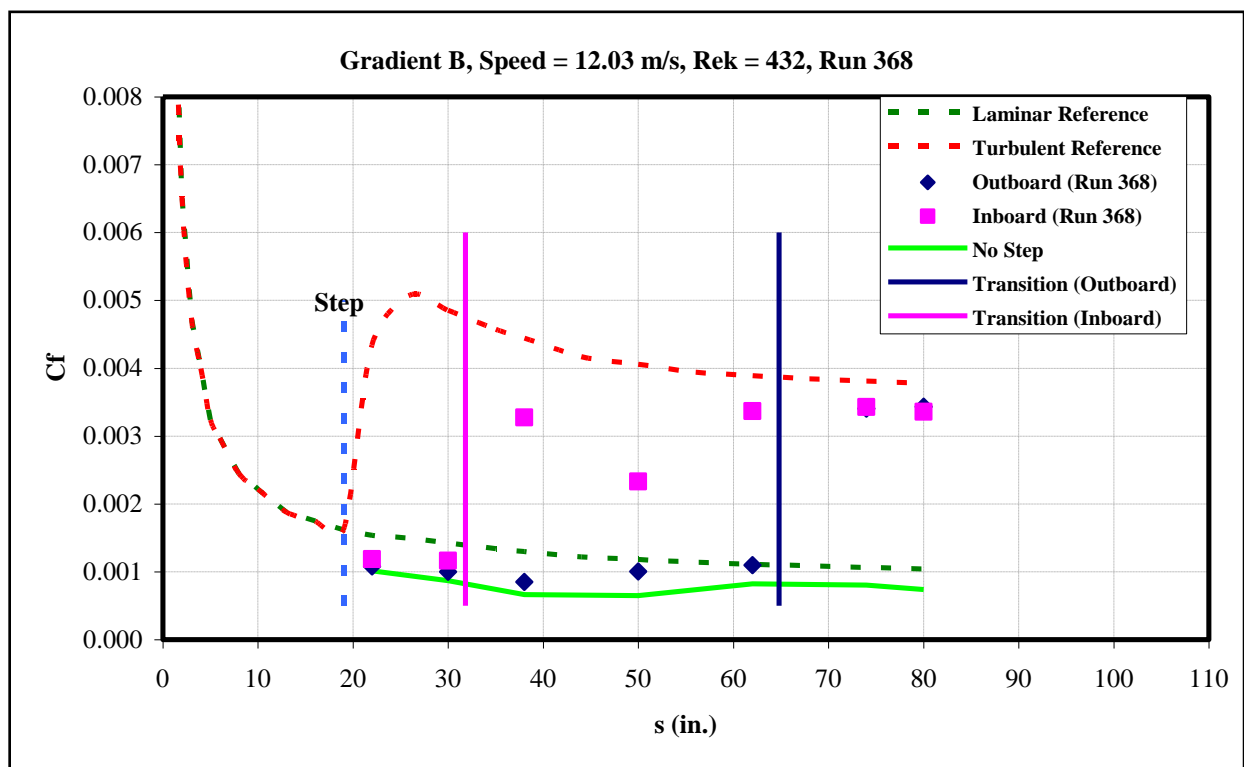


Figure 313: Gradient-B, $k=0.035$ -in aft step, $U=12.03$ m/s skin-friction distribution.

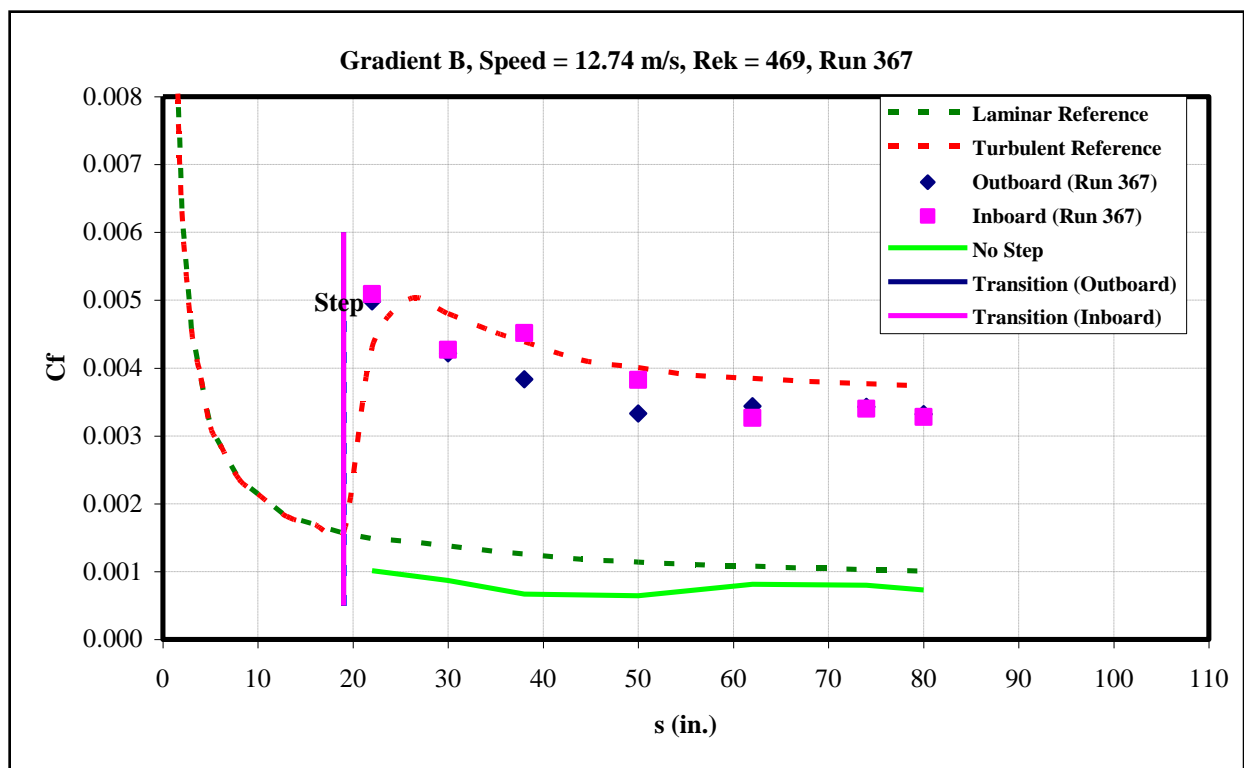


Figure 314: Gradient-B, $k=0.035$ -in aft step, $U=12.74$ m/s skin-friction distribution.

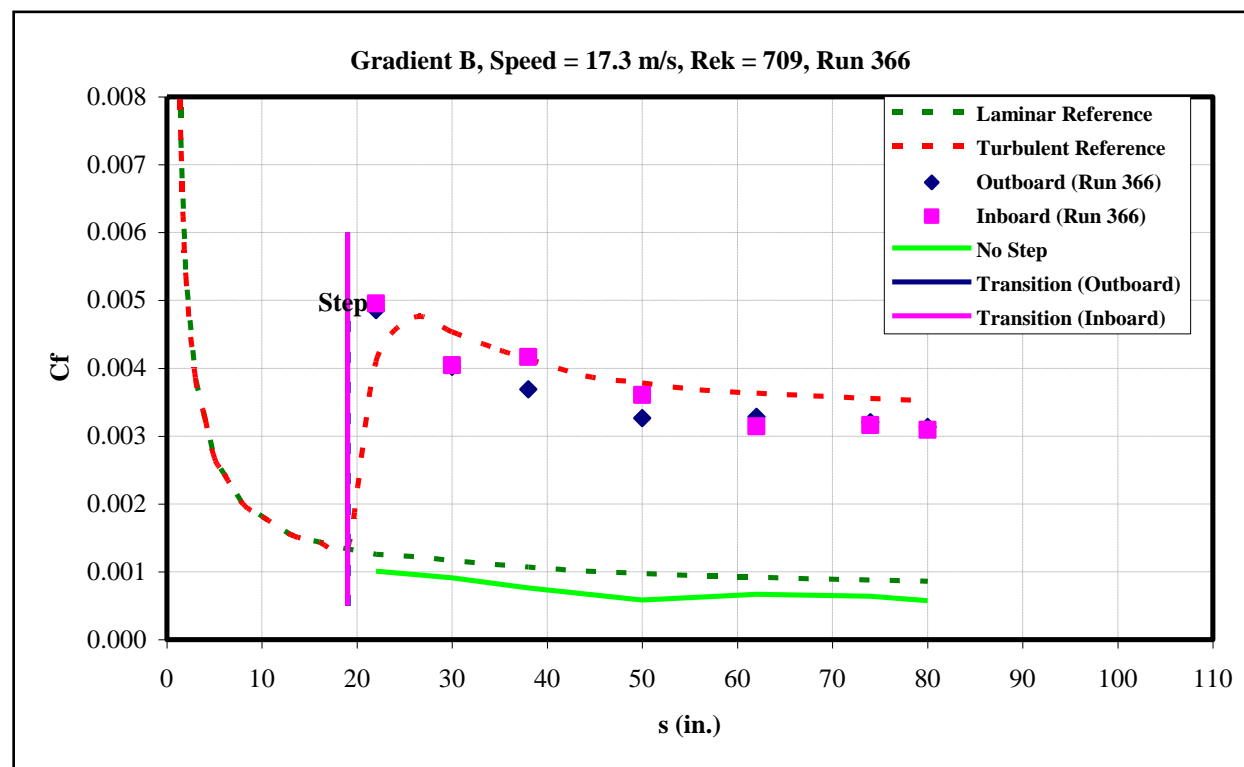


Figure 315: Gradient-B, $k=0.035$ -in aft step, $U=17.3$ m/s skin-friction distribution.

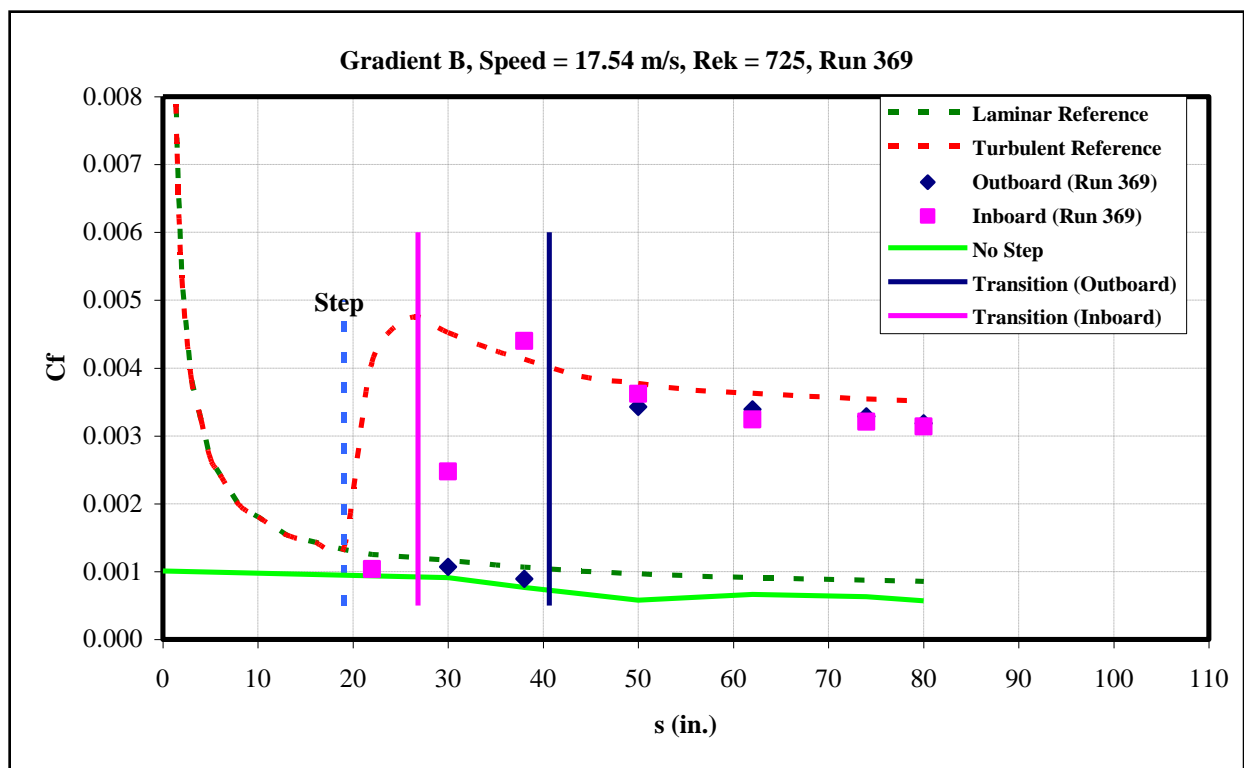


Figure 316: Gradient-B, $k=0.035$ -in aft step, $U=17.54$ m/s skin-friction distribution.

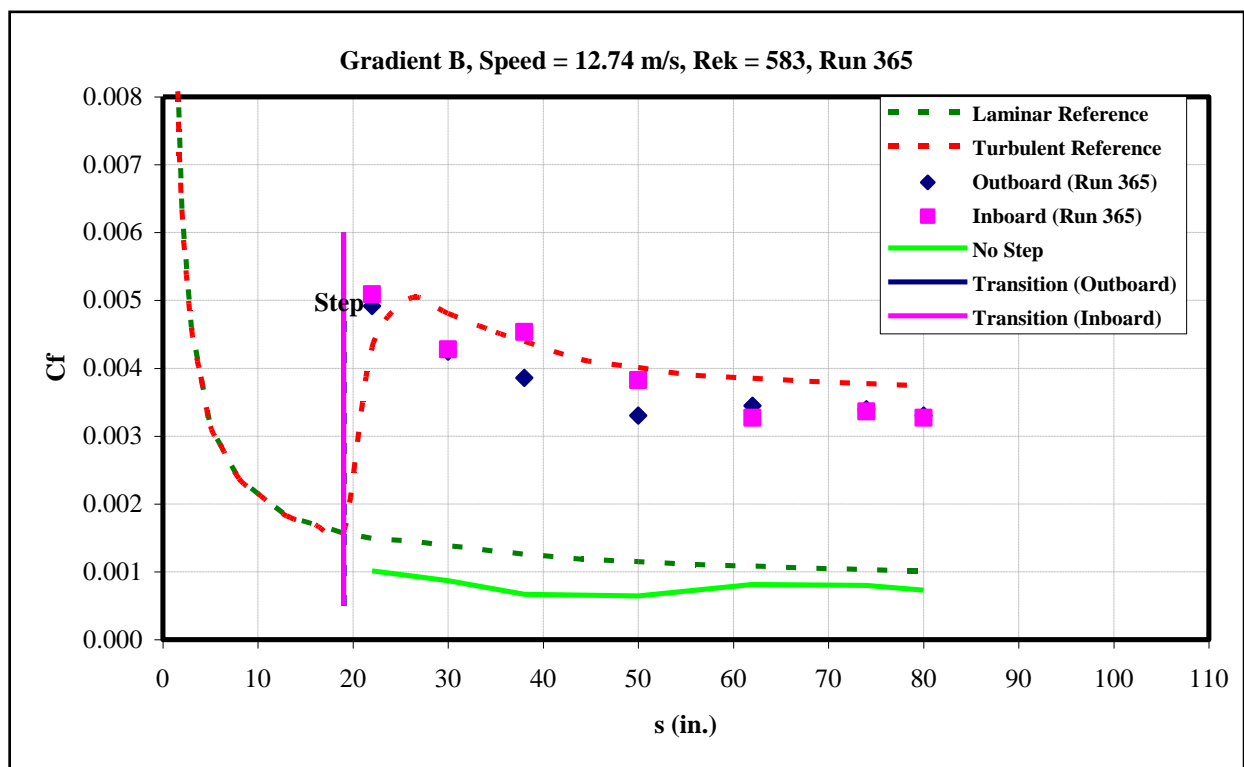


Figure 317: Gradient-B, $k=0.04$ -in aft step, $U=12.74$ m/s skin-friction distribution.

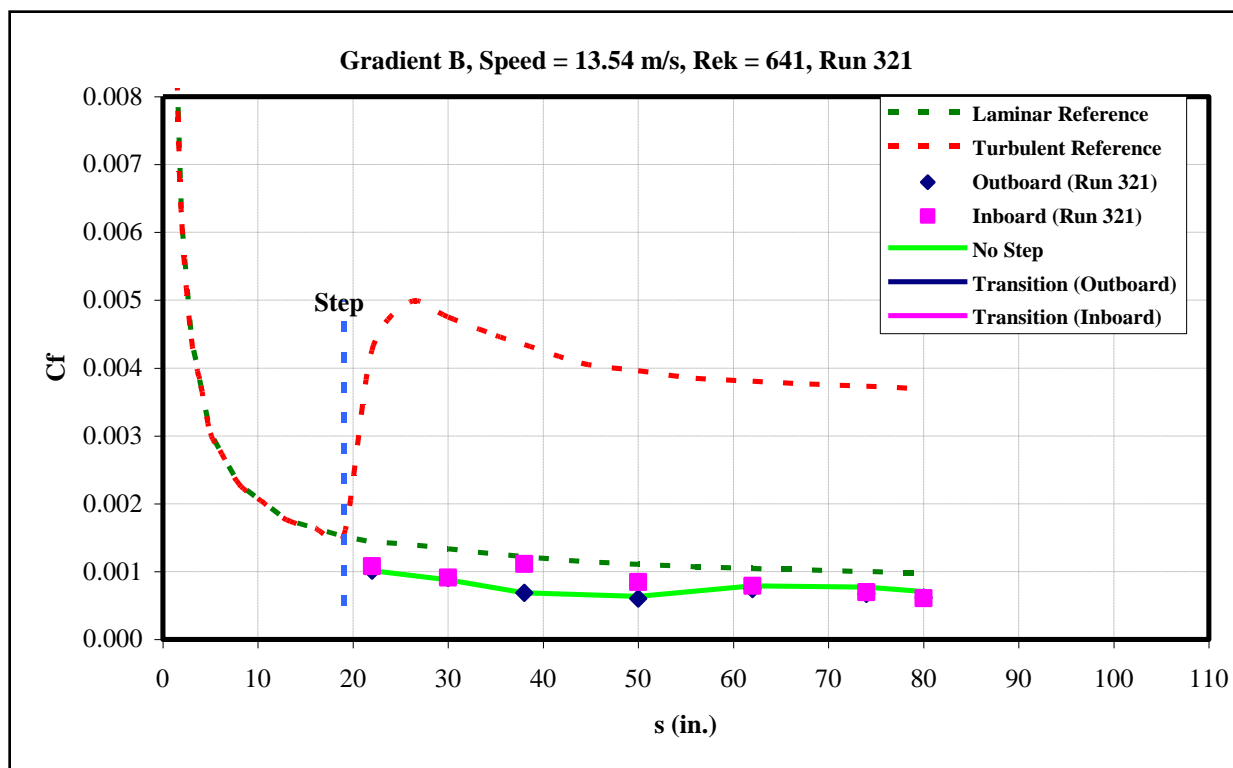


Figure 318: Gradient-B, $k=0.04$ -in aft step, $U=13.54$ m/s skin-friction distribution.

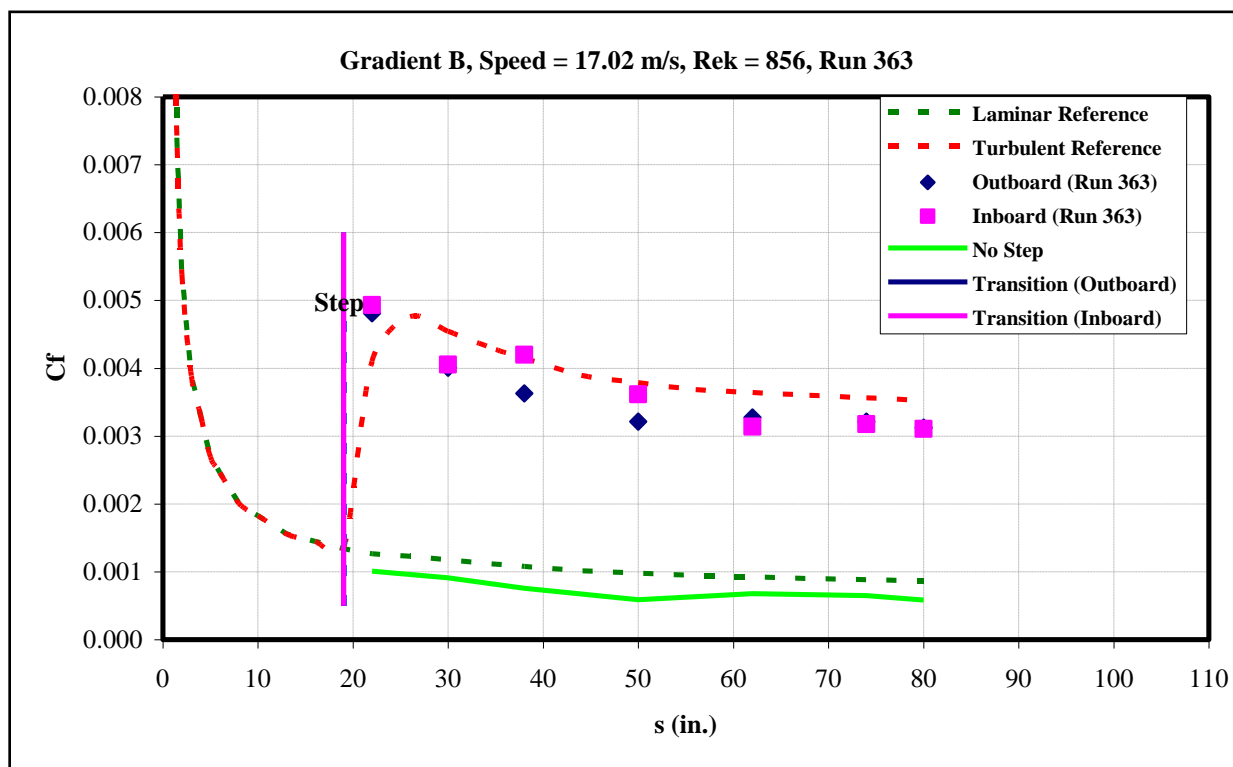


Figure 319: Gradient-B, $k=0.04$ -in aft step, $U=17.02$ m/s skin-friction distribution.

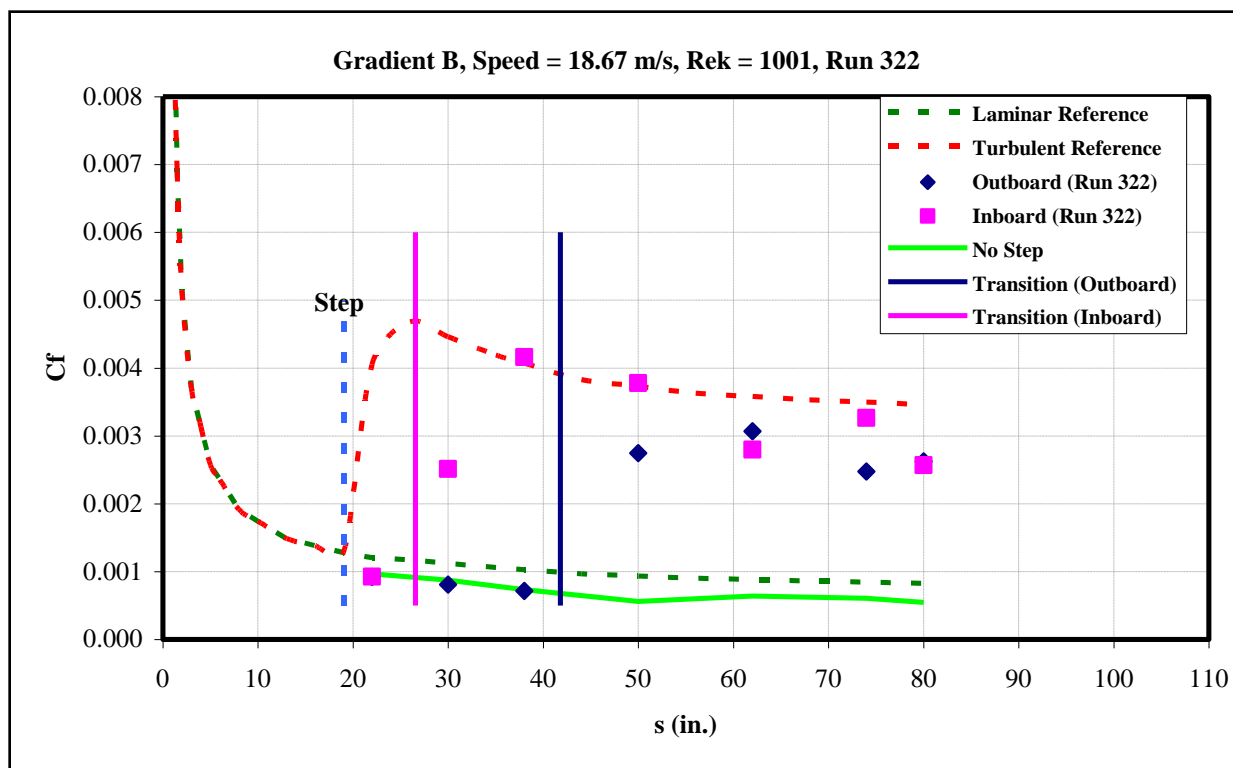


Figure 320: Gradient-B, $k=0.04$ -in aft step, $U=18.67$ m/s skin-friction distribution.

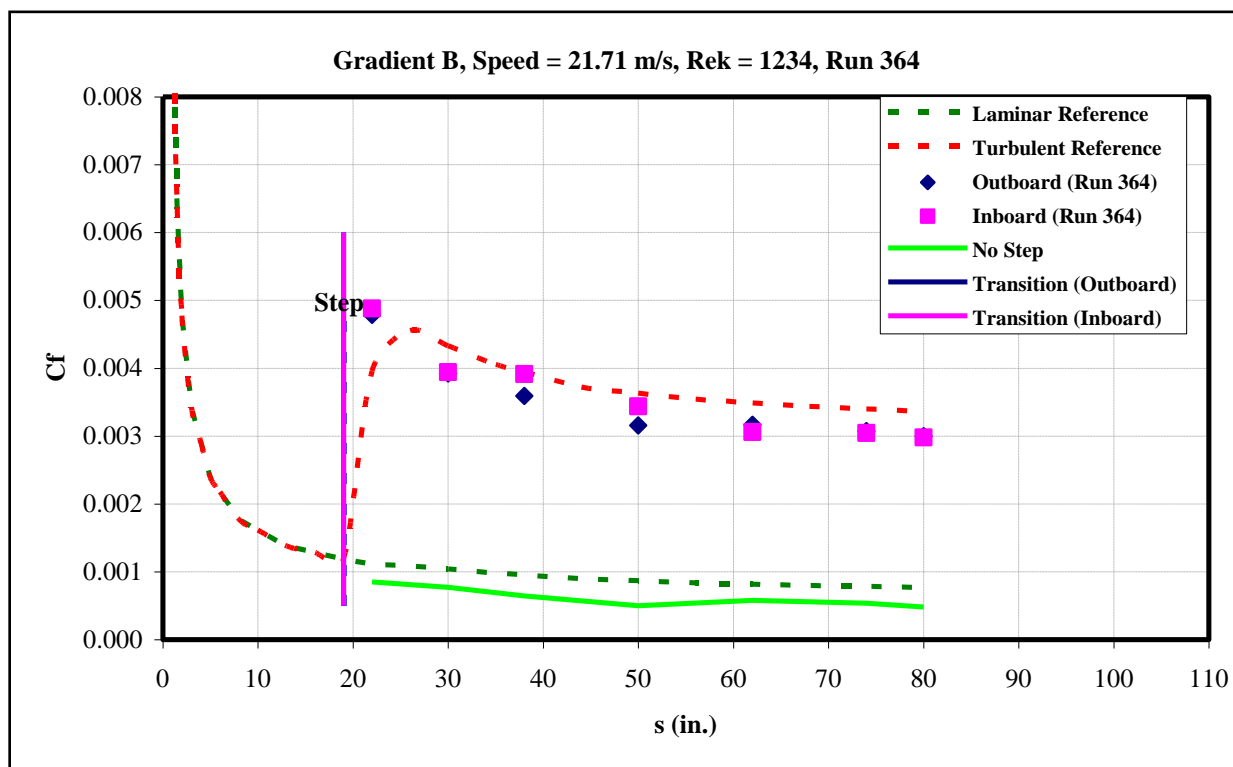


Figure 321: Gradient-B, $k=0.04$ -in aft step, $U=21.71$ m/s skin-friction distribution.

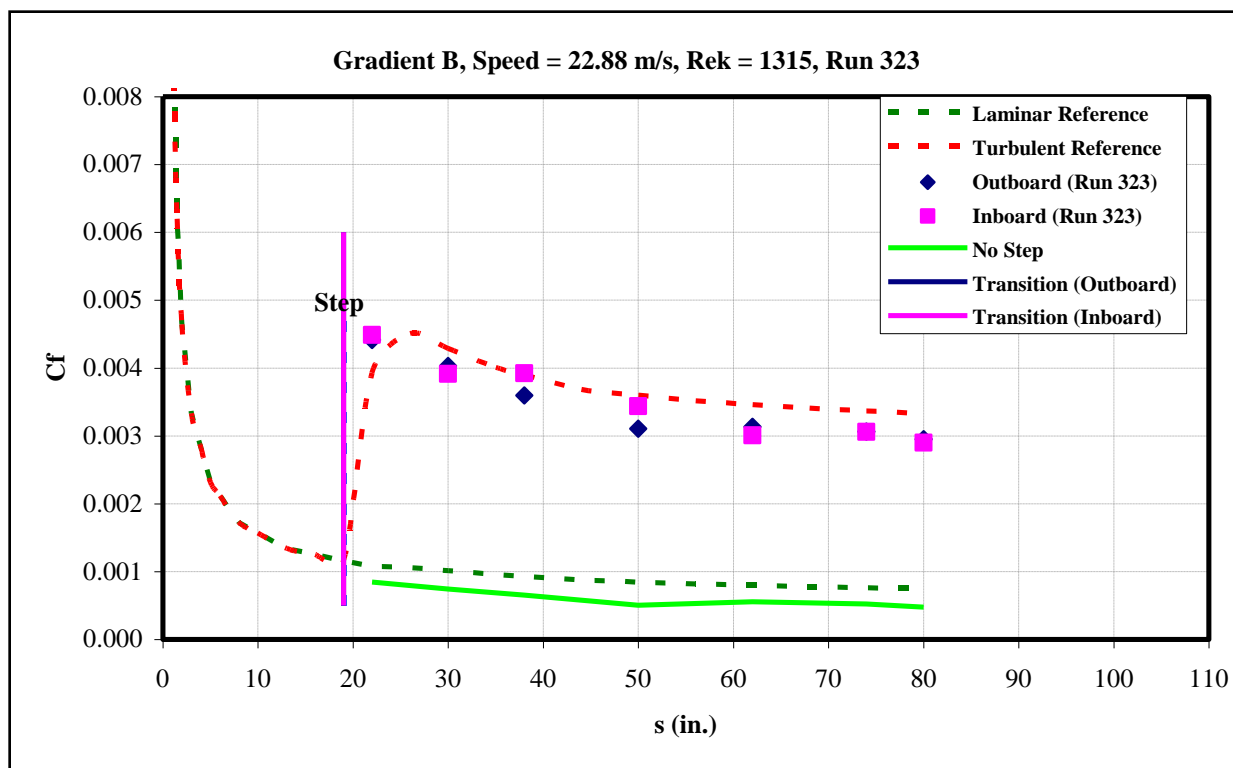


Figure 322: Gradient-B, $k=0.04$ -in aft step, $U=22.88$ m/s skin-friction distribution.

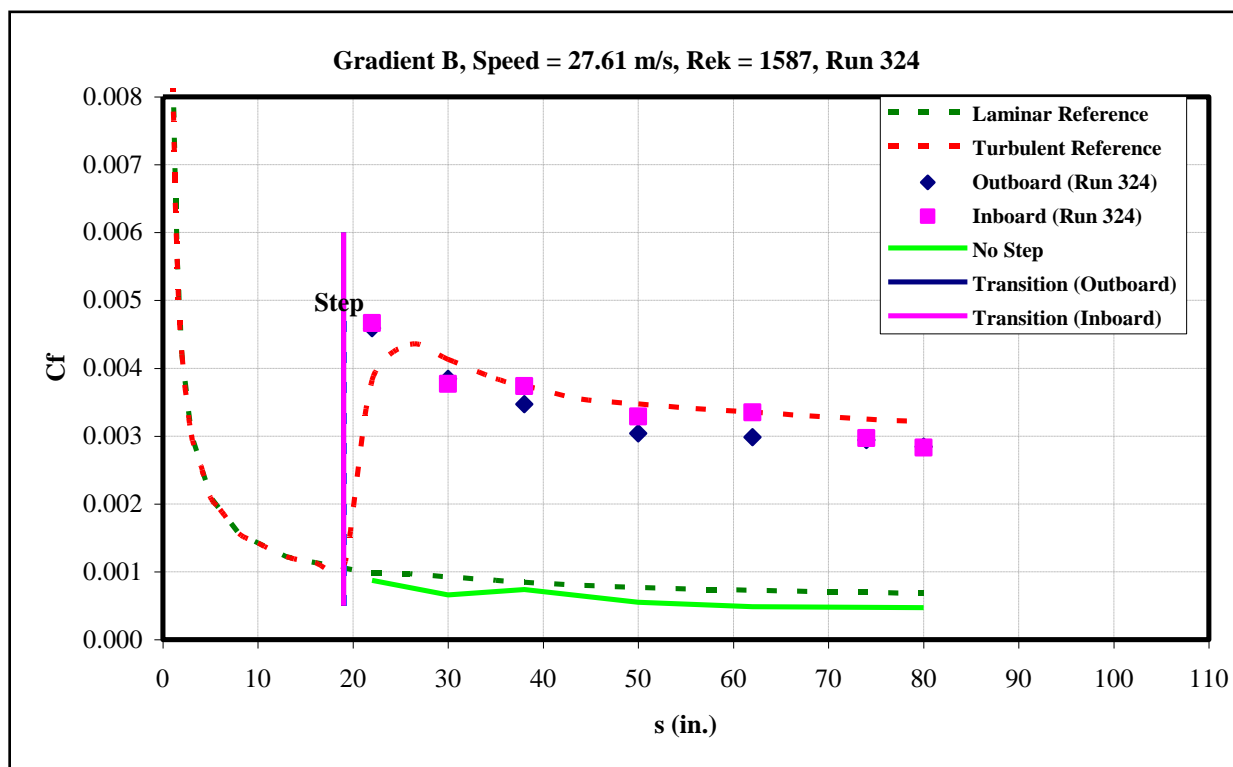


Figure 323: Gradient-B, $k=0.04$ -in aft step, $U=27.61$ m/s skin-friction distribution.

7.5 Hotwire Anemometry

The account has two sections. The first sections (7.5.1-7.5.6) describe the equipment and procedures used in the hot-wire anemometry measurements. Section 7.5.7 contains the experimental results, including the velocity time series obtained using hot wires and the power spectra and velocity RMS calculated from them, and accelerometer measurements. The detailed measurements of velocity profiles in the boundary layer at a range of flow speeds made with traversing hot-wire probe are also presented.

The results on flow uniformity testing also contain important free stream turbulence intensity measurements. It is known that increase in freestream turbulence intensity decreases the transition Reynolds number and at some high level of freestream turbulence in a dangerous range of frequencies the mechanism of transition can change from linear with Tollmien-Schlichting (T-S) waves to another mechanism, deemed “bypass transition.” The accelerometer vibration spectra are presented simultaneously with hot-wire velocity measurements for each run. The model vibrations could be considered as contributors to freestream turbulence and they needed to be measured separately in order to check their relative influence on the velocity power spectra.

The detailed description of flow characteristics in streamwise direction is presented for a range of flow speeds for all three models. These characteristics are: freestream velocity profiles, displacement thickness, shape factor, pressure parameters and acceleration coefficient. At the end, a detailed comparison of our experimental results with stability predictions for our flows is performed. The presented results show the growth (decay) of T-S waves amplitudes in a quantified way as growth (decay) of spectral peaks found in our velocity power spectra. The corresponding normalized frequencies were put on the stability diagram to check if the amplified frequencies in the spectra lay in the region of unstable disturbances and an N-factor analysis, a commonly used transition prediction technique, was performed.

7.5.1 Hotwire Anemometry Setup

A standard four-channel constant temperature hot-wire anemometer (AA Lab System AN-1005) was used for flow velocity measurements (Figure 324). The specifications are given in Table 5. All four channels were used simultaneously with the same hot-wire boundary-layer probes (Figure 325). The standard procedure of balancing the bridge of the anemometer and other required adjustments are given in the Calibration Procedure (see Appendix E) and in more details in the Anemometer Manual¹¹. The signal from the bridge was fed to the internal low noise amplifier of the anemometer to obtain a ± 10 V range. The output signal after the amplifiers was acquired by two data acquisition systems: a National Instruments Data Acquisition card driven by a Dell laptop and an IoTech LogBook, as described below.



Figure 324: AA Lab Systems Hot-wire anemometer AN-1005.

Table 5: Anemometer Specifications

Component	Specifications
Analog BNC output	+/- 12 V
Ultra-low noise amplifier gain	1-20
Digital serial port output	700 KBps
A/D resolution	16 bits
Sampling	500 kHz (gross for all channels)
Interface	USB2
Dimensions	40cm x 40cm x 40cm
Weight	10 kg

The boundary layer probes and supports were made by Dantec (Figure 325). The probes

were single gold-plated boundary layer probes (Dantec #55P05) and the probe supports were Dantec #55H21. The probe support dimensions were 4mm x 23.5cm with a 0.8m cable.

The specially-designed home-made aluminum mounting holders were used to attach the hot-wire probes to the surface (Figure 870, Appendix G). They were L-shaped and were attached to the surface with a leg facing outward from the region of measurements to prevent contamination of the next hot-wire. The L-shaped holder allowed rough adjustment of the distance between the hot-wire sensor and the surface. For more accurate final adjustment of the distance between the hot-wire sensor and the surface the specially designed home-made aluminum height adjusters were used (Figure 871, Appendix G). A Nikon D300 digital camera with a Tamron SPAF 180 mm lens was used to determine the hot-wire height (see Table 6 for specifications). The distance between a hot-wire sensor and surface was obtained from the image with pixel accuracy which was about 50-100 microns.

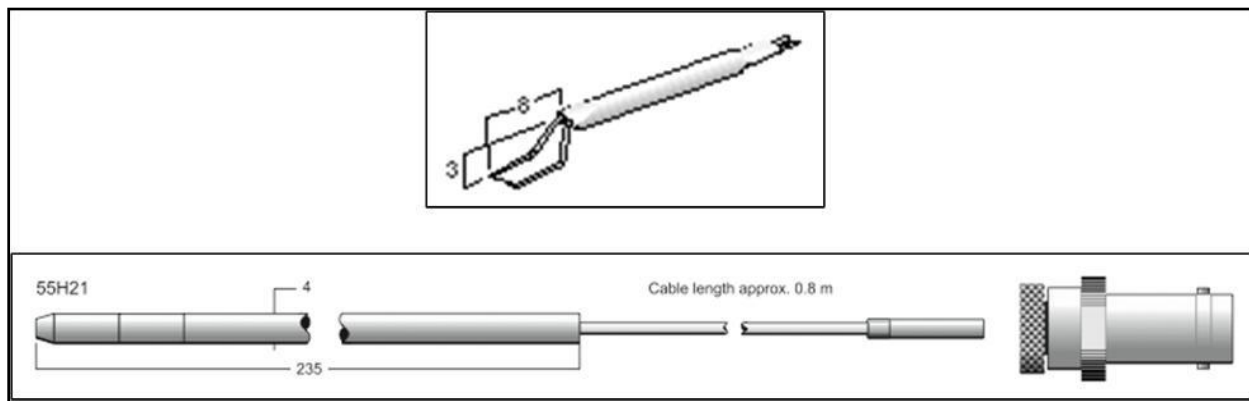


Figure 325: Dantec boundary layer hot-wire probe (top) and probe support (bottom), dimensions in mm.

Table 6: Nikon Camera Specifications

Component	Specifications
Type	Single-lens reflex digital camera
Lens Mount	Nikon F mount
Effective pixels	12.3 million
Image size (pixels)	4,288 x 2,848 (L)
File format	NEF(raw), TIFF, JPEG
Media	Compact Flash memory card
Release mode	Single frame, Continuous, Live view
Interface	USB
Power	AC adapter, Rechargeable Li-ion battery
Lens model	SPAF 180mm F/3.5 Di LD [IF] Macro1:1 (Model B01)

A calibrator (Figure 326) was required for calibration of the hot-wire voltage versus a known flow velocity measured directly with a differential pressure transducer (Figure 327). The (CIT) calibrator was made from raw aluminum materials. The calibrator consists of a settling box, a converging cylindrical tube with a 6:1 converging nozzle that increases the flow velocity approximately 36 times, replaceable converging nozzles that allow for further increase of flow

velocity, and a holder for a hot-wire probe support and Pitot tube. The settling box was attached to the cylindrical tube with four steel rods through an O-ring. A special Plexiglas conical insert was used when installing a nozzle in order to center it with respect to the cylindrical tube opening. A nozzle of 9/16-inch diameter allowed simultaneous measurements by both the Caltech-made Pitot tube and the hot-wire probe. The air was fed to the calibrator from an external air pump through a MAC series air filter. A pressure regulator with a Matheson Tri-Gas gage was connected to the calibrator by a 0.25 inch hose and allowed incremental control of the pressure during calibration.

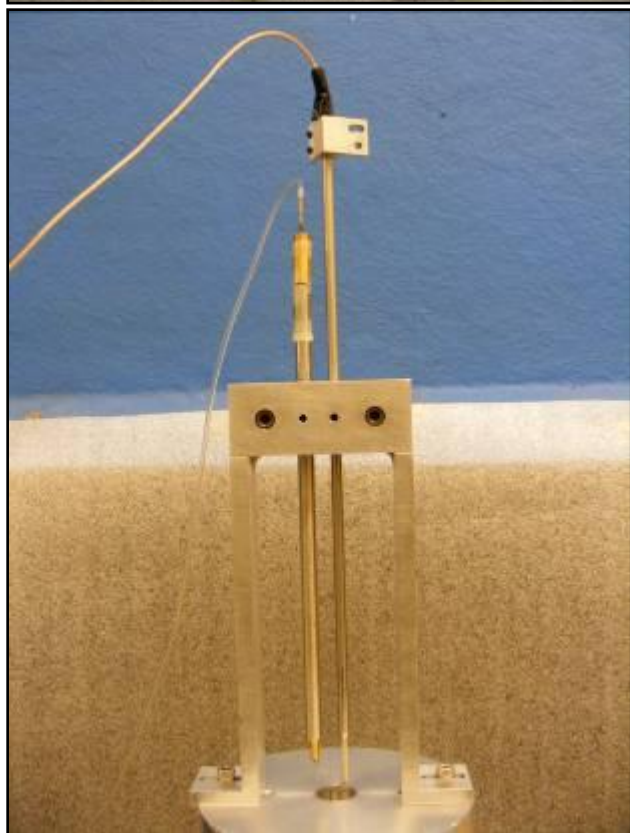


Figure 326: Calibrator, air filter and pressure regulator (left), Pitot tube and hot-wire probe support in the calibrator holder (right)



Figure 327: Pressure transducer and its power supply.

The holder for the Pitot tube and hot-wire probe support was designed to permit the removal of the hot-wire probe support after calibration without disconnecting the hot-wire probe from its support. The hot-wire sensor and the Pitot tube were aligned at the same level slightly below the nozzle edge approximately in the center of the nozzle opening. The Pitot tube was glued to the holder for convenience.

Air pressure was measured using an MKS Instruments 223-model transducer, a general purpose differential baratron allowing accurate measuring of low differential pressures generated by air. A user-supplied bipolar power supply of ± 11 to 18VDC was required to operate it. The transducer is manufacturer-calibrated and the calibration curve is shown below (Figure 328). The specifications of the transducer and the hot wire calibrator are given in Table 7. One pressure input of the transducer was connected to the Pitot tube and the other was connected to a free tube attached somewhere close to the calibrator nozzle so that pressure signal from the Pitot was measured with respect to atmospheric pressure. The flow velocity measured with the pressure transducer is given by equation 11.

$$V = \left(2 \cdot \frac{\Delta P}{\rho} \right)^{1/2} \quad (11)$$

Where: V is the velocity at the exit of nozzle, ΔP is the pressure as read by the transducer, and ρ is air density.

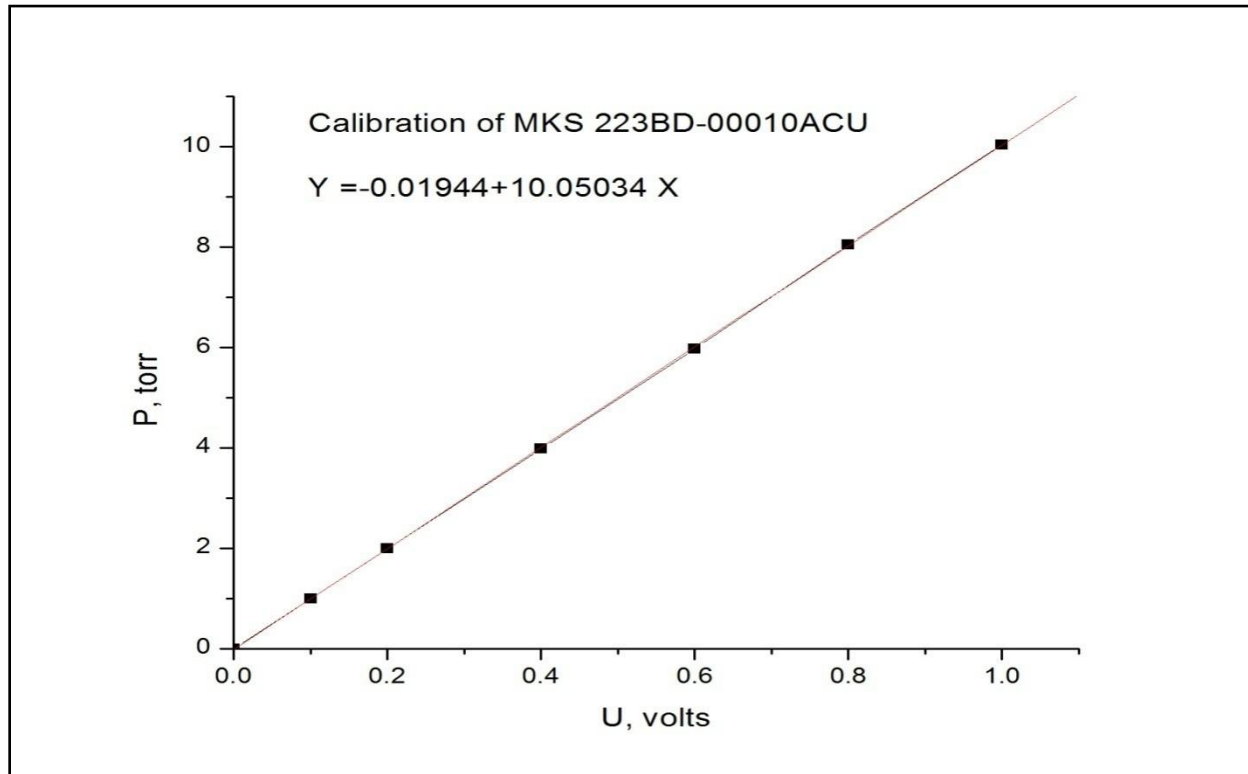


Figure 328: Calibration of the MKS 223BD pressure transducer.

Table 7: Hot-wire Calibrator and Pressure Transducer Specifications

Component	Specifications
Air Filter	Product # MAC-85-3/4-CC, MAC series compressed air filter assembly, for flows to 85 SCFM @ 100 PSIG, 3/4 in. NPT connections.
Pressure Regulator	Matheson Tri-Gas, Model 3200 Series, Single-Stage High-Purity/High Flow Brass and Stainless Steel Regulator. Delivery pressure range: 0-50 psig, pressure gage: 0-100 psig, Maximum Inlet Pressure: 3000 psig, Maximum Flow Rate: 100 SCFM (2832 SLPM).
Pressure Transducer	MKS Instruments, 223BD-00010ACU, 10 torr baratron differential capacitance manometer, Power Required ± 11 to 18 VDC @ 25 mA, Maximum Line Pressure 40 psig (275 kPa), Output: 0 to ± 1 VDC into $> 10K \Omega$ load.
Power Supply	MASTECH, HY3003F-3, dual 0-30V @ 3A, 5V @ 3A power supply

The hot wire calibration procedure is given in Appendix E. The error in velocity measurements could be related to variation in many different parameters such as ambient temperature and humidity, sensor resistivity, change of the anemometer settings due to

temperature drift, etc. To get an estimation of the velocity error, the hot-wire calibration was performed before and after measurements (usually at the beginning and at the end of a day). It was found that the error was 1-5%.

7.5.2 Hot wire Repair Station

A hot wire repair station was setup at the Towing Wind Tunnel in order to repair any broken wires in-situ. The hot-wire repair station (Figure 329) consisted of a microscope, one XYZ small translational stage and two micro manual rotary stages, a repair kit including a Dantec 10-wire cartridge, a soldering iron, soldering paste and tin wire. One rotation stage was attached to a XYZ translational stage. This complex translation stage was used for manipulation of a wire cartridge. Another rotation stage was attached to a base plate for manipulation with a broken hot-wire probe. Adjustment of all these stages plus a possibility to adjust the base plate allowed fine manipulations during hot-wires repair process. The specifications of the hot wire repair station are shown in Table 8.

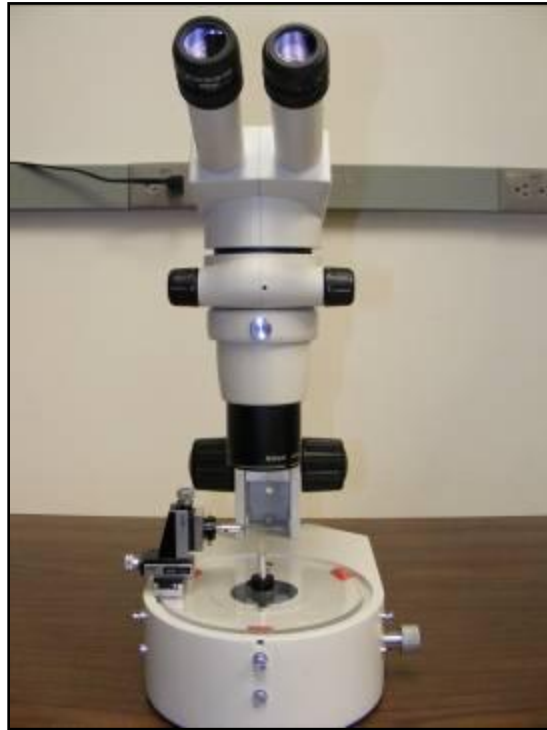


Figure 329: Microscope and micro manipulation stages.

Table 8: Hot-wire Repair Station

Component	Specifications
Microscope	Nikon SMZ-800 Zoom Stereo
Micro Rotational and Translational Stages	Edmund Optics small XYZ leadscrew drive stage, part #NT56-339 Edmund Optics micro manual rotary stages, part #NT56-572; 17 degrees fine adjustment, 360 degrees coarse adjustment

Repair Kit	Dantec 1 wire cartridge (10 wires), #9055P
Solder Paste	# 71 stainless steel solder paste
Tin Wire	Superior Flux & Mfg. Co. 96% tin 4% silver solder solid wire

The procedure for fixing a broken hot-wire is given in Appendix F.

7.5.3 *Vibration Measurements*

Possible model vibrations were recorded with two accelerometers (Figure 330) so that two components of vibrations were obtained simultaneously. Vibrations could be considered as a source of flow fluctuations and need to be monitored and controlled, if necessary. Accelerometers were glued with Super Glue to the model surface (Figure 331). Each accelerometer had its own power supply with internal rechargeable battery, which worked simultaneously as an amplifier with adjustable gain. The specifications of the accelerometer systems are given in Table 9. The voltage signal from the power supply/amplifier output was recorded directly to the LogBook.



Figure 330: Accelerometer (right) and its power supply/amplifier (left).

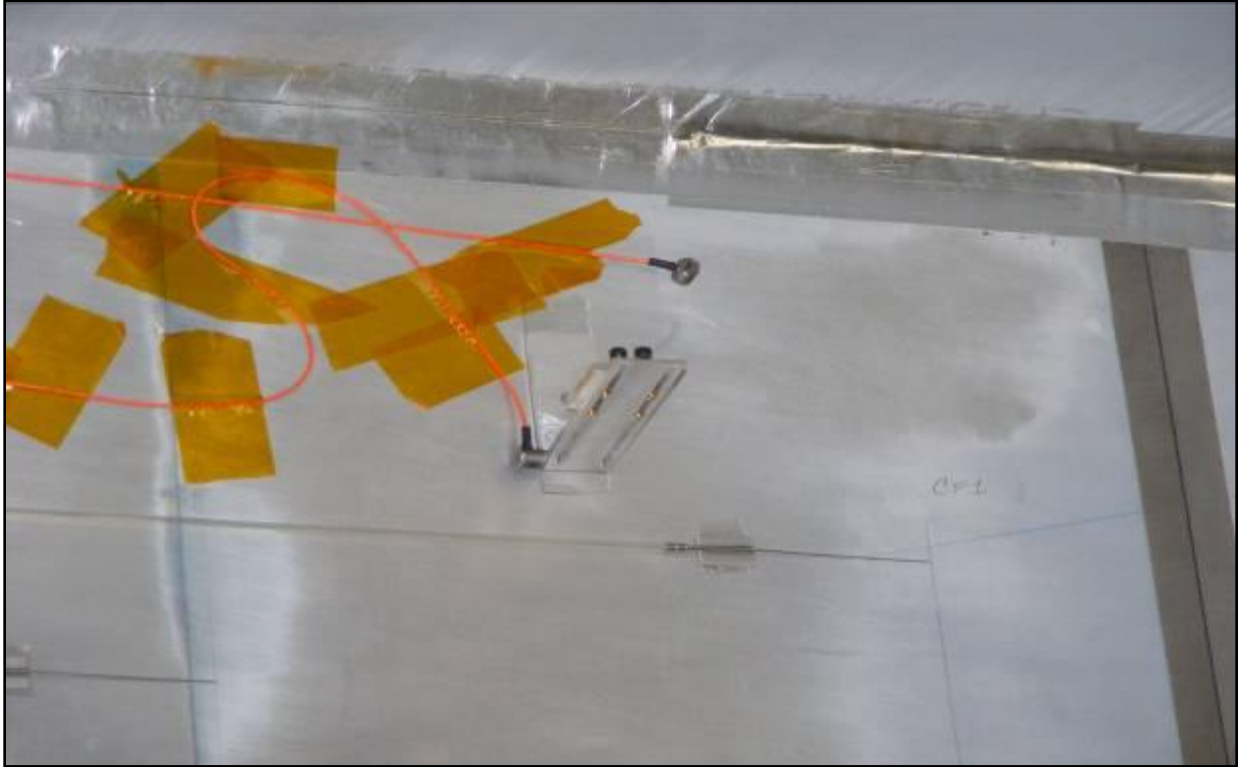


Figure 331: One accelerometer is glued to testing side of the model to measure k-component of vibrations; second accelerometer is glued to L-bracket to measure s-component.

Table 9: Accelerometer Specifications

Component	Specifications
Accelerometers	Omega #ACC104A. Sensitivity: 10mV/g @ 100Hz. Bandwidth: 1Hz-10kHz. Amplitude range: +/-500g. Dimensions: 7mm x 7mm x 6mm
Battery power supply/amplifier	Omega #ACC-PS2. Gain: x1, x10, x100, single channel. Dimensions: 12.1cm x 4.4cm x 4.5cm

7.5.4 Temperature Control

Knowledge of the temperature in the test section was required as it could be different from the temperature at calibration station. The corrections should be then applied to calibration coefficients in case of significant difference in temperatures. The temperature was measured with a thermocouple connected to a temperature meter (Figure 332). The thermocouple was calibrated first versus a known temperature (Figure 333) and the calibration coefficients were input to the acquisition program. The signal from the thermocouple meter was recorded through the DAQ to the laptop in real-time. It was found that the temperature difference was around 0.5°C between the test section and the calibration station and thus temperature correction was not applied due to its smallness. The velocity spectra were found not to be sensitive to this temperature difference. The thermocouple specifications are given in Table 10.

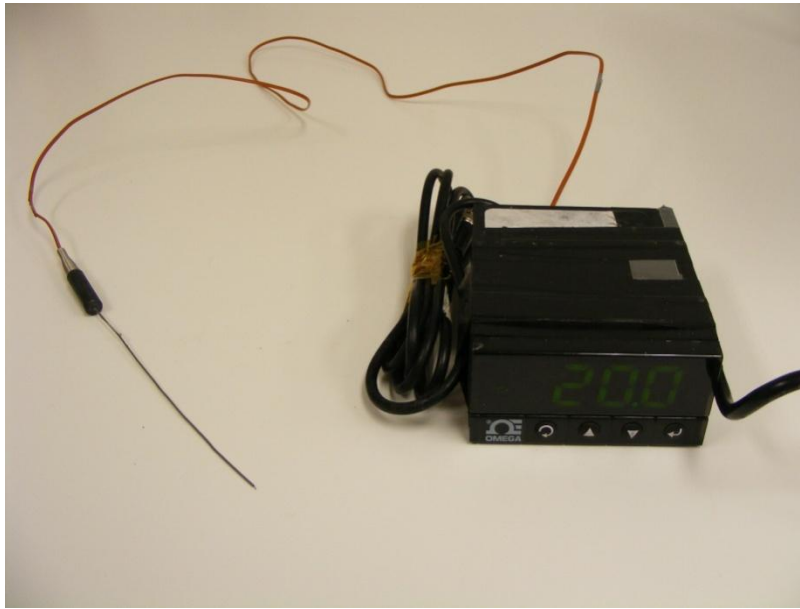


Figure 332: Thermocouple (left) and its controller (right) .

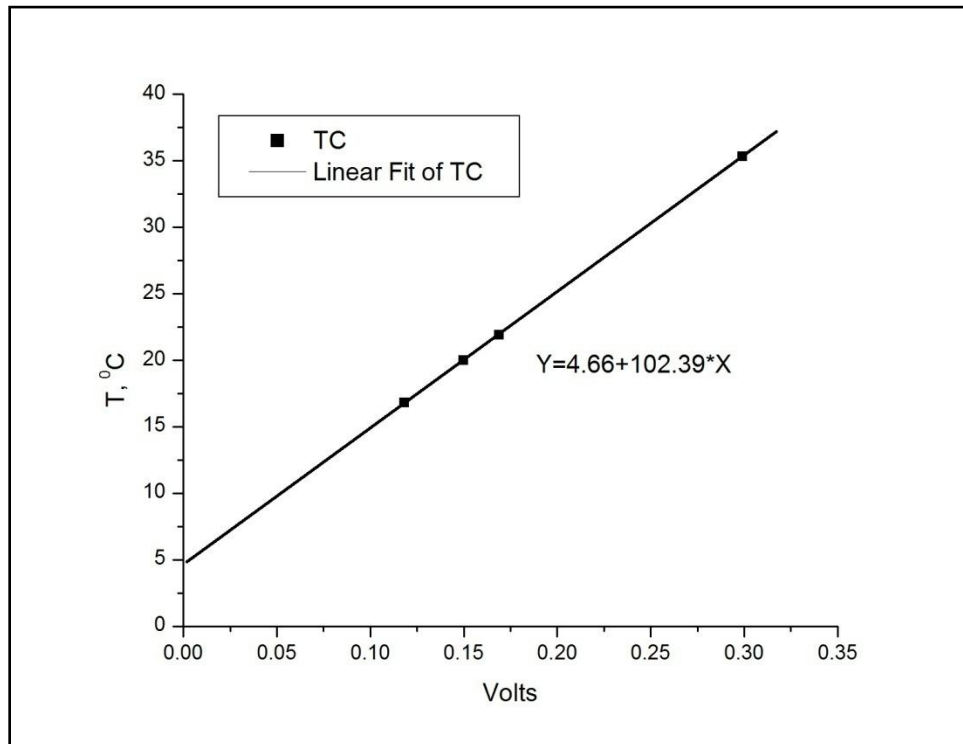


Figure 333: Calibration of thermocouple (TC).

Table 10: Thermocouple Specifications

Component	Specifications
Thermocouple	Omega #JMTSS-040E-6
Temperature meter	Omega #DPi8A, analog output, accuracy 0.03%

7.5.5 Data Acquisition System

The flow velocity, model vibrations and temperature fluctuations measured during the testing were recorded using two devices: a laptop computer together with a National Instruments data acquisition card and an IOTech LogBook.

The signals from the amplifier outputs of the anemometer were fed to the Data Acquisition card (DAQ) and, after digitizing, recorded to the laptop through a USB port in real-time (Figure 334). The DAQ was also used simultaneously for digitizing the voltage signal from a thermocouple controller, which was transformed by a computer program to a temperature signal. The FS/GS grounding switches of the DAQ were set to the FS position as it was found to lower noise in the signal¹². The laptop software preinstalled included a program for communication with the DAQ through the USB port, LabView for data acquisition from DAQ, LogView for uploading data from CompactFlash memory card from LogBook, and Matlab.

The IOTech LogBook (Figure 335) was used to record (duplicate) the signals from the amplifier outputs of the anemometer and also for the recording of vibration signals from the accelerometers. To provide a stand-alone experiment the Uninterrupted Power Supply (UPS) was used to power all devices (Figure 336). The charge of the UPS internal battery was not enough for a full day of experiments; therefore, three additional external 12V batteries (connected in series to supply 36V) were connected in parallel with the internal battery. This allowed running the experiment for a full day with recharging required only overnight.

The specifications of the data acquisition system are given in Table 11.



Figure 334: Laptop (left) and Data Acquisition card (right).



Figure 335: LogBook: front view (left) and rear view (right).



Figure 336: Uninterrupted Power Supply (UPS).

Table 11: Data Acquisition Specifications

Component	Specifications
Laptop	Dell XPS M1330. Intel® Core™ 2 Duo T5550 (2MB cache/1.83GHz/667Mhz FSB). Genuine Windows Vista® Home Premium Edition SP1
DAQ	National Instruments #USB-6221 BNC
LogBook	IoTech. A/D resolution: 16 bits. Memory: RAM 4 MB (gross) plus Hard Disk 1 GB. 8 BNC analog inputs (active) +/-10V, accuracy +/- 1.5 mV. Digital inputs. Sampling 100 kHz (gross). Triggering: analog (TTL), digital and software. Software: LogView for setup, PostView for post-acquisition viewing. SanDisk CompactFlash PCMCIA Adapter for connection of Hard Disk to PC. Power consumption: 0.9 V, 15VDC. Power supply: 120VAC. Weight: 4.1 kg. Dimensions: 280mm x 356mm x 44mm.
Uninterrupted Power Supply (UPS)	ISE Inc. output 120VAC, 700W (internal battery 49min @ 170W). Dimensions: 44.3cm x 88cm x 38.5cm, (rack mount). Weight: 17 kg.

Several software packages were used for data acquisition and post processing. The software included LabView, DAQ software, LogView, Matlab and Camera Control Pro 2.

Labview was used for data acquisition during experiment and during hot-wire calibration. The DAQ software was required for working with DAQ, while the LogView software was required for uploading data from and for downloading acquisition configuration to a CompactFlash memory card of the LogBook. Matlab was used for data post processing after the experiment and calibration. Camera ControlPro2 was used for communication between Laptop and Nikon Camera in live mode (which was convenient during hot-wire probe adjustment) and transferring images to computer.

The list of additional required (SETS-developed) programs is:

HW_acquisition_calib.vi – for data acquisition through DAQ;

cal_power_2.m – for successive data processing and obtaining velocity spectra;

calib_pressure_HW.vi – during hot-wire calibration;

calibrator.m – for successive data processing and obtaining calibration coefficients;

accpower.m – for accelerometer data processing and obtaining spectra.

See the calibration procedure (Appendix E) and the hot-wire experimental procedure (Appendix G) for details on these programs. In the analysis, only the velocity data recorded through DAQ were post processed and velocity data recorded to LogBook were kept as a backup.

7.5.6 Review of Linear Stability Theory

The Blasius momentum equation for a flat plate laminar boundary layer flow with a zero pressure gradient is¹³:

$$f''' + ff'' = 0 \quad (12)$$

where: $f' = u/U$.

For the case of a flat plate the boundary layer solution is self-similar in the sense that two profiles $u(x,y)$ at different values of x differ only by a scale factor in y . For geometries more complicated than a flat plate, self similar solutions are also found. Falkner and Skan (1931) showed that similarity is achieved with a power-law freestream velocity distribution:

$$U(x) \sim x^m \quad (13)$$

The most common form of the Falkner-Skan equation for similar flows is:

$$f''' + ff'' + \beta(1 - f'^2) = 0 \quad (14)$$

where: $\beta = 2m/(1+m)$.

The parameter β is a measure of the pressure gradient dp/dx . $\beta=0$ corresponds to flat plate (Blasius) flow. If β is positive, the pressure gradient is negative (favorable), which was the case for the downstream segments of the SETS models.

The power-law free stream velocity distribution for positive β can be reached over a wedge (Figure 337). These self-similar flows have constant β and are easily treated numerically but difficult to realize in practice. The flows over the SETS models are not similar, but the surface of each model can be presented as a set of such wedges with continuously changing angles: $\beta(x)\pi/2$. The β parameter now is not constant but a function of distance x . We call such flows “locally similar” because β varies with stream wise location.

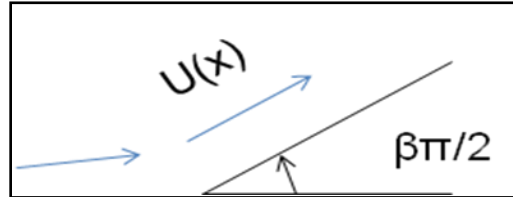


Figure 337: Interpretation of β parameter for a similar wedge flow.

These self-similar flows have constant β and are easily treated numerically but difficult to realize in practice. The flows over the SETS models are not similar, but the surface of each model can be presented as a set of such wedges with continuously changing angles: $\beta(x)\pi/2$. The β parameter now is not constant but a function of distance x . We call such flows “locally similar” because β varies with stream wise location.

Stability analysis of the Navier-Stokes and continuity equations results in the famous Orr-Sommerfeld equation:

$$(U - c)(u'' - \alpha^2 u) - U''u + \frac{iv}{\alpha}(u'''' - 2\alpha^2 u'' + \alpha^4 u) = 0 \quad (15)$$

with disturbances specified by:

$$u = u(y) \exp[i\alpha(x \cos(\phi) + z \sin(\phi) - ct)] \quad (16)$$

where: α is the wave number, c is the propagation speed, ϕ is the angle of propagation and u is the Fourier coefficient of disturbance velocity.

The disturbances are referred to as Tollmien-Schlichting waves, which are first (infinitesimal) indications of laminar-flow instability. At a certain critical Reynolds number, Re_{δ^*crit} , the infinitesimal disturbances are amplified. The region of Reynolds numbers where the disturbances are amplified is bounded by the neutral stability curve. Outside this region all disturbances are damped.

The stability diagram obtained from the (parallel flow) numerical computations of Wazzan¹⁴, for the Blasius flow, assuming parallel flow (constant boundary layer thickness), is shown in the Figure 338. In the same plot the non-parallel flow experimental results of Ross and Barnes¹⁵ are presented for comparison. The frequency was made non-dimensional, $F = 2\pi f\nu/U^2$, and Reynolds number is $Re_{\delta^*} = \delta^*U/\nu$. The main difference between the parallel and non-parallel cases is that for parallel flow the $Re_{\delta^*crit} \approx 580$ and for non-parallel $Re_{\delta^*crit} \approx 400$. The difference becomes very small for Re_{δ^*} larger than 800 for the Blasius case.

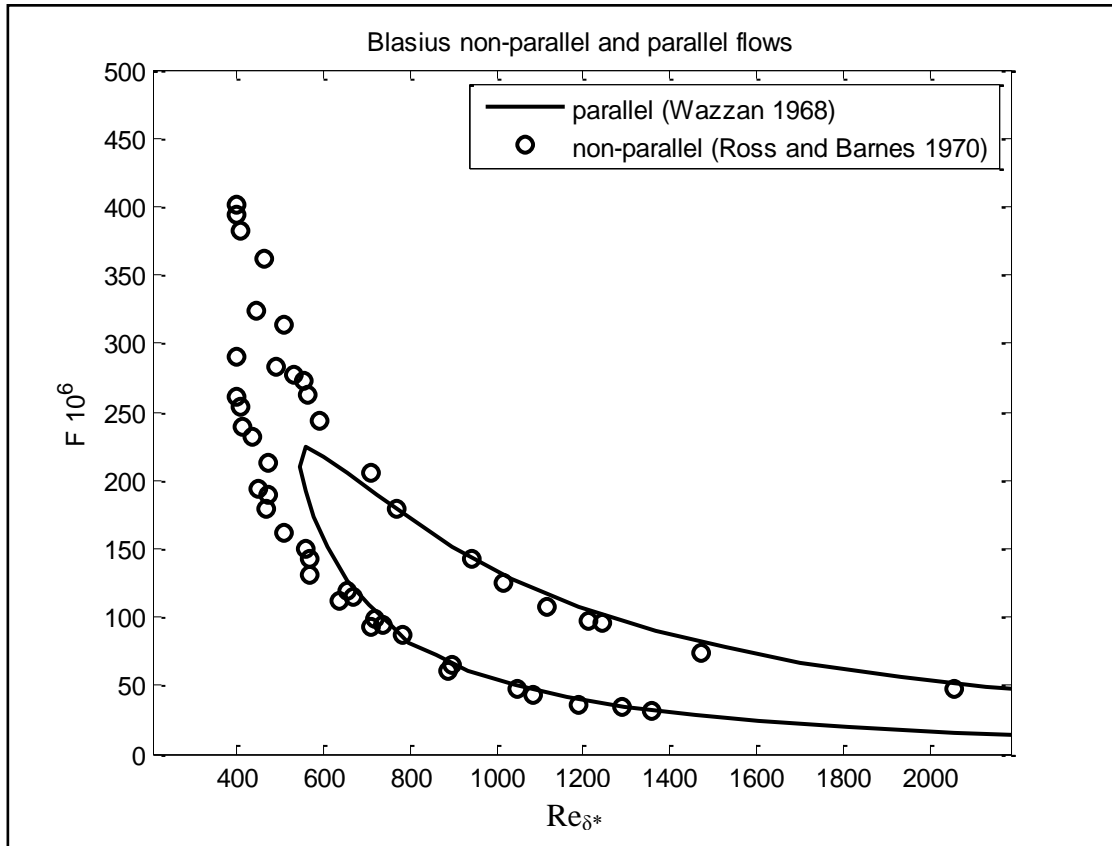


Figure 338: Stability diagram for Blasius non-parallel and parallel flows.

The effect of favorable (negative) pressure gradient on the stability curve is shown in Figure 339. The (parallel-flow) computations were performed for the Falkner-Skan wedge flows for different values of pressure gradient parameter β . The case of $\beta=0$ corresponds to the shown in the previous plot Blasius parallel flow. It can be seen that the stability diagram shrinks towards higher Reynolds numbers with increase of pressure gradient and to a more narrow range of unstable frequencies. Thus favorable (negative) pressure gradient stabilizes the boundary layer flow.

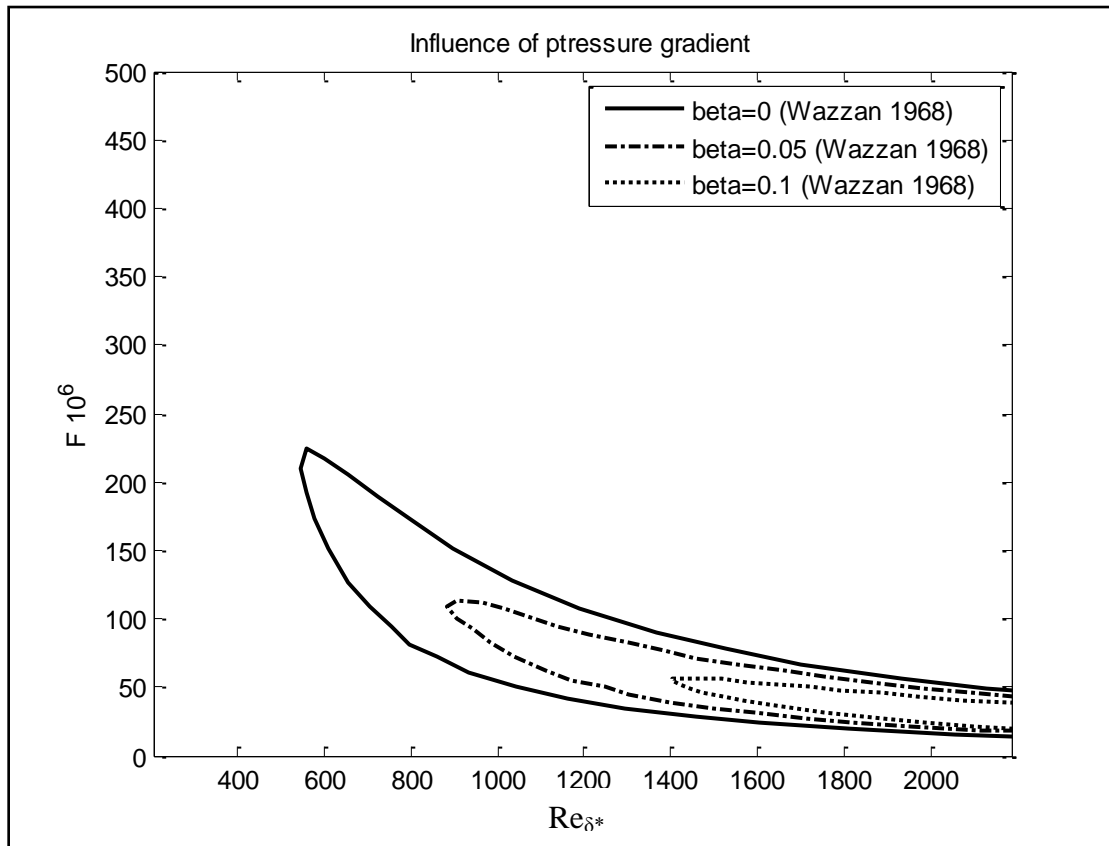


Figure 339: Stability diagram for different pressure gradients.

The linear stability theory cannot predict the onset of turbulence. There are three general types of boundary layer transition processes¹⁶. The first is called *natural transition* for a flow with low freestream turbulence level and smooth walls. The flow changes from T-S waves to turbulent flow slowly through three-dimensional waves, vortex breakdown and turbulent spots. The commonly used transition prediction technique for this transition mechanism (and to be used in the following comparison with the experimental data for Gradient-Zero model) is the e^N method. It assumes that transition occurs when the overall amplification of T-S waves reaches a particular value $N=9$ (from Smith and Gamberoni¹⁷, $N=10$ (from Jaffe et al (1970)¹⁸; where: $N=\ln(a/a_0)$, a and a_0 – are the final (at transition point) and initial amplitudes of T-S wave correspondingly. The receptivity of the boundary layer to external disturbances sets the initial amplitude. The presence of a step can be considered as local stability modification which can lead to increase of local amplification rate. As a result the amplitude of T-S waves increases at the step location and transition moves upstream closer to the step. So long as transition does not

occur too close to the step, the effect of step has been described by a roughness dependent change to N , ΔN ^{19,20}.

If the freestream turbulence level is high, the wall is rough or the surface is vibrating, etc., the flow may skip the early stages of natural instability and go directly to vortex breakdown or turbulent spots. Large disturbances cause *bypass transition*.

The last type is called *separated-flow transition*, when transition occurs in a separated shear layer.

High freestream turbulence intensity (TI) is known to reduce the transitional N-factor²¹. In his work Mack proposed that turbulence is related to the initial level of disturbances, which would then modify the e^9 method into “ e^N ” prediction. He suggested the following modification of the transitional N-factor:

$$N \approx -8.43 - 2.4 \cdot \ln(TI) \quad (17)$$

where: TI is given by a fraction (not percent). The formula is valid for $TI=0.0007 - 0.0298$.

7.5.7 Hot-wire Anemometry Results

The experimental results on power spectra and velocity time series measured with hot-wires in the test section for all three models are presented in this section. Hot-wires were placed in the boundary layer at the same heights of about $k \approx 0.02$ in (the detailed information on hot-wire locations and parameters of each run were documented in the Run Matrix). Hot-wires were placed on the model in stepwise order outside of the contamination angle and were numbered successively starting from the first upstream hot-wire, usually placed close to the step excrescence. The basic experimental parameters were as follows. The sample time in the test section was about 5-25sec, the sampling frequency was 300Hz, and the freestream speed (measured with Pitot tube) ranged from $U \approx 8$ -30m/s. Each plot shows first the power spectra for hot-wires and then the corresponding velocity time series. In the later sections, the useful comparison of the spectra for different freestream speeds, stream-wise distances, and models are presented. The results on the velocity RMS calculated from the velocity time series are also presented. Each plot shows the RMS for several runs (different U), but for the same model and step height. Finally, the traversing results are presented. Each plot shows the mean velocity profiles and velocity RMS profiles as function of distance from the wall for several runs (different U), but for the same model and step height.

7.5.7.1

Velocity Time Series and Spectra

The velocity time series and spectra results in this section are presented first for the Gradient-Zero model, then for the Gradient-A model, and finally for the Gradient-B model.

Table 13 below gives information about all runs that were performed for the Gradient-Zero model. It contains the basic parameters for the Gradient-Zero model, including run number, freestream speed, step height, and Reynolds number calculated at the step position. Information on the hot-wire locations, frequencies of peaks (if found in velocity power spectra) attributed to possible T-S waves, and their amplitudes and corresponding N-factors is provided also in the

Table 13. Table 12 gives a detailed description of each parameter used in Table 13.

Table 12: Parameters used in Table 13

Component	Specifications
U	upstream freestream speed measured with Pitot tube (highlighted in yellow – U was not measured but extrapolated based on the measured speeds; in orange – car speed, U_{car})
k	step height (positive for forward facing and negative for aft facing)
k/δ^*_k	step height normalized with displacement thickness at step location
$Re_{\delta^*, k}$	$= \delta^*_k U / \nu$
Re_k	$k U_k / \nu$
A0	level of noise in the velocity power spectra for the first upstream hw1 taken as initial amplitude of T-S wave
s1-s4	streamwise positions of hot-wires hw1-hw4
f1 – f4	frequency of T-S waves
A1-A4	power of T-S waves (A1 coincides with A0 because no T-S waves were detected for the first hw1 in all runs)
N1-N4	N-factors for hw1-hw4 calculated from the spectra as $N_i = 0.5 \cdot \ln(A_i/A_0)$, where i is the hot wire number
Δf	half width of a frequency peak at its half height

Table 13: Gradient-Zero hot-wire matrix

Basic parameters						hw1			
Run #	U (m/s)	k (in)	k/ δ^*k	Re δ^*k	A0	s1 (in)	f1 (Hz)	A1	N1
125	14.1	0.00	0.000	1296	--	18.5	--	--	--
124	18.4	0.00	0.000	1273	--	18.5	--	--	--
123	23.2	0.00	0.000	1440	--	18.5	--	--	--
144	12.7	0.00	0.000	1067	0.001	16.5	--	0.001	--
145	17	0.00	0.000	1235	0.004	16.5	--	0.004	--
146	19.3	0.00	0.000	1312	0.004	16.5	--	0.004	--
147	22.3	0.00	0.000	1418	0.003	16.5	--	0.003	--
130	14.2	0.04	0.850	1296	0.002	16.5	--	0.002	--
131	14.6	0.04	0.850	1296	0.002	16.5	--	0.002	--
132	19.6	0.04	0.996	1333	0.01	16.5	--	0.01	--
133	22	0.04	1.065	1399	0.02	16.5	--	0.02	--
134	24	0.04	1.095	1480	0.02	16.5	--	0.02	--
128	18	0.04	0.996	1224	0.02	16.5	--	0.02	--
126	22.1	0.04	1.065	1406	0.04	16.5	--	0.04	--
127	23.5	0.04	1.095	1454	0.06	16.5	--	0.06	--
129	24	0.04	1.095	1480	0.03	16.5	--	0.03	--
148	13	0.04	0.806	1092	0.002	16.5	--	0.002	--
149	17.3	0.04	0.932	1257	0.003	16.5	--	0.003	--
150	20	0.04	0.996	1360	0.004	16.5	--	0.004	--
151	22.6	0.04	1.065	1437	0.004	16.5	--	0.004	--
152	22.5	0.04	1.065	1431	--	16.5	--	--	--
135	13	-0.04	0.806	1092	0.001	16.5	--	0.001	--
136	17.2	-0.04	0.932	1250	--	16.5	--	--	--
137	19.6	-0.04	0.996	1333	--	16.5	--	--	--
138	22.6	-0.04	1.065	1437	--	16.5	--	--	--
139	8.6	-0.04	0.677	982	0.001	16.5	--	0.001	--
140	12.5	-0.04	0.806	1050	0.001	16.5	--	0.001	--
141	16.6	-0.04	0.932	1206	--	16.5	--	--	--
142	19.6	-0.04	0.996	1333	--	16.5	--	--	--
143	22	-0.04	1.065	1399	--	16.5	--	--	--

Table 13: Gradient-Zero hot-wire matrix (continued)

hw2				hw3				hw4			
s2 (in)	f2 (Δf_2) (Hz)	A2	N2	s3 (in)	f3 (Δf_3) (Hz)	A3	N3	s4 (in)	f4 (Δf_4) (Hz)	A4	N4
39.5	--	--	--	57	--	--	--	78	--	--	--
39.5	--	--	--	57	--	--	--	78	--	--	--
39.5	--	--	--	57	--	--	--	78	--	--	--
27	153(36)	0.012	1.2	32	144(29)	0.004	0.7	--	--	--	--
27	232 (41)	0.21	2	32	216 (33)	0.02	0.8	--	--	--	--
27	268 (46)	0.35	2.3	32	248 (30)	0.04	1.2	--	--	--	--
27	322 (33)	0.7	2.7	32	318 (41)	0.05	1.4	--	--	--	--
27	200 (28)	0.9	3.1	32	181 (26)	30	4.8	36.5	159 (38)	0.15	2.15
27	200 (28)	0.7	2.9	32	181 (26)	30	4.8	36.5	161 (38)	0.15	2.15
27	283 (40)	60	4.35	32	270 (48)	640	5.5	36.5	255 (38)	4	3
27	325 (41)	280	4.75	32	316 (44)	1100	5.45	36.5	300 (36)	20	3.5
27	327 (31)	550	5.1	32	327 (24)	1800	5.7	36.5	--	--	--
		--	--			--	--			--	--
27	275 (37)	45	3.85	32	266 (48)	270	4.75	36.5	233 (30)	220	4.65
27	323 (37)	200	4.25	32	322 (33)	1600	5.25	36.5	316 (37)	420	4.6
27	329 (33)	700	4.7	32	327 (22)	2200	5.25	36.5	327 (20)	250	4.15
27	329 (33)	500	4.85	32	329 (26)	1400	5.35	36.5	--	--	--
		--	--			--	--			--	--
27	159 (37)	0.15	2.15	32	144 (37)	0.11	2	37	140 (41)	0.27	2.45
27	249 (37)	7.7	3.9	32	229 (37)	1.9	3.25	37	225 (33)	2.4	3.35
27	297 (59)	40	4.6	32	282 (44)	9	3.85	37	--	--	--
27	326 (30)	200	5.4	32	--	--	--	37	--	--	--
27	--	--	--	32	--	--	--	37	--	--	--
27	150 (33)	10	4.6	32	--	--	--	36.5	--	--	--
27	--	--	--	32	--	--	--	36.5	--	--	--
27	--	--	--	32	--	--	--	36.5	--	--	--
27	--	--	--	32	--	--	--	36.5	--	--	--
27	83 (37)	0.45	3	32	77 (33)	0.45	3	36.5	68 (26)	0.3	2.85
27	150 (52)	10	4.6	32	--	--	--	36.5	--	--	--
27	--	--	--	32	--	--	--	36.5	--	--	--
27	--	--	--	32	--	--	--	36.5	--	--	--
27	--	--	--	32	--	--	--	36.5	--	--	--

Table 14 contains information about transition locations found from velocity and skin friction measurements. The data from velocity measurements are based on qualitative analysis of the velocity time series and spectra. The criteria for the transition were: the broadening of velocity power spectra and about 100% intermittency in the velocity time series.

Table 14: Gradient-Zero hot-wire transition locations

Basic parameters			Transition location	
Run #	U (m/s)	k (in)	s, from HW (in)	s, from Cf (in)
125	14.1	0.00	--	--
124	18.4	0.00	--	--
123	23.2	0.00	--	--
144	12.7	0.00	--	--
145	17	0.00	--	--
146	19.3	0.00	--	--
147	22.3	0.00	--	--
130	14.2	0.04	--	--
131	14.6	0.04	--	--
132	19.6	0.04	--	--
133	22	0.04	--	--
134	24	0.04	16.5 - 27	30.1
128	18	0.04	--	--
126	22.1	0.04	--	--
127	23.5	0.04	16.5 - 27	30.1
129	24	0.04	16.5 - 27	30.1
148	13	0.04	--	--
149	17.3	0.04	--	--
150	20	0.04	32 - 37	--
151	22.6	0.04	16.5 - 27	30.1
152	22.5	0.04	16.5 - 27	30.1
135	13	-0.04	--	--
136	17.2	-0.04	16.5 - 27	31.01
137	19.6	-0.04	16.5 - 27	20.99
138	22.6	-0.04	16.5 - 27	22.6
139	8.6	-0.04	--	--
140	12.5	-0.04	--	--
141	16.6	-0.04	16.5 - 27	31.01
142	19.6	-0.04	16.5 - 27	20.99
143	22	-0.04	16.5 - 27	22.6

The plots of velocity time series and corresponding power spectra are shown in the order corresponding to run numbers as given in Table 14. The spikes observed in the spectra beginning at about 230Hz and spaced by 120Hz are related to electronic noise. The specific of this open-field experiment was no grounding and proximity of other equipment which could introduce the

noise, especially the HART vehicle itself. In a separate laboratory test no spikes were observed in the spectra (Figure 340). The electronic noise effectively contributes to the velocity RMS and turbulence intensity and is correlated between wires (Figure 341); therefore its influence can be removed using simple cross-correlation (differencing techniques), e.g. . Reshotko *et al*²². In the subsequent analysis the calculated values for the velocity RMS and turbulence intensity are biased from the true values by the contribution of correlated noise, however a true measure of the turbulence intensity after use of the differencing technique is given in the Section 7.5.7.5. It should also be noted that the finite extent of the test section led to shorter run times than would be desirable to fully-resolve the low-frequency part of the spectrum.

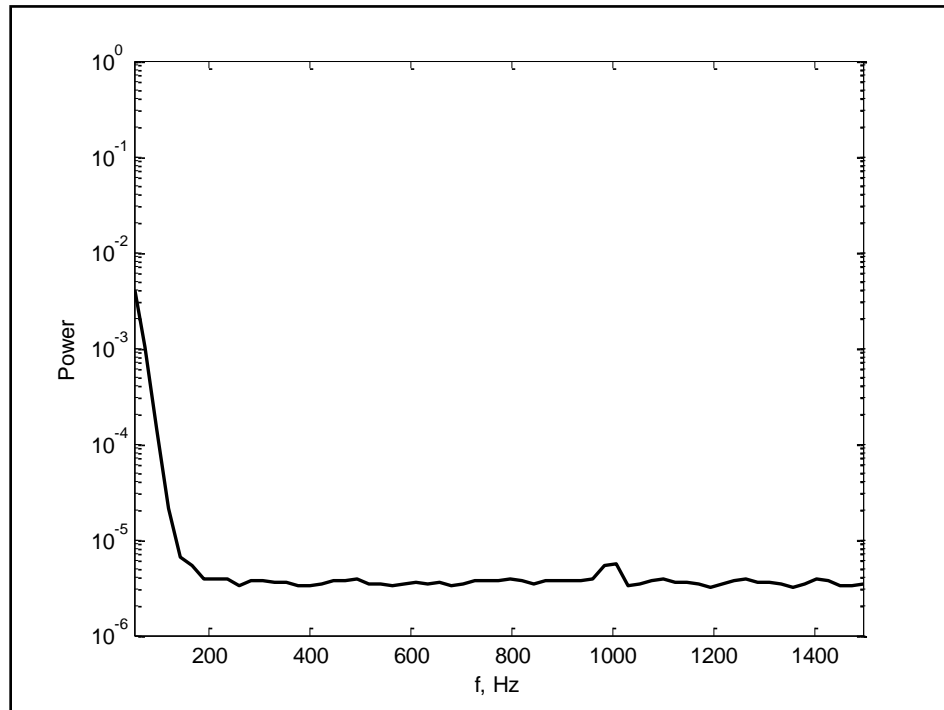


Figure 340: Velocity power spectrum for zero flow in calm environment (lab test).

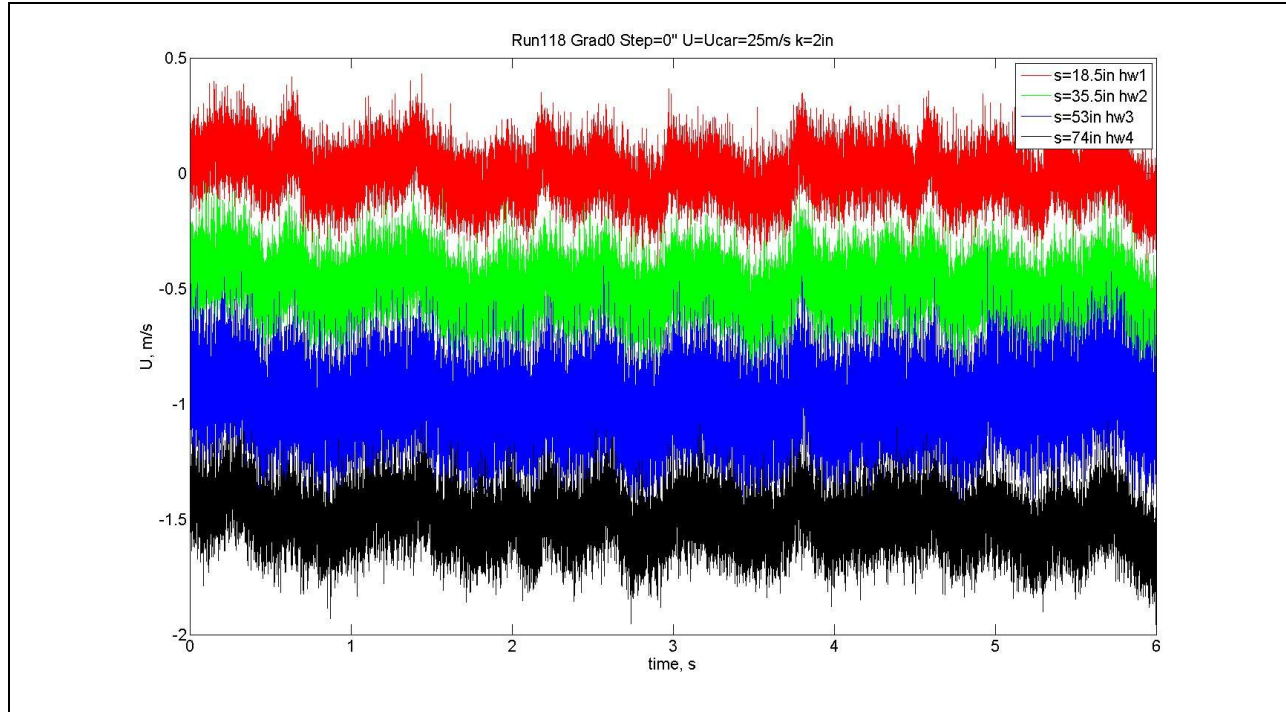


Figure 341: Comparison of fluctuating velocity time series for all wires, Run 118. Note that the traces for HWs 2-4 are offset by -0.5 from the previous wires for clarity.

Runs 123-125 (Figures 342-347) correspond to zero step (clean plate) and large separation between the hot-wires. The velocity time series show laminar flow conditions with the appearance of intermittent spikes corresponding to localized spots of turbulence that increase with freestream speed. The spectra do not show T-S waves, which are estimated to be in 100-300Hz range of frequencies.

Runs 144-147 (Figures 348-355) correspond to zero step (clean plate) and smaller separation between the hot-wires. The velocity time series show pure laminar flow. There are possible T-S waves observed for the hw2 and hw3 locations. Their frequency increases from about 150Hz to 320Hz as freestream speed increases from 12.7m/s to 22.3m/s and it decreases slightly with increase of streamwise distance. The N-factors increase with freestream speed and decrease with stream-wise distance.

Runs 130-134 (Figures 356-365), Runs 126-129 (Figures 366-373), and Runs 148-152 (Figures 374-383) are for the case of a 0.04-inch forward-facing step. In general, the velocity time series show more fluctuations than for the previous case without the step excrescence. The spectra show possible T-S waves in the same range of frequencies. N-factors are larger than for the case without a step. The N-factors increase with freestream speed and drop with stream-wise distance, except for the runs when transition to turbulence is observed (Run 134, Run 129, Run 151). Qualitatively, the transition to turbulence is described by a high level of fluctuations in velocity time series and the broadening of spectra in those runs.

Runs 135-138 (Figures 384-391) and runs 139-143 (Figures 392-401) are for the case of a -0.04-inch aft-facing step. Most of the plots show turbulence for all hot-wires and no T-S waves except for run 135 and runs 139-140, corresponding to low freestream speeds.

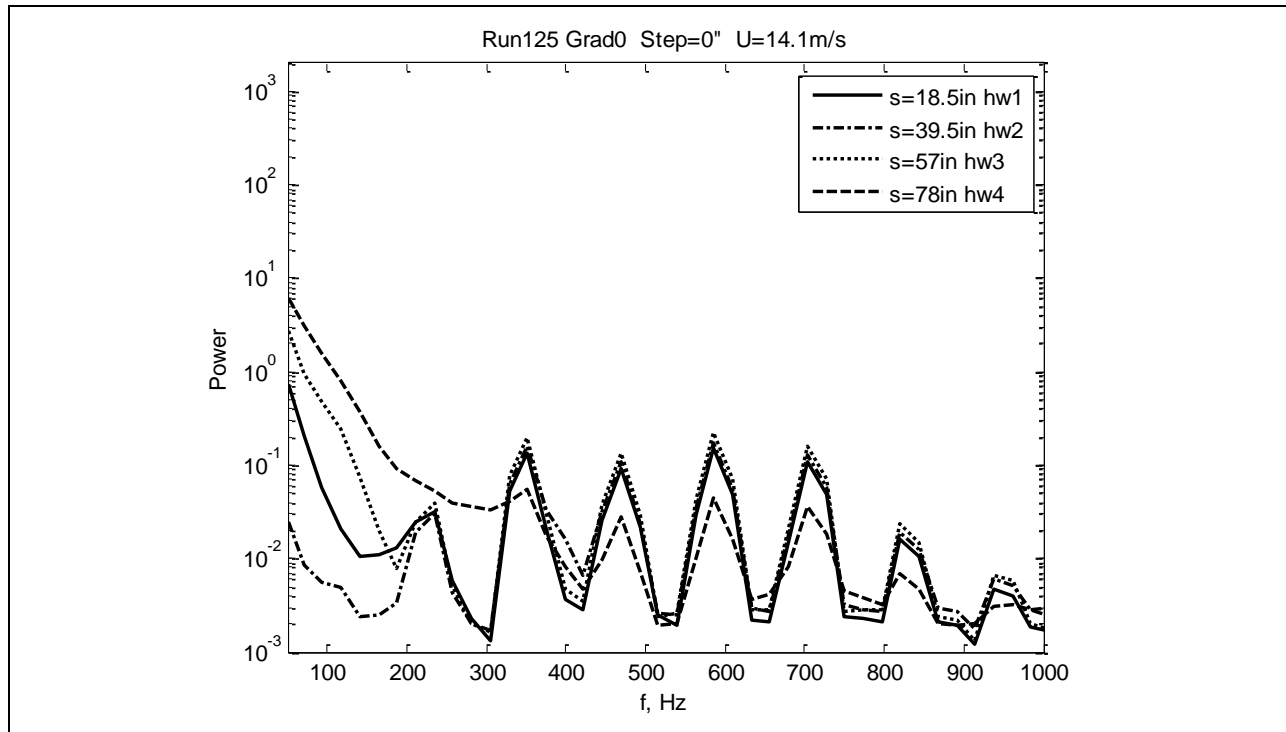


Figure 342: Measured power spectra.

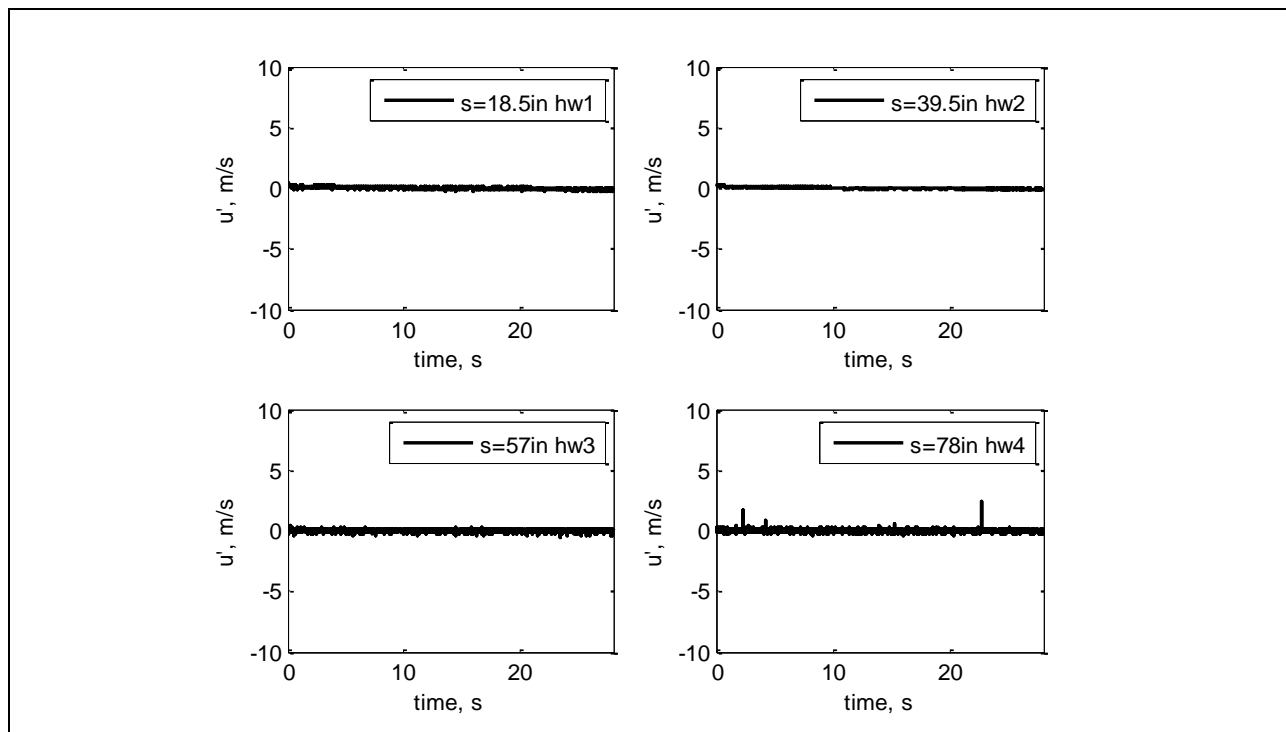


Figure 343: Measured velocity time history.

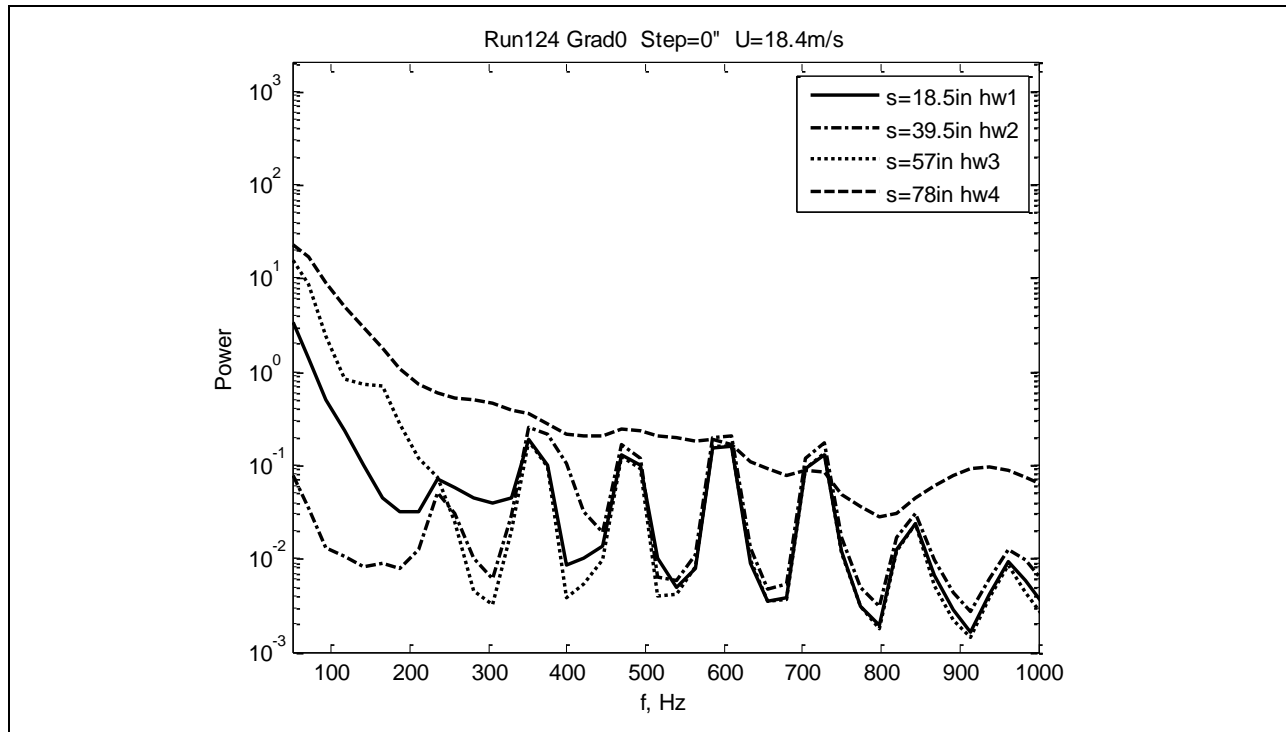


Figure 344: Measured power spectra.

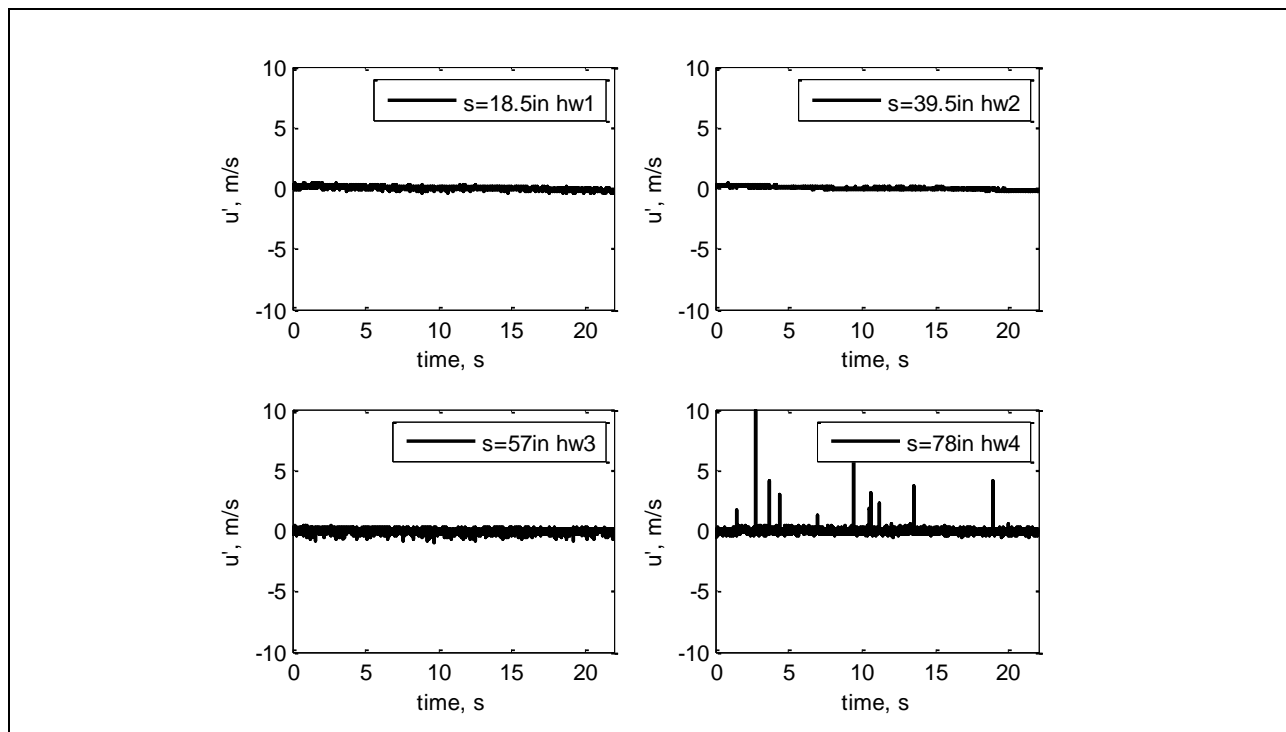


Figure 345: Measured velocity time history.

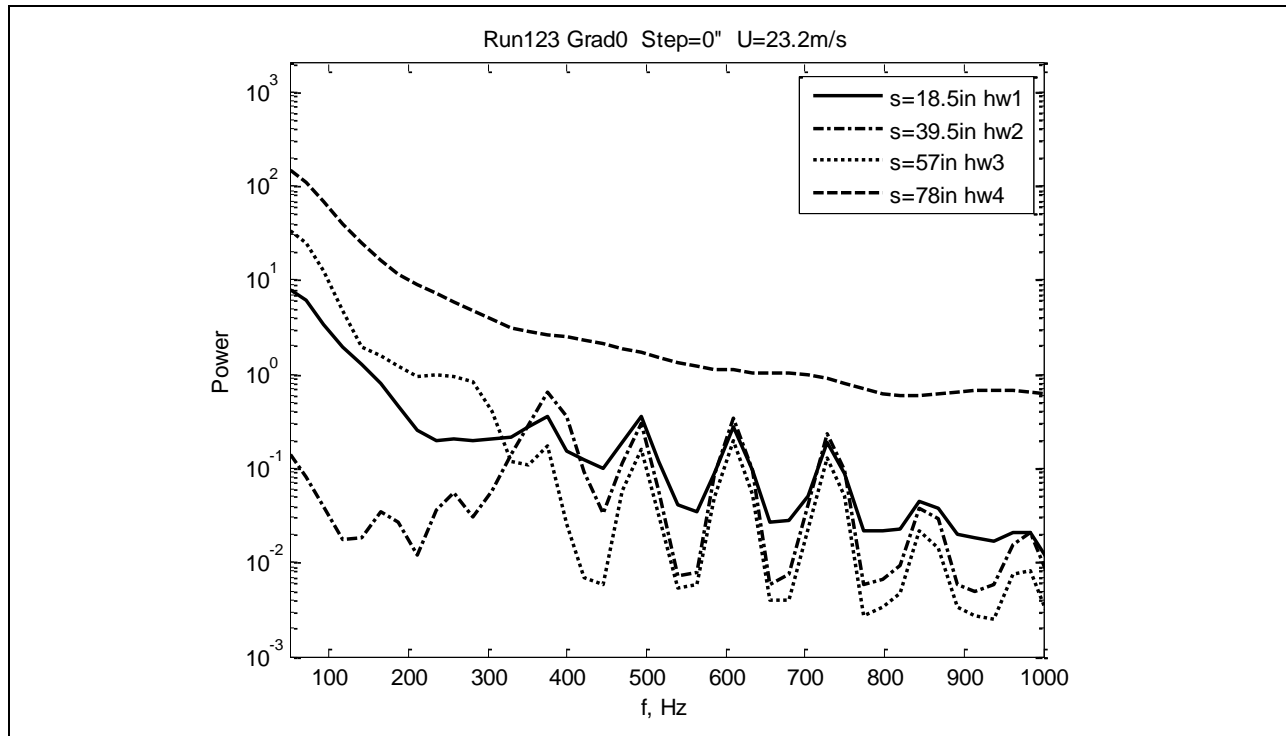


Figure 346: Measured power spectra.

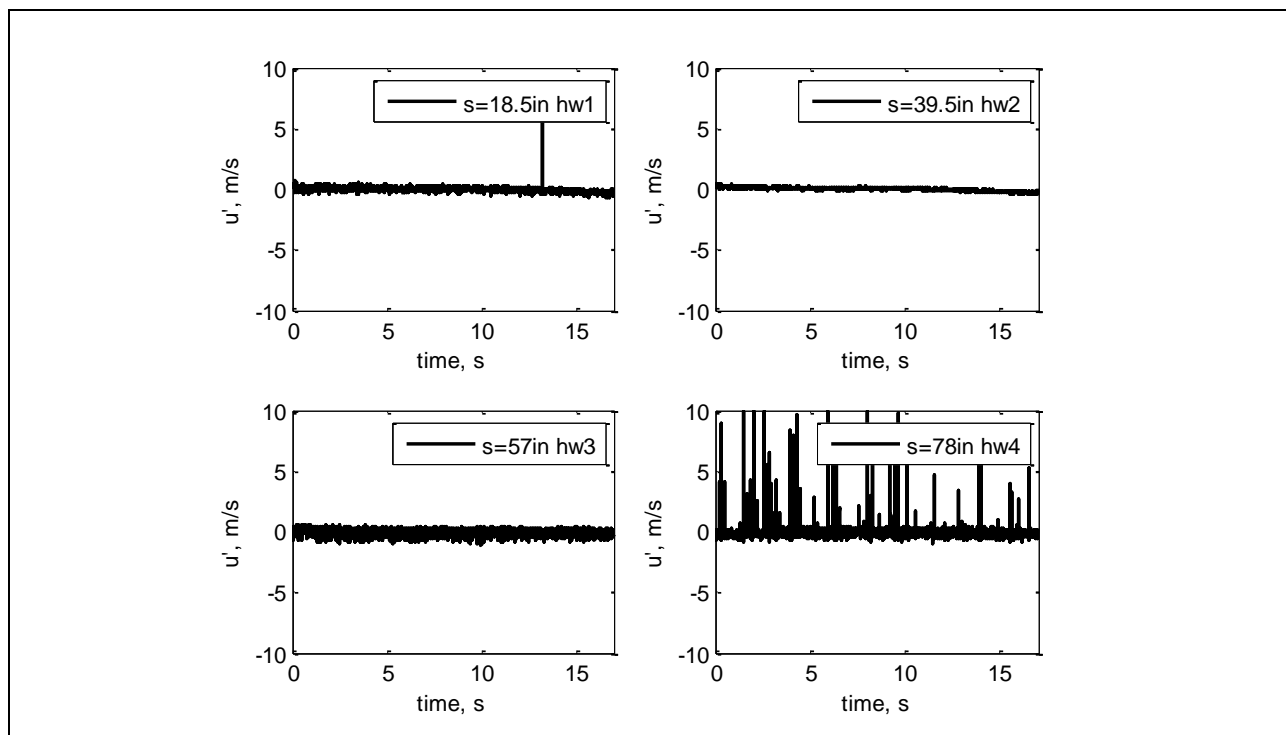


Figure 347: Measure velocity time history.

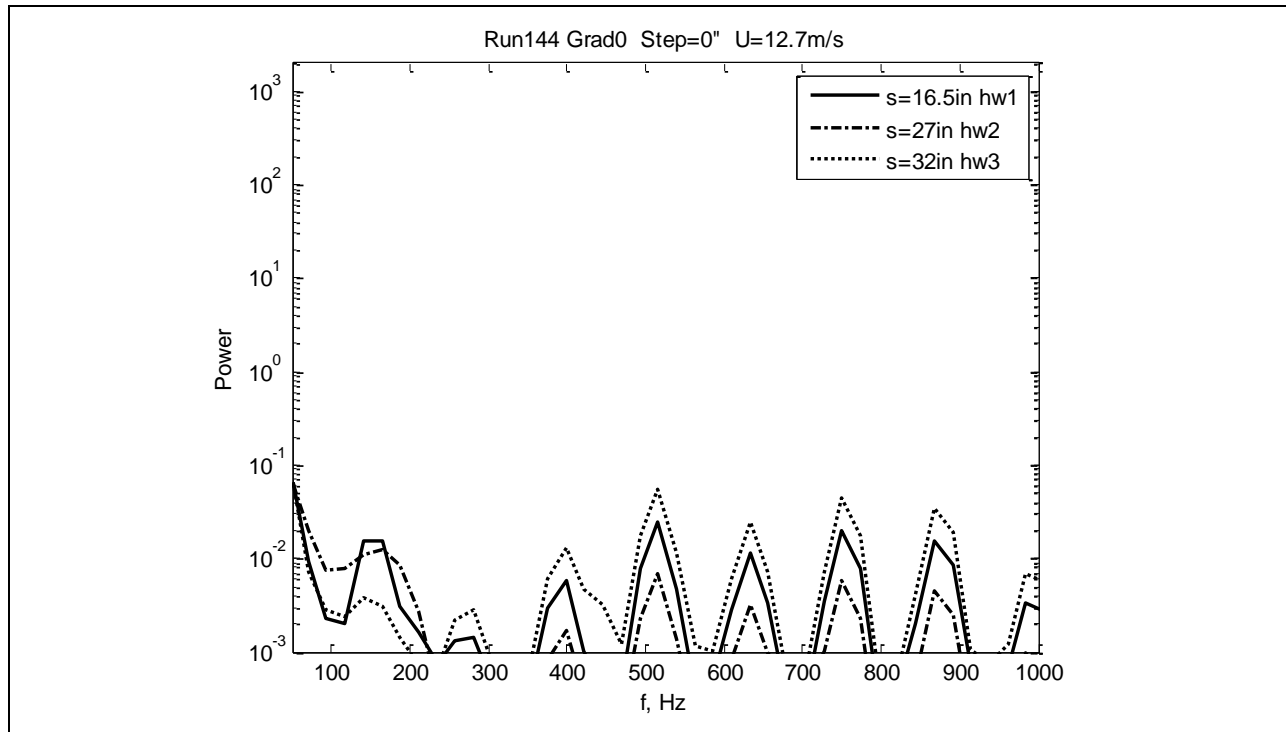


Figure 348: Measured power spectra.

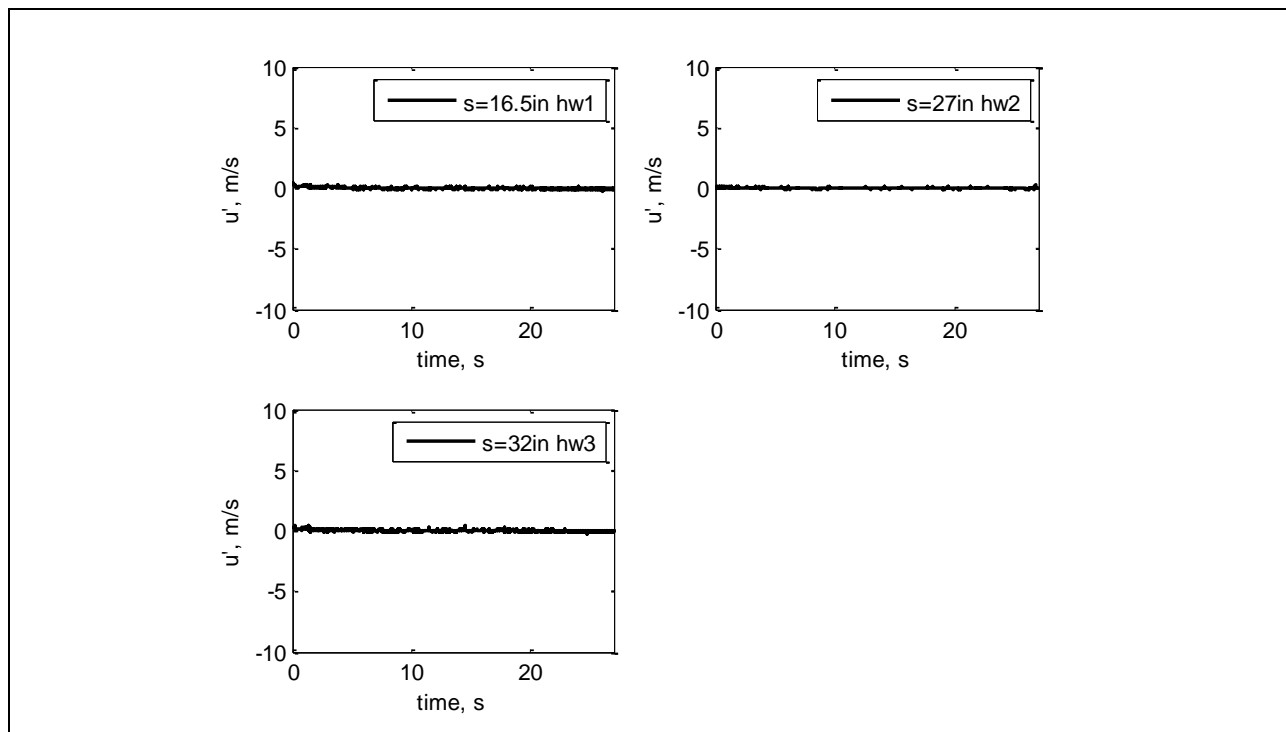


Figure 349: Measured velocity time history.

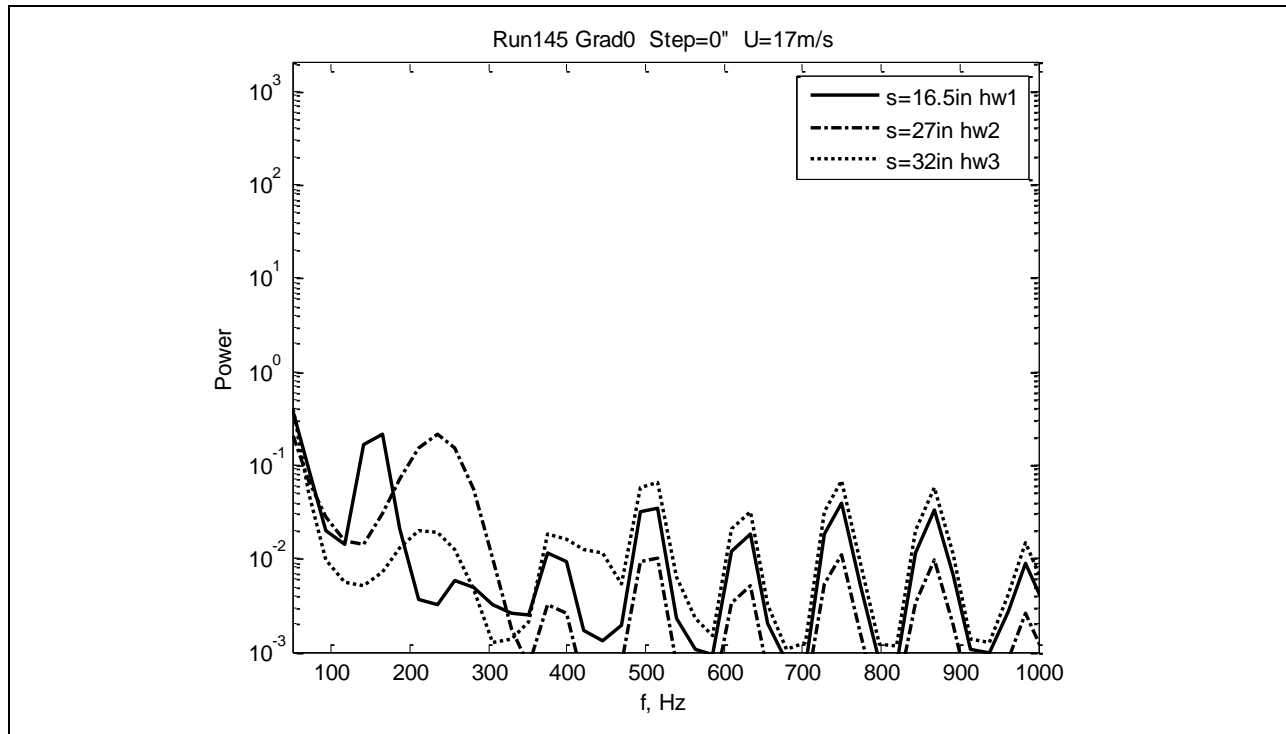


Figure 350: Measured power spectra.

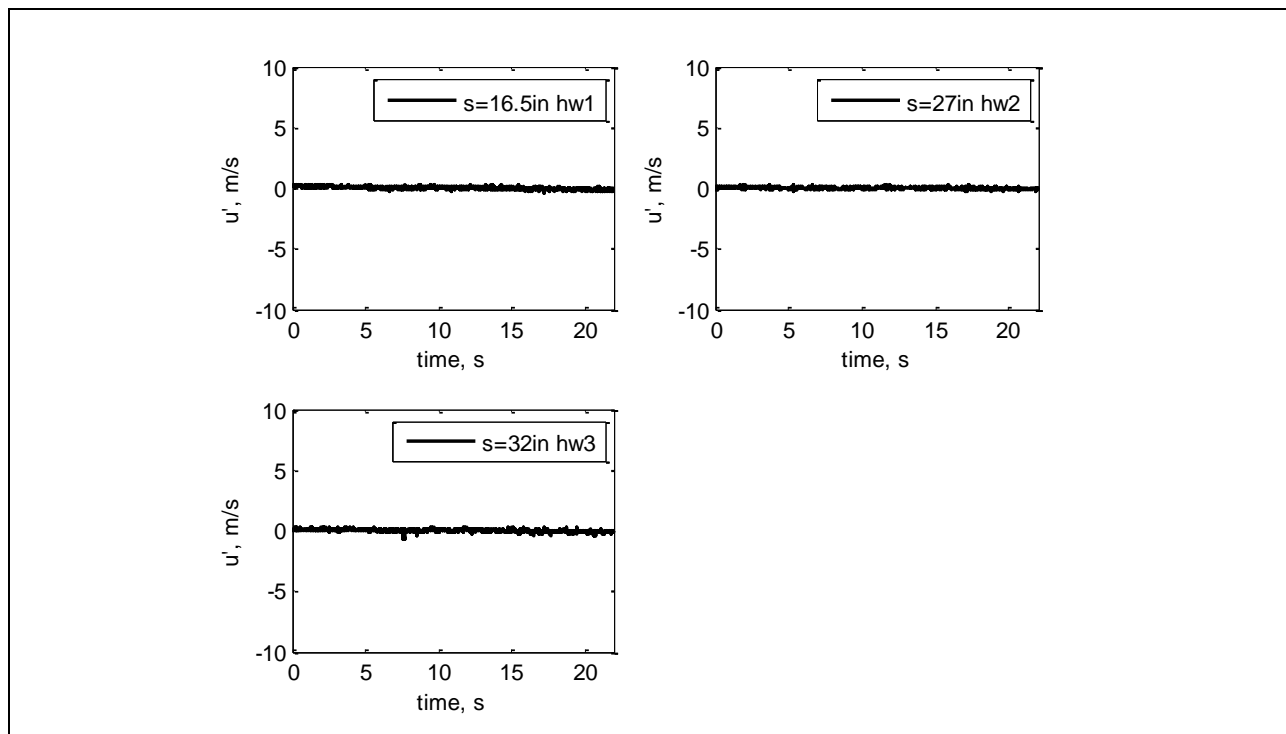


Figure 351: Measured velocity time history.

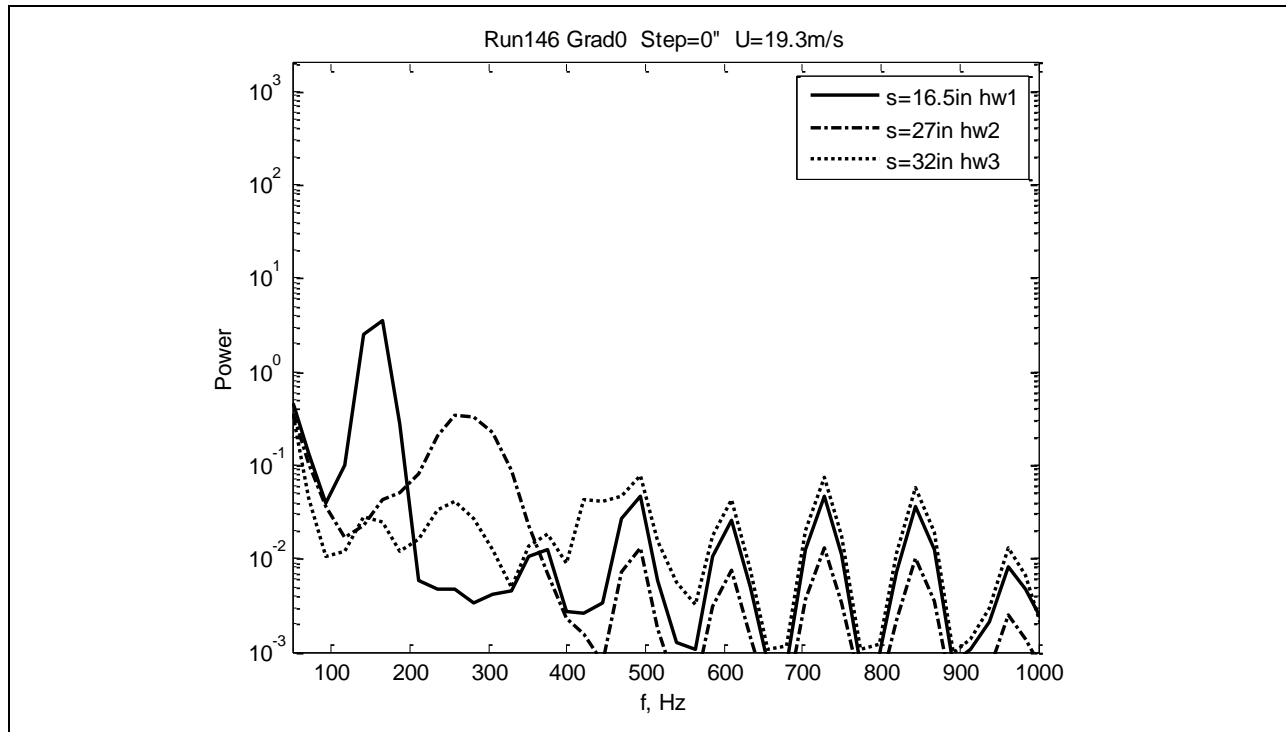


Figure 352: Measured power spectra.

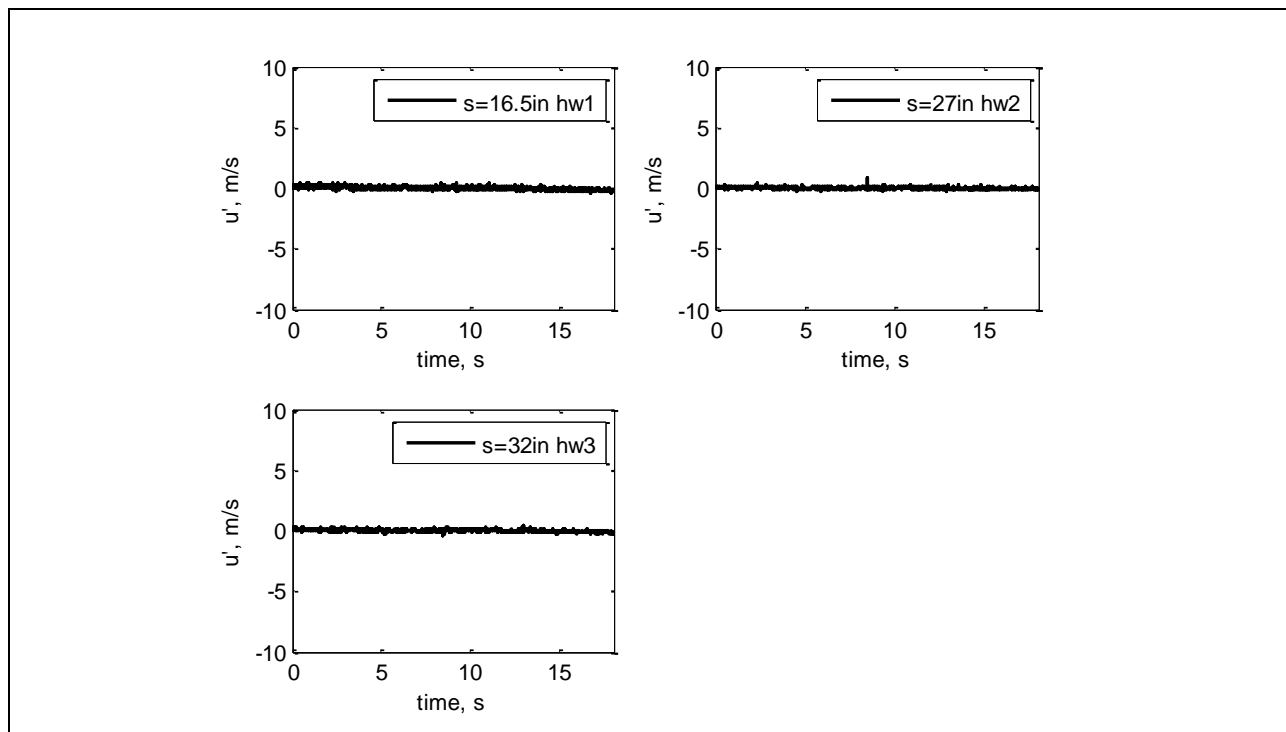


Figure 353: Measured velocity time history.

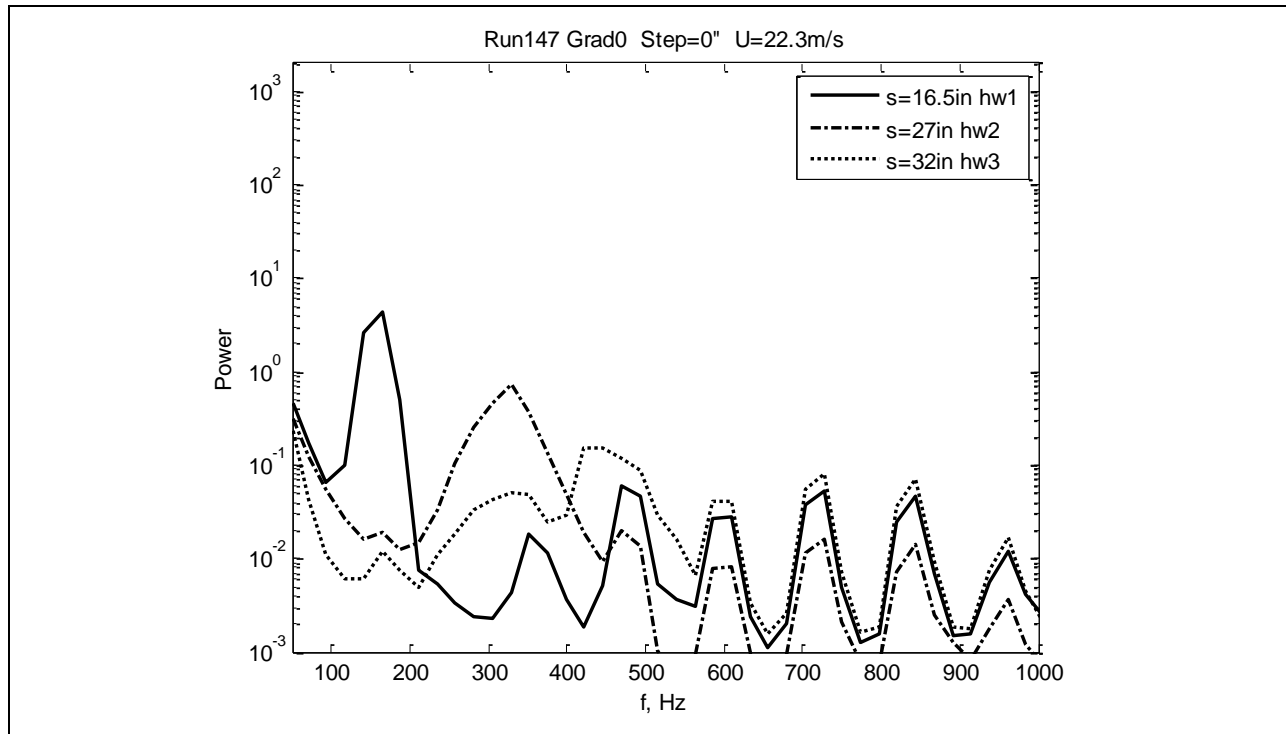


Figure 354: Measured power spectra.

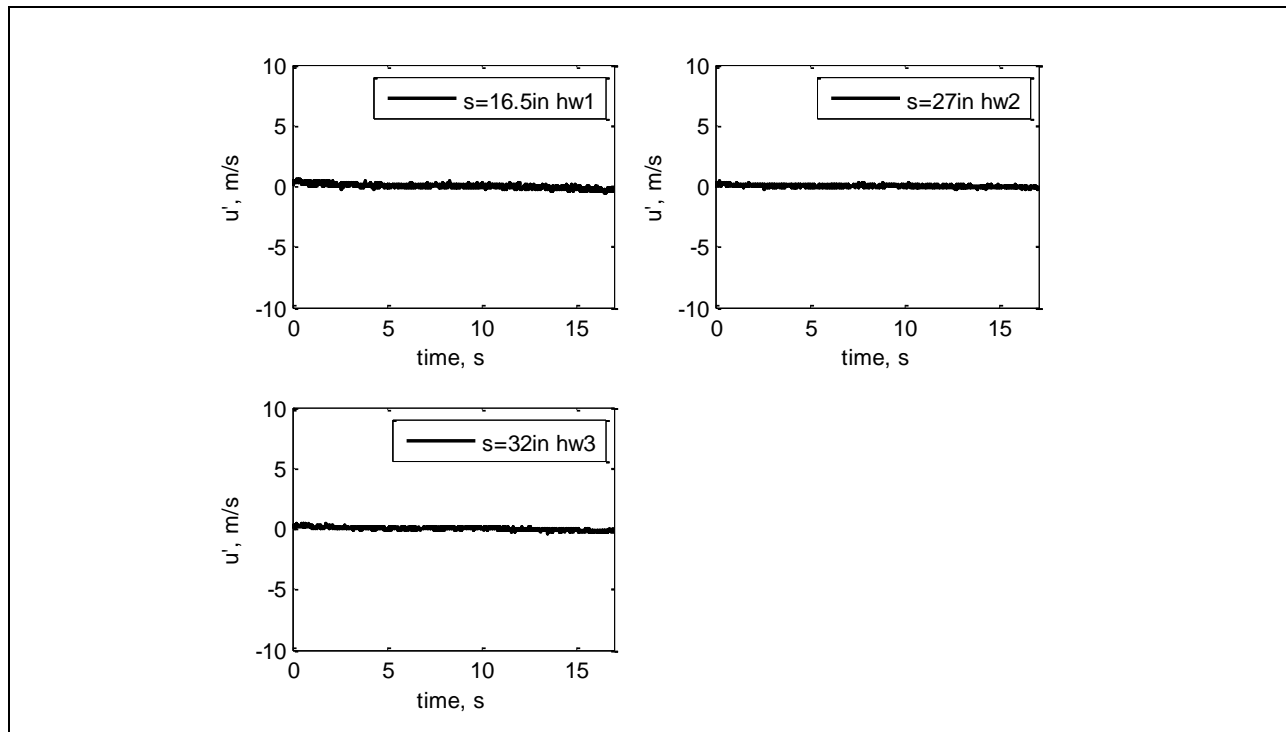


Figure 355: Measured velocity time history.

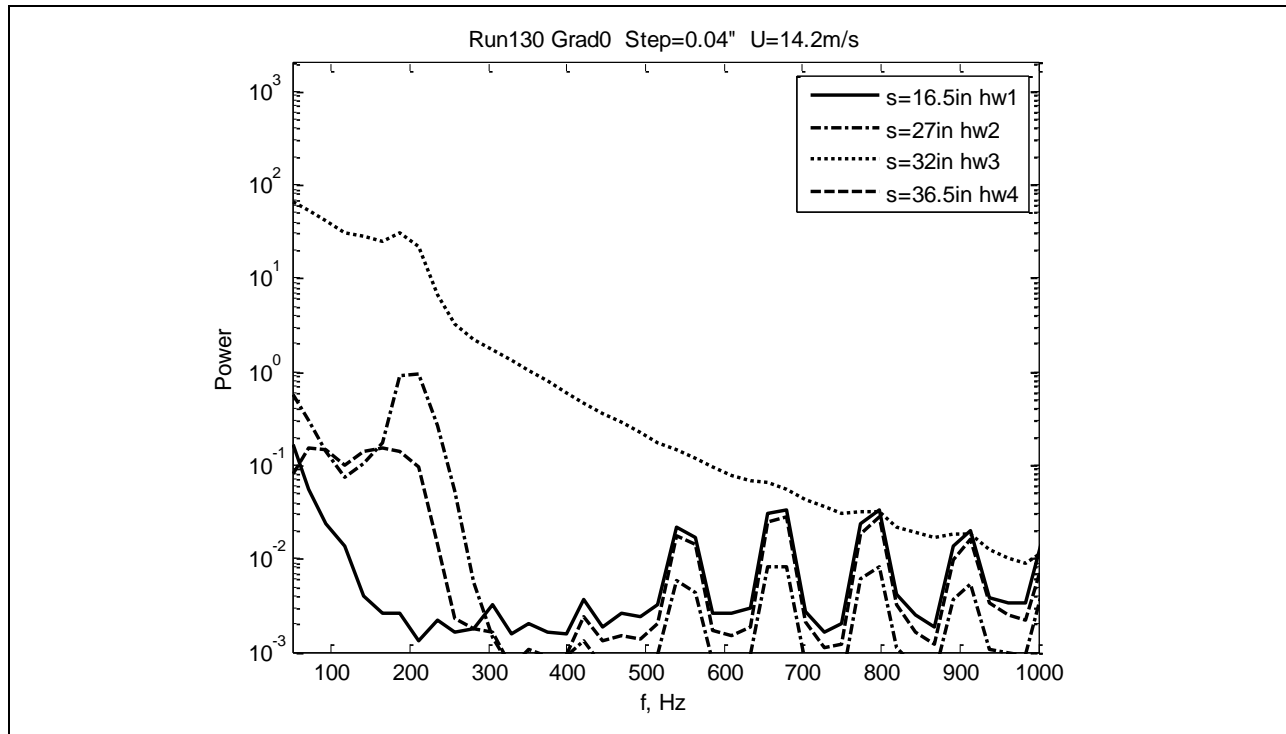


Figure 356: Measured power spectra.

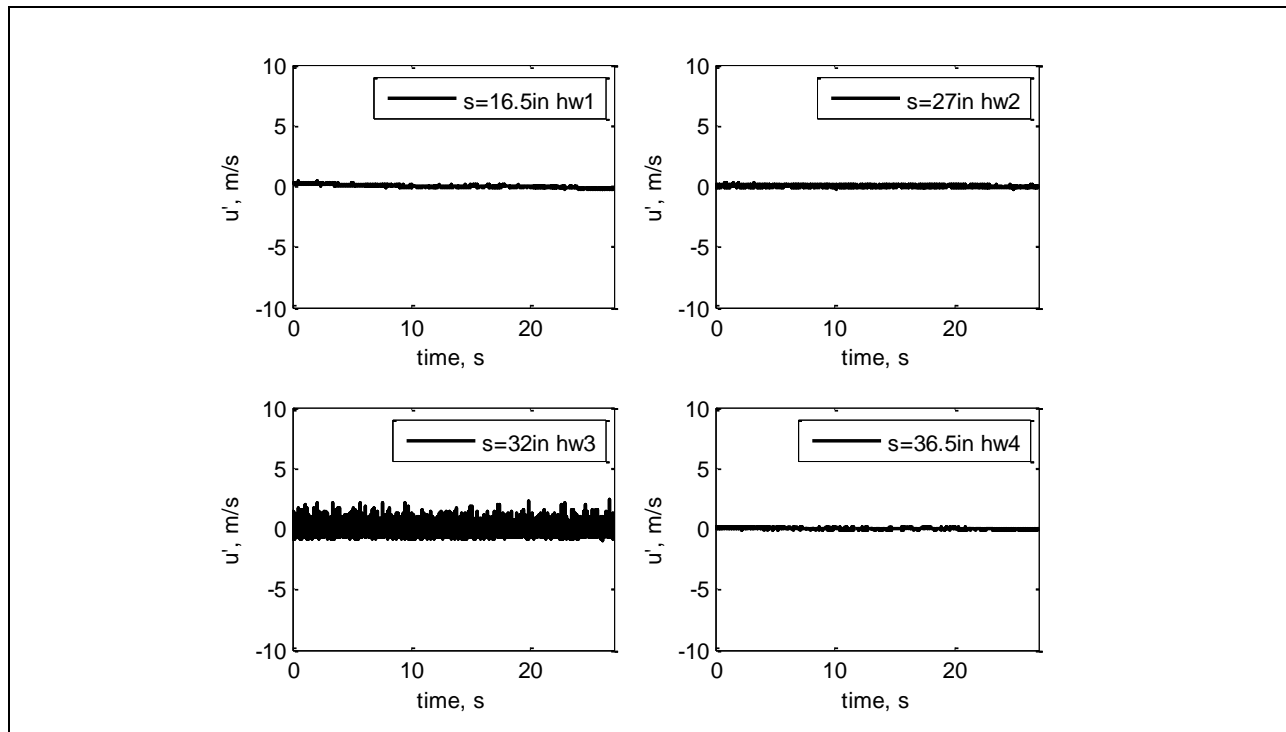


Figure 357: Measured velocity time history.

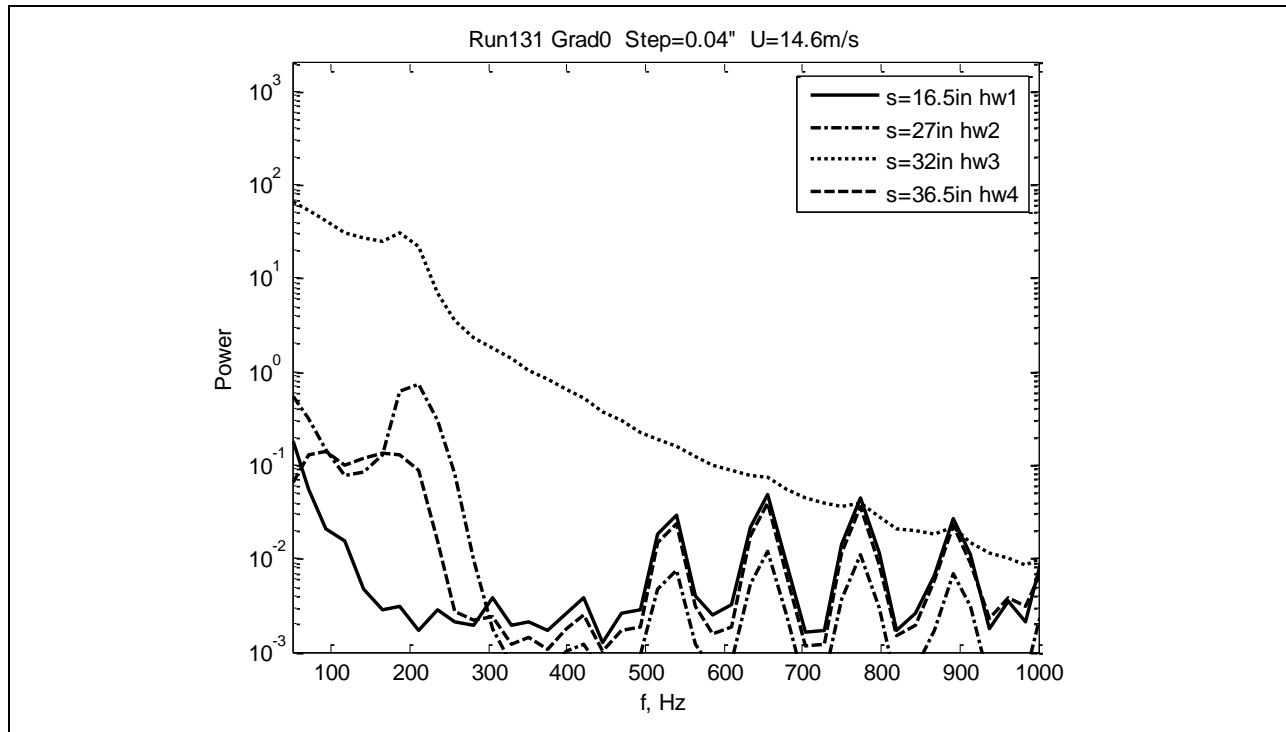


Figure 358: Measured power spectra.

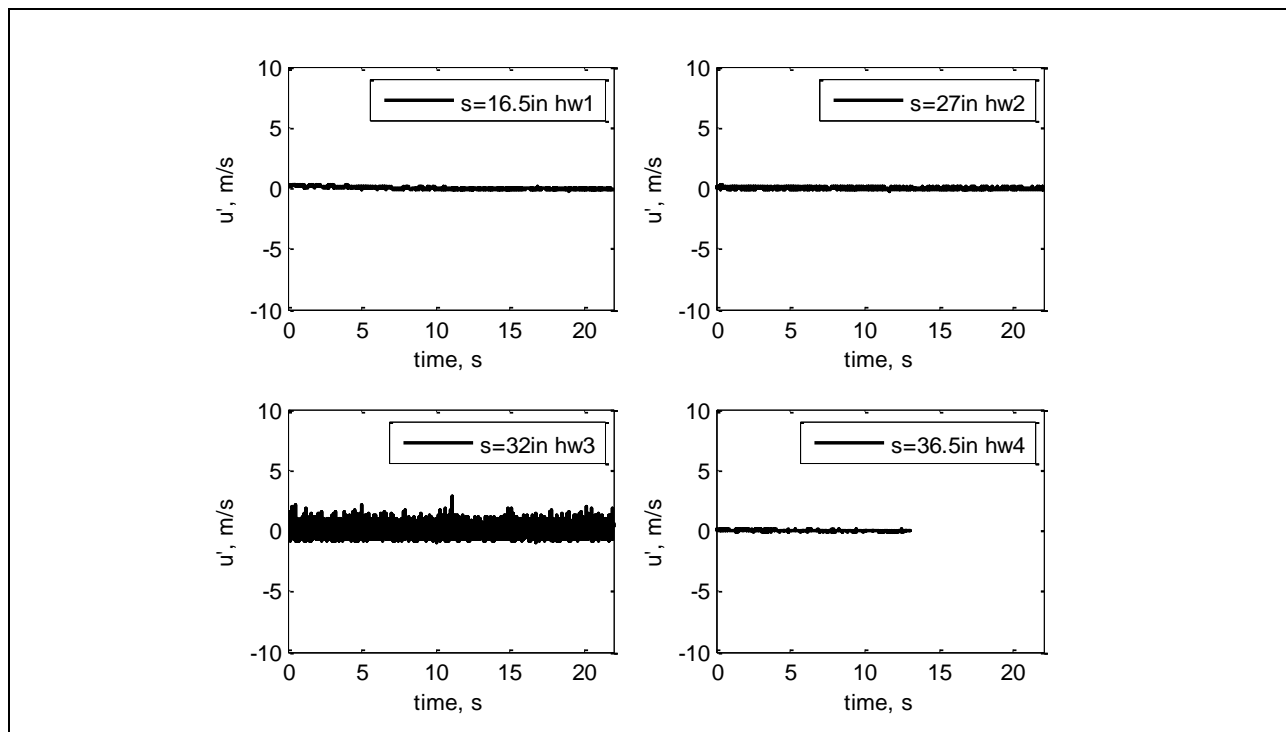


Figure 359: Measured velocity time history.

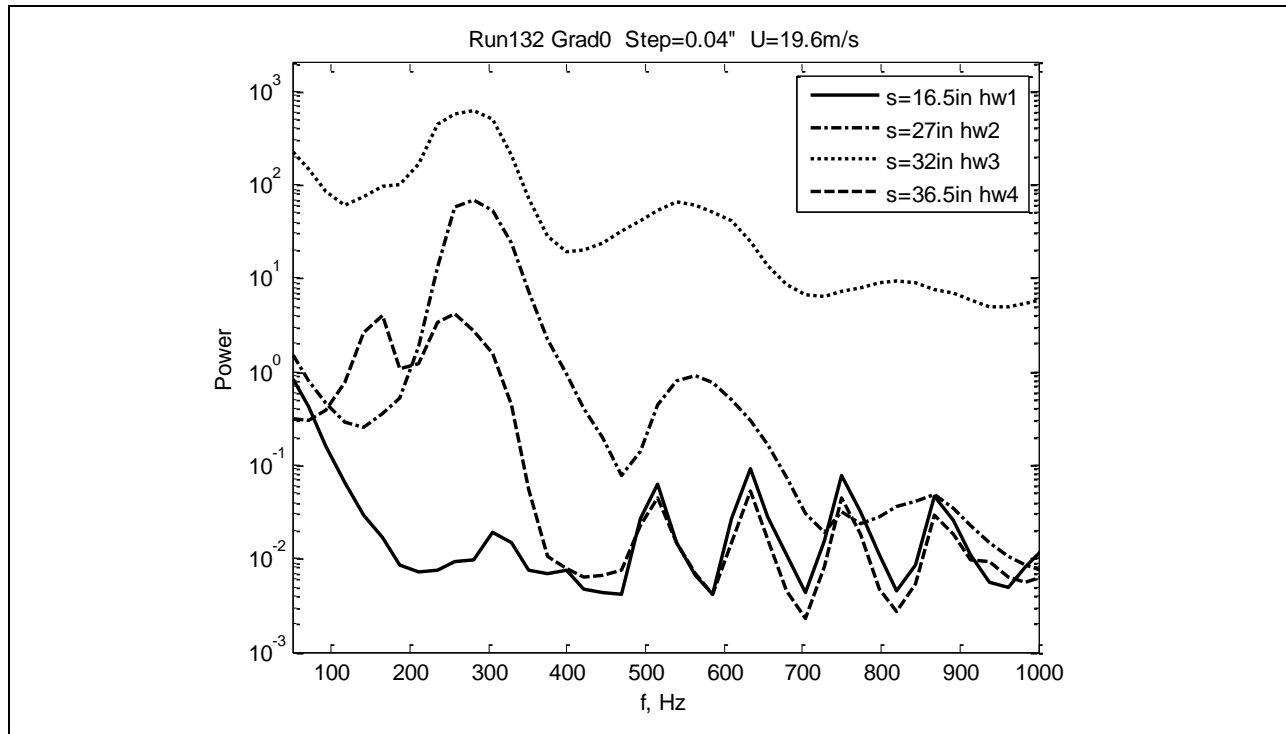


Figure 360: Measured power spectra.

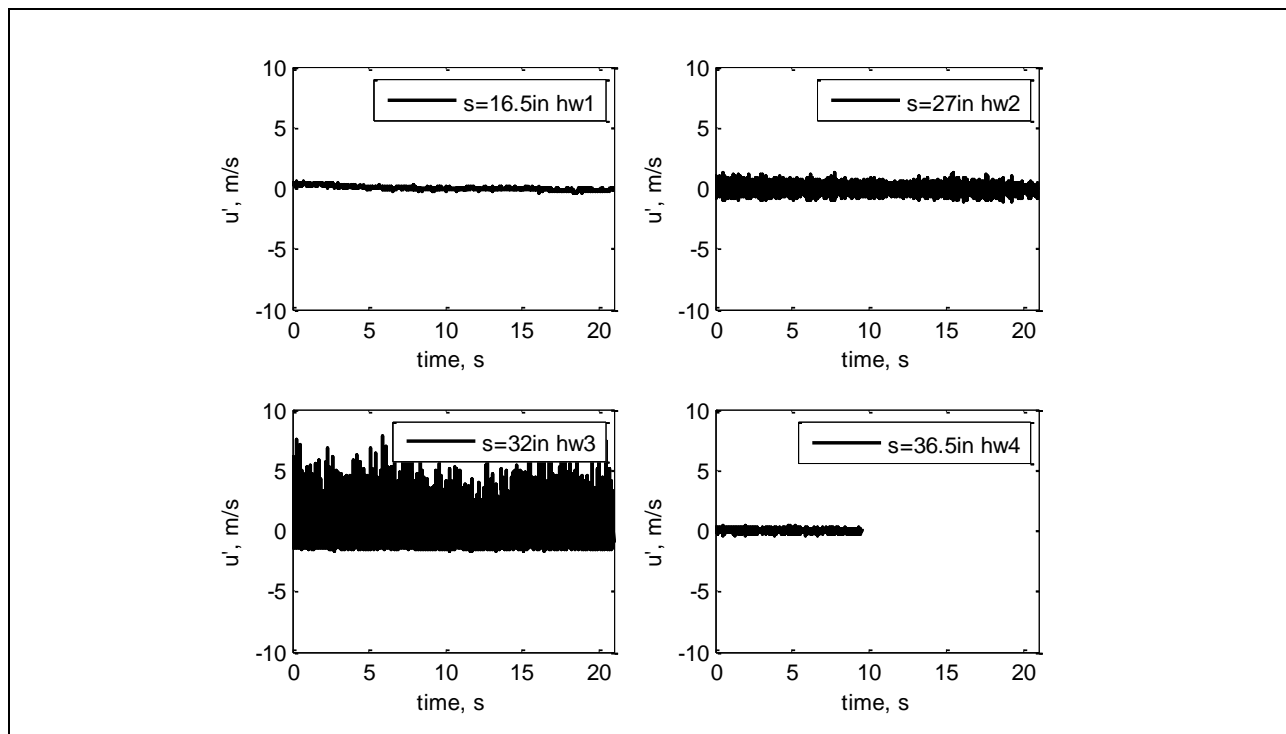


Figure 361: Measured velocity time history.

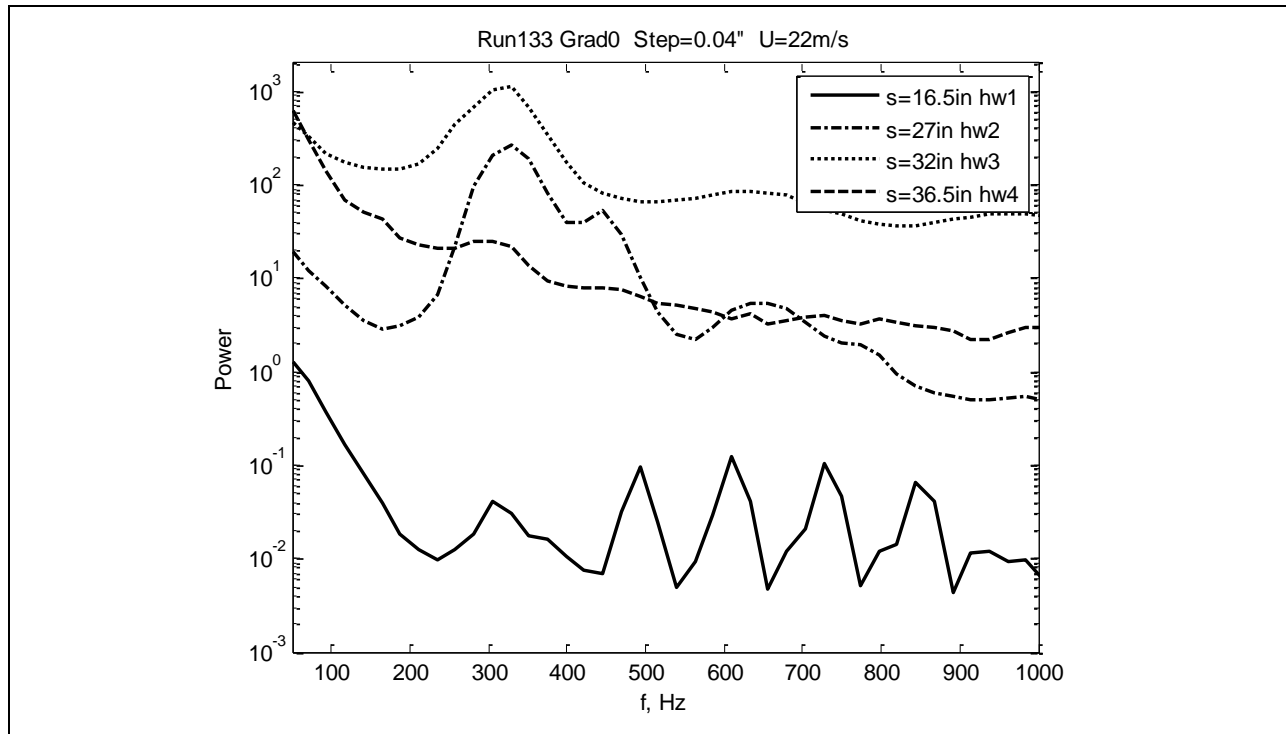


Figure 362: Measured power spectra.

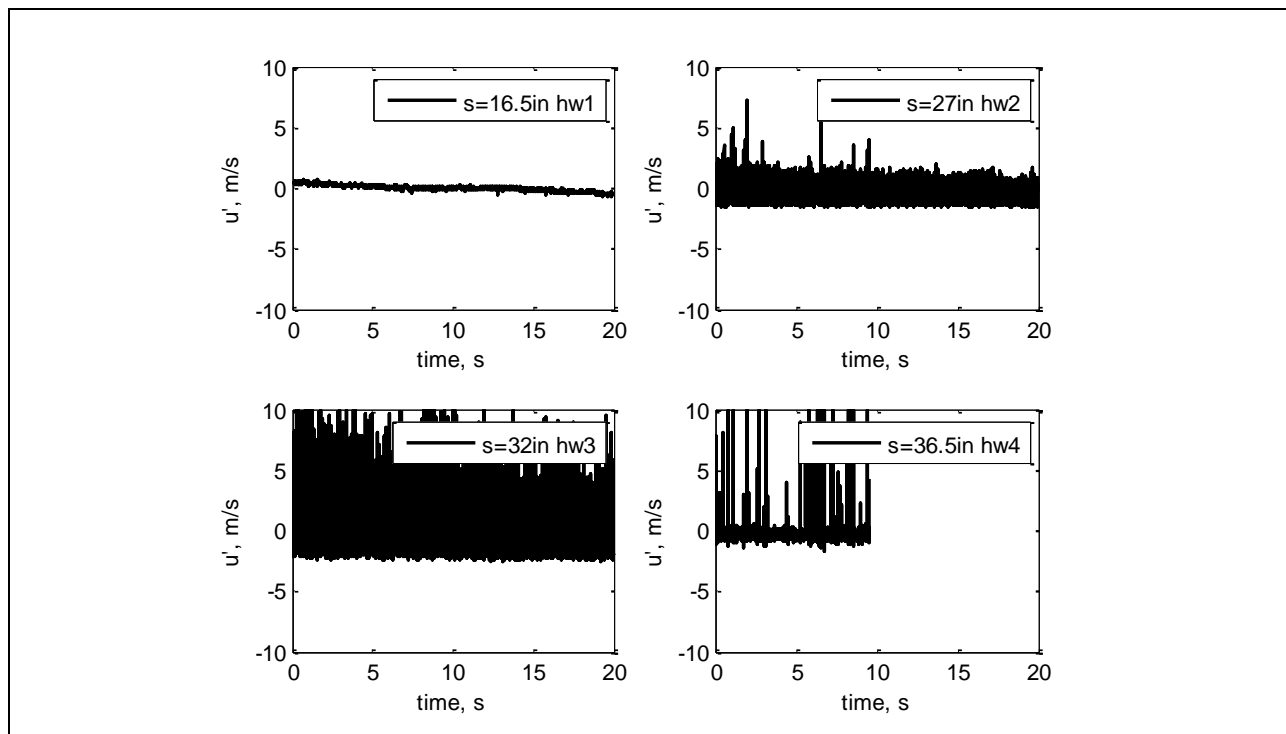


Figure 363: Measured velocity time history.

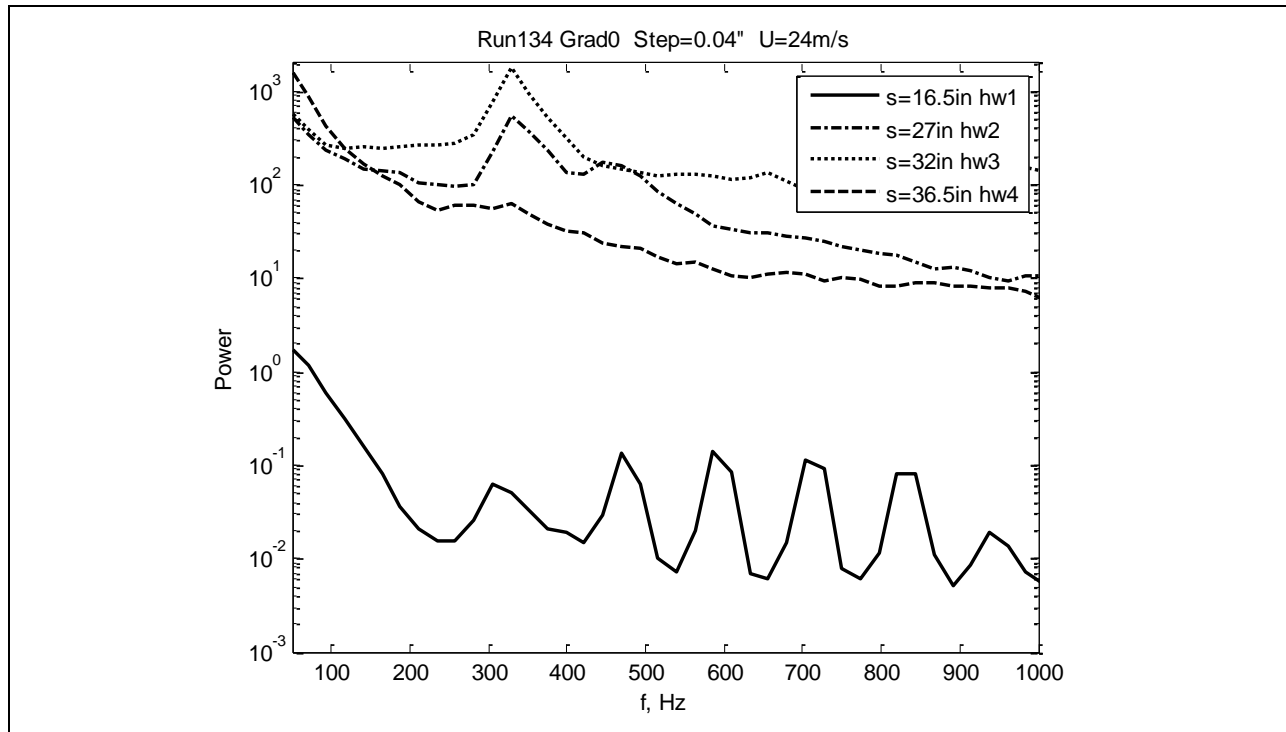


Figure 364: Measured power spectra.

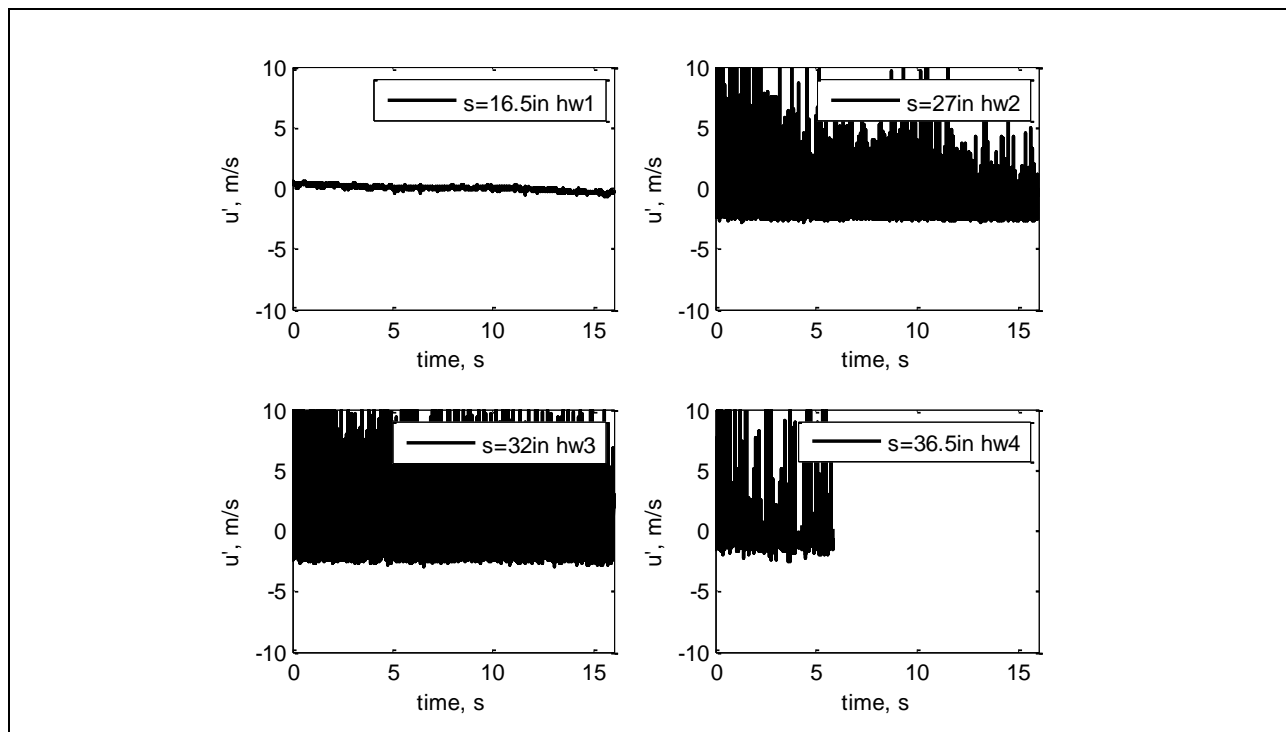


Figure 365: Measured velocity time history.

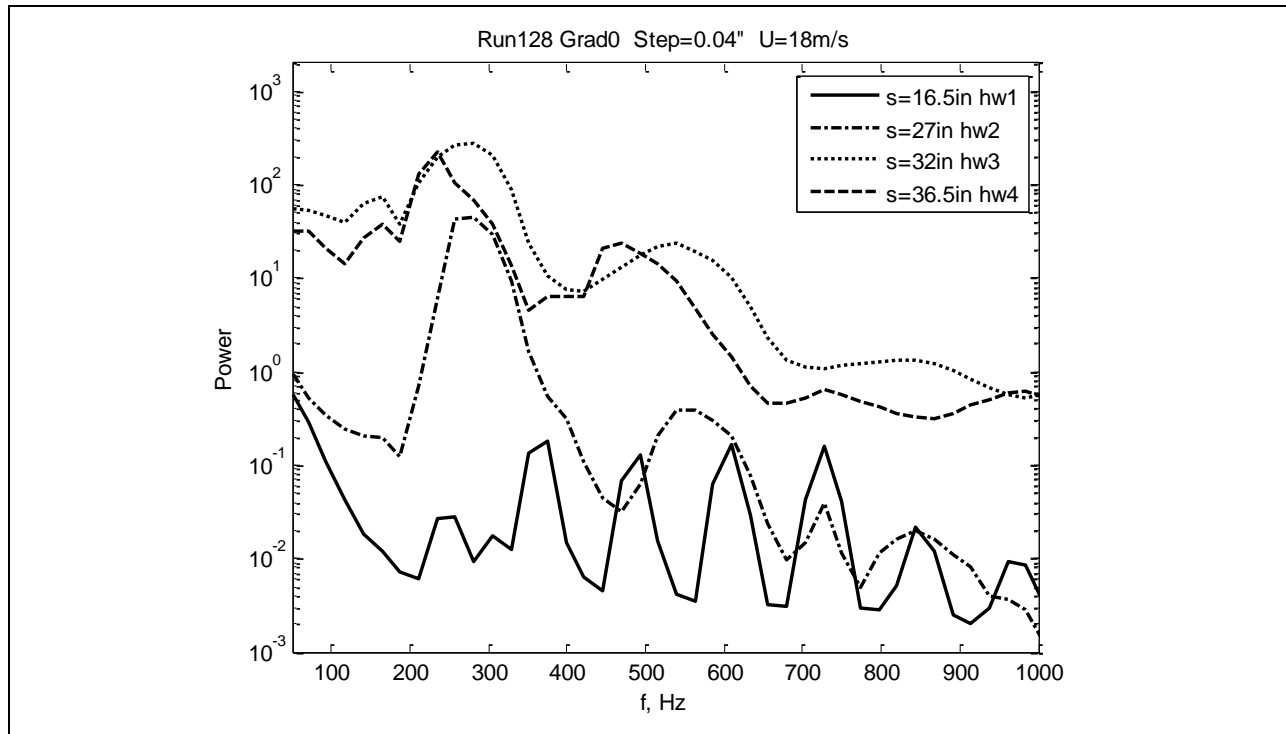


Figure 366: Measured power spectra.

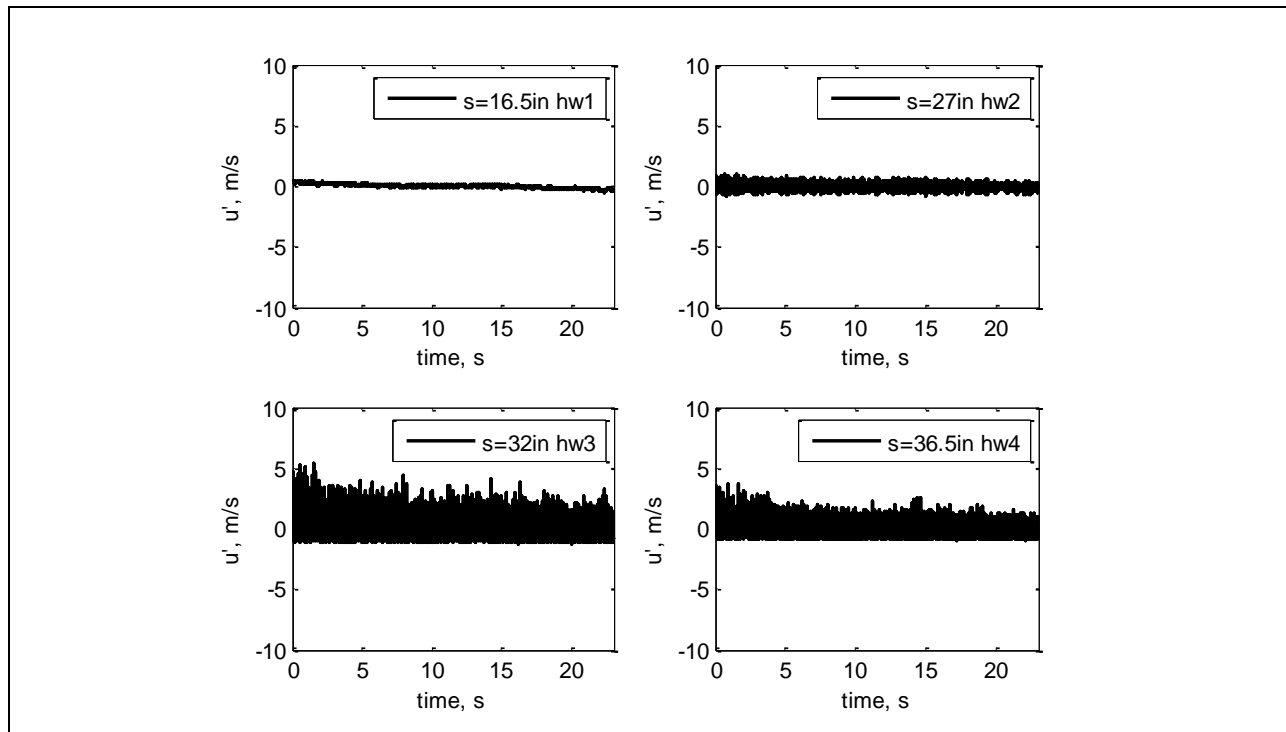


Figure 367: Measured velocity time history.

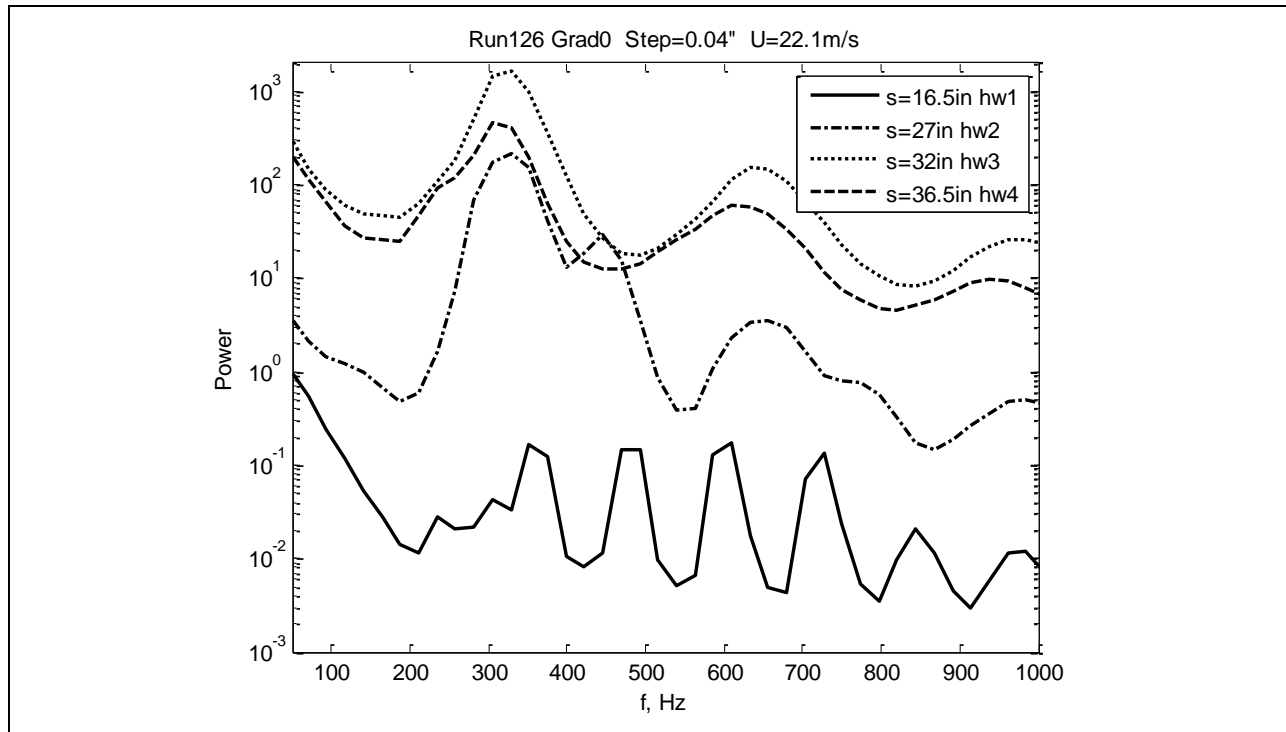


Figure 368: Measured power spectra.

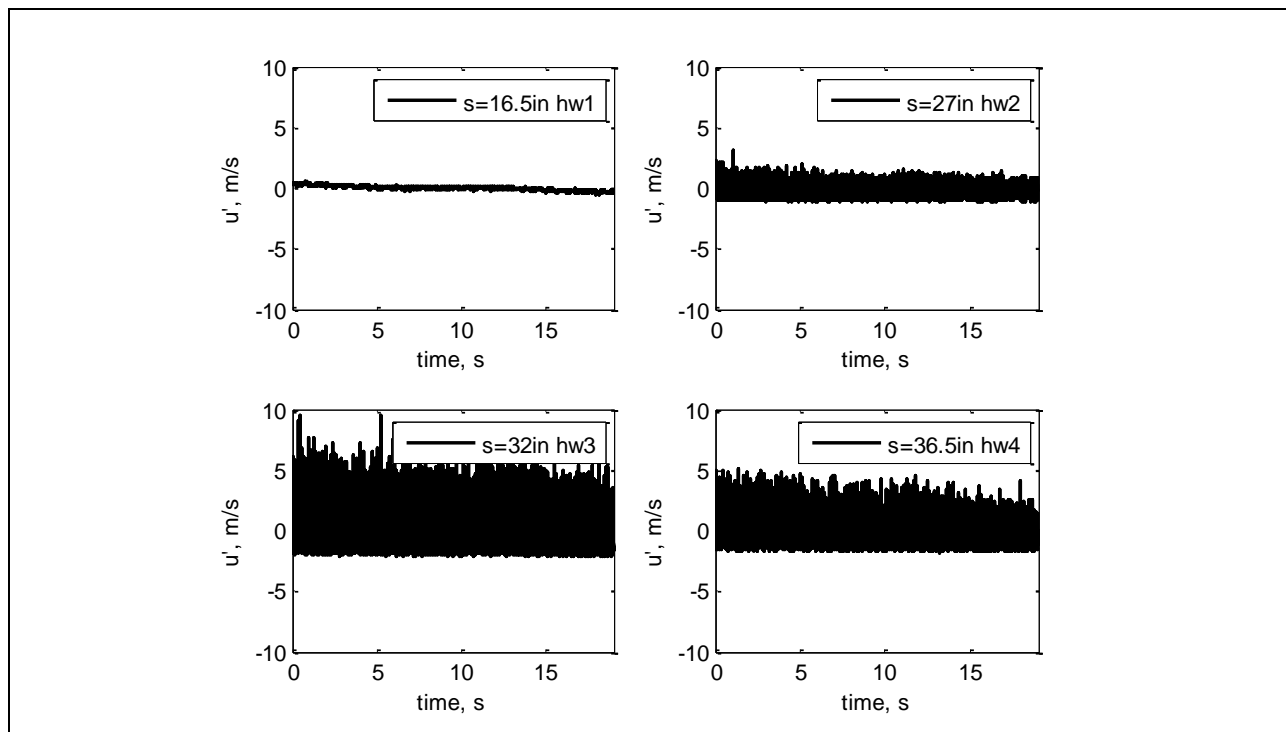


Figure 369: Measured velocity time history.

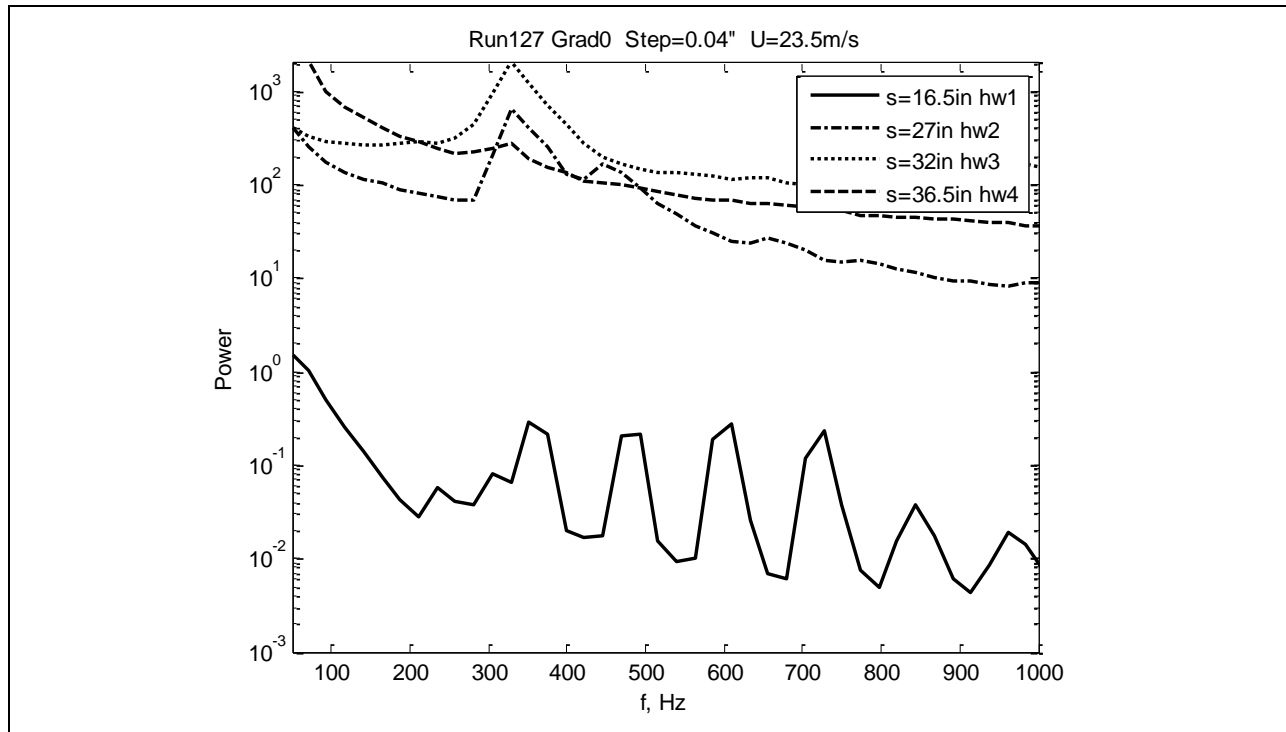


Figure 370: Measured power spectra.

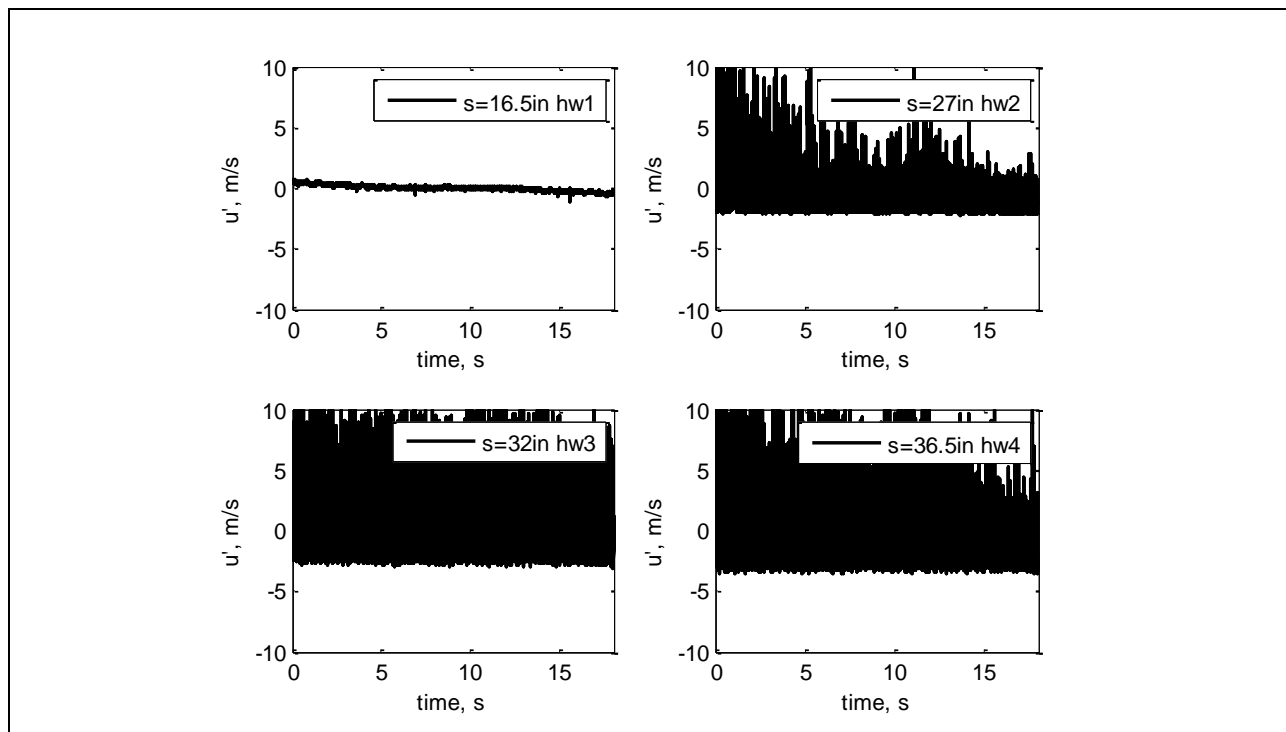


Figure 371: Measured velocity time history.

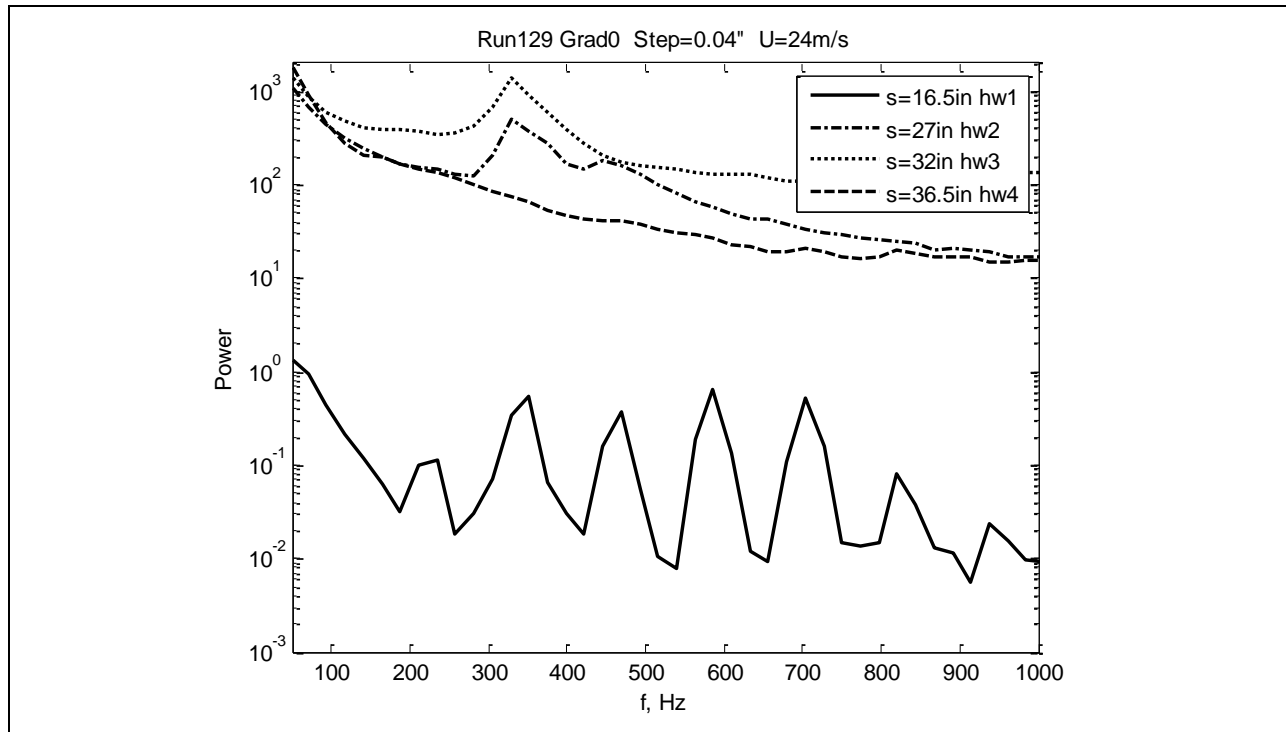


Figure 372: Measured power spectra.

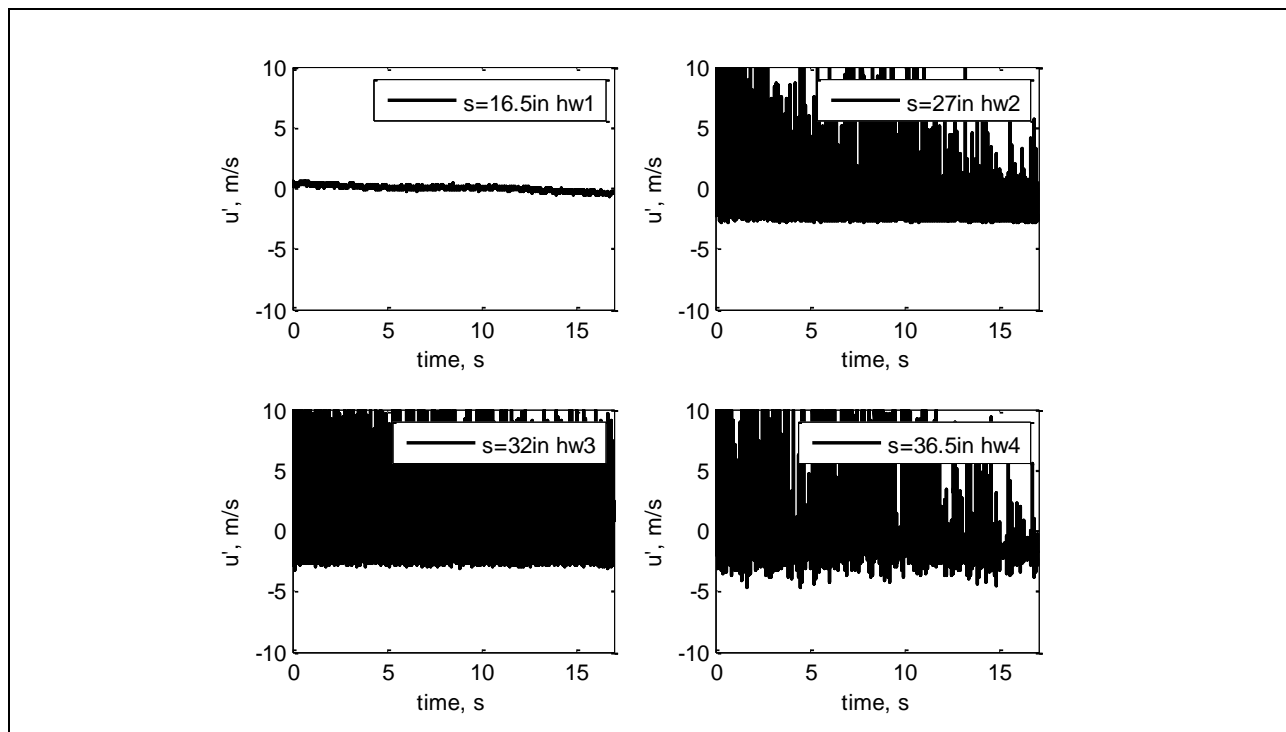


Figure 373: Measured velocity time history.

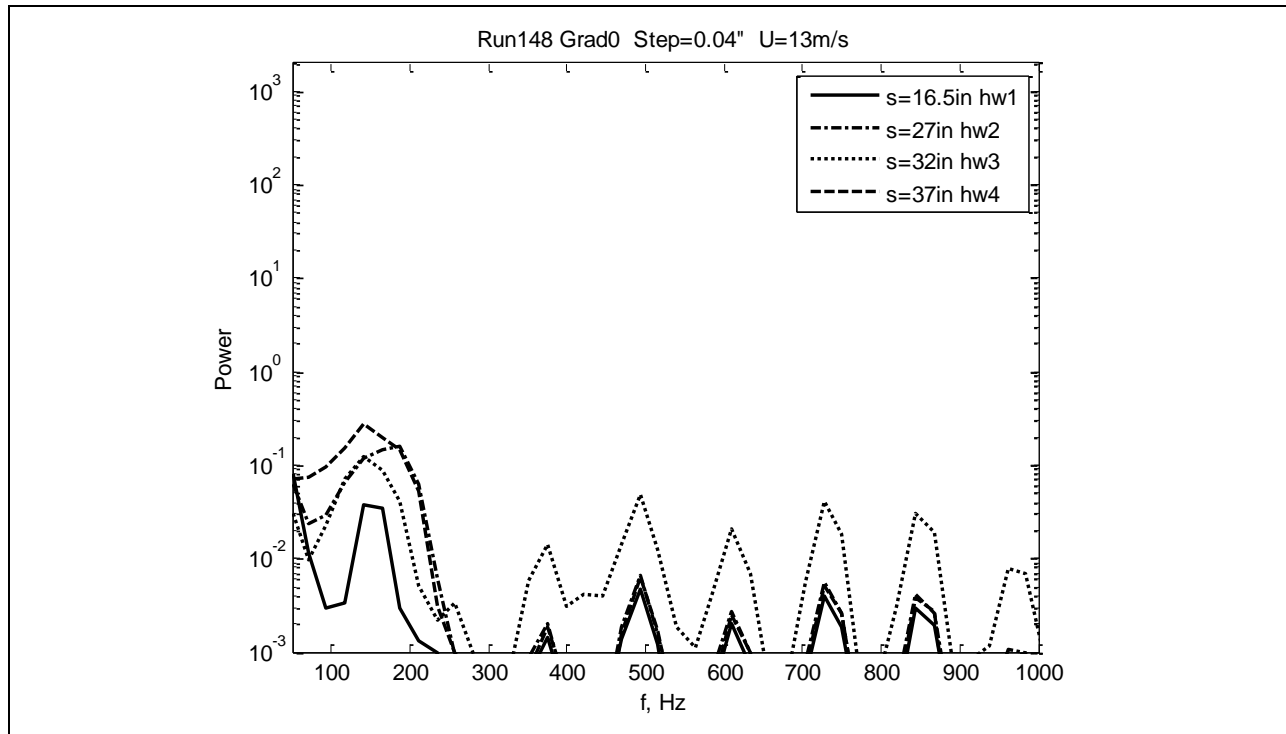


Figure 374: Measured power spectra.

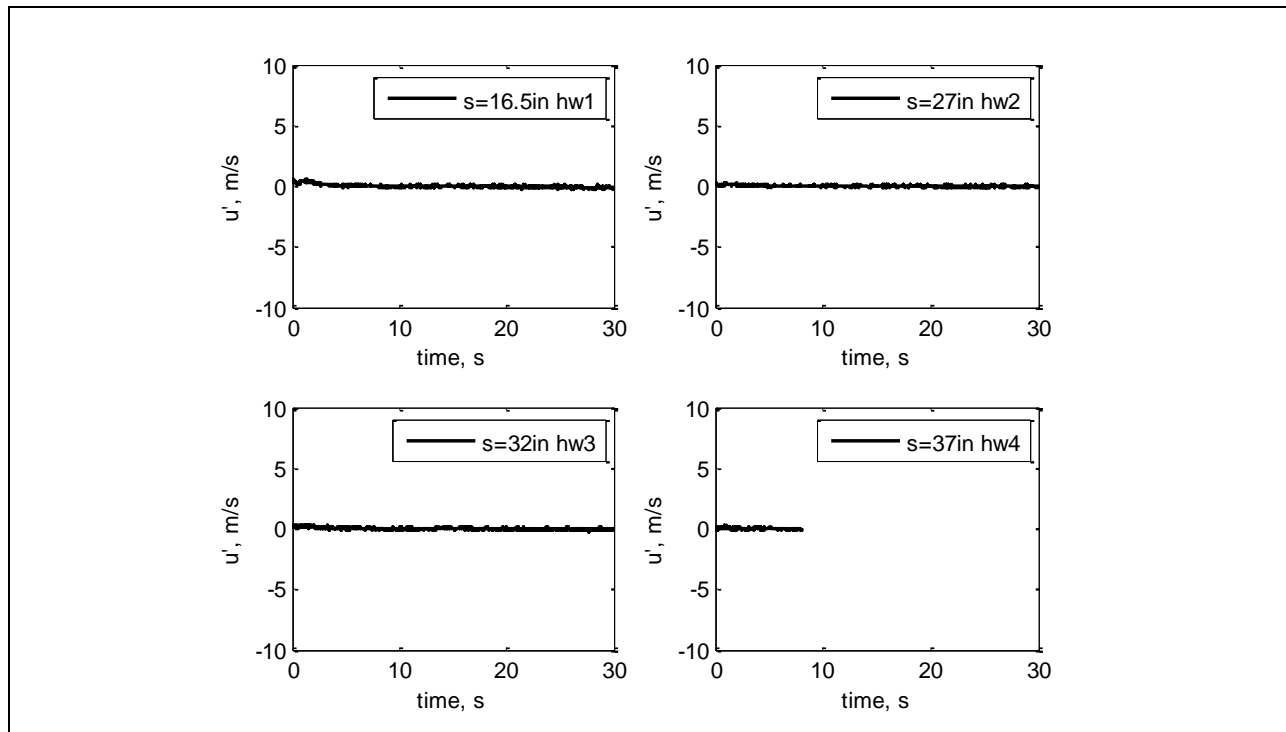


Figure 375: Measured velocity time history.

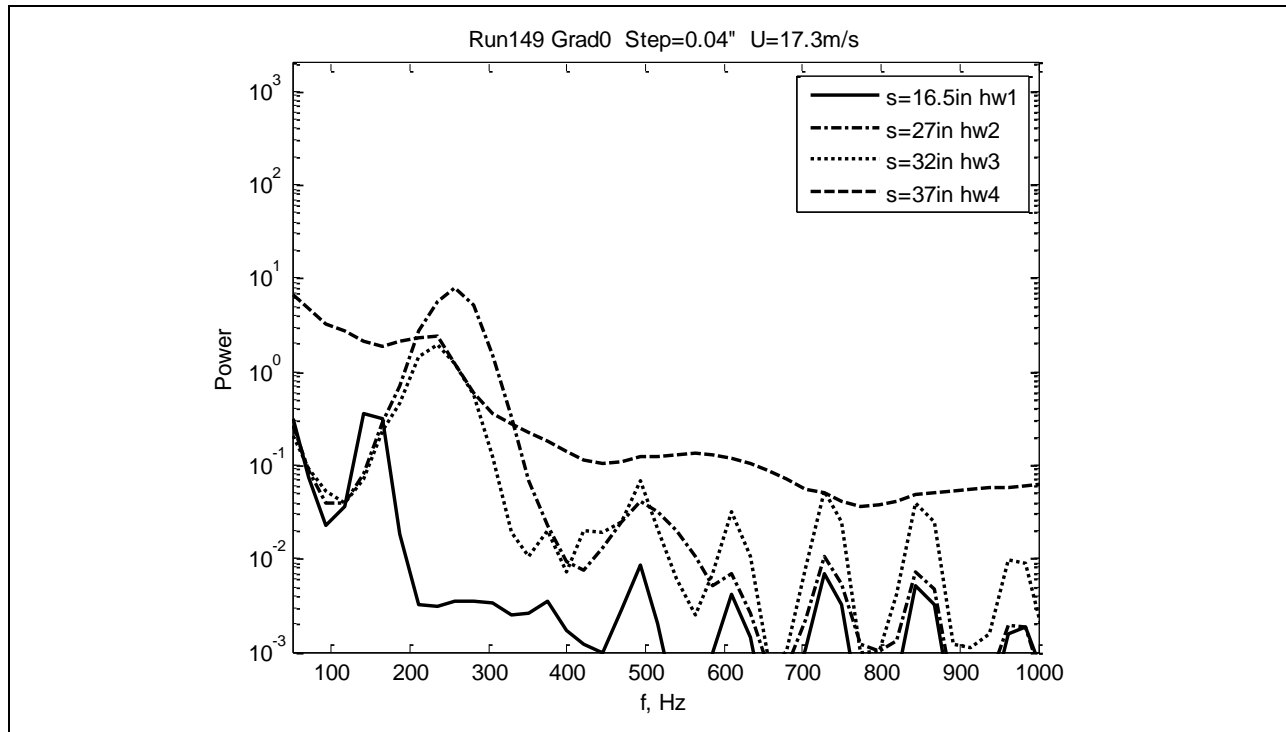


Figure 376: Measured power spectra.

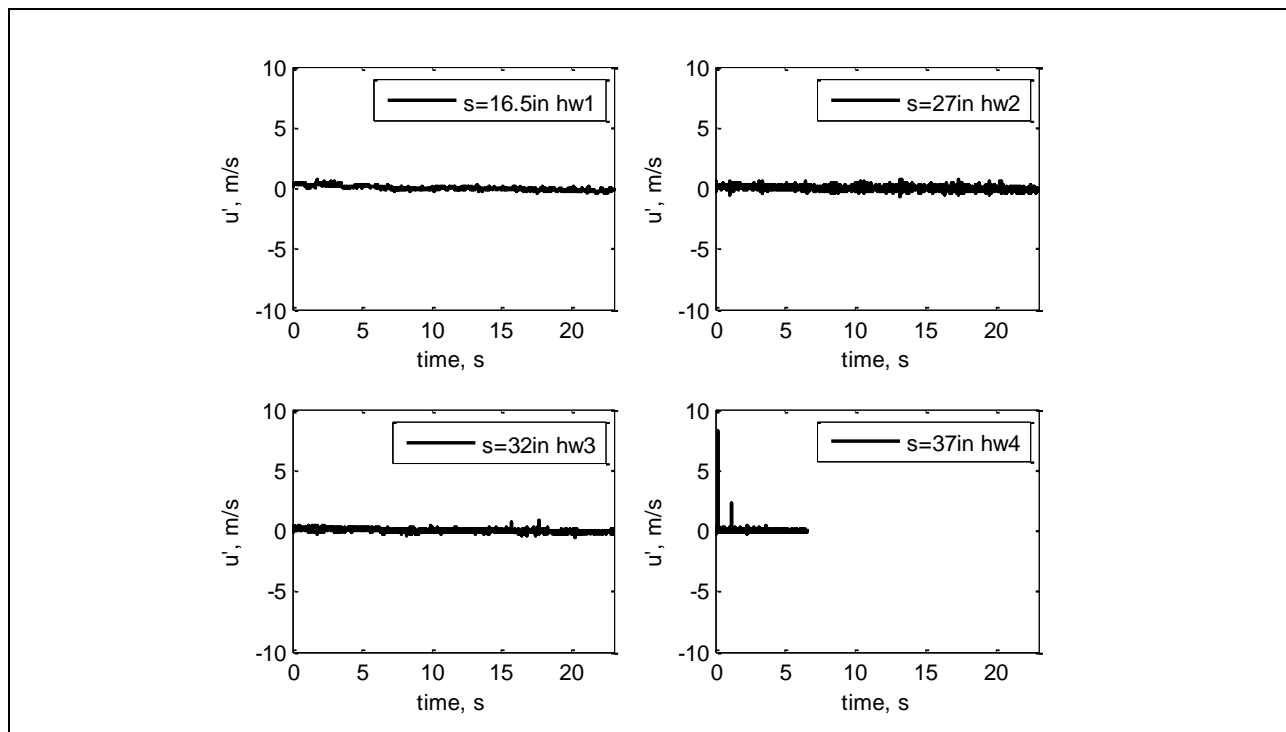


Figure 377: Measured velocity time history.

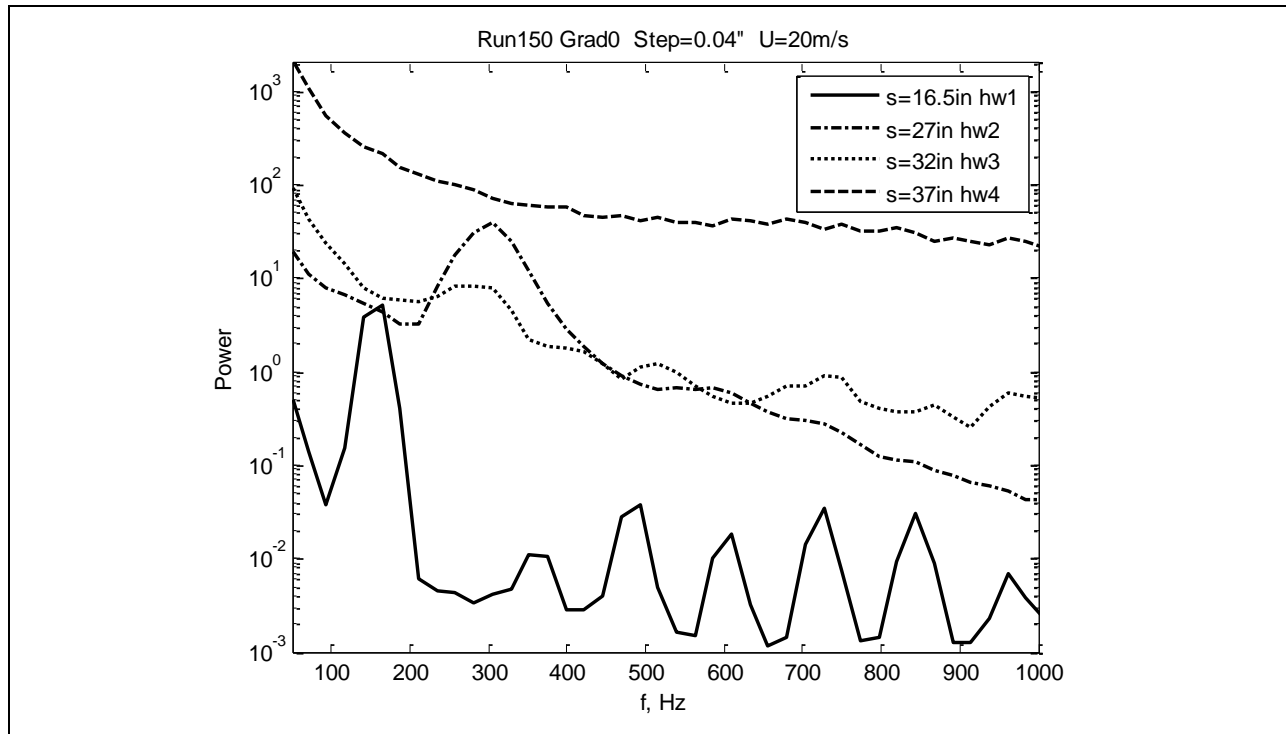


Figure 378: Measured power spectra.

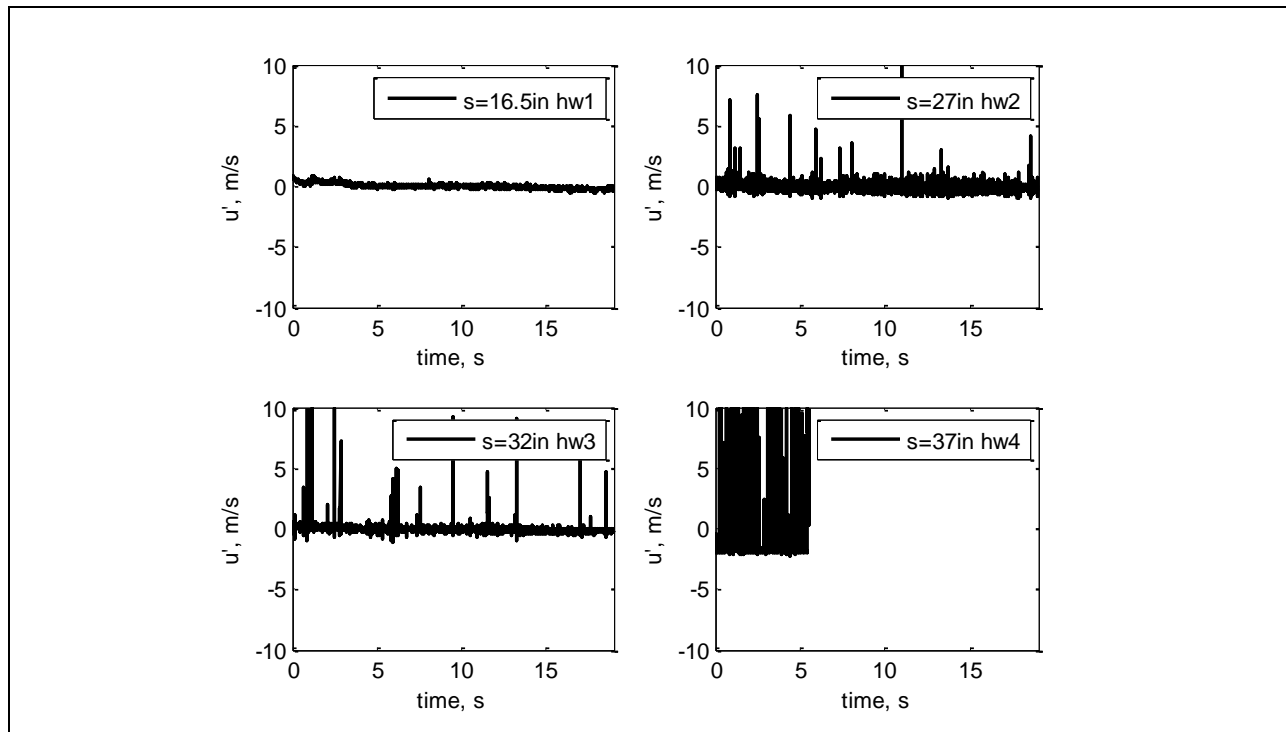


Figure 379: Measured velocity time history.

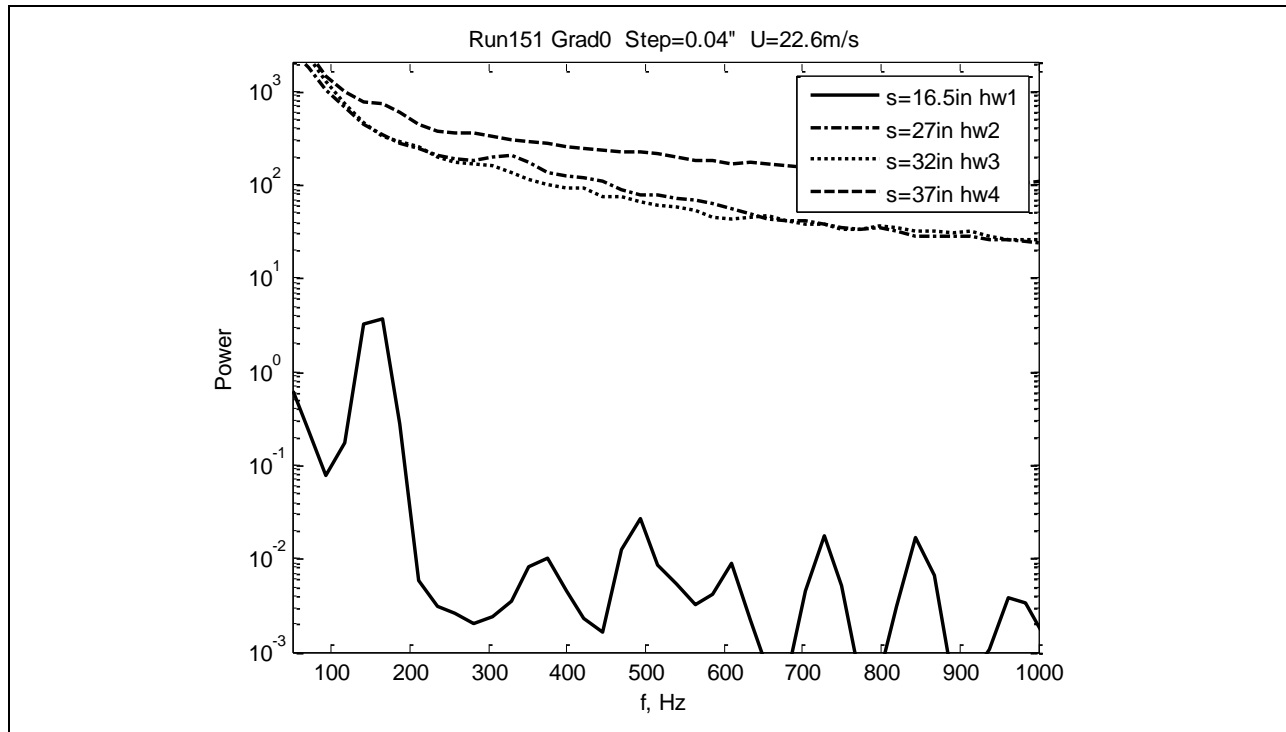


Figure 380: Measured power spectra.

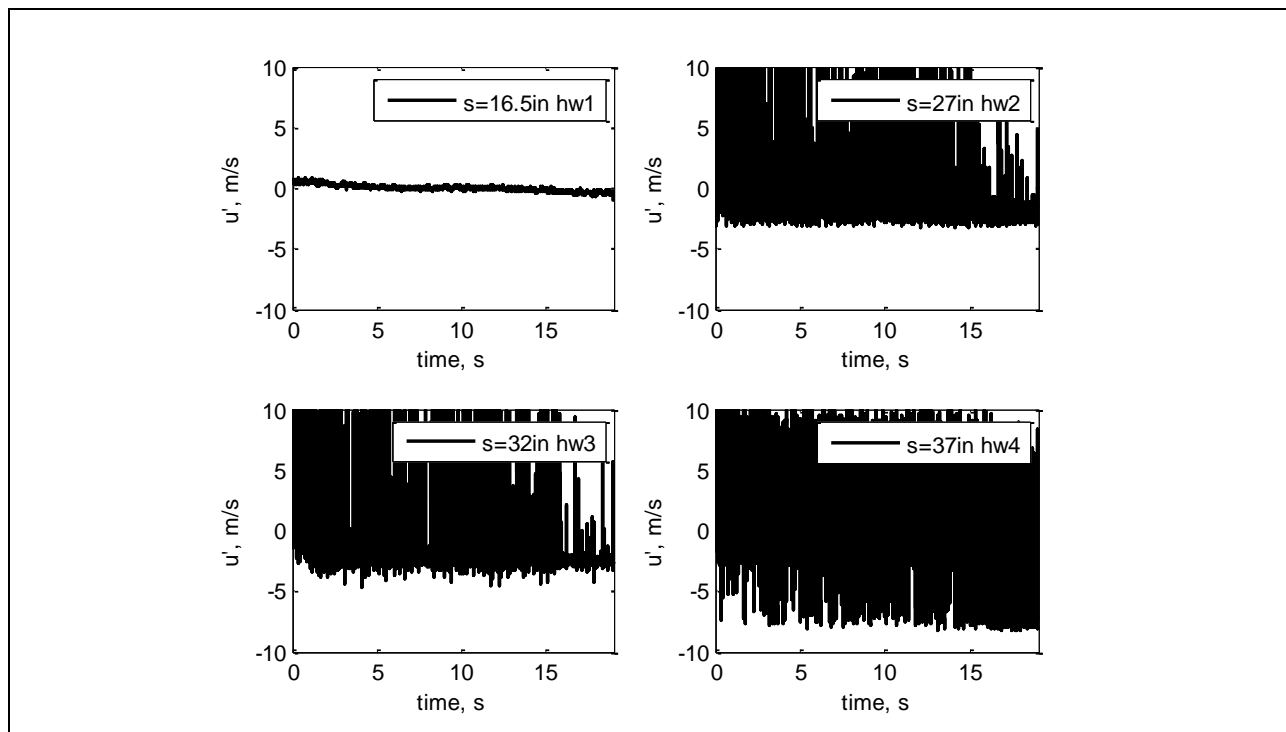


Figure 381: Measured velocity time history.

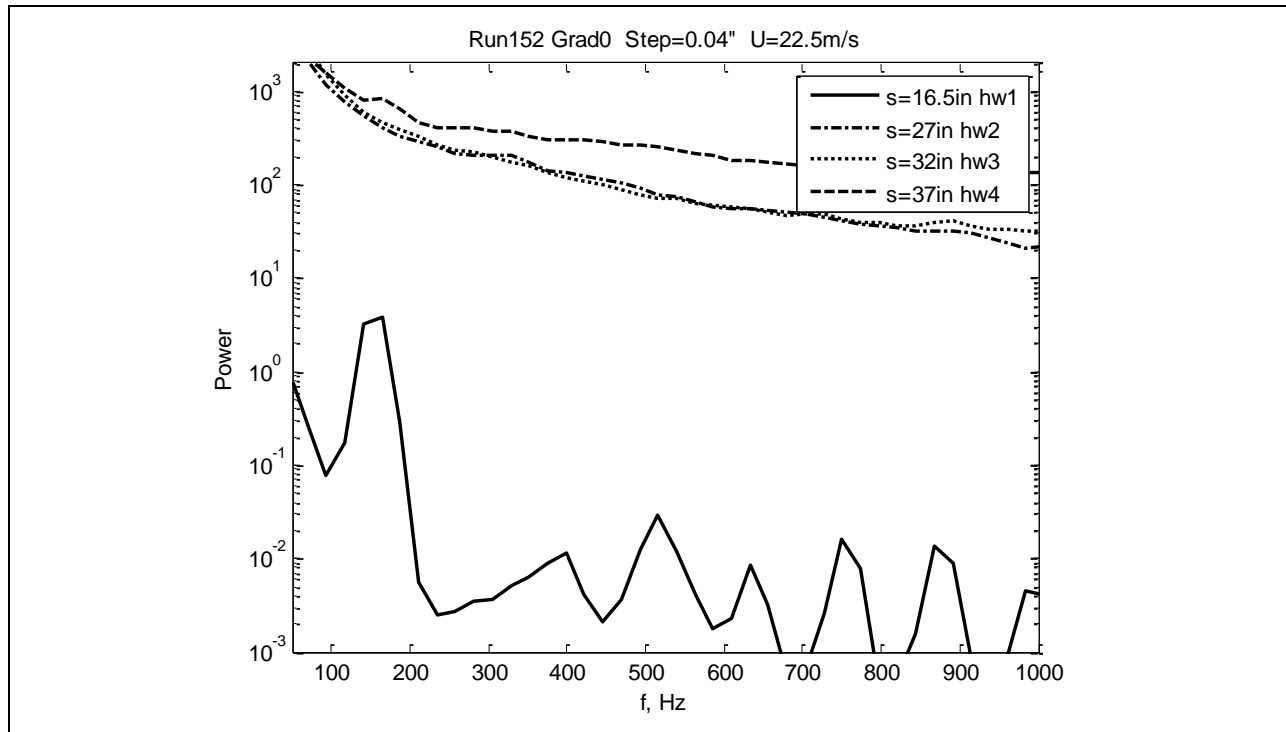


Figure 382: Measured power spectra.

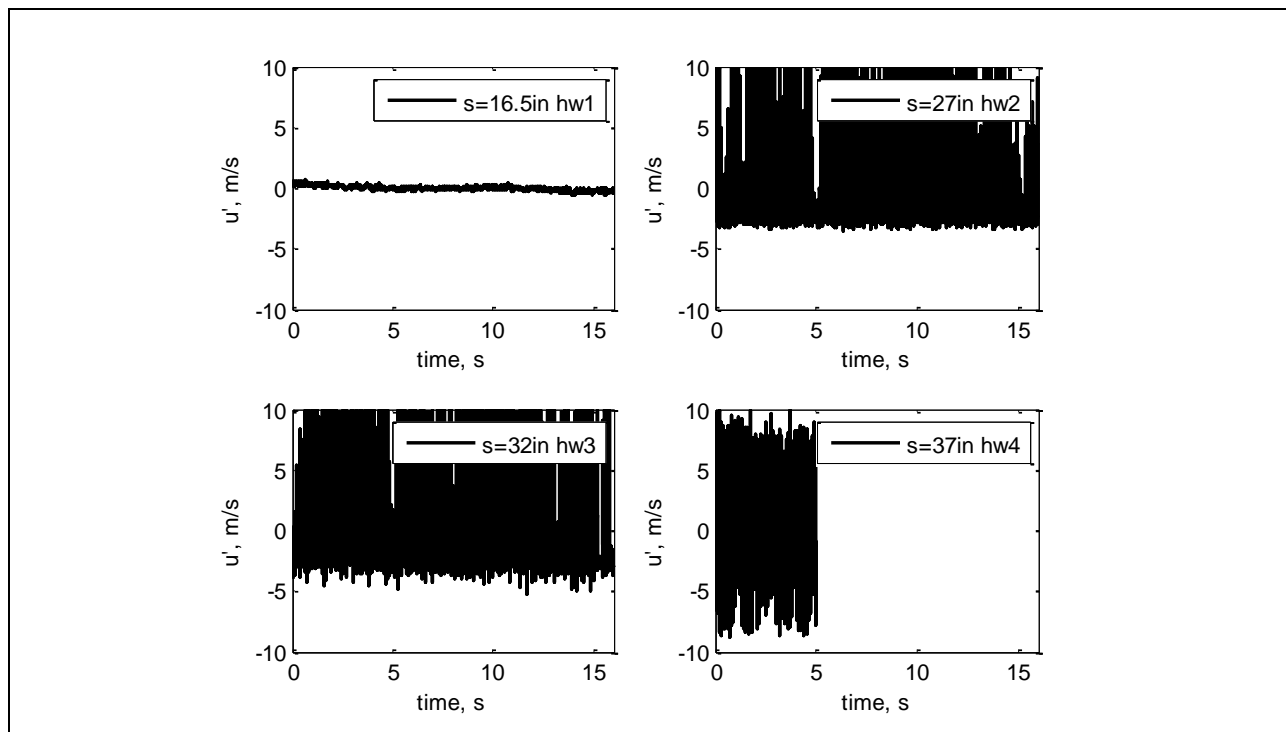


Figure 383: Measured velocity time history.

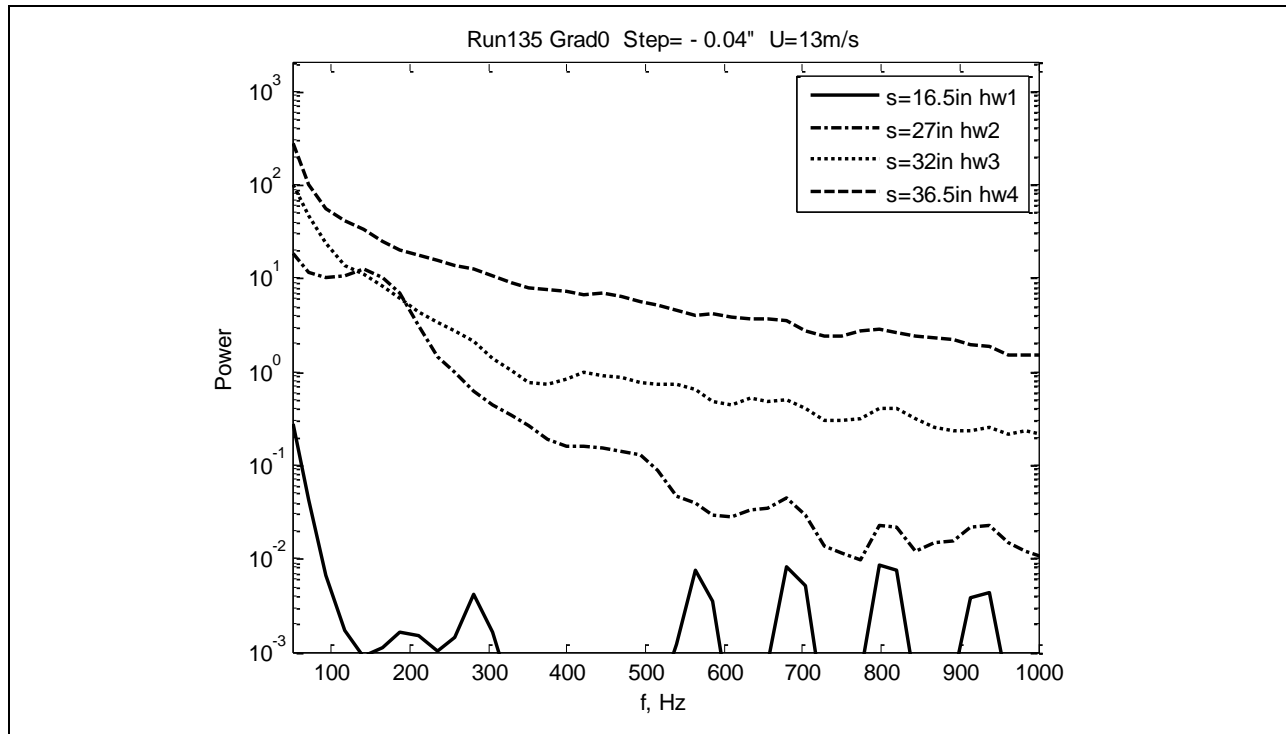


Figure 384: Measured power spectra.

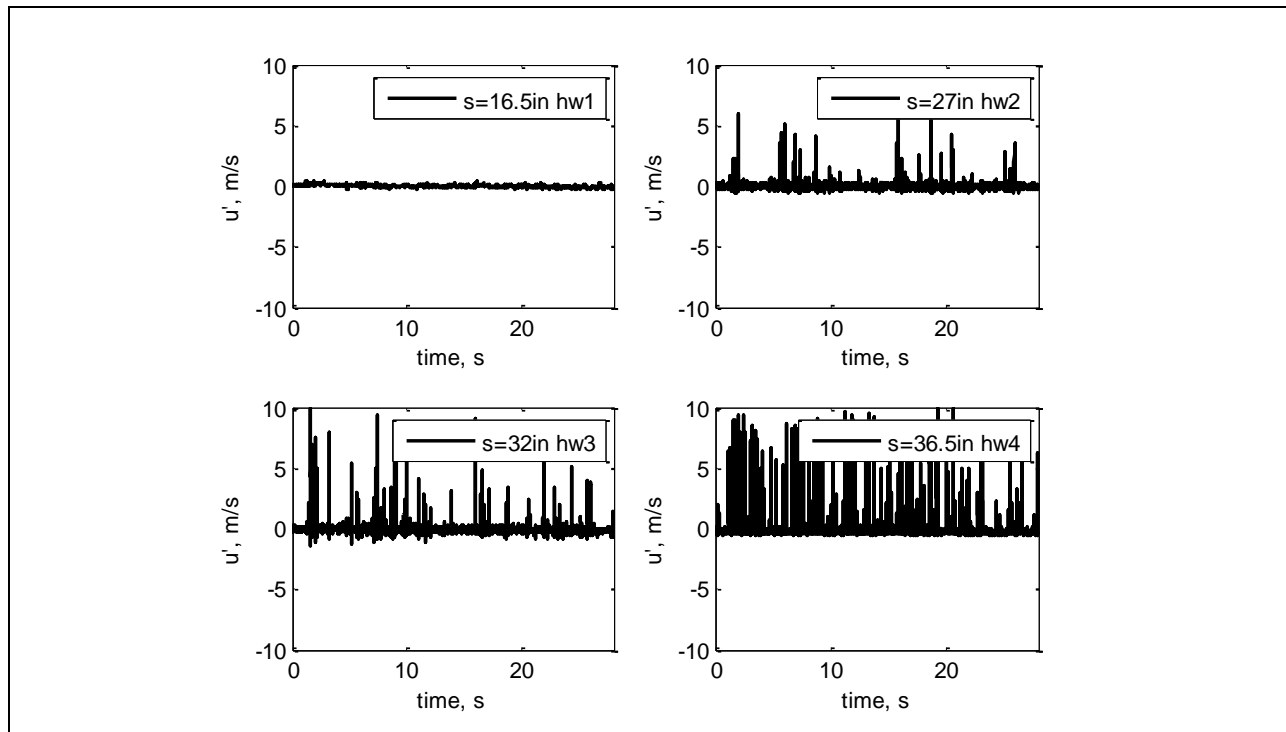


Figure 385: Measured velocity time history.

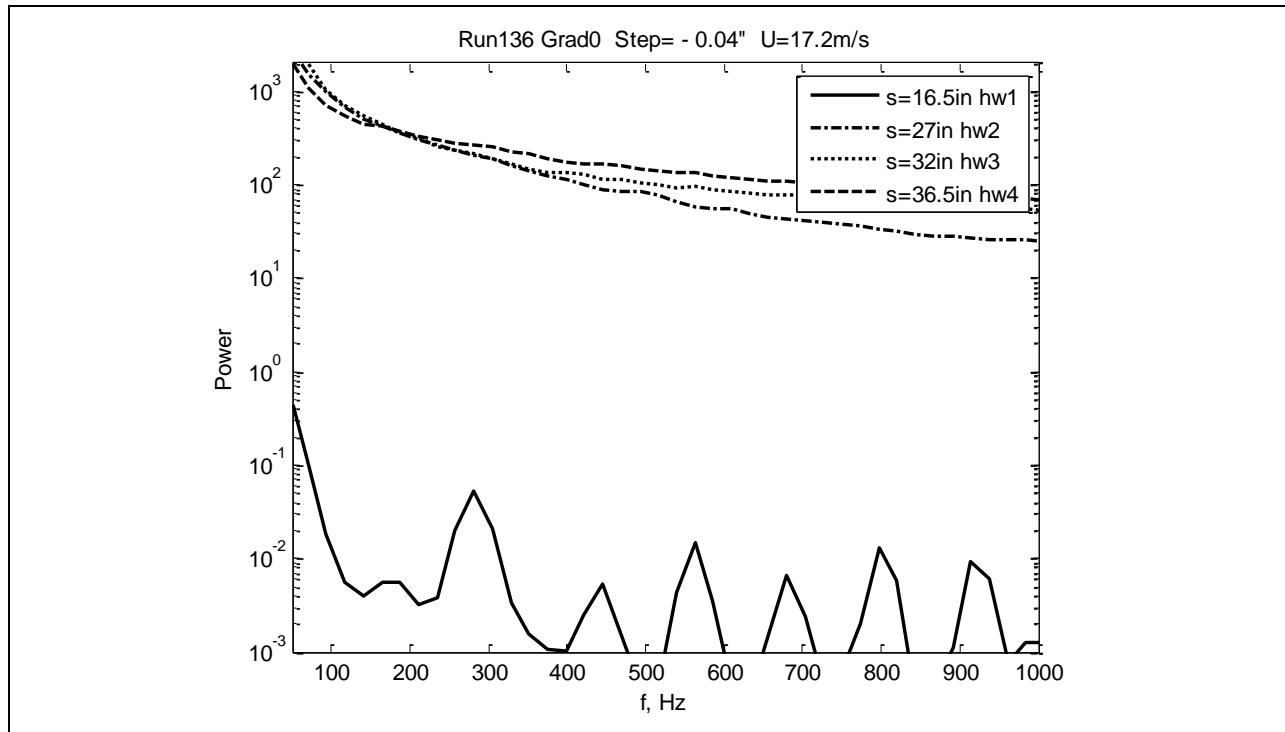


Figure 386: Measured power spectra.

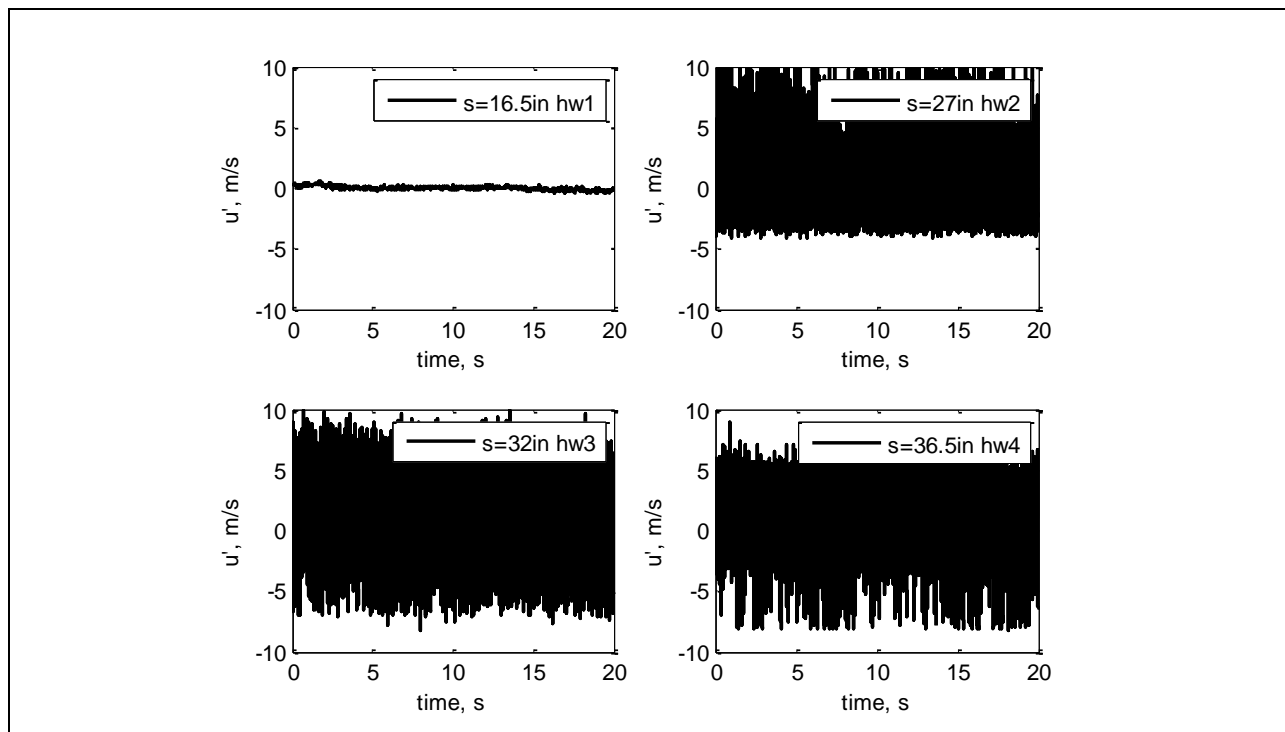


Figure 387: Measured velocity time history.

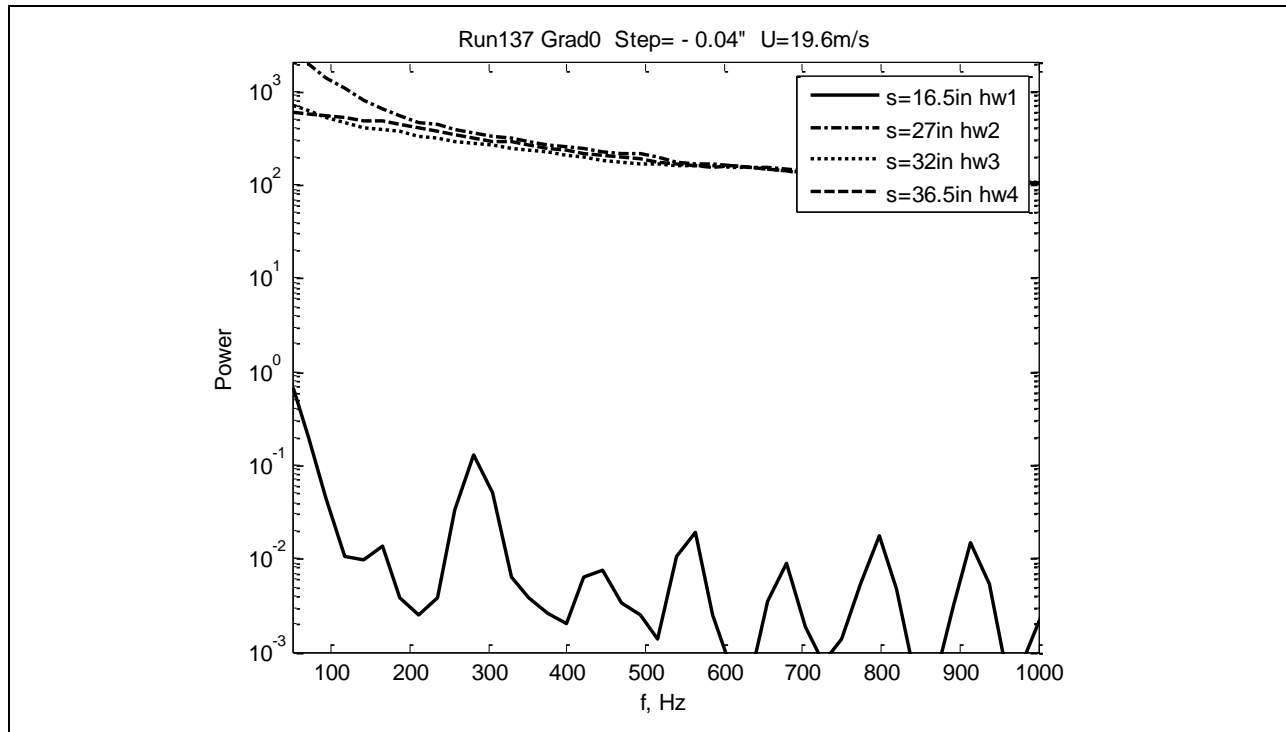


Figure 388: Measured power spectra.

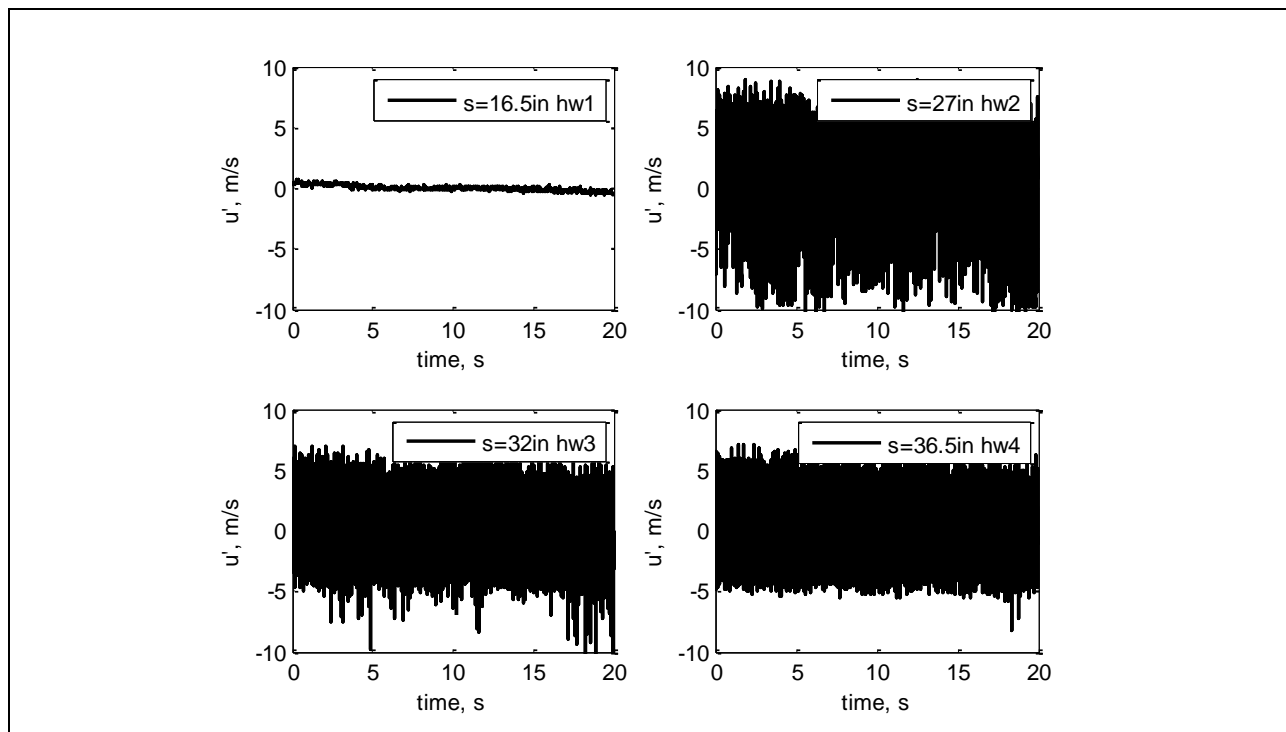


Figure 389: Measured velocity time history.

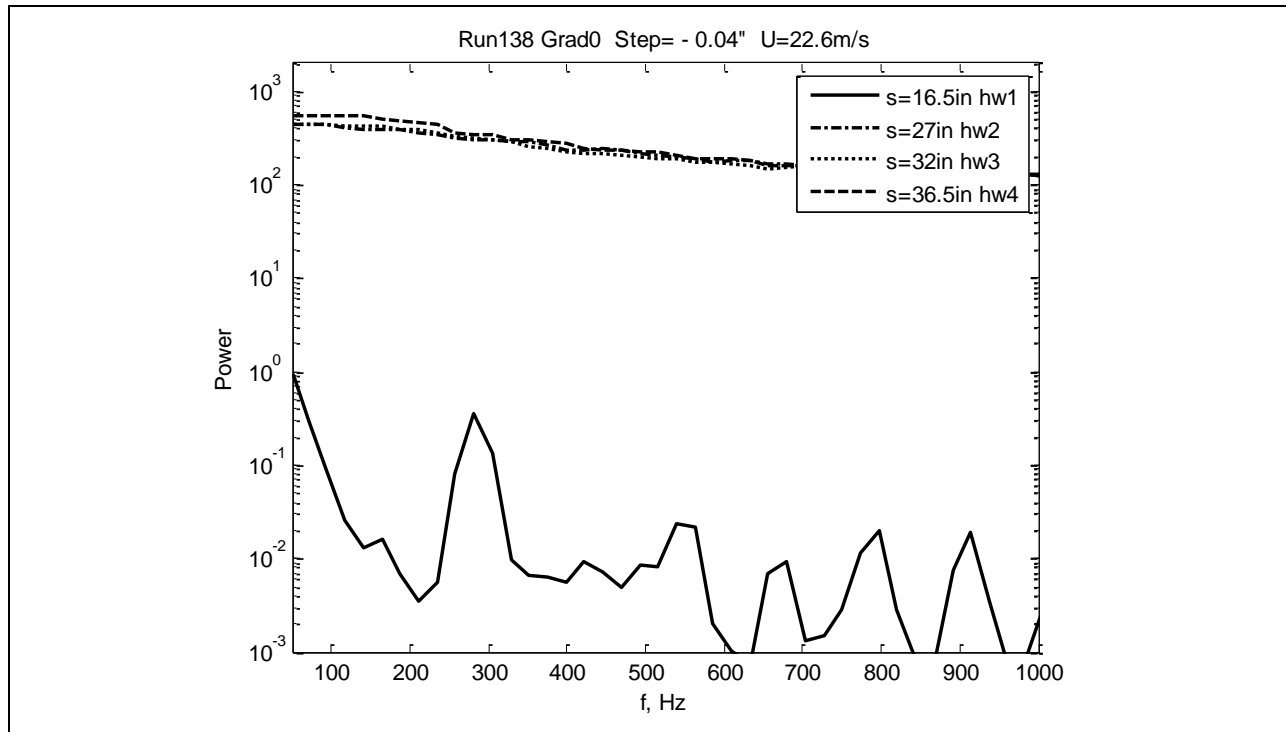


Figure 390: Measured power spectra.

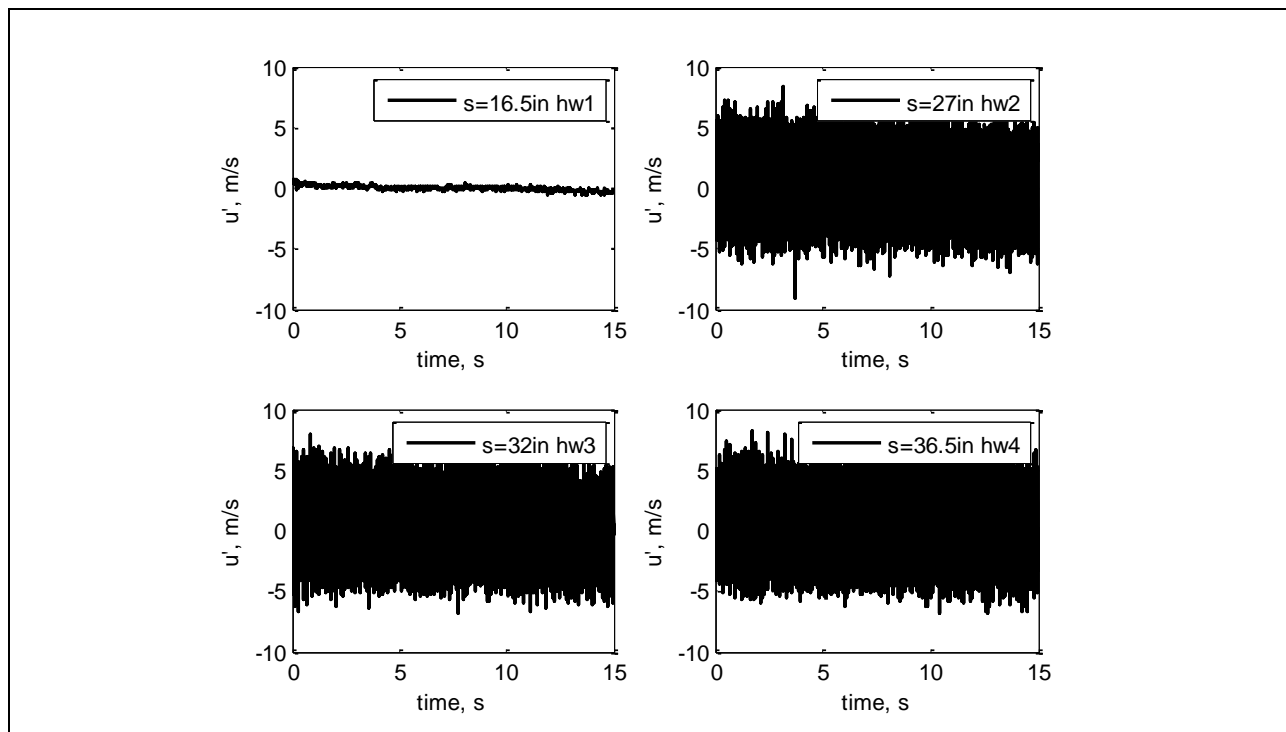


Figure 391: Measured velocity time history.

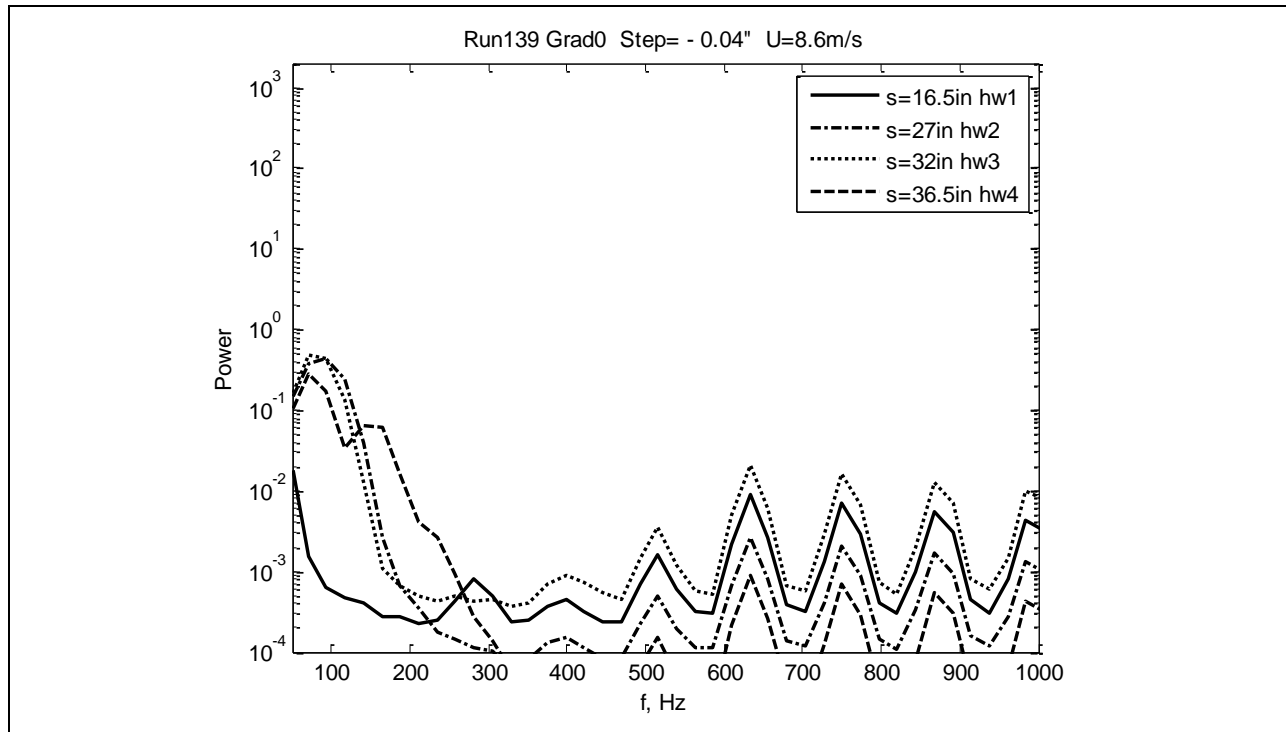


Figure 392: Measured power spectra.

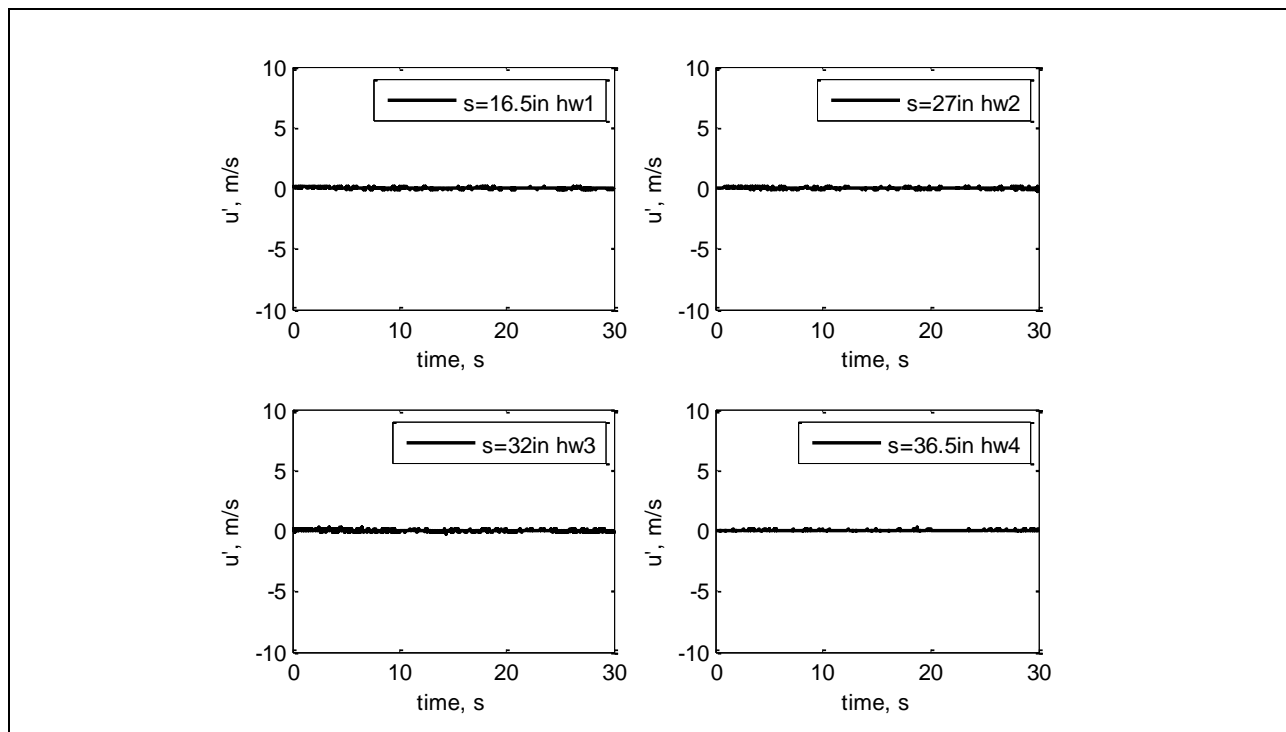


Figure 393: Measured velocity time history.

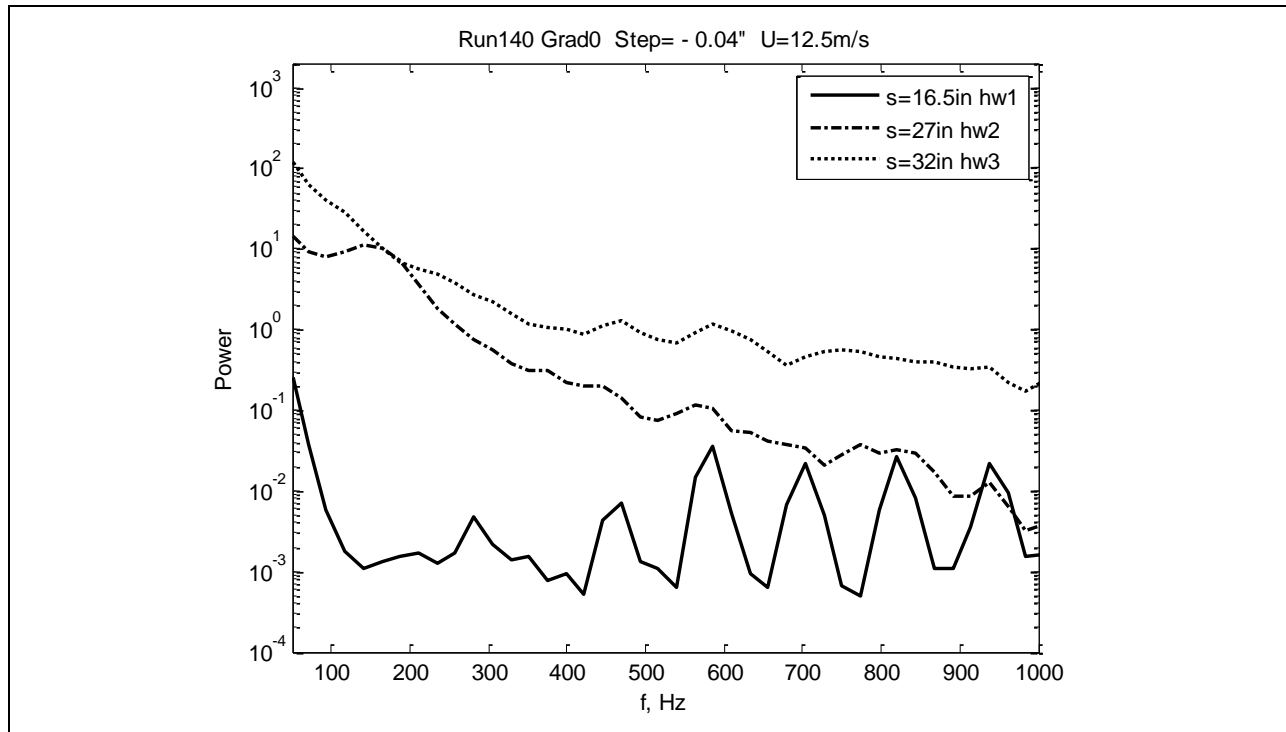


Figure 394: Measured power spectra.

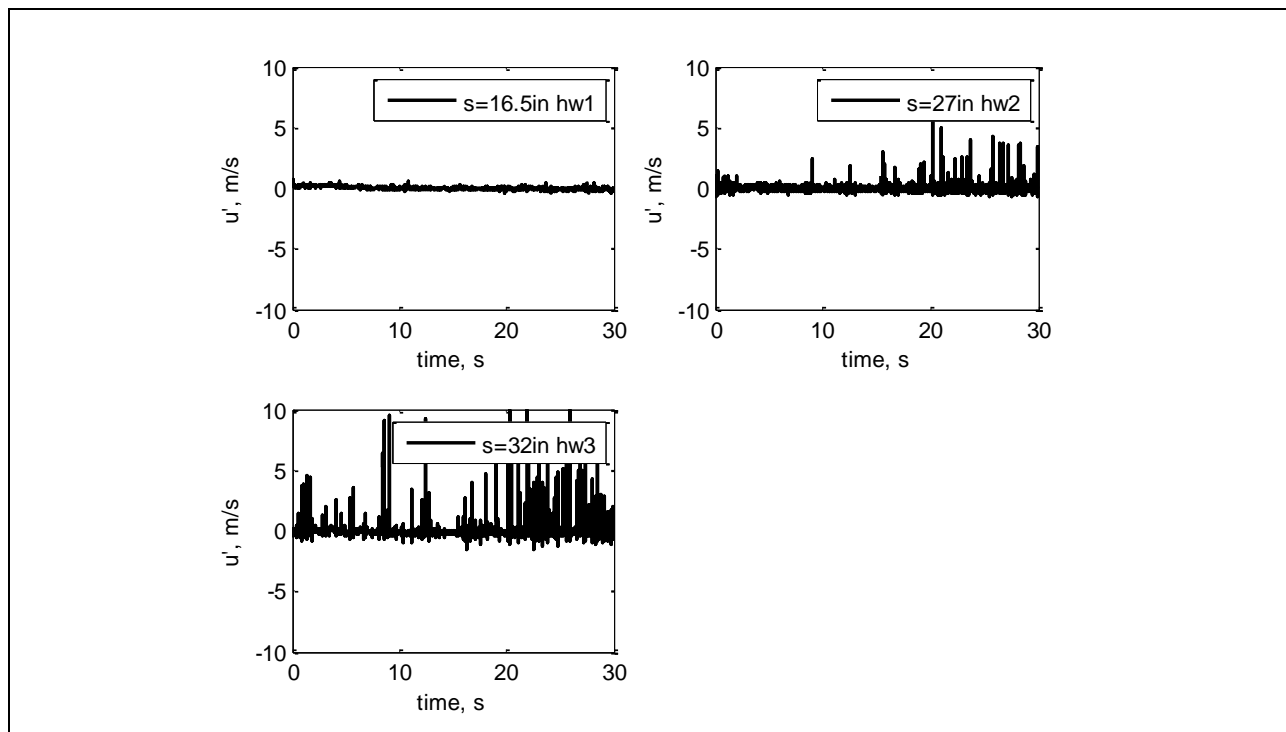


Figure 395: Measured velocity time history.

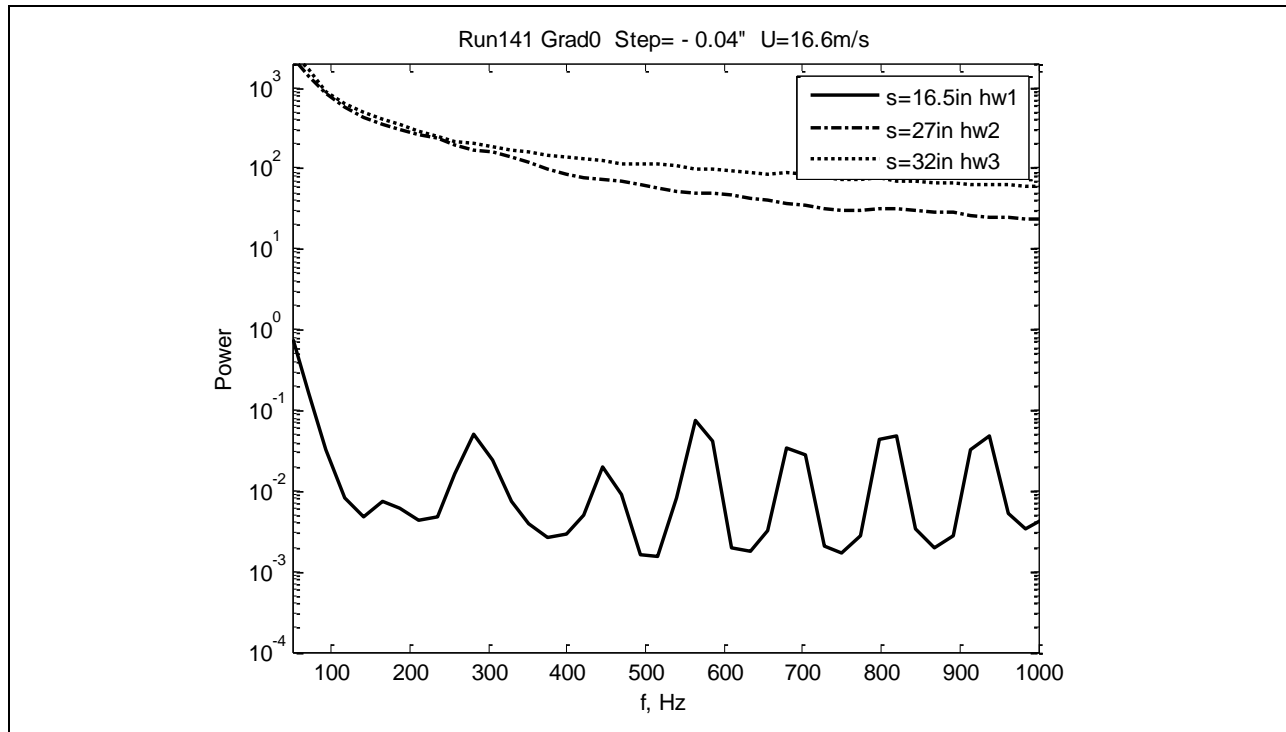


Figure 396: Measured power spectra.

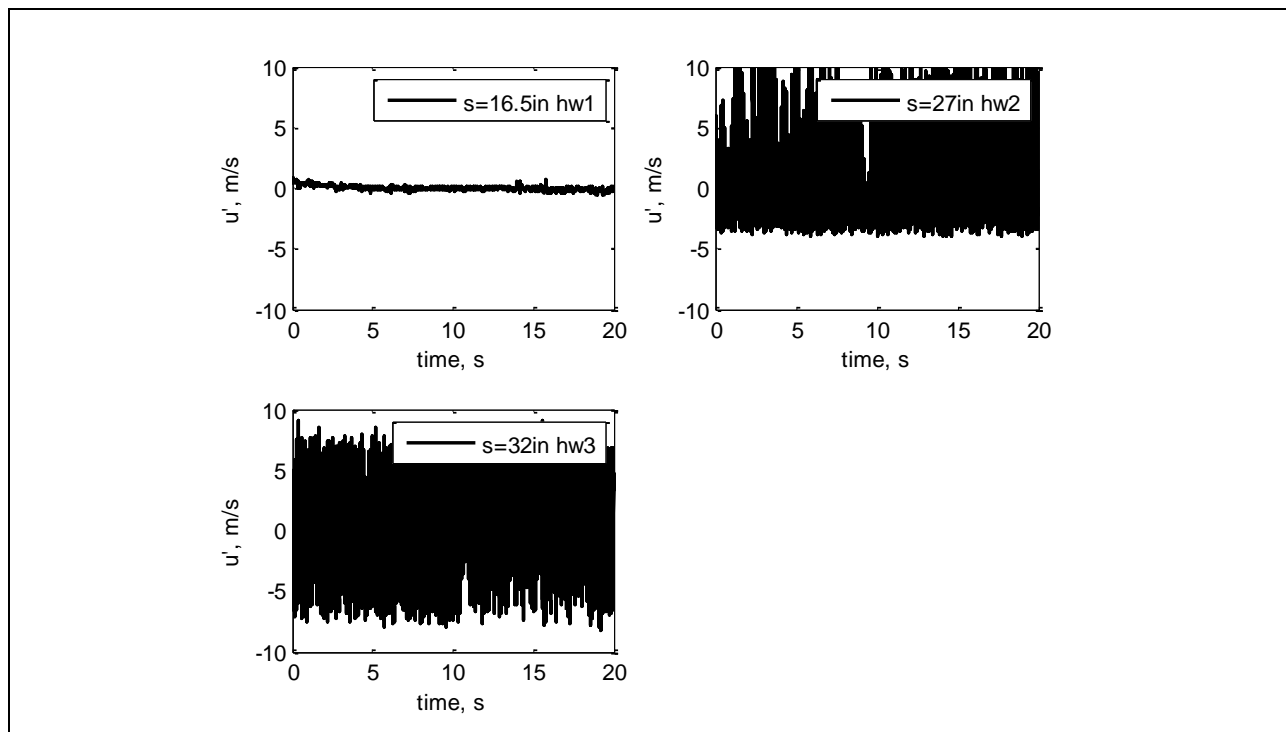


Figure 397: Measured velocity time history.

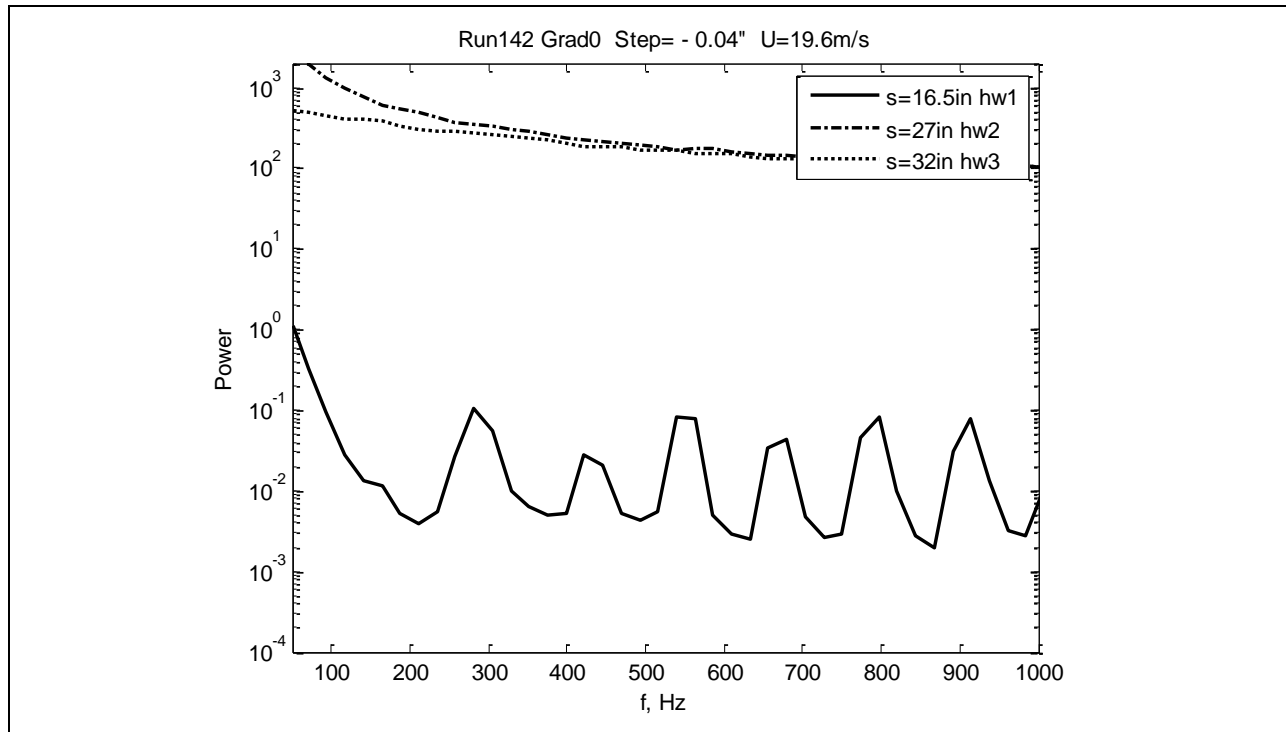


Figure 398: Measured power spectra.

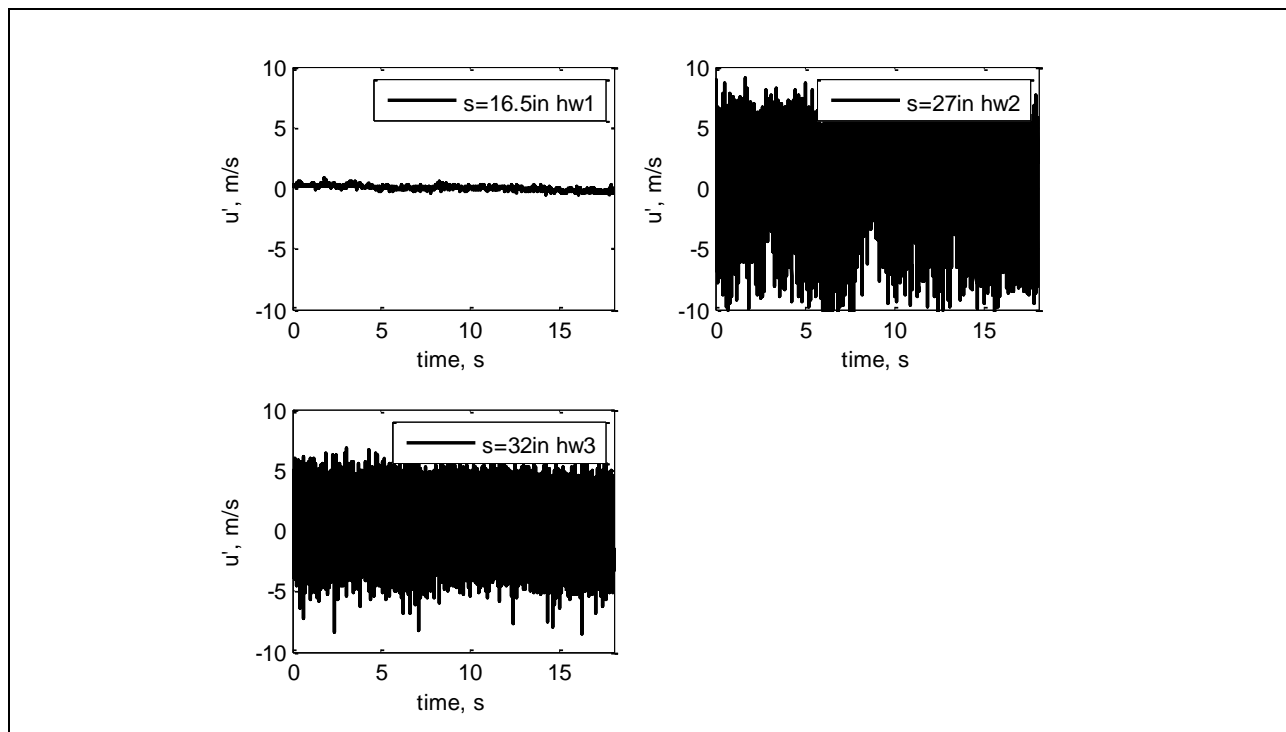


Figure 399: Measured velocity time history.

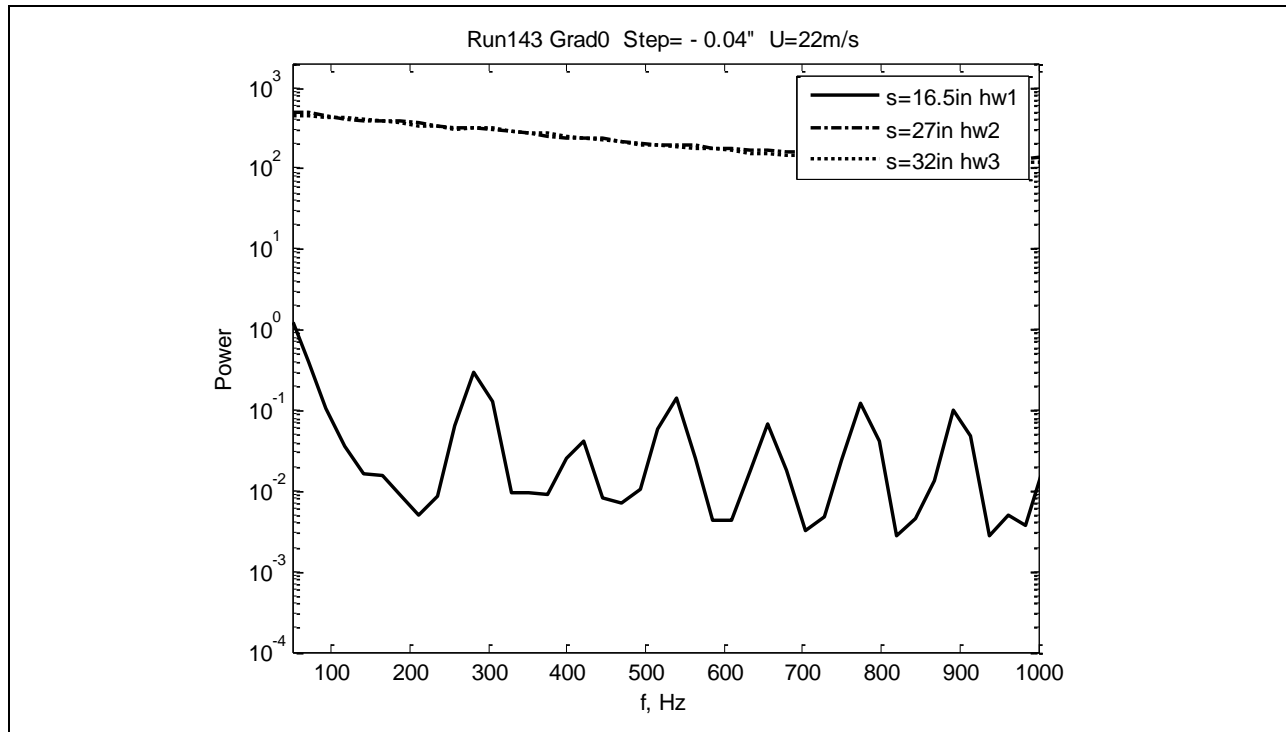


Figure 400: Measured power spectra.

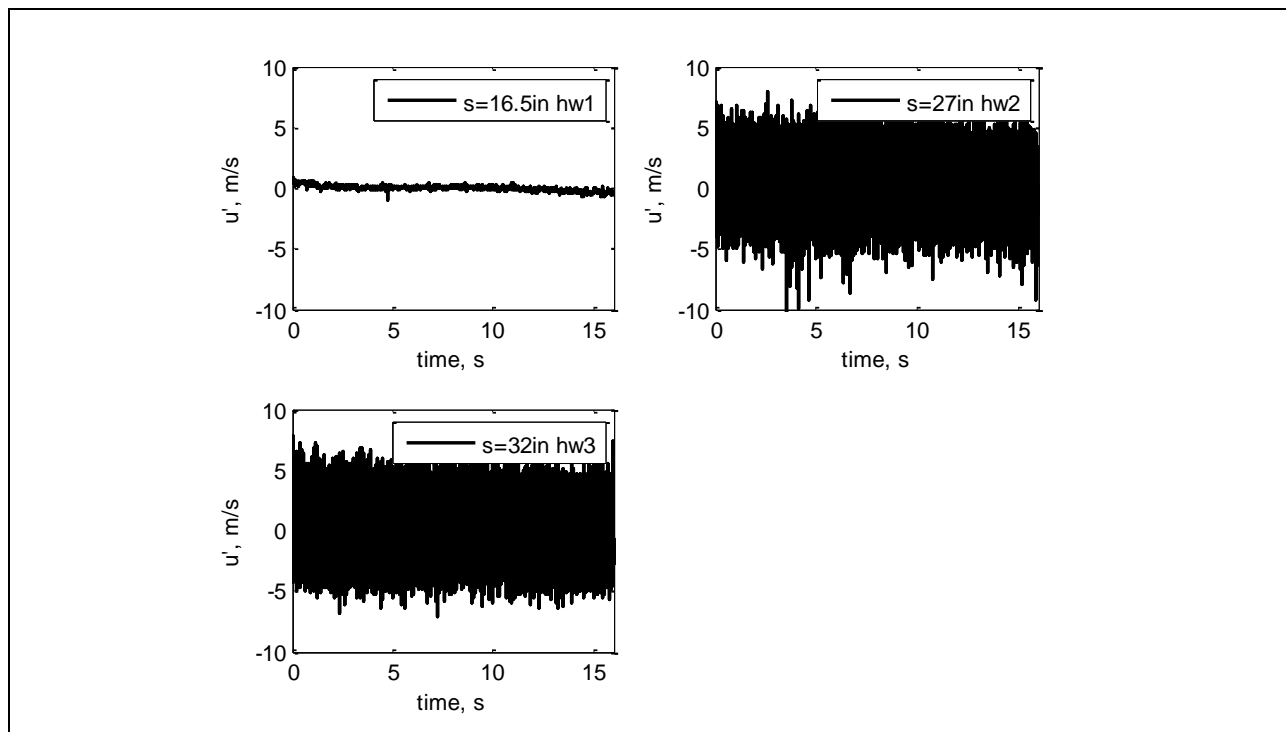


Figure 401: Measured velocity time history.

Table 16 below gives information about all runs that were performed for the Gradient-A model. It contains the basic parameters for the Gradient-A model, including run number, freestream speed, step height, and Reynolds number calculated at the step position. Information on the hot-wire locations, frequencies of peaks (if found in velocity power spectra) attributed to possible T-S waves, and their amplitudes and corresponding N-factors is provided also in the Table 16. Table 15 gives a detailed description of each parameter used in Table 16.

Table 15: Parameters used in Table 16

Component	Specifications
U	upstream freestream speed measured with Pitot tube (highlighted in yellow – U was not measured but extrapolated based on the measured speeds; in orange – car speed, U_{car})
k	step height (positive for forward facing and negative for aft facing)
k/δ_k^*	step height normalized with displacement thickness at step location
$Re_{\delta_k^*, k}$	$= \delta_k^* U / \nu$
Re_k	$k U_k / \nu$
A0	level of noise in the velocity power spectra for the first upstream hw1 taken as initial amplitude of T-S wave
s1-s4	streamwise positions of hot-wires hw1-hw4
f1 – f4	frequency of T-S waves
A1-A4	power of T-S waves (A1 coincides with A0 because no T-S waves were detected for the first hw1 in all runs)
N1-N4	N-factors for hw1-hw4 calculated from the spectra as $N_i = 0.5 \cdot \ln(A_i/A_0)$, where i is the hot wire number
Δf	half width of a frequency peak at its half height

Highlighted in orange in Table 16 is the speed set by the car driver, U_{car} . It was usually slightly higher than the real speed by 1-2m/s.

Table 16: Gradient-A hot-wire matrix

Basic parameters						hw1			
Run #	U (m/s)	k (in)	k/ δ^* k	Re δ^* ,k	A0	s1 (in)	f1 ($\Delta f1$) (Hz)	A1	N1
189	14.3	0.00	0.000	890	0.0017	22	--	--	--
188	18.3	0.00	0.000	1001	0.016	22	--	--	--
190	23	0.00	0.000	1124	0.005	22	--	--	--
187	24	0.00	0.000	1149	0.1	22	--	--	--
275	13	-0.04	1.034	847	0.001	30	244 (28)	0.1	2.3
278	15	-0.04	1.089	933	0.003	30	262 (21)	2	3.25
276	17.6	-0.04	1.208	987	0.004	30	262 (21)	2	3.1
277	20	-0.04				30	--	--	--
282	17.7	0.065	1.960	992	0.002	30	256 (22)	2.2	3.5
279	20.8	0.065	2.139	1071	0.003	30	256 (19)	3	3.45
280	23.6	0.065	2.277	1141	0.02	30	256 (23)	2	2.3
281	27.6	0.065			--	30	--	--	--
285	8.7	-0.055			--	20	--	--	--
283	9.1	-0.055			--	20	--	--	--
284	12	-0.055			--	20	--	--	--
286	16.4	-0.055			--	20	--	--	--
292	17.5	-0.04			--	20	--	--	--
293	20	-0.04			--	20	--	--	--
294	22.5	-0.04			--	20	--	--	--
295	17.5	0.065			--	20	--	--	--
296	20	0.065			--	20	--	--	--
297	22.5	0.065			--	20	--	--	--
298	25	0.065			--	20	--	--	--

Table 16: Gradient-A hot-wire matrix (continued)

hw2				hw3				hw4			
s2 (in)	f2 (Δf_2) (Hz)	A2	N2	s3 (in)	f3 (Δf_3) (Hz)	A3	N3	s4 (in)	f4 (Δf_4) (Hz)	A4	N4
36.5	--	--	--	54	--	--	--	69.5	--	--	--
36.5	--	--	--	54	--	--	--	69.5	--	--	--
36.5	--	--	--	54	--	--	--	69.5	--	--	--
36.5	--	--	--	54	--	--	--	69.5	--	--	--
44	200 (24)	7.5	4.45	53	171 (22)	1	3.45	65.5	118	0.2	2.6
44	--	--	--	53	--	--	--	65.5	--	--	--
44	--	--	--	53	--	--	--	65.5	--	--	--
44	--	--	--	53	--	--	--	65.5	--	--	--
44	197 (24)	1	3.1	53	171 (26)	3	3.65	65.5	122 (24)	2	3.45
44	199 (23)	2.7	3.4	53	170 (23)	7	3.9	65.5	--	--	--
44	--	--	--	53	--	--	--	65.5	--	--	--
44	--	--	--	53	--	--	--	65.5	--	--	--
25	--	--	--	30	--	--	--	35	--	--	--
25	--	--	--	30	--	--	--	35	--	--	--
25	--	--	--	30	--	--	--	35	--	--	--
25	--	--	--	30	--	--	--	35	--	--	--
35	--	--	--	--	--	--	--	--	--	--	--
35	--	--	--	--	--	--	--	--	--	--	--
35	--	--	--	--	--	--	--	--	--	--	--
35	--	--	--	--	--	--	--	--	--	--	--
35	--	--	--	--	--	--	--	--	--	--	--
35	--	--	--	--	--	--	--	--	--	--	--
35	--	--	--	--	--	--	--	--	--	--	--
35	--	--	--	--	--	--	--	--	--	--	--
35	--	--	--	--	--	--	--	--	--	--	--

Table 17 summarizes transition locations found from velocity and skin friction measurements. The data from velocity measurements are based on quantitative analysis of the velocity time series and spectra. The criteria for the transition were qualitative: the broadening of velocity power spectra and 100% intermittency in the velocity time series.

Table 17: Gradient-A hot-wire transition locations

Basic parameters			Transition location	
Run #	U (m/s)	k (in)	s, from HW (in)	s, from Cf (in)
189	14.3	0.00	--	--
188	18.3	0.00	--	--
190	23	0.00	--	--
187	24	0.00	--	--
275	13	-0.04	--	--
278	15	-0.04	53 - 65.5	--
276	17.6	-0.04	30 - 44	--
277	20	-0.04	30 - 44	63.01
282	17.7	0.065	--	--
279	20.8	0.065	--	--
280	23.6	0.065	30 - 44	63.69
281	27.6	0.065	< 30	51.5
285	8.7	-0.055	--	--
283	9.1	-0.055	--	--
284	12	-0.055	--	44.18
286	16.4	-0.055	20 - 25	no run

The plots of velocity time series and corresponding power spectra are shown in the order corresponding to run numbers as given in the Table 17.

Runs 187-190 (Figures 402-409) correspond to zero step (clean plate) and large separation between the hot-wires. The velocity time series show laminar flow conditions with slight increase of velocity fluctuations with increase of freestream speed. The spectra show weak peaks in 250-300Hz range of frequencies. The following stability analysis will determine whether they correspond to unstable T-S waves.

Runs 275-278 (Figures 410-417) are for the case of a -0.04-inch aft-facing step. The possible T-S waves can be found for the Run 275 in the range 120-250Hz (the peak shifts to lower frequency with increase of stream-wise distance). In Run 278 transition to turbulence is observed for the last hw4 with preceding spikes in velocity time series for hw2 and hw3. Run 276 and Run 277 show turbulence for all hot-wires except for the first one.

Runs 279-282 (Figures 418-425) are for the case of a 0.065-inch forward-facing step. In the Run 282 all hot-wires show laminar flow with the presence of possible T-S waves in the range 120-250Hz (the peak shifts to lower frequency with increase of stream-wise distance). In Run 279 last hw4 shows broadening of the spectra with a lot of spikes in the velocity time series and hw1-hw3 show laminar flow with possible T-S waves. In Run 280 all hot-wires except the first one show turbulence and in Run 281 all hot-wires show turbulence.

Runs 283-286 (Figures 426-433) are for the case of a -0.055-inch aft-facing step. In Run 285 all hot-wires show laminar flow, in Run 283 and Run 284 there is continuous broadening of

spectra and spikes in velocity time series. No T-S waves are observed for this case. In Run 286 transition to turbulence happens - all three hot-wires except the first one show turbulent flow.

Runs 292-294 (Figures 434-439) are for the case of a -0.04-inch aft facing step. These runs are a repetition of the case -0.04in step as in Runs 275-278 but for intermediate stream-wise locations and only two hot-wires were used (hw1 and hw2). No T-S waves can be found in these runs.

Runs 295-298 (Figures 440-447) are for the case of a 0.065-inch forward-facing step. These runs are repetition of the case 0.065in step as in Runs 279-282 but for intermediate hot-wire locations and only two hot-wires were used (hw1 and hw2). No T-S waves can be found in these runs.

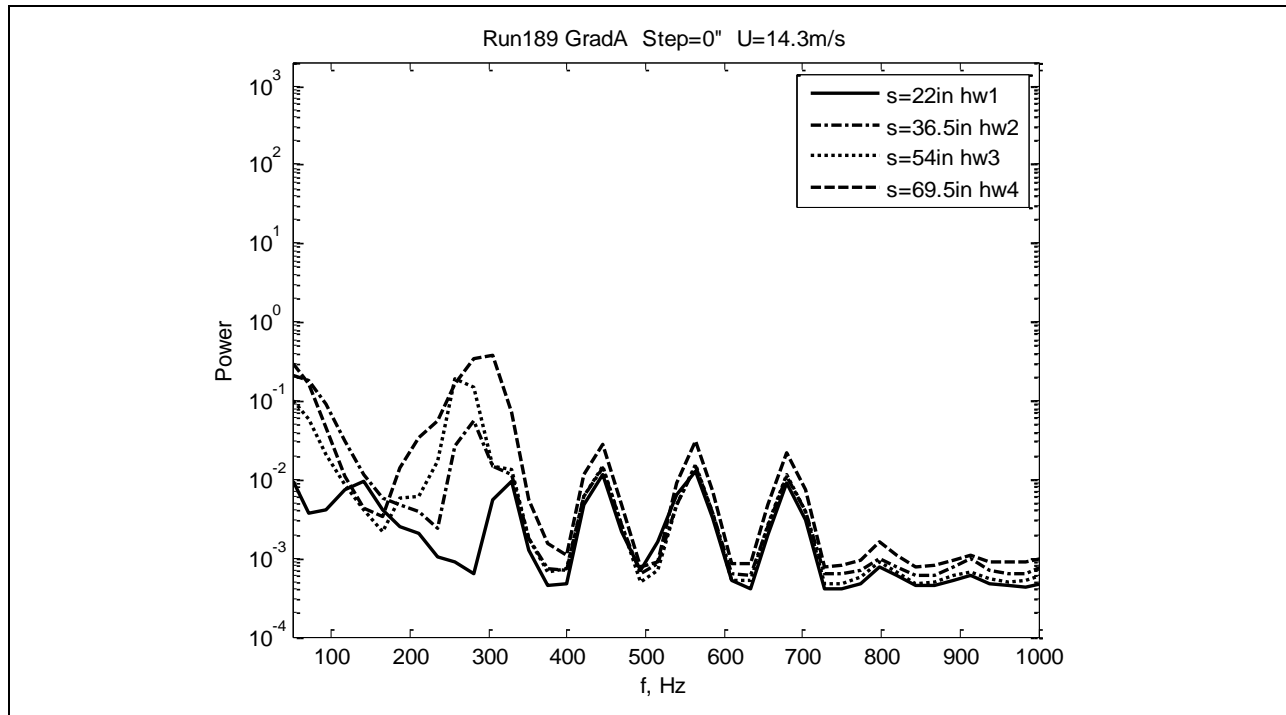


Figure 402: Measured power spectra.

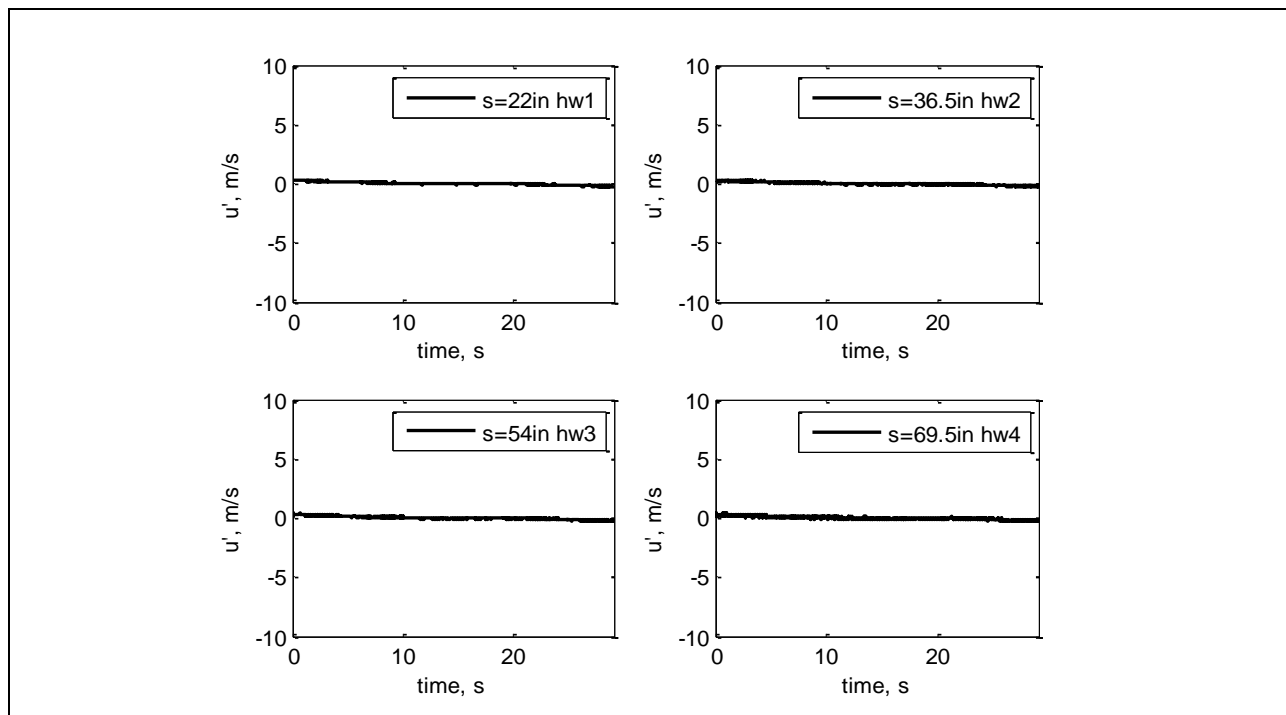


Figure 403: Measured velocity time history.

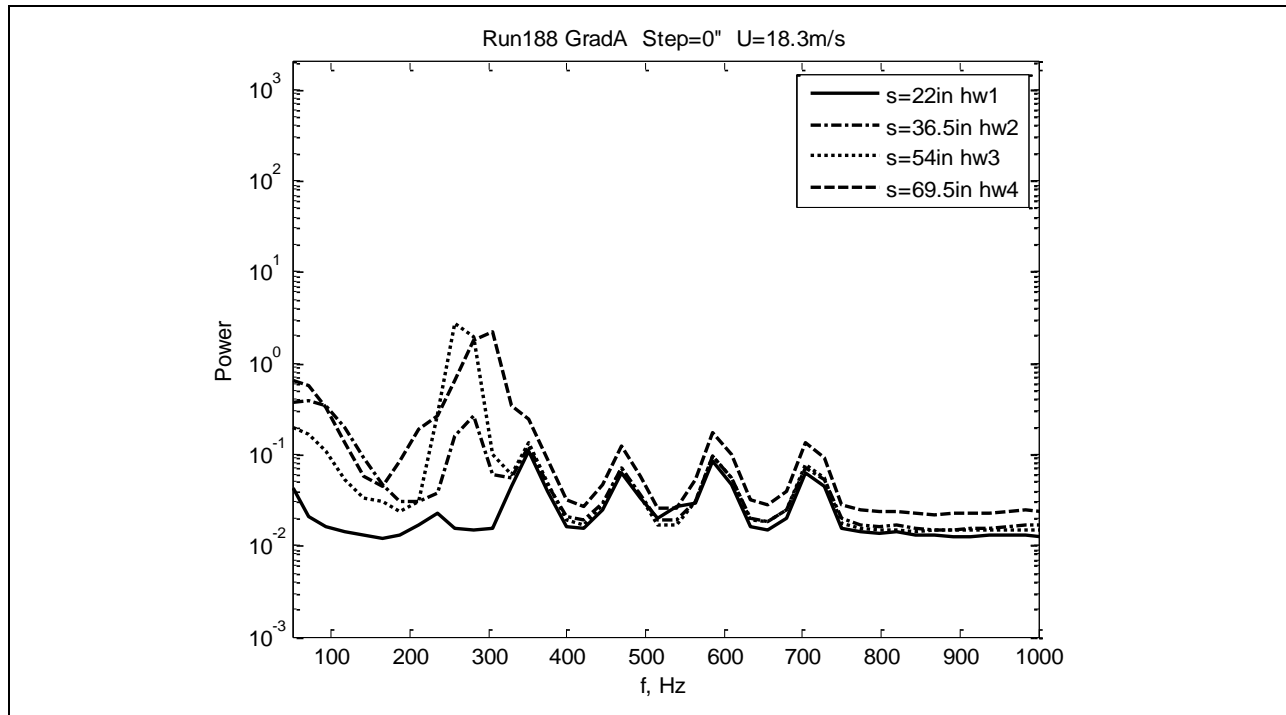


Figure 404: Measured power spectra.

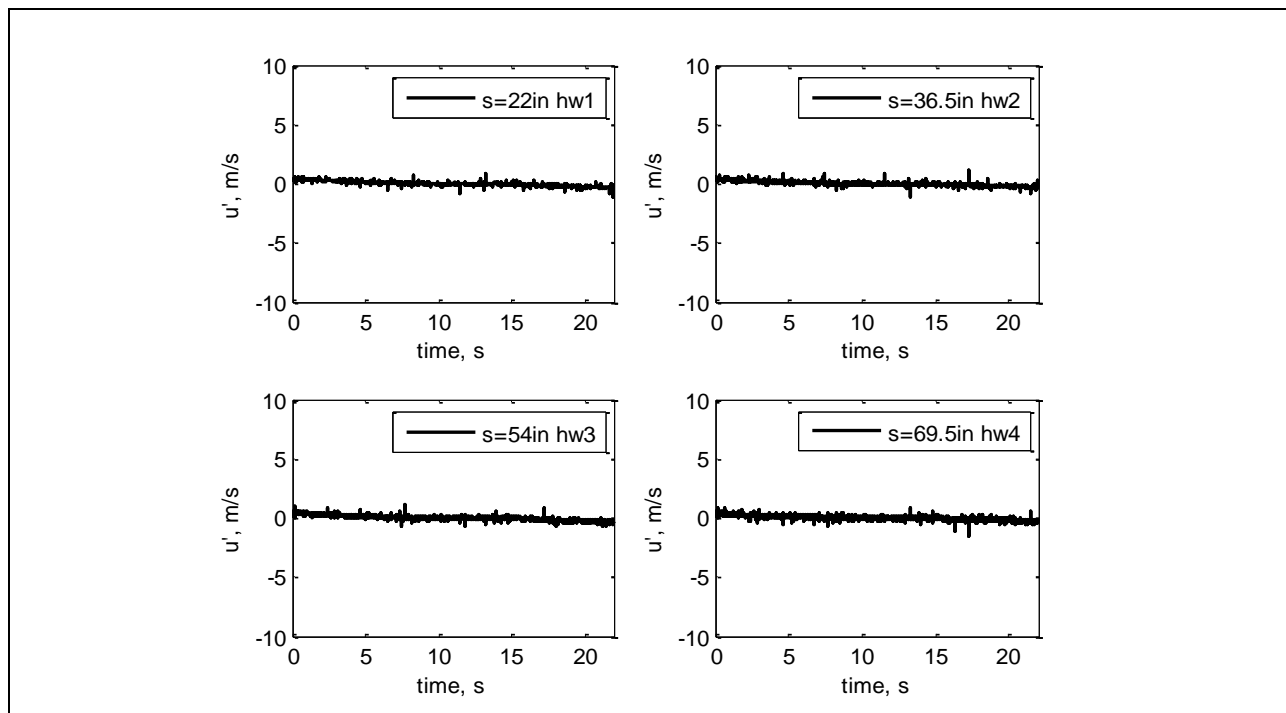


Figure 405: Measured velocity time history.

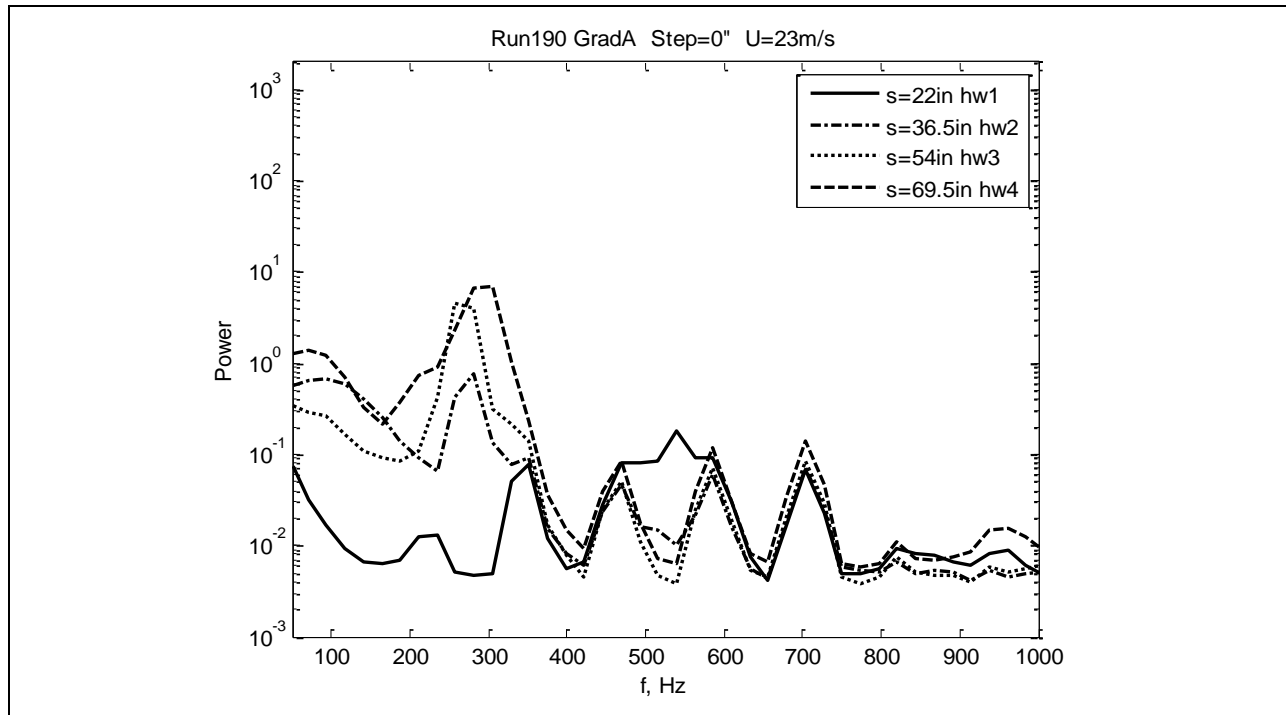


Figure 406: Measured power spectra.

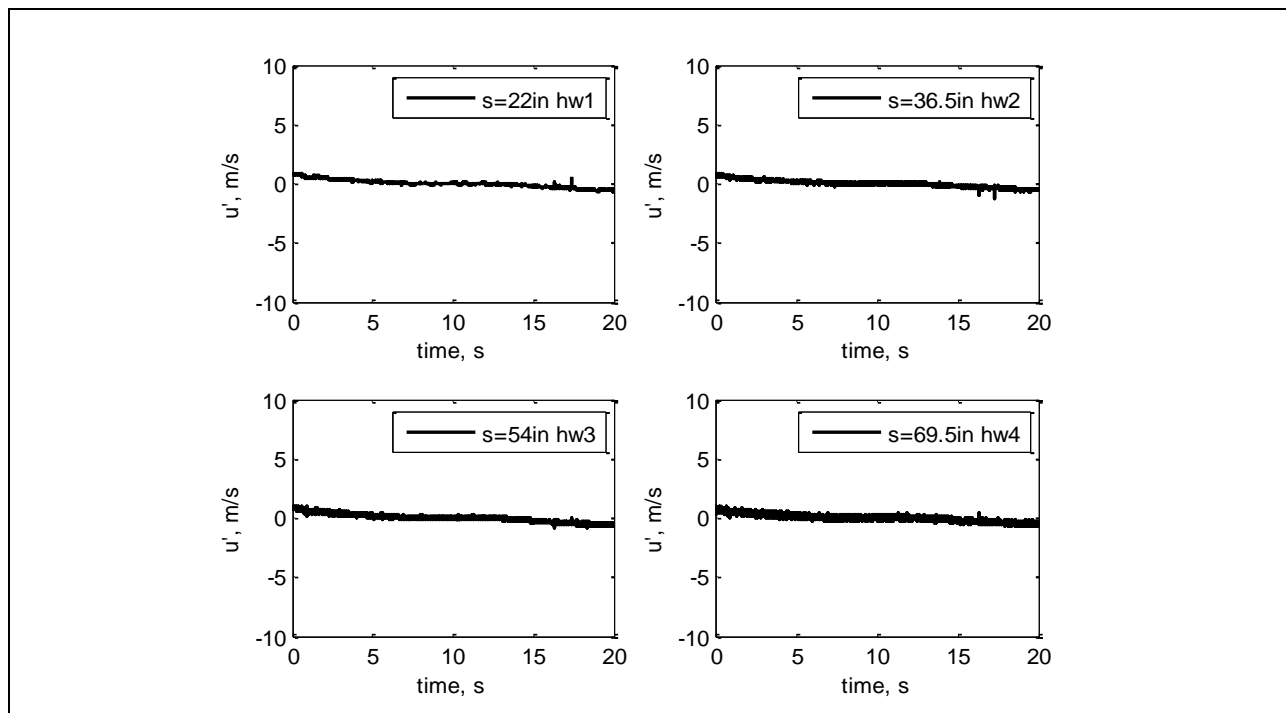


Figure 407: Measured velocity time history.

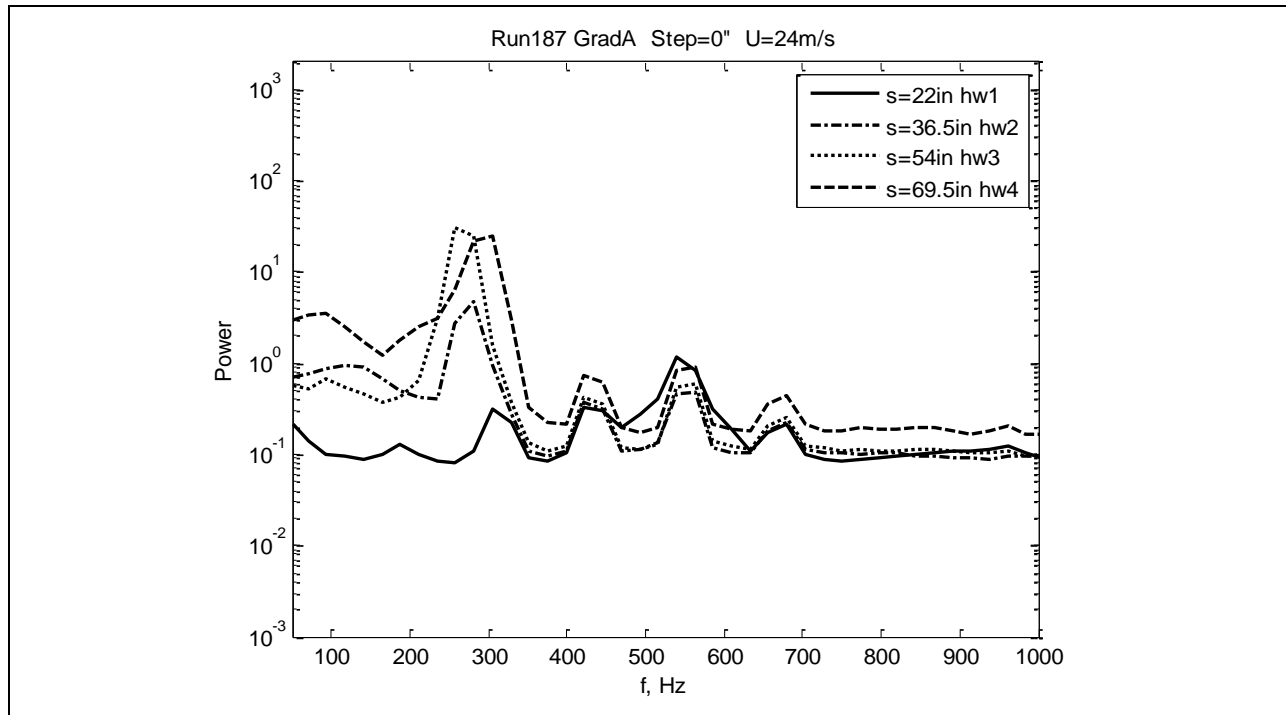


Figure 408: Measured power spectra.

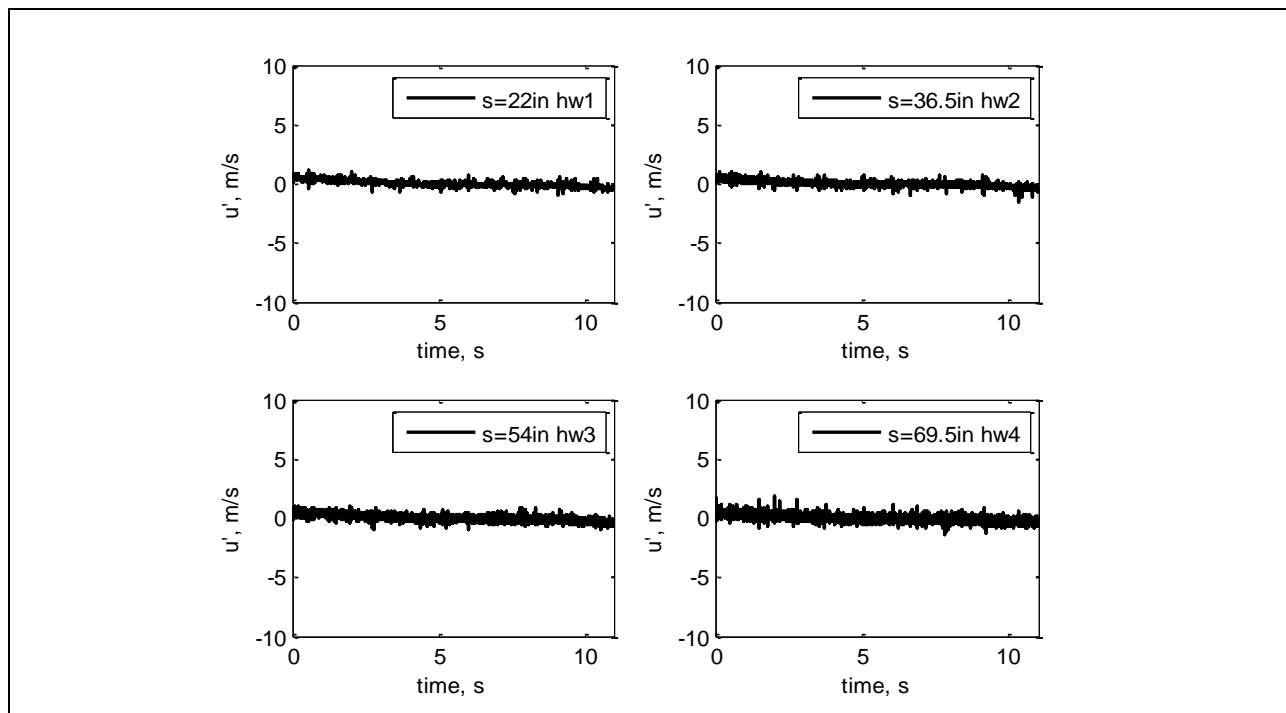


Figure 409: Measured velocity time history.

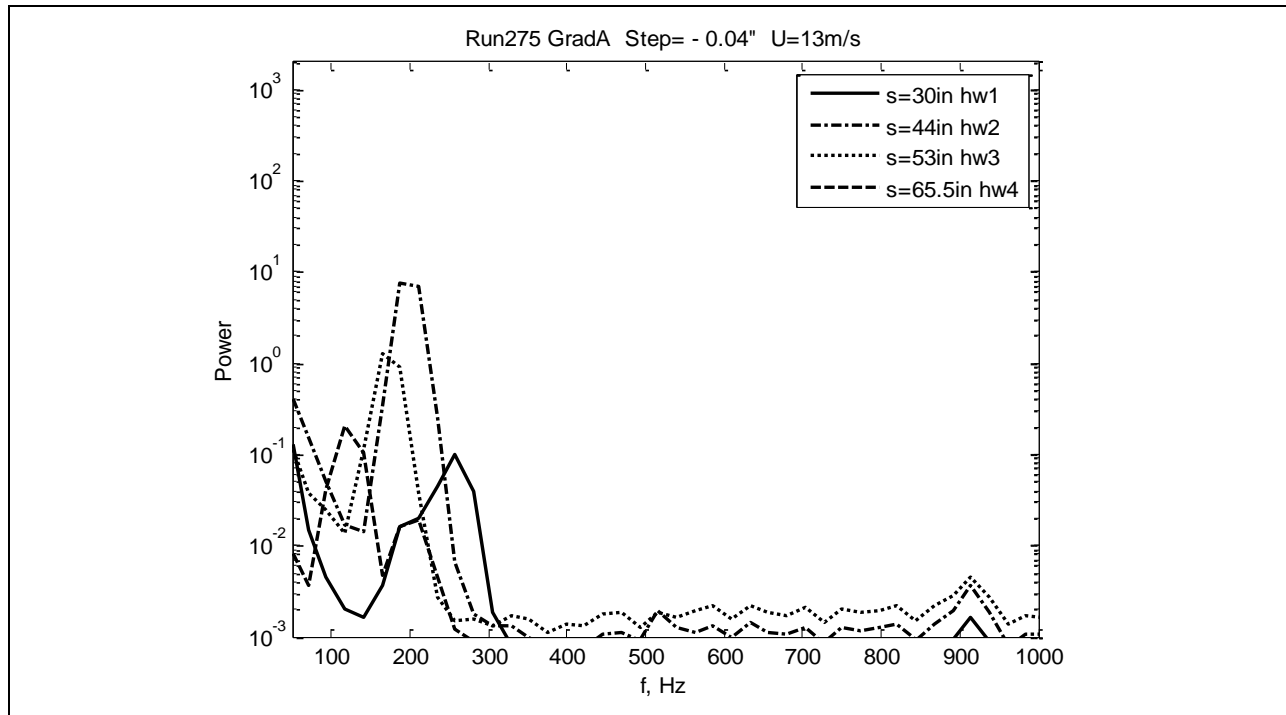


Figure 410: Measured power spectra.

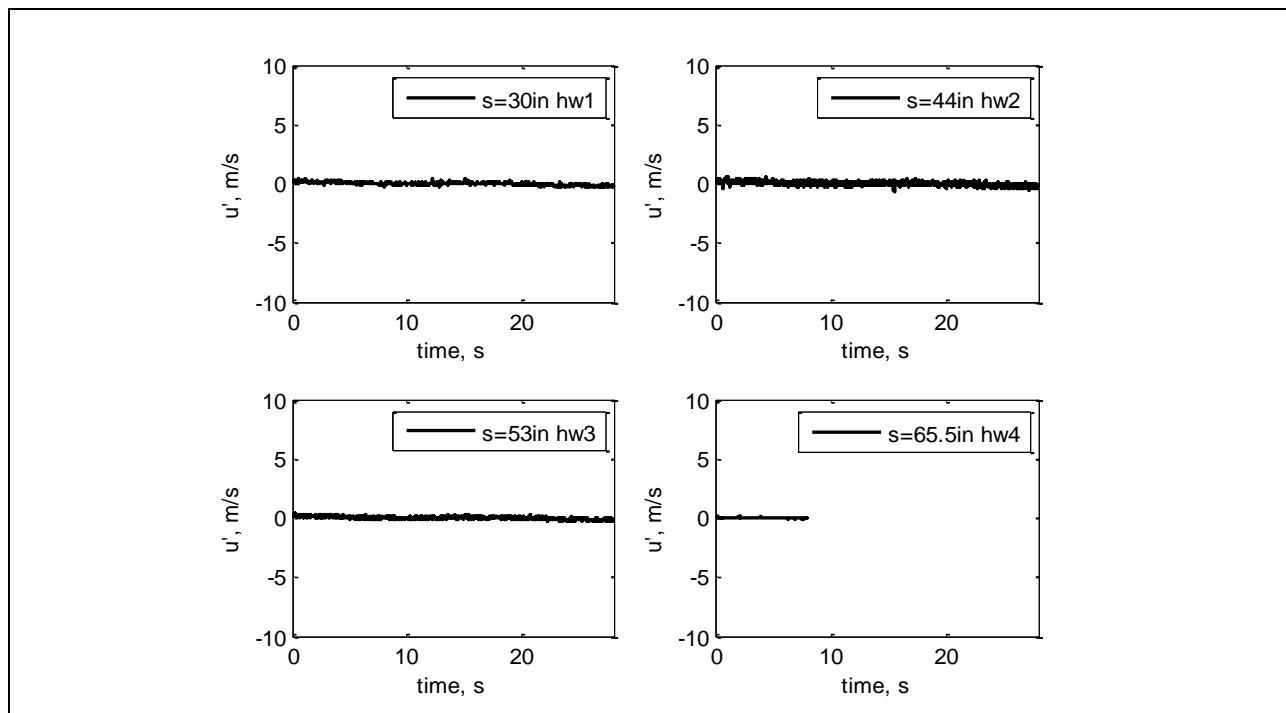


Figure 411: Measured velocity time history.

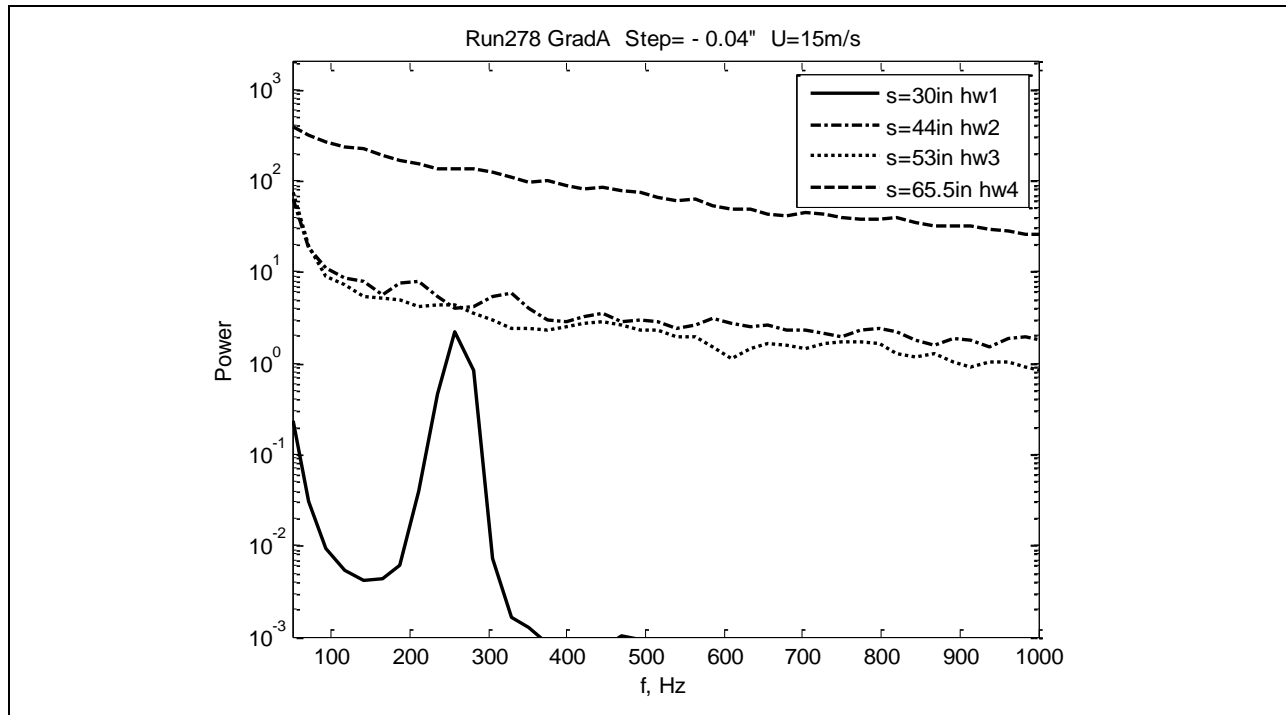


Figure 412: Measured power spectra.

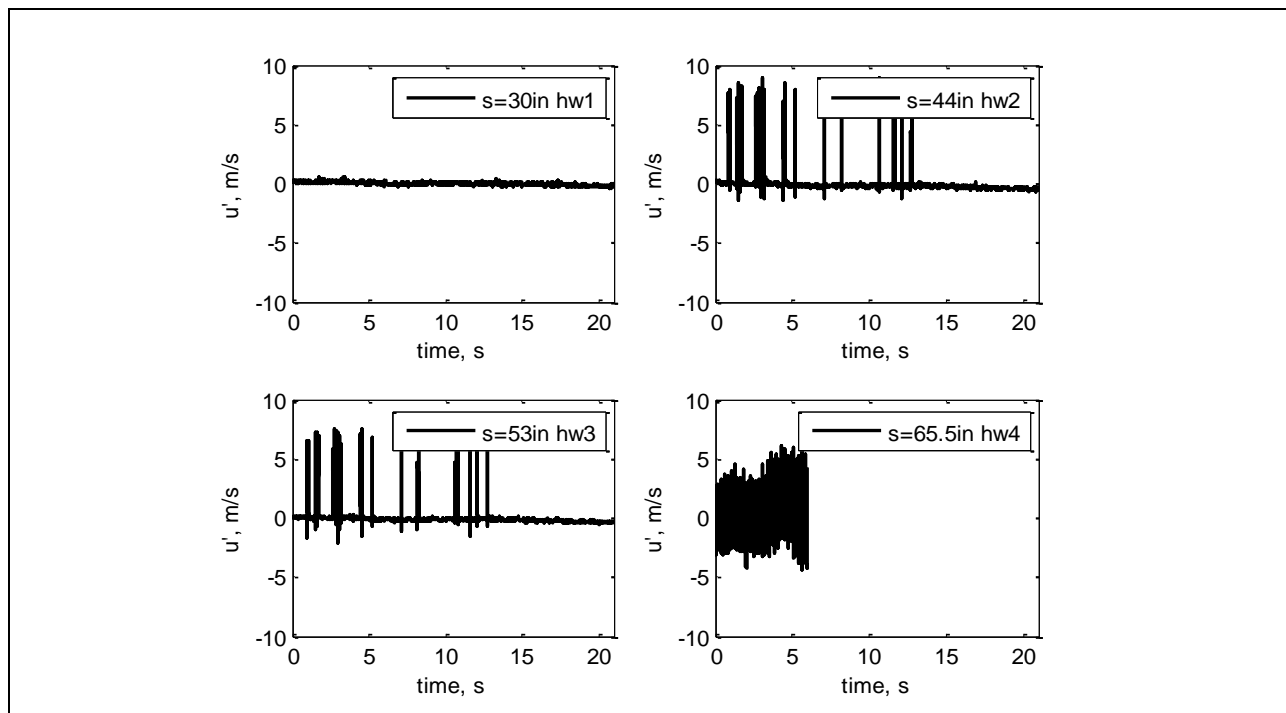


Figure 413: Measured velocity time history.

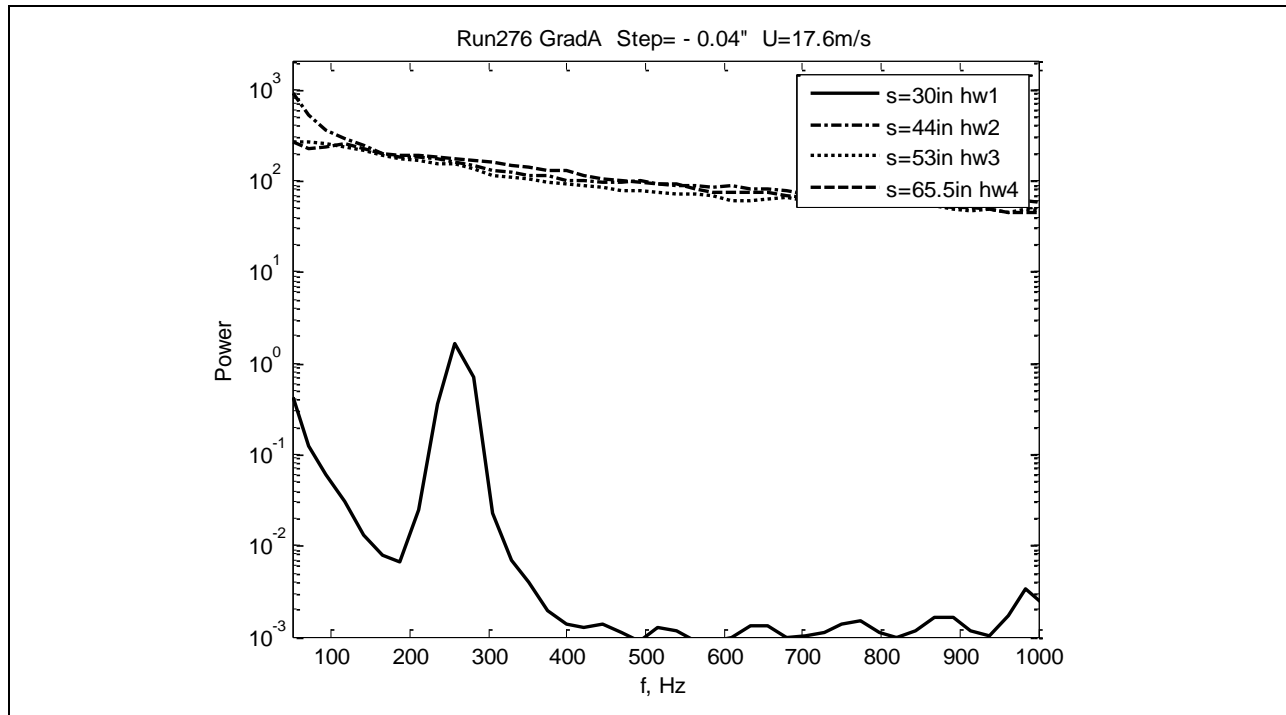


Figure 414: Measured power spectra.

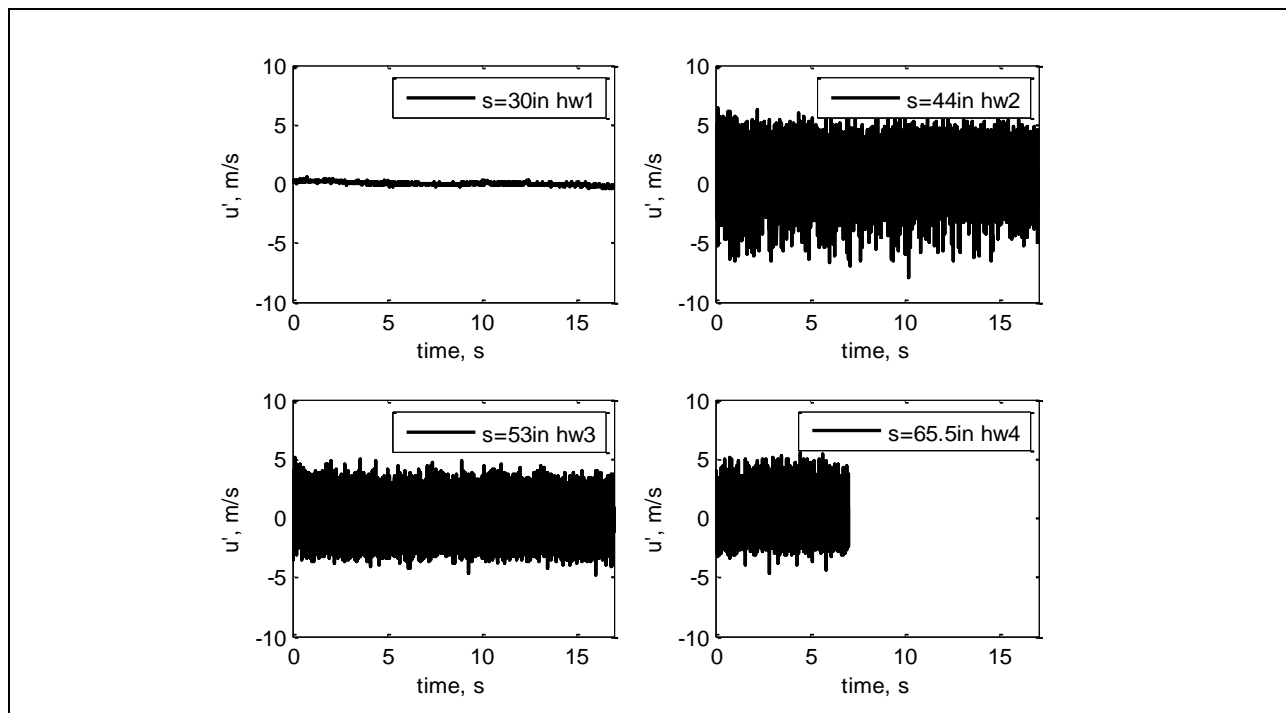


Figure 415: Measured velocity time history.

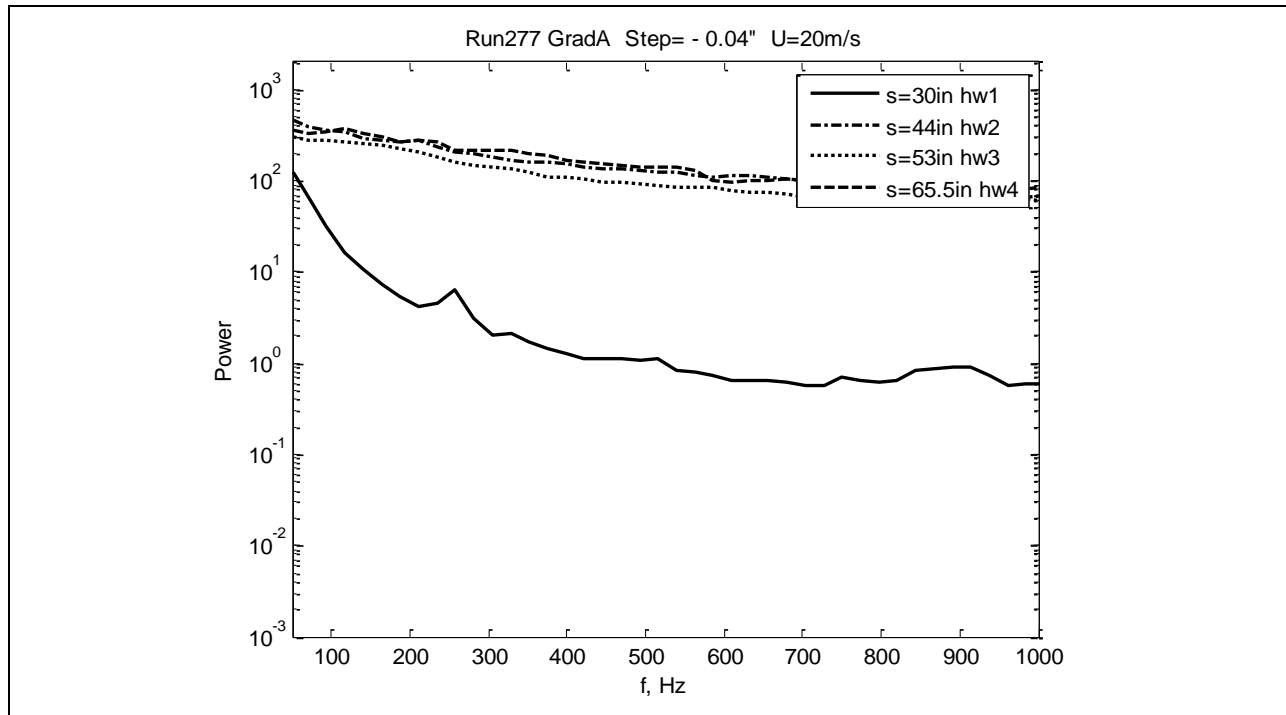


Figure 416: Measured power spectra.

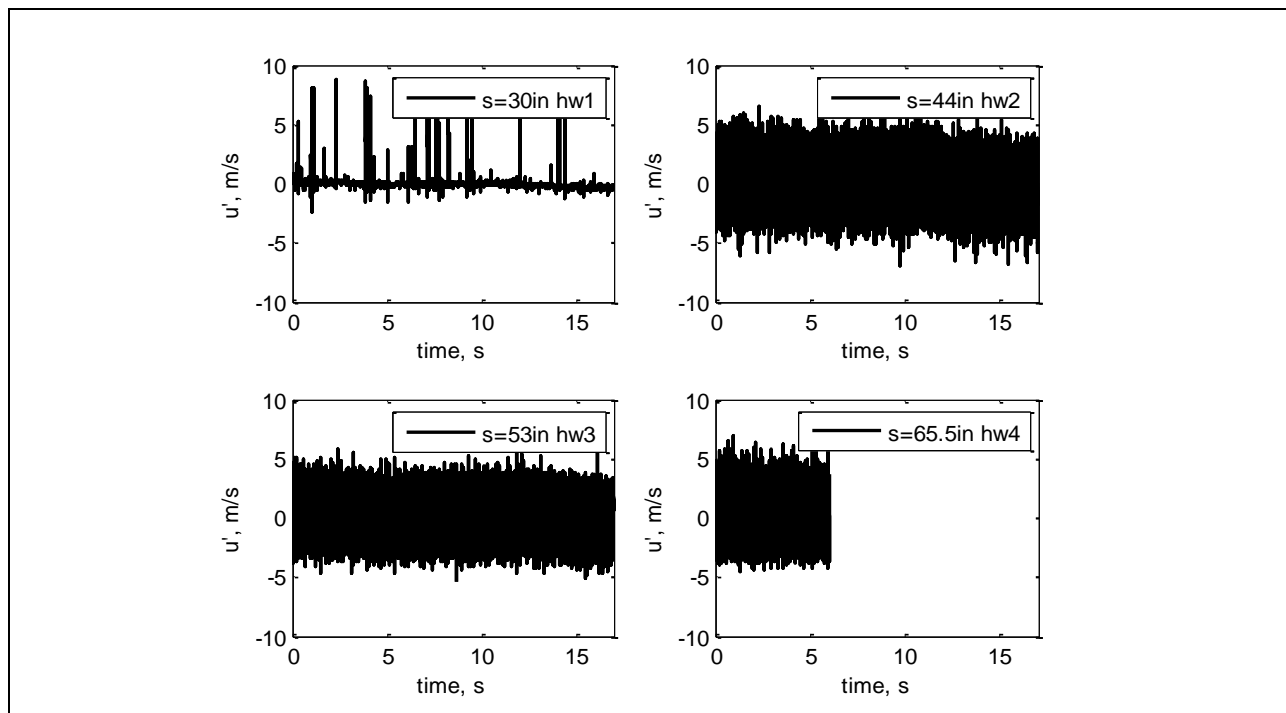


Figure 417: Measured velocity time history.

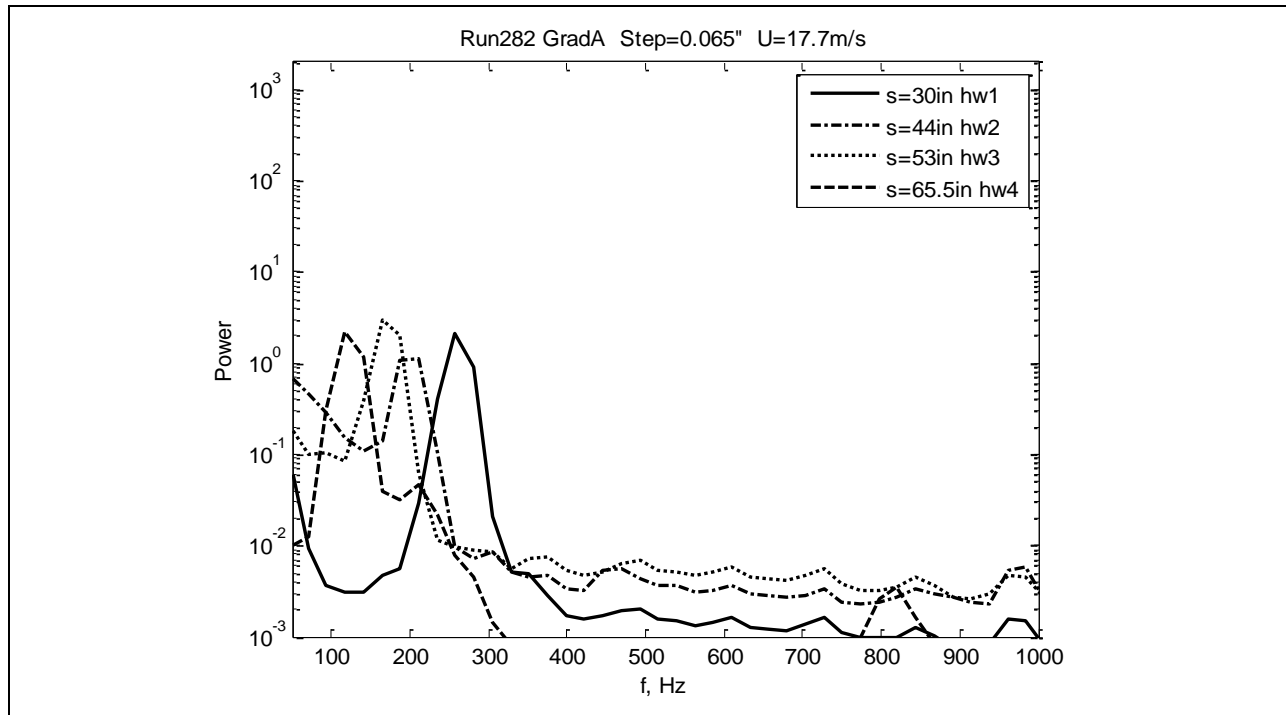


Figure 418: Measured power spectra.

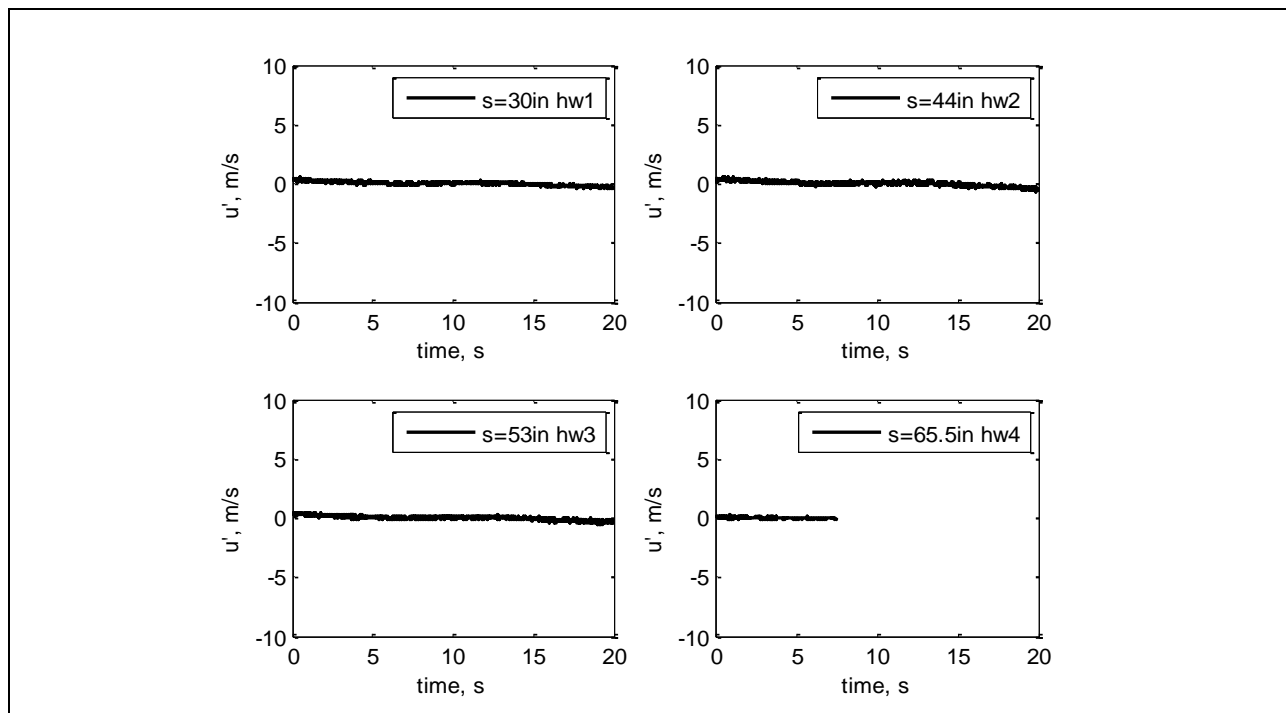


Figure 419: Measured velocity time history.

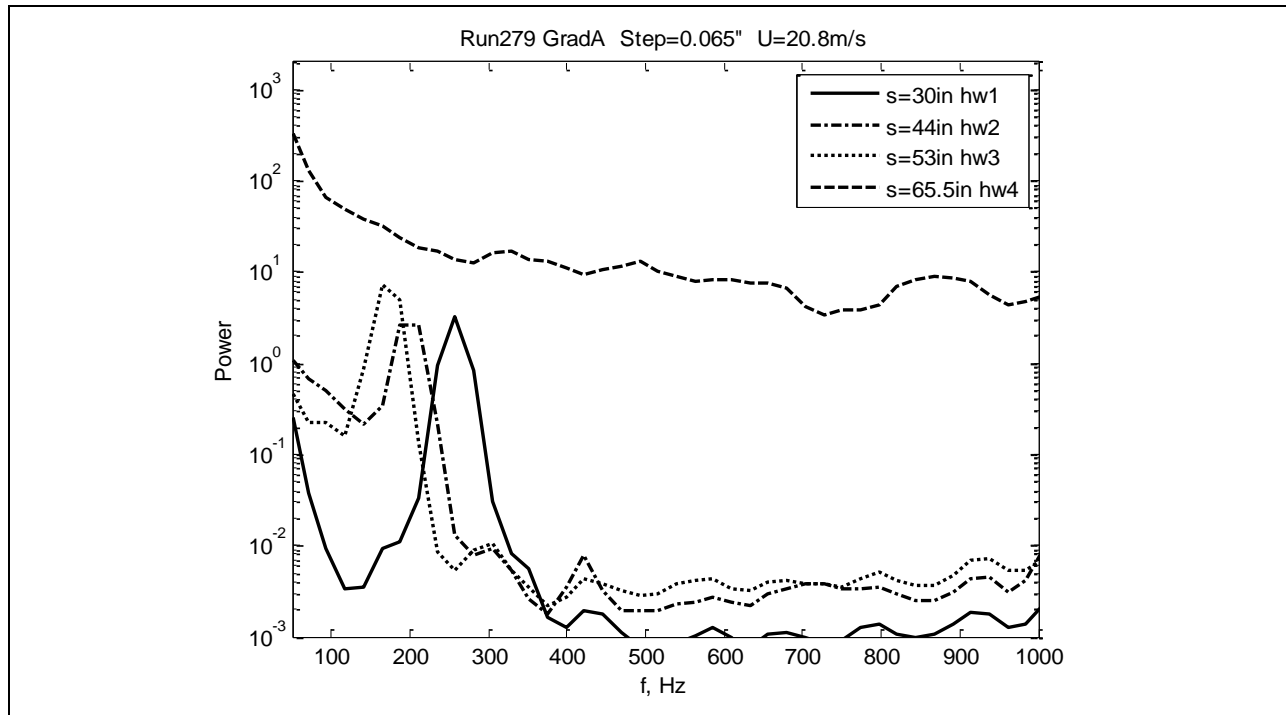


Figure 420: Measured power spectra.

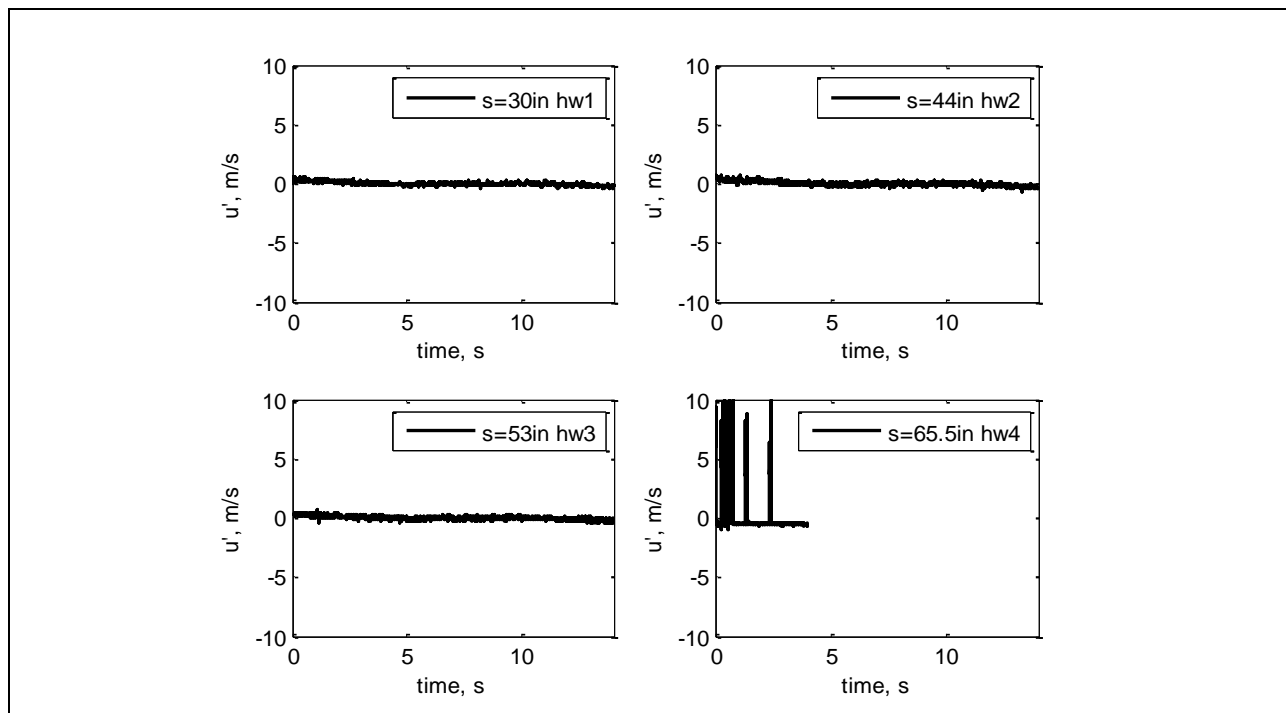


Figure 421: Measured velocity time history.

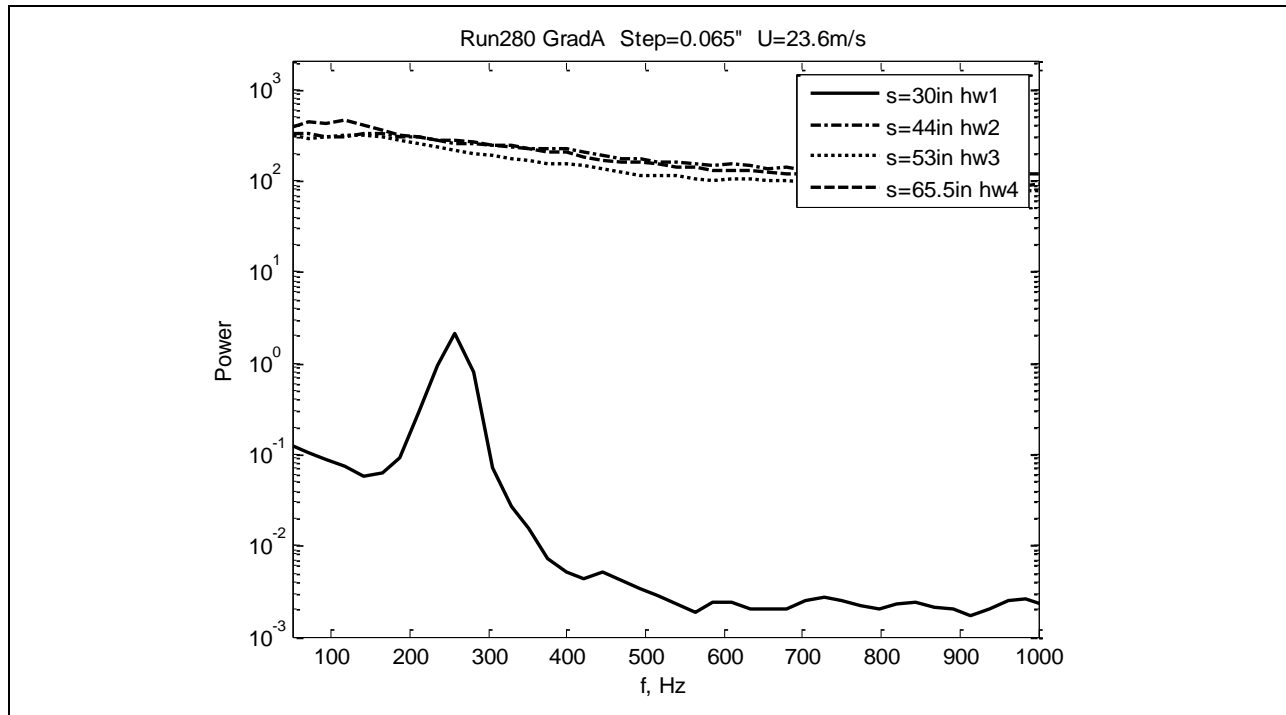


Figure 422: Measured power spectra.

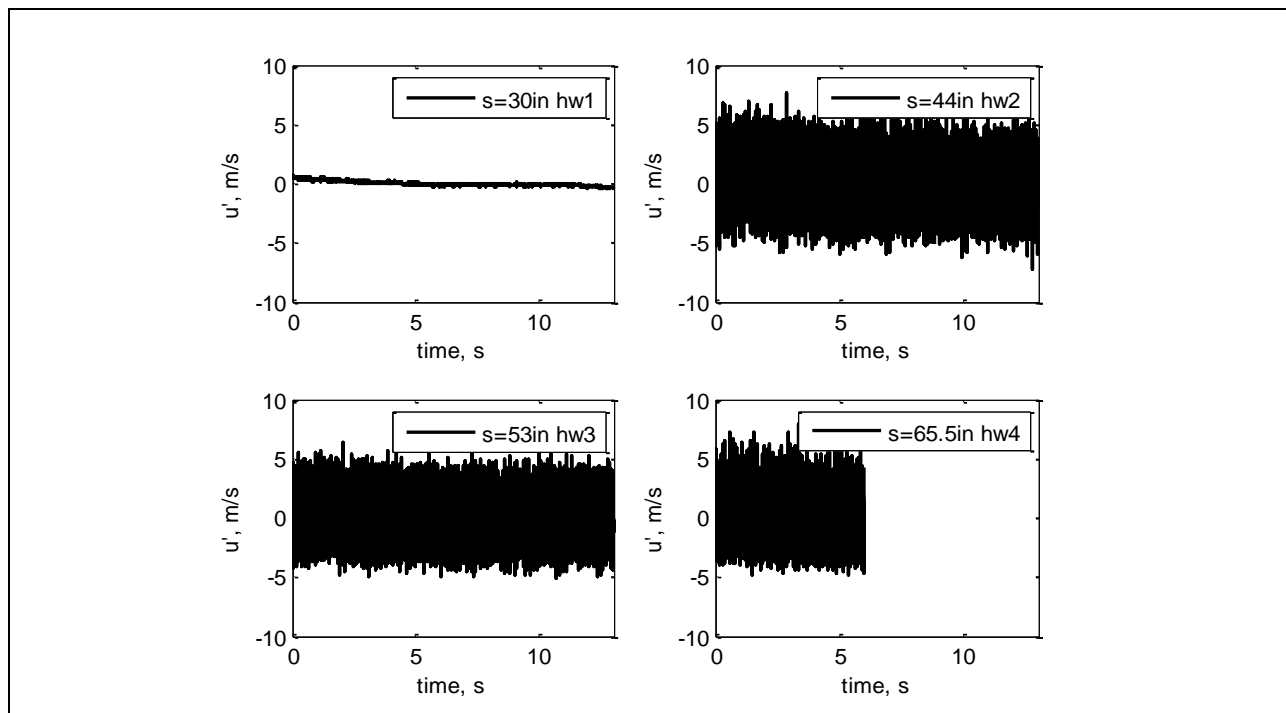


Figure 423: Measured velocity time history.

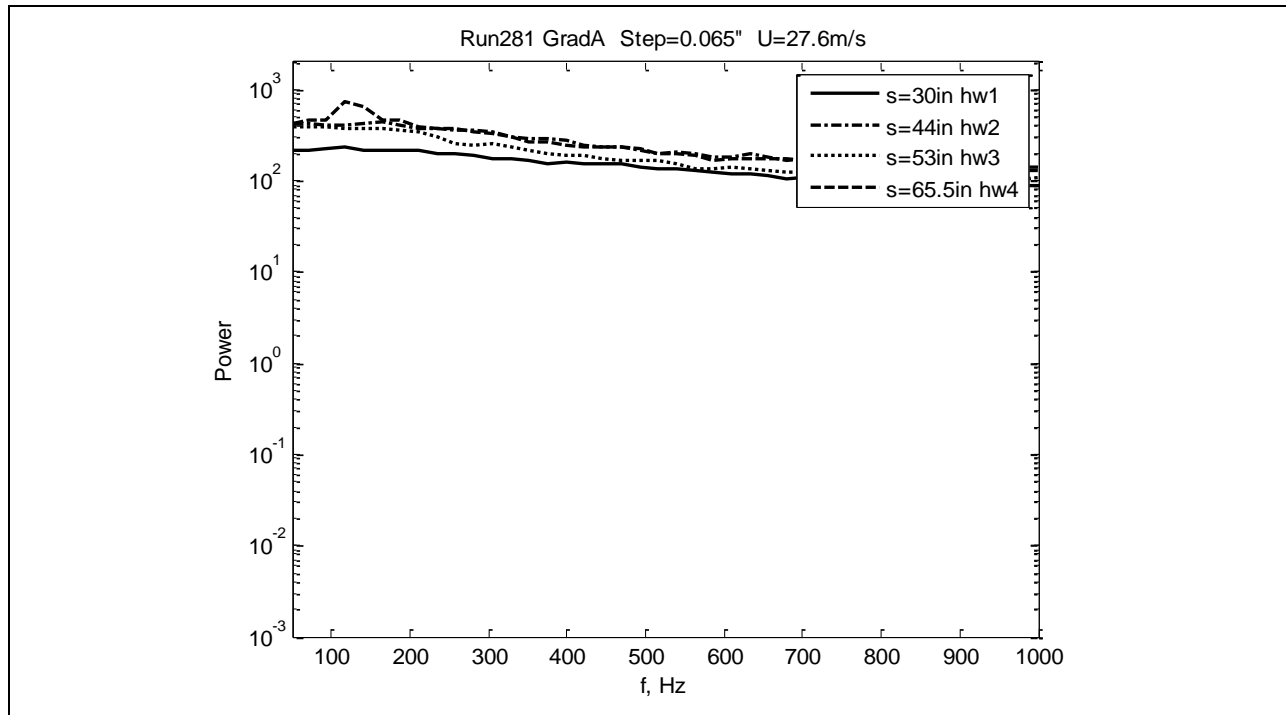


Figure 424: Measured power spectra.

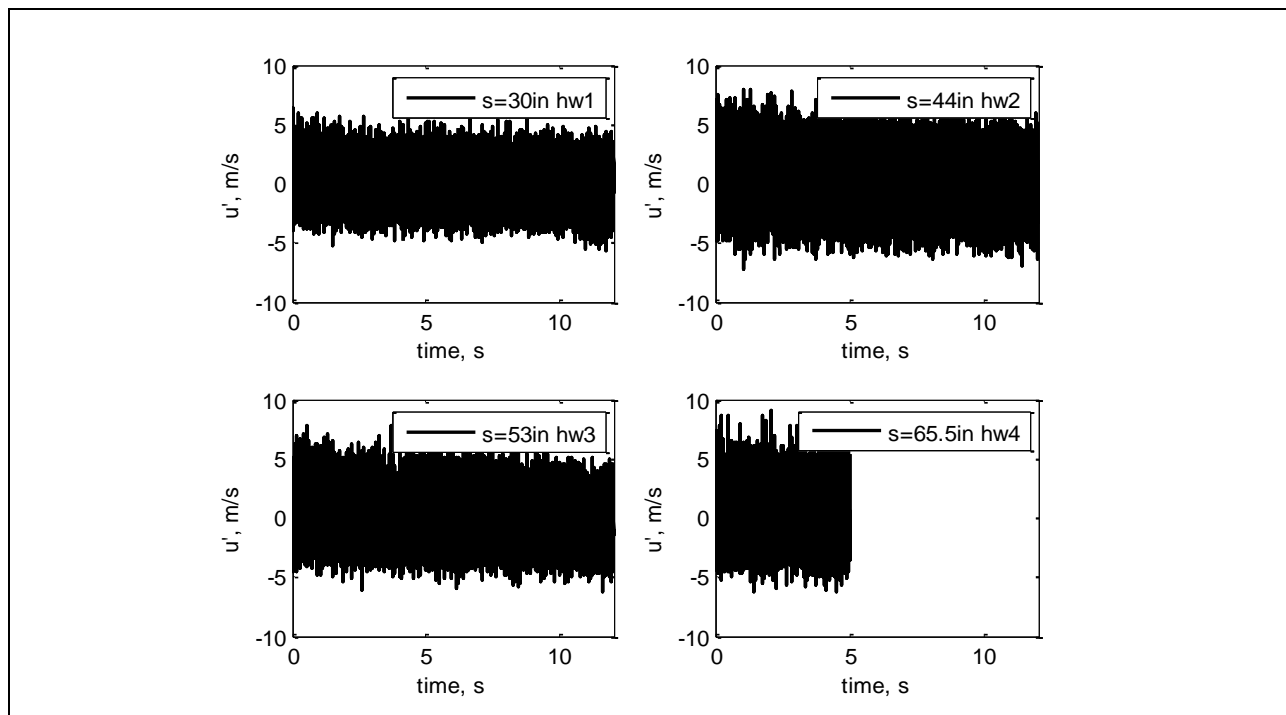


Figure 425: Measured velocity time history.

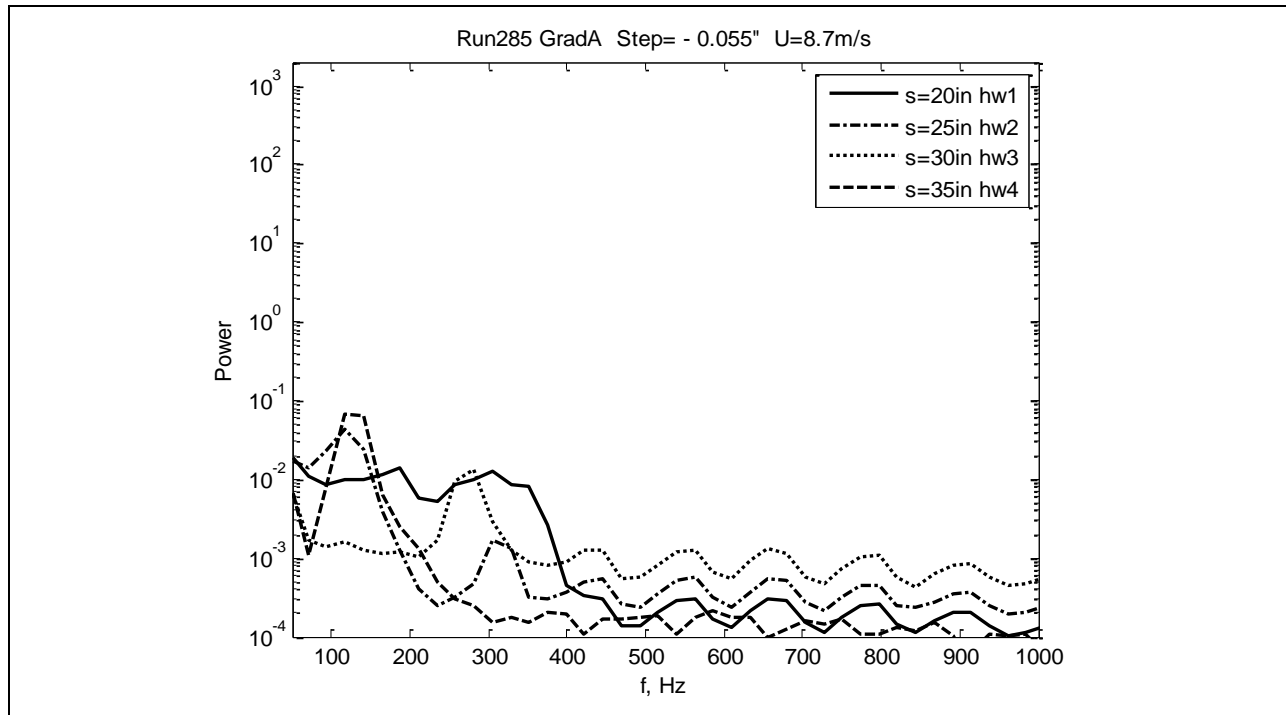


Figure 426: Measured power spectra.

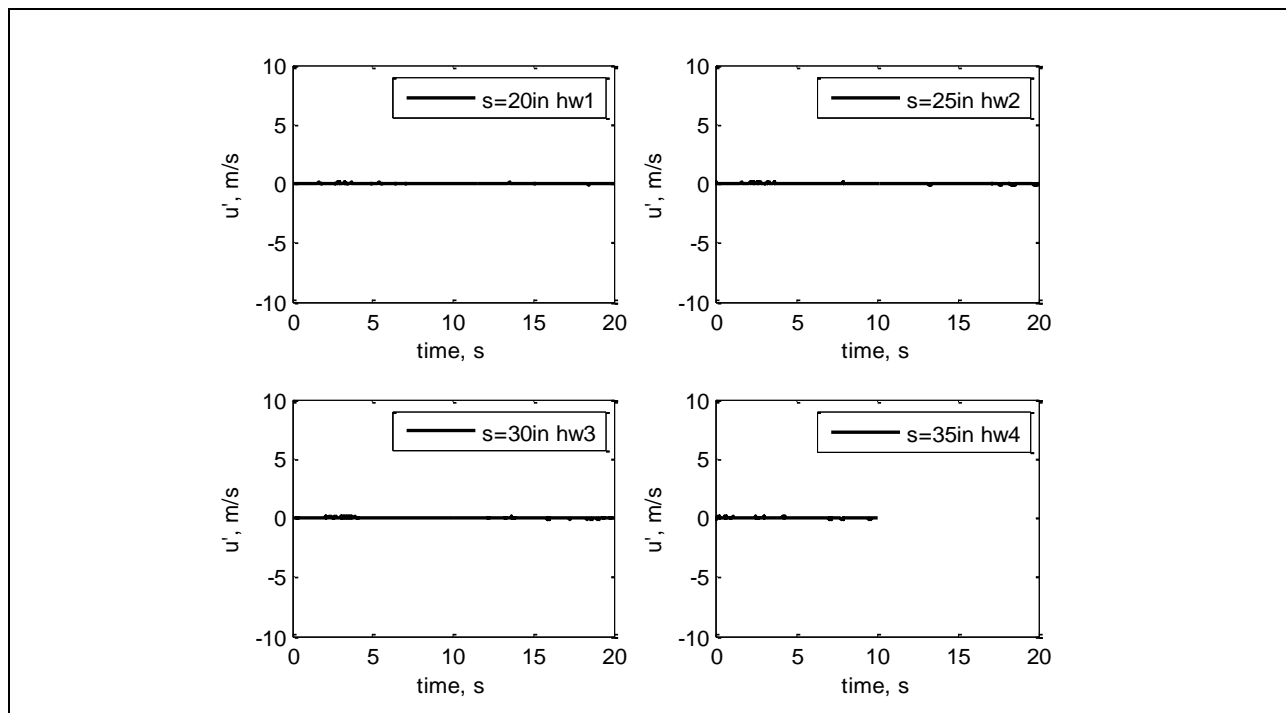


Figure 427: Measured velocity time history.

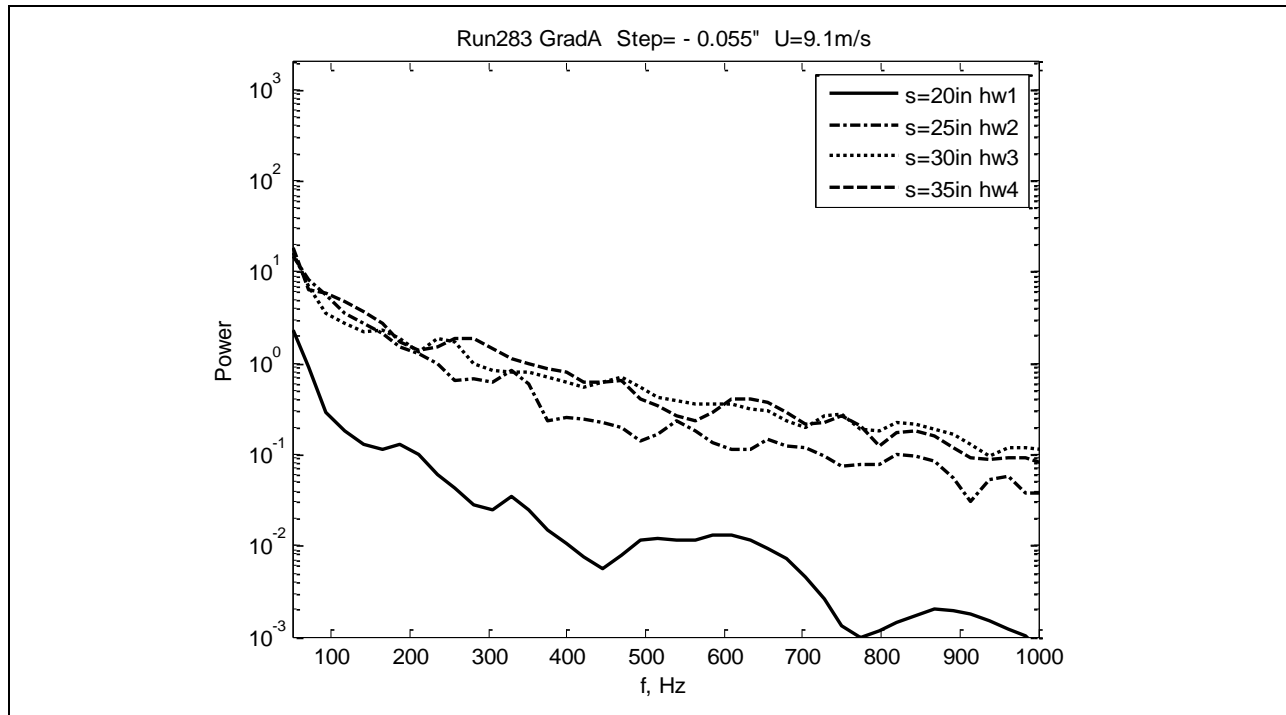


Figure 428: Measured power spectra.

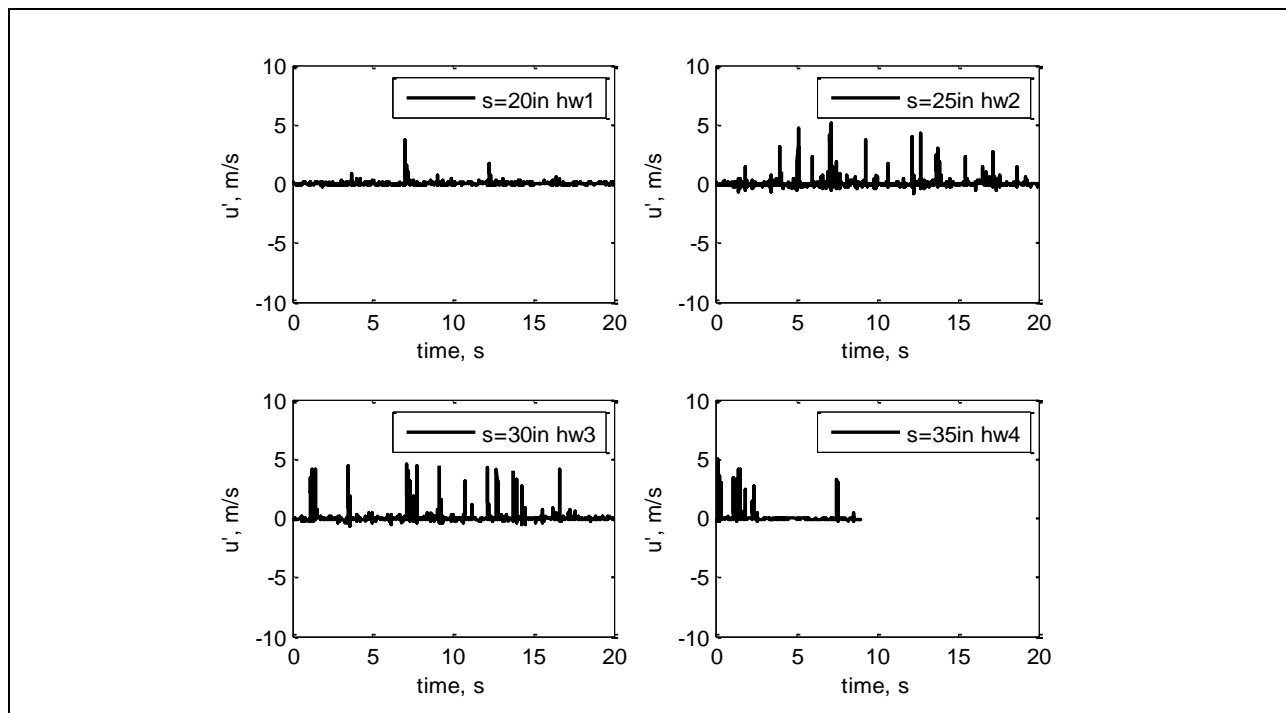


Figure 429: Measured velocity time history.

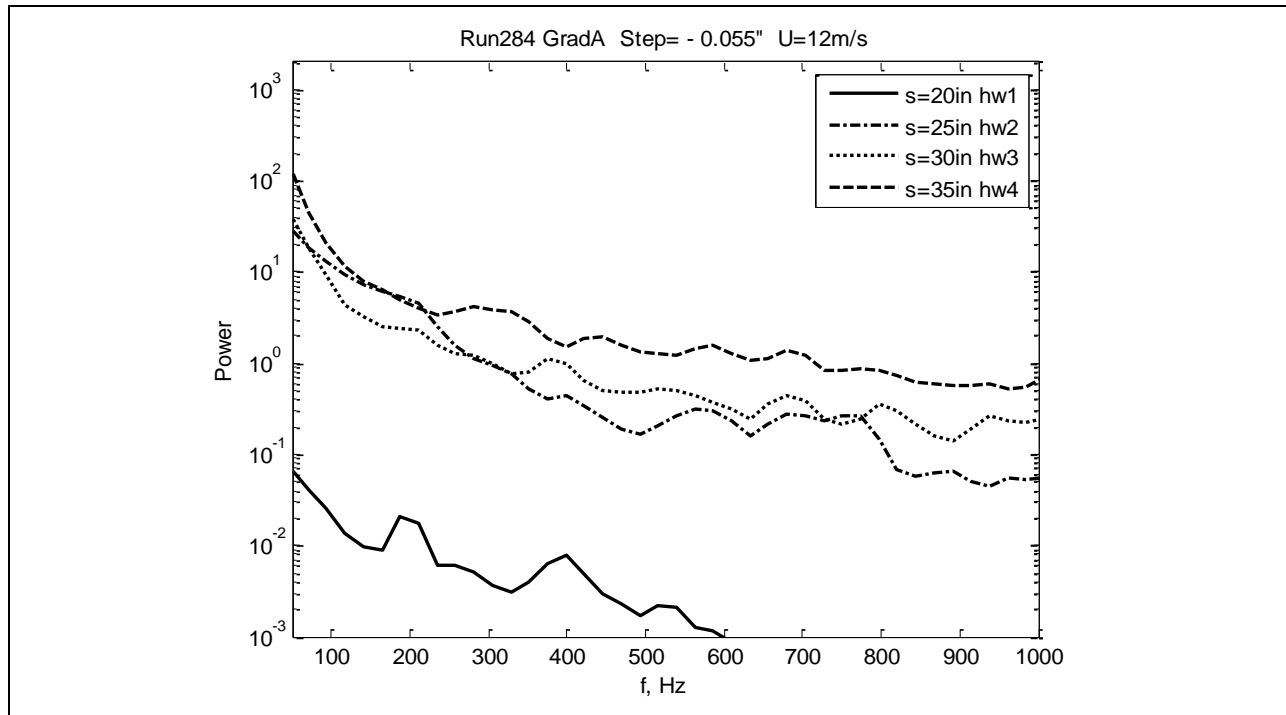


Figure 430: Measured power spectra.

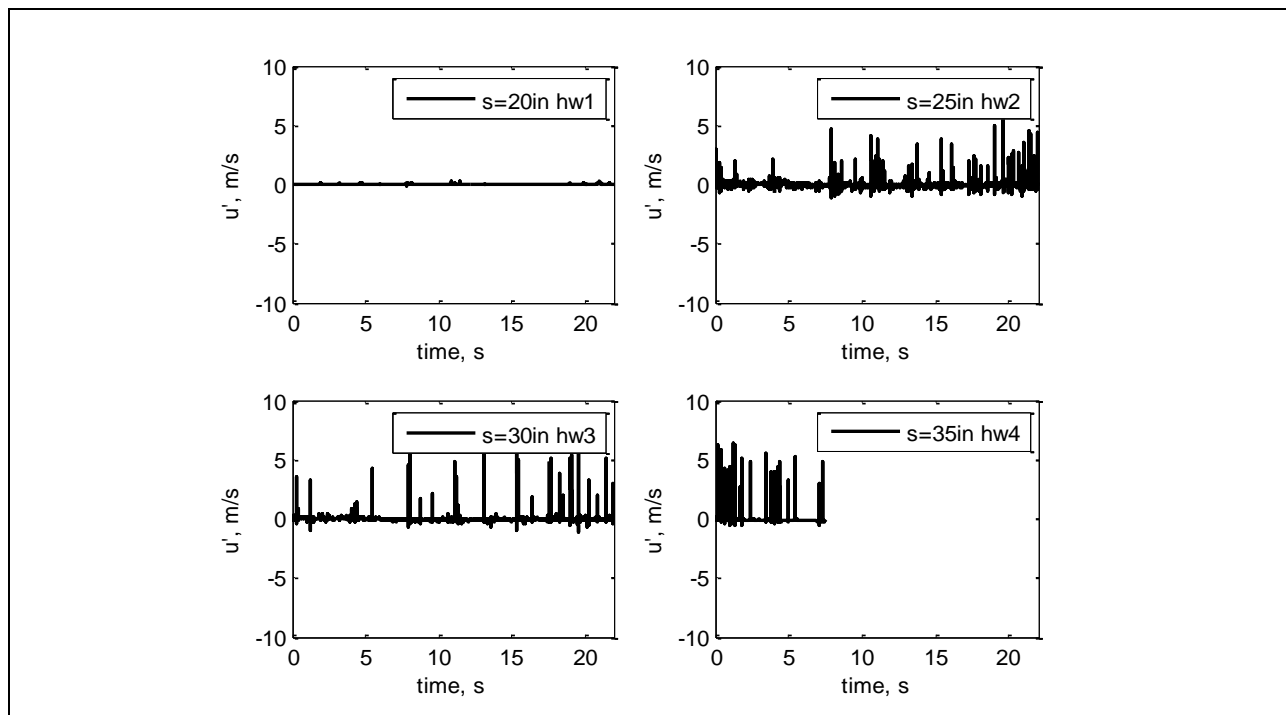


Figure 431: Measured velocity time history.

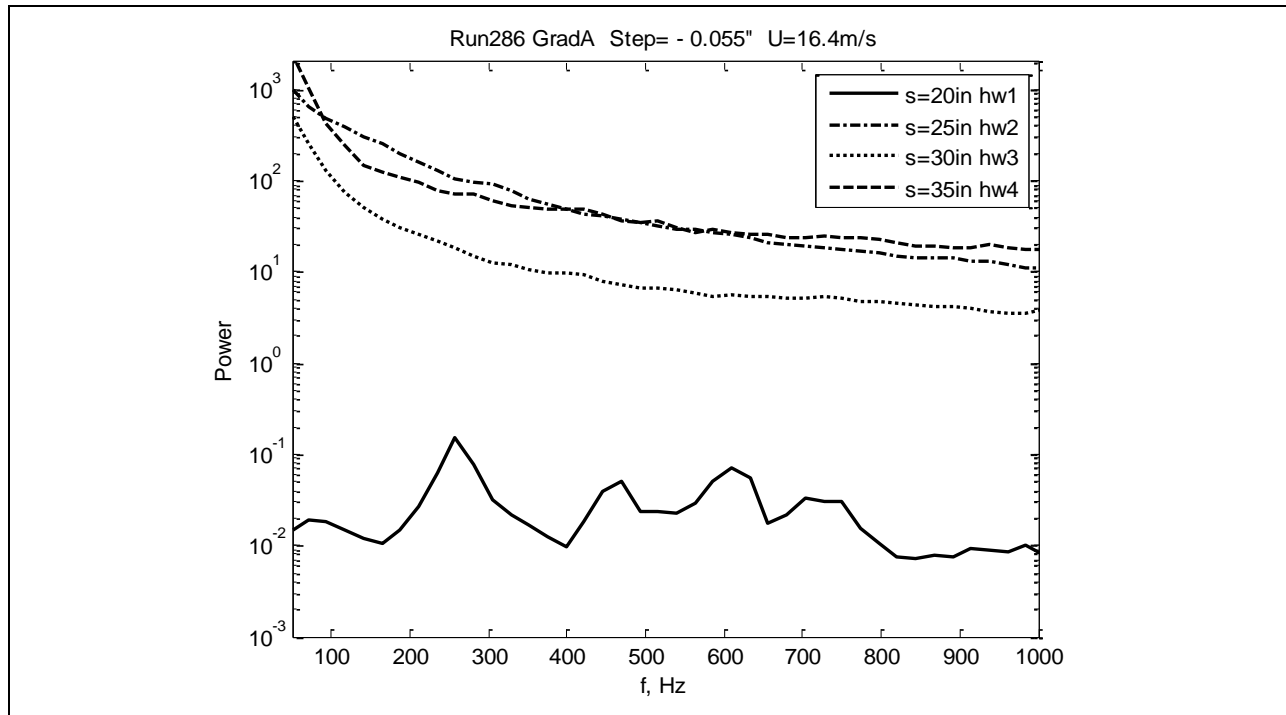


Figure 432: Measured power spectra.

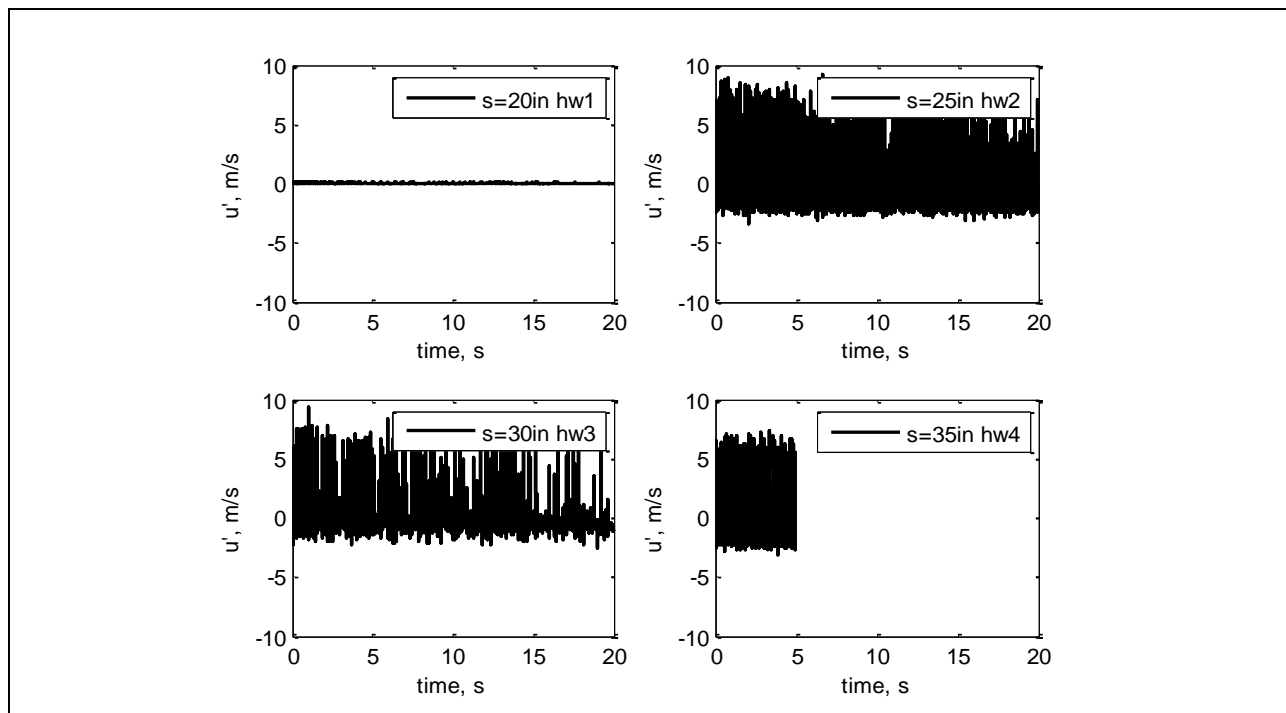


Figure 433: Measured velocity time history.

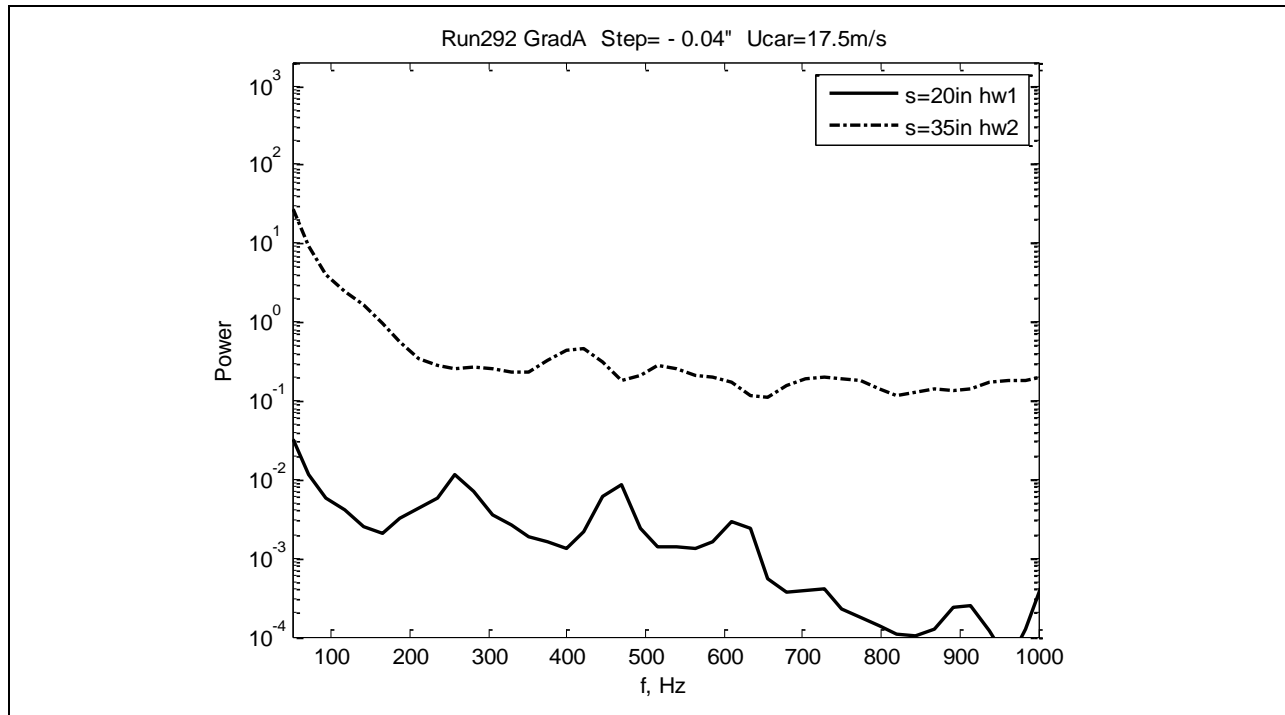


Figure 434: Measured power spectra.

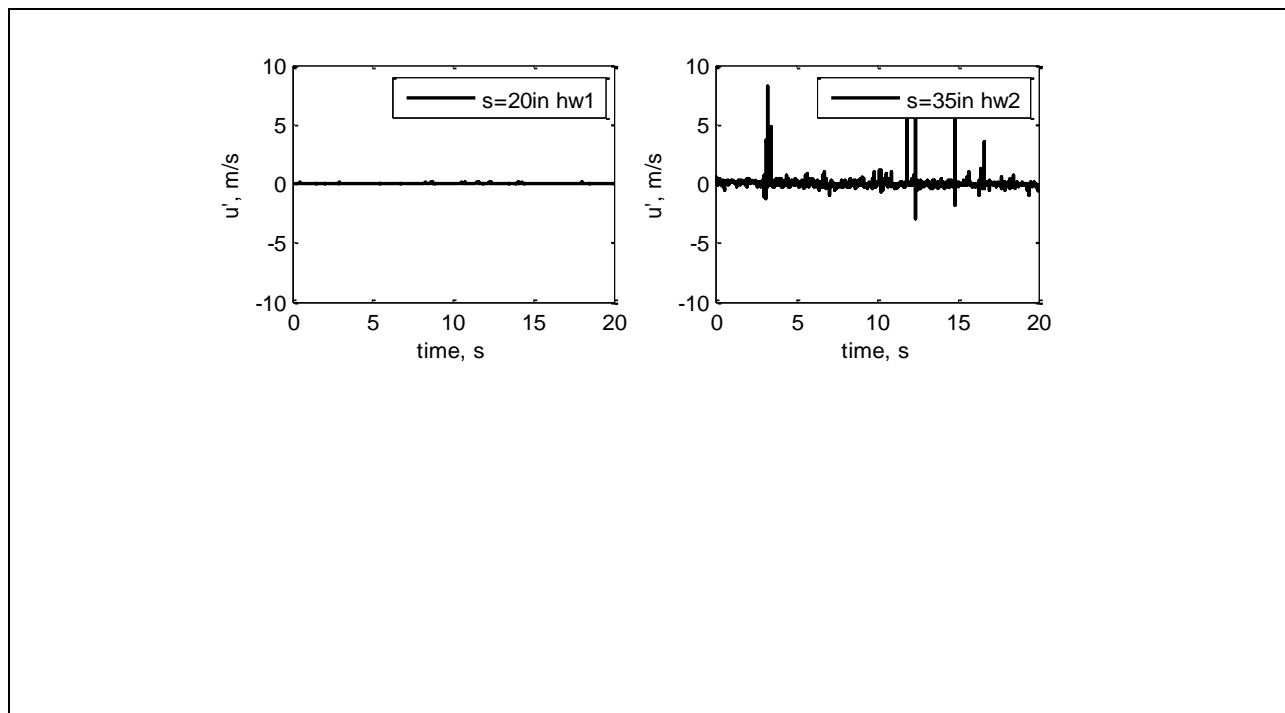


Figure 435: Measured velocity time history.

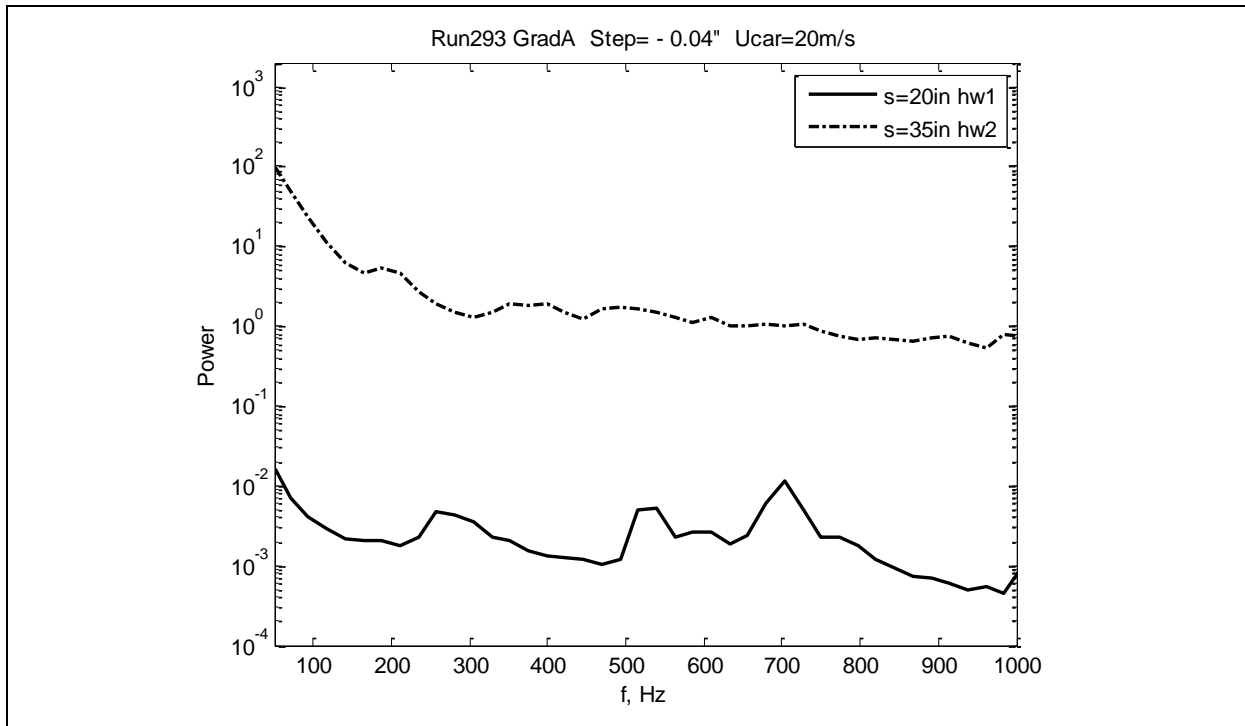


Figure 436: Measured power spectra.

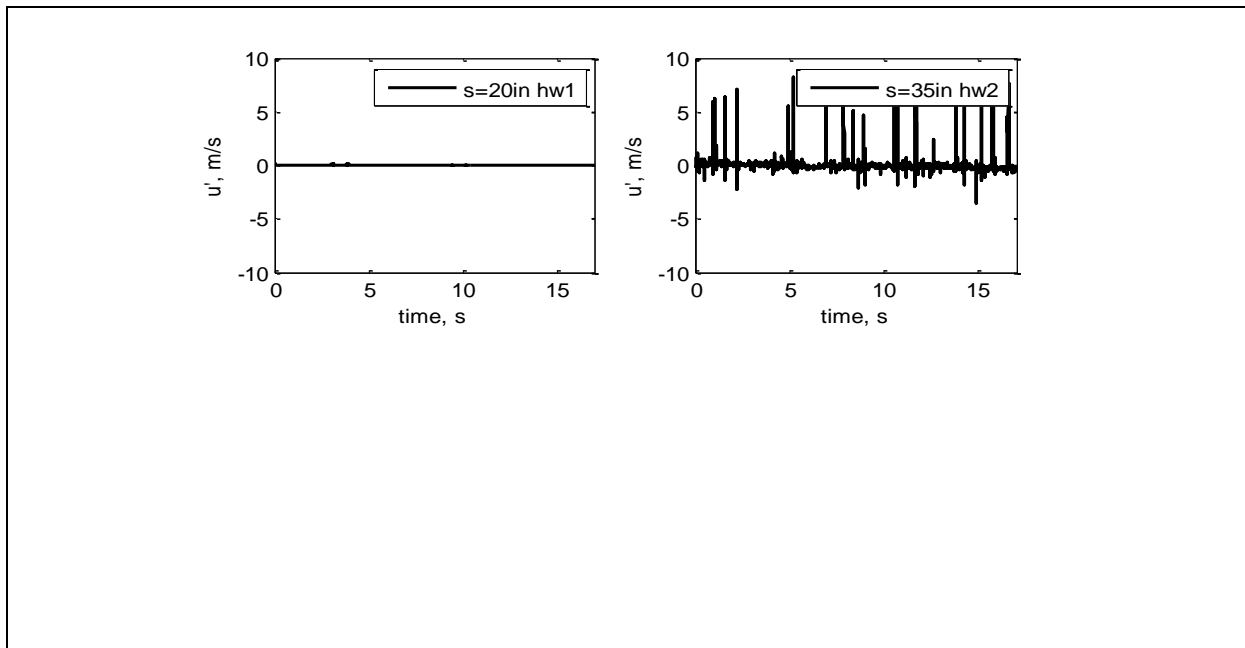


Figure 437: Measured velocity time history.

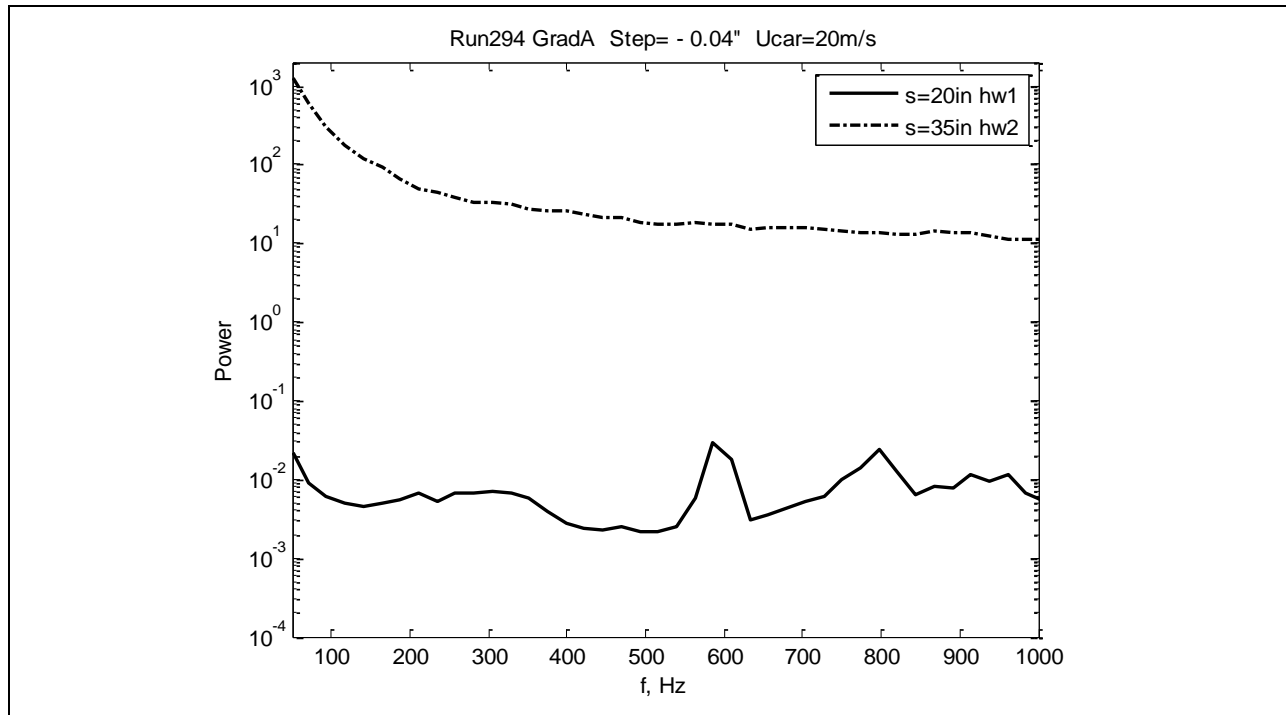


Figure 438: Measured power spectra.

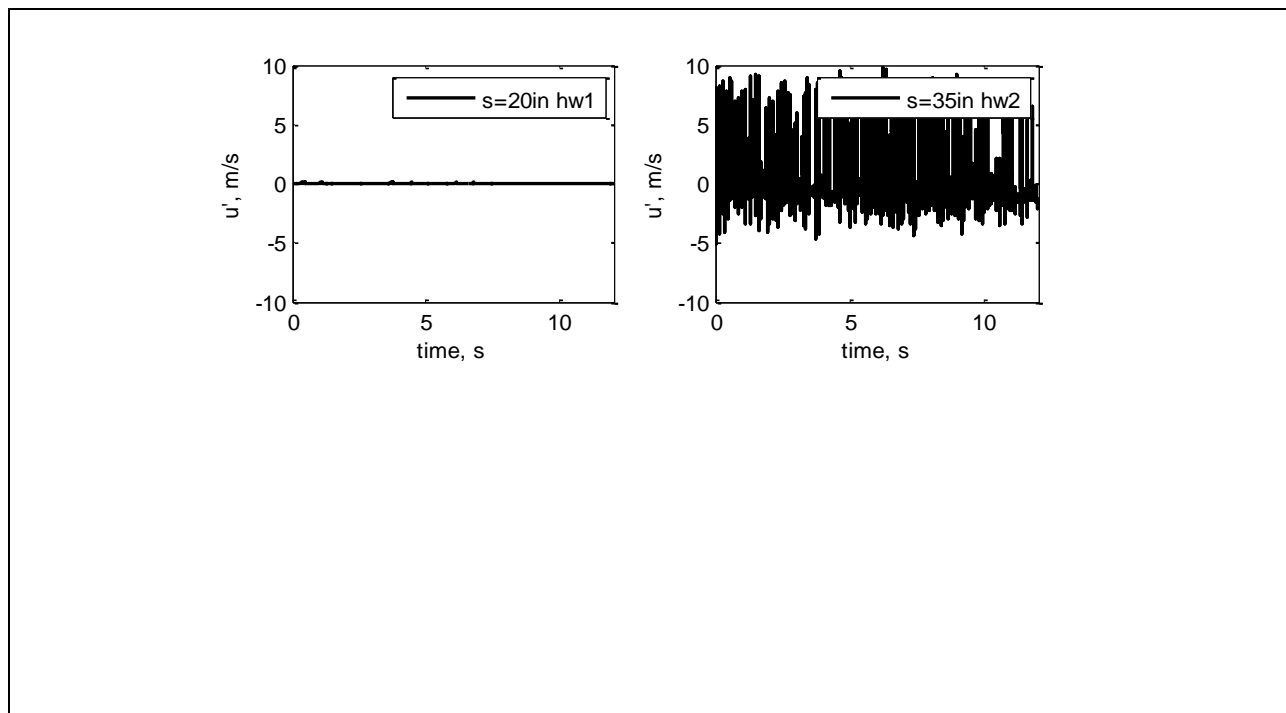


Figure 439: Measured velocity time history.

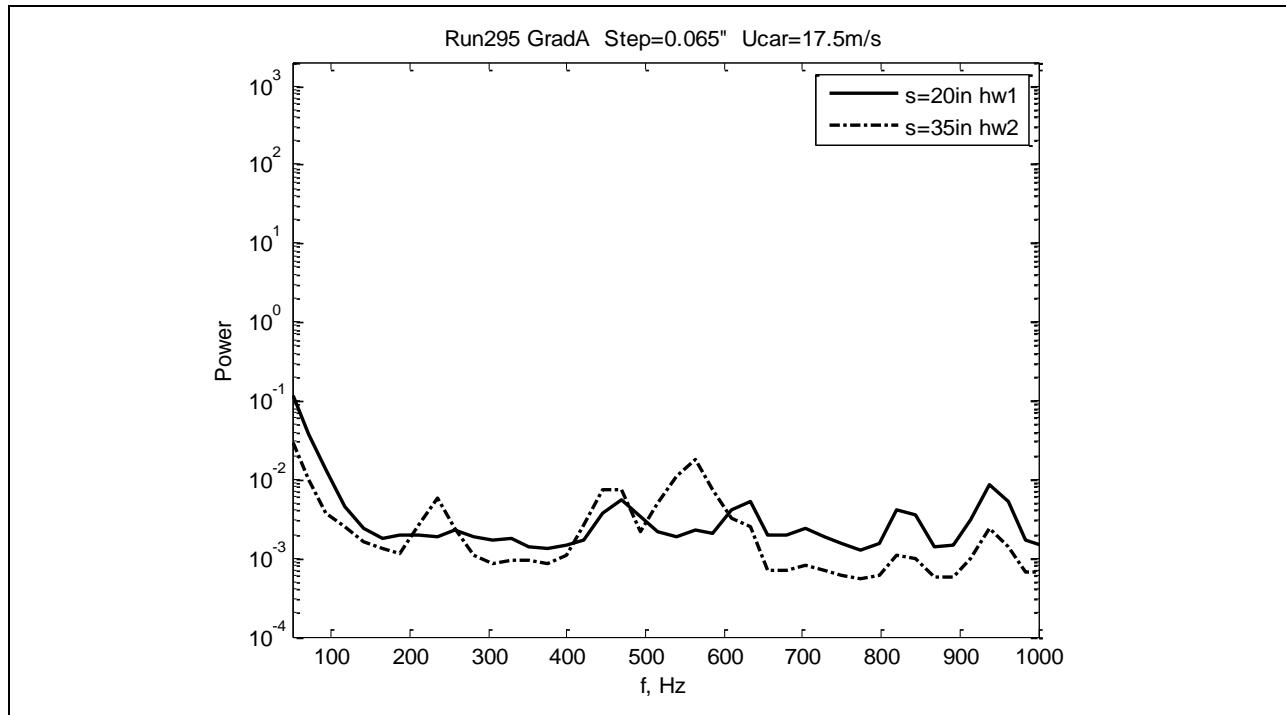


Figure 440: Measured power spectra.

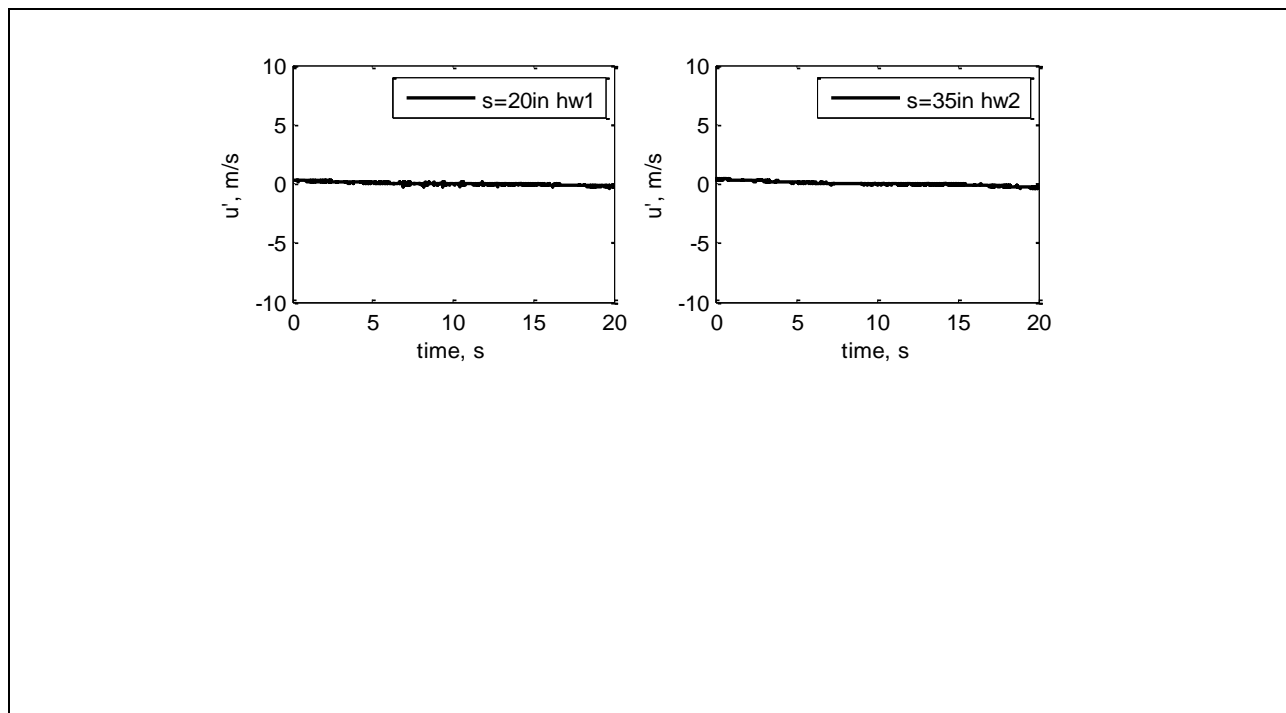


Figure 441: Measured velocity time history.

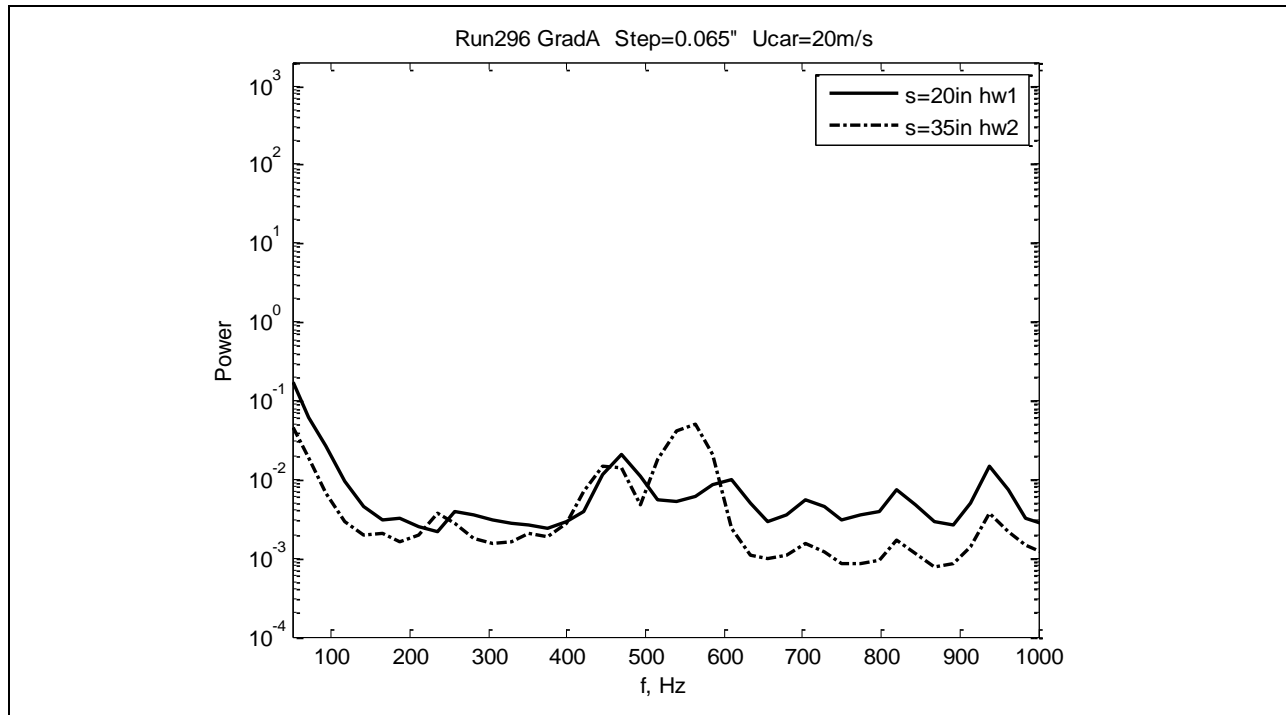


Figure 442: Measured power spectra.

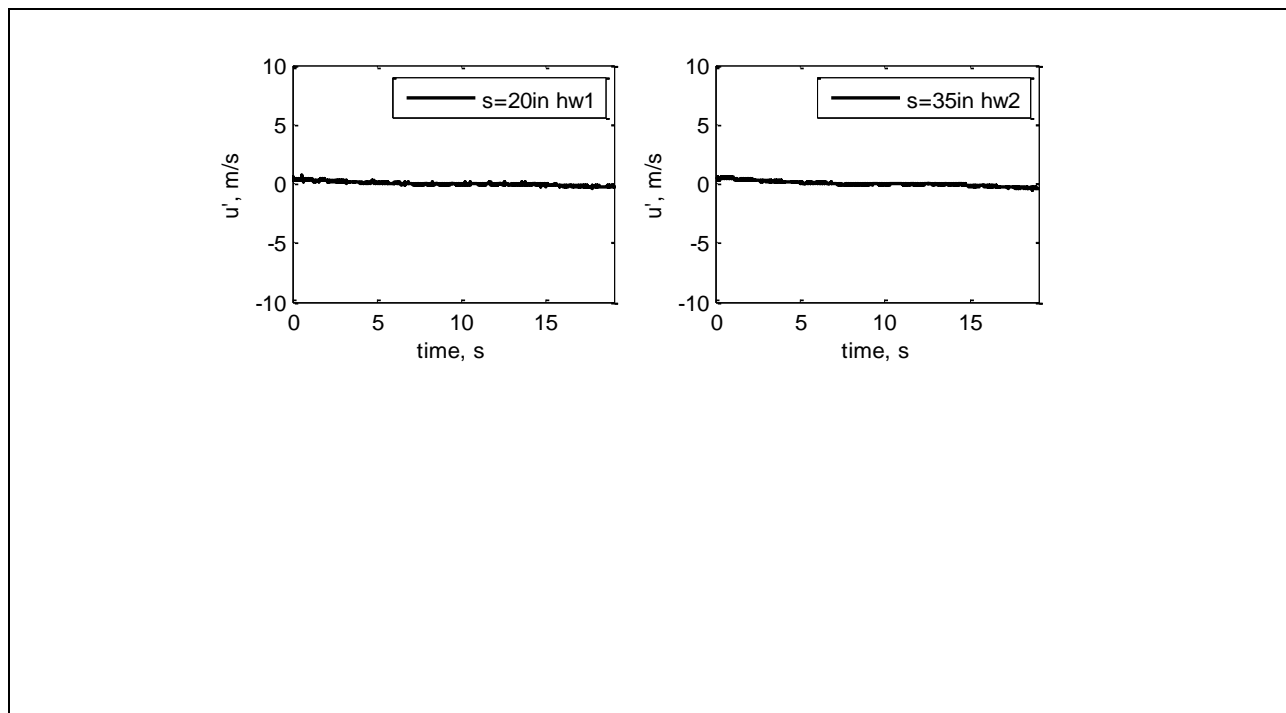


Figure 443: Measured velocity time history.

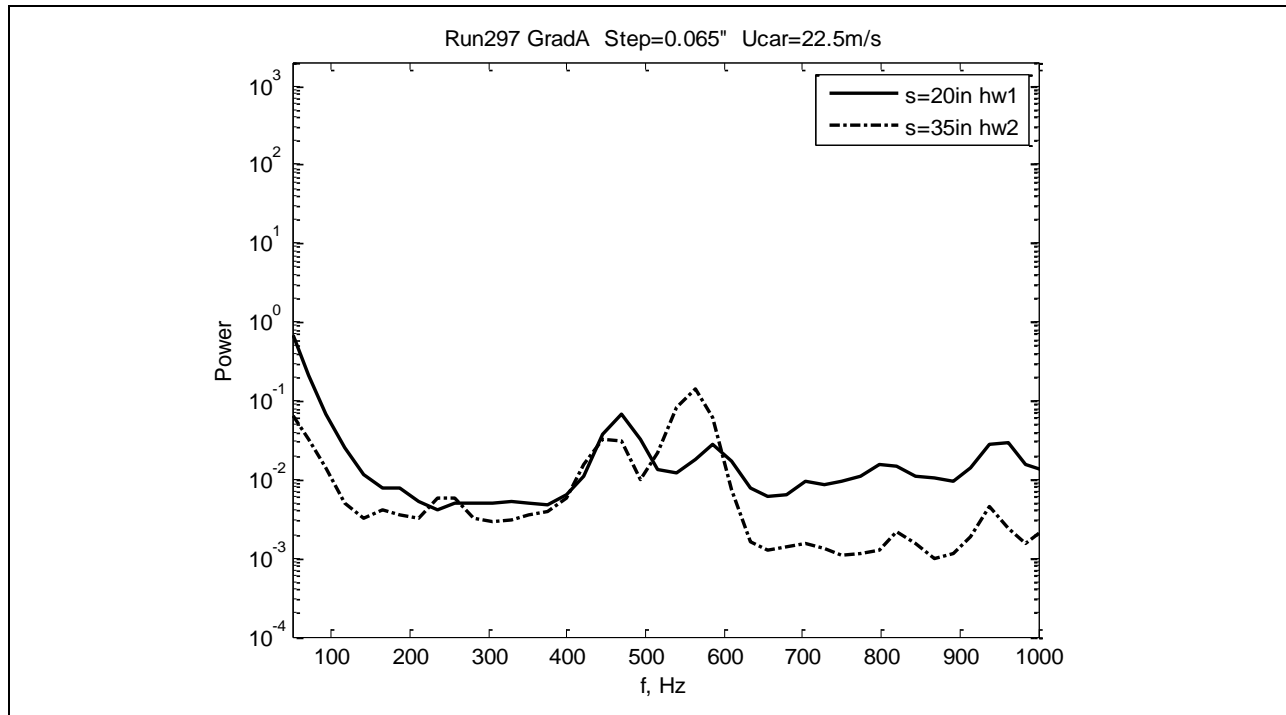


Figure 444: Measured power spectra.

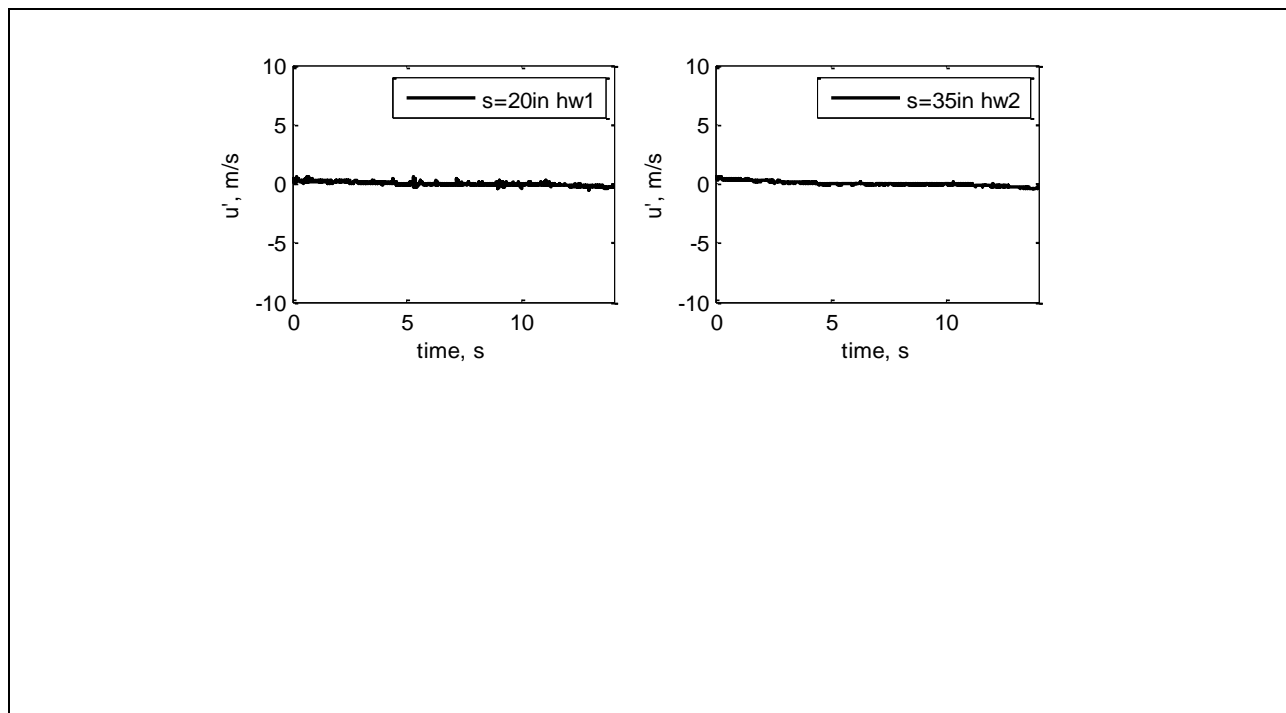


Figure 445: Measured velocity time history.

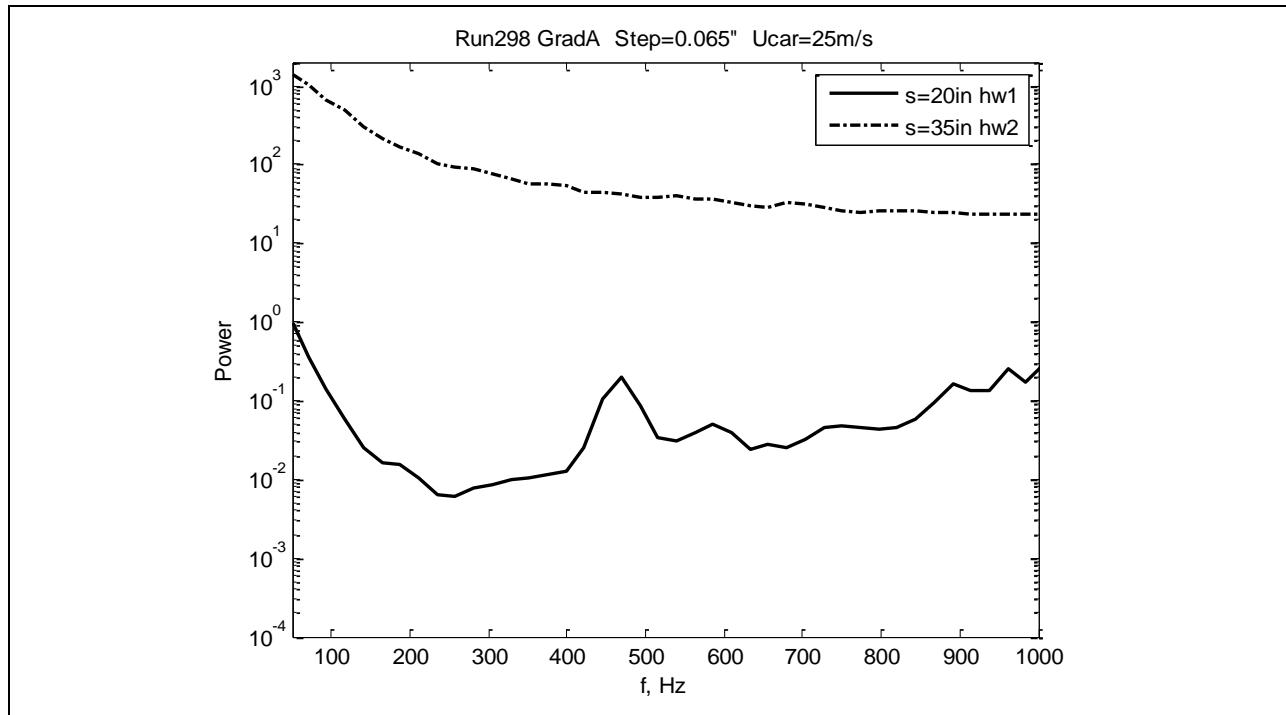


Figure 446: Measured power spectra.

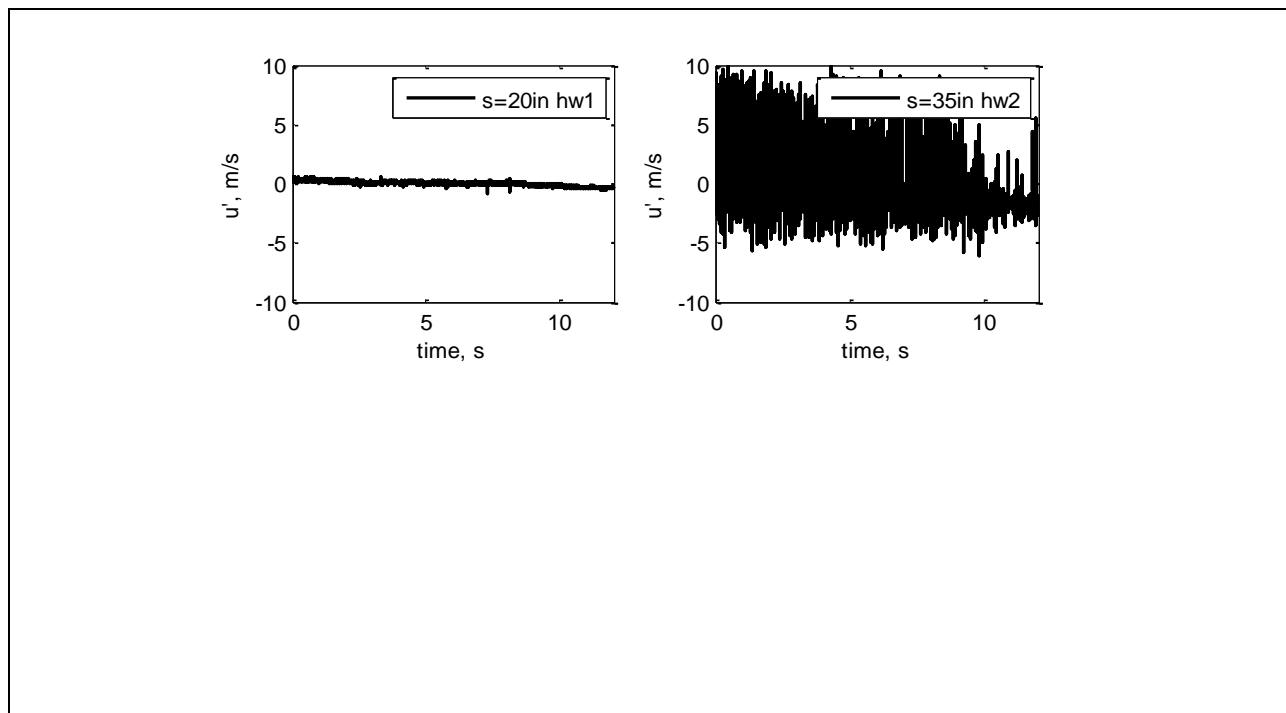


Figure 447: Measured velocity time history.

Table 19 below gives information about all runs that were performed for the Gradient-B model. It contains the basic parameters for the Gradient-B model, including run number, freestream speed, step height, and Reynolds number calculated at the step position. Information on the hot-wire locations, frequencies of peaks (if found in velocity power spectra) attributed to possible T-S waves, and their amplitudes and corresponding N-factors is provided also in Table 19. Table 18 gives a detailed description of each parameter used in Table 19.

Table 18: Parameters used in Table 19

Component	Specifications
U	upstream freestream speed measured with Pitot tube (highlighted in yellow – U was not measured but extrapolated based on the measured speeds; in orange – car speed, U_{car})
k	step height (positive for forward facing and negative for aft facing)
k/δ_k^*	step height normalized with displacement thickness at step location
$Re_{\delta_k^*, k}$	$= \delta_k^* U / \nu$
Re_k	$k U_k / \nu$
A0	level of noise in the velocity power spectra for the first upstream hw1 taken as initial amplitude of T-S wave
s1-s4	streamwise positions of hot-wires hw1-hw4
f1 – f4	frequency of T-S waves
A1-A4	power of T-S waves (A1 coincides with A0 because no T-S waves were detected for the first hw1 in all runs)
N1-N4	N-factors for hw1-hw4 calculated from the spectra as $N_i = 0.5 \cdot \ln(A_i/A_0)$, where i is the hot wire number
Δf	half width of a frequency peak at its half height

Highlighted in orange in Table 19 is the speed set by the car driver, U_{car} . It was usually slightly higher the real speed by 1-2m/s.

Table 19: Gradient-B hot-wire matrix

Basic parameters						hw1			
Run #	U (m/s)	k (in)	k/ δ^*k	Re δ^*,k	A0	s1 (in)	f1 (Hz)	A1	N1
325	14.2	0.00	0.00	809	--	18.5	--	--	--
326	18.9	0.00	0.00	930	--	18.5	--	--	--
327	23.8	0.00	0.00	1060	--	18.5	--	--	--
328	25.8	0.00	0.00	1096	--	18.5	--	--	--
329	28.3	0.00	0.00		--	18.5	--	--	--
344	13.5	0.04			--	18.5	--	--	--
345	17.7	0.04			--	18.5	--	--	--
346	22.8	0.04			--	18.5	--	--	--
347	27.2	0.04			--	18.5	--	--	--
348	13.1	0.055			--	18.5	--	--	--
349	16.6	0.055			--	18.5	--	--	--
350	20.2	0.055			--	18.5	--	--	--
376	14	0.055			--	19.75	--	--	--
377	18.3	0.055			--	19.75	--	--	--
378	23	0.055			--	19.75	--	--	--
379	27.2	0.055			--	19.75	--	--	--
383	23.3	0.045			--	19.75	--	--	--
385		0.045			--	19.75	--	--	--
386	23.4	-0.03			--	19.75	--	--	--
387	18.7	-0.03			--	19.75	--	--	--
388	12.2	-0.03			--	19.75	--	--	--
389	7.1	-0.03			--	19.75	--	--	--
411	12.9	-0.015			--	19.75	--	--	--
412	20	-0.015			--	19.75	--	--	--
413	25	-0.015			--	19.75	--	--	--
414	30	-0.015			--	19.75	--	--	--
416	12.5	-0.02			--	19.75	--	--	--
417	14	-0.02			--	19.75	--	--	--
415	15	-0.02			--	19.75	--	--	--
419	17.5	-0.02			--	19.75	--	--	--
420	20	-0.02			--	19.75	--	--	--
421	10	-0.03			--	19.75	--	--	--
422	15	-0.03			--	19.75	--	--	--
423	20	-0.03			--	19.75	--	--	--
426	25	-0.03			--	19.75	--	--	--
425	30	-0.03			--	19.75	--	--	--

Table 19: Gradient-B hot-wire matrix (*continued*)

hw2				hw3				hw4			
s2 (in)	f2 (Hz)	A2	N2	s3 (in)	f3 (Hz)	A3	N3	s4 (in)	f4 (Hz)	A4	N4
37	--	--	--	54	--	--	--	77	--	--	--
37	--	--	--	54	--	--	--	77	--	--	--
37	--	--	--	54	--	--	--	77	--	--	--
37	--	--	--	54	--	--	--	77	--	--	--
37	--	--	--	54	--	--	--	77	--	--	--
27	--	--	--	33	--	--	--	40	--	--	--
27	--	--	--	33	--	--	--	40	--	--	--
27	--	--	--	33	--	--	--	40	--	--	--
27	--	--	--	33	--	--	--	40	--	--	--
27	--	--	--	33	--	--	--	40	--	--	--
27	--	--	--	33	--	--	--	40	--	--	--
27	--	--	--	33	--	--	--	40	--	--	--
22.75	--	--	--	26	--	--	--	30	--	--	--
22.75	--	--	--	26	--	--	--	30	--	--	--
22.75	--	--	--	26	--	--	--	30	--	--	--
22.75	--	--	--	26	--	--	--	30	--	--	--
22.75	--	--	--	25.75	--	--	--	29.5	--	--	--
22.75	--	--	--	25.75	--	--	--	29.5	--	--	--
22.75	--	--	--	25.75	--	--	--	29.5	--	--	--
22.75	--	--	--	25.75	--	--	--	29.5	--	--	--
22.75	--	--	--	25.75	--	--	--	29.5	--	--	--
22.75	--	--	--	25.75	--	--	--	29.5	--	--	--
22.75	--	--	--	25.75	--	--	--	29.5	--	--	--
22.75	--	--	--	25.75	--	--	--	29.5	--	--	--
22.75	--	--	--	25.75	--	--	--	29.5	--	--	--
22.75	--	--	--	25.75	--	--	--	29.5	--	--	--
22.75	--	--	--	25.75	--	--	--	29.5	--	--	--
22.75	--	--	--	25.75	--	--	--	29.5	--	--	--
22.75	--	--	--	25.75	--	--	--	29.5	--	--	--
22.75	--	--	--	25.75	--	--	--	29.5	--	--	--
22.75	--	--	--	25.75	--	--	--	29.5	--	--	--

Table 20 summarizes transition locations found from velocity and skin friction measurements. The data from velocity measurements are based on quantitative analysis of the velocity time series and spectra. The criteria for the transition were qualitative: the broadening of velocity power spectra and 100% intermittency in the velocity time series.

Table 20: Gradient-B hot-wire transition locations

Basic parameters			Transition location	
Run #	U (m/s)	k (in)	s, from HW (in)	s, from Cf (in)
325	14.2	0.00	--	--
326	18.9	0.00	--	--
327	23.8	0.00	--	--
328	25.8	0.00	--	--
329	28.3	0.00	--	--
344	13.5	0.04	--	--
345	17.7	0.04	--	--
346	22.8	0.04	--	--
347	27.2	0.04	--	--
348	13.1	0.055	--	--
349	16.6	0.055	--	--
350	20.2	0.055	--	--
376	14	0.055	--	--
377	18.3	0.055	--	--
378	23	0.055	<19.7 then laminar	19
379	27.2	0.055	< 19.7	no run
383	23.3	0.045	--	--
385		0.045	--	--
386	23.4	-0.03	< 19.7	no run
387	18.7	-0.03	< 19.7	no run
388	12.2	-0.03	< 19.7	no run
389	7.1	-0.03	--	--
411	12.9	-0.015	--	--
412	20	-0.015	--	--
413	25	-0.015	--	--
414	30	-0.015	--	--
416	12.5	-0.02	--	--
417	14	-0.02	--	--
415	15	-0.02	25.7 - 29.5	no run
419	17.5	-0.02	25.7 - 29.5	no run
420	20	-0.02	22.7 - 25.7	no run
421	10	-0.03	--	--
422	15	-0.03	--	--
423	20	-0.03	--	--
426	25	-0.03	25.7 - 29.5	no run
425	30	-0.03	19.7 - 22.7	no run

The plots of velocity time series and corresponding power spectra are shown in the order corresponding to run numbers as given in Table 20.

Runs 325-329 (Figures 448-457) correspond to zero step (clean plate) and large separation between the hot-wires. The velocity time series show laminar flow conditions with slight increase of velocity fluctuations with increase of freestream speed. The peak which appears in spectra at about 300Hz for hw3 is not present for the next hw4. No transition to turbulence is observed and there are no reliable T-S waves.

Runs 344-347 (Figures 458-465) are for a 0.04-inch forward-facing step. The separation between hot-wires is smaller than in the previous runs. All hot-wires show laminar flow for all freestream speeds. Some peaks are observed in all spectra in the range of 300-400Hz.

Runs 348-350 (Figures 466-471) are for a 0.055-inch forward-facing step. Run 348 and Run 349 show laminar flow for all hot-wires. The peaks in the spectra are observed in 300-400Hz range. In Run 350 the second hw2 shows turbulence, but with a return to a laminar signal for hw3 and hw4.

Runs 376-379 (Figures 472-479) are for a 0.055-inch forward-facing step but for smaller separation between hot-wires than in the previous case and with the first hw1 located downstream of the step. Run 376 and Run 377 show laminar flow, the peaks in spectra are around 200-300Hz, which may be T-S waves. Run 378 shows turbulence for hw1 and hw2 and then laminar flow is restored for hw3 and hw4. Run 379 shows everything turbulent.

Runs 383,385 (Figures 480-483) are for a 0.045-inch forward-facing step show laminar flow with the peaks in the spectra in the range 200-400Hz. In Run 385, hw2 shows turbulence, but it is restored to laminar flow for the next hw3 and hw4.

Runs 386-389 (Figures 484-491) are for a -0.03-inch aft-facing step. All hot-wires for all runs show turbulence except for Run 389 (for the lowest freestream speed), which appears to be close to turbulence.

Runs 411-414 (Figures 492-499) are for a -0.015-inch aft-facing step. All hot-wires for all runs show laminar flow. The peaks in the spectra are observed at 250-350Hz range.

Runs 415-420 (Figures 500-509) are for a -0.02-inch aft-facing step. Run 416 and Run 417 show laminar flow with the peaks in the spectra in 250-350Hz range. Run 415, Run 419 and Run 420 show laminar flow for hw1 and hw2 and close to turbulent or turbulent for hw3 and hw4. The transition point stays between hw2 and hw3 independently of freestream speed.

Supplementary Runs 421-426 (Figures 510-519) were performed under the same conditions as Runs 386-389 except a seal (thin tape) was applied to cover the gap created just after the step. Comparison of these two sets made in the following subsection shows high sensitivity to the presence of the gap.

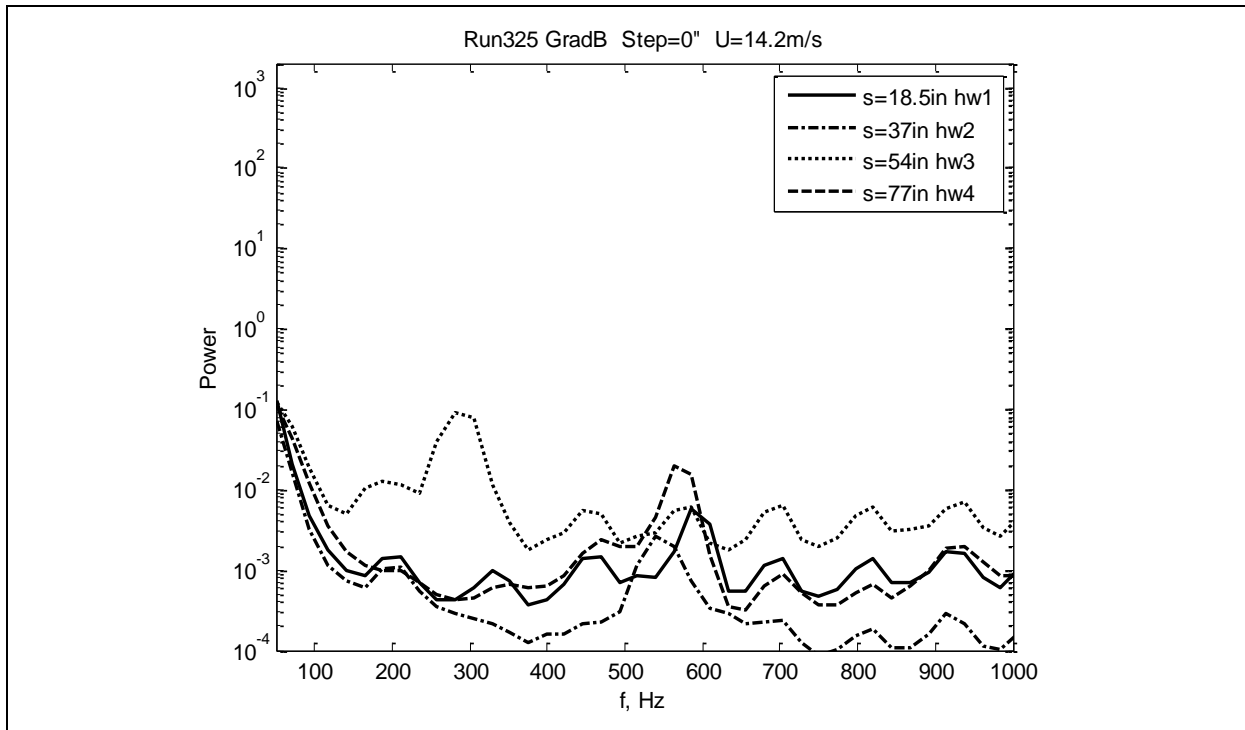


Figure 448: Measured power spectra.

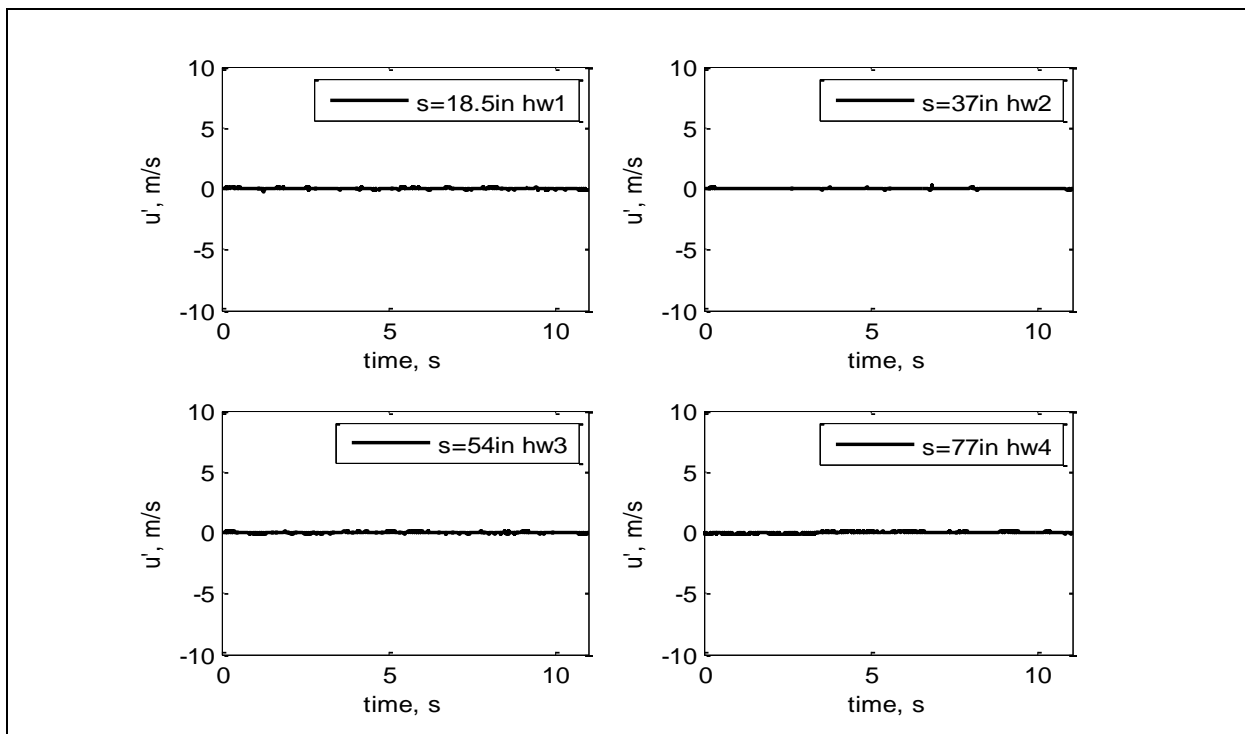


Figure 449: Measured velocity time history.

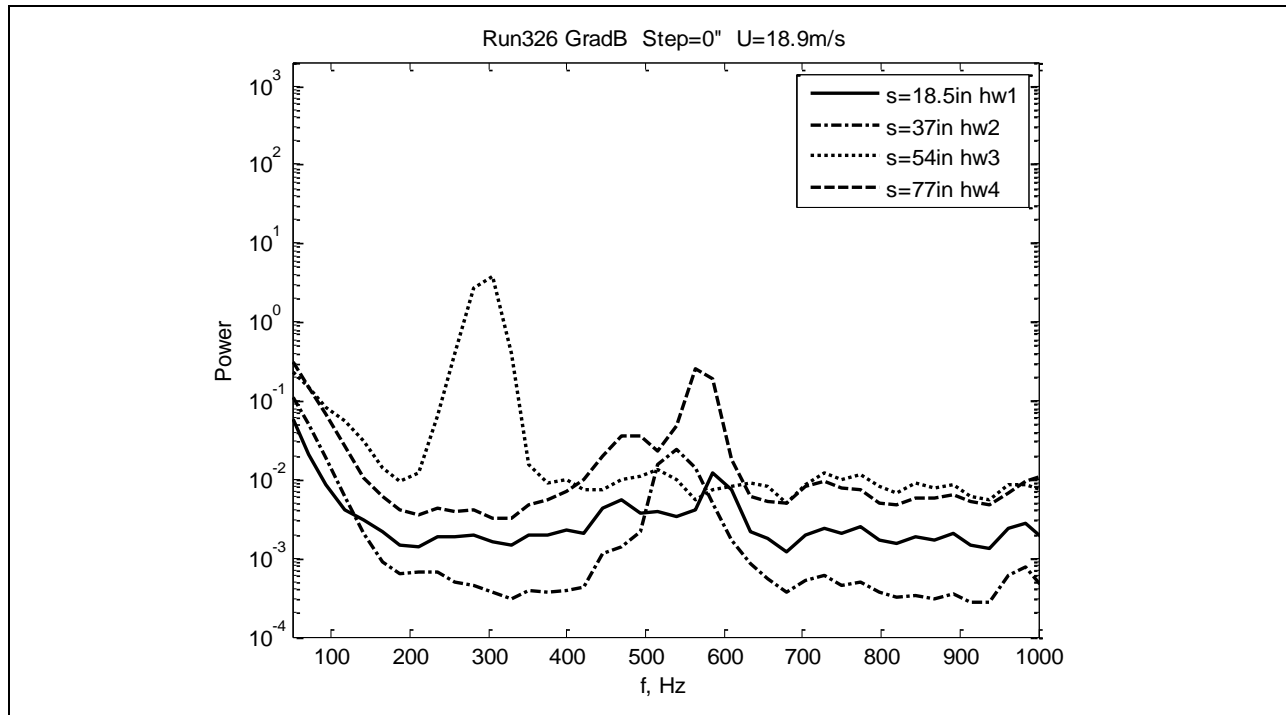


Figure 450: Measured power spectra.

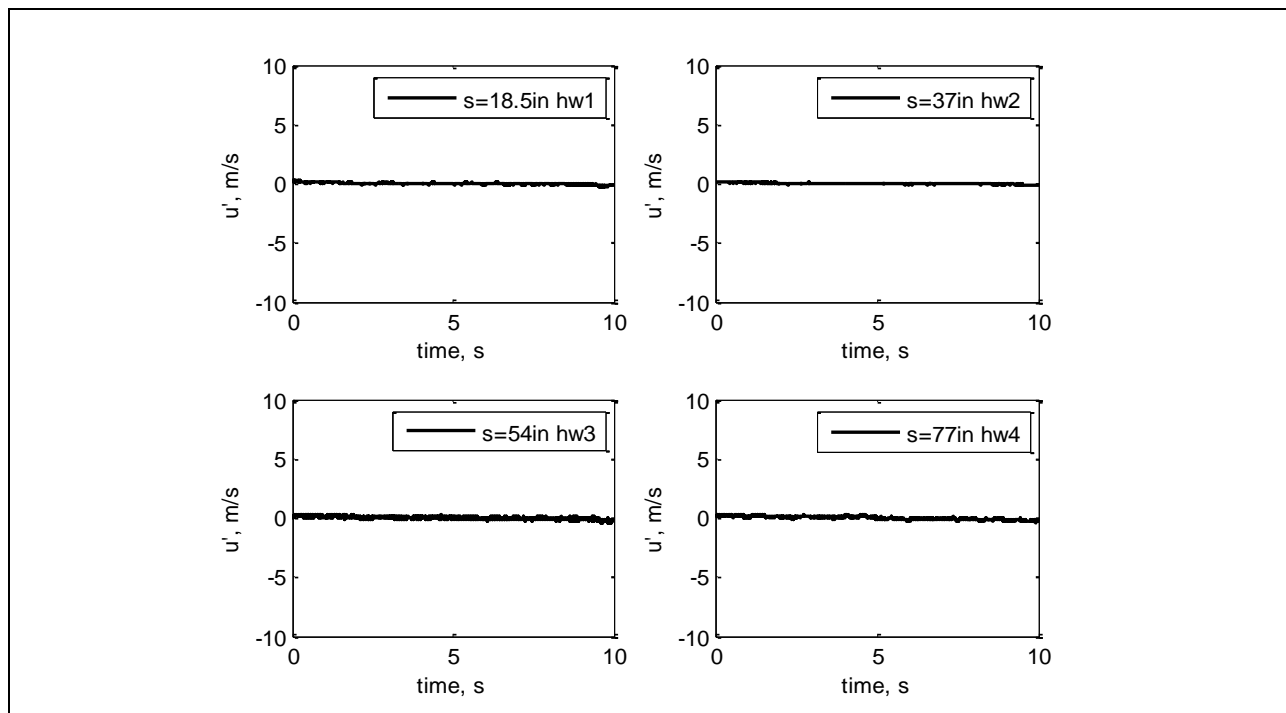


Figure 451: Measured velocity time history.

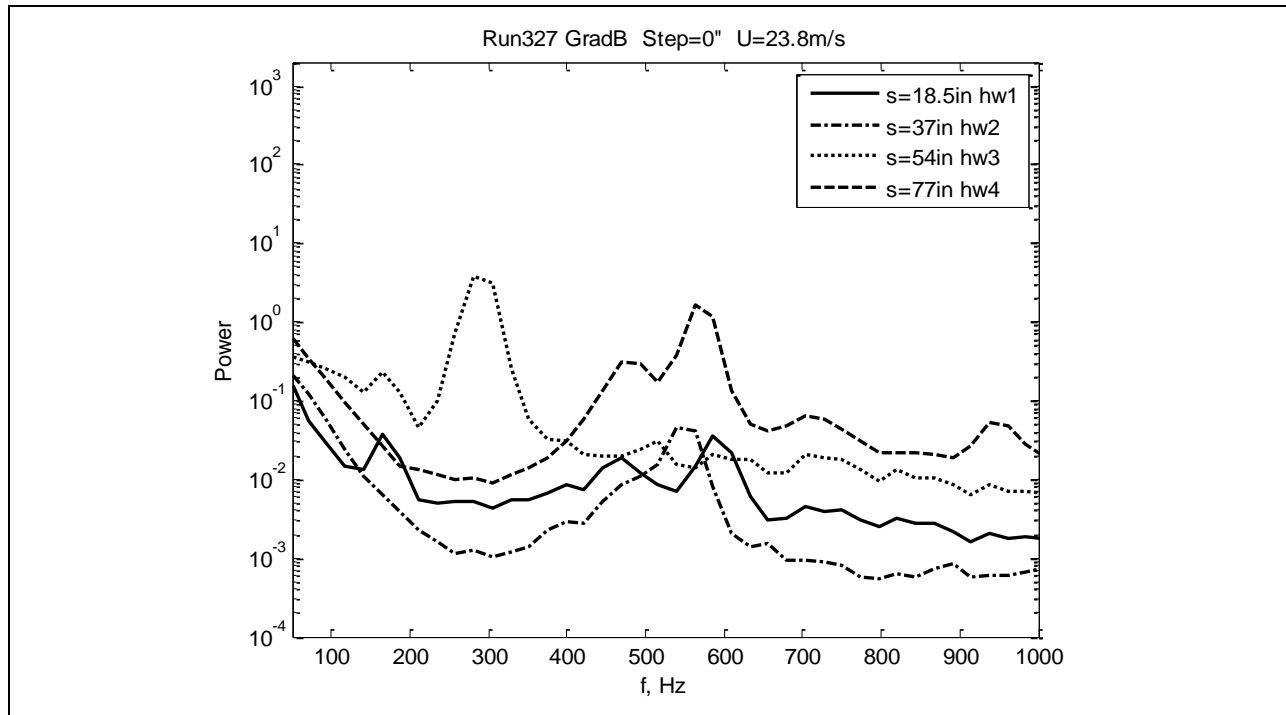


Figure 452: Measured power spectra.

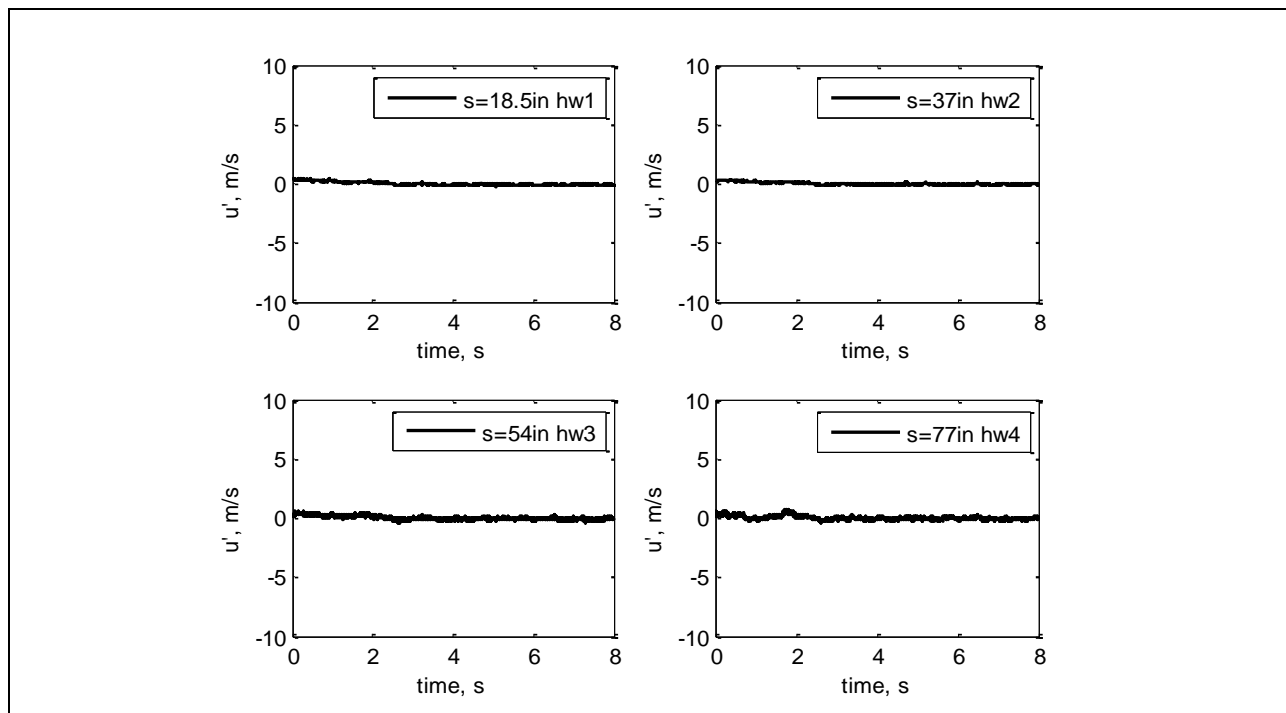


Figure 453: Measured velocity time history.

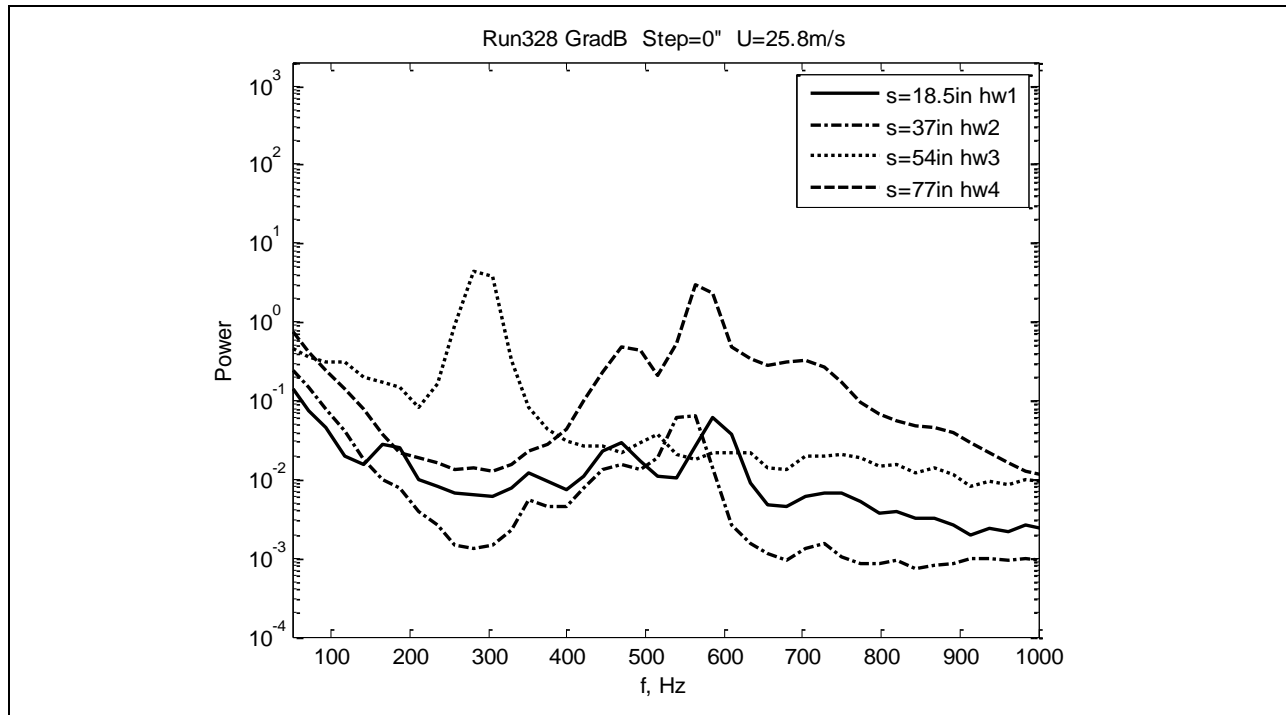


Figure 454: Measured power spectra.

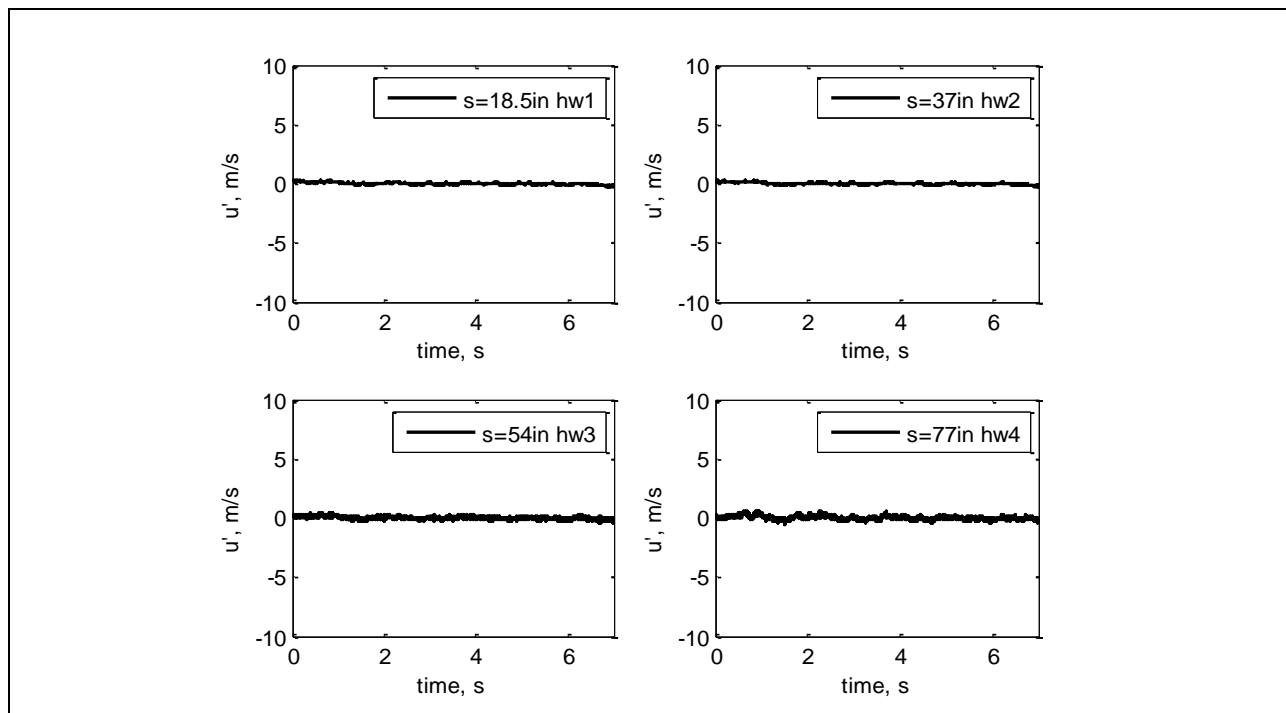


Figure 455: Measured velocity time history.

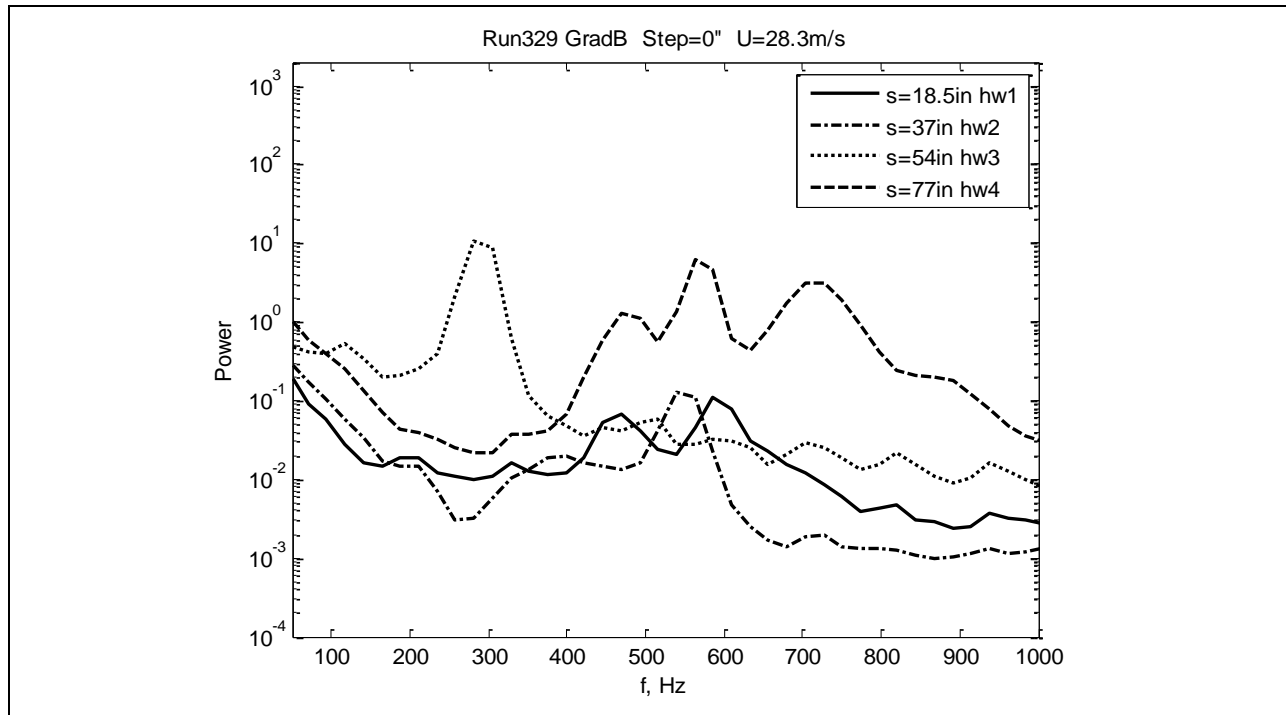


Figure 456: Measured power spectra.

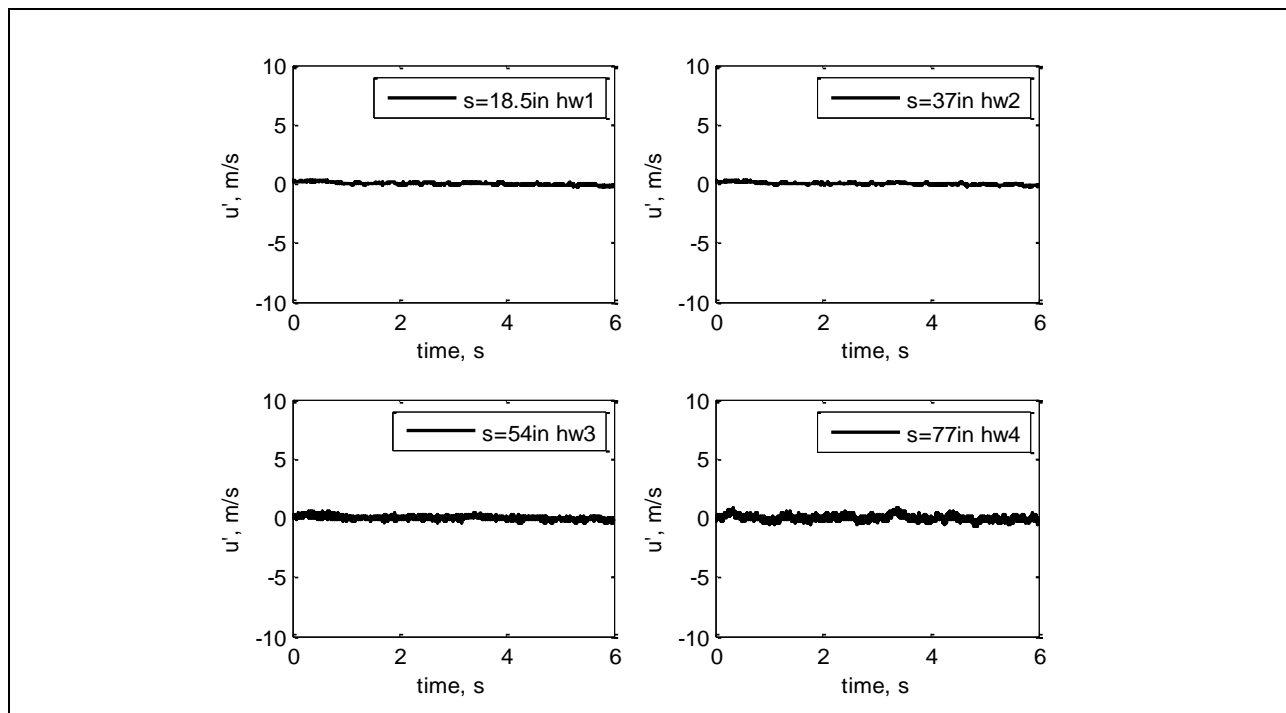


Figure 457: Measured velocity time history.

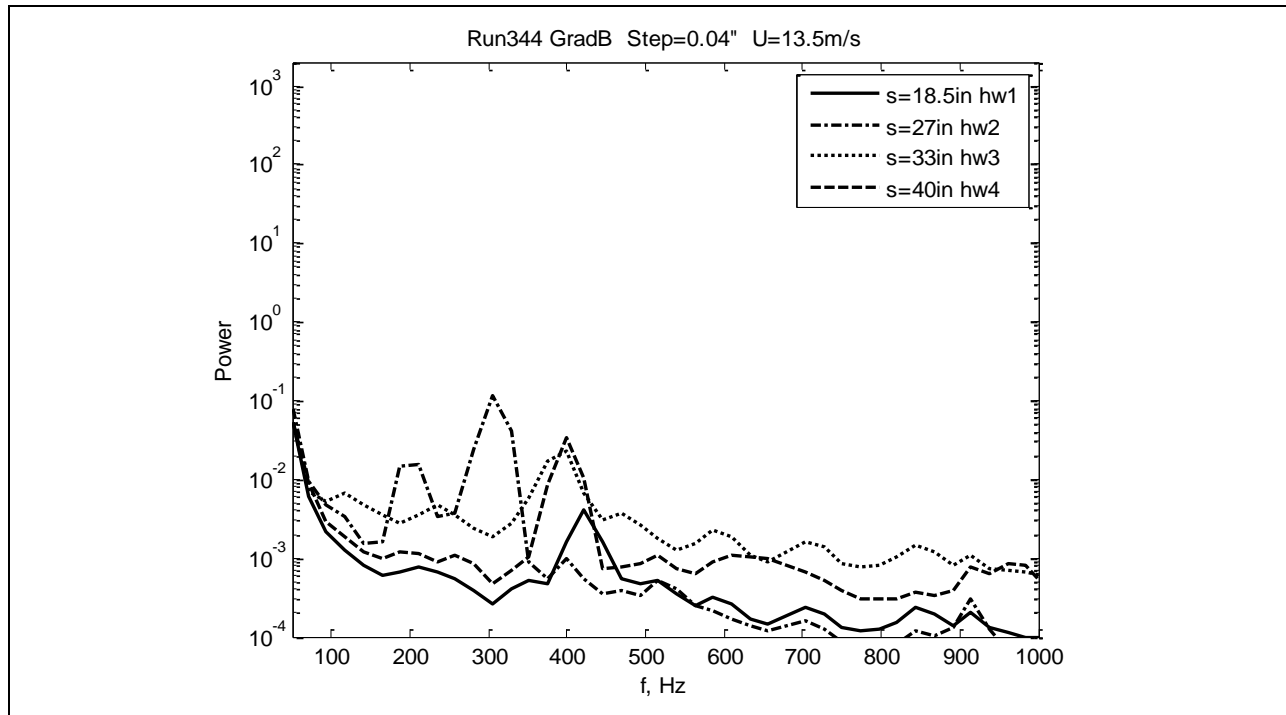


Figure 458: Measured power spectra.

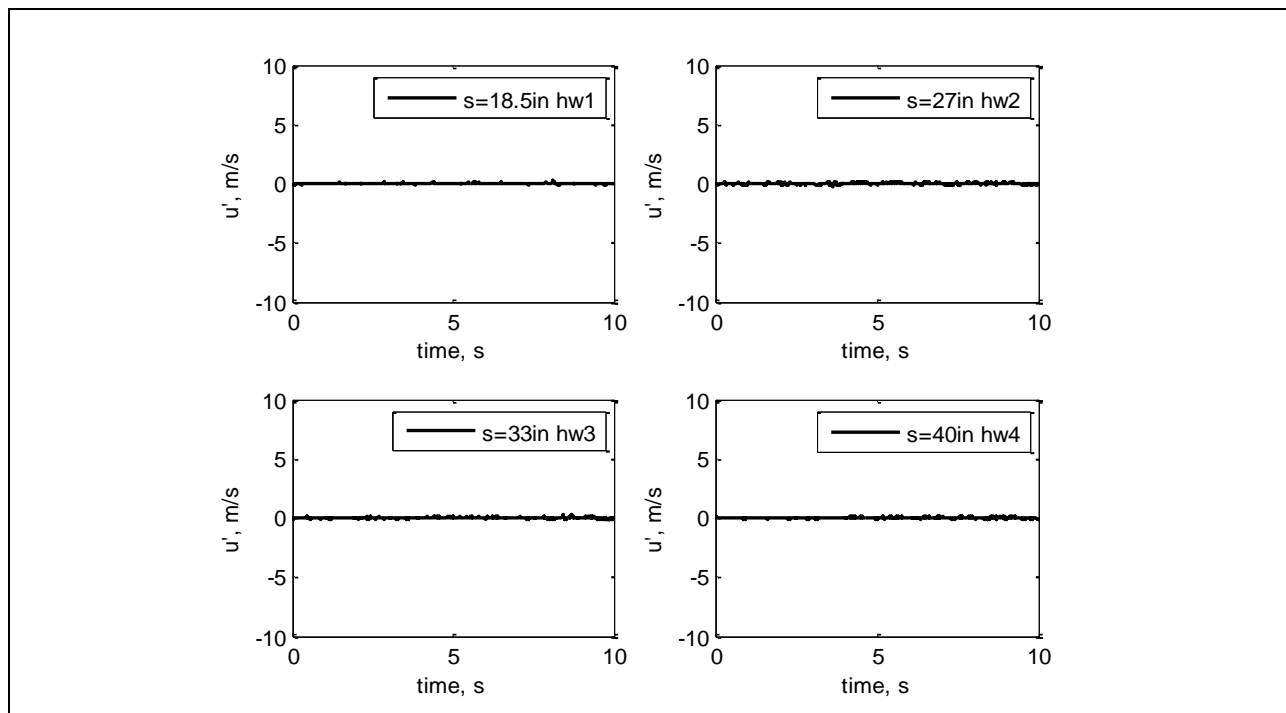


Figure 459: Measured velocity time history.

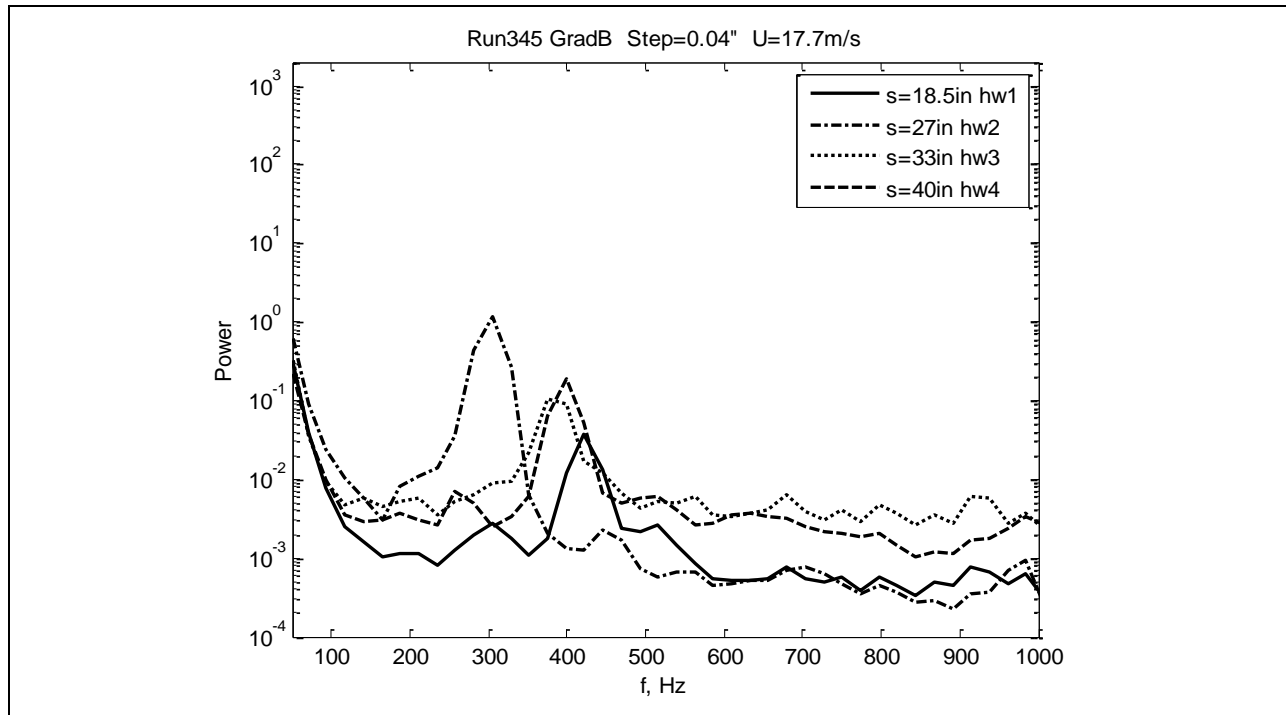


Figure 460: Measured power spectra.

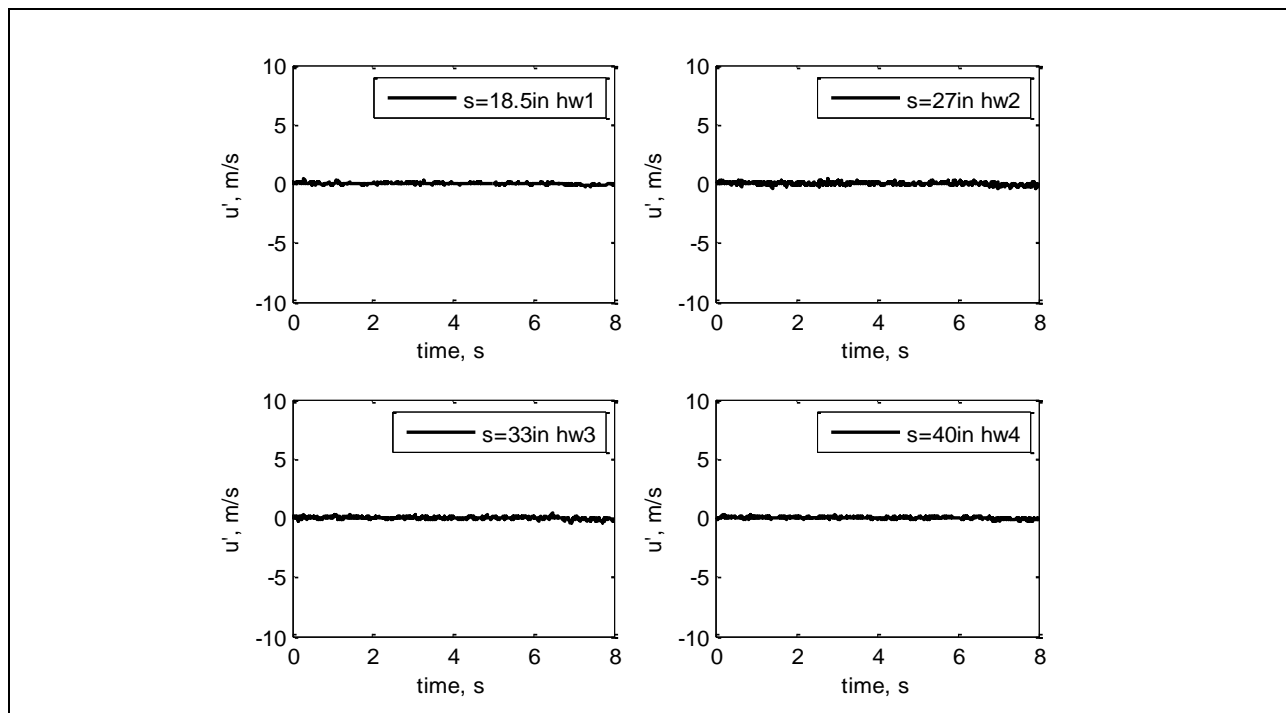


Figure 461: Measured velocity time history.

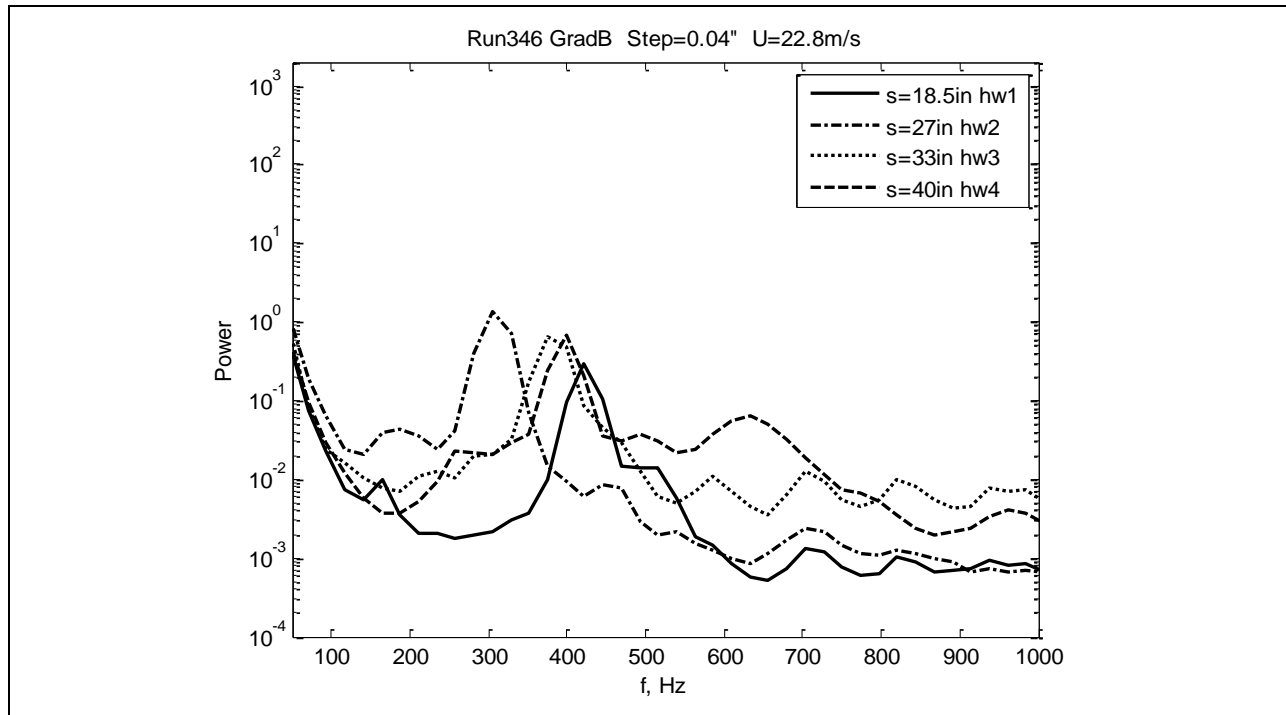


Figure 462: Measured power spectra.

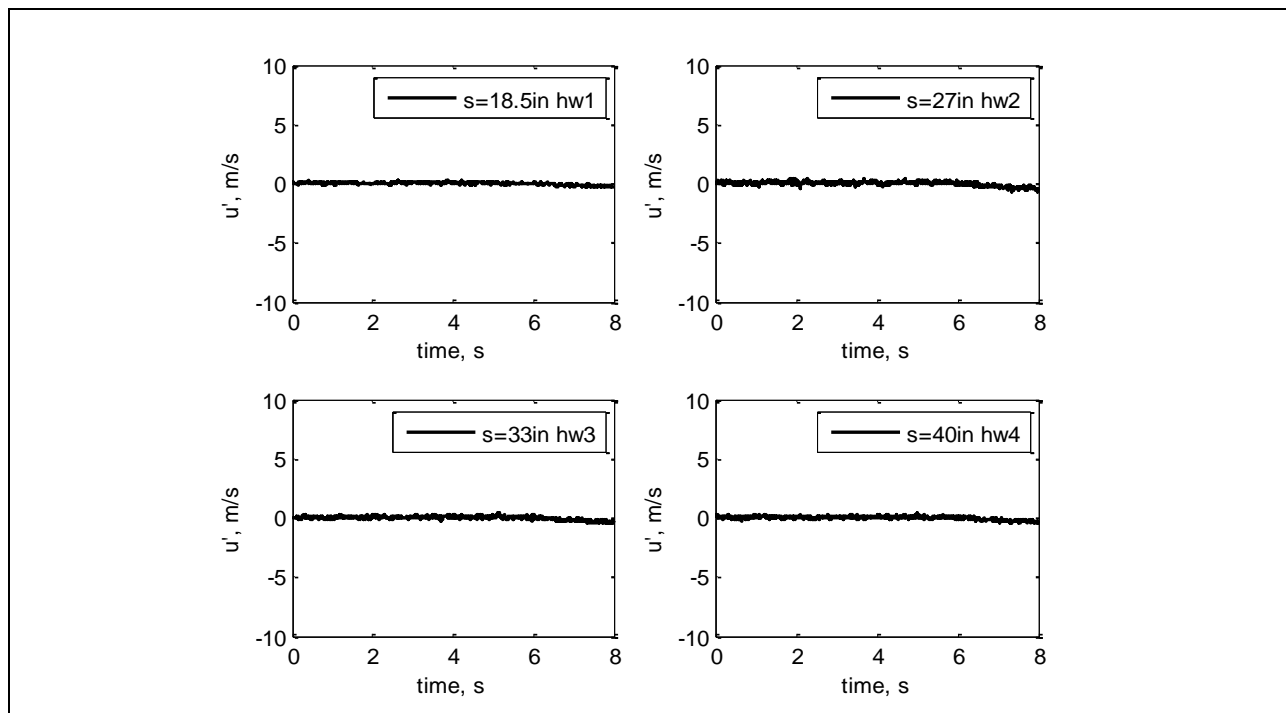


Figure 463: Measured velocity time history.

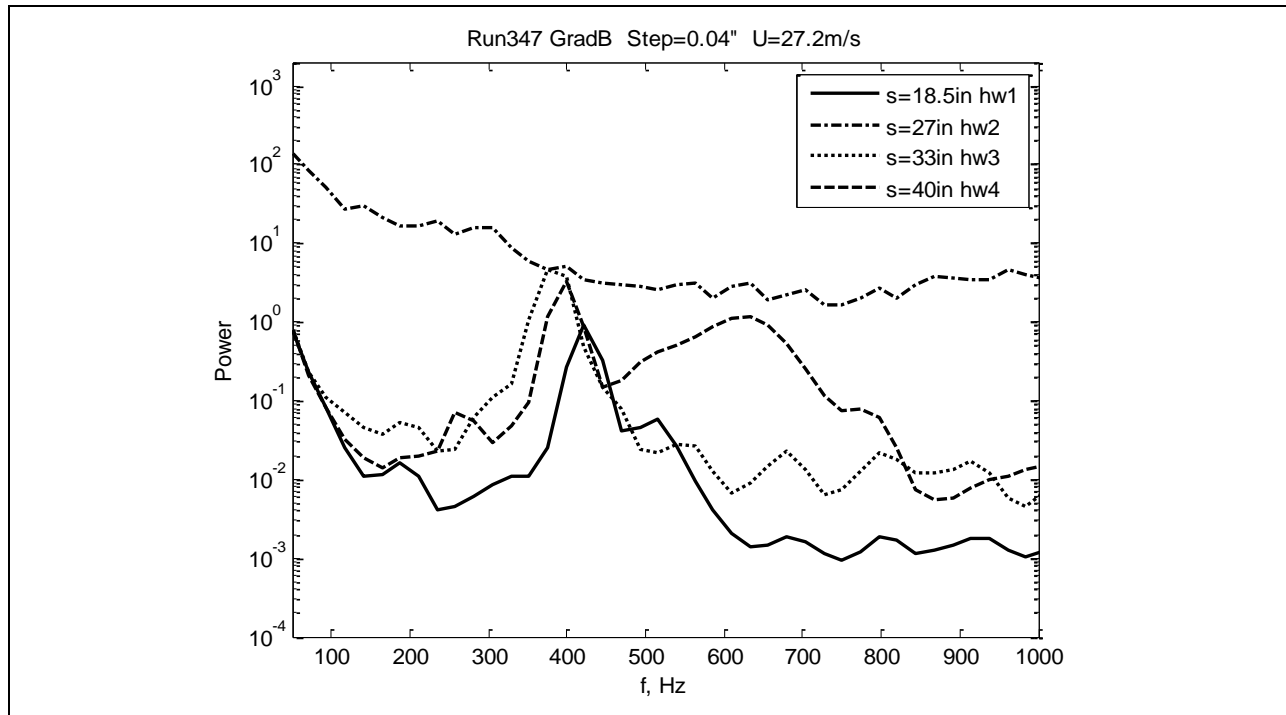


Figure 464: Measured power spectra.

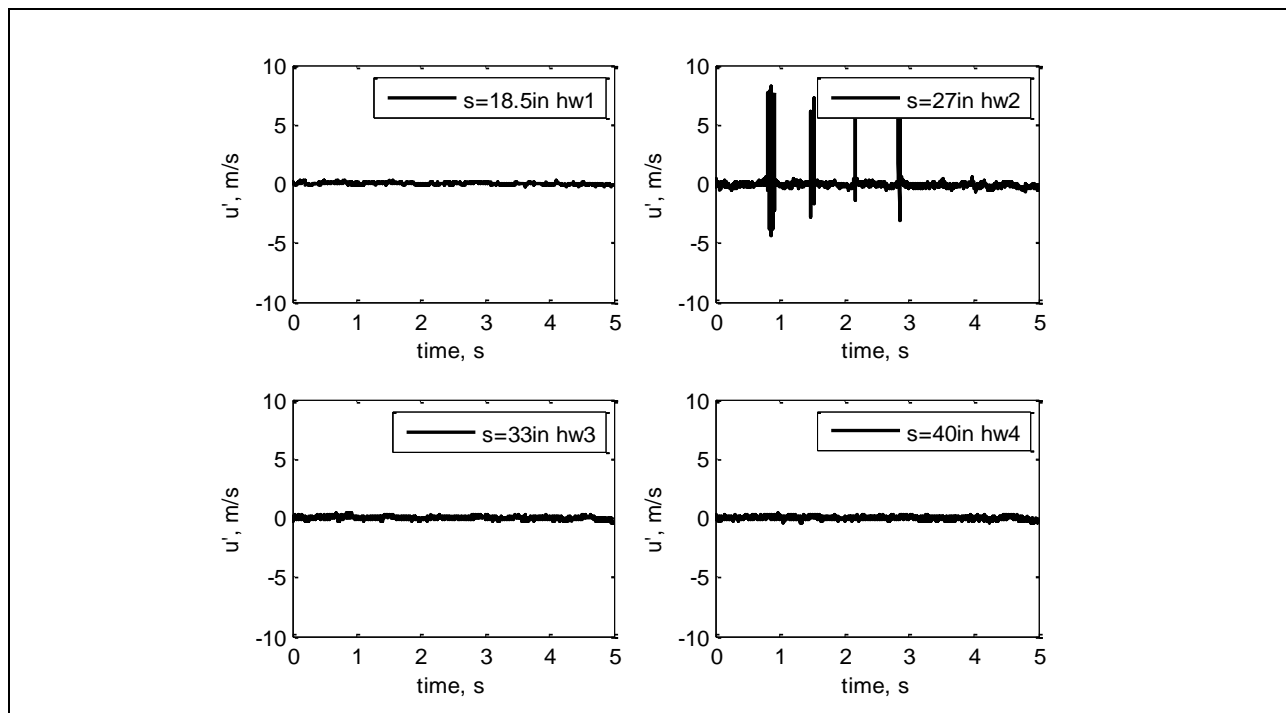


Figure 465: Measured velocity time history.

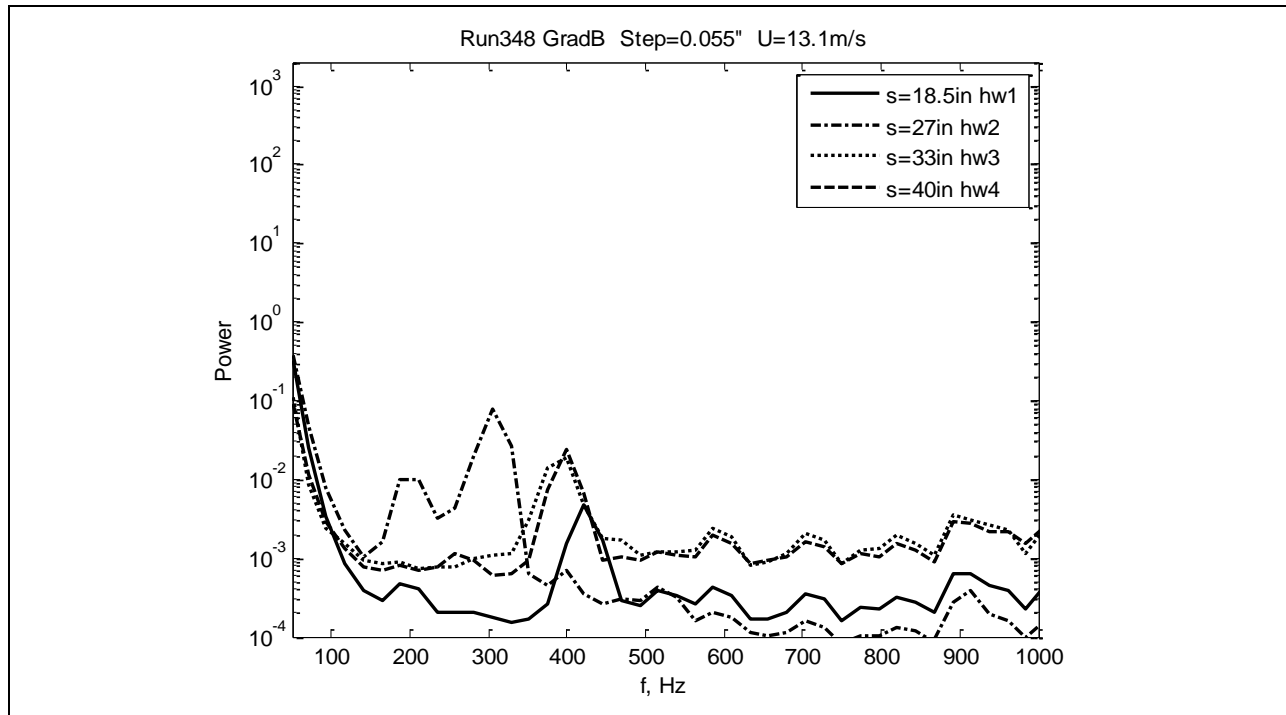


Figure 466: Measured power spectra.

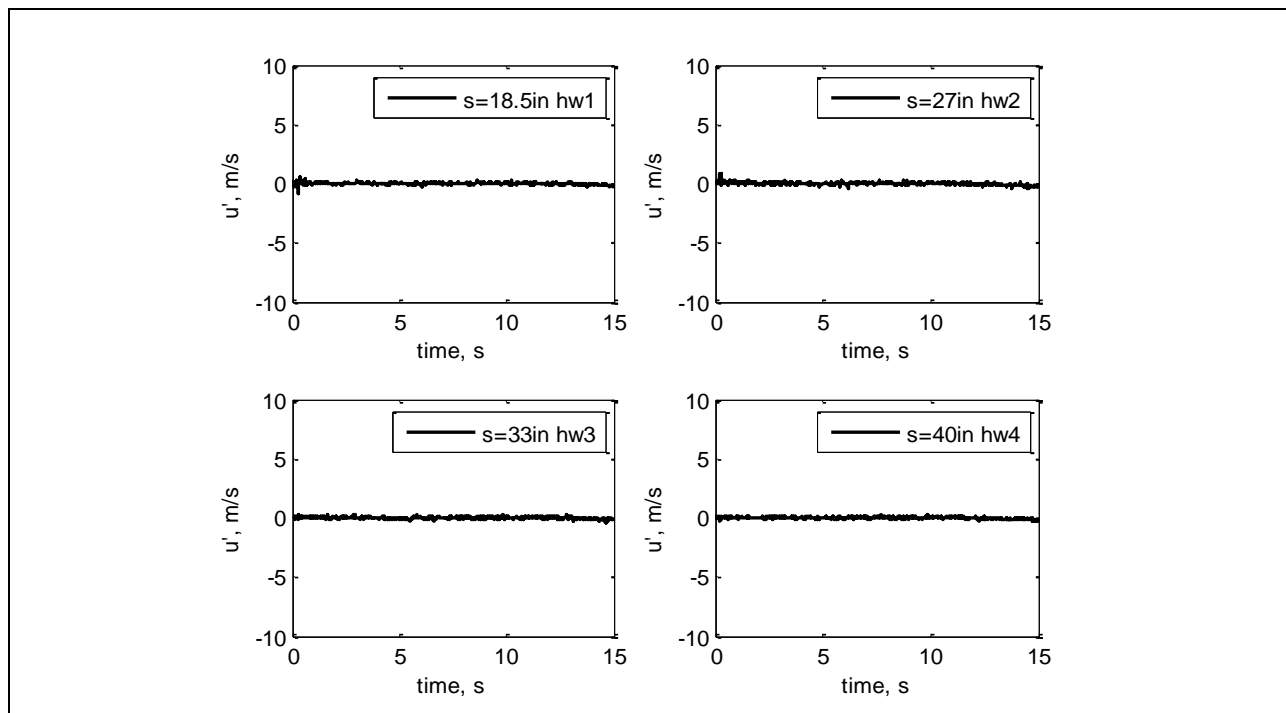


Figure 467: Measured velocity time history.

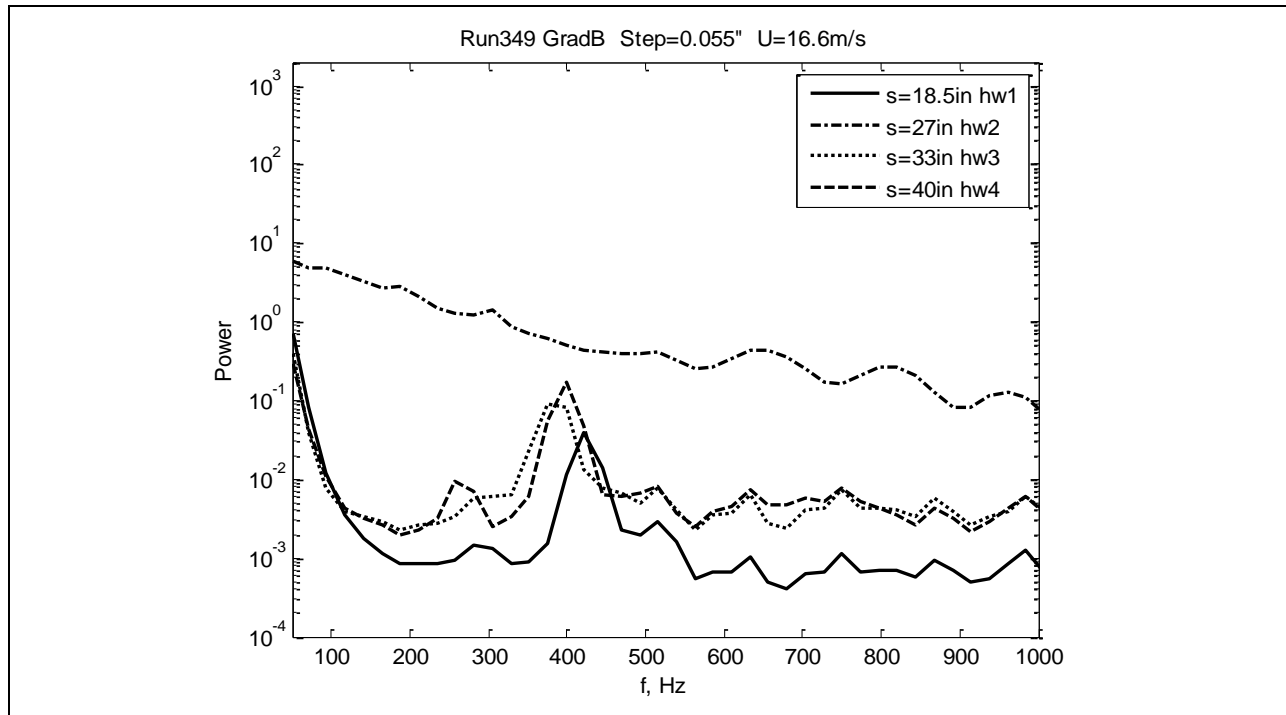


Figure 468: Measured power spectra.

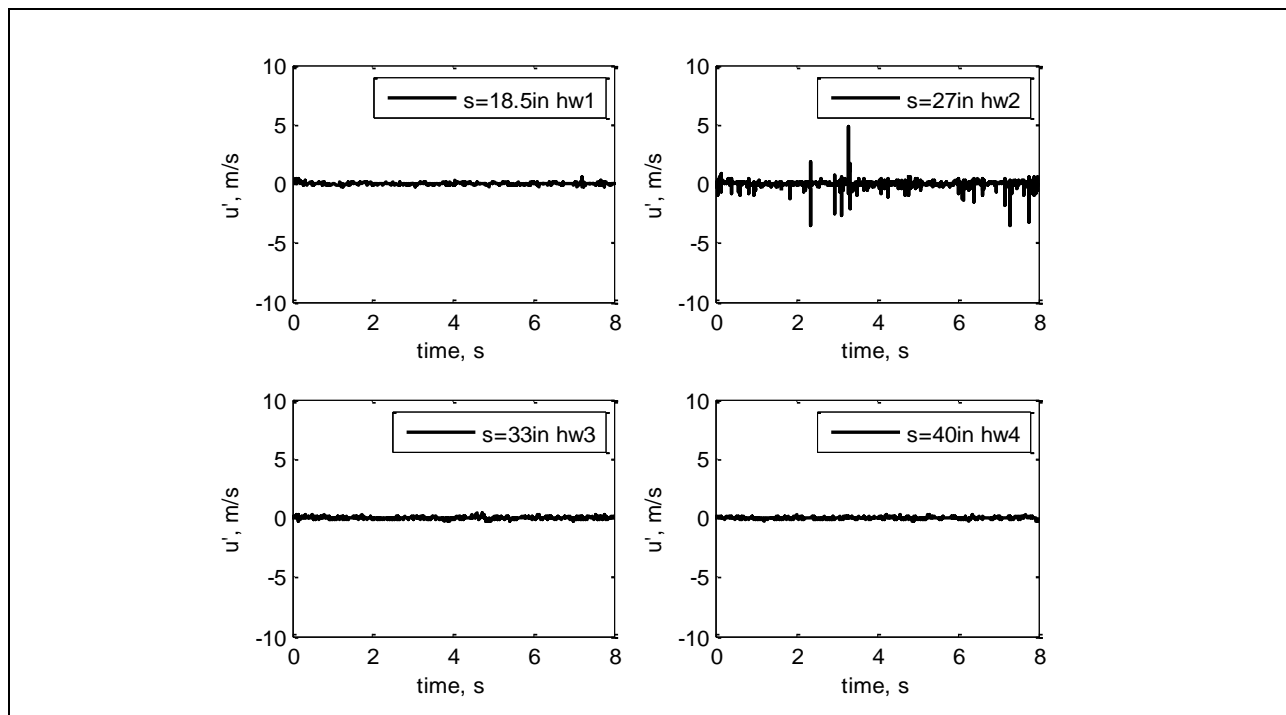


Figure 469: Measured velocity time history.

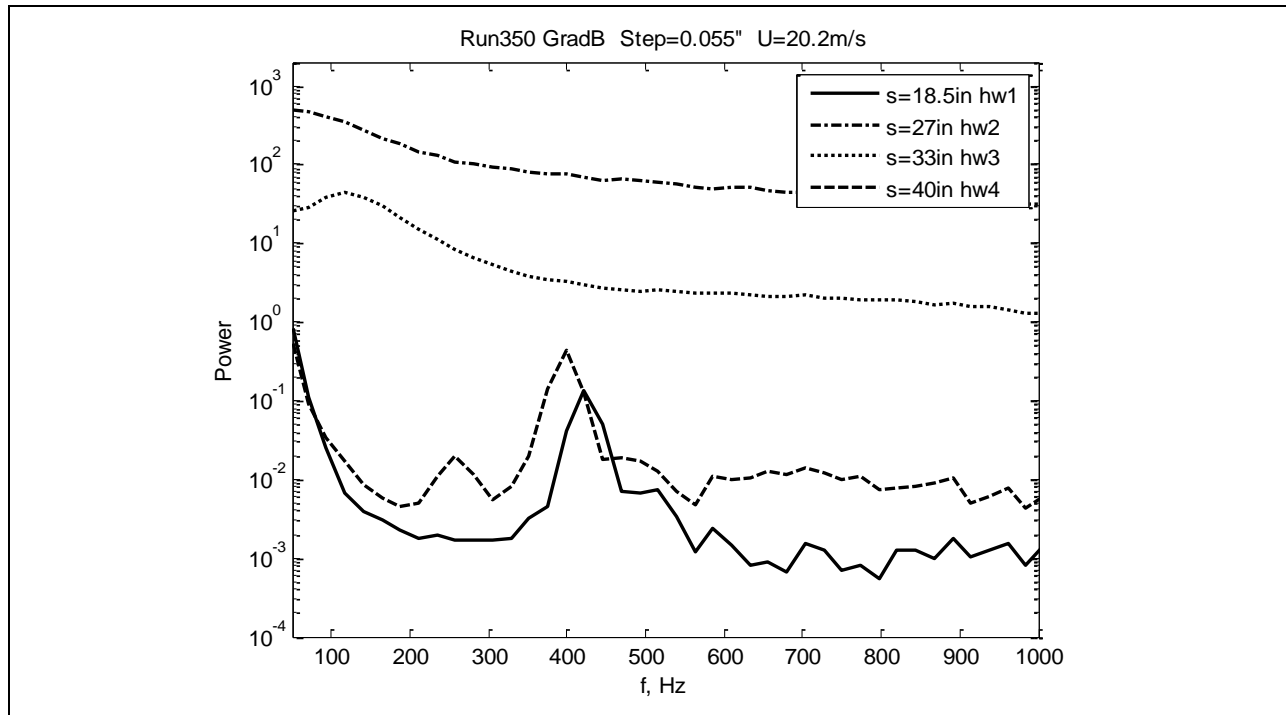


Figure 470: Measured power spectra.

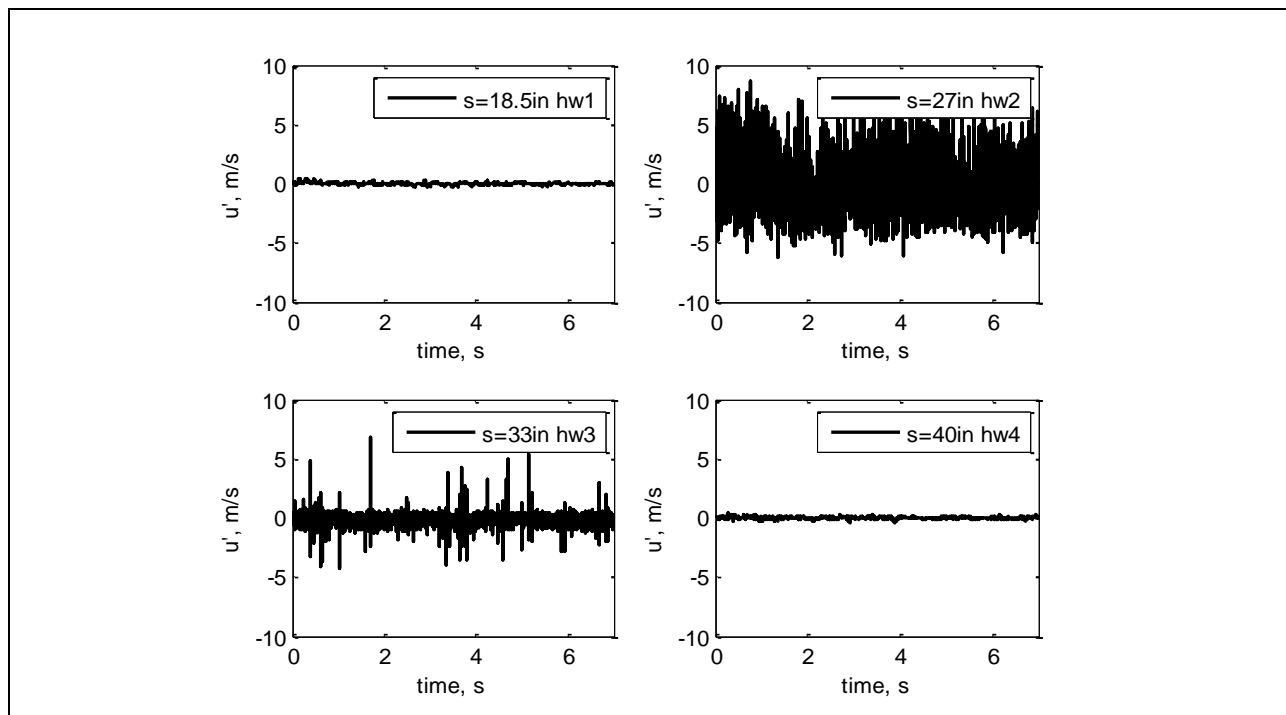


Figure 471: Measured velocity time history.

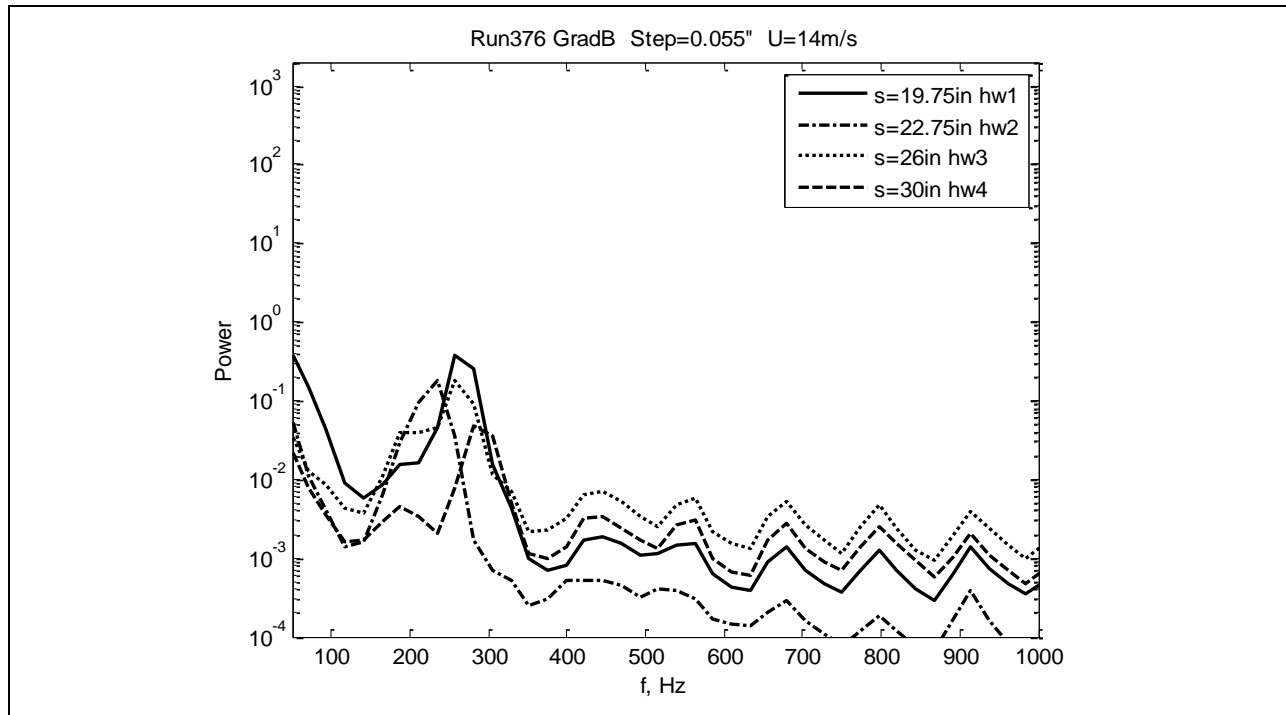


Figure 472: Measured power spectra.

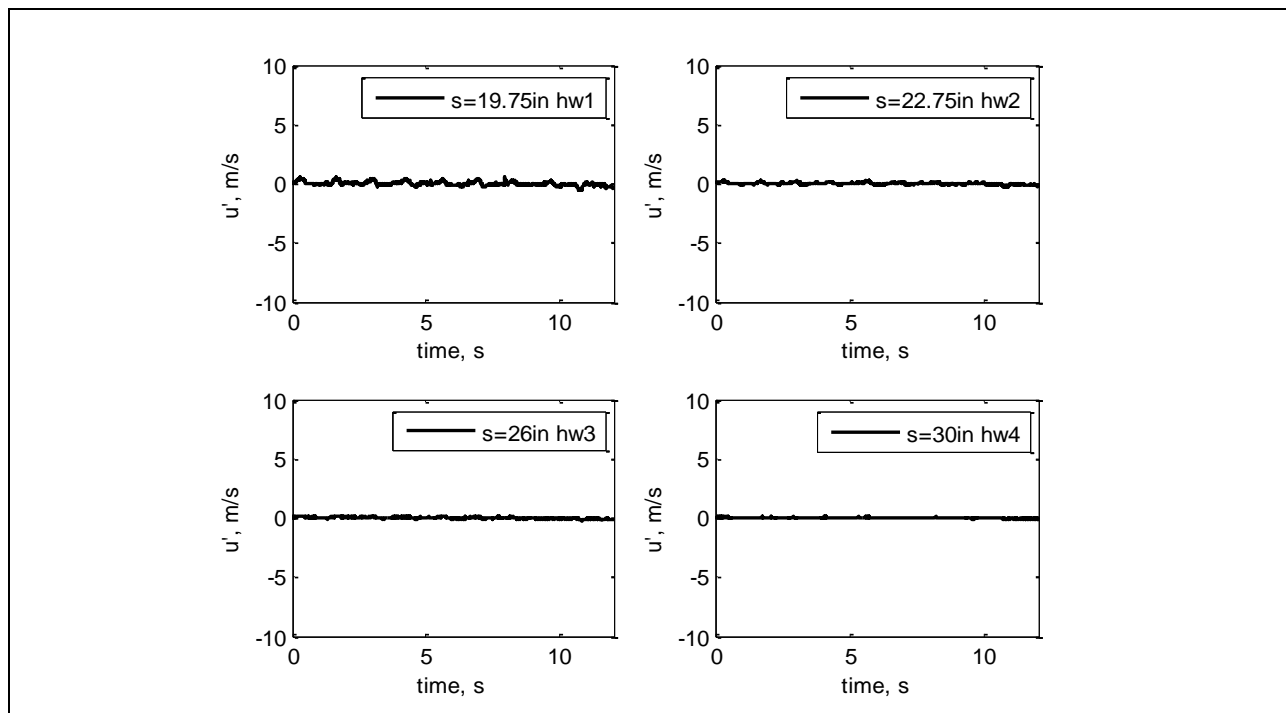


Figure 473: Measured velocity time history.

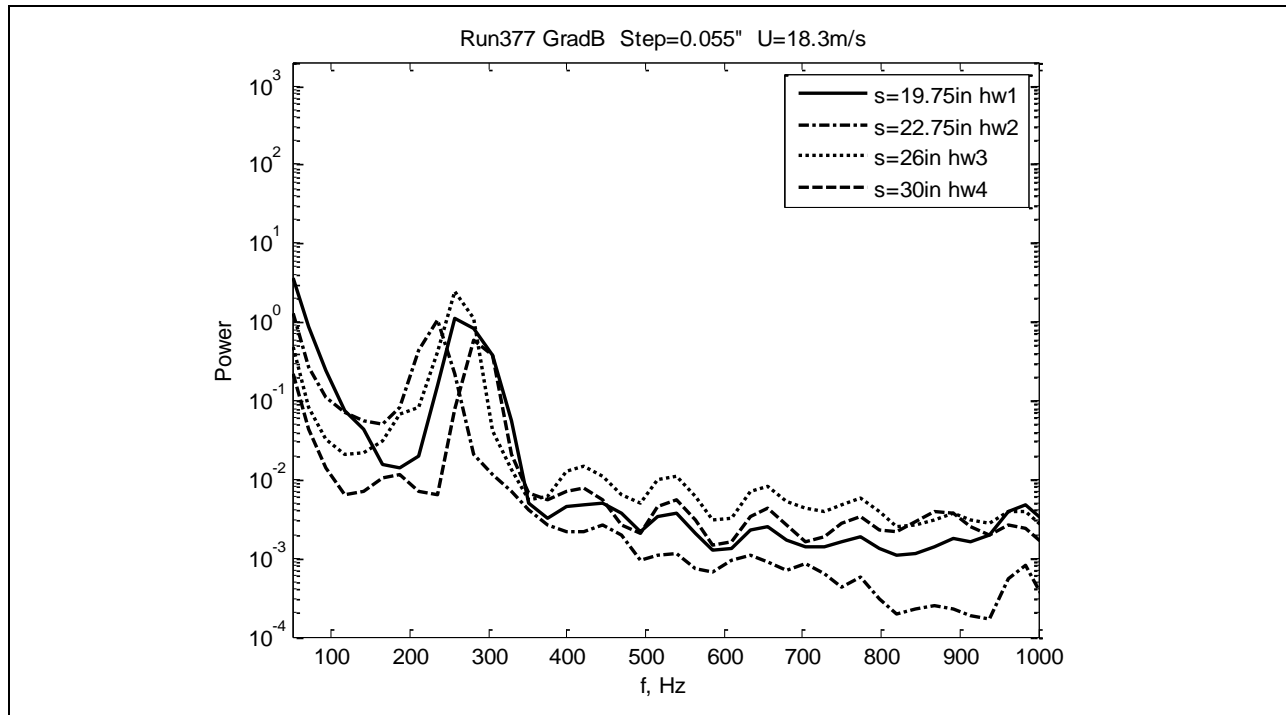


Figure 474: Measured power spectra.

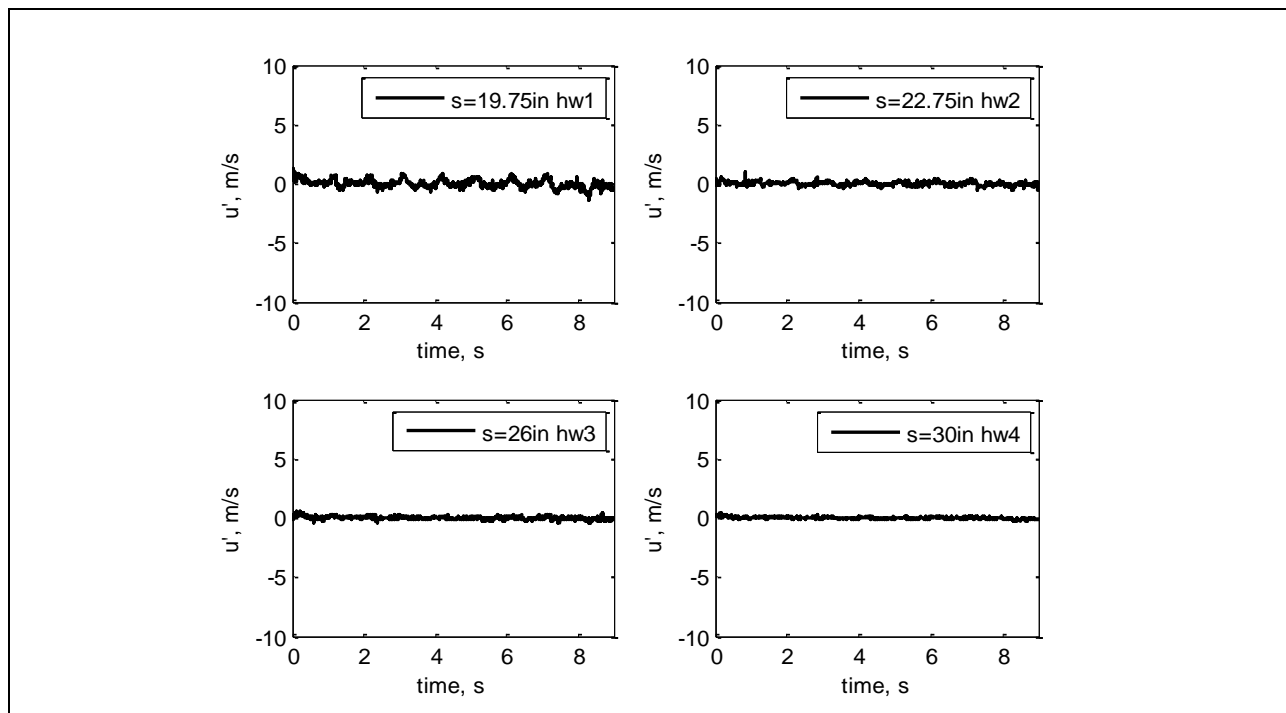


Figure 475: Measured velocity time history.

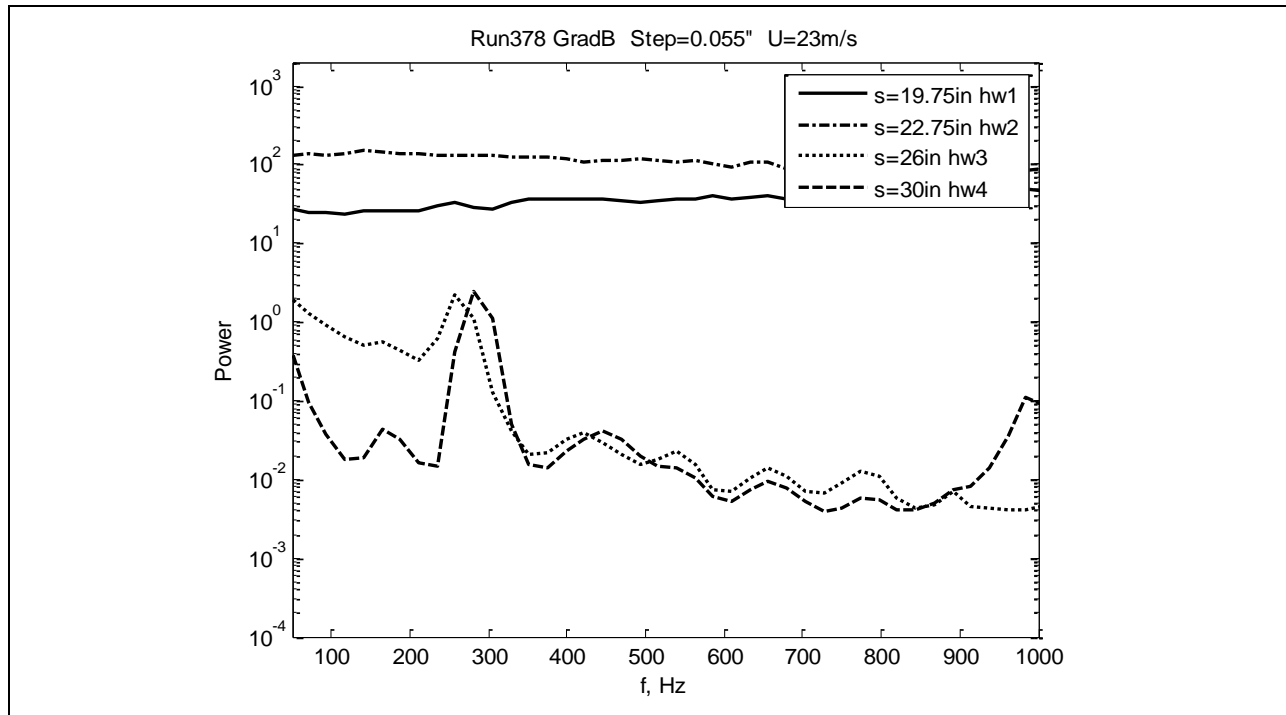


Figure 476: Measured power spectra.

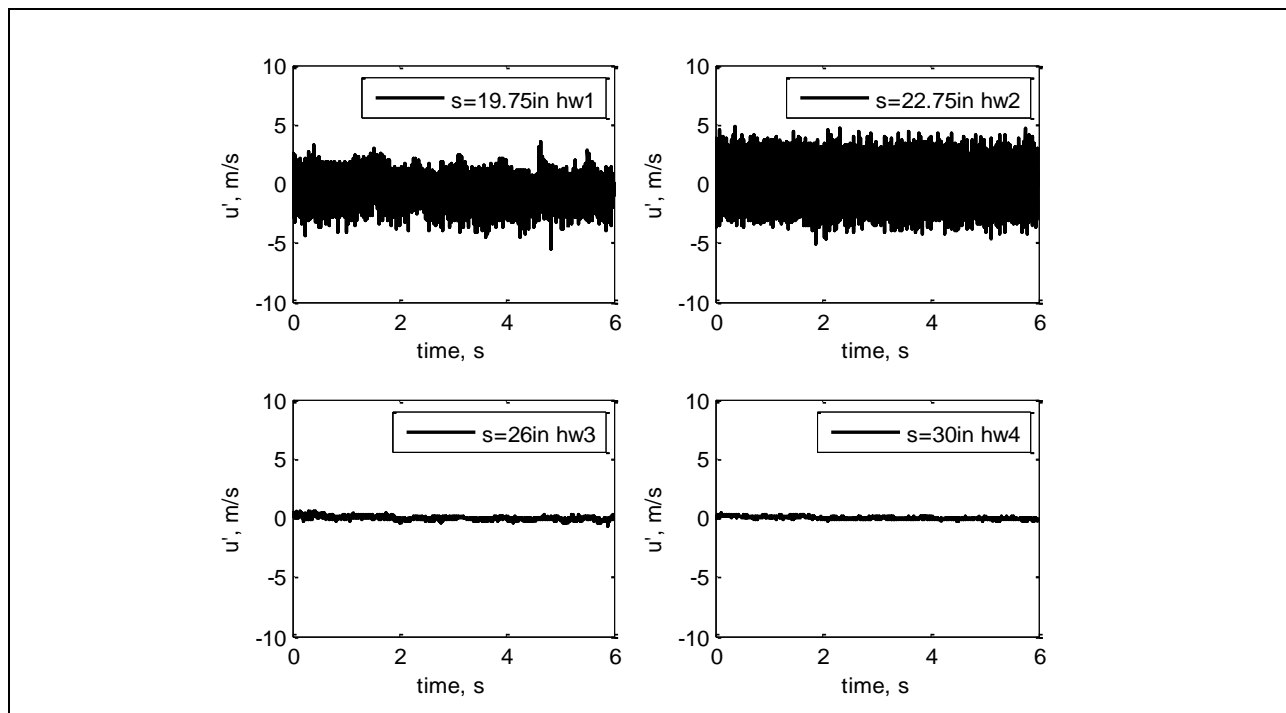


Figure 477: Measured velocity time history.

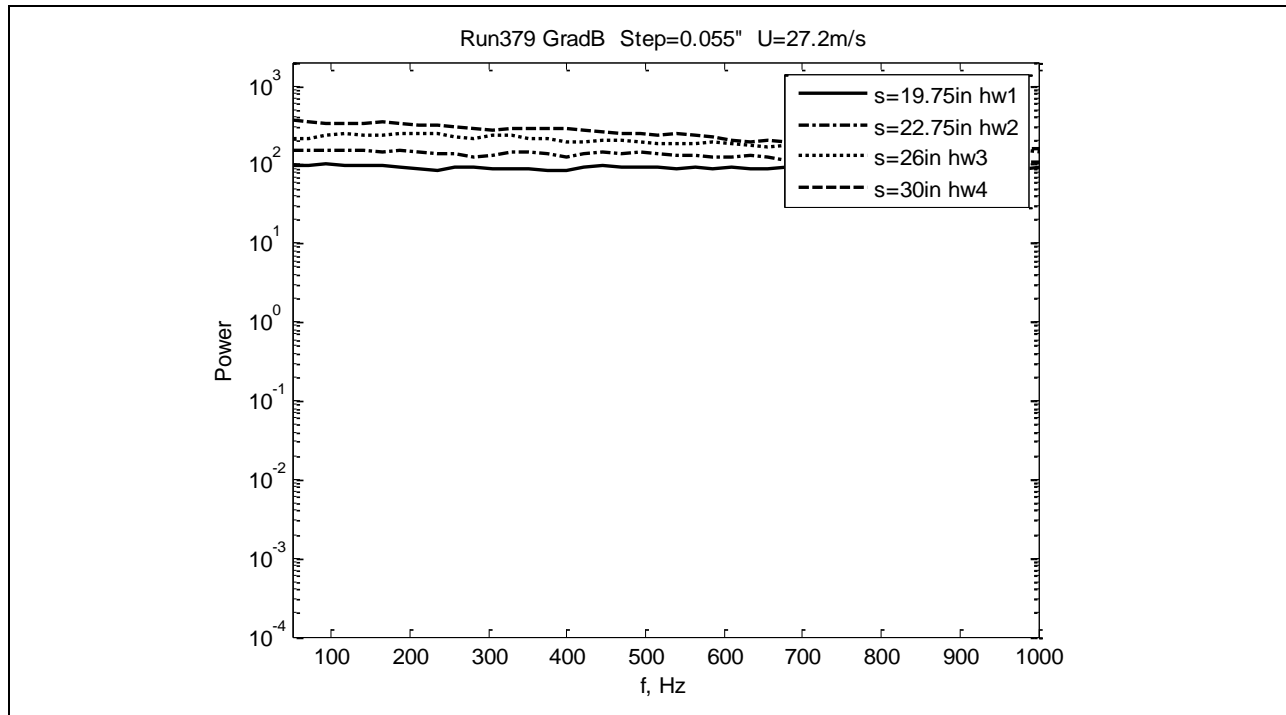


Figure 478: Measured power spectra.

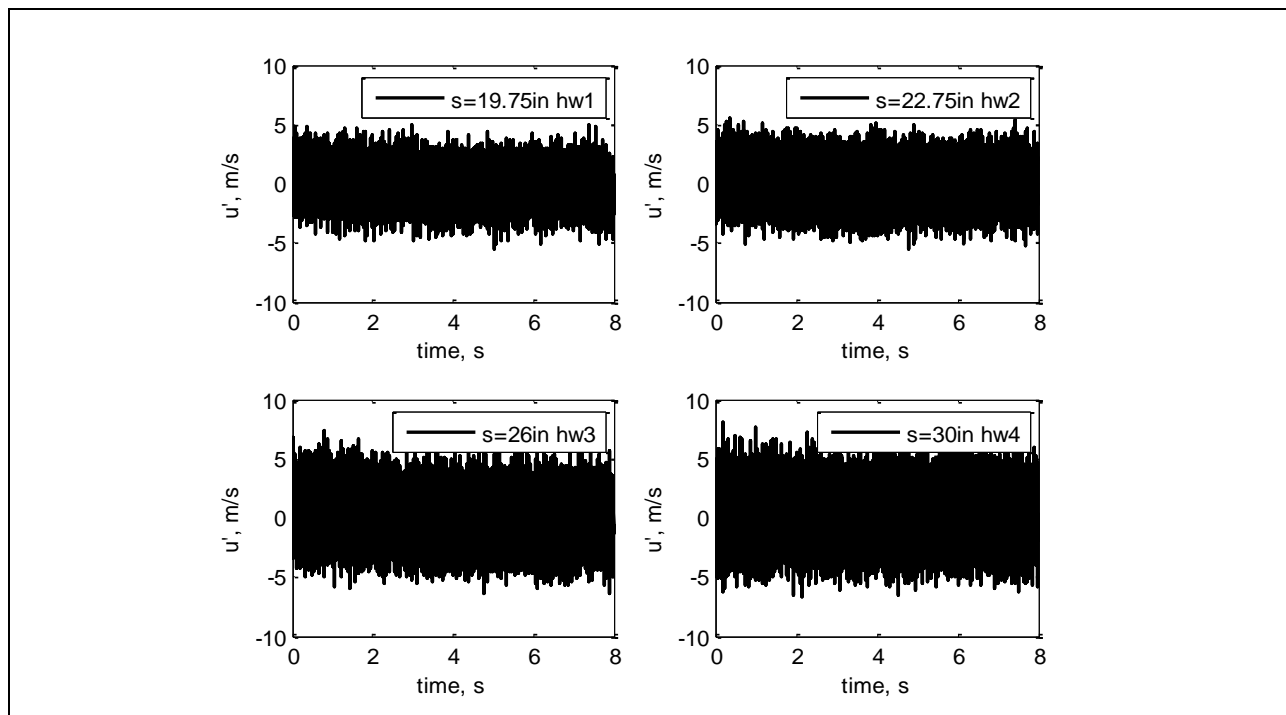


Figure 479: Measured velocity time history.

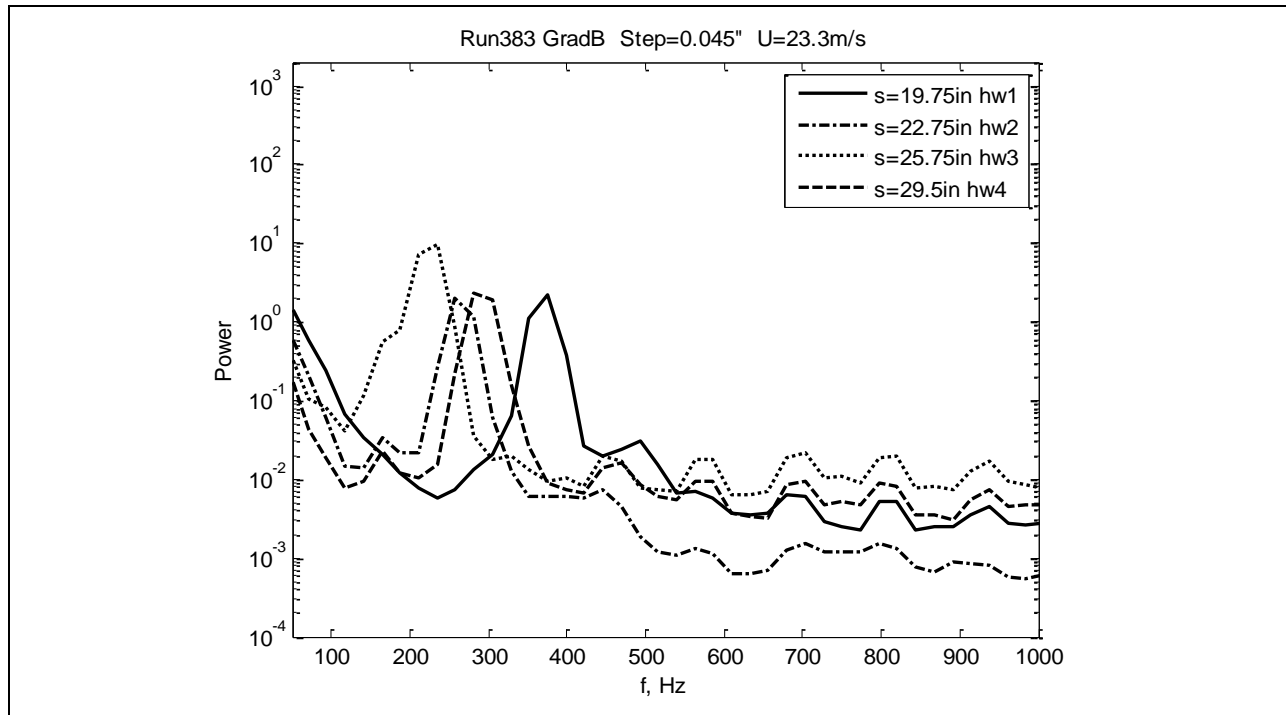


Figure 480: Measured power spectra.

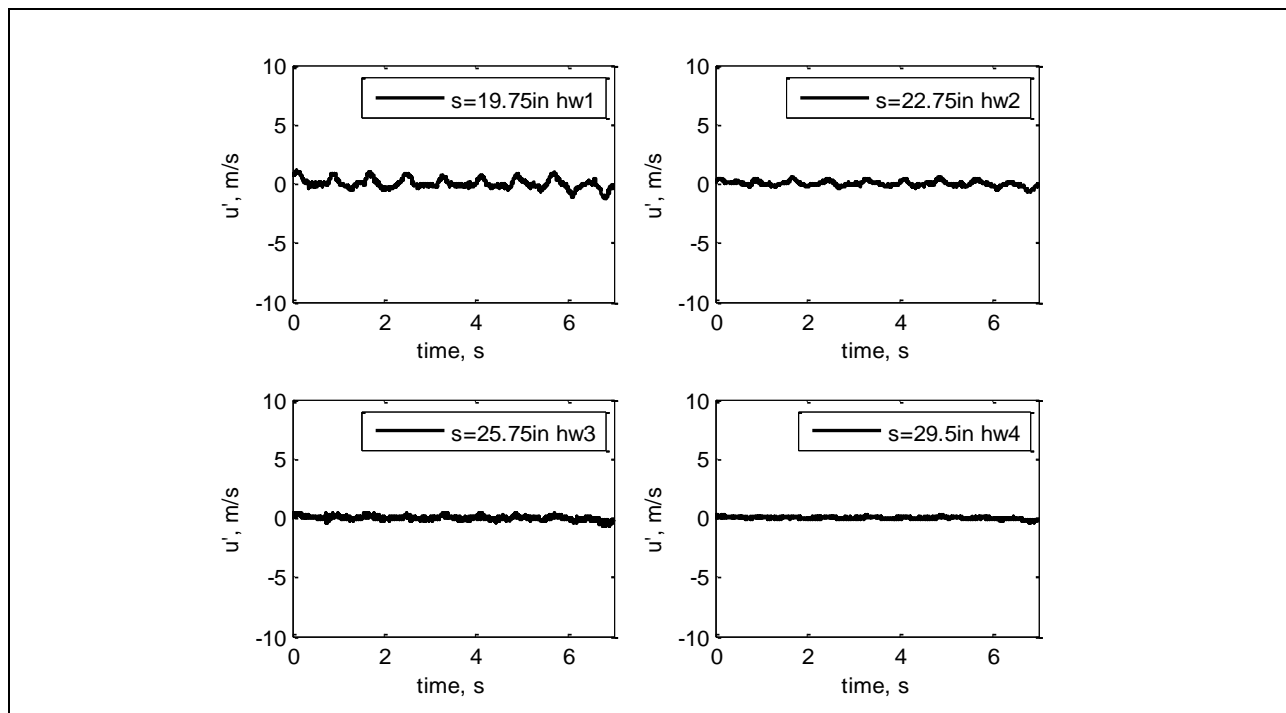


Figure 481: Measured velocity time history.

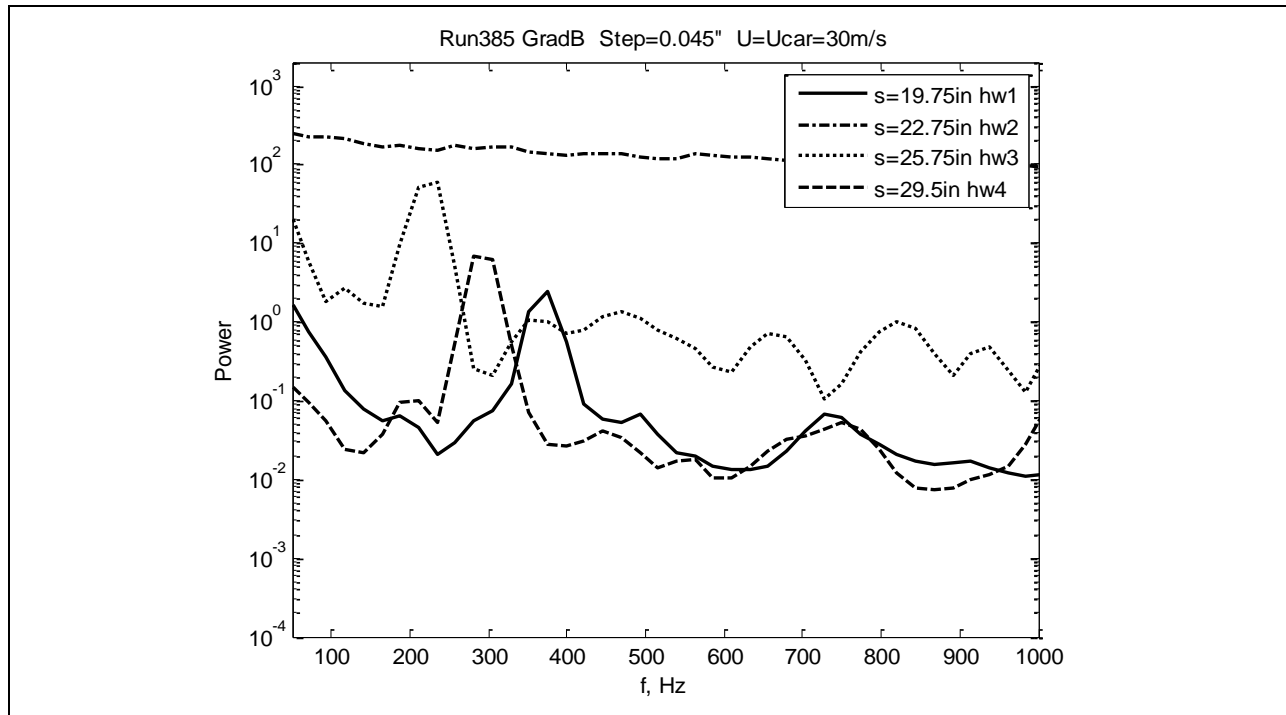


Figure 482: Measured power spectra.

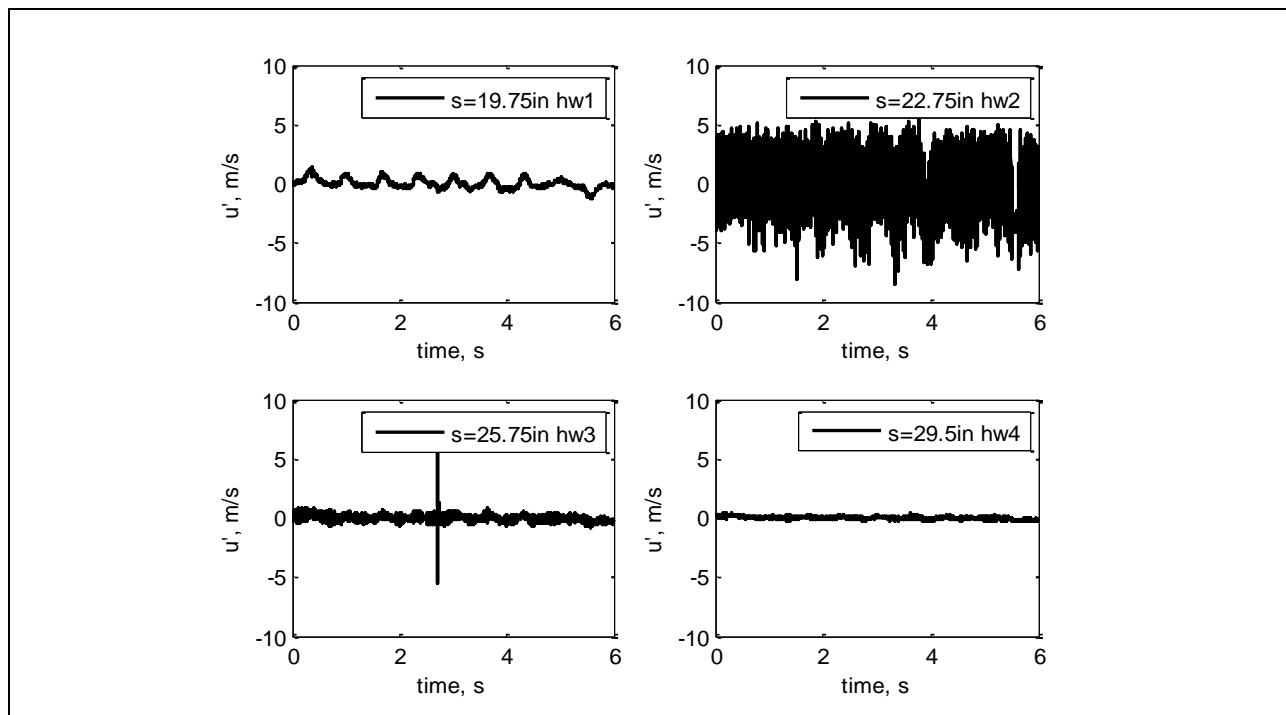


Figure 483: Measured velocity time history.

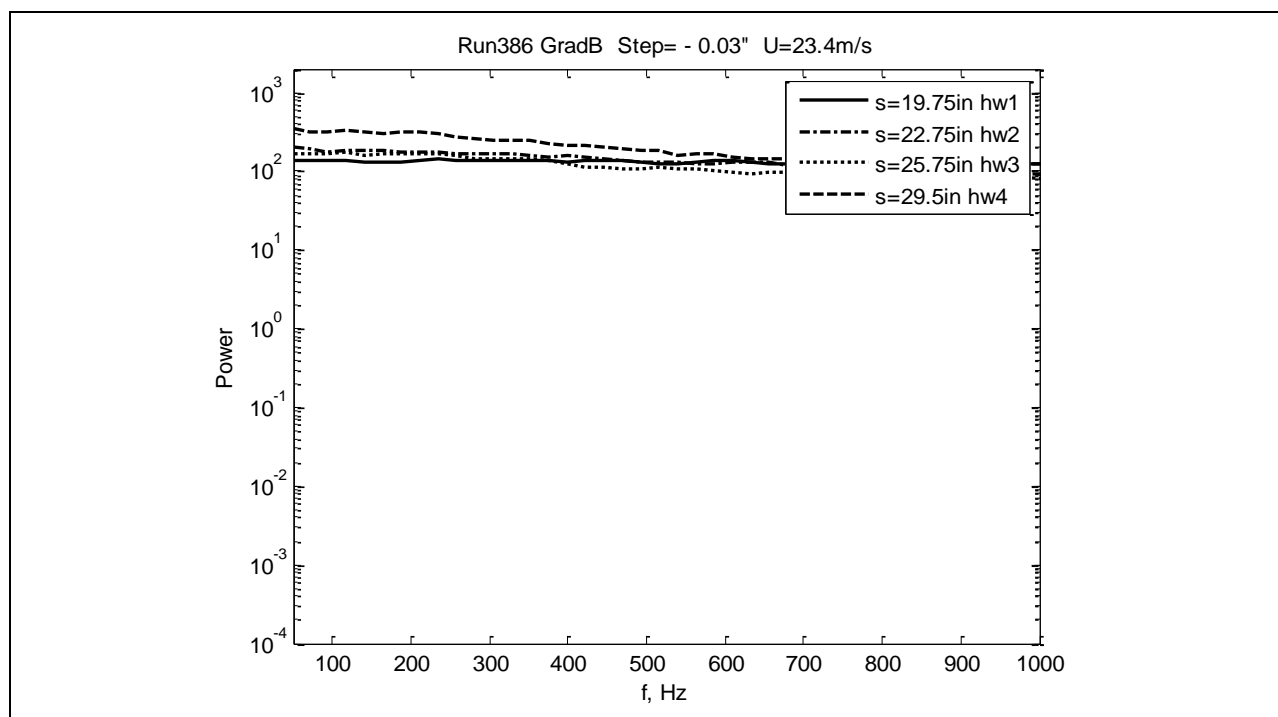


Figure 484: Measured power spectra.

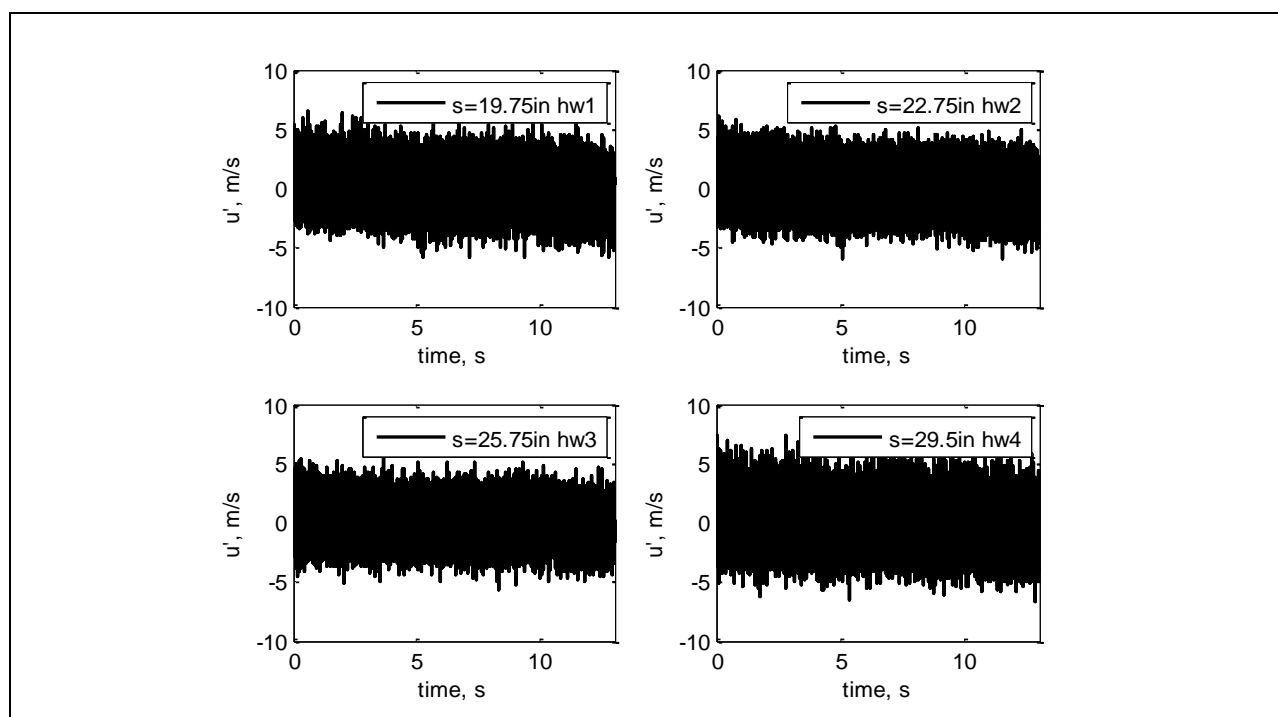


Figure 485: Measured velocity time history.

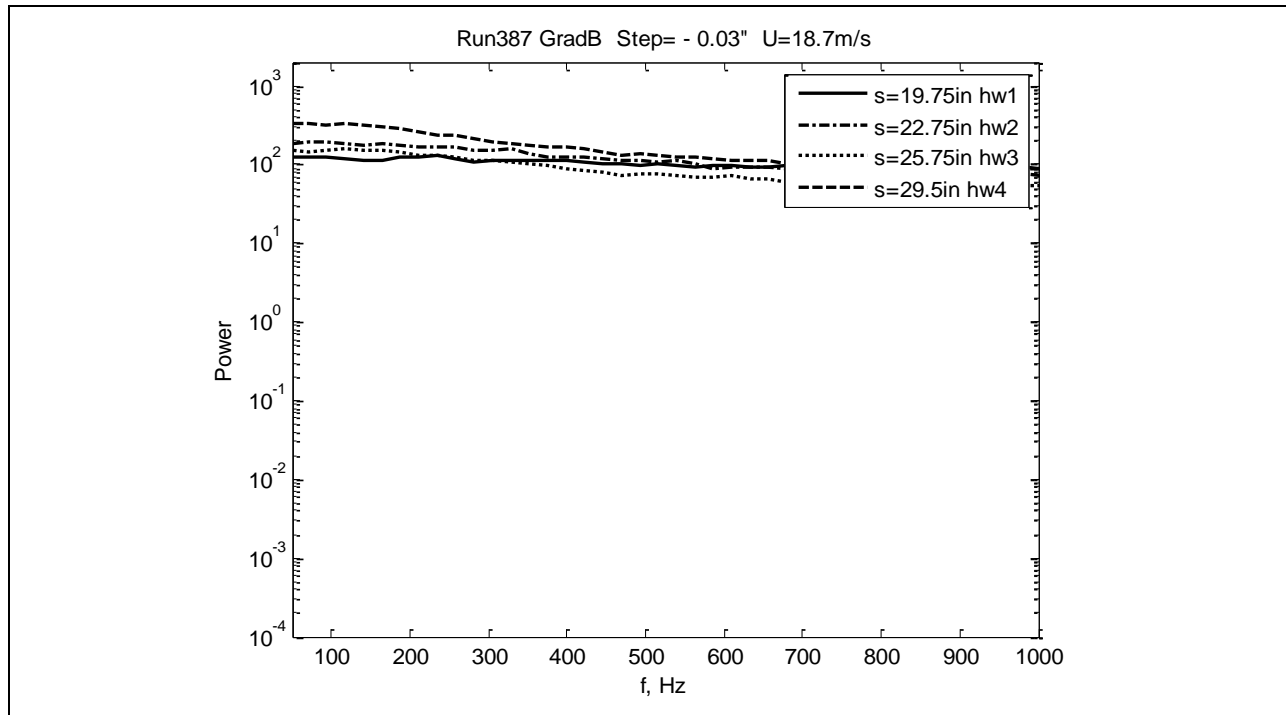


Figure 486: Measured power spectra.

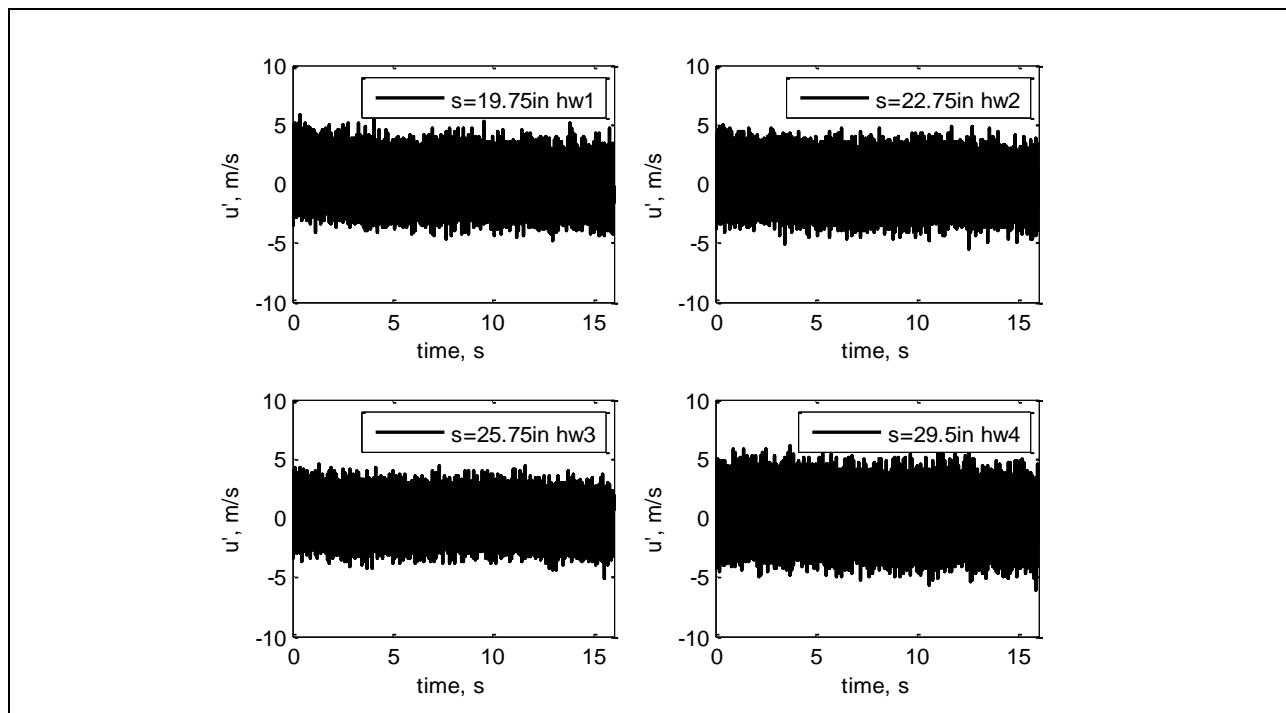


Figure 487: Measured velocity time history.

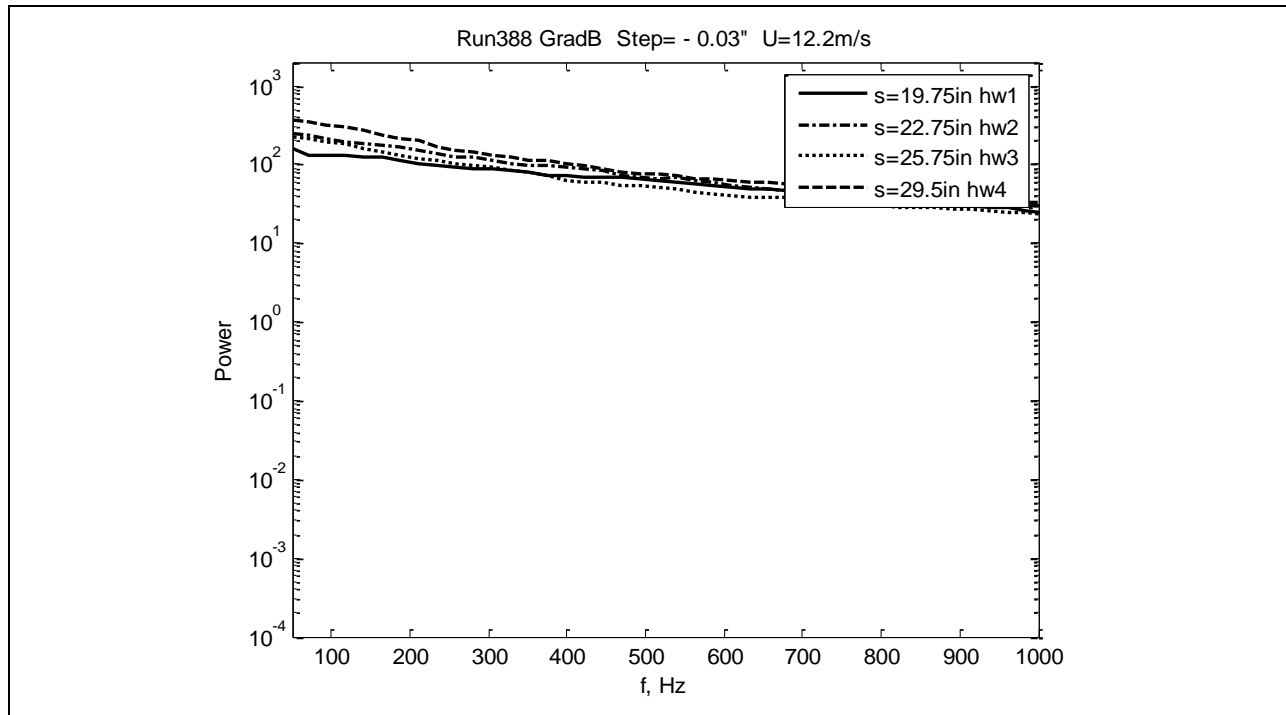


Figure 488: Measured power spectra.

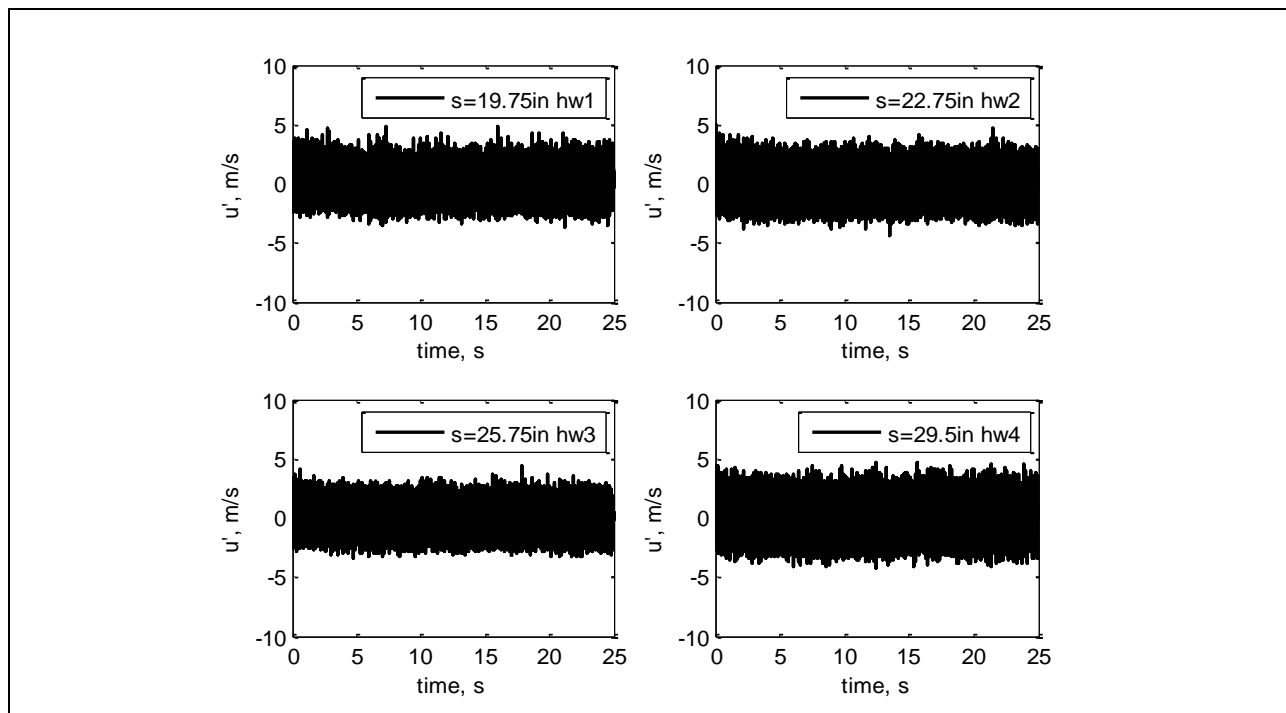


Figure 489: Measured velocity time history.

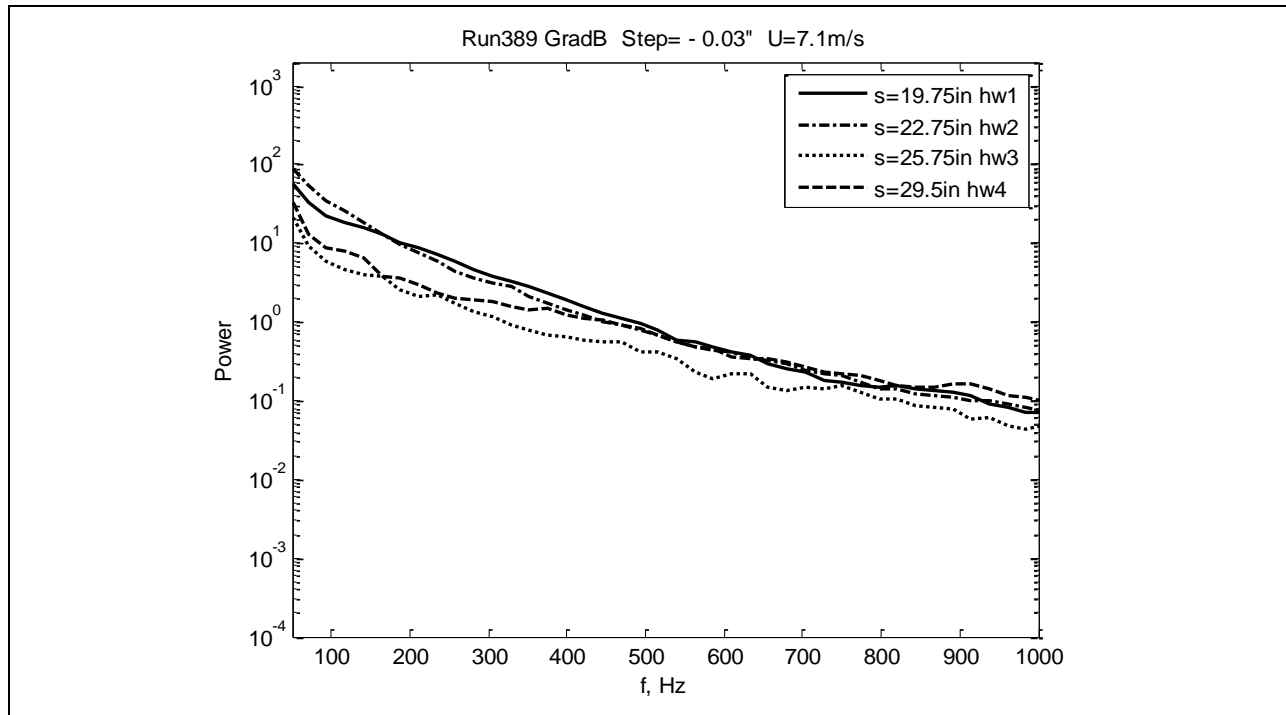


Figure 490: Measured power spectra.

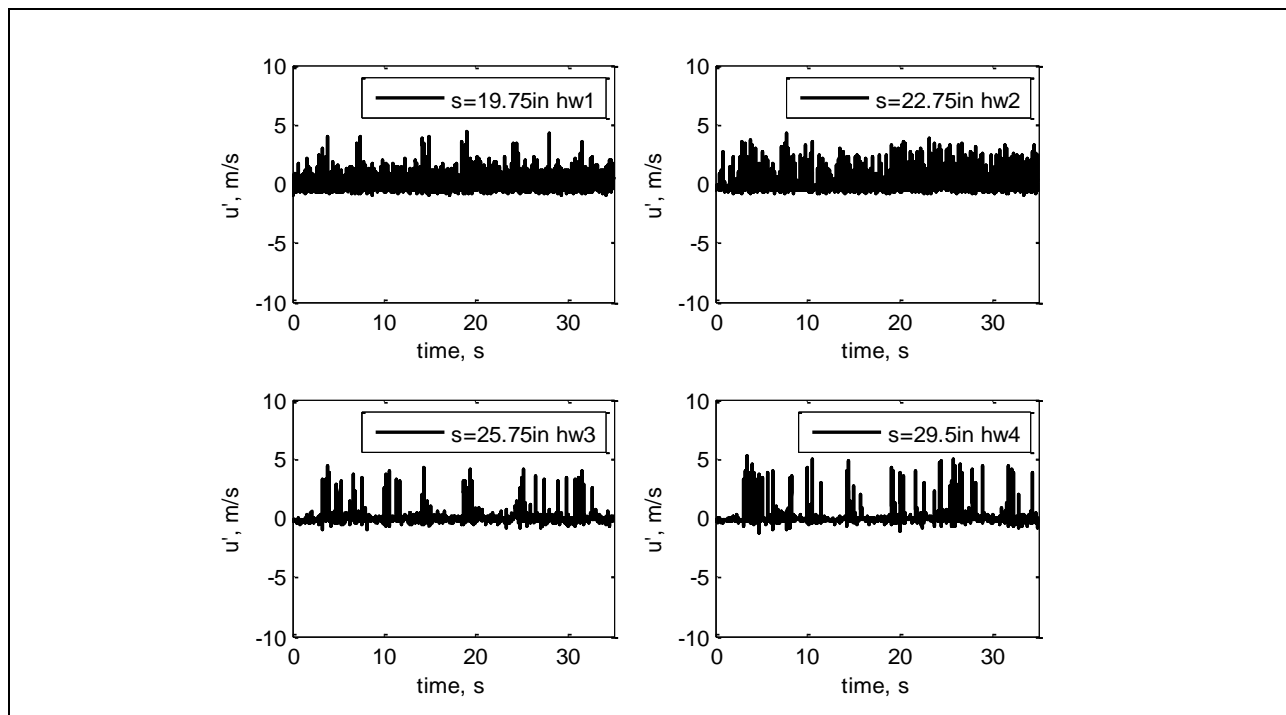


Figure 491: Measured velocity time history.

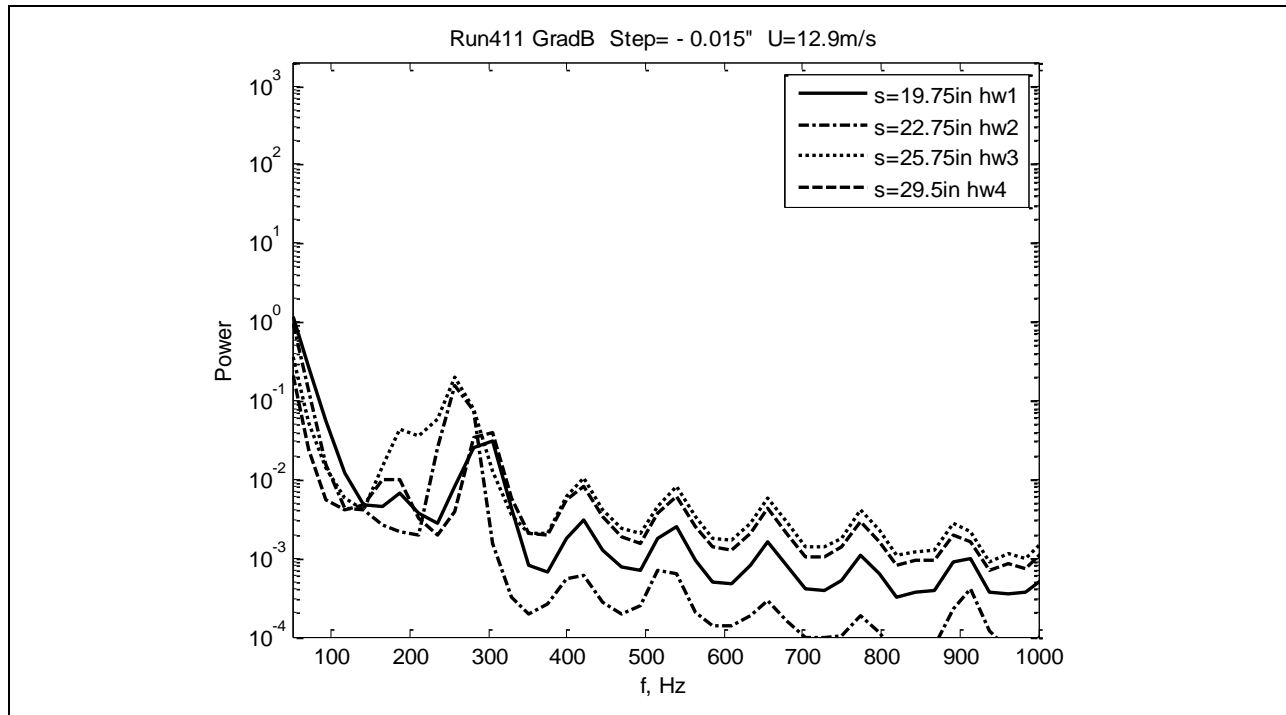


Figure 492: Measured power spectra.

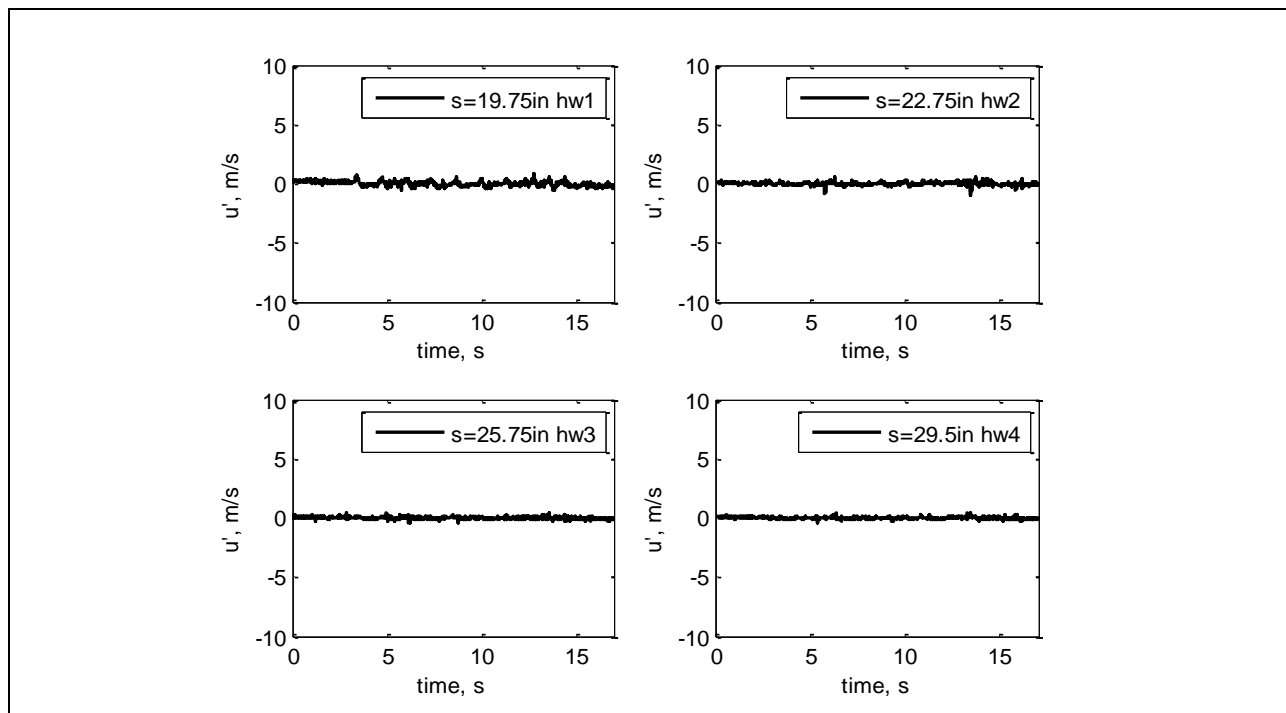


Figure 493: Measured velocity time history.

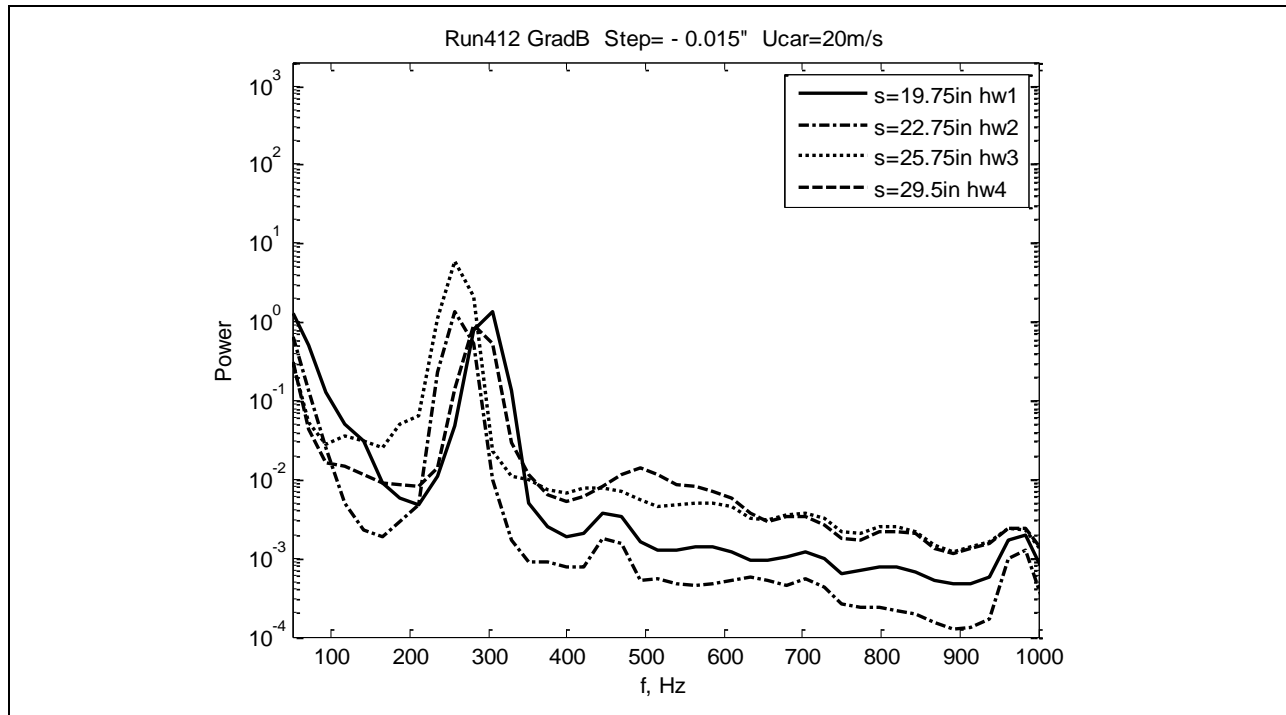


Figure 494: Measured power spectra.

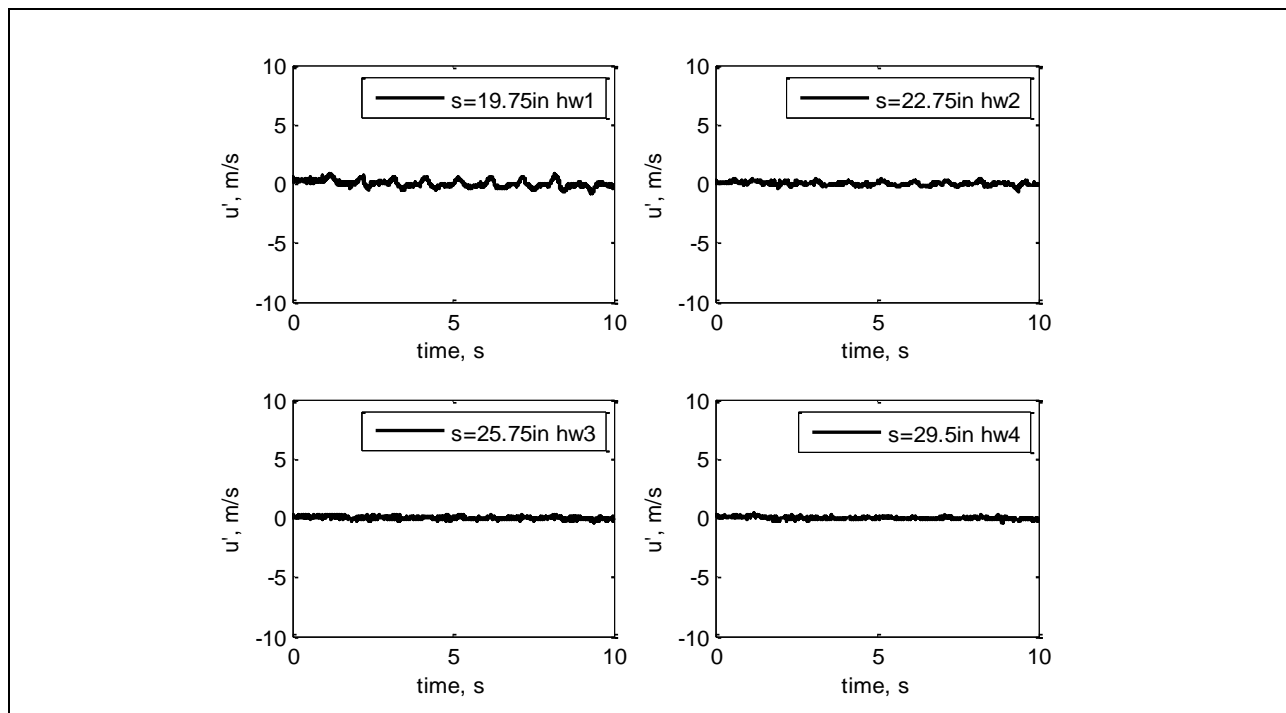


Figure 495: Measured velocity time history.

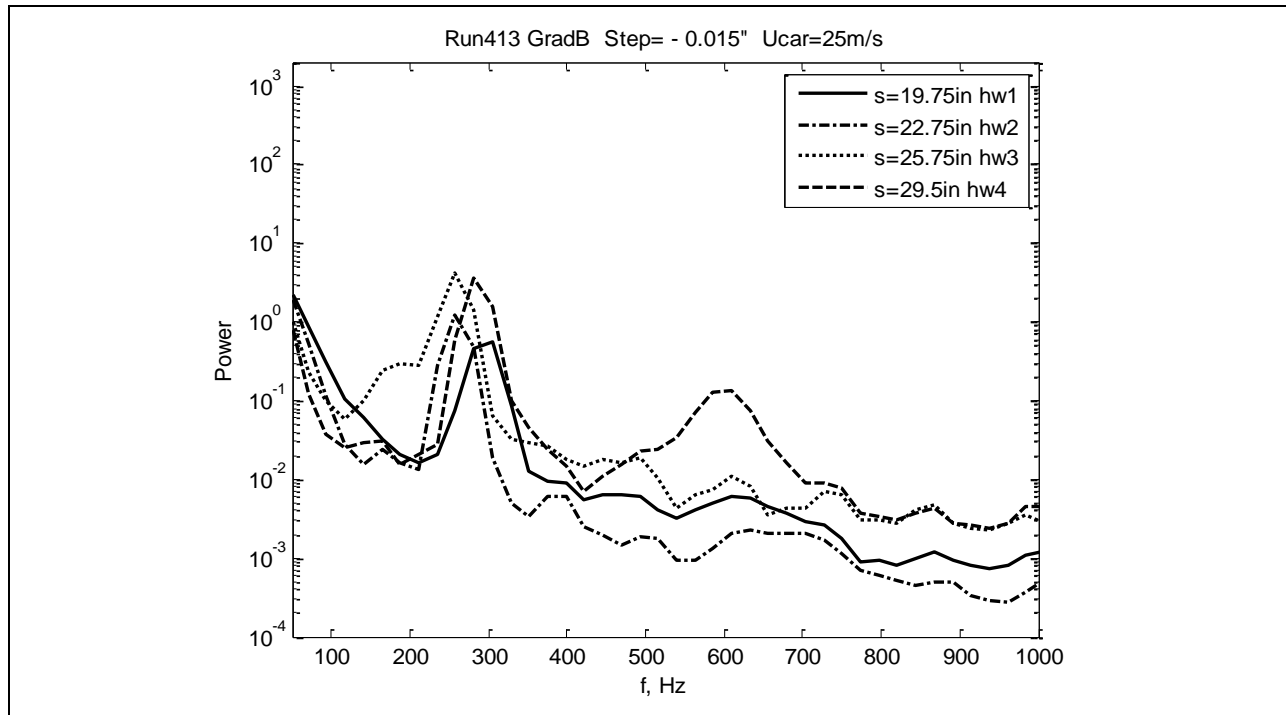


Figure 496: Measured power spectra.

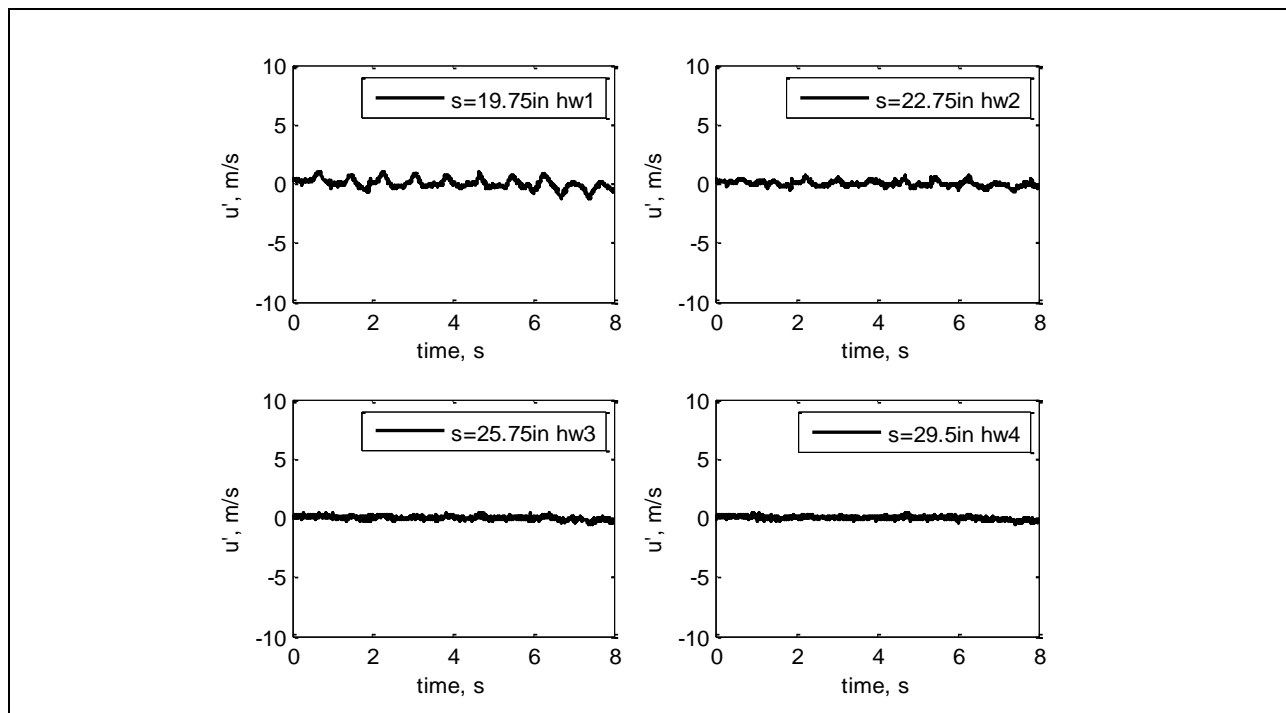


Figure 497: Measured velocity time history.

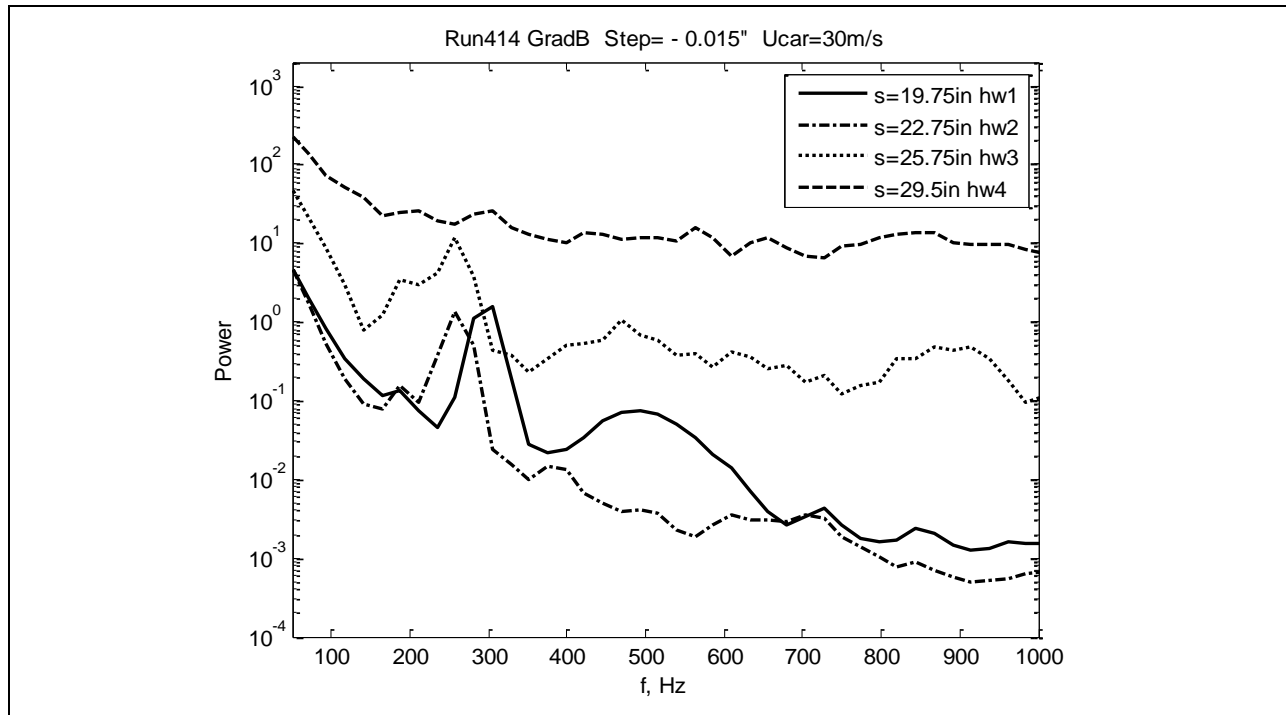


Figure 498: Measured power spectra.

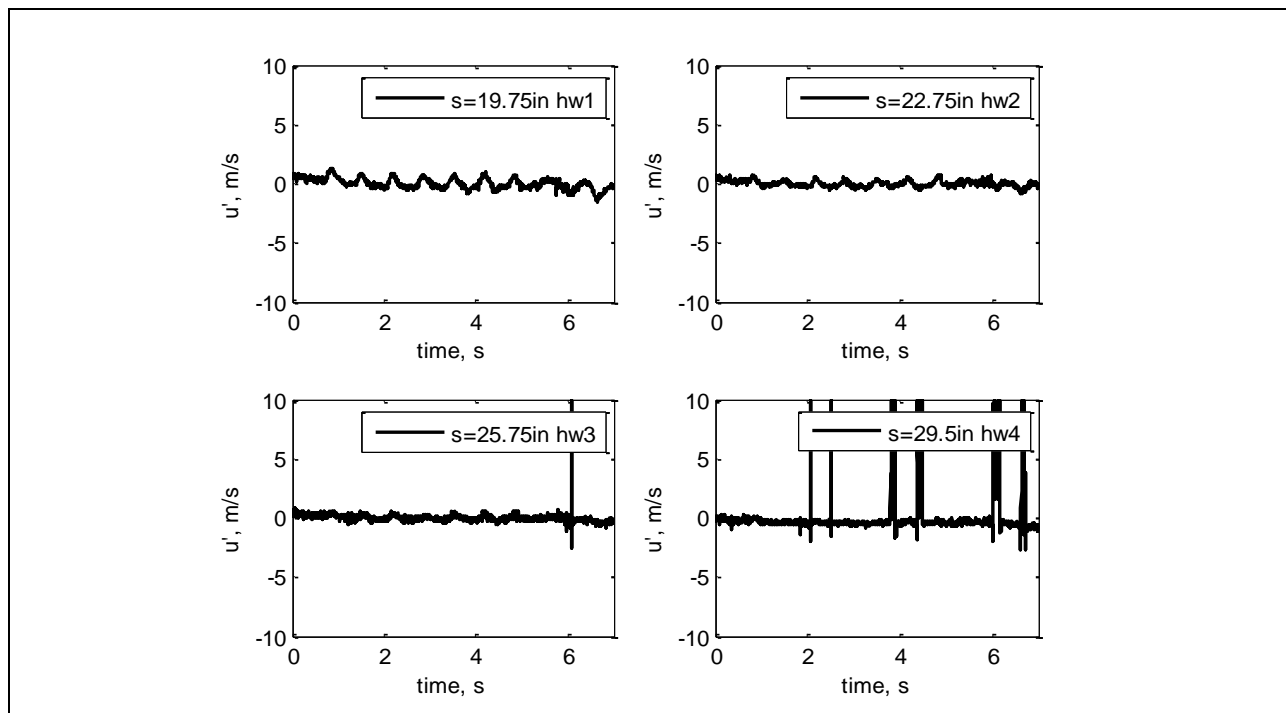


Figure 499: Measured velocity time history.

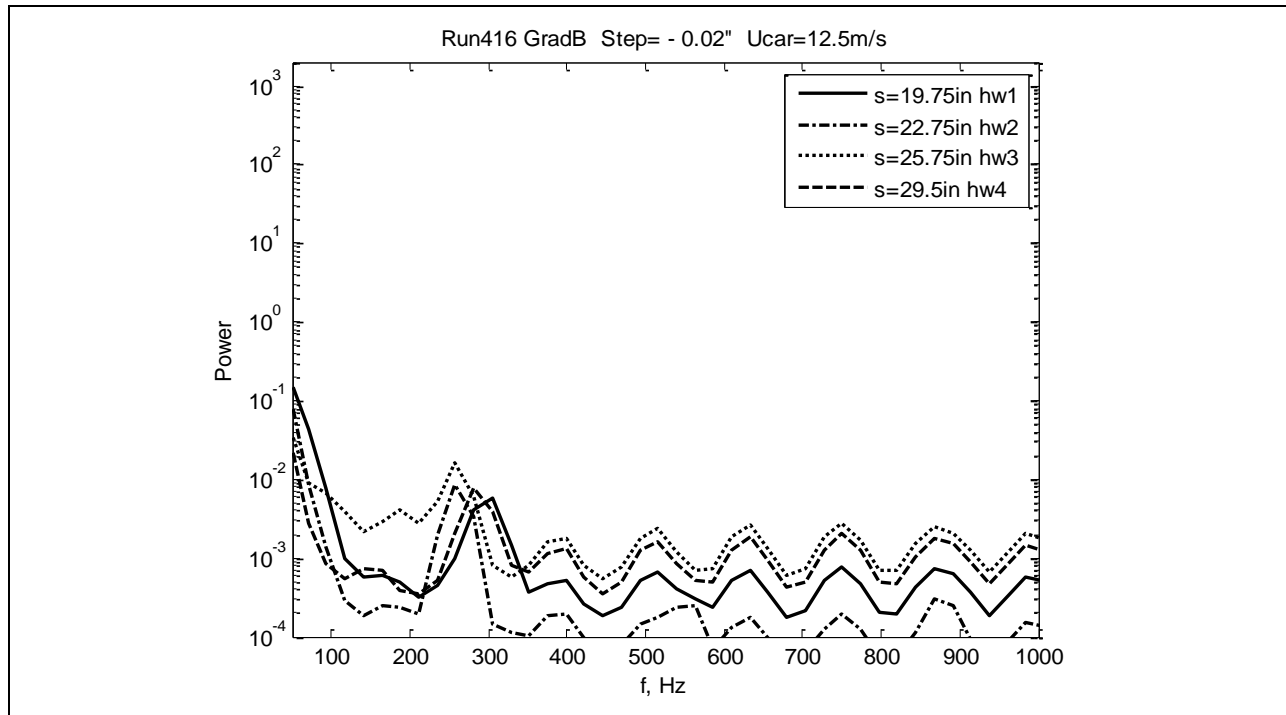


Figure 500: Measured power spectra.

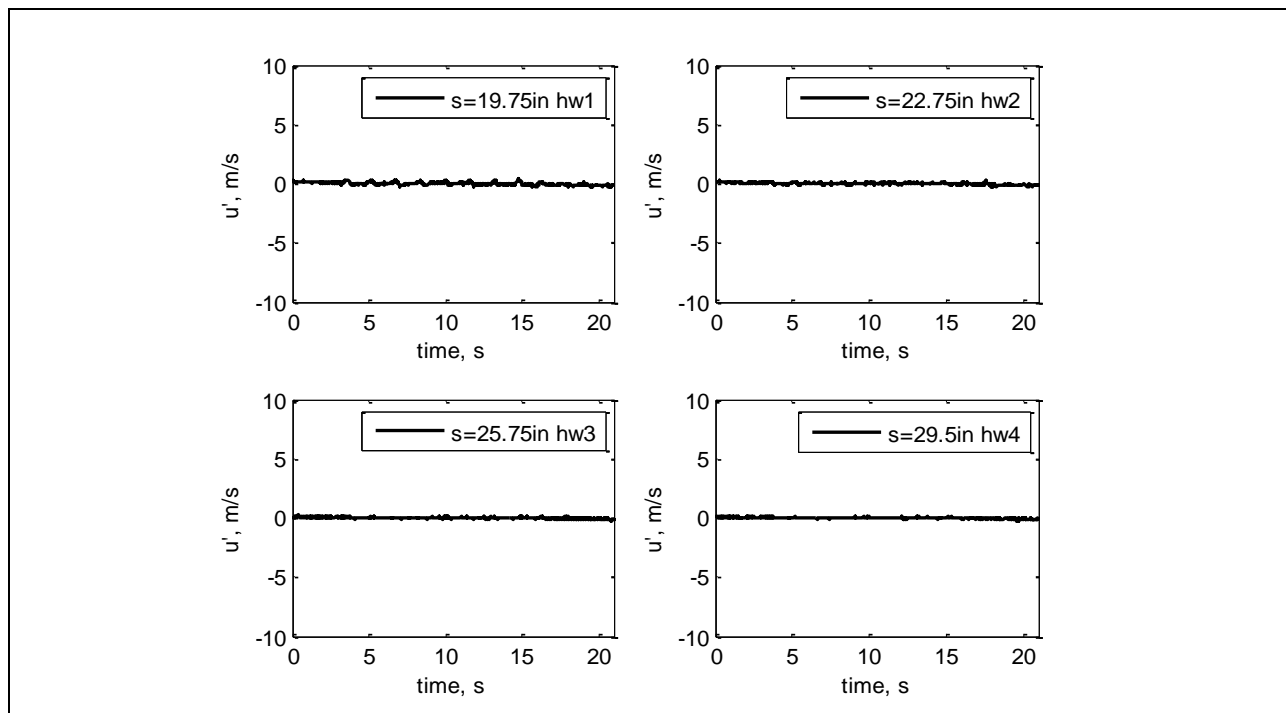


Figure 501: Measured velocity time history.

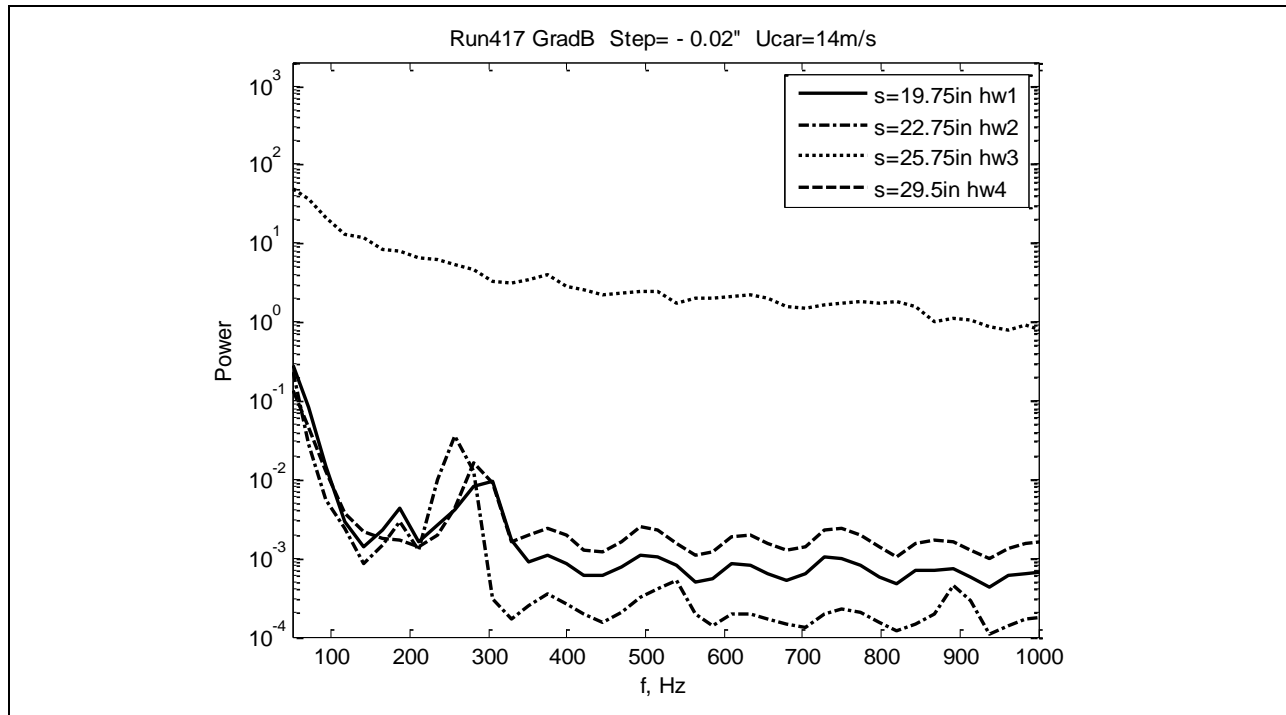


Figure 502: Measured power spectra.

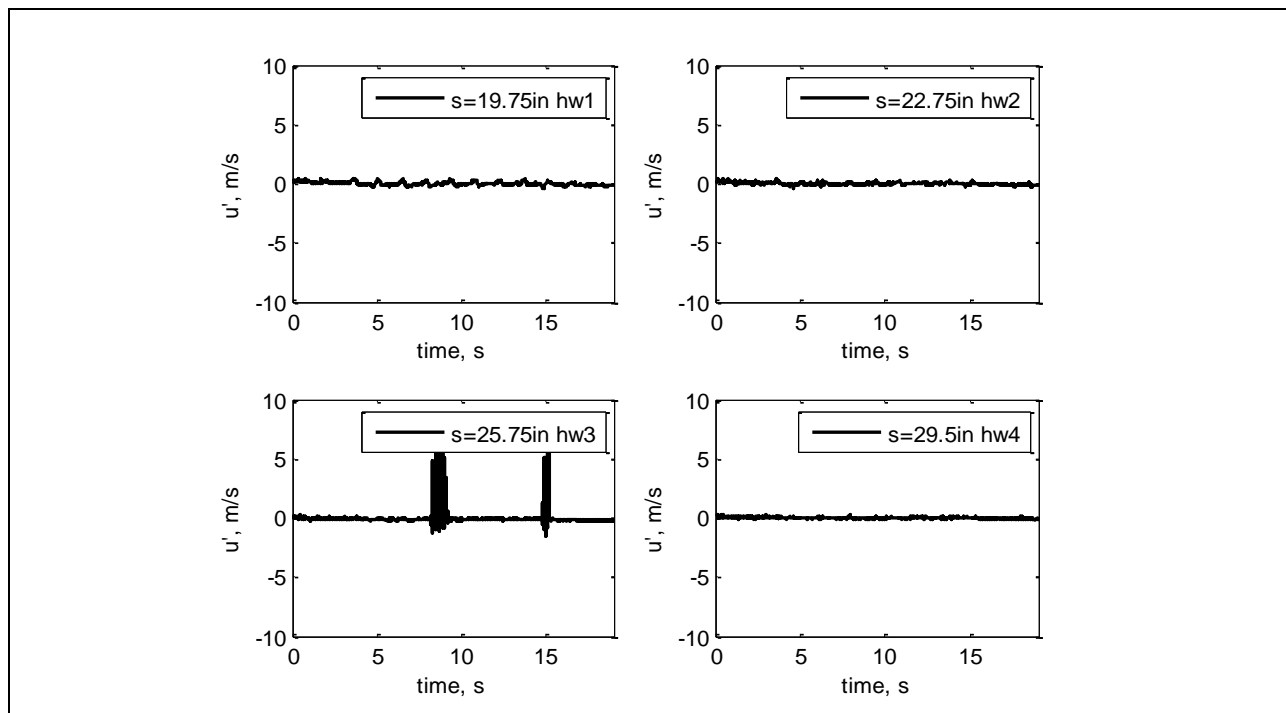


Figure 503: Measured velocity time history.

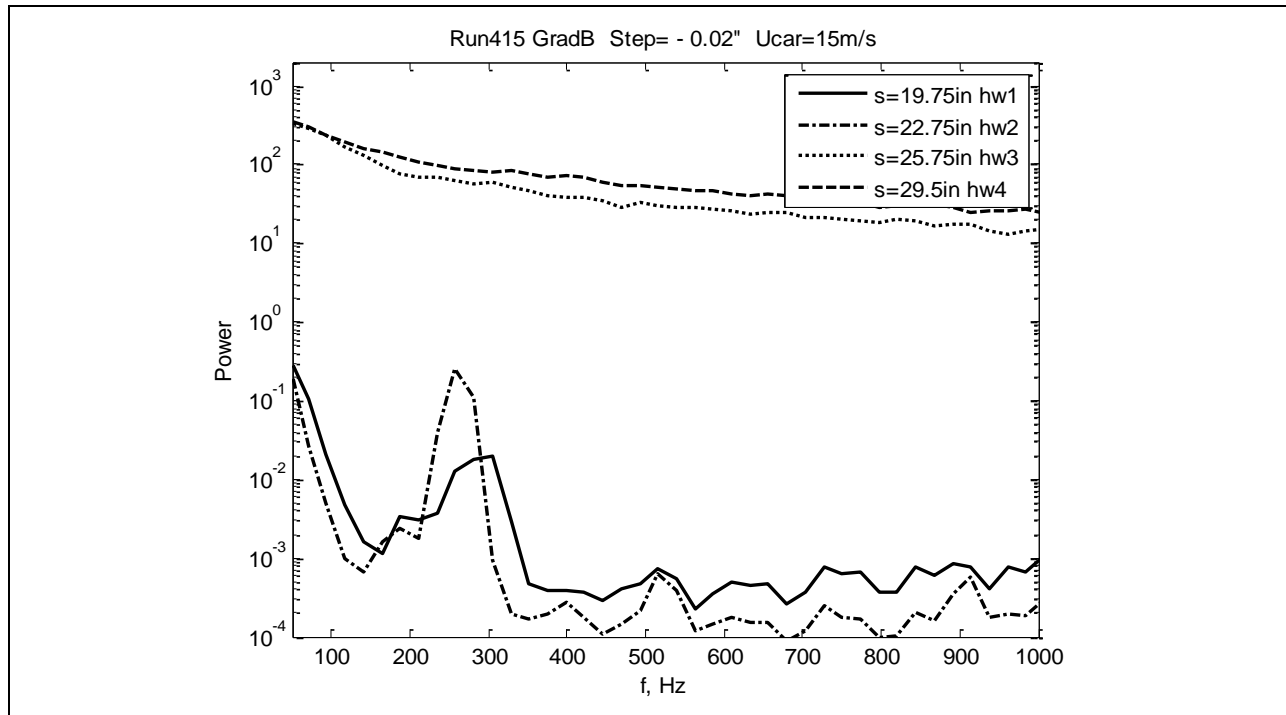


Figure 504: Measured power spectra.

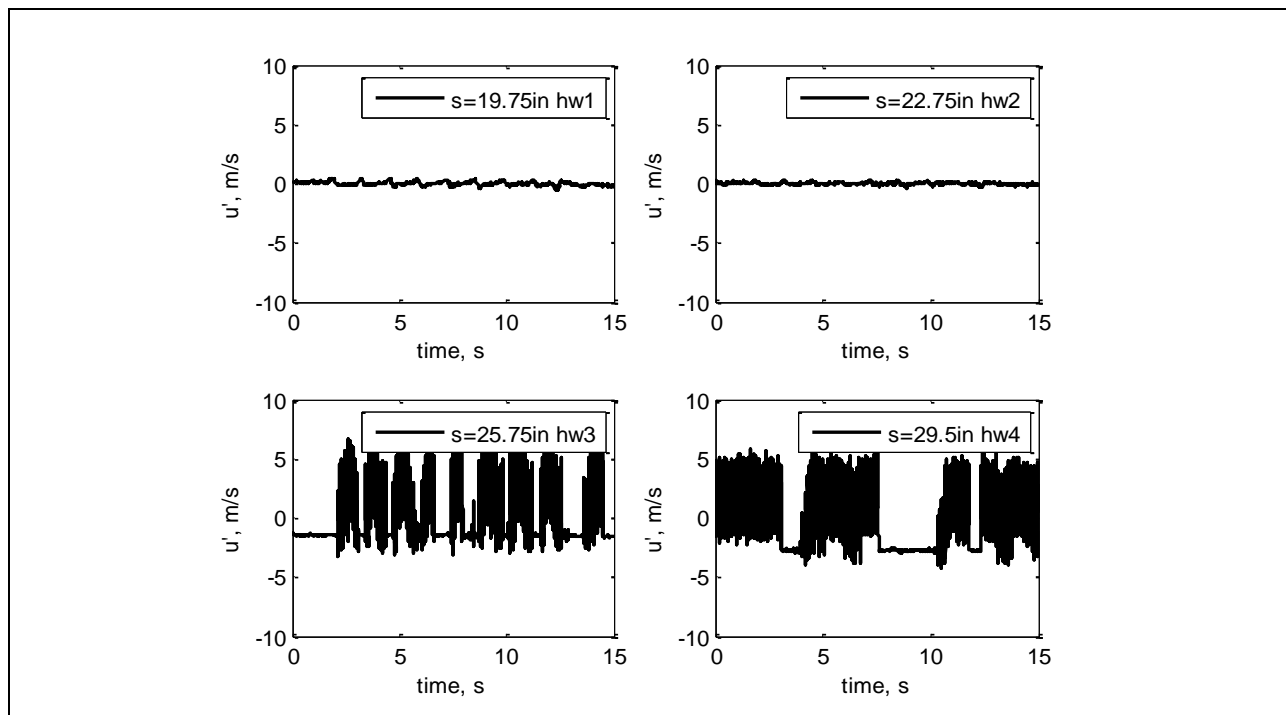


Figure 505: Measured velocity time history.

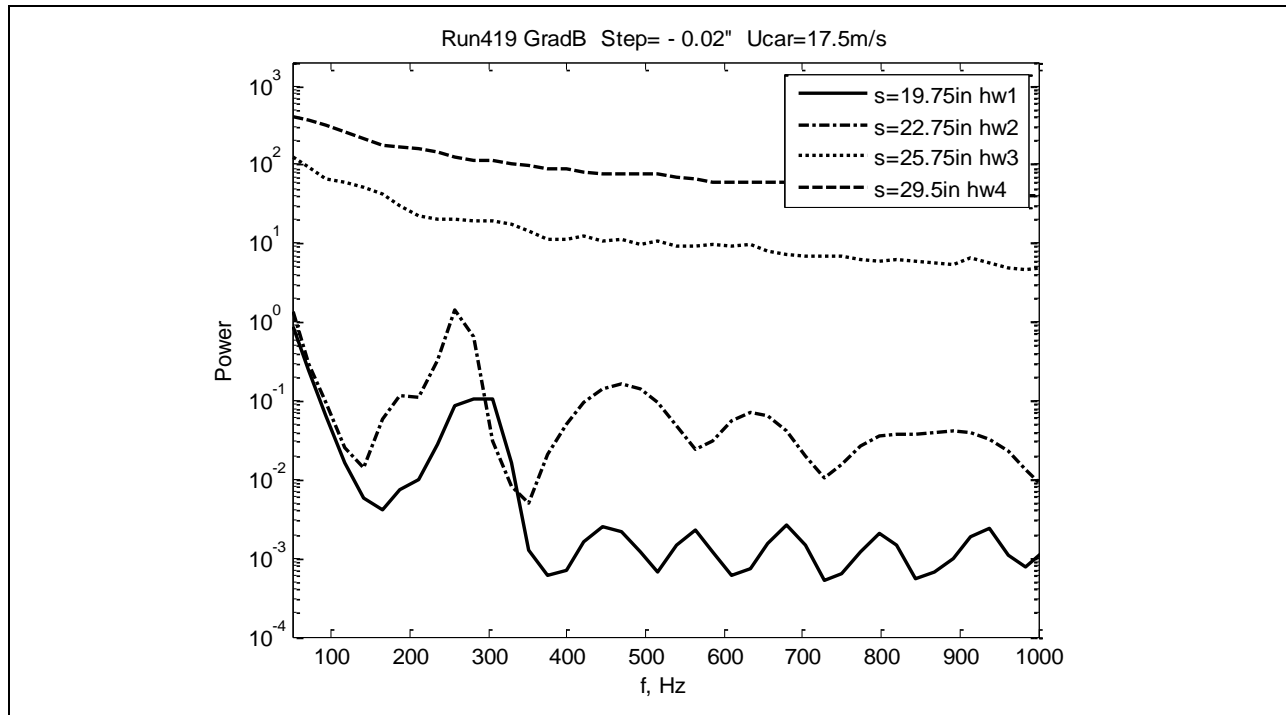


Figure 506: Measured power spectra.

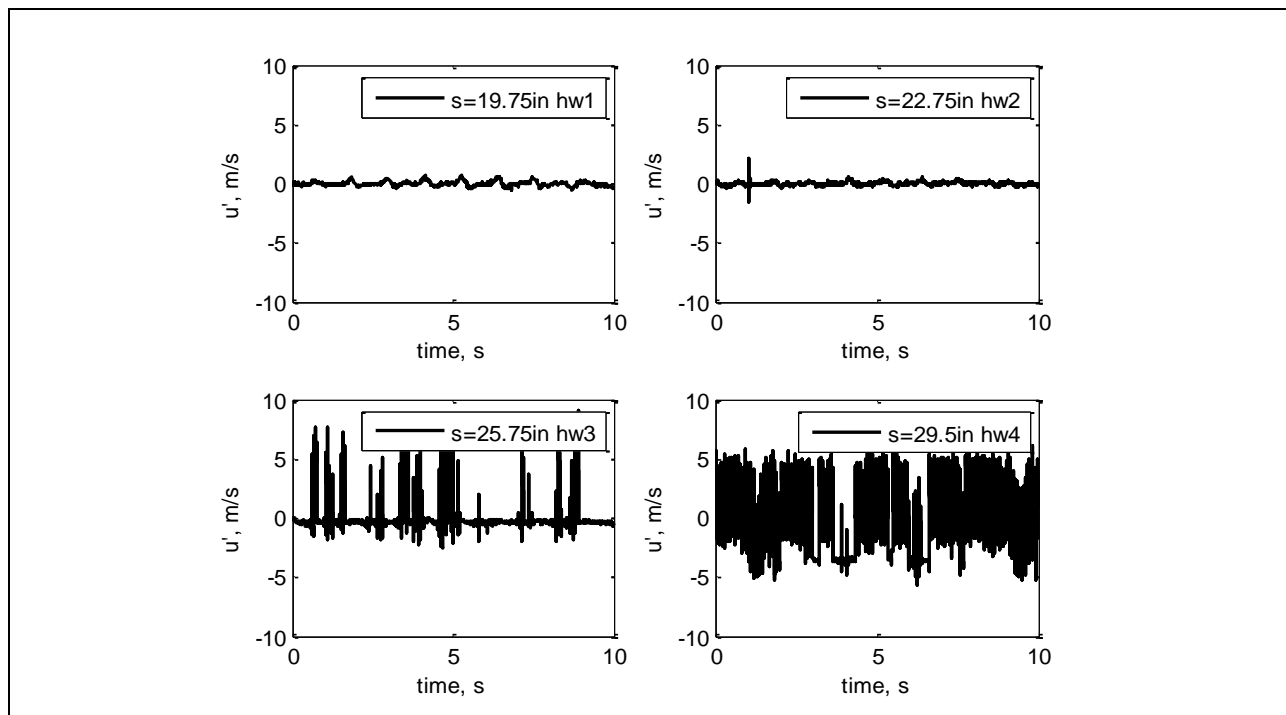


Figure 507: Measured velocity time history.

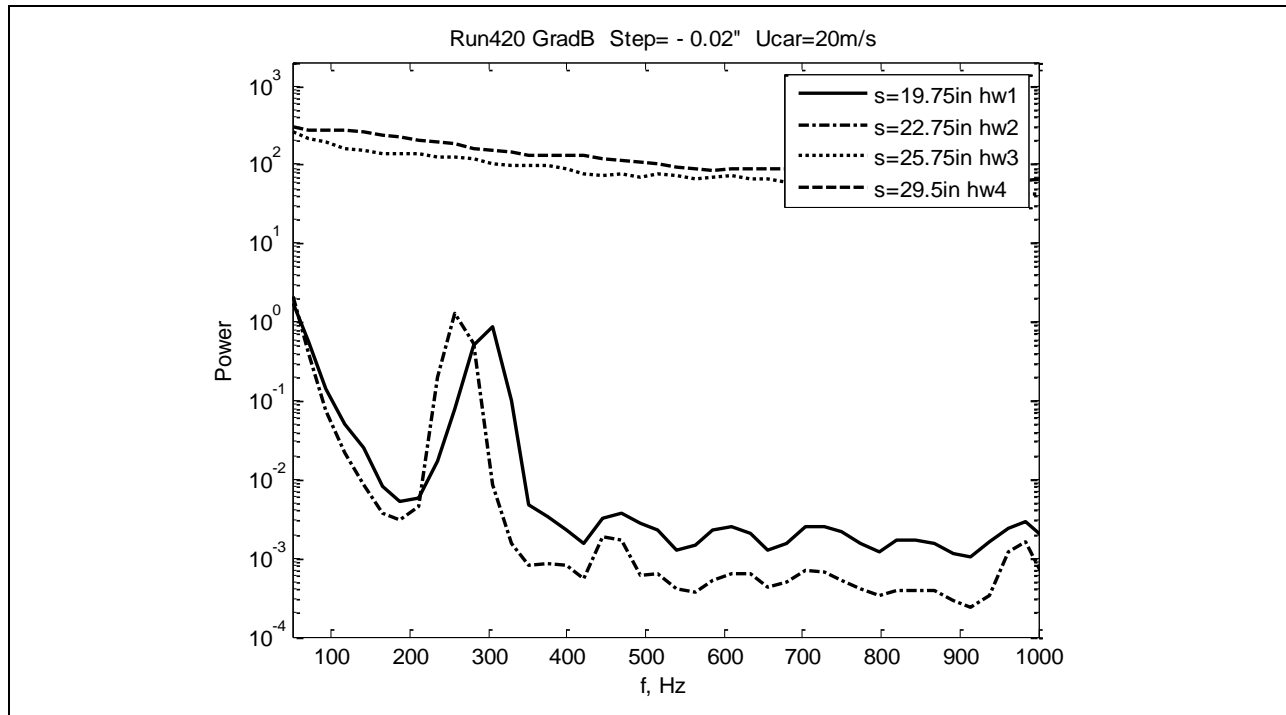


Figure 508: Measured power spectra.

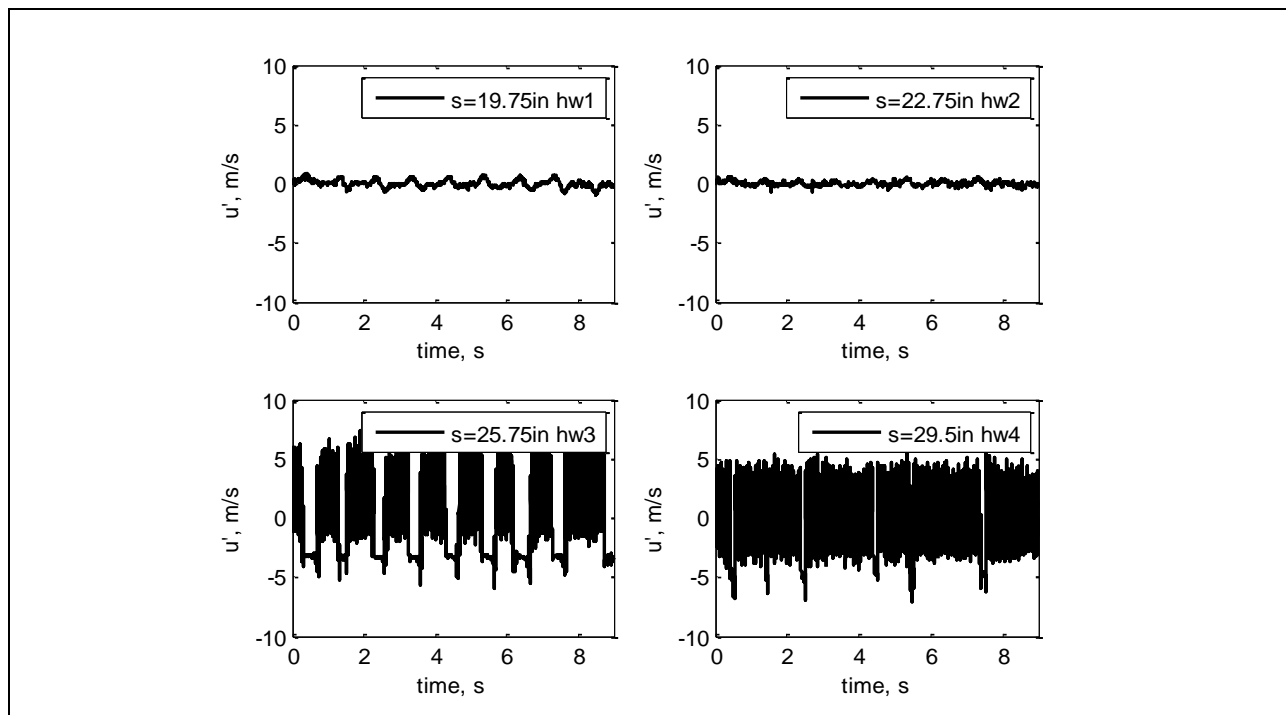


Figure 509: Measured velocity time history.

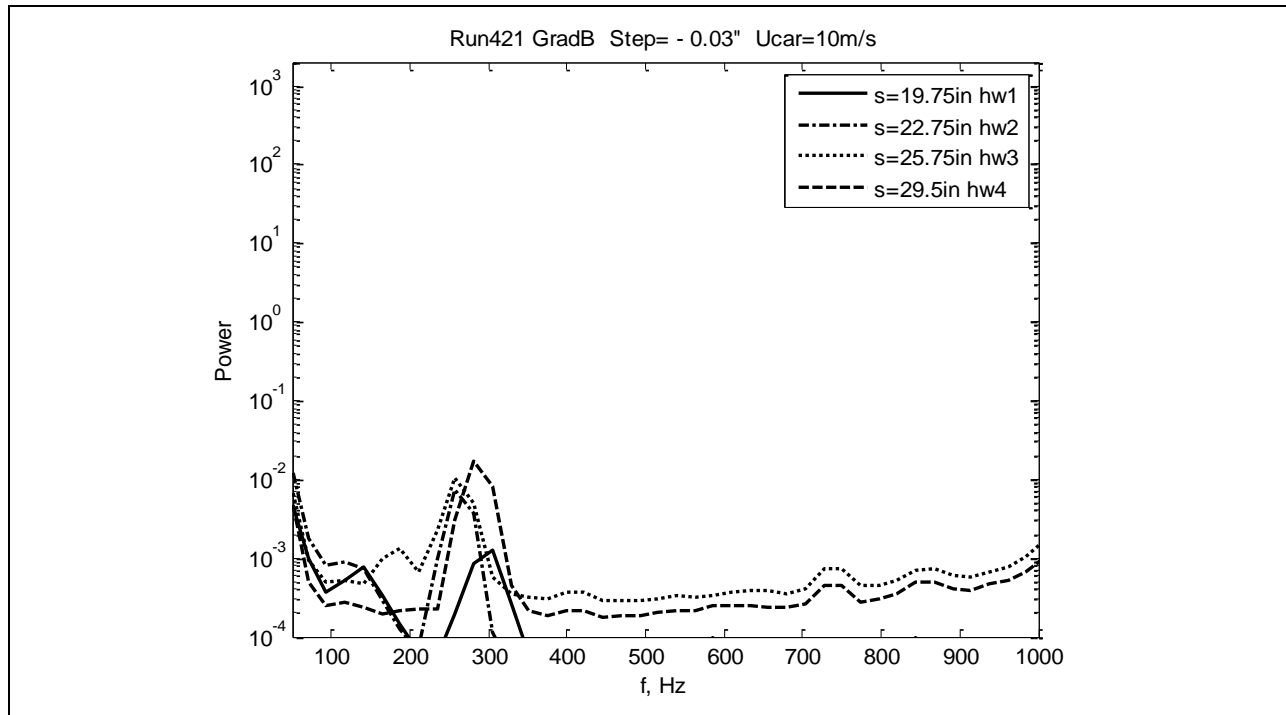


Figure 510: Measured power spectra.

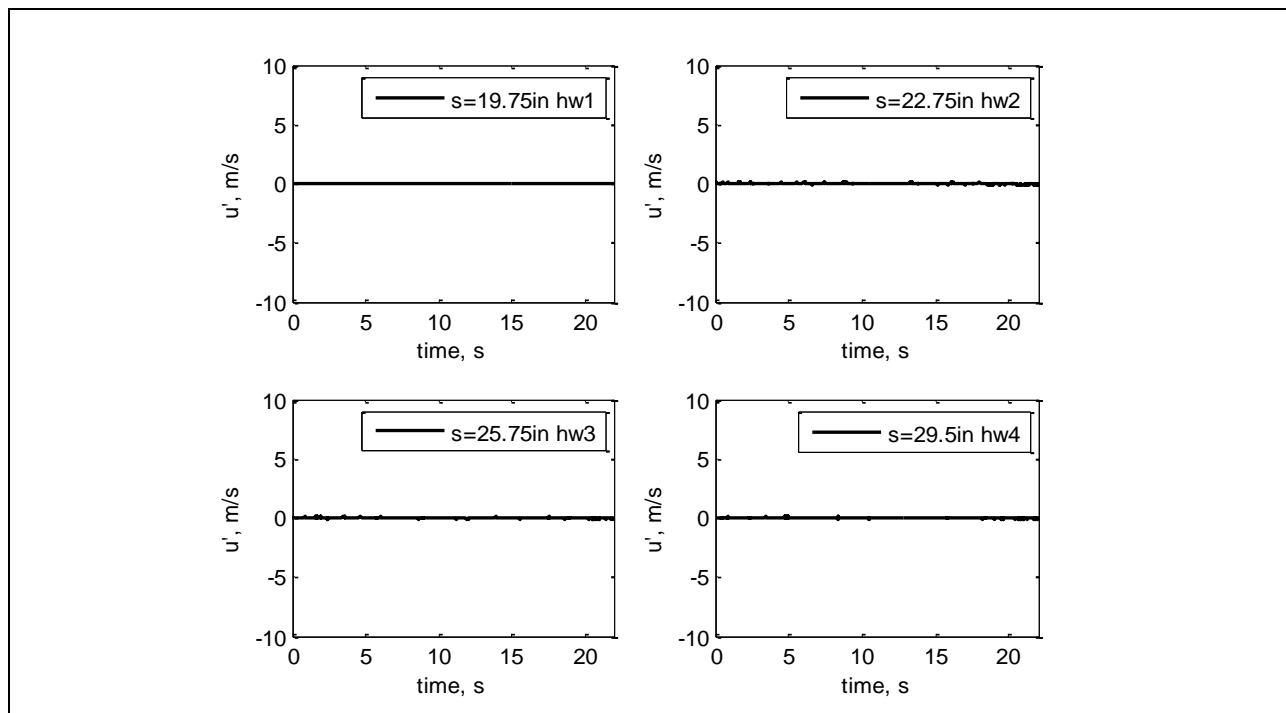


Figure 511: Measured velocity time history.

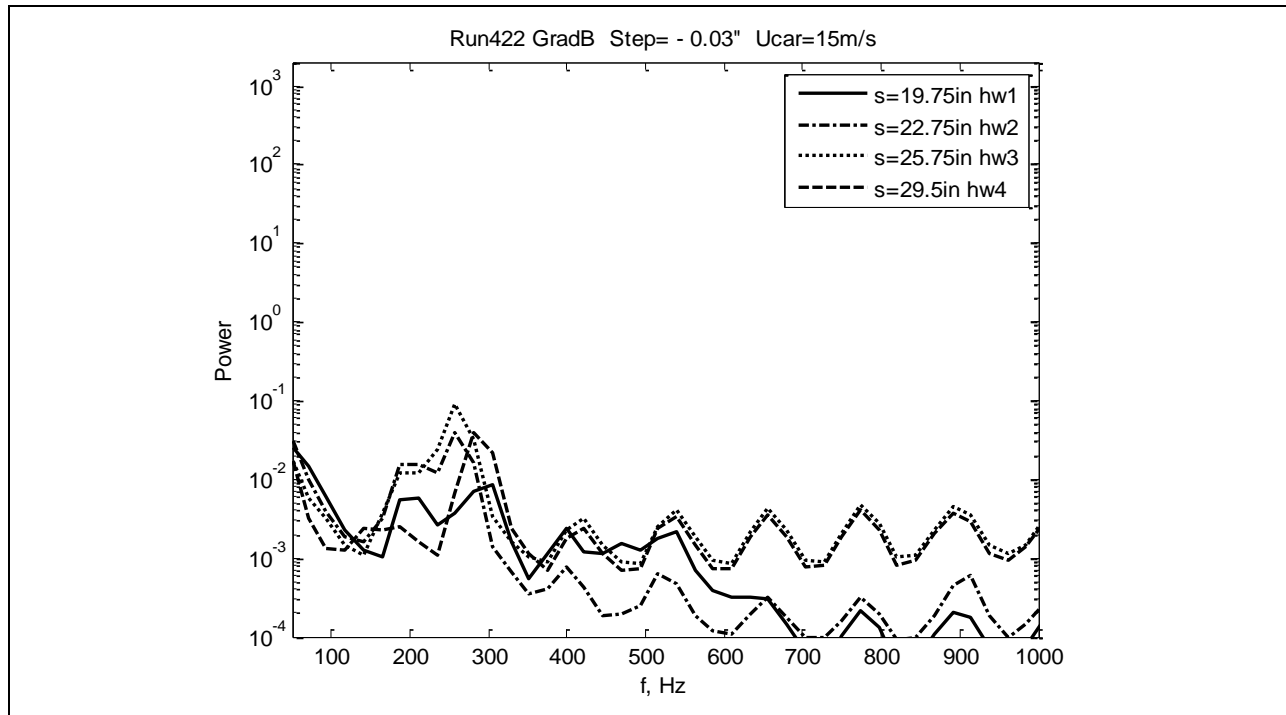


Figure 512: Measured power spectra.

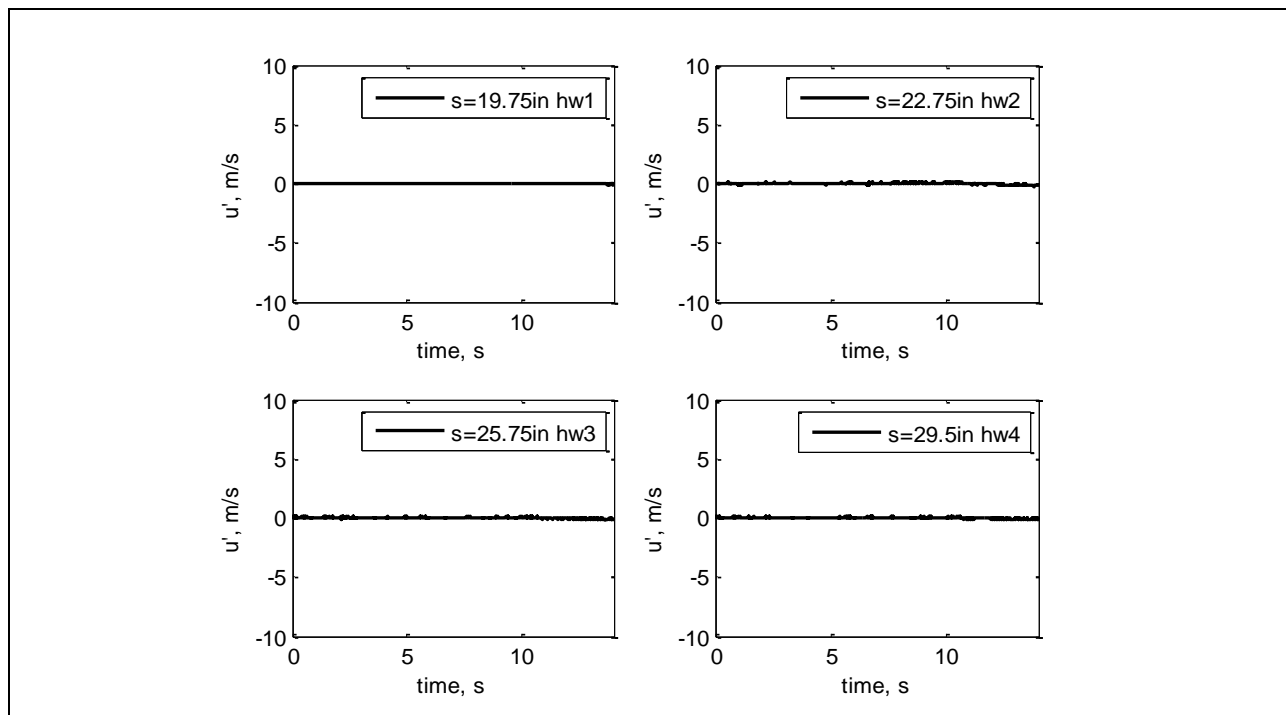


Figure 513: Measured velocity time history.

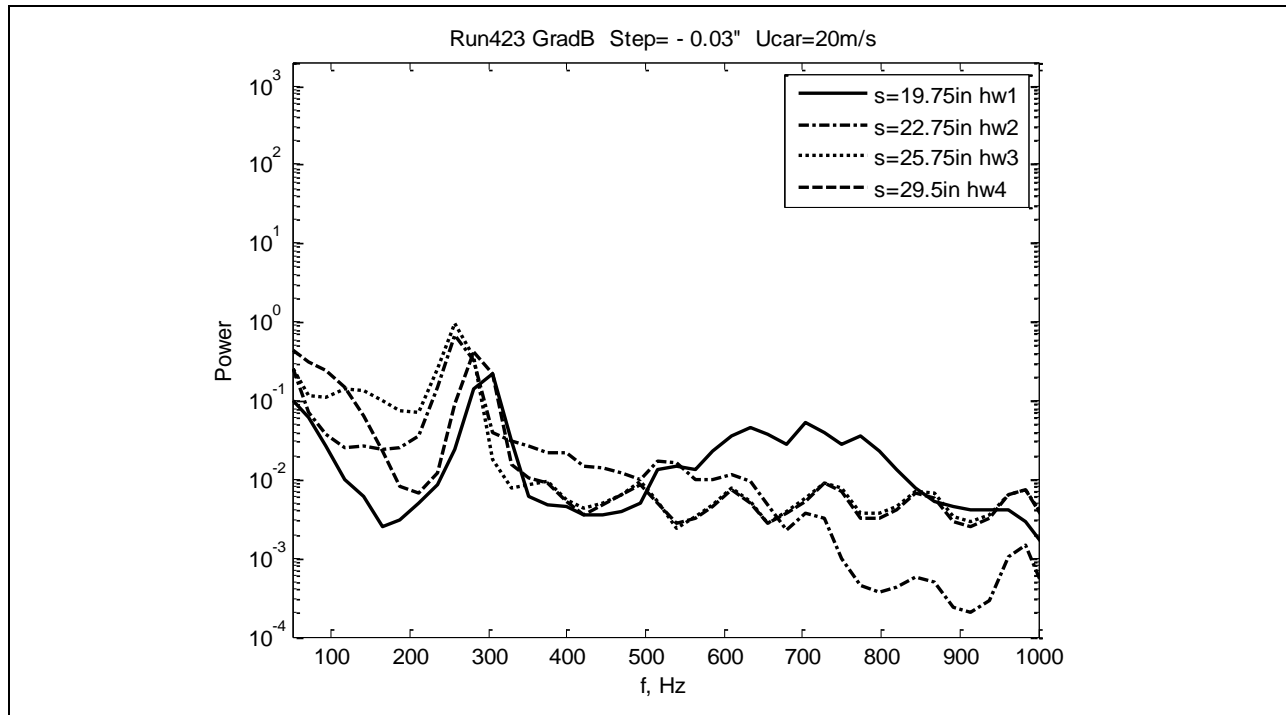


Figure 514: Measured power spectra.

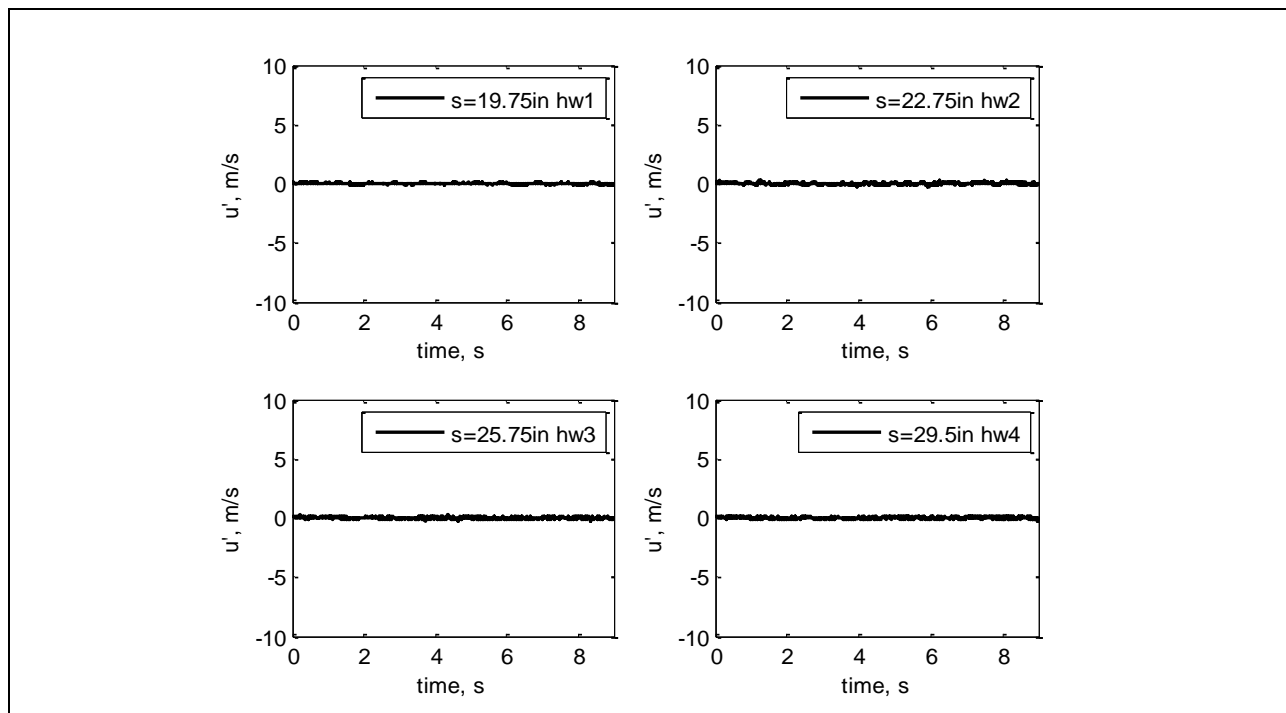


Figure 515: Measured velocity time history.

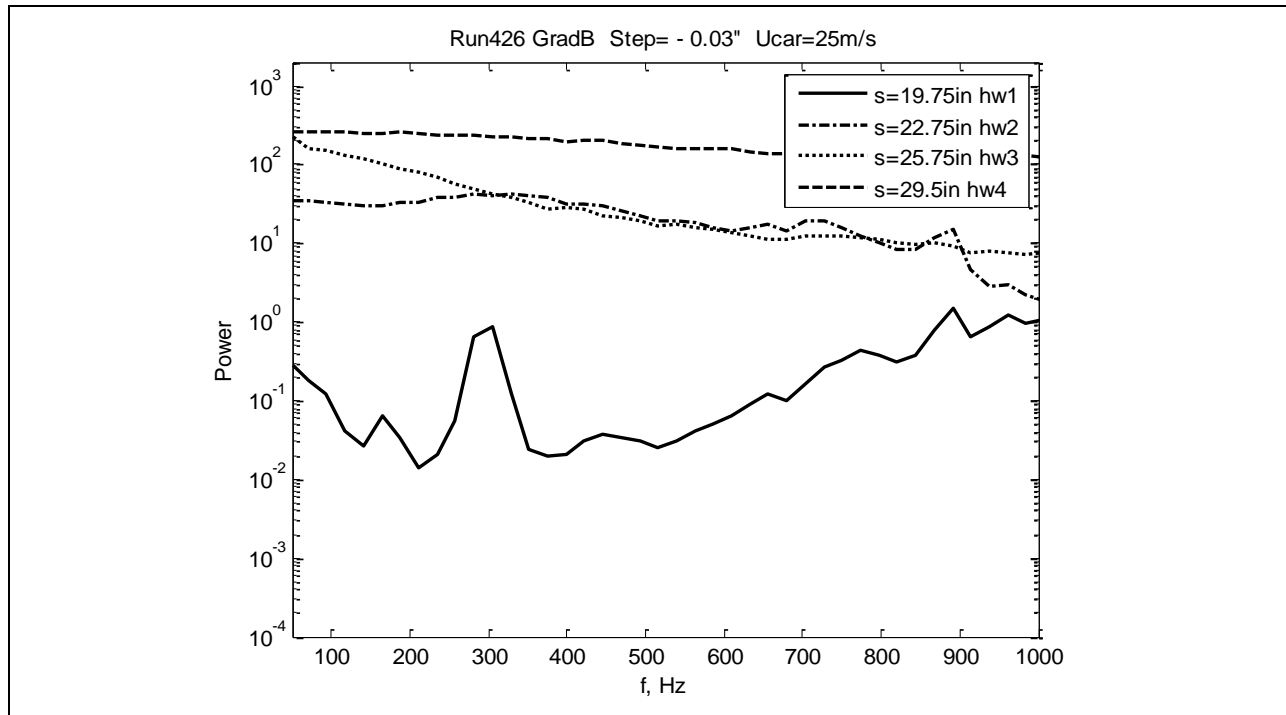


Figure 516: Measured power spectra.

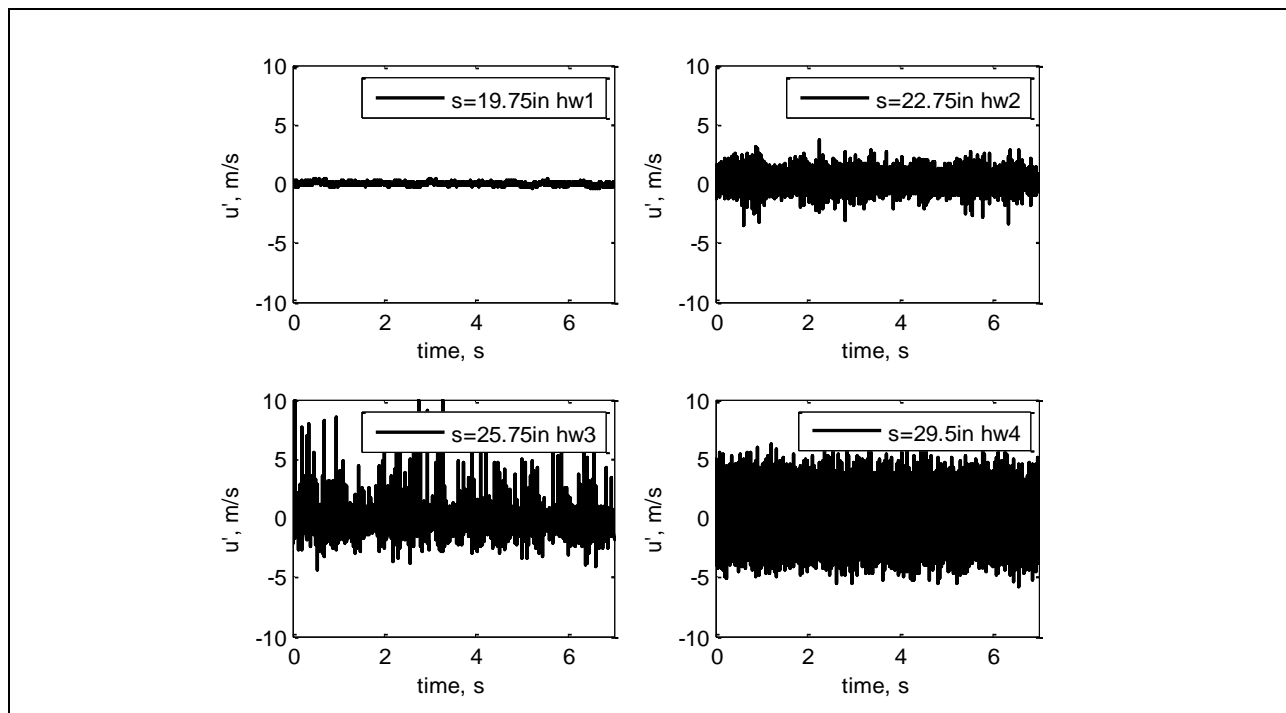


Figure 517: Measured velocity time history.

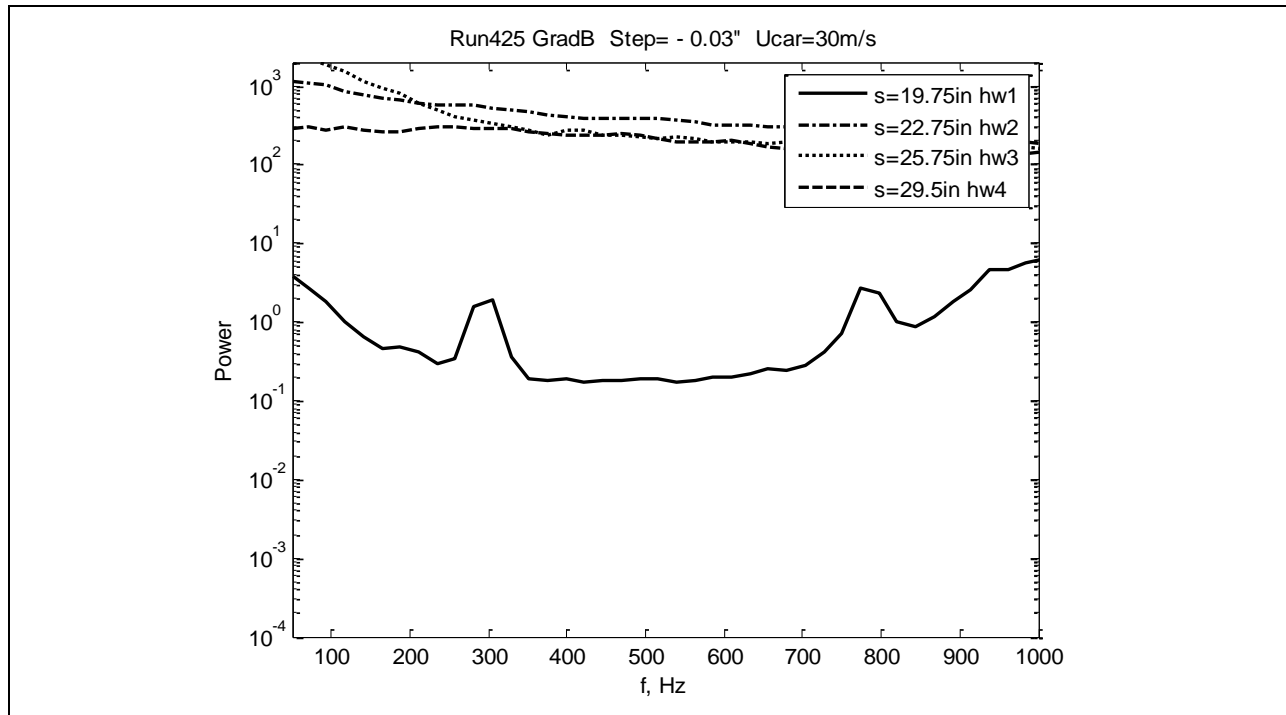


Figure 518: Measured power spectra.

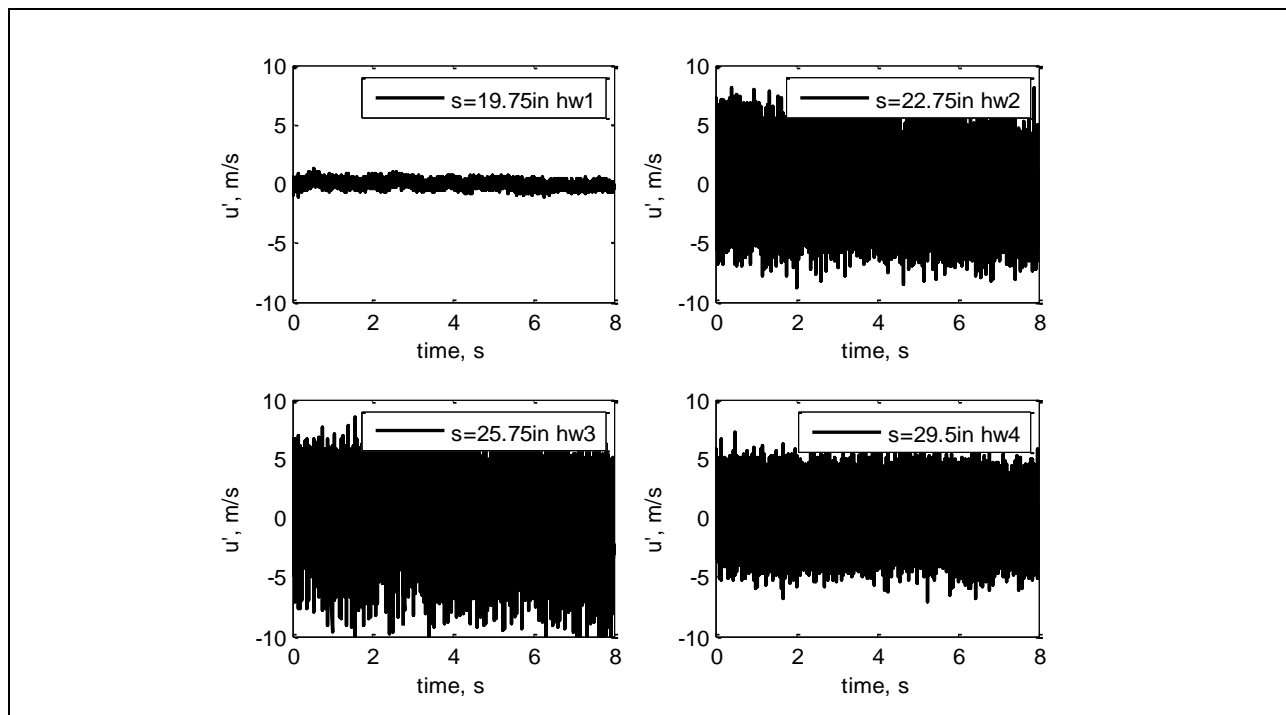


Figure 519: Measured velocity time history.

A comparison was made for Gradient-B between runs where the gap near the step location was unsealed and runs where the gap was sealed with tape.

The comparison for the car speed $U_{car}=10\text{m/s}$ was made between Run 389 (unsealed gap) (Figures 520-521) and Run 421 (gap sealed with tape) (Figures 522-523). A dramatic difference in the velocity time series and power spectra for the sealed and unsealed cases can be seen. In the next figure the comparison for higher car speed $U_{car}=15\text{m/s}$ was made between Run 388 (unsealed gap) (Figures 524-525) and Run 422 (sealed with tape gap) (Figures 526-527). It can be seen that the transition to turbulence happens at about step location for the unsealed case, whereas for the sealed case everything is laminar. The gap consequently is an additional source for disturbances. Application of the seal as it was done with tape, on the other hand, modifies the shape of the step which also influences the transition.

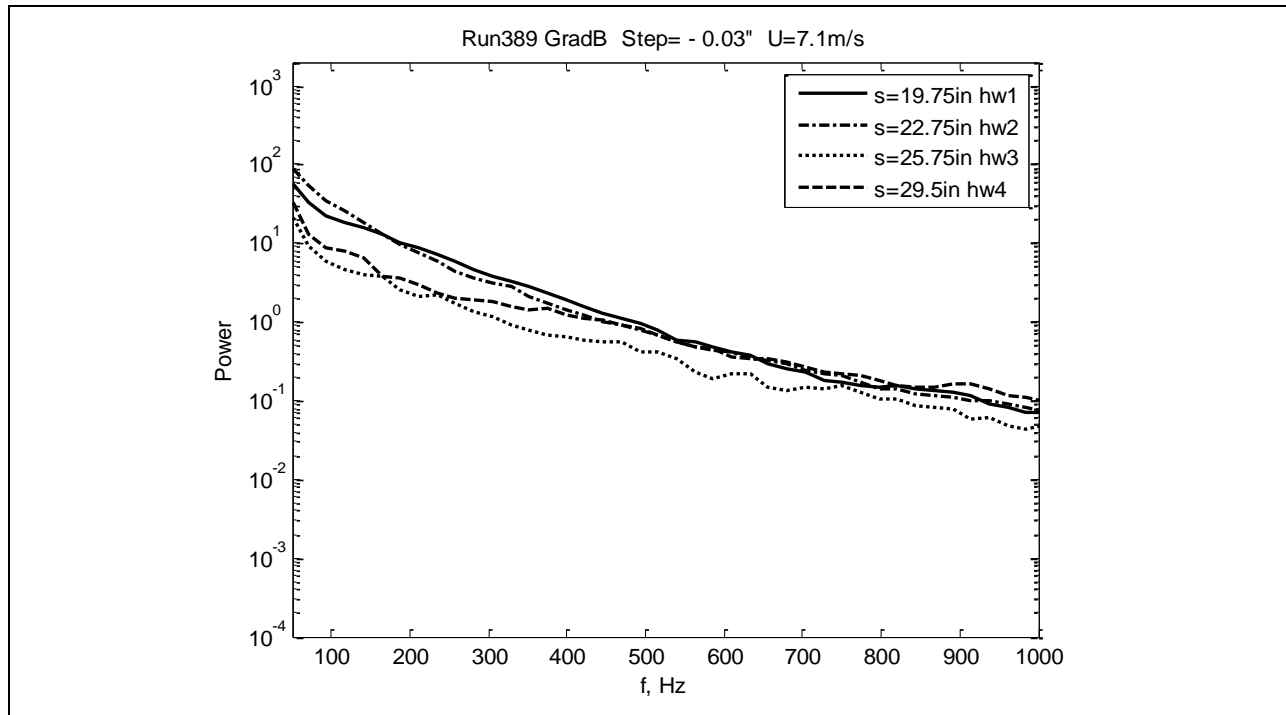


Figure 520: Measured power spectra.

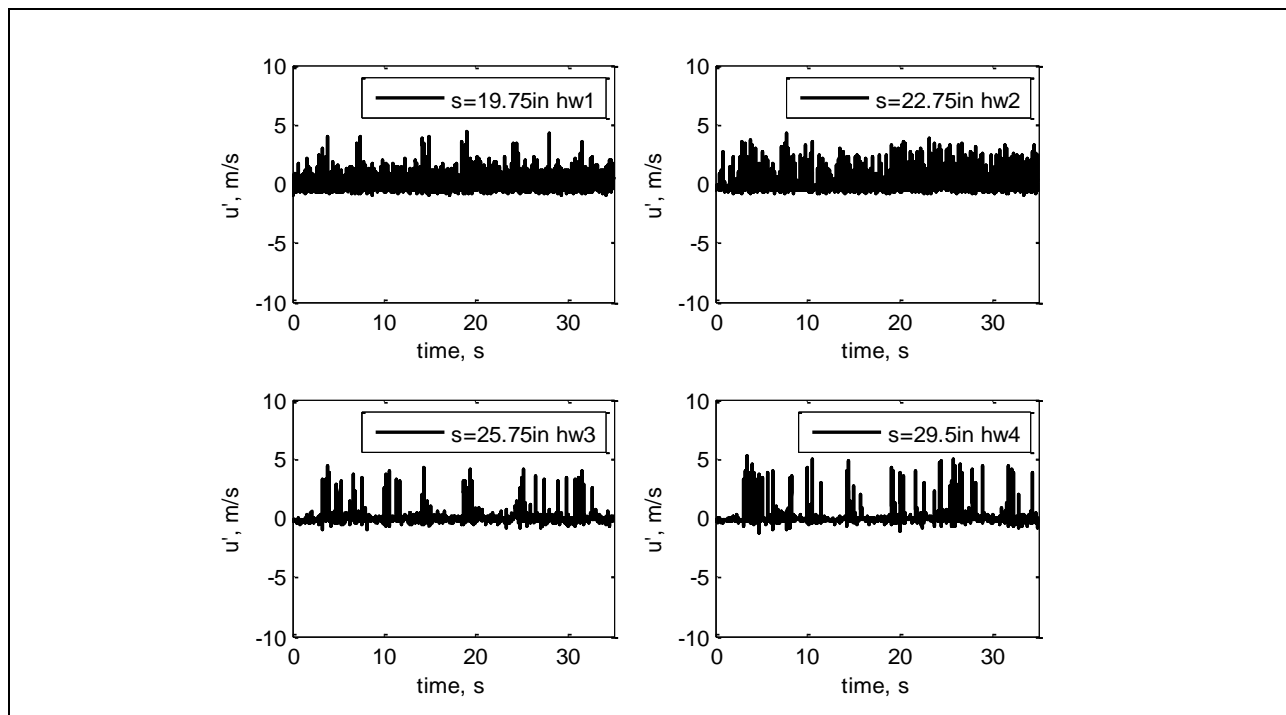


Figure 521: Measured velocity time history.

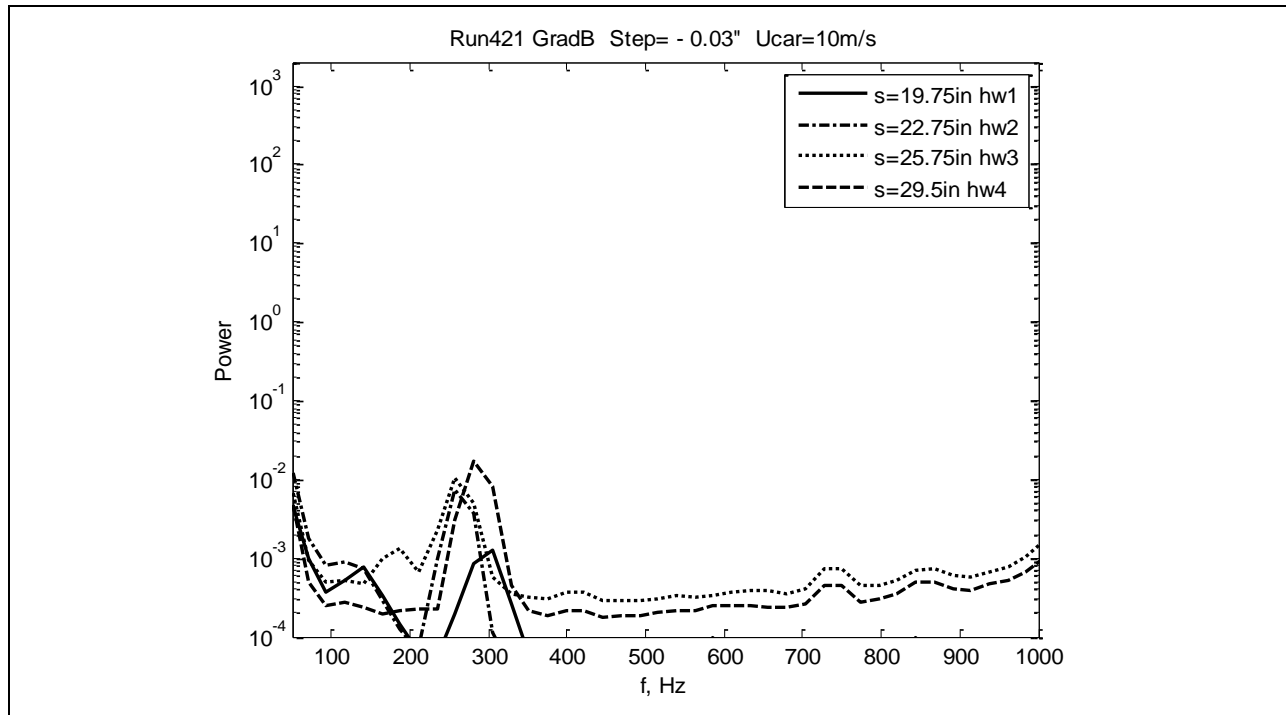


Figure 522: Measured power spectra.

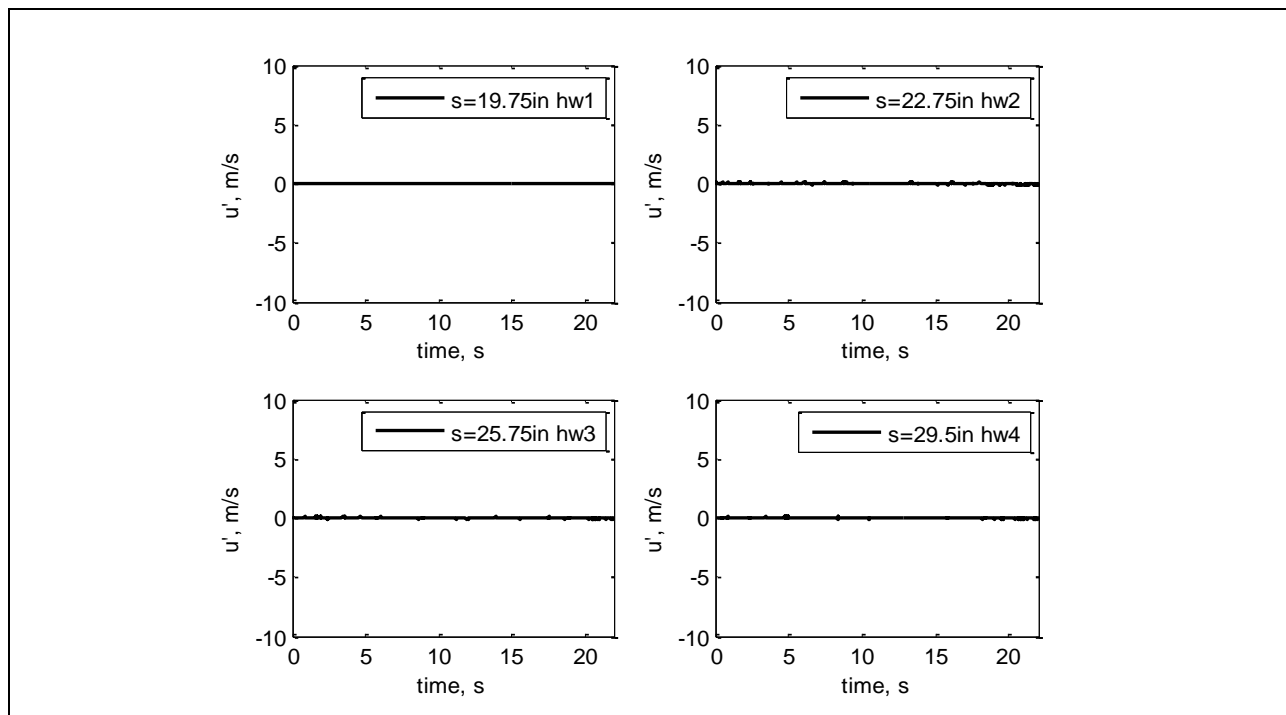


Figure 523: Measured velocity time history.

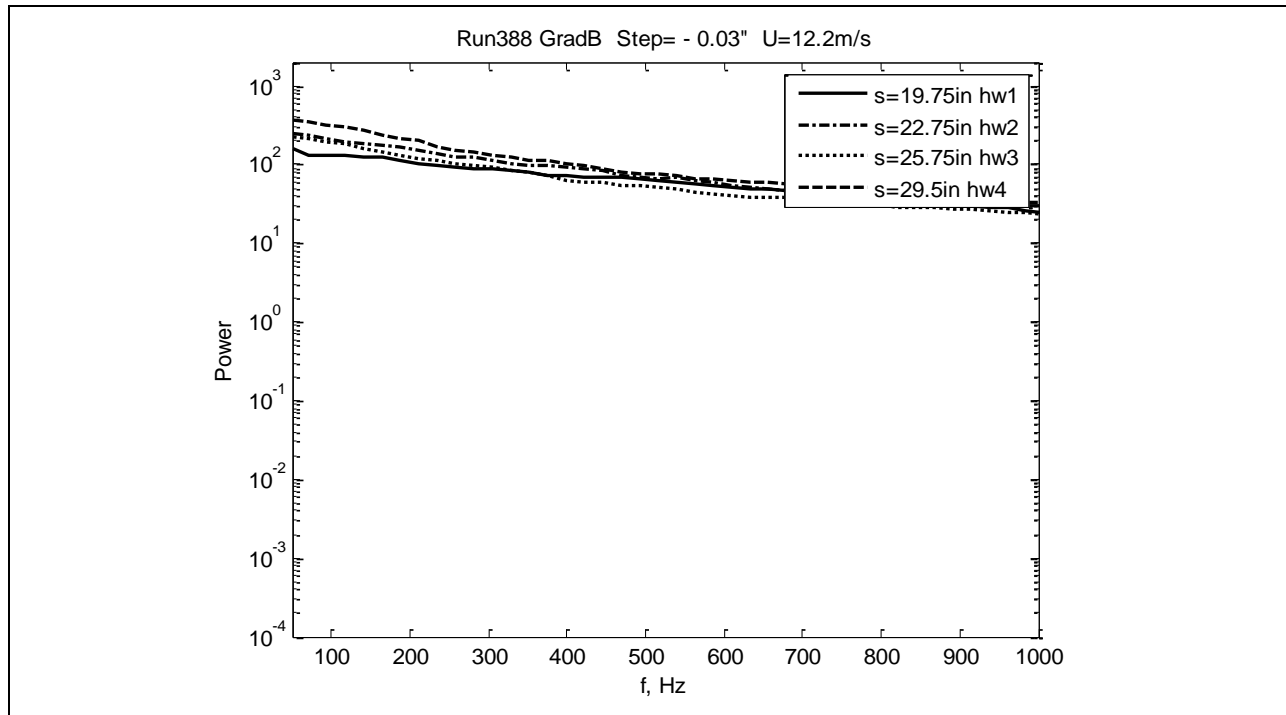


Figure 524: Measured power spectra.

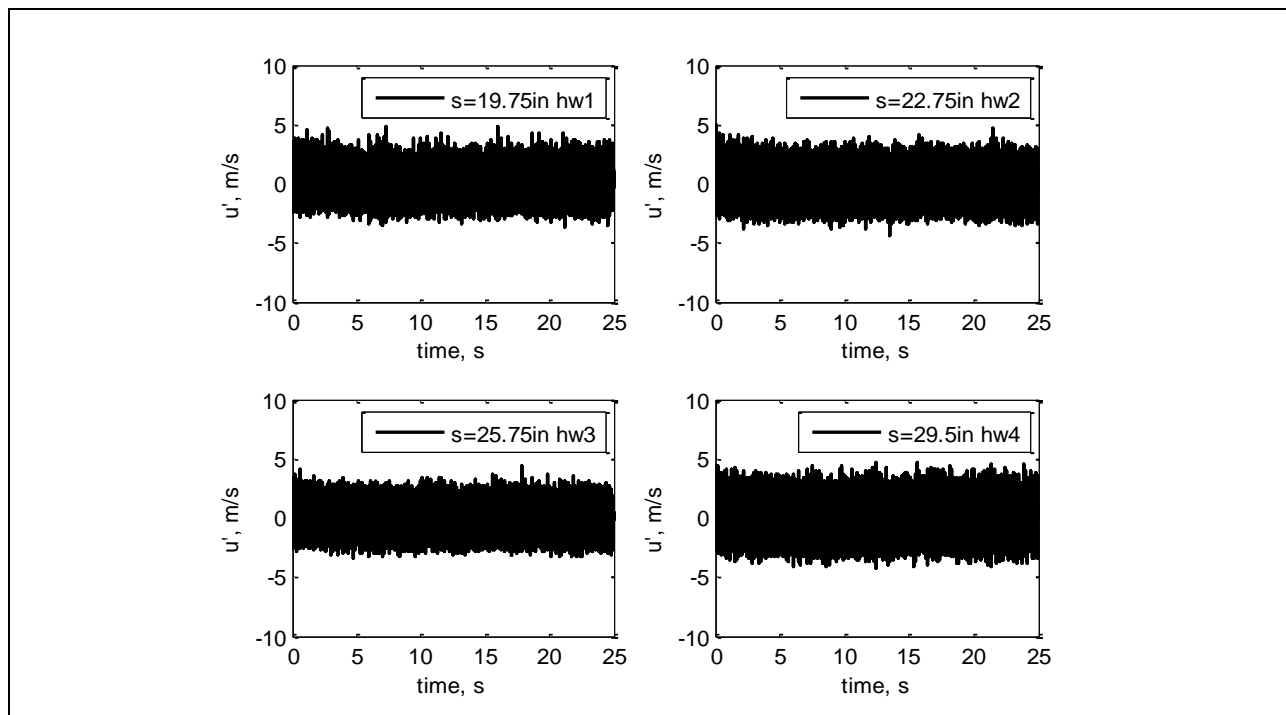


Figure 525: Measured velocity time history.

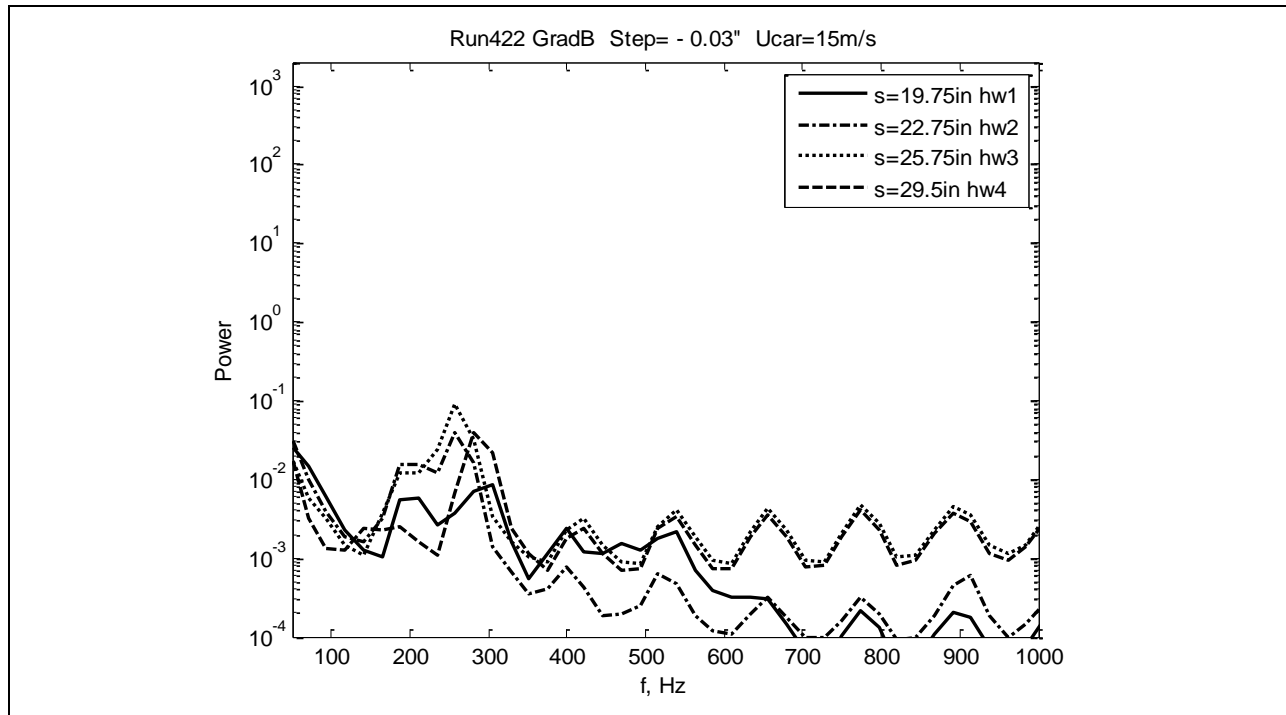


Figure 526: Measured power spectra.

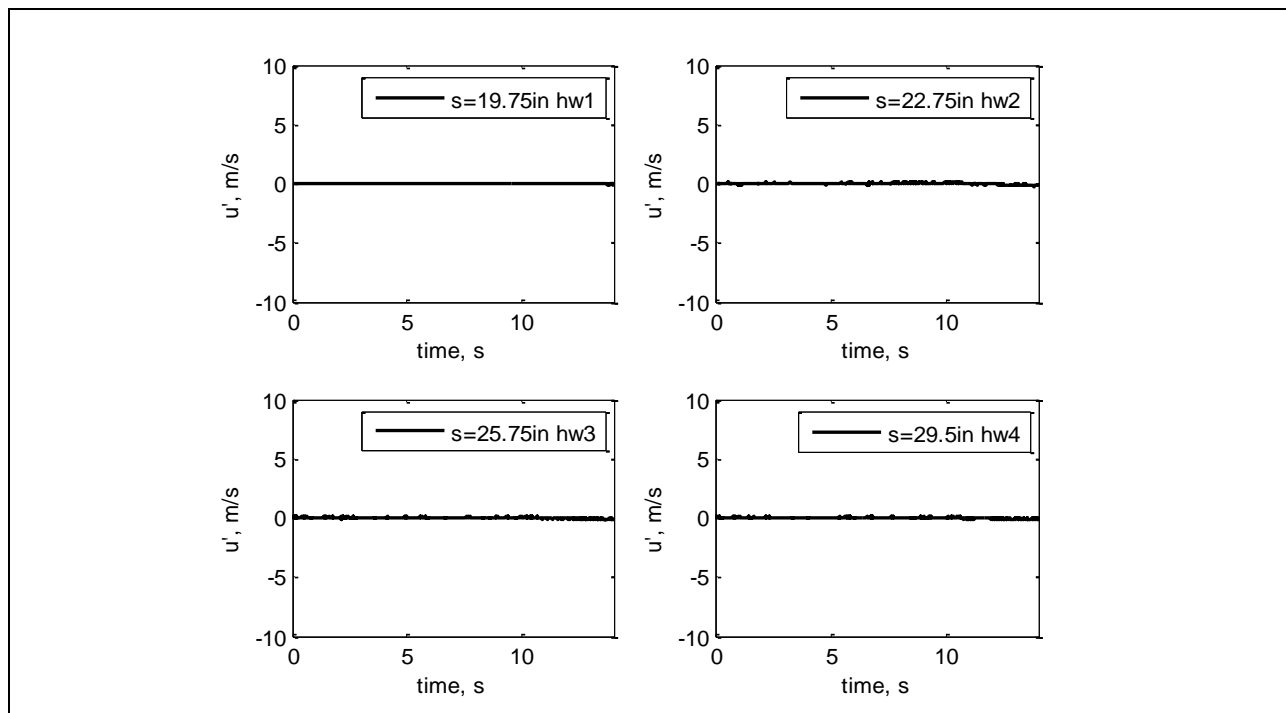


Figure 527: Measured velocity time history.

7.5.7.2

Selected Comparison of Spectra

The following three plots (Figures 528-530) show the changes in the spectra for Gradient-Zero model with freestream speed (i.e. linear stability characteristics) for three different steps.

Figure 528 shows how the peak of possible T-S waves can grow with freestream speed and shift to higher frequency. All spectra were taken at the same stream-wise position $s=27\text{in}$ and with zero step.

Figure 529 shows the same tendency for the peak as in the previous case but also shows spectrum broadening with freestream speed. All spectra were taken at the same stream-wise position $s=27\text{in}$ and with a forward-facing 0.04-inch step.

Figure 530 shows spectrum broadening with freestream speed which more pronounced than for the previous case. All spectra were taken at the same stream-wise position $s=27\text{in}$ and with an aft-facing -0.04-inch step.

It can be seen from the comparison of the three cases that the influence of the aft-facing step of -0.04-inch is more pronounced on the spectrum change than of the forward-facing step of 0.04-inch.

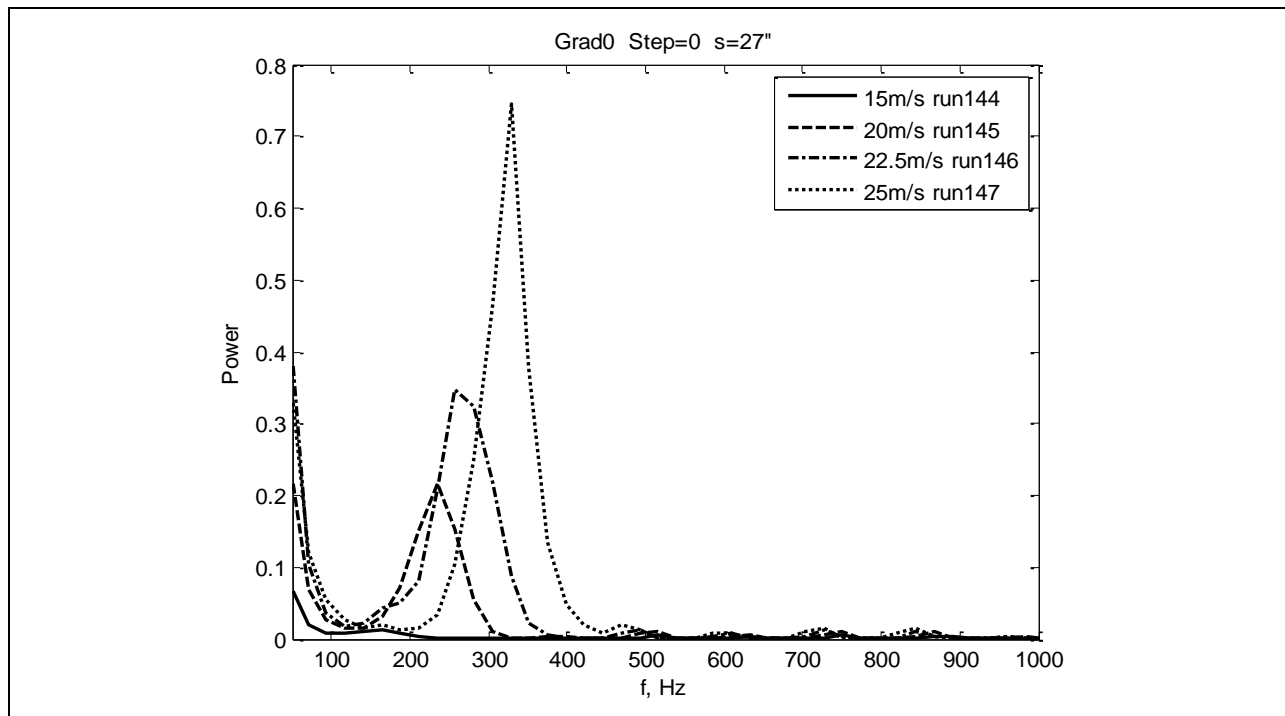


Figure 528: Measured power spectra.

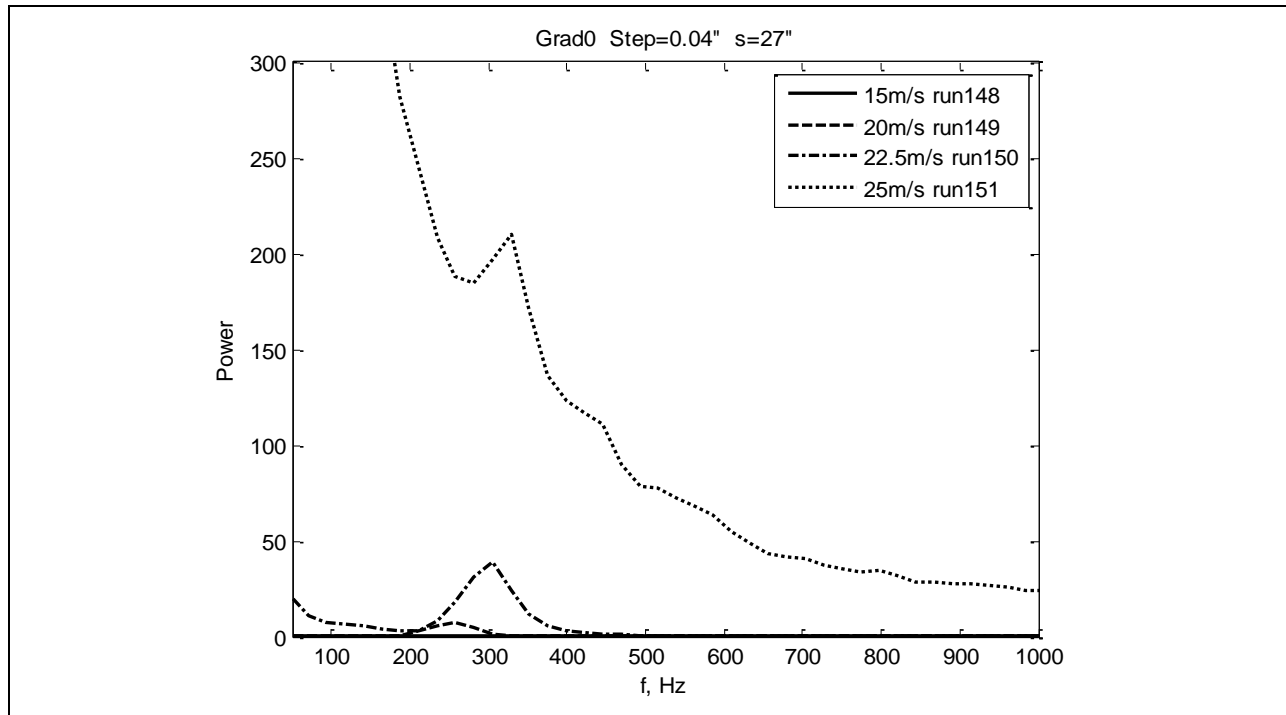


Figure 529: Measured power spectra.

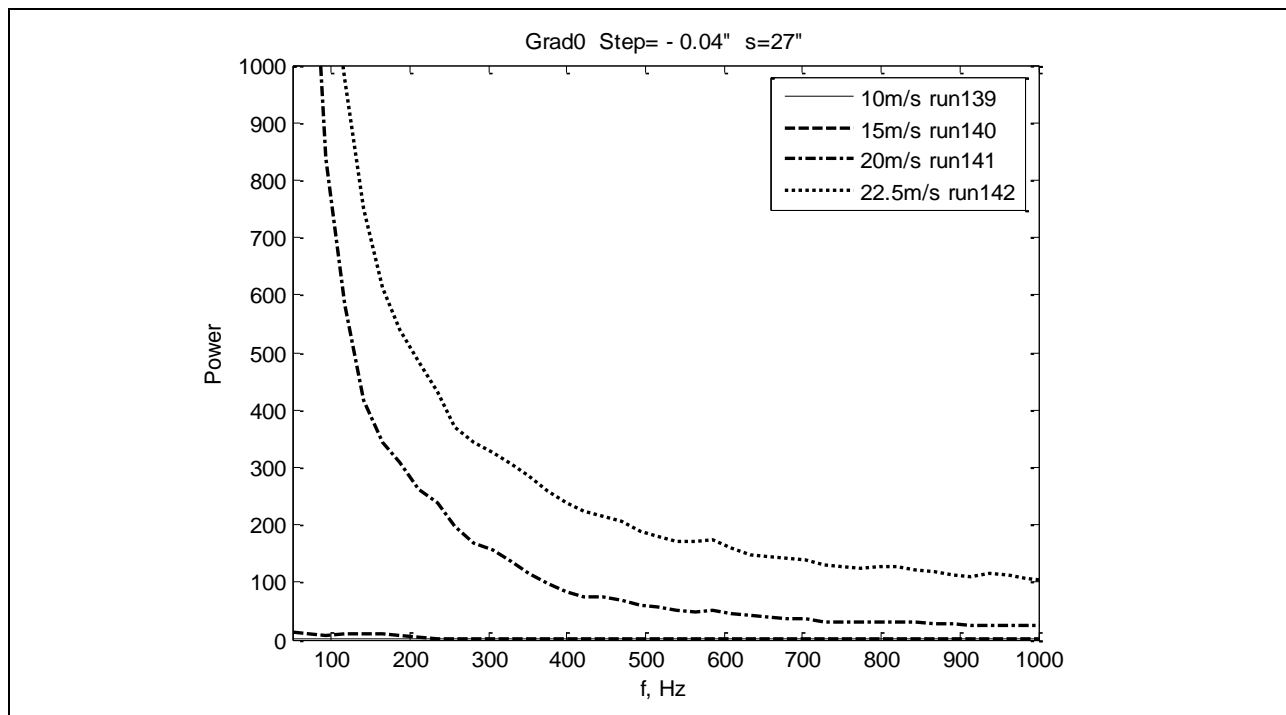


Figure 530: Measured power spectra.

The following plot (Figure 531) shows the changes in the spectra for the Gradient-Zero model for three different steps at the same freestream speed and stream-wise position. The spectrum for the aft-facing step of -0.04in is much broader than for either the zero step or the forward-facing step of 0.04in.

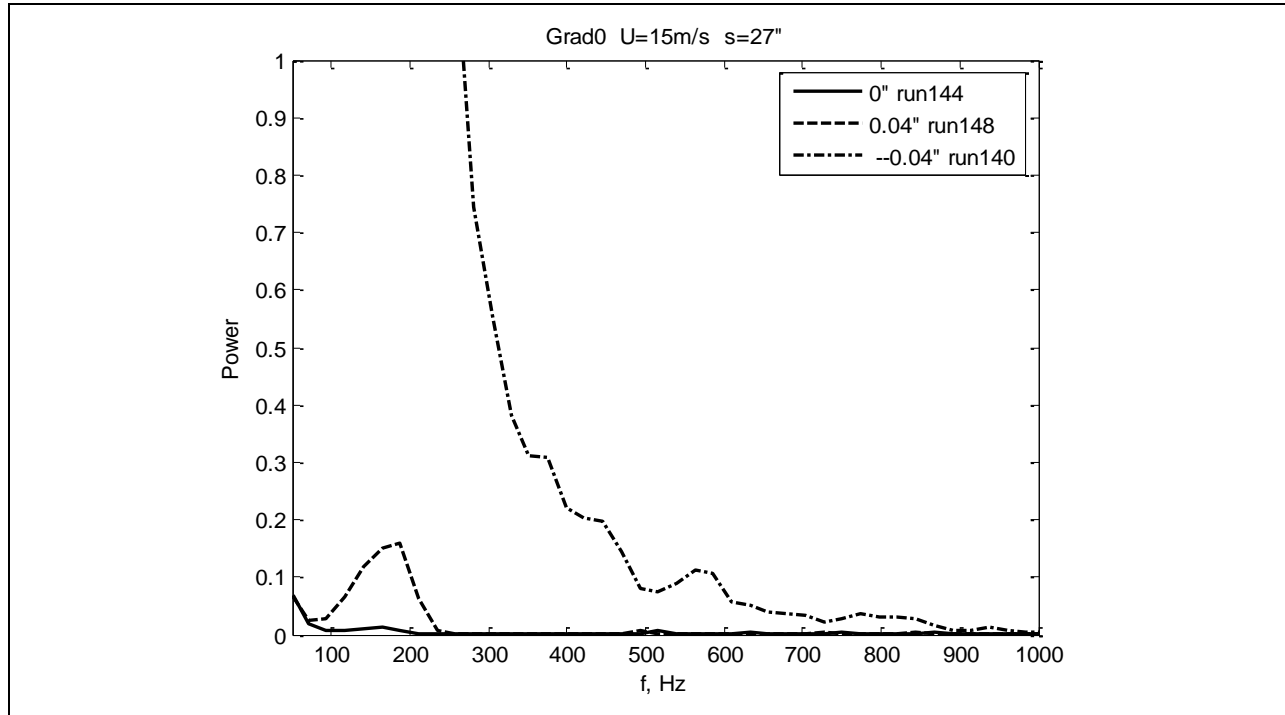


Figure 531: Measured power spectra.

The following plot (Figure 532) shows how the peak corresponding to possible T-S waves can grow, decay and shift in frequency with increase of stream-wise distance. All spectra were taken for the same Gradient-Zero model, at the same free stream speed of $U=17.3\text{m/s}$ and at the same step height.

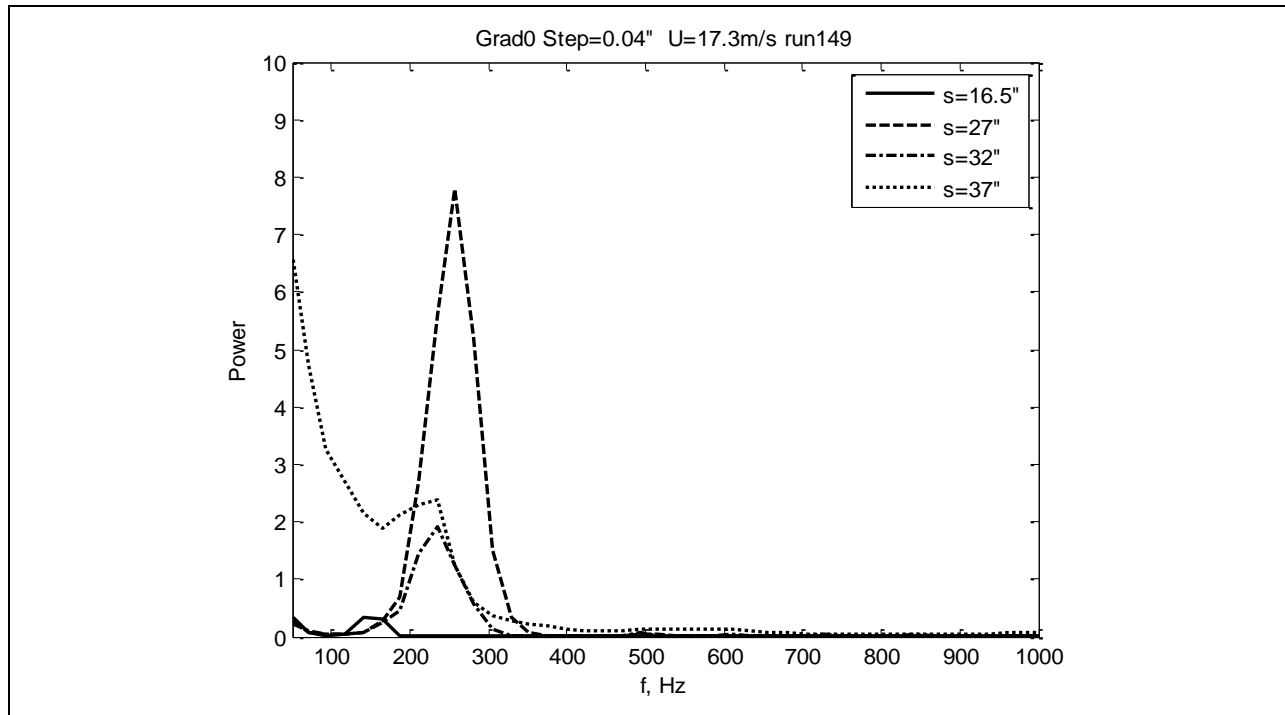


Figure 532: Measured power spectra.

The following three plots (Figures 533-535) show the changes in the spectra for the Gradient-A model with freestream speed for three different step cases.

Figure 533 shows how peak of possible T-S wave can grow with freestream speed. There are negligible shifts in frequency as compared with Gradient-Zero shown above. All spectra were taken at the same stream-wise position $s=36.5$ in and with zero step.

Figure 534 shows the same tendency for the peak as in the previous case but also shows spectrum broadening with freestream speed. All spectra were taken at the same stream-wise position $s=36.5$ in and with the aft-facing -0.04-inch step.

Figure 535 shows similar tendency for spectrum but for a forward-facing 0.065-inch step.

It can be seen from comparison of the three cases that influence of the aft-facing step -0.04-inch is even more pronounced on the spectrum than of the larger forward-facing step of 0.065-inch.

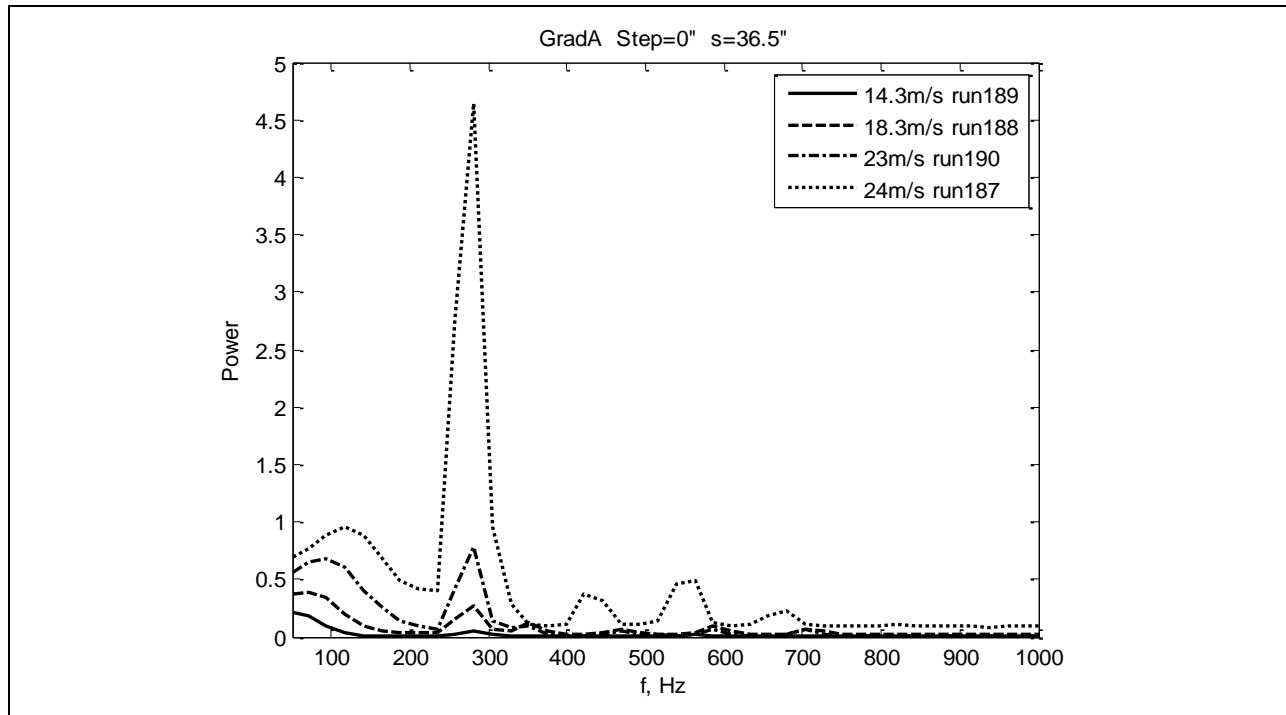


Figure 533: Measured power spectra.

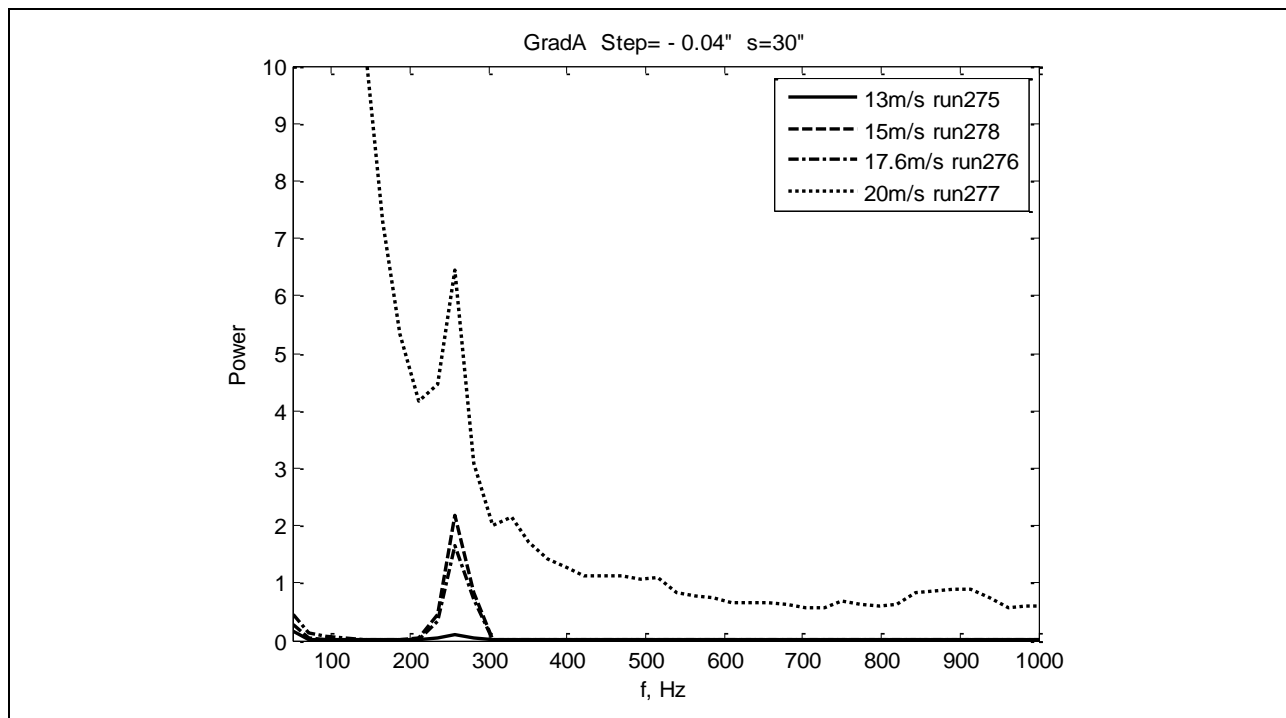


Figure 534: Measured power spectra.

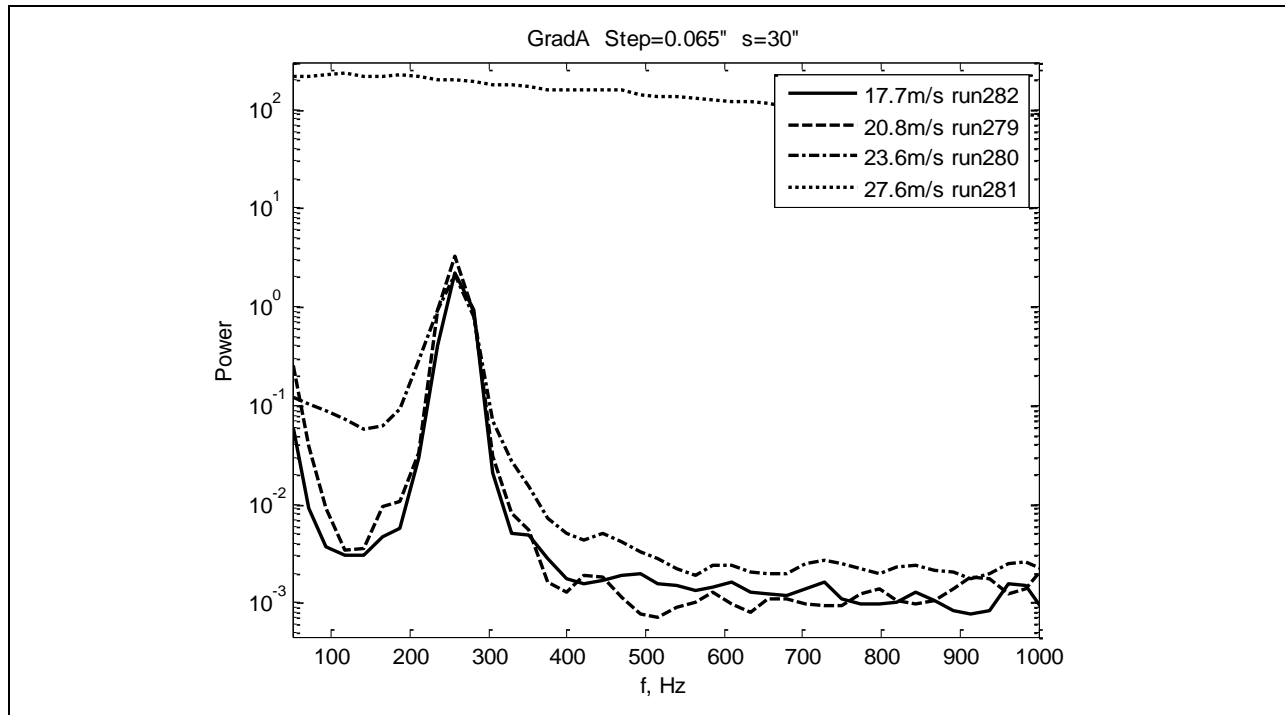


Figure 535: Measured power spectra.

The following two plots (Figures 536-537) show comparison of spectra for Gradient-A for two different steps (0.065-inch and -0.04-inch) at the same freestream speed.

Figure 536 shows the $s=30$ in stream-wise position. Figure 537 shows $s=44$ in. For the smaller distance ($s=30$ in), the spectra are the same for different steps, but with the increase of distance ($s=44$ in), the aft-facing step of 0.04in shows a broader spectrum than the forward-facing step of 0.065in.

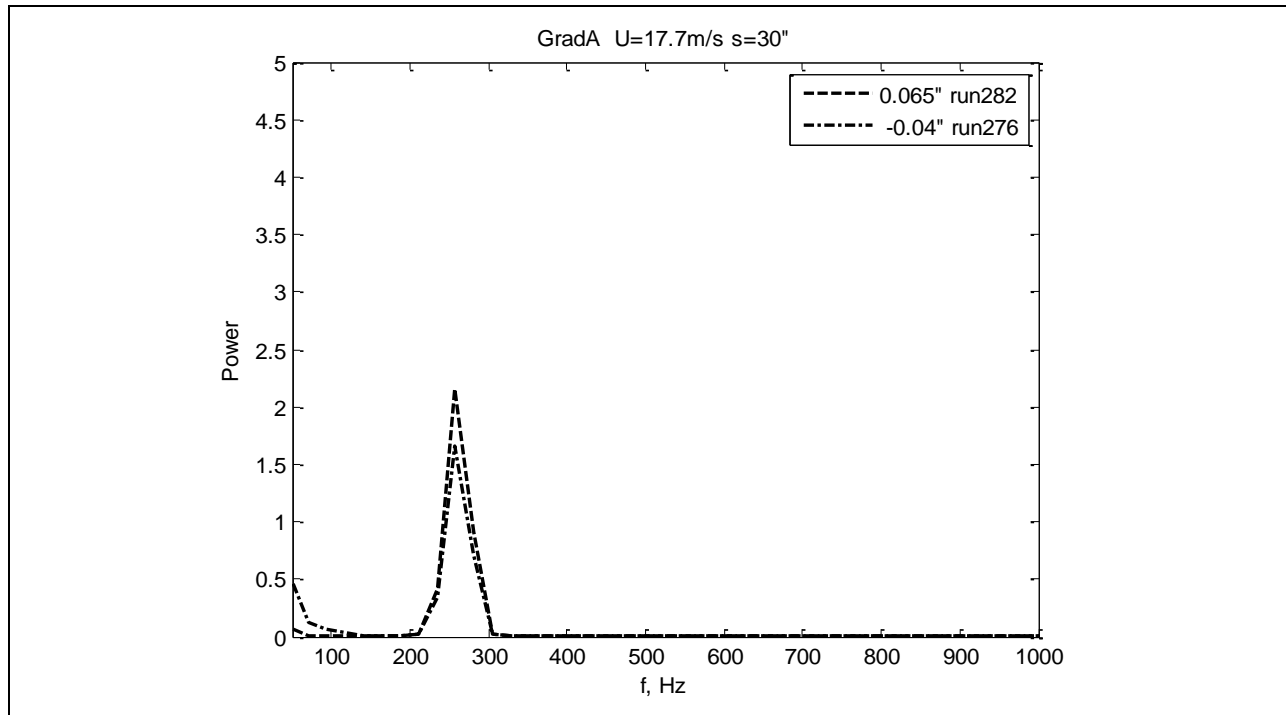


Figure 536: Measured power spectra.

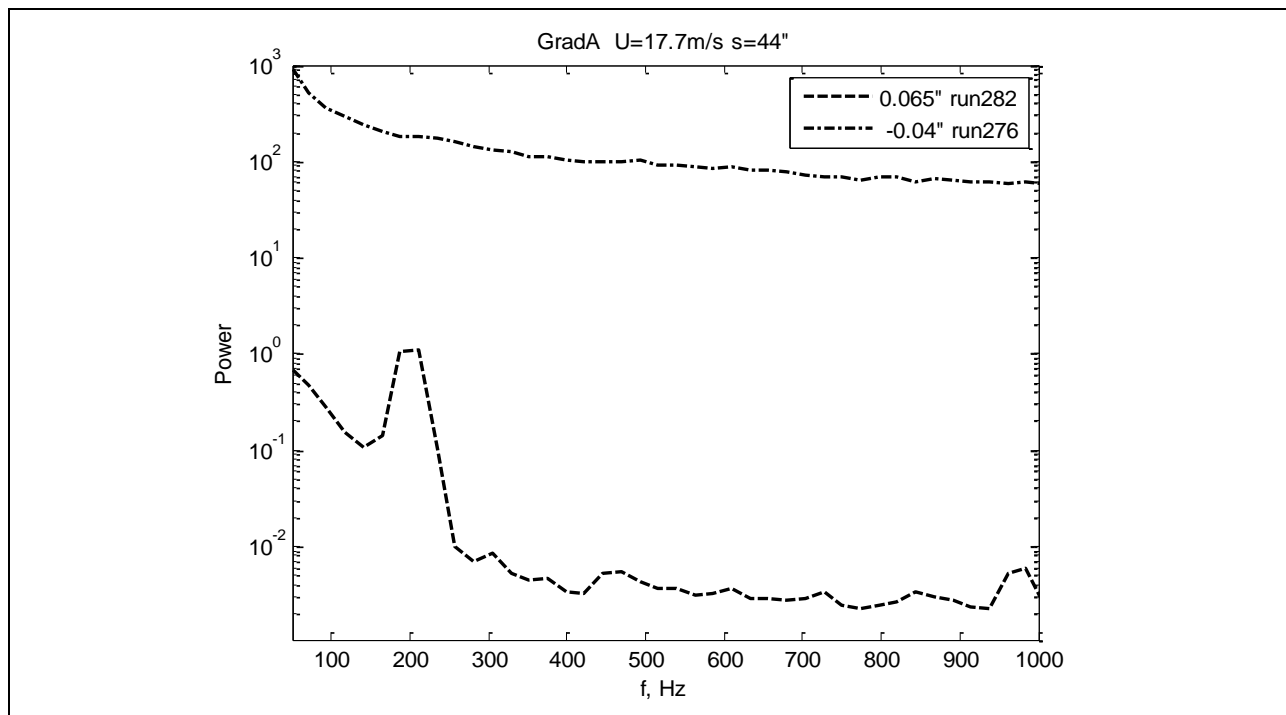


Figure 537: Measured power spectra.

The following three plots (Figures 538-540) show how the spectrum changes with the increase of stream-wise distance for three different cases. First is a forward-facing step of 0.065in at $U=17.7\text{m/s}$. Second is an aft-facing step of -0.04in and $U=13\text{m/s}$. Third is an aft-facing step of -0.04 and $U=17.6\text{m/s}$. The shift to lower frequency is observed with increase of stream-wise distance and more pronounced effect of the aft-facing step is also shown.

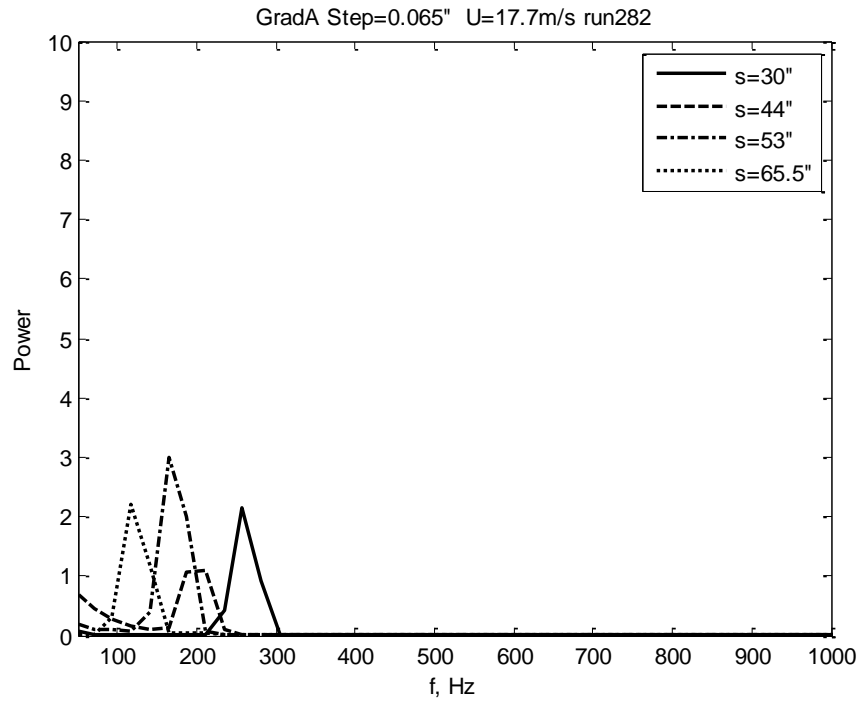


Figure 538: Measured power spectra.

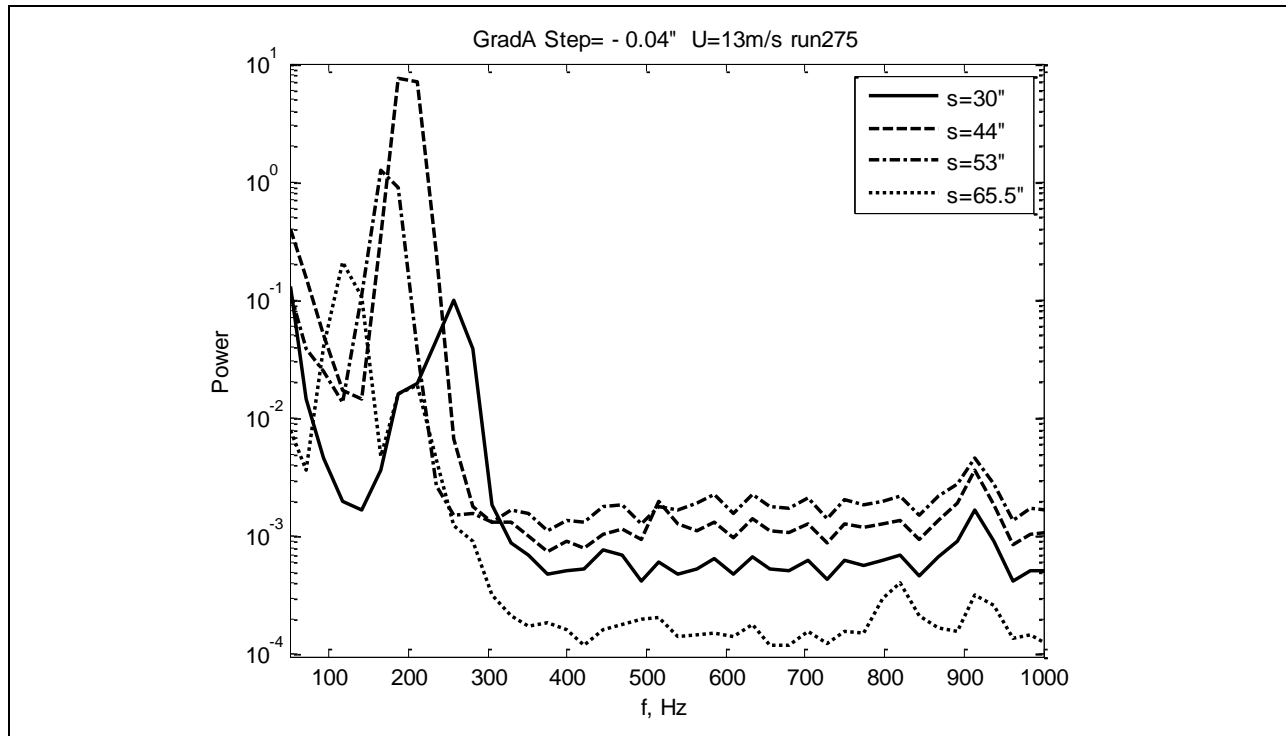


Figure 539: Measured power spectra.

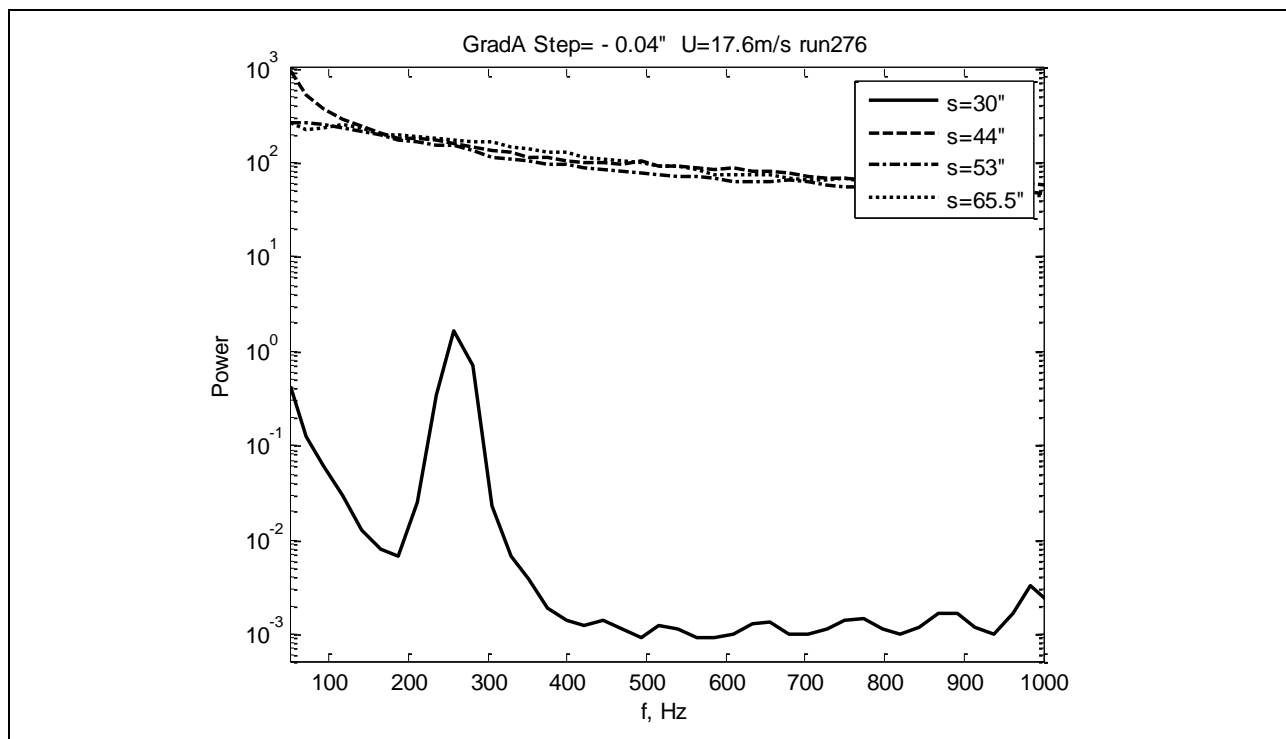


Figure 540: Measured power spectra.

Spectra comparison of the Gradient-Zero and Gradient-A models are given in the following eight plots (Figures 541-548).

Run 147 and Run 190 compare Gradient-Zero and Gradient-A for similar speeds and zero step. Spectra for both are similar, except the range of possible T-S waves for Gradient-Zero is 300-350Hz and for Gradient-A is 250-300Hz. Both runs show laminar flow for all hot-wires.

Run 140 and Run 275 compare Gradient-Zero and Gradient-A for similar speeds and an aft-facing -0.04in step. Spectrum broadening is observed for Gradient-Zero whereas for Gradient-A all spectra show laminar flow with well-distinguished possible T-S waves in the range 100-300Hz.

Run 149 and Run 282 compare Gradient-Zero with a smaller forward-facing step of 0.04in to Gradient-A with a larger forward-facing step of 0.065in for approximately the same freestream velocity. The tendency can be seen in the broadening of the spectrum which happens earlier for Gradient-Zero, even though the step height is smaller for this model than for Gradient-A.

Run 150 and Run 279 compare the same as for previous case but for higher freestream velocity.

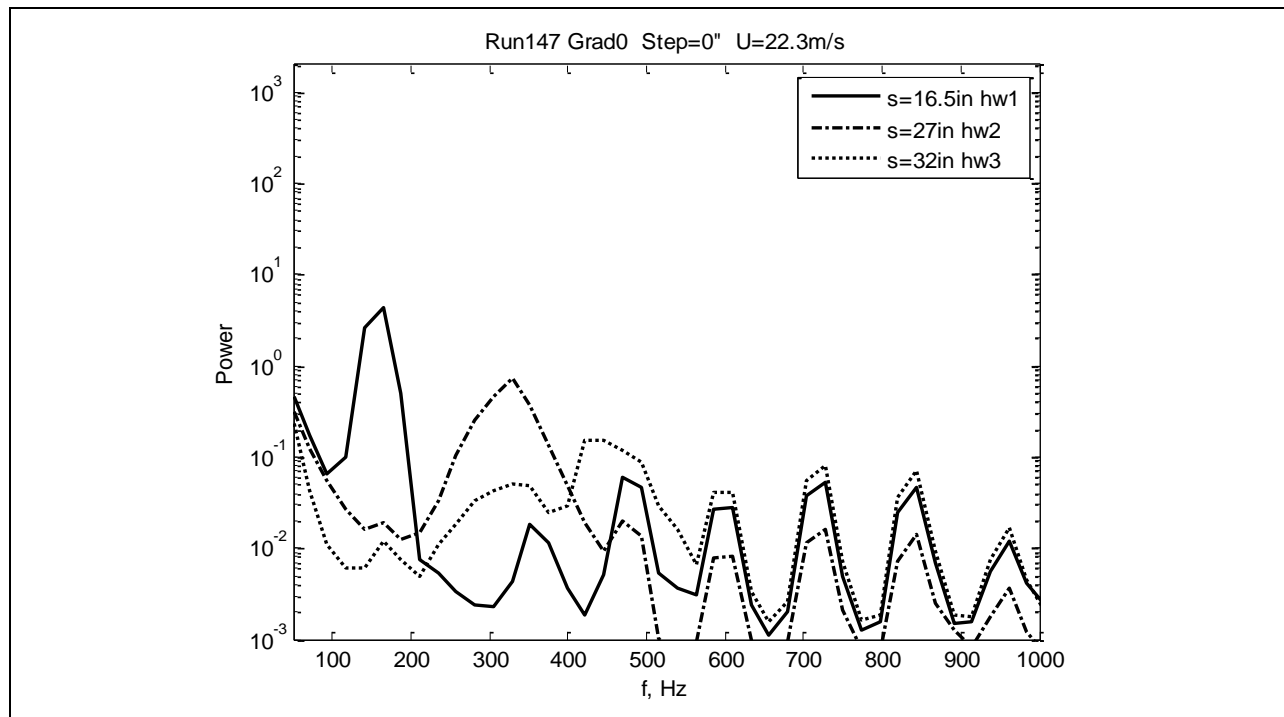


Figure 541: Measured power spectra.

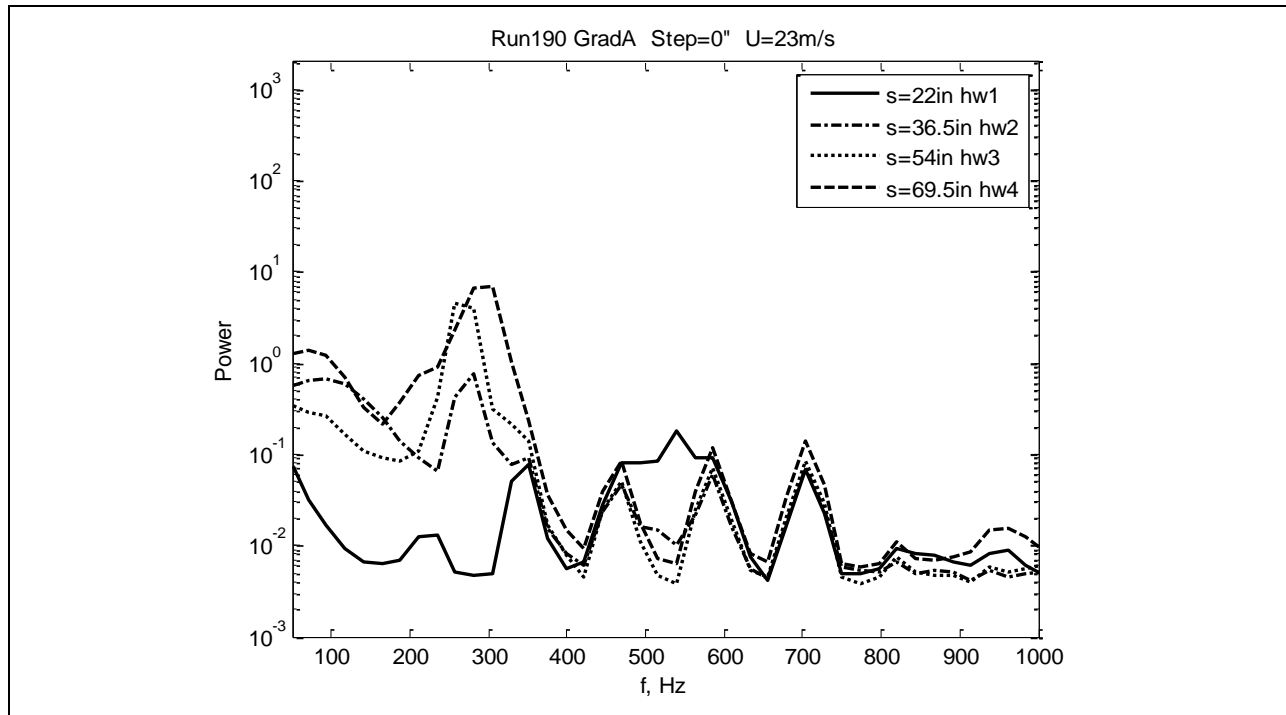


Figure 542: Measured power spectra.

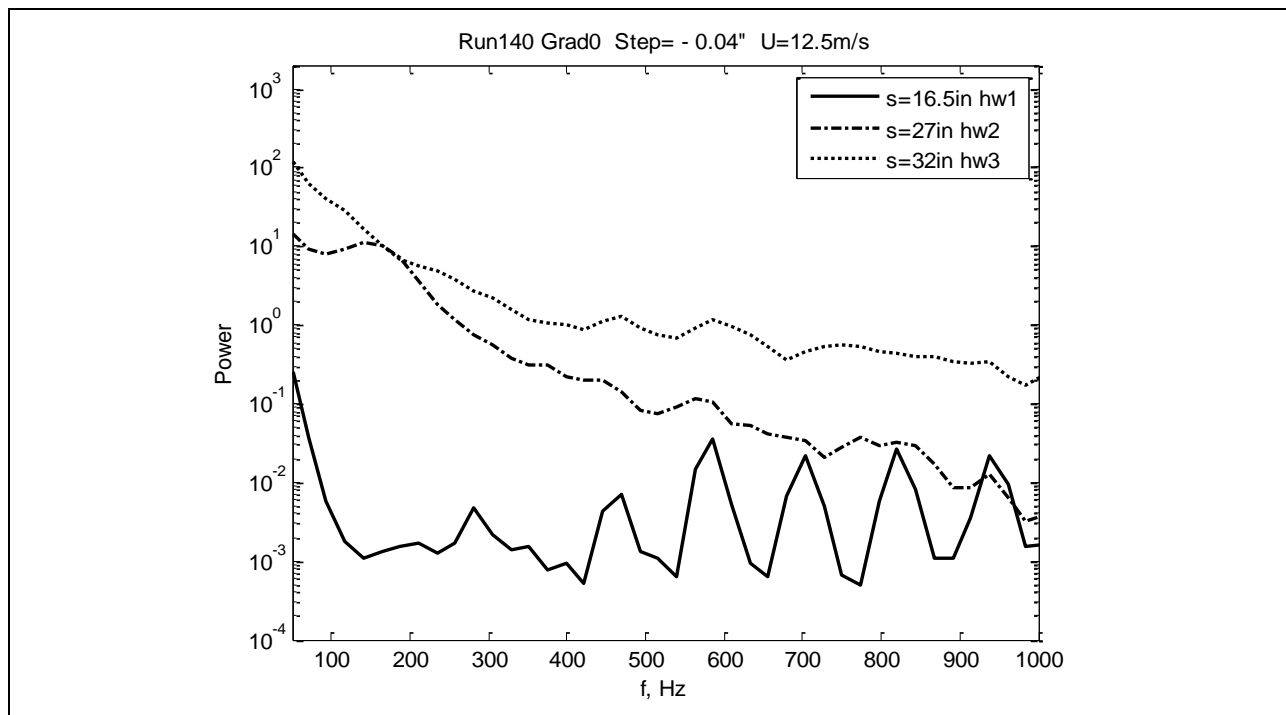


Figure 543: Measured power spectra.

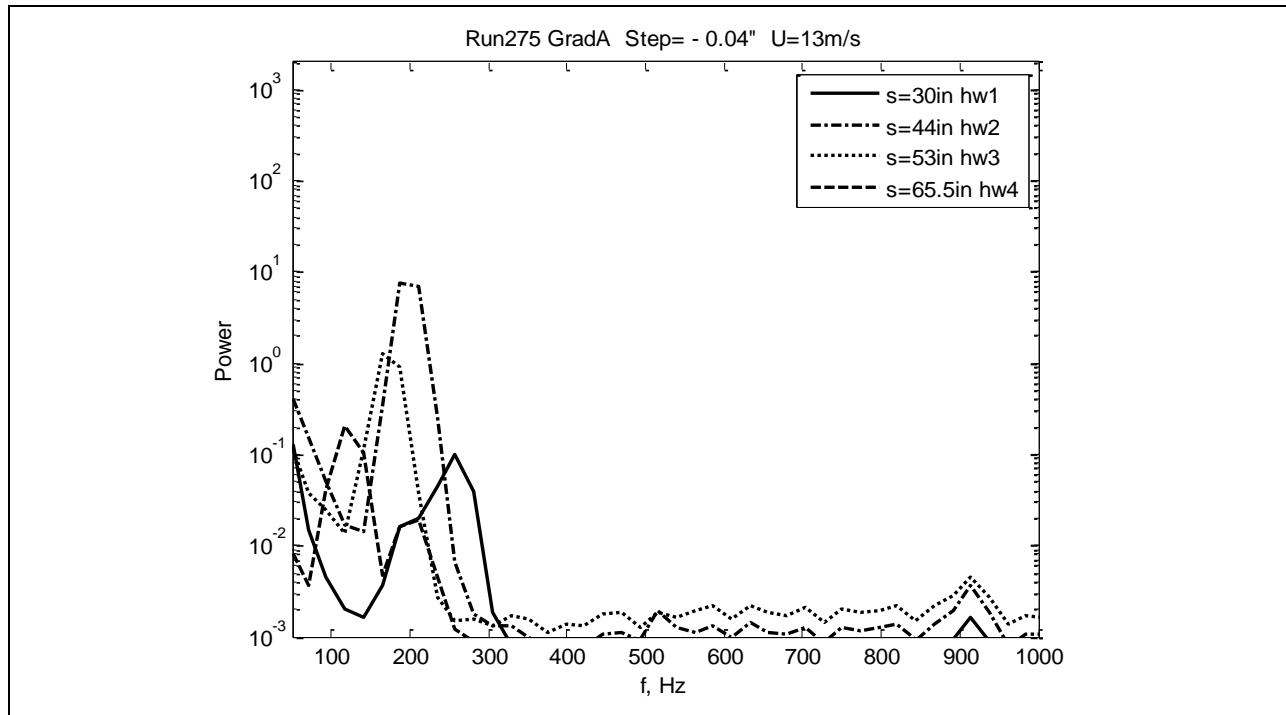


Figure 544: Measured power spectra.

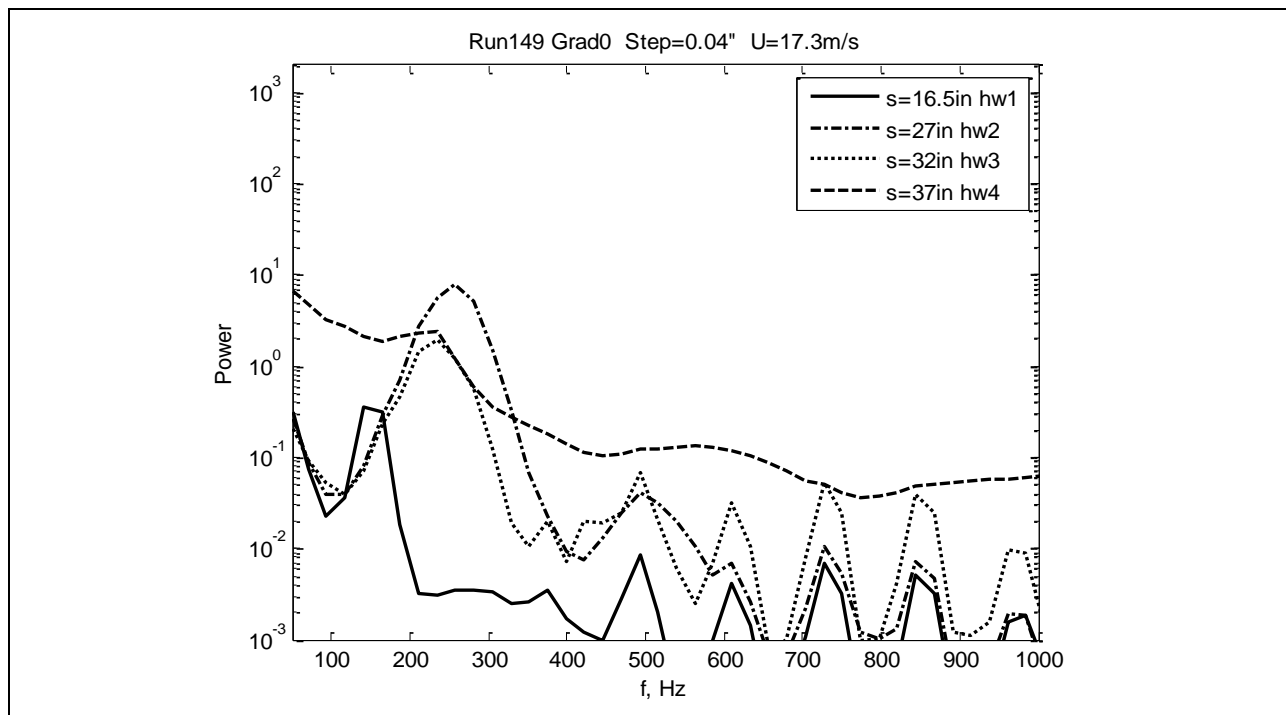


Figure 545: Measured power spectra.

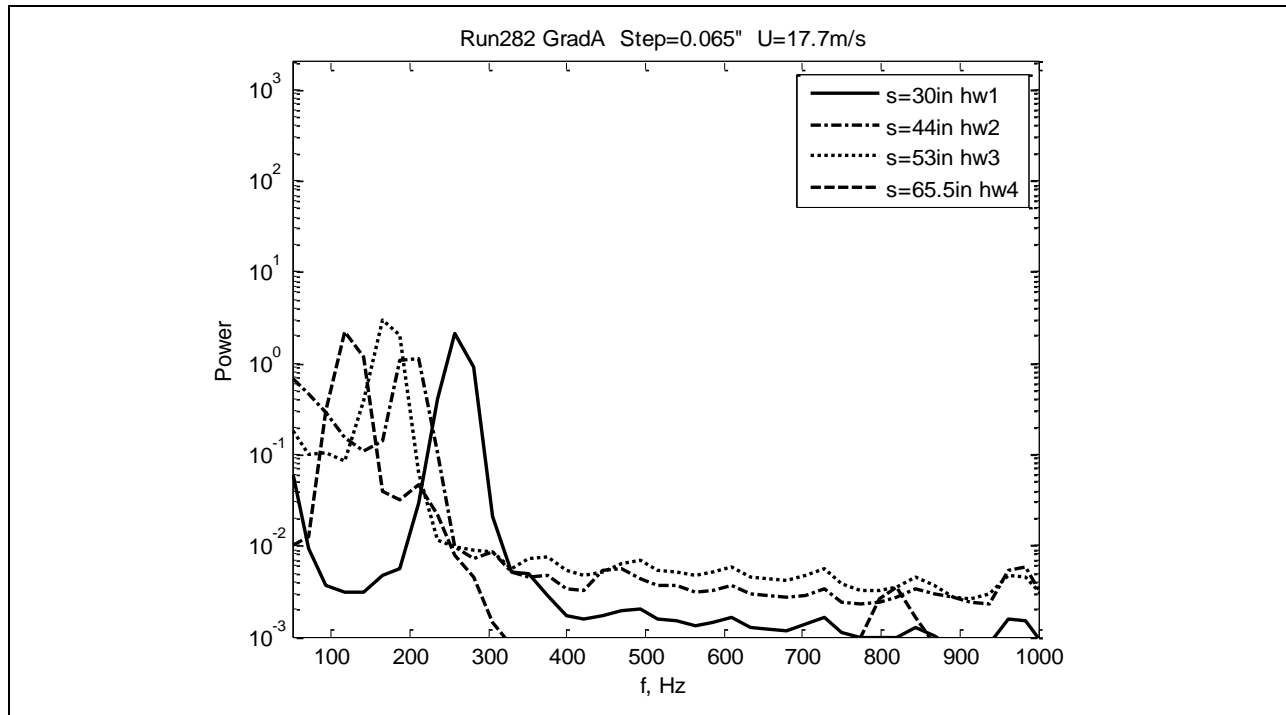


Figure 546: Measured power spectra.

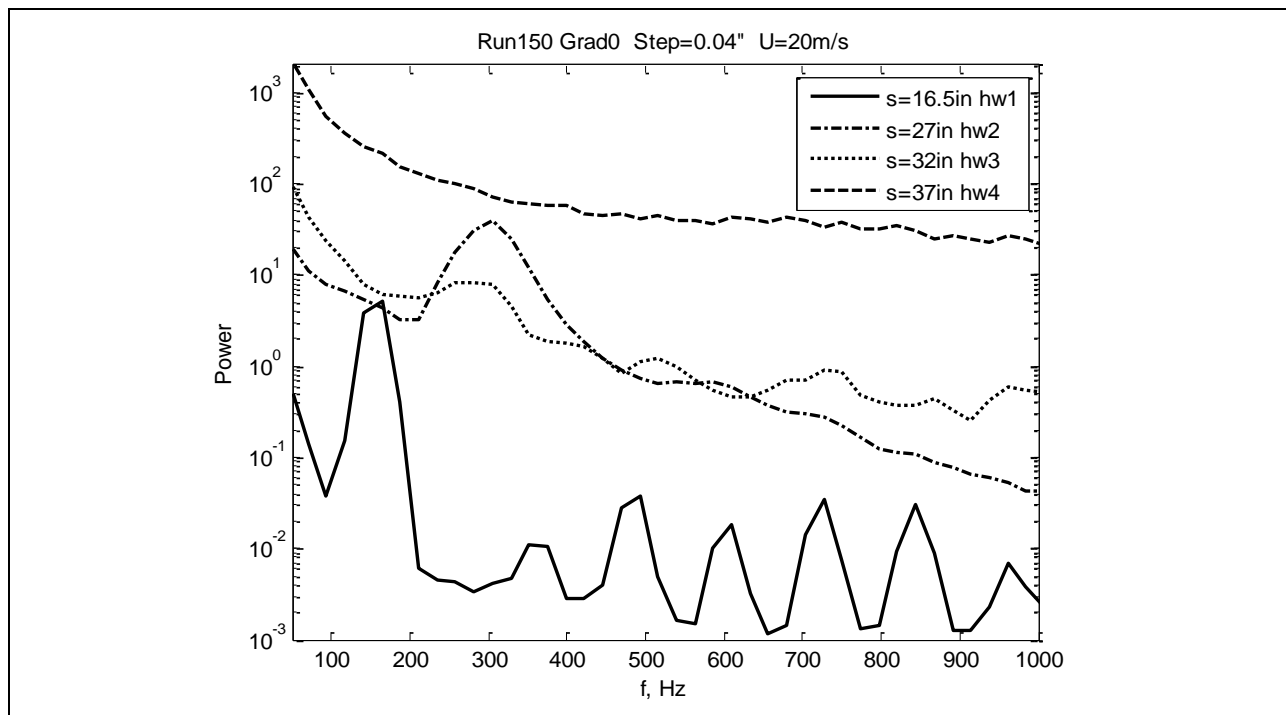


Figure 547: Measured power spectra.

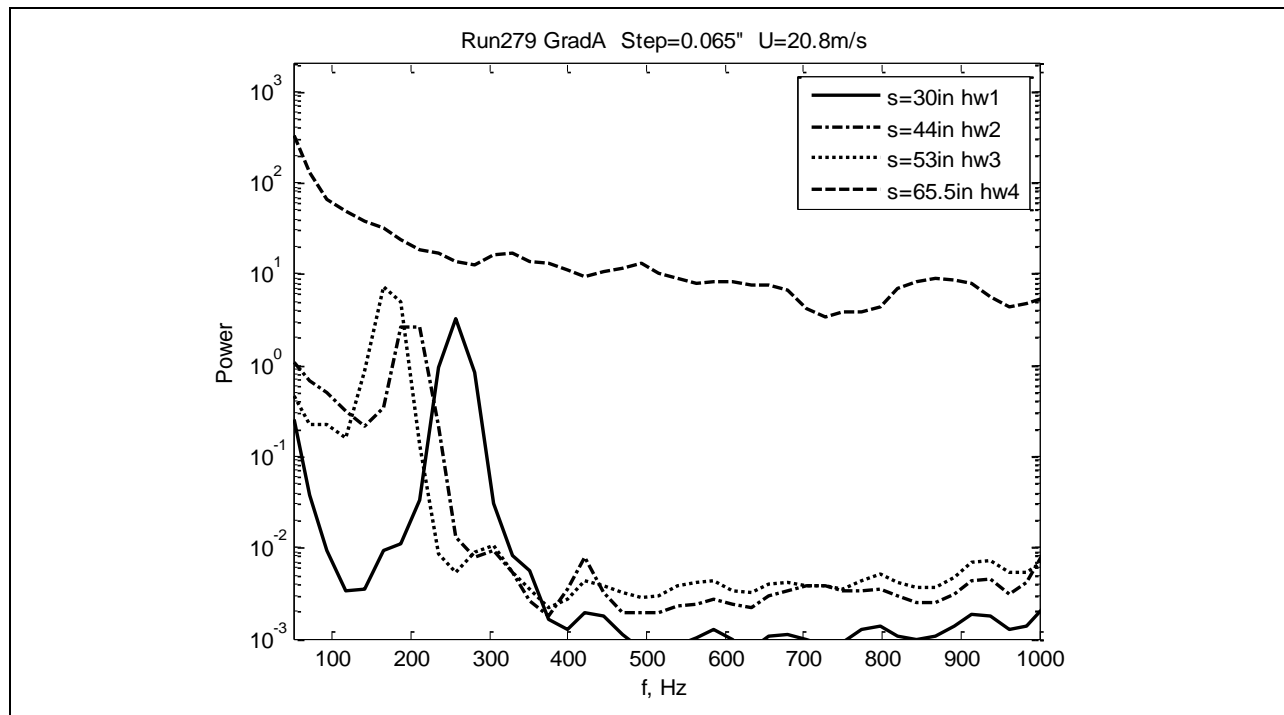


Figure 548: Measured power spectra.

A spectra comparison of the Gradient-A and Gradient-B models is given in the following six plots (Figures 549-554).

Run 275 and Run 388 compare Gradient-A and Gradient-B approximately for the same freestream velocity and slightly different aft-facing step heights (-0.04in for Gradient-A and -0.03in for Gradient-B). It can be seen that spectra are broad for Gradient-B even with smaller step although this model has a more-favorable pressure gradient and is supposed to stabilize flow better than Gradient-A. The reason may be related to the presence of an unintentional (manufacturing defect) gap just after the step for Gradient-B model, which introduces additional disturbances to the flow. Attempts were made to seal this gap during the Gradient-B testing.

Run 282 and Run 377 compare Gradient-A and Gradient-B approximately for the same freestream velocity and slightly different forward-facing step heights (0.065in for Gradient-A and 0.055in for Gradient-B). Both show laminar flows for all hot-wires.

Run 280 and Run 378 the same as previous case but for higher freestream velocity. Gradient-A (Run 280) shows broadening of the spectra starting from the second hot-wire, hw2. Gradient-B (Run 378) shows first two hot-wires, hw1 and hw2, with broad spectrum but then starting from hw3, the laminar flow is restored.

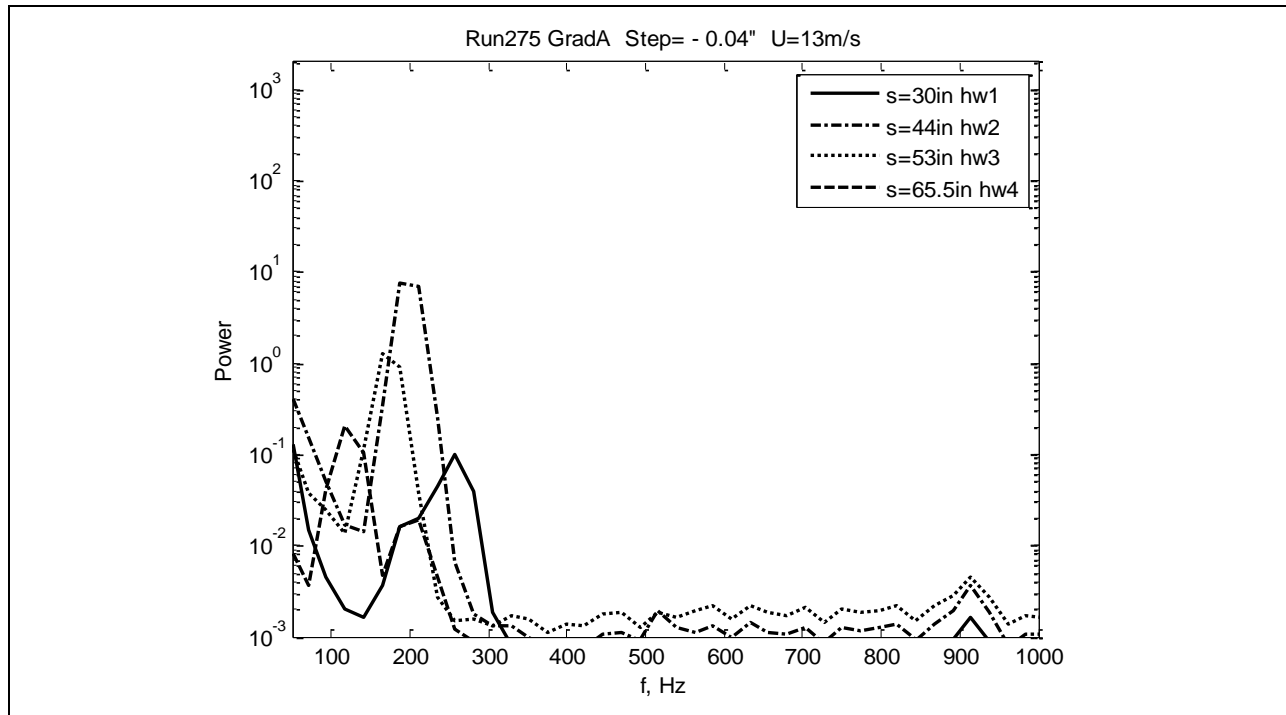


Figure 549: Measured power spectra.

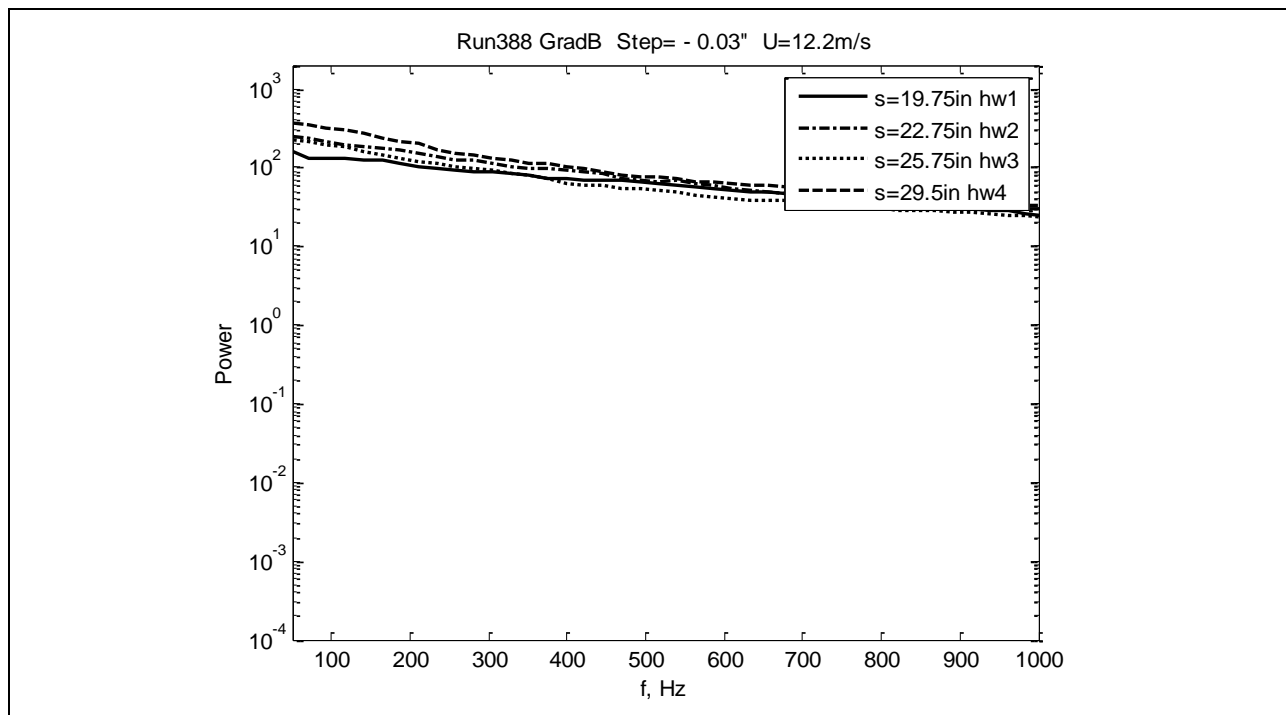


Figure 550: Measured power spectra.

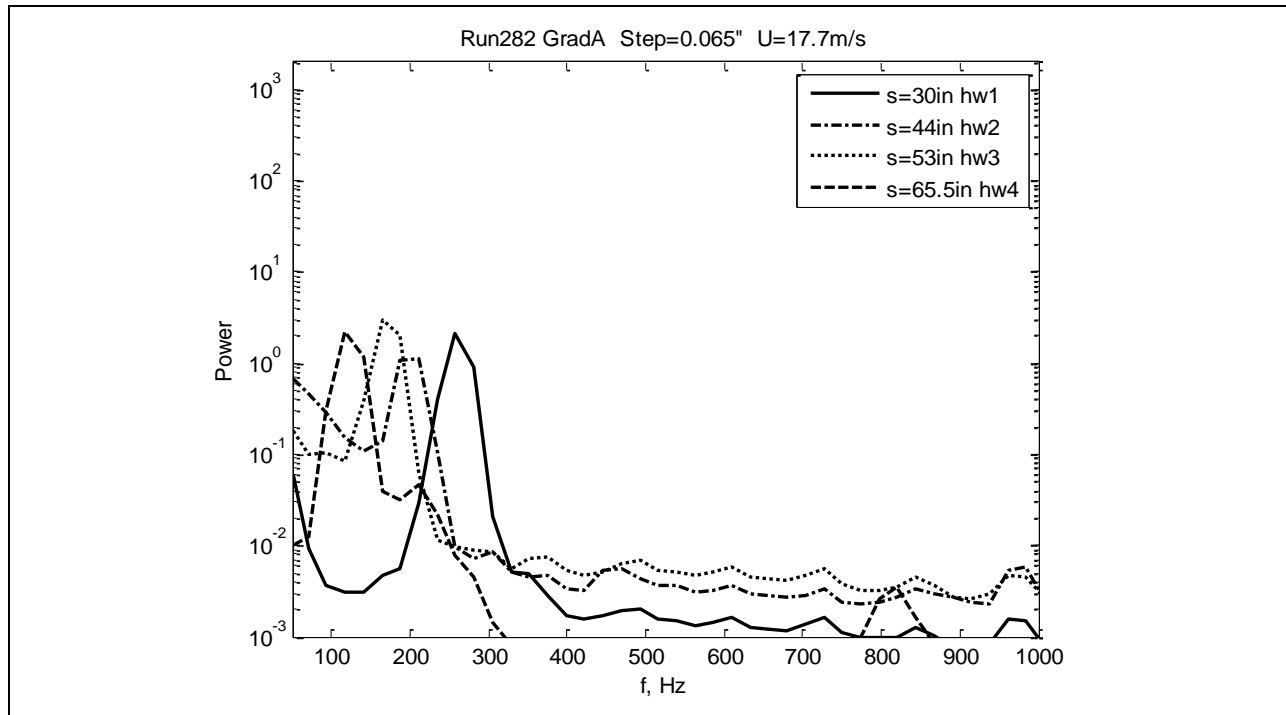


Figure 551: Measured power spectra.

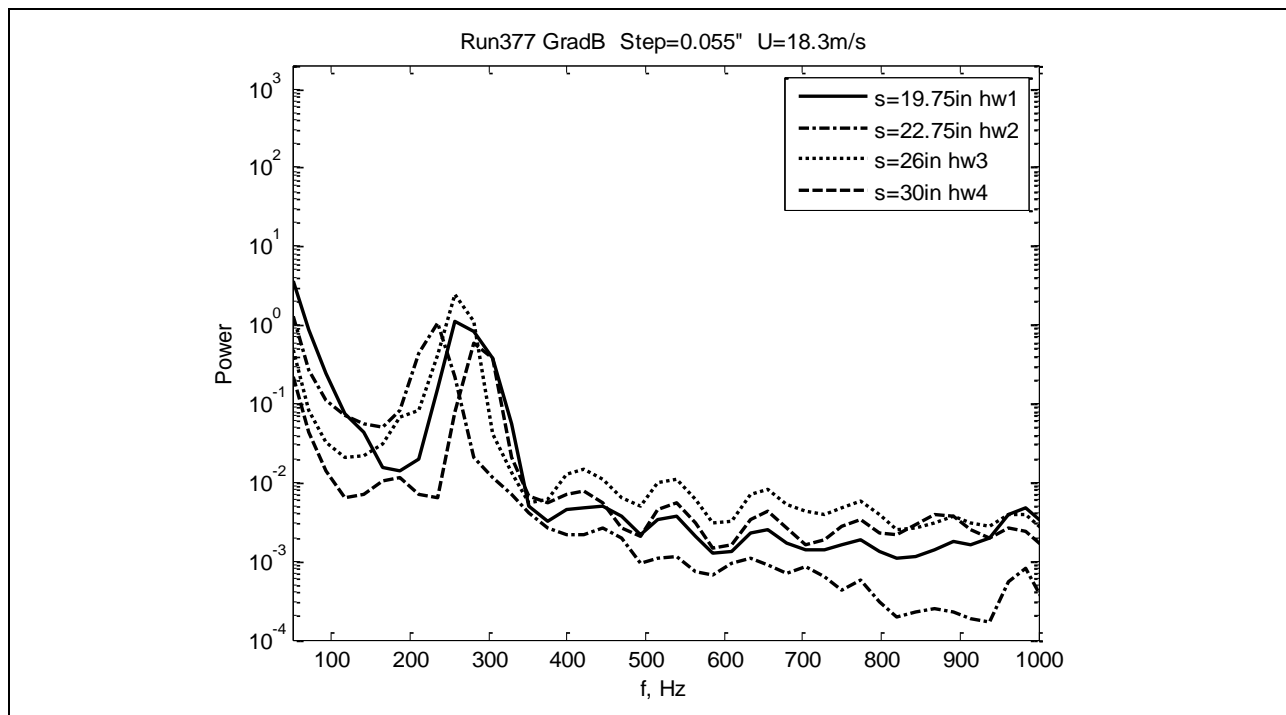


Figure 552: Measured power spectra.

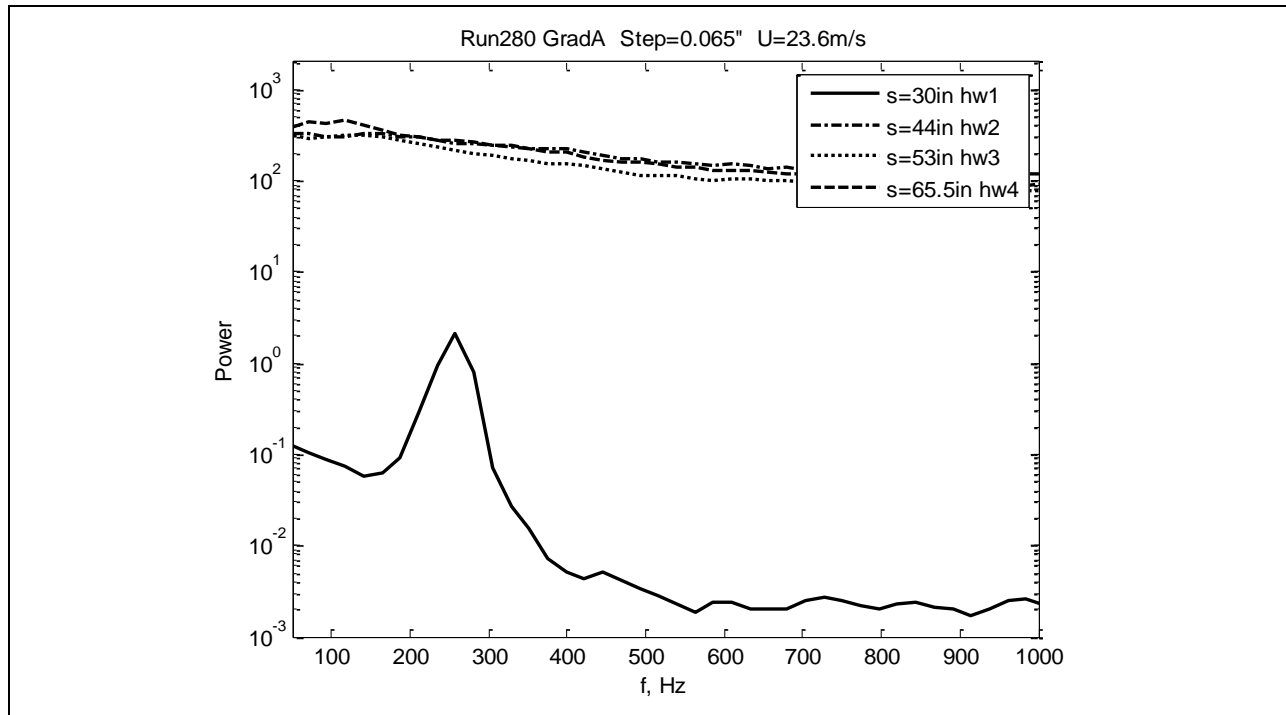


Figure 553: Measured power spectra.

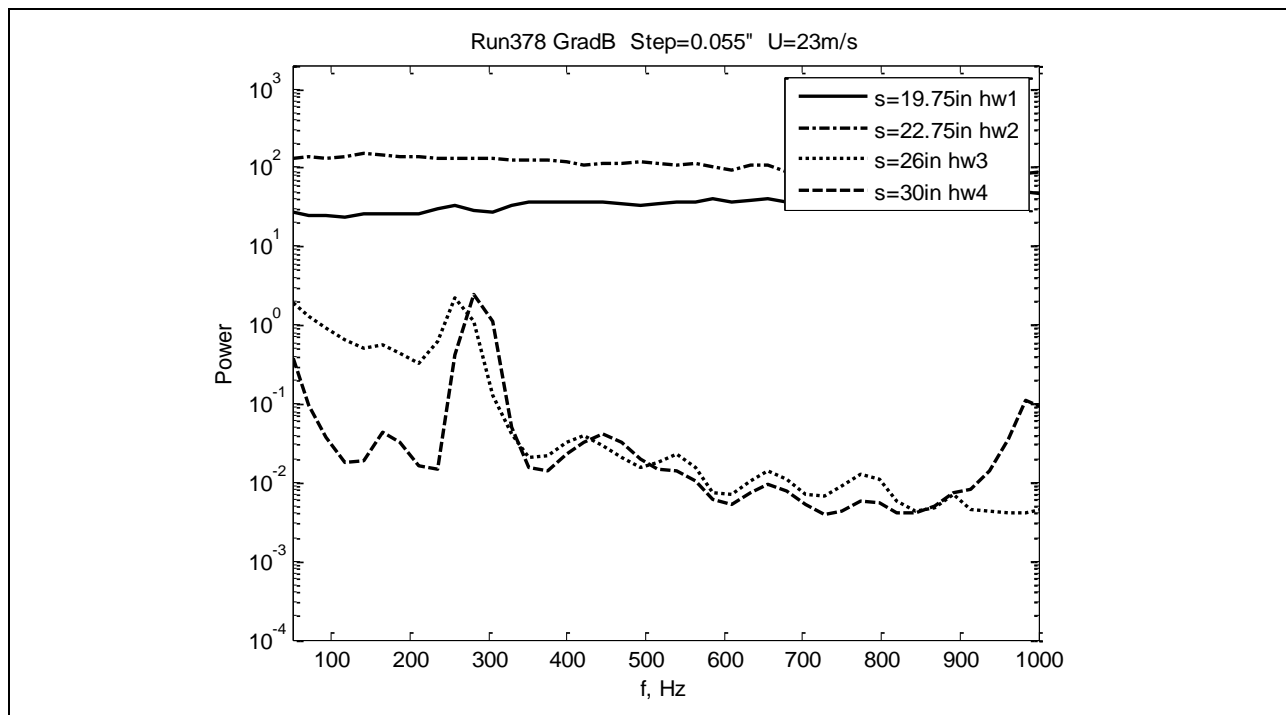


Figure 554: Measured power spectra.

7.5.7.3

Velocity Root Mean Square (RMS)

The root-mean-square (RMS) velocities were calculated from the velocity time series for Gradient-Zero model (above in Section 7.5.7.2). Figures 555-561 below show the calculated velocity RMS values. The electronic noise observed in the velocity signal (see spectra in hot-wire anemometry results in Section 7.5.7.1) contributes to the velocity RMS: the calculated values for the velocity RMS in this section are biased from the true values by this contribution. Each plot contains set of runs for different freestream speeds but for the same model and step height. The laminar flows show usually low RMS (below 0.5m/s). If transition to turbulence happened, the RMS increased to 2-4m/s. Some plots show continuous growth of RMS with stream-wise distance when transition happened, some plots show first growth and then drop of RMS probably because of the stabilizing effect of the favorable (negative) pressure gradient.

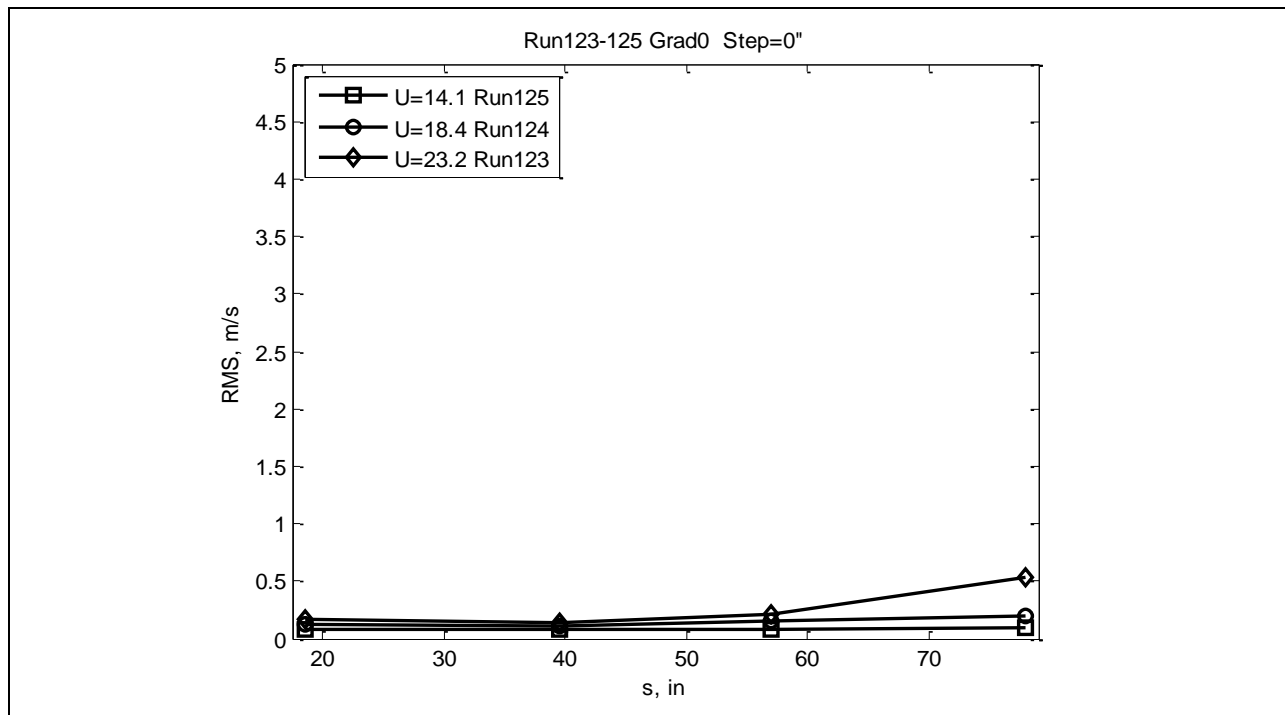


Figure 555: Stream-wise RMS velocity.

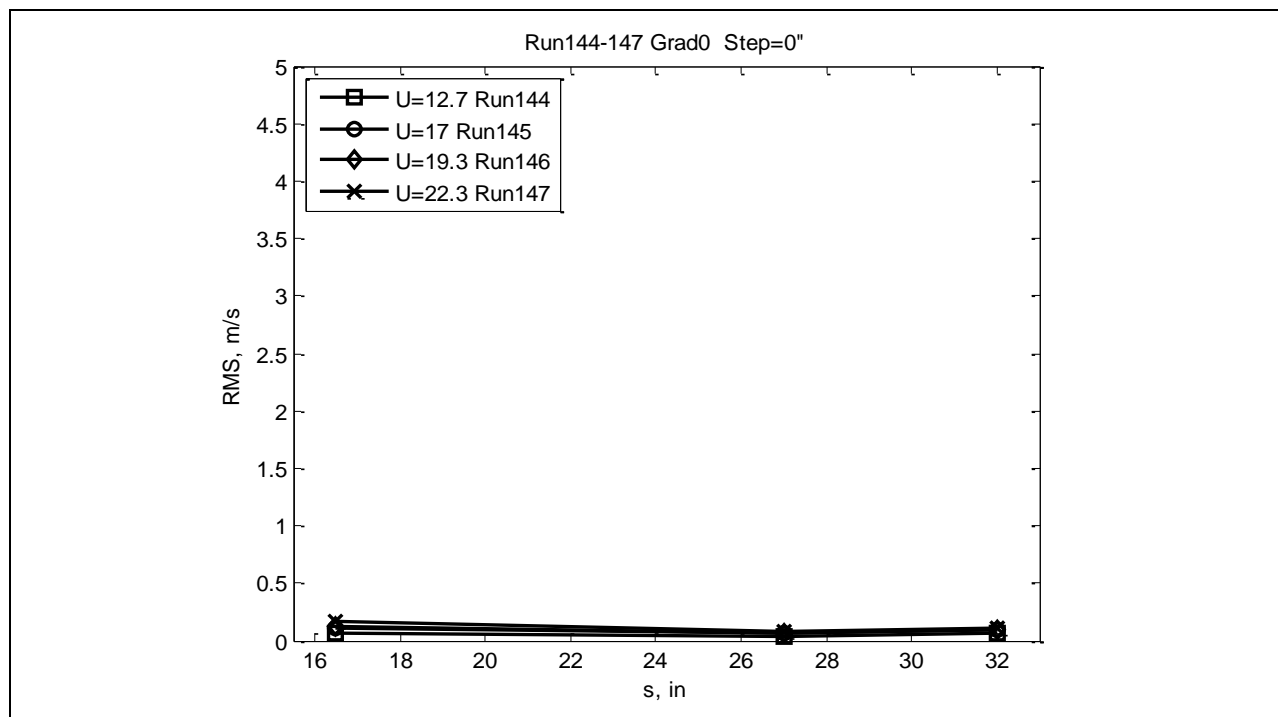


Figure 556: Stream-wise RMS velocity.

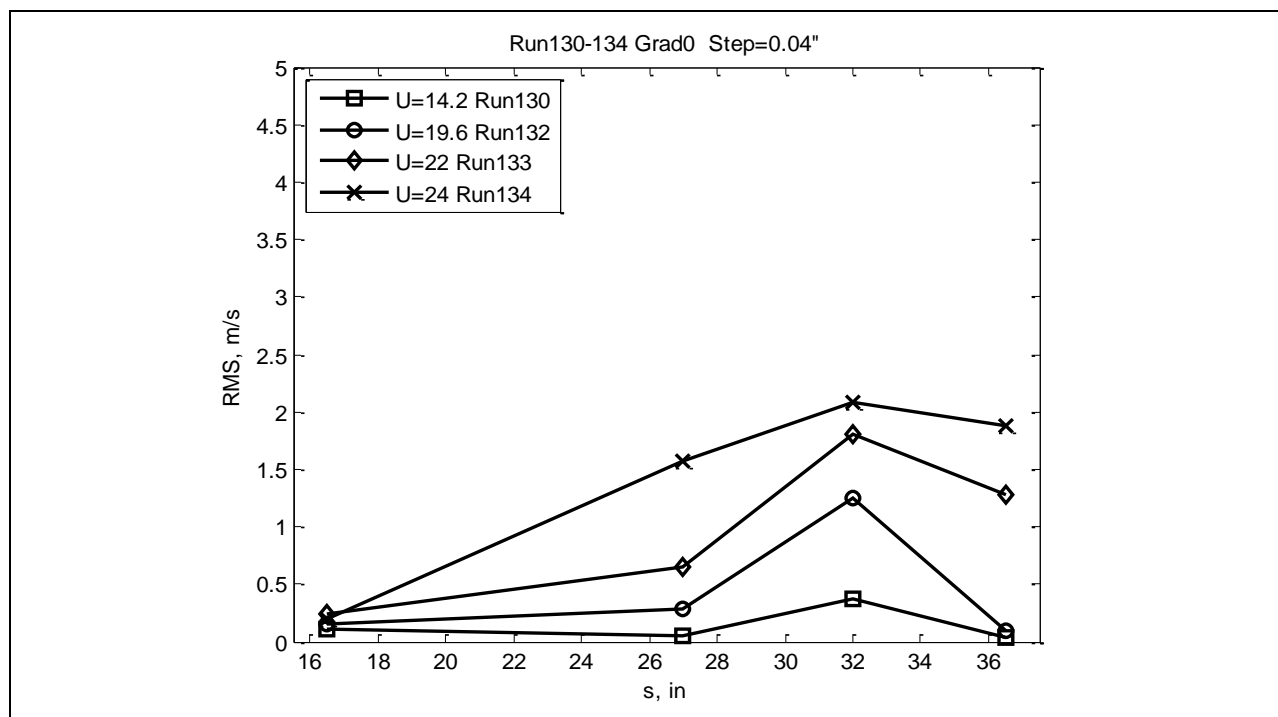


Figure 557: Stream-wise RMS velocity.

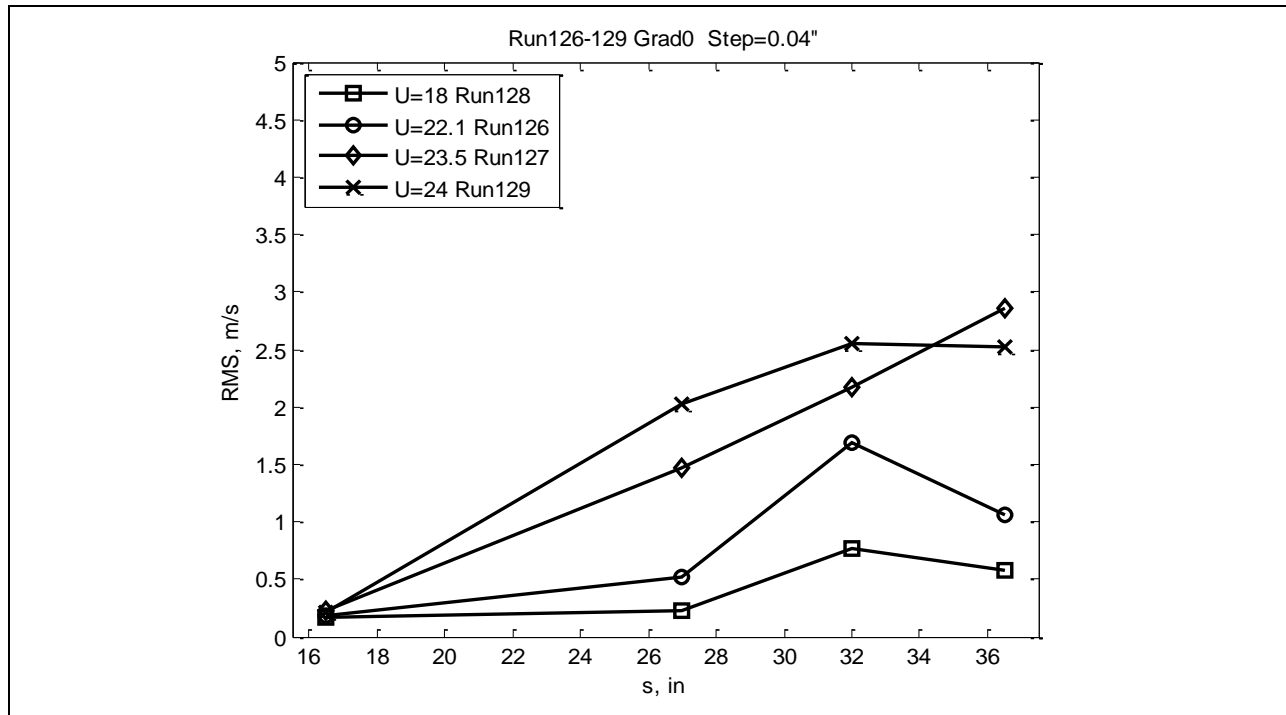


Figure 558: Stream-wise RMS velocity.

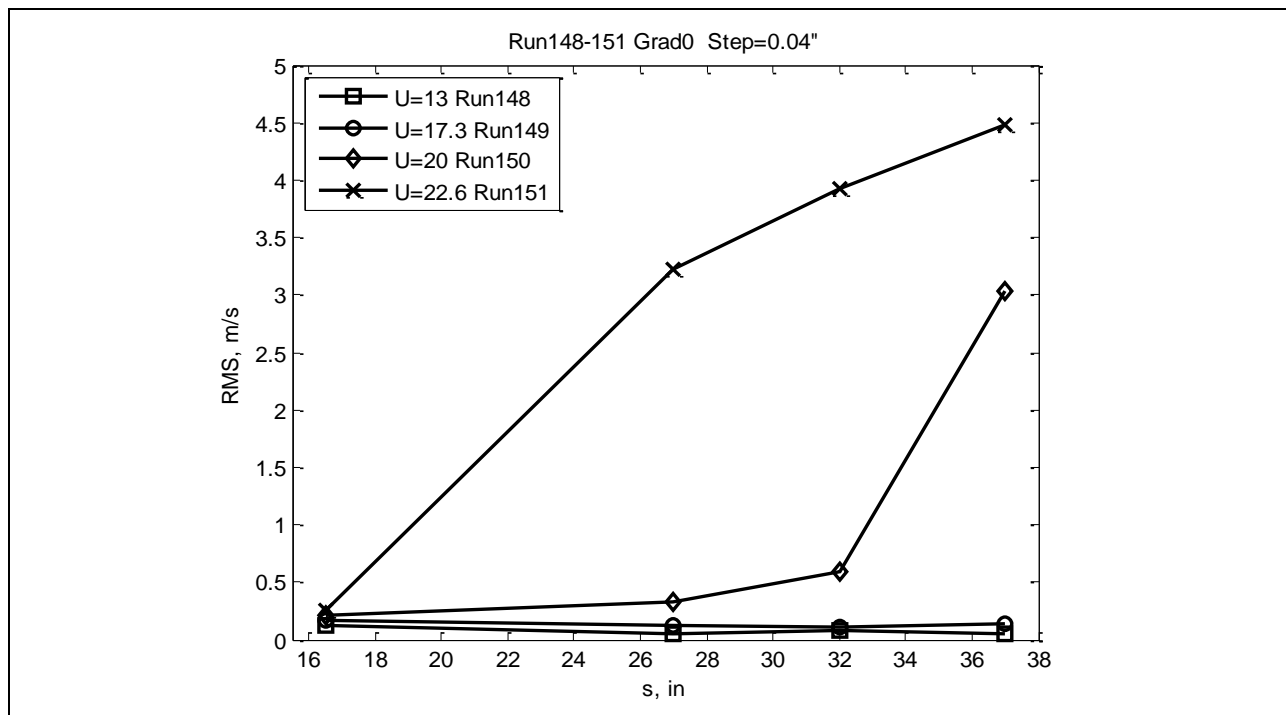


Figure 559: Stream-wise RMS velocity.

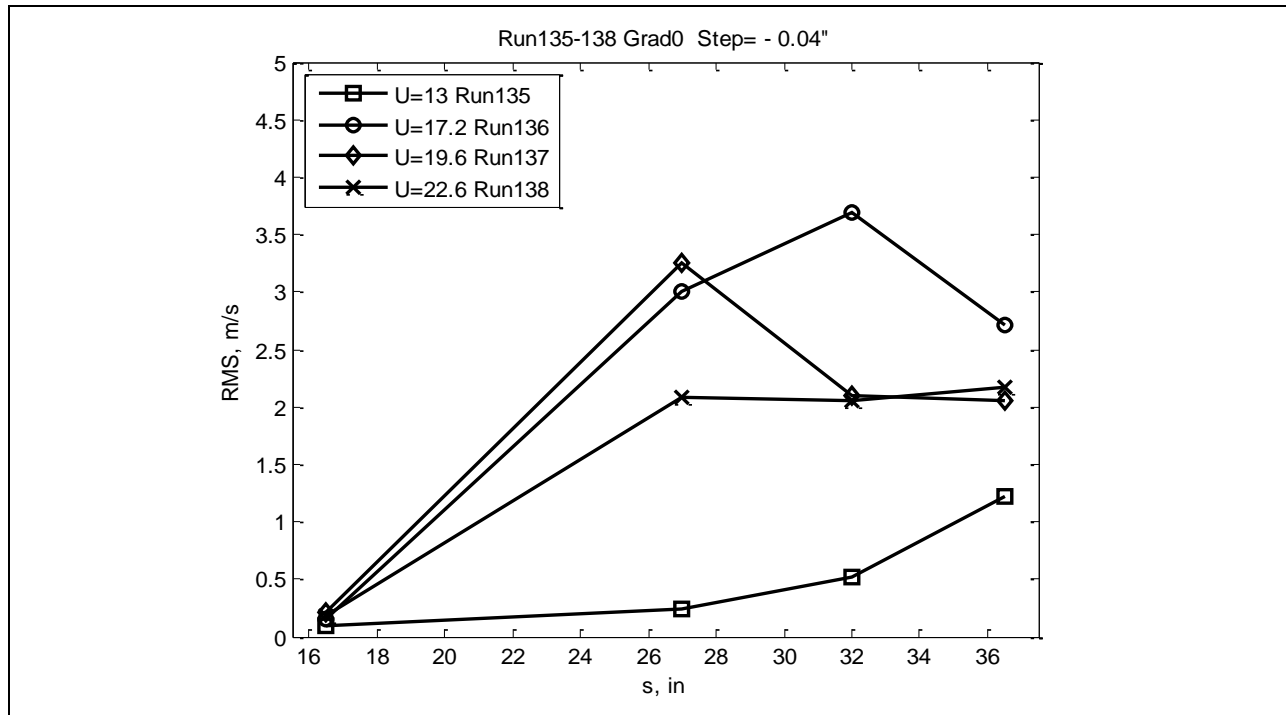


Figure 560: Stream-wise RMS velocity.

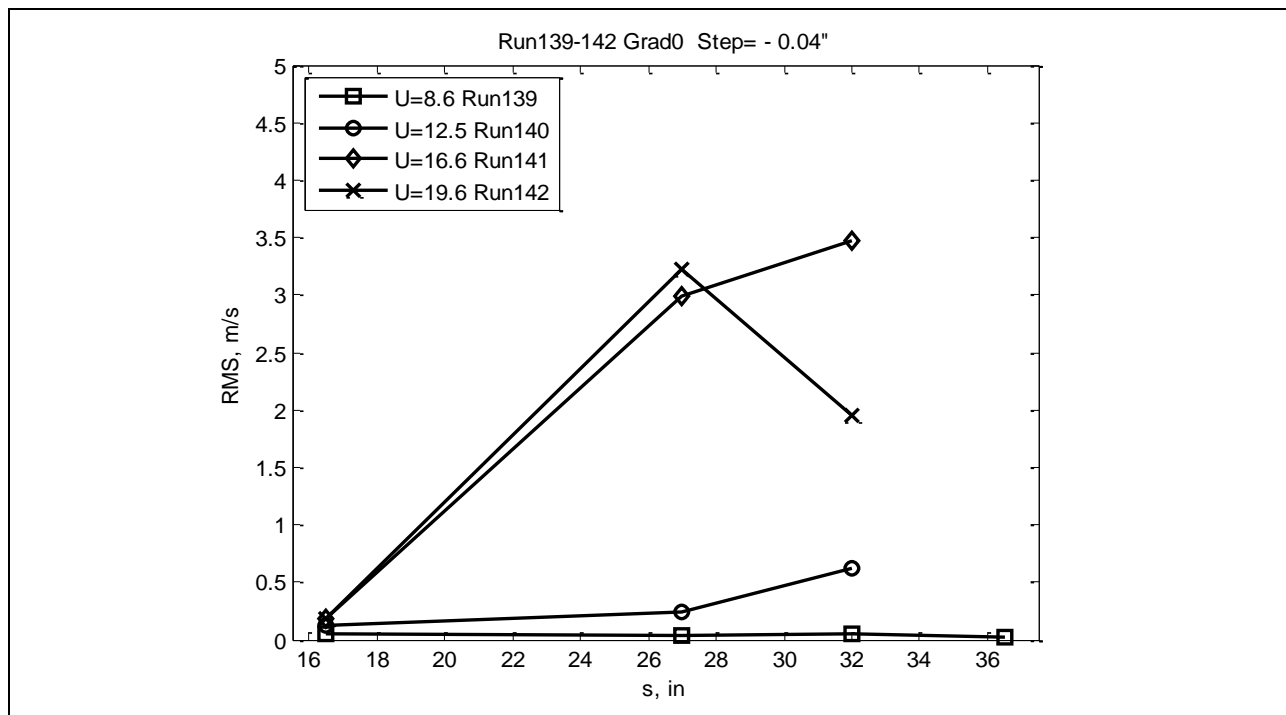


Figure 561: Stream-wise RMS velocity.

The RMS velocities were calculated from the velocity time series for Gradient-A model and the results are shown in Figures 562-565. The electronic noise observed in the velocity signal (see spectra in hot-wire anemometry results in Section 7.5.7.1) contributes to the velocity RMS: the calculated values for the velocity RMS in this section are biased from the true values by this contribution. Each plot contains set of runs for different freestream speeds but for the same model and step height. The laminar flows showed usually low RMS (below 0.5m/s). If transition to turbulence happened, the RMS increased to 2-4m/s. Some plots show continuous growth of RMS with stream-wise distance when transition happened, some plots show first growth and then drop of RMS probably because of stabilizing effect of the favorable (negative) pressure gradient.

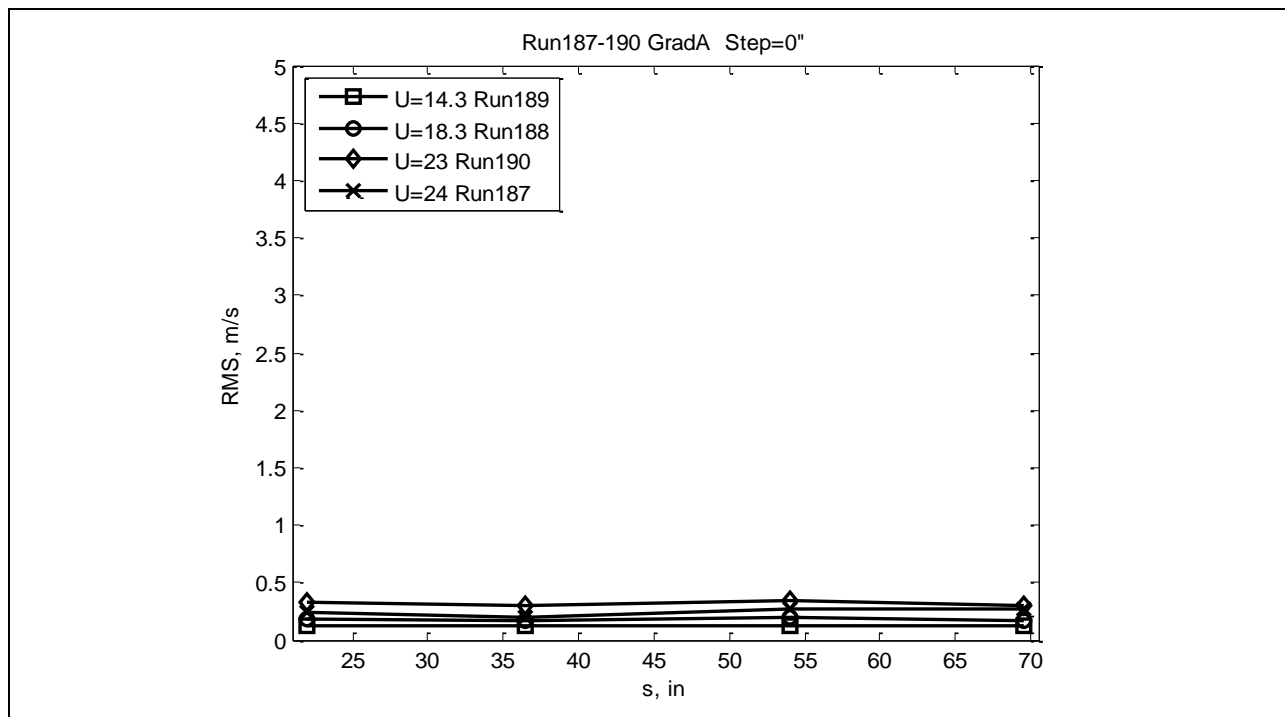


Figure 562: Stream-wise RMS velocity.

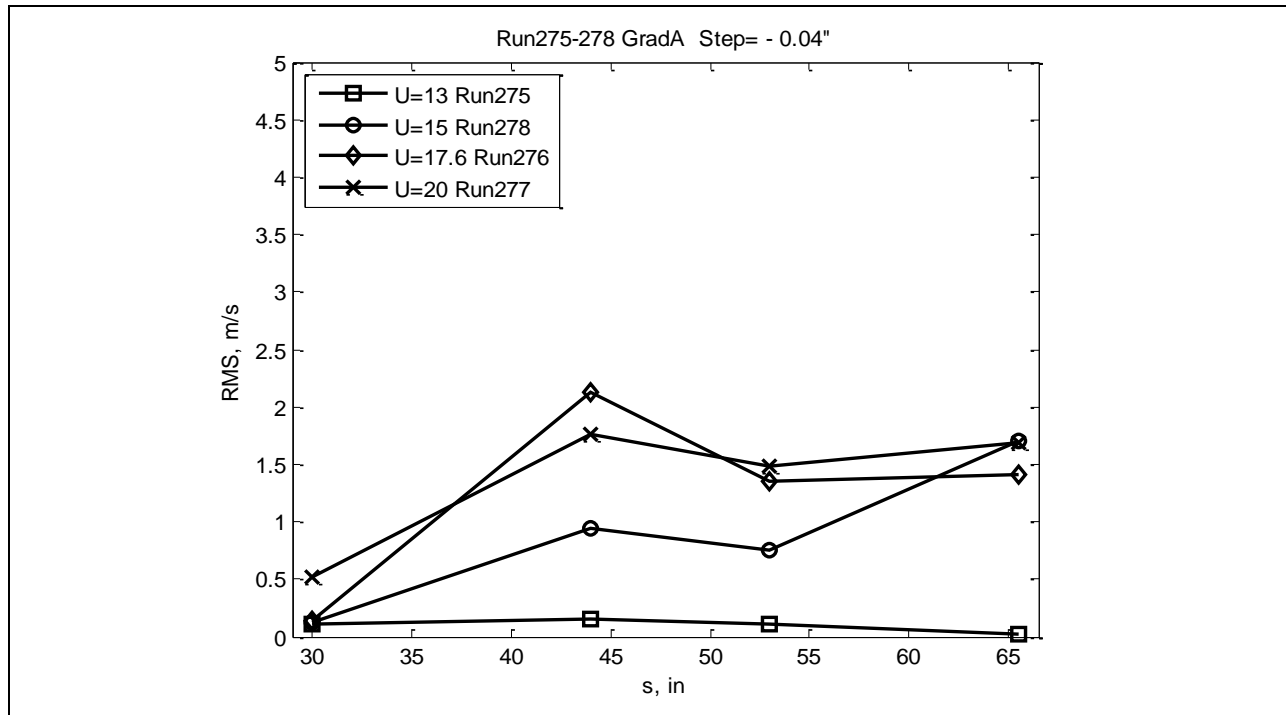


Figure 563: Stream-wise RMS velocity.

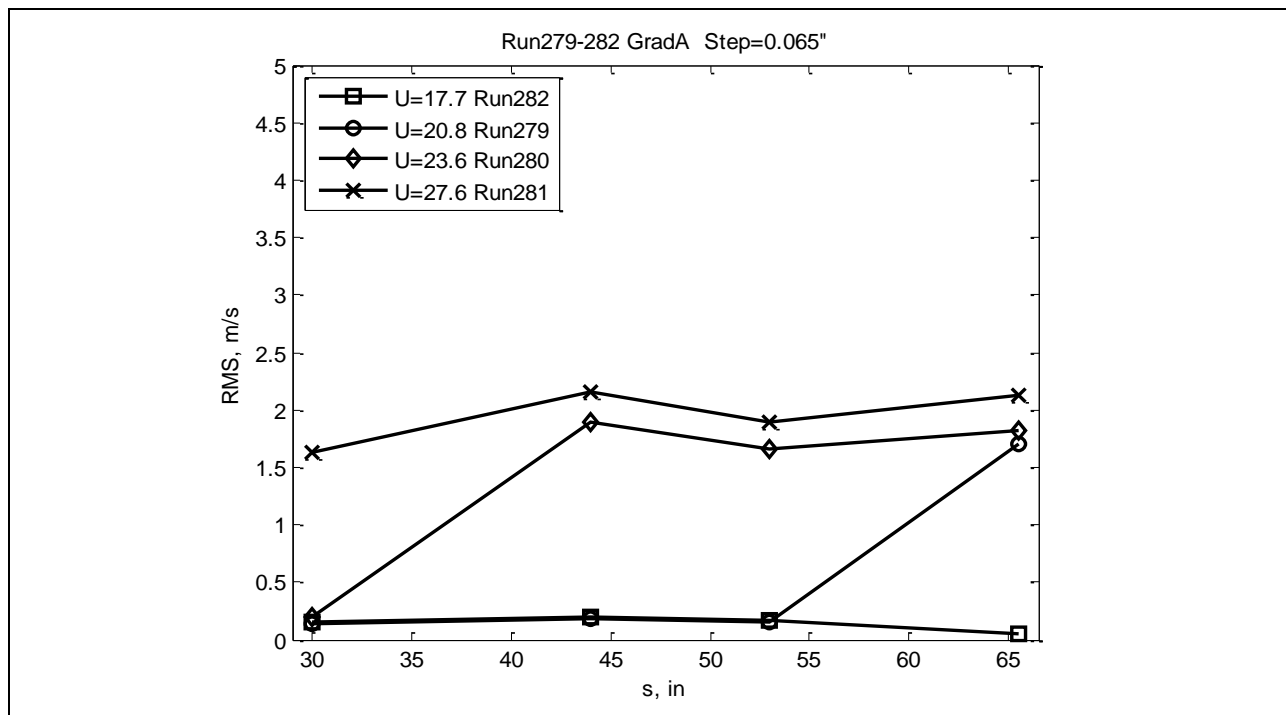


Figure 564: Stream-wise RMS velocity.

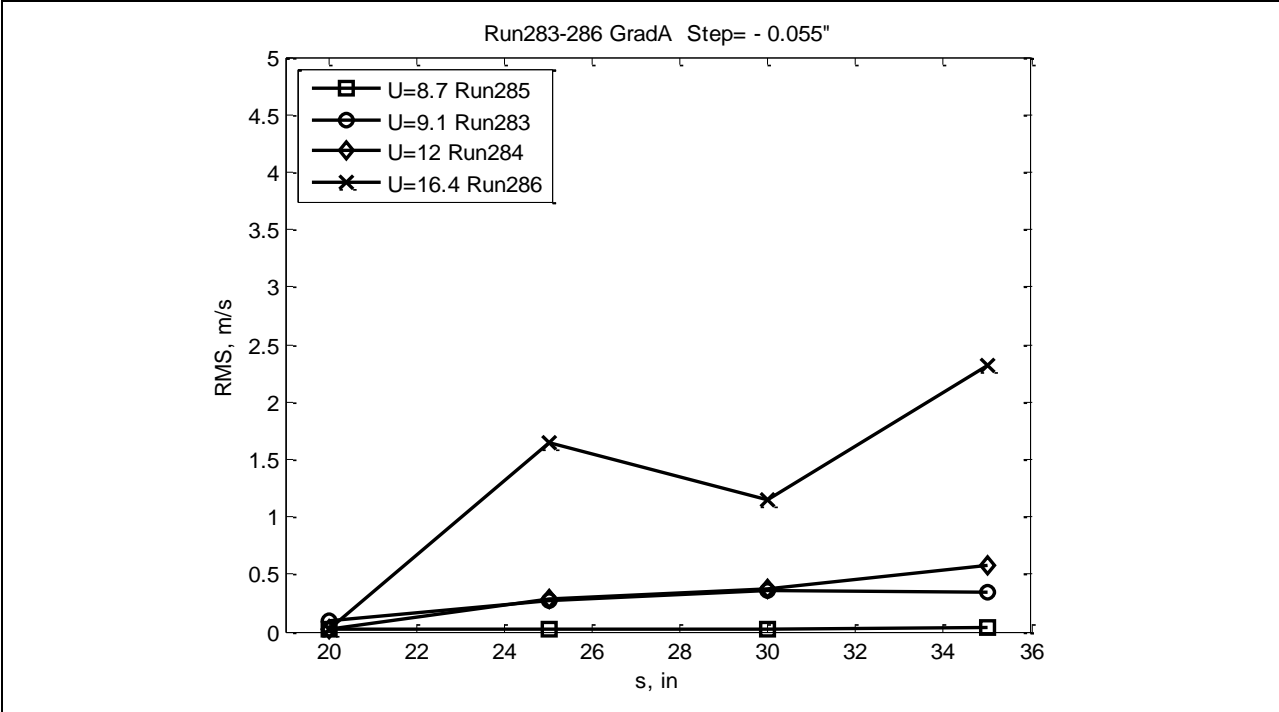


Figure 565: Stream-wise RMS velocity.

The RMS velocities were calculated from the velocity time series for Gradient-B model (Figures 566-573). The electronic noise observed in the velocity signal (see spectra in hot-wire anemometry results in Section 7.5.7.1) contributes to the velocity RMS: the calculated values for the velocity RMS in this section are biased from the true values by this contribution. Each plot contains set of runs for different freestream speeds but for the same model and step height. The laminar flows showed usually low RMS (below 0.5m/s). If transition to turbulence happened, the RMS increased to 2-4m/s. Some plots show continuous growth of RMS with stream-wise distance when transition happened, some plots show first growth and then drop of RMS probably because of stabilizing effect of the favorable (negative) pressure gradient.

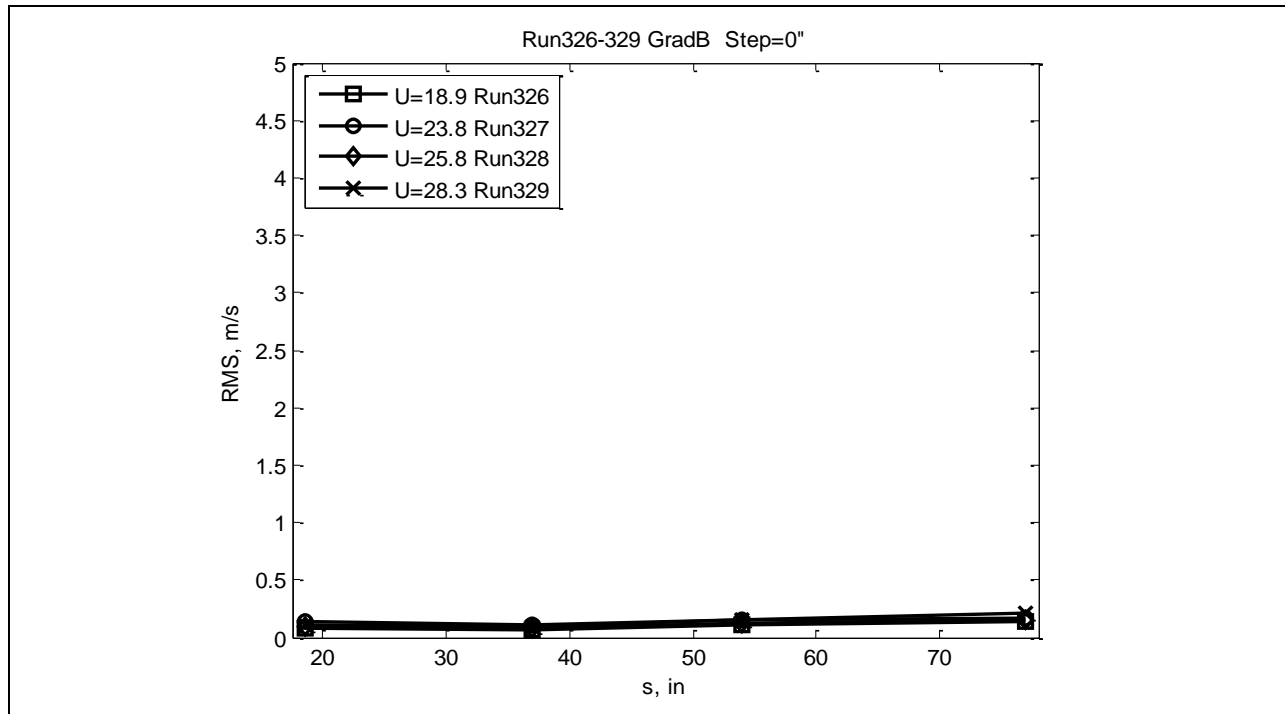


Figure 566: Stream-wise RMS velocity.

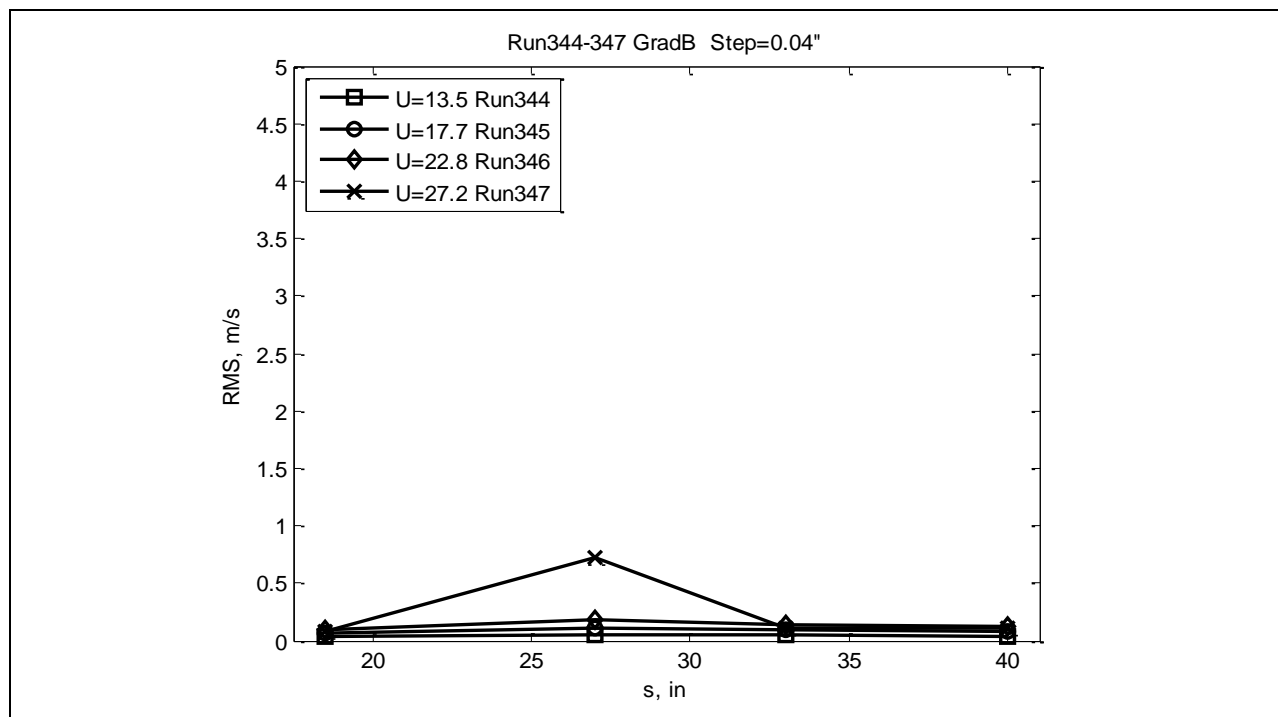


Figure 567: Stream-wise RMS velocity.

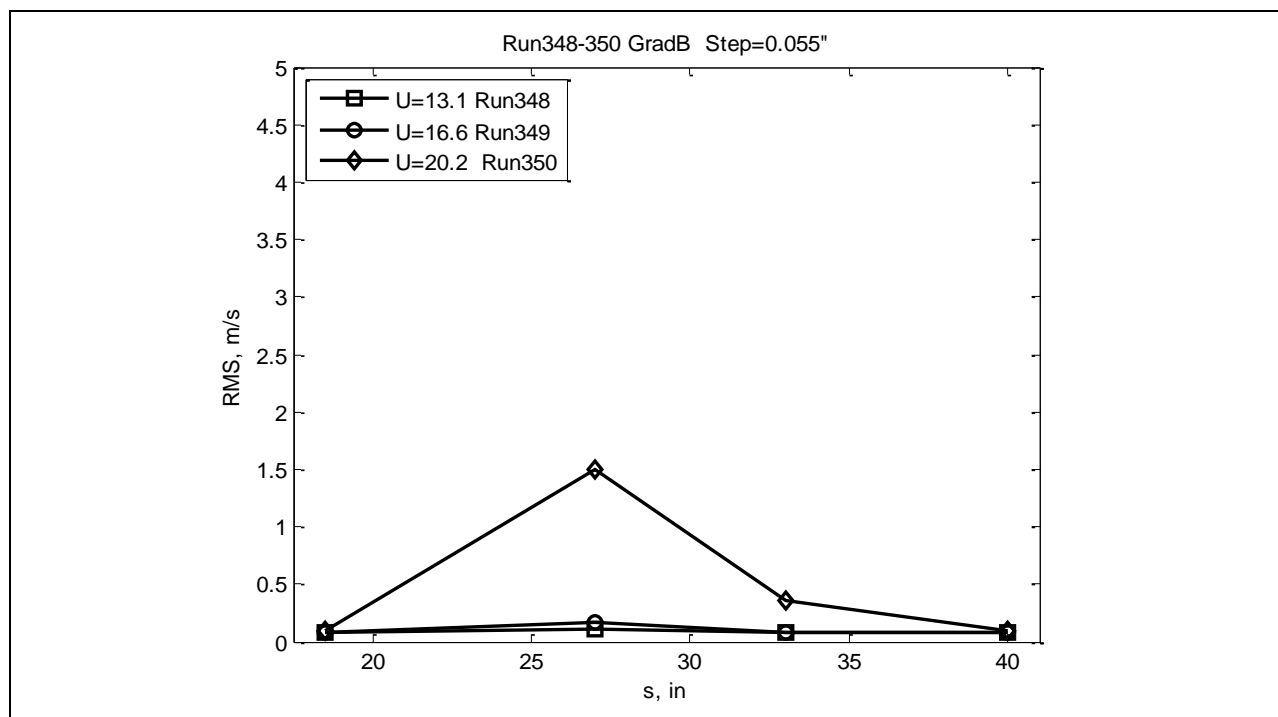


Figure 568: Stream-wise RMS velocity.

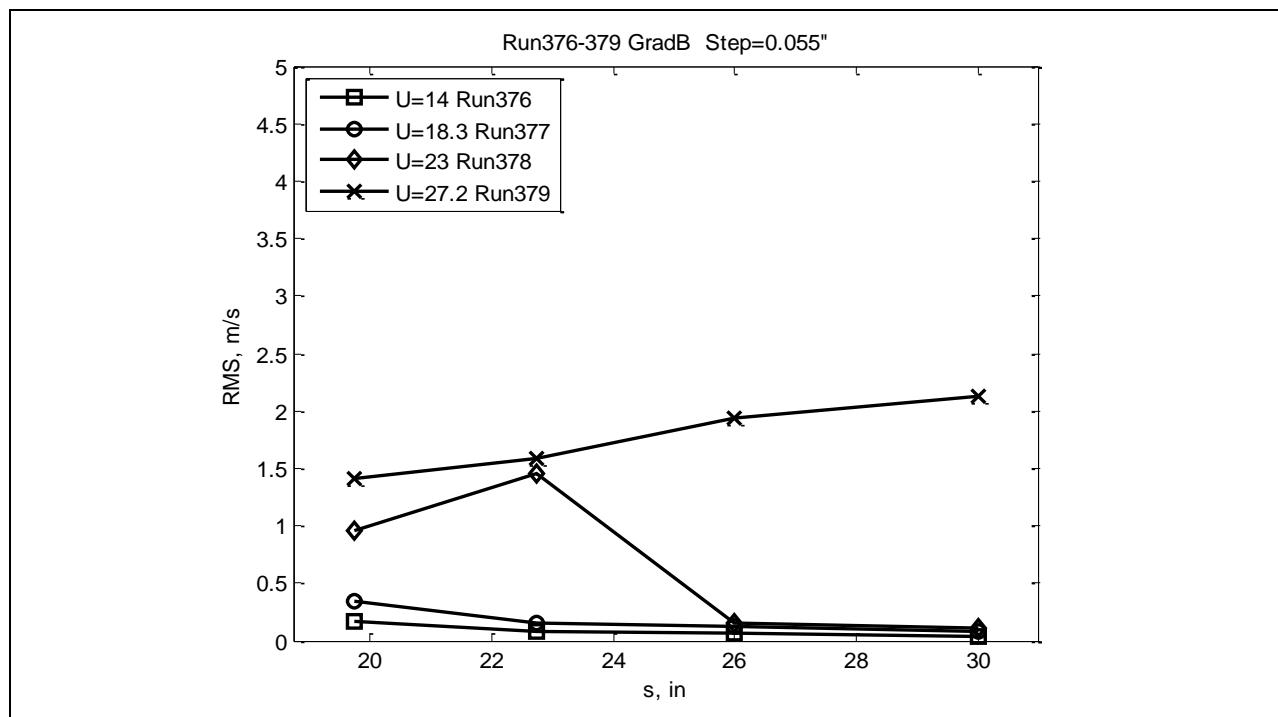


Figure 569: Stream-wise RMS velocity.

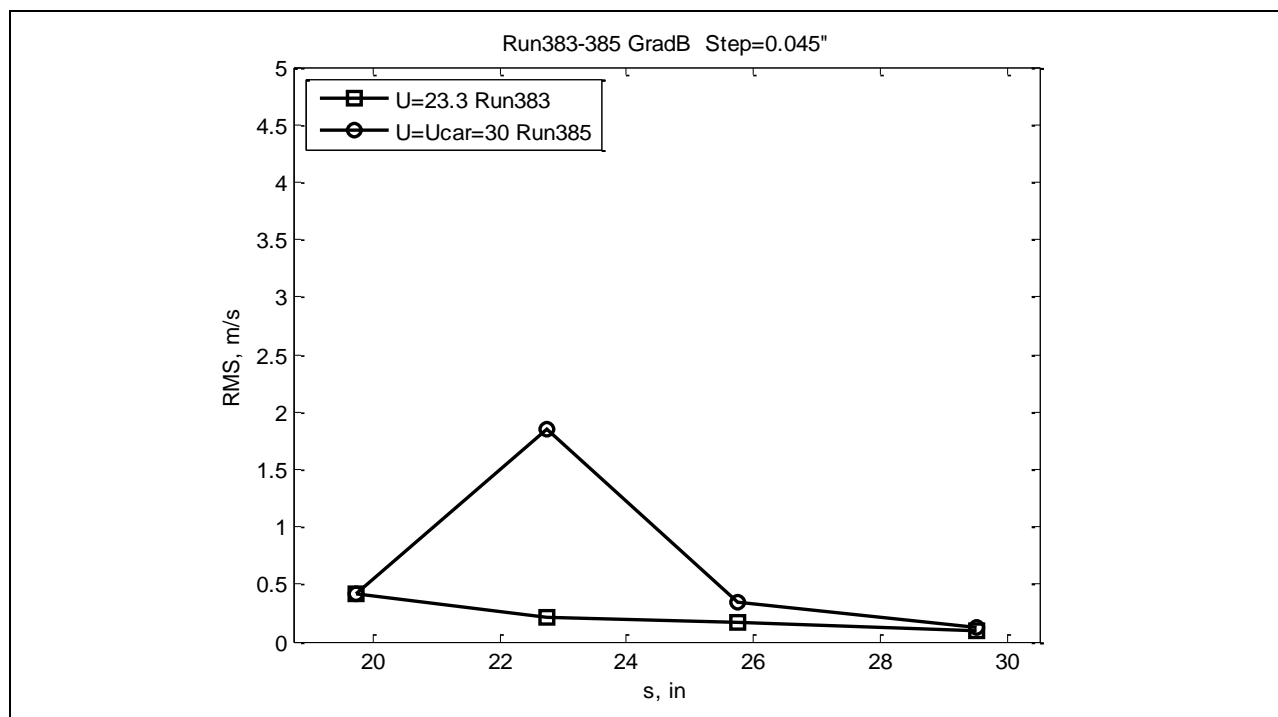


Figure 570: Stream-wise RMS velocity.

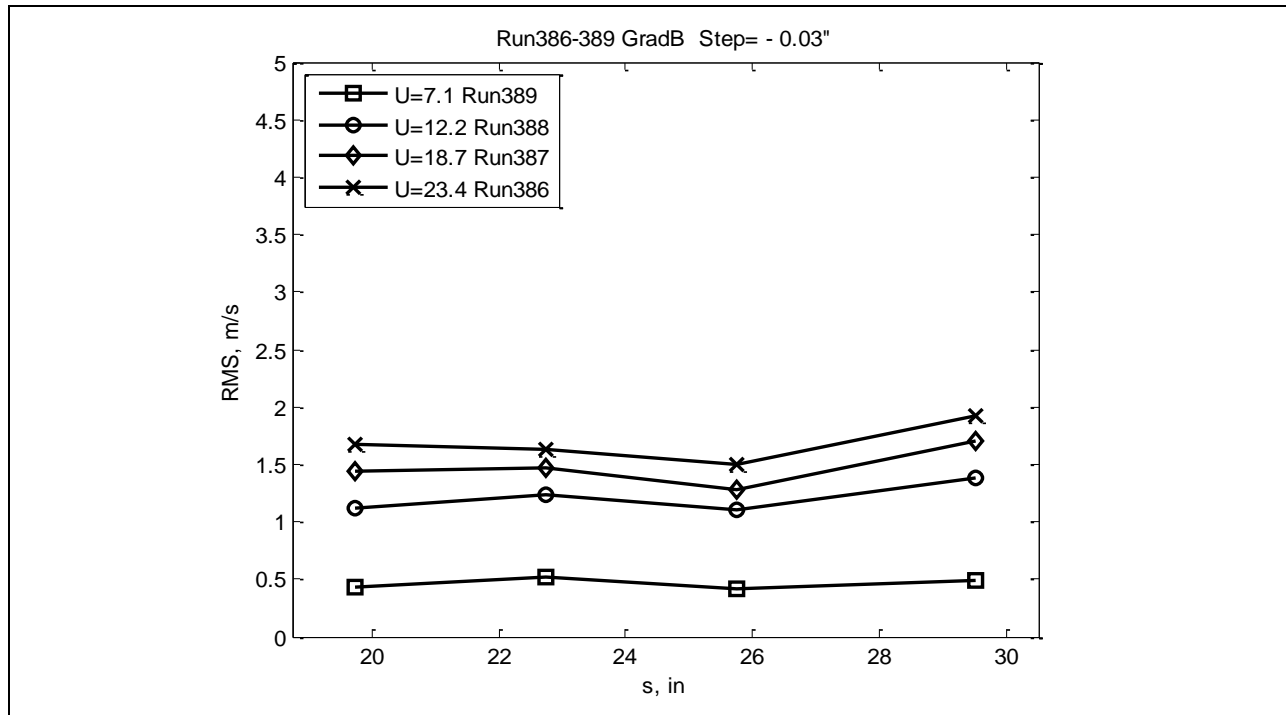


Figure 571: Stream-wise RMS velocity.

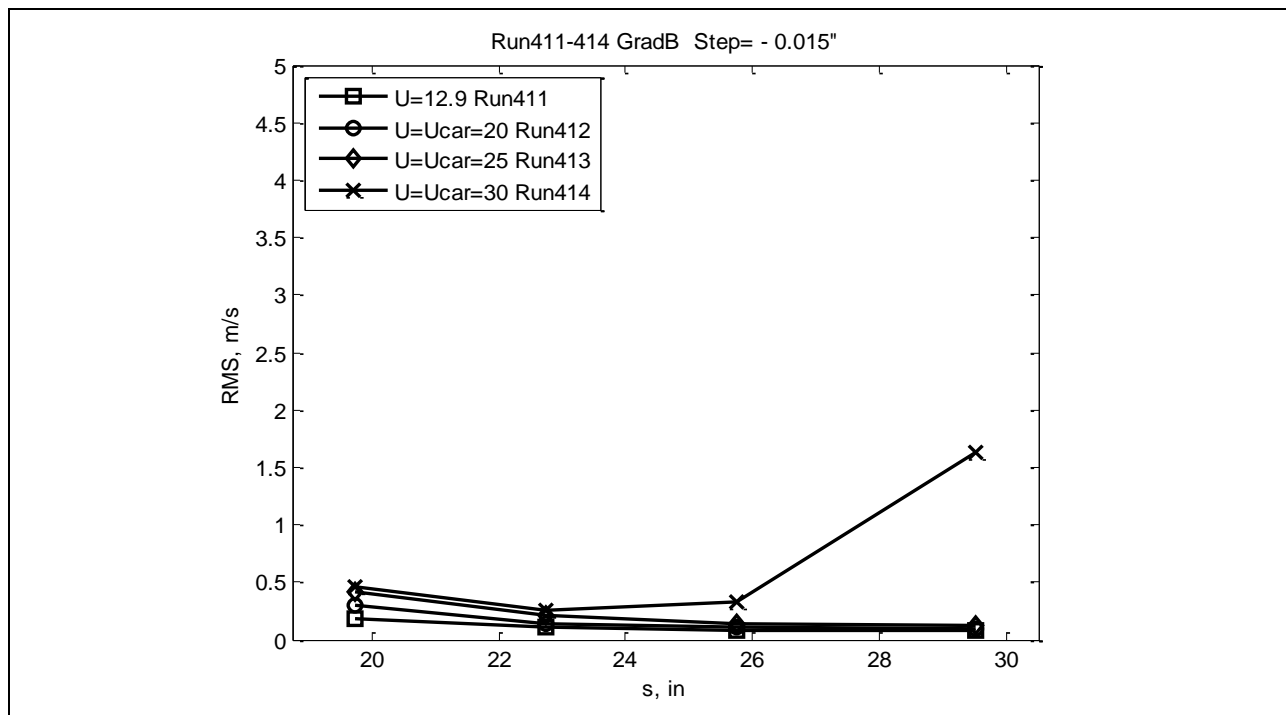


Figure 572: Stream-wise RMS velocity.

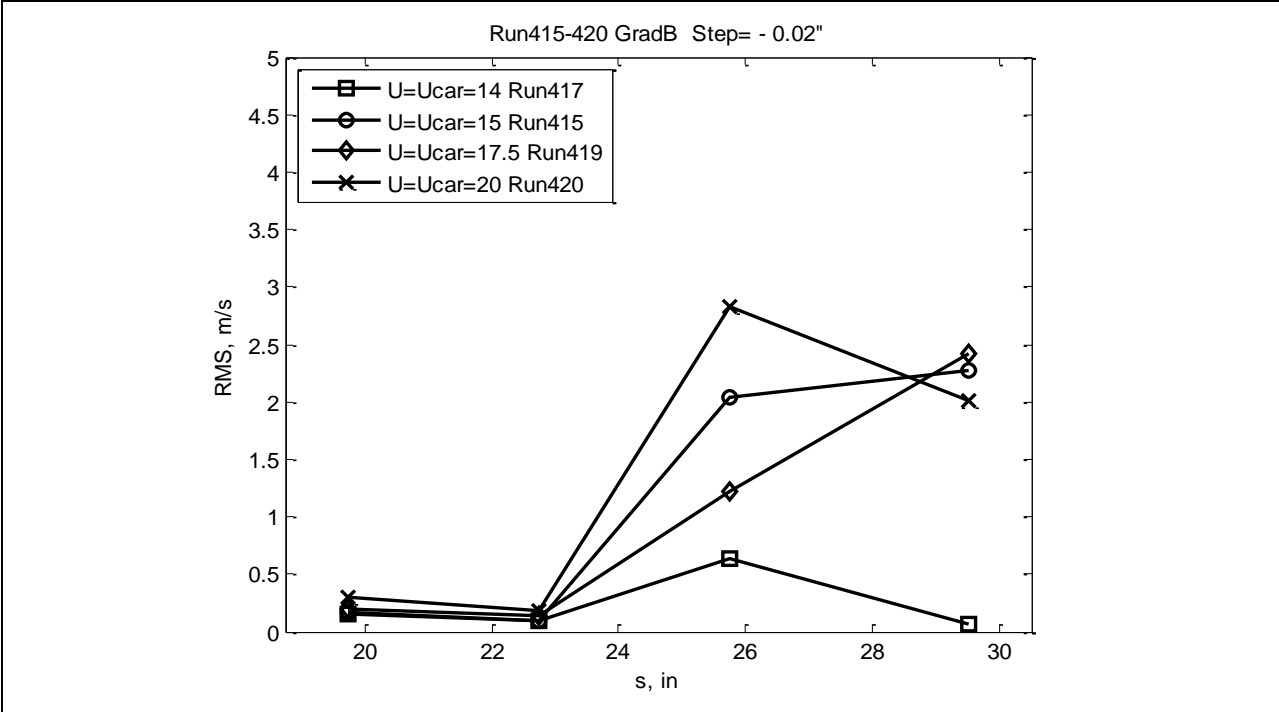


Figure 573: Stream-wise RMS velocity.

7.5.7.4

Traversing Data

The traversing of a hotwire probe through the boundary layer was done using the Boundary Layer Data System (BLDS) described in Section 7.3.3. The plots below (Figures 574-577) show the mean velocity profiles and velocity RMS as function of distance from the wall for Gradient-Zero. The data are collected for a set of runs (different freestream velocity) but for the same model and step height in one plot. If transition happened, the velocity profile changed to typical turbulent one and the RMS increased correspondingly as can be seen in Figure 576 for 22.5m/s and in Figure 577 for 19.6m/s and 22m/s. The change in the velocity profile during transition was used to compare with the C_f distribution change during transition obtained from Preston tube measurements.

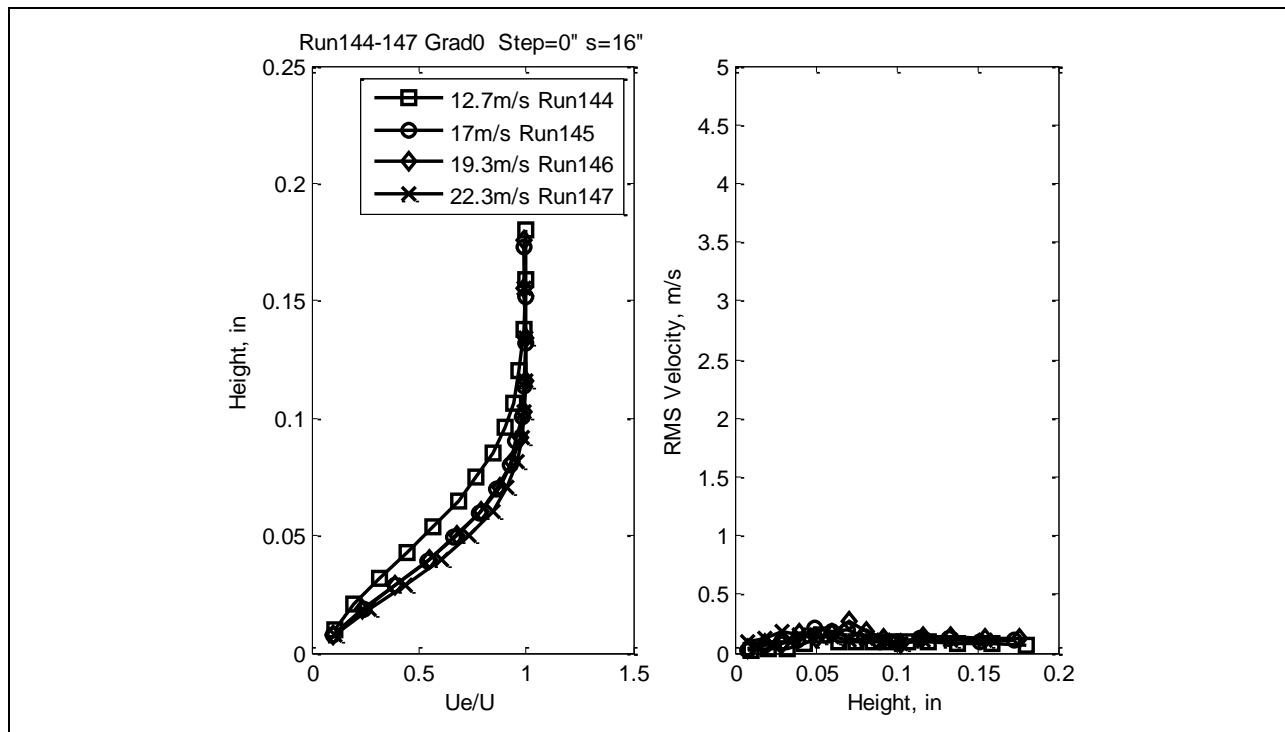


Figure 574: Mean velocity profile (left) and RMS velocity (right), as a function of distance from the surface.

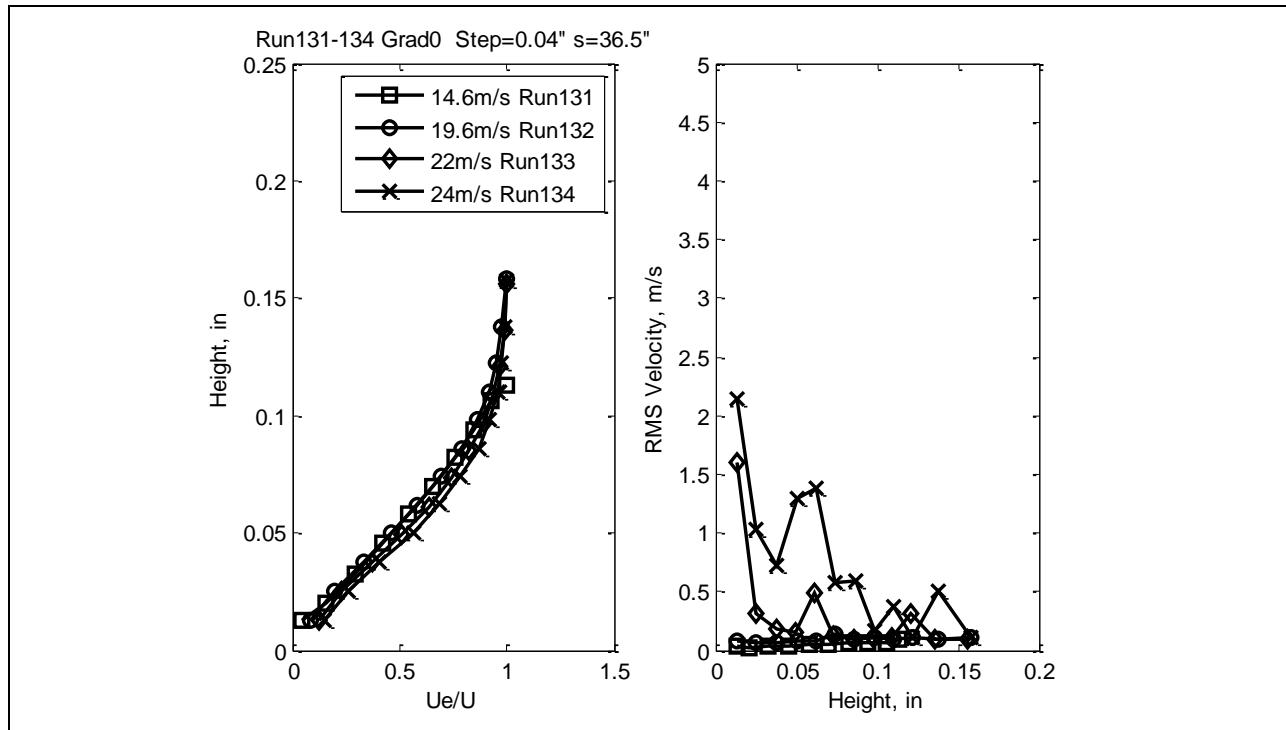


Figure 575: Mean velocity profile (left) and RMS velocity (right), as a function of distance from the surface.

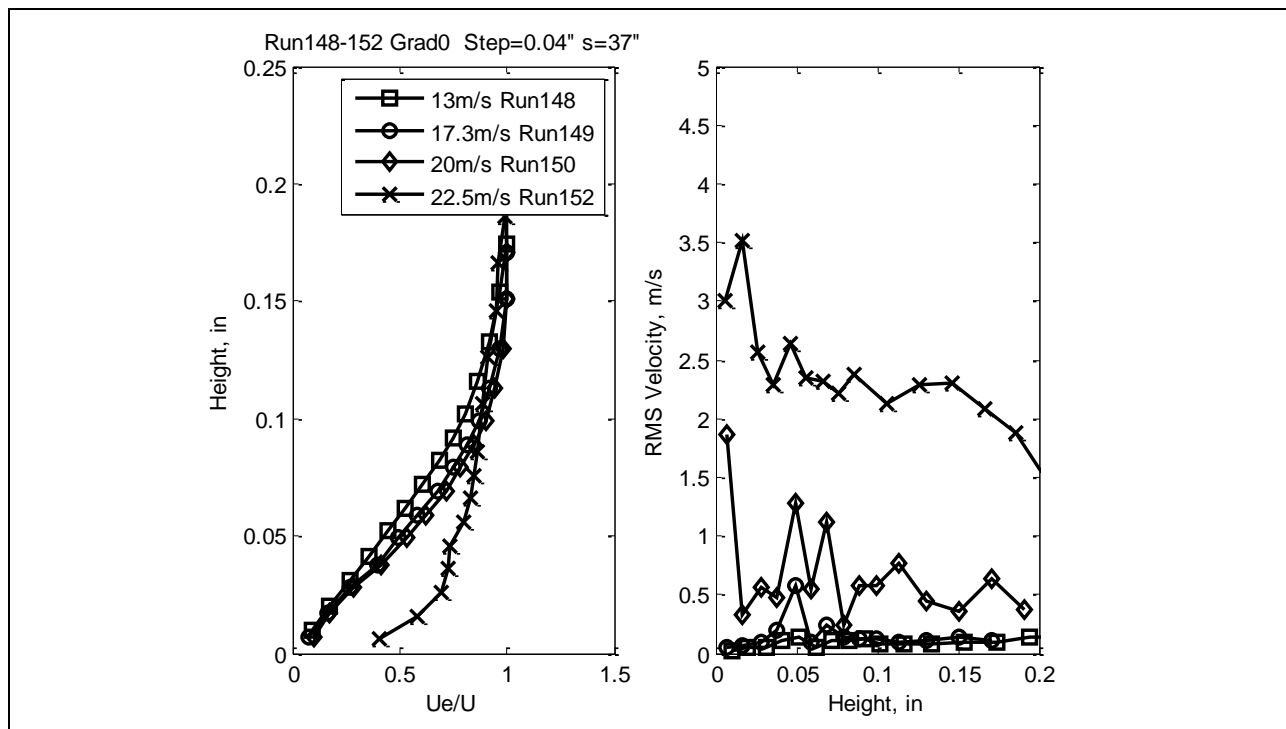


Figure 576: Mean velocity profile (left) and RMS velocity (right), as a function of distance from the surface.

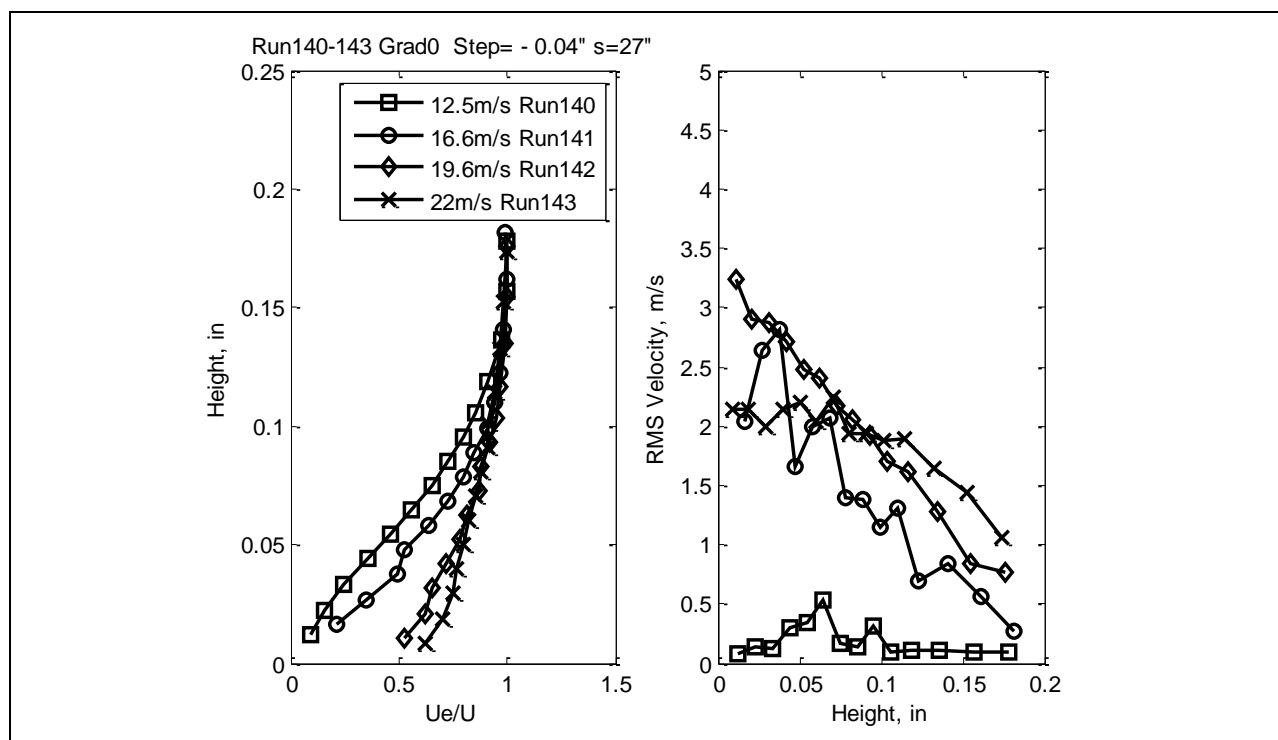


Figure 577: Mean velocity profile (left) and RMS velocity (right), as a function of distance from the surface.

The traversing of a hotwire probe through the boundary layer was done using the Boundary Layer Data System (BLDS) described in Section 7.3.3. The plots below (Figures 578-581) show the mean velocity profiles and velocity RMS as function of distance from the wall for Gradient-A. The data are collected for a set of runs (different freestream velocity) but for the same model and step height in one plot. If transition happened, the velocity profile changed to a typical turbulent one and the RMS increased correspondingly as can be seen in Figure 579 for 17.6m/s and 20m/s in Figure 580 for 23.6m/s and 27.6m/s. The change in velocity profile during transition was used to compare with a skin friction distribution change during transition obtained from Preston tube measurements.

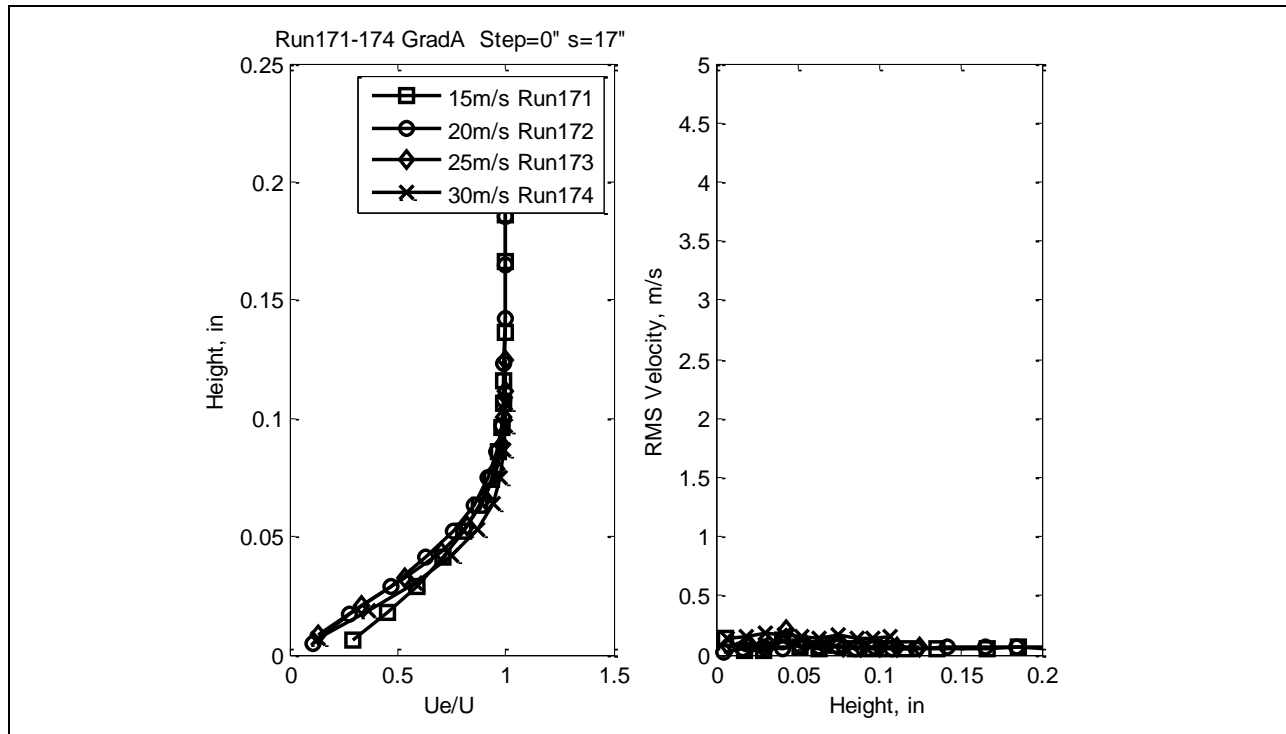


Figure 578: Mean velocity profile (left) and RMS velocity (right), as a function of distance from the surface.

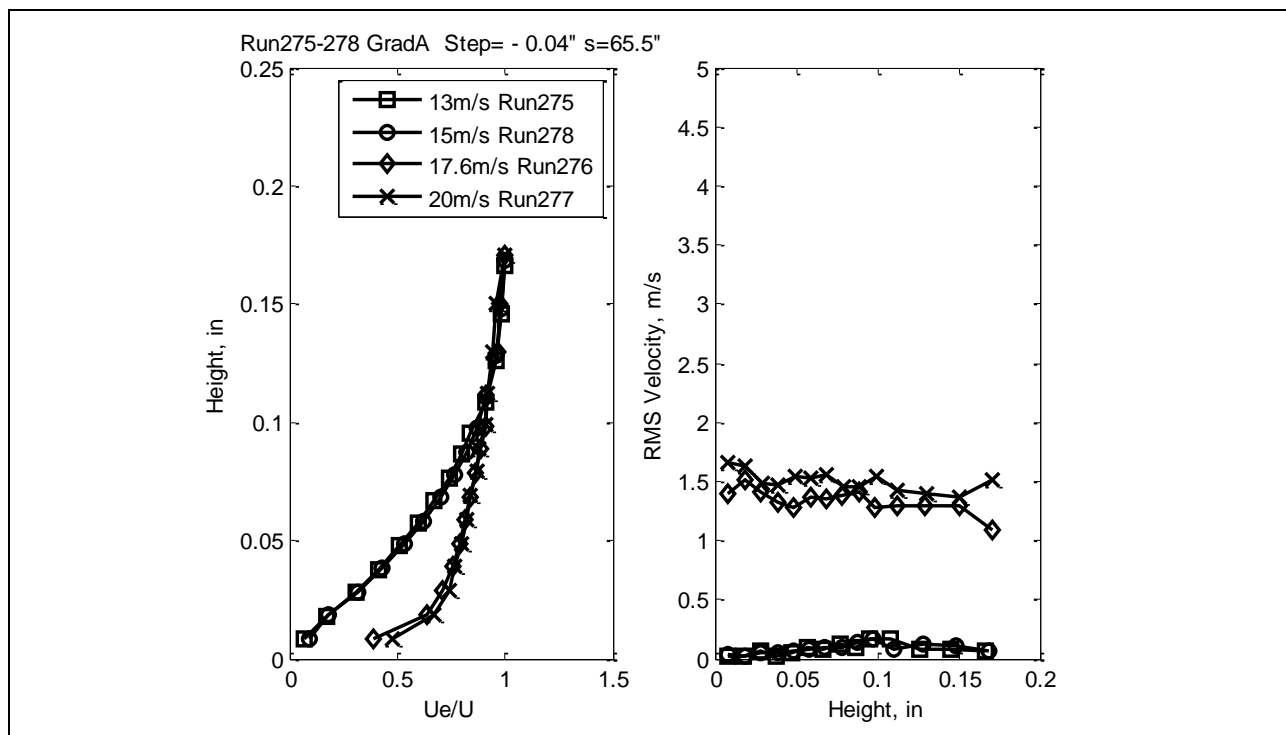


Figure 579: Mean velocity profile (left) and RMS velocity (right), as a function of distance from the surface.

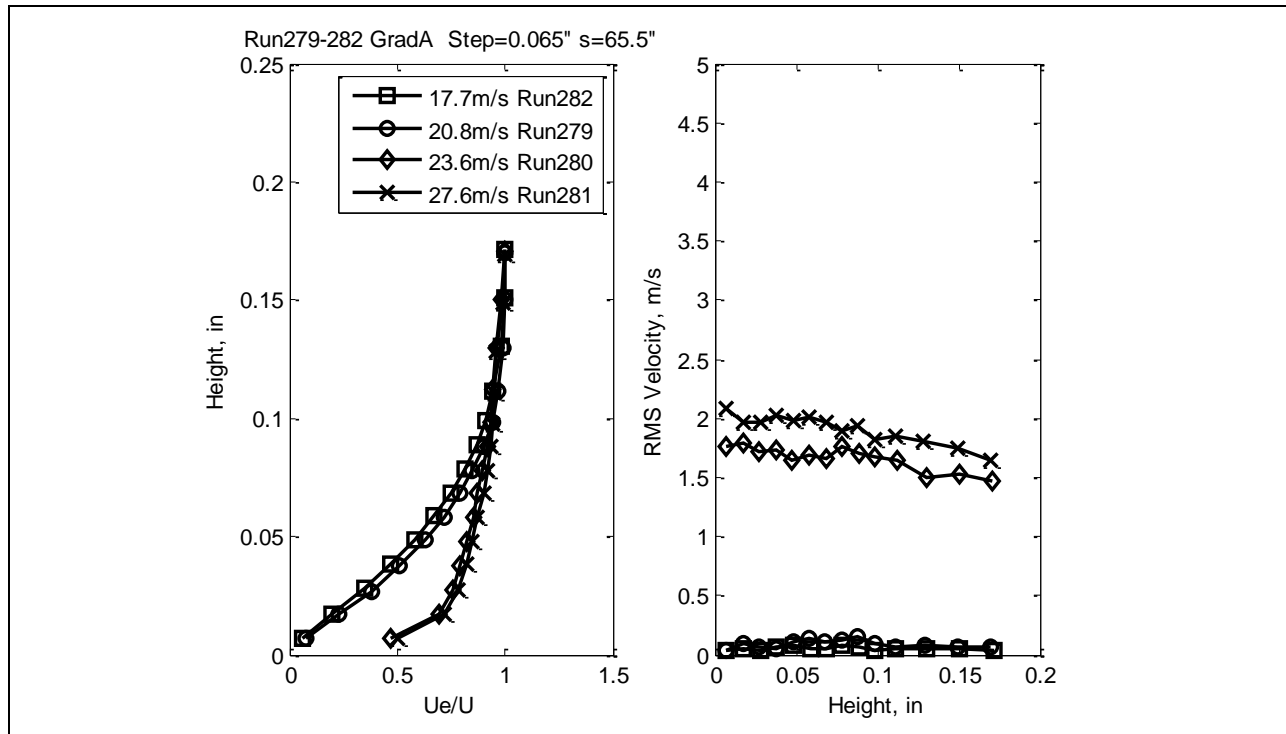


Figure 580: Mean velocity profile (left) and RMS velocity (right), as a function of distance from the surface.

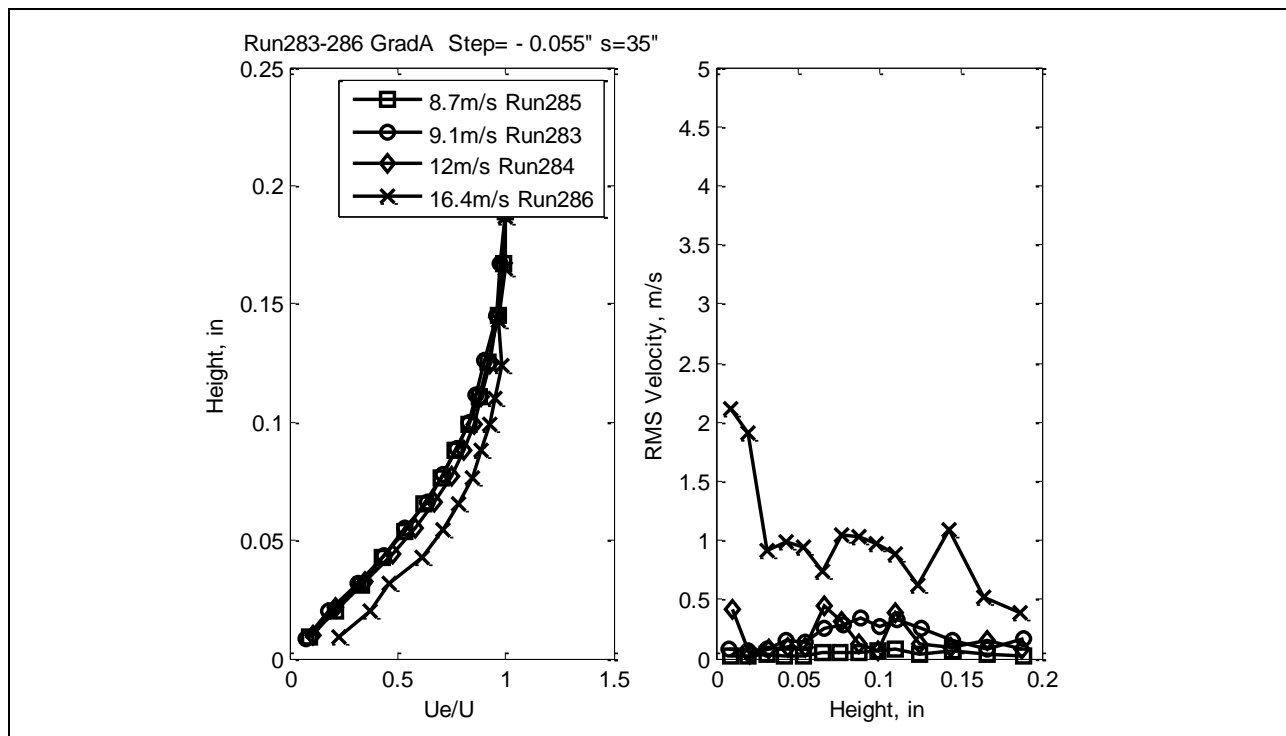


Figure 581: Mean velocity profile (left) and RMS velocity (right), as a function of distance from the surface.

This section, along with Section 7.5.7.6, contains additional data on flow uniformity measured with hot-wires and possible model vibrations measured with accelerometers. The origin of non-uniformity could be related with asymmetry of the flow in the test section introduced by the flow geometry (car, model distortion etc.). The model vibrations naturally could appear during car motion. It was crucial to have good flow uniformity especially in span-wise direction because during measurements the hot-wires were placed at some separation in span-wise direction to prevent their influence on each other. It should be guaranteed that possible span-wise flow variation is negligible compared to flow change in stream-wise direction.

Turbulence intensity (TI) was measured during flow uniformity testing. The obtained values on the one hand underestimate the real ones because only one velocity component (stream-wise) was measured. On the other hand, the electronic noise observed in the velocity signal (see spectra in Section 7.5.7.1) could effectively contribute to the TI.

Flow uniformity measurements are first presented for Gradient-Zero, then Gradient-A, and finally, Gradient-B.

Span-wise uniformity testing in freestream at the step location for Gradient-Zero for zero step (clean plate) is reported here. Run 39 (Figures 582-583) and Run 46 (Figures 584-585) show spectra, velocity time series and corresponding plots of TI (Figure 586 and Figure 587) in freestream ($k=2\text{in}$) slightly upstream of the step location for two different freestream speeds as function of span-wise distance. The spectra show no difference for different span-wise positions and the uncorrected TI varies from 0.25 to 0.4% for Run 39 and stays at the level 0.4% for Run 46.

Span-wise uniformity testing was also undertaken in the boundary layer at the step location for zero step. Run 48 (Figure 588-589) and Run 49 (Figures 590-591) show spectra, velocity time series and corresponding plots of TI (Figure 592 and Figure 593) in a boundary layer ($k=0.02\text{in}$) slightly upstream of the step location for two different freestream speeds as function of span-wise distance. The spectra and the uncorrected TI are the same ($\text{TI}=0.3\%$) for all except for the uppermost location ($\text{TI}=0.6\text{-}1.2\%$).

Stream-wise uniformity testing in freestream for zero step is reported here. Run 117 (Figures 594-595) and Run 118 (Figures 596-597) show spectra, velocity time series and corresponding plots of TI (Figure 598 and Figure 599) in freestream ($k=2\text{in}$) at different stream-wise positions (hot-wires were separated in span-wise direction in order to prevent their influence on each other) for two different freestream speeds. The spectra show no difference for different stream-wise positions and the uncorrected TI is about 0.4%.

The differencing technique outlined in Reshotko *et al*²² was applied to the data and led to a significant reduction in the turbulence intensity. For all runs, the TI was found to be in the range 0.05-0.10%, despite the low frequency uncertainty associated with the short run time.

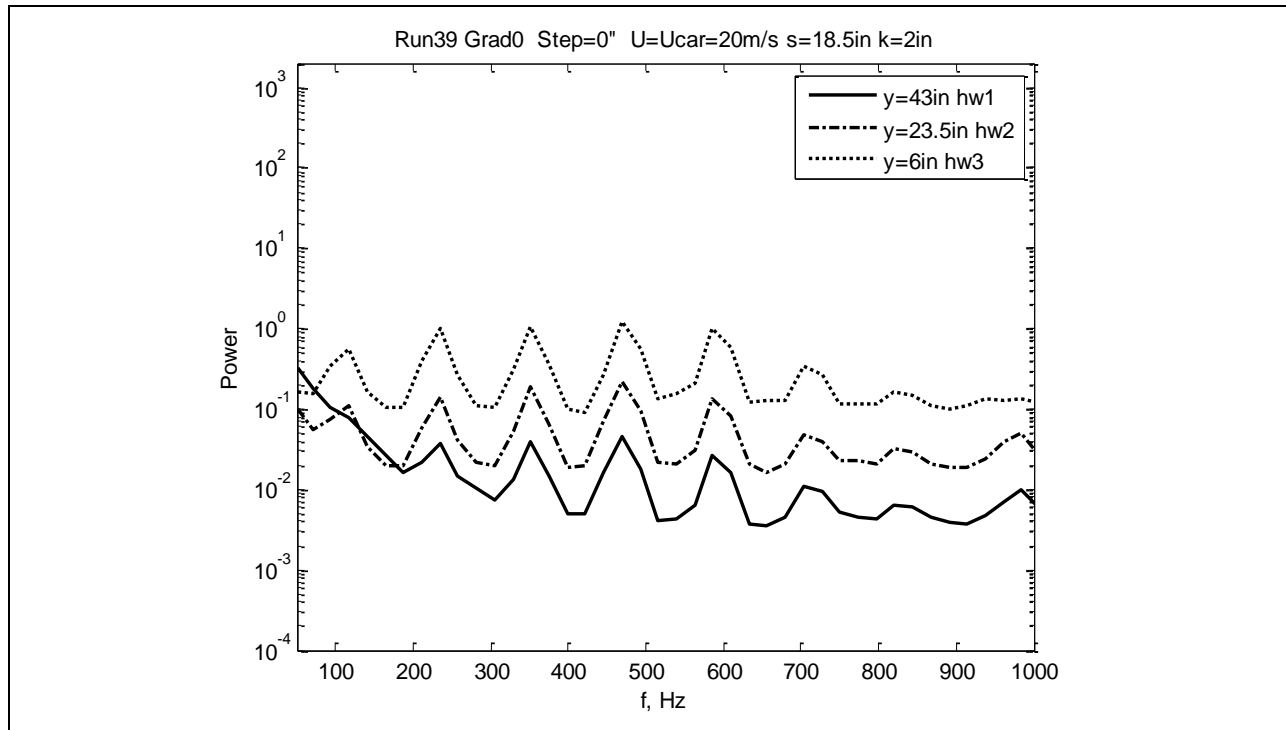


Figure 582: Power spectra.

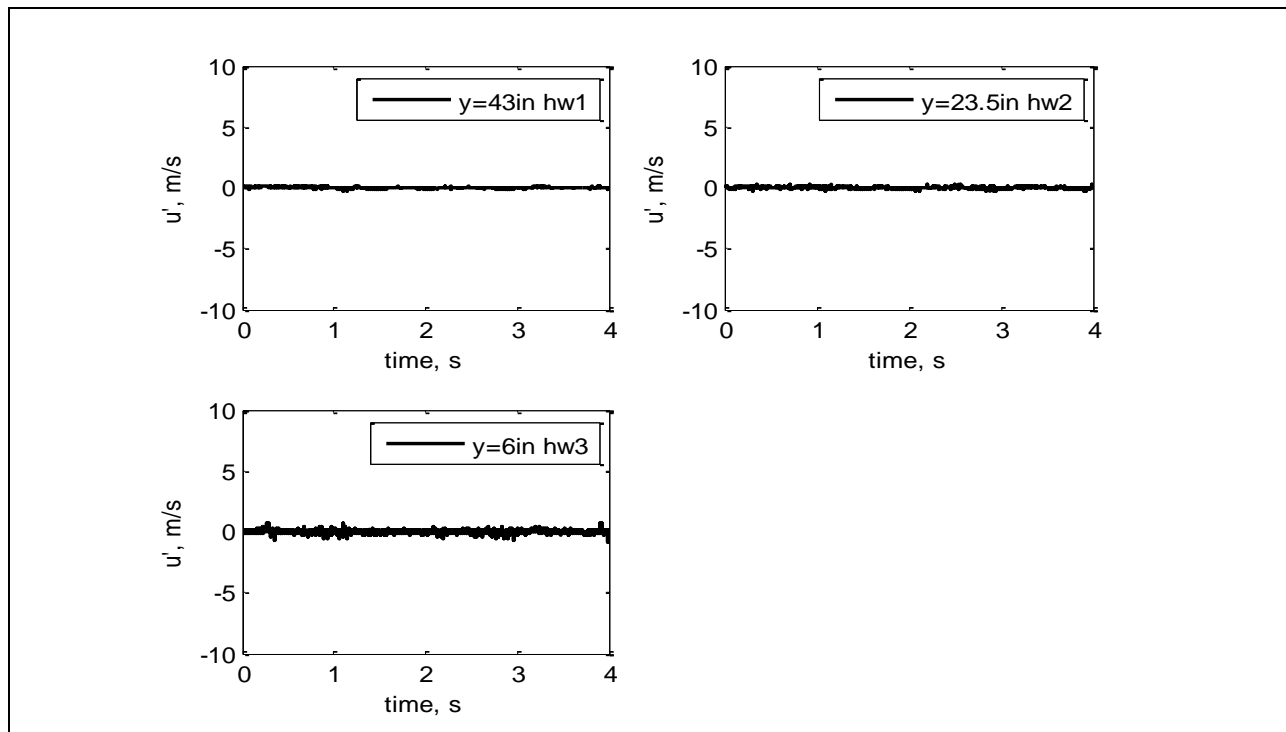


Figure 583: Velocity time series.

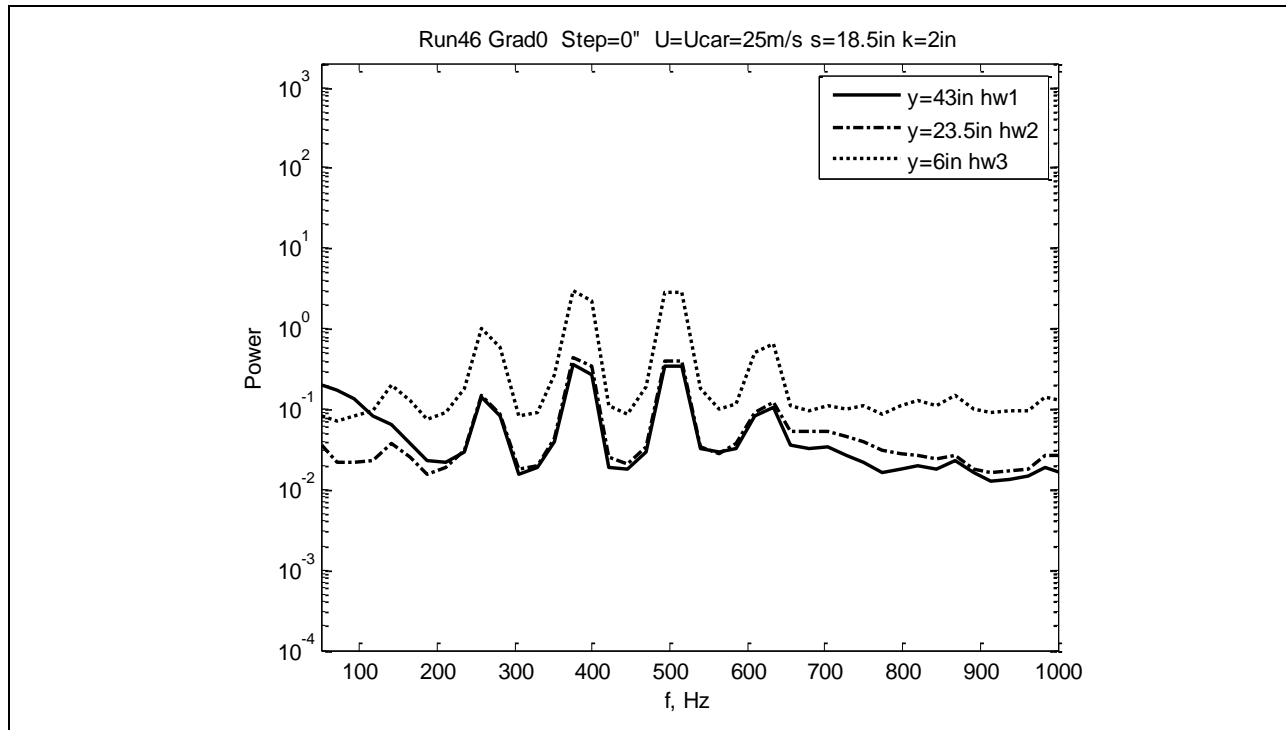


Figure 584: Power spectra.

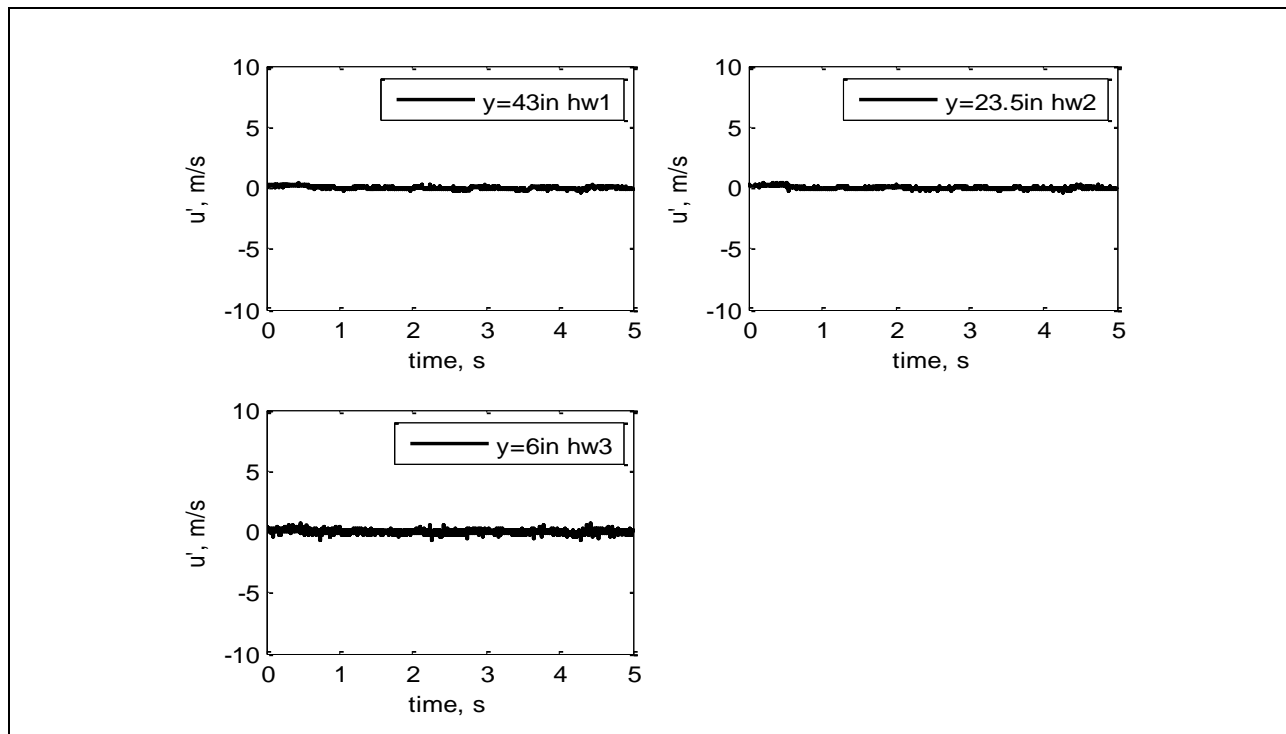


Figure 585: Velocity time series.

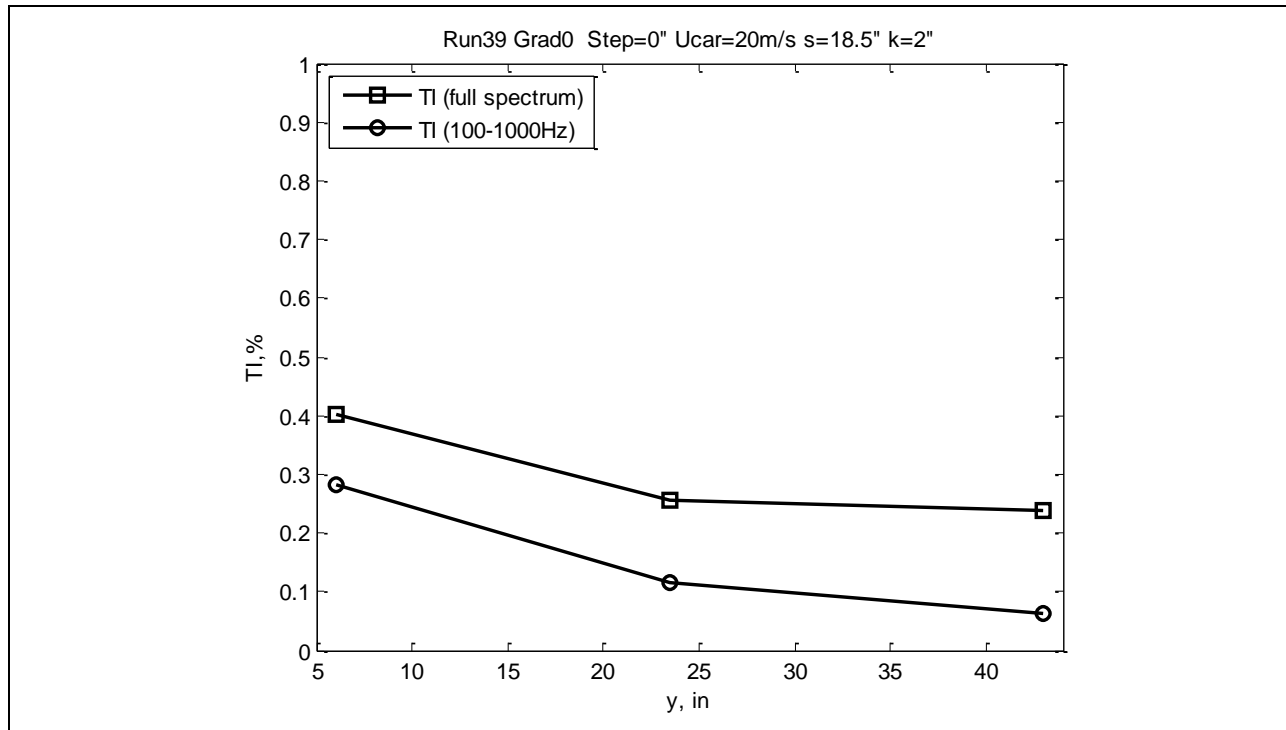


Figure 586: Turbulence intensity.

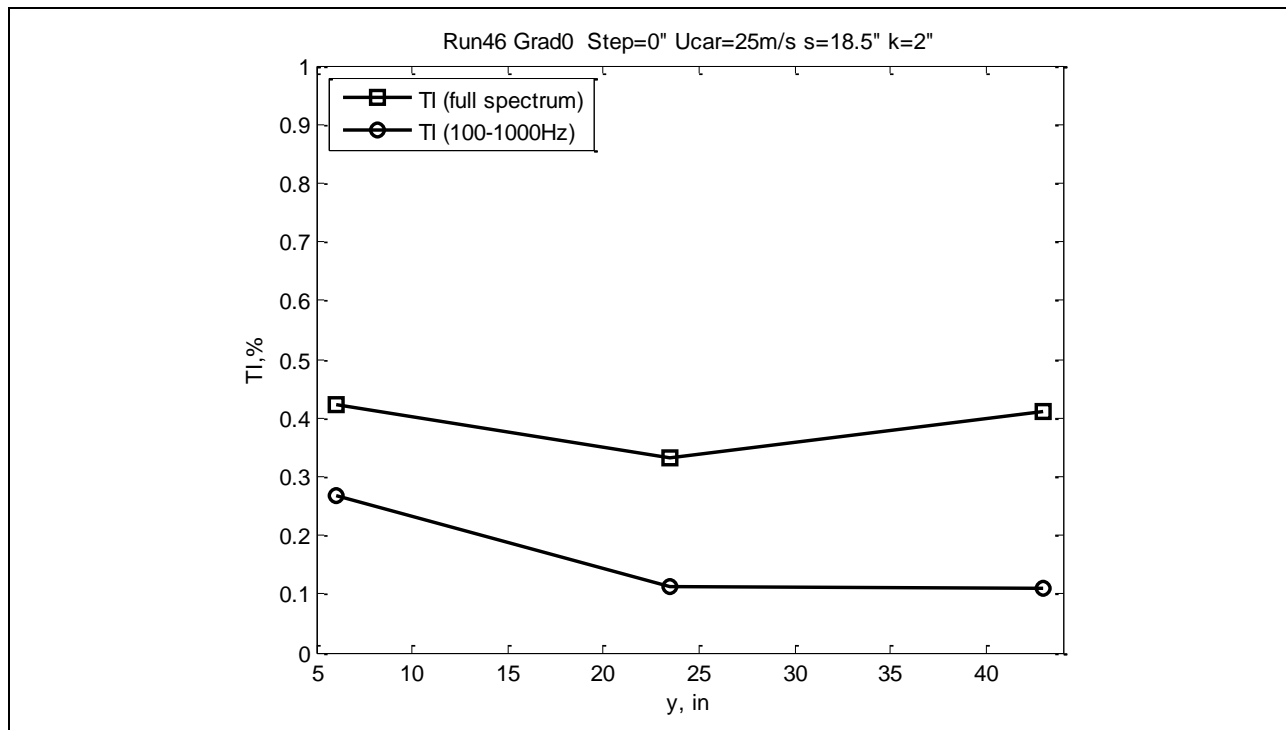


Figure 587: Turbulence intensity.

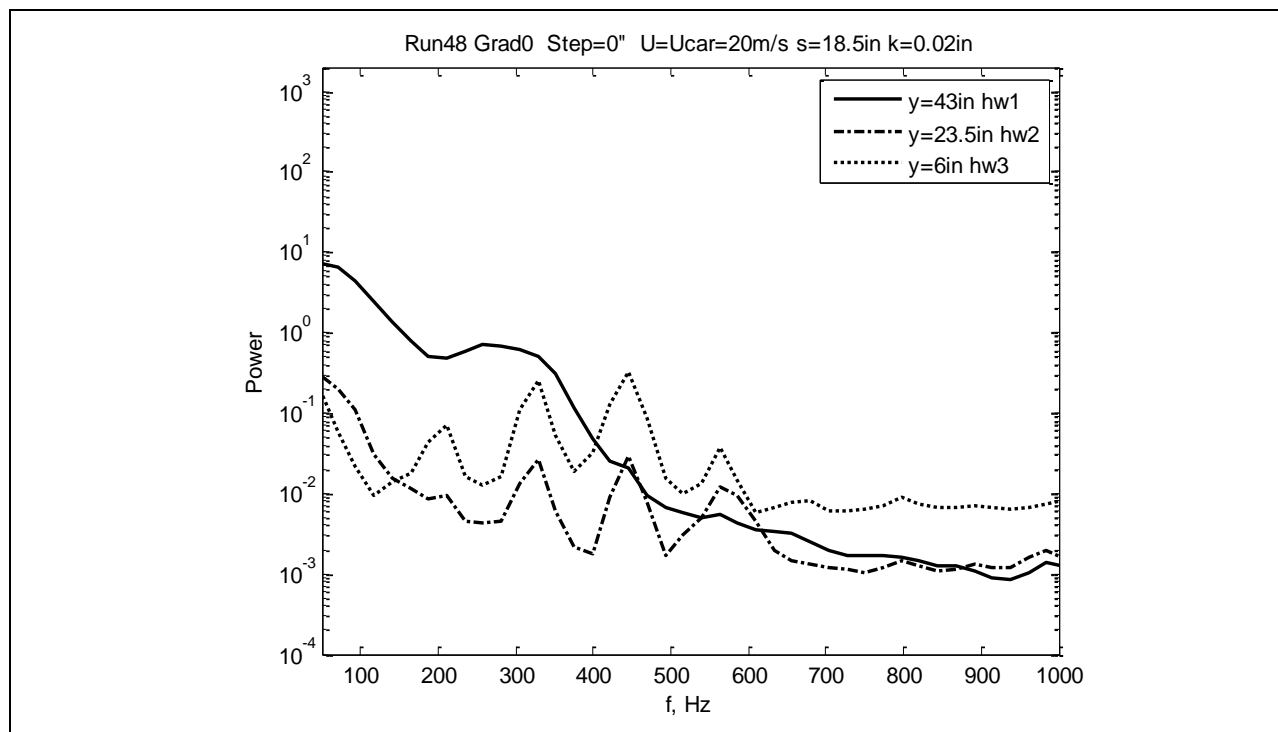


Figure 588: Power spectra.

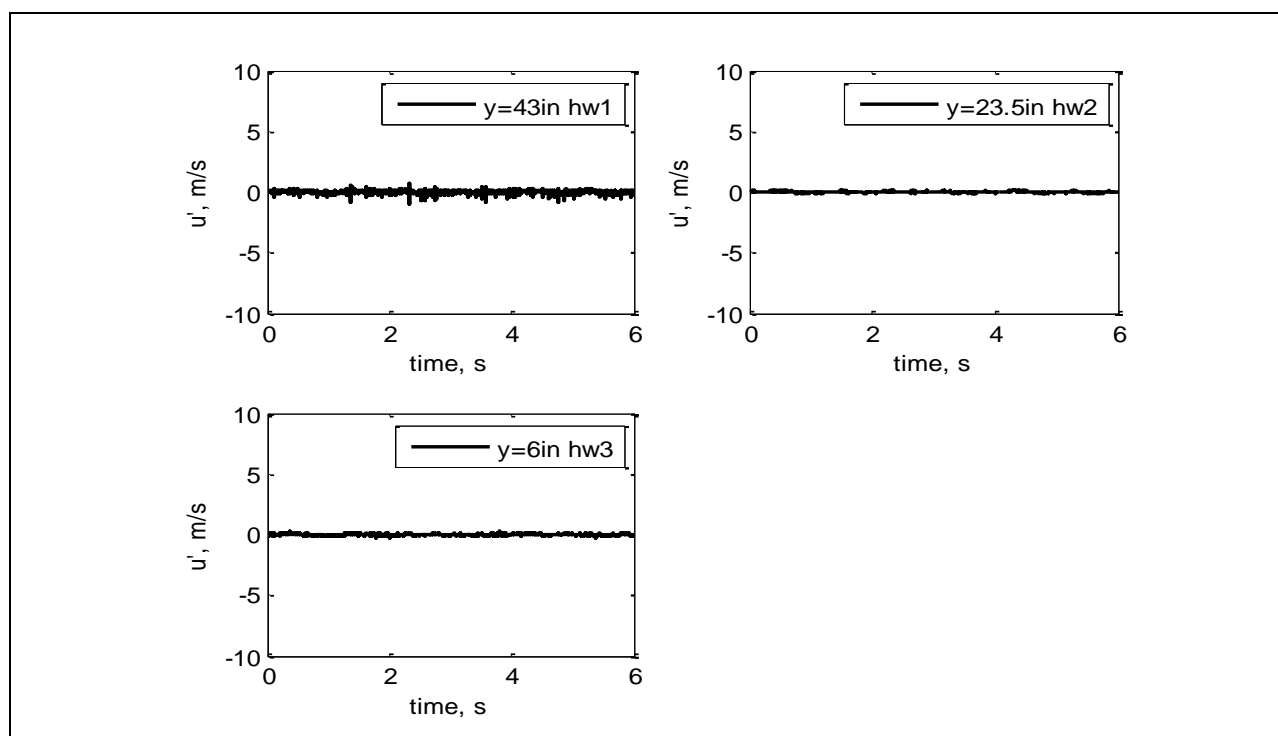


Figure 589: Velocity time series.

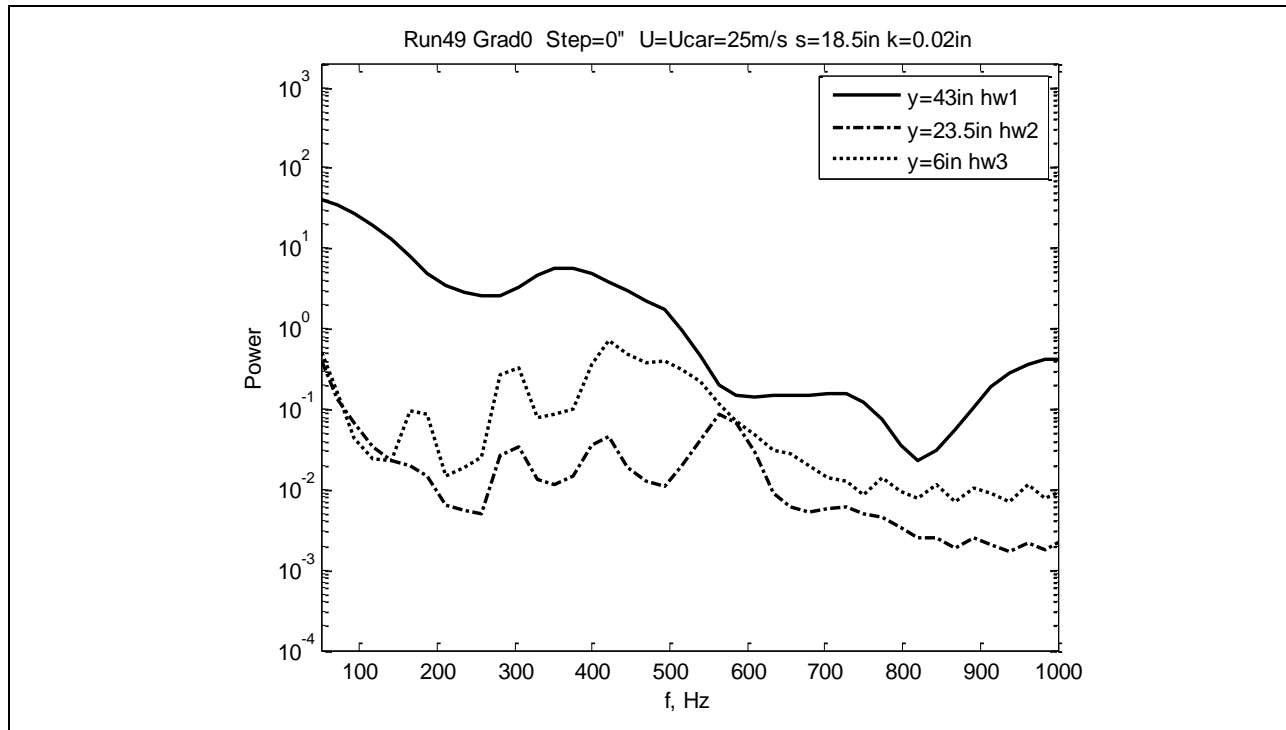


Figure 590: Power spectra.

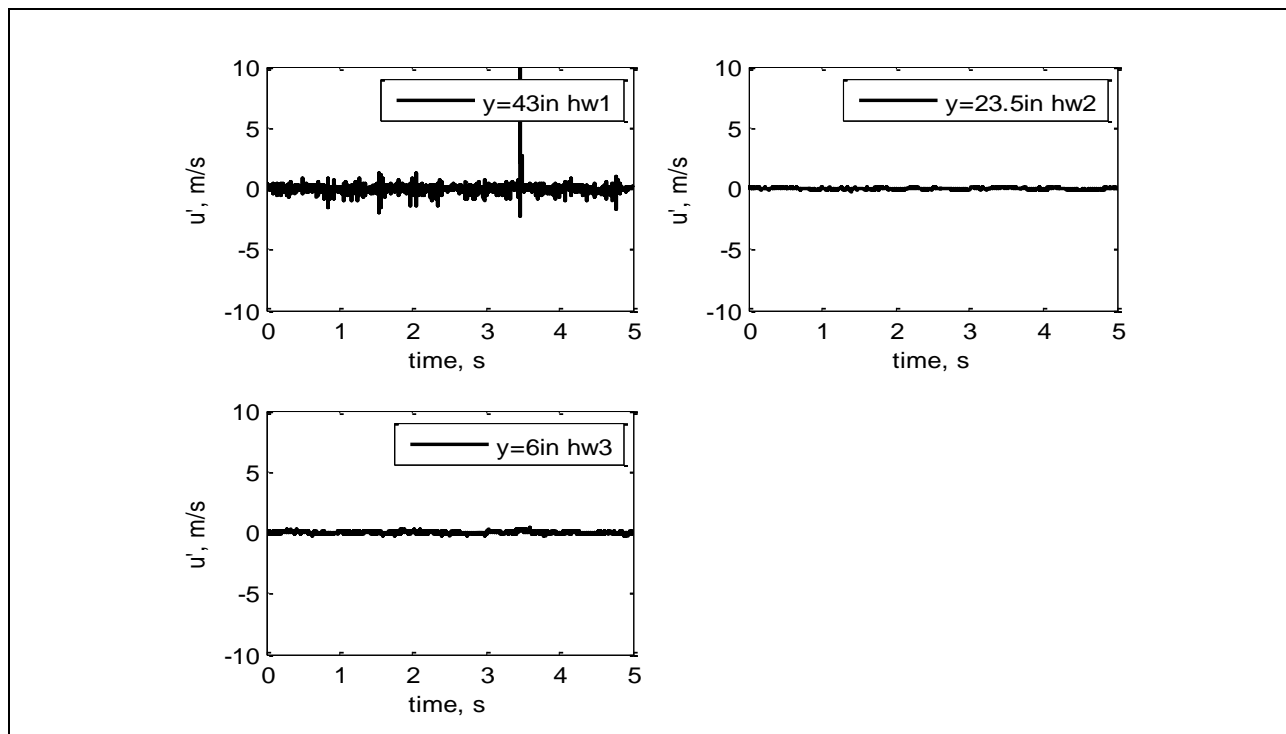


Figure 591: Velocity time series.

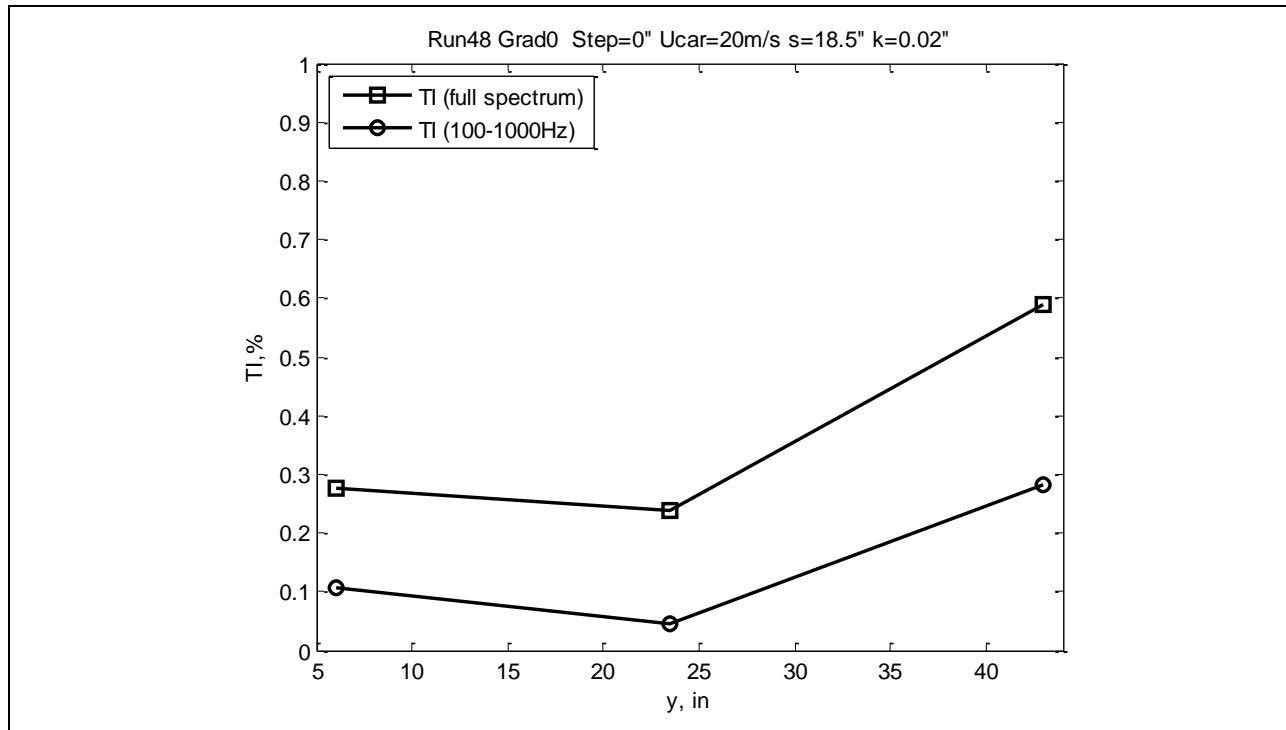


Figure 592: Turbulence intensity.

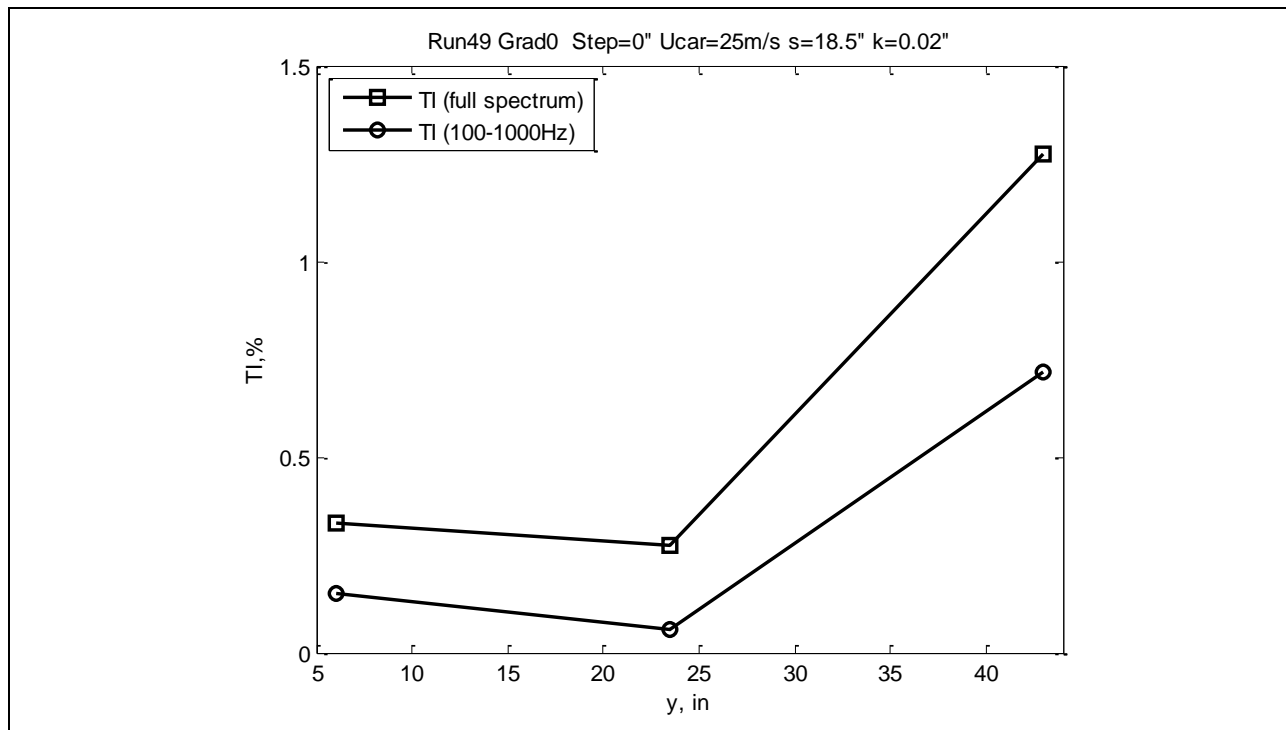


Figure 593: Turbulence intensity.

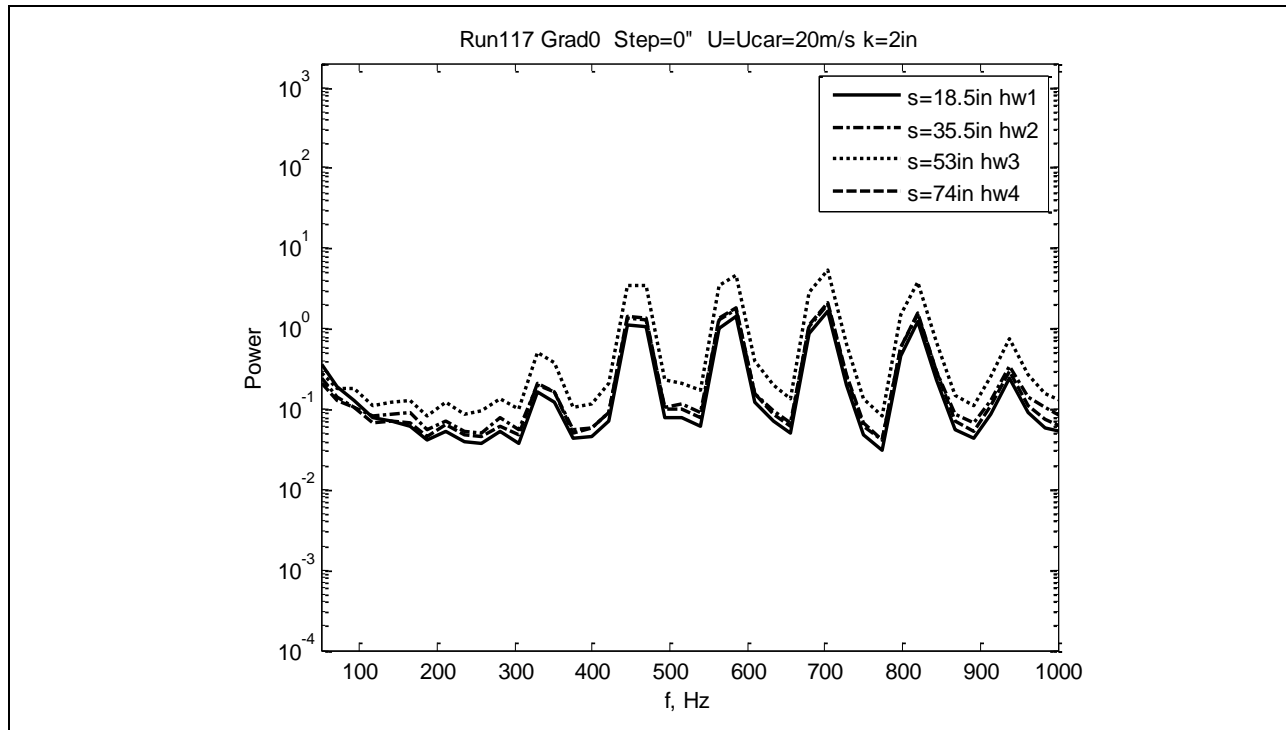


Figure 594: Power spectra.

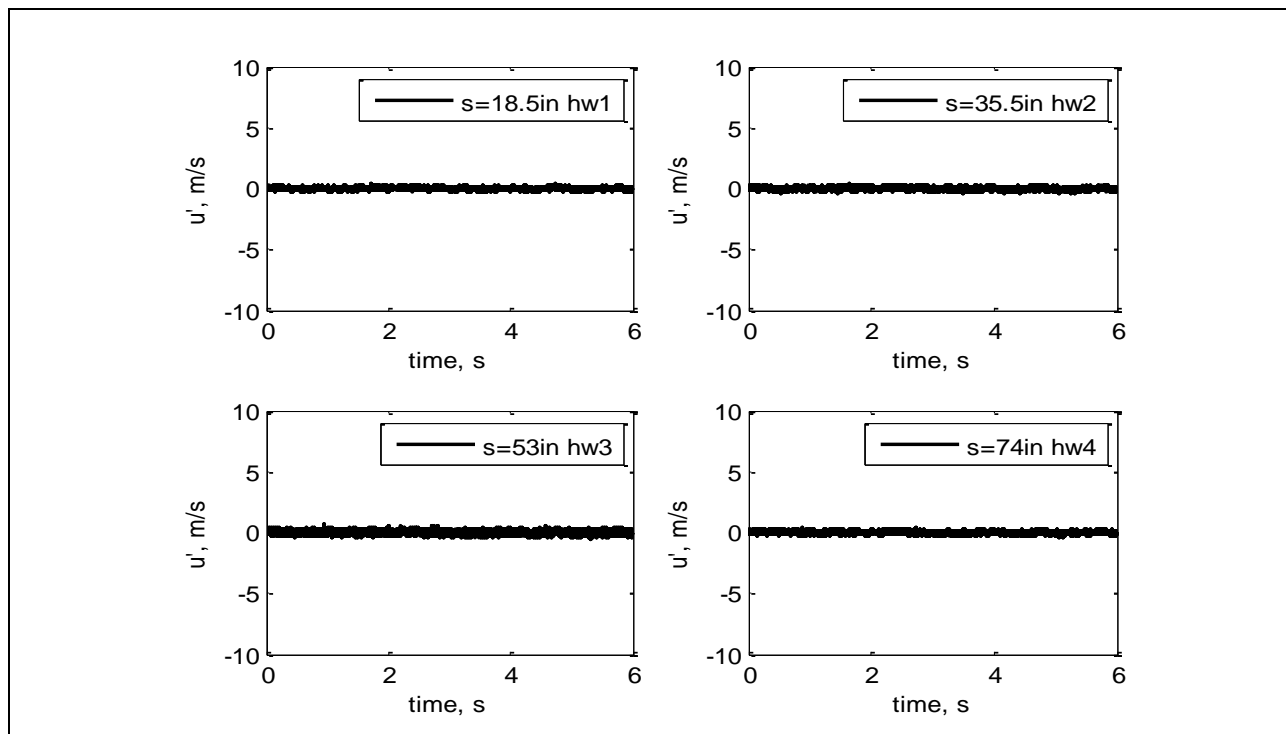


Figure 595: Velocity time series.

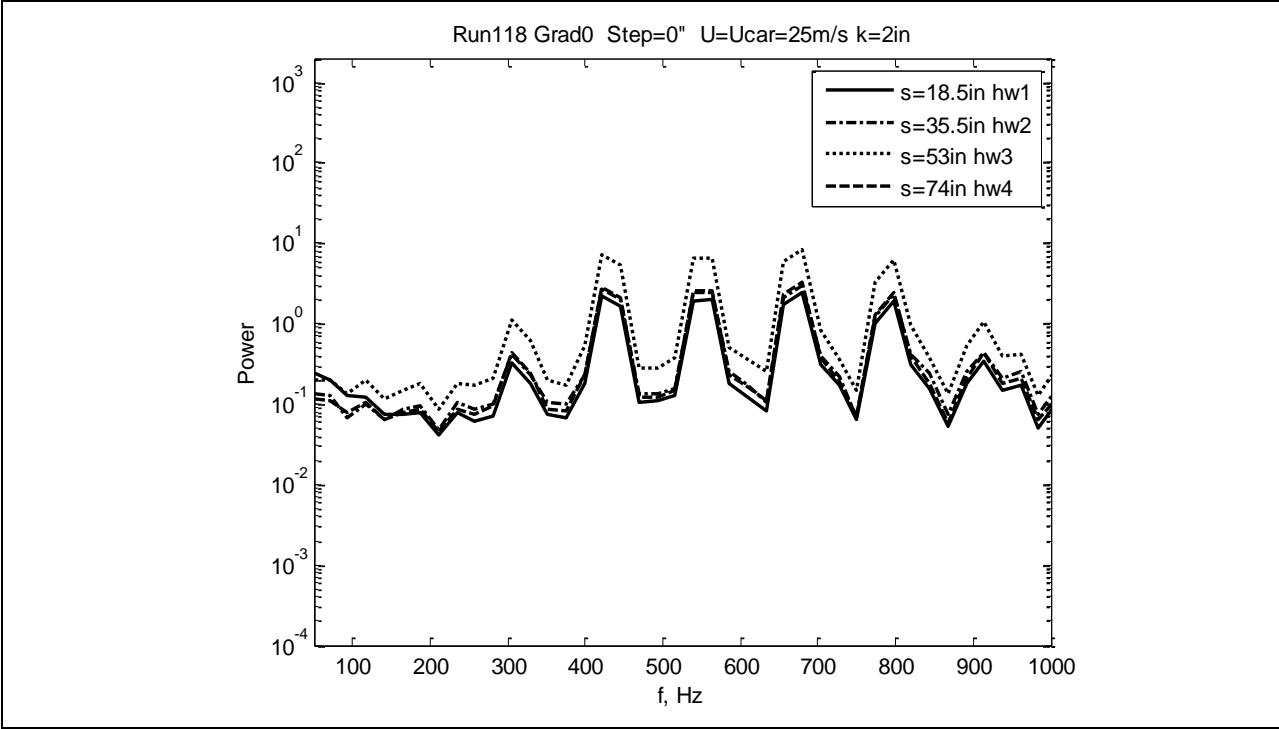


Figure 596: Power spectra.

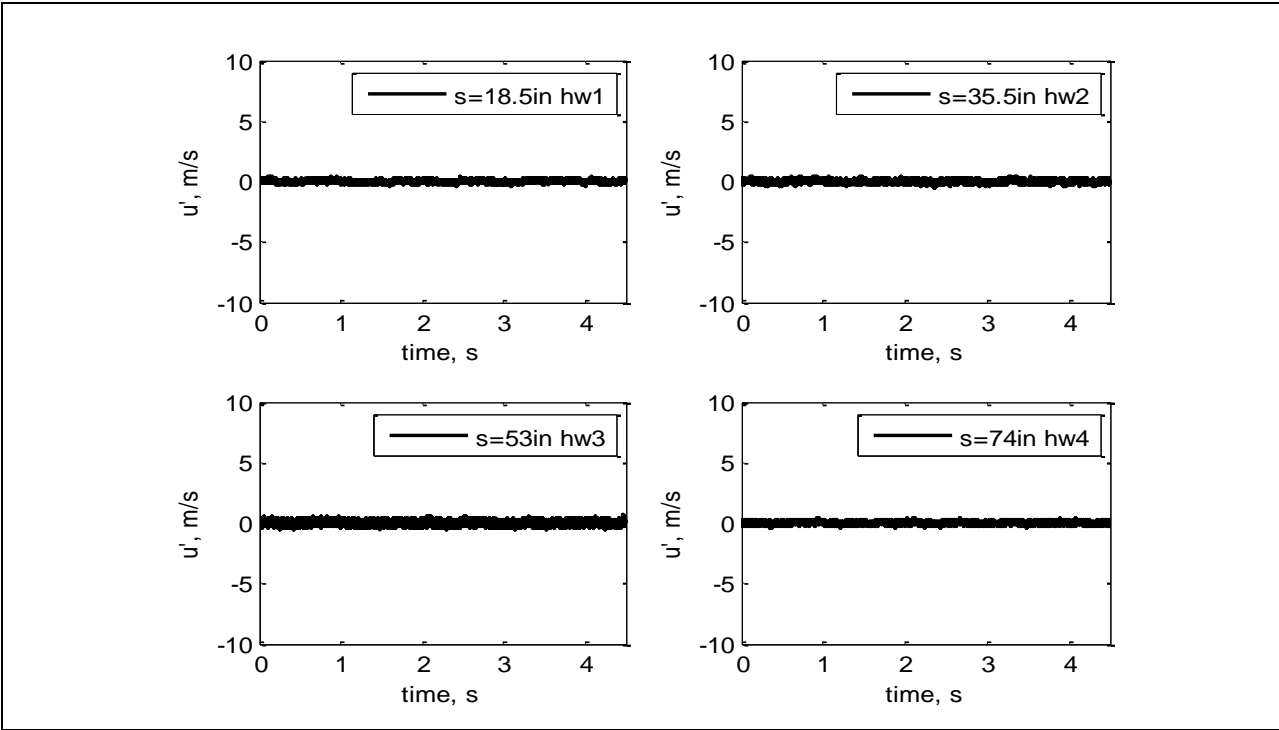


Figure 597: Velocity time series.

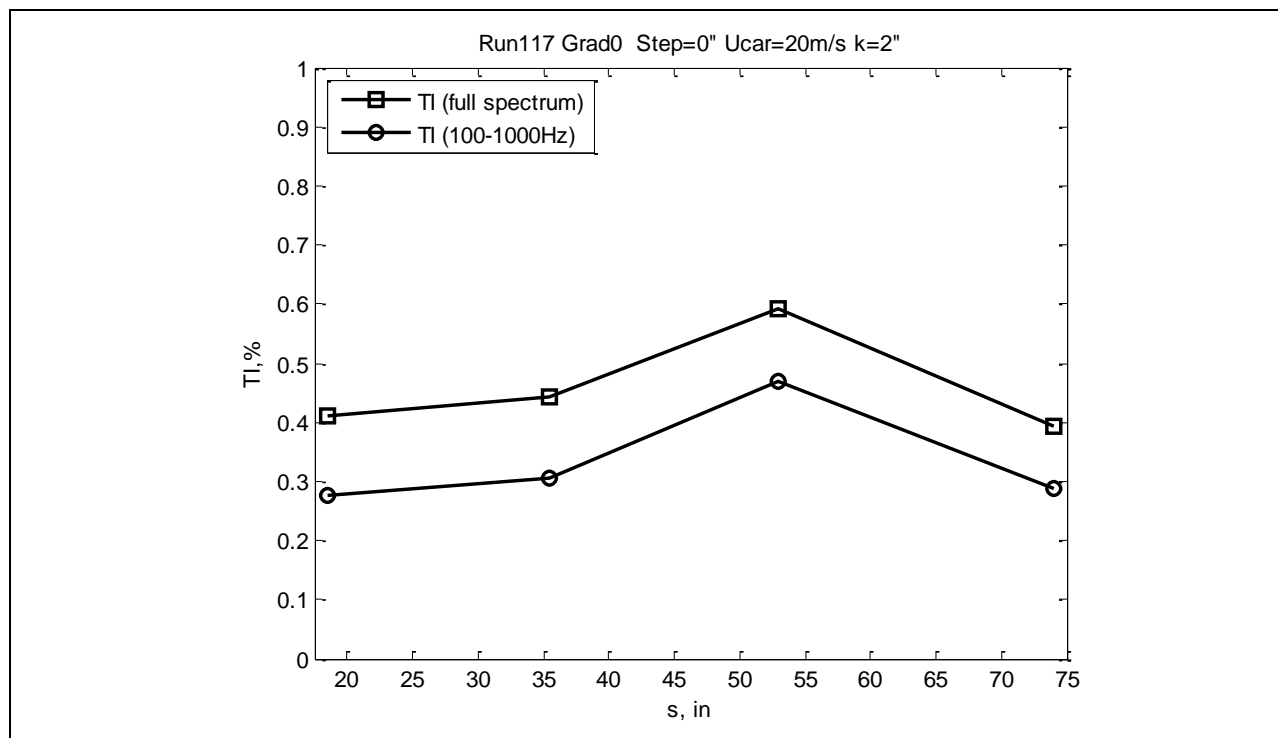


Figure 598: Turbulence intensity.

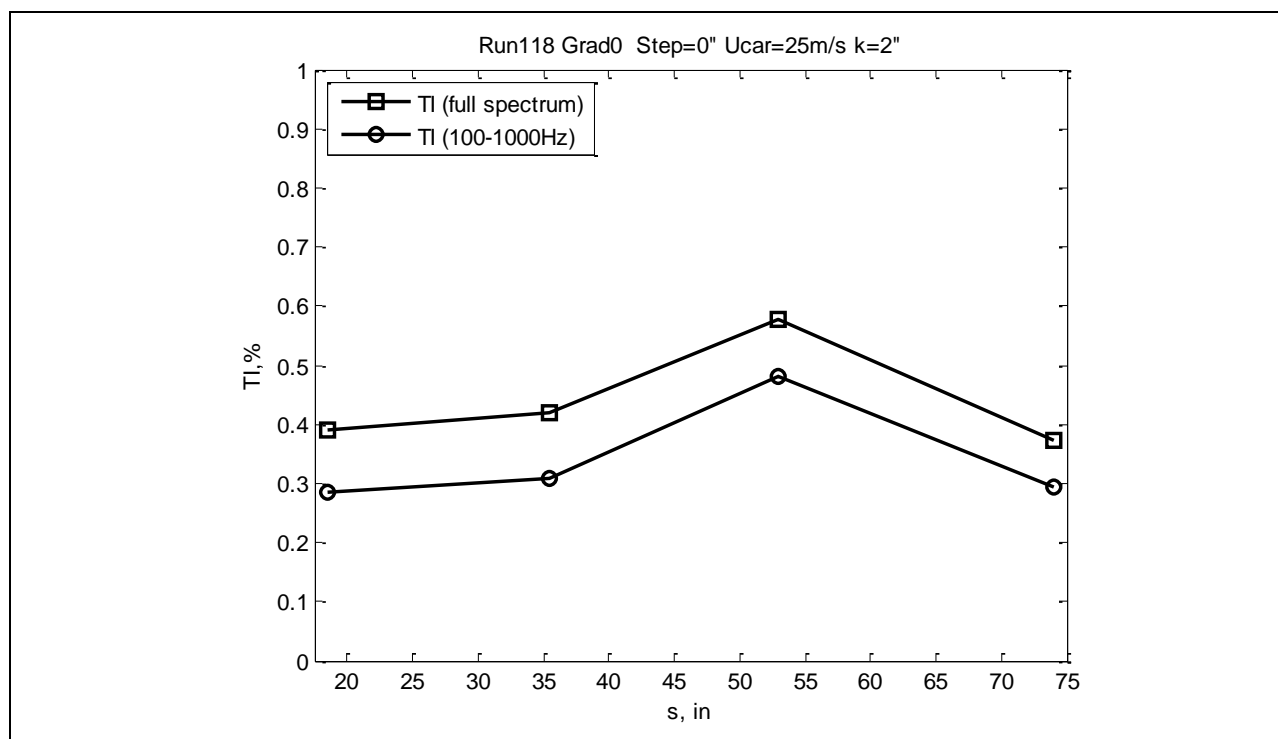


Figure 599: Turbulence intensity.

Flow uniformity testing for Gradient-A is reported here. Spanwise uniformity testing in the freestream at the step location for zero step (clean plate) is shown in Figures 600-605. Run 172 (Figures 600-601) and Run 173 (Figures 602-603) show the spectra, velocity time series and corresponding plots of turbulence intensity (Figure 604 and Figure 605) in the freestream ($k=1.4\text{in}$) slightly upstream of the step location for two different freestream speeds as function of spanwise distance. The spectra show no difference for different spanwise positions and the uncorrected TI is about 0.5% for all locations.

Spanwise uniformity testing in boundary layer at the step location for zero step (clean plate) is shown in Figures 606-611. Run 176 (Figures 606-607) and Run 177 (Figures 608-609) show the spectra, velocity time series and corresponding plots of TI (Figure 610 and Figure 611) in the boundary layer ($k=0.02\text{in}$) slightly upstream of the step location for two different freestream speeds as function of spanwise distance. The spectra show no variation and the uncorrected TI varies from 0.1% to 0.25% for Run 176 and from 0.2% to 0.6% for Run 177.

Streamwise uniformity testing in freestream for zero step (clean plate) is shown in Figures 612-617. Run 182 (Figures 612-613) and Run 183 (Figures 614-615) show the spectra, velocity time series and corresponding plots of uncorrected TI (Figure 616 and Figure 617) in the freestream ($k=1.4\text{in}$) at different streamwise positions (hot-wires were separated in spanwise direction too in order to prevent their influence on each other) for two different freestream speeds. The spectra show no variation and uncorrected TI varies from 0.45% to 0.55% for the Run 182 and from 0.5% to 0.6% for the Run 183.

Spanwise uniformity testing in boundary layer downstream of step for zero step (clean plate) is shown in Figures 618-623. Run 253 (Figures 618-619) and Run 254 (Figures 620-621) show the spectra, velocity time series and corresponding plots of TI (Figure 622 and Figure 623) in boundary layer ($k=0.02\text{in}$) downstream of the step ($s=31.5\text{in}$) for two different freestream speeds as function of spanwise distance. The spectra look similar for different spanwise positions and uncorrected TI varies from 0.1% to 0.2% for Run 253 and from 0.15% to 0.4% for Run 254.

Spanwise uniformity testing in boundary layer downstream of step for non-zero step is shown in Figures 624-629. Run 248 (Figures 624-625) and Run 249 (Figures 626-627) show the spectra, velocity time series and corresponding plots of TI (Figure 628 and Figure 629) in the boundary layer ($k=0.02\text{in}$) down-stream of the step ($s=31.5\text{in}$) for two different freestream speeds as function of spanwise distance. For the lower speed (Run 248), the spectra look similar to the zero step case, but for the higher speed (Run 249), there is significant variation in the spectra with span-wise distance and TI also varies significantly from 0.2% to 2.2%. This may be related to the fact that when the Reynolds number increased, the flow became more unstable and very sensitive to small variations of the initial and boundary conditions which were present in spanwise direction.

The differencing technique outlined in Reshotko *et al*²² was applied to the data and led to a significant reduction in the turbulence intensity. For the streamwise runs, the TI was found to be in the range 0.05-0.10%, despite the low frequency uncertainty associated with the short run time, while the variation with spanwise distance observed in the uncorrected spectra persisted, with a maximum corrected TI of 0.2%

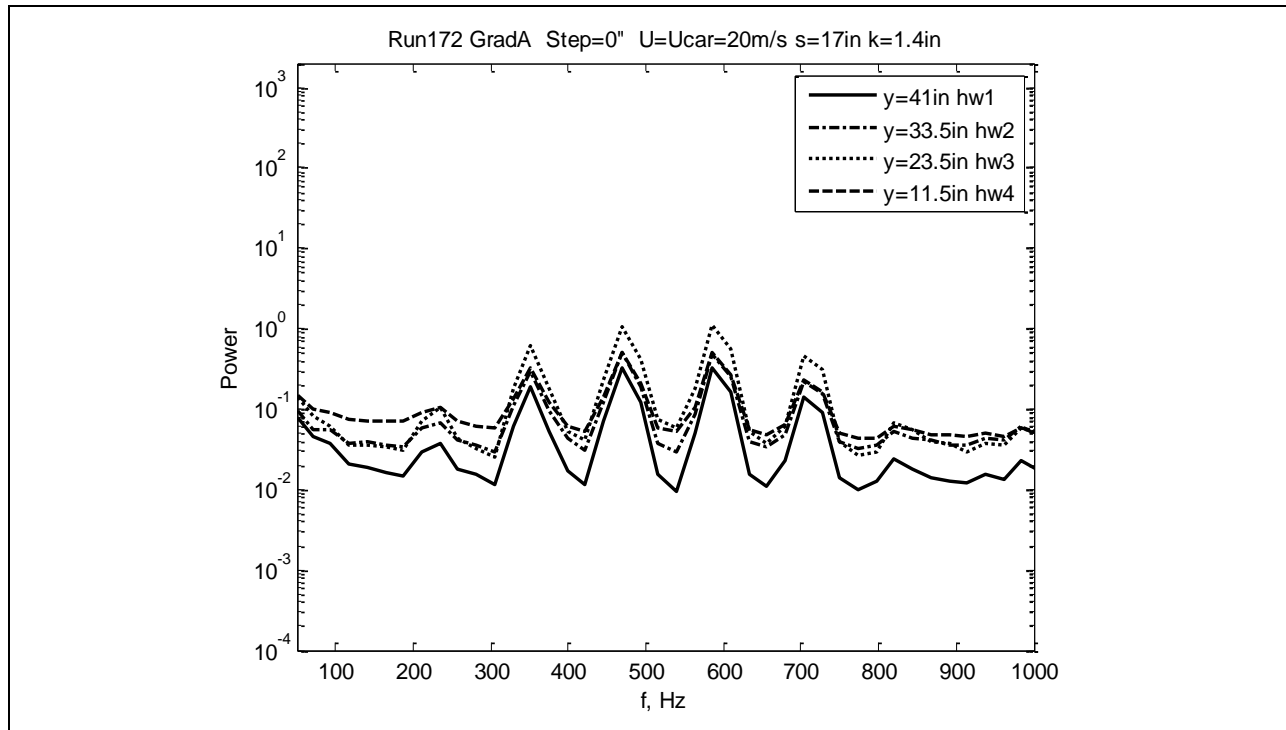


Figure 600: Power spectra.

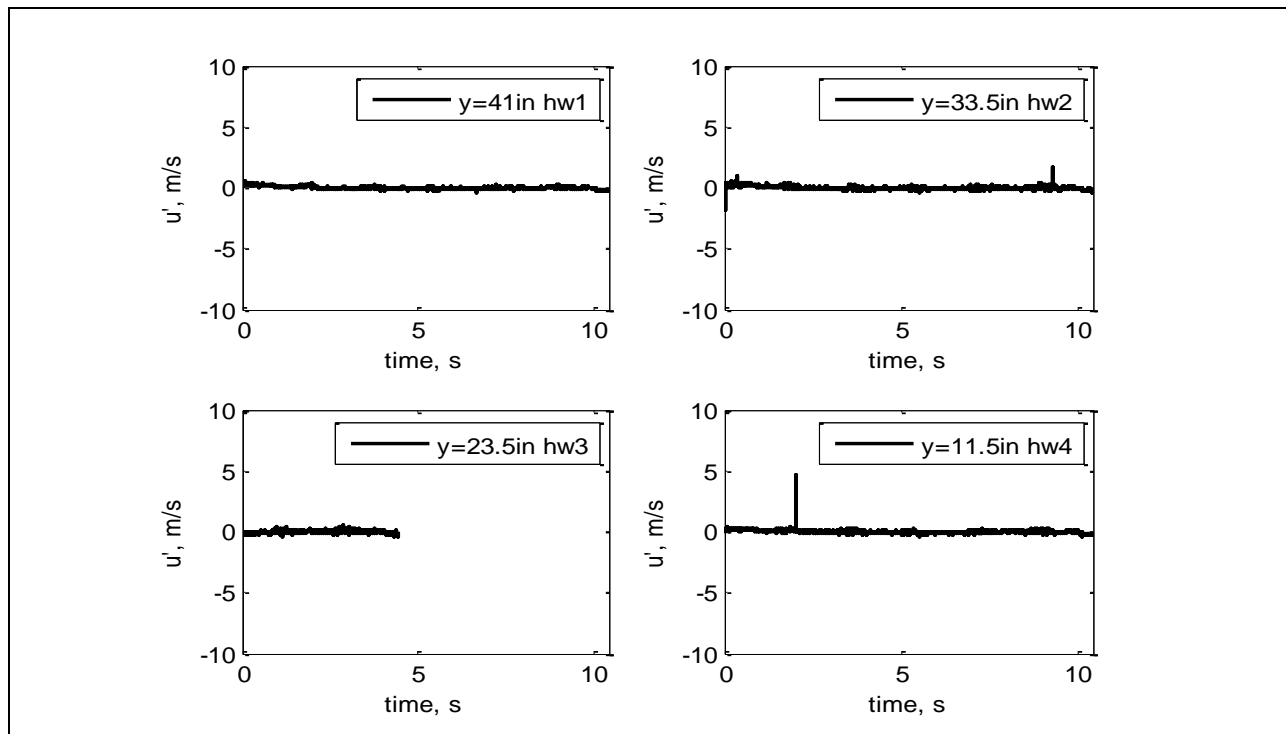


Figure 601: Velocity time series.

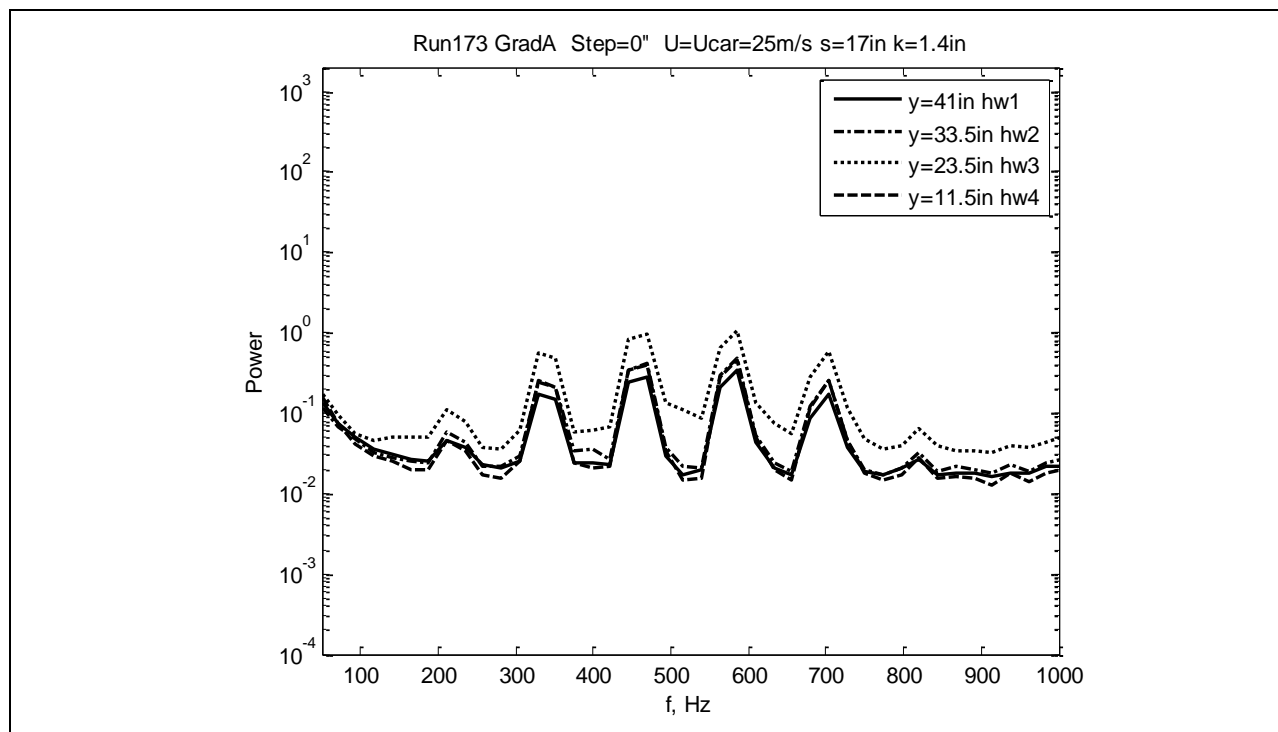


Figure 602: Power spectra.

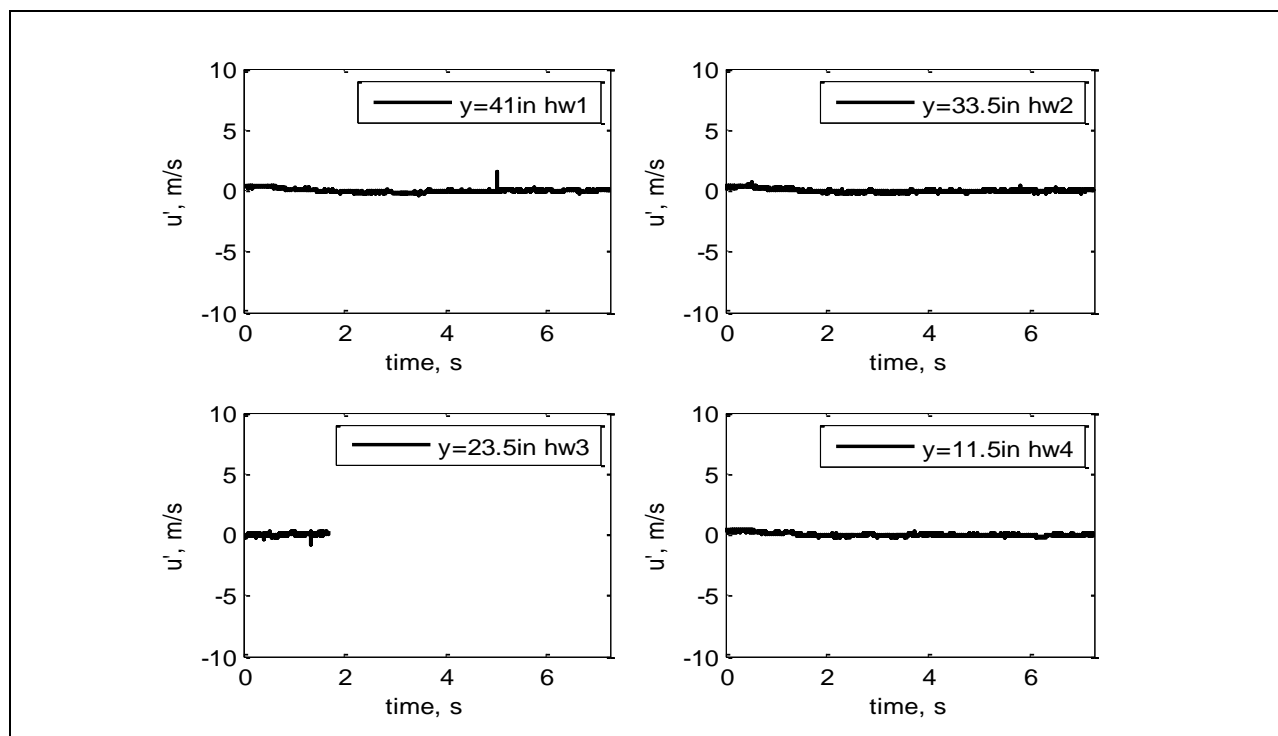


Figure 603: Velocity time series.

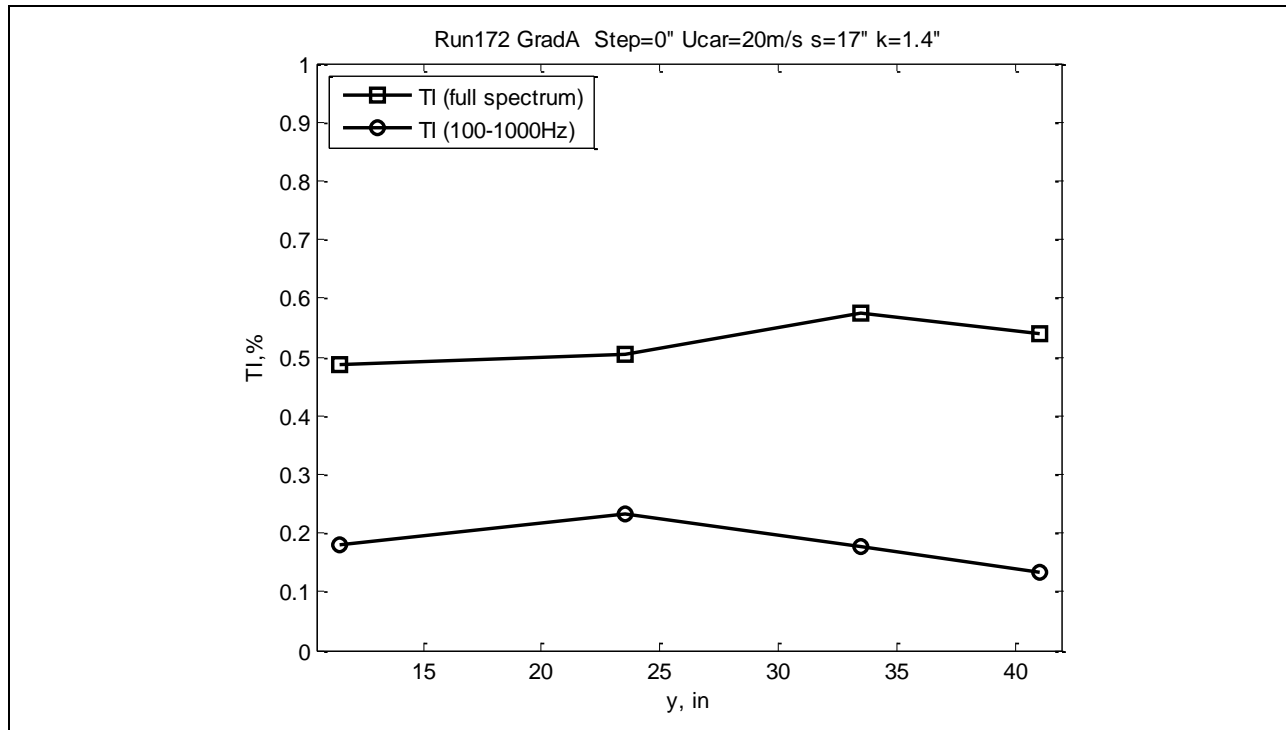


Figure 604: Turbulence intensity.

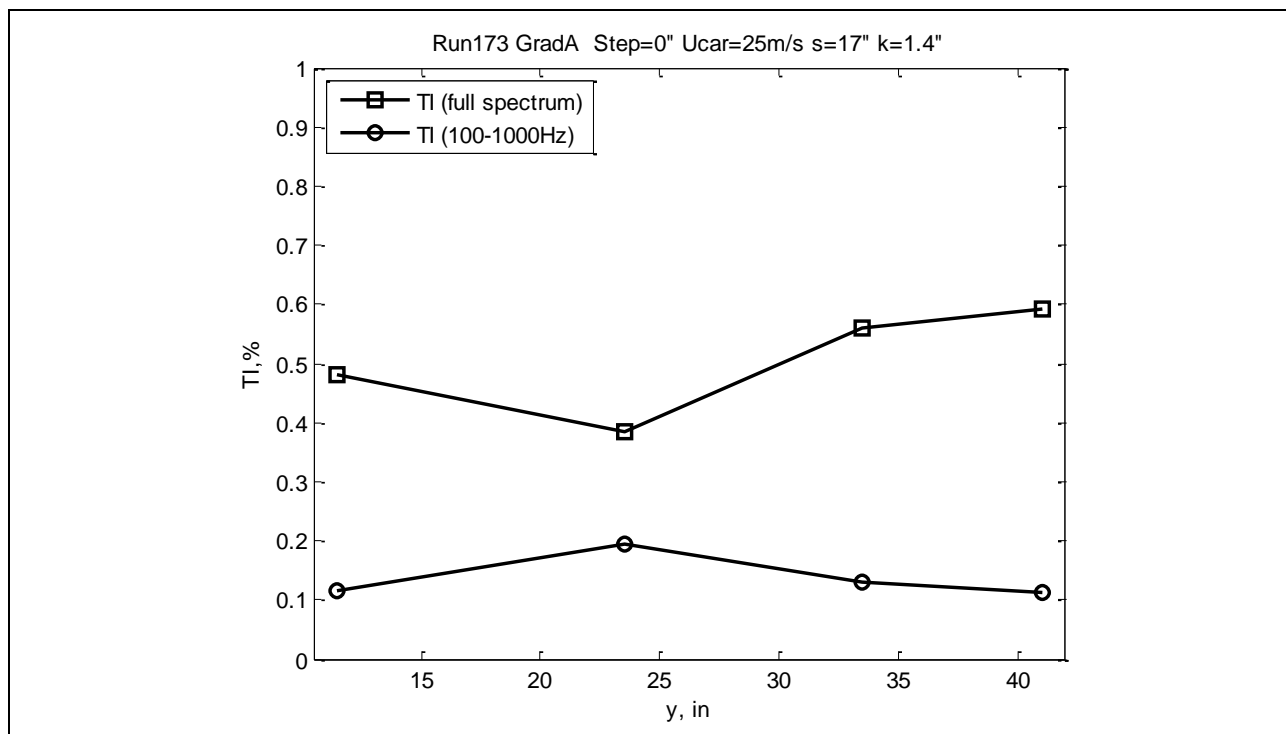


Figure 605: Turbulence intensity.

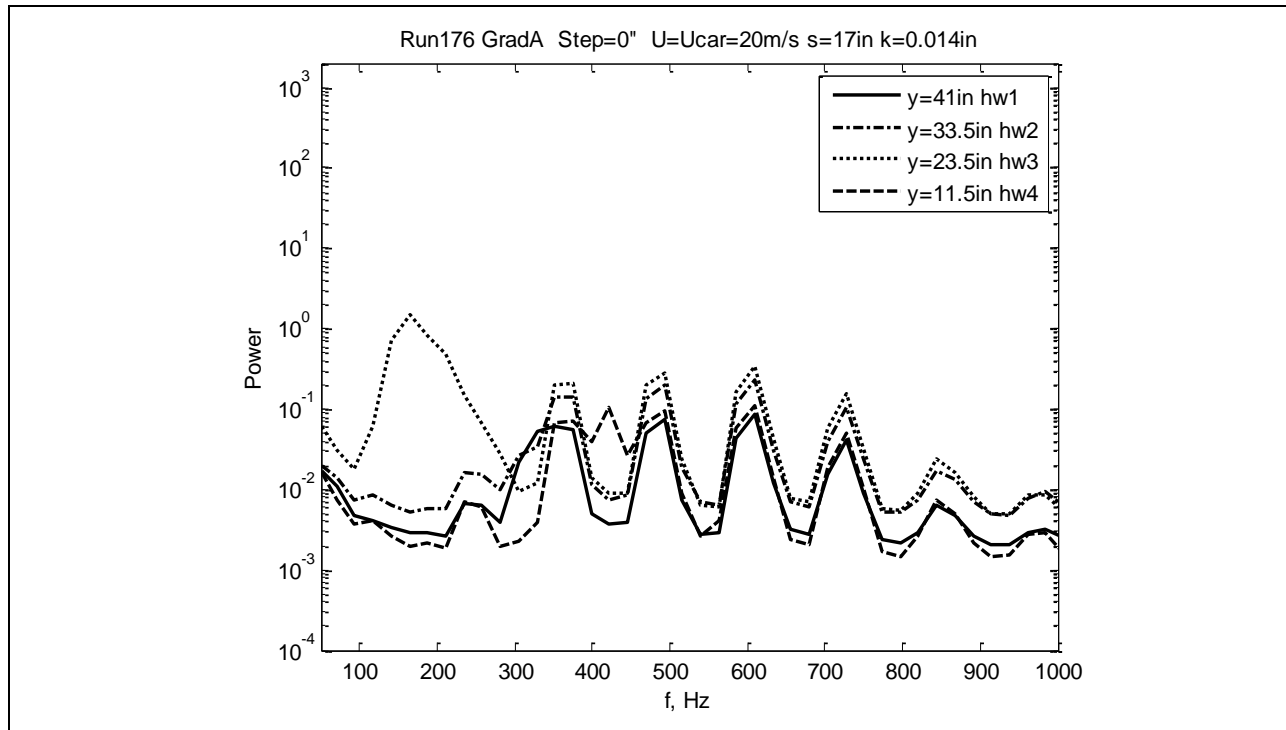


Figure 606: Power spectra.

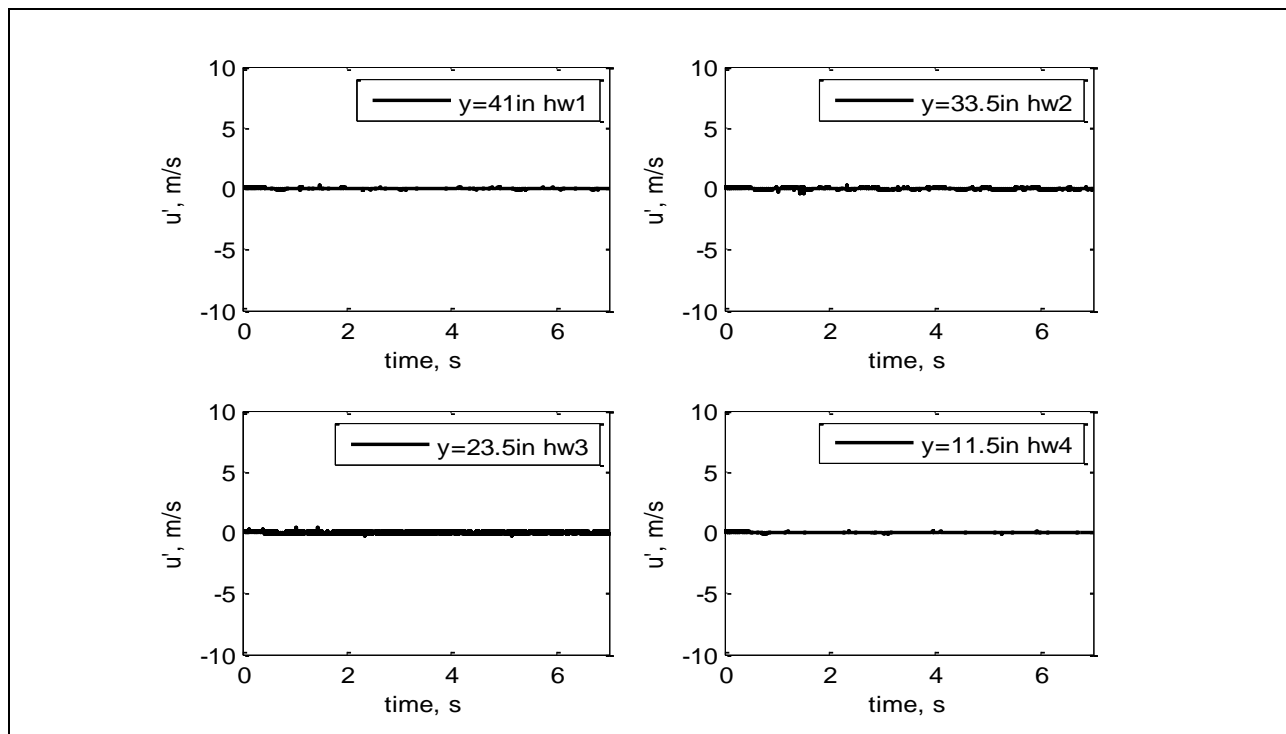


Figure 607: Velocity time series.

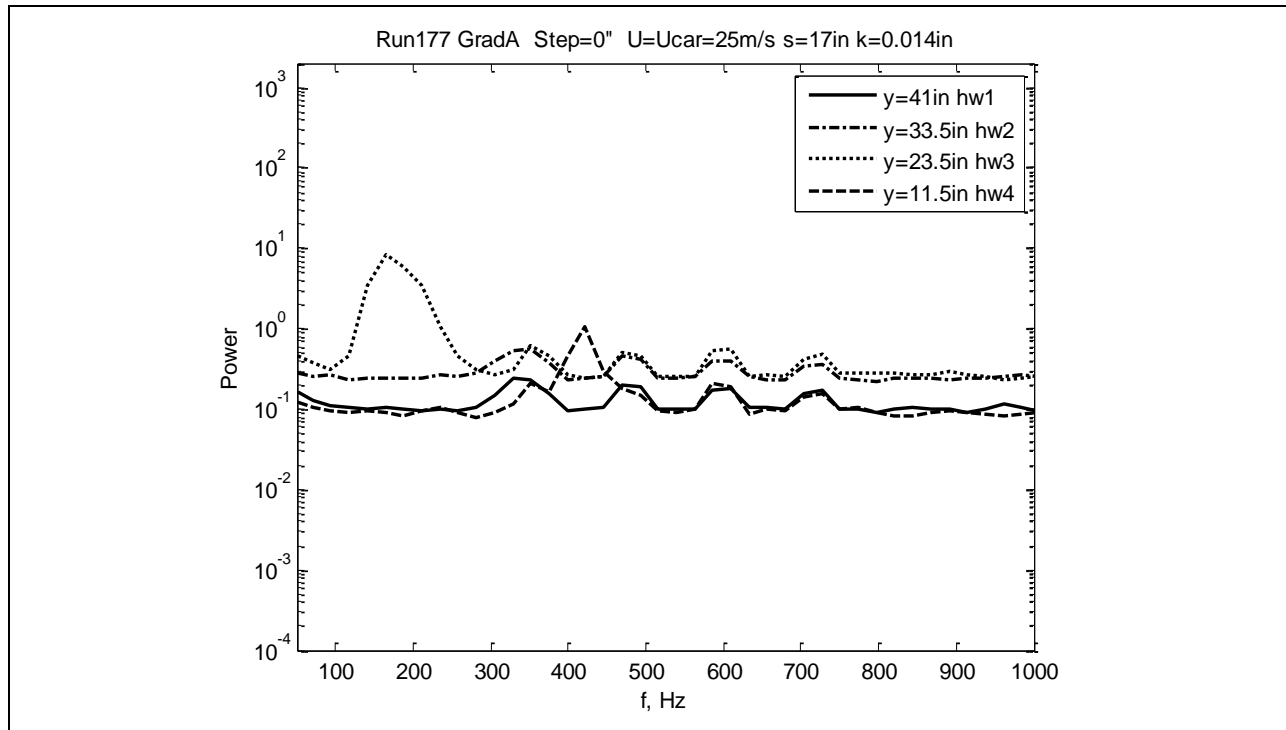


Figure 608: Power spectra.

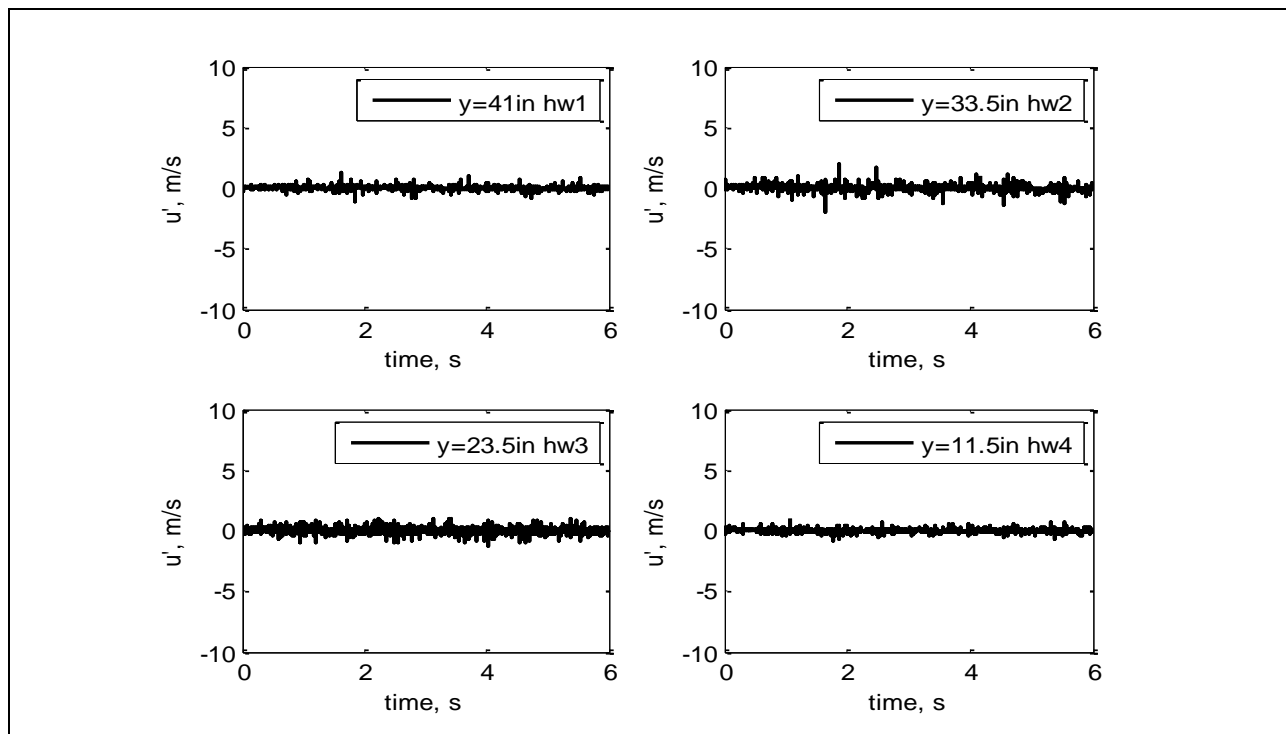


Figure 609: Velocity time series.

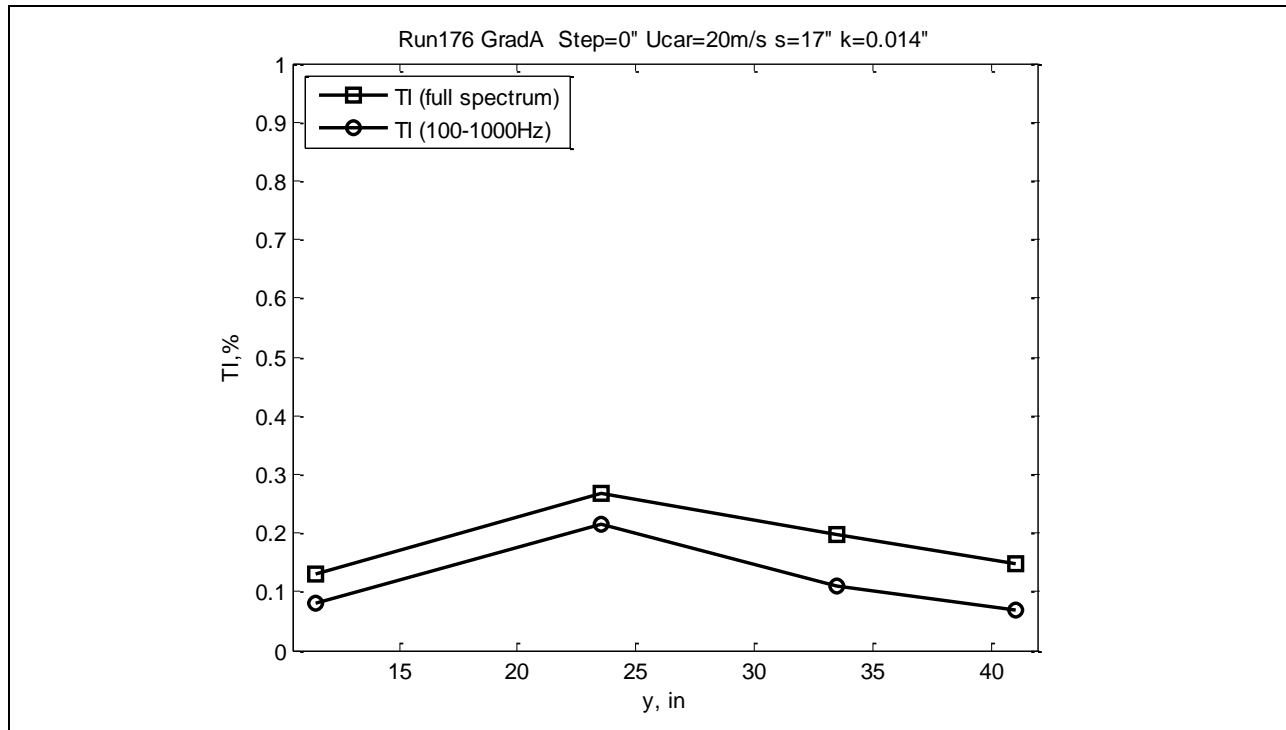


Figure 610: Turbulence intensity.

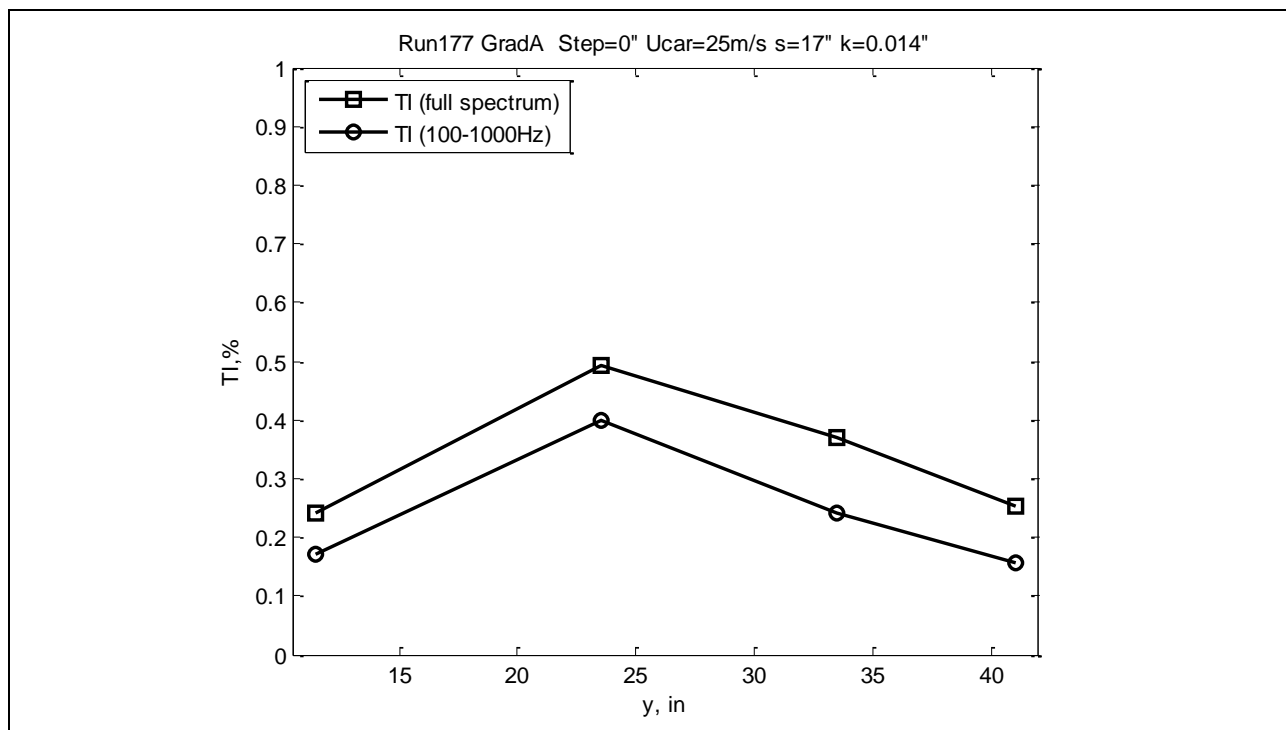


Figure 611: Turbulence intensity.

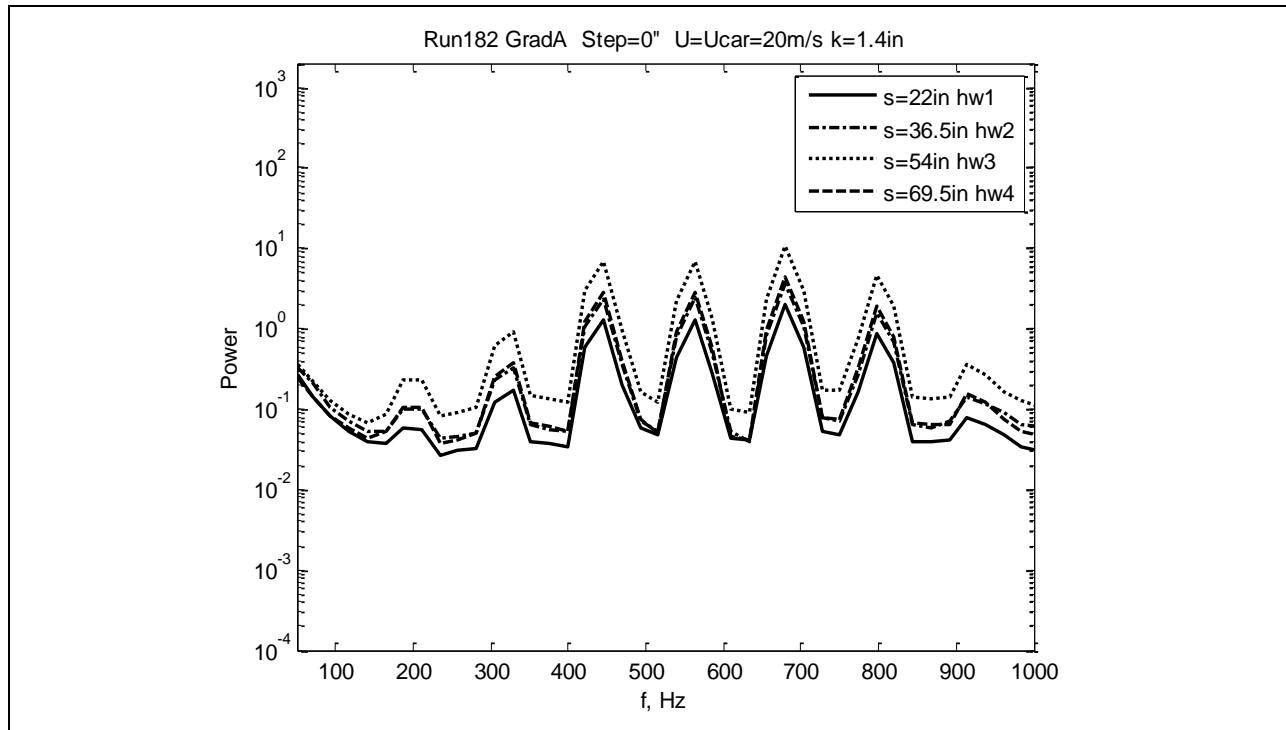


Figure 612: Power spectra.

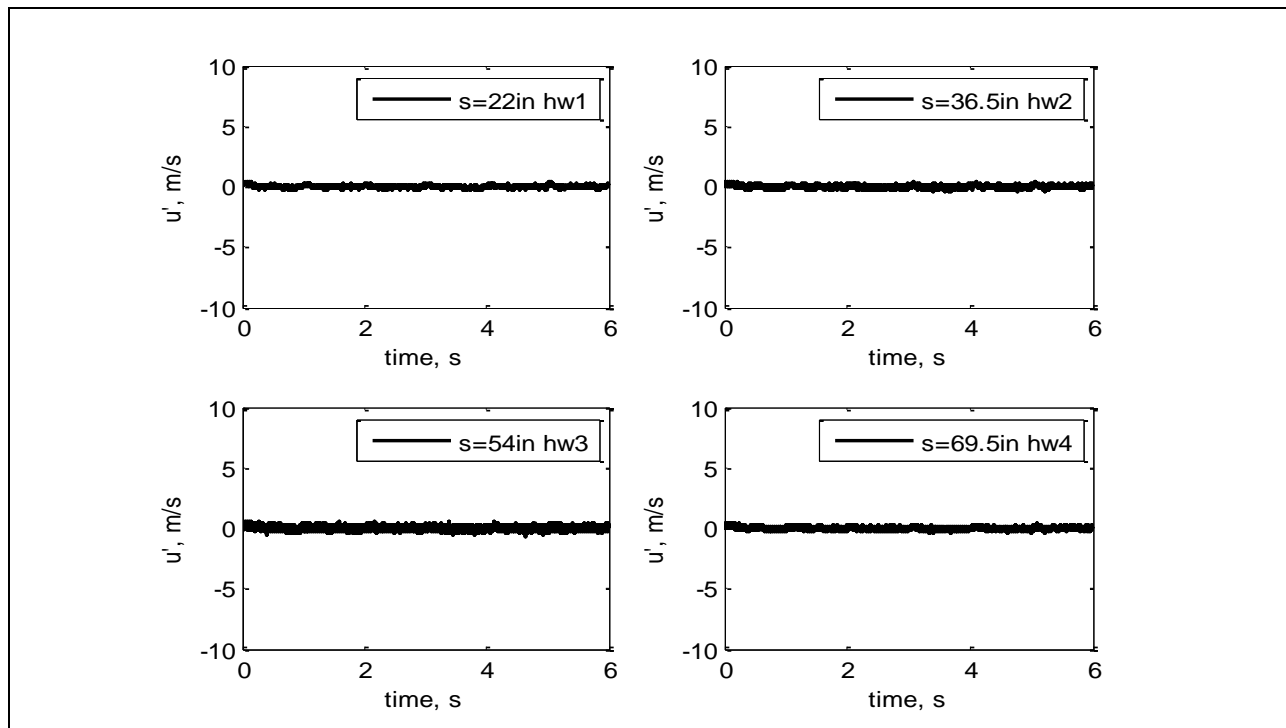


Figure 613: Velocity time series.

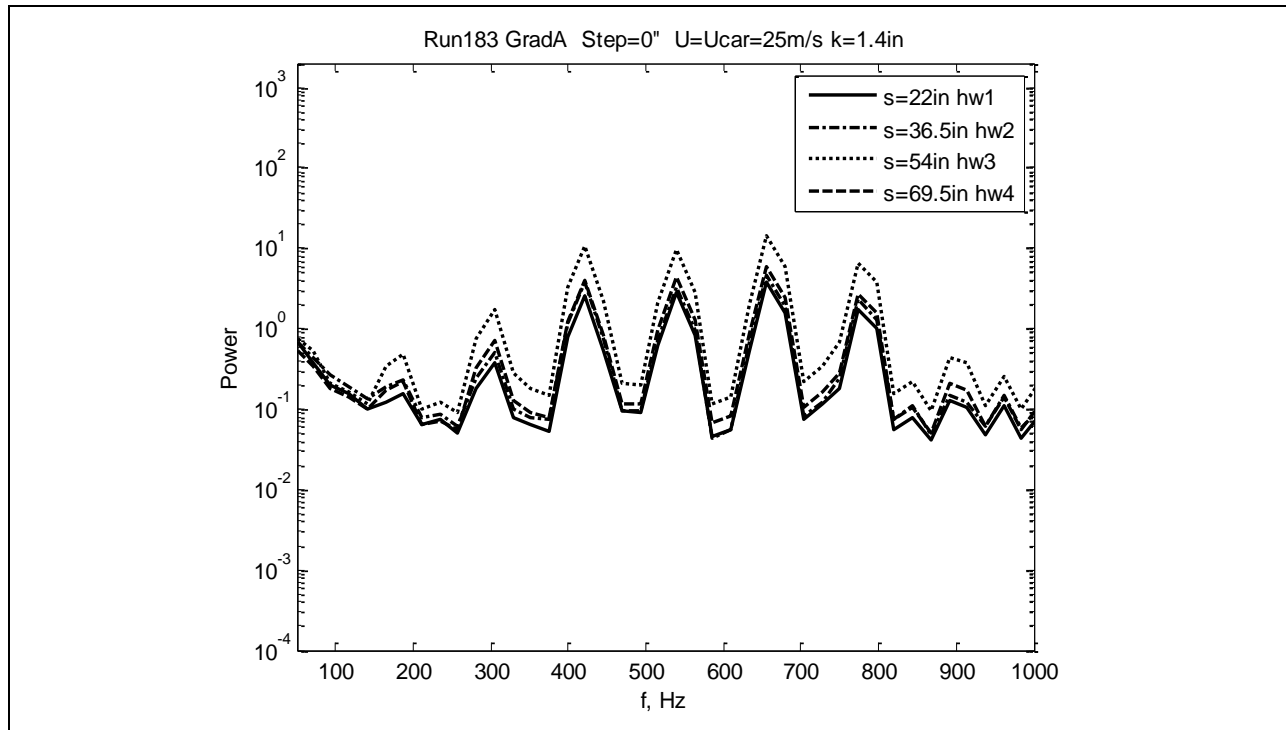


Figure 614: Power spectra.

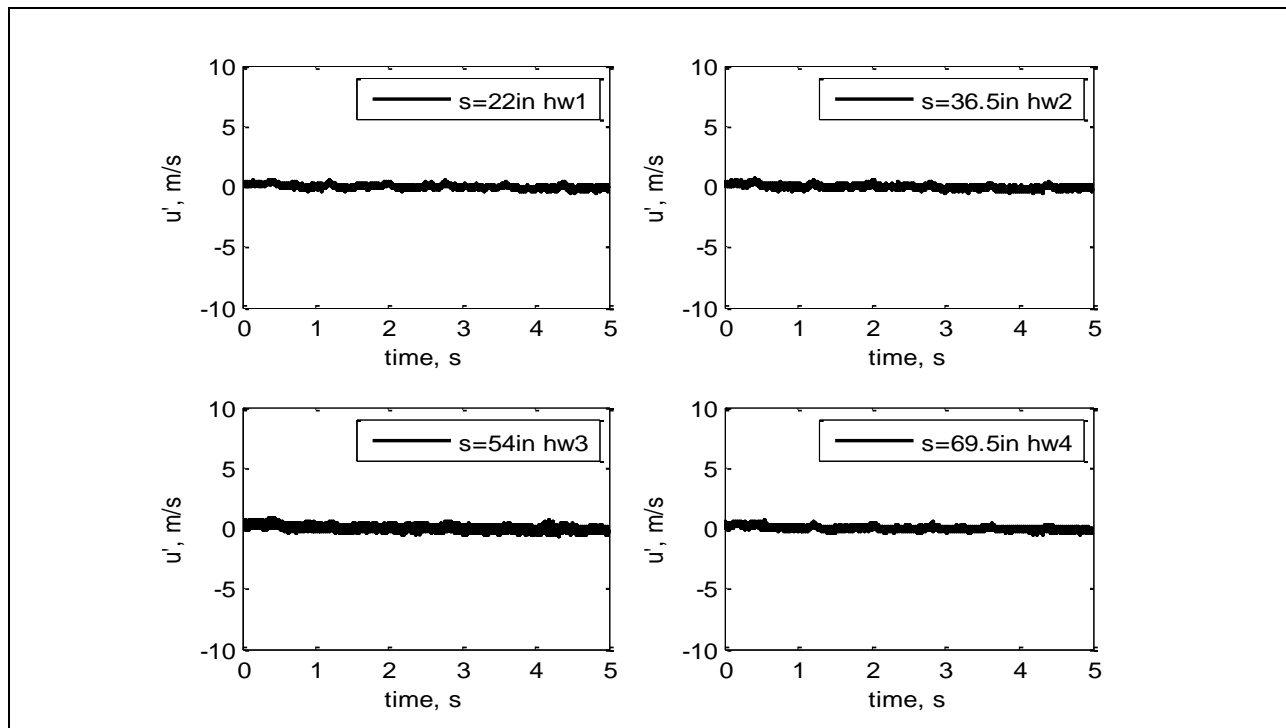


Figure 615: Velocity time series.

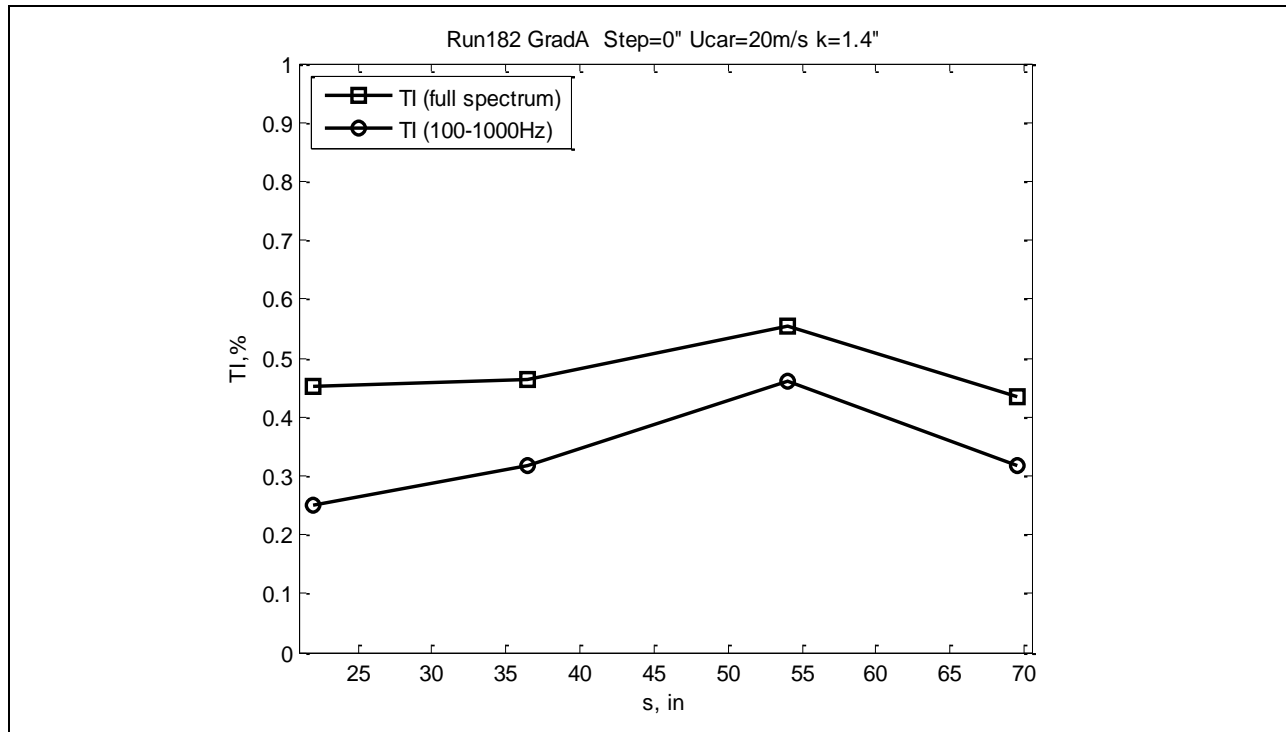


Figure 616: Turbulence intensity.

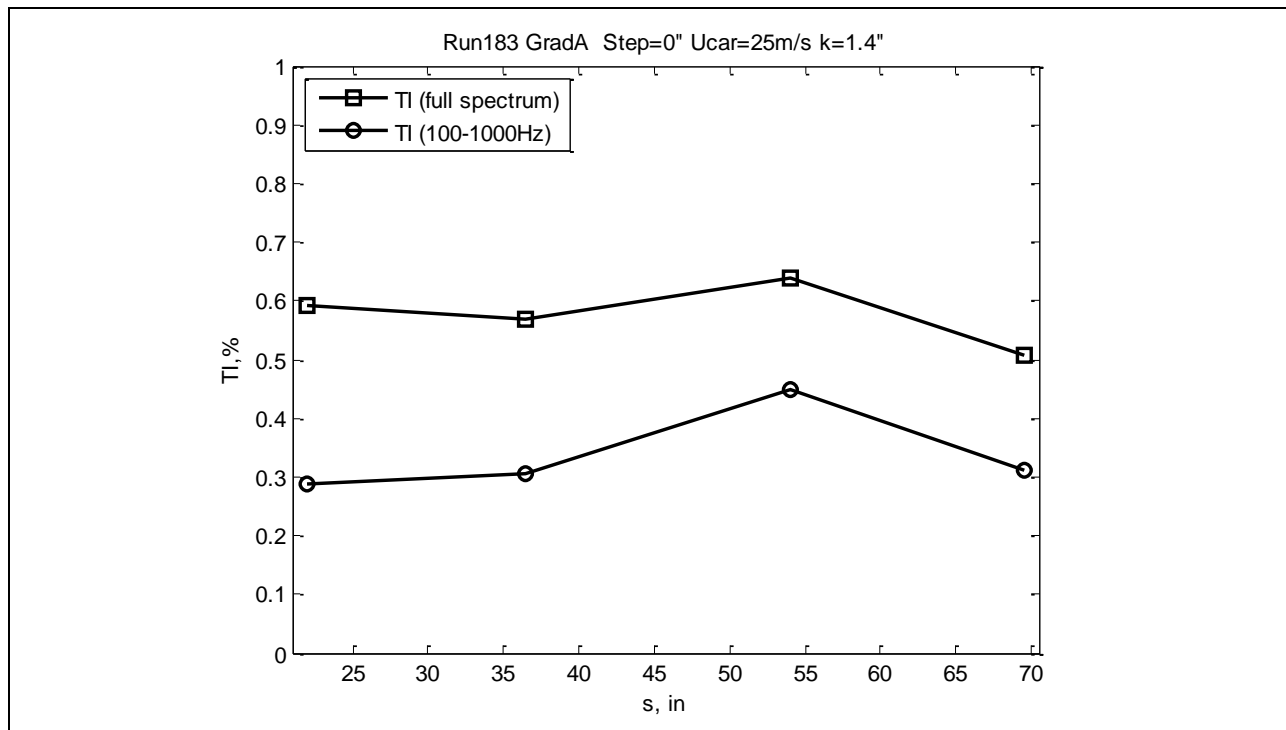


Figure 617: Turbulence intensity.

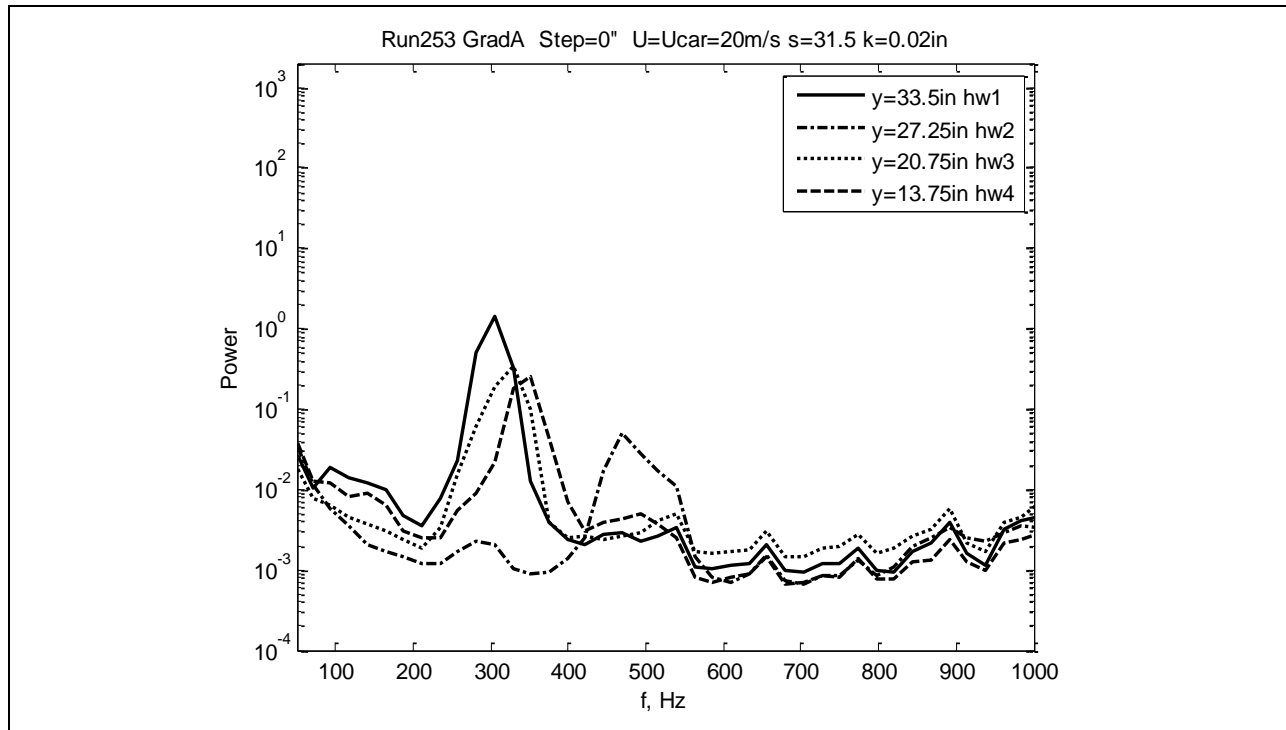


Figure 618: Power spectra.

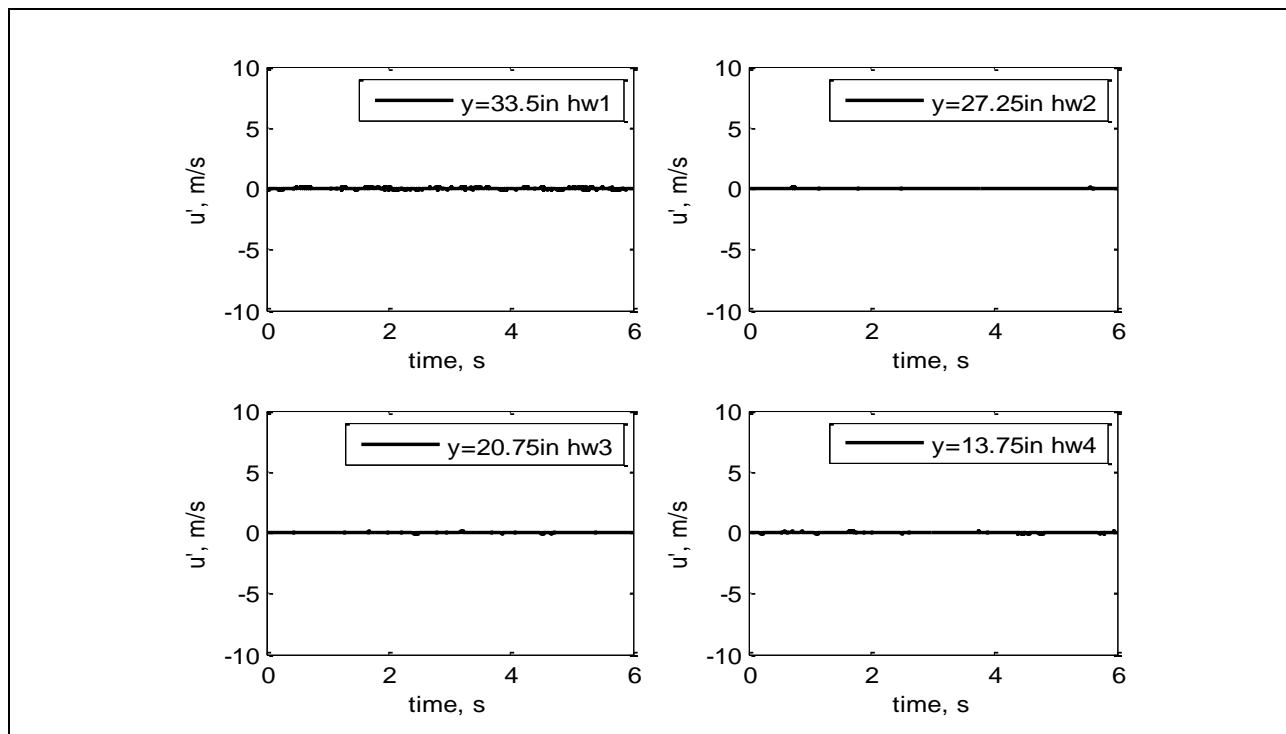


Figure 619: Velocity time series.

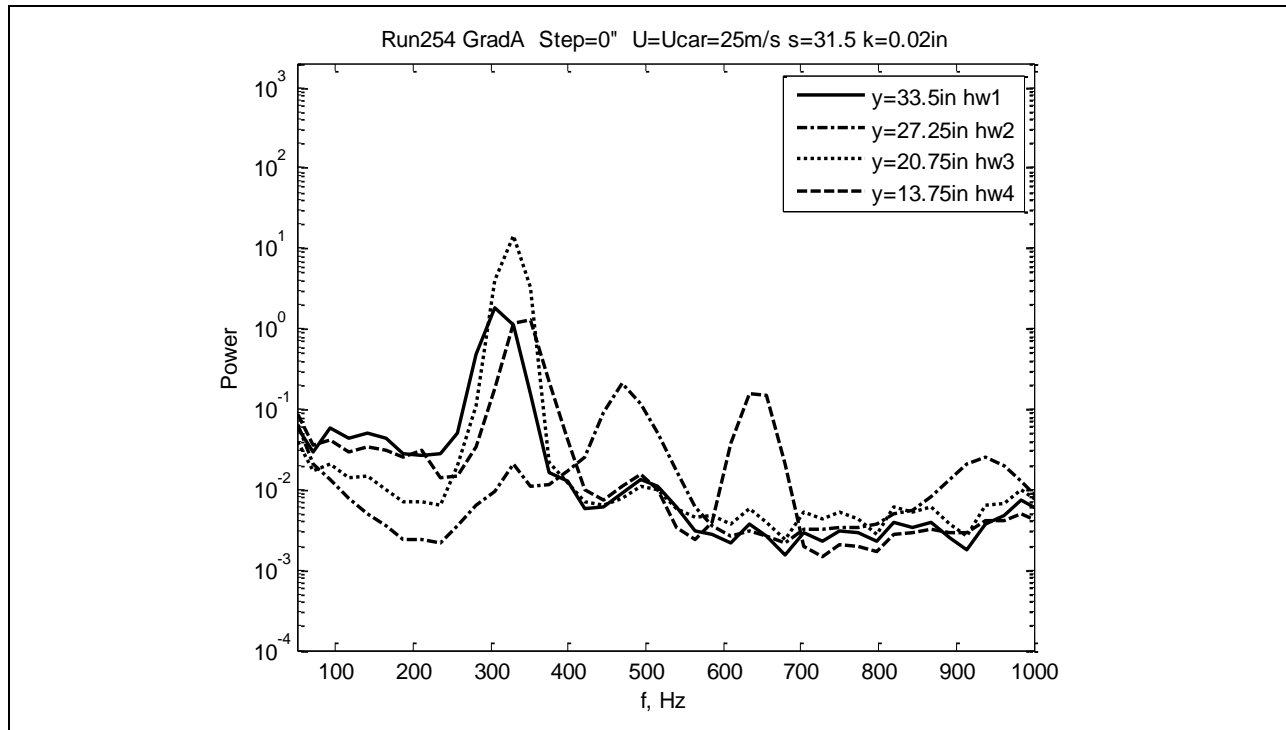


Figure 620: Power spectra.

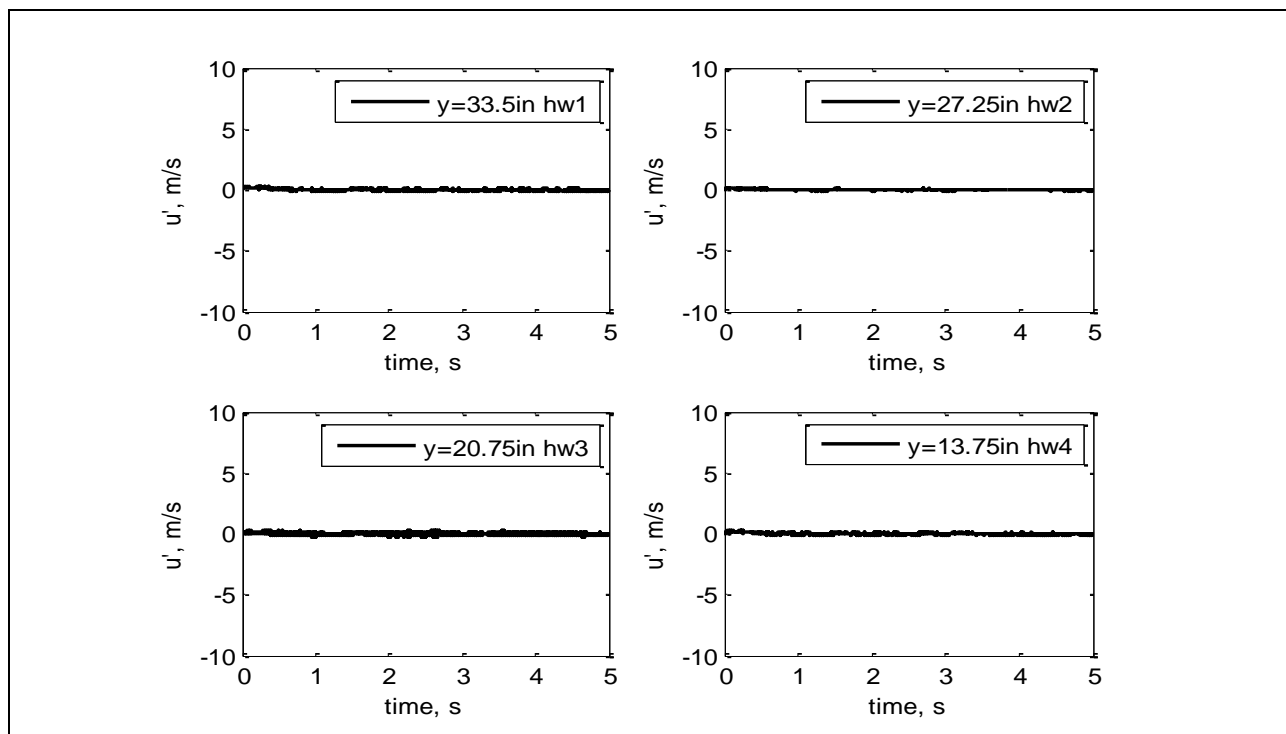


Figure 621: Velocity time series.

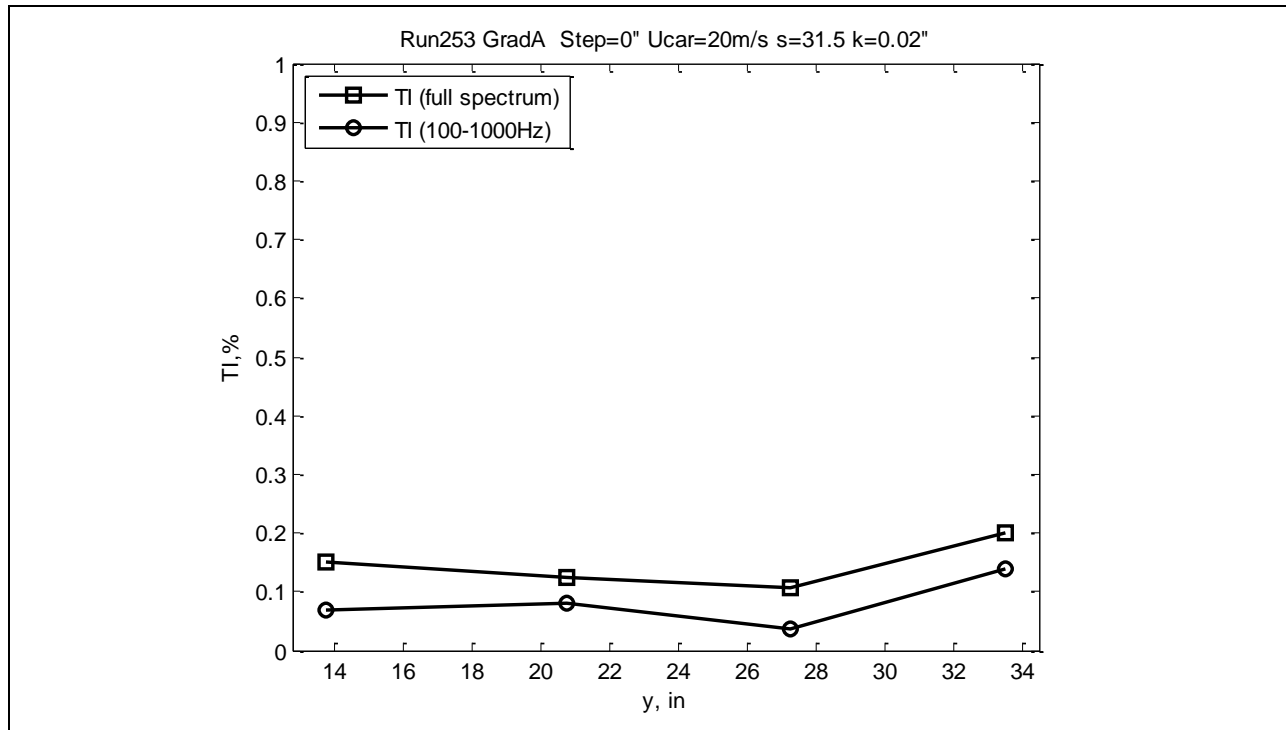


Figure 622: Turbulence intensity.

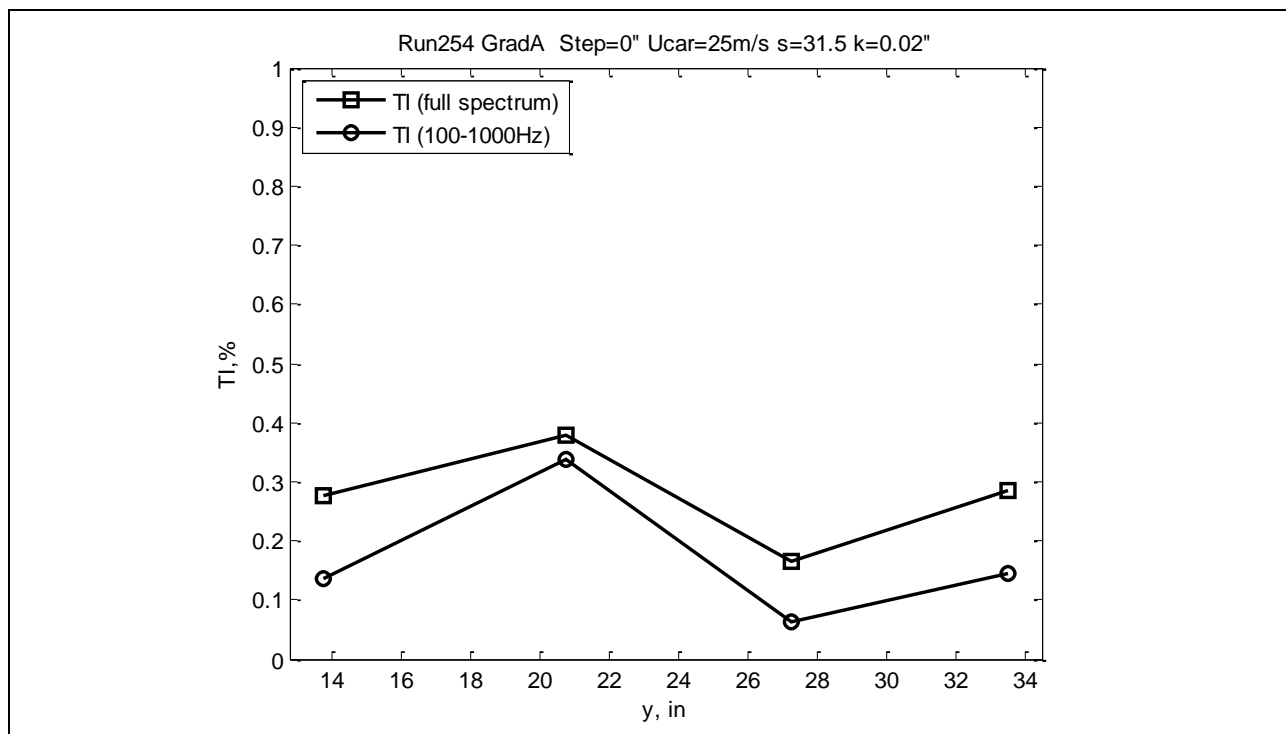


Figure 623: Turbulence intensity.

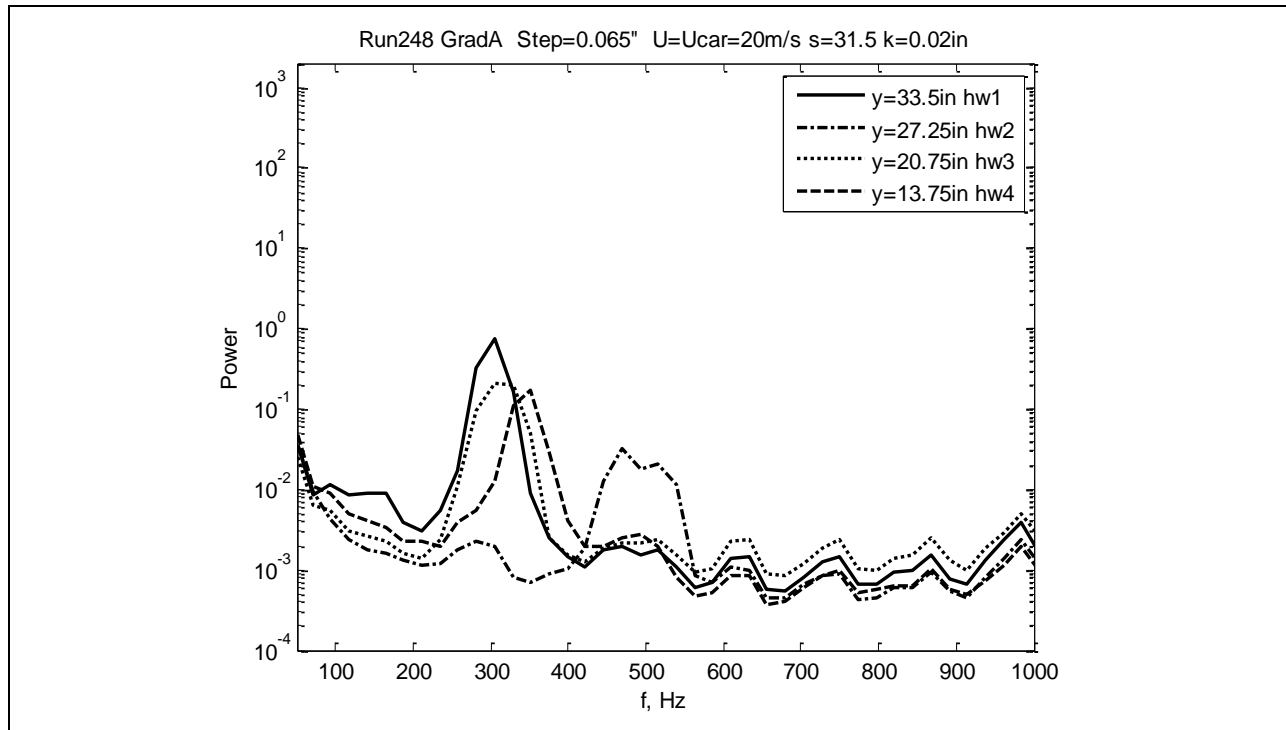


Figure 624: Power spectra.

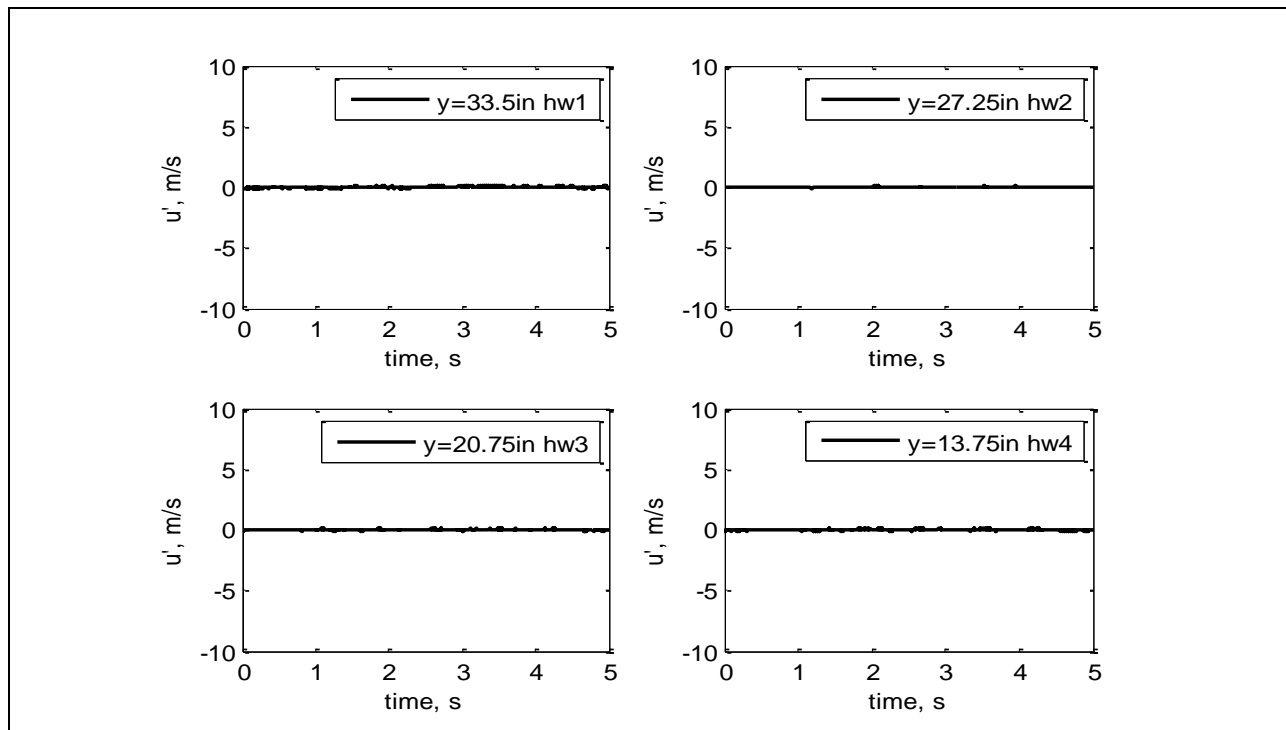


Figure 625: Velocity time series.

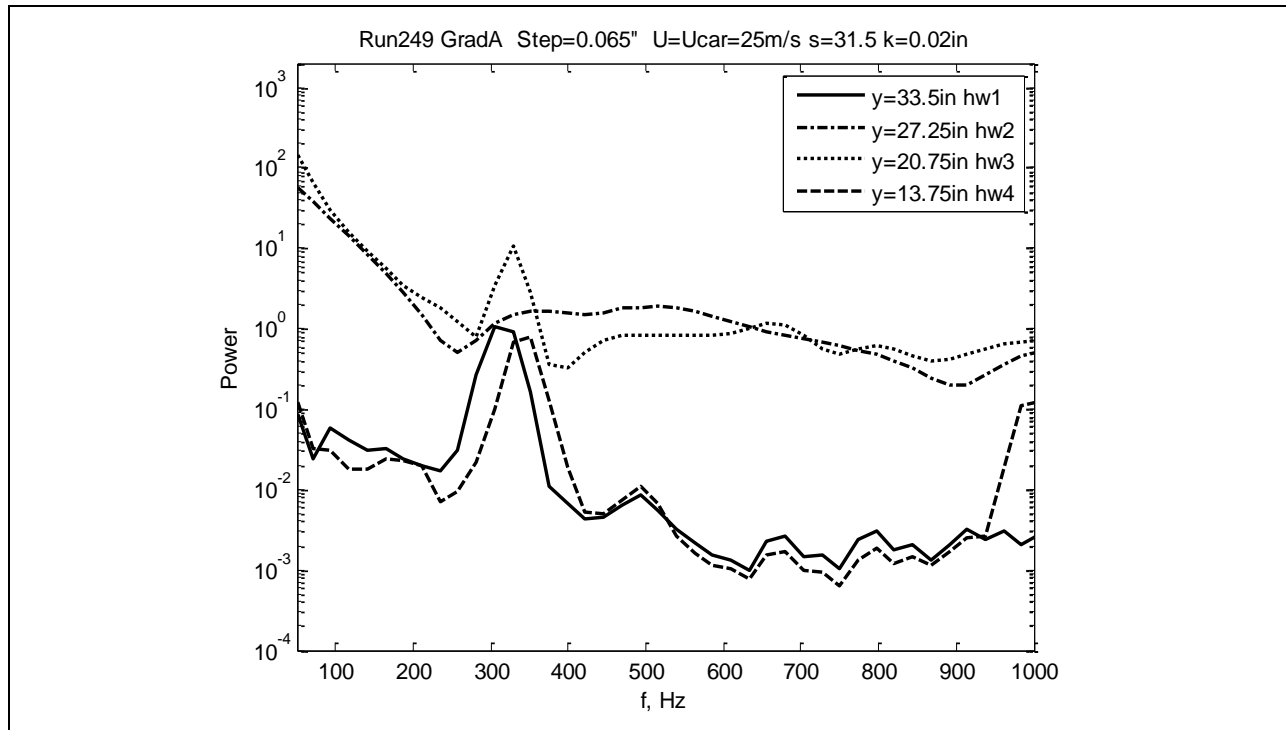


Figure 626: Power spectra.

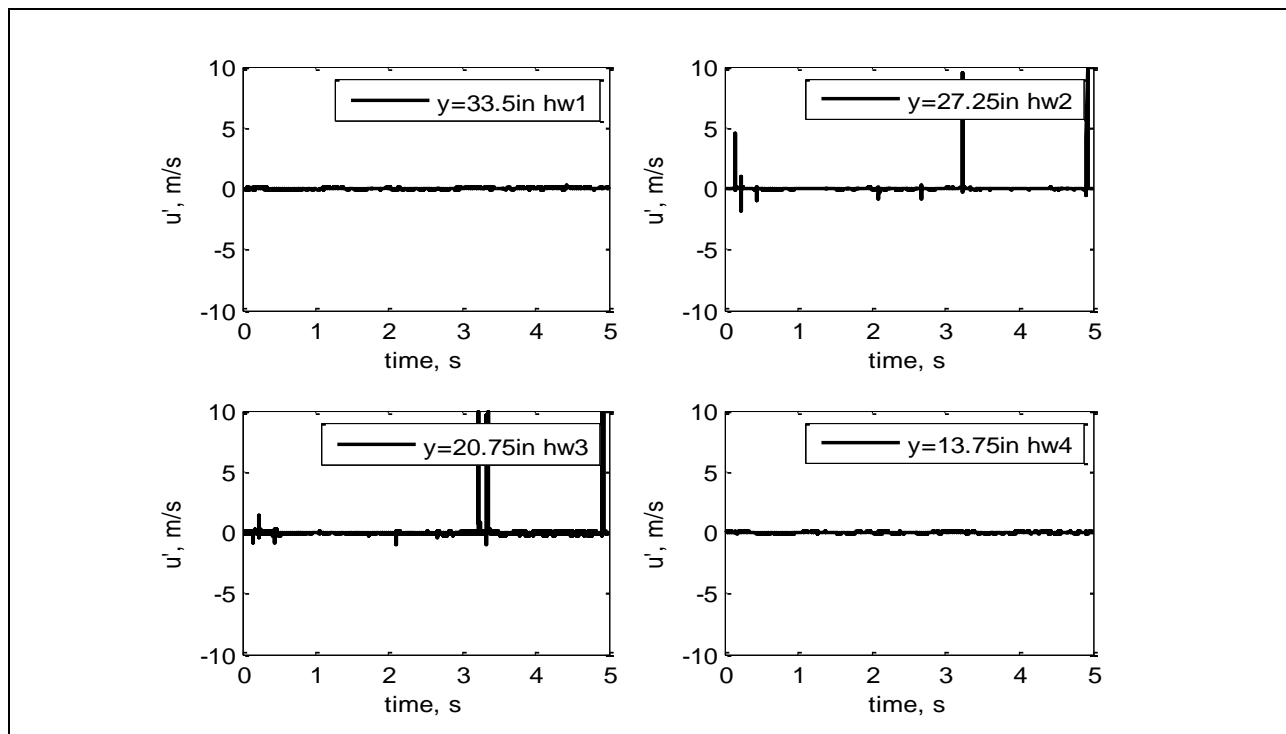


Figure 627: Velocity time series.

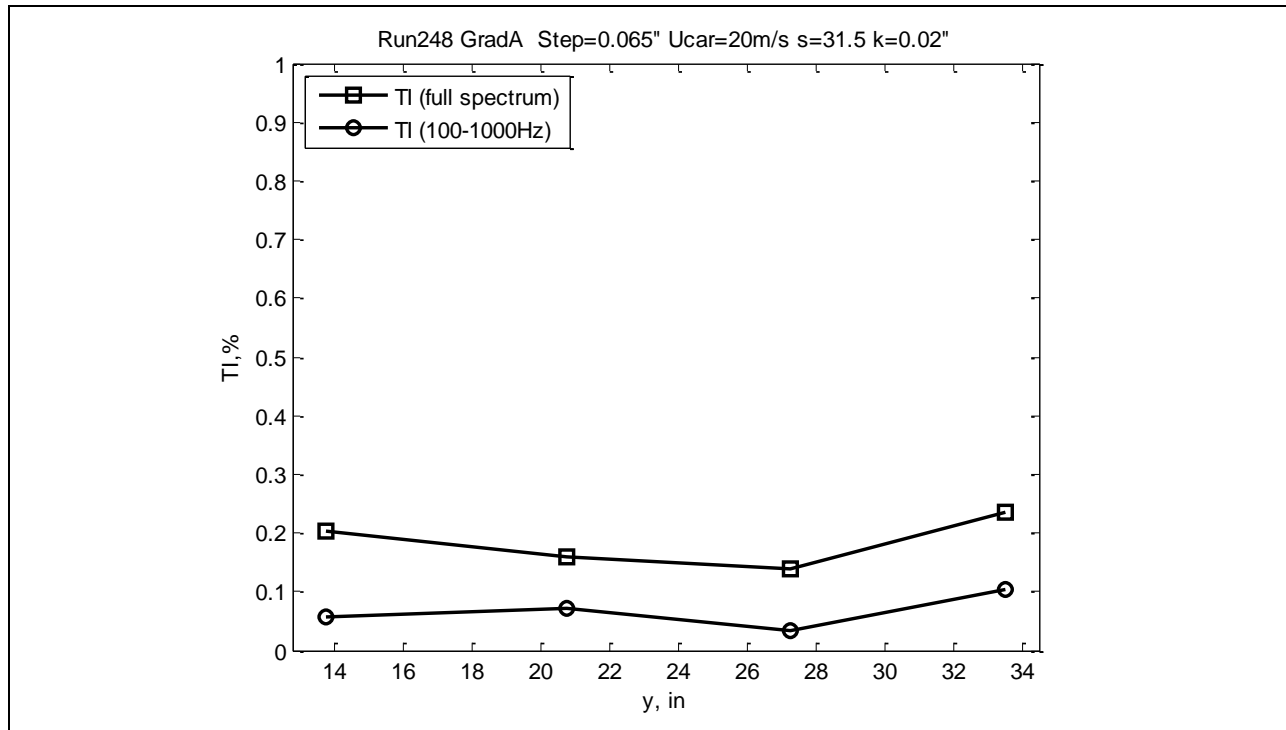


Figure 628: Turbulence intensity.

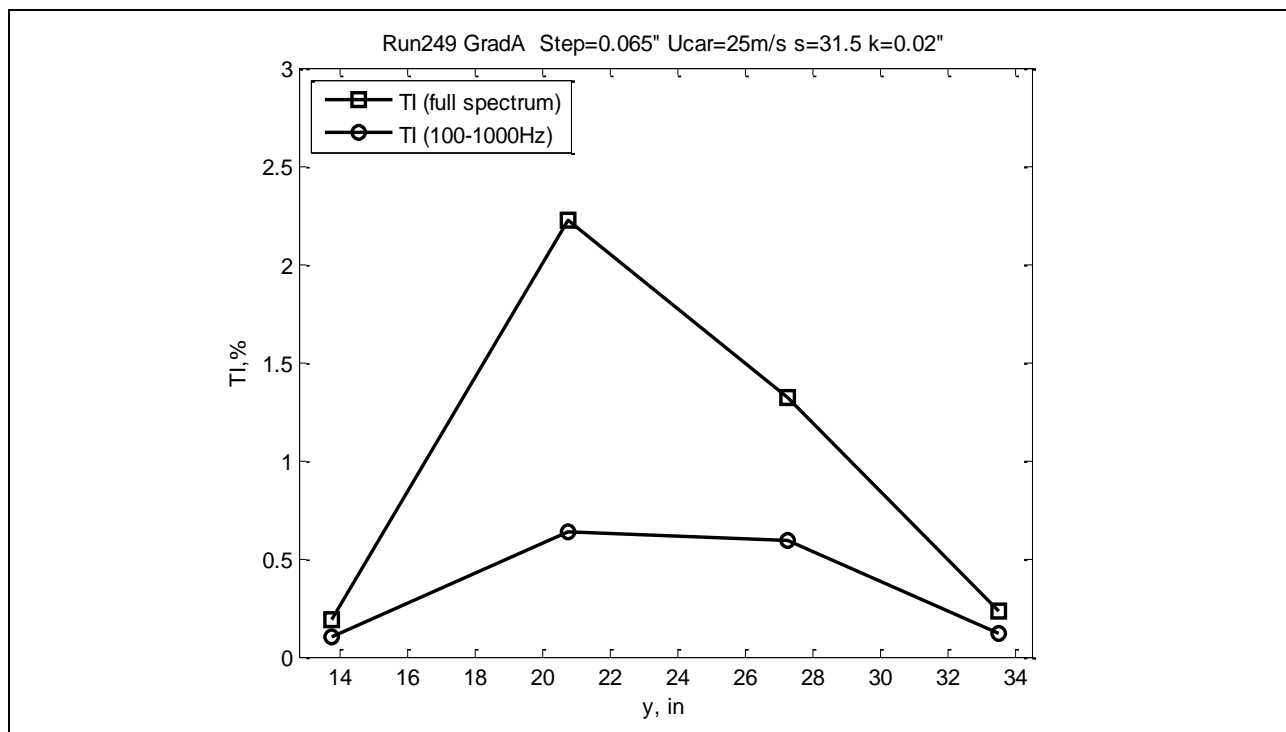


Figure 629: Turbulence intensity.

Spanwise uniformity testing in boundary layer downstream of step for Gradient-B for non-zero step is shown in Figures 630-635. Run 380 (Figures 630-631) and Run 381 (Figures 632-633) show the spectra, velocity time series and corresponding plots of TI (Figure 634 and Figure 635) in the boundary layer ($k=0.02\text{in}$) downstream of the step ($s=19.75\text{in}$) for two different freestream speeds as function of span-wise distance. For the lower speed Run 380 the spectra look similar to zero step case for Gradient-A model (see above) but for the higher speed Run 381 there is significant variation in the spectra with span-wise distance and the uncorrected TI varies significantly too from 1.8% to 3%. This may be related to the fact that when Reynolds number increased, the flow becomes more unstable and very sensitive to small variations of the initial and boundary conditions which were present in spanwise direction.

The differencing technique outlined in Reshotko *et al*²² was applied to the data and led to a significant reduction in the turbulence intensity. For the streamwise runs, the TI was found to be in the range 0.05-0.10%, despite the low frequency uncertainty associated with the short run time.

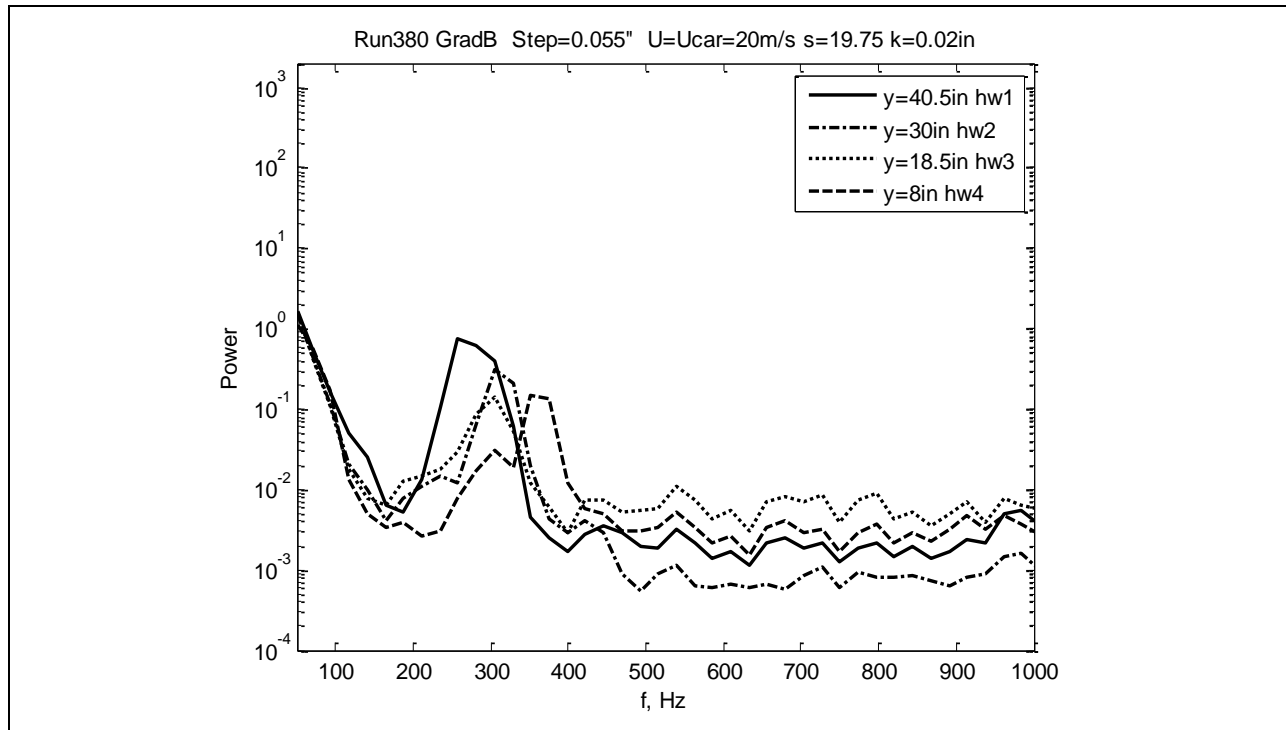


Figure 630: Power spectra.

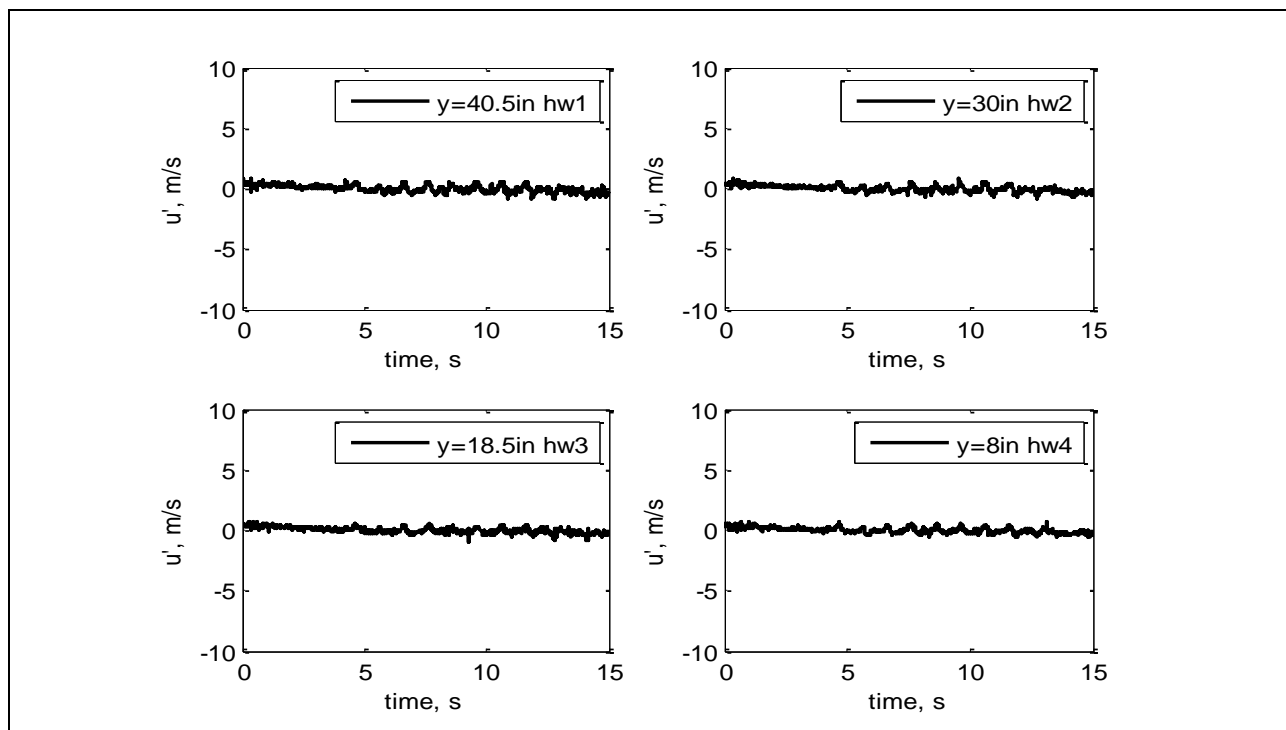


Figure 631: Velocity time series.

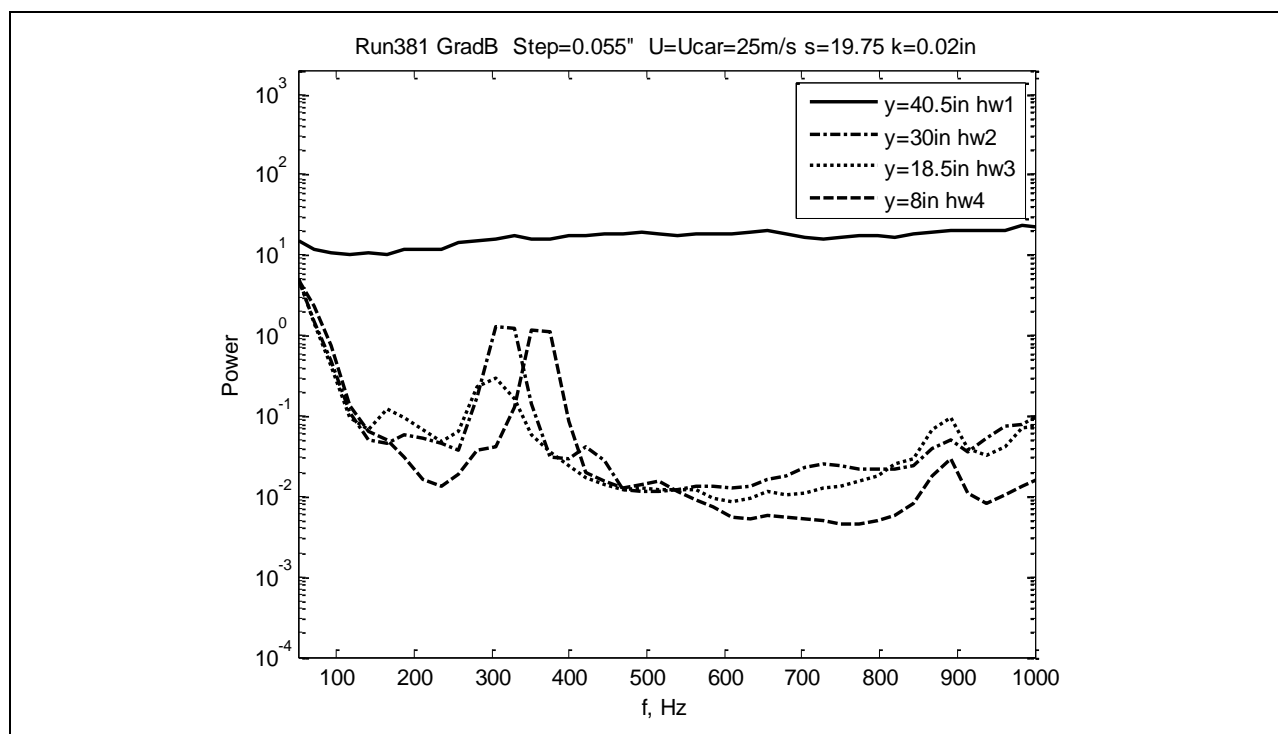


Figure 632: Power spectra.

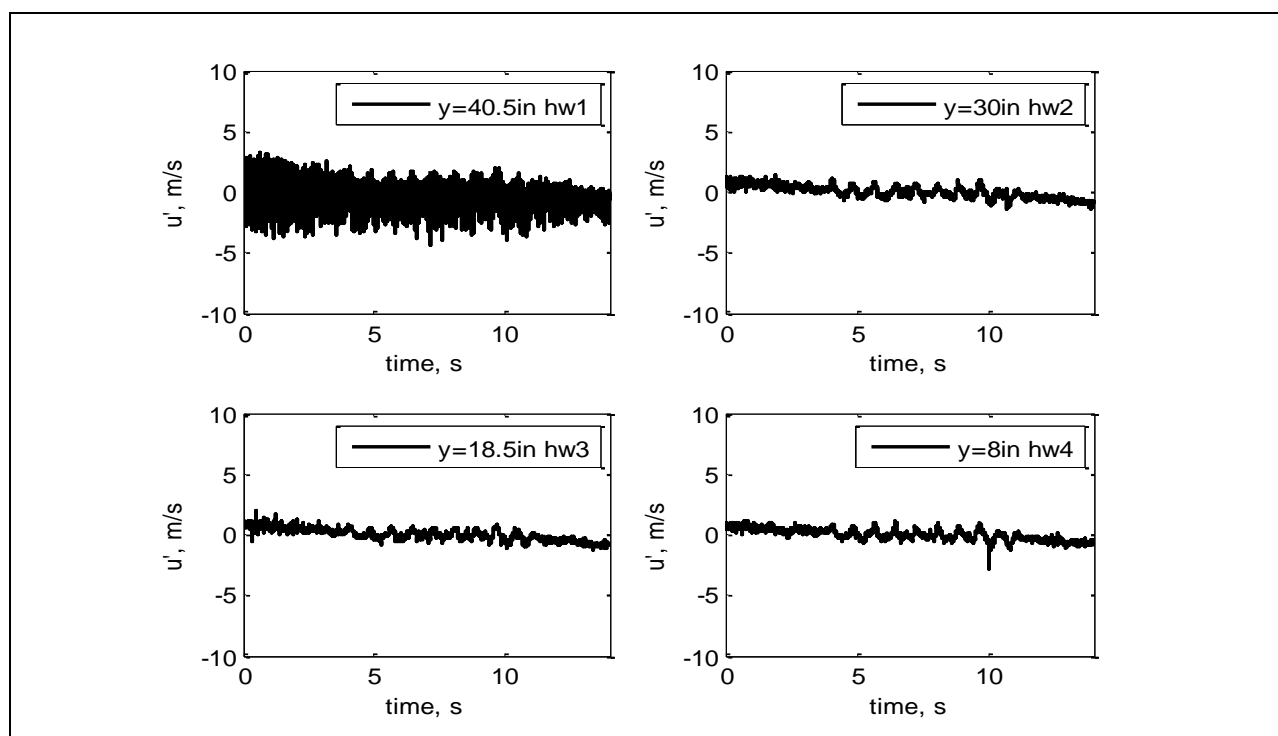


Figure 633: Velocity time series.

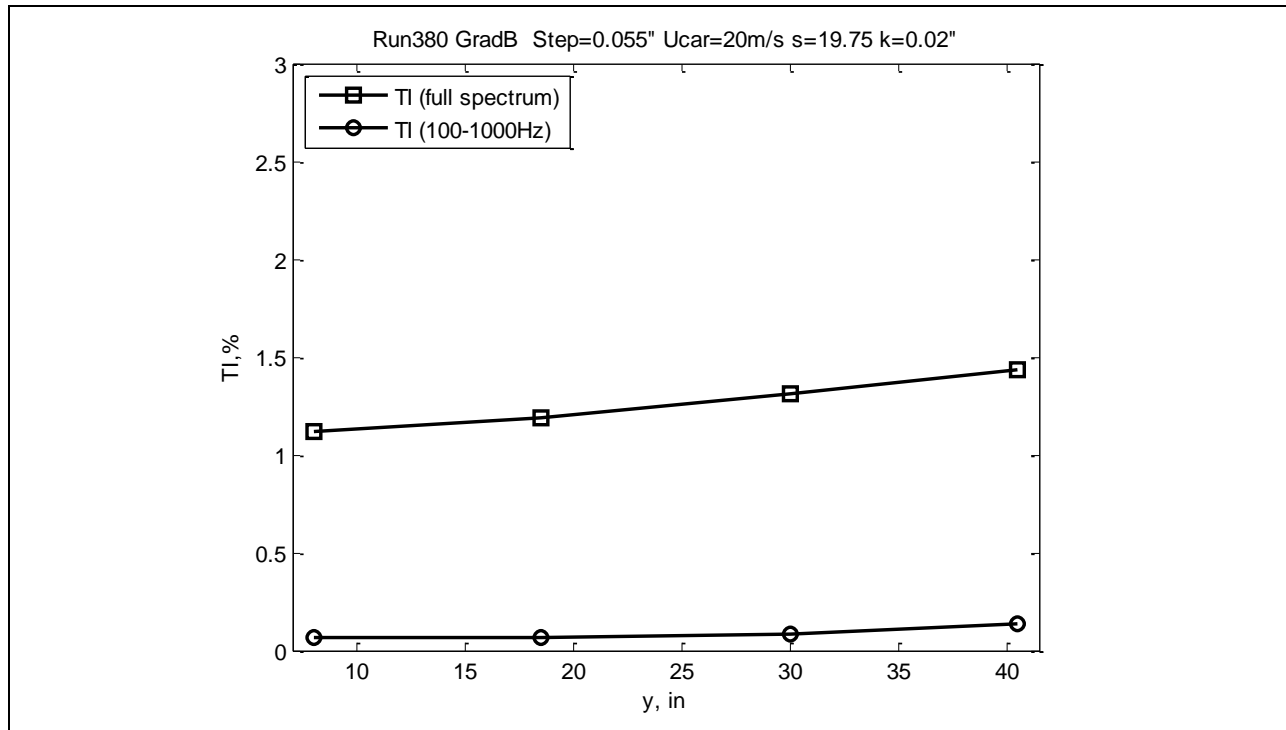


Figure 634: Turbulence intensity.

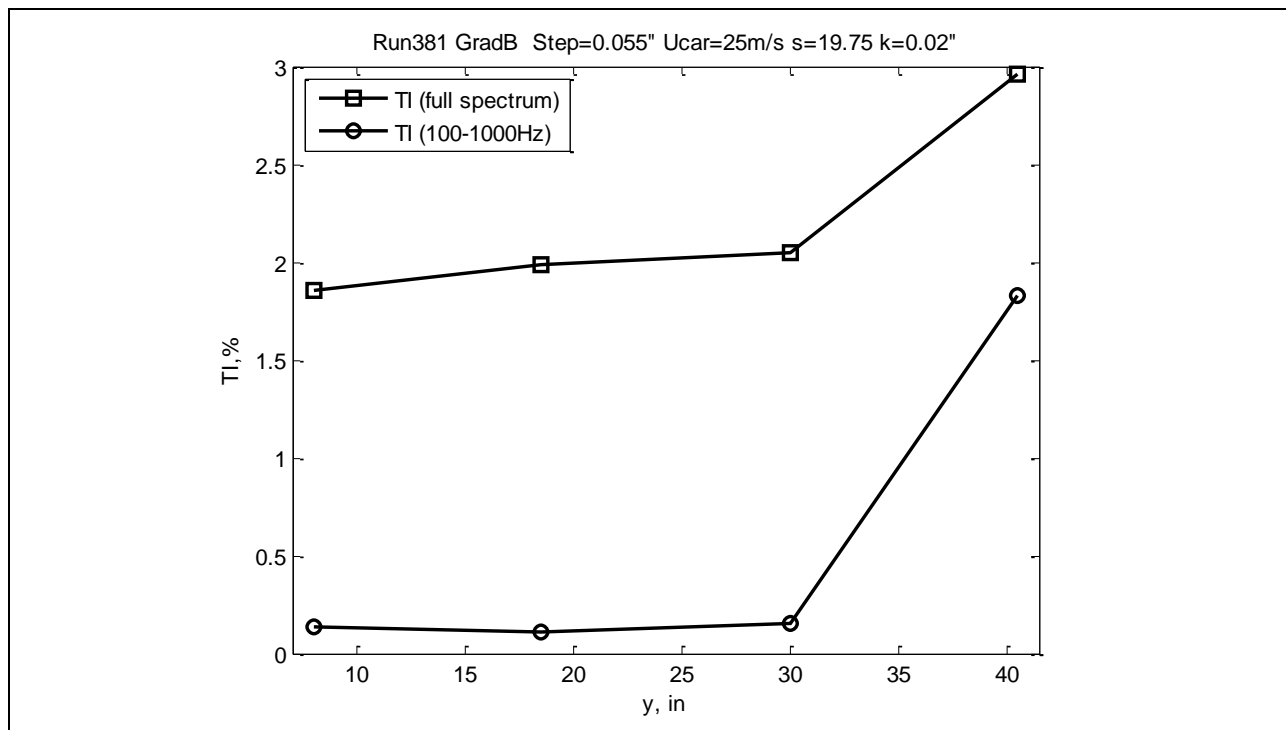


Figure 635: Turbulence intensity.

7.5.7.6

Supplementary data: accelerometer results

This section contains data on possible model vibrations measured with accelerometers. This data is presented first for Gradient-Zero, next for Gradient-A, then finally for Gradient-B.

The results of vibration measurements for the Gradient-Zero model are presented in this section (Figures 636-691). The measurements of vibrations were performed simultaneously with hot-wire measurements for each run. The results showed that the level of vibrations was low (low power in the spectra) and no single frequency was detected in the frequency range where T-S waves were expected (50-400Hz). Two components were measured simultaneously – the k-component (wall normal direction) and the s-component (streamwise direction). The plots below for a given run number show the power spectra calculated from voltage fluctuations in the test section and voltage fluctuations for the total run time in order to check how vibrations changed during the run. The power spectrum for the case when no vibrations were expected (still car) is included for each run also for reference. From the data it can be seen that the level of vibrations in the test section is comparable with that for a still car. The spectra do not show single frequencies in the range of interest (50-400Hz). The single peak and noticeable increase in vibrations are observed at higher speeds (over 20m/s) like in Run 146 and Run 147, for example, for the s-component. But the peak in these cases is located at 400-500Hz, which is out of range of interest and its power is very low. There was sometimes a slow variation of the DC component in the voltage (as for example in Run 144 (Figures 642-643)), which is related to some transient processes in battery or accelerometer itself. It did not contribute to the range of frequencies of interest.

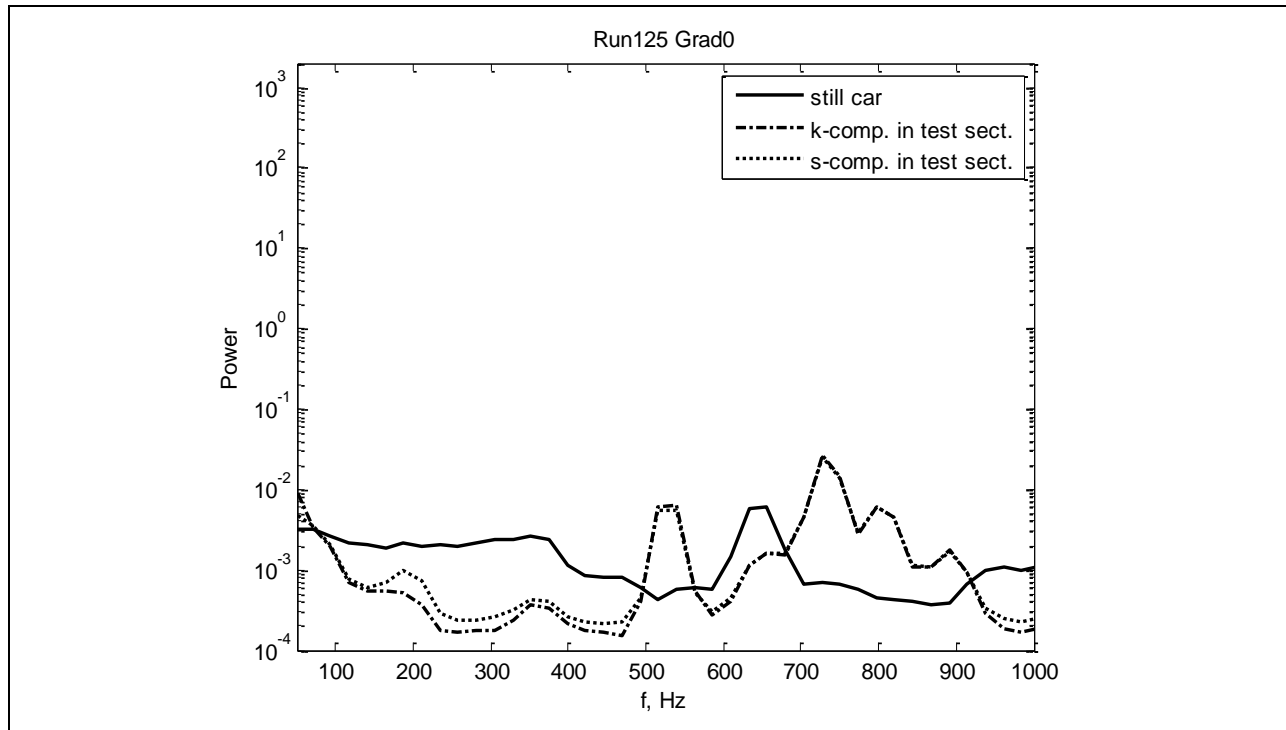


Figure 636: Power spectra in test section.

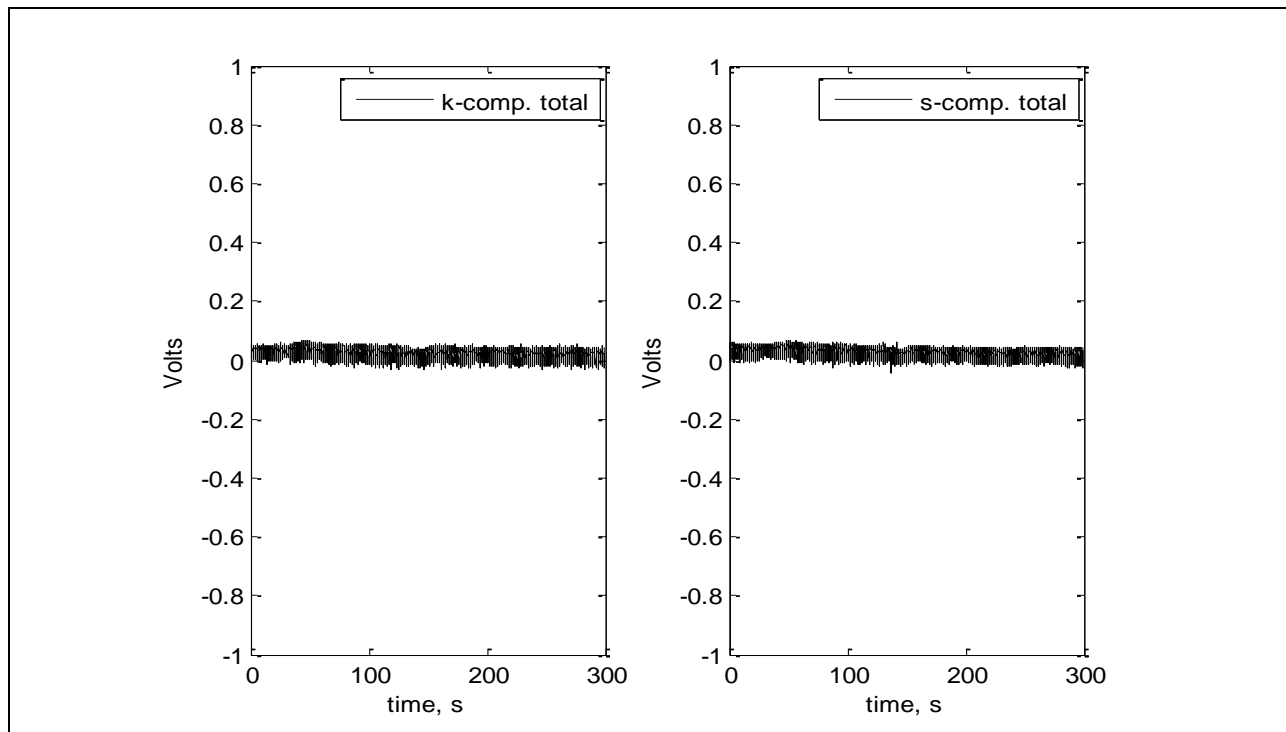


Figure 637: Voltage for full run.

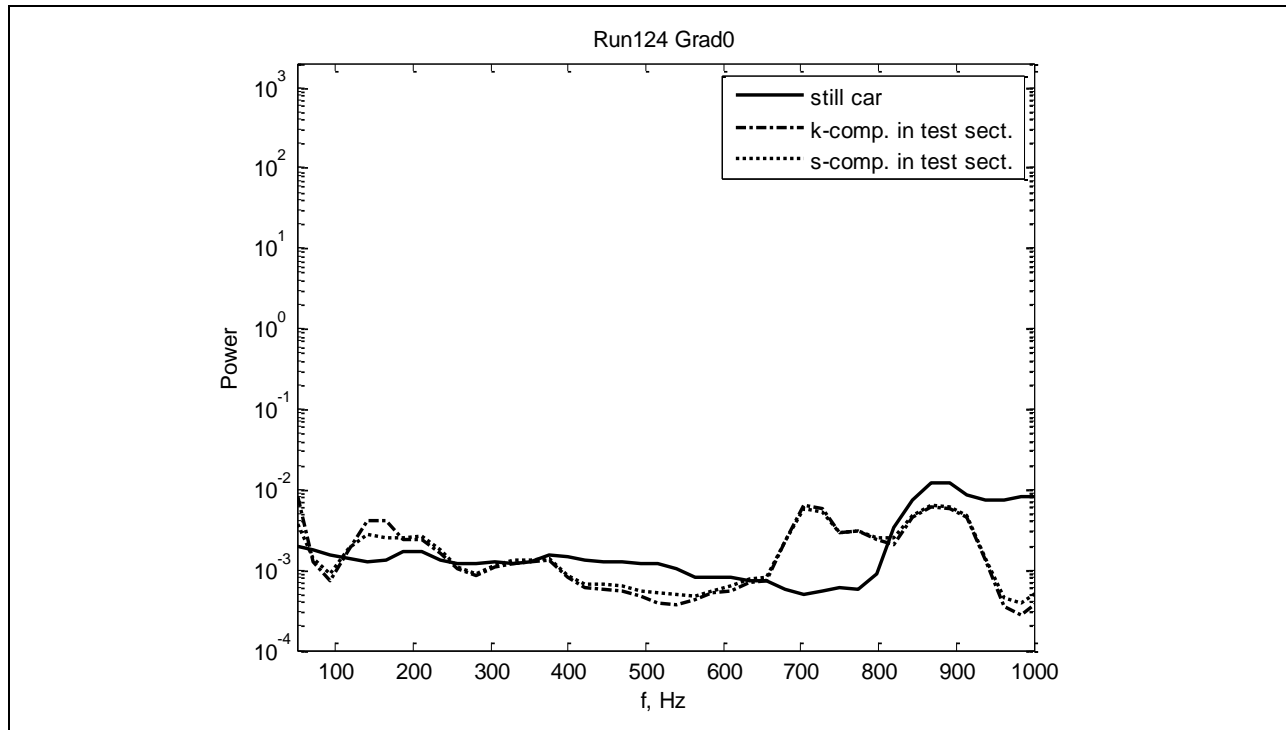


Figure 638: Power spectra in test section.

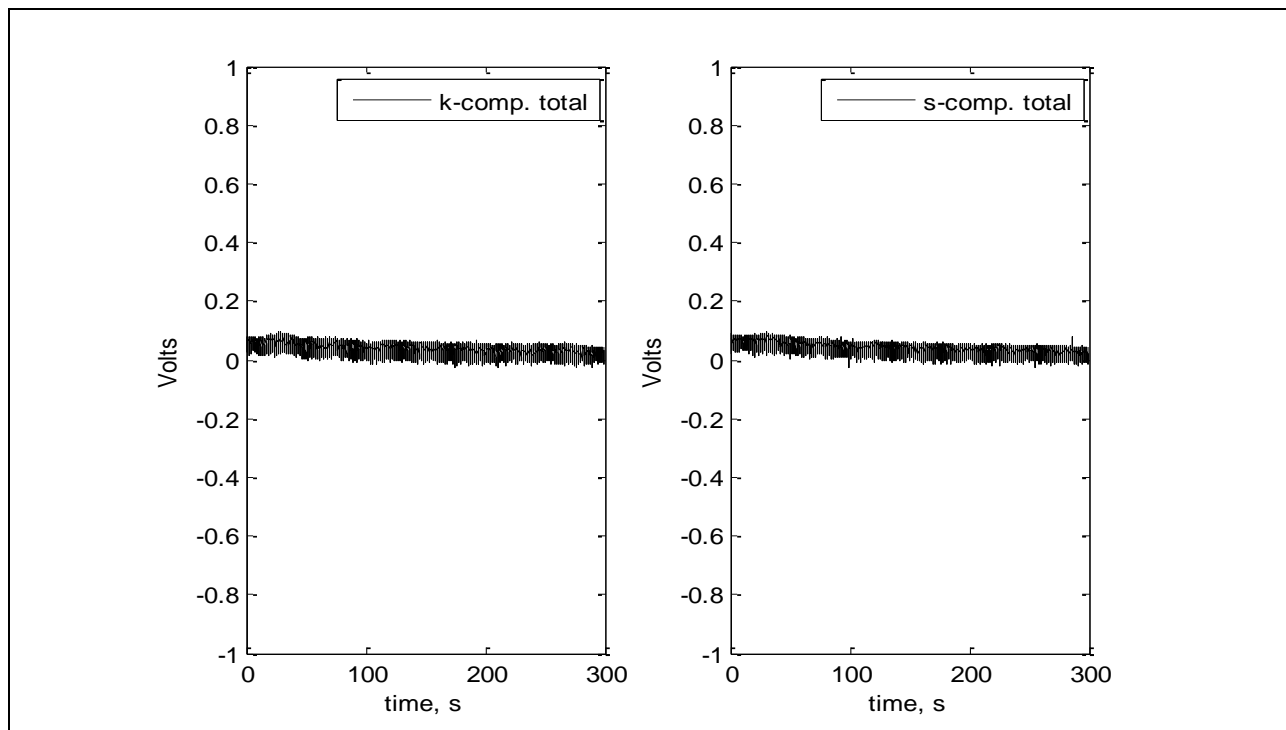


Figure 639: Voltage for full run.

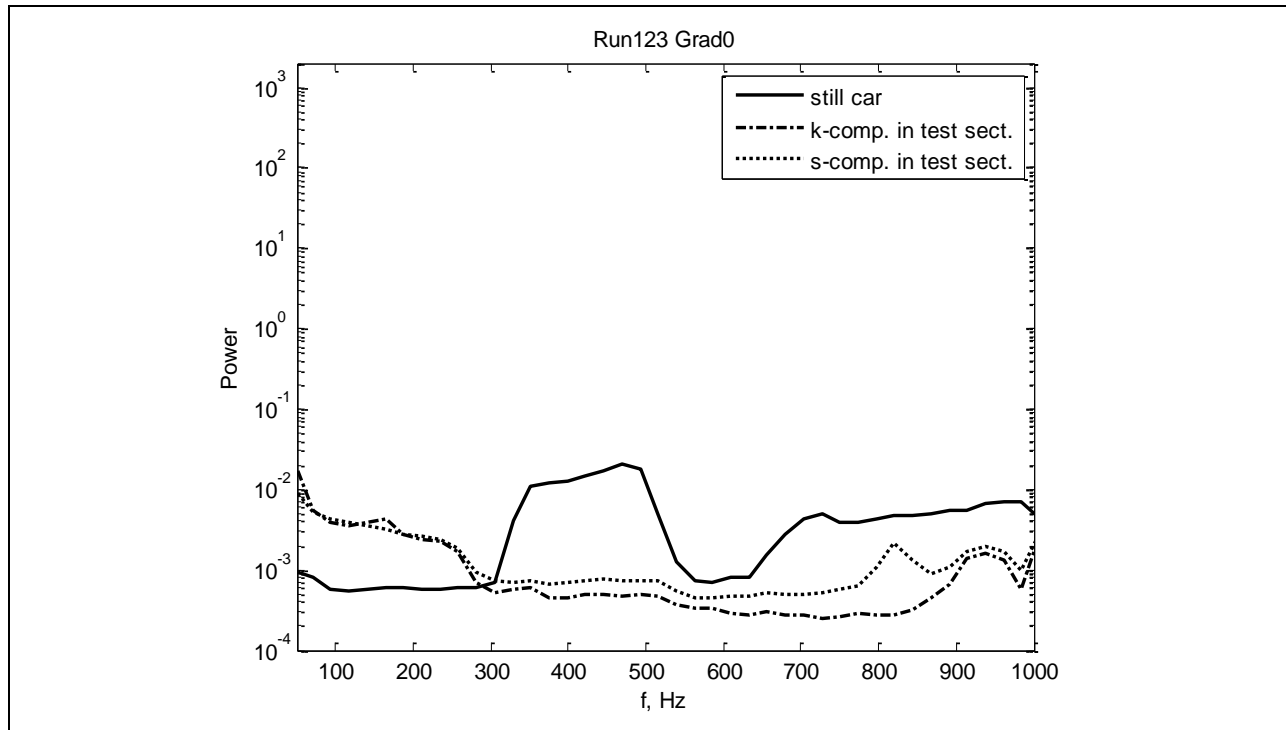


Figure 640: Power spectra in test section.

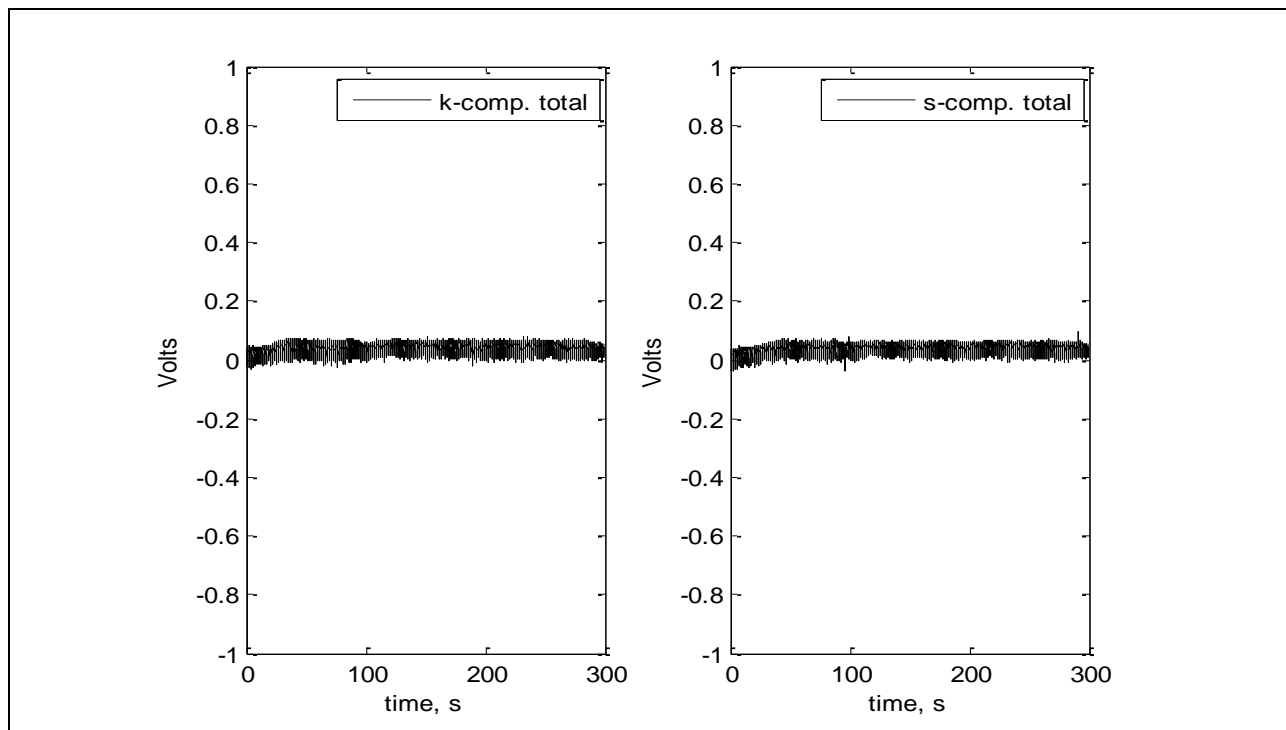


Figure 641: Voltage for full run.

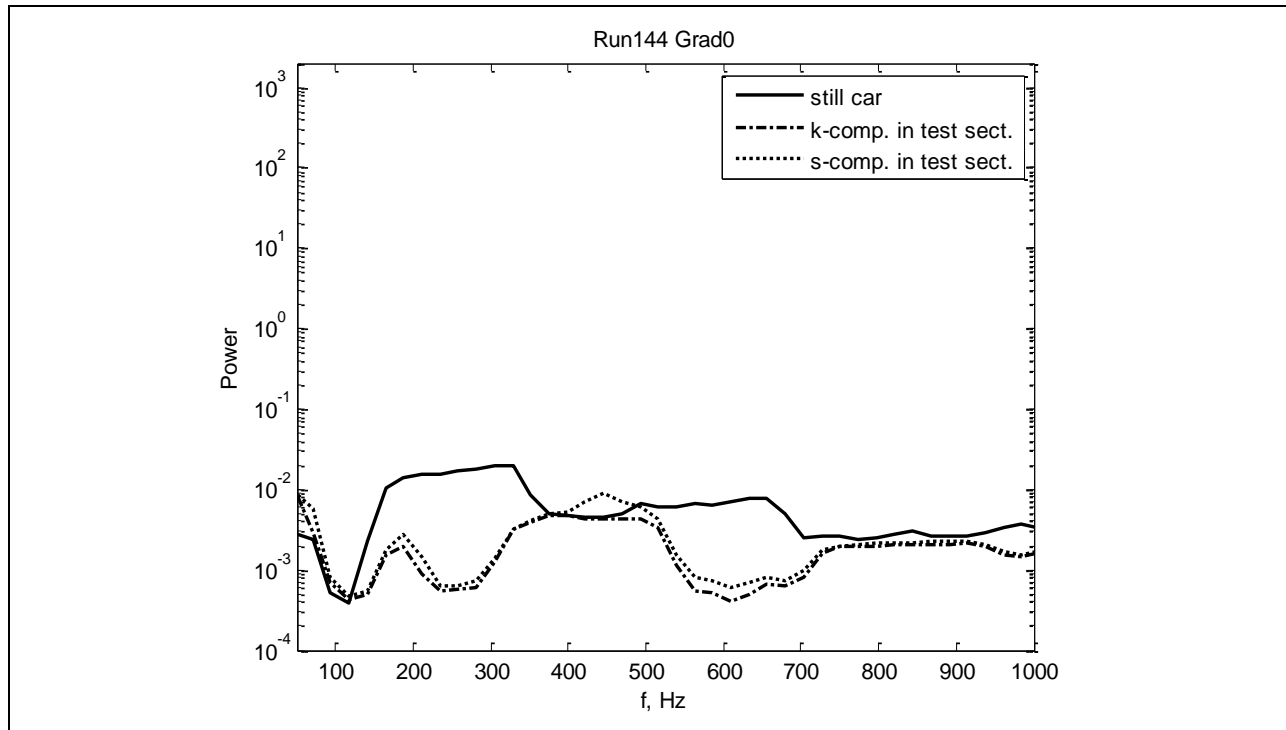


Figure 642: Power spectra in test section.

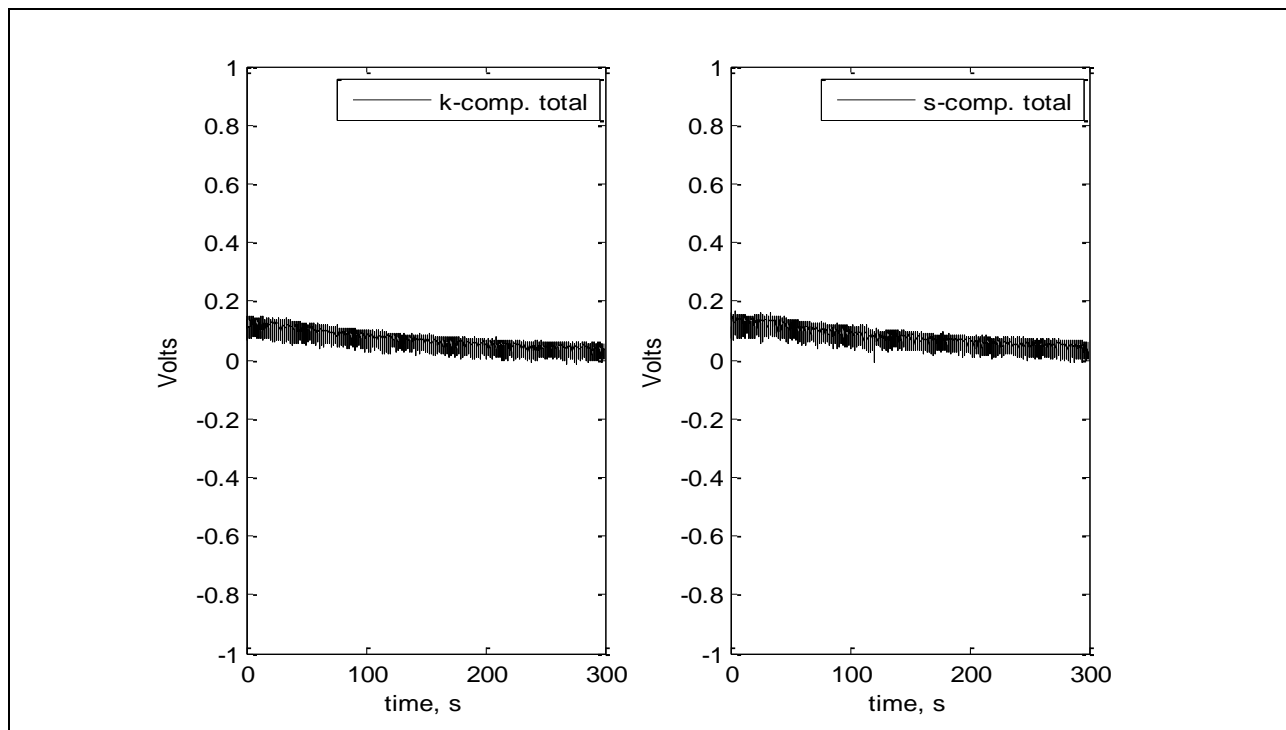


Figure 643: Voltage for full run.

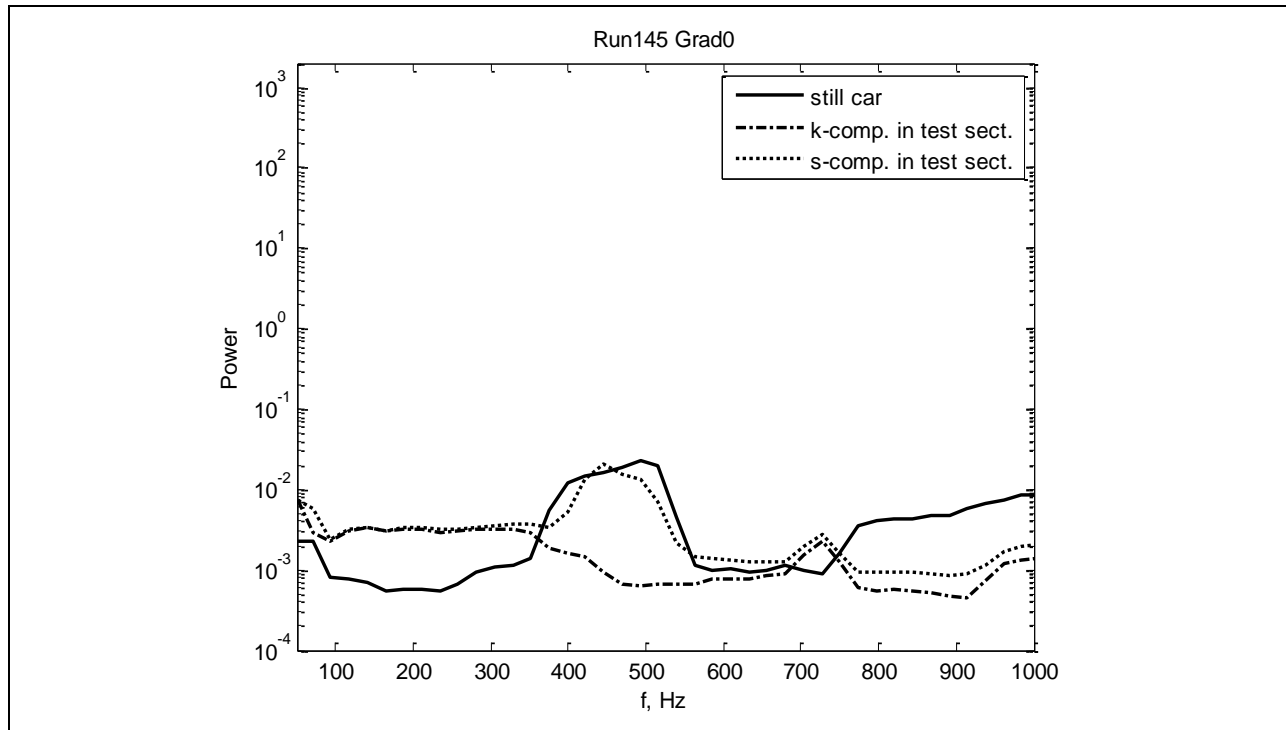


Figure 644: Power spectra in test section.

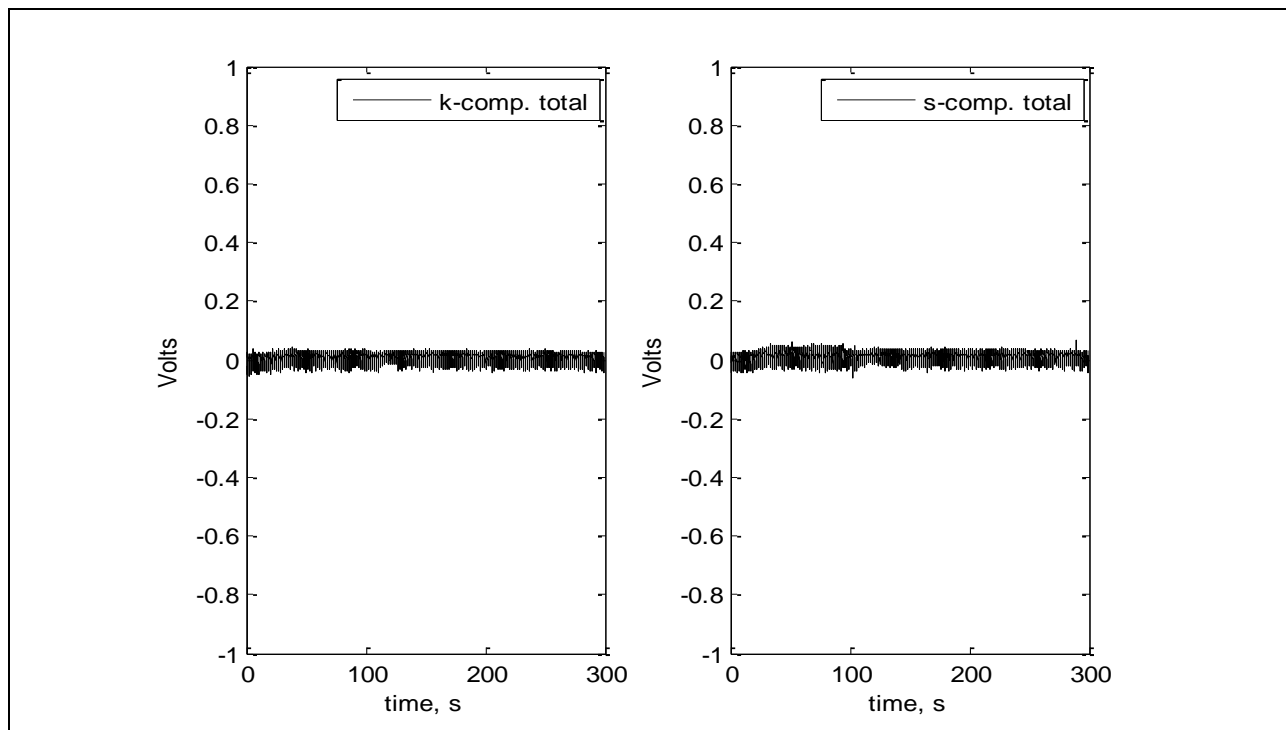


Figure 645: Voltage for full run.

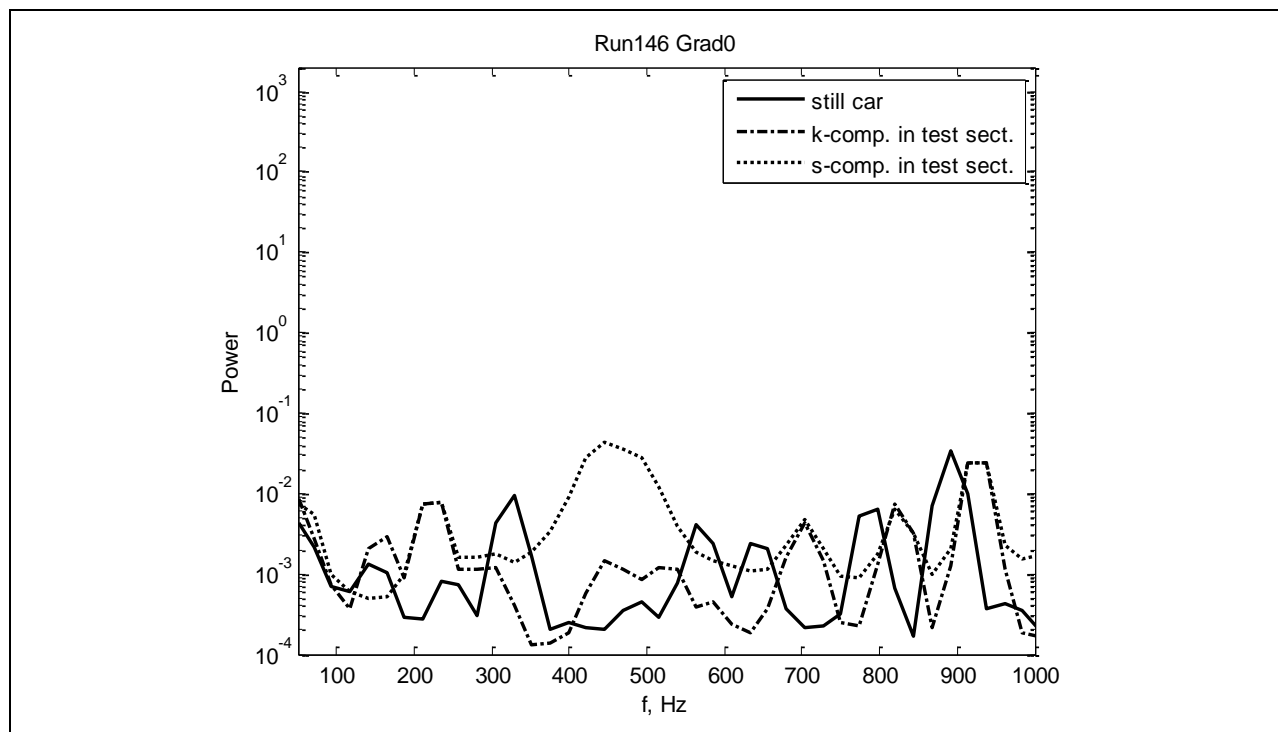


Figure 646: Power spectra in test section.

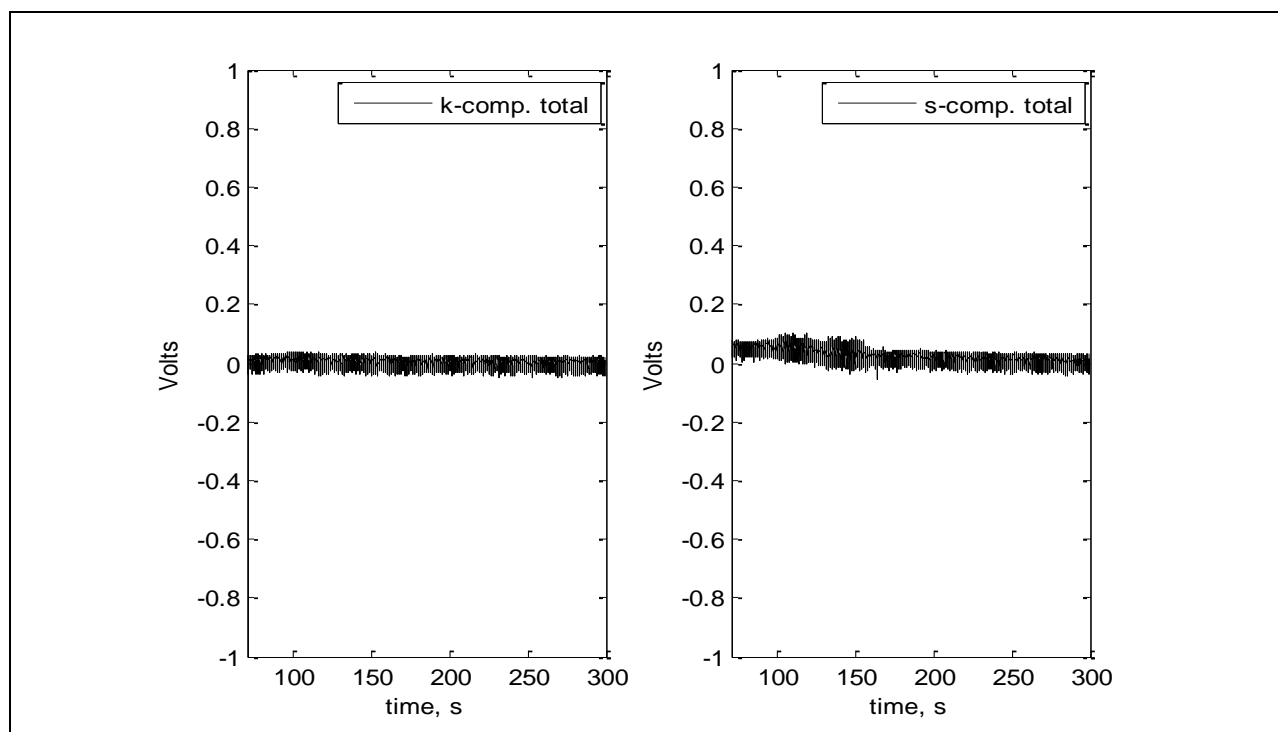


Figure 647: Voltage for full run.

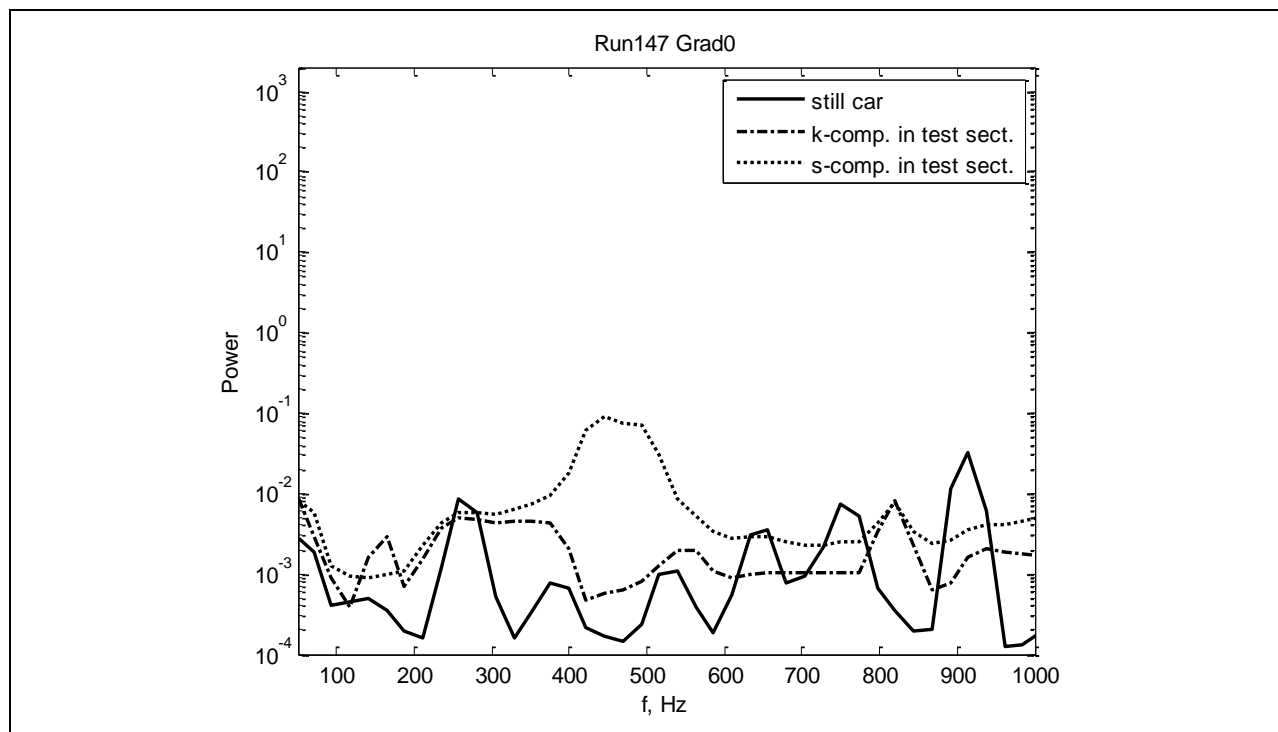


Figure 648: Power spectra in test section.

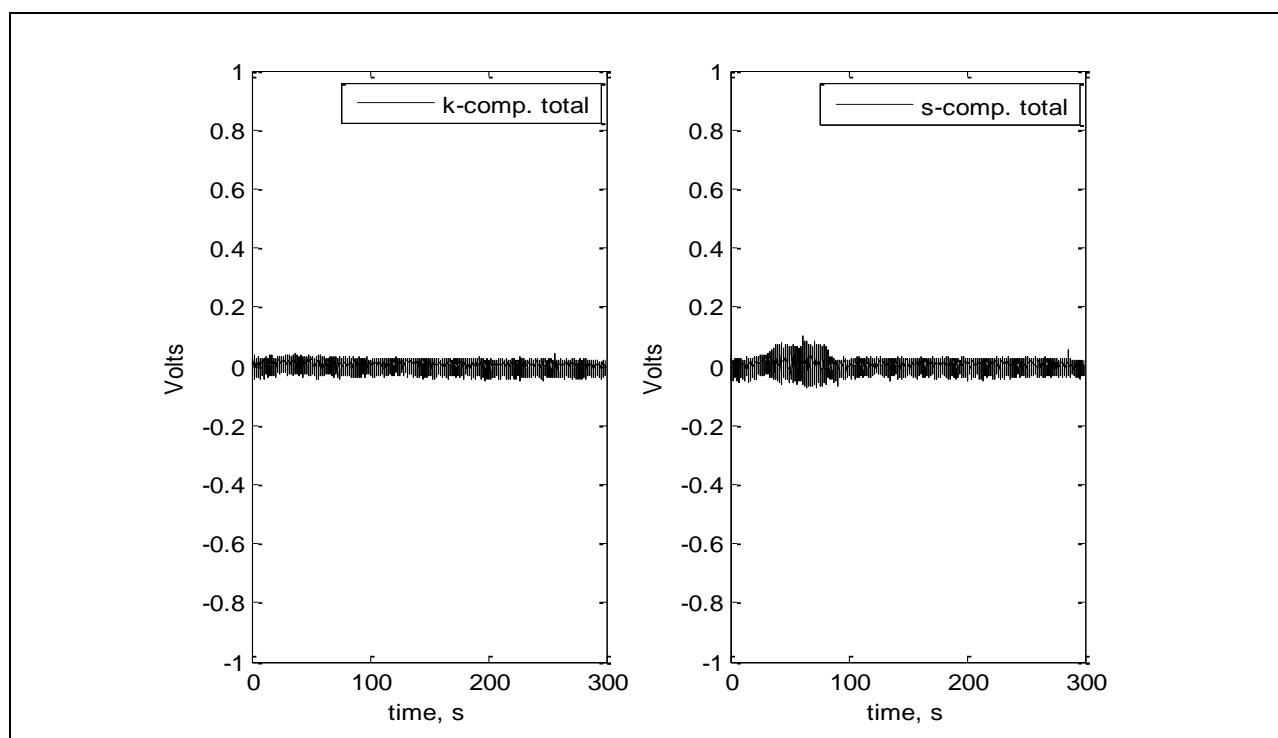


Figure 649: Voltage for full run.

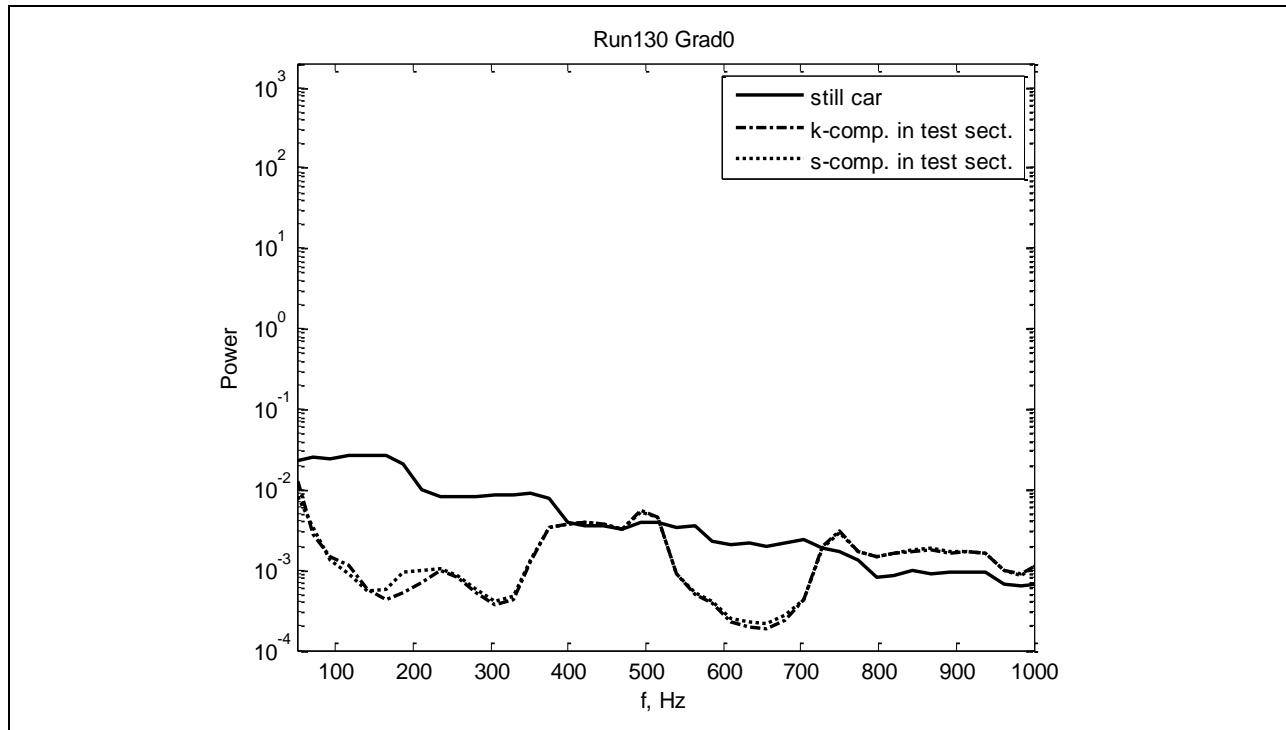


Figure 650: Power spectra in test section.

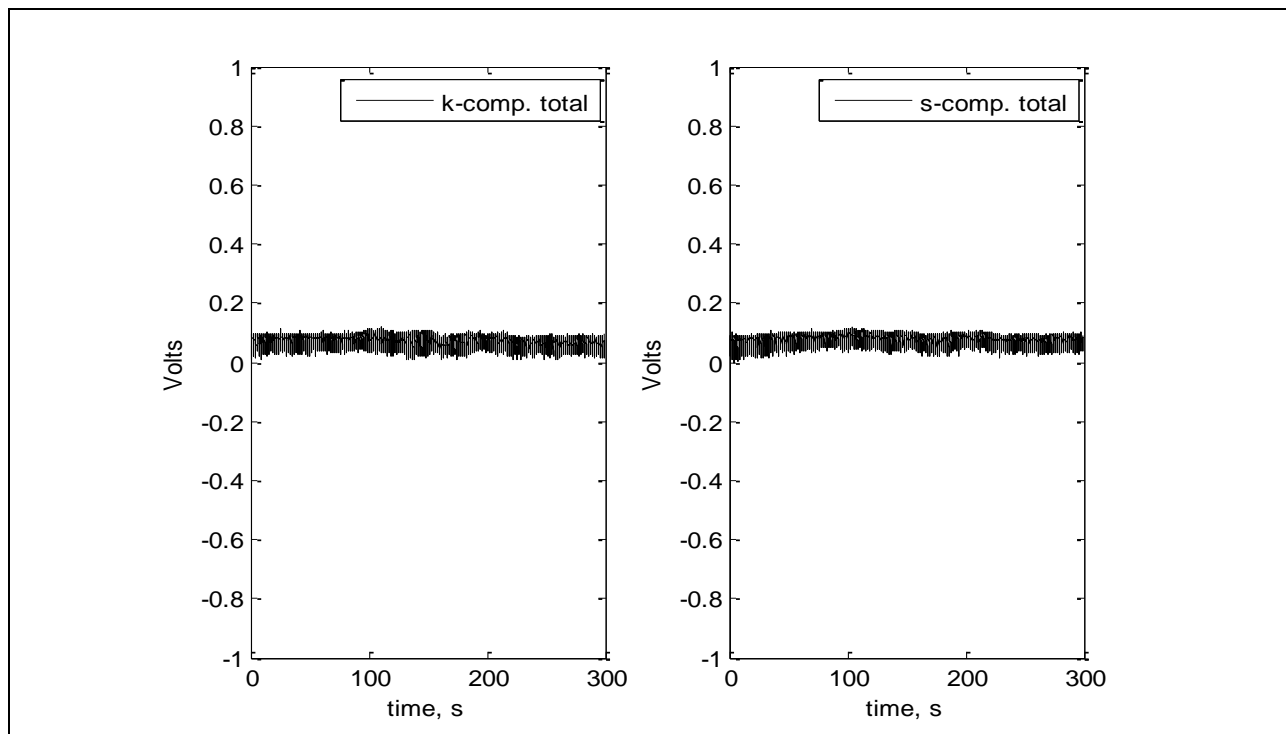


Figure 651: Voltage for full run.

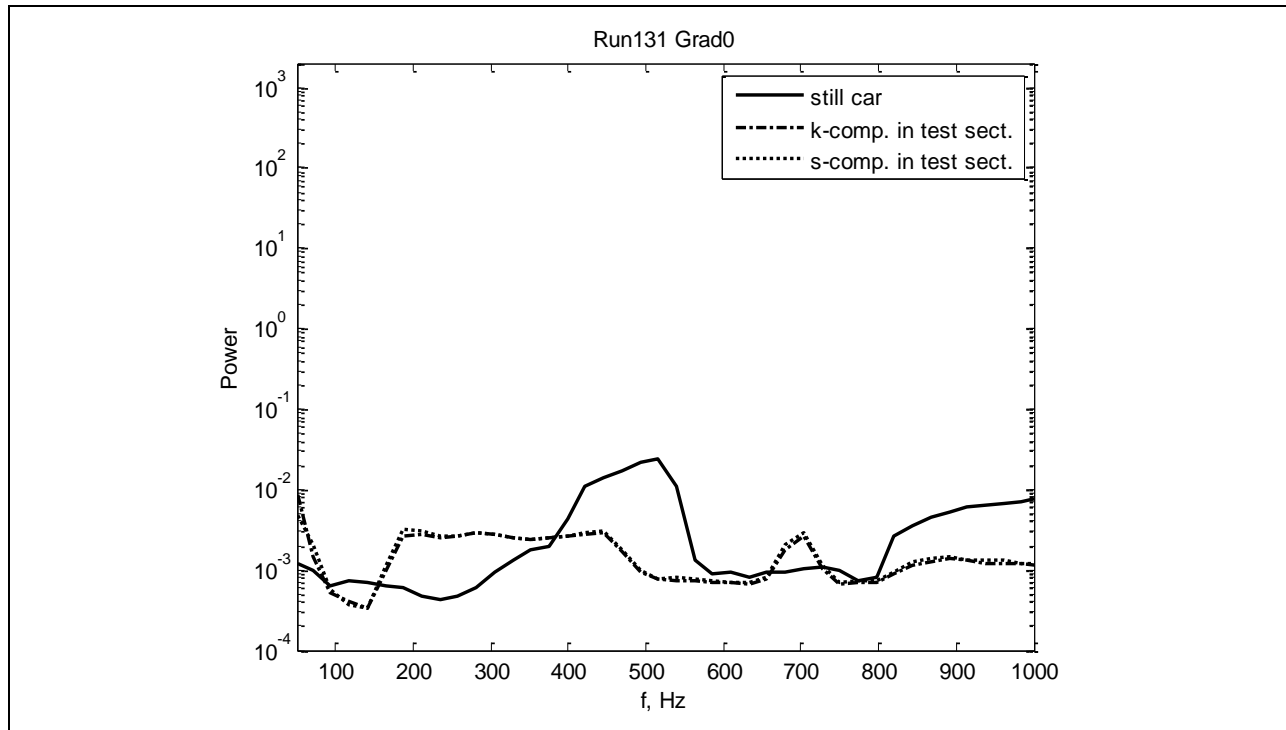


Figure 652: Power spectra in test section.

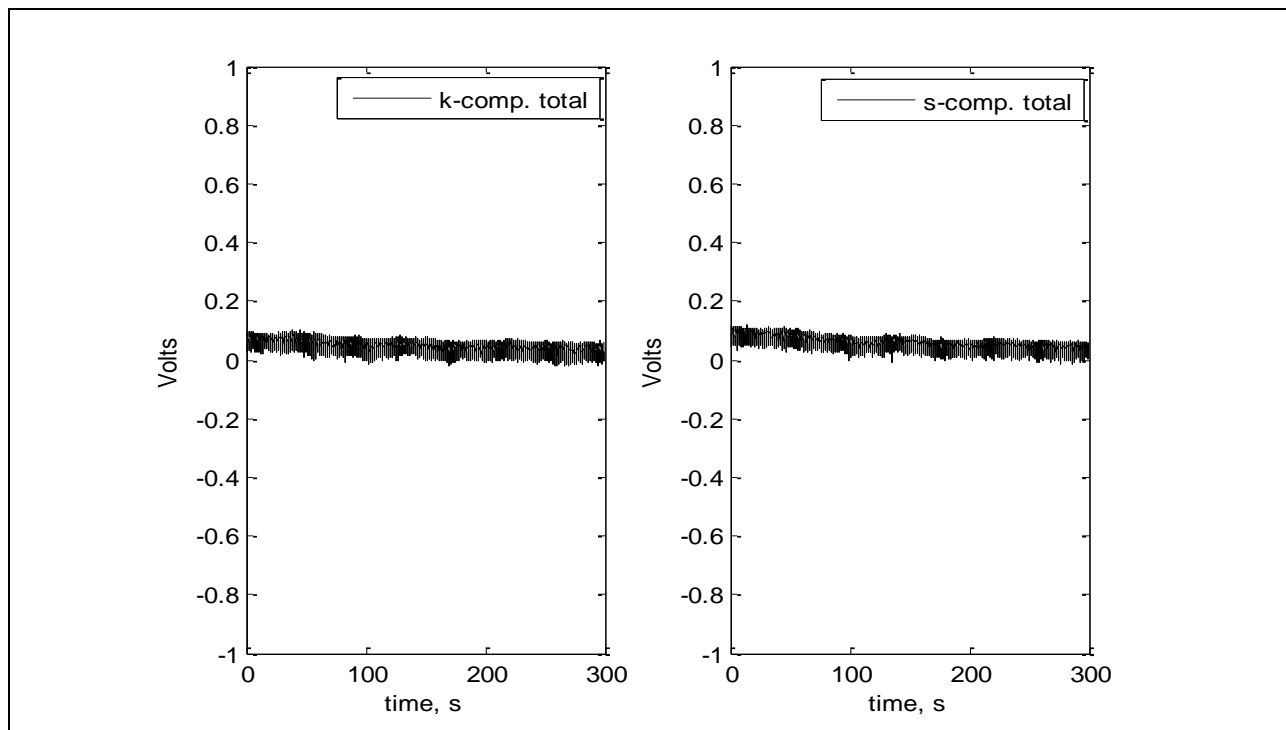


Figure 653: Voltage for full run.

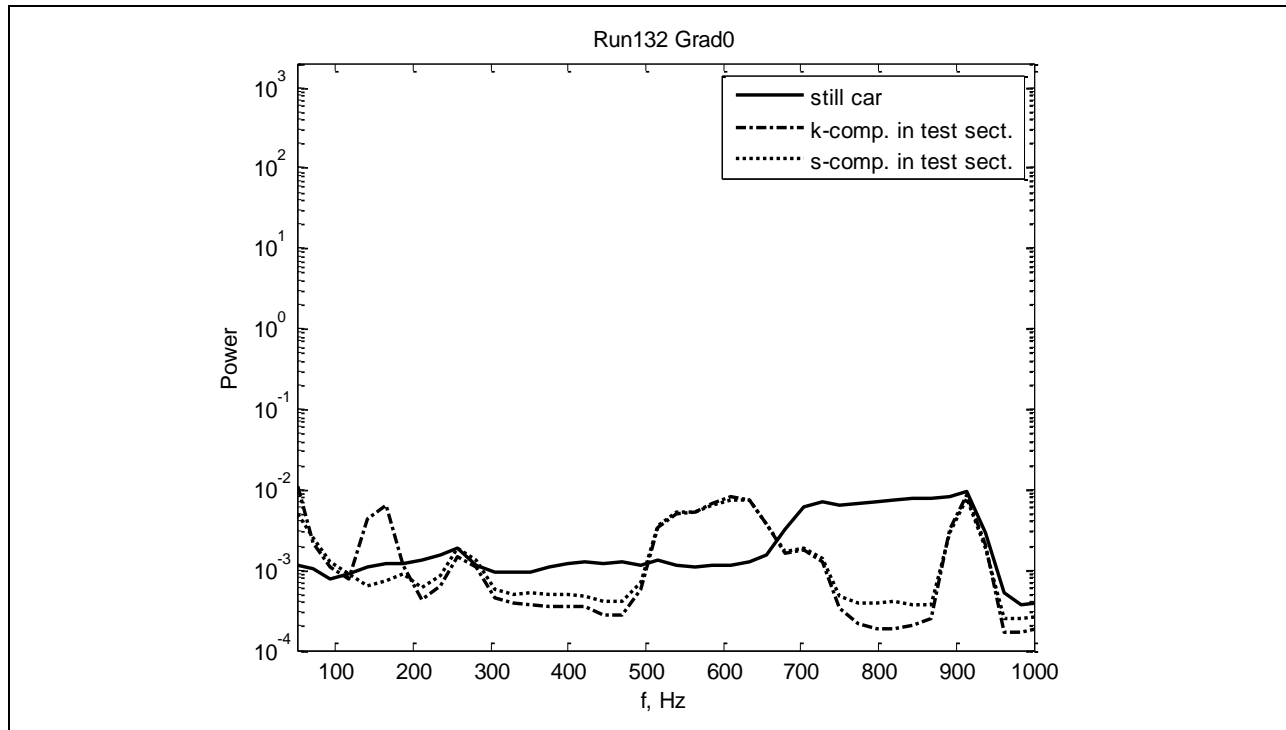


Figure 654: Power spectra in test section.

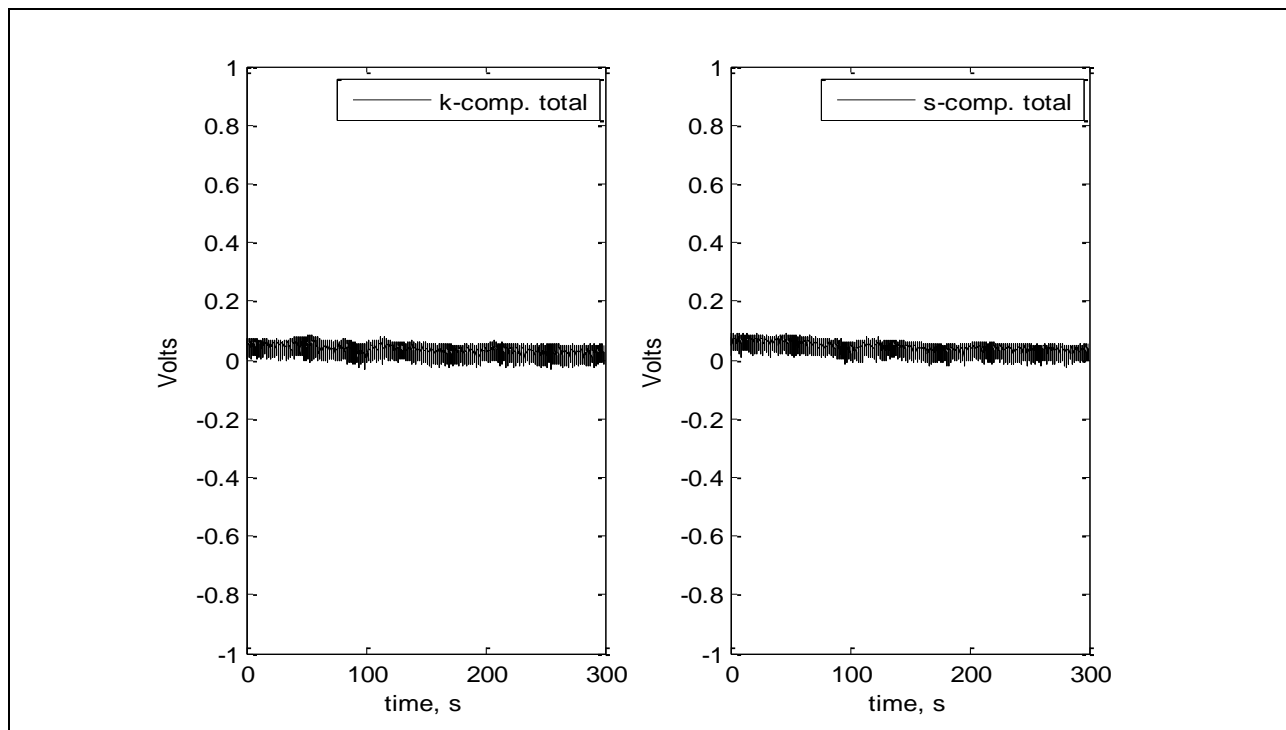


Figure 655: Voltage for full run.

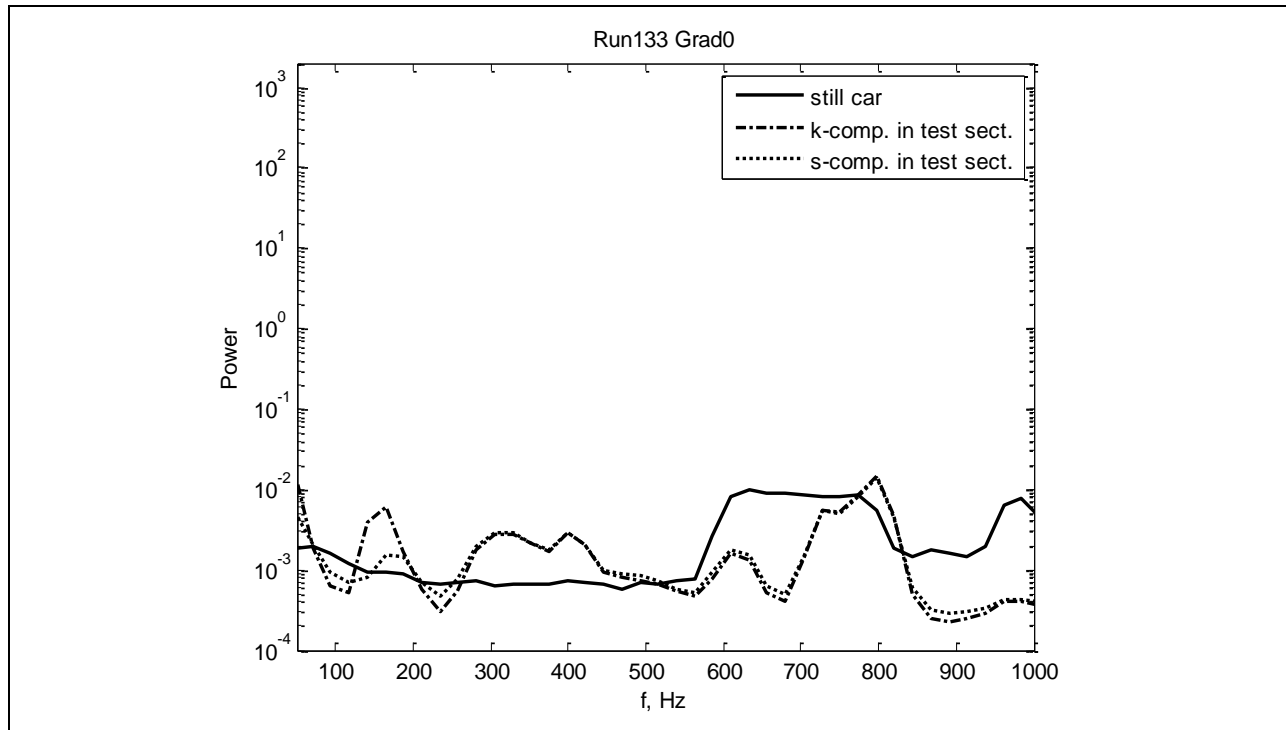


Figure 656: Power spectra in test section.

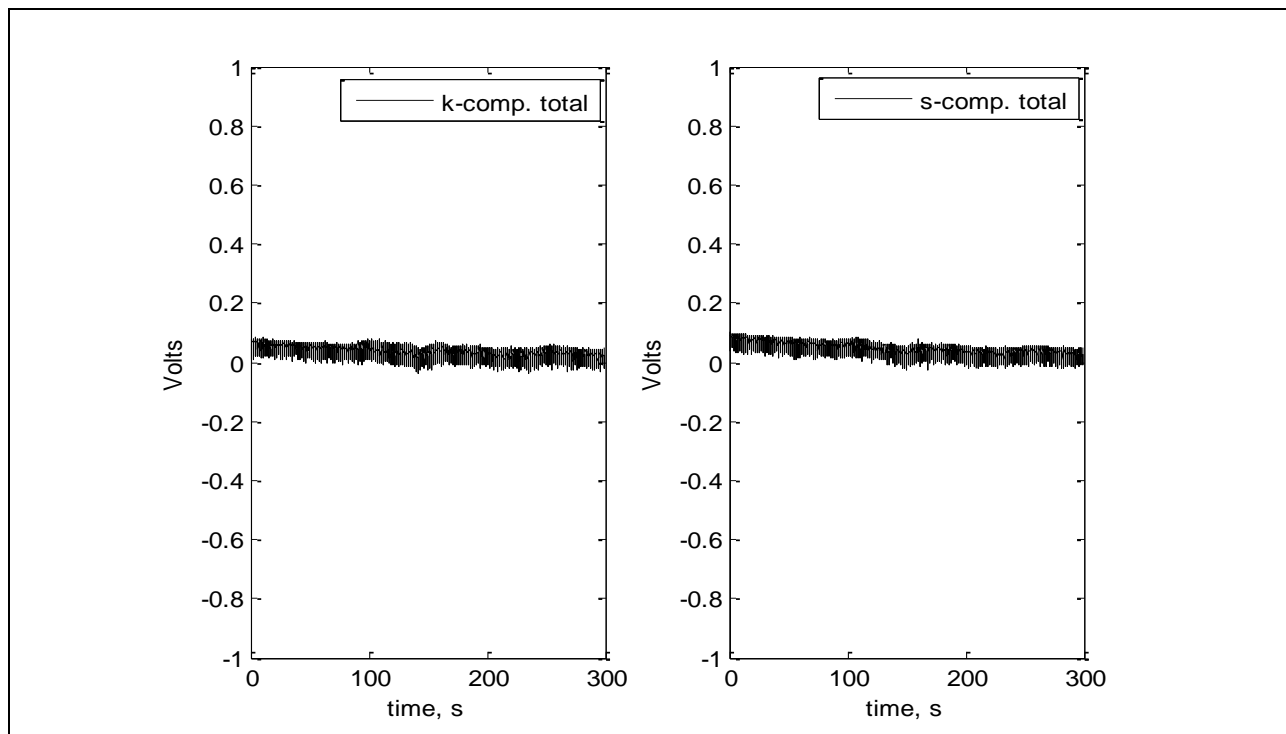


Figure 657: Voltage for full run.

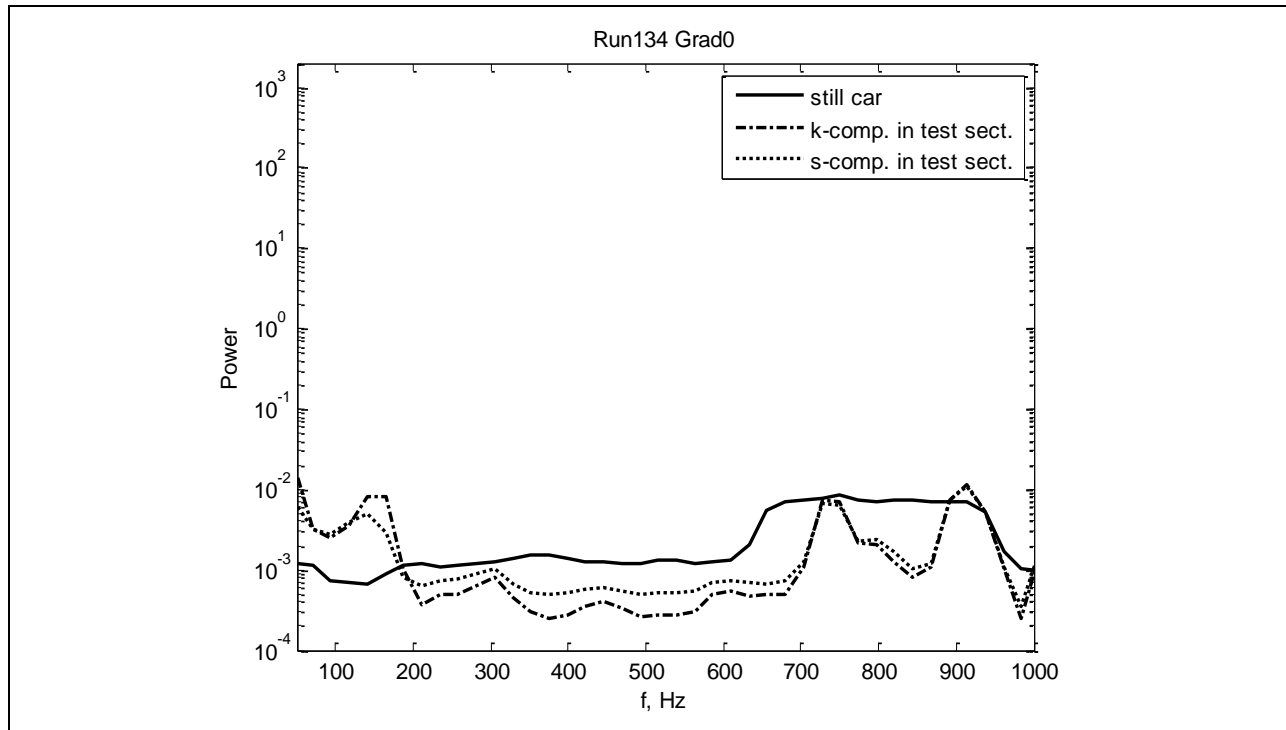


Figure 658: Power spectra in test section.

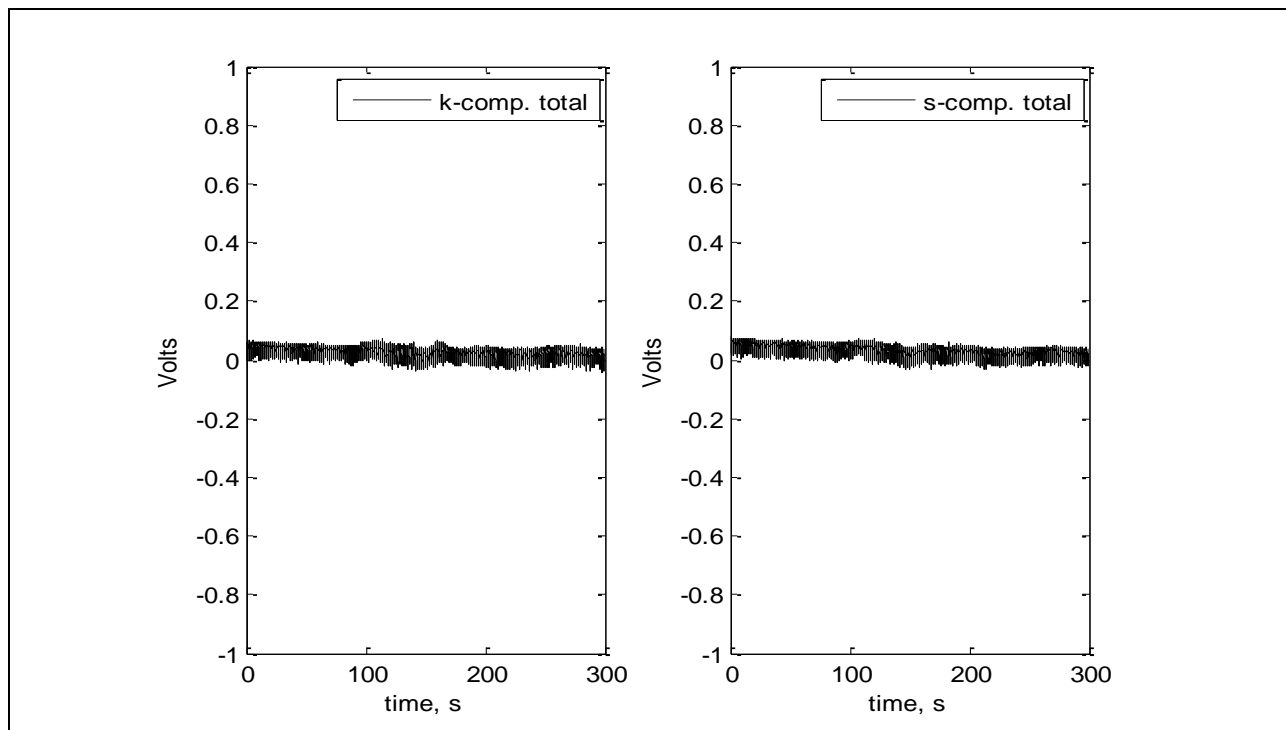


Figure 659: Voltage for full run.

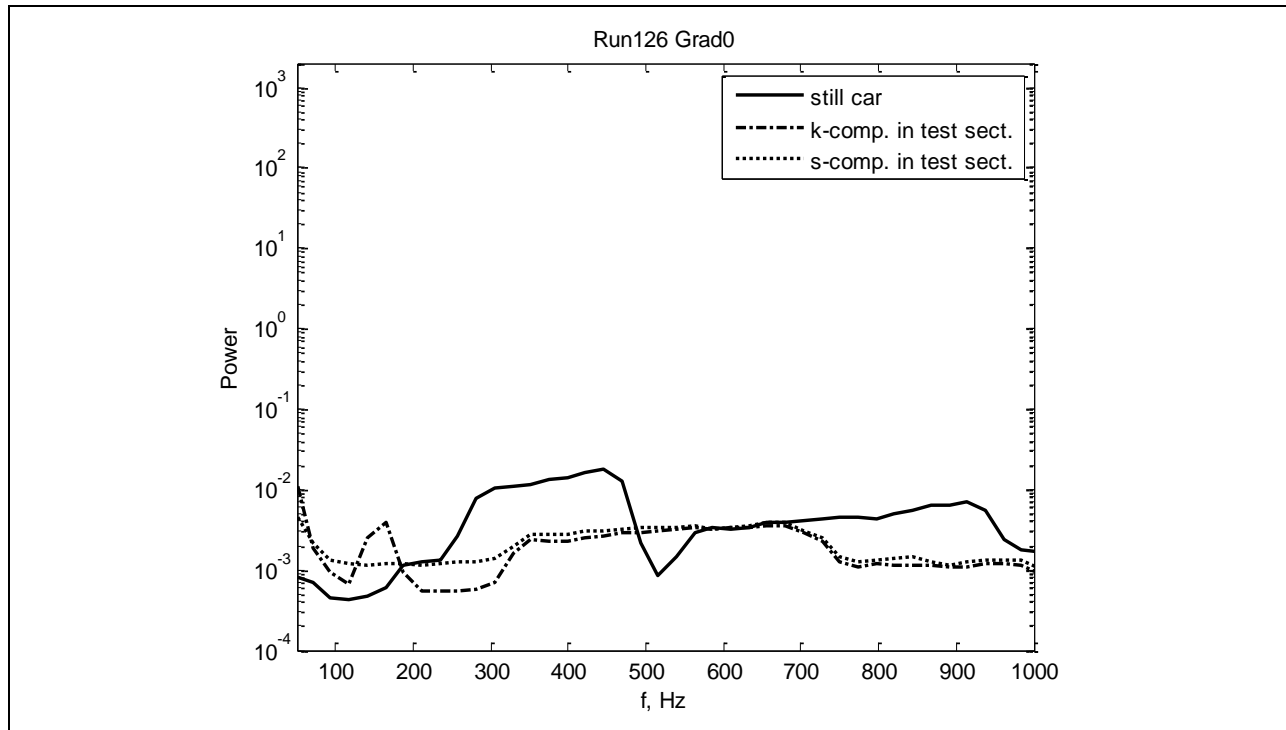


Figure 660: Power spectra in test section.

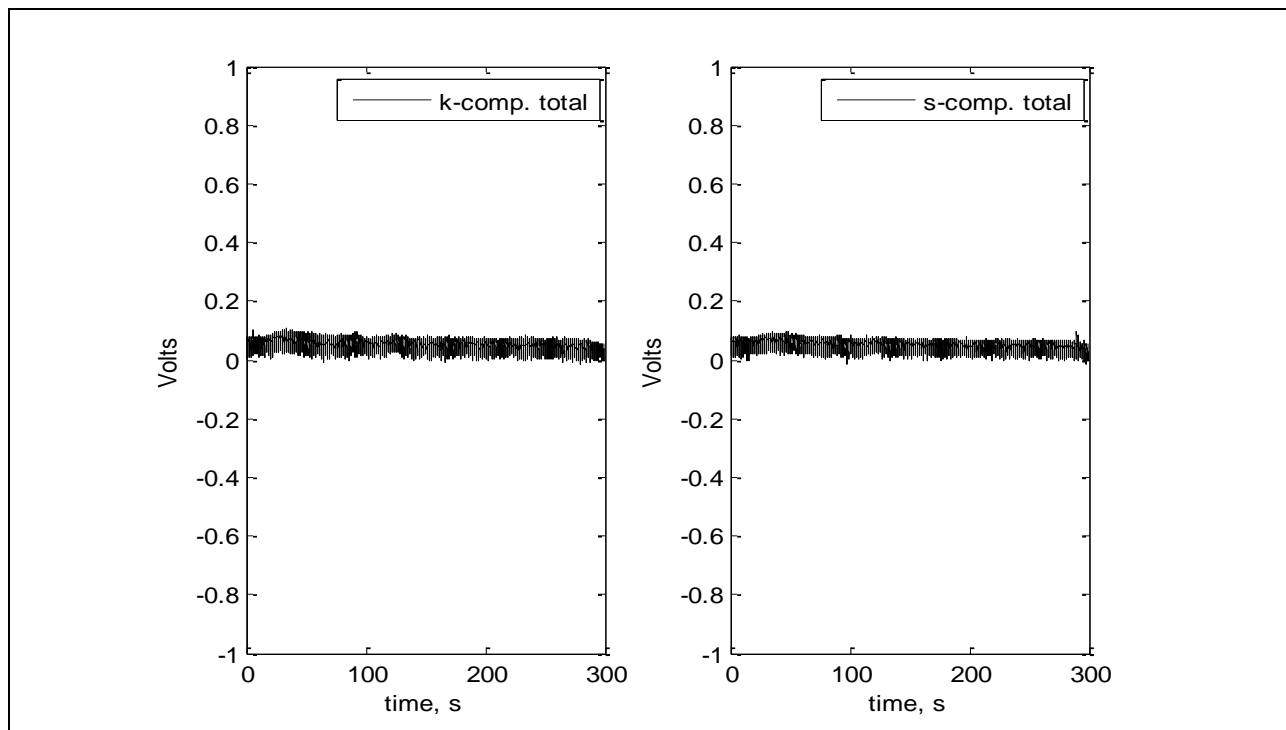


Figure 661: Voltage for full run.

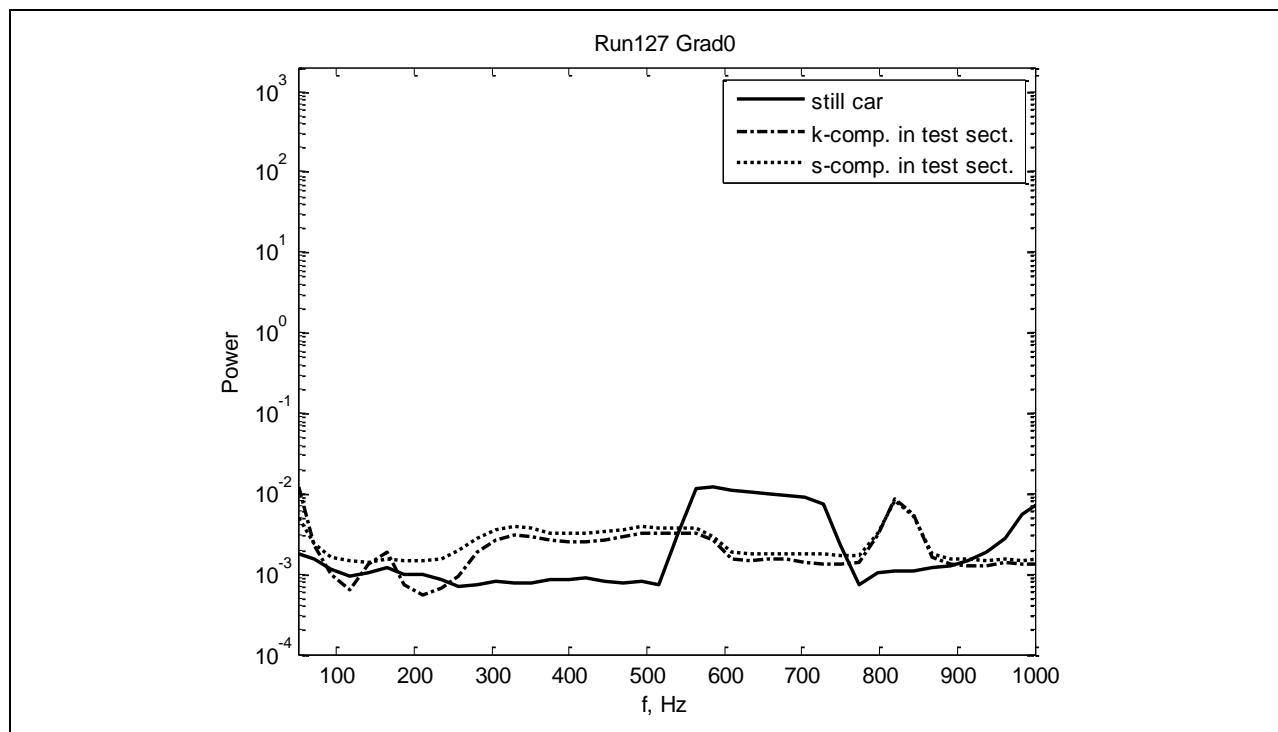


Figure 662: Power spectra in test section.

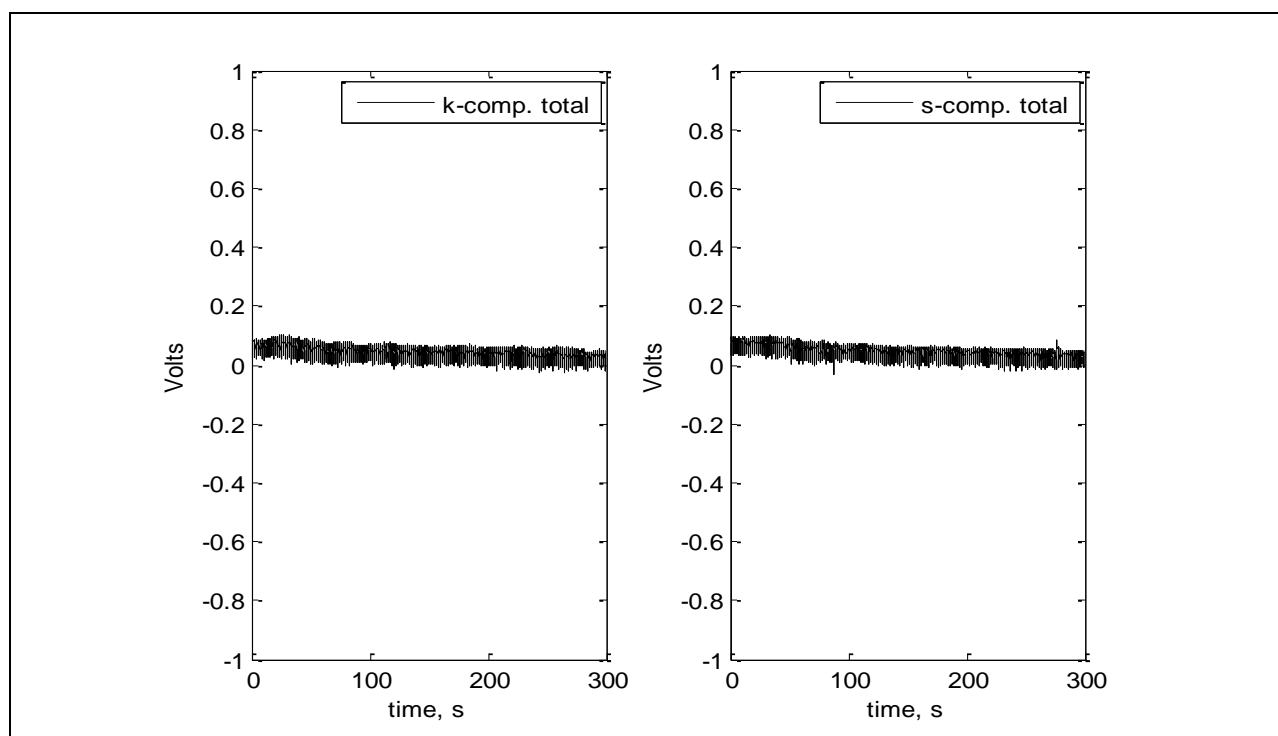


Figure 663: Voltage for full run.

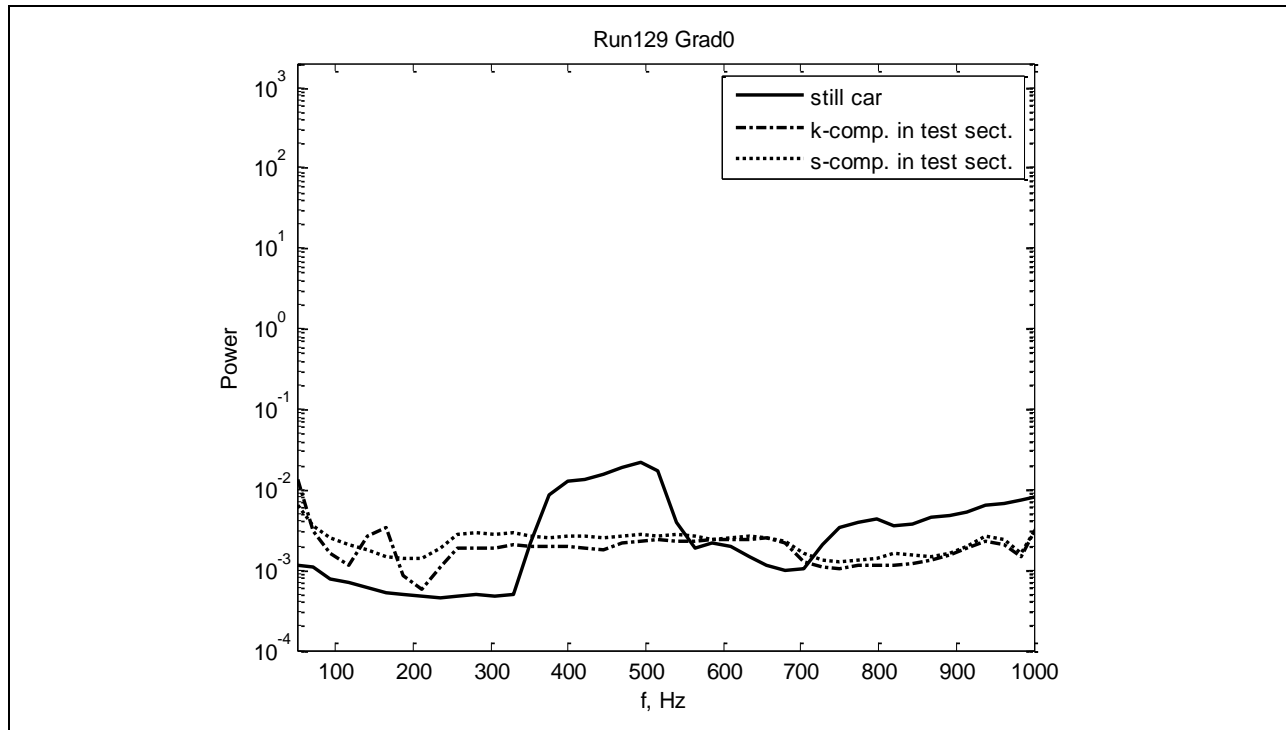


Figure 664: Power spectra in test section.

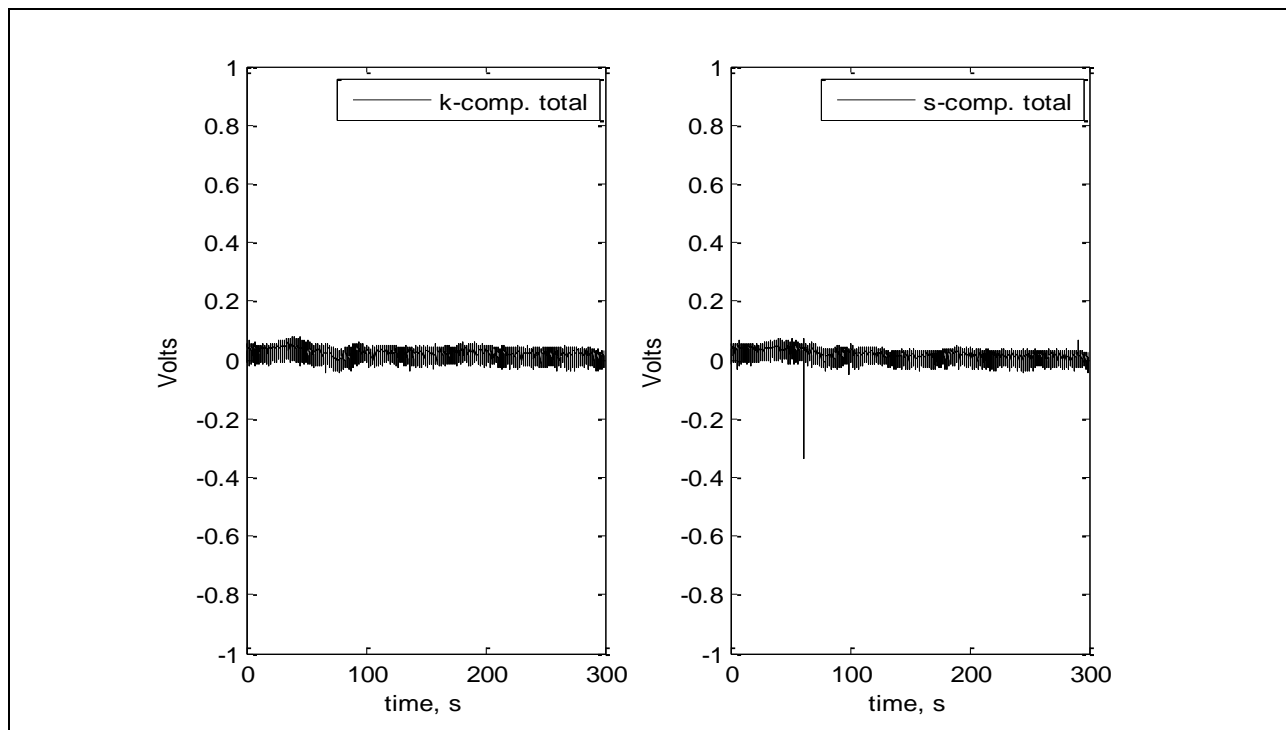


Figure 665: Voltage for full run.

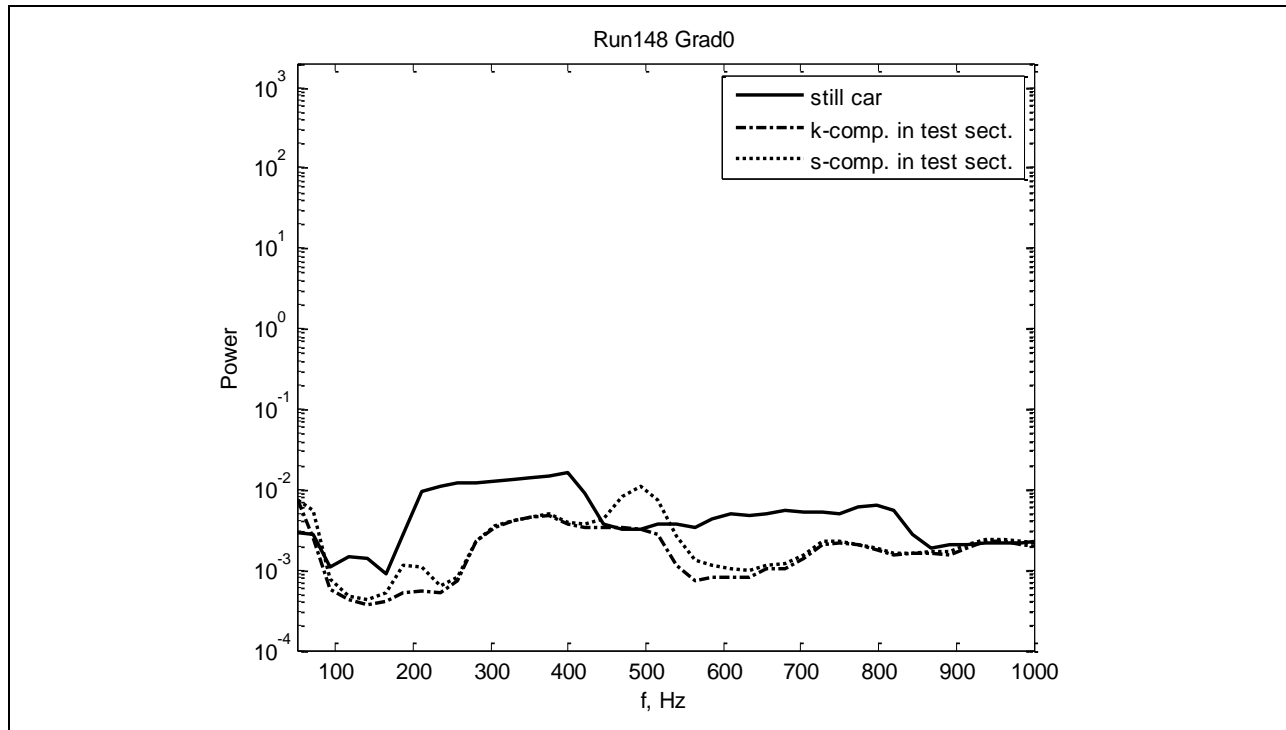


Figure 666: Power spectra in test section.

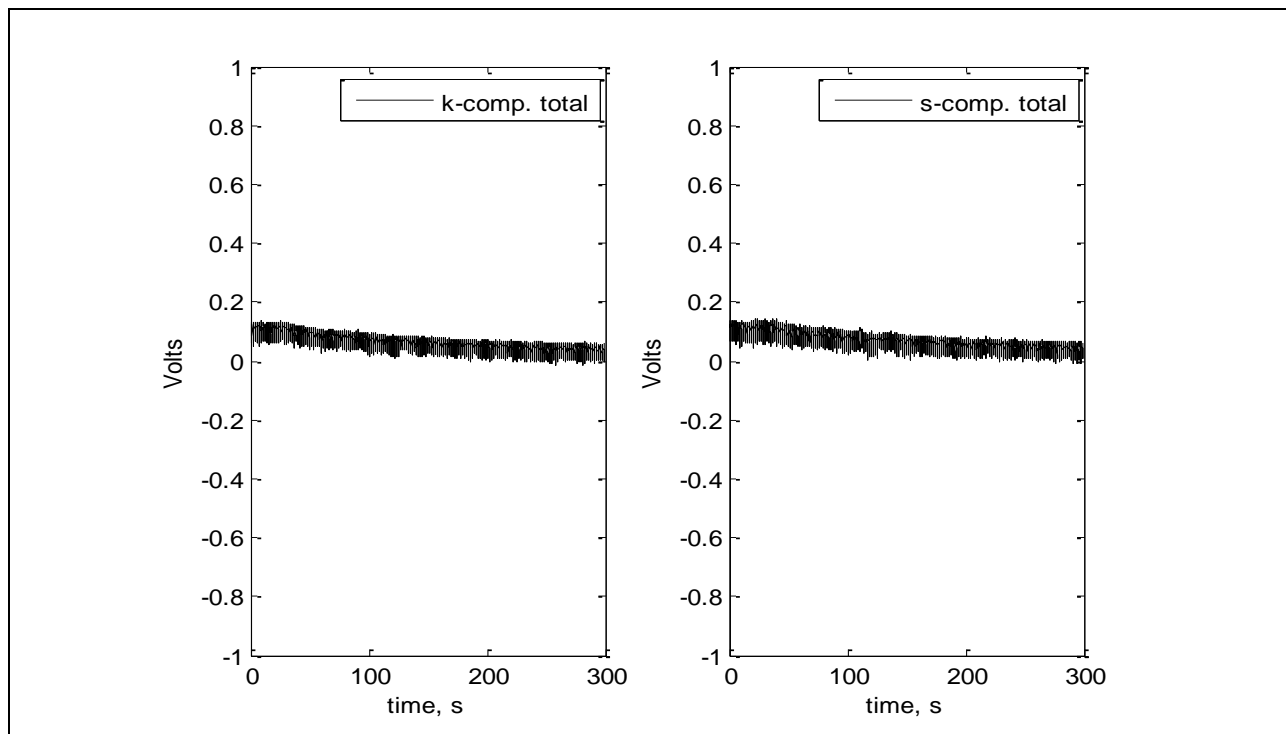


Figure 667: Voltage for full run.

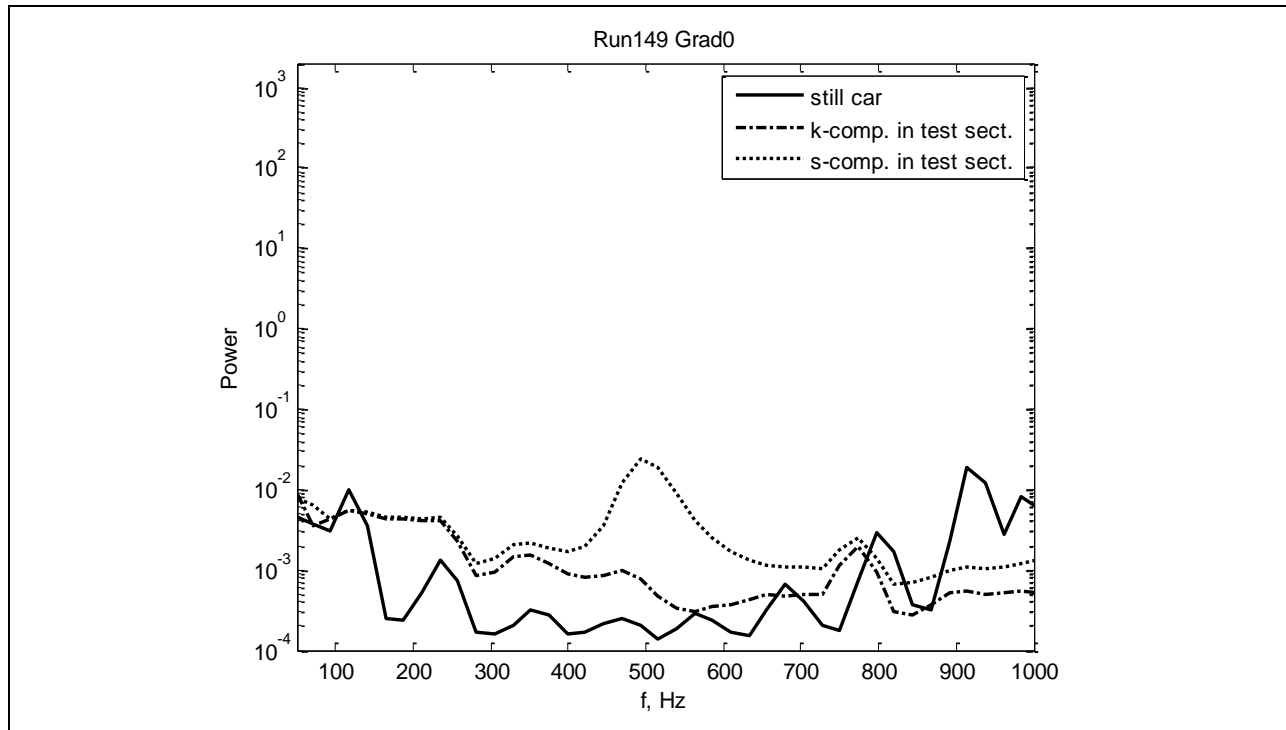


Figure 668: Power spectra in test section.

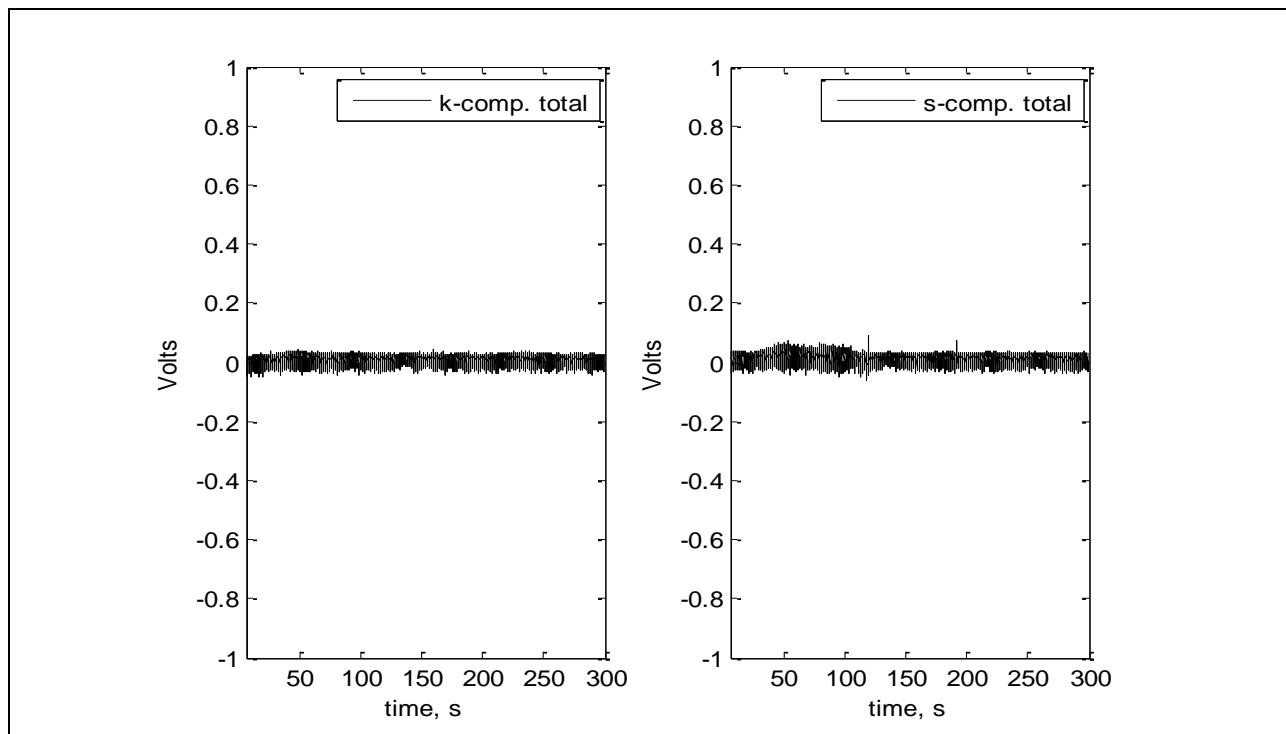


Figure 669: Voltage for full run.

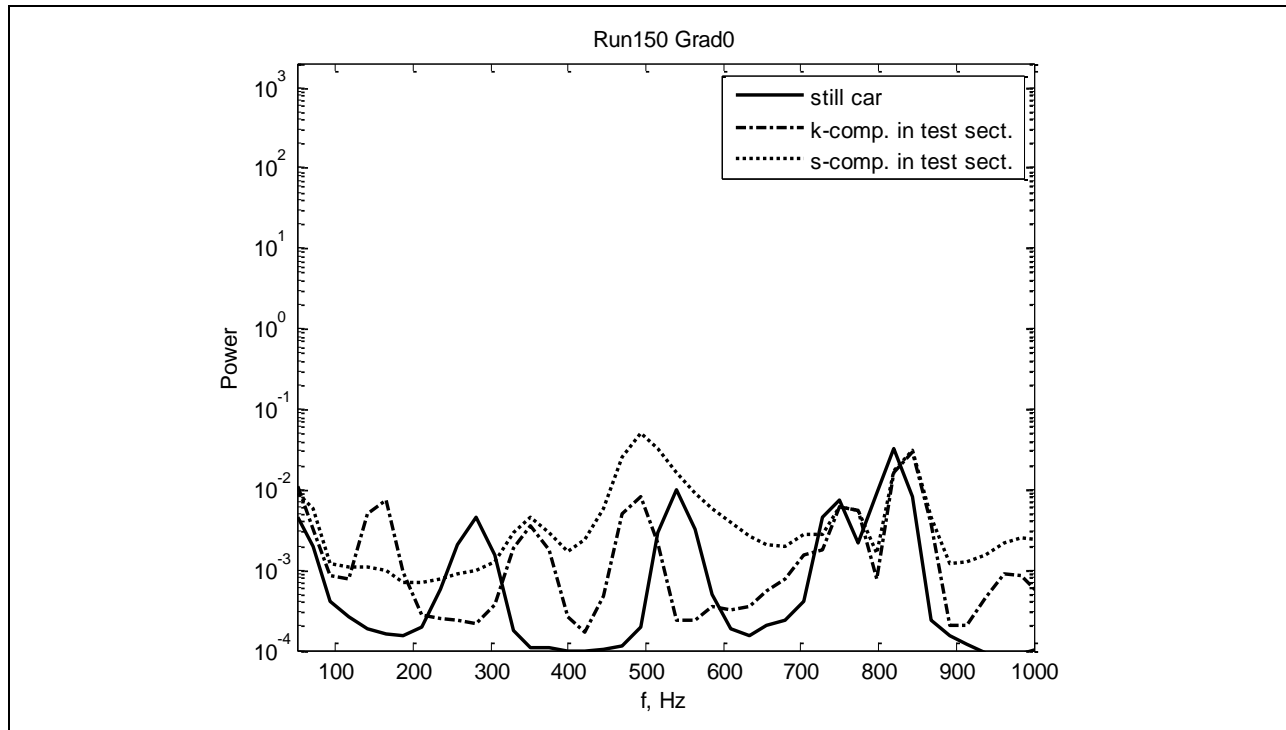


Figure 670: Power spectra in test section.

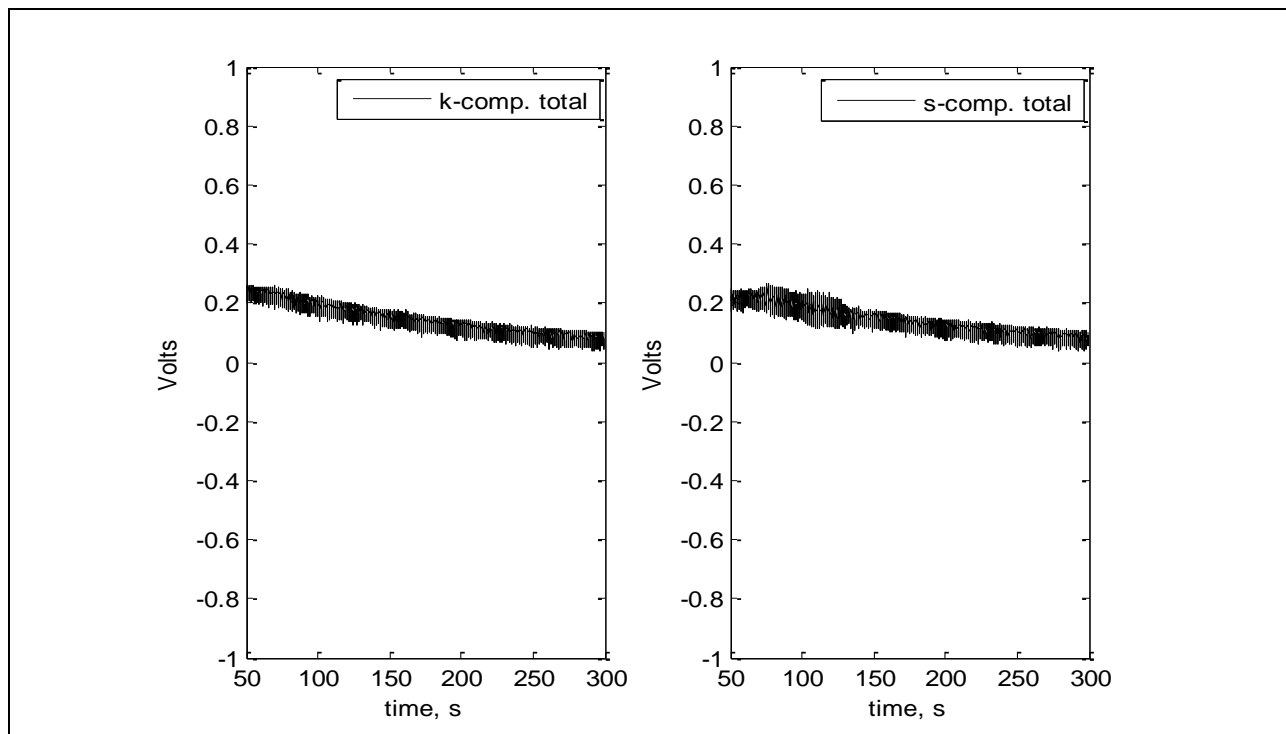


Figure 671: Voltage for full run.

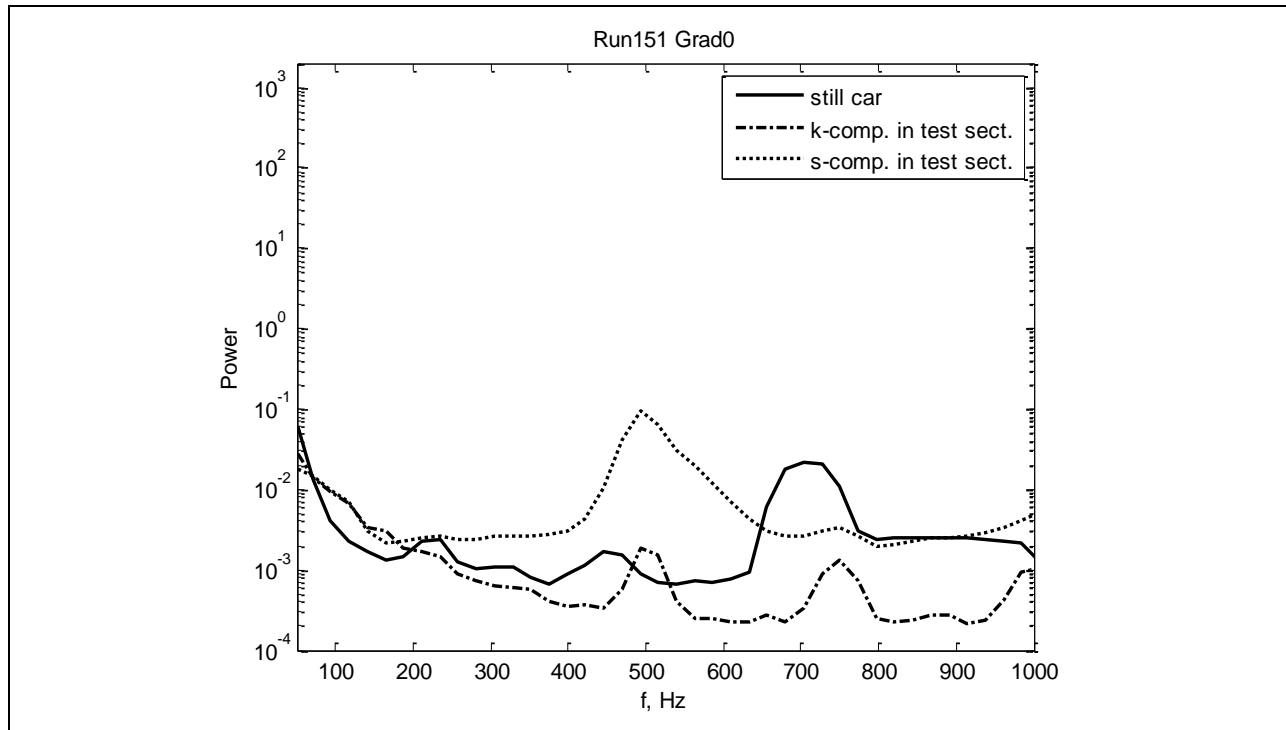


Figure 672: Power spectra in test section.

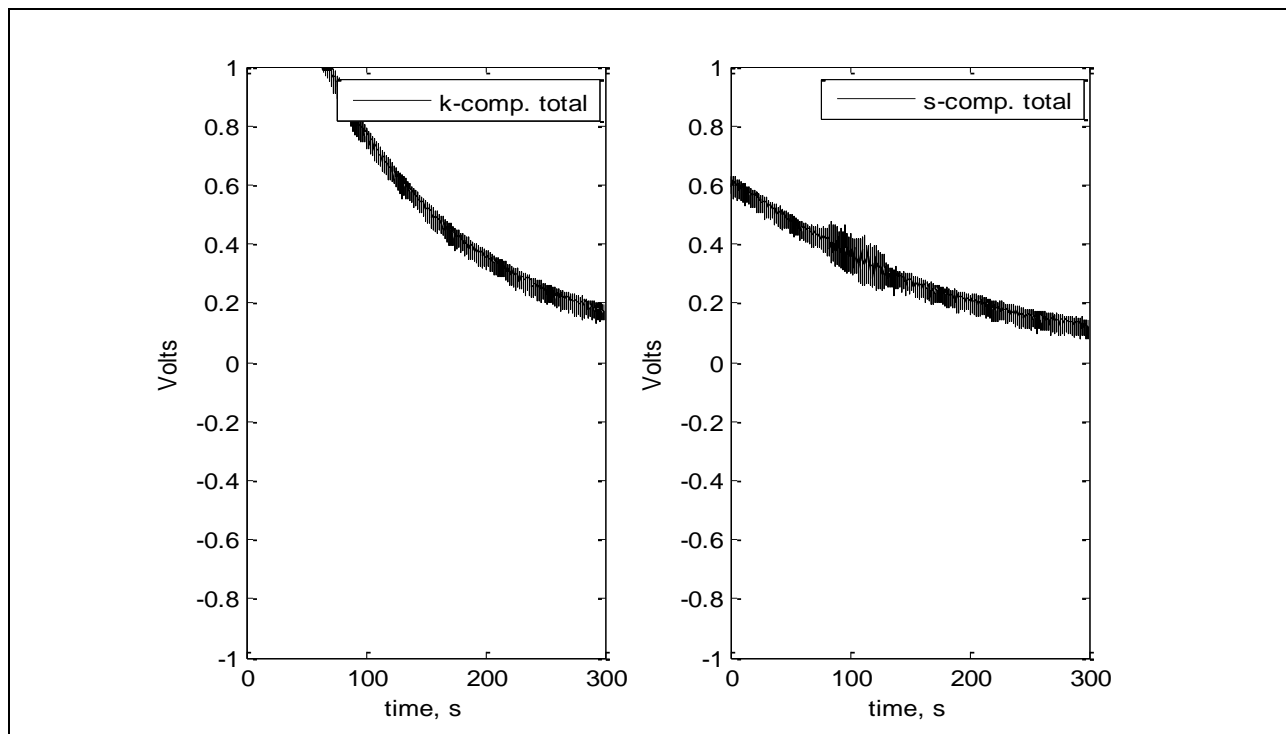


Figure 673: Voltage for full run.

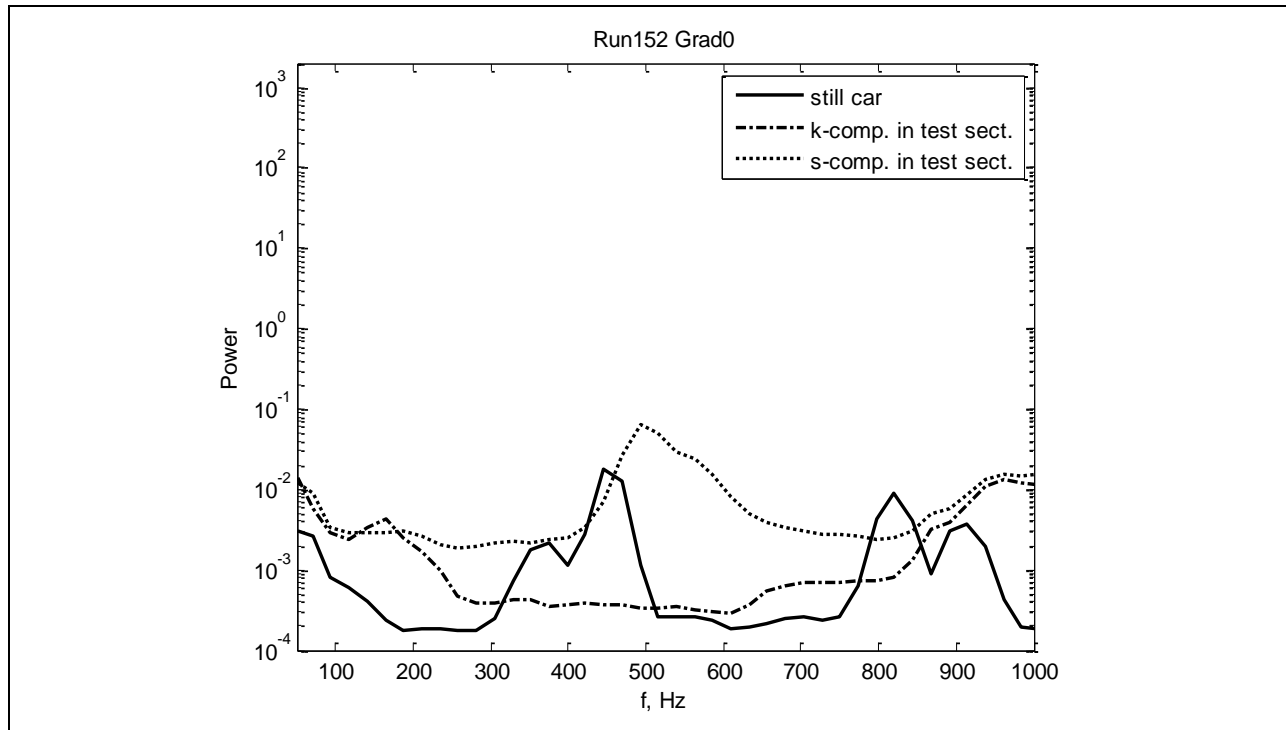


Figure 674: Power spectra in test section.

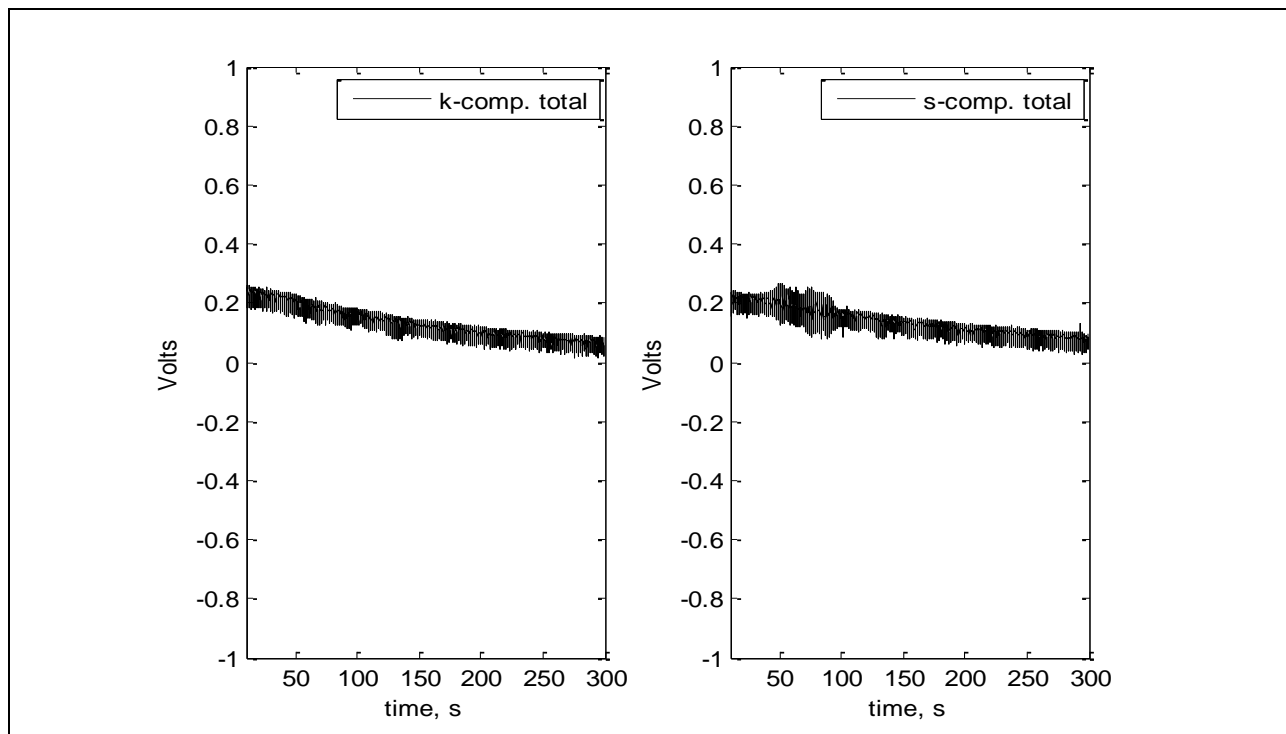


Figure 675: Voltage for full run.

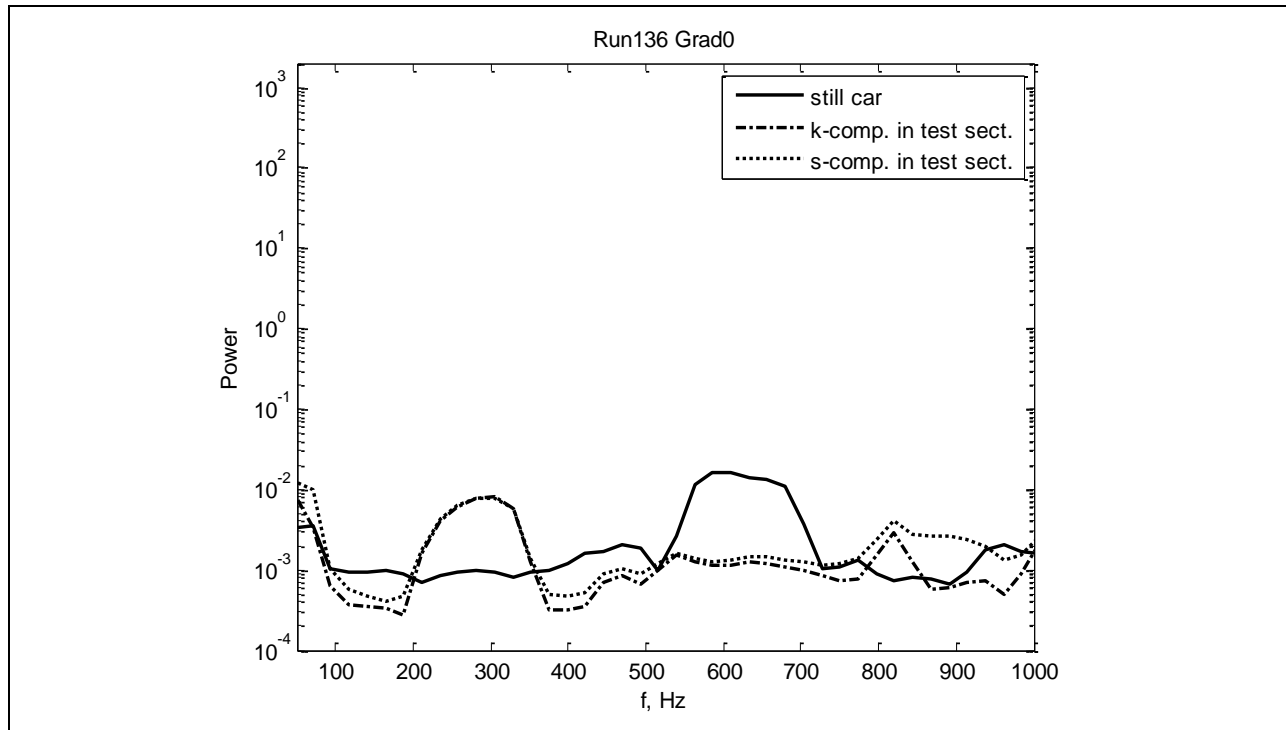


Figure 676: Power spectra in test section.

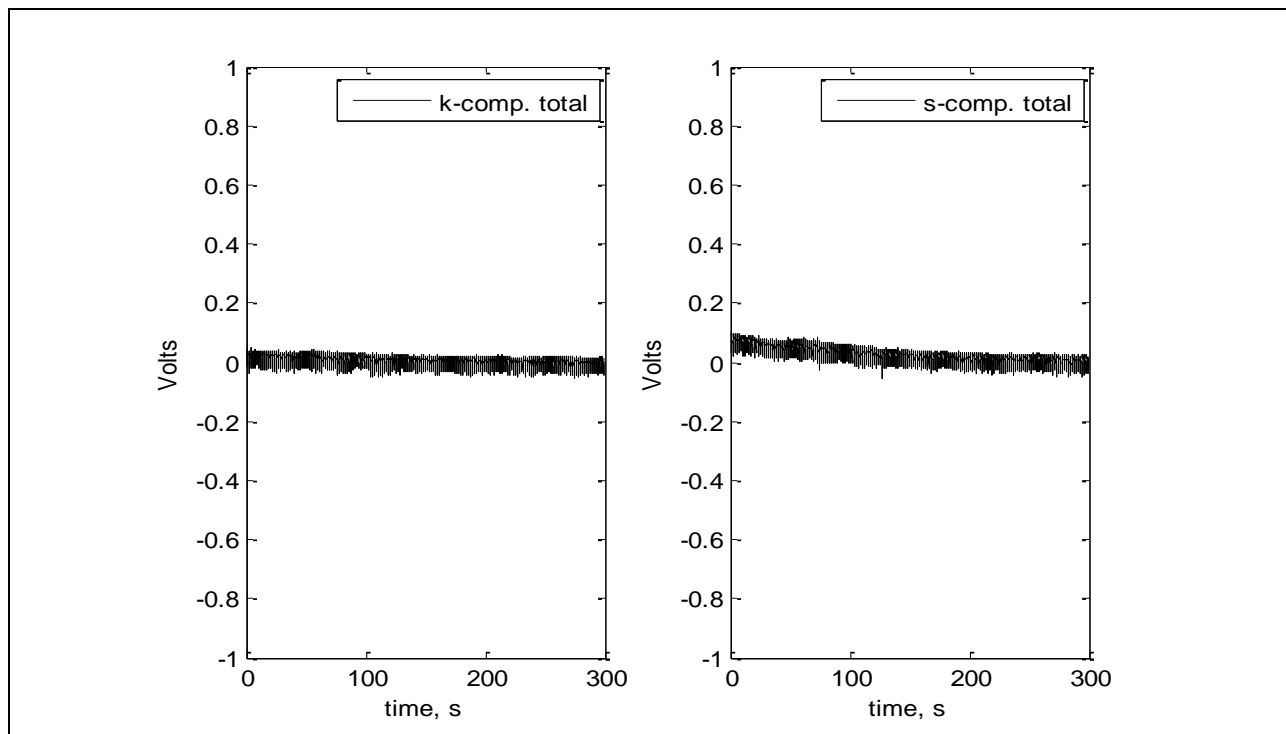


Figure 677: Voltage for full run.

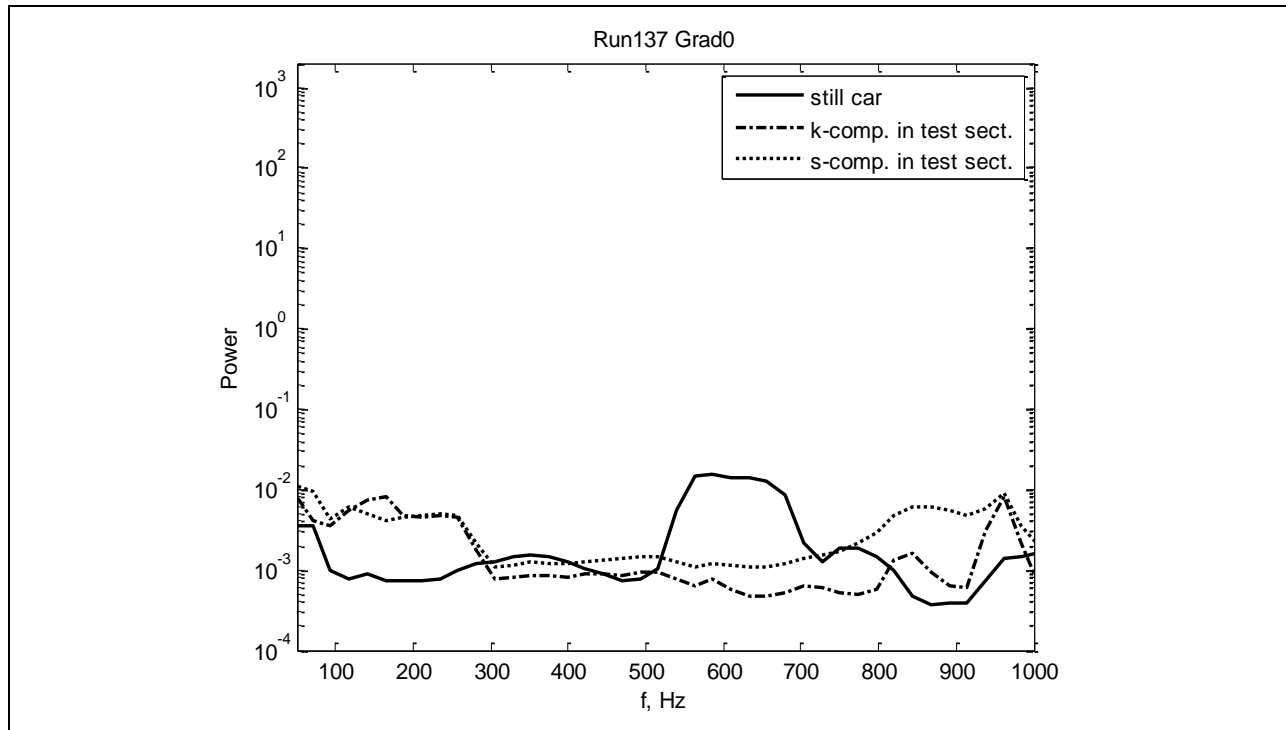


Figure 678: Power spectra in test section.

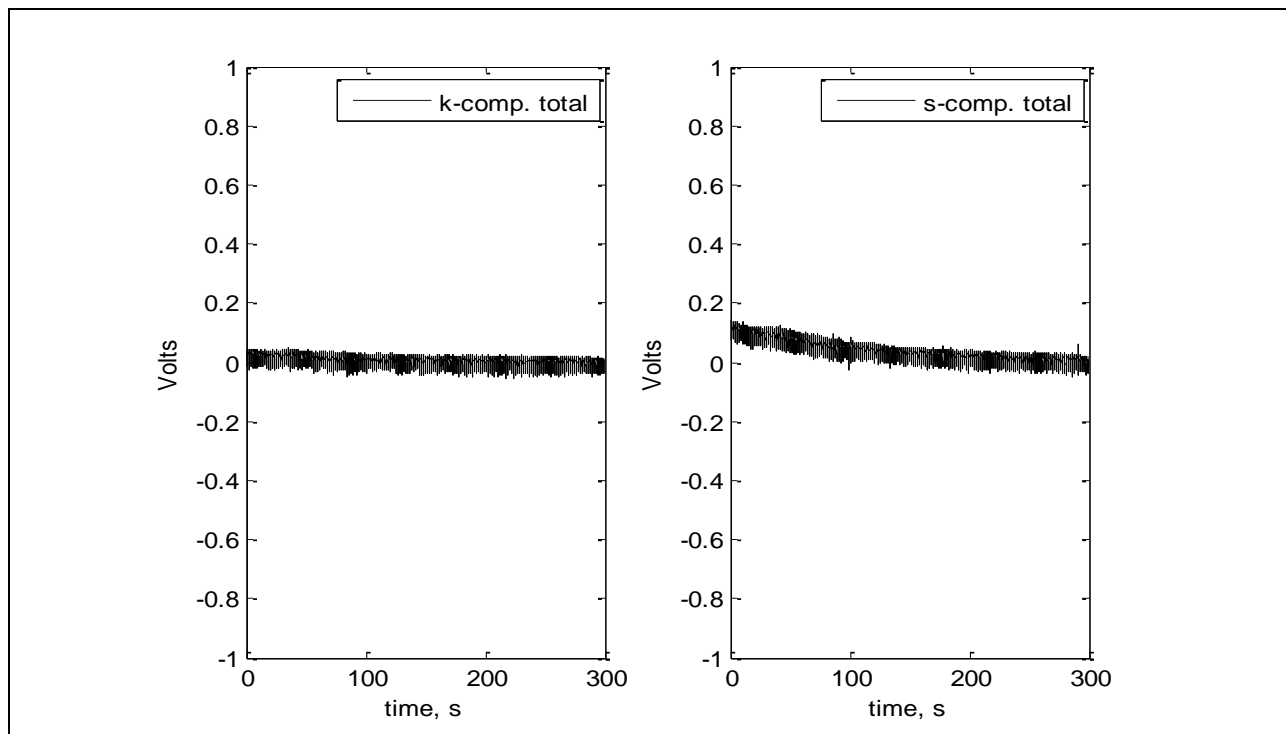


Figure 679: Voltage for full run.

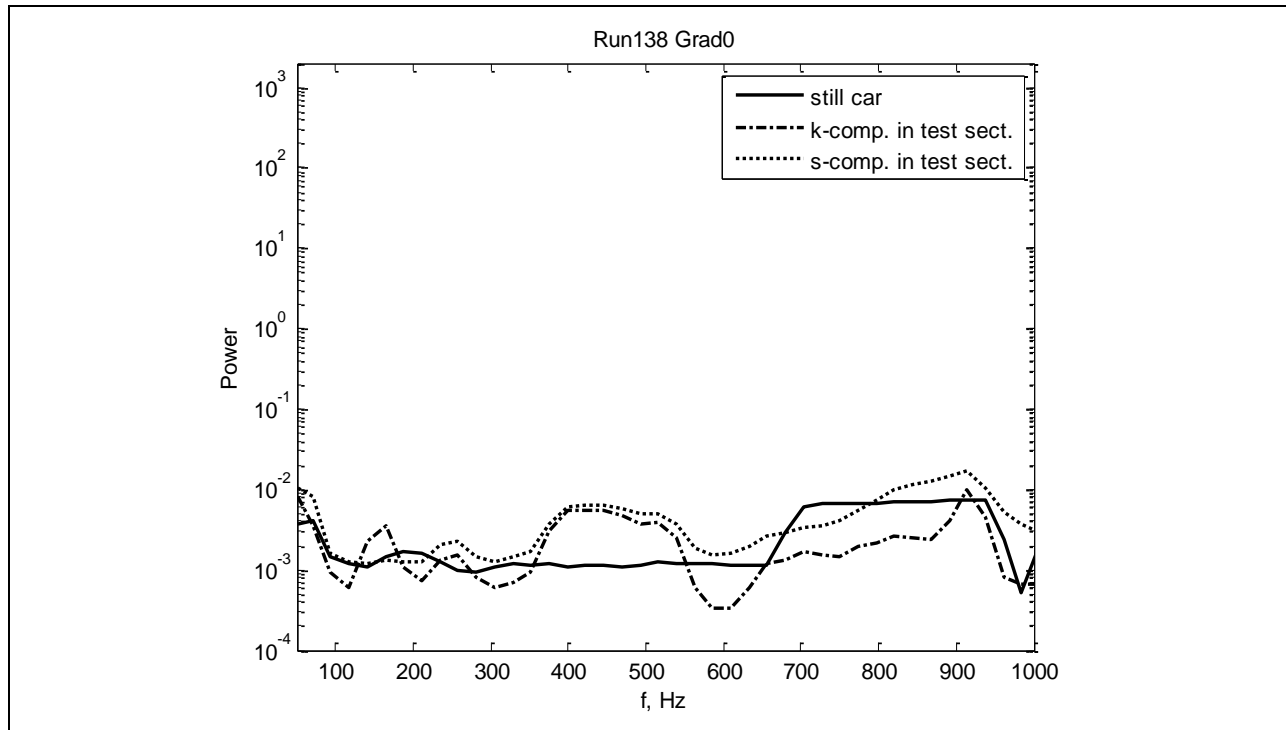


Figure 680: Power spectra in test section.

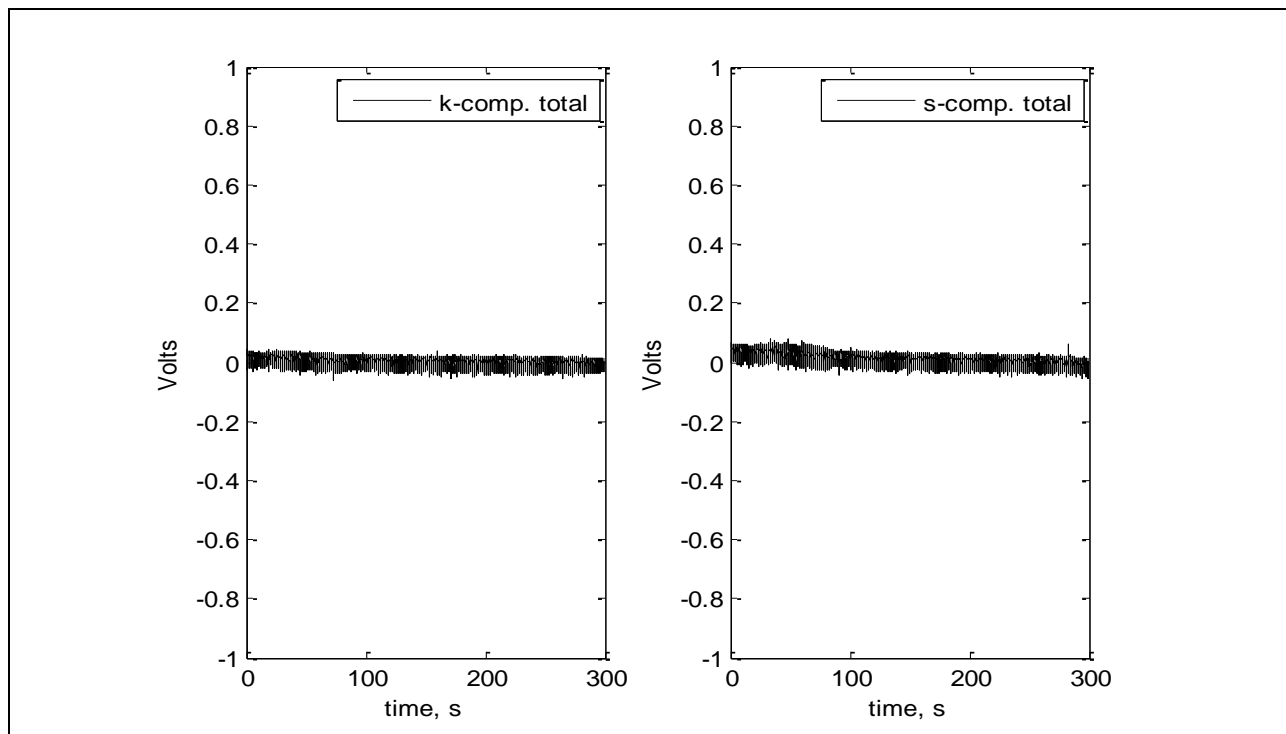


Figure 681: Voltage for full run.

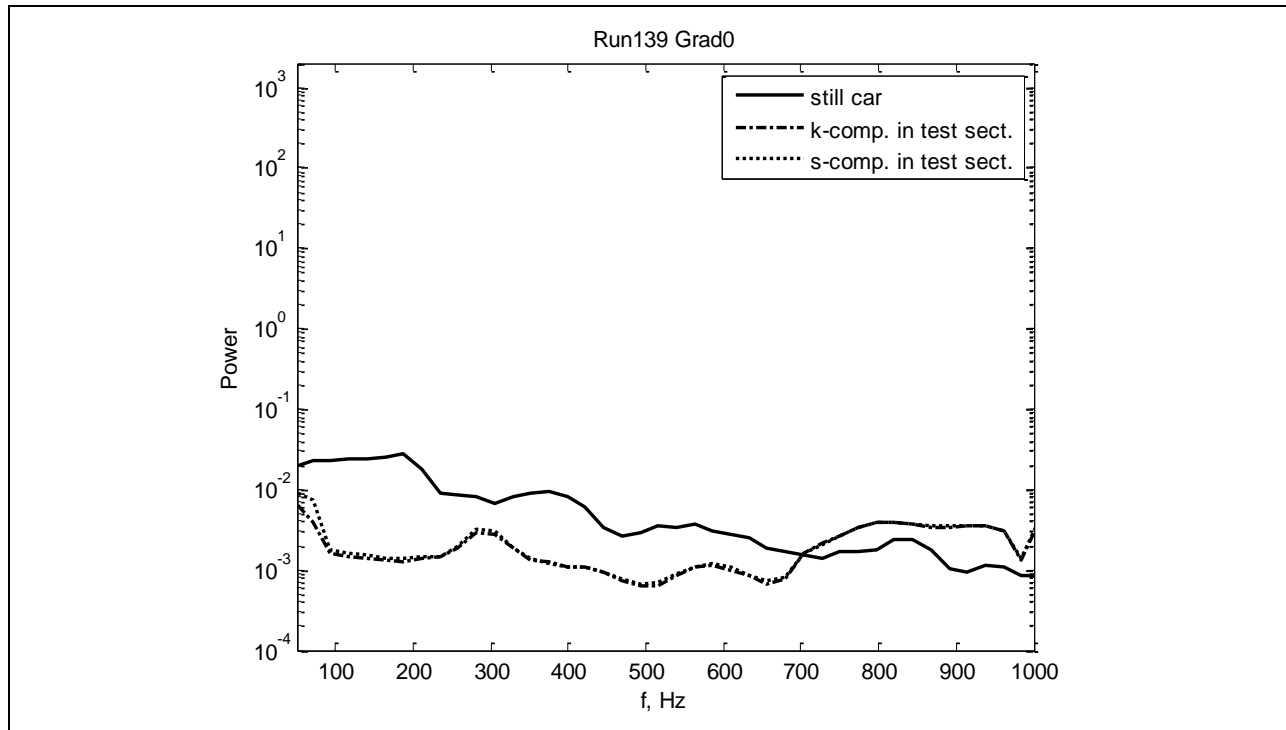


Figure 682: Power spectra in test section.

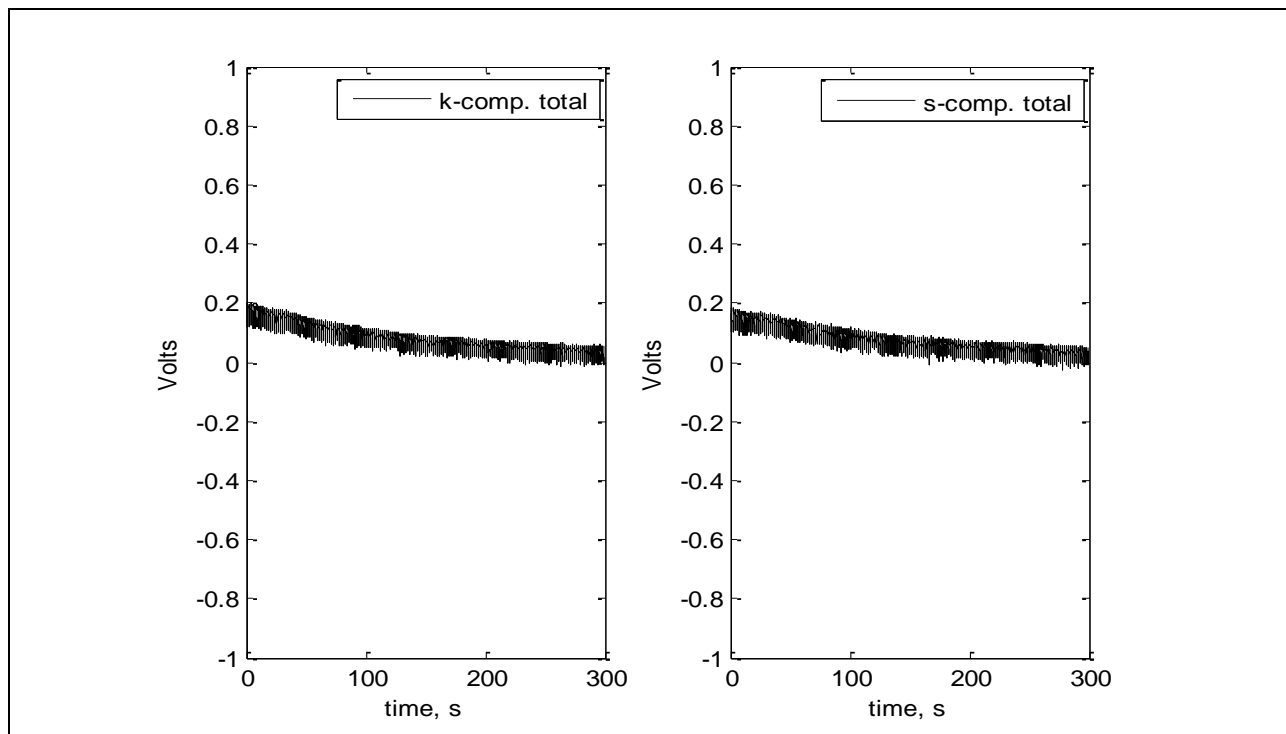


Figure 683: Voltage for full run.

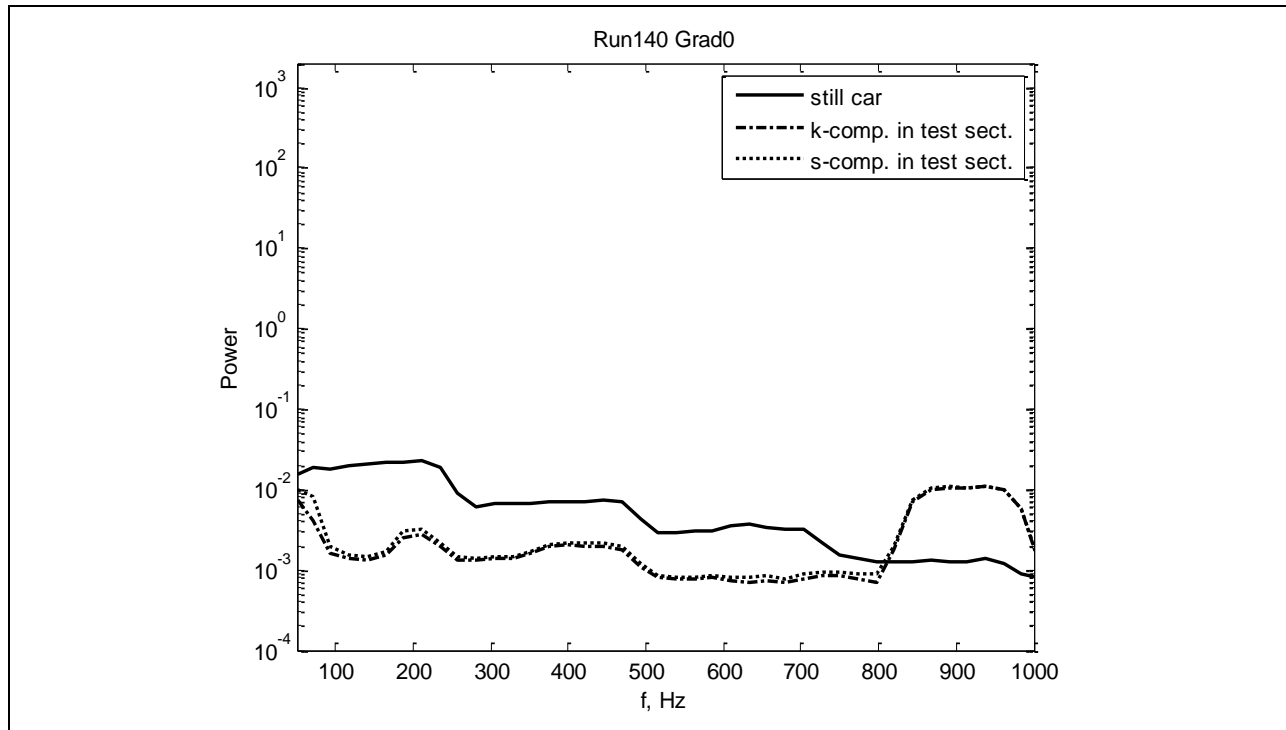


Figure 684: Power spectra in test section.

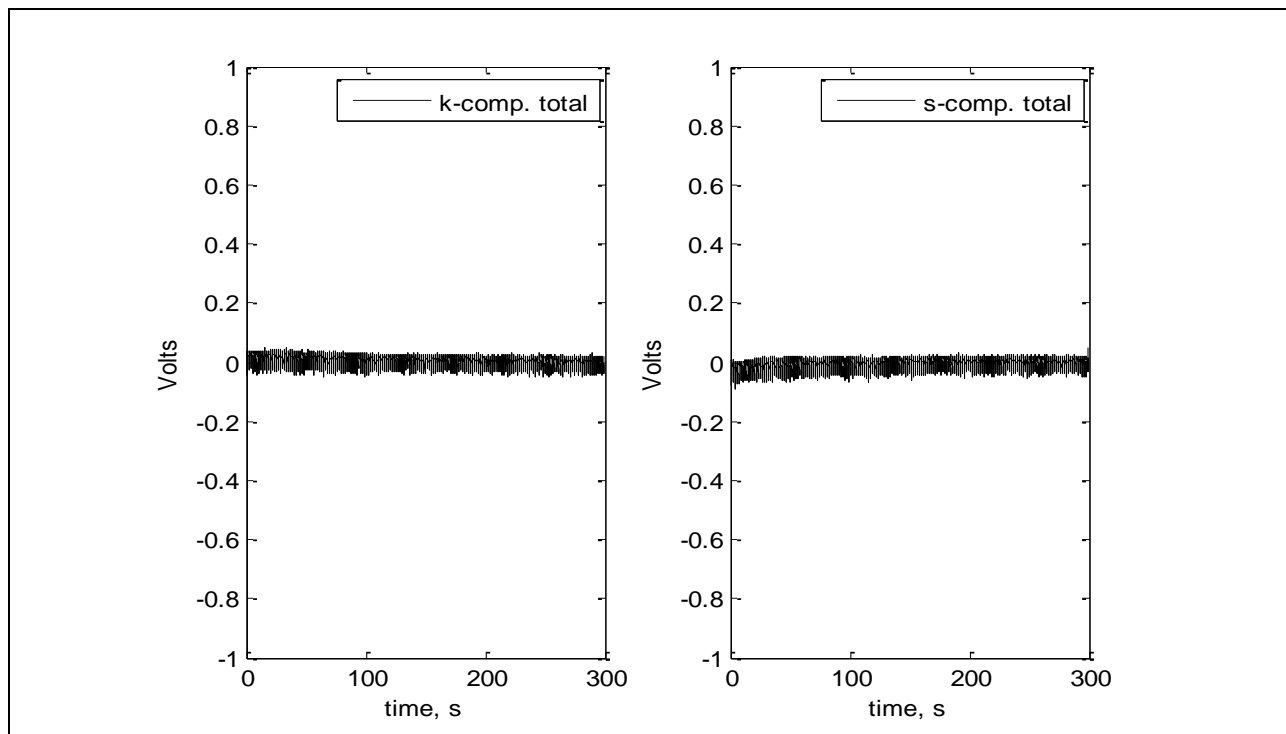


Figure 685: Voltage for full run.

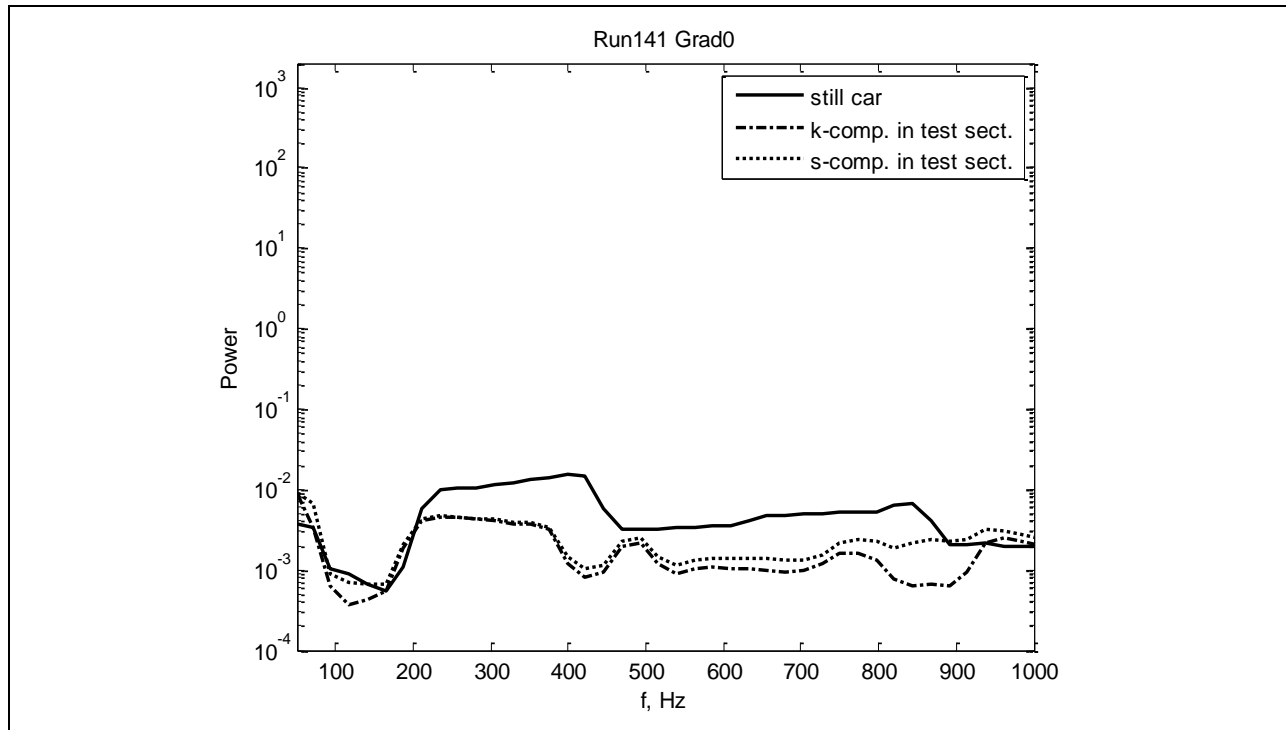


Figure 686: Power spectra in test section.

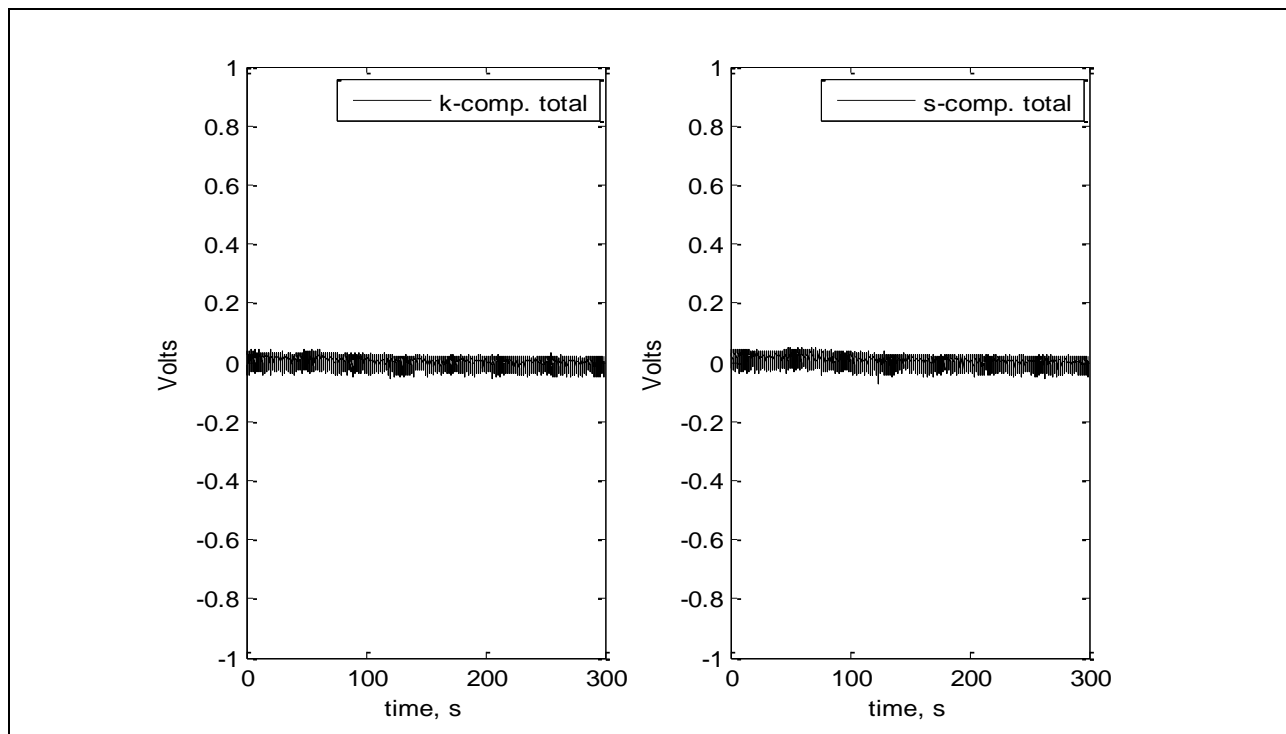


Figure 687: Voltage for full run.

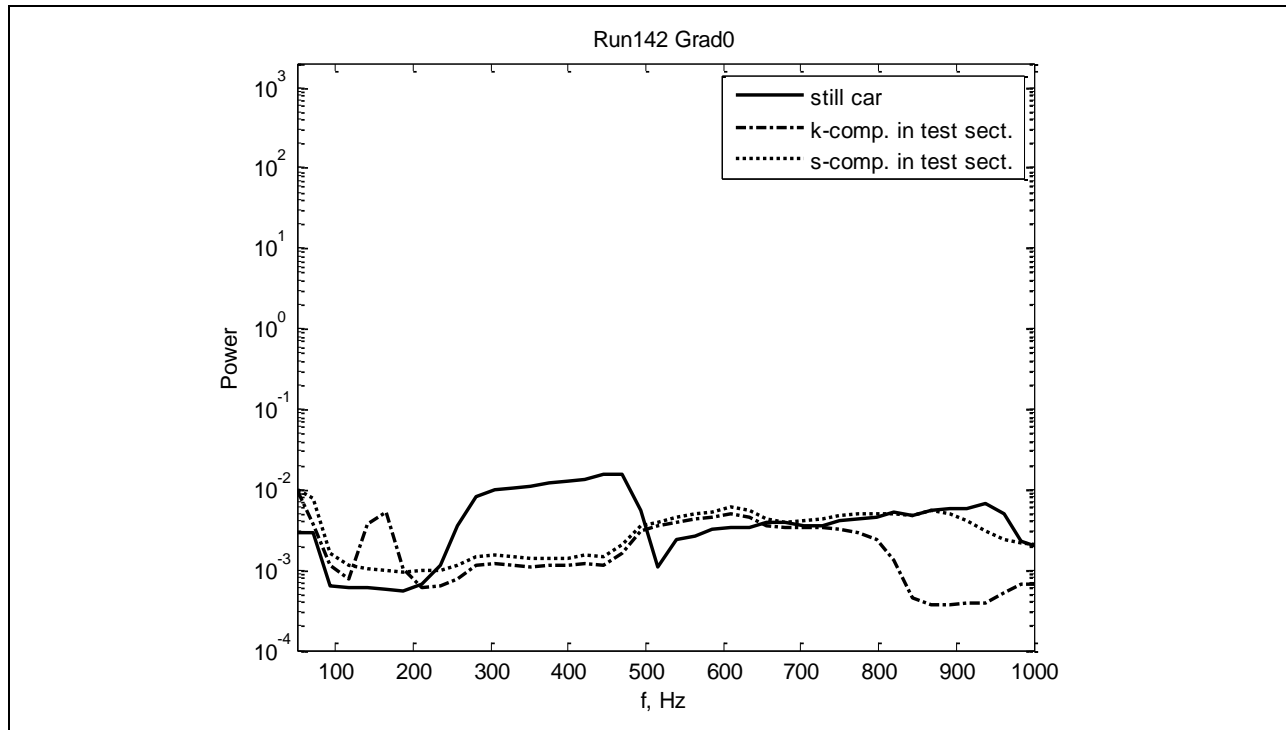


Figure 688: Power spectra in test section.

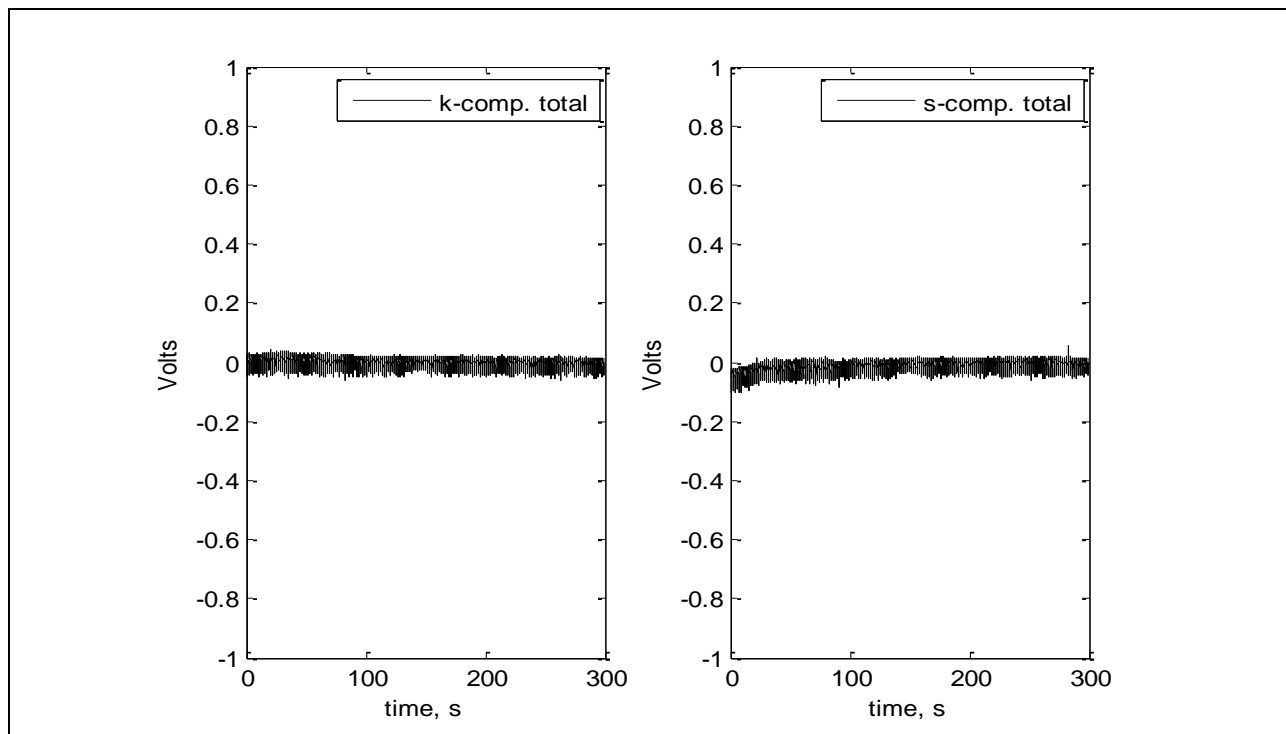


Figure 689: Voltage for full run.

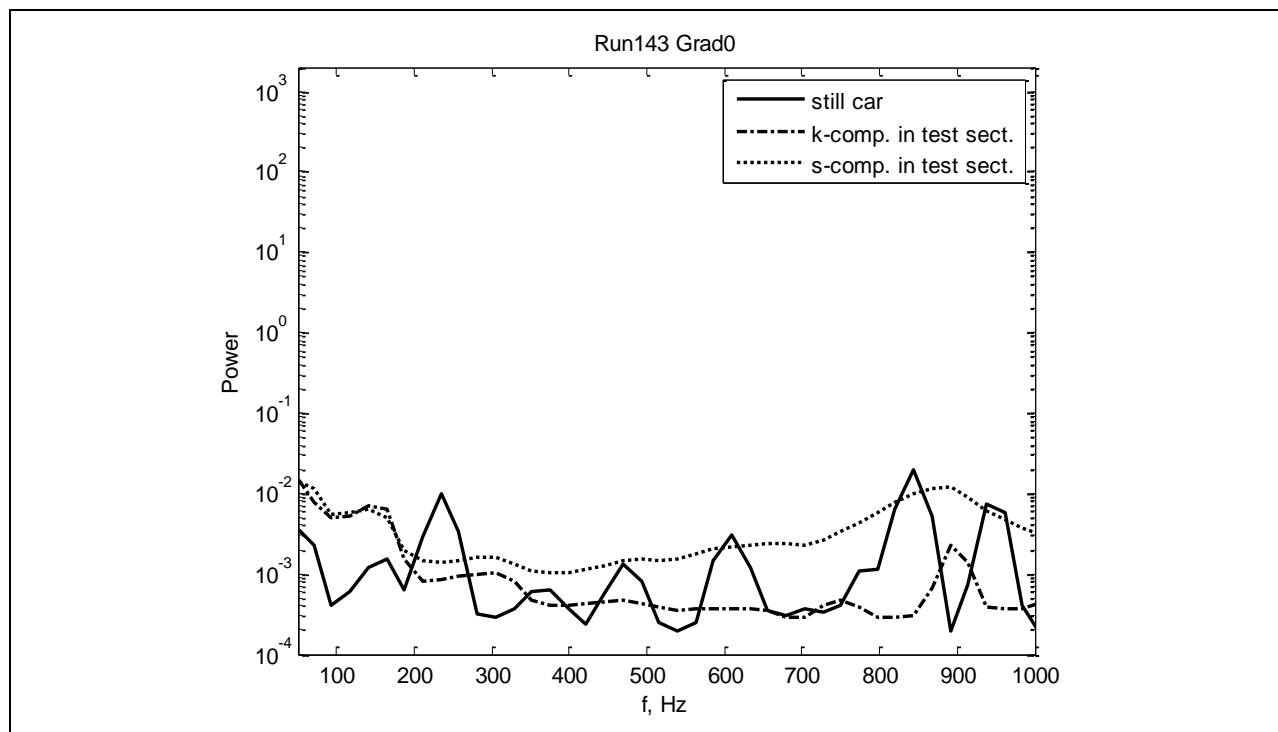


Figure 690: Power spectra in test section.

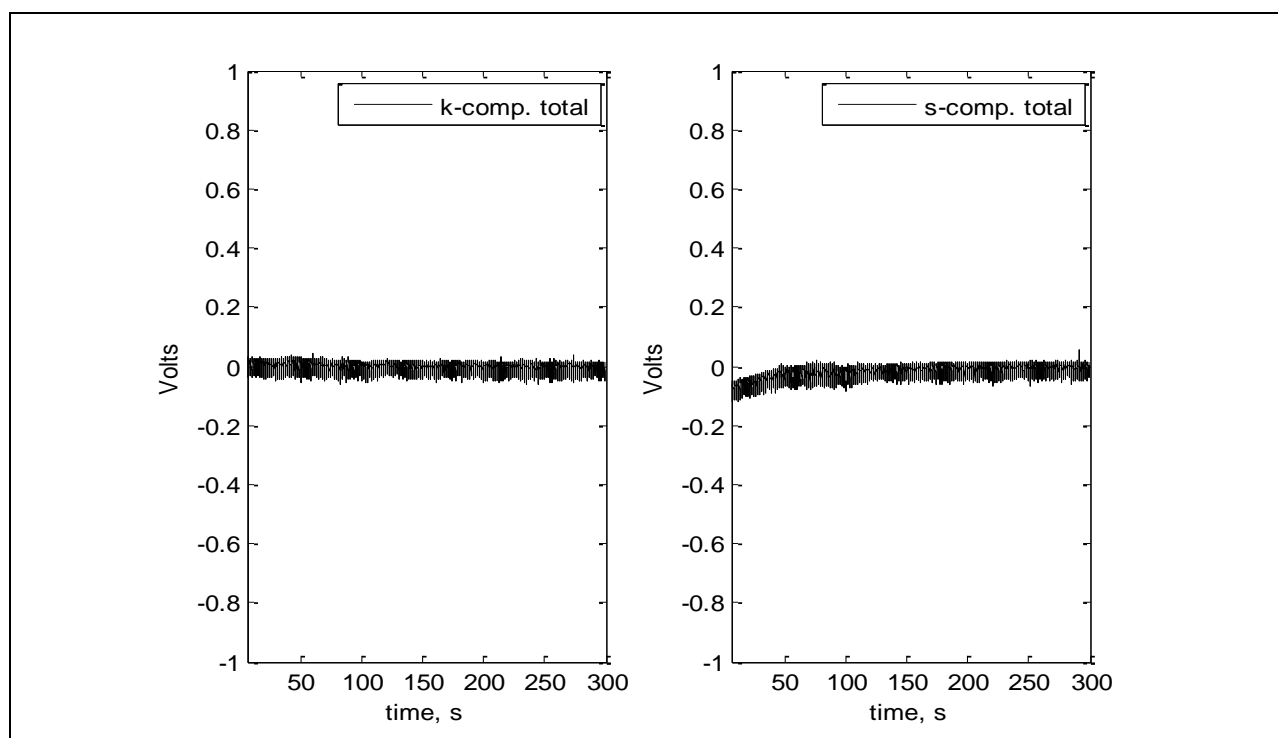


Figure 691: Voltage for full run.

The results of the vibration measurements for the Gradient-A model are shown in Figures 692-717. The measurements were performed simultaneously with hot-wire measurements. The results showed that the level of vibrations was low (low power in the spectra) and no single frequency was detected in the frequency range where T-S waves were expected (50-400Hz). Two components were measured simultaneously – the k-component (wall normal direction) and the y-component (spanwise direction). The plots below for a given run number show the power spectra calculated from voltage fluctuations in the test section and voltage fluctuations for the total run time in order to check how vibrations changed during the run. The power spectrum for the case when no vibrations were expected (still car) is also included for each run for reference. From the data it can be seen that the level of vibrations in the test section is comparable with that for the still car. The spectra do not show single frequencies in the range of interest (50-400Hz). The noisy spikes in the voltage signal as observed for example in Run 187 (Figures 692-693) for both components and in the Run 275 (Figures 694-695) for the k-component can be attributed to external noise, or problems inside of the accelerometers, because they appeared in the signal intermittently and independently of the car speed.

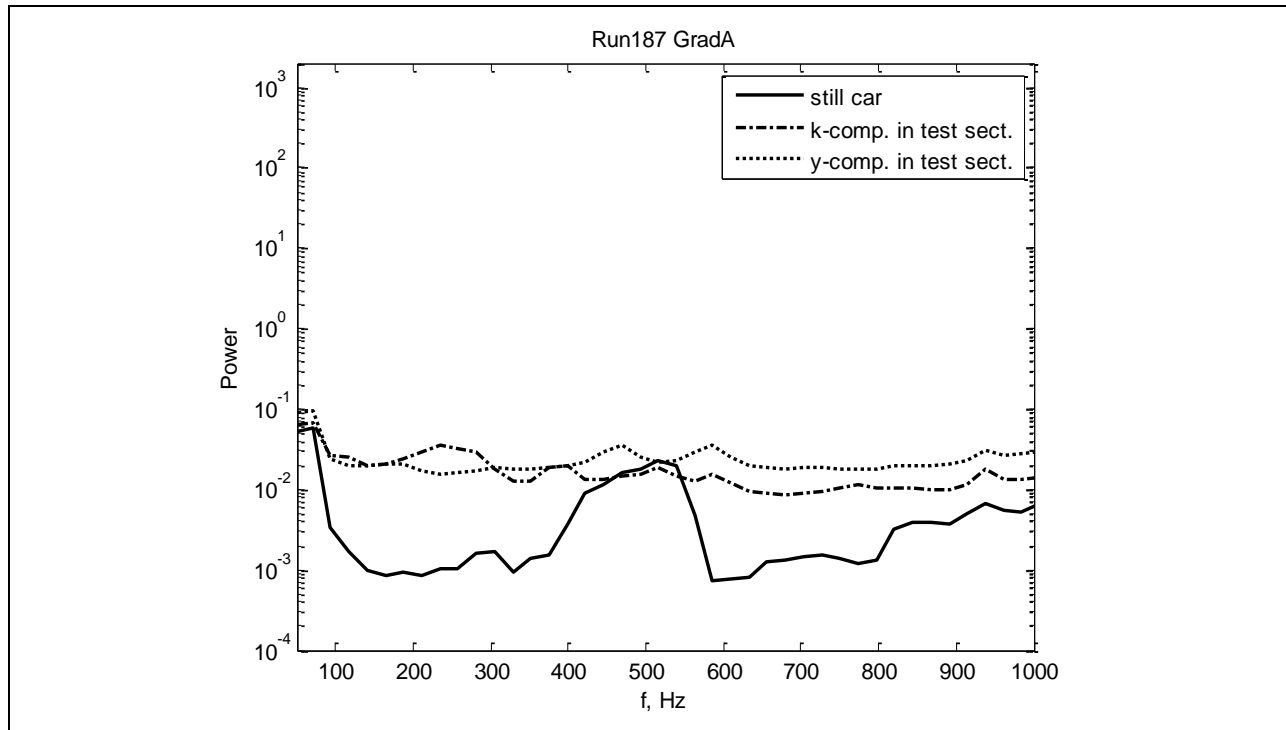


Figure 692: Power spectra in test section.

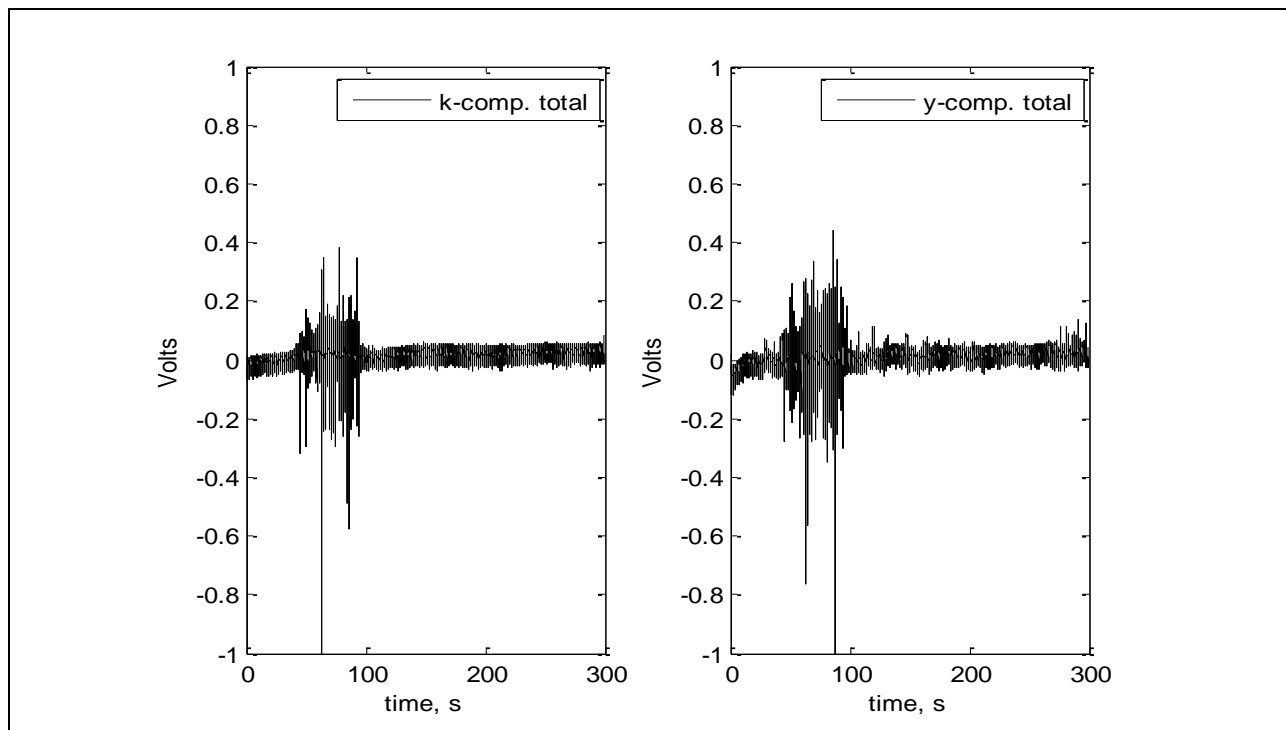


Figure 693: Voltage for full run.

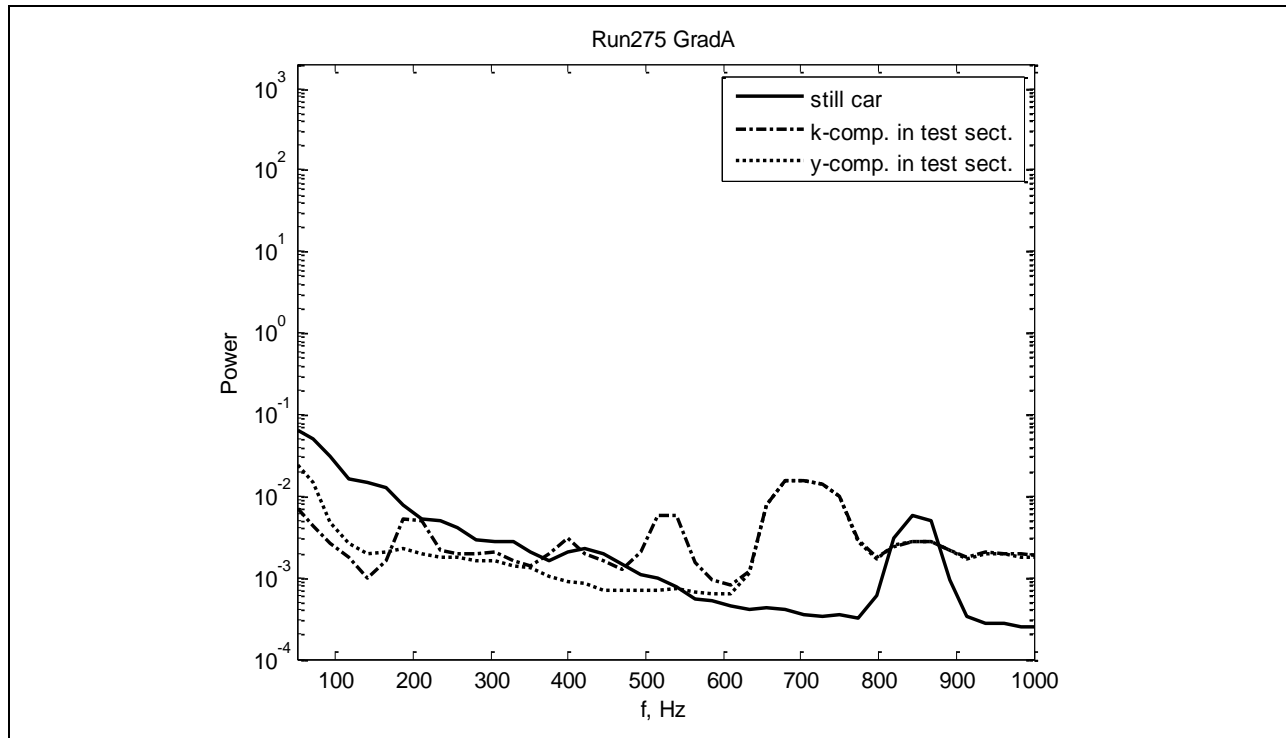


Figure 694: Power spectra in test section.

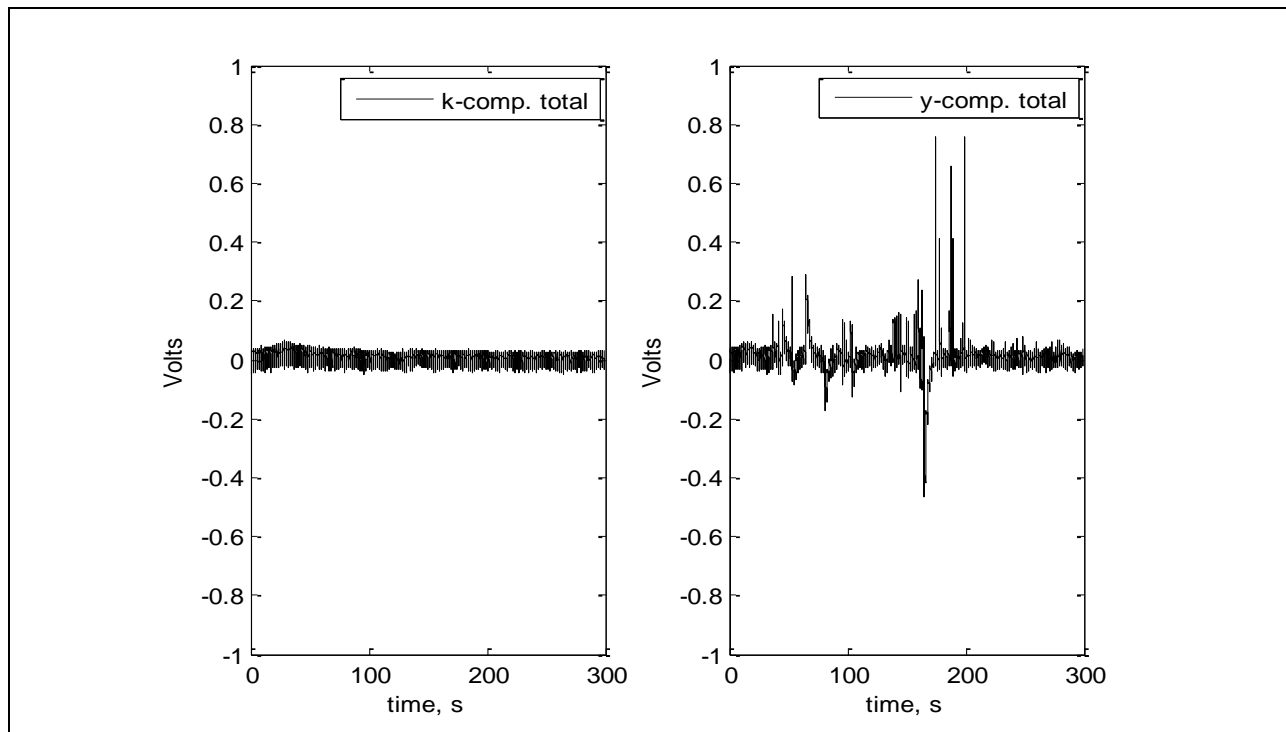


Figure 695: Voltage for full run.

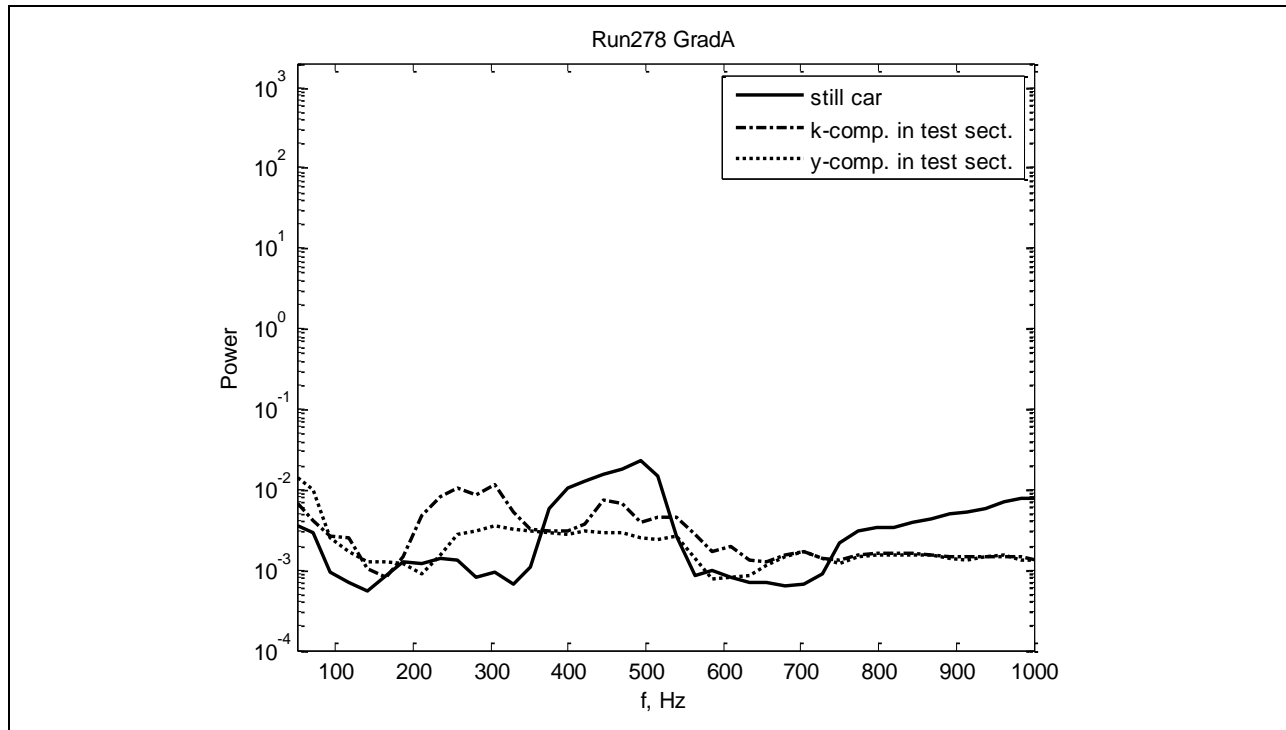


Figure 696: Power spectra in test section.

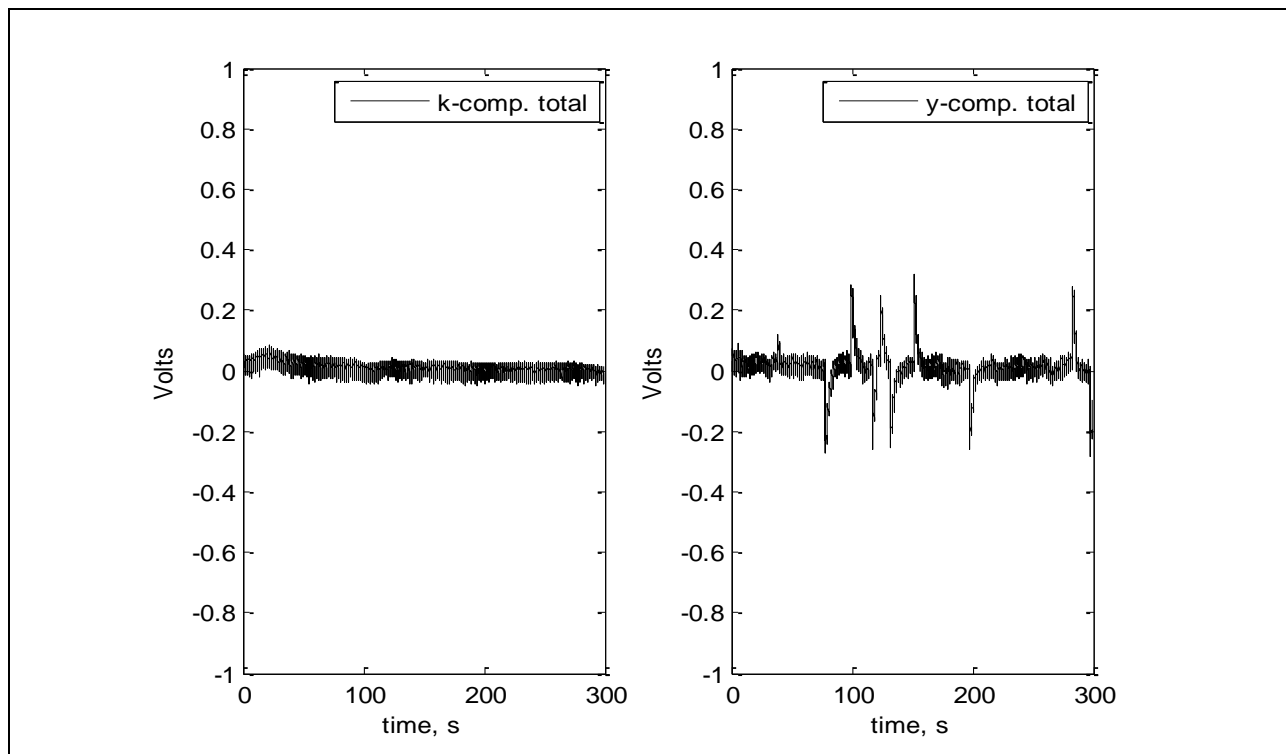


Figure 697: Voltage for full run.

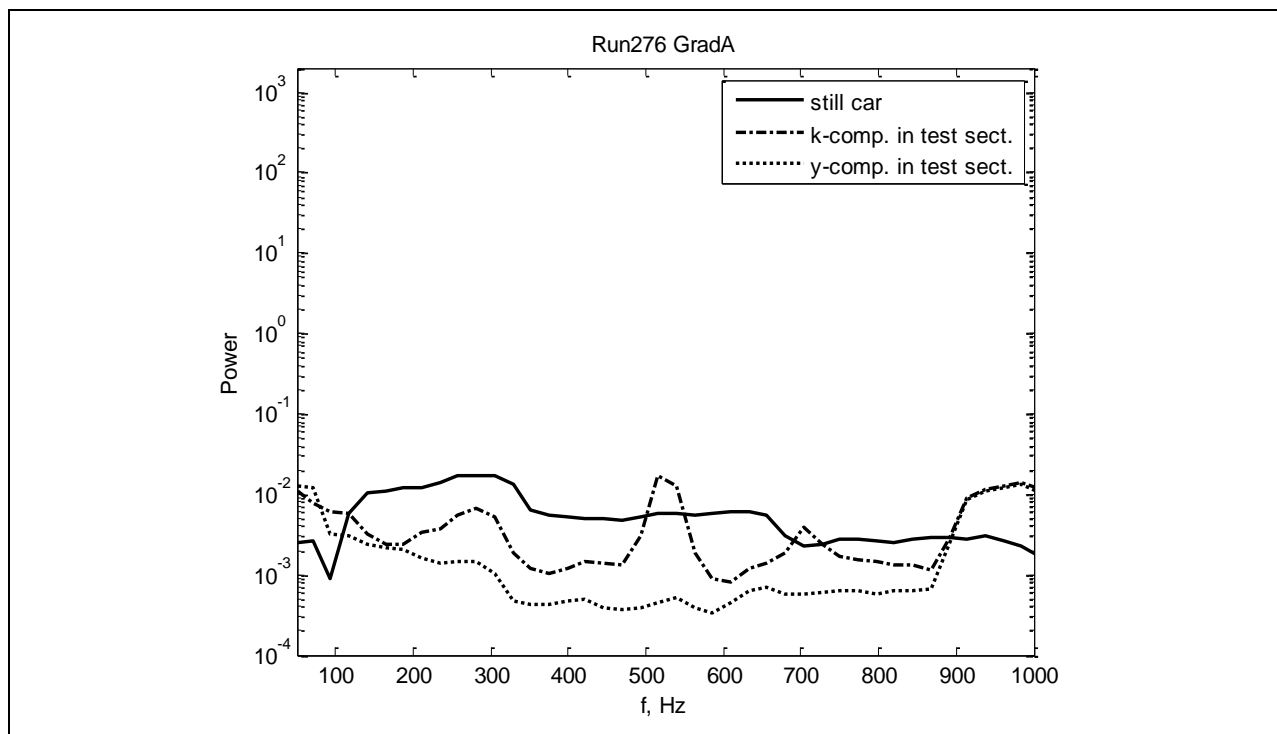


Figure 698: Power spectra in test section.

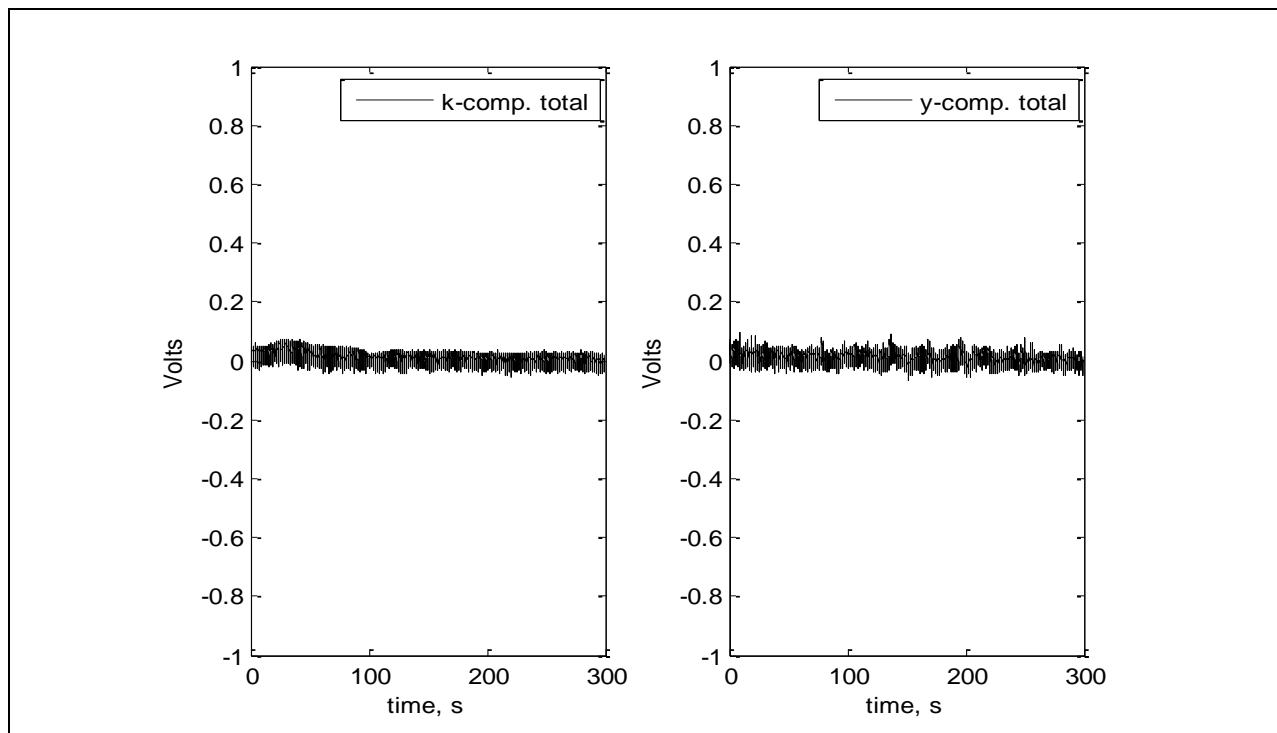


Figure 699: Voltage for full run.

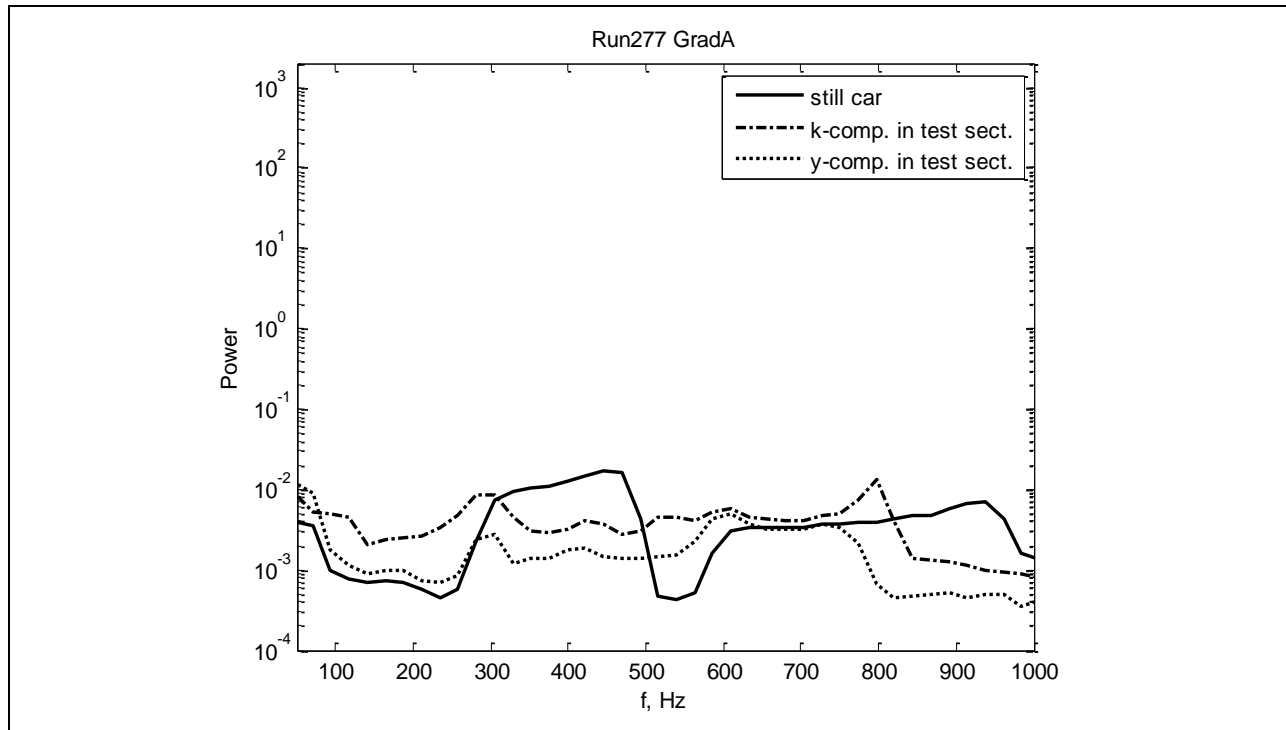


Figure 700: Power spectra in test section.

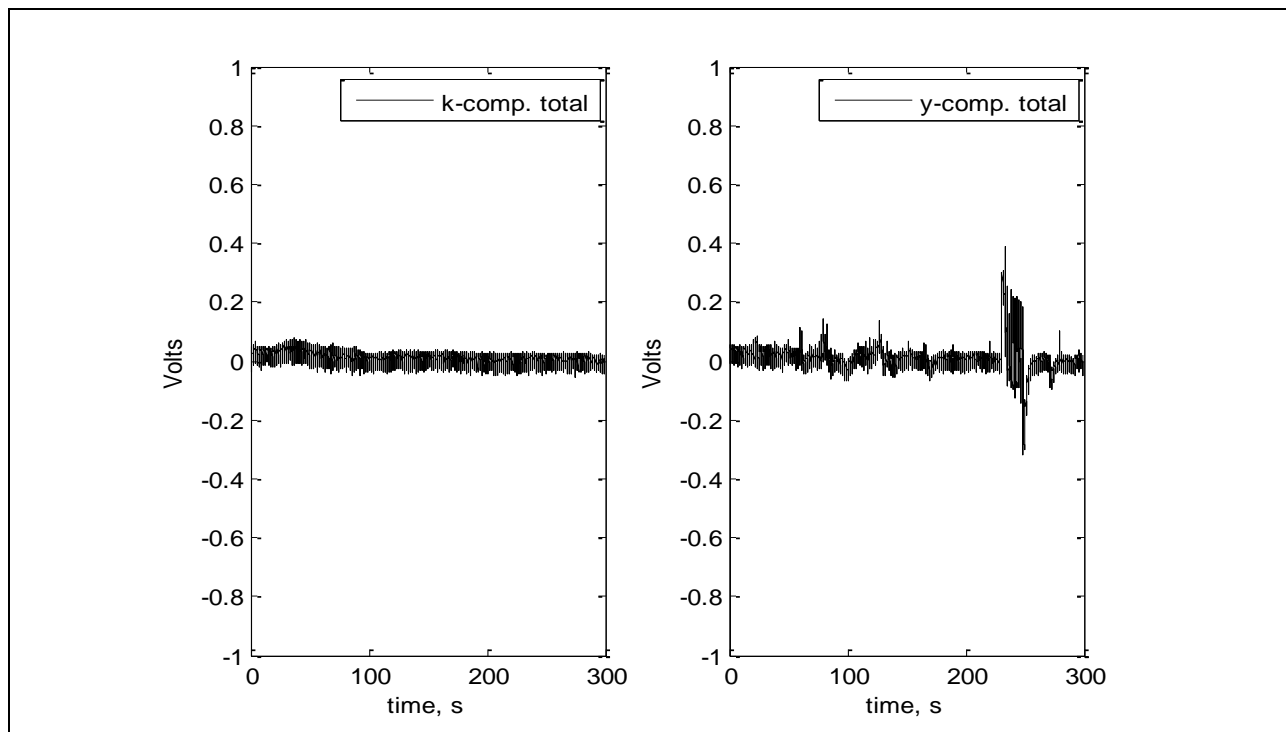


Figure 701: Voltage for full run.

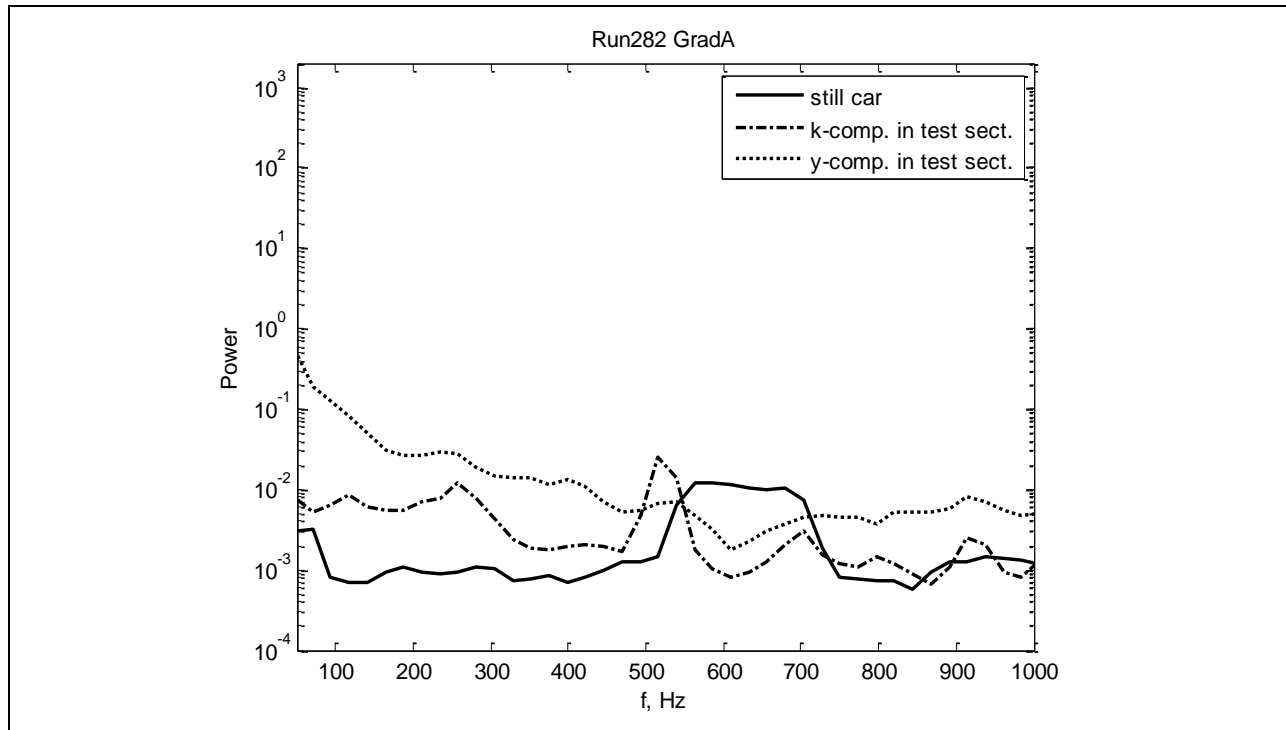


Figure 702: Power spectra in test section.

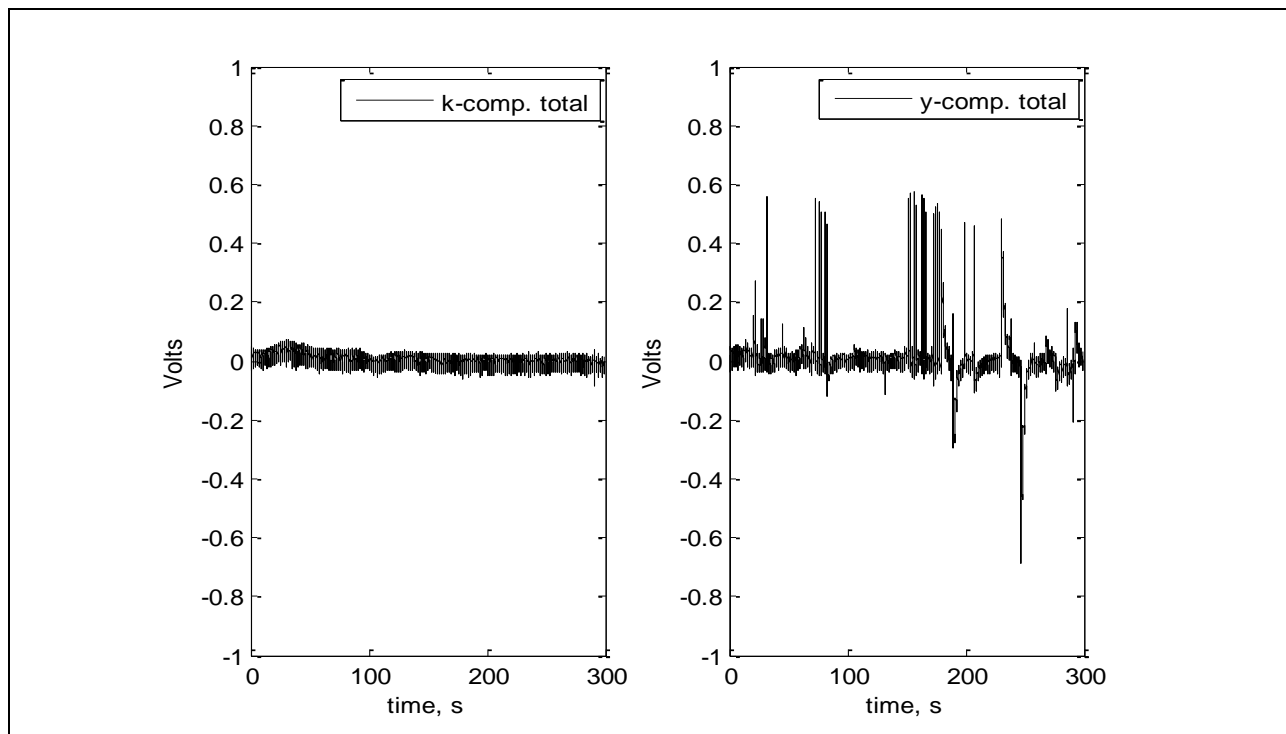


Figure 703: Voltage for full run.

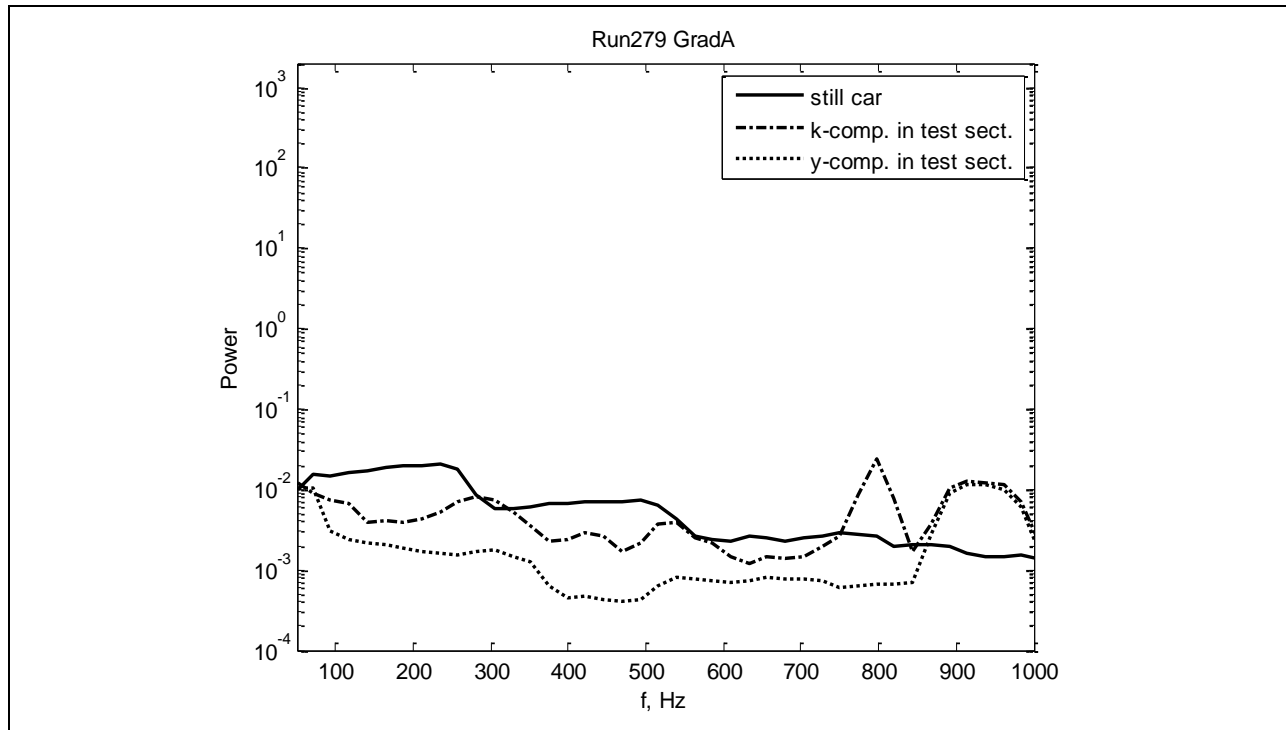


Figure 704: Power spectra in test section.

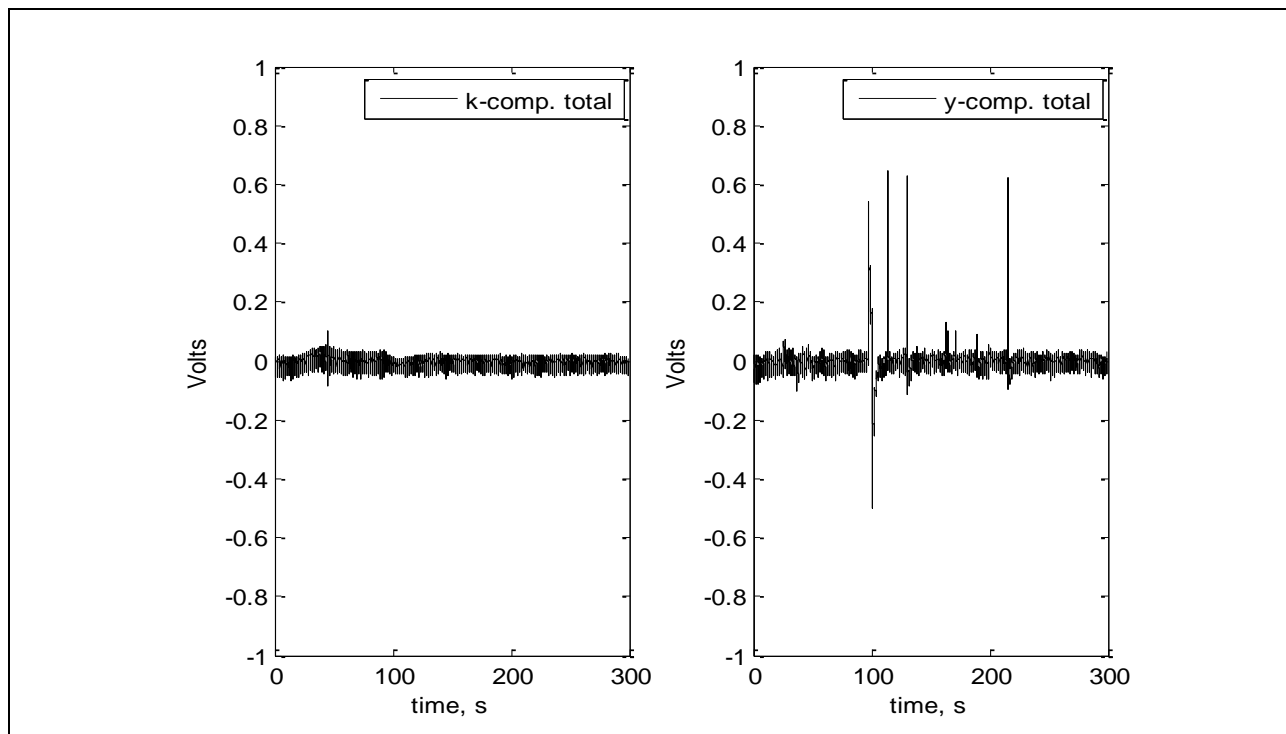


Figure 705: Voltage for full run.

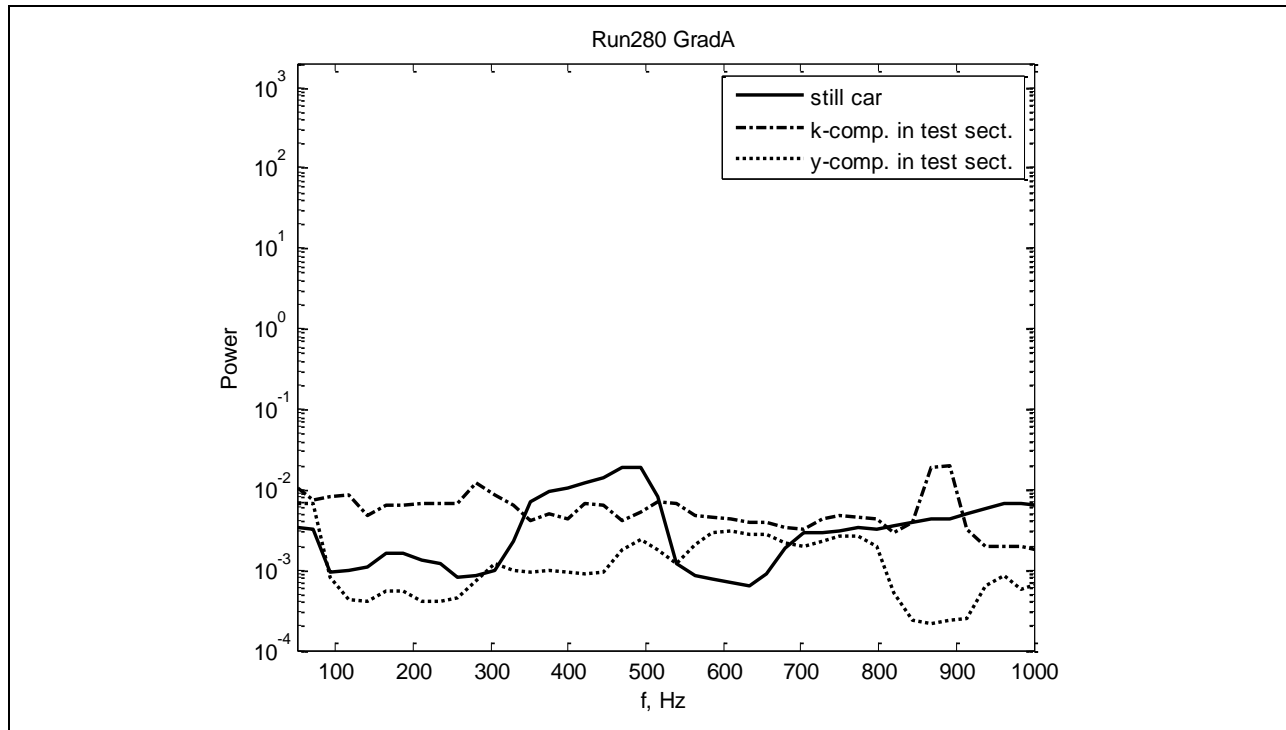


Figure 706: Power spectra in test section.

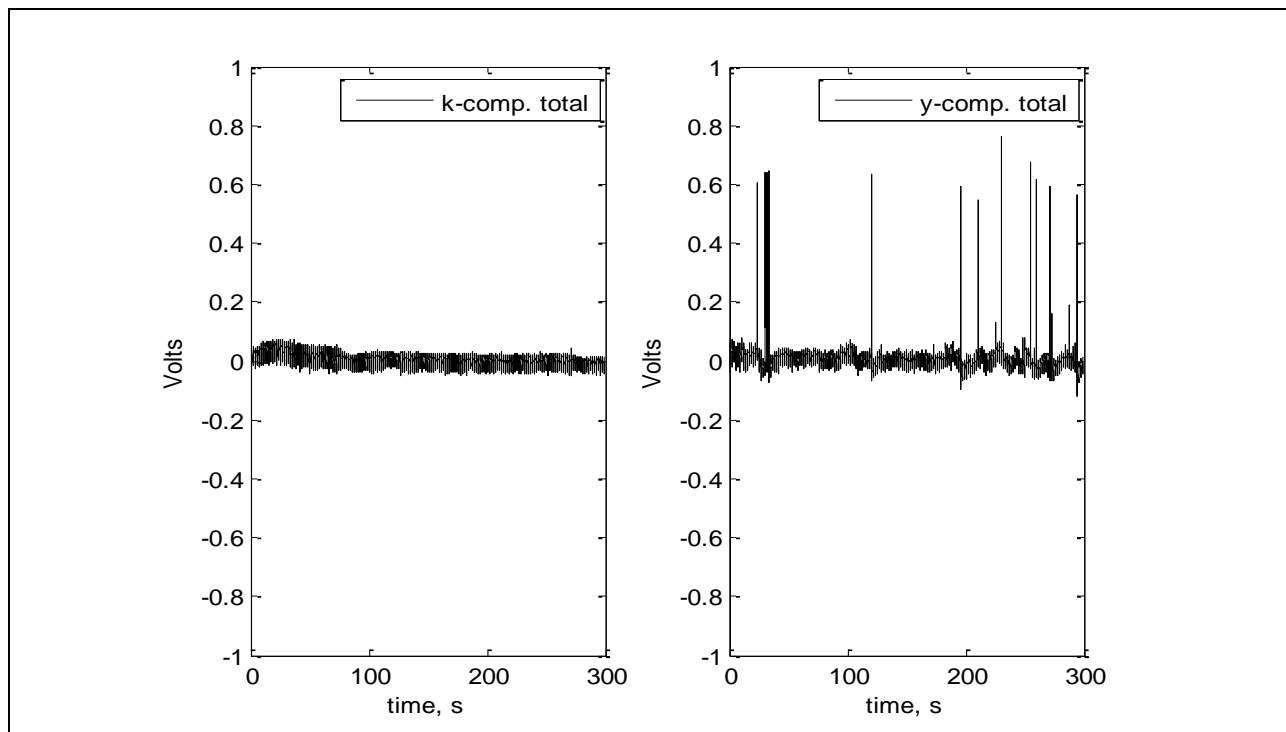


Figure 707: Voltage for full run.

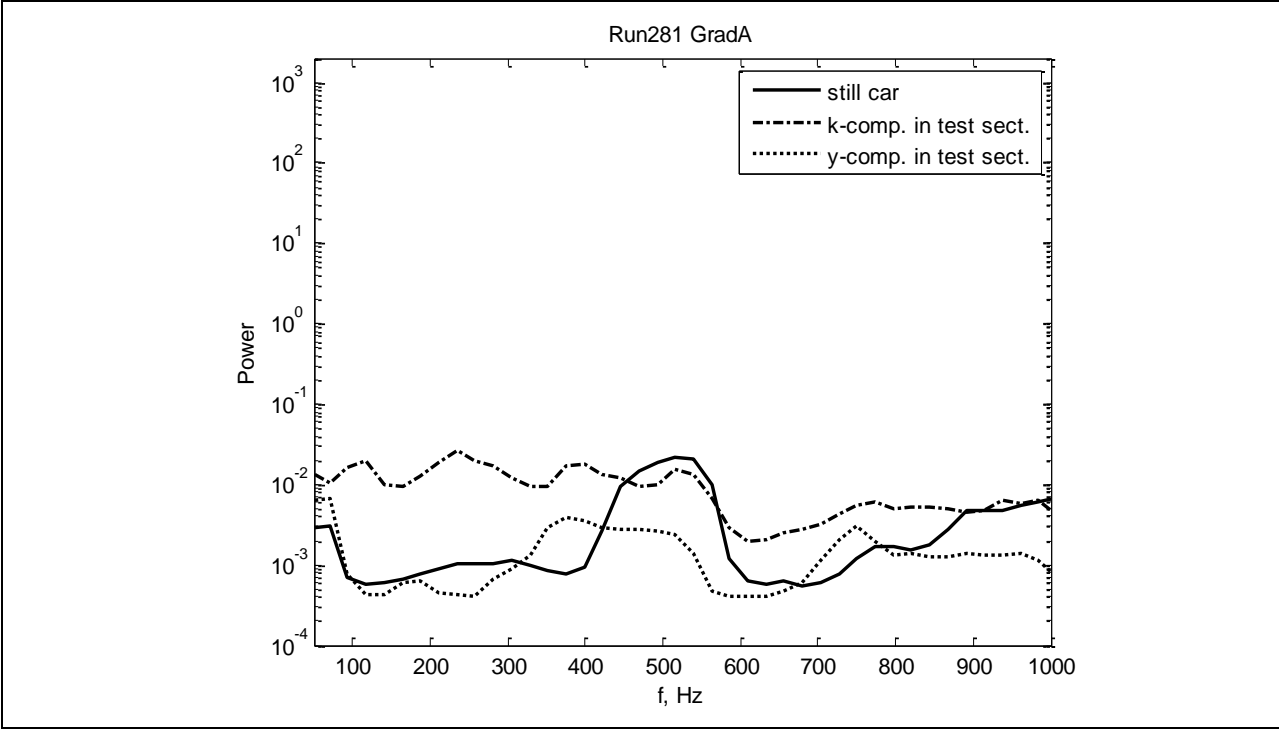


Figure 708: Power spectra in test section.

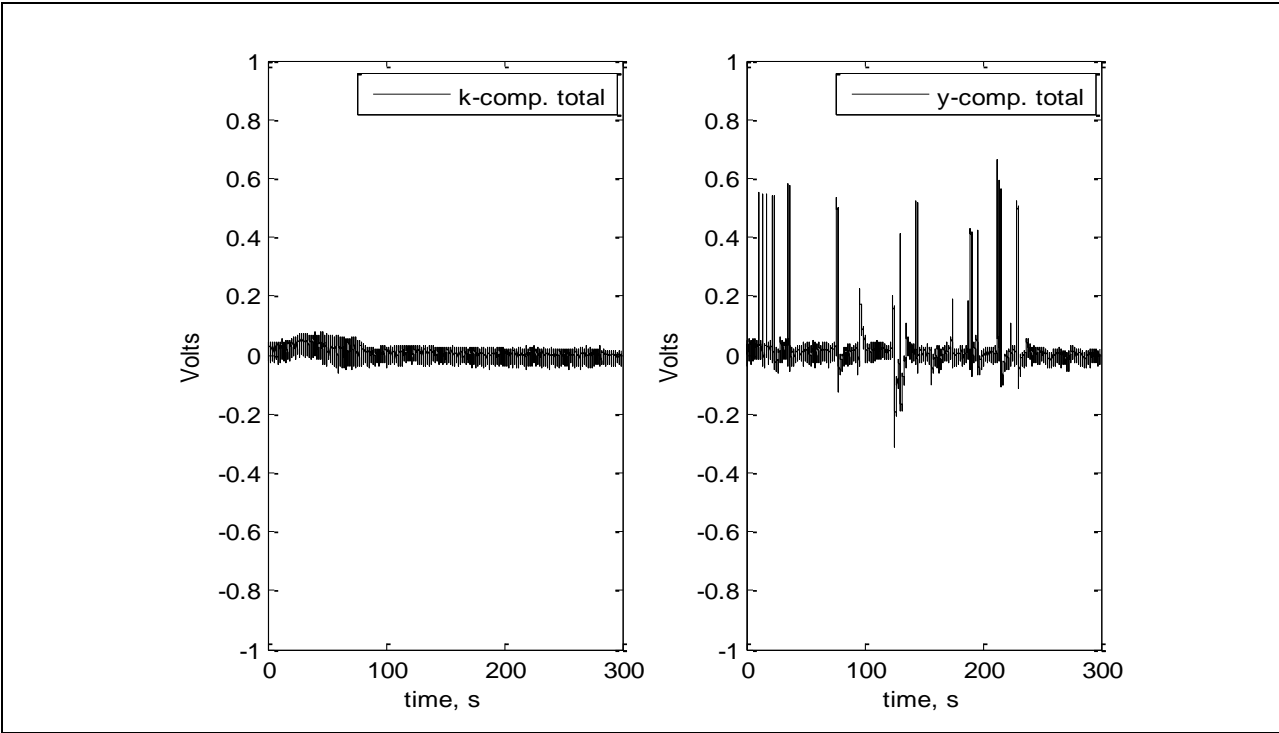


Figure 709: Voltage for full run.

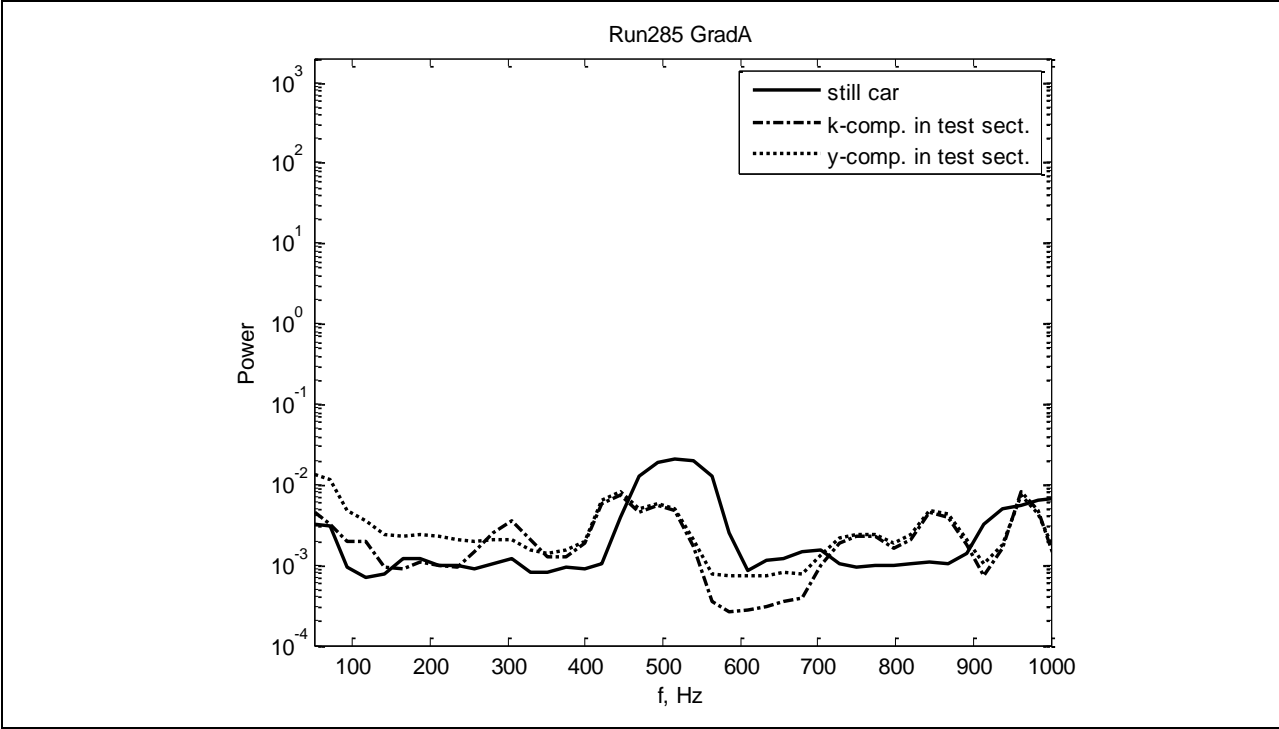


Figure 710: Power spectra in test section.

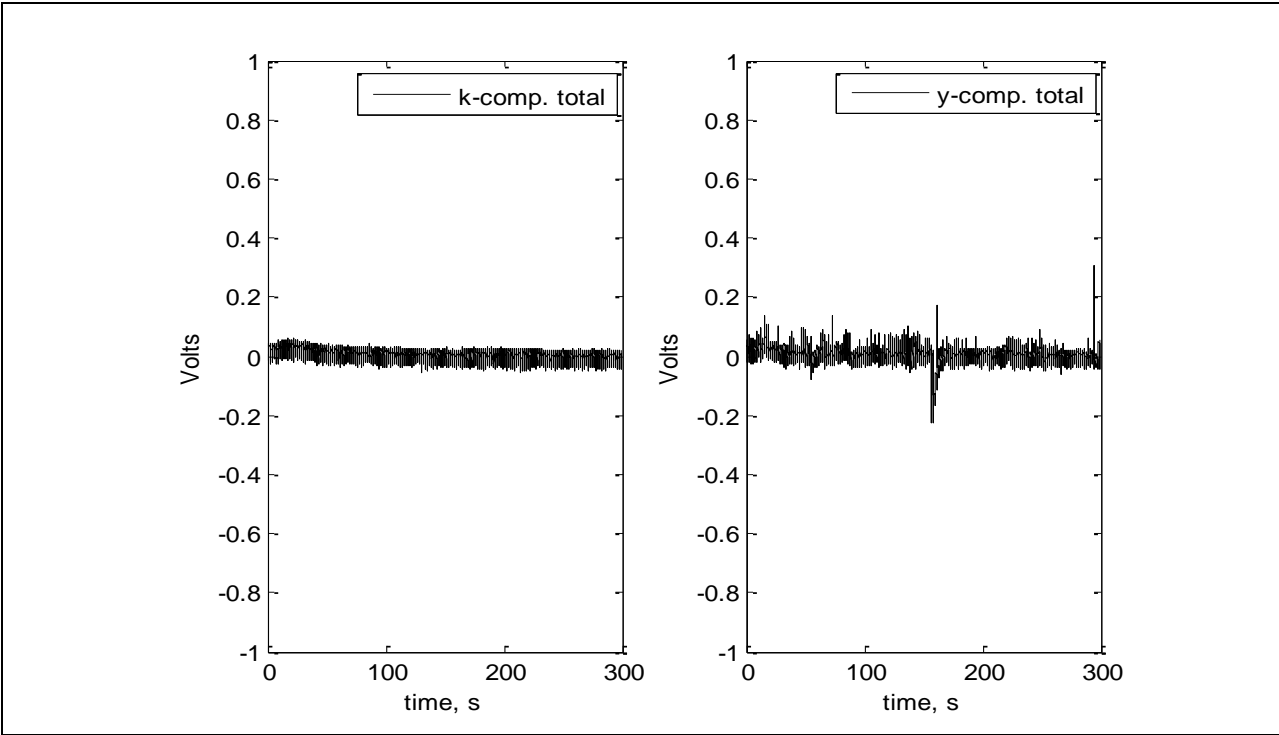


Figure 711: Voltage for full run.

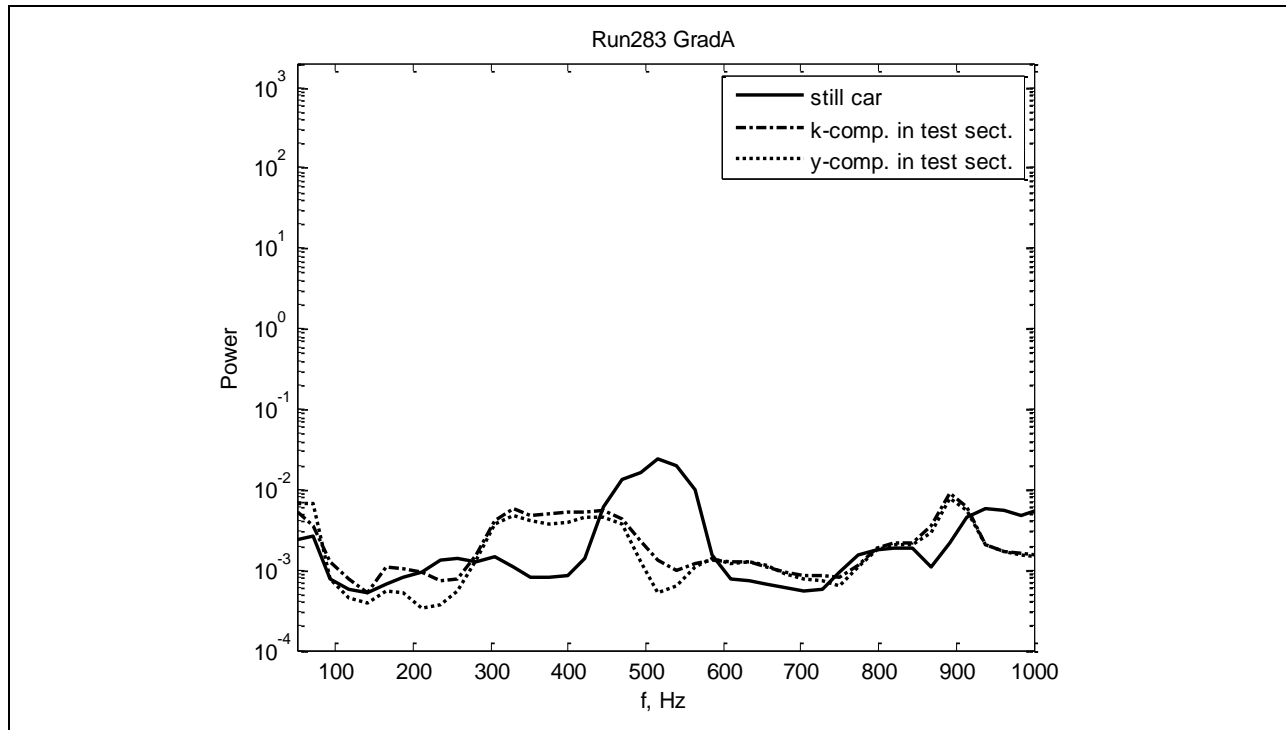


Figure 712: Power spectra in test section.

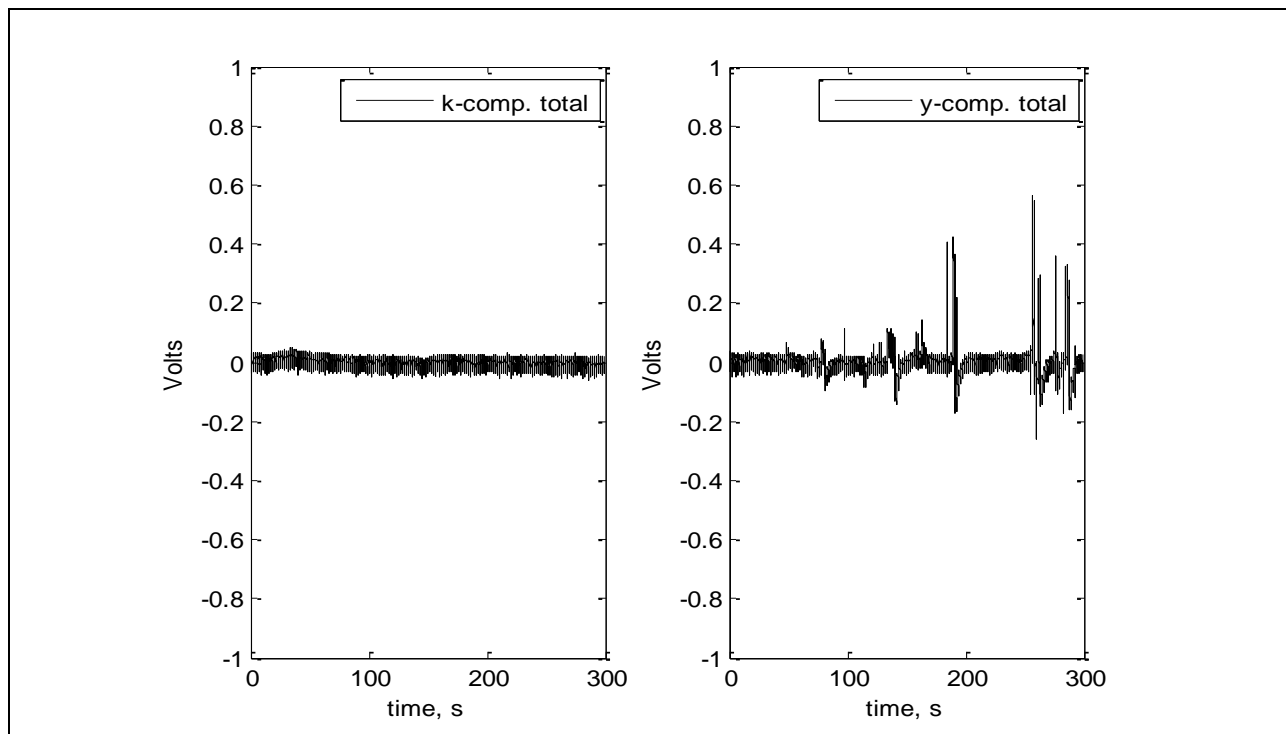


Figure 713: Voltage for full run.

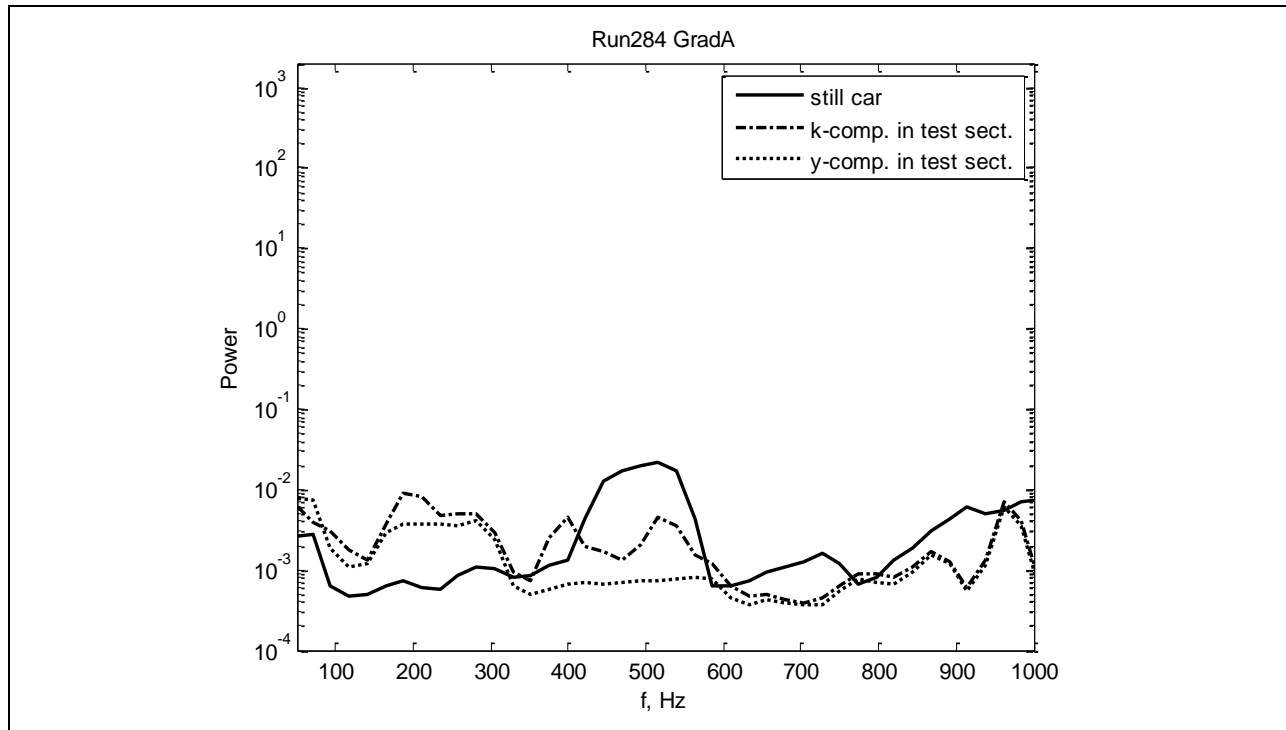


Figure 714: Power spectra in test section.

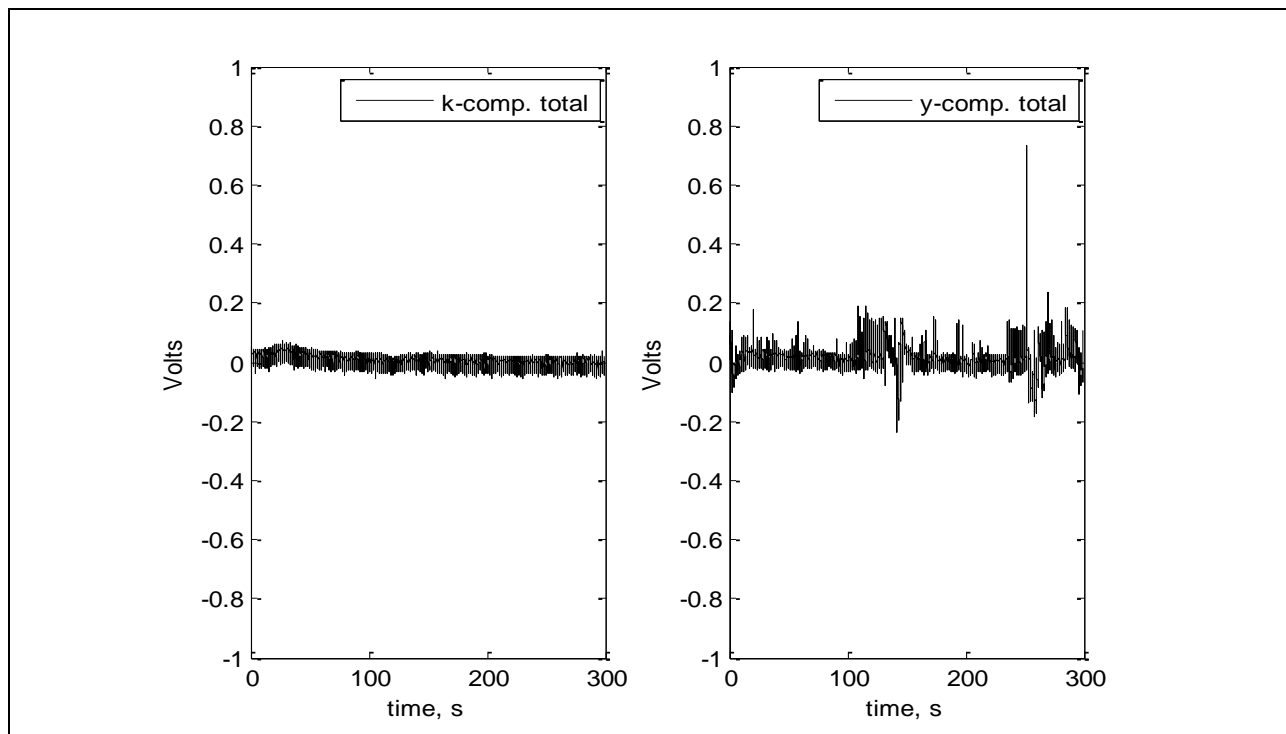


Figure 715: Voltage for full run.

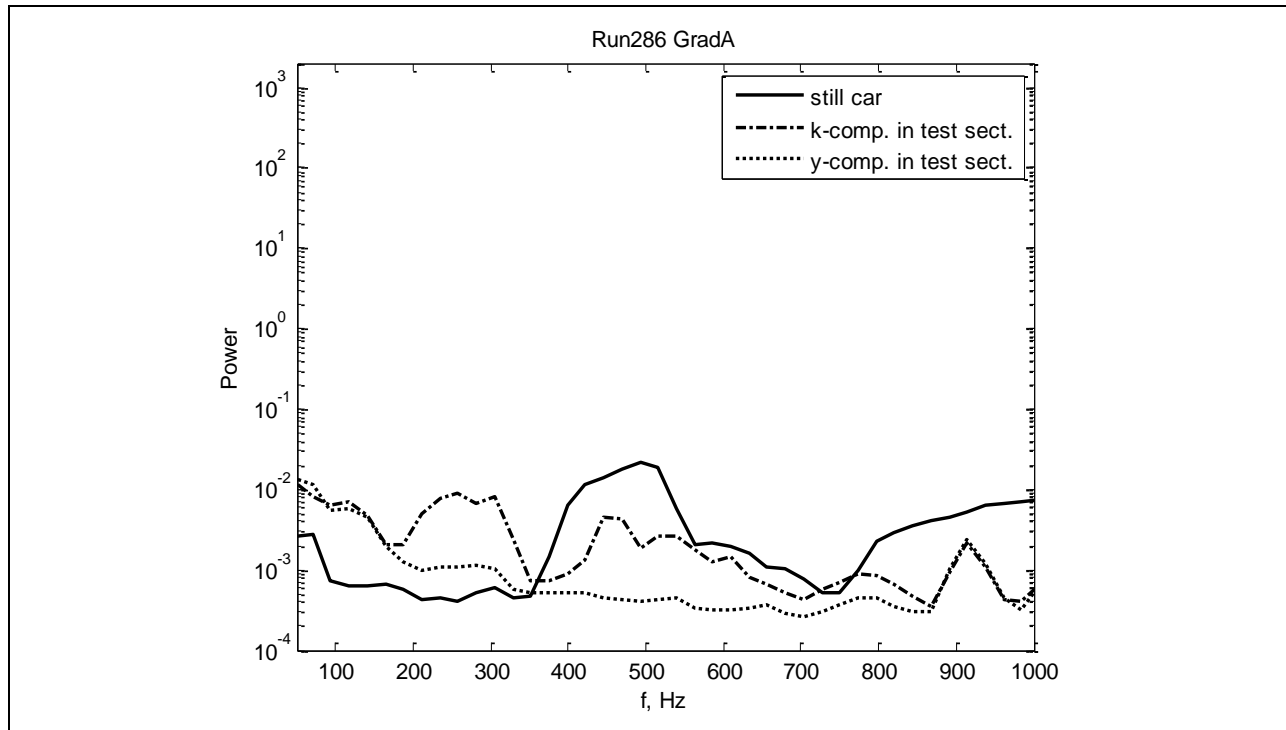


Figure 716: Power spectra in test section.

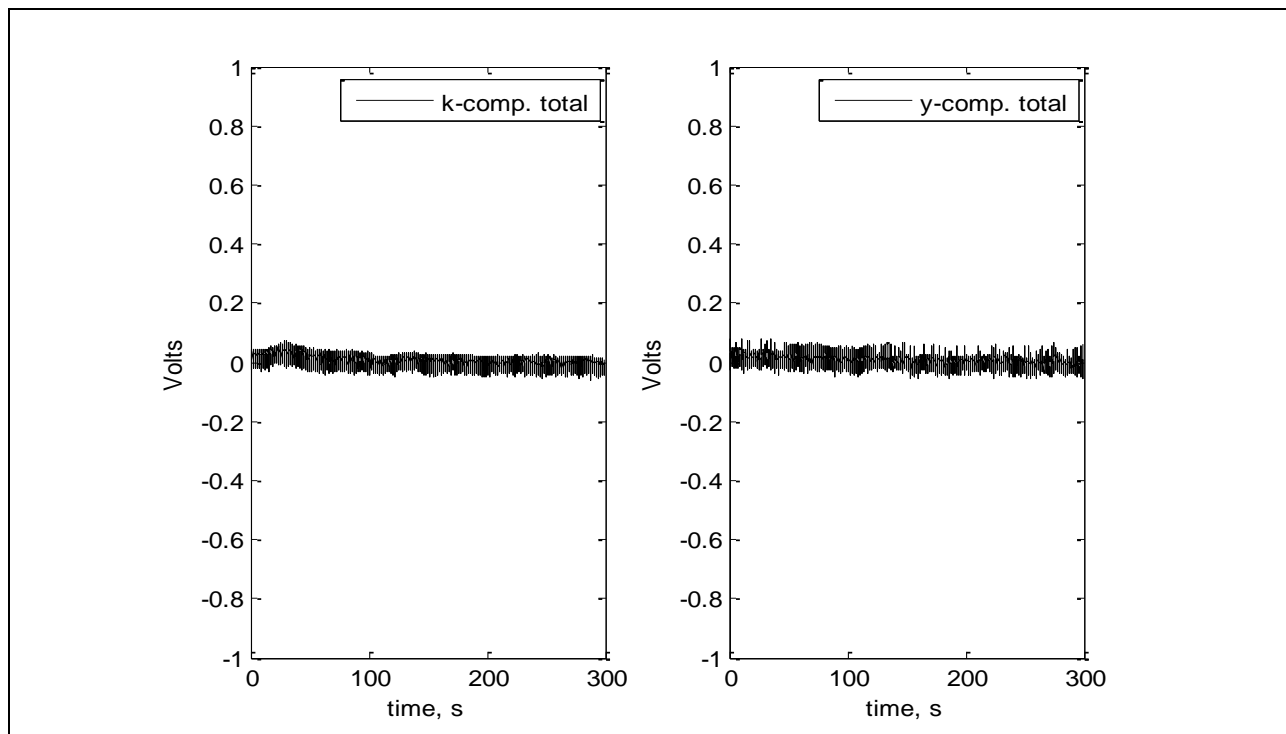


Figure 717: Voltage for full run.

The results of the vibration measurements for the Gradient-B model are presented in Figures 718-765. The measurements were performed simultaneously with hot-wire measurements. The results showed that the level of vibrations was low (low power in the spectra) and no single frequency was detected in the frequency range where T-S waves were expected (50-400Hz). Only the k-component (wall normal direction) was measured in these runs because the second accelerometer started to give noise. The plots below for a given run number show the power spectrum calculated from voltage fluctuations in the test section and voltage fluctuations for the total run time in order to check how vibrations changed during the run. The power spectrum for the case when no vibrations are expected (still car) is also included for each run for reference. From the data it can be seen that the level of vibrations in the test section is comparable with that for a still car. The spectra do not show single frequencies in the range of interest (50-400Hz). For some high speed runs at about 30m/s – for example, for Run 347 (Figures 724-725) and Run 385 (Figures 742-743) – higher power is observed in the spectrum in test section as compared to that for a still car (about an order of magnitude).

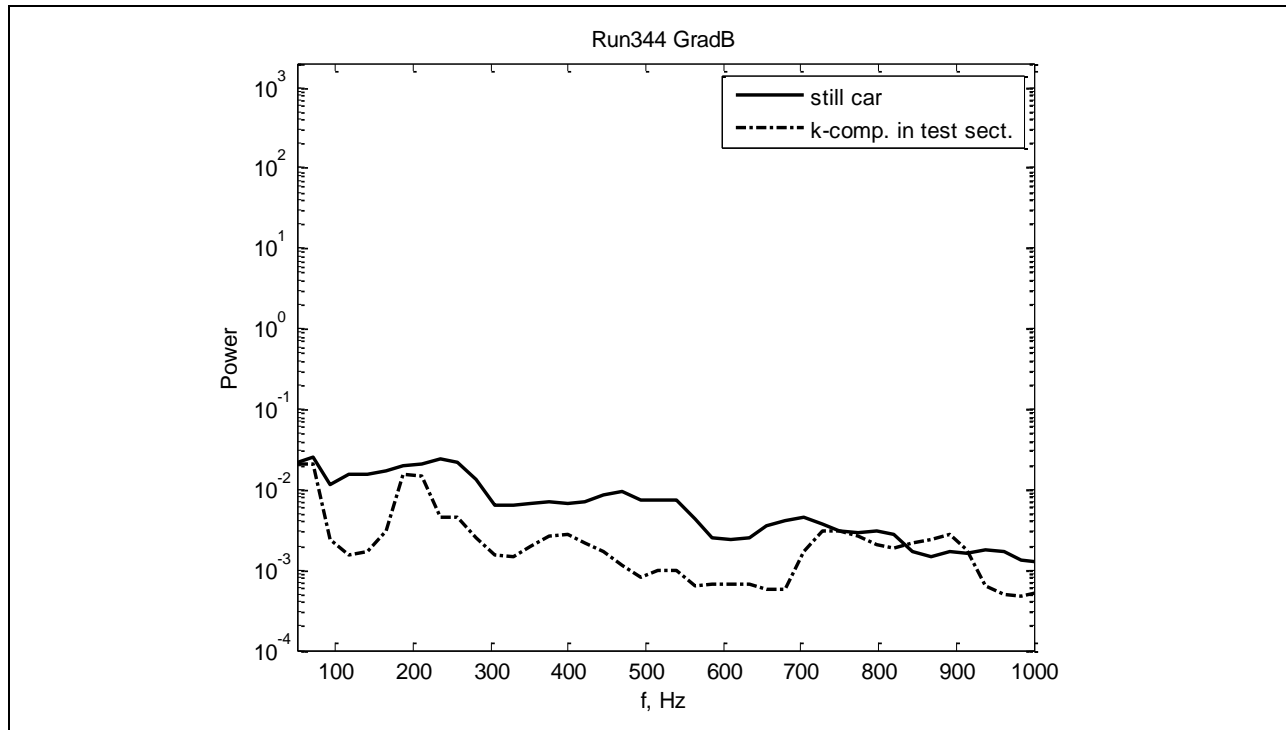


Figure 718: Power spectra in test section.

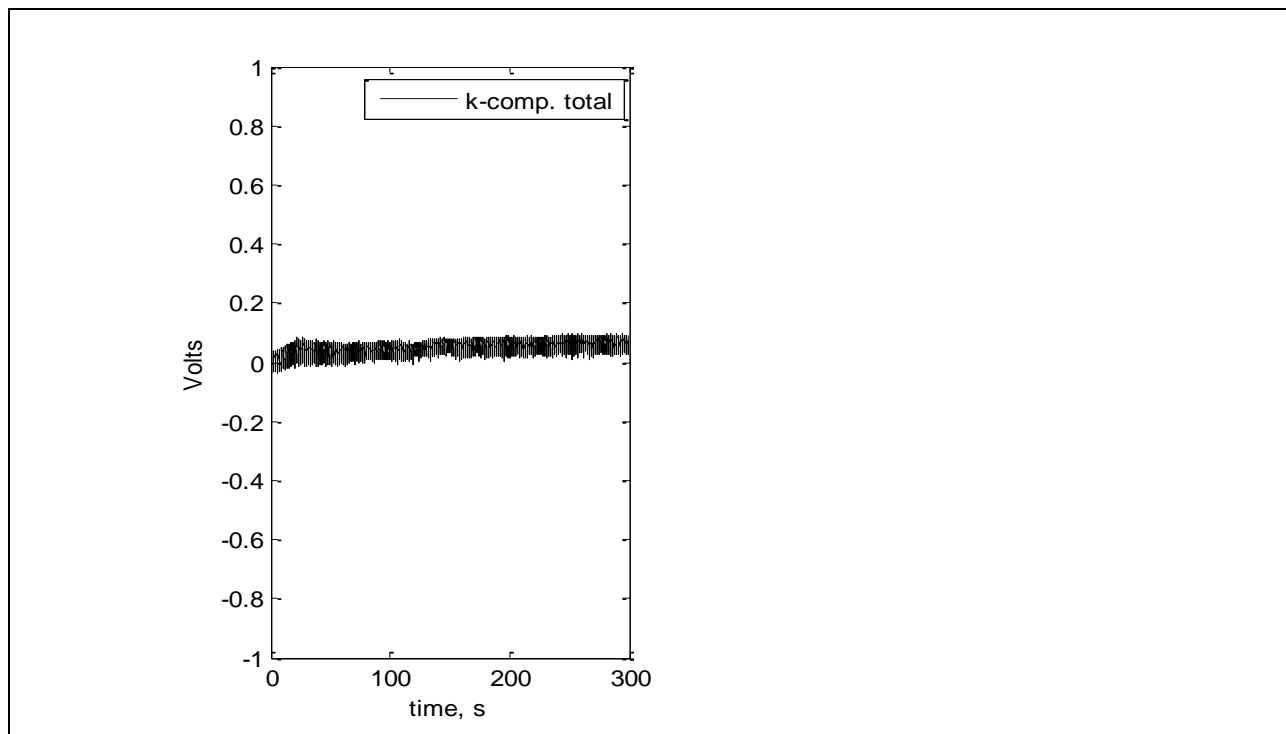


Figure 719: Voltage for full run.

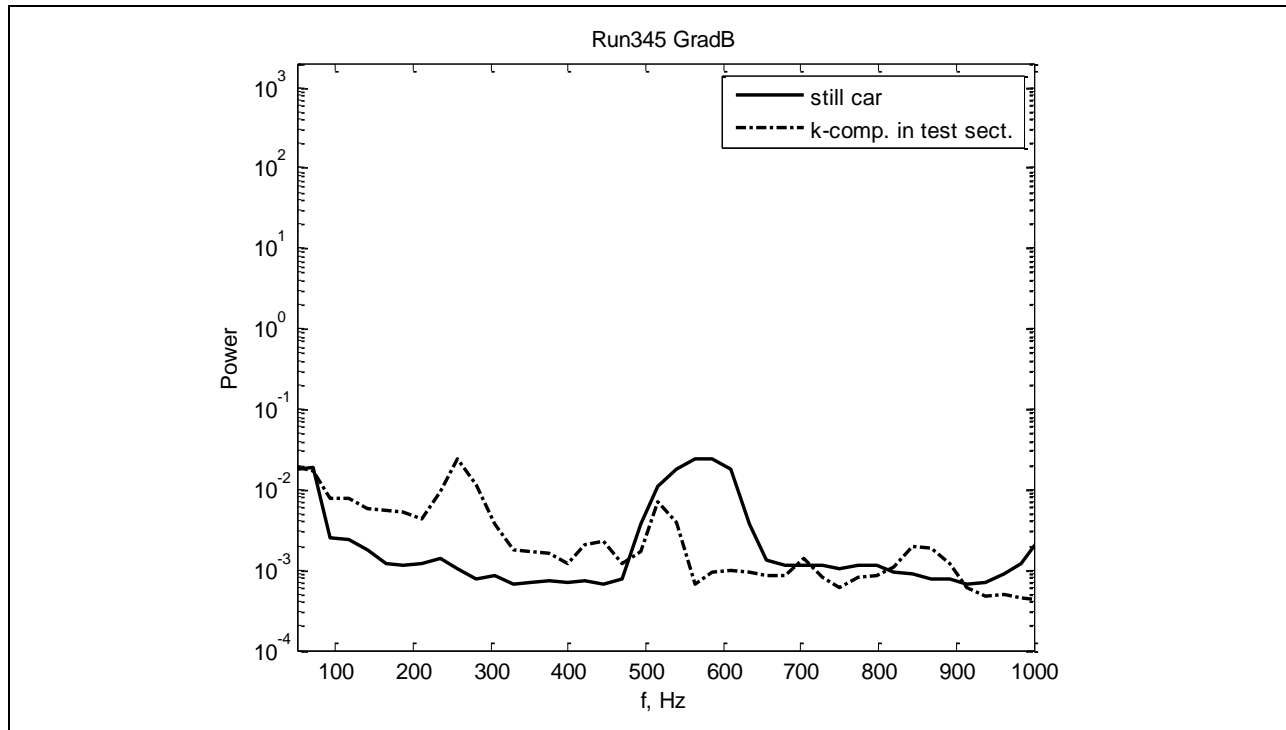


Figure 720: Power spectra in test section.

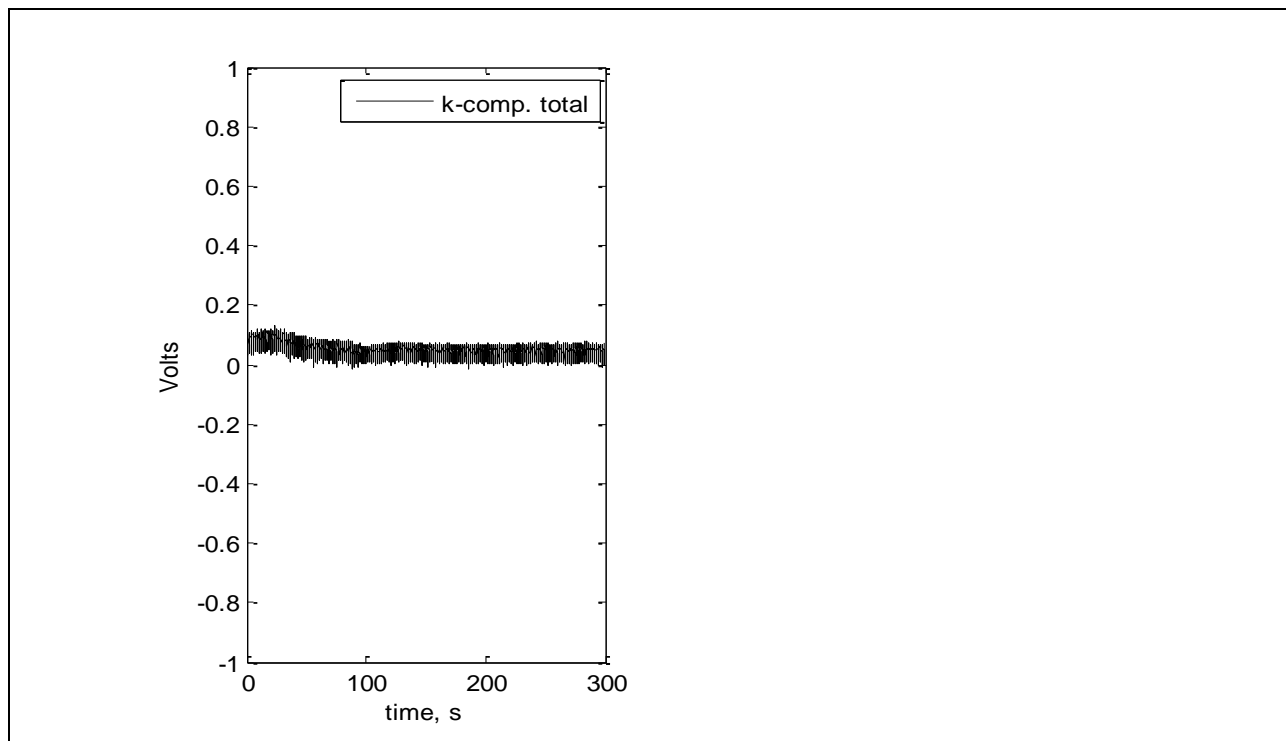


Figure 721: Voltage for full run.

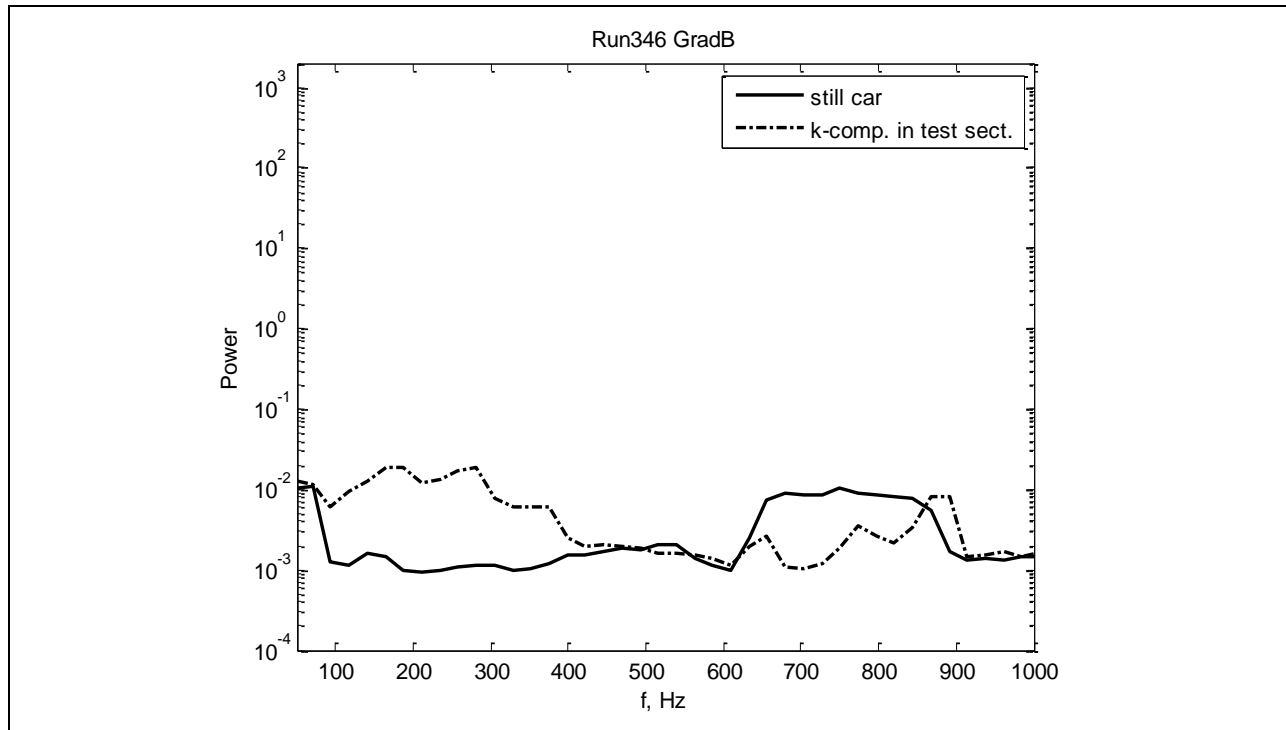


Figure 722: Power spectra in test section.

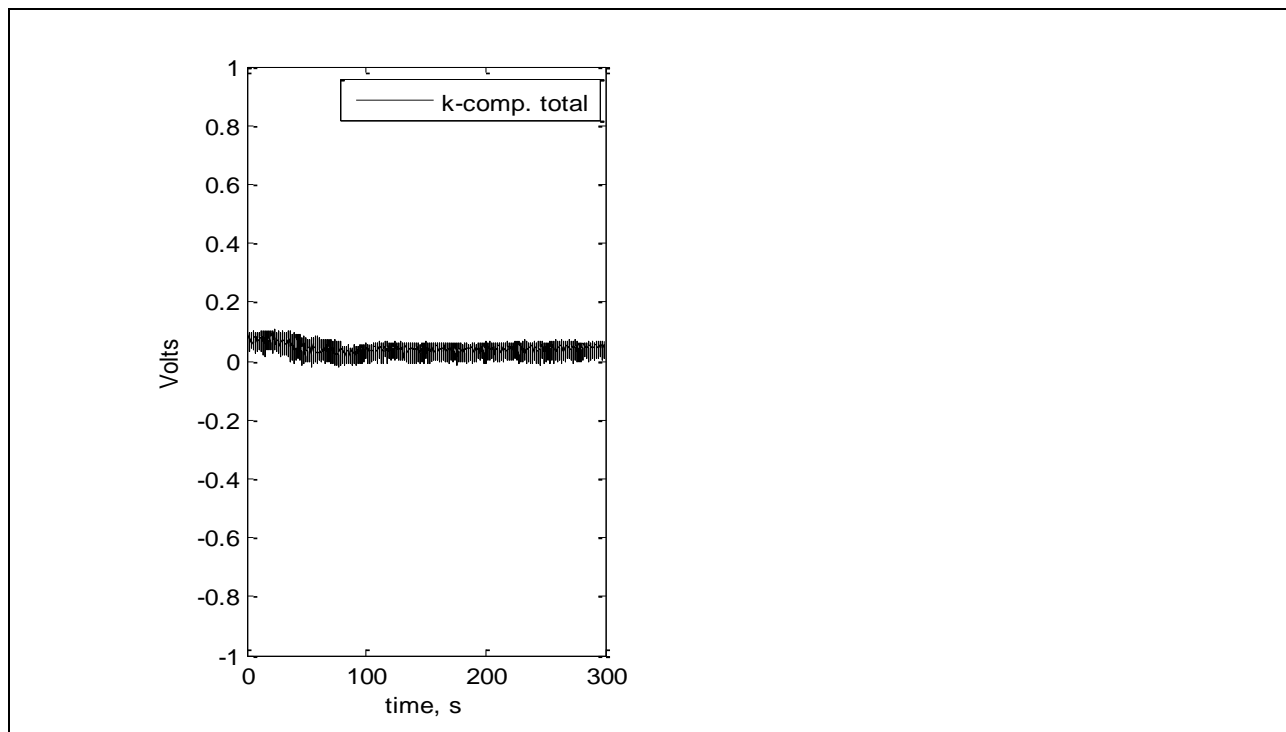


Figure 723: Voltage for full run.

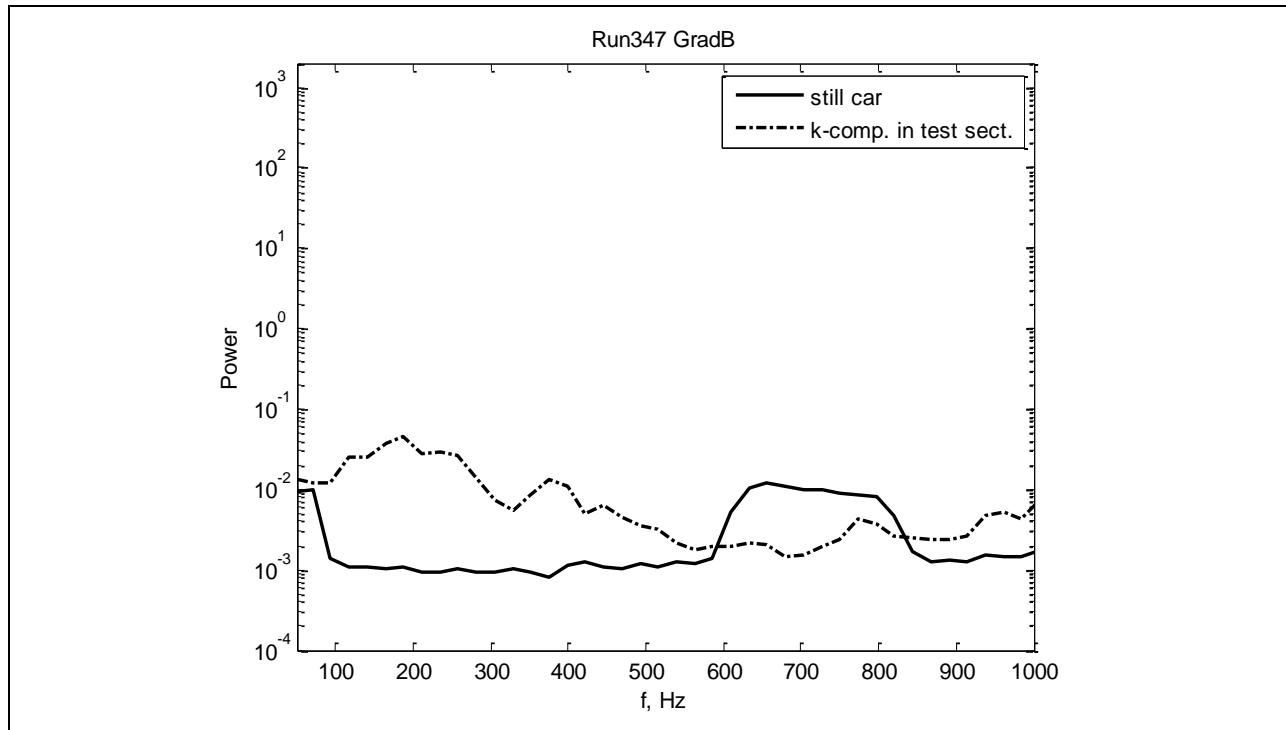


Figure 724: Power spectra in test section.

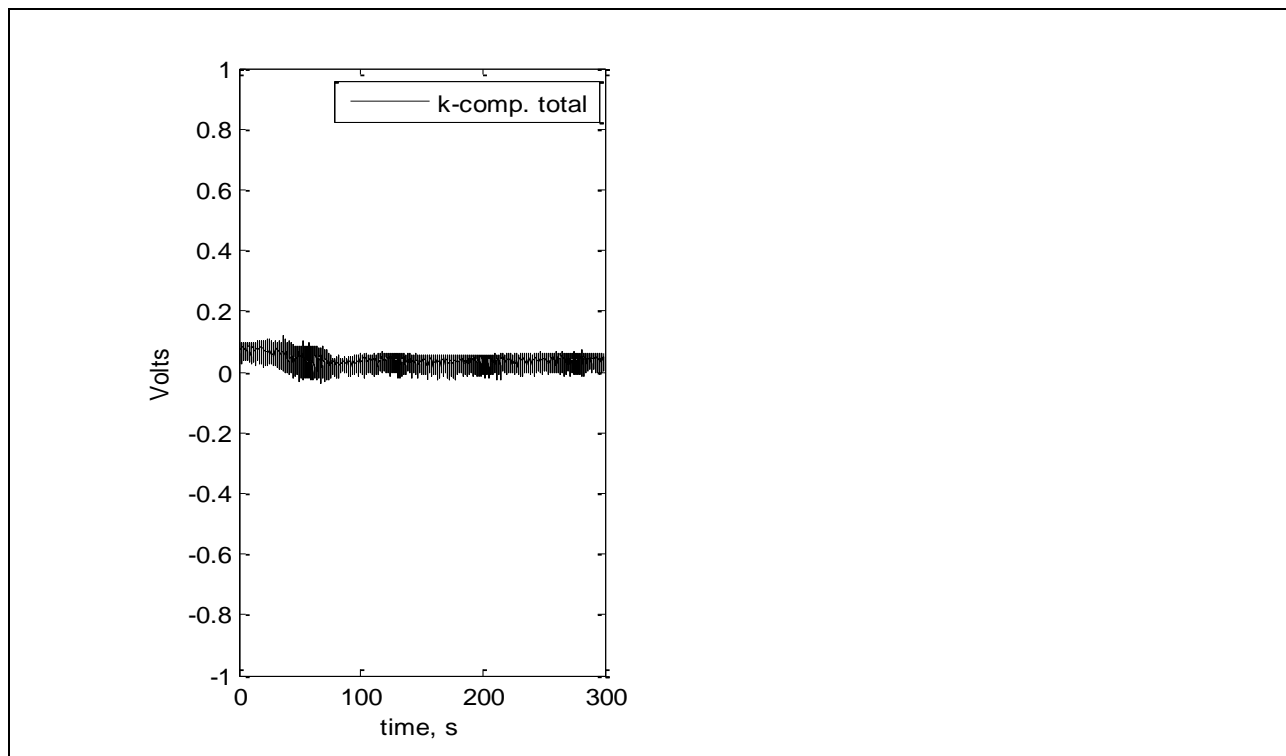


Figure 725: Voltage for full run.

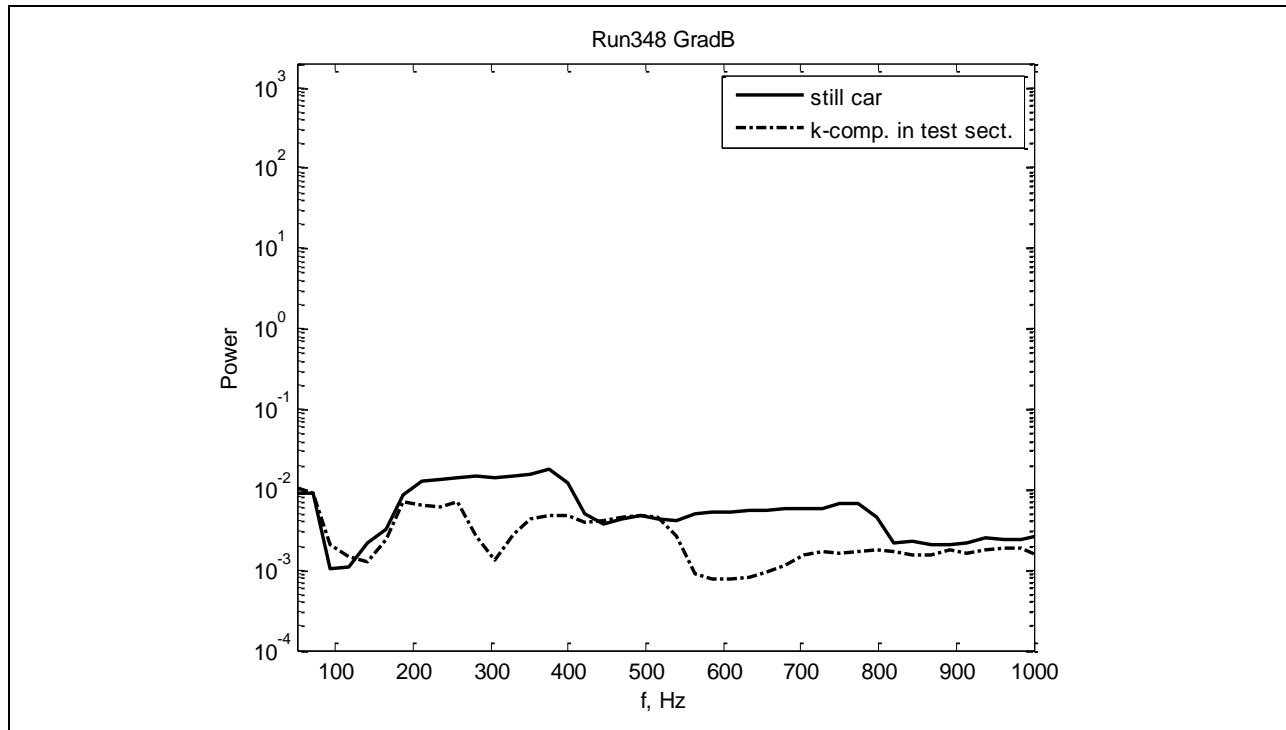


Figure 726: Power spectra in test section.

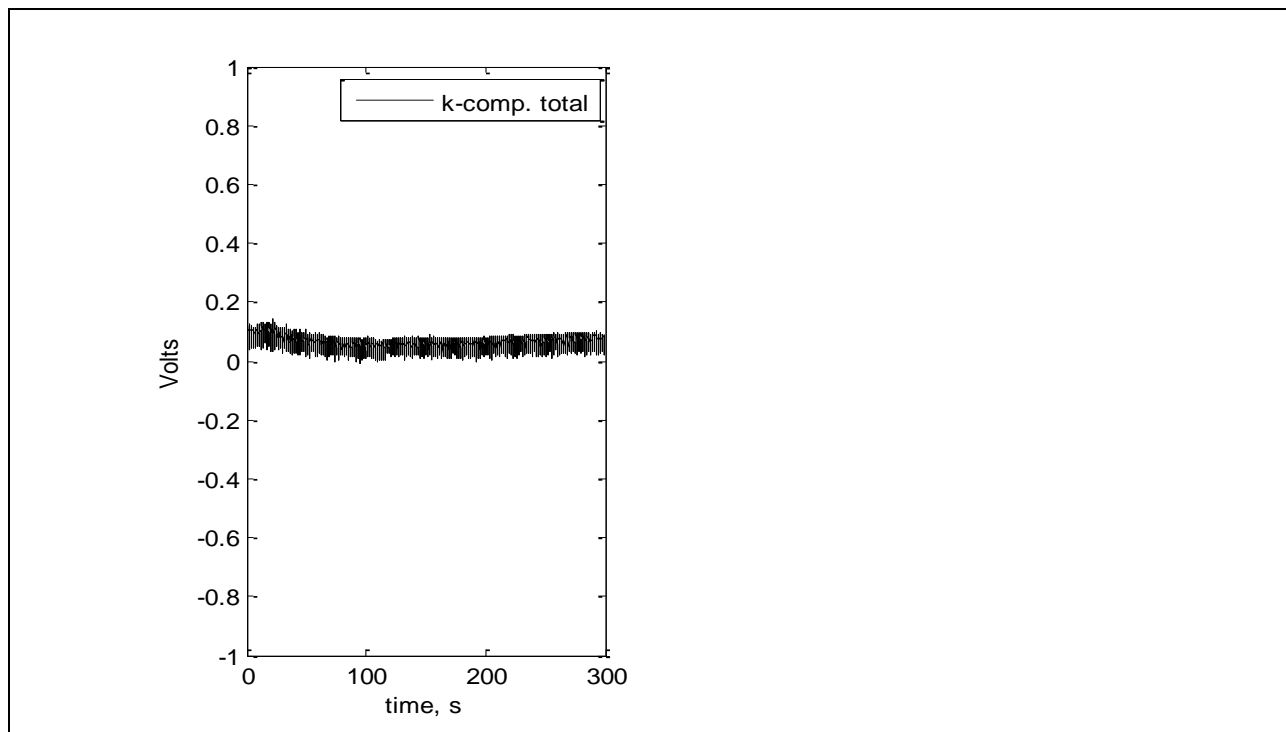


Figure 727: Voltage for full run.

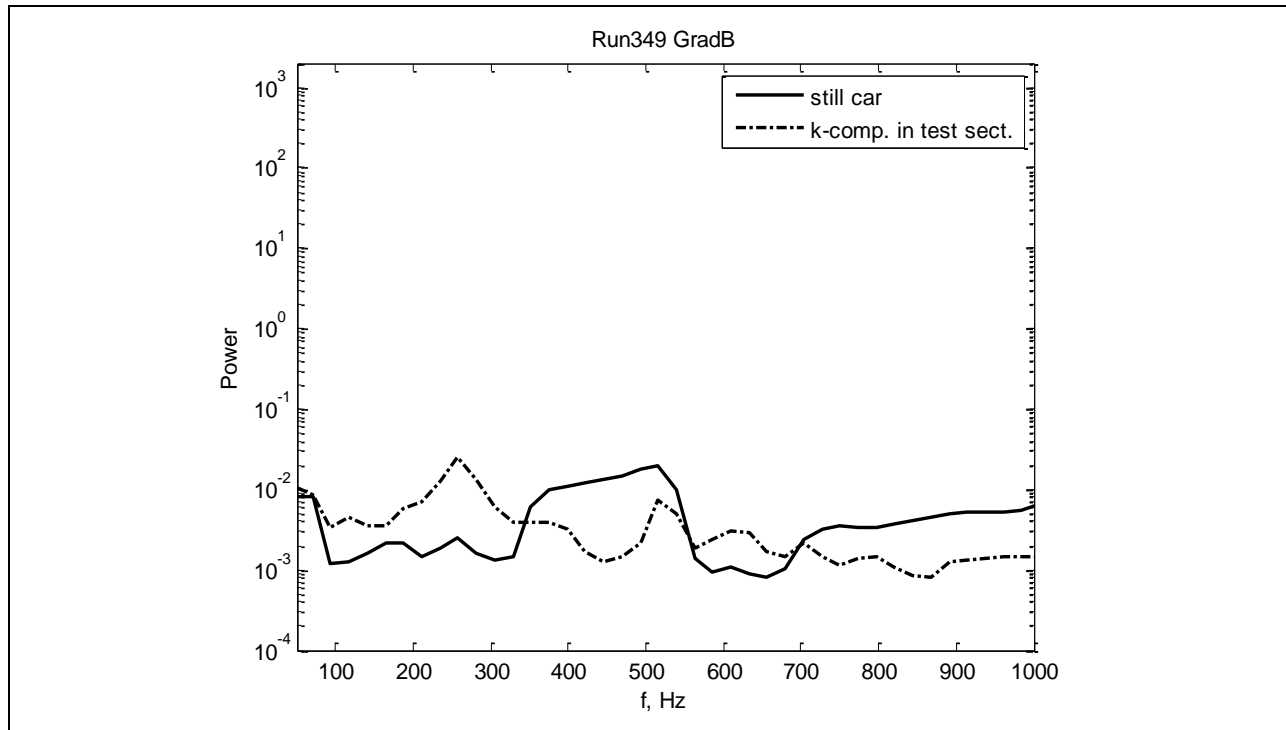


Figure 728: Power spectra in test section.

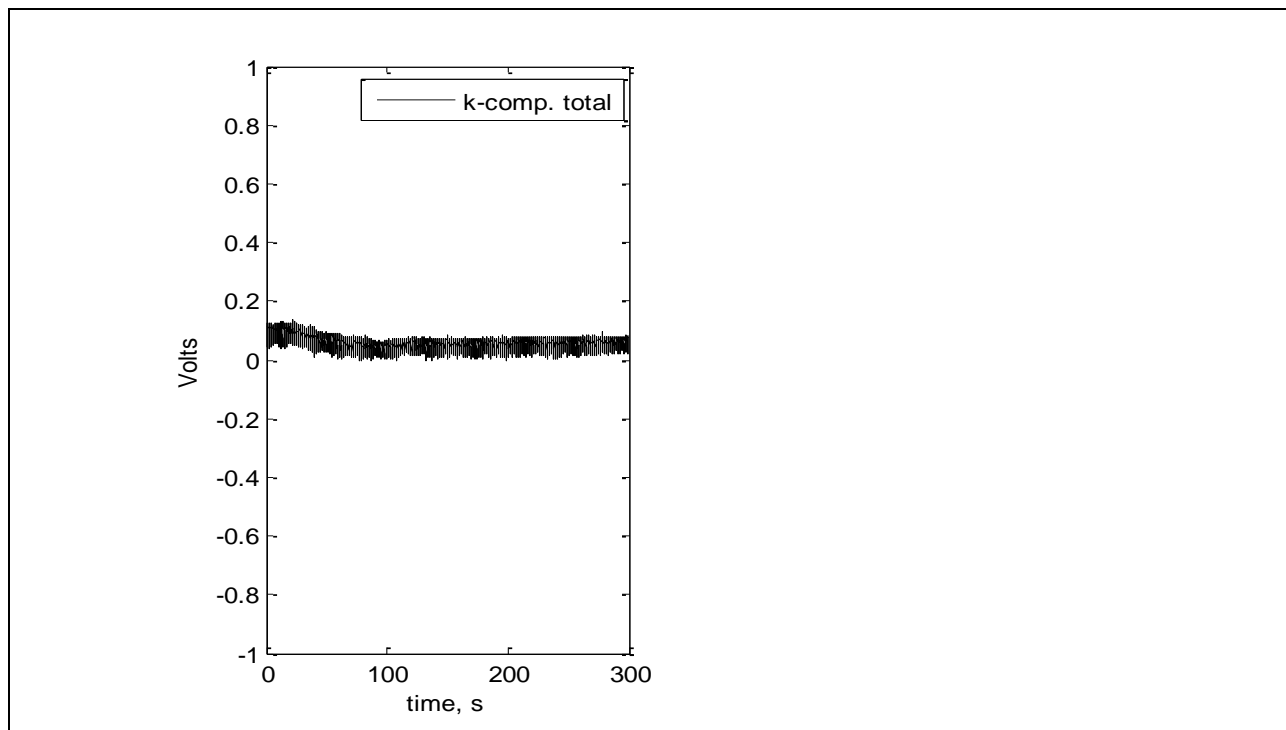


Figure 729: Voltage for full run.

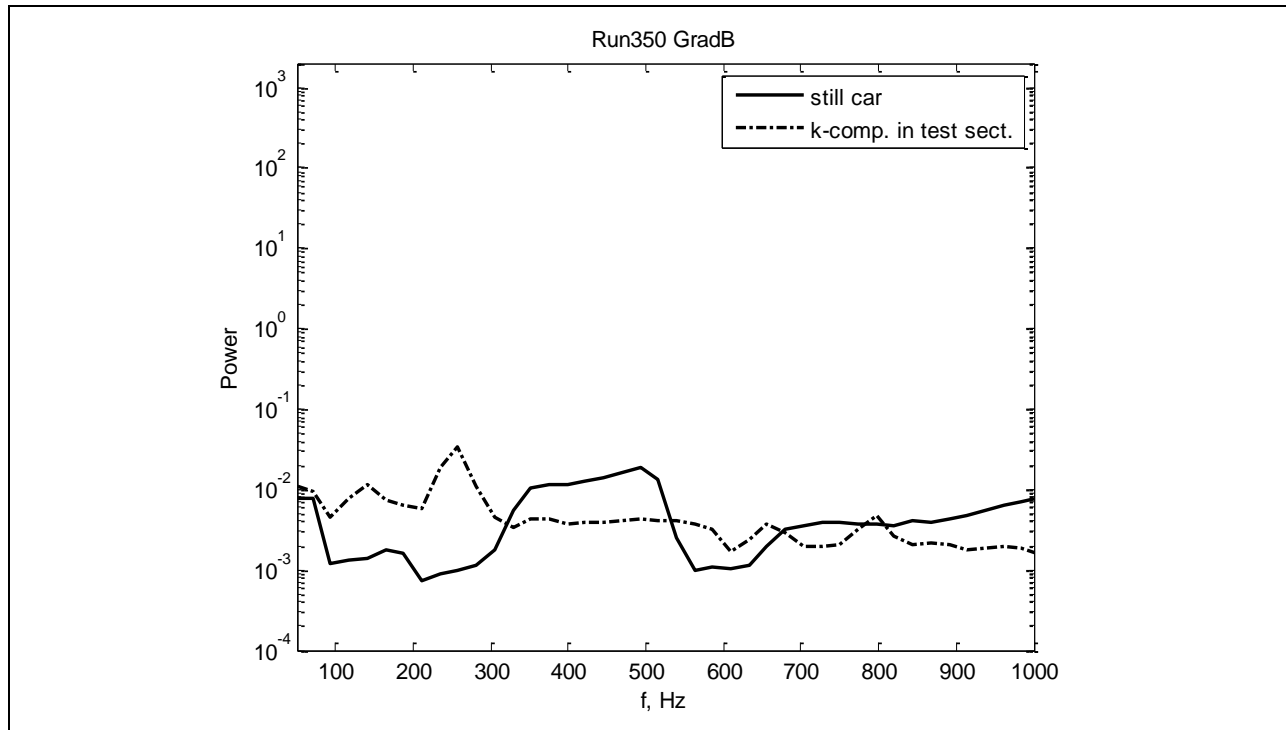


Figure 730: Power spectra in test section.

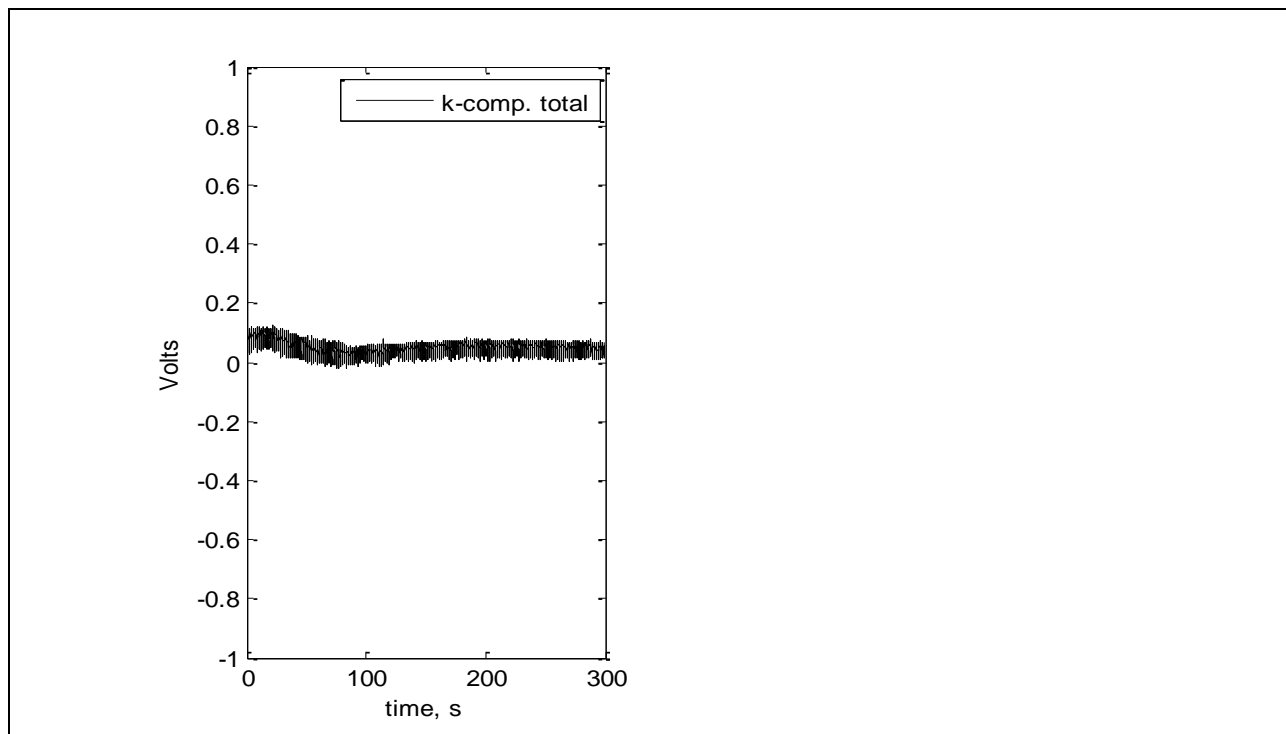


Figure 731: Voltage for full run.

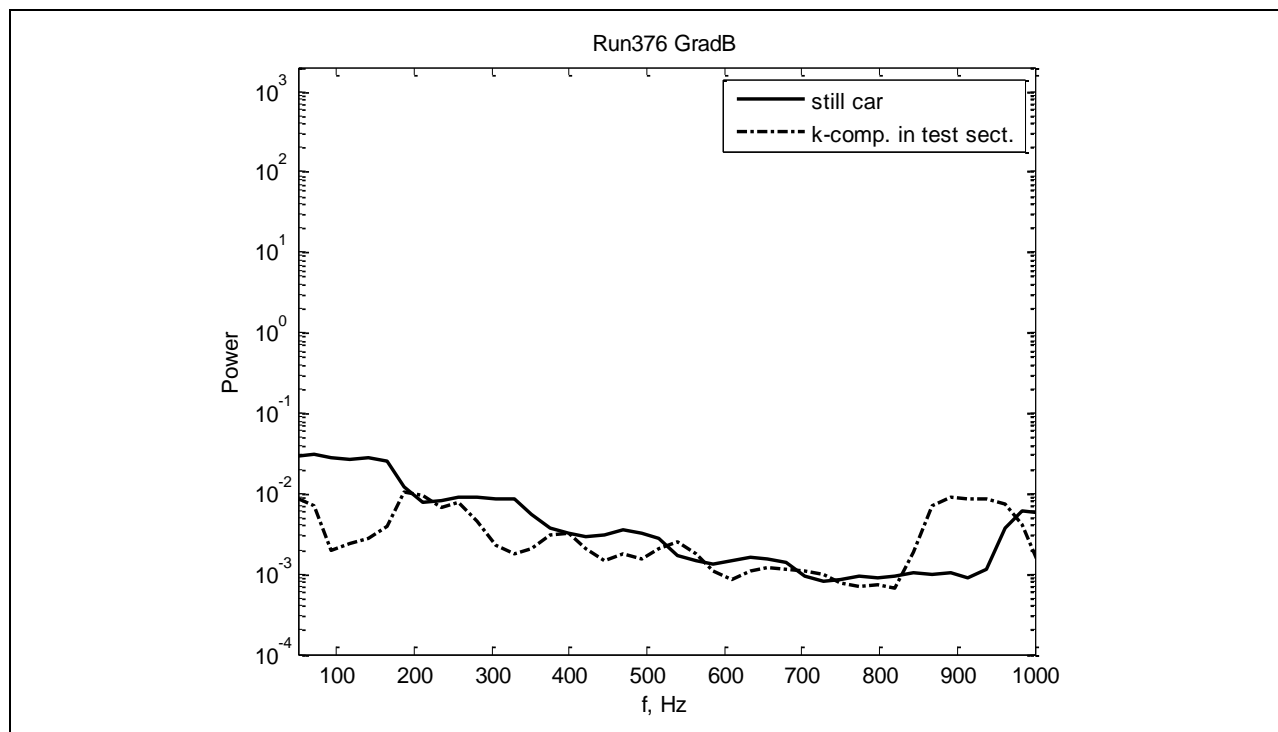


Figure 732: Power spectra in test section.

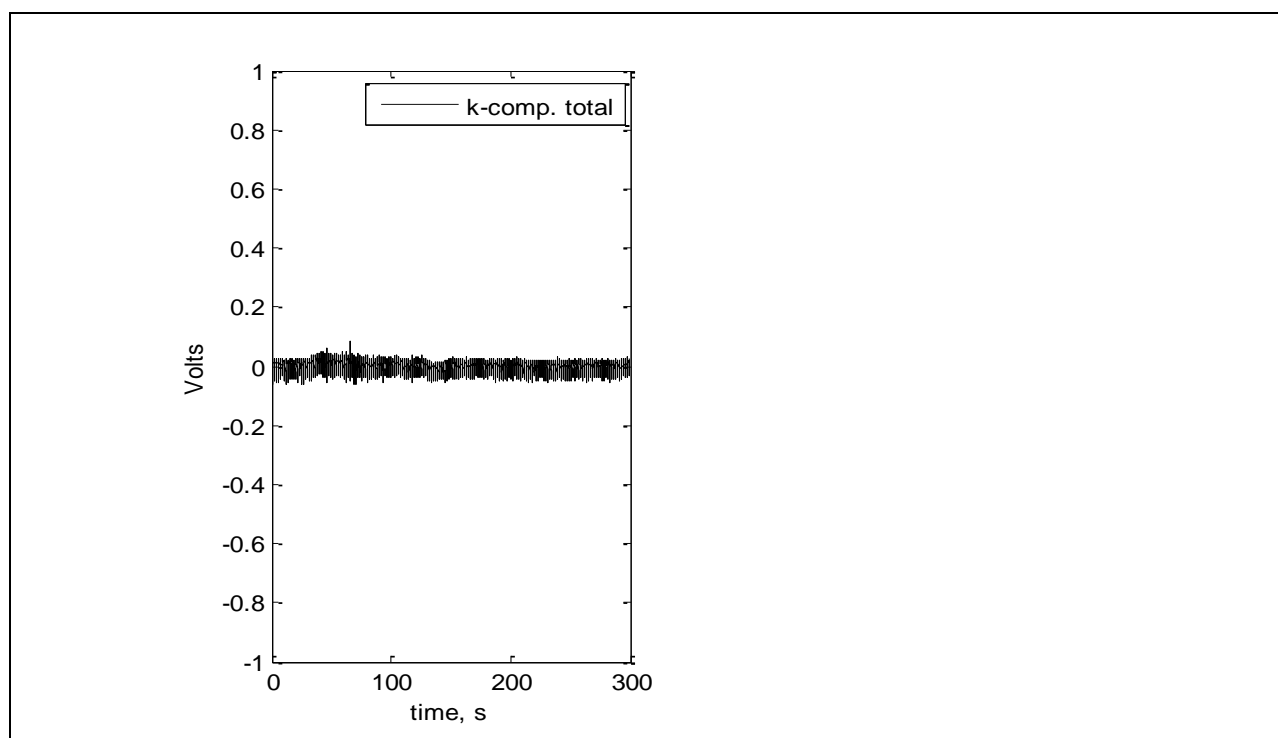


Figure 733: Voltage for full run.

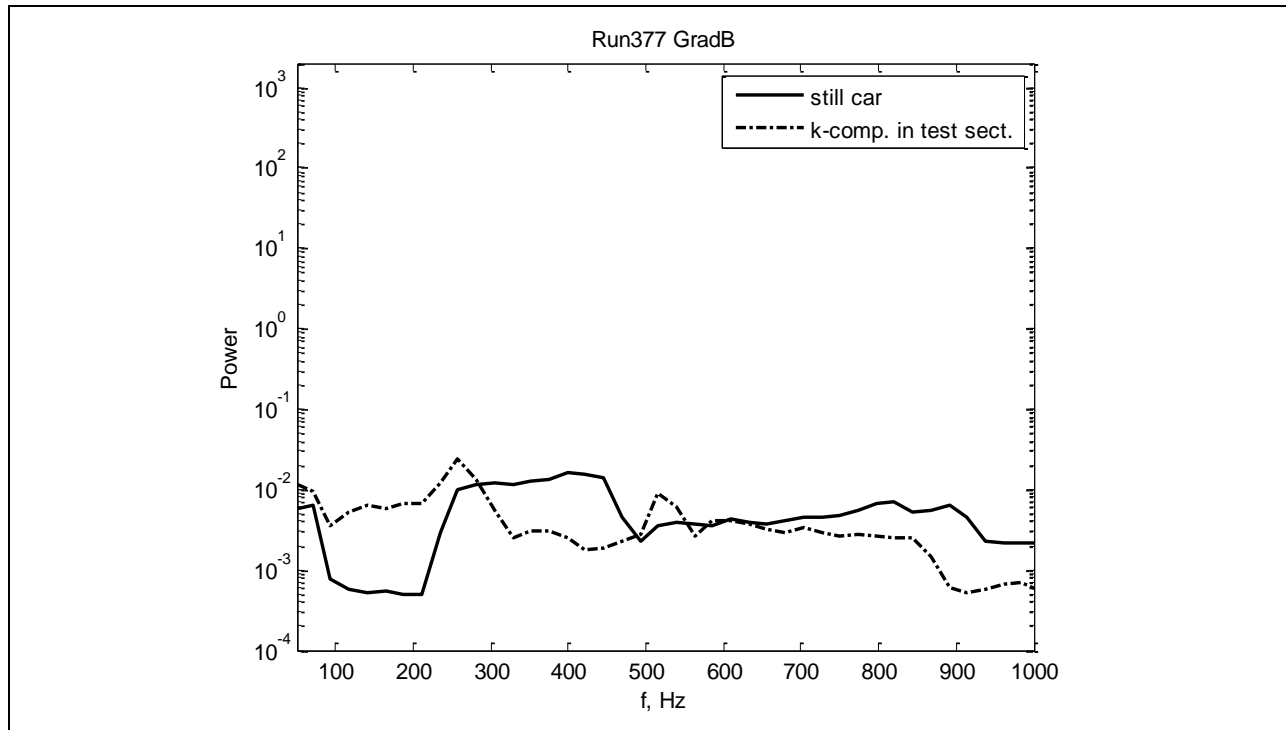


Figure 734: Power spectra in test section.

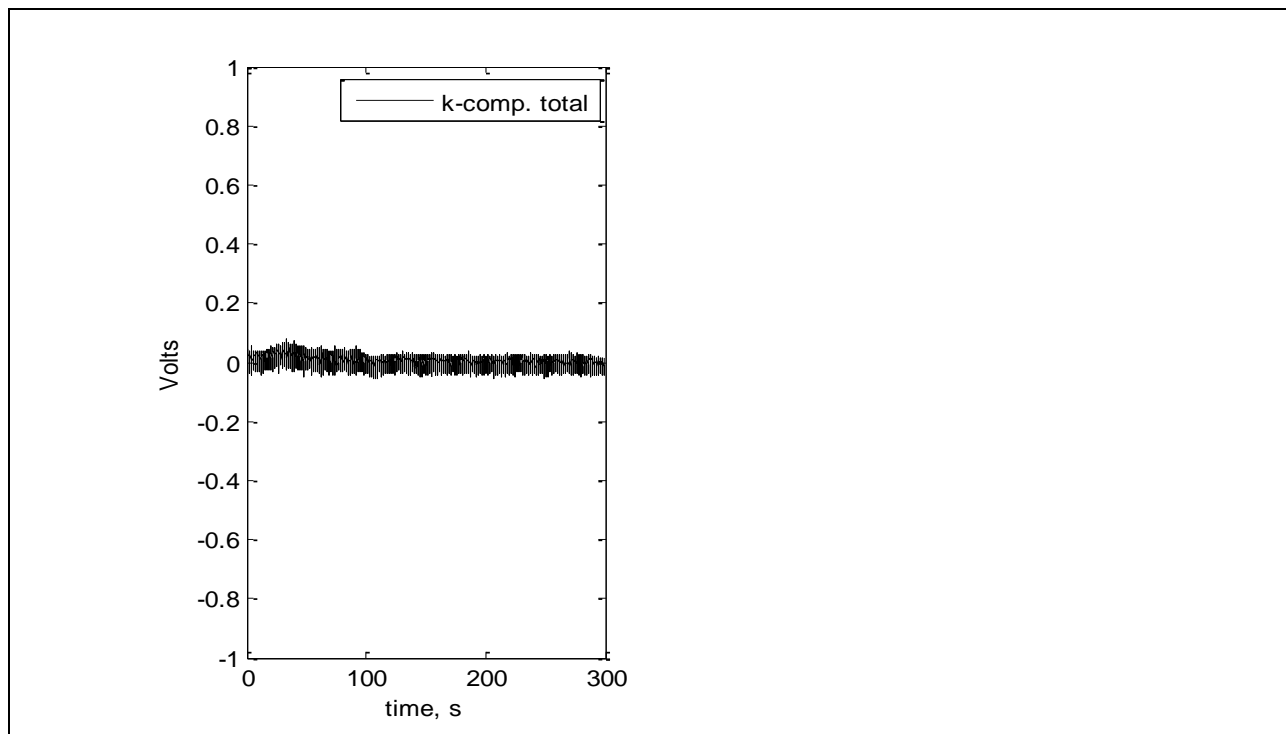


Figure 735: Voltage for full run.

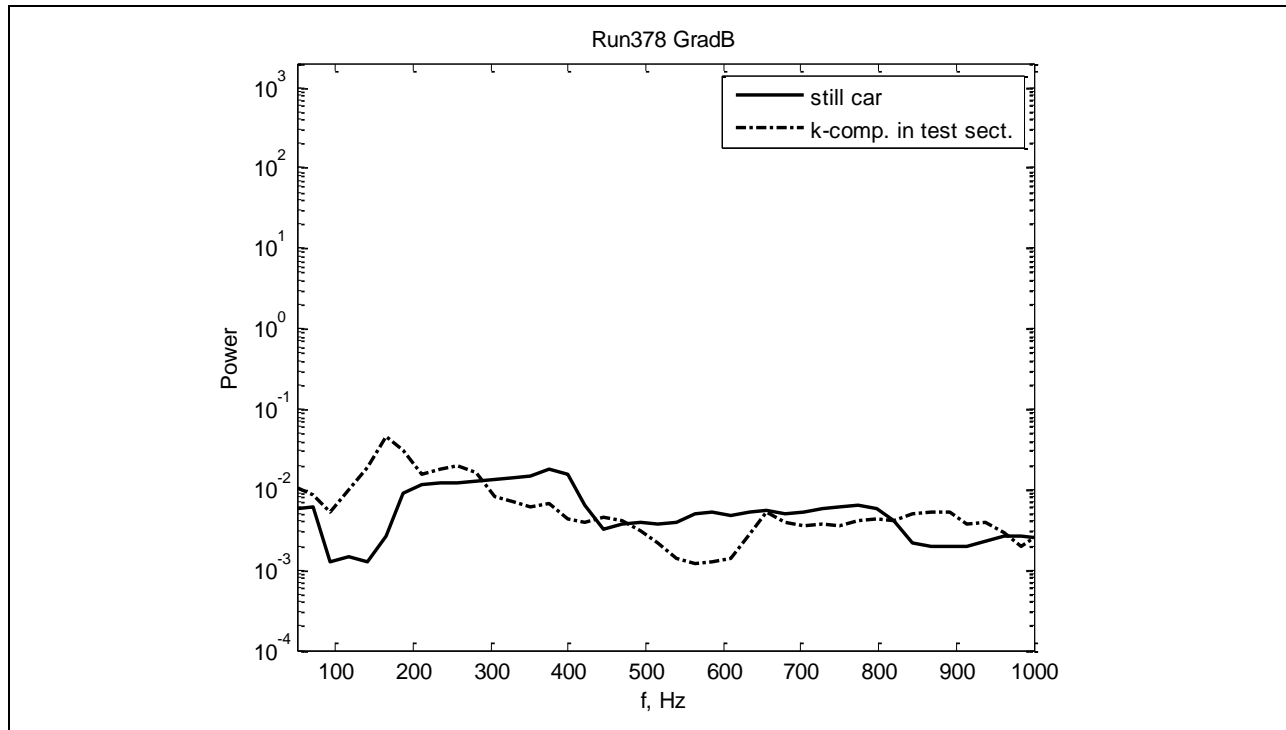


Figure 736: Power spectra in test section.

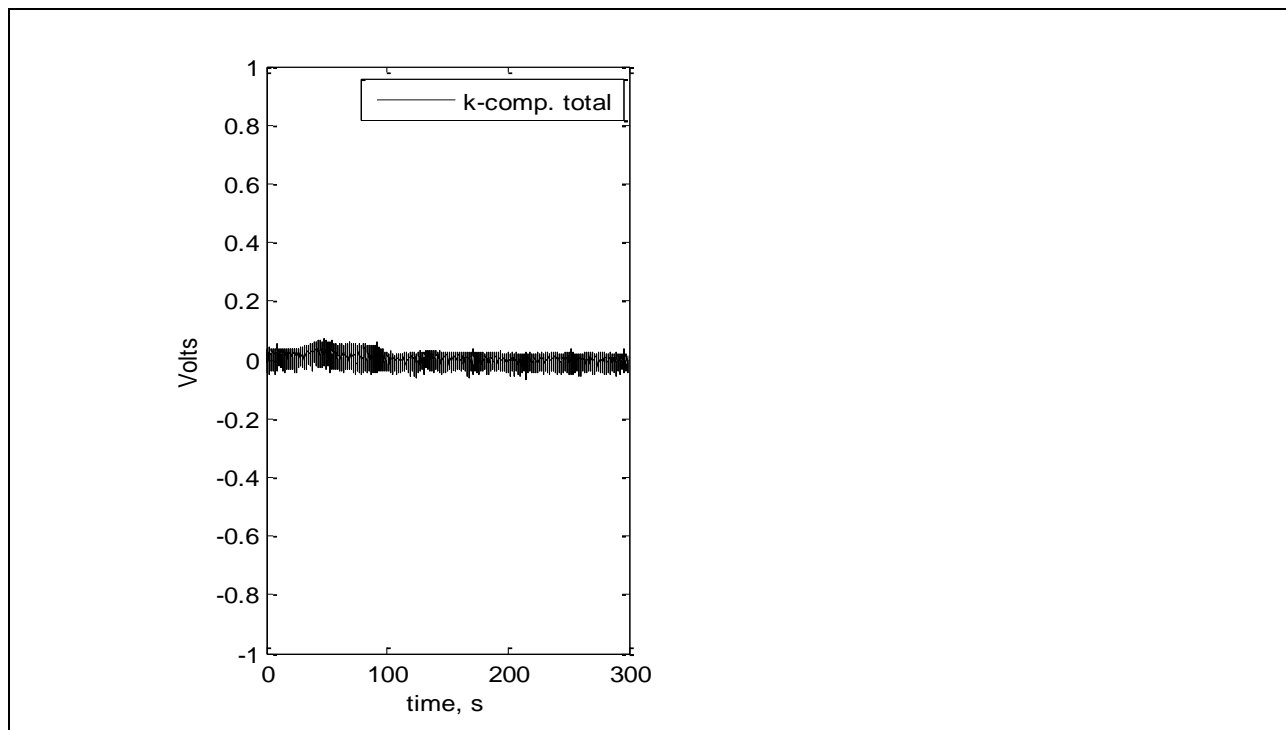


Figure 737: Voltage for full run.

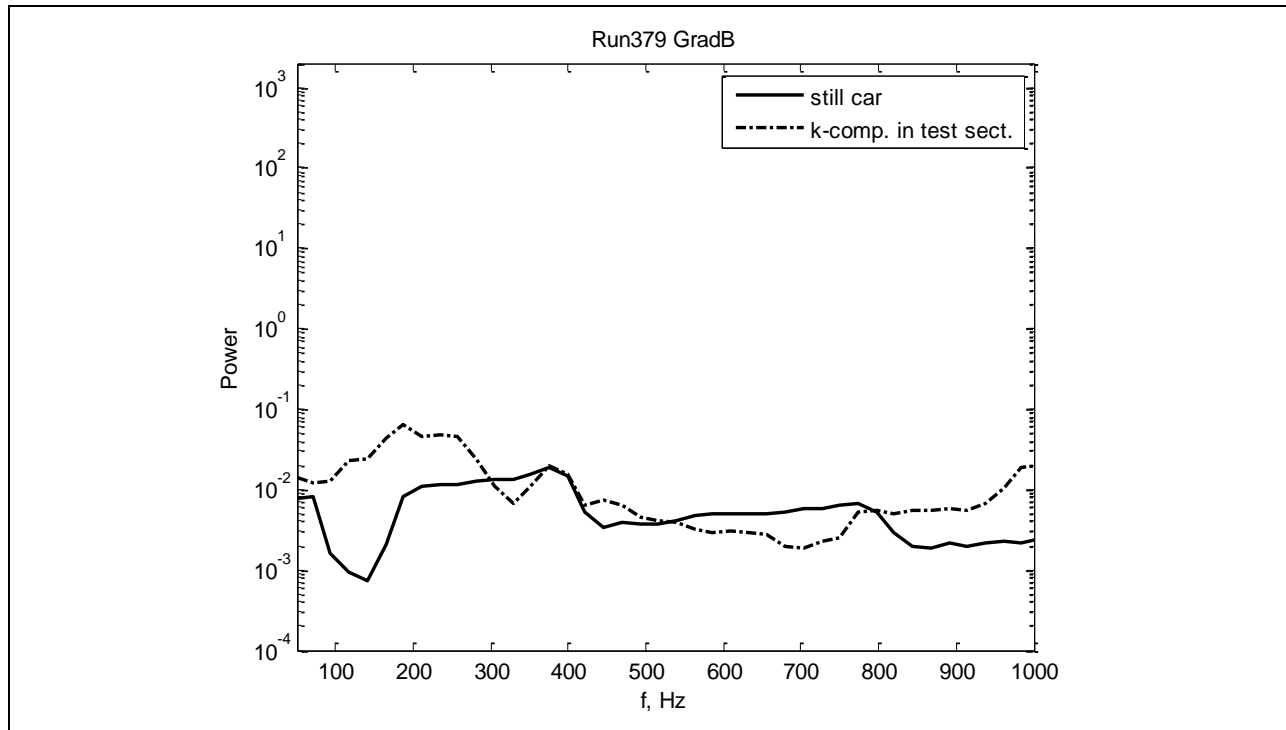


Figure 738: Power spectra in test section.

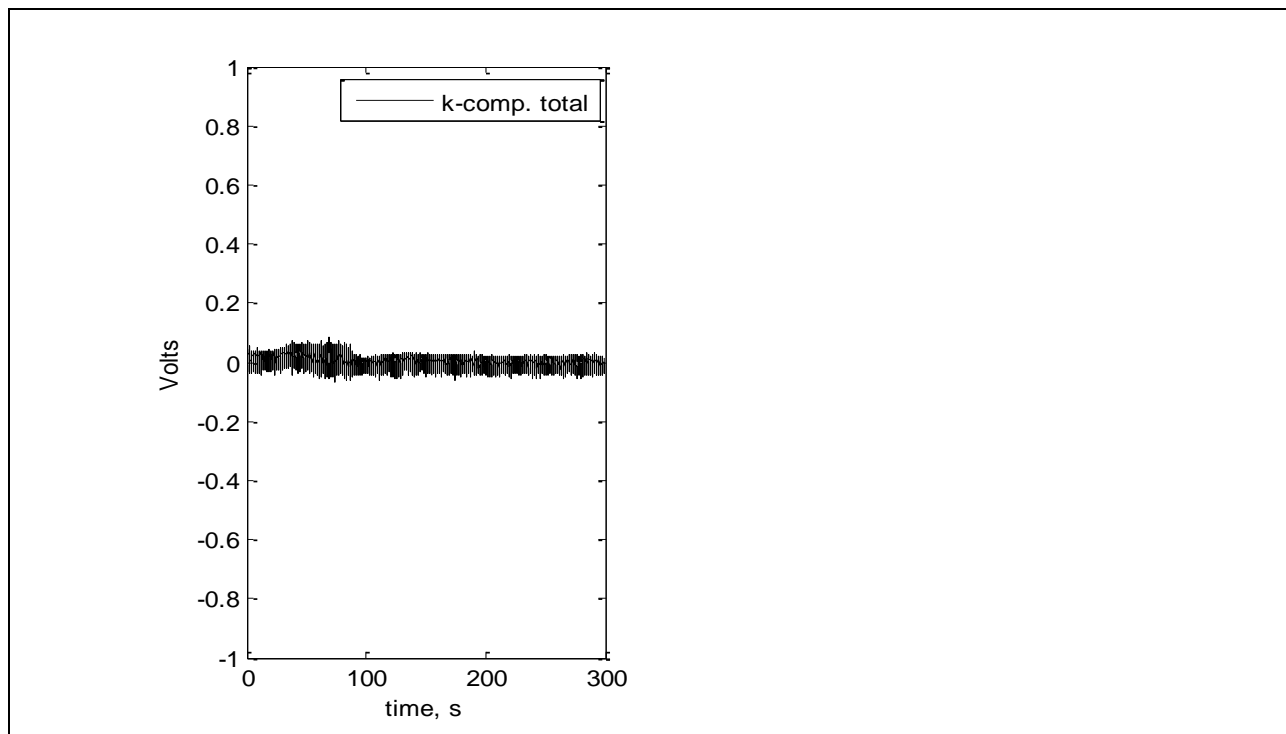


Figure 739: Voltage for full run.

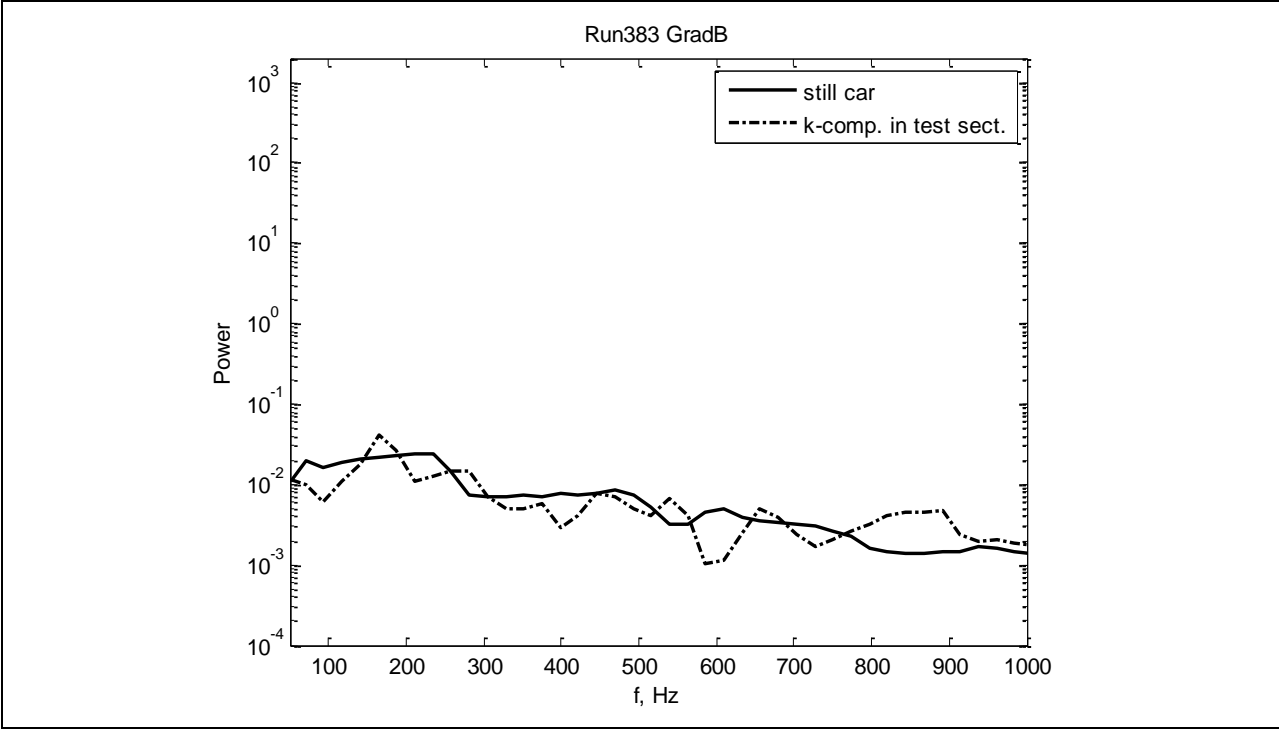


Figure 740: Power spectra in test section.

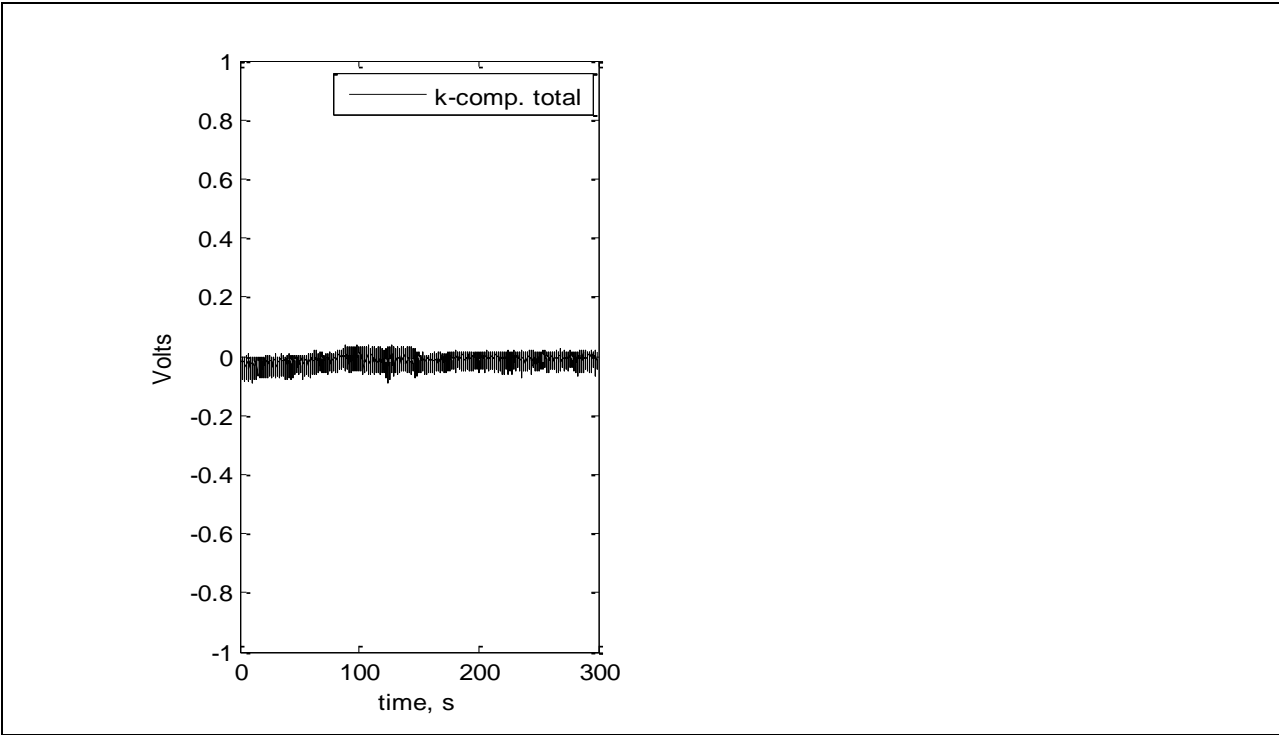


Figure 741: Voltage for full run.

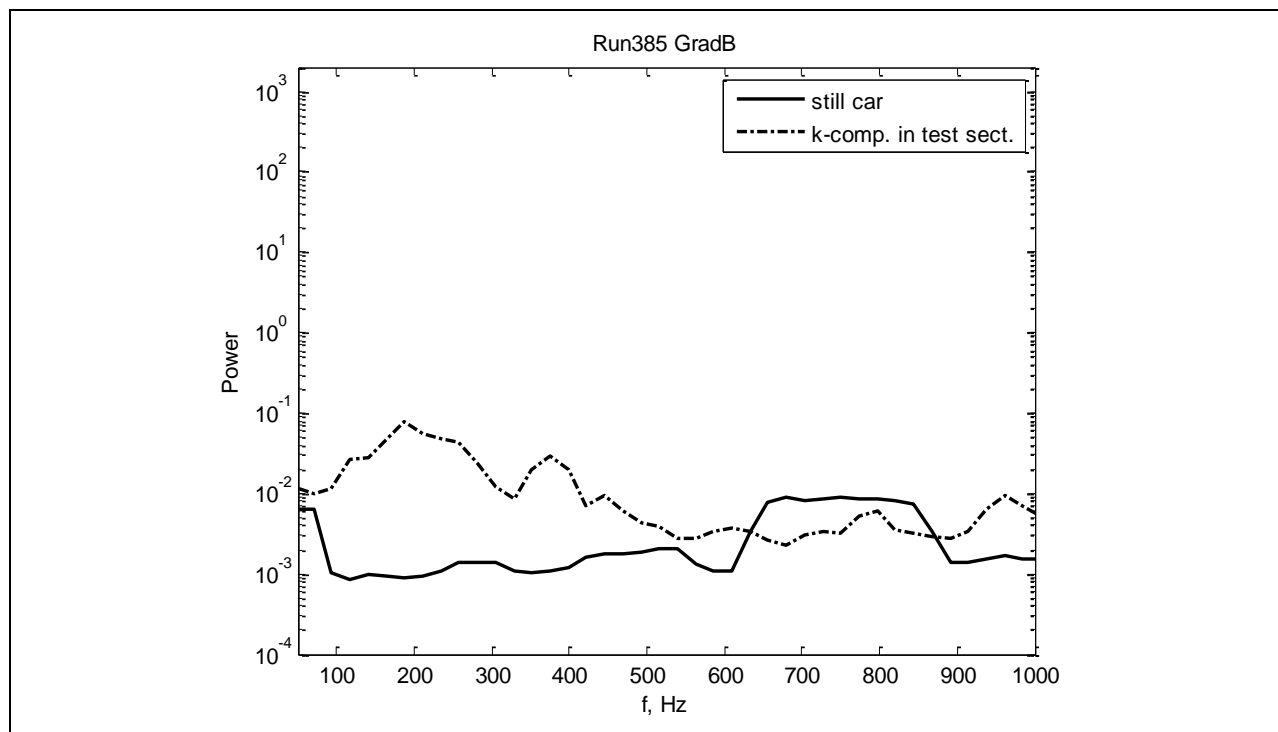


Figure 742: Power spectra in test section.

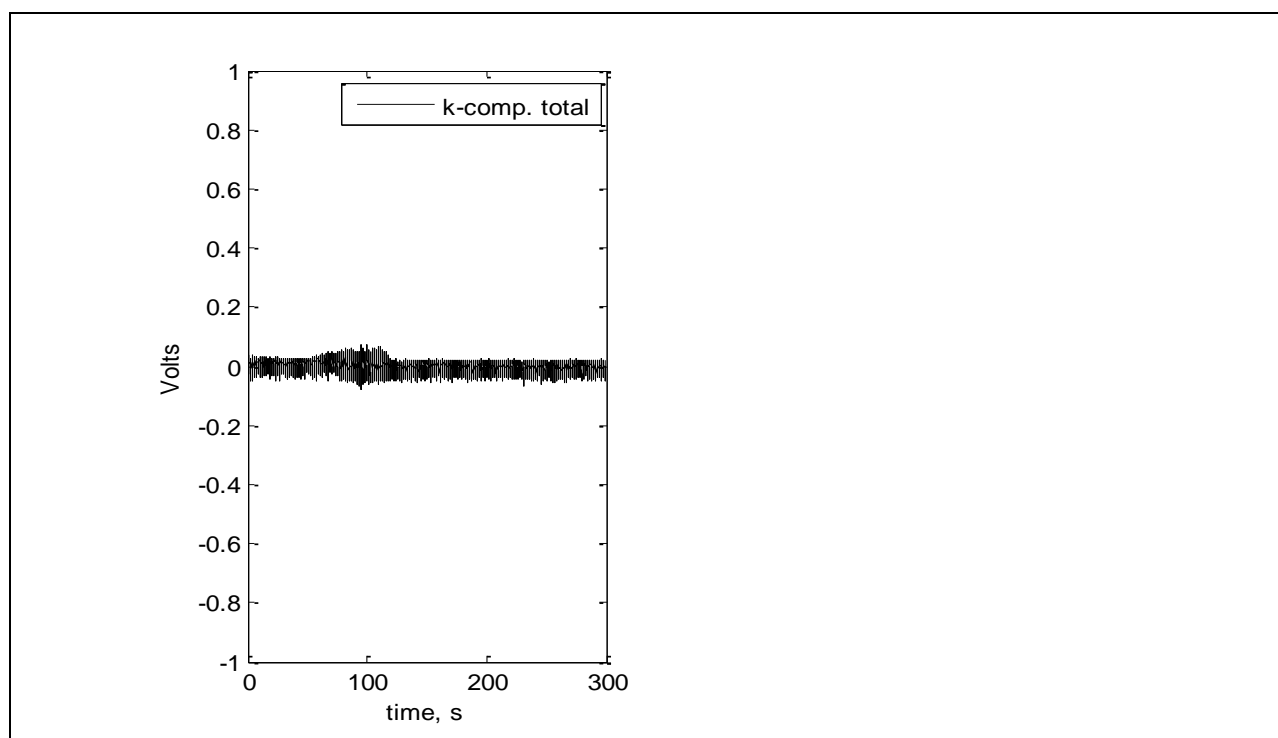


Figure 743: Voltage for full run.

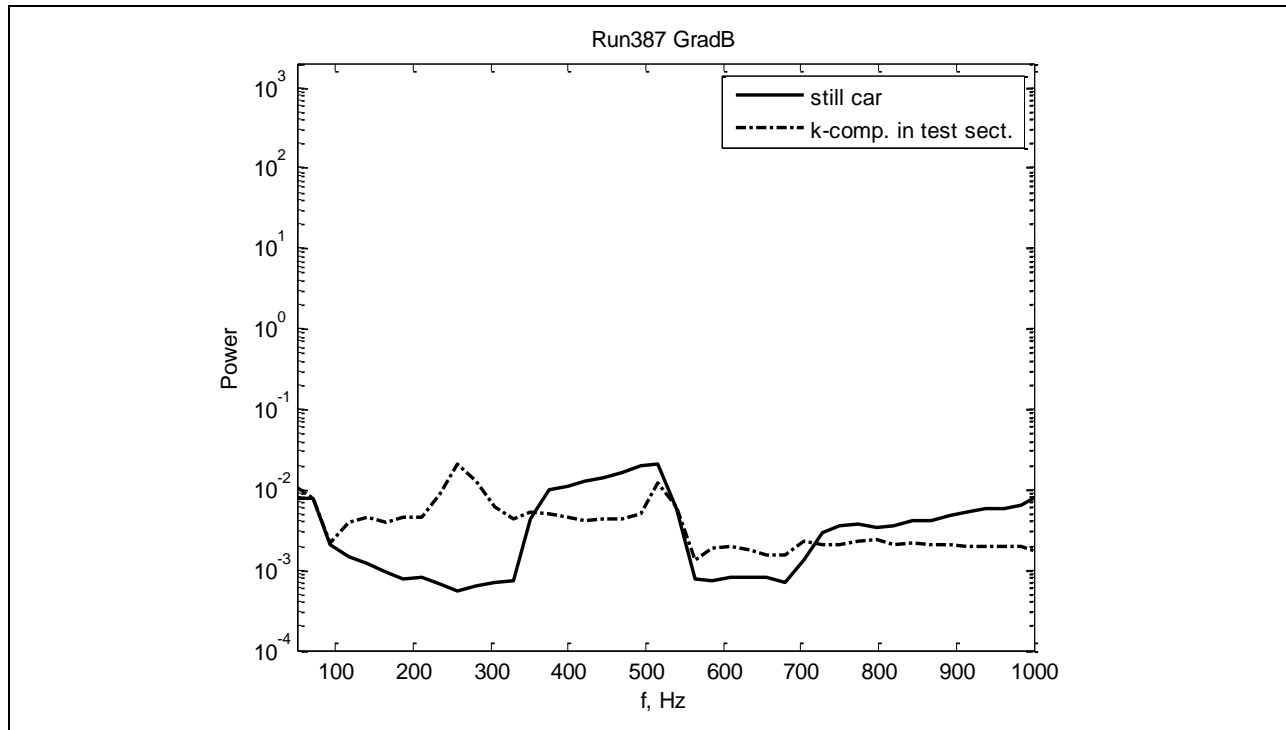


Figure 744: Power spectra in test section.

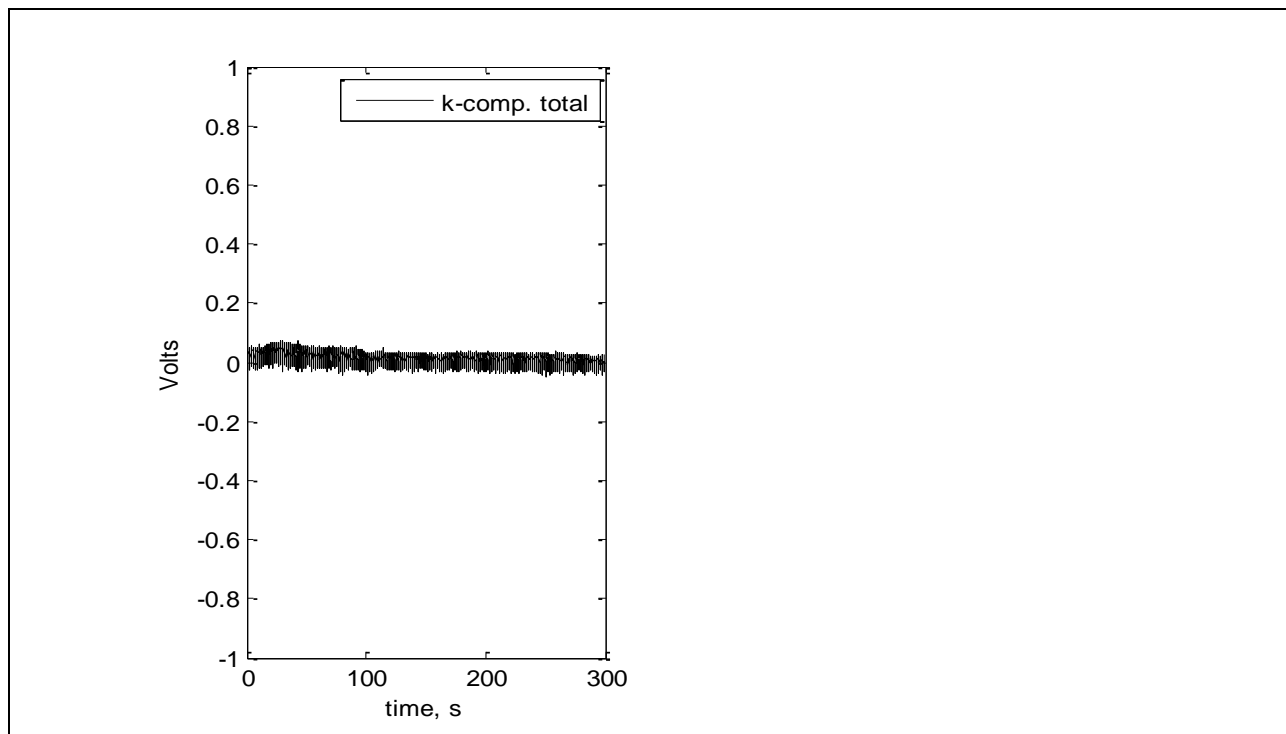


Figure 745: Voltage for full run.

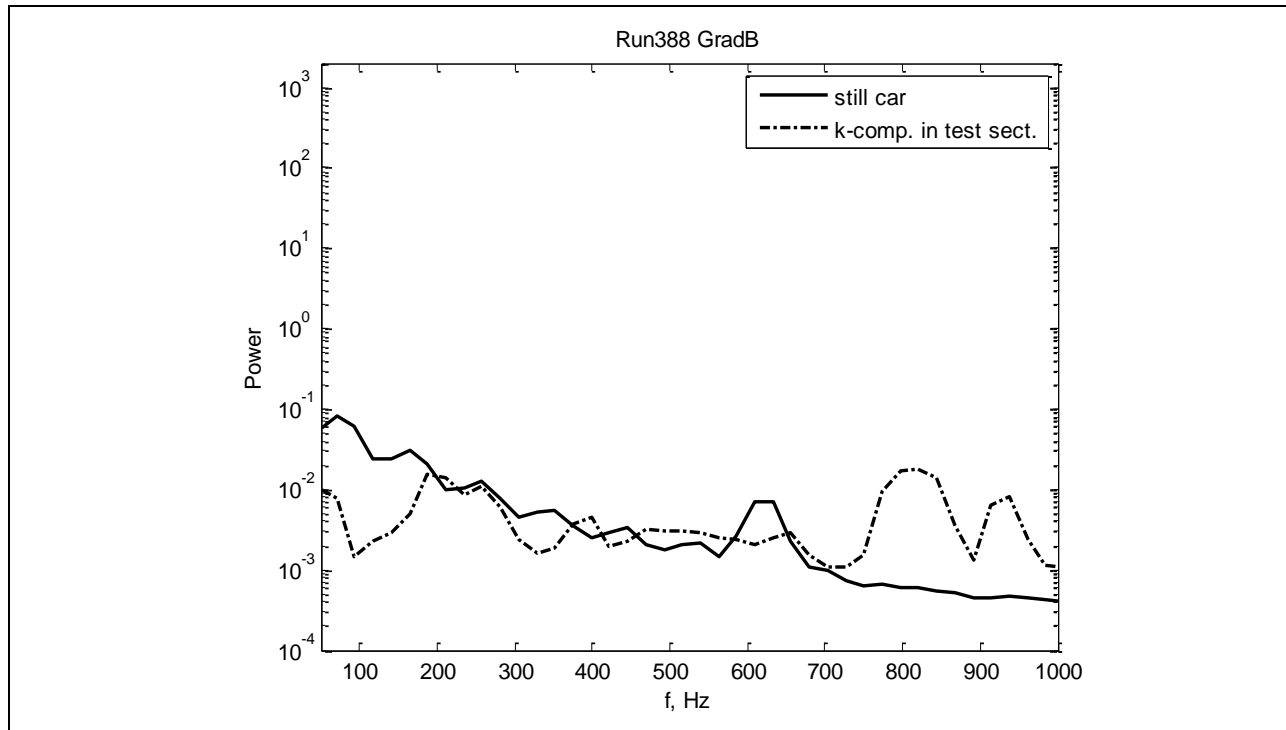


Figure 746: Power spectra in test section.

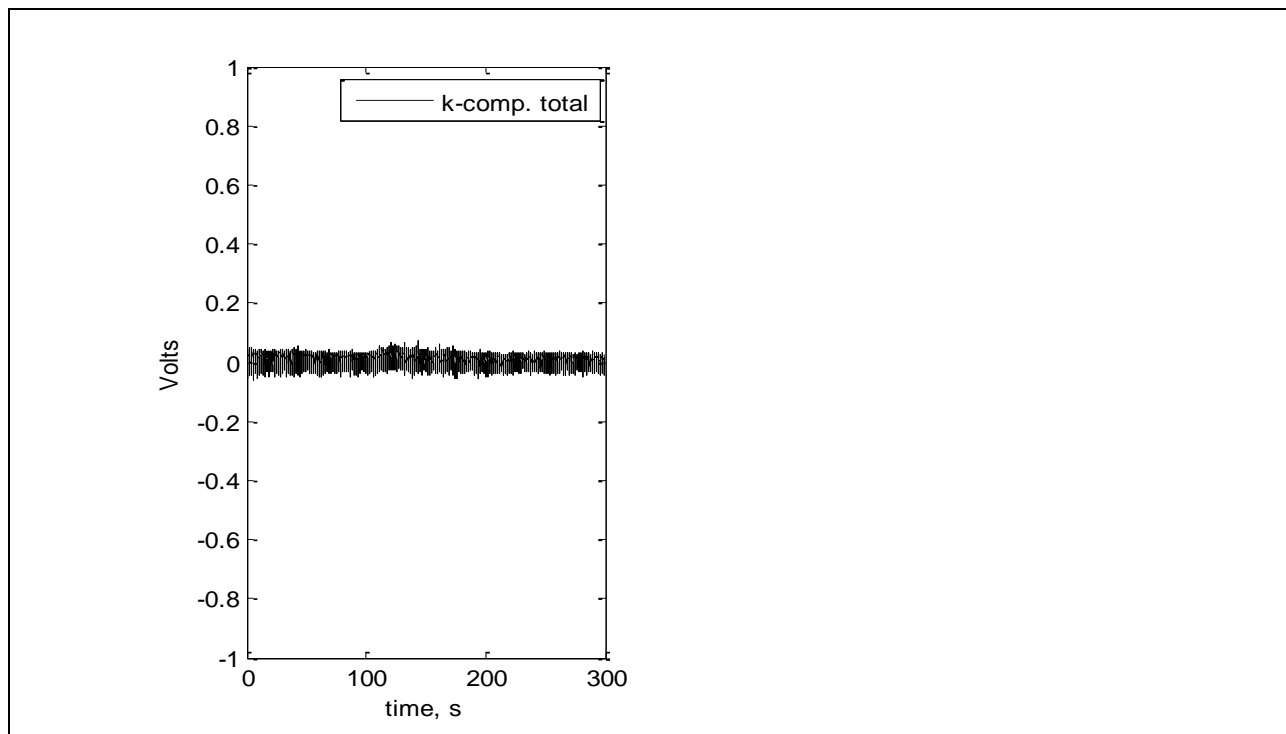


Figure 747: Voltage for full run.

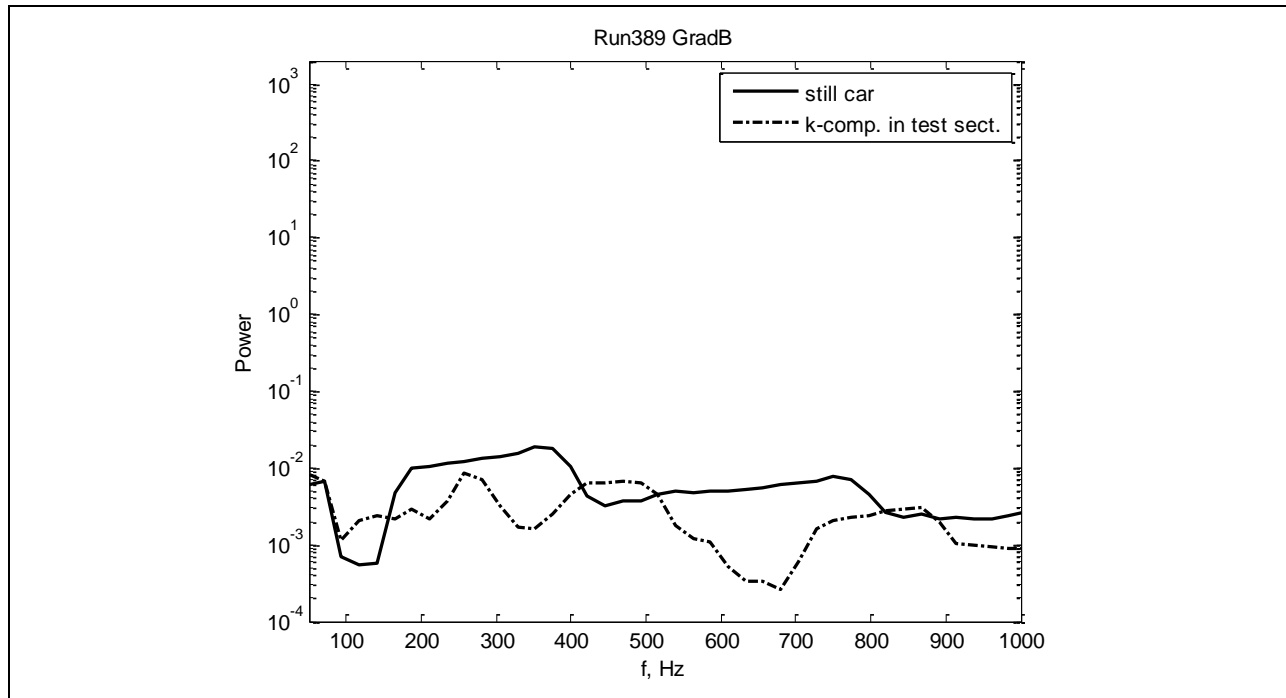


Figure 748: Power spectra in test section.

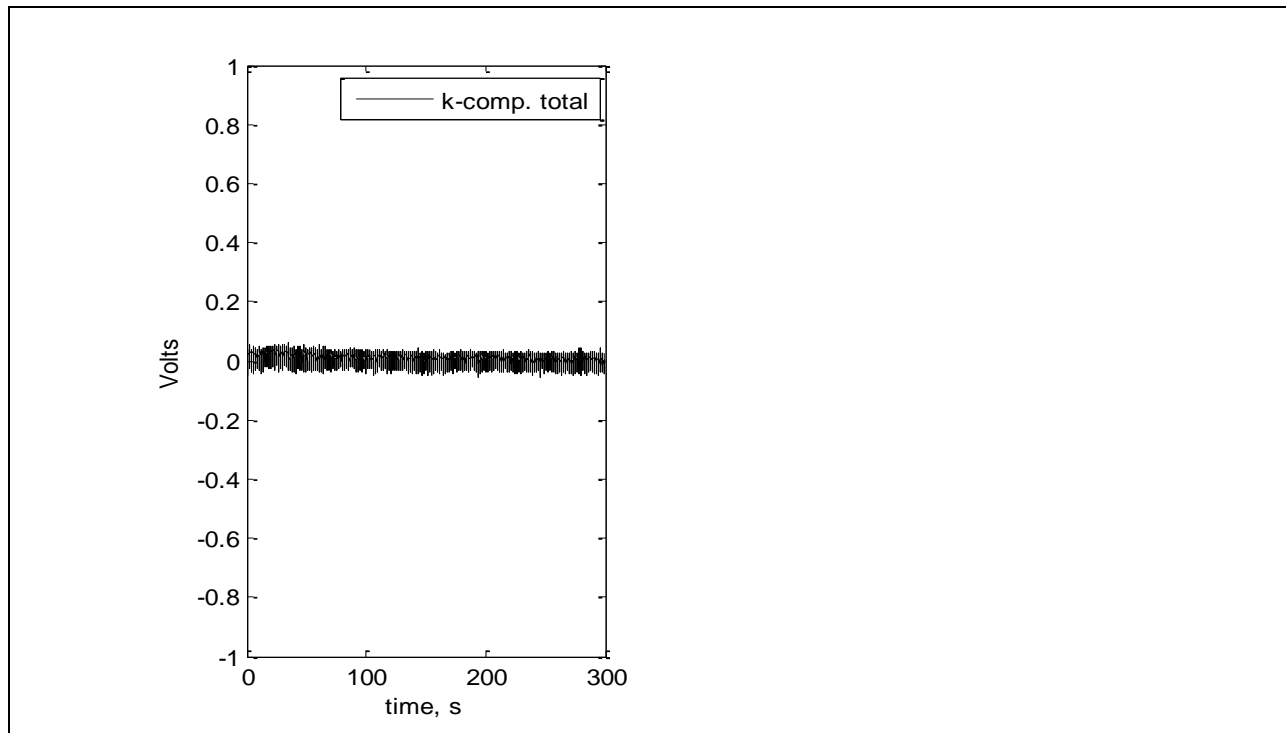


Figure 749: Voltage for full run.

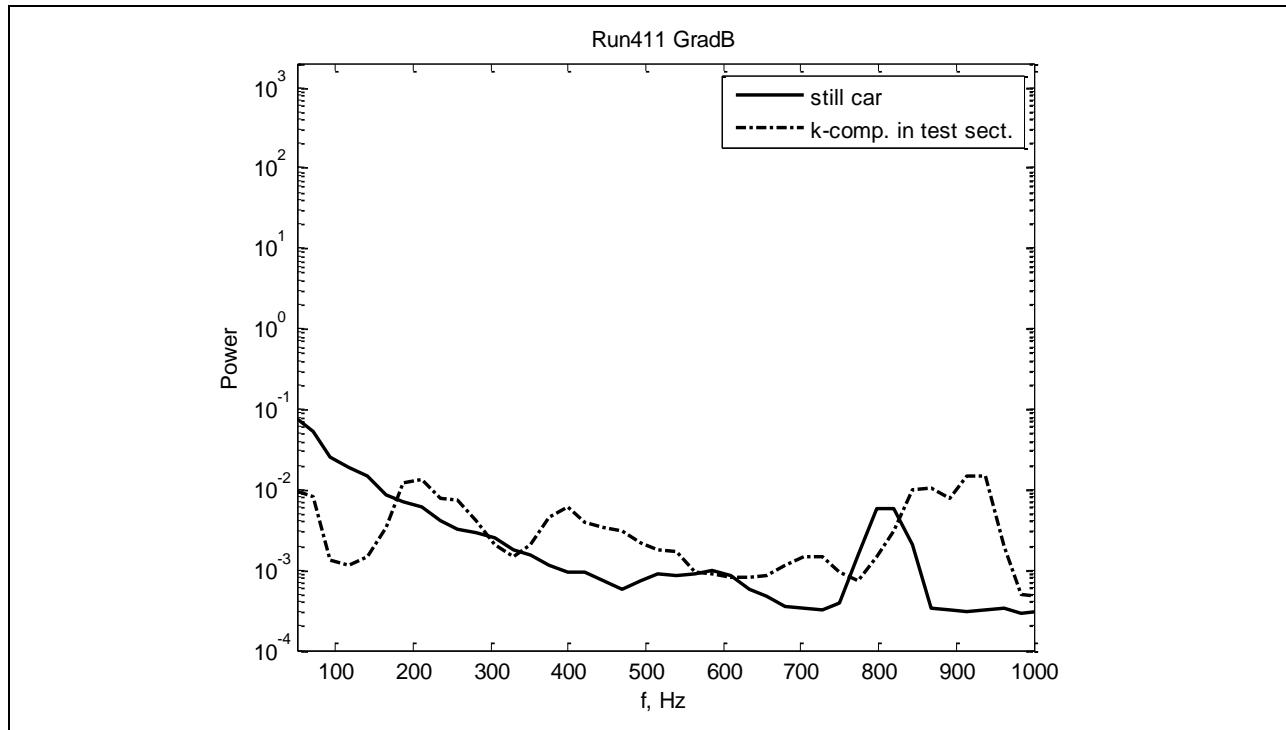


Figure 750: Power spectra in test section.

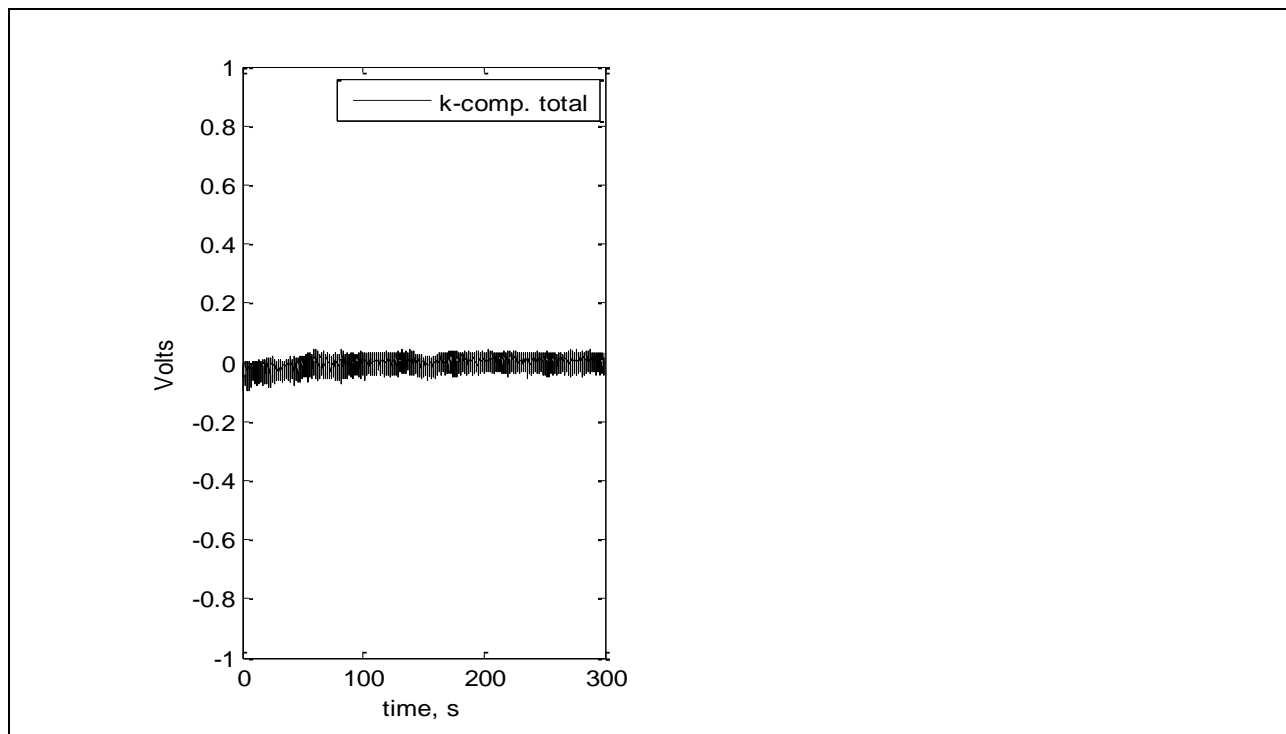


Figure 751: Voltage for full run.

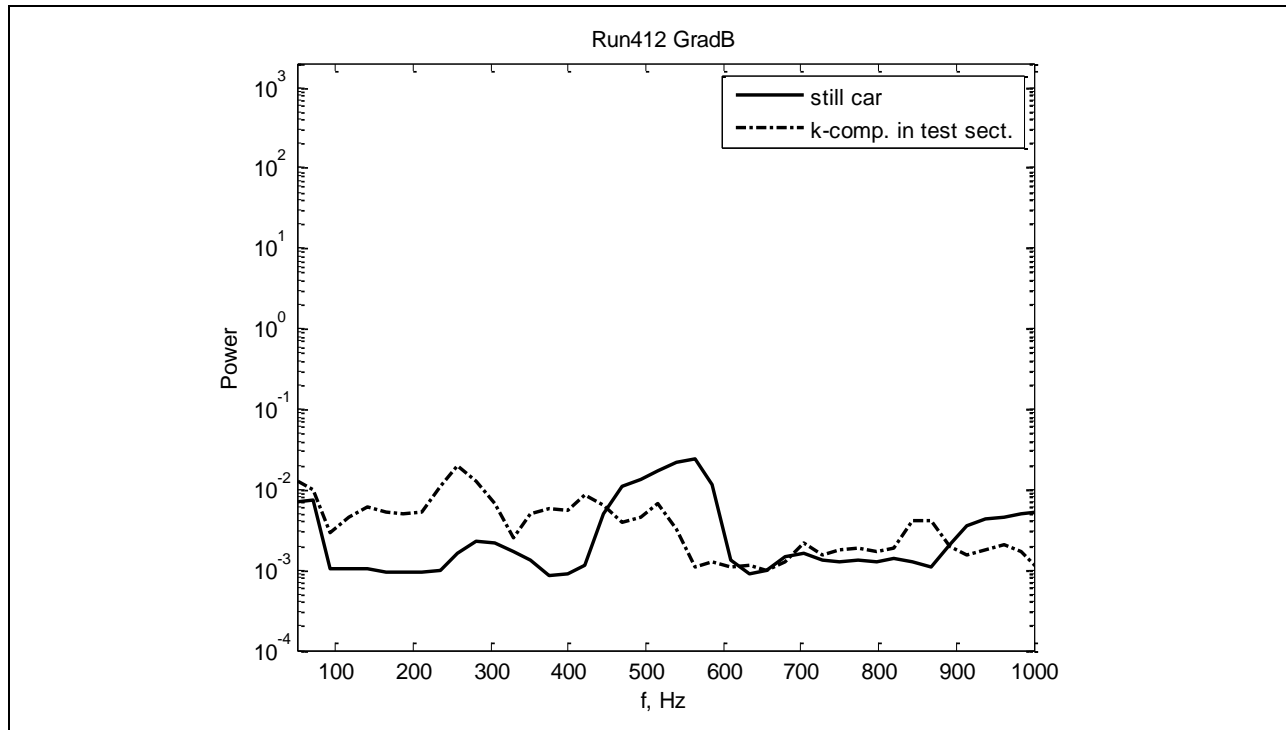


Figure 752: Power spectra in test section.

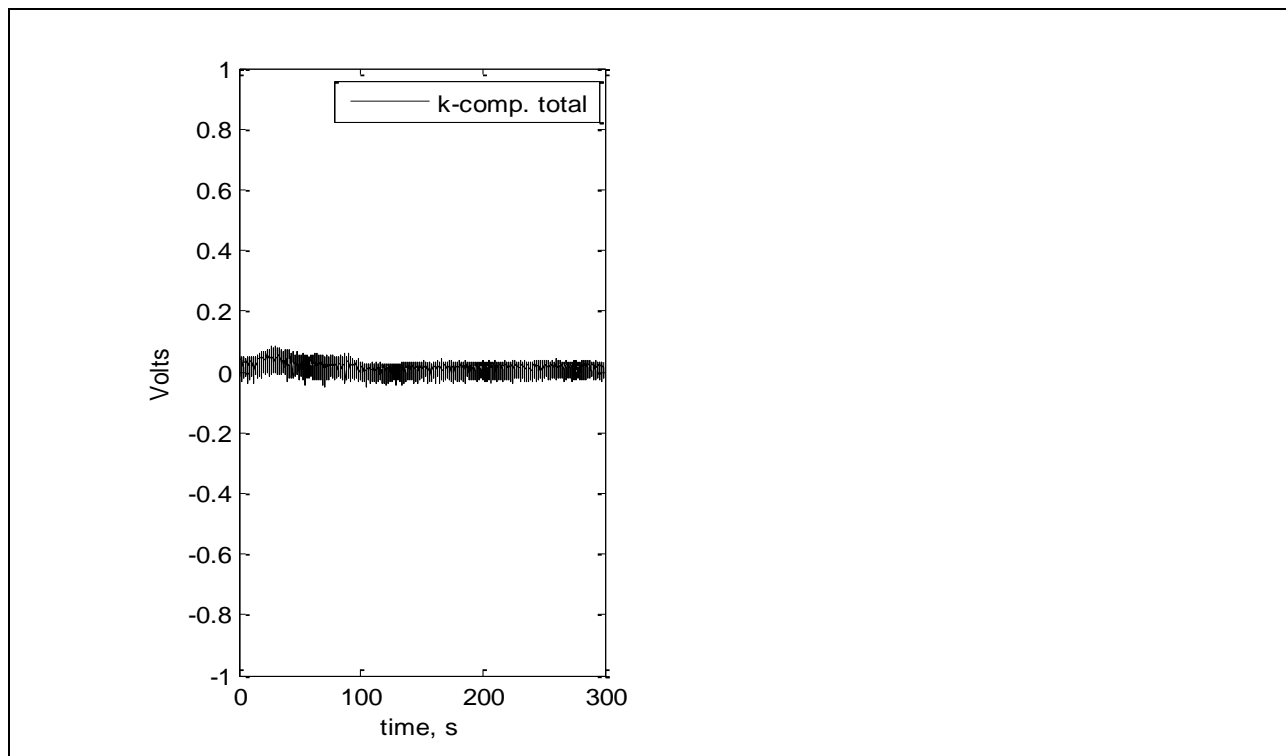


Figure 753: Voltage for full run.

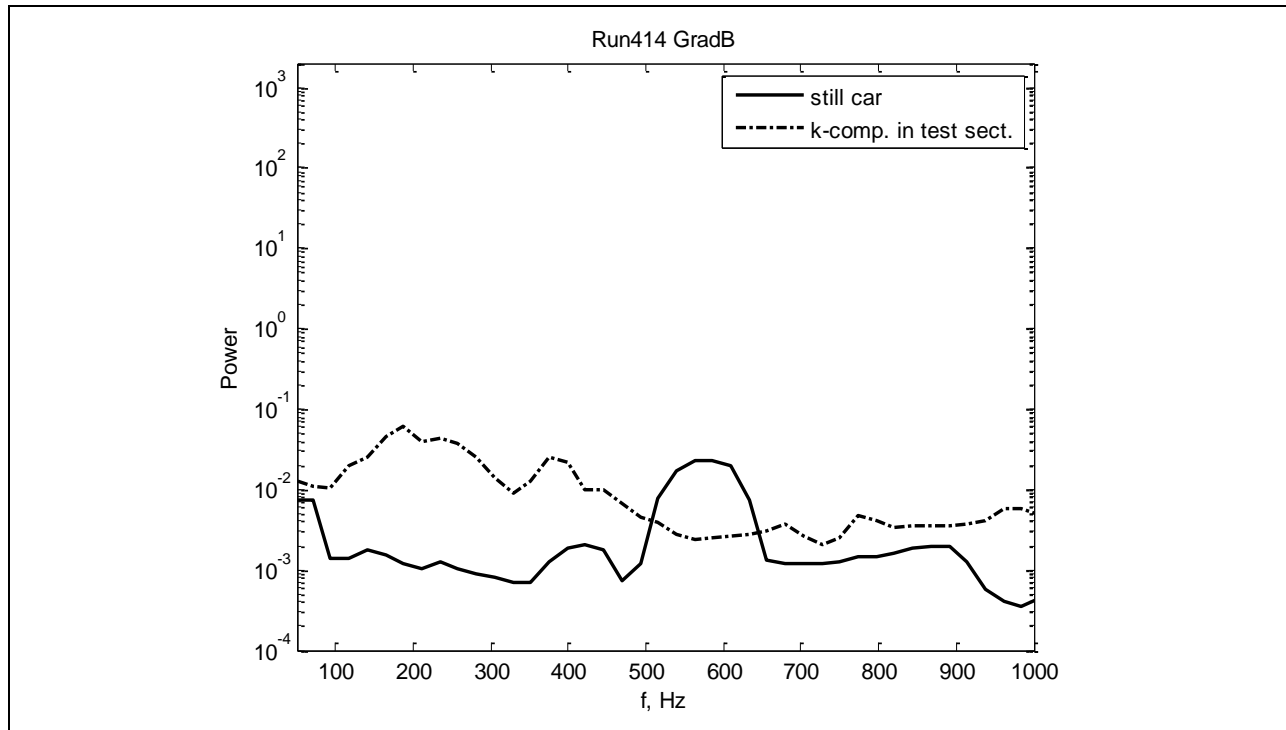


Figure 754: Power spectra in test section.

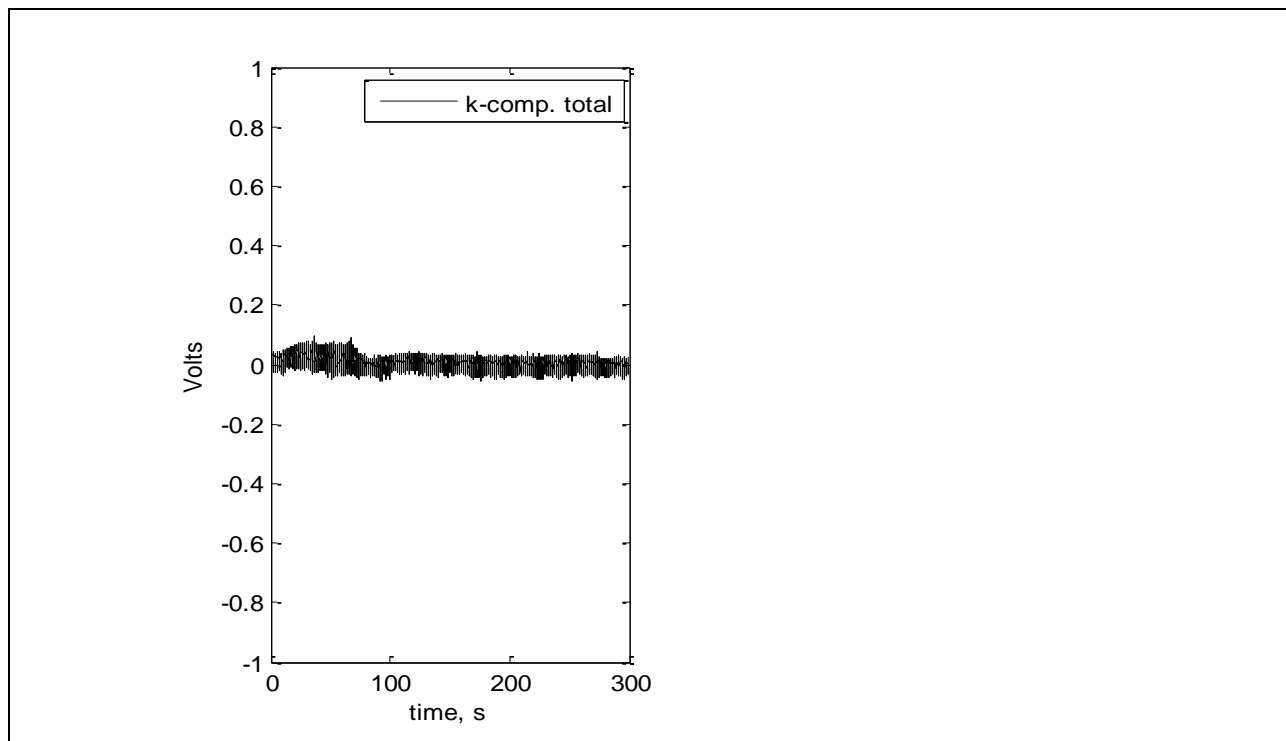


Figure 755: Voltage for full run.

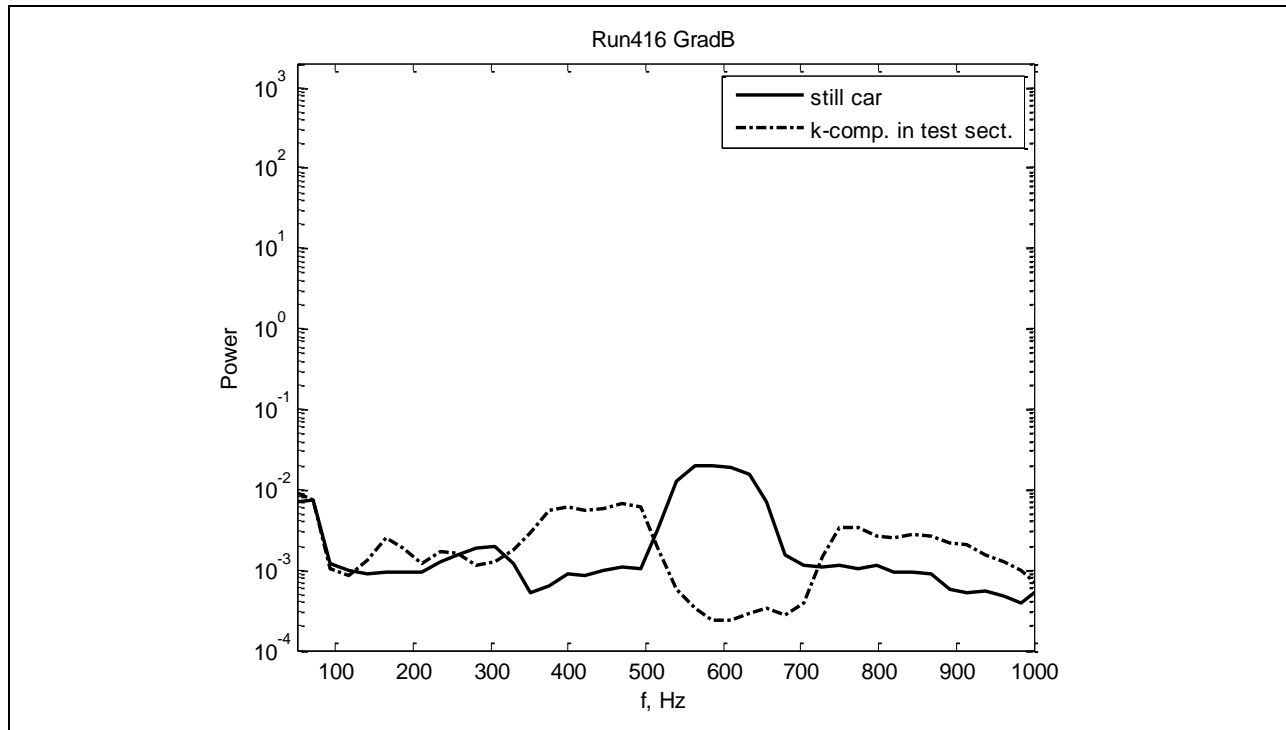


Figure 756: Power spectra in test section.

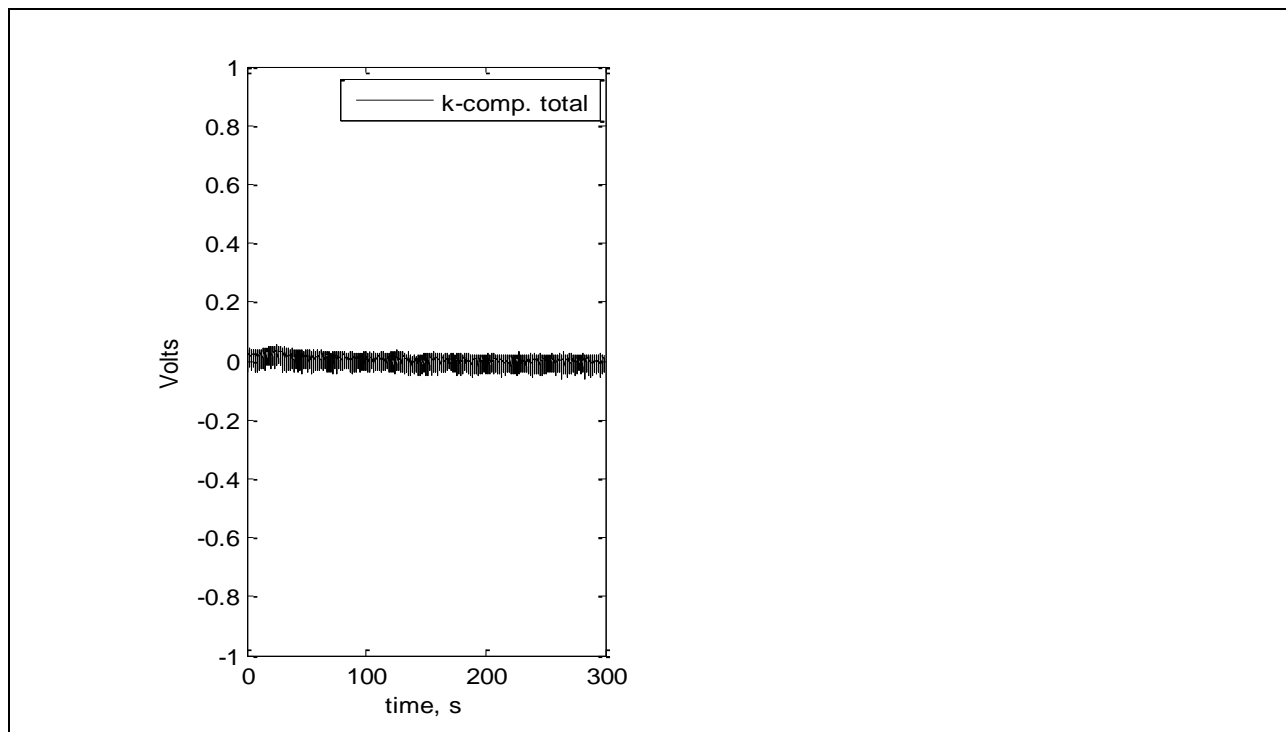


Figure 757: Voltage for full run.

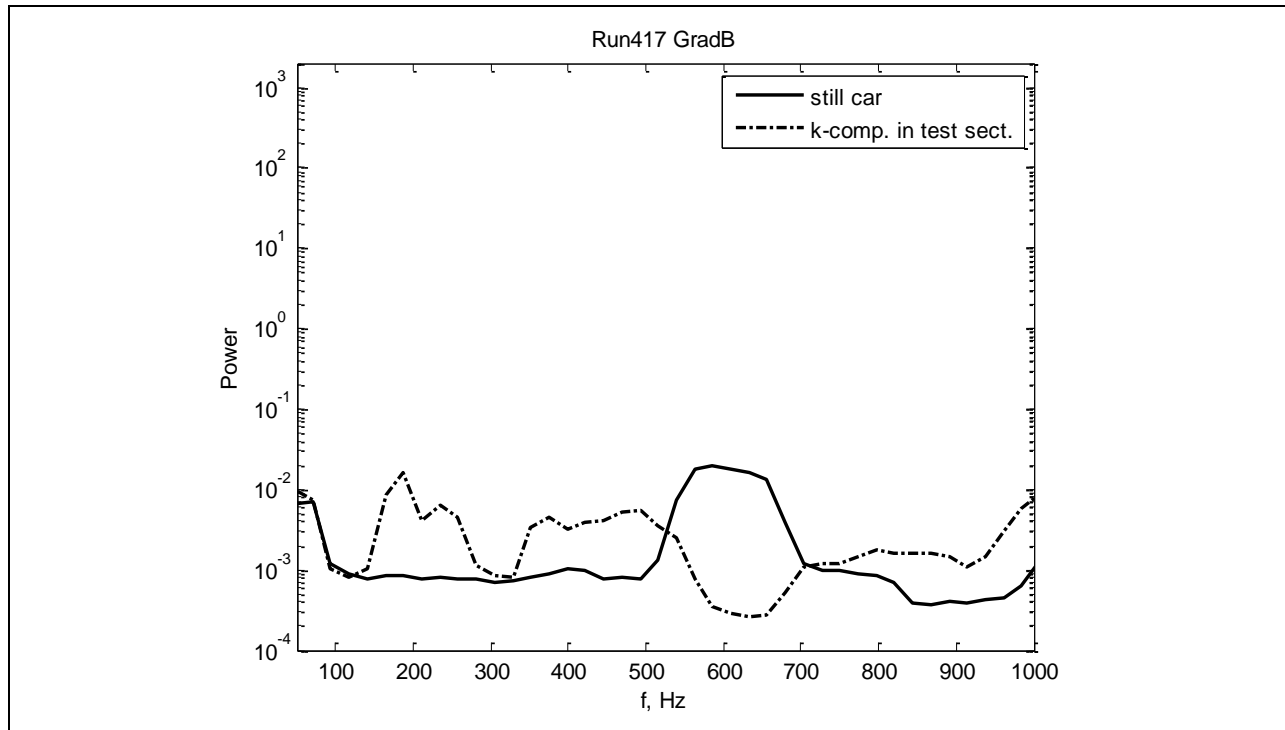


Figure 758: Power spectra in test section.

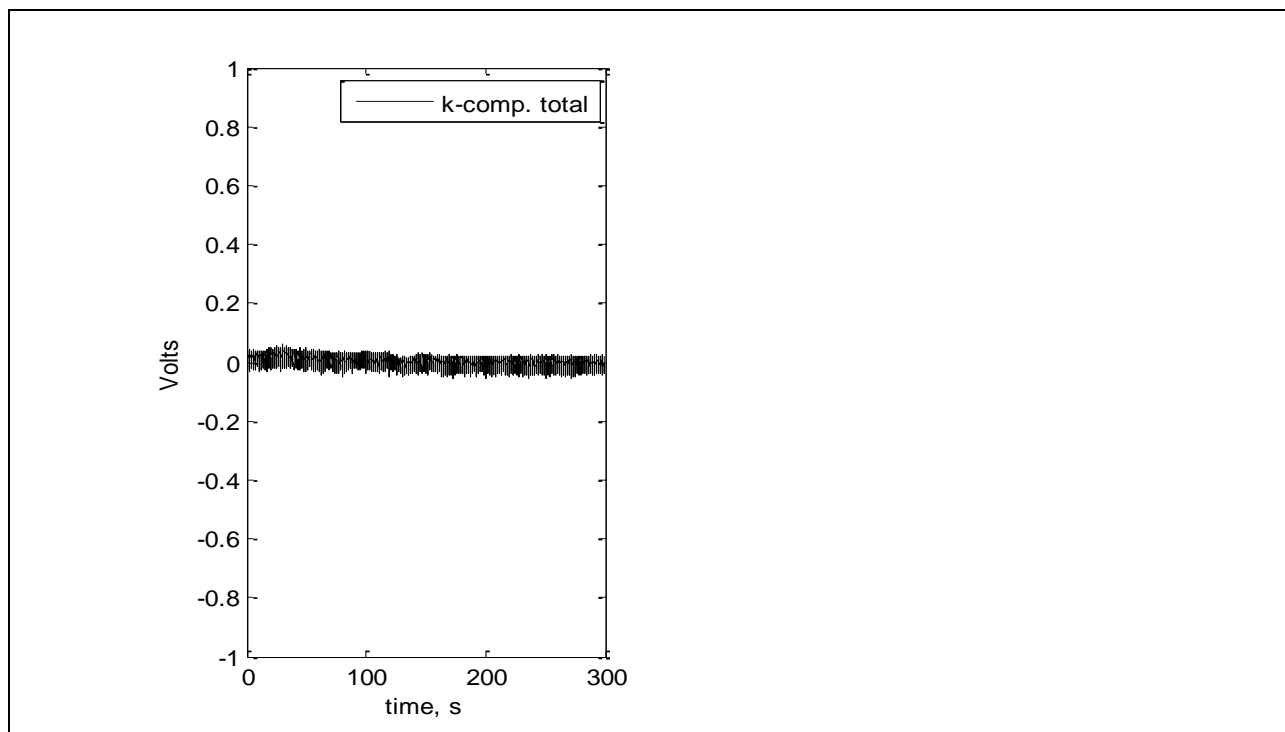


Figure 759: Voltage for full run.

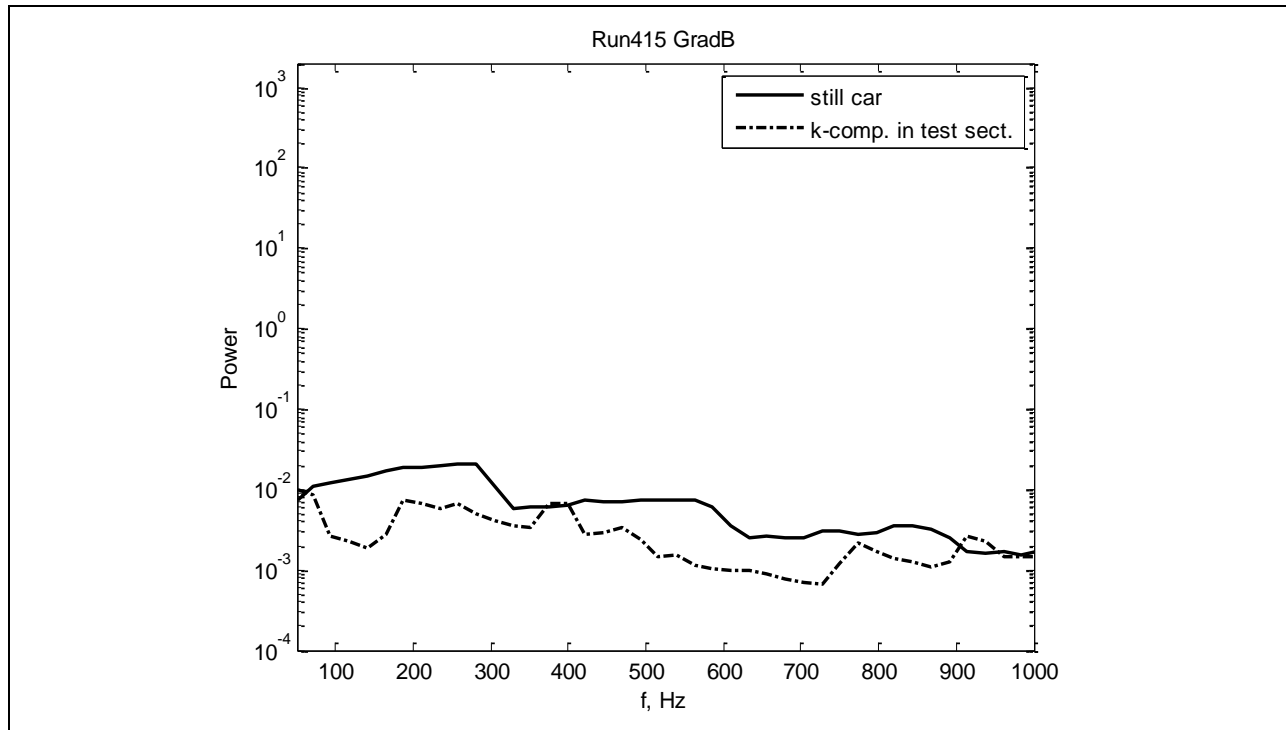


Figure 760: Power spectra in test section.

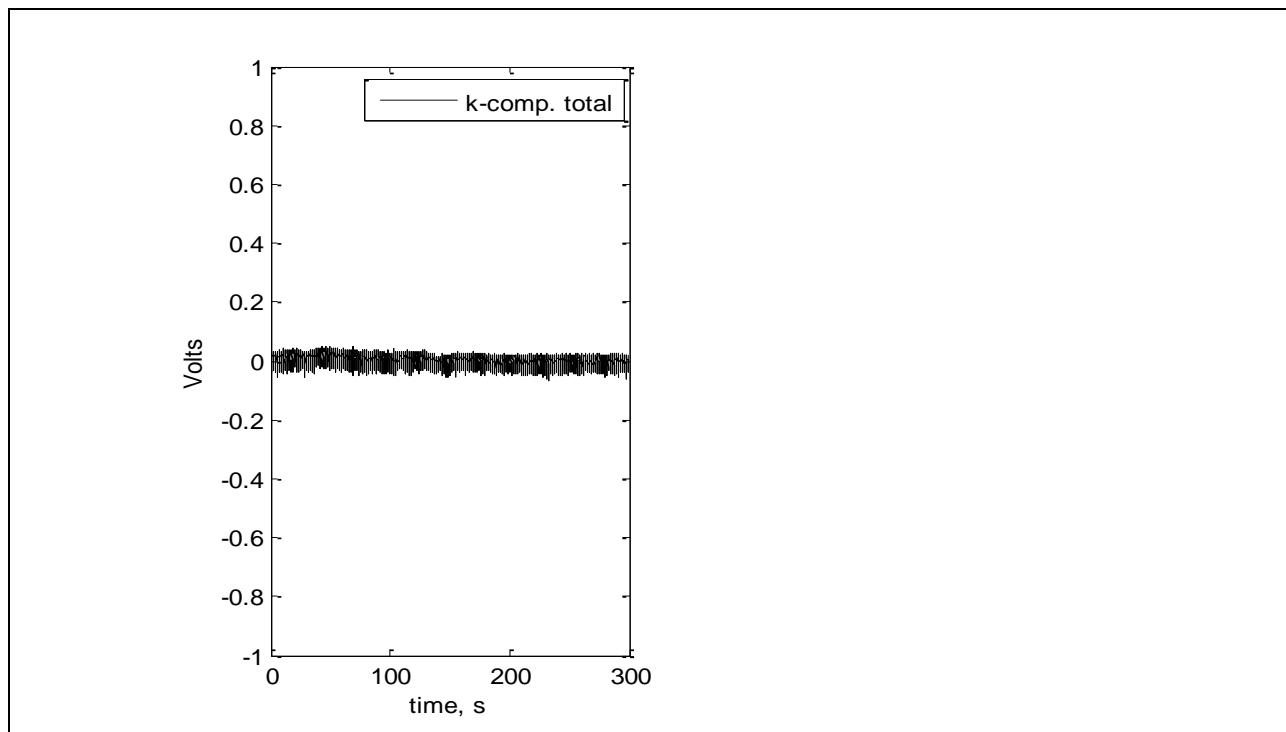


Figure 761: Voltage for full run.

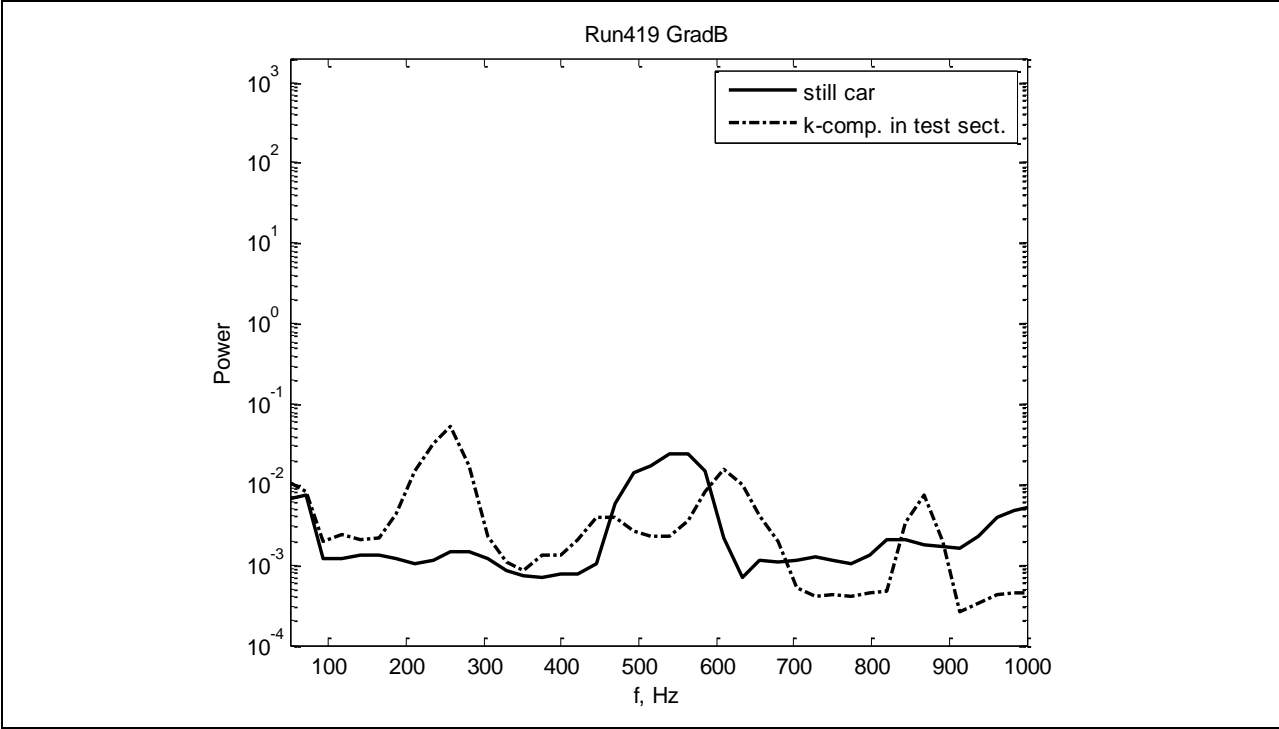


Figure 762: Power spectra in test section.

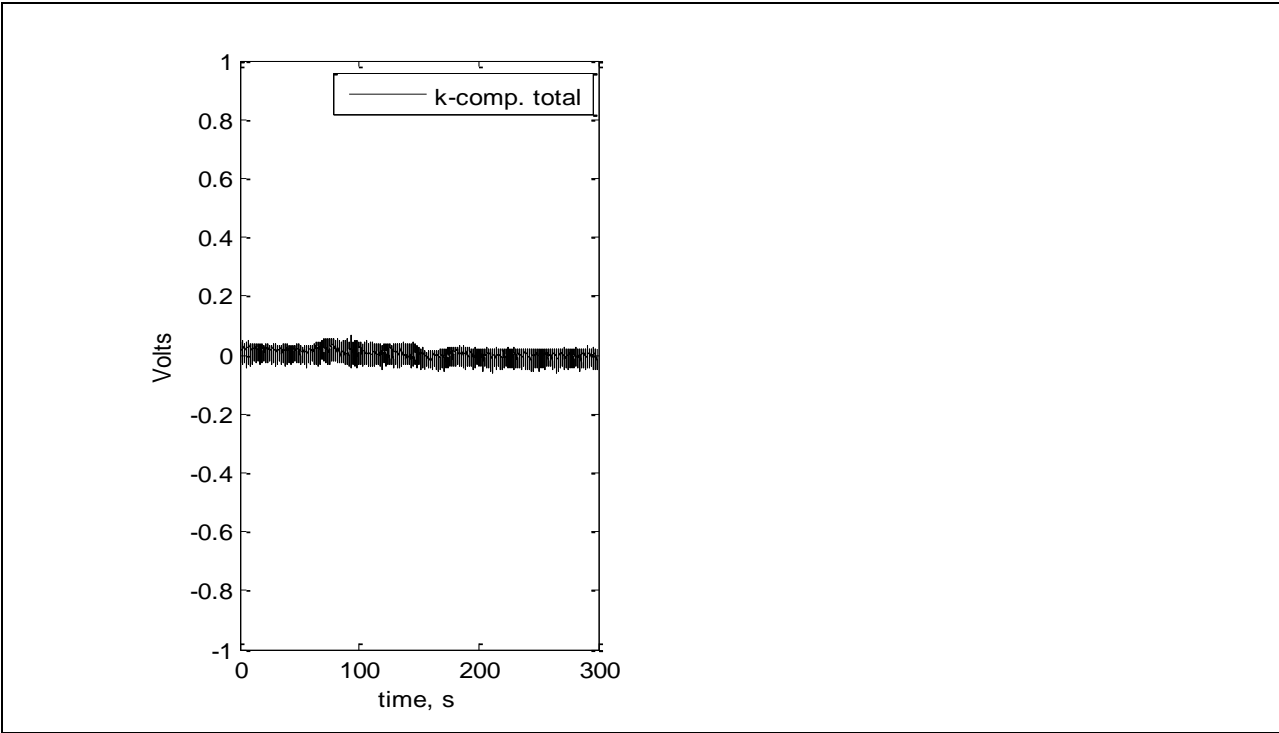


Figure 763: Voltage for full run.

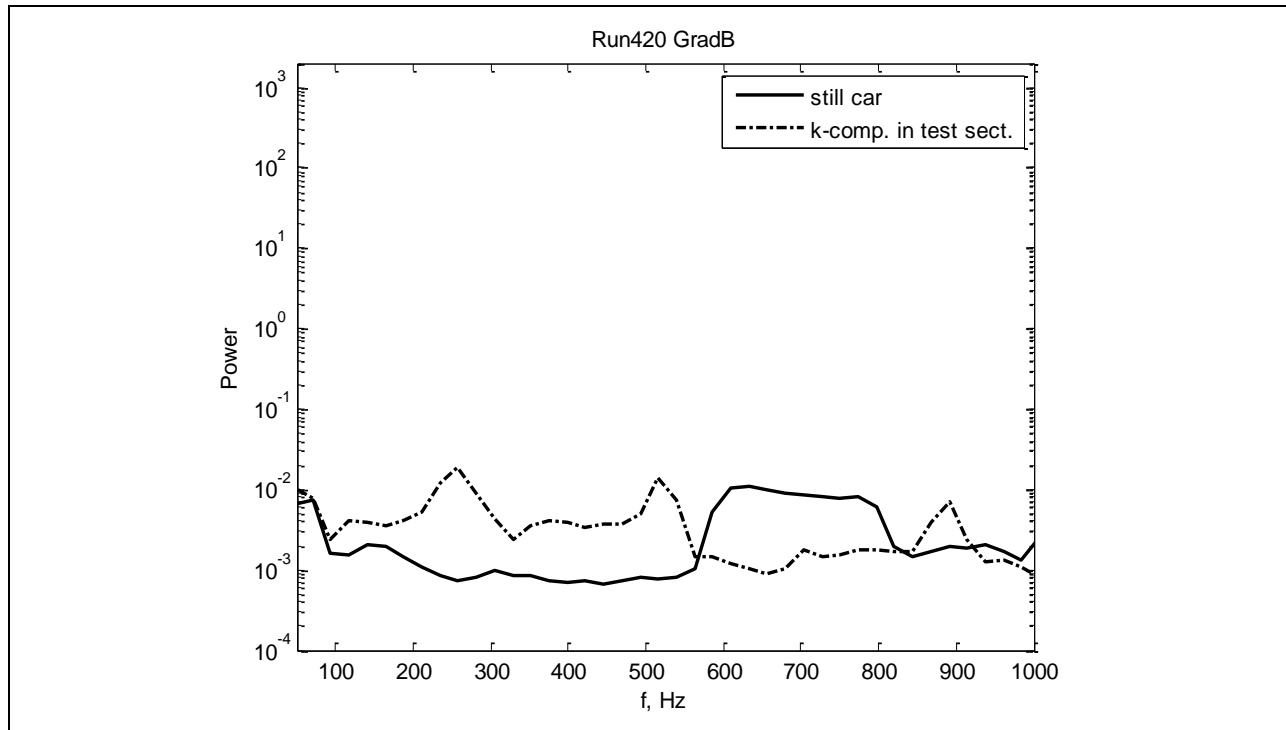


Figure 764: Power spectra in test section.

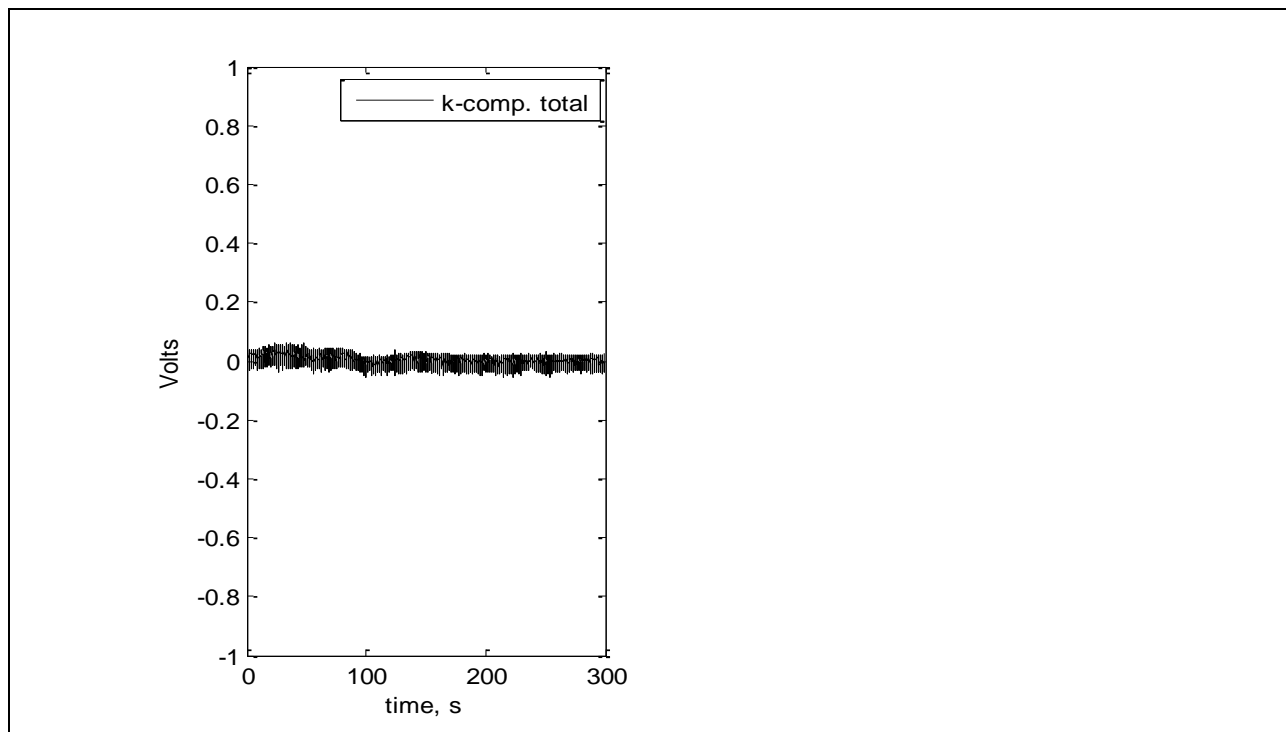


Figure 765: Voltage for full run.

7.5.7.7

Flow characterization

Plots of the following flow parameters for all three models (Gradient-Zero, Gradient-A, and Gradient-B, in that order) are presented below.

Profiles of the local freestream speed, U_e , normalized with upstream freestream speed, U_e/U_∞ , are shown in Figure 766, Figure 773 and Figure 779 for Gradient-Zero, Gradient-A and Gradient-B, correspondingly. The distributions are given for two different speeds and show approximately the same velocity gradient after the step location along the model.

The displacement thicknesses, δ^* (denoted delta* in the plot) are shown in Figure 767, Figure 774 and Figure 780 for Gradient-Zero, Gradient-A and Gradient-B, correspondingly. The distributions are given for two different speeds and show that displacement thickness depends on freestream speed.

The coefficient of pressure, C_p , is shown in Figure 768, Figure 775 and Figure 781 for Gradient-Zero, Gradient-A and Gradient-B, correspondingly. The distribution is given for the highest speed (it looks almost the same for all other speeds). After the leading edge section, it is negative and decreasing with streamwise distance meaning that the pressure drops with streamwise distance.

The acceleration parameter (or nondimensional pressure gradient), $K = v_e/U_e^2 dU_e/ds$ is shown in Figure 769, Figure 776 and Figure 782 for Gradient-Zero, Gradient-A and Gradient-B, correspondingly. After the step location it is relatively constant along each model, and positive, meaning that flow is accelerating and slightly depends on freestream speed.

The shape factor, $H = \delta^*/\theta$ is shown in Figure 770, Figure 777 and Figure 783 for Gradient-Zero, Gradient-A and Gradient-B, correspondingly. It has a weak dependence on freestream speed and decreases with streamwise distance after step location.

The pressure parameter, β (denoted beta in the plot) is shown in Figure 771, Figure 778 and Figure 784 for Gradient-Zero, Gradient-A and Gradient-B, correspondingly. It has a weak dependence on freestream speed and grows with stream-wise distance after the step location. The β parameter was found using the assumption of local similarity of the flow (see explanations below).

An additional plot relating the pressure parameter, β , to the shape factor, H , for similar flows is given in Figure 772. Data for this plot are taken from Obremski et al (1969)²³.

The variation of the shape factors with streamwise distance indicates that the flows for all three models are not similar (and the flow for Gradient-Zero model is not of Blasius type). However we can consider our flows as locally similar: the shape of the model can be thought as a set of very small wedges. Each such wedge has its own inclination angle and the flow over such wedge is similar having constant H and β independent on streamwise position¹³. Under the assumption of local similarity and knowing the value of H at each streamwise position and using the unique relation between H and β for similar flows (see Obremski et al 1969²³), we can find β for all streamwise positions for our flows.

Comparisons of H and β as functions of streamwise distance for all three models are shown in Figure 785 and Figure 786, respectively.

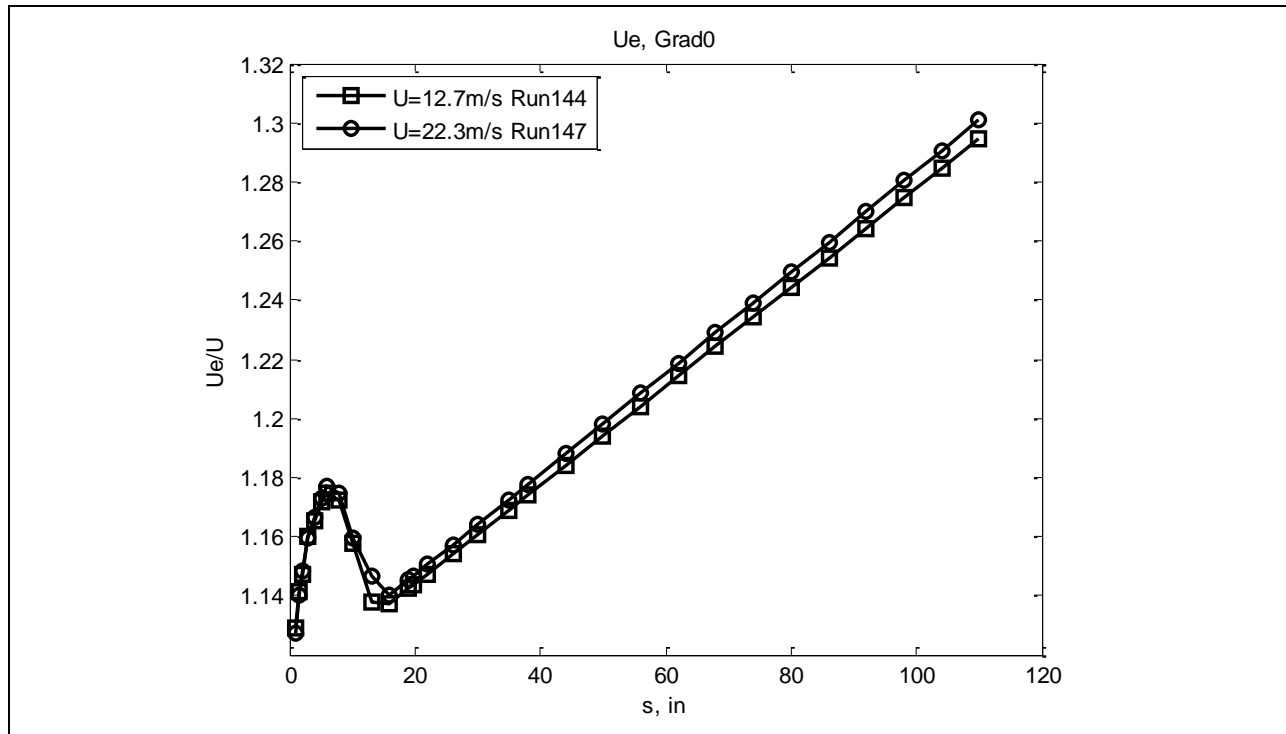


Figure 766: Local freestream speed.

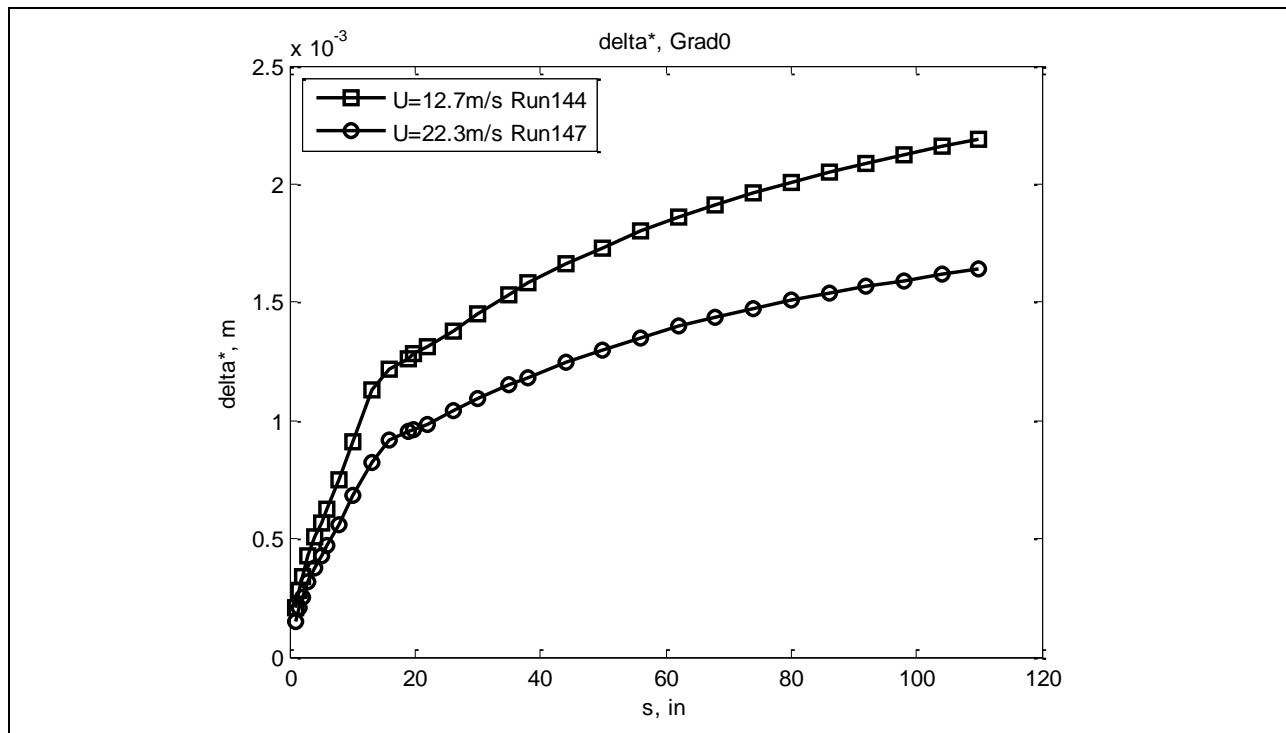


Figure 767: Displacement thickness.

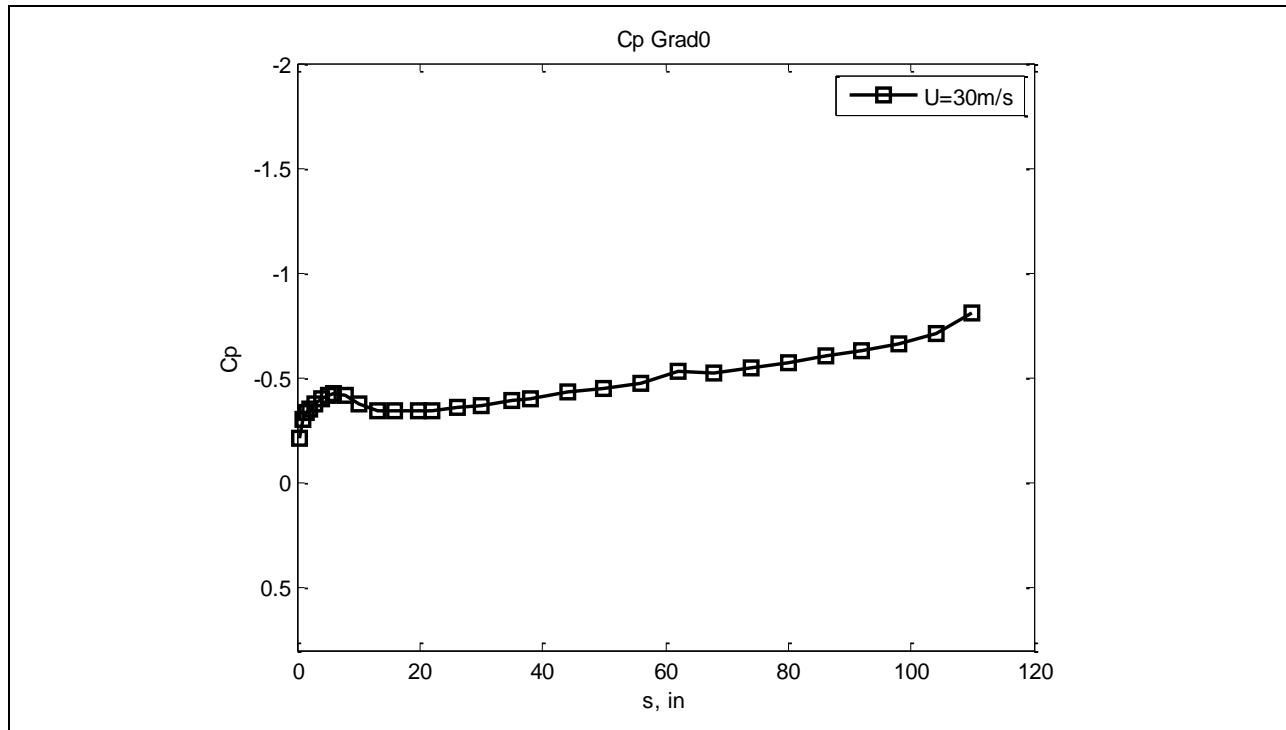


Figure 768: Coefficient of pressure.

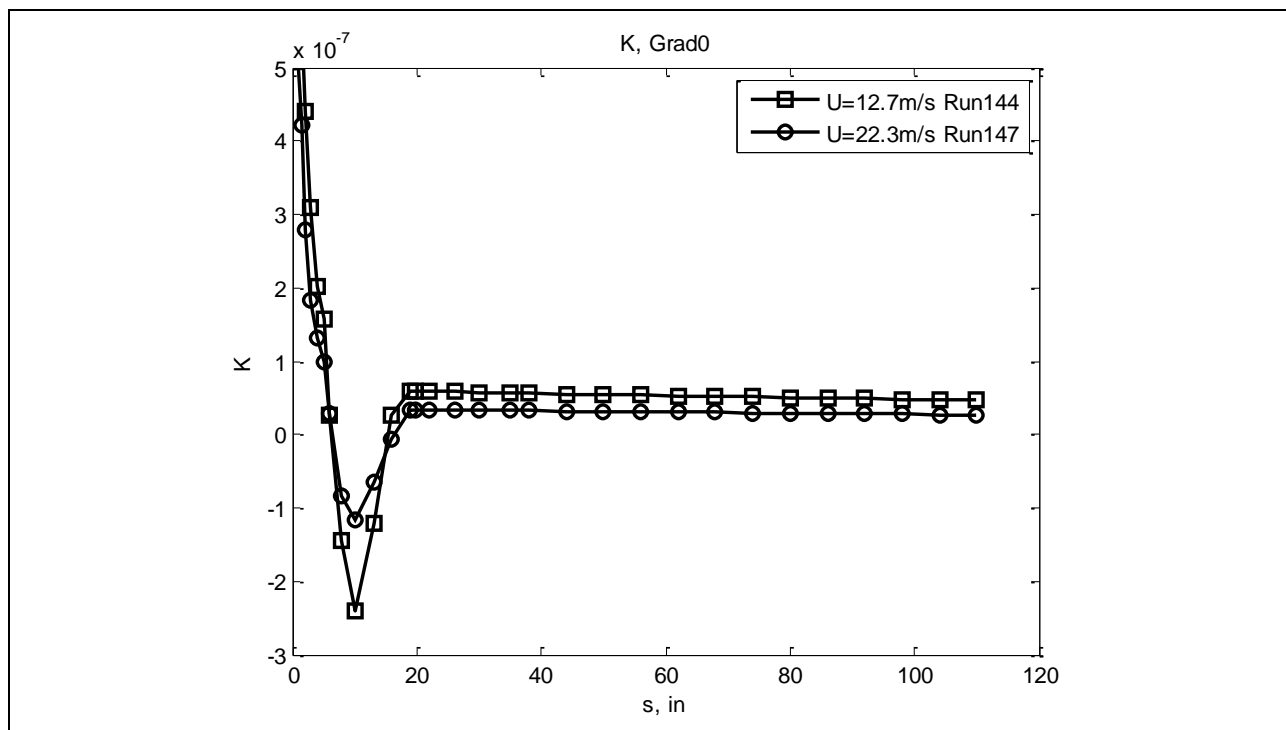


Figure 769: Nondimensional pressure gradient.

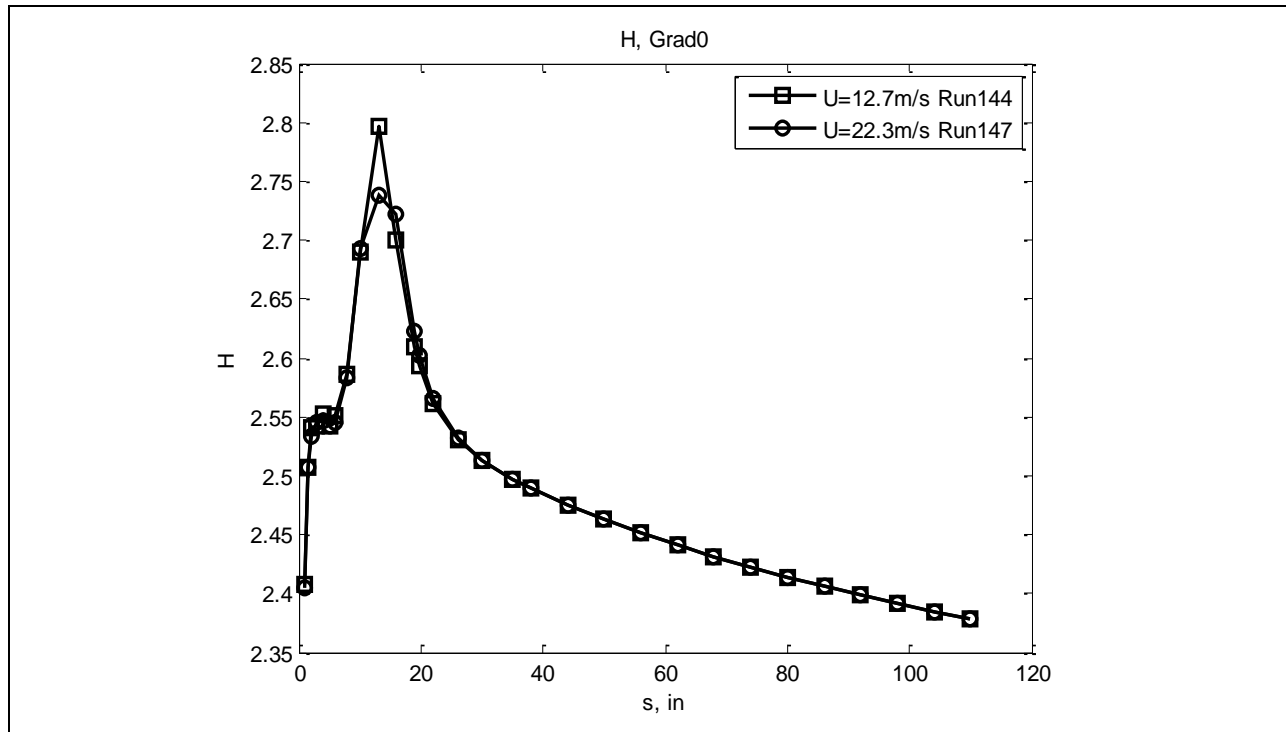


Figure 770: Shape factor.

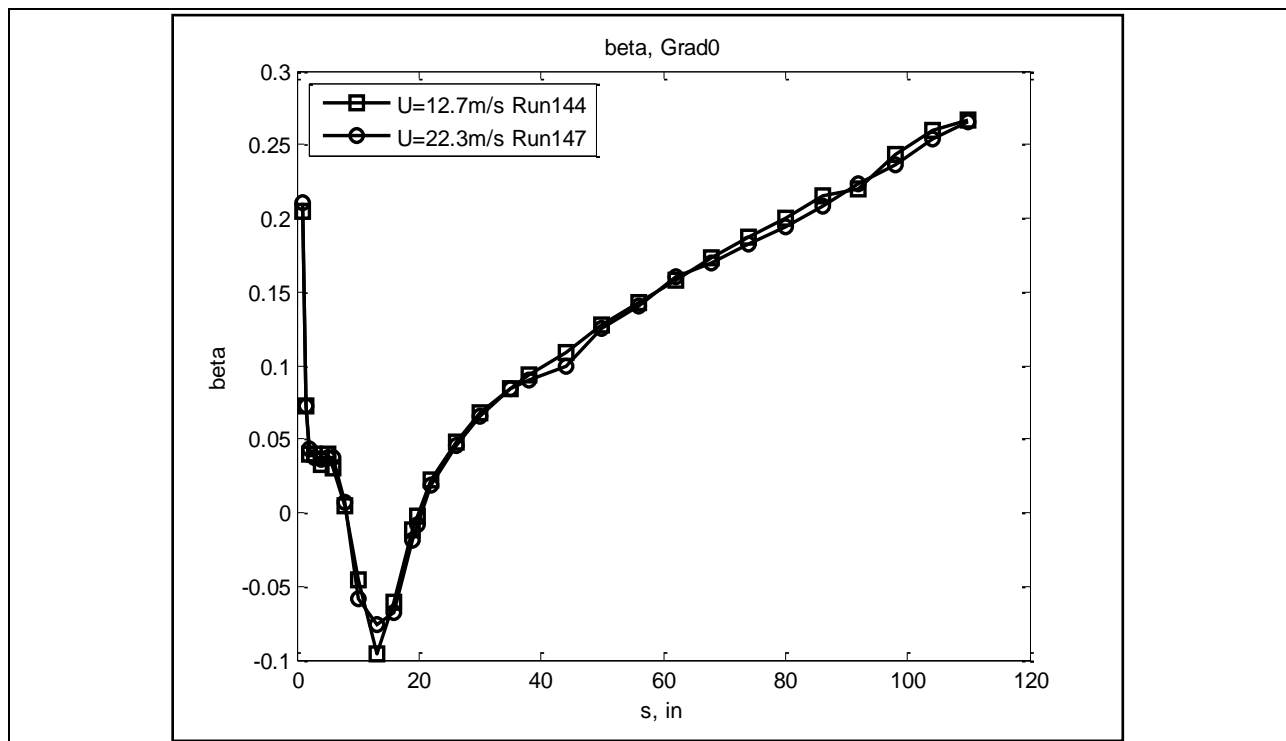


Figure 771: Pressure parameter versus shape factor.

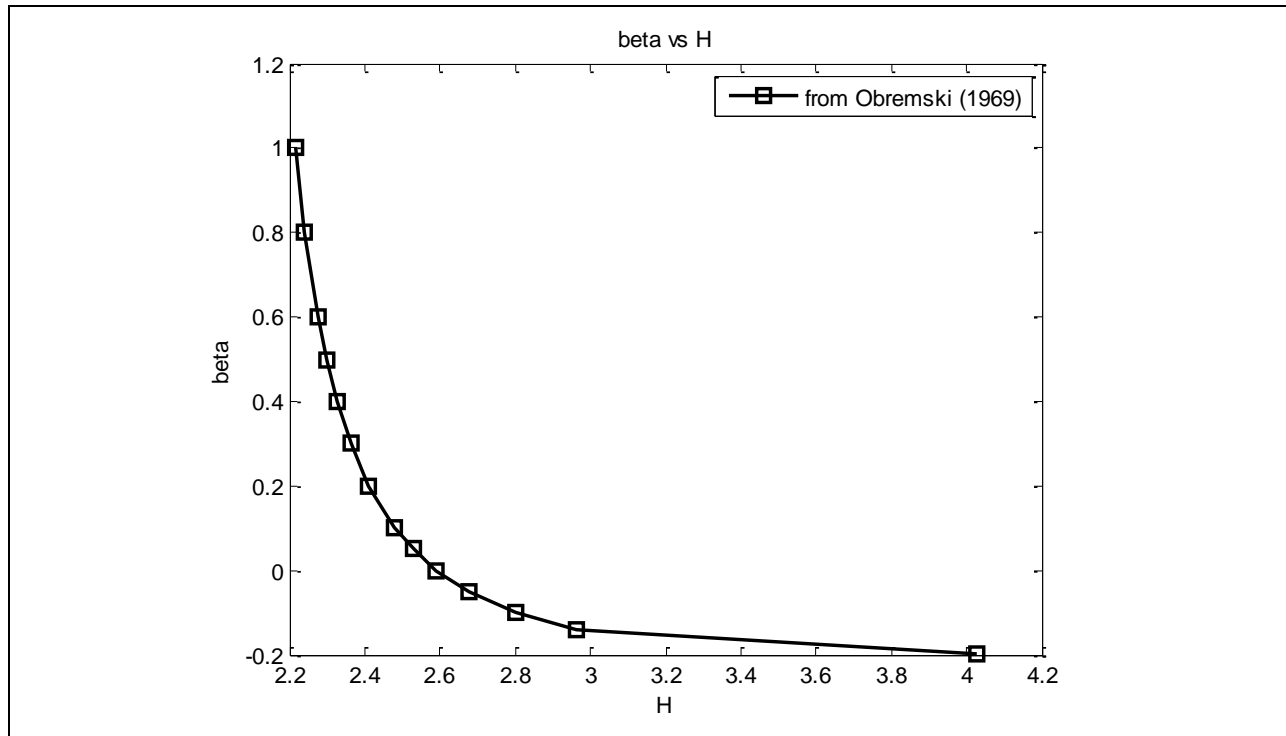


Figure 772: Pressure parameter.

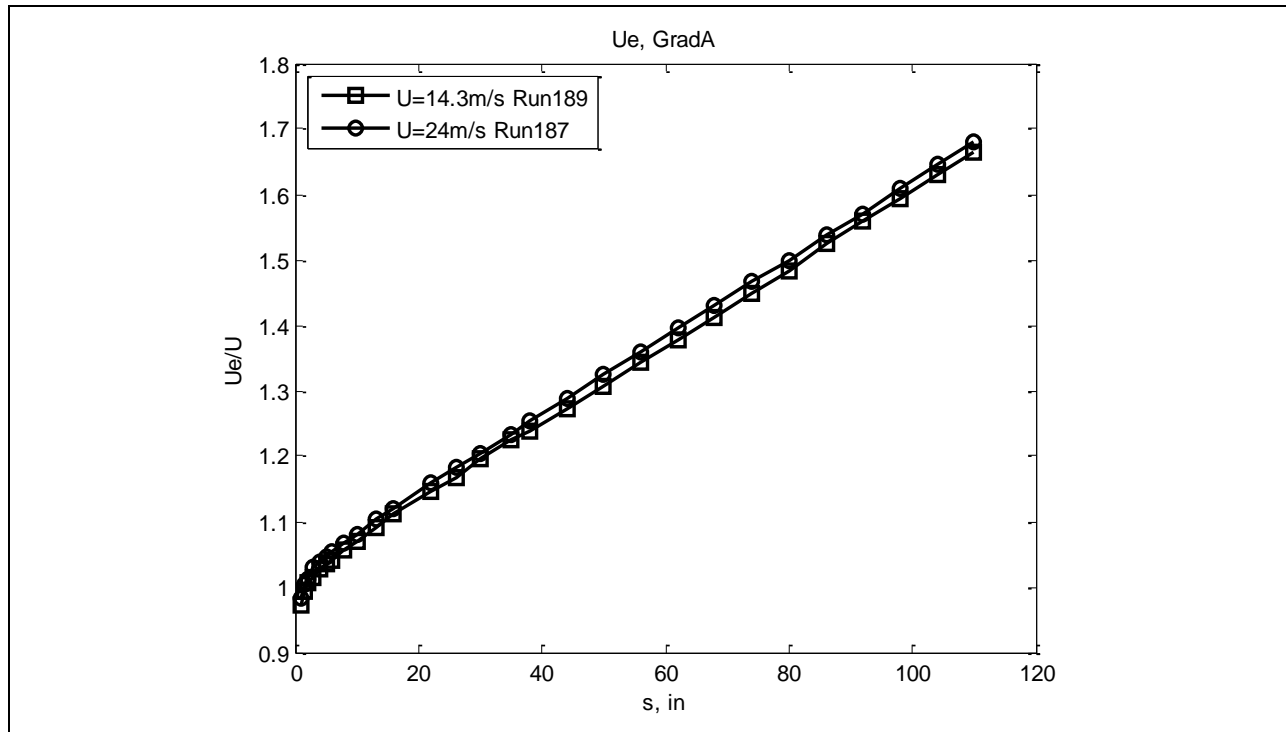


Figure 773: Local freestream speed.

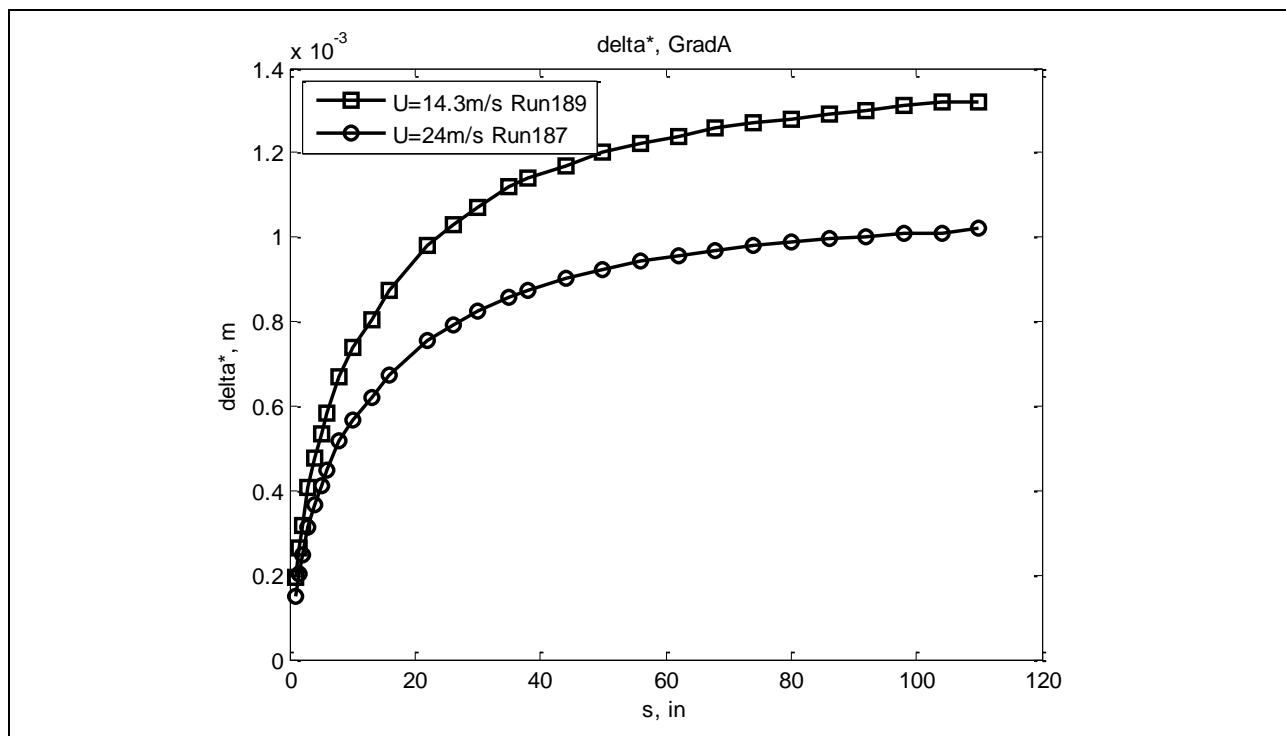


Figure 774: Displacement thickness.

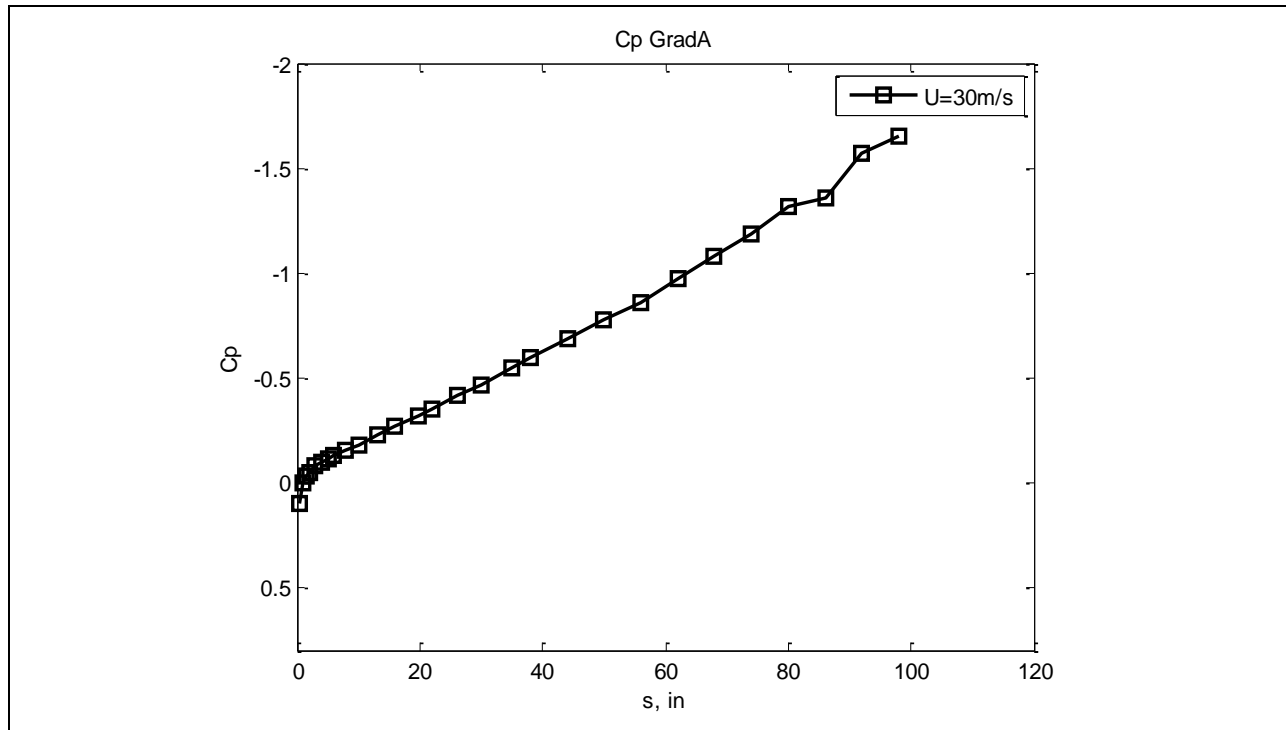


Figure 775: Coefficient of pressure.

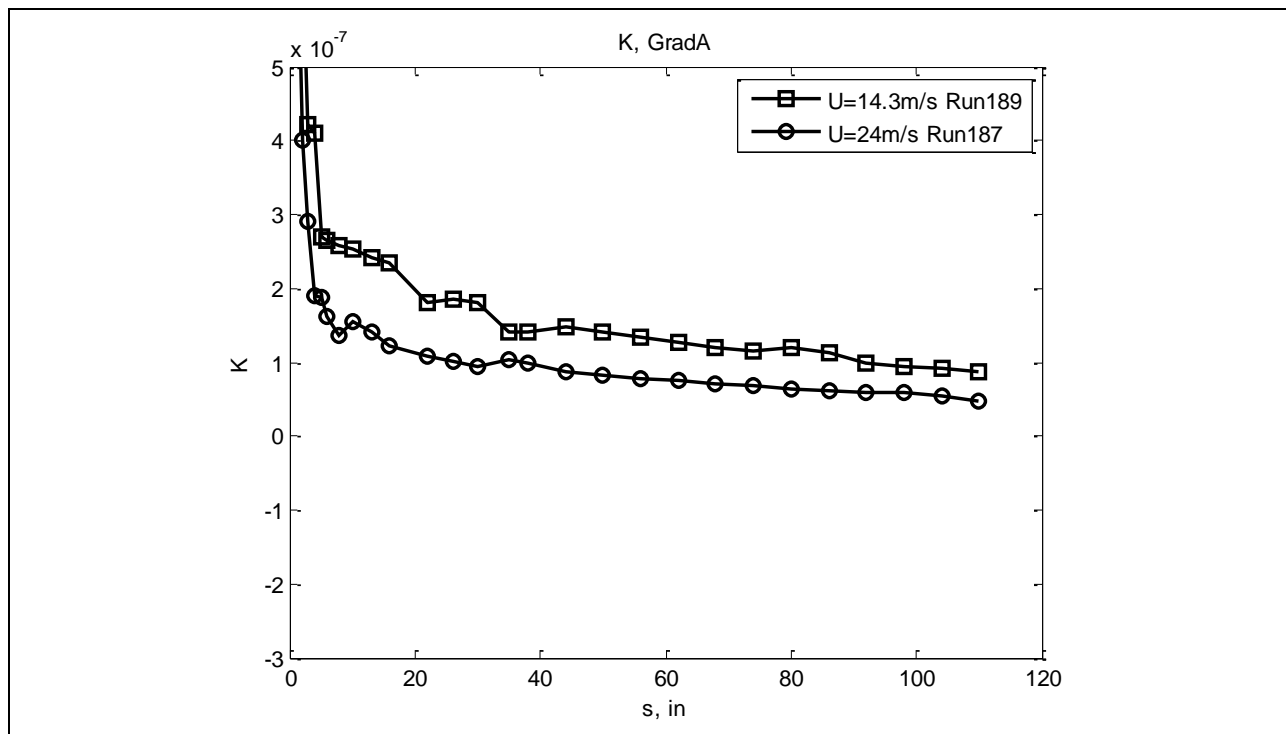


Figure 776: Nondimensional pressure gradient.

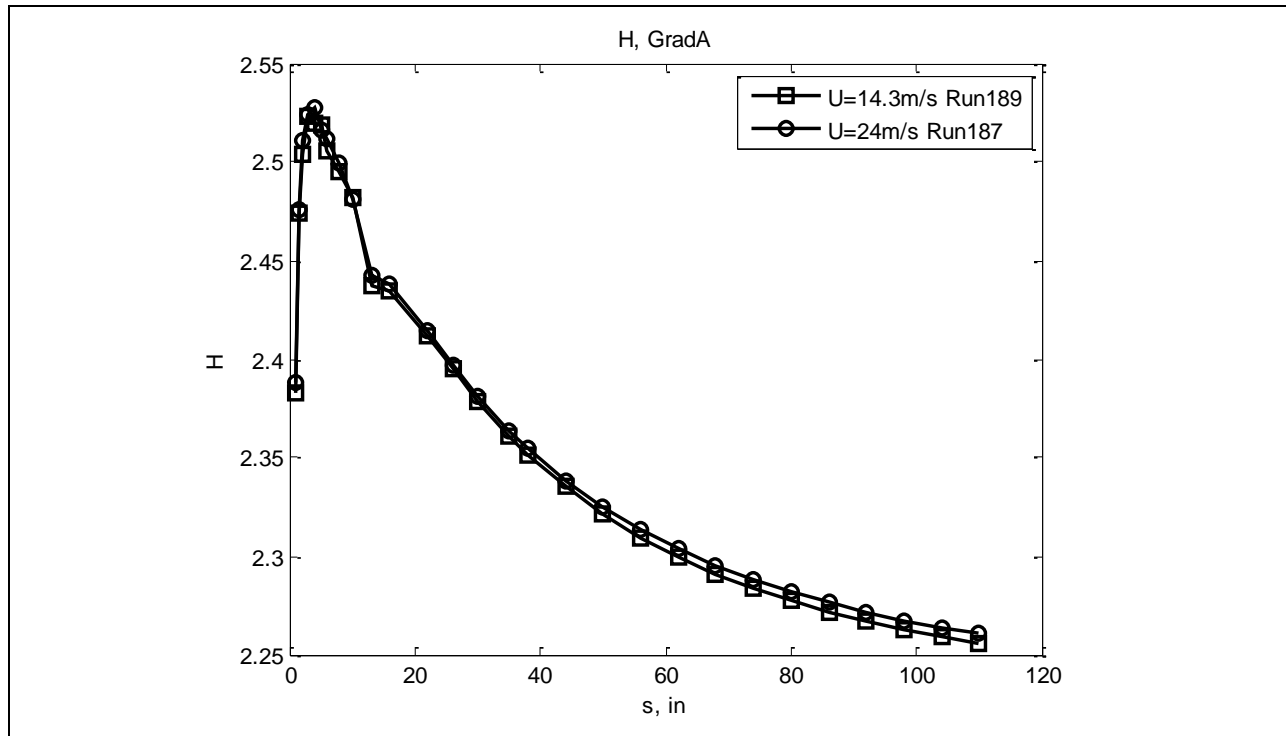


Figure 777: Shape factor.

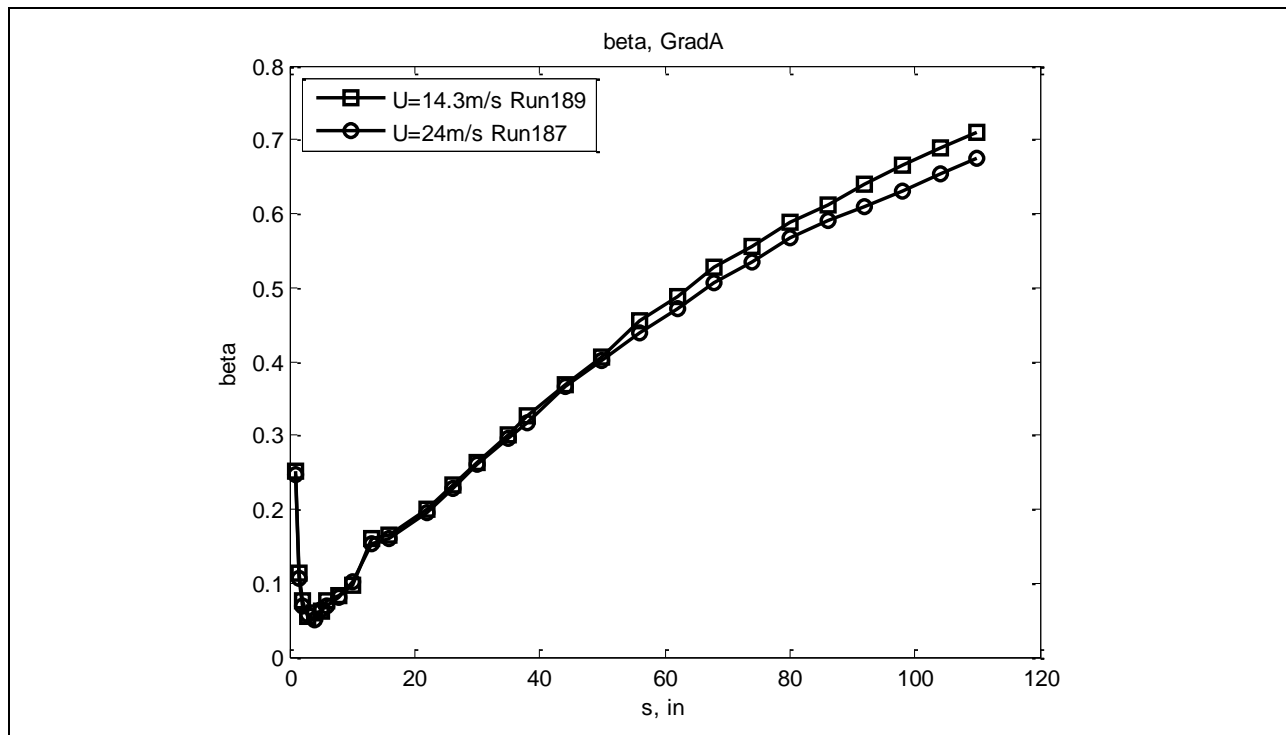


Figure 778: Pressure parameter.

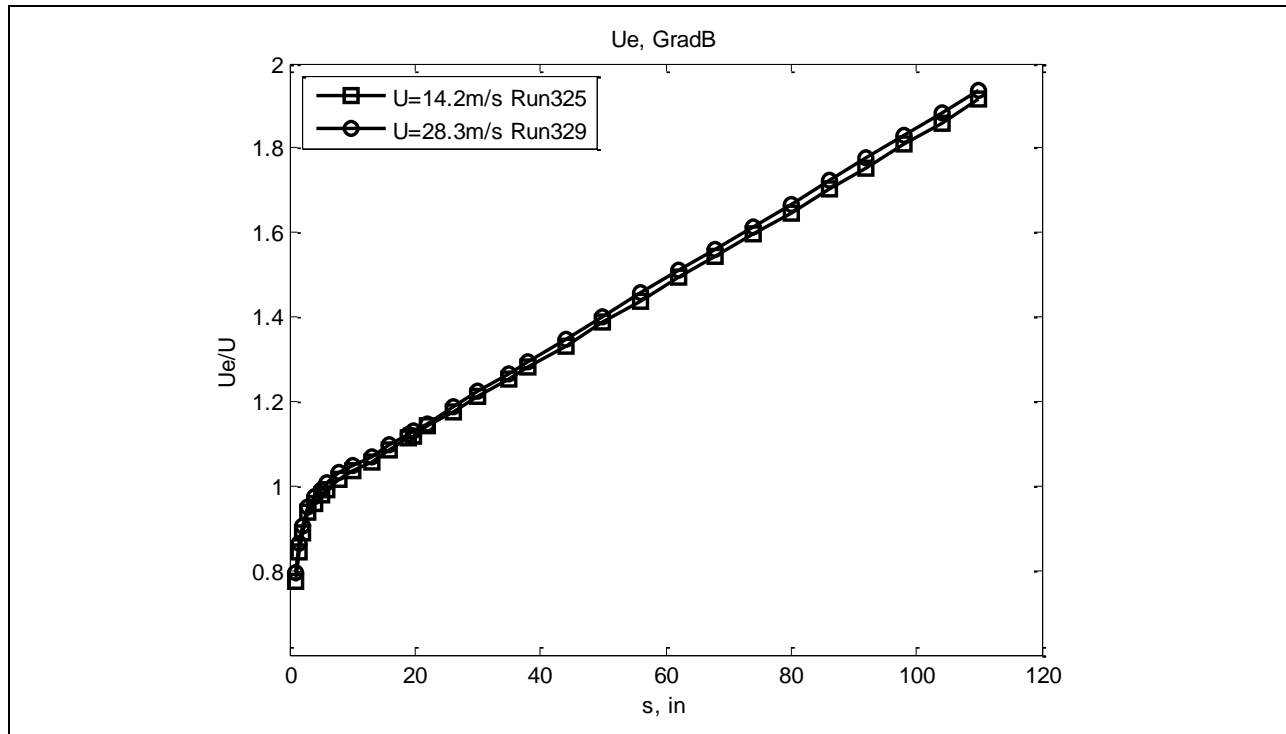


Figure 779: Local freestream speed.

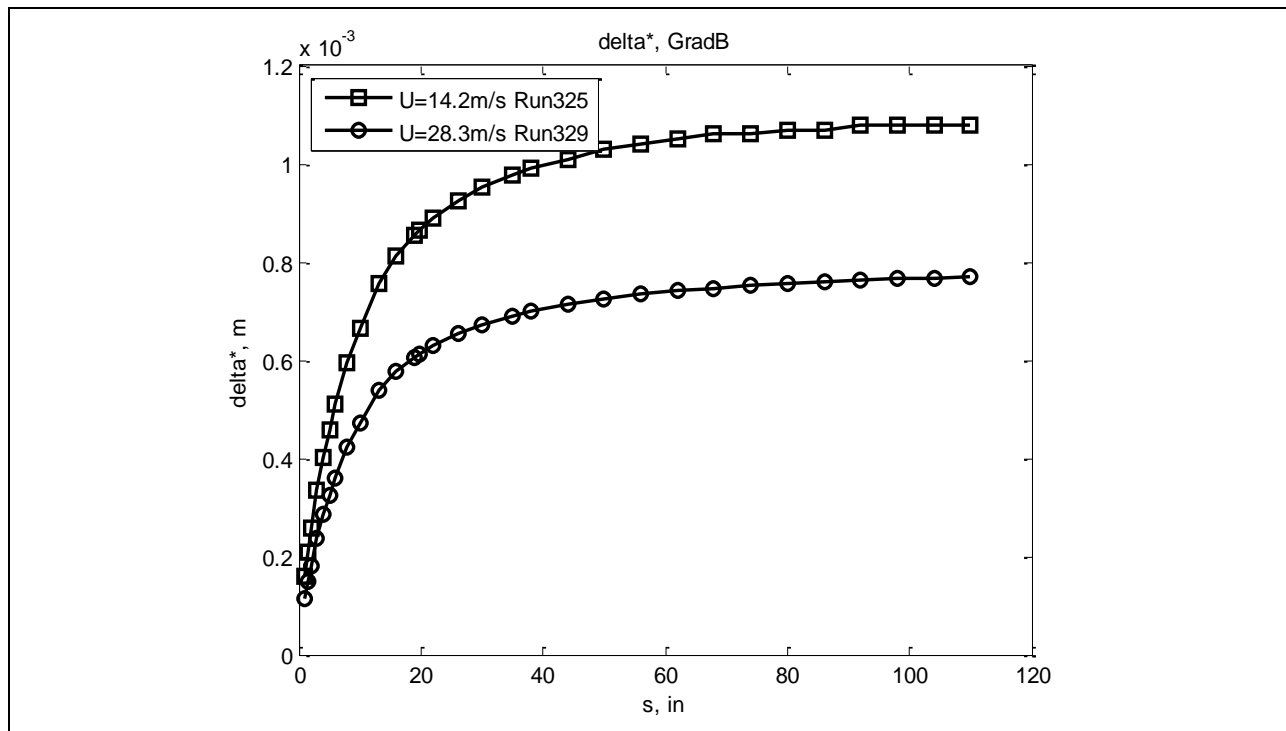


Figure 780: Displacement thickness.

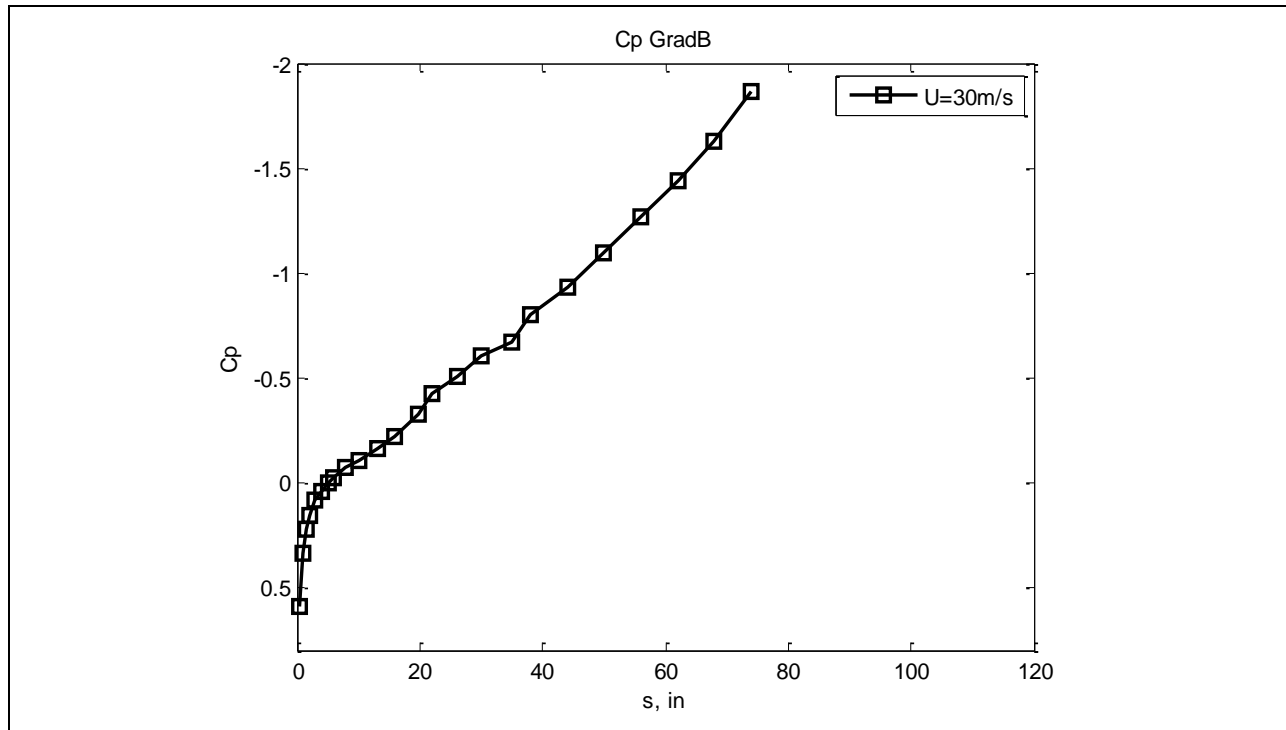


Figure 781: Coefficient of pressure.

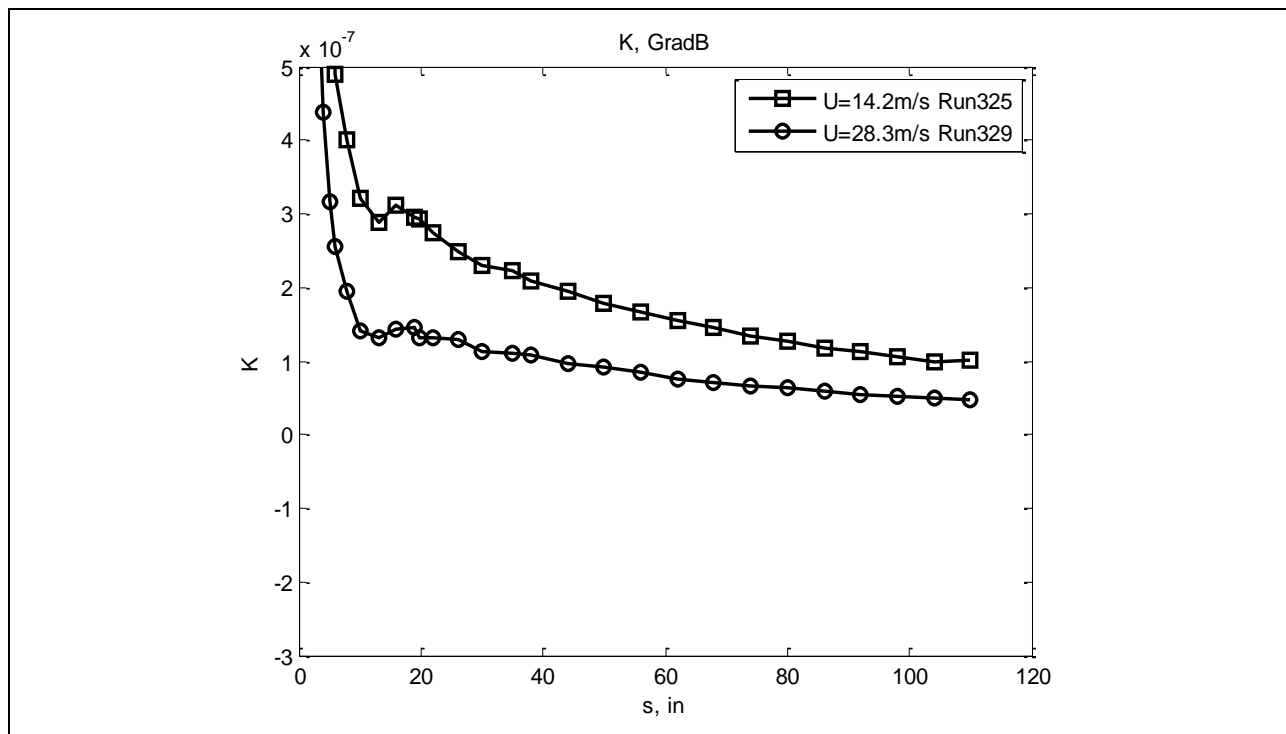


Figure 782: Nondimensional pressure gradient.

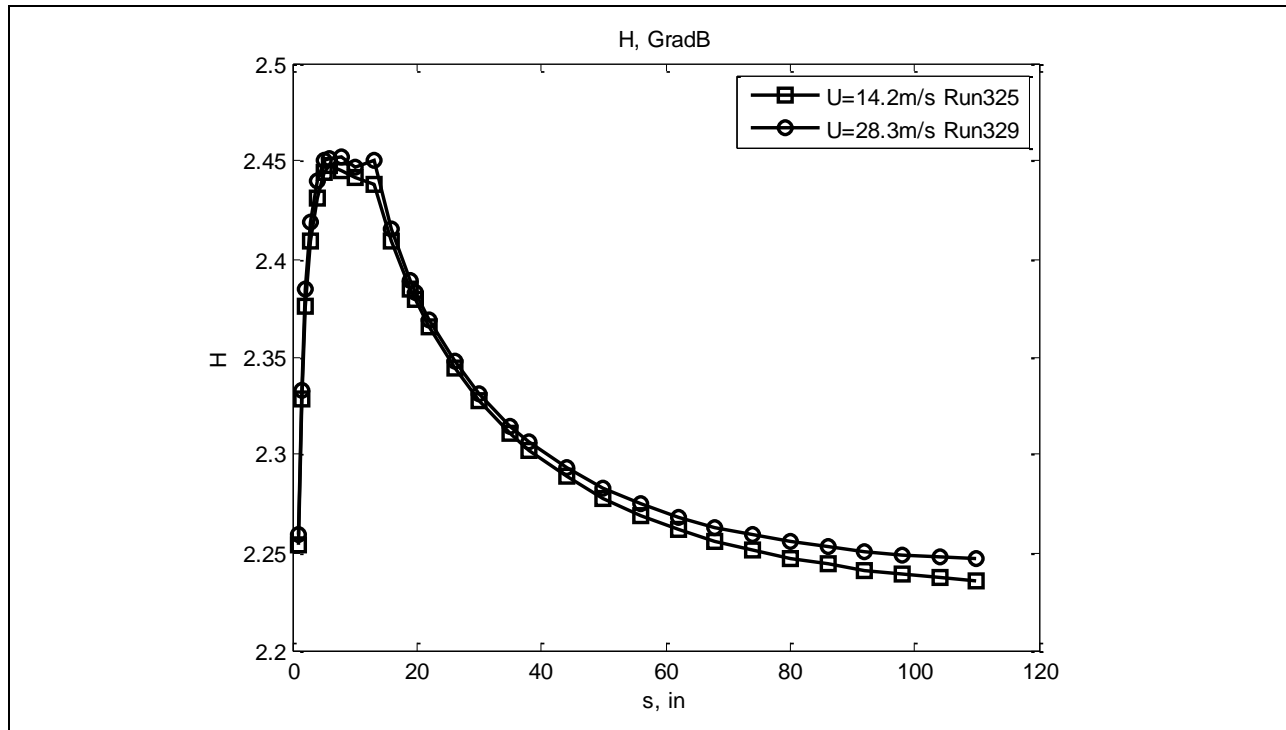


Figure 783: Shape factor.

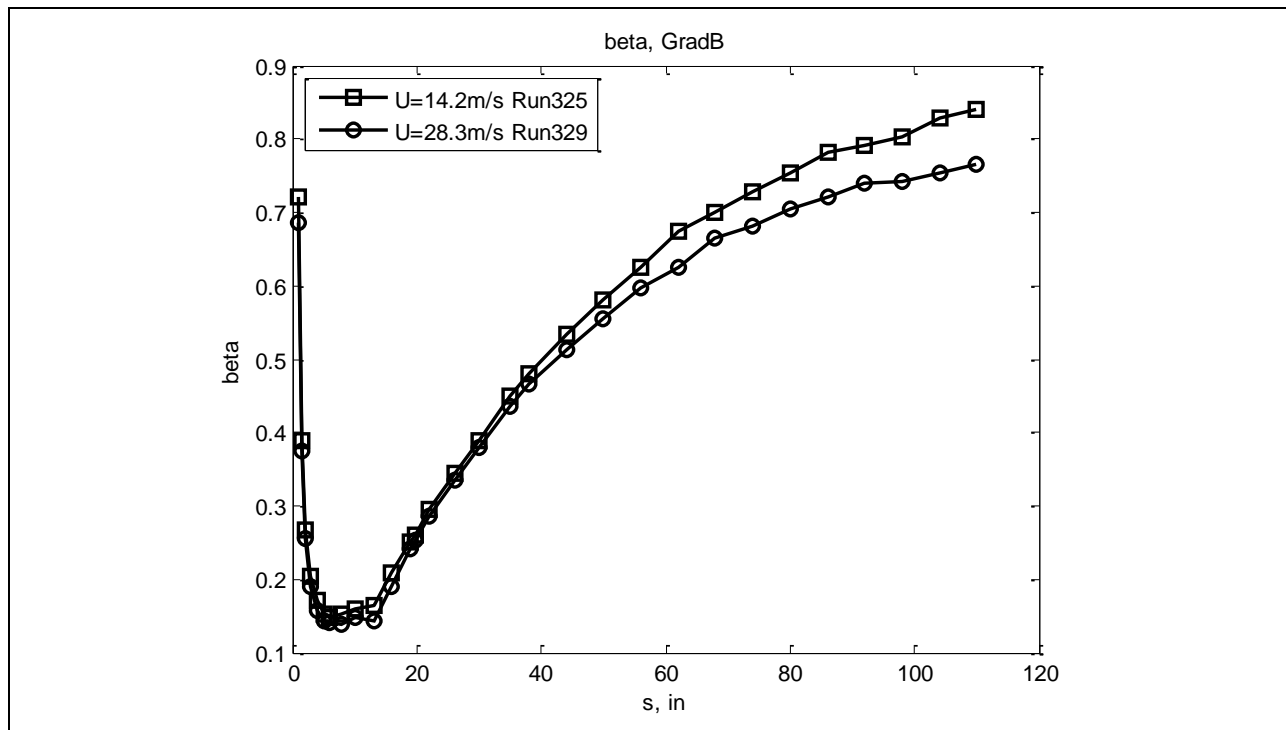


Figure 784: Pressure parameter.

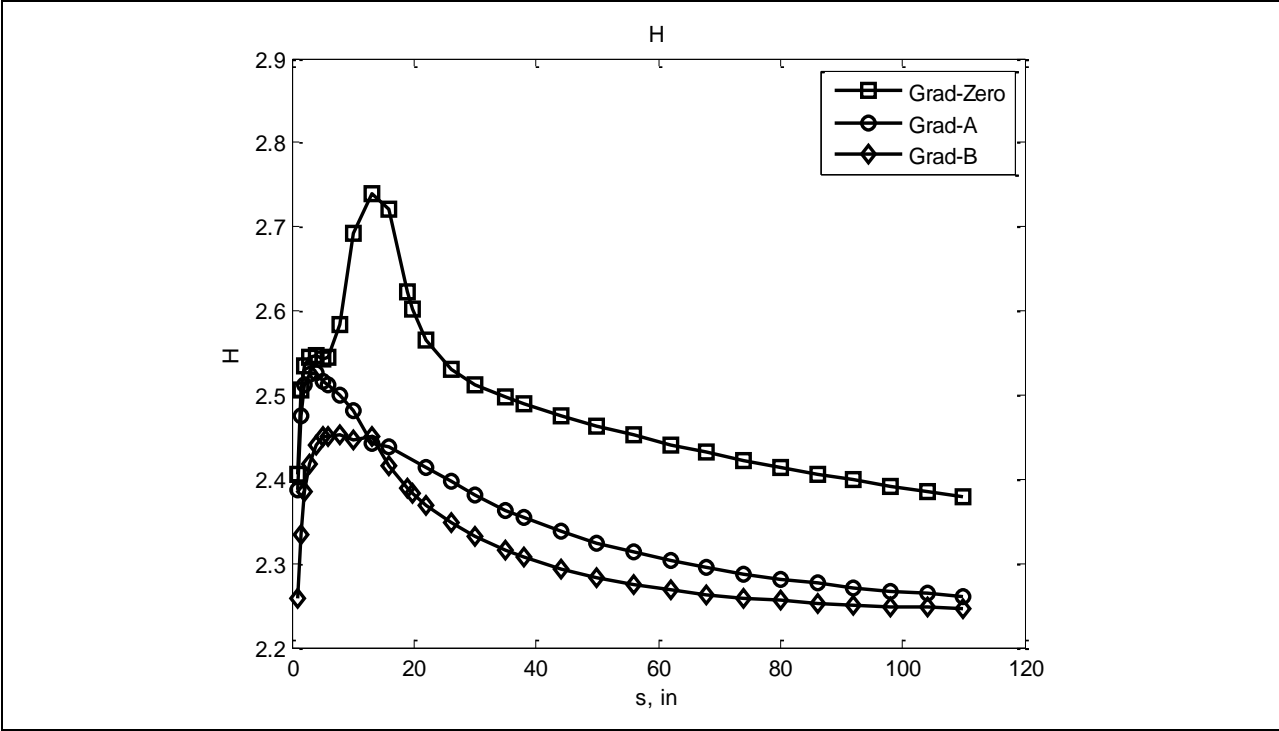


Figure 785: Shape factor.

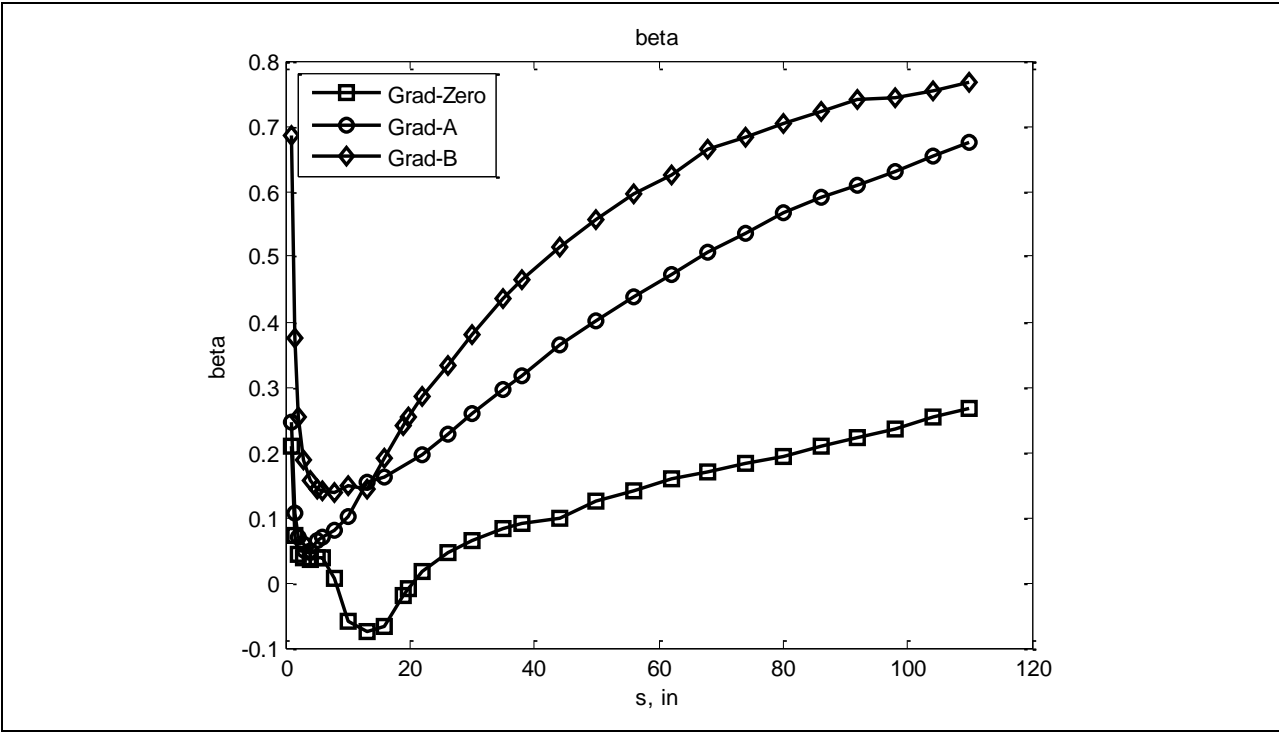


Figure 786: Pressure parameter.

7.5.8 Comparison with Stability Analysis

The comparison with stability analysis is presented first for Gradient-Zero and then for Gradient-A. A discussion on Gradient-B follows at the end of this section.

To obtain the following plots, the data on the powers, A , of possible T-S waves given in Section 7.5.7.1 were used. Amplification of possible T-S waves plots show the normalized amplitudes, a/a_0 , for Gradient-Zero model as function of streamwise distance (where: $a=(A)^{1/2}$). For a_0 , we used a conservative estimate from the level of noise in the power spectra for the first hot-wire, hw1. This estimation for a_0 has two drawbacks. First, the level of noise may be higher than the real amplitude of T-S wave. Second, the first hot-wire location available (which was about 20 inches from the leading edge) probably does not correspond to the spot where T-S wave first appears. For these reasons, another estimation was also used for a_0 , namely, the level of noise in the power spectra for zero flow speed in calm environment (obtained in a separate laboratory test, Figure 340). The comparison in the T-S wave amplification for different choice of a_0 is shown only for one flow speed (Run 147) in Figure 787 for the amplitudes and in Figure 792 for N-factors, correspondingly. N-factors of possible T-S waves plots show the N-factors for Gradient-Zero model as function of stream-wise distance. Each plot is for a given step height and contains a set of different runs corresponding to different freestream velocities.

The case for zero step (Figure 787) shows that the amplitude first increases at $s=27$ in and then drops at $s=36$ in for $U=22.3$ m/s. No transition to turbulence is observed for this case.

The case for a forward-facing step of 0.04in (Figure 788, Figure 789 and Figure 790) shows higher amplification at $s=32$ in for $U=24$ m/s (Run 134) and at $s=27$ in for $U=22.6$ m/s (Run 151). In these cases transition to turbulence is observed downstream of these locations.

In the case for an aft-facing step of -0.04in (Figure 791), the transition to turbulence happens at $s=27$ in at a lower speed, $U=12.6$ m/s (Run 140).

The plots for N-factors for the three different step heights show a similar tendency (Figures 792-796). It is worthwhile to note that when no transition is observed the N-factor grew up to 3 as for the case of zero step, $U=22.3$ (Run147). For the cases when transition is observed the N-factor grew up to 5-6 as for the forward-facing step of 0.04in. case, $U=24$ m/s (Run 134), $U=22.6$ m/s (Run 151) and the aft-facing step of -0.04in case, $U=12.5$ m/s (Run 140).

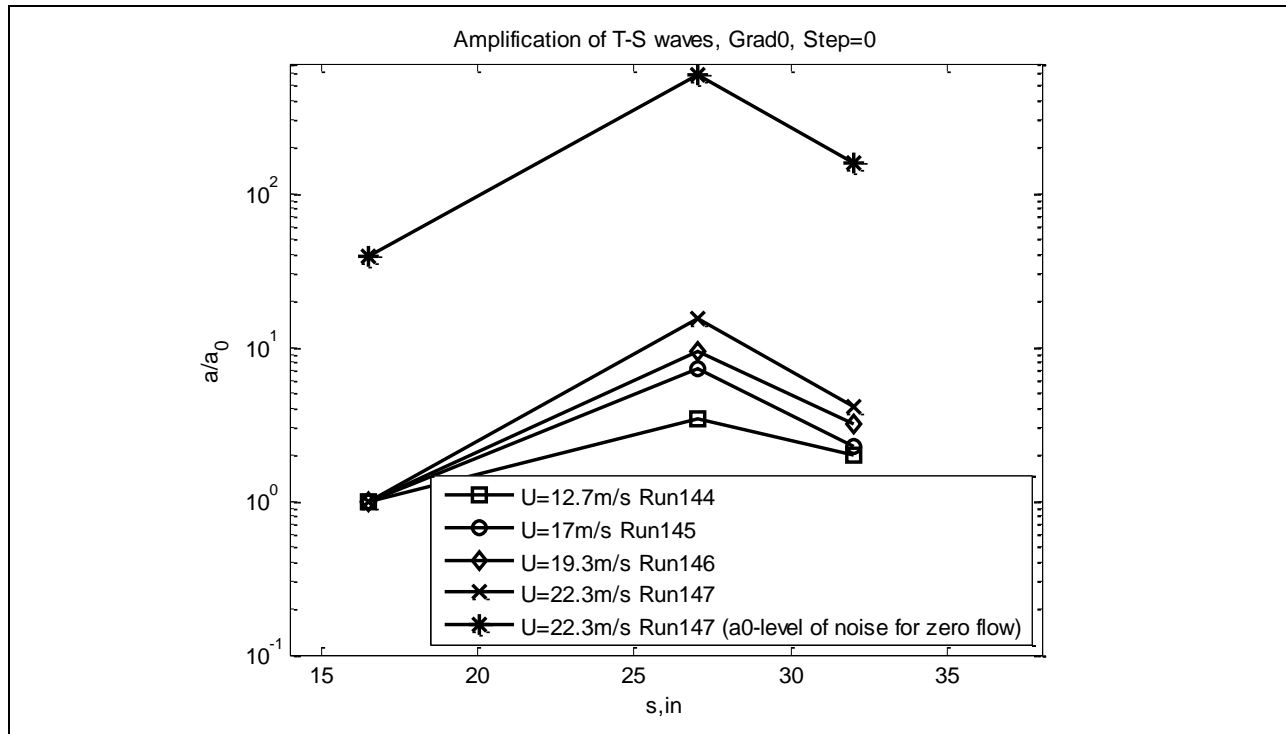


Figure 787: T-S wave normalized amplitudes.

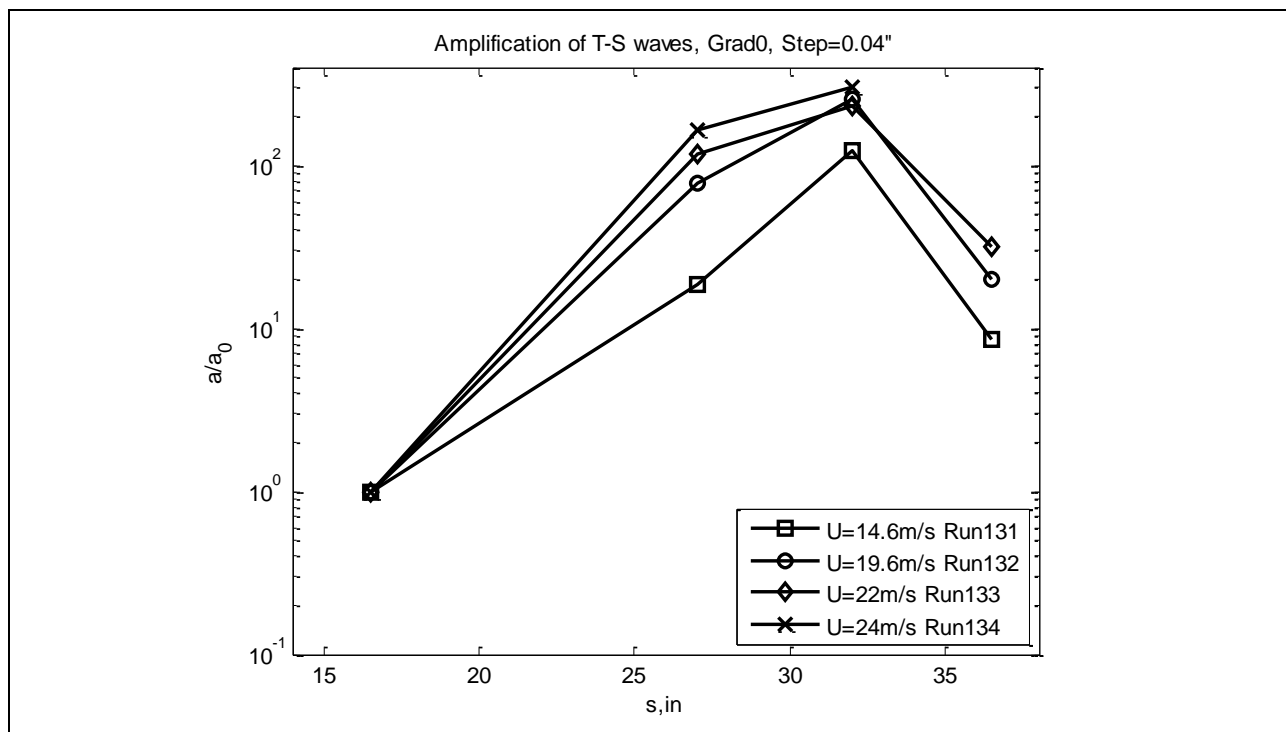


Figure 788: T-S wave normalized amplitudes.

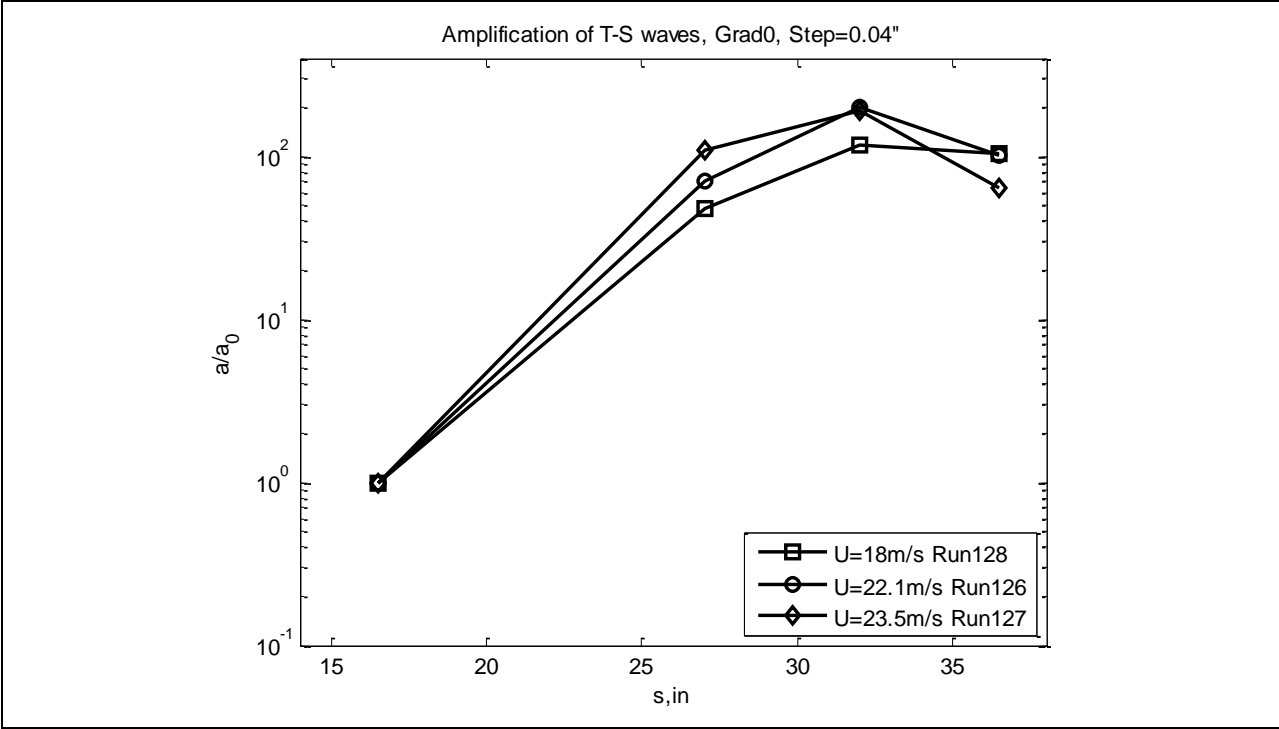


Figure 789: T-S wave normalized amplitudes.

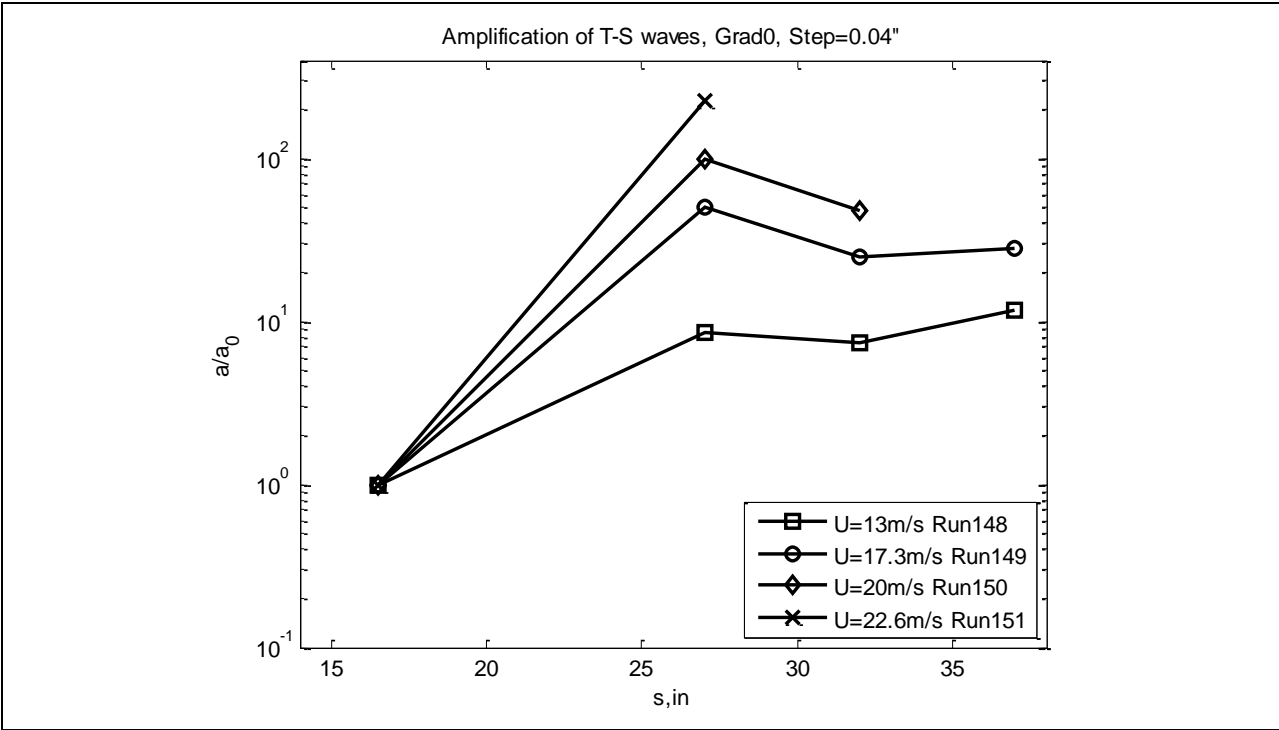


Figure 790: T-S wave normalized amplitudes.

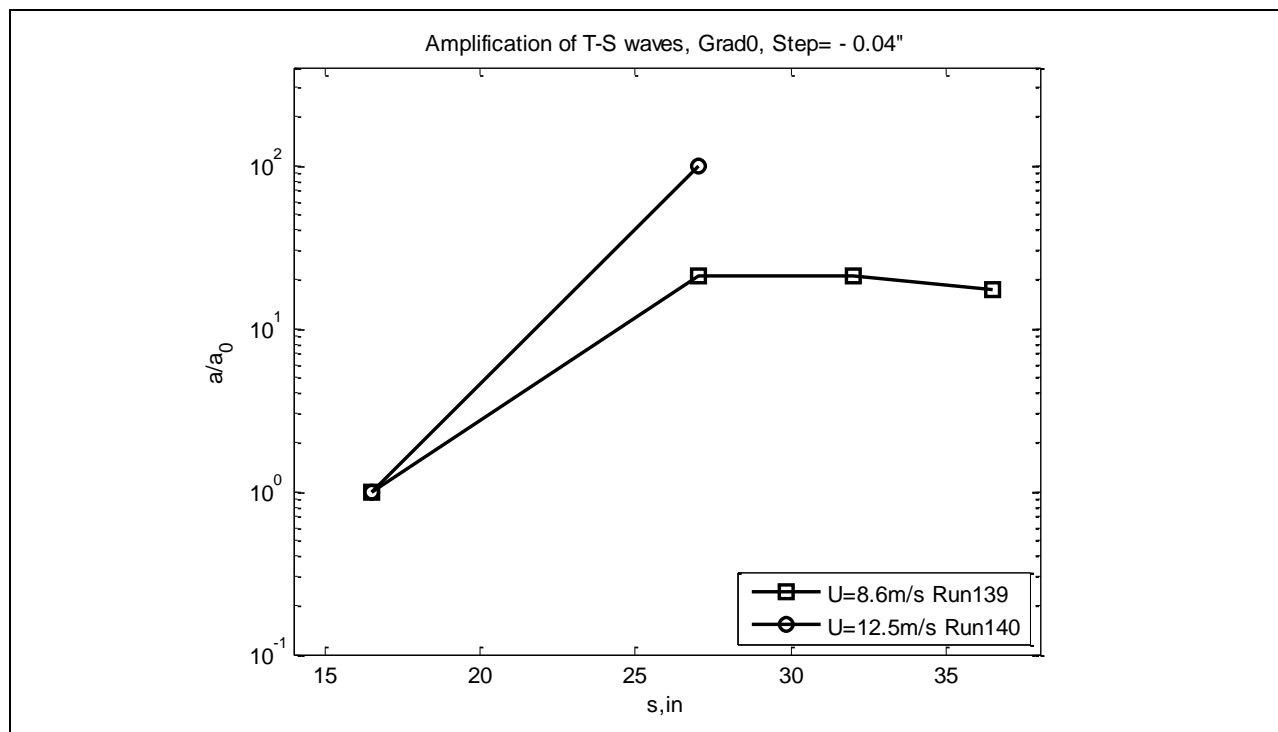


Figure 791: T-S wave normalized amplitudes.

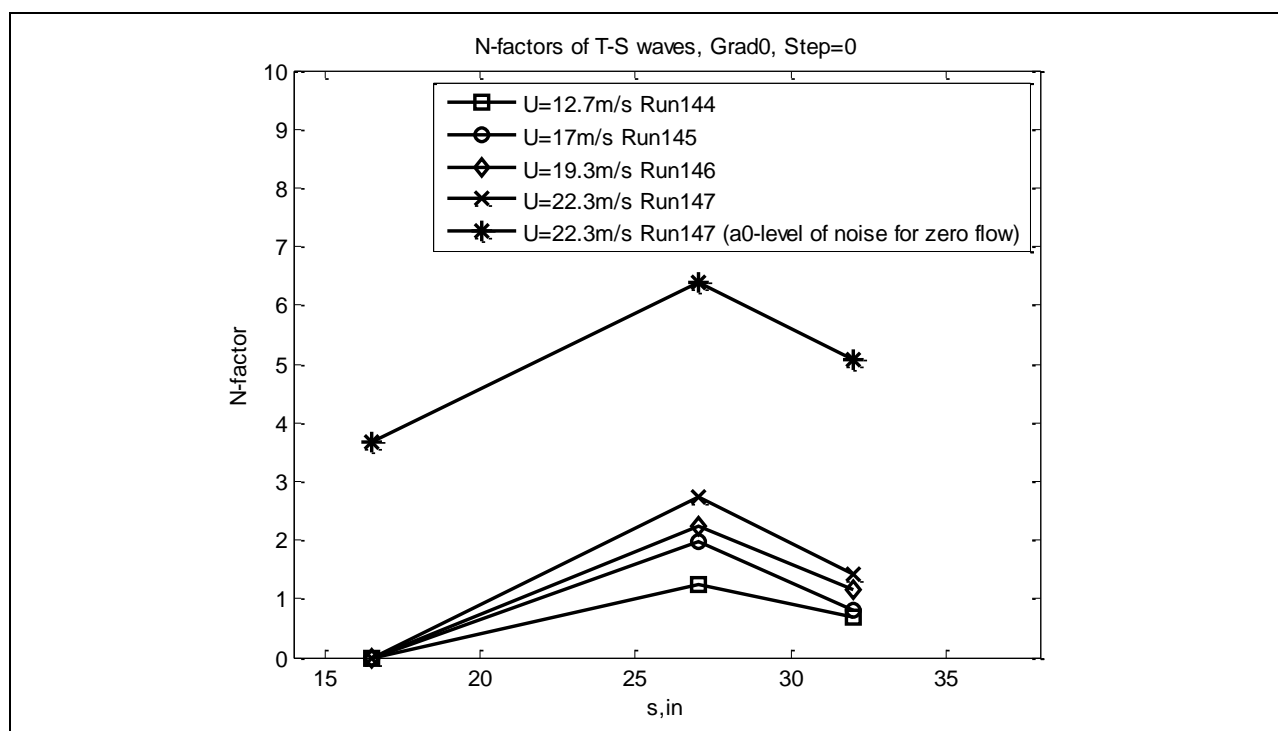


Figure 792: T-S wave normalized amplitudes.

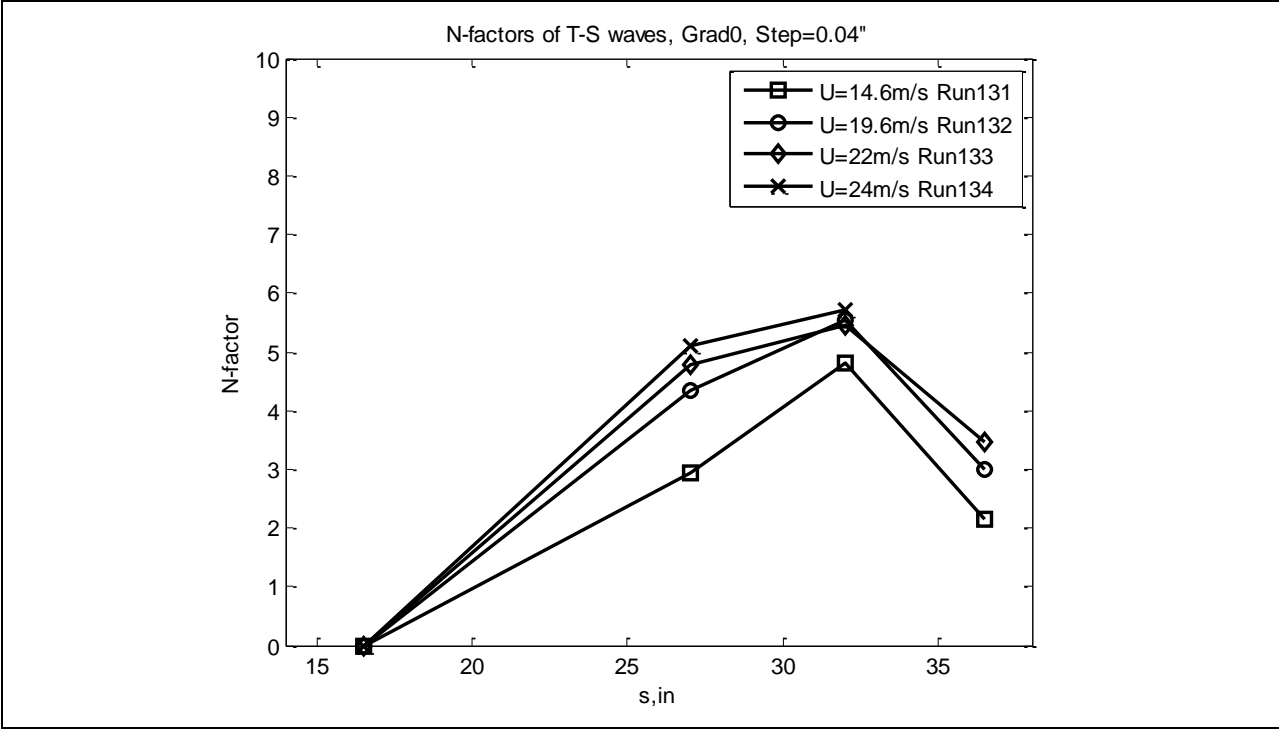


Figure 793: T-S wave normalized N-factors.

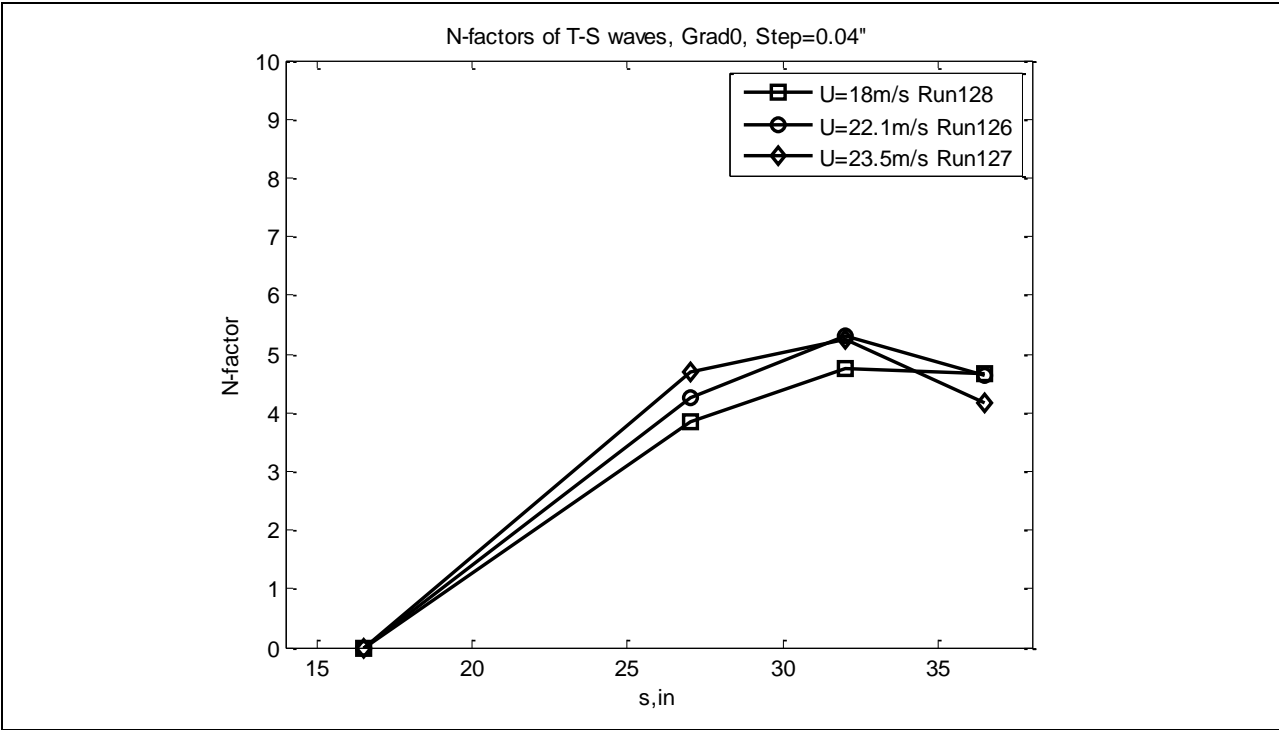


Figure 794: T-S wave normalized N-factors.

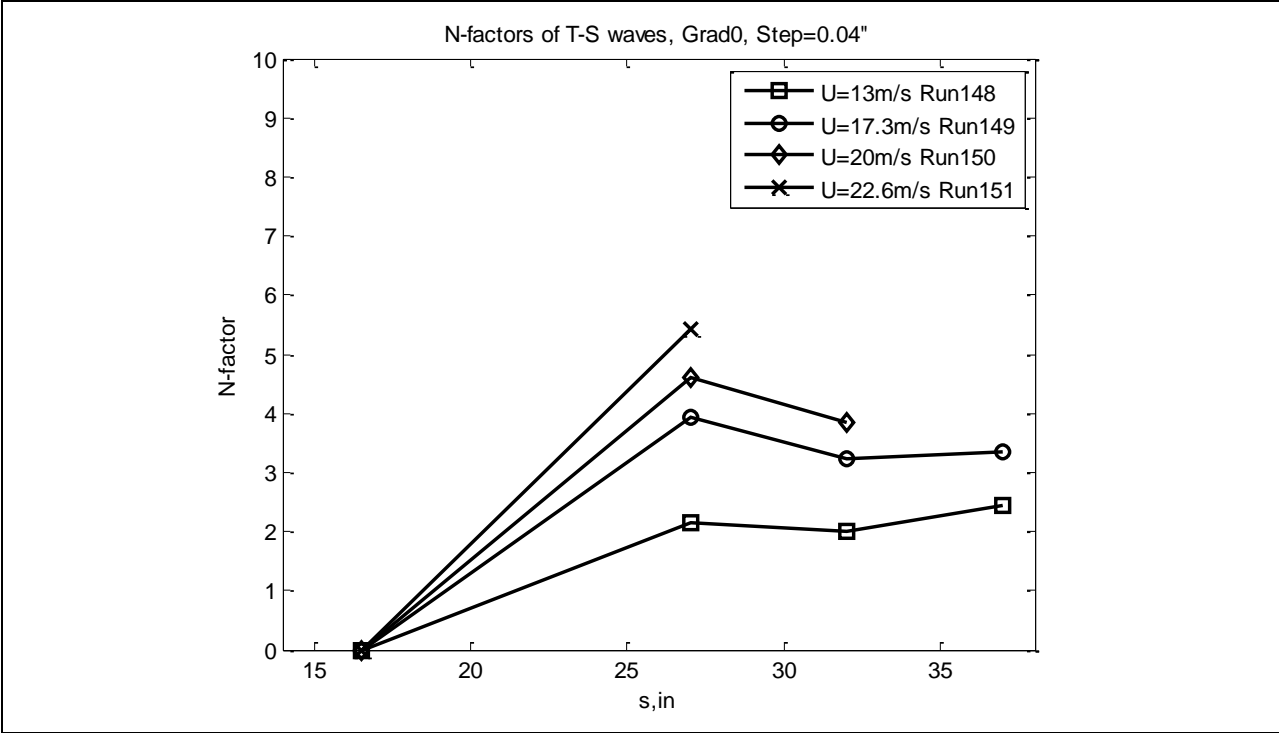


Figure 795: T-S wave normalized N-factors.

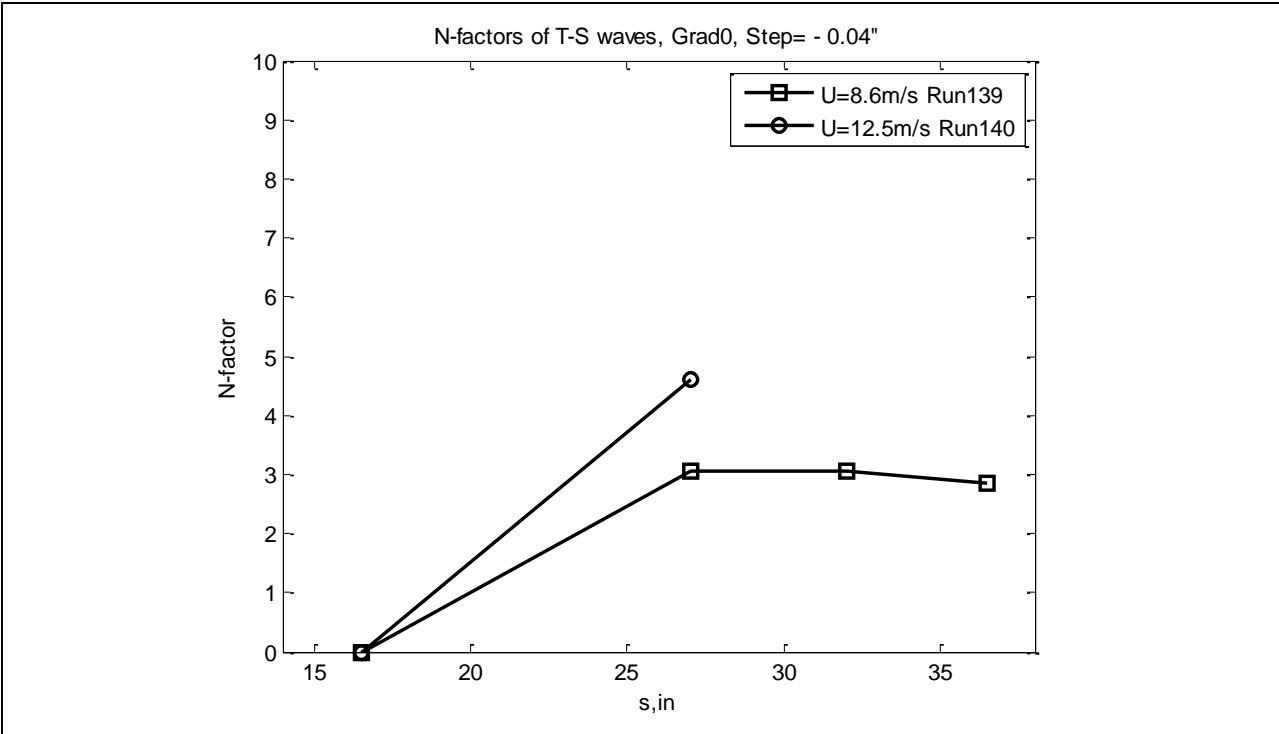


Figure 796: T-S wave normalized N-factors.

Figure 797 shows a stability diagram with the range of frequencies that are unstable for a given Reynolds number and pressure parameter. The lines in the plot are neutral stability curves taken from simulations of Wazzan (1968)¹⁴ for parallel similar flows with stream-wise pressure gradient. The lines in the plot correspond to three different pressure gradients (different β). The symbols in the plot are our experimental data for the case of Gradient-Zero model and zero step (Runs 144-147). The two different values of $\beta=0.052$ and 0.073 are for two different stream-wise positions $s=27\text{in}$ and 32in correspondingly. The values of β for our points are very close to the case of $\beta=0.05$ from Wazzan (1968). It can be seen that our points are well inside of the unstable region and we can conclude that our frequencies observed in the spectra for the case of Gradient-Zero model, zero step, correspond to unstable T-S waves. It can be seen also that our points with larger β correspond to higher local Re_{δ^*} .

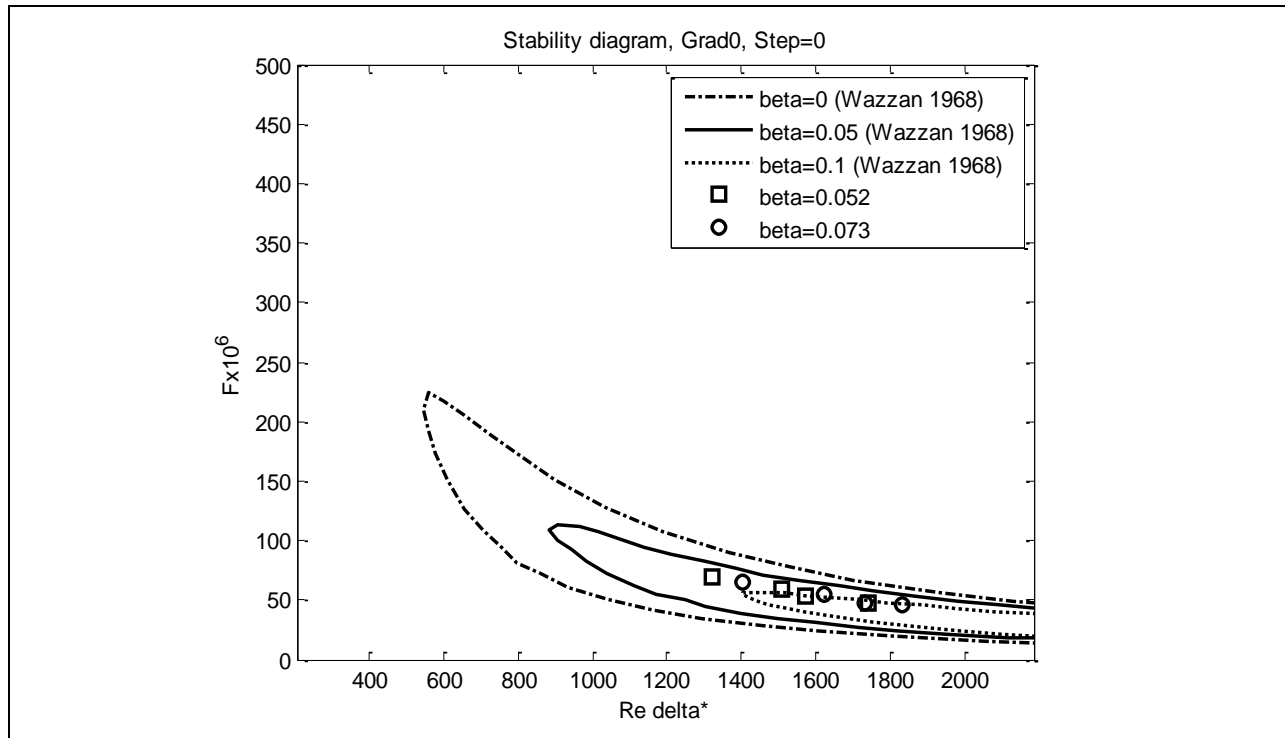


Figure 797: Stability diagram.

The comparison of the Rapid N-factor computations described in Gaster et al (1994)²⁴ and Gaster (1997)²⁵ with the experimentally found N-factors for the Gradient-Zero model with a zero step is shown in Figures 798-801 for four different freestream speeds. The lines in the plots show N-factors computed for individual frequencies as functions of stream-wise position. The envelope to the lines gives maximal N-factor. The symbols are the experimental N-factors determined from the velocity power spectra (see Section 7.5.7.1). It can be seen that the experimental data are in the right range of stream-wise locations where the maximal amplification is observed and the corresponding experimental frequencies are close to computed ones (compare, for example, in Figure 798 for $U=12.7\text{m/s}$ the experimental 153Hz and 144Hz points with 167Hz and 150Hz lines which have maximal N-factors for the same streamwise positions). Two different ways of calculating of the experimental N-factors were used. The open symbols in the plots correspond to the case when the level of noise for the first upstream

hot-wire was used as the initial power of T-S waves. The values of the N-factors calculated this way are smaller than computed ones which can be explained by high level of the noise. The measured level of noise in the power spectra in the boundary layer could be related to both TI (including freestream turbulence, vibrations, shedding from leading edge etc.) and electronic noise. High freestream TI is known to reduce N-factors (see Mack's modification of the e^9 method, Mack 1977²¹). For the level of turbulence measured in the test section the transitional N-factor can drop from its zero-freestream turbulence value 9 to 3.9. It is comparable with the observed difference between experiments and simulations (Figures 798-801). If the electronic noise is high, it can lead to the overestimation of the initial power too.

The filled symbols correspond to the case when the level of noise for a zero flow in calm environment (Figure 340) was taken as the initial power. The N-factors in this case showed much closer agreement to the simulations (Figures 798-801).

The T-S wave frequency didn't depend on the step height as can be concluded from the data on frequencies of T-S waves for different steps in Section 7.5.7.1 (within the accuracy of peak determination which can be estimated by half-width at half-height). The presence of the step increased amplitudes of T-S waves and N-factors (see Figures 787-791 and Figures 792-796).

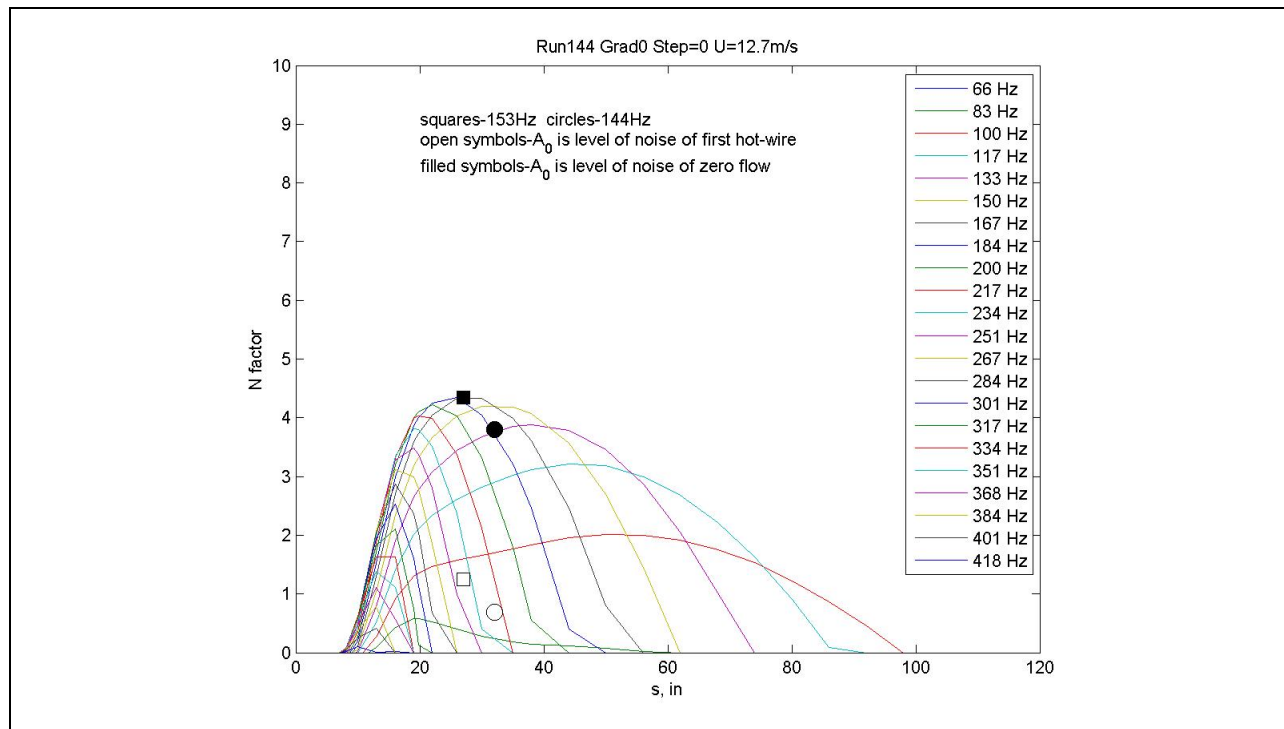


Figure 798: N-factors (comparison with simulation).

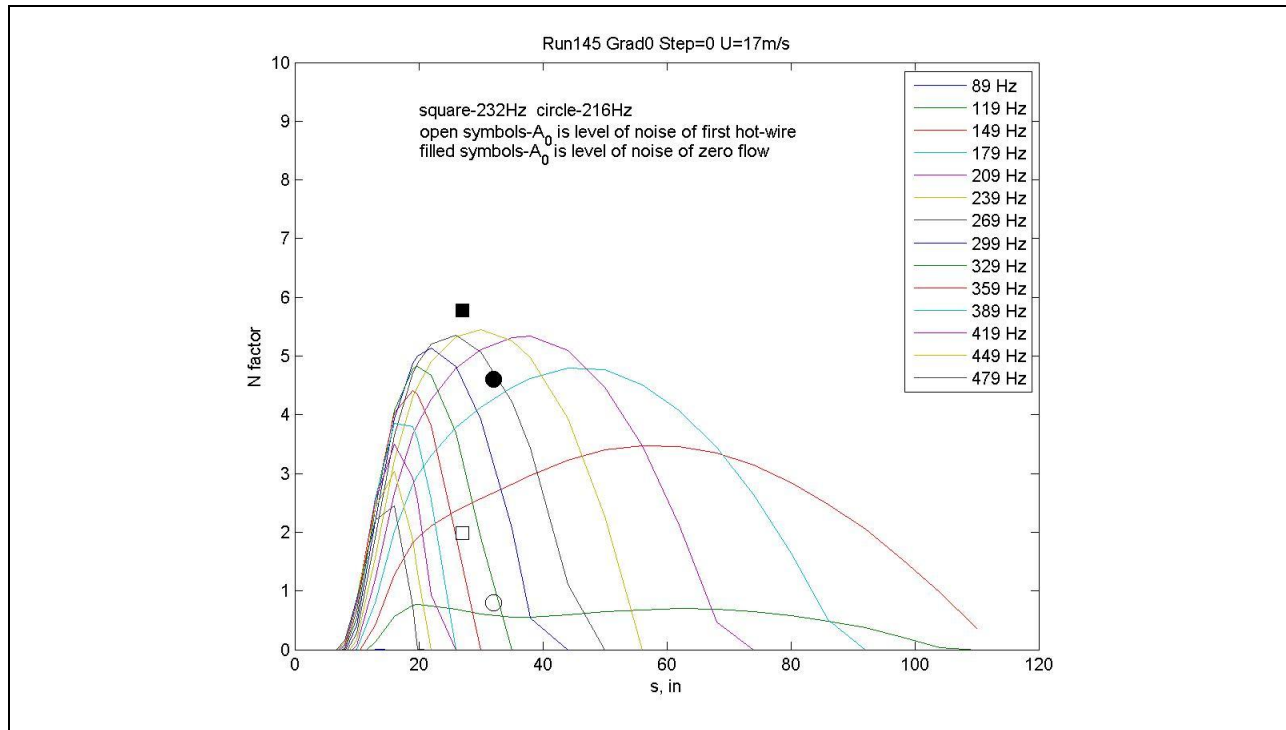


Figure 799: N-factors (comparison with simulation).

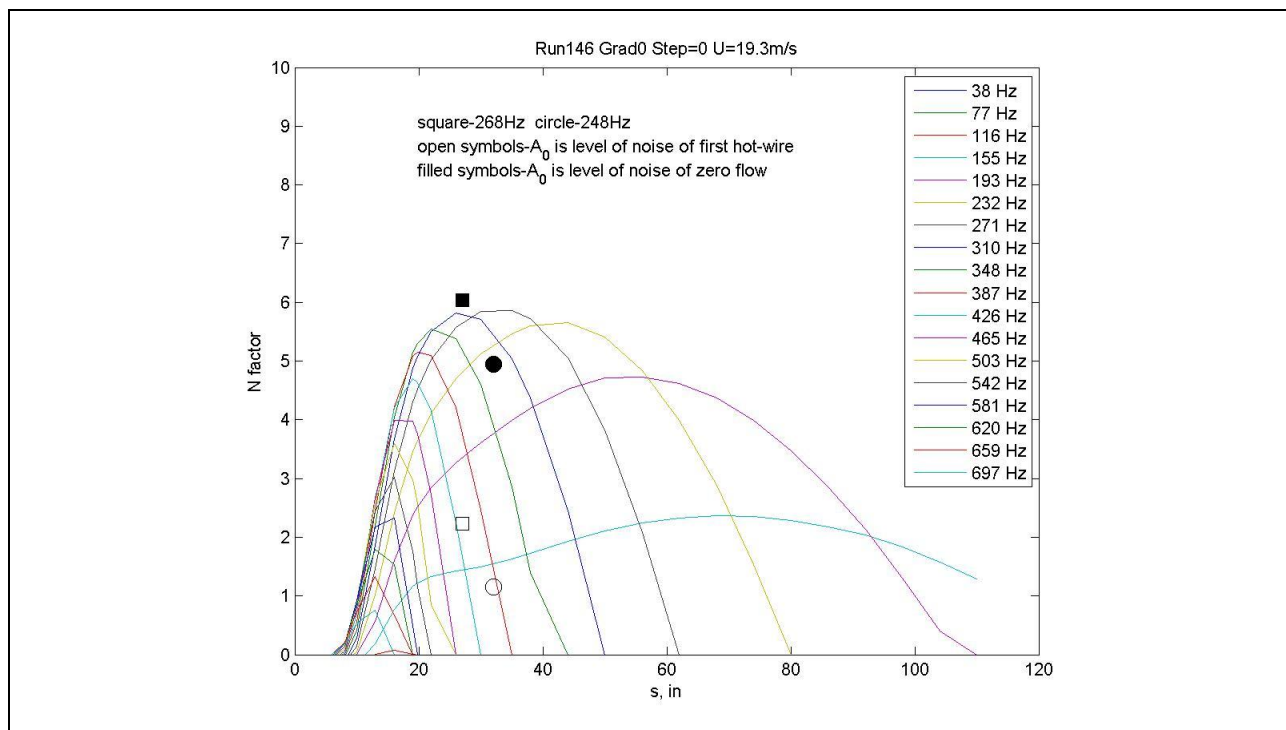


Figure 800: N-factors (comparison with simulation).

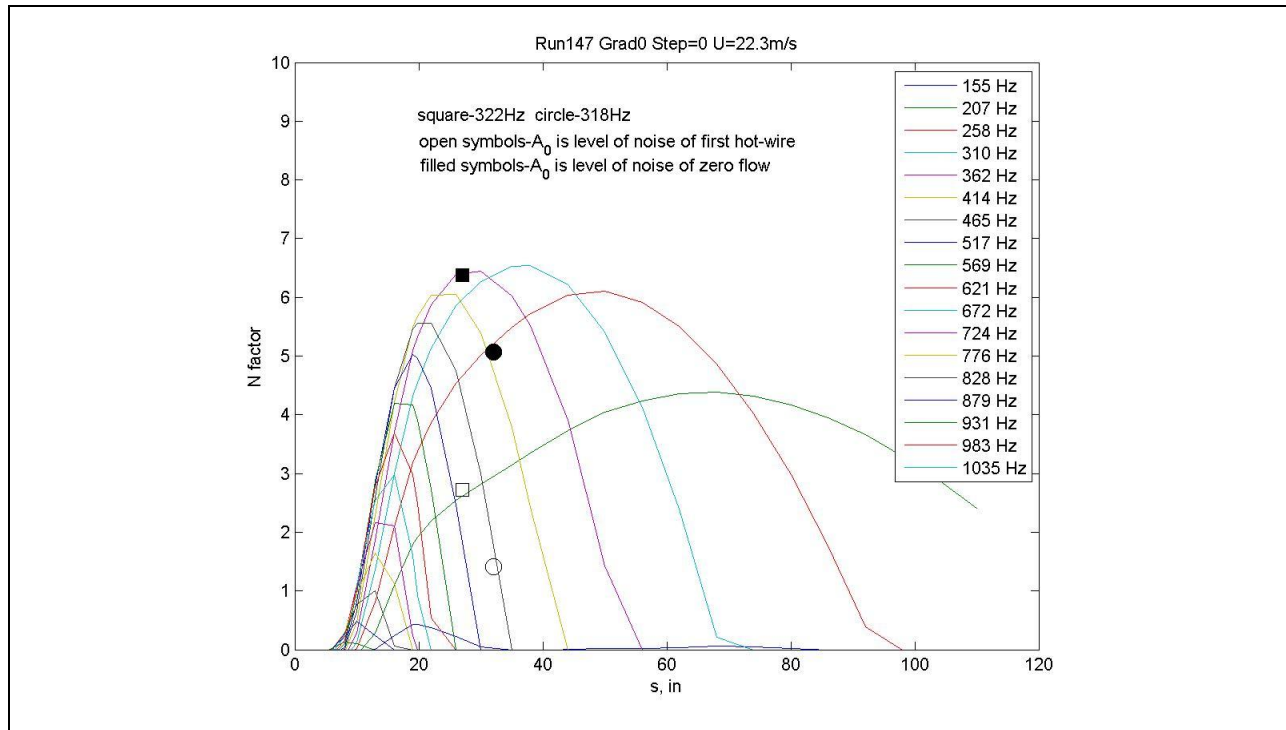


Figure 801: N-factors (comparison with simulation).

To obtain the following plots, the data for the powers, A , of possible T-S waves given in Section 7.5.7.1 were used for Gradient-A. Amplification of possible T-S waves plots show the normalized amplitudes, a/a_0 , for Gradient-A model as function of stream-wise distance (where: $a=(A)^{1/2}$, and a_0 is the level of noise for the first hot-wire, hw1). N-factors of possible T-S waves plots show the N-factors for Gradient-A model as function of stream-wise distance. Each plot is for a given step height and contains a set of different runs corresponding to different freestream velocities.

The case of an aft-facing step of -0.04in (Figure 802) shows an amplification factor of between 10 and 100 times. The amplitude first increases at $s=44$ in and then drops to the same level at $s=65.5$ in for $U=13$ m/s. No transition to turbulence is observed for this case.

The case of a forward-facing step of 0.065in (Figure 803) shows approximately the same level of amplification as for the previous case, but without a change with stream-wise distance.

The plots for N-factors (Figure 804 and Figure 805) for the two different step heights show similar tendencies to the amplitudes behavior. The N-factors are about 3-4 and almost do not change with streamwise distance.

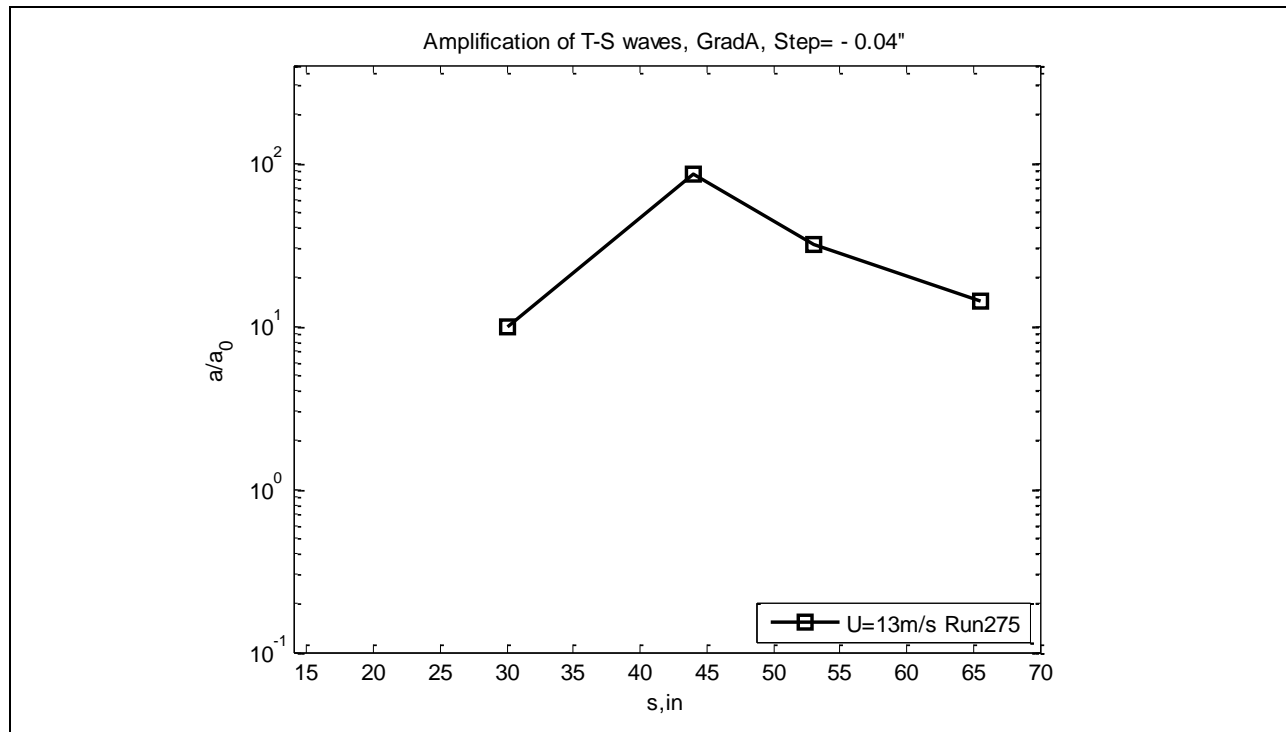


Figure 802: T-S wave normalized amplitudes.

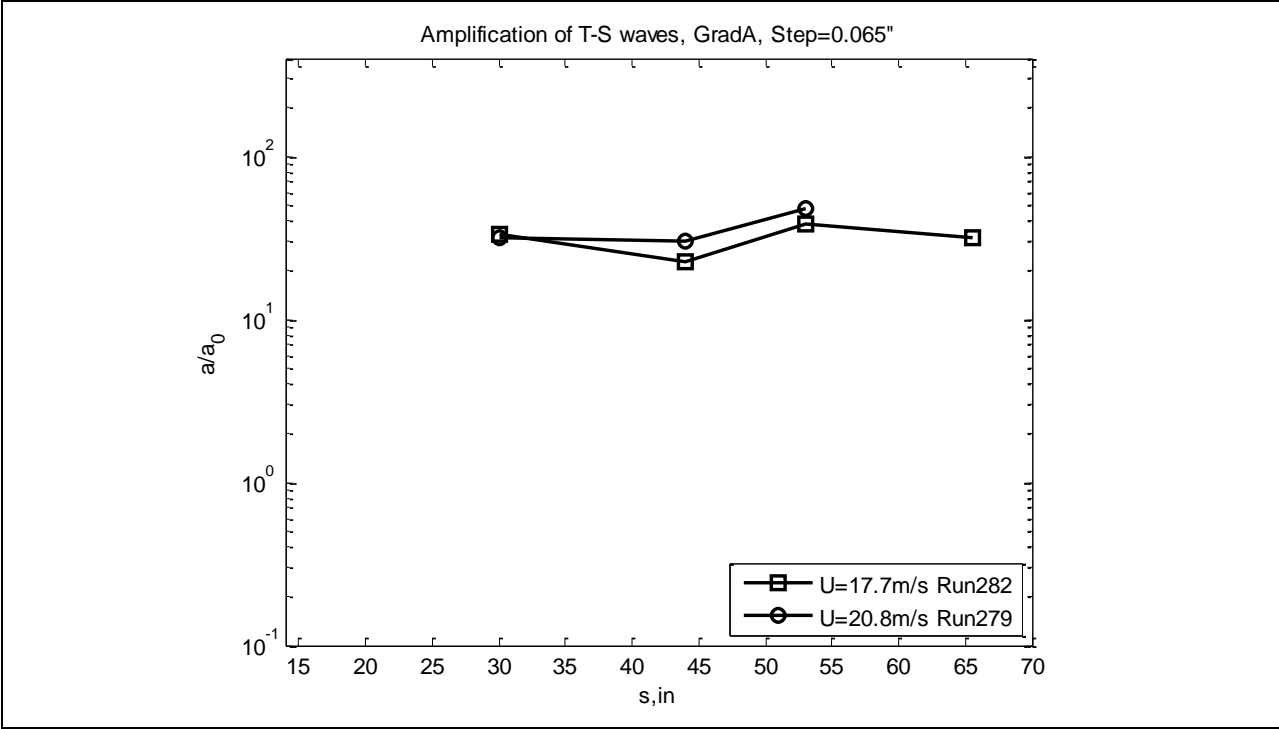


Figure 803: T-S wave normalized amplitudes.

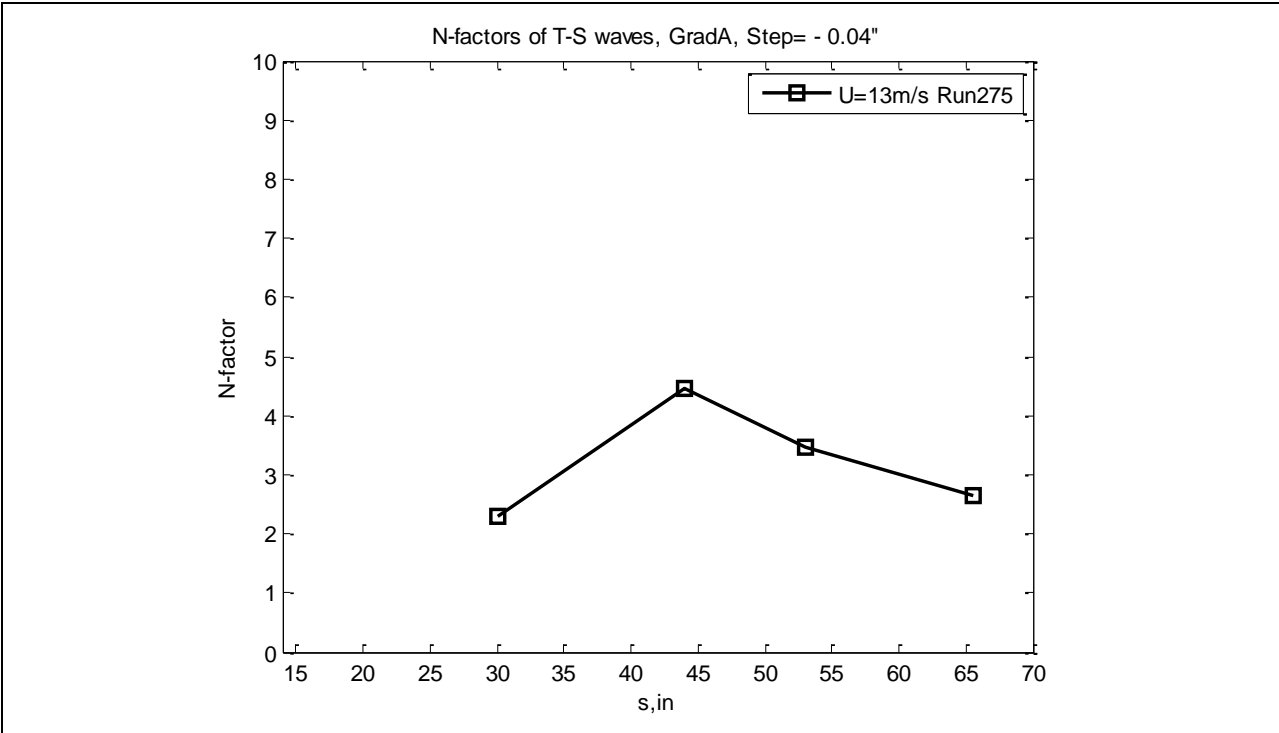


Figure 804: T-S wave normalized amplitudes.

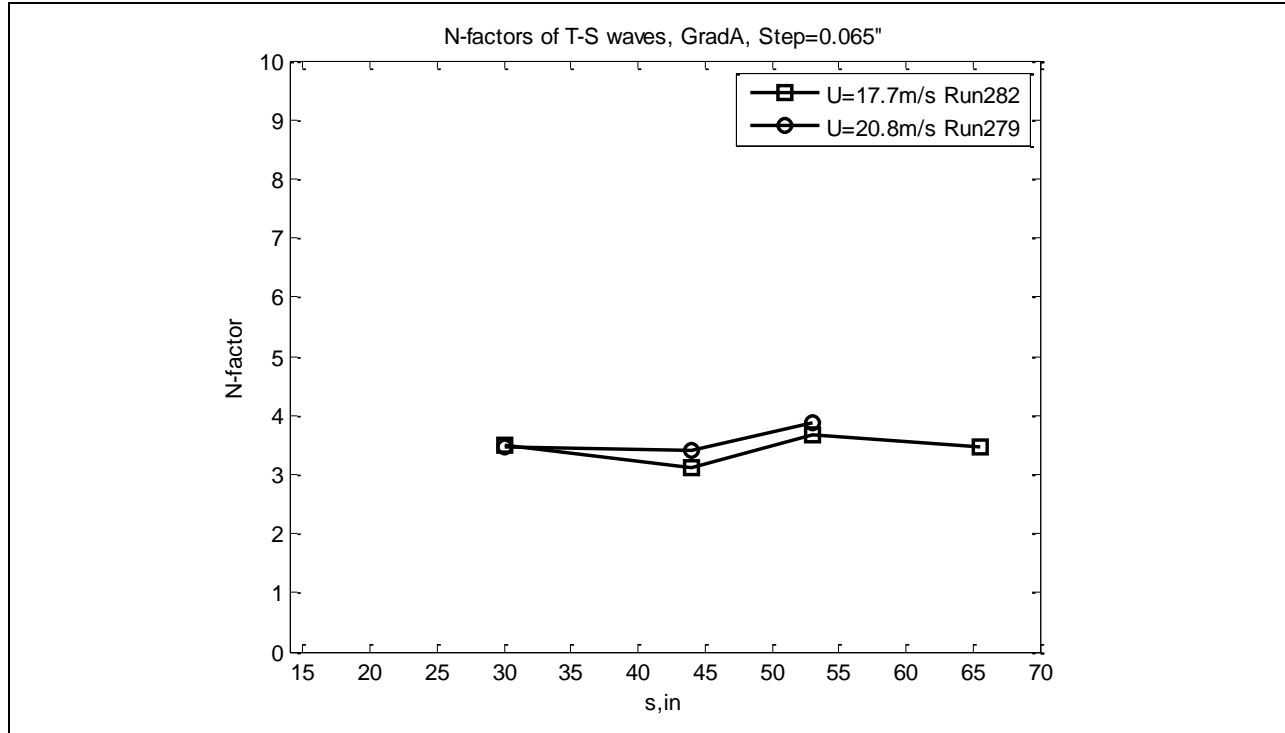


Figure 805: T-S wave normalized N-factors.

Figure 806 is the stability diagram for Gradient-A model. The lines in the plot are the neutral stability curves taken from simulations of Wazzan (1968)¹⁴ for parallel, similar flows with stream-wise pressure gradient. The lines correspond to two values of $\beta=0.2$ and 0.5 . The symbols correspond to frequencies of possible T-S waves found in the spectra for the cases of -0.04 in step (Run 275) and 0.065 in step (Run 282 and Run 279). The different values of $\beta=0.26, 0.36, 0.42$ and 0.5 for the experimental points correspond to different stream-wise locations $s=30$ in, 44 in, 53 in and 65.5 in. It can be seen that our points are well outside of the unstable region. It can be hypothesized that either the frequencies observed in the spectra for the case of Gradient-A model do not correspond to unstable T-S waves or our simple assumptions fail because of the increase in receptivity associated with the region of deceleration after the leading edge suction peak. The other sets of runs (Runs 187-190 for zero step, Runs 283-286 for Step= -0.055 in, Runs 292-294 for Step= -0.04 in, Runs 295-298 for Step= 0.065 in) did not show unstable T-S waves either (see corresponding plots for Gradient-A model in Section 7.5.7.1).

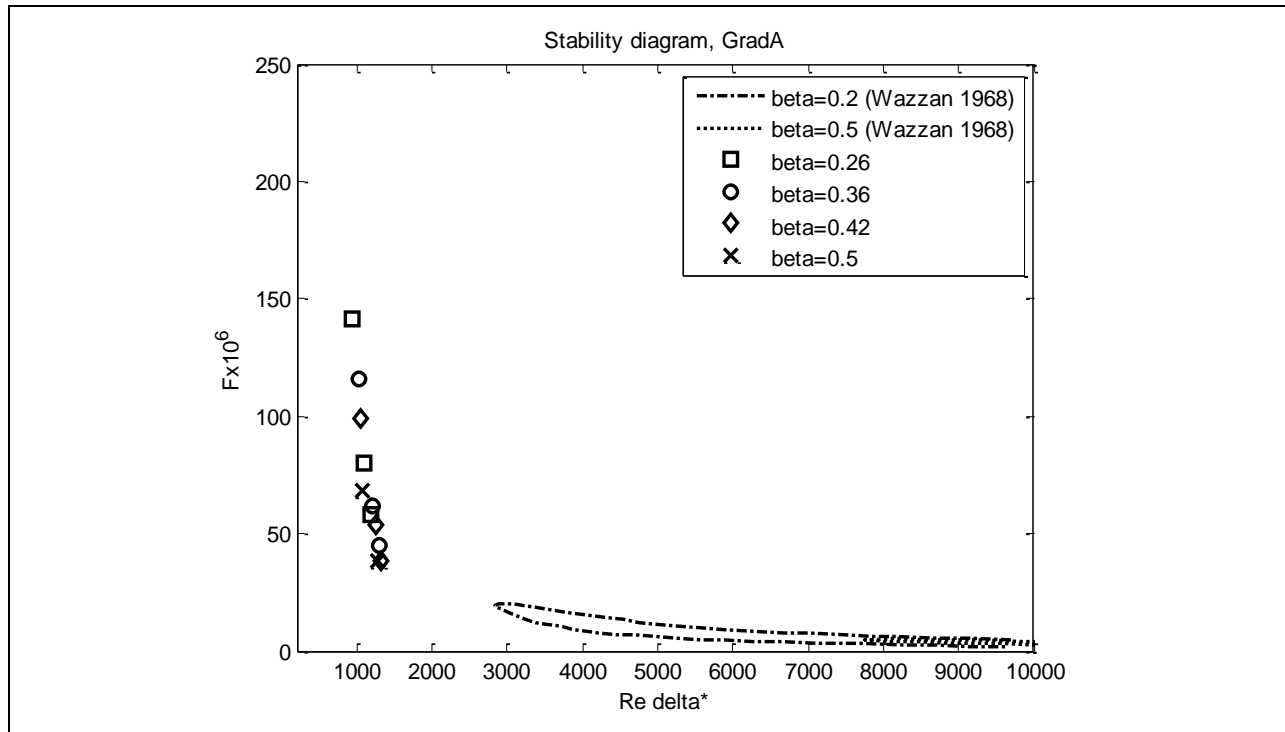


Figure 806: Stability diagram.

No T-S waves were observed in the spectra for the Gradient-B model. The pressure parameter β varied from 0.2 to 0.8 starting from the step location to the fairing of the model correspondingly. The maximal experimental Re_{δ^*} was about 1500 which is lower than the minimal critical $Re_{\delta^*_{crit}}=3000$ required for T-S to exist for $\beta=0.2$ (parallel flow analysis). So, the zeroth order condition for the amplified T-S waves was not reached. However, the transition happened as indicated the broadening in the velocity power spectra and C_f measurements.

7.5.9 Comparison with Skin Friction Measurements

The comparison of the hot-wire results with the skin friction distribution results from the Preston tube measurements are made in this section. First the results are presented for Gradient-Zero, followed by Gradient-A. This comparison was not made for the Gradient-B model.

Figure 807 (velocity RMS) and Figure 808 (Cf distribution measurements) both show laminar flow in the boundary layer for all speeds and all stream-wise locations for Gradient-Zero and zero step. The RMS is at the level of 0.2-0.5m/s and Cf at 0.0005 for laminar flow. Figure 809 and Figure 810 show the corresponding traversing data.

Figure 811 shows Cf distribution measurements for the case of Gradient-A and a forward-facing 0.04in step. According to the Cf distribution (Figure 811), transition happens at $U=23\text{m/s}$ at $s=35\text{in}$. The traversing hot-wire data (Figure 810) show that the boundary layer profile changes to a turbulent one at $U=22.5\text{m/s}$ and $s=37\text{in}$, which are very close to the corresponding U and s values for transition obtained from the Cf distribution. As Figure 809 shows, the RMS velocity increased from the laminar value earlier than the change to a turbulent velocity profile was observed. All this confirms that the RMS velocity reflects only the magnitude of perturbations to the laminar velocity profile, while Cf responds to the change in the mean velocity profile itself (which explains the reason why the former showed transition earlier than latter).

Figures 812-814 show the velocity RMS, corresponding traversing data, and Cf distribution measurements for the case of Gradient-A and an aft-facing -0.04in step. According to the Cf distribution (Figure 814) transition happens at $U=20\text{m/s}$ at $s=35\text{in}$. The traversing hot-wire data (Figure 813) show that the boundary layer profile changes to turbulent one at $U=19.6\text{m/s}$ at $s=27\text{in}$, which are close to the corresponding U and s for transition from Cf distribution. Figure 812 shows that velocity RMS increases from laminar to turbulent earlier than the velocity profile changes from laminar to turbulent, reinforcing our conclusion from above.

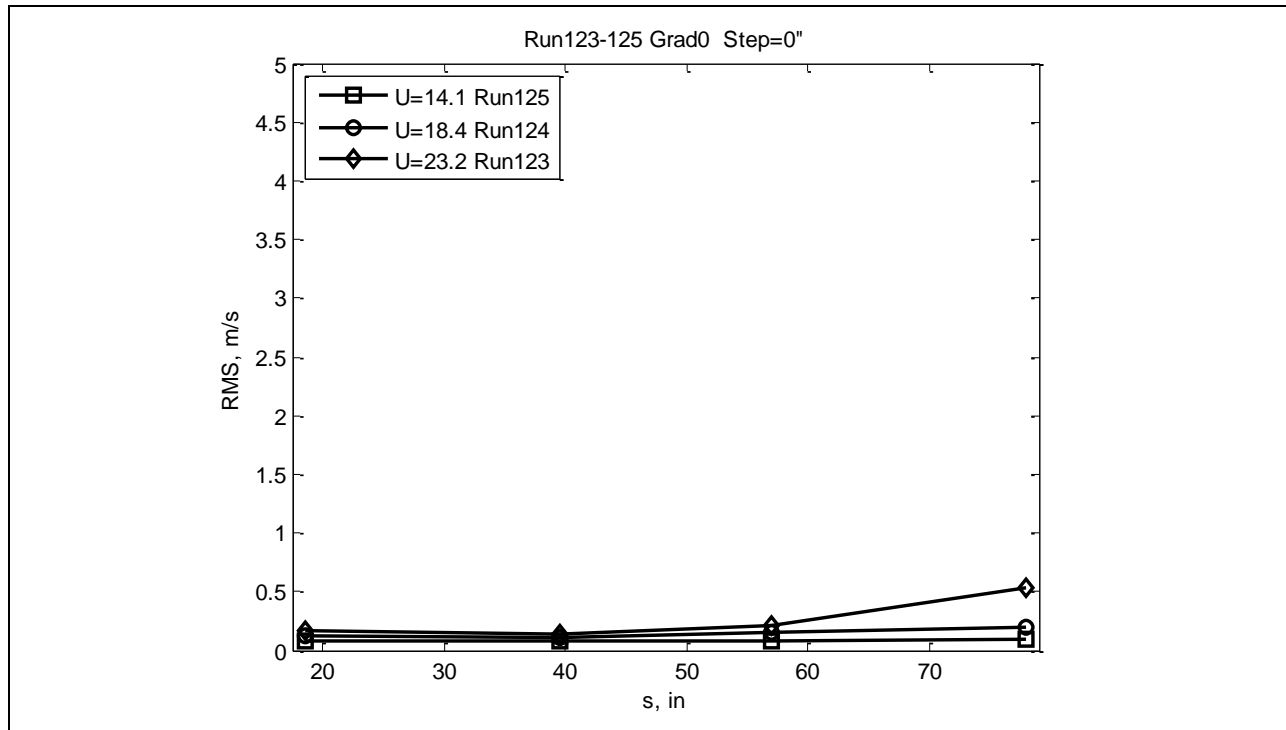


Figure 807: Velocity RMS.

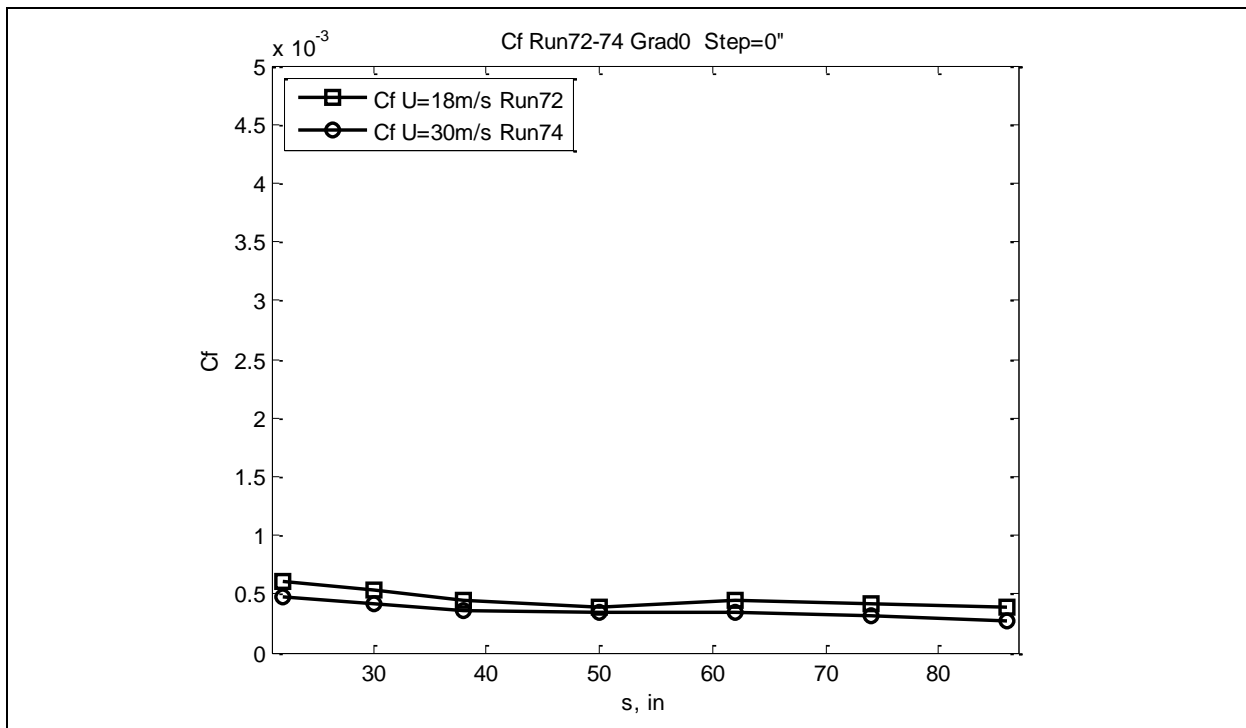


Figure 808: Cf distribution.

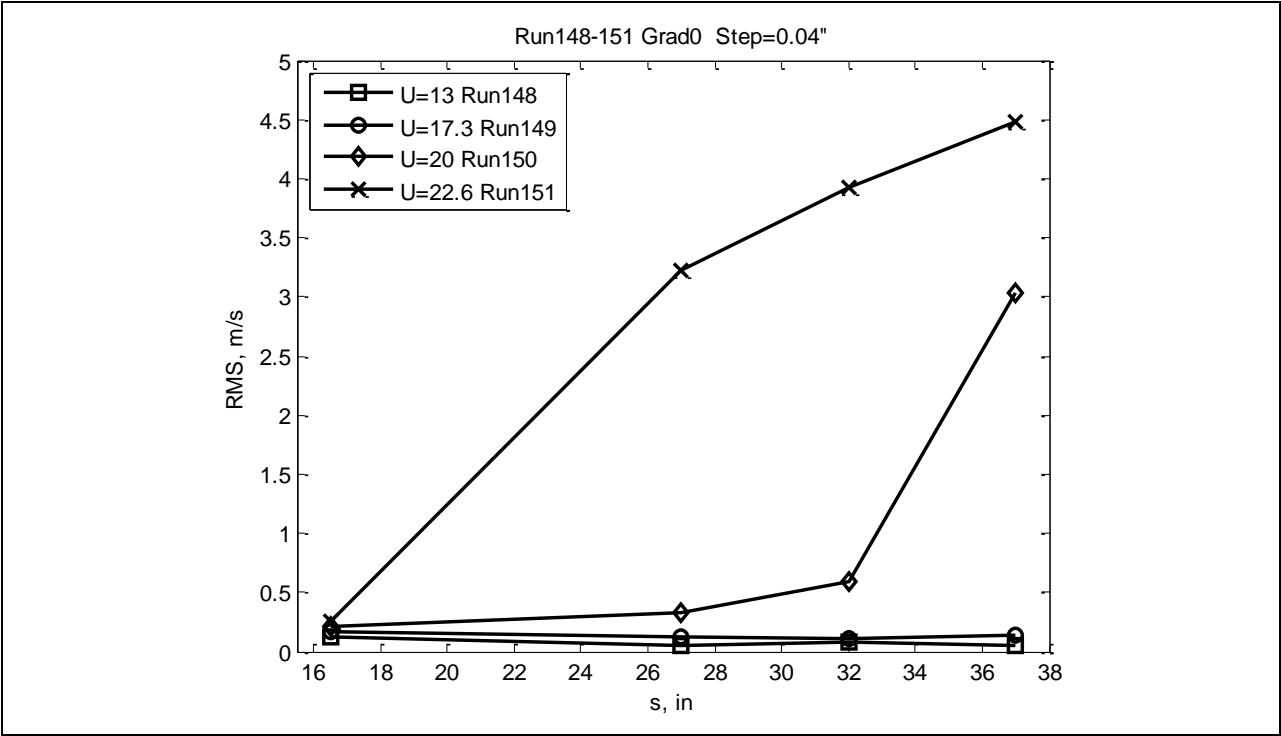


Figure 809: Velocity RMS.

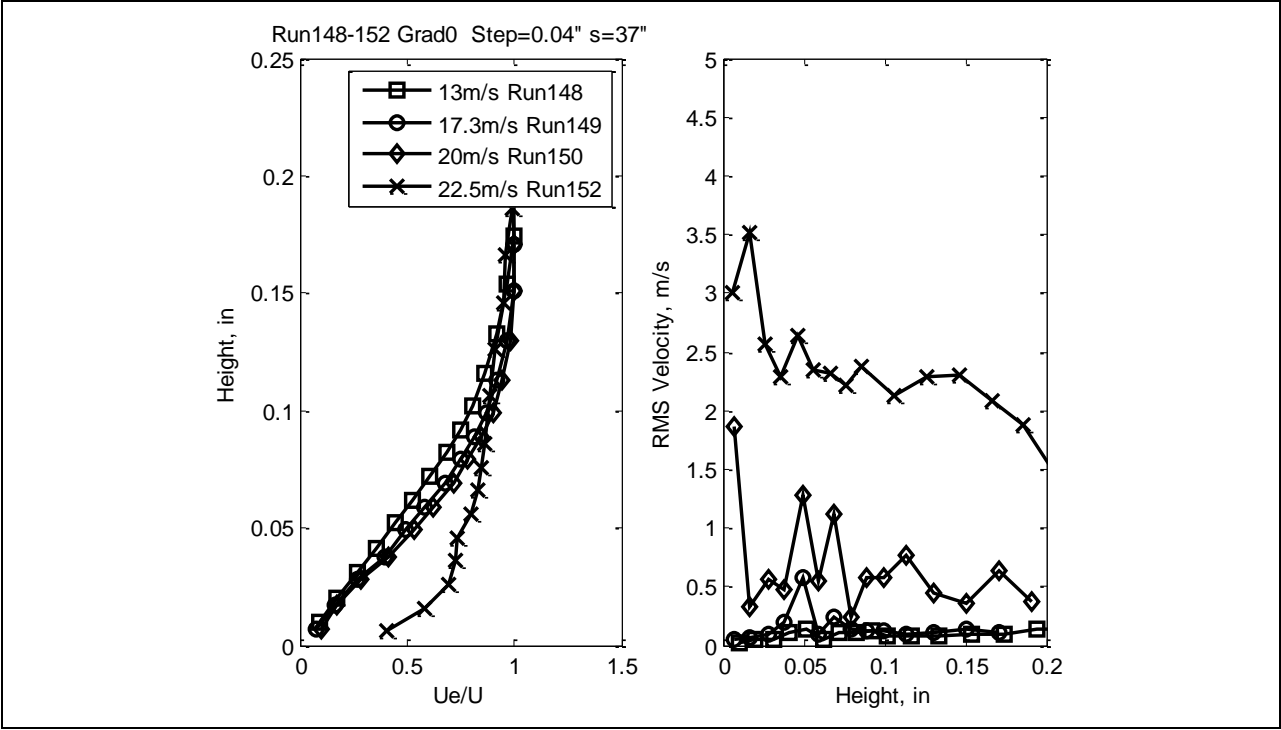


Figure 810: Velocity (left) and RMS (right) profiles.

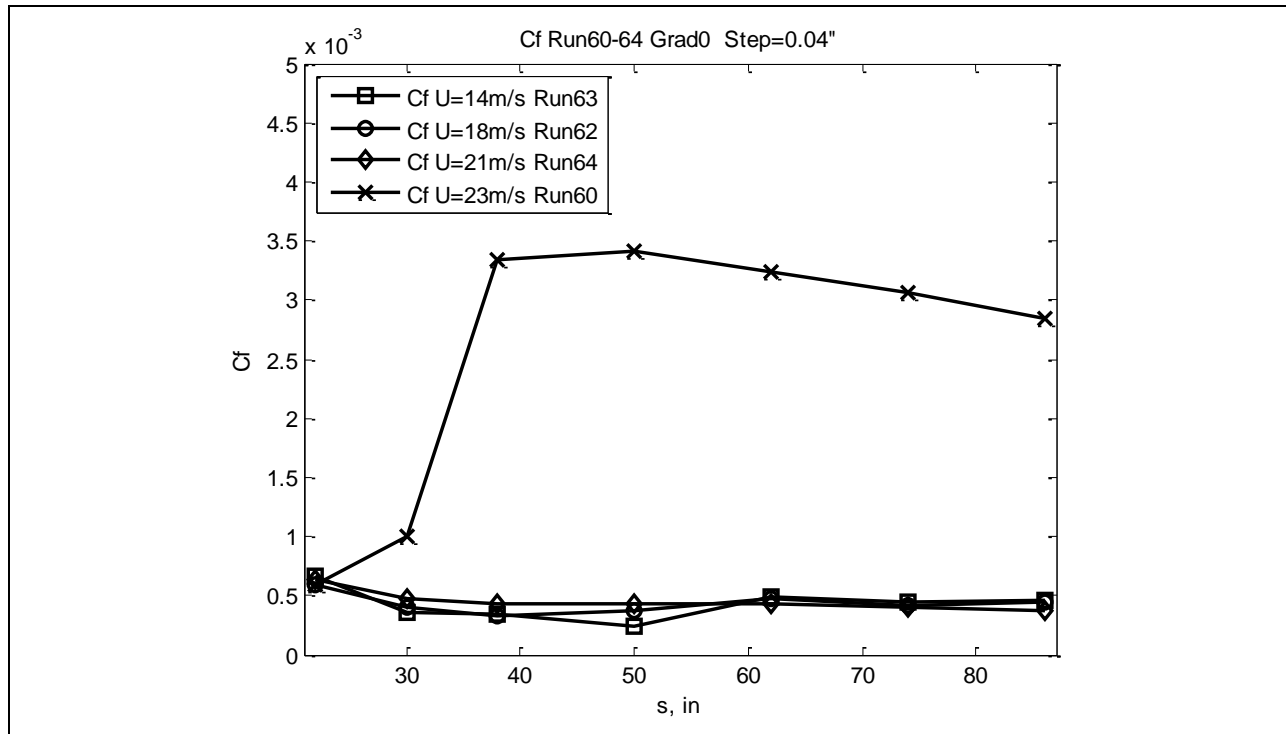


Figure 811: Cf distribution.

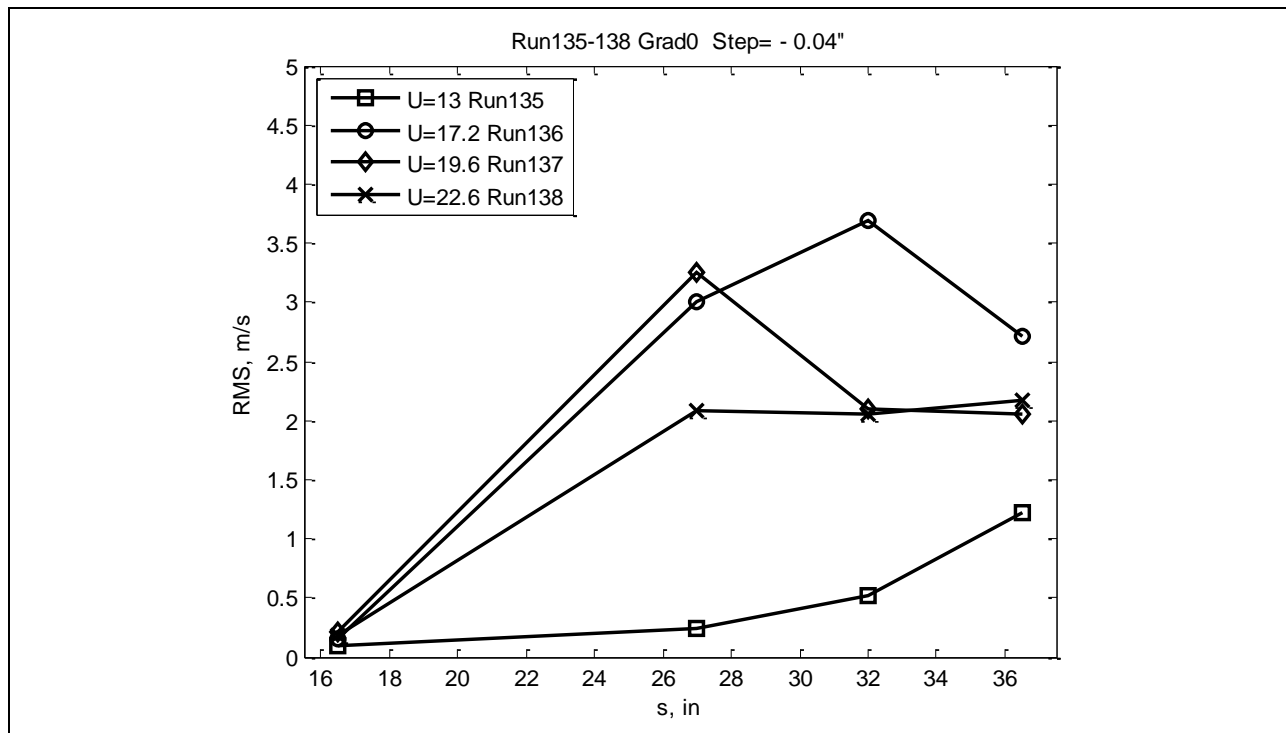


Figure 812: Velocity RMS.

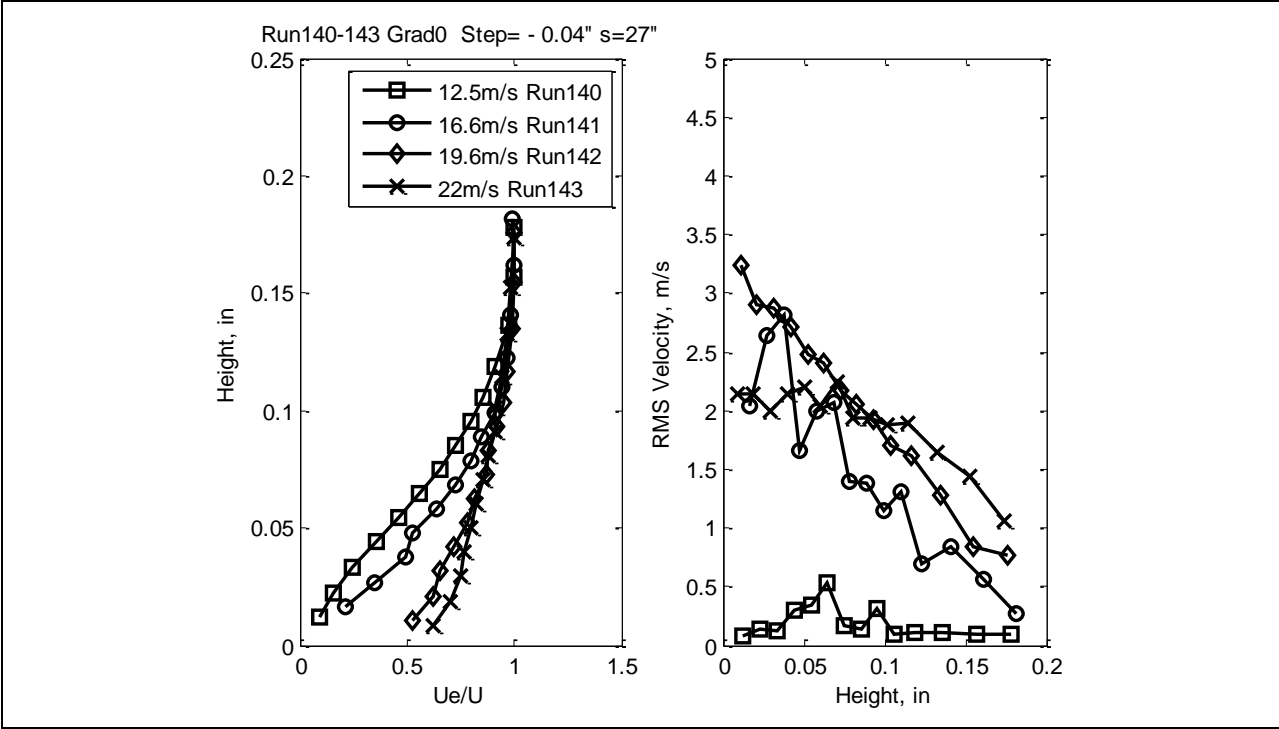


Figure 813: Velocity (left) and RMS (right) profiles.

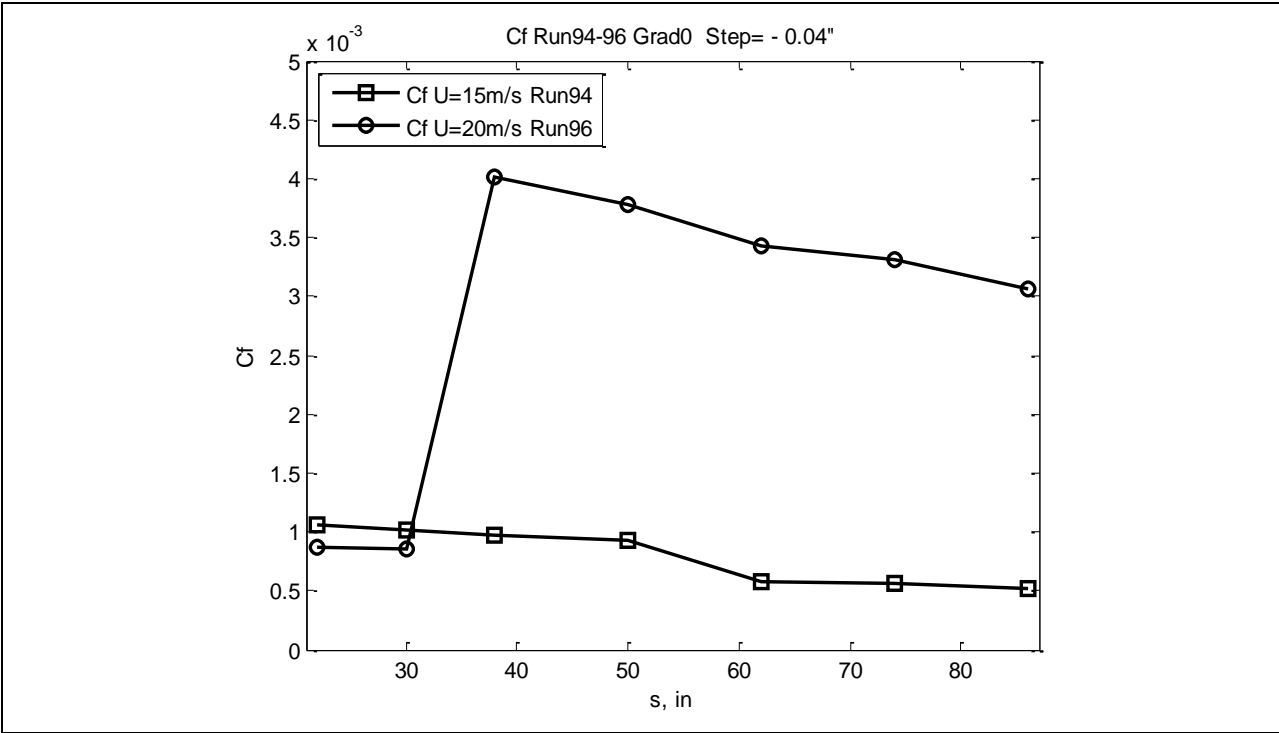


Figure 814: Cf distribution.

Figure 815 (RMS velocity) and Figure 816 (Cf distribution) both show laminar flow in boundary layer for all speeds and all stream-wise locations for Gradient-A and zero step. The RMS is at the level of 0.1-0.3m/s and Cf at 0.0005 for laminar flow.

Figures 817-819 are for the case of Gradient-A and a forward-facing 0.065in step. According to the Cf distribution (Figure 819), transition happens at $U=30\text{m/s}$ at about $s=55\text{in}$. The traversing hot-wire data (Figure 818) show that the boundary layer profile changes to a turbulent one at $U=23.6\text{m/s}$ at $s=65.5\text{in}$, which is consistent with the U and s for transition from Cf distribution. Figure 817 shows that velocity RMS increases from laminar to turbulent earlier than the velocity profile changes from laminar to turbulent.

Figures 820-822 are for the case of Gradient-A and an aft-facing -0.04in step. According to the Cf distribution (Figure 822), transition happens at $U=23\text{m/s}$ at about $s=70\text{in}$. The traversing hot-wire data (Figure 821) show that the boundary layer profile changes to turbulent one at $U=17.6\text{m/s}$ at $s=65.5\text{in}$, which is close to the U and s for transition from Cf distribution. The Figure 820 shows that velocity RMS increases from laminar to turbulent earlier than the velocity profile changed from laminar to turbulent.

All the results above confirm that the RMS velocity is a sensitive indicator of perturbations to the laminar velocity profile, but even the use of spectral broadening as an indicator of transition can lead to a false prediction because of the stabilizing nature of the downstream flow on these models. The skin friction, Cf, responds to a change in mean velocity profile which explains the reason why the former shows transition earlier than the latter.

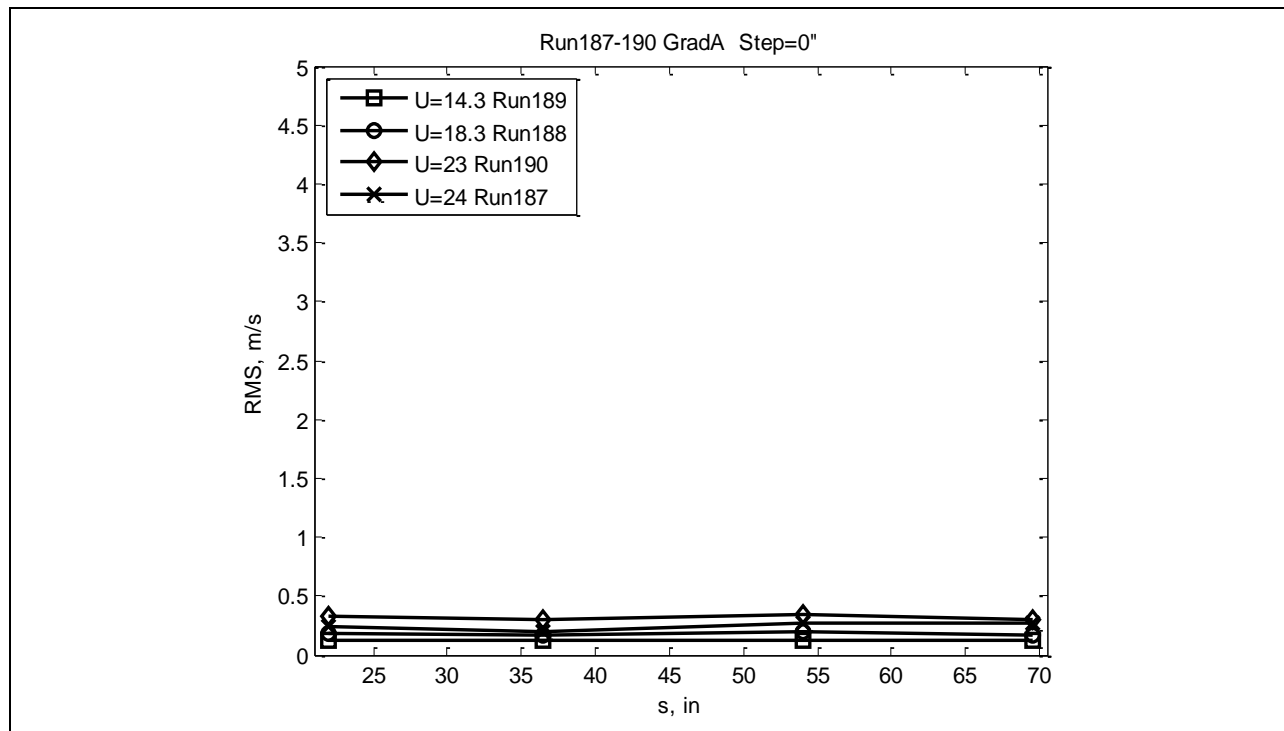


Figure 815: Velocity RMS.

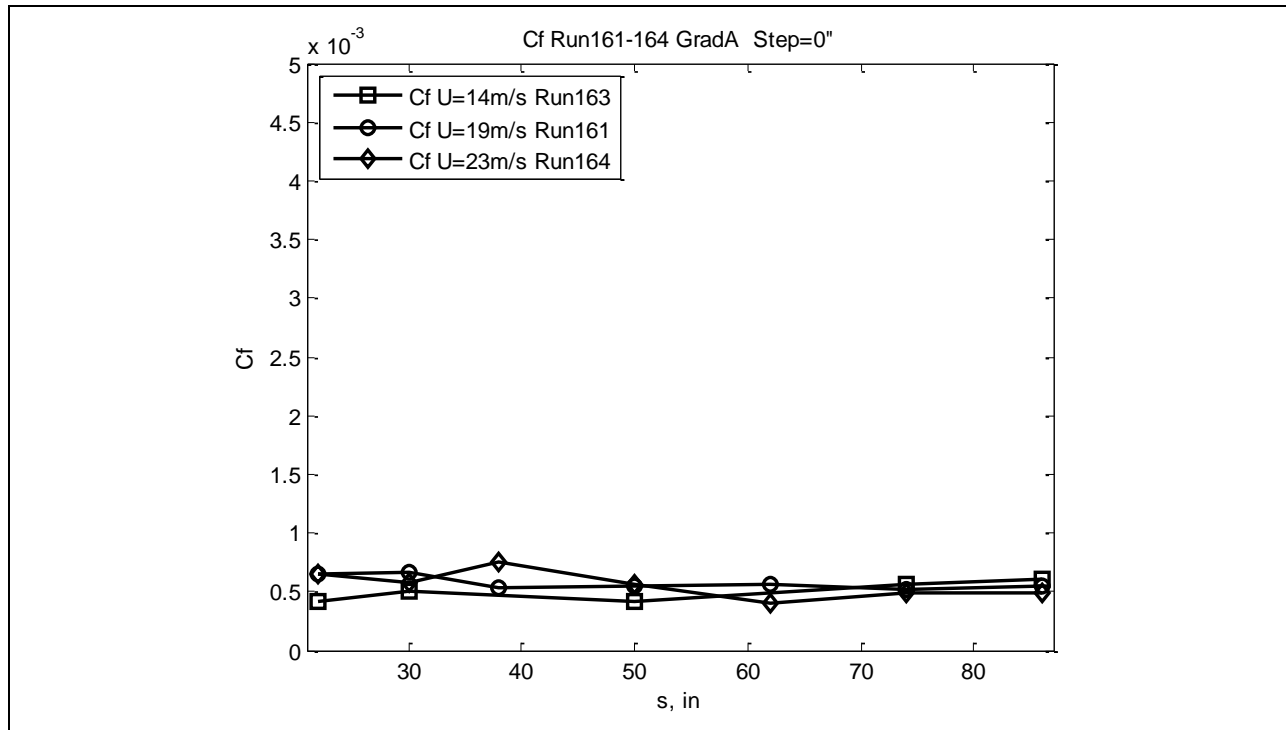


Figure 816: Cf distribution.

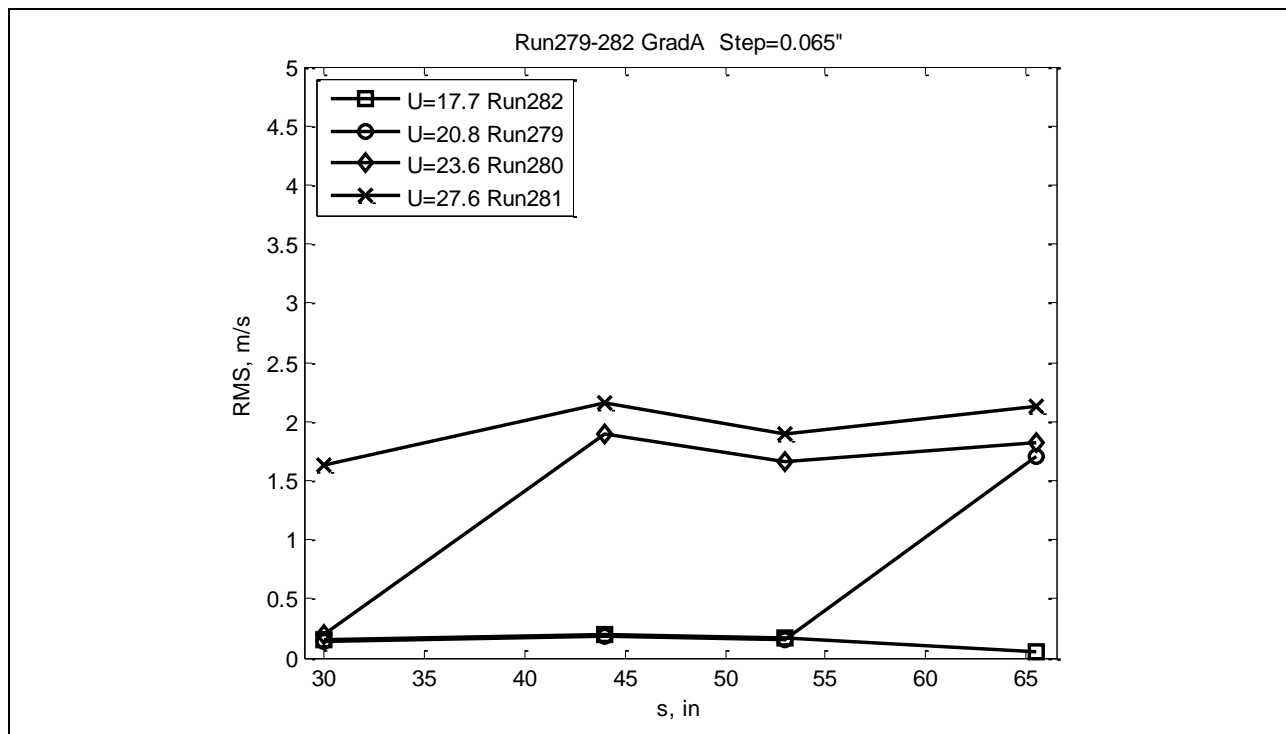


Figure 817: Velocity RMS.

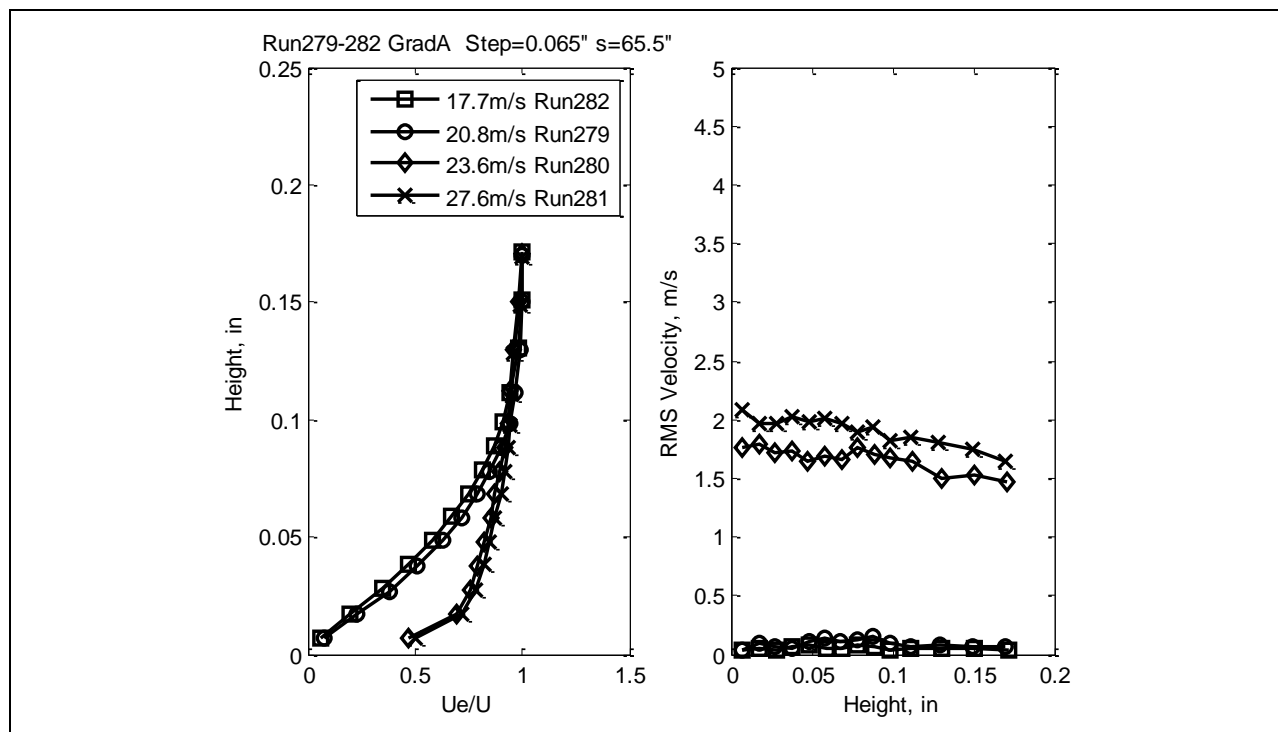


Figure 818: Velocity (left) and RMS (right) profiles.

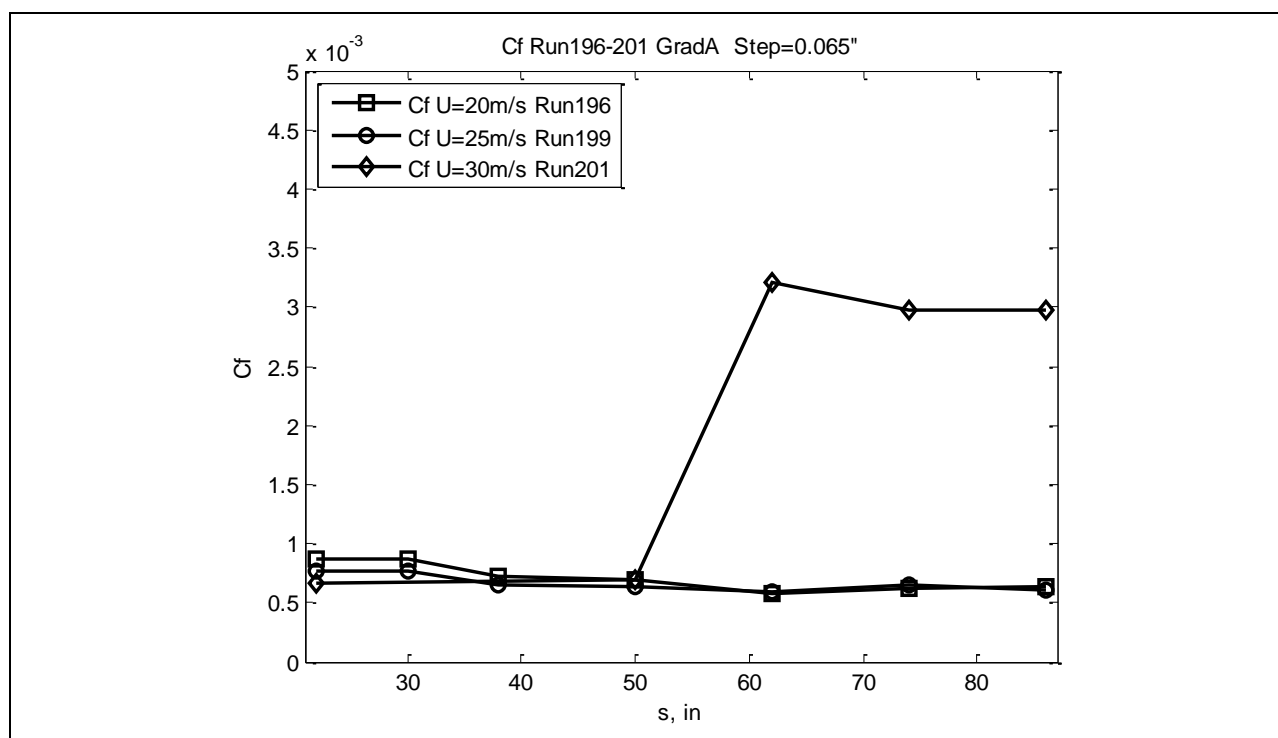


Figure 819: Cf distribution.

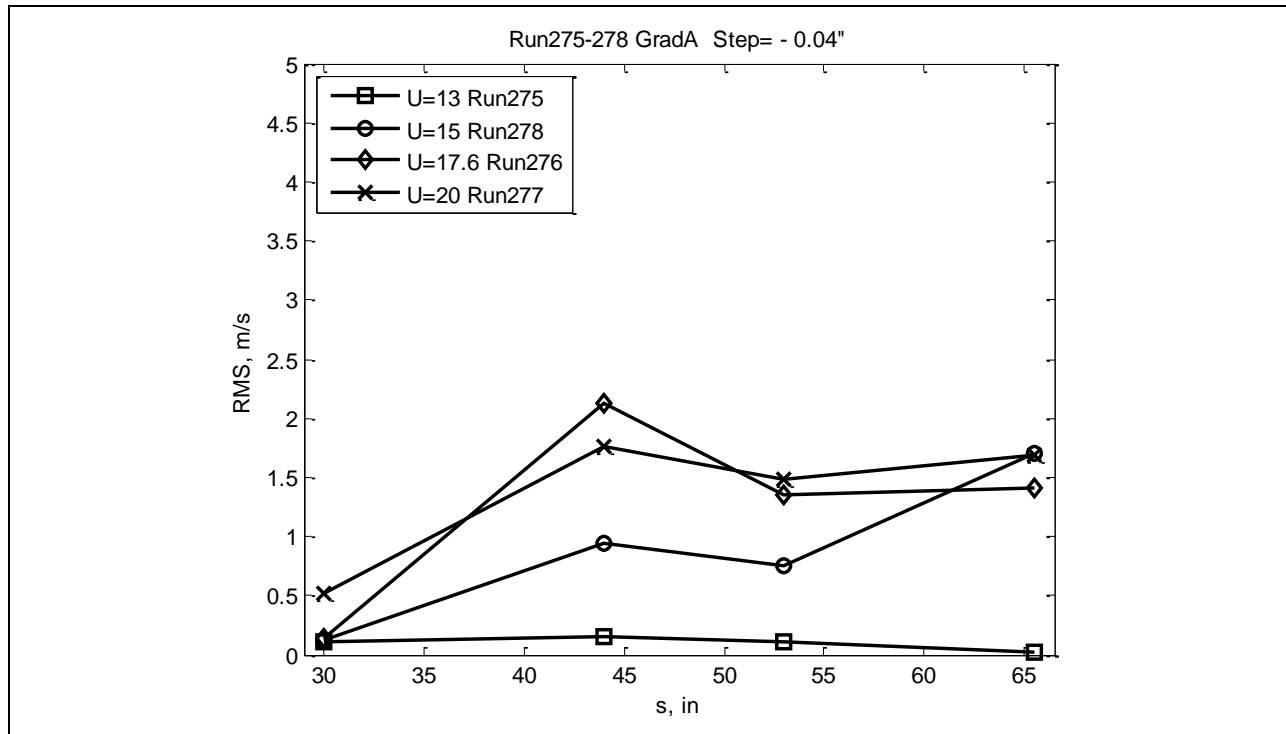


Figure 820: Velocity RMS.

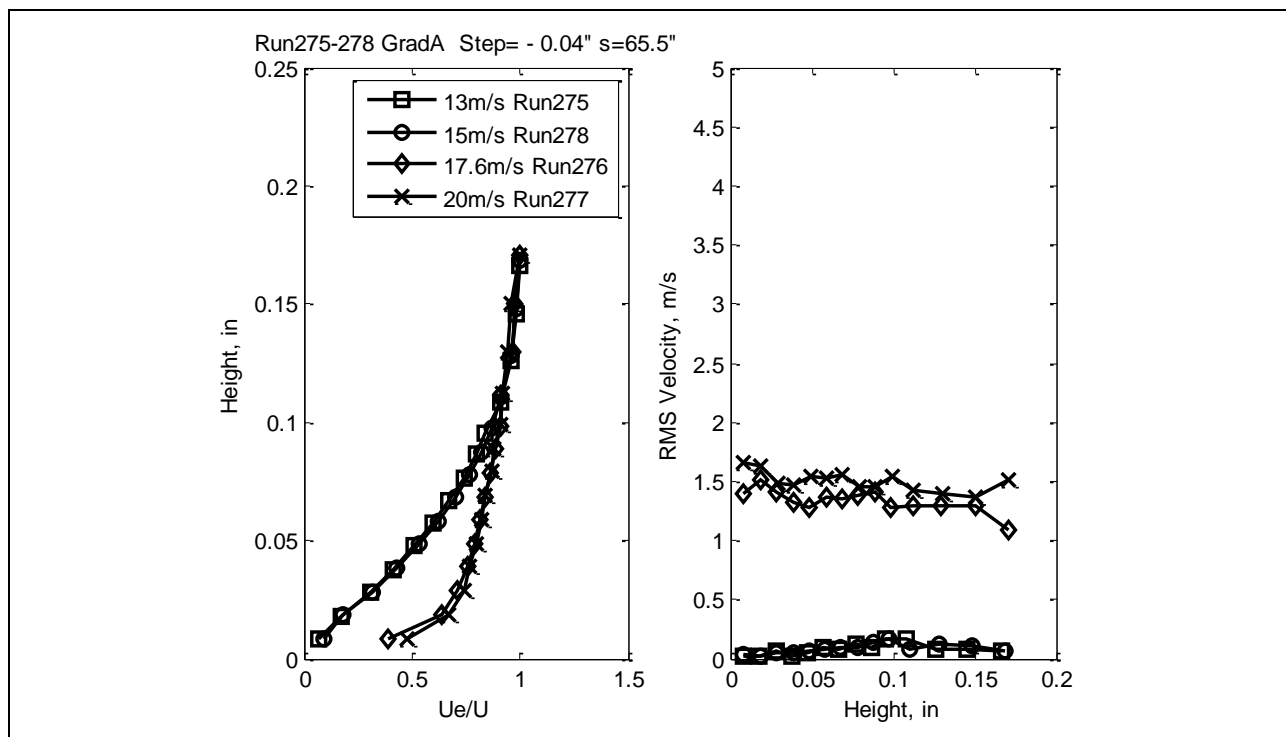


Figure 821: Velocity (left) and RMS (right) profiles.

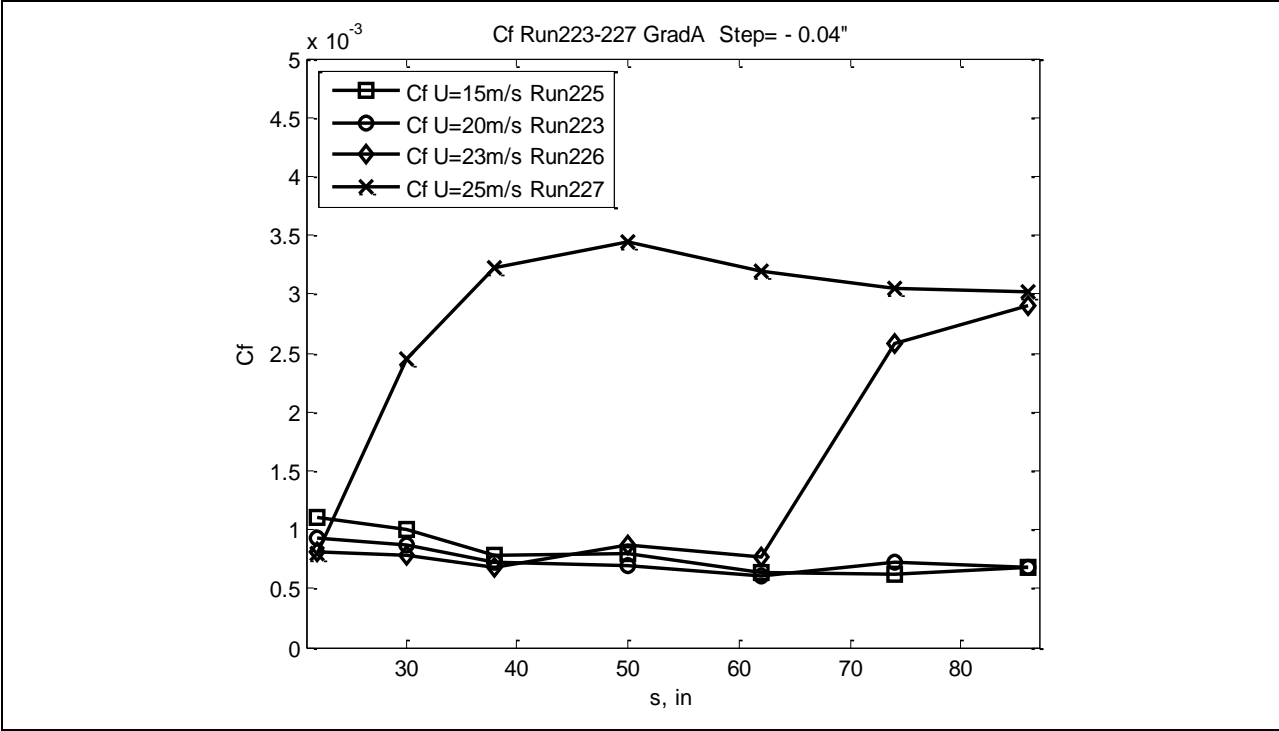


Figure 822: Cf distribution.

8.0 EXCRESCENCE RELATIONS

The excrescence relations shown in Figures 823-836 were developed from the skin friction results shown in Section 7.4.3. The excrescence relations are plots of dimensionless step height (Re_k) versus transition Reynolds number (Re_{tr}). There is one plot for each model and step geometry (e.g. forward- or aft-facing step), showing the relationship between step height and transition Reynolds number. Different colored symbols represent different dimensionless excrescence locations (Re_{xk}), which varied by virtue of the change in freestream speed. There is also one additional plot per model and step geometry that collapses the different Re_{xk} results into a single trendline.

The closed symbols on the plots below represent measured transition locations. The open symbols represent runs wherein transition was not measured on the plate (i.e. the flow was all laminar for that condition). The transition Reynolds number value of the open symbols is shown at the end of the measurement section of the model – transition is at least greater than that Re_{tr} value. In some cases (for example, Figure 827), the trendlines are shown to follow these open symbols – this is a conservative use of the open symbol data since the open symbols do not represent measured transition locations. The Gradient-B data is shown as a dashed line because the data is somewhat suspect due to the gap that was present near the step location. The significance of the excrescence relations is discussed in Section 9.0, Conclusions.

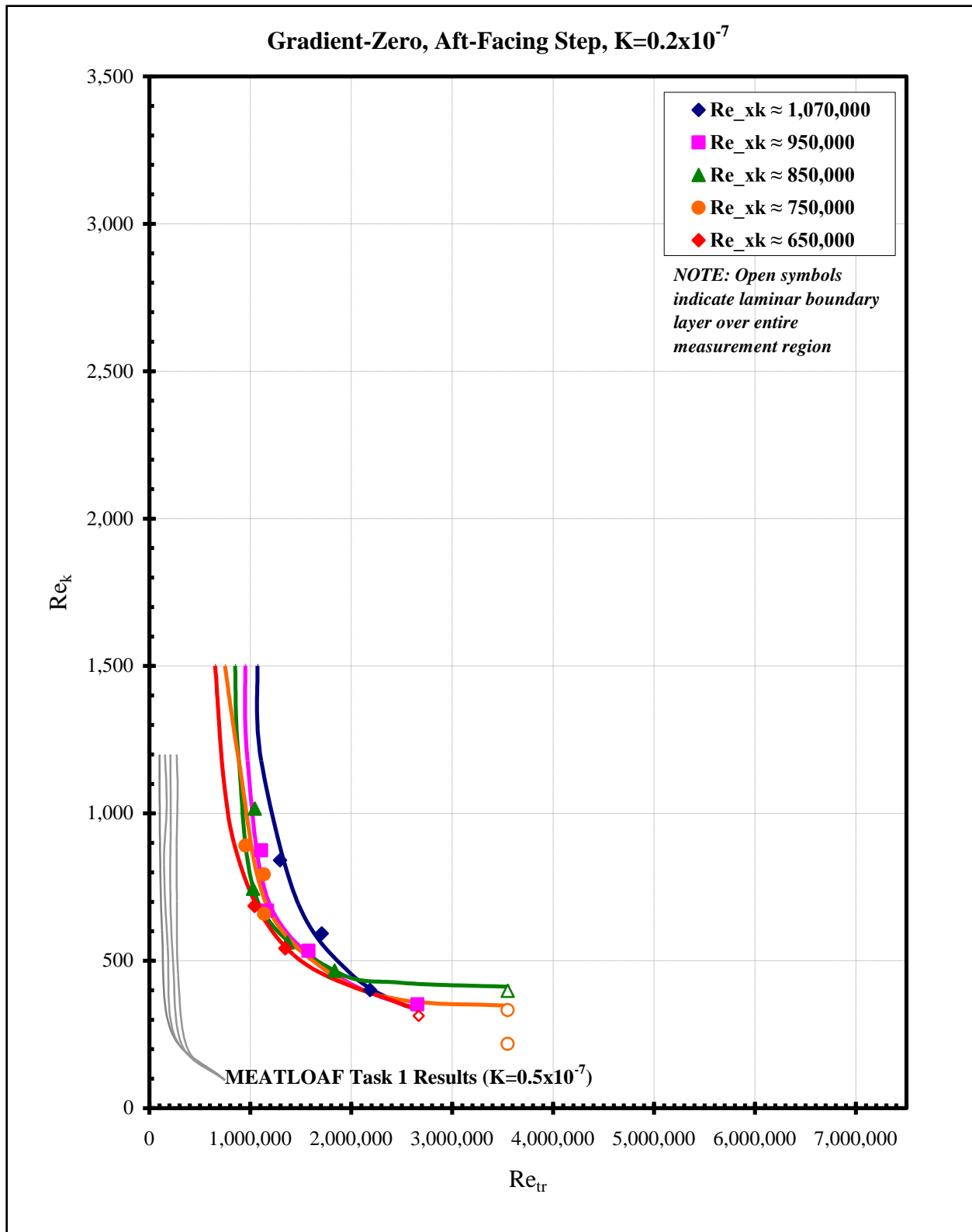


Figure 823: Transition location for aft-facing steps on Gradient-Zero model.

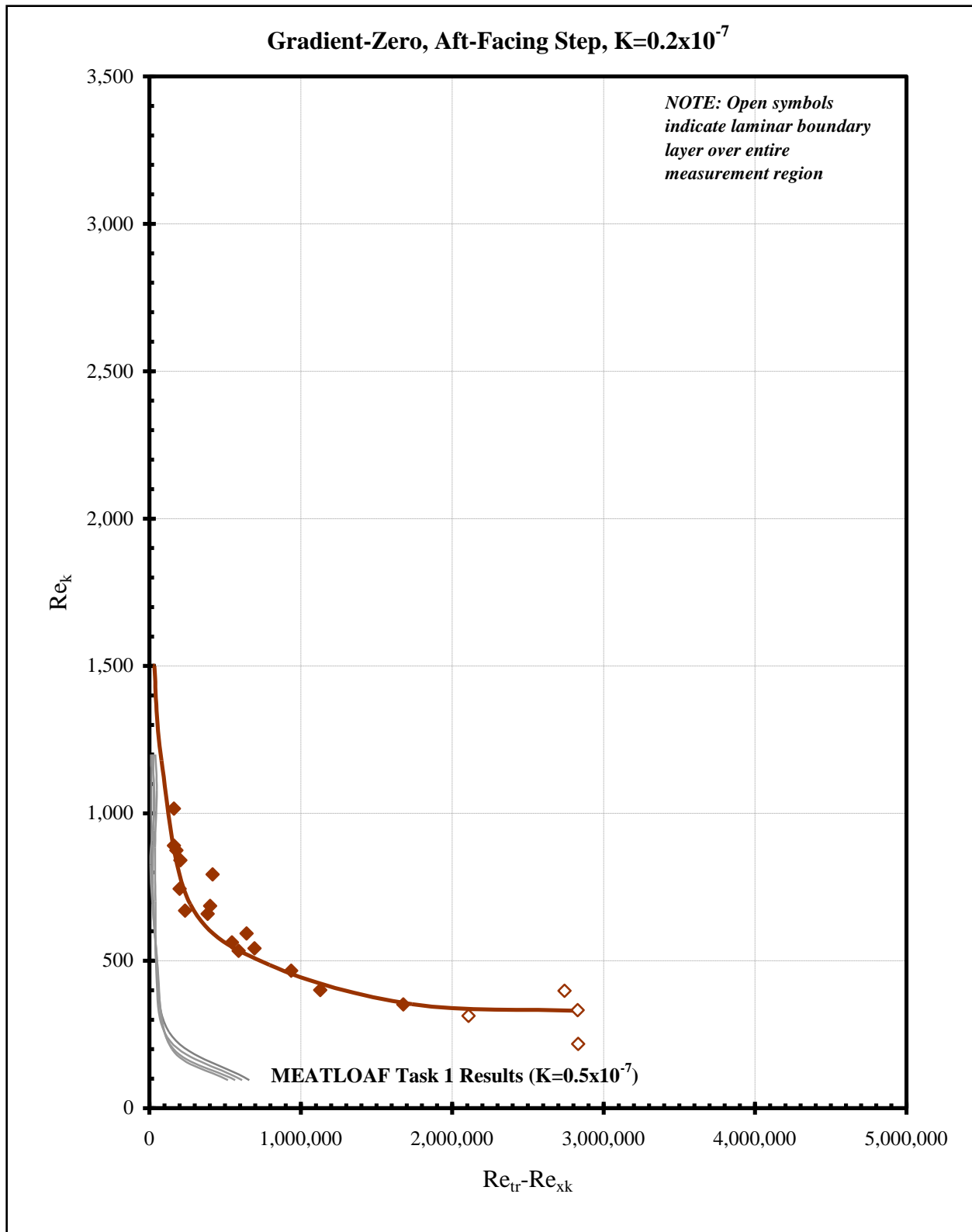


Figure 824: Transition location for aft-facing steps on Gradient-Zero model.

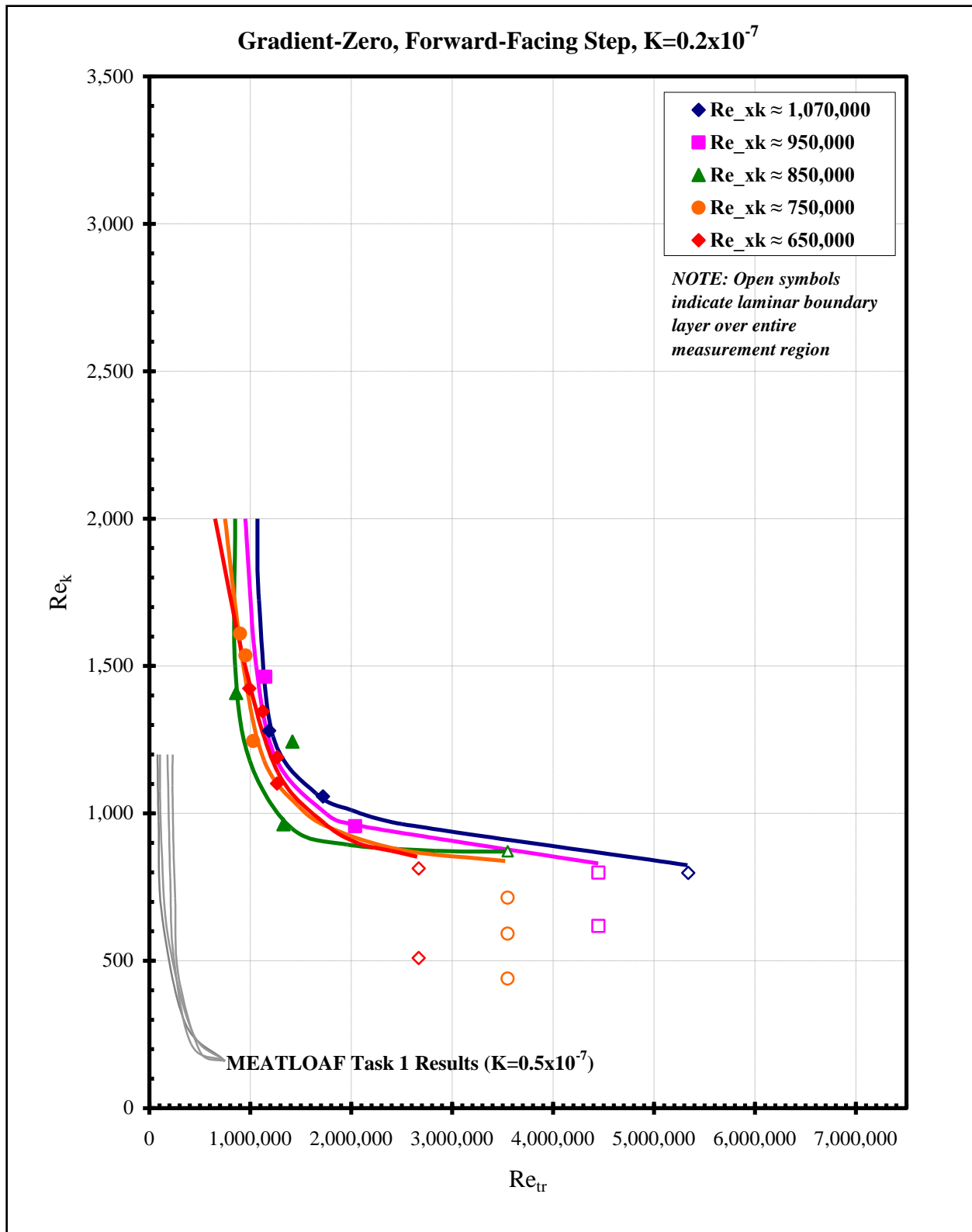


Figure 825: Transition location for forward-facing steps on Gradient-Zero model.

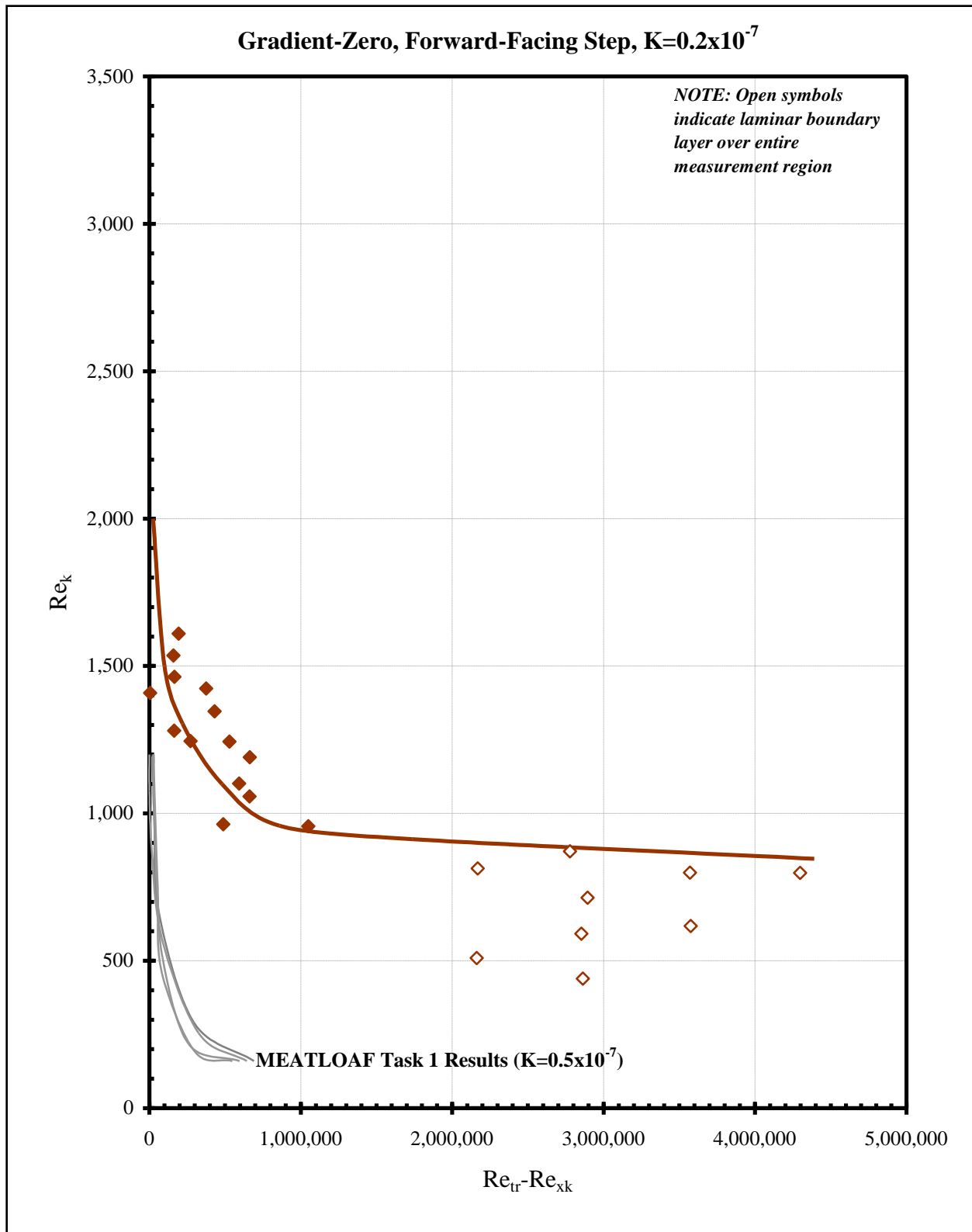


Figure 826: Transition location for forward-facing steps on Gradient-Zero model.

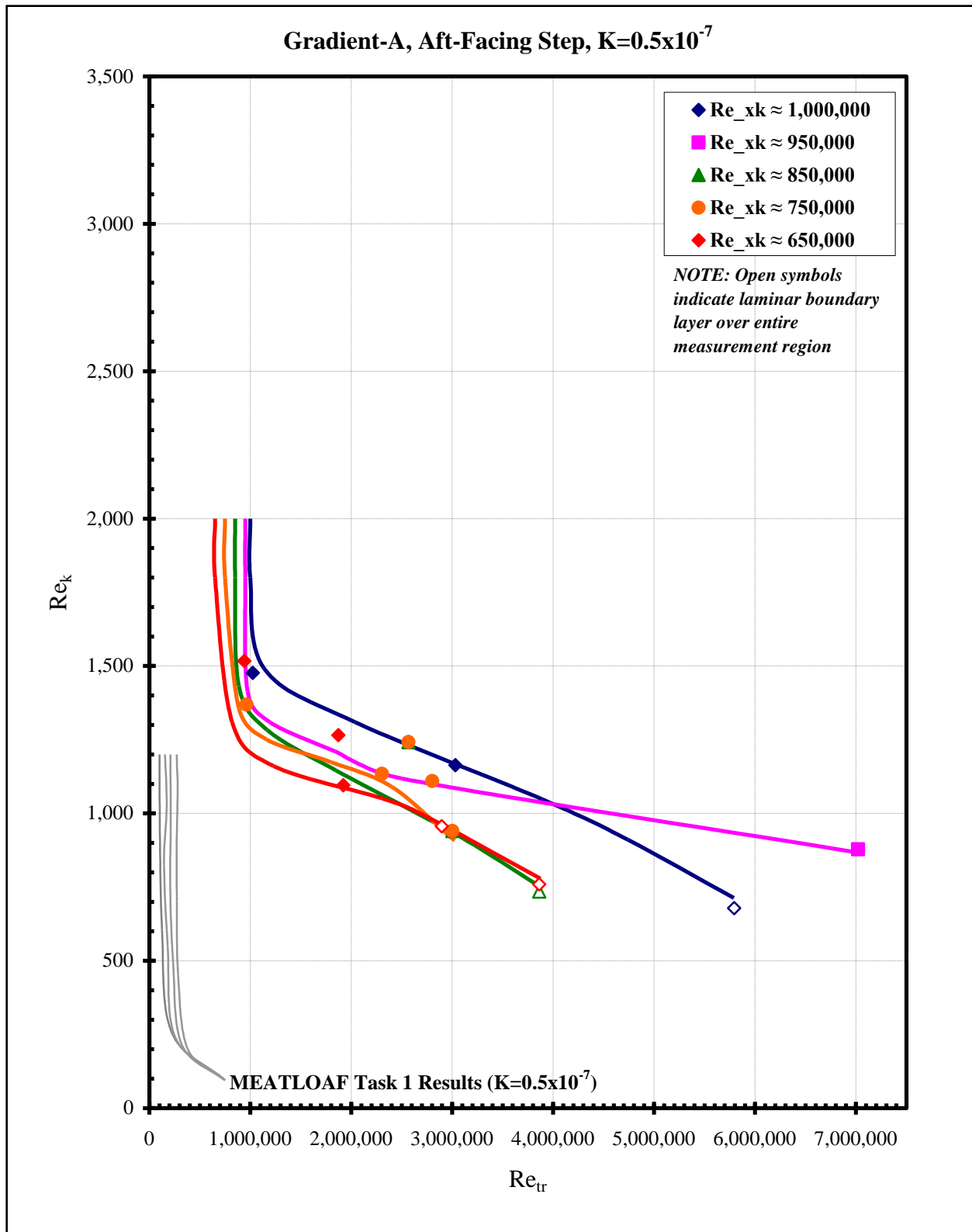


Figure 827: Transition location for aft-facing steps on Gradient-A model.

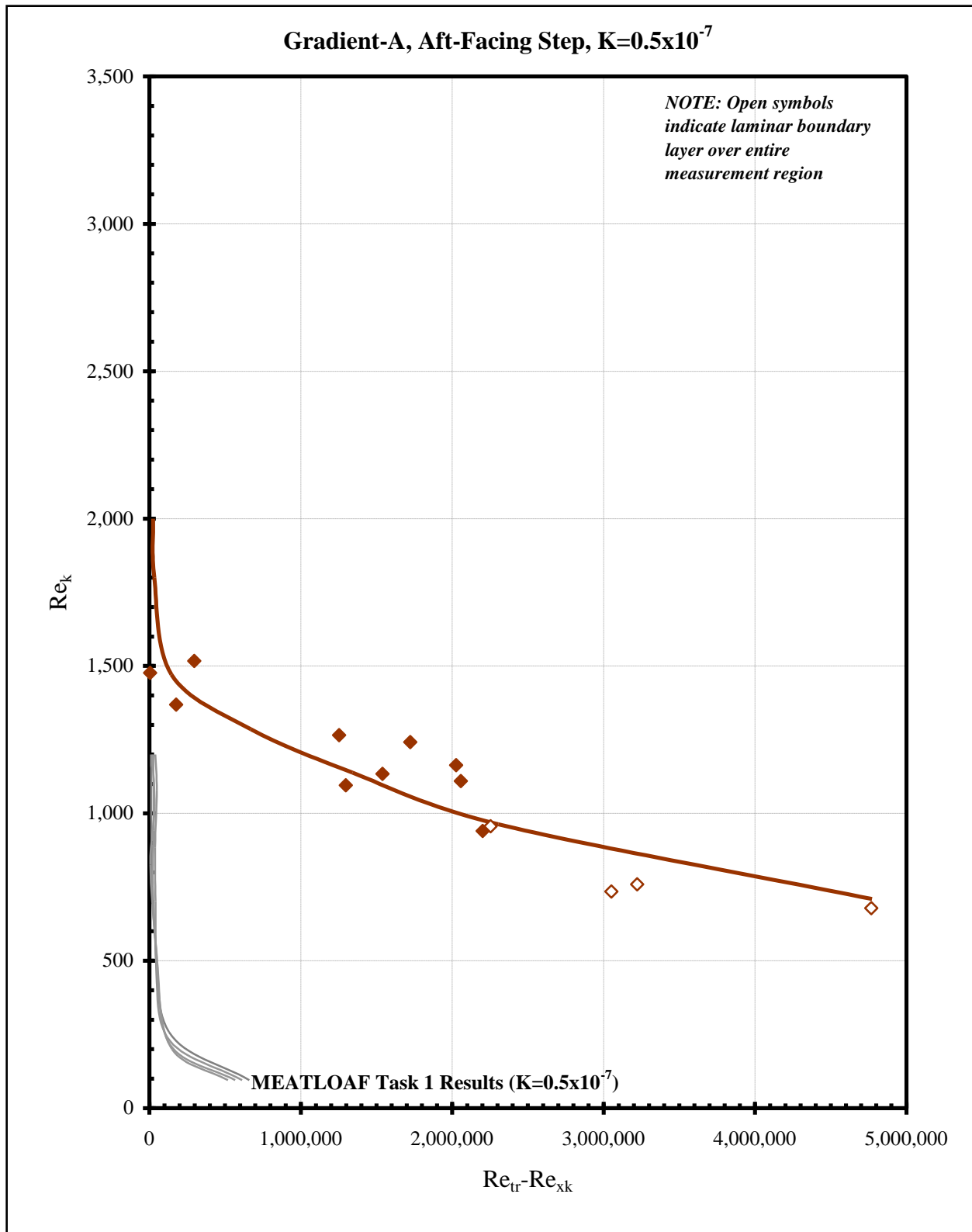


Figure 828: Transition location for aft-facing steps on Gradient-A model.

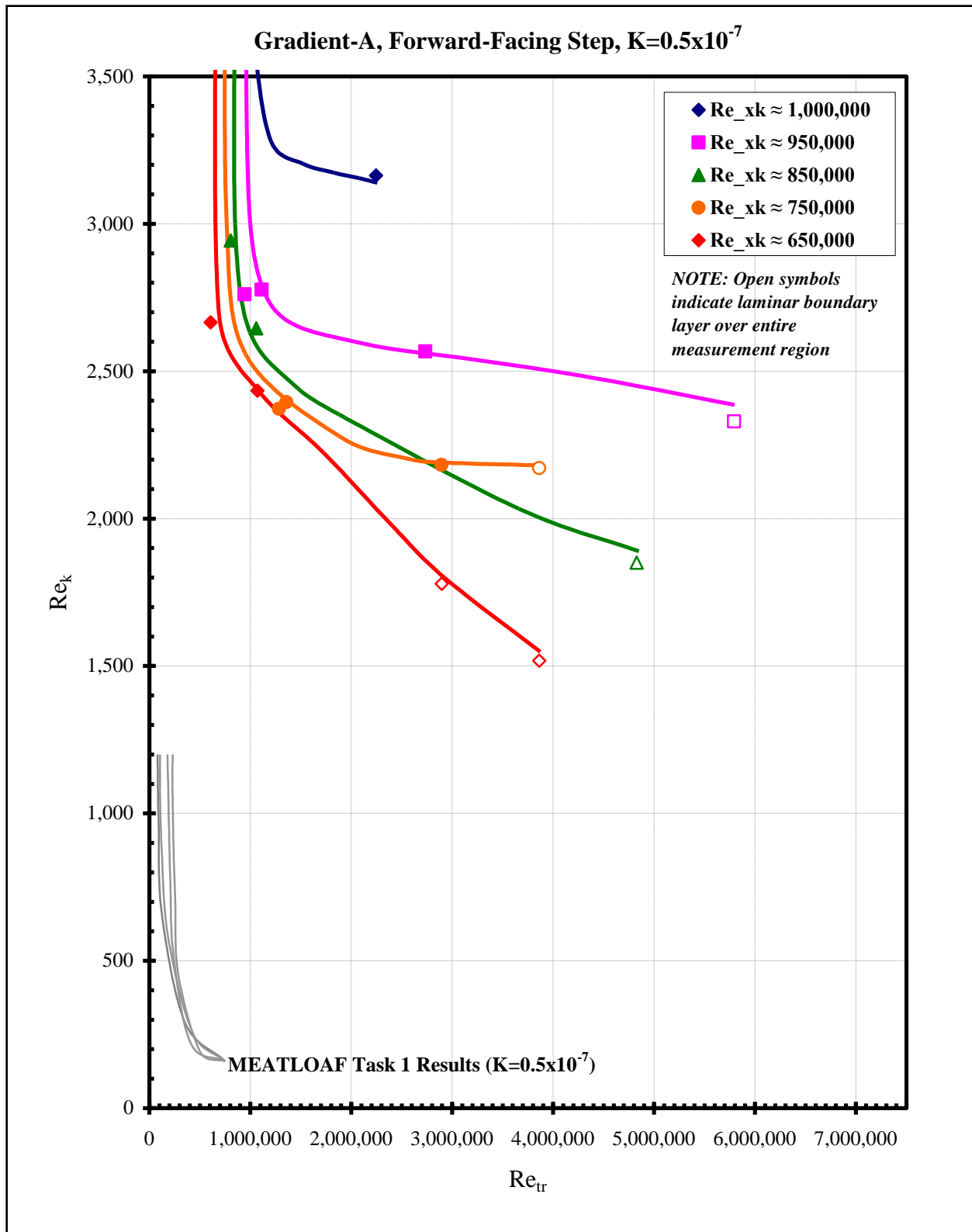


Figure 829: Transition location for forward-facing steps on Gradient-A model.

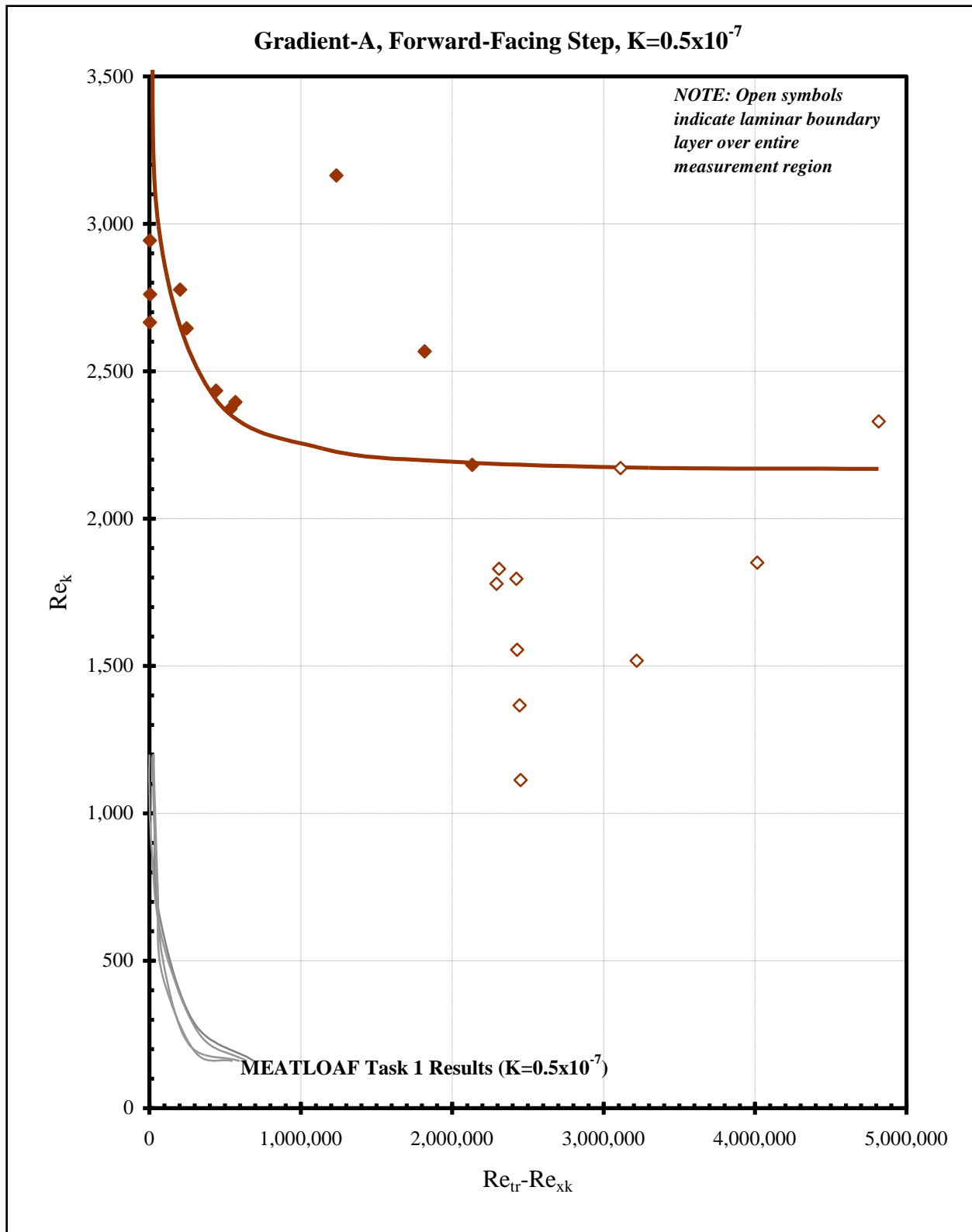


Figure 830: Transition location for forward-facing steps on Gradient-A model.

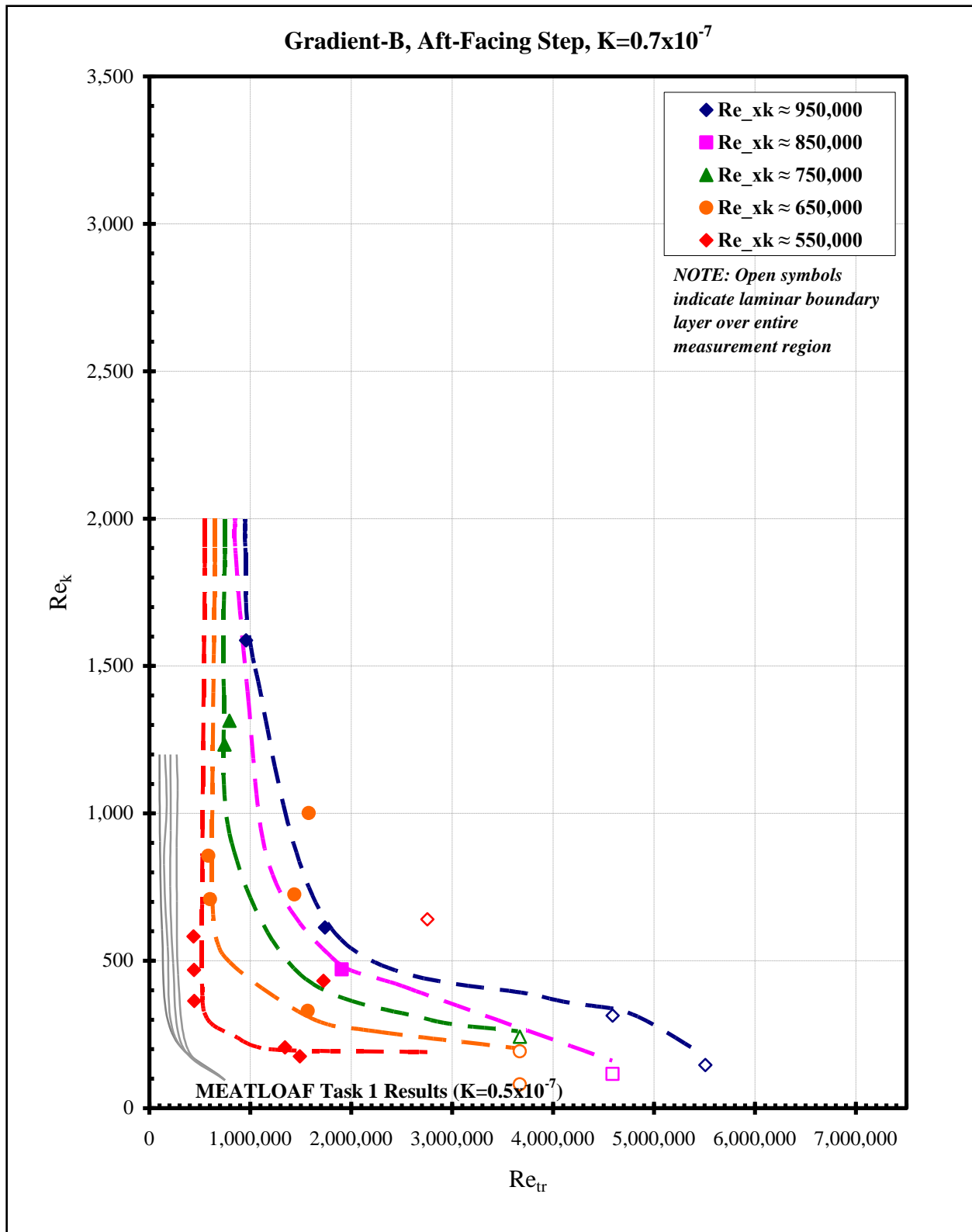


Figure 831: Transition location for aft-facing steps on Gradient-B model.

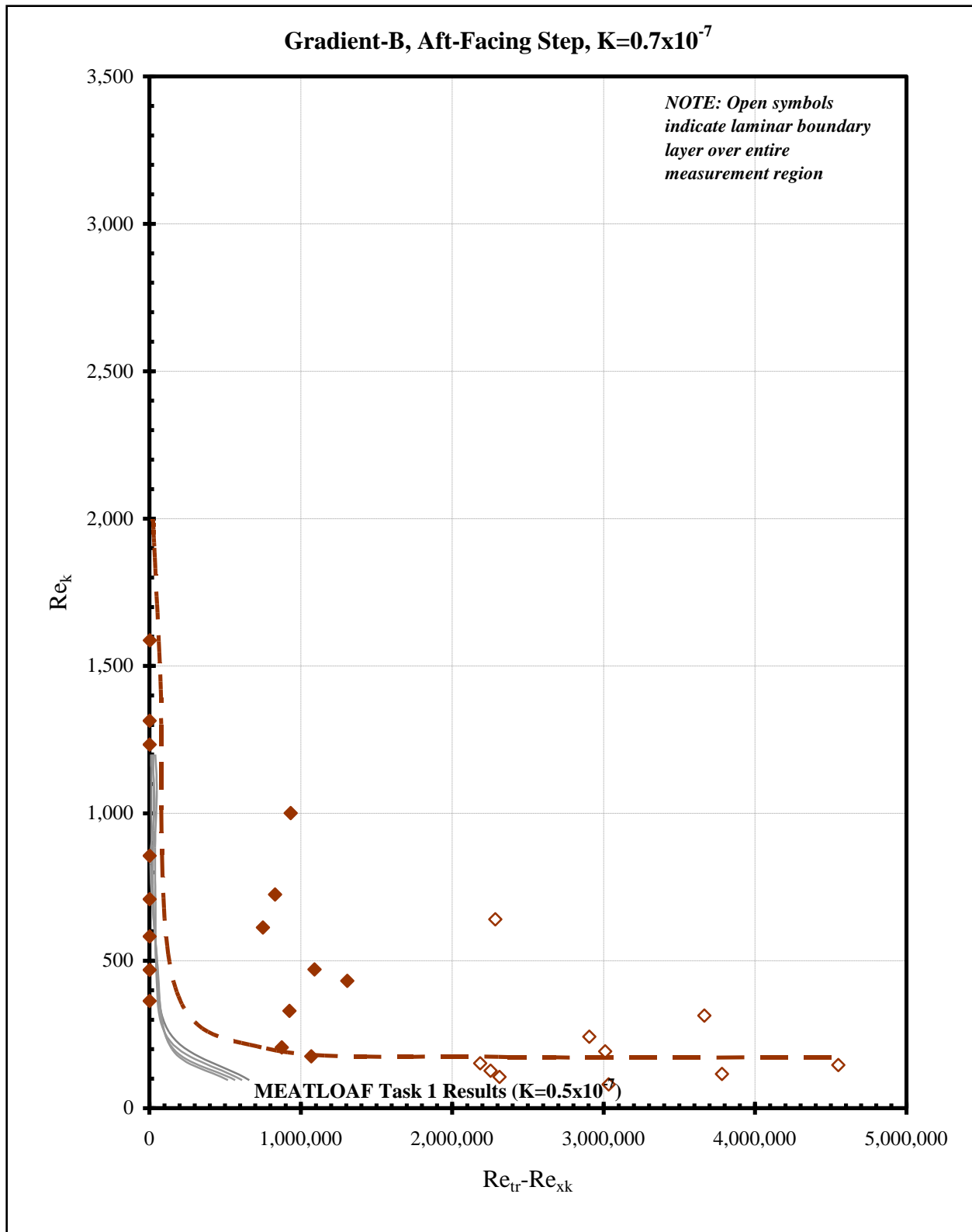


Figure 832: Transition location for aft-facing steps on Gradient-B model.

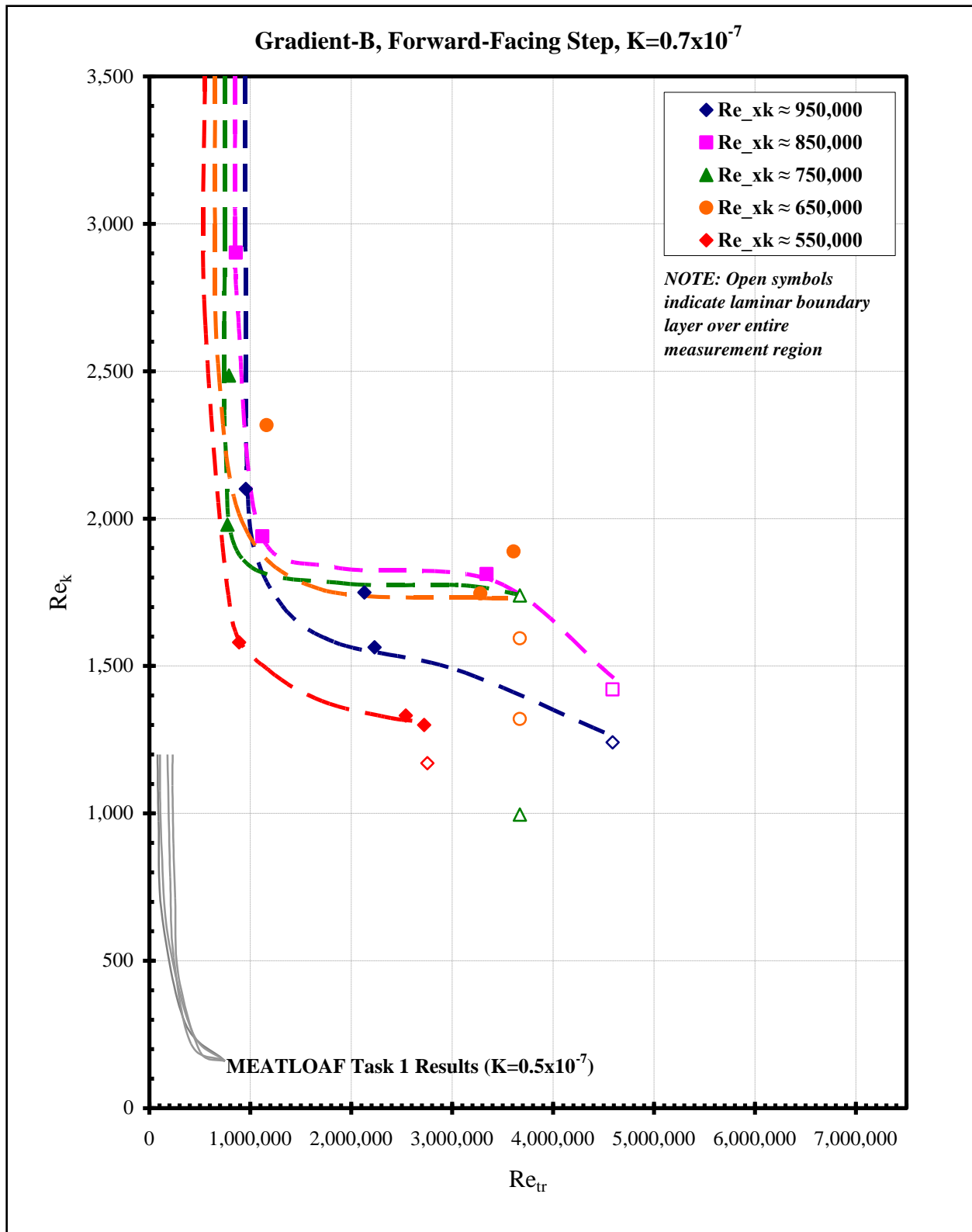


Figure 833: Transition location for forward-facing steps on Gradient-B model.

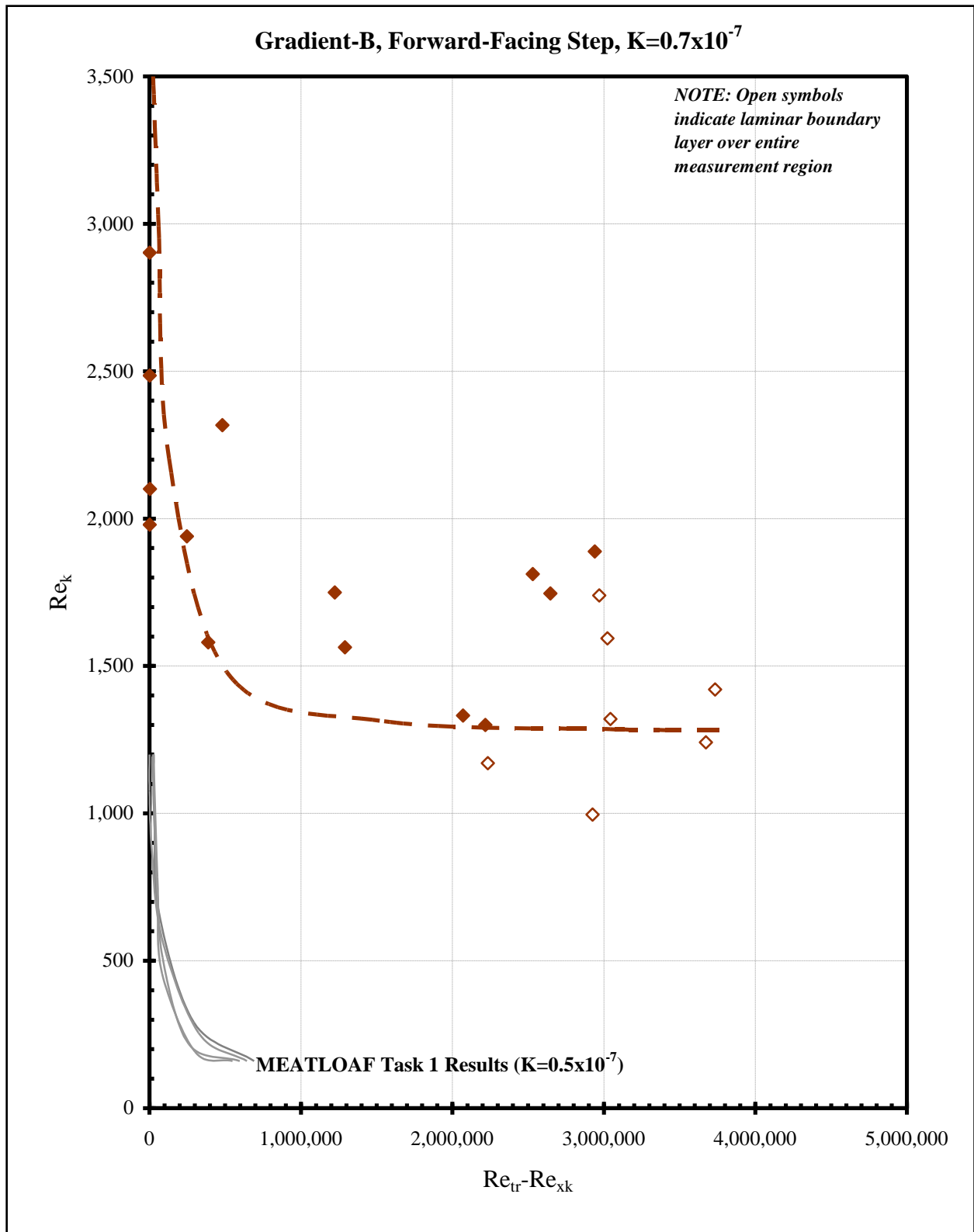


Figure 834: Transition location for forward-facing steps on Gradient-B model.

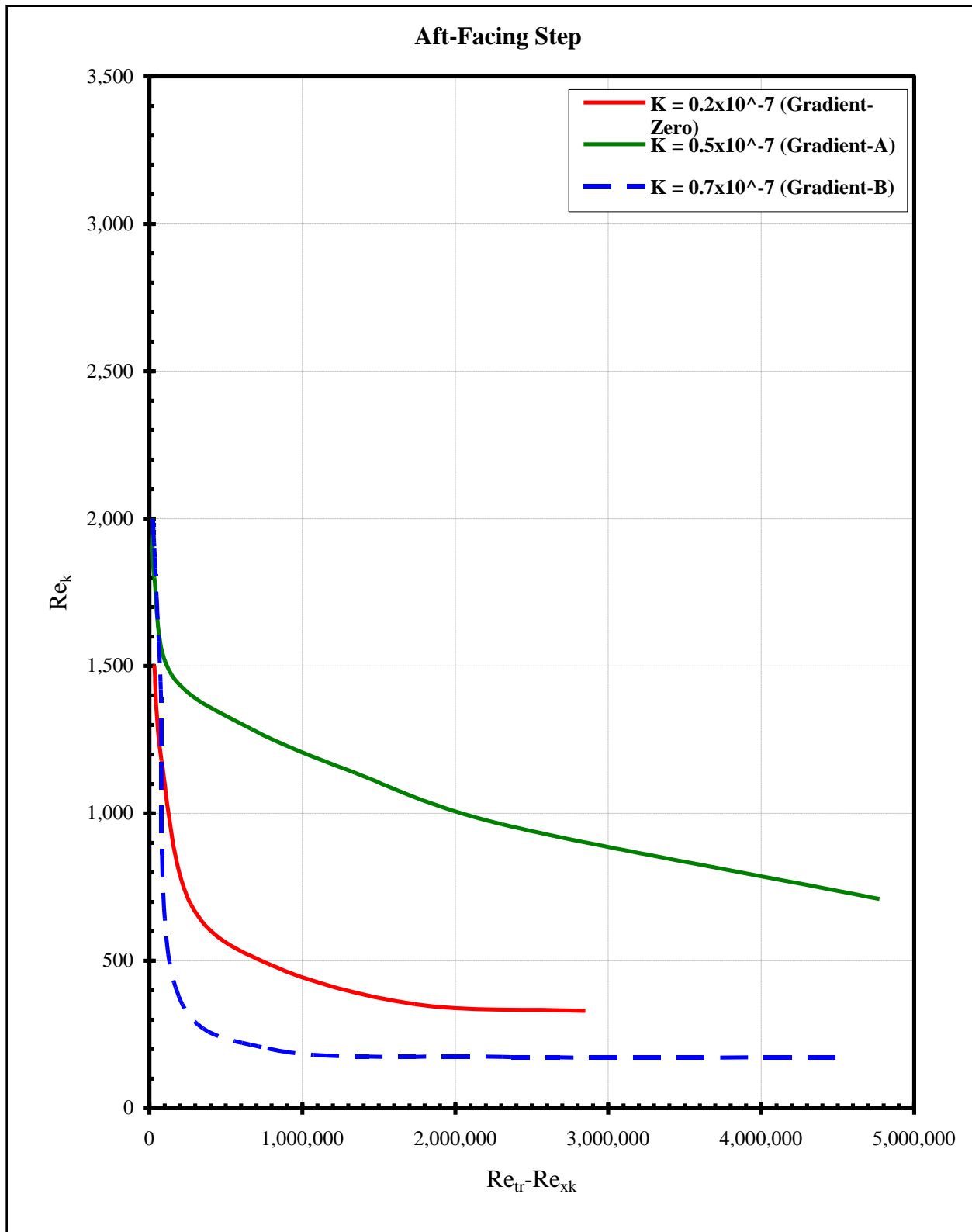


Figure 835: Aft-facing step transition locations.

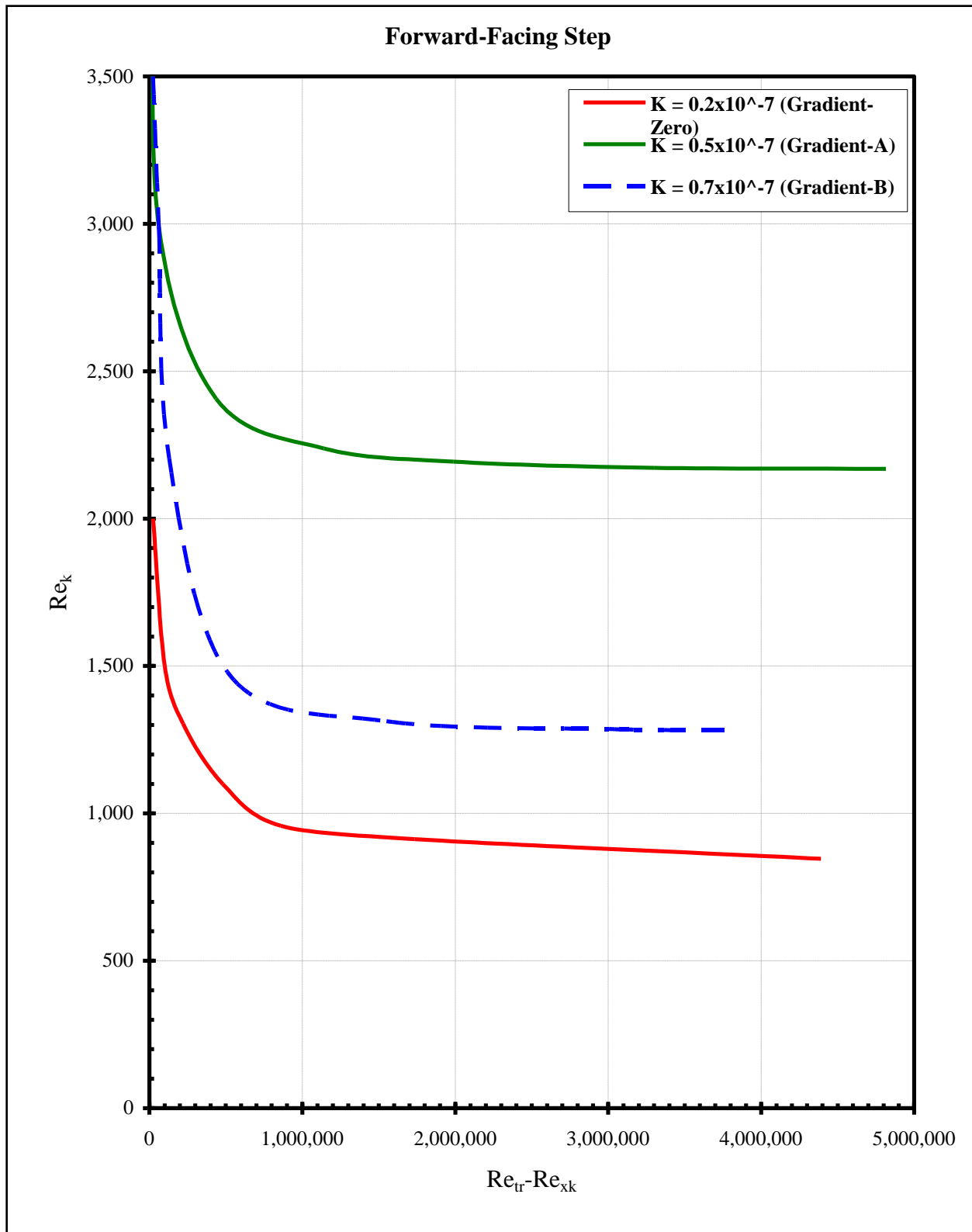


Figure 836: Aft-facing step transition locations.

9.0 CONCLUSIONS

The results of the SETS testing have allowed the transition relations, Re_k as a function of Re_{tr} , to be extended to significantly higher Reynolds numbers. These relations are applicable to current and future laminar flow aircraft and can be used as a basis for determining the required manufacturing tolerances. The allowable heights of step excrescences obtained in the SETS study are significantly larger than previous studies have indicated. This will allow for loosening of tolerances on laminar flow aircraft which could contribute to more practical applications of the technology.

Models designed for the Towing Wind Tunnel test facility provided the desired pressure gradients and fully exploited the capabilities of the facility. The shakedown wind tunnel testing conducted was instrumental in identify a number of minor shortcomings in the hardware. This allowed those to be fixed prior to shipping the models and instrumentation to the overseas test facility. The Gradient-B model, which was the only hardware element that was not tested in the shakedown wind tunnel test, experienced significant issues during the test that negatively impacted the results.

The flow characterization for all three SETS models showed (see Section 7.5.7.7) that starting from the step location and with increase of the stream-wise distance the boundary layers have linearly growing velocity profiles, increasing (and freestream velocity sensitive) displacement thicknesses, negative and decreasing coefficients of pressure, positive and almost constant (but freestream velocity sensitive) acceleration parameters, monotonically decreasing and independent of the freestream velocity shape factors, monotonically increasing and independent of the freestream velocity pressure parameters. The last observation indicates that the boundary layer flows are not similar for the SETS models.

The TI measurements showed a high level of turbulence in freestream (probably still an underestimate because only one velocity component was measured). On the other hand, the (correlated) electronic noise observed in the velocity signal (see spectra in Section 7.5.7.1) effectively contributed to the TI. Depending on a particular run and type of a model the uncorrected TI varied on average from 0.33-0.57% for a full frequency range 0-1500Hz of the velocity spectra and from 0.15-0.4% for the 100-1000Hz confining the most dangerous part of the frequency range where unstable T-S wave can be amplified (100-300Hz). These values are larger than would be expected based on the T-S wave results. The maximal span-wise variation in TI was about 0.1% for both frequency ranges (see Section 7.5.7.5 flow uniformity measurements). Use of a differencing technique to remove the rms velocity component that was correlated between wires led to a more reasonable estimate of TI of 0.05-0.1%, which is acceptable for transition studies.

The acceleration measurements provided information about model vibration (see Section 7.5.7.6 on accelerometer results). In general, the vibration spectra revealed low power over a broad range of frequencies. They did not show any sharp peaks for the most dangerous part of the frequency range where unstable T-S waves can be present.

The transition location found from the hot-wire measurements was compared with that found from Preston tube measurements. The qualitative criteria for the transition in the first approach were the fully intermittent velocity history and broad power spectrum. The criterion for the transition in the second approach was a 50% increase of the C_f from its laminar reference level. Although the low spatial resolution in the hot-wire measurements did not usually permit determination of the exact location of the transition point, the transition onset estimated from the velocity data occurred earlier than that determined from the C_f distributions (see Table 14 and

Table 17). This can be explained by the fact that the velocity spectral broadening and the degree of intermittency (and RMS) are sensitive to the perturbations to the mean velocity profile, whereas the C_f increases when the boundary layer velocity profile significantly changes from laminar to turbulent. The latter is confirmed in the plots shown in the Comparison with skin friction measurements section: whenever increase in C_f happened, the velocity profile changed from laminar to turbulent.

Gradient-Zero model: The frequency peaks found in the velocity spectra from about 100Hz-350Hz for the Gradient-Zero model were attributed to the amplified T-S waves as they fitted to the interval of unstable frequencies (see stability diagram in Figure 797). The amplification and N-factors first increased and then decreased with the stream wise distance (see Table 13 and Figures 787-796) because of the stabilization effect of the favorable downstream pressure gradient. The presence of a step did not change the frequency of the T-S waves but changed the amplification and N-factors. The amplification of the T-S waves for a zero step (clean plate) served as a baseline and was presented in terms of N-factors. The initial power of the T-S wave, A_0 , was determined in two ways. When it was taken as the level of noise in the power spectrum for the first hot-wire (which was usually located close to a step and about 20 inches away from the leading edge where the T-S could be first generated), the N-factors were consistently lower than the values found from the Rapid-N results (Figures 798-801). This can be explained by the presence of the correlated noise leading to a high level of the freestream turbulence, TI. If the latter contribution is high, it can lead to the overestimation of the initial power A_0 and underestimated values of the N-factors. When A_0 was taken as the level of noise for zero flow in calm environment (Figure 340), the N-factors showed much closer values to those obtained in the simulations (Figures 798-801). The presence of steps increased the amplification and N-factors of the T-S waves (see Table 13 and Figures 787-796. The transition location moved closer to the step location. The aft-facing steps were more efficient amplifiers than forward-facing steps (see Table 13 and Figures 529-530). It can be concluded that the transition process for Gradient-Zero model was linear through the generation of unstable T-S waves although significant level of TI and uncertainty in the determination of the initial amplitude of T-S waves resulted in lower values of the N-factors as compared with simulation results.

Gradient-A model: The observed frequencies in the velocity power spectra for Gradient-A model in the presence of the step (see Table 16) did not agree with the unstable region of frequencies (Figure CIT 326) from the literature, likely because the pressure gradient varies significantly along the length of the plate. However, transition happened as indicated the broadening in the velocity power spectra, high intermittency in the velocity history and sharp increase in the C_f distributions.

Gradient-B model: Sealing at the gap led to significant run-to-run variation in the hot-wire results. No T-S waves were observed for Gradient-B model, likely because the critical Reynolds number was not reached. However, transition happened as indicated the broadening in the velocity power spectra, high intermittency in the velocity history and sharp increase in the C_f distributions.

Comparison of Gradient-Zero and Gradient-A model: The stabilizing effect of the pressure gradient can be clearly seen from the comparison of, for example, spectral evolution in the boundary layer in the streamwise direction for Gradient-Zero (Figure 543) and Gradient-A (Figure 544) models. It can be seen that the flow was already unstable at $s=27$ inches for Gradient-Zero model, whereas the flow was completely stable at least up to $s=66$ inches for Gradient-A model. The higher negative pressure gradient makes flow more stable with respect to

disturbances.

10.0 RECOMMENDATIONS

The results of the SETS testing provide data on the effects of surface excrescences on boundary layer transition due to pressure gradient at Reynolds numbers closer to many laminar flow aircraft flight conditions than have been previously available. This data should be incorporated into the development of manufacturing tolerances for laminar flow aircraft. It is likely that tolerances developed based, in part, on SETS data will be significantly looser than tolerances based only on previously existing information. These looser tolerances could have a significant impact on manufacturing costs or feasibility assessments.

Follow-on activities should be undertaken to more fully understand the effects of excrescences on boundary layer transition. Excrescences of importance to laminar flow aircraft include more than just the forward and aft facing steps examined in the SETS and MEATLOAF studies. Additional excrescence types that should be examined include three-dimensional excrescences, surface waves, multiple excrescences, and surface patterns. By examining these additional types of excrescences, increased confidence in the setting of manufacturing tolerances can be obtained.

Work in the SETS study focused on understanding the influence of pressure gradient, largely because it was expected to have a significant effect on the transition behavior. Examining the influences of additional parameters is important in fully-developing excrescence relations. The parameters that remain to be examined are sweep angle (of both the leading edge and of the excrescence itself), Mach number, and extensions in Reynolds number to even higher levels.

Follow-on activities to investigate an expanded set of excrescence geometries could also examine a different mechanism of transition, namely bypass transition – so called because it bypasses linear mechanisms. Additional data, in particular from the different flow environment, could prove key to developing the relation between stability analysis and excrescence effects on transition. Analysis of SETS data and comparisons with linear stability analysis has opened the door to utilizing stability analysis to supplement – and potentially significantly substitute for – an experimentally developed database of excrescence effects.

REFERENCES

1. Drake, Bender, Solomon, and Vavra, "Air Vehicle Technology Integration Program (AVTIP) Delivery Order 0020: Prediction of Manufacturing Tolerances for Laminar Flow Final Report," AFRL-VA-WP-TR-2005-3060, June 2005.
2. Bender, and Drake, "Air Vehicle Technology Integration Program (AVTIP) Delivery Order 0020: Prediction of Manufacturing Tolerances for Laminar Flow Task 6 Final Report," AFRL-VA-WP-TR-2007-3086, September 2006.
3. Krist, S. L. and Biedron, R. T. and Rumsey, C. L., "CFL3D User's Manual (Version 5.0)," NASA TM-1998-208444, June 1998.
4. Murphy, J. D. and Davies, C.A., Users Guide – Ames Inlet Boundary Layer Program MK I. NASA TM X-62211, January 1973.
5. Yoshioka, Kikuchi, Ohta, Kato, Song, and Kohama, "Measurement of ground effect and boundary-layer transition by towing wind tunnel," 2009 Fluid Dyn. Res. 41 021408 (12pp)
6. Takahashi, K., "The outline of MLU002N on Miyazaki test track," Int. Conf. on Speedup Technology for Railway and MAGLEV Vehicles vol 1 pp 329–33, 1993.
7. Westphal, Bleazard, Drake, Bender, et al, "A Compact, Self-Contained System for Boundary Layer Measurement in Flight", AIAA 2006-3828.
8. Bender, Drake, Westphal, et al., "Development and Flight Demonstration of Self-Contained Boundary Layer Measurement Devices ," AIAA-2008-7333.
9. Poll, P.I.A., "A Note on the Use of Surface Pitot Tubes for the Measurement of Skin Friction in Laminar Boundary Layers", College of Aeronautics Report 8307, Cranfield Institute of Technology, Cranfield, Bedford, U.K., March 1983.
10. Patel, V.C., "Calibration of the Preston Tube and Limitations on its Use in Pressure Gradients", Engineering Laboratory, Cambridge University, December 21, 1964.
11. AN-1005 User's Manual, Hot Wire & Film Anemometry System, A.A. Lab Systems LTD.
12. DAQ Getting Started Guide, National Instruments Corporation, 2008.
13. White, F.M., "Viscous fluid flow", McGraw-Hill International Edition, 2006.
14. Wazzan, A.R., Gazley C., and Smith, A.M.O., "Spatial and temporal stability charts for the Falkner-Skan boundary layer profiles," Douglas aircraft Co. Report DAC-67087, 1968.
15. Ross, J.A. and Barnes, F.H., "The flat plate boundary layer, part 3, comparison of theory with experiment," J. Fluid Mech, 43, pp. 819-832, 1970.
16. Morkovin M.V., "The many faces of transition", in Viscous Drag, C.S.Wells (Ed.). Plenum Press, New York, 1969.
17. Smith, A.M.O., Gamberoni, N., "Transition, pressure gradient and stability theory," Douglas Aircraft Co., technical report no ES-26388, 1956.
18. Jaffe N.A, Okamura T.T. and Smith A.M.O., "Determination of spatial amplification factors and their application to predicting transition", AIAA J., vol.8, no.2, pp. 301-308, 1970.
19. Wang, Y.U. and Gaster, M., "Effect of surface steps on boundary layer transition," Exp. In Fluids, 39, pp. 679-686, 1997.
20. Crouch, J. D., Kosorygin, V. S. and Ng, L. L. (2006) "Modeling the effects of steps on boundary-layer transition," in *IUTAM Symposium on Laminar-Turbulent Transition*, ed.

21. Mack L.M., "Transition prediction and linear stability theory", AGARD pp. 1-1-1-22, 1977.
22. Reshotko, E., Saric, W. S. & Nagib, H. M. Flow quality issues for large wind tunnels. AIAA Paper 97-0225 (1997).
23. Obremski, H.J., et al., "A portfolio of stability characteristics of incompressible boundary layers," AGARDograph No.134, NATO, Paris, 1969.
24. Gaster, M. and Jiang, F., "A rapid scheme for estimating transition on wings by linear stability theory," Proc. 19th Congress of ICAS, Vol. 2, pp. 1104-1113, Anaheim, CA, September 1994.
25. Gaster, M., "Rapid Estimator of Eigenvalues for N-factor Calculation," Tech. rep., Queen Mary and Westfield College, London, 1997.
26. Hool, J.N., "Measurement of Skin Friction Using Surface Tubes", School of Mechanical Engineering, New South Wales University of Technology, February 1956.
27. P.R. Spalart, "Young-Person's Guide to Detached-Eddy Simulation Grids", Boeing Commercial Airplanes
28. Govindarajan, R., pp 37-44, Fluid Mechanics and its Applications (vol. 78), Springer Netherlands.
29. Schubauer, G.B, and Skramstad, H., "Laminar boundary layer oscillations and transition on a flat plate", J. Res. Nat. Bur. Stand., vol.38, pp.251-292, 1947.
30. van Ingen, J.L., "A suggested semi-empirical method for the calculation of the boundary layer transition region," Department of Aeronautics Engineering, Delft Institute of Technology, Delft, The Netherlands, report VTH-74, 1956.

APPENDIX A

Model Static Pressure Tap Locations

Zero					A					B				
tap no.	s (in.)	x (in.)	y (in.)	z (in.)	tap no.	s (in.)	x (in.)	y (in.)	z (in.)	tap no.	s (in.)	x (in.)	y (in.)	z (in.)
1	-1	0.877256	-0.397612	12	1	-1	0.803094	-0.5263	12	1	-1	0.608984	-0.748483	12
2	-0.5	0.394234	-0.269375	12	2	-0.5	0.341144	-0.336055	12	2	-0.5	0.220538	-0.43524	12
3	0.5	0.394234	0.269375	12	3	0.5	0.341144	0.336055	12	3	0.5	0.220538	0.43524	12
4	1	0.877256	0.397612	12	4	1	0.803094	0.5263	12	4	1	0.608984	0.748483	12
5	1.5	1.368273	0.491681	12	5	1.5	1.279858	0.676724	12	5	1.5	1.038872	1.003397	12
6	2	1.862393	0.56803	12	6	2	1.762185	0.808396	12	6	2	1.486226	1.226536	12
7	3	2.854953	0.689369	12	7	3	2.734545	1.04171	12	7	3	2.405945	1.618638	12
8	4	3.850454	0.783845	12	8	4	3.712005	1.252778	12	8	4	3.342808	1.968181	12
9	5	4.847655	0.85835	12	9	5	4.691972	1.451912	12	9	5	4.289455	2.290394	12
10	6	5.845998	0.91556	12	10	6	5.673498	1.643227	12	10	6	5.24176	2.595488	12
11	8	7.84479	0.98253	12	11	8	7.639111	2.012476	12	11	8	7.156643	3.172621	12
12	10	9.844688	0.999641	12	12	10	9.606654	2.371316	12	12	10	9.079318	3.723324	12
13	13	12.84469	1.000372	12	13	13	12.5599	2.898908	12	13	13	11.96994	4.525983	12
14	16	15.84469	1.000379	12	14	16	15.51469	3.417718	12	14	16	14.86454	5.314178	12
15	19.75	19.59469	1.000379	12	15	19.75	19.21005	4.055569	12	15	19.75	18.48697	6.283953	12
16	22	21.84469	1.000378	12	16	22	21.42822	4.432647	12	16	22	20.66253	6.857928	12
17	26	25.84469	1.000378	12	17	26	25.37363	5.091216	12	17	26	24.5341	7.863371	12
18	30	29.84469	1.000377	12	18	30	29.32178	5.733189	12	18	30	28.41084	8.848656	12
19	35	34.84469	1.000376	12	19	35	34.26117	6.509272	12	19	35	33.26485	10.04801	12
20	38	37.84469	1.000375	12	20	38	37.22729	6.958819	12	20	38	36.18143	10.75049	12
21	44	43.84469	1.000374	12	21	44	43.16553	7.817217	12	21	44	42.02461	12.11315	12
22	50	49.84469	1.000373	12	22	50	49.11212	8.615672	12	22	50	47.88506	13.39942	12
23	56	55.84469	1.000372	12	23	56	55.06749	9.345603	12	23	56	53.76325	14.60173	12
24	62	61.84469	1.000371	12	24	62	61.0322	9.994828	12	24	62	59.6633	15.69149	12
25	68	67.84469	1.00037	12	25	68	67.00713	10.54186	12	25	68	65.5873	16.64134	12
26	74	73.84469	1.000369	12	26	74	72.99157	10.97141	12	26	74	71.53948	17.39379	12
27	80	79.84469	1.000368	12	27	80	78.98441	11.25826	12	27	80	77.51686	17.90268	12
28	86	85.84469	1.000367	12	28	86	84.98307	11.36063	12	28	n/a	n/a	n/a	n/a
29	92	91.84469	1.000366	12	29	92	90.98067	11.2202	12	29	n/a	n/a	n/a	n/a
30	98	97.84469	1.000365	12	30	98	96.96236	10.76666	12	30	n/a	n/a	n/a	n/a
31	104	103.8447	1.000364	12	31	n/a	n/a	n/a	n/a	31	n/a	n/a	n/a	n/a
32	110	109.8447	1.000363	12	32	n/a	n/a	n/a	n/a	32	n/a	n/a	n/a	n/a
33	-1	0.877256	-0.397612	36	33	-1	0.803094	-0.5263	36	33	-1	0.608984	-0.748483	36
34	-0.5	0.394234	-0.269375	36	34	-0.5	0.341144	-0.336055	36	34	-0.5	0.220538	-0.43524	36
35	0.5	0.394234	0.269375	36	35	0.5	0.341144	0.336055	36	35	0.5	0.220538	0.43524	36
36	1	0.877256	0.397612	36	36	1	0.803094	0.5263	36	36	1	0.608984	0.748483	36
37	1.5	1.368273	0.491681	36	37	1.5	1.279858	0.676724	36	37	1.5	1.038872	1.003397	36
38	2	1.862393	0.56803	36	38	2	1.762185	0.808396	36	38	2	1.486226	1.226536	36
39	3	2.854953	0.689369	36	39	3	2.734545	1.04171	36	39	3	2.405945	1.618638	36
40	4	3.850454	0.783845	36	40	4	3.712005	1.252778	36	40	4	3.342808	1.968181	36
41	5	4.847655	0.85835	36	41	5	4.691972	1.451912	36	41	5	4.289455	2.290394	36
42	6	5.845998	0.91556	36	42	6	5.673498	1.643227	36	42	6	5.24176	2.595488	36
43	8	7.84479	0.98253	36	43	8	7.639111	2.012476	36	43	8	7.156643	3.172621	36
44	10	9.844688	0.999641	36	44	10	9.606654	2.371316	36	44	10	9.079318	3.723324	36
45	13	12.84469	1.000372	36	45	13	12.5599	2.898908	36	45	13	11.96994	4.525983	36
46	16	15.84469	1.000379	36	46	16	15.51469	3.417718	36	46	16	14.86454	5.314178	36
47	19.75	19.59469	1.000379	36	47	19.75	19.21005	4.055569	36	47	19.75	18.48697	6.283953	36
48	22	21.84469	1.000378	36	48	22	21.42822	4.432647	36	48	22	20.66253	6.857928	36
49	26	25.84469	1.000378	36	49	26	25.37363	5.091216	36	49	26	24.5341	7.863371	36
50	30	29.84469	1.000377	36	50	30	29.32178	5.733189	36	50	30	28.41084	8.848656	36
51	35	34.84469	1.000376	36	51	35	34.26117	6.509272	36	51	35	33.26485	10.04801	36
52	38	37.84469	1.000375	36	52	38	37.22729	6.958819	36	52	38	36.18143	10.75049	36
53	44	43.84469	1.000374	36	53	44	43.16553	7.817217	36	53	44	42.02461	12.11315	36
54	50	49.84469	1.000373	36	54	50	49.11212	8.615672	36	54	50	47.88506	13.39942	36
55	56	55.84469	1.000372	36	55	56	55.06749	9.345603	36	55	56	53.76325	14.60173	36
56	62	61.84469	1.000371	36	56	62	61.0322	9.994828	36	56	62	59.6633	15.69149	36
57	68	67.84469	1.00037	36	57	68	67.00713	10.54186	36	57	68	65.5873	16.64134	36
58	74	73.84469	1.000369	36	58	74	72.99157	10.97141	36	58	74	71.53948	17.39379	36
59	80	79.84469	1.000368	36	59	80	78.98441	11.25826	36	59	80	77.51686	17.90268	36
60	86	85.84469	1.000367	36	60	86	84.98307	11.36063	36	60	n/a	n/a	n/a	n/a
61	92	91.84469	1.000366	36	61	92	90.98067	11.2202	36	61	n/a	n/a	n/a	n/a
62	98	97.84469	1.000365	36	62	98	96.96236	10.76666	36	62	n/a	n/a	n/a	n/a
63	104	103.8447	1.000364	36	63	n/a	n/a	n/a	n/a	63	n/a	n/a	n/a	n/a
64	110	109.8447	1.000363	36	64	n/a	n/a	n/a	n/a	64	n/a	n/a	n/a	n/a
65	35	33.84469	1.000376	8	65	35	33.27278	6.357282	8	65	35	32.29309	9.812018	8
66	35	33.84469	1.000376	18	66	35	33.27278	6.357282	18	66	35	32.29309	9.812018	18
67	35	33.84469	1.000376	24	67	35	33.27278	6.357282	24	67	35	32.29309	9.812018	24
68	35	33.84469	1.000376	30	68	35	33.27278	6.357282	30	68	35	32.29309	9.812018	30
69	35	33.84469	1.000376	40	69	35	33.27278	6.357282	40	69	35	32.29309	9.812018	40

APPENDIX B

The model stress report follows below.

SETS TOWING STRESS REPORT

MODEL:

0709 - GRADIENT 0, A, AND B

Prepared by:

Concurrence:

Pauline Nyon
Engineer 2
310-332-9196

Carlos Ruiz
Project Lead Design Engineer
(310) 332-9195

May 28, 2008

Introduction

The stress report is to verify the strength of the SETS towing model. The model consists of 3 different airfoil shapes, but utilizes the same main frame. The 3 submodels are gradient 0, gradient A, and gradient B. Gradient 0 has the smallest axial area and gradient B has the largest axial area, producing drag.

In this report, gradient 0 is analyzed. The last page of the report calculates the drag area of gradient B and verifies that the air load due to the axial area is minimal compared to the side load. The side load used was received from the aeroscience group.

The model is analyzed to a maximum speed of 40 m/s. The report does not address crosswinds larger than what Yuto Shinagawa has stated below. It is not recommended to test the three models if conditions above 40 m/s with crosswinds larger than 220 lbs are anticipated.

From Yuto Shinagawa on 5/13/2008:

Side force on model

Max side force at 40m/s, 15kts crosswind = $SF = 20.5\text{psf} * (4\text{ft} * 8\text{ft}) * 0.33 = \mathbf{220\text{ lbf}}$ (valid for all three models)

0.33 is the force coefficient on a model of this particular aspect ratio (4ft wide, about 8ft long)

The neutral point for the side force should be at 35% of the chord for gradient A and B, and 25% of the chord for gradient zero.

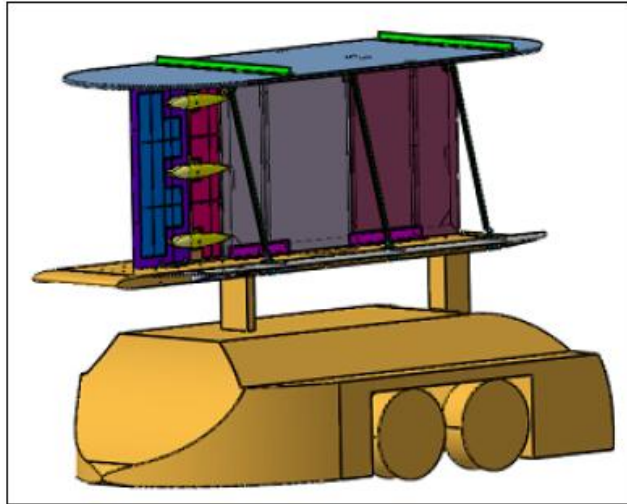
Lift force on top splitter plate

Max lift force at 40m/s = $L = 20.5\text{psf} * (4.5\text{ft} * 12\text{ft}) * 0.05 = \mathbf{55\text{ lbf}}$

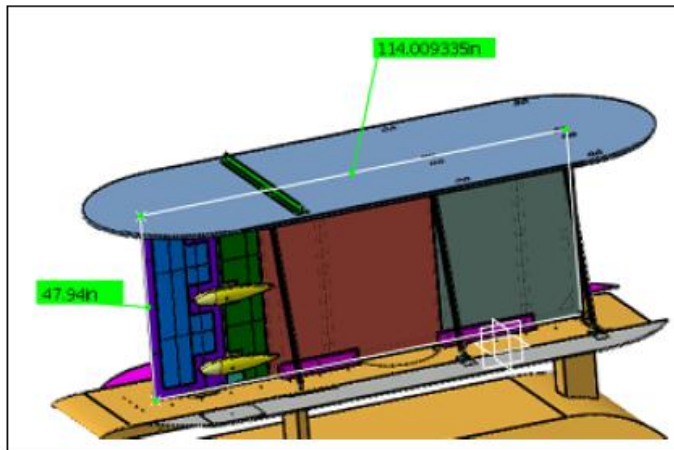
4.5ft and 12ft are roughly the width and length of the splitter plate, and 0.05 is the expected lift coefficient at an incidence of 5 degrees.

<u>PAGE</u>	<u>DESCRIPTION</u>	<u>MIN FS</u>	<u>COMMENTS</u>
	Gradient 0 model		
2	Turnbuckle stress	HIGH	
3	Turnbuckle buckling	3.162	
3	Rod end stress	11.929	
4	Lwr turnbuckle brkt shear tearout	5.853	
4	Lwr turnbuckle brkt bearing	5.888	
5	Lwr turnbuckle brkt bending	4.922	
5	Lwr turnbuckle brkt bolt tensile	18.08	
6	Lwr forward brace bending	3.981	
7	Lwr forward brace bolt tensile	4.491	
7	Lwr forward brace bolt shear	n/a	Small force
8	Frame brace bending	12.729	
9	Uppr splitter plate bolt tensile	n/a	Small force
11	Leading Edge assembly bolt tensile	HIGH	
11	Leading Edge assembly bolt shear	HIGH	
12	Lower splitter plate bolt tensile	HIGH	
	Gradient A and B models		Drag from lrger airfoil shape is minimal compared to side force
	SF > 20 are HIGH		

Maximum Q = 20.5 psf
Maximum CL = .33



Handling loads and crosswinds will be the largest forces on the model. The forces are found.



$$\text{Area} := 47.94 \cdot 114 \cdot \text{in}$$

$$\text{Area} = 5465.16 \text{ in}^2$$

$$\text{Force}_s := \text{Area} \cdot Q \cdot C_L$$

$$\text{Force}_s = 256.749 \text{ lbf}$$

$$Q := 20.5 \cdot \frac{\text{lbf}}{\text{ft}^2} \quad (\text{Crosswind})$$

$$C_L := .33$$

The turnbuckle forces are found.

The angle from horizontal is 73.7 degrees. The force on each of the three turnbuckles is:

$$F_{tb} := \frac{\text{Force}_s}{\cos(73.7 \cdot \text{deg}) \cdot 3}$$

$$F_{tb} = 304.927 \text{ lbf}$$

Cross-sectional properties of turnbuckle:

$$I := .059 \cdot \text{in}^4$$

$$A := .756 \cdot \text{in}^2$$

$$\sigma_{\text{ten}} := \frac{F_{tb}}{A}$$

$$\sigma_{\text{ten}} = 403.343 \text{ psi}$$

Turnbuckle material is aluminum (assumed to be 6061-T6)

$$\text{SF} := \frac{42000 \cdot \text{psi}}{\sigma_{\text{ten}}}$$

$$\text{SF} = 104.13 \quad \text{HIGH}$$

Buckling

Assuming the force acts towards the turnbuckle, the buckling is found:

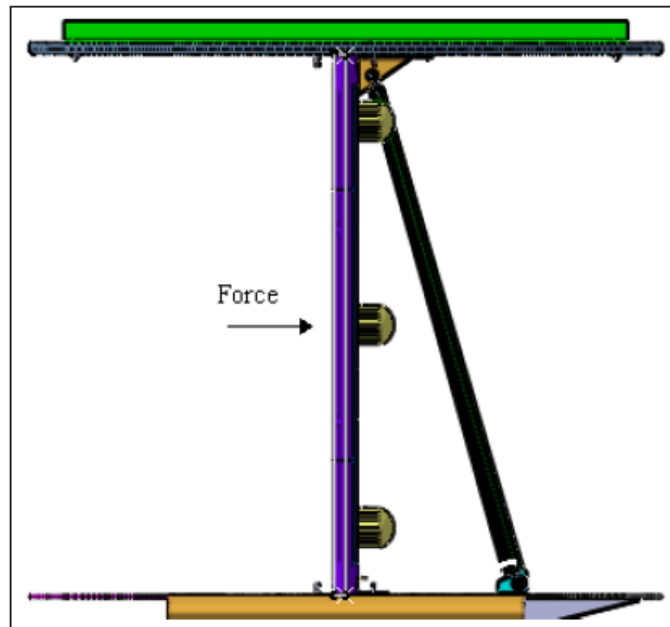
$$I = 0.059 \text{ in}^4$$

$$E := 10.3 \times 10^6 \cdot \text{psi}$$

$$L := 44.5 \cdot \text{in}$$

$$P_{\text{cr}} := \frac{\pi \cdot E \cdot I}{L^2}$$

$$P_{\text{cr}} = 964.093 \text{ lbf}$$



The force on each turnbuckle is:

$$F_{tb} = 304.927 \text{ lbf}$$

$$SF := \frac{P_{cr}}{F_{tb}}$$

$$SF = 3.162$$

Rod End Bending

Assuming the force acts at the center of the airfoil shape at 25% chord, the force and moment of the rod end is found.

Shear force (found previously):

$$F_{tb} = 304.927 \text{ lbf}$$

Force due to moment:

$$M_1 := F_{tb} \cdot \frac{(47.9 \cdot \text{in})}{2}$$

$$M_1 = 7303.004 \text{ in}\cdot\text{lbf}$$

$$F_m := \frac{M_1}{14.75 \cdot \text{in}}$$

$$F_m = 495.119 \text{ lbf}$$

Sum of the forces acting on the rod end is:

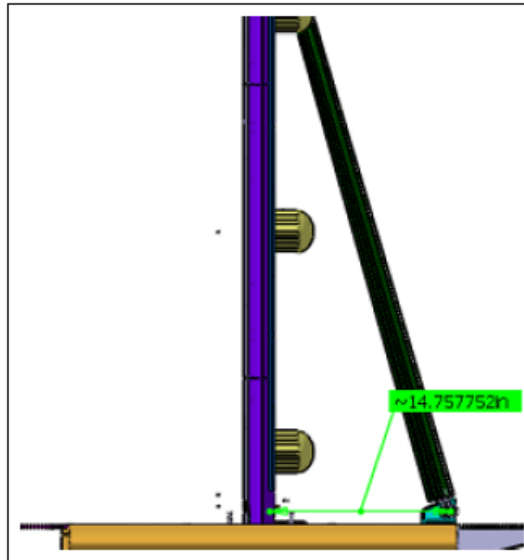
$$F_{rod} := F_{tb} + F_m$$

$$F_{rod} = 800.046 \text{ lbf}$$

The allowable radial force on this rod end is 9544 lbs (taken from specification sheet). The factor of safety of the rod end is:

$$SF := \frac{9544 \cdot \text{lbf}}{F_{rod}}$$

$$SF = 11.929$$



Lower Turnbuckle Bracket Shear Tearout and Bearing

The force found previously is:

$$F_{\text{rod}} = 800.046 \text{ lbf}$$

The bolt hole is .375" in diameter. The shear tearout of the lower bracket is:

$$F_{\text{sh}} := \frac{\frac{F_{\text{rod}}}{2}}{\left(.65 \cdot \text{in} - \frac{.375 \cdot \text{in}}{2} \right) \cdot .1875 \cdot \text{in}}$$

$$F_{\text{sh}} = 4612.878 \text{ psi}$$

The allowable for 6061-T6 Al is 27 ksi. The factor of safety is:

$$SF := \frac{27000 \cdot \text{psi}}{F_{\text{sh}}}$$

$$SF = 5.853$$

Bearing on the lower bracket is:

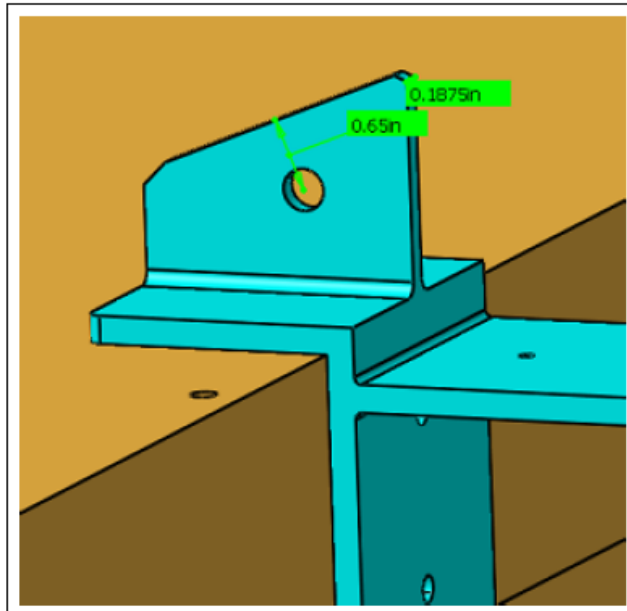
$$F_b := \frac{F_{\text{rod}}}{(.375 \cdot \text{in}) \cdot (.1875 \cdot \text{in})}$$

$$F_b = 11378.433 \text{ psi}$$

The allowable bearing for 6061-T6 is 78 ksi. The factor of safety is:

$$SF := \frac{67000 \cdot \text{psi}}{F_b}$$

$$SF = 5.888$$



Lower Turntable Bracket Bending and Bolt Loads

The force on the rod used was found previously. The direction of the force is perpendicular to the turntable. The force is found.

$$F_{\text{rod}} = 800.046 \text{ lbf}$$

$$d := (1.00 - .25) \cdot \text{in} \quad (\text{Asymmetric bracket})$$

$$M_{\text{ax}} := F_{\text{rod}} \cdot d$$

$$M_{\text{ax}} = 600.035 \text{ in} \cdot \text{lbf}$$

$$c := \frac{.375 \cdot \text{in}}{2}$$

$$I := \frac{1}{12} \cdot (3 \cdot \text{in}) \cdot (.375 \cdot \text{in})^3$$

$$I = 0.01318 \text{ in}^4$$

$$\sigma := \frac{M_{\text{ax}} \cdot c}{I}$$

$$\sigma = 8533.824 \text{ psi}$$

Allowable for 6061-T6 Al = 42 ksi.

$$\text{SF} := \frac{42000 \cdot \text{psi}}{\sigma}$$

$$\text{SF} = 4.922$$

The bolt forces are found:

The distance between the two bolts is 1.57 in.

$$F_{\text{bolt}} := \frac{M_{\text{ax}}}{1.57 \cdot \text{in}}$$

$$F_{\text{bolt}} = 382.188 \text{ lbf}$$

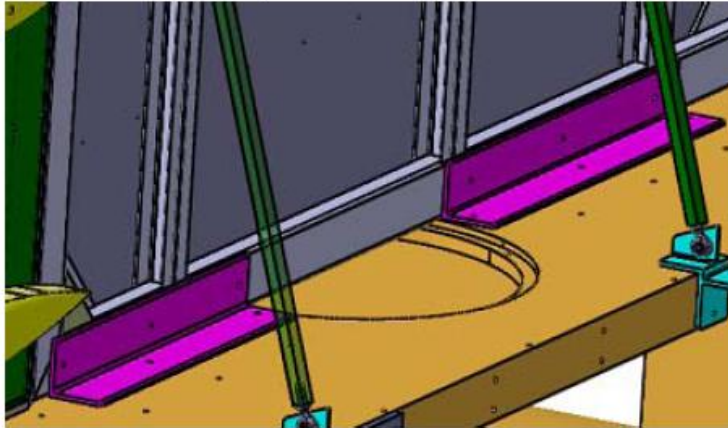
The allowable for .25" dia bolt is 6910 lbs. The factor of safety is:

$$\text{SF} := \frac{6910 \cdot \text{lbf}}{F_{\text{bolt}}}$$

$$\text{SF} = 18.08$$

Using the force found on the model, the bolt loading and bending of the bracket is found.

Lower Forward Brace Bending



Bending in the bracket is found using *Roark's Formulas for Stress and Strain*. The model is analyzed as a beam with one end simply supported and one end fixed. The moment at the bracket, or the fixed end, is found.

$$d := 47.94 \cdot \text{in}$$

$$\frac{d}{2} = 23.97 \text{ in}$$

$$\text{Force}_s = 256.7 \text{ lbf}$$

$$M := \left(\frac{-\text{Force}_s \cdot \frac{d}{2}}{2 \cdot d^2} \right) \left[d^2 - \left(\frac{d}{2} \right)^2 \right]$$

$$M = -2307.85 \text{ in} \cdot \text{lbf}$$

The cross-sectional properties of the bracket is:

$$l := 21 \cdot \text{in}$$

$$t := .25 \cdot \text{in}$$

$$I := \frac{1}{12} \cdot l \cdot t^3$$

$$c := \frac{.25 \cdot \text{in}}{2}$$

$$I = 0.027 \text{ in}^4$$

$$c = 0.125 \text{ in}$$

Assuming the the forward 21" bracket takes the entire of the load, the stress is conservatively:

$$\sigma := \frac{M \cdot c}{I}$$

$$\sigma = -10550.169 \text{ psi}$$

The aluminum bending allowable is 42 ksi. The factor of safety is:

$$SF := \frac{42000 \cdot \text{psi}}{|\sigma|}$$

$$SF = 3.981$$

Bolt Tensile

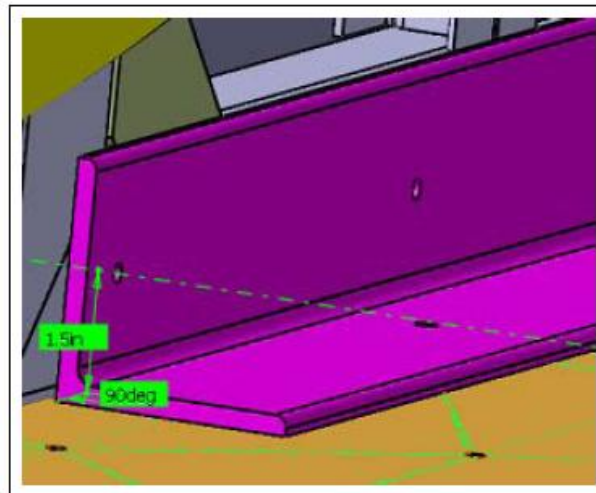
$$F_{\text{bolt}} := \frac{|M|}{1.5 \cdot \text{in}}$$

$$F_{\text{bolt}} = 1538.566 \text{ lbf}$$

1/4 - 28 Bolt Allowable = 6910 lbs

$$SF := \frac{6910 \cdot \text{lbf}}{F_{\text{bolt}}}$$

$$SF = 4.491$$



Bolt Shear

Axial Area:

$$A_{\text{ax}} := (2 \cdot \text{in}) \cdot (47.94 \cdot \text{in})$$

$$A_{\text{ax}} = 95.88 \text{ in}^2$$

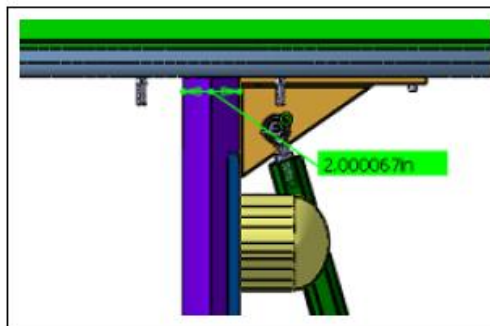
$$Q = 20.5 \frac{\text{lbf}}{\text{ft}^2}$$

$$C_L = 0.33$$

$$F_{\text{ax}} := A_{\text{ax}} \cdot Q \cdot C_L$$

$$F_{\text{ax}} = 4.504 \text{ lbf}$$

The load is small compared to 1/4-28 bolt shear allowable.



Bending in Beam on Frame

Assuming the frame is a beam pinned on one end and fixed on the other, the moment at the center is used to find the stress through the center. *Roark's Formulas for Stress and Strain* is used.

$$l := 42 \text{ in}$$

$$\text{Force}_s = 256.749 \text{ lbf}$$

$$a := \frac{1}{2}$$

$$a = 21 \text{ in}$$

$$M := \left(\frac{\text{Force}_s \cdot a}{2 \cdot l^3} \right) \cdot (l - a)^2 \cdot (2 \cdot l + a)$$

$$M = 1684.913 \text{ in} \cdot \text{lbf}$$

$$c := \frac{1.5 \text{ in}}{2}$$

$$I := .383 \text{ in}^4$$

$$\sigma := \frac{M \cdot c}{I}$$

(very conservative - taken
from 1 vertical cross-section,
shown below)

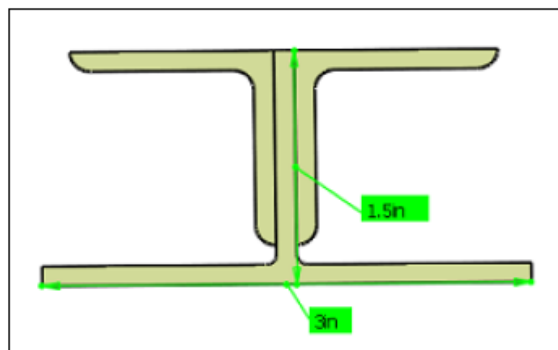
$$\sigma = 3299.438 \text{ psi}$$



The aluminum tensile strength of 6061-T6 is 42 ksi. The factor of safety is:

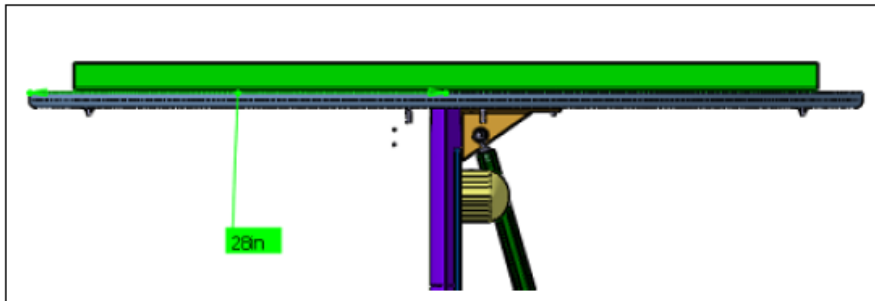
$$\text{SF} := \frac{42000 \cdot \text{psi}}{\sigma}$$

$$\text{SF} = 12.729$$



Upper Splitter Plate Assembly

The upper splitter plate will create a lift resulting in 55 lbs of force. Half that value is applied to half the model, and the center of applied force for this analysis is shown below.



$$d := 14 \text{ in}$$

$$F := 19.89 \text{ lbf} \quad (\text{distance from applied force center and edge of wedged portion of gusset})$$

Case 1: Bending on gusset from one side of loading

$$M := F \cdot d$$

$$M = 278.46 \text{ lbf} \cdot \text{in}$$

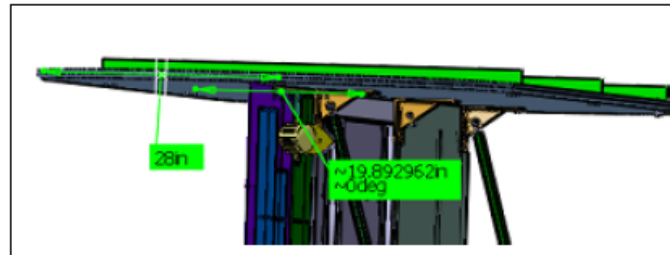
The distance between the two line of bolts is 5.5", but the distance from the wedge edge to the inboard bolt is 4.143".

$$F_{\text{bolt}} := \frac{M}{4.143 \text{ in}}$$

$$F_{\text{bolt}} = 67.212 \text{ lbf}$$

The force on the bolts is minimal compared to .25" bolt allowables.

SF = HIGH



Leading Edge Assembly

There are 3 shoulder bolts attaching the frame to the subassembly. The weight of the model and the airoload is used to find the shear and tensile of the shoulder bolts.

$$W_{LE} := 205 \cdot \text{lbf}$$

$$\text{Force}_s = 256.749 \text{ lbf}$$

Although the side force on the model is located at 25% of the chord (24" aft of LE), the leading edge weight and the entire side air load is conservatively applied at the center of LE area.

$$F_{\text{tot}} := W_{LE} + \text{Force}_s$$

$$F_{\text{tot}} = 461.749 \text{ lbf}$$

$$d := \frac{30.85 \cdot \text{in}}{2}$$

$$d = 15.425 \text{ in}$$

$$M := d \cdot F_{\text{tot}}$$

$$M = 7122.473 \text{ in} \cdot \text{lbf}$$

Area of fairing:

$$A_{\text{fairing}} := 11.01 \cdot \text{in}^2$$

$$Q_{\text{fairing}} := 100 \cdot \frac{\text{lbf}}{\text{ft}^2} \quad C_L = 0.33$$

$$F_{\text{fairing}} := A_{\text{fairing}} \cdot Q_{\text{fairing}} \cdot C_L$$

$$F_{\text{fairing}} = 2.523 \text{ lbf}$$

The force due to fairing is minimal compared to F_{tot} . It is negligible.

The distance between the edge of the assembly and the line of shoulder bolts is .55". The force on each bolt is:

$$F := \frac{M}{.55 \cdot \text{in} \cdot 3}$$

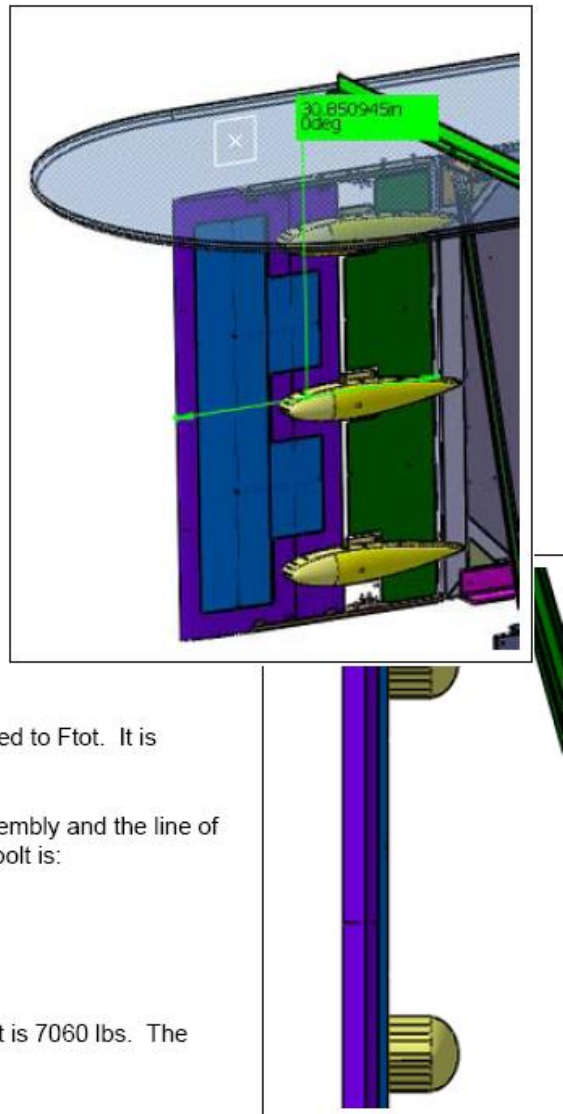
$$F = 4316.65 \text{ lbf}$$

The allowable force on a 3/8" shoulder bolt is 7060 lbs. The factor of safety is:

$$SF := \frac{7060 \cdot \text{lbf}}{F}$$

$$SF = 1.636$$

See next sheet for additional bolts added.



There will be 2 additional bolts added to from the 1F-004 upper plate to the 0-012 top tie plate. Assuming a **flat plate** with **2 adjacent sides fixed** and **2 free** with a **uniform load on the entire plate**, Roark's Formulas for Stress and Strain is used.

$$a := 30.85 \cdot \text{in}$$

$$b := 47.94 \cdot \text{in}$$

$$\frac{a}{b} = 0.644$$

Taken from Roark's:

$$\gamma_1 := 1.129$$

$$F_{\text{tot}} = 461.749 \text{ lbf} \quad (\text{found previously, weight and side force})$$

$$q := \frac{F_{\text{tot}}}{a \cdot b}$$

$$q = 0.312 \text{ psi}$$

$$R := \gamma_1 \cdot q \cdot b$$

$$R = 16.898 \frac{\text{lbf}}{\text{in}}$$

By definition, R is the force per unit length normal to plate surface exerted by the boundary support on the edge of the plate. If R is multiplied by the entire edge a, the force on the line of bolts is found.

$$F_{\text{bolt}} := \frac{R \cdot a}{2} \quad (\text{there are 2 bolts})$$

$$F_{\text{bolt}} = 260.657 \text{ lbf}$$

$$SF := \frac{7060 \cdot \text{lbf}}{F_{\text{bolt}}}$$

$$SF = 27.085$$

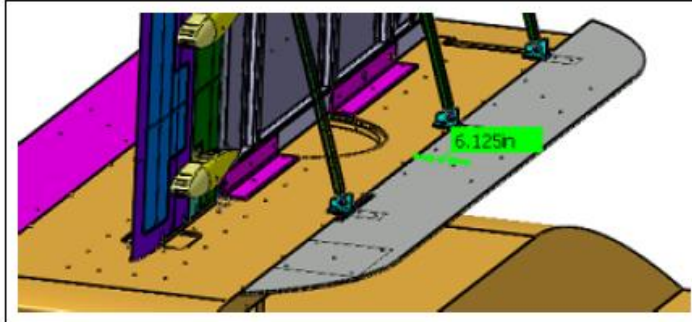
Shear Strength

$$F_{\text{tot}} = 461.749 \text{ lbf}$$

The allowable shear on a 3/8" shoulder bolt is 10500 lbs.

$$SF := \frac{10500 \cdot \text{lbf}}{F_{\text{tot}}}$$

$$SF = 22.74$$

Lower Splitter Plate

There is an assumption that there is lift on the lower splitter plate equivalent to the lift on upper splitter plate. Using the same C_L and Q , the force is found on the lower splitter plate. The location of force application is the center of area.

$$\text{Area}_{\text{spl}} := 1512.45 \cdot \text{in}^2$$

$$Q := 20.5 \cdot \frac{\text{lbf}}{\text{ft}^2}$$

$$C_L := .05$$

$$F_{\text{spl}} := \text{Area}_{\text{spl}} \cdot Q \cdot C_L$$

$$F_{\text{spl}} = 10.766 \text{ lbf}$$

$$d := 6.125 \cdot \text{in}$$

$$M_{\text{spl}} := F_{\text{spl}} \cdot d$$

$$M_{\text{spl}} = 65.94 \text{ in} \cdot \text{lbf}$$



There are (3) lower extension support and (3) lower turnbuckle attach bracket. The turnbuckle attach brackets are ignored and the lower extension supports are analyzed. There are (4) bolts attaching each support to the cart. The bolts loads are found.

$$d := 1.57 \cdot \text{in} \quad (\text{distance between the two line of bolts})$$

$$F_{\text{bolt}} := \frac{M_{\text{spl}}}{d}$$

$$F_{\text{bolt}} = 42 \text{ lbf} \quad (\text{conservative - assuming only 2 bolts hold entire plate})$$

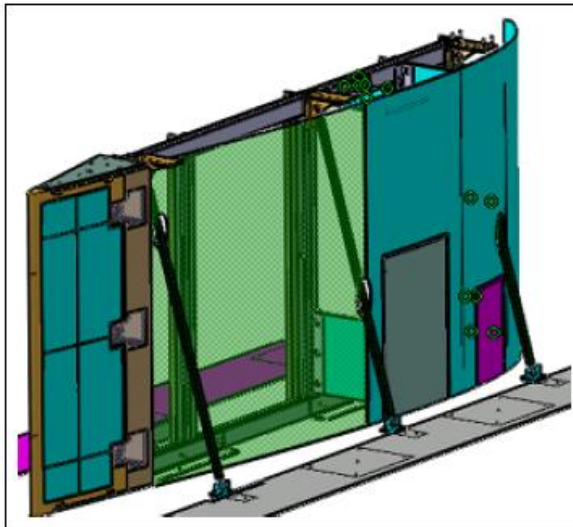
Bolt Size and Allowable Tensile Strength = 1/4-28 SHCS, 6910 lbf

$$SF := \frac{6910 \cdot \text{lbf}}{F_{\text{bolt}}}$$

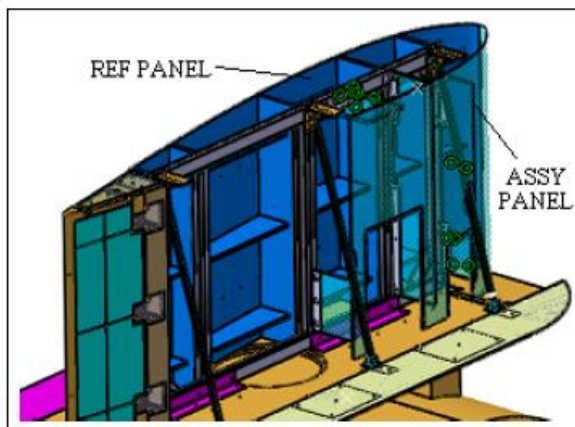
$$SF = 164.524 \quad \text{HIGH}$$

Gradient A and B Models

The gradient A and B models consist of new forward and aft assembly and reference panels and a new forward subassembly. In addition to the new parts, the rest of the model will be reviewed for high SF.



There are stiffeners attaching the aft assembly and the frame. Drag is added to analyze the attachment of the panels.



The area used to take a look at the drag of the panels for gradient B is conservatively half the rectangle show to the right.

$$\text{Area} := (47.98 - 22.473) \cdot \text{in}^2$$

$$\text{Area} = 1078.255 \text{ in}^2$$

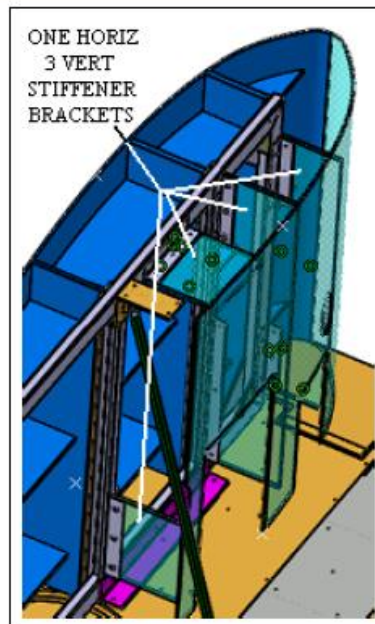
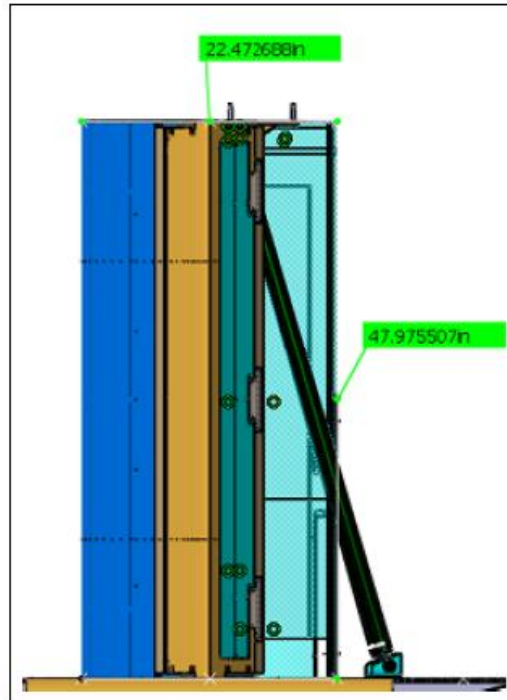
$$Q = 20.5 \frac{\text{lbf}}{\text{ft}^2}$$

$$C_D := 1.2$$

$$F := \frac{\text{Area}}{2} \cdot Q \cdot C_D$$

$$F = 92.101 \text{ lbf}$$

The shear and moment on the 5 stiffeners will be a fraction of the drag force calculated, 92 lbs. The shear is minimal. The layup plan minimum of 3 plies and bolt attachment is sufficient.



APPENDIX C

Model Installation in 7x10 for Shakedown Test

The installation of the model in the 7x10-ft Wind Tunnel was designed to replicate the installation in the TWT as closely as possible. A splitter plate based on the one that is integral to the HART carrier vehicle of the TWT was fabricated (see Figure 837) and mounted to the existing model support system in the wind tunnel. The installation of the model and instrumentation was done in the same manner as planned for the TWT.

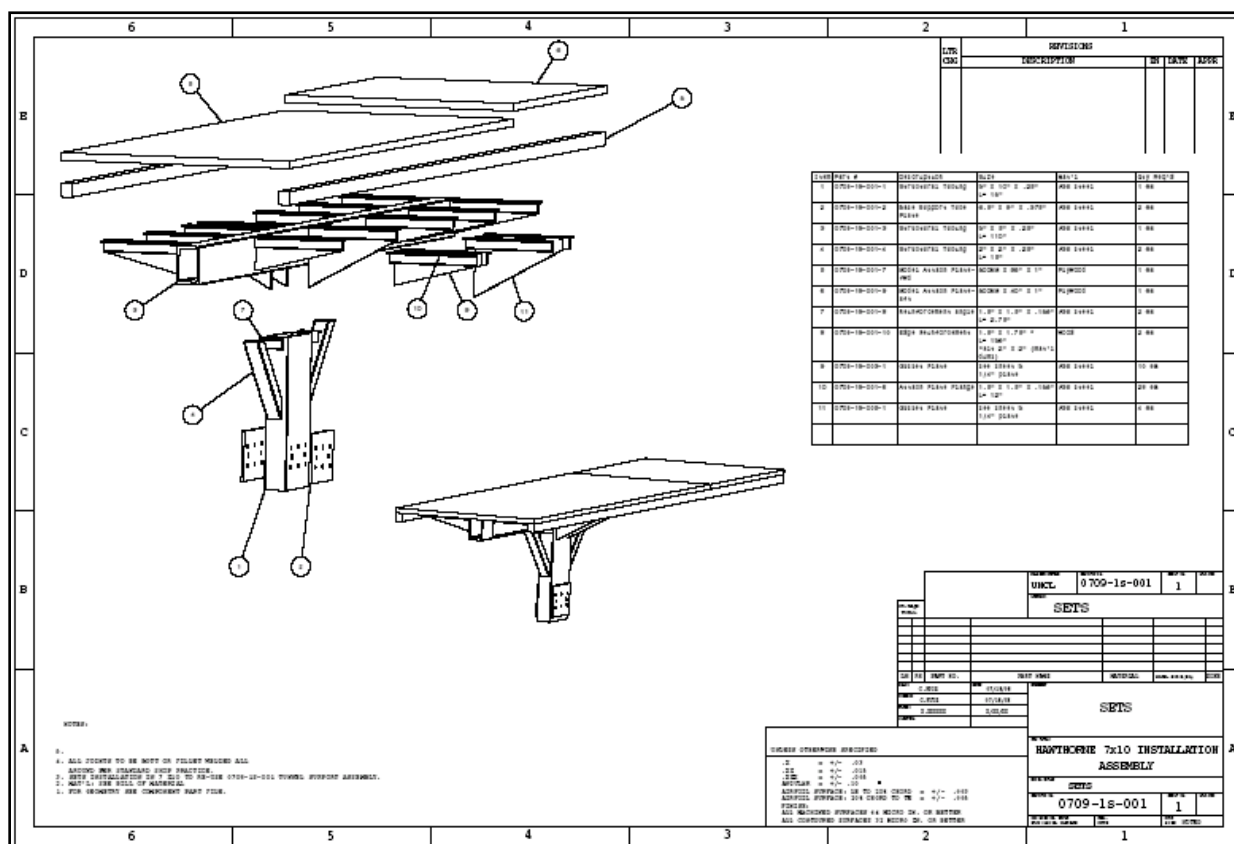


Figure 837: Model installation support for SETS models in NGC 7x10-ft wind tunnel.

The models used a common internal frame as their core support. This common frame was mounted to the splitter plate and supported with braces on the non-measurement side of the model. These braces were fabricated as turnbuckles to allow fine tuning of their length once installed (see Figure 838).



Figure 838: Common frame installed on support structure in NGC 7x10-ft wind tunnel.

Once the frame had been mounted to the splitter plate, the leading edge assembly was installed. This leading edge assembly was unique to each of the three models; Figure 839 shows the frame with the Gradient-Zero leading edge installed, viewed from downstream. Pressure tubing for the static pressure taps in the leading edge assembly was passed through specifically installed holes in the frame and combined with tubing for the static pressure taps on the measurement side of the model (see Figure 840). The measurement side skin was installed to the frame once the leading edge had been installed. This allowed all of the routing of the pressure tubing to be done before the non-measurement side skin had been installed, allowing for easy access. All of the static pressure tubes exited the model at the downstream end and were run externally to the pressure transducers.



Figure 839: Leading edge (background) and measurement-side skin installed on frame.



Figure 840: Upper and lower splitter plates installed; pressure routing complete.

The upper splitter plate was installed on the model after the measurement side skin was installed. The upper splitter plate was a single piece assembly built with an aluminum honeycomb core. Despite its large size, it was relatively light and proved fairly easy to handle. For the Gradient-Zero model, the non-measurement side skin was divided into two separate panels. This made installation simpler (see Figure 841). For the Gradient-A and Gradient-B models this was not possible, since the support for the cross-sectional shape was integral to the skin assembly. For the Gradient-A and Gradient-B models, access panels were installed in the non-measurement side skin to allow access to the model internal components, including the fasteners to join the skin assembly to the frame.



Figure 841: Non-measurement side skin being installed.

The lower splitter plate that was an integral part of the HART carrier vehicle was insufficient in span to meet the needs of the SETS models. Splitter plate extension were fabricated and attached to the lower splitter plate to provide the required size (see Figures 842-844). Pressure instrumentation was mounted to the lower side of these splitter plate extensions (see Figure 846). The arrangement of the HART carrier vehicle at the TWT necessitated the mounting of this instrumentation on the splitter plate. In order to replicate that setup, the instrumentation was mounted in similar locations during the shakedown test (see Figures 845-847). This arrangement resulted in the testing in the 7x10-ft Wind Tunnel being substantially less efficient than could have been the case if instrumentation installation had been optimized for that facility. However, since the objective of the shakedown test was to prepare for the testing in the TWT, rather than obtain the maximum quantity of data, this approach was preferred.

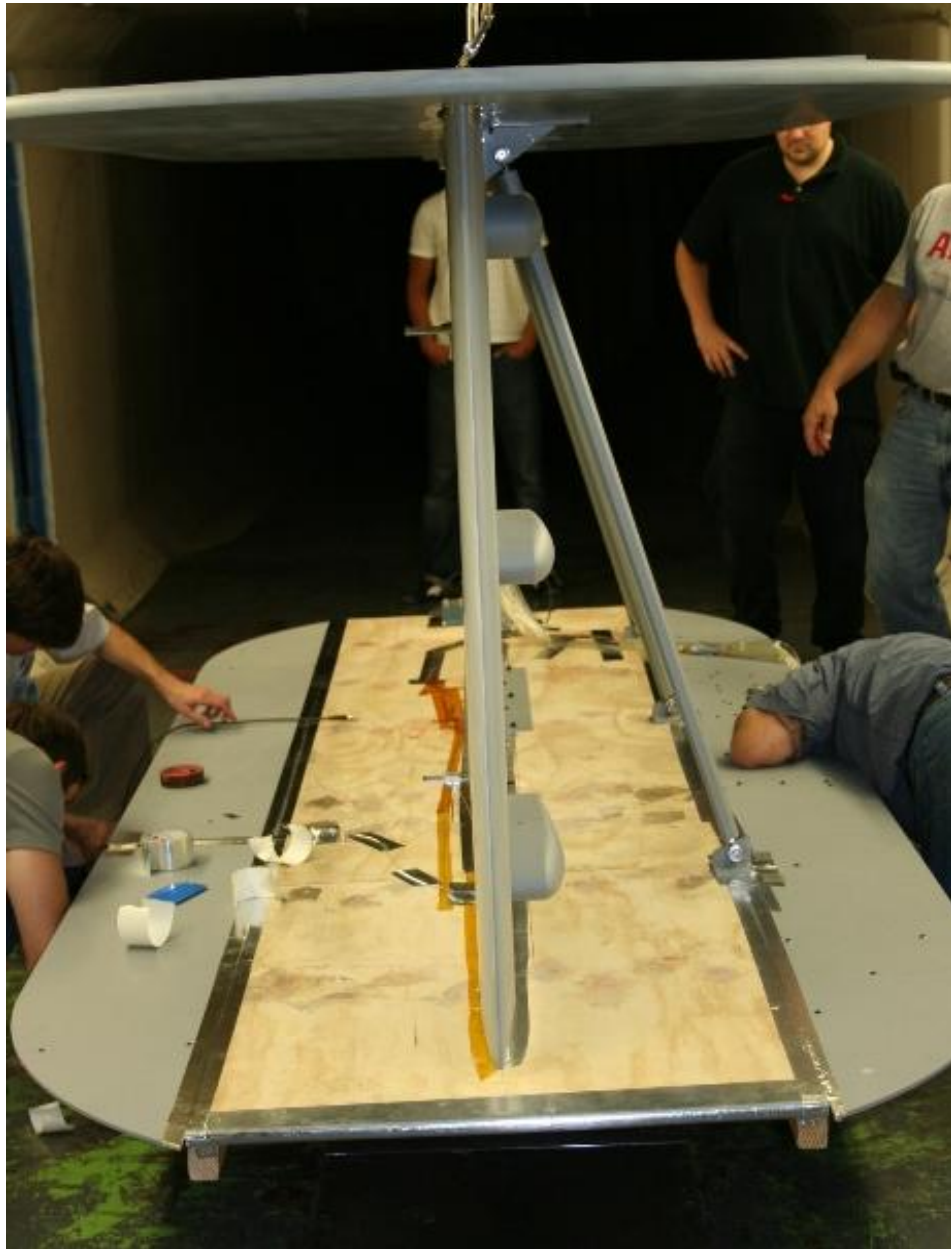


Figure 842: Gradient-Zero installed in NGC 7x10-ft wind tunnel (leading edge view)

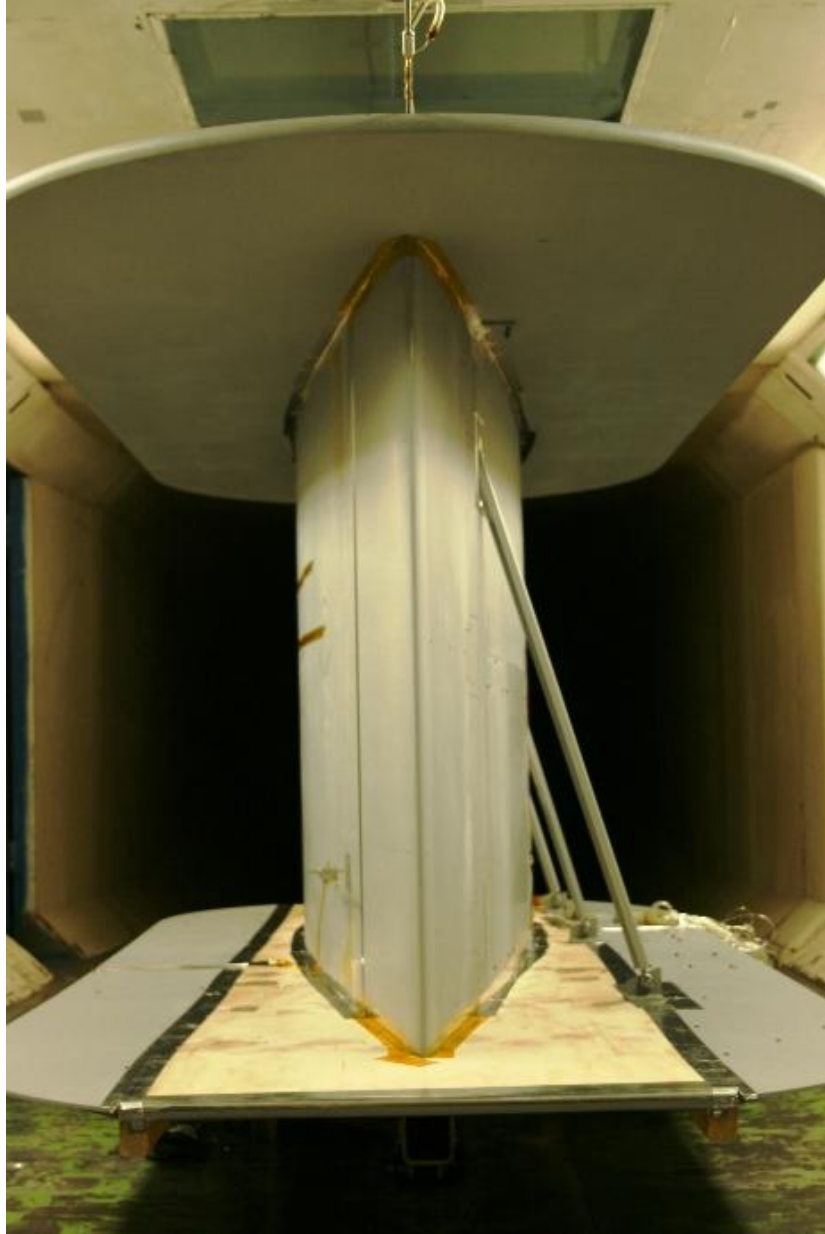


Figure 843: Gradient-A installed in NGC 7x10-ft wind tunnel (leading edge view)



Figure 844: Gradient-A installed in NGC 7x10-ft wind tunnel (flow is right-to-left)



Figure 845: Hot wire instrumentation installed underneath model during shakedown test.



Figure 846: Pressure instrumentation installed underneath lower splitter plate during shakedown test.

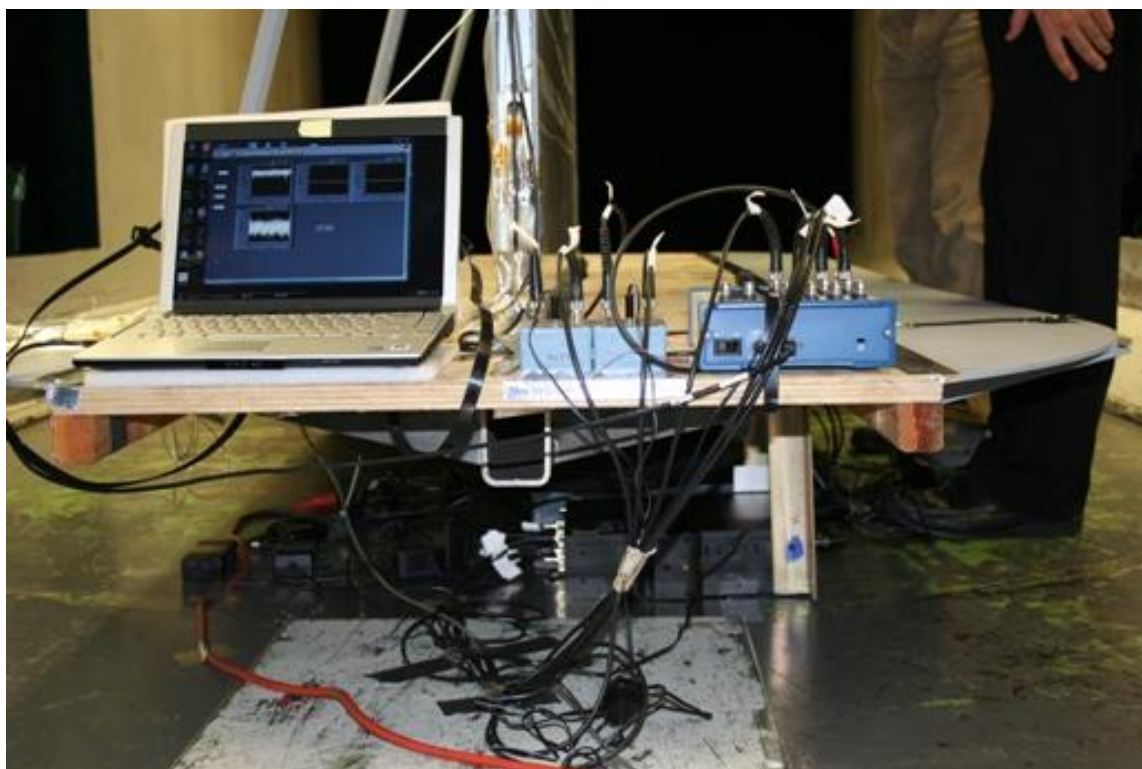


Figure 847: Laptop, accelerometers, and NI DAQ installed at aft end of model during shakedown test.

APPENDIX D

The measured velocity profiles are shown below in Figures 848-868. See Section 7.3.3 for further details.

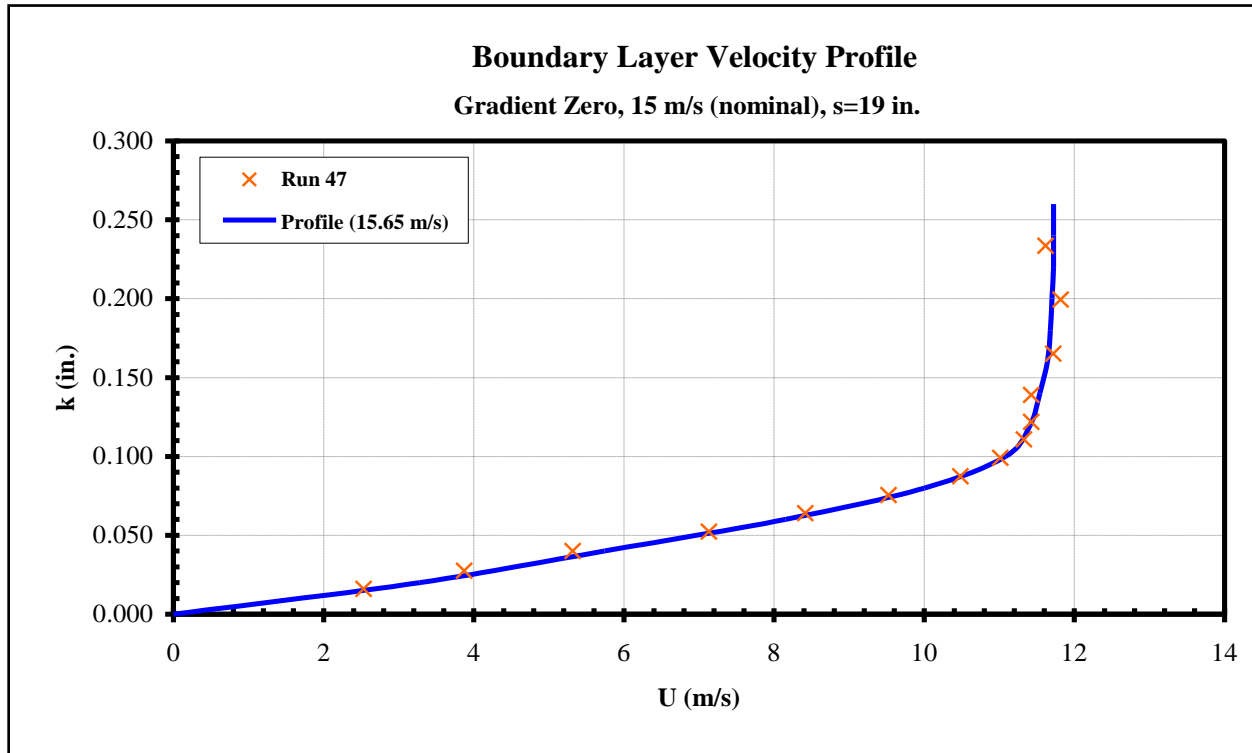


Figure 848: Gradient-Zero boundary layer velocity profile, U=15 m/s (nominal).

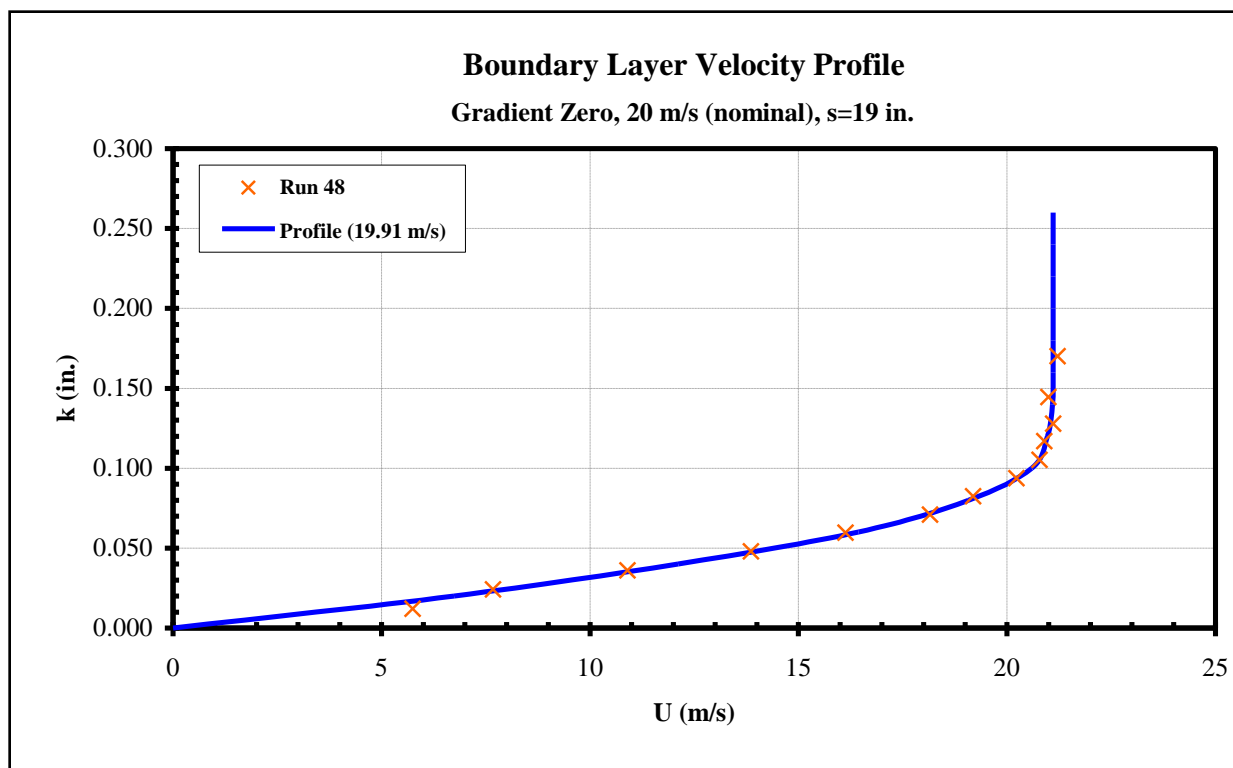


Figure 849: Gradient-Zero boundary layer velocity profile, U=20 m/s (nominal).

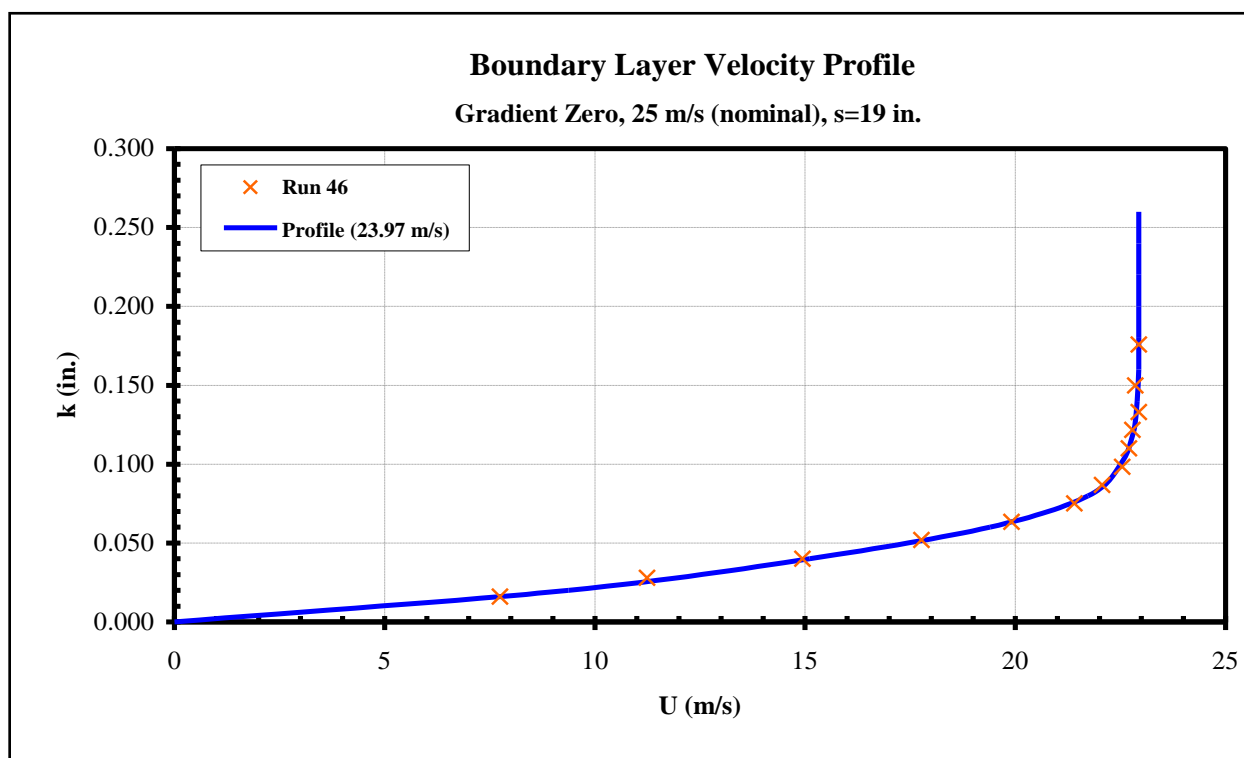


Figure 850: Gradient-Zero boundary layer velocity profile, U=25 m/s (nominal).

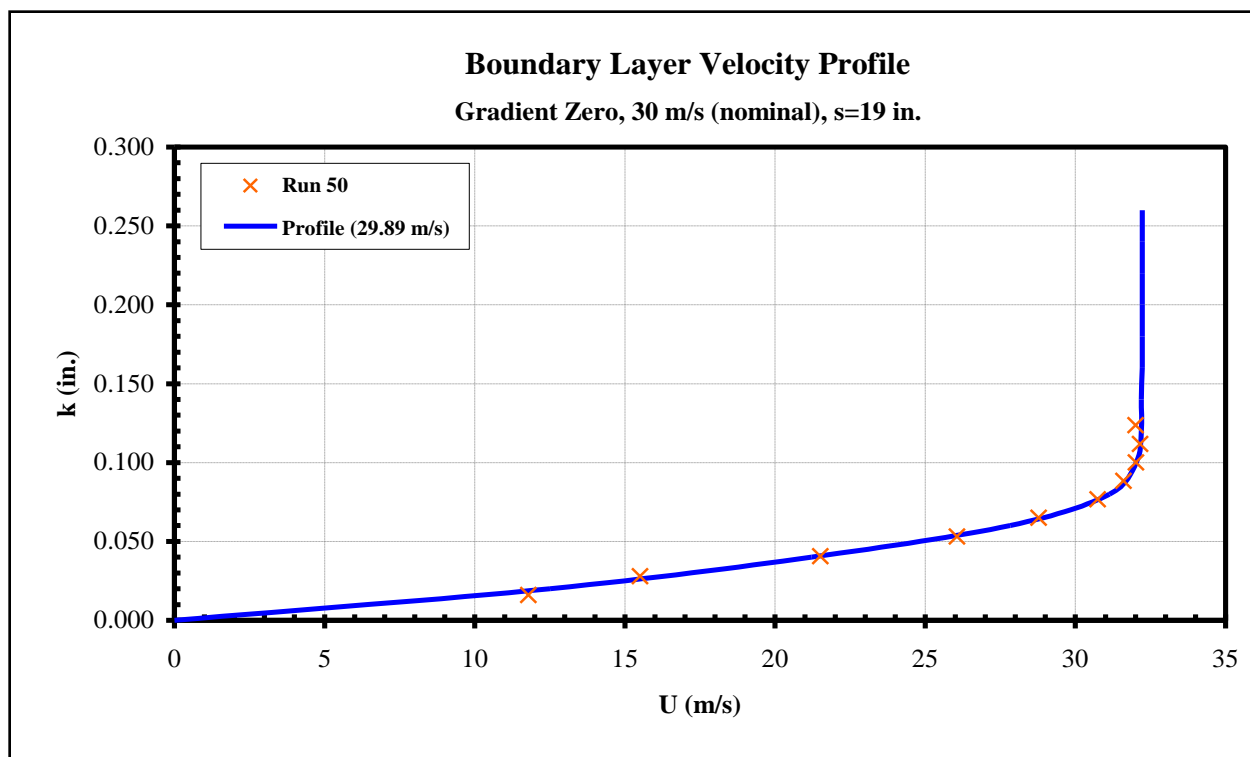


Figure 851: Gradient-Zero boundary layer velocity profile, U=30 m/s (nominal).

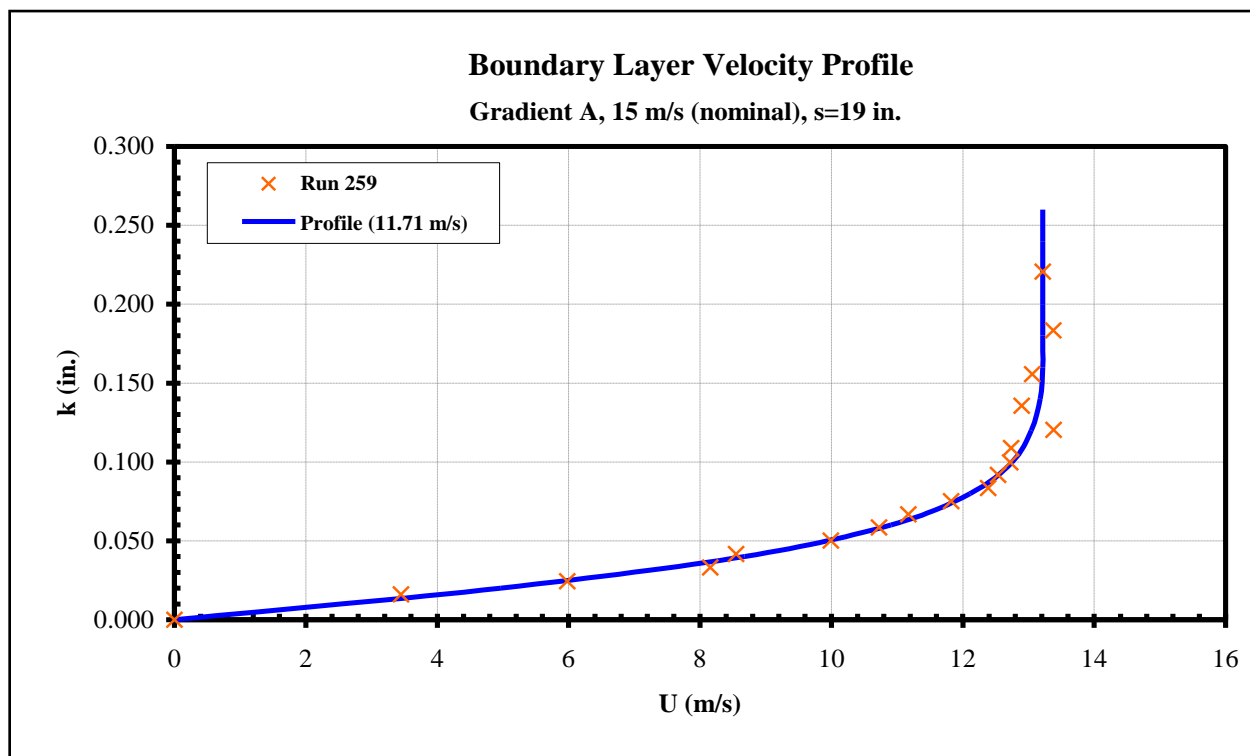


Figure 852: Gradient-A boundary layer velocity profile, U=15 m/s (nominal).

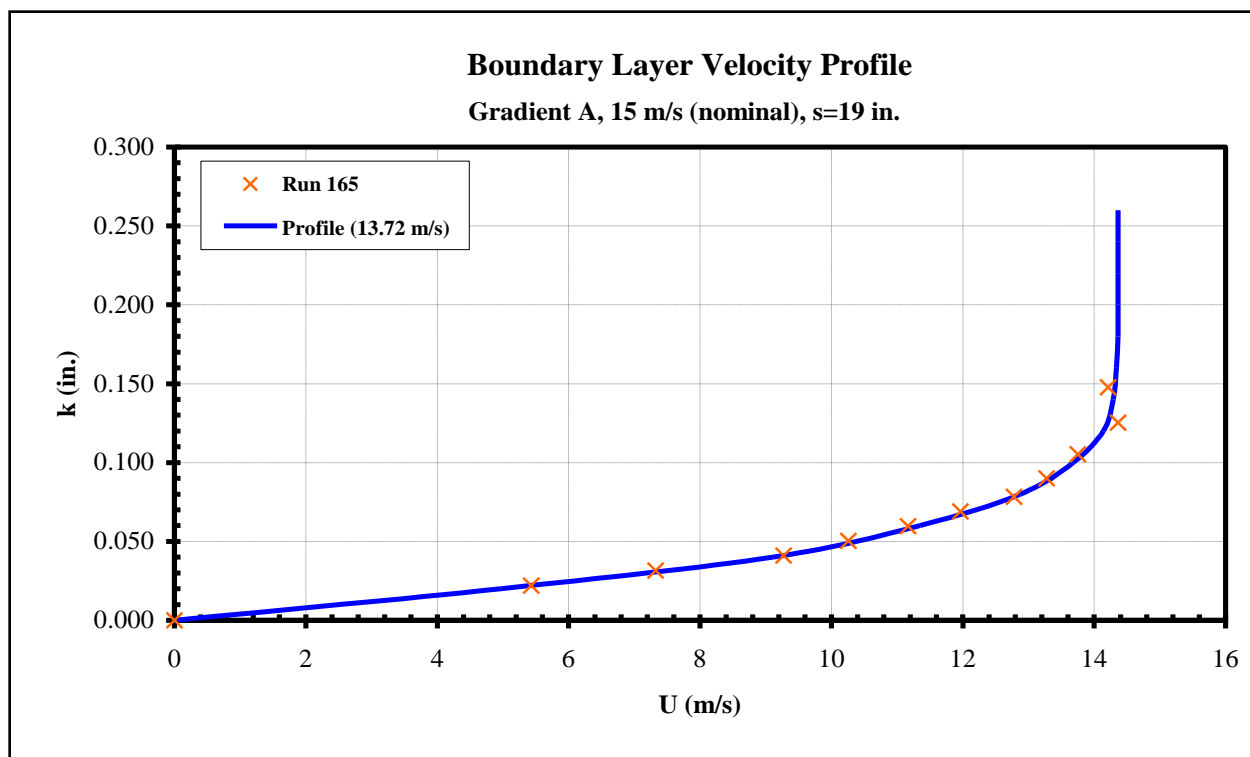


Figure 853: Gradient-A boundary layer velocity profile, U=15 m/s (nominal).

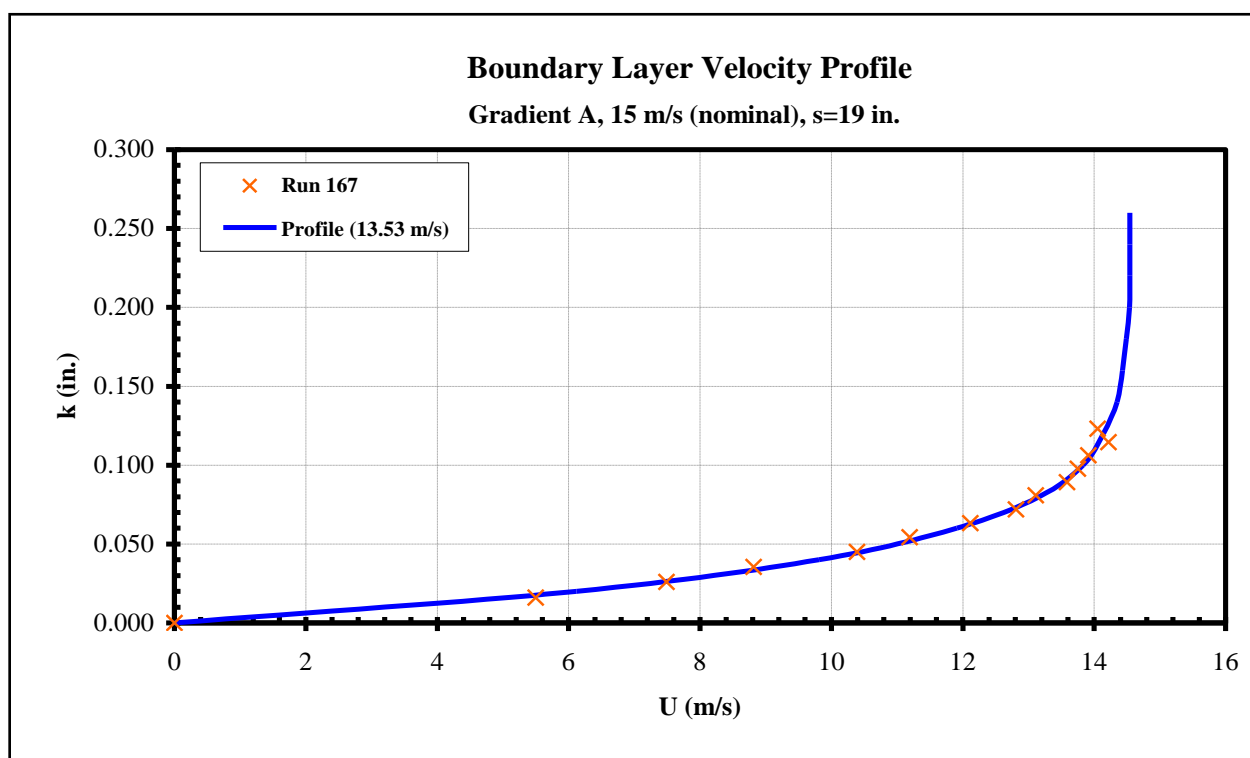


Figure 854: Gradient-A boundary layer velocity profile, U=15 m/s (nominal).

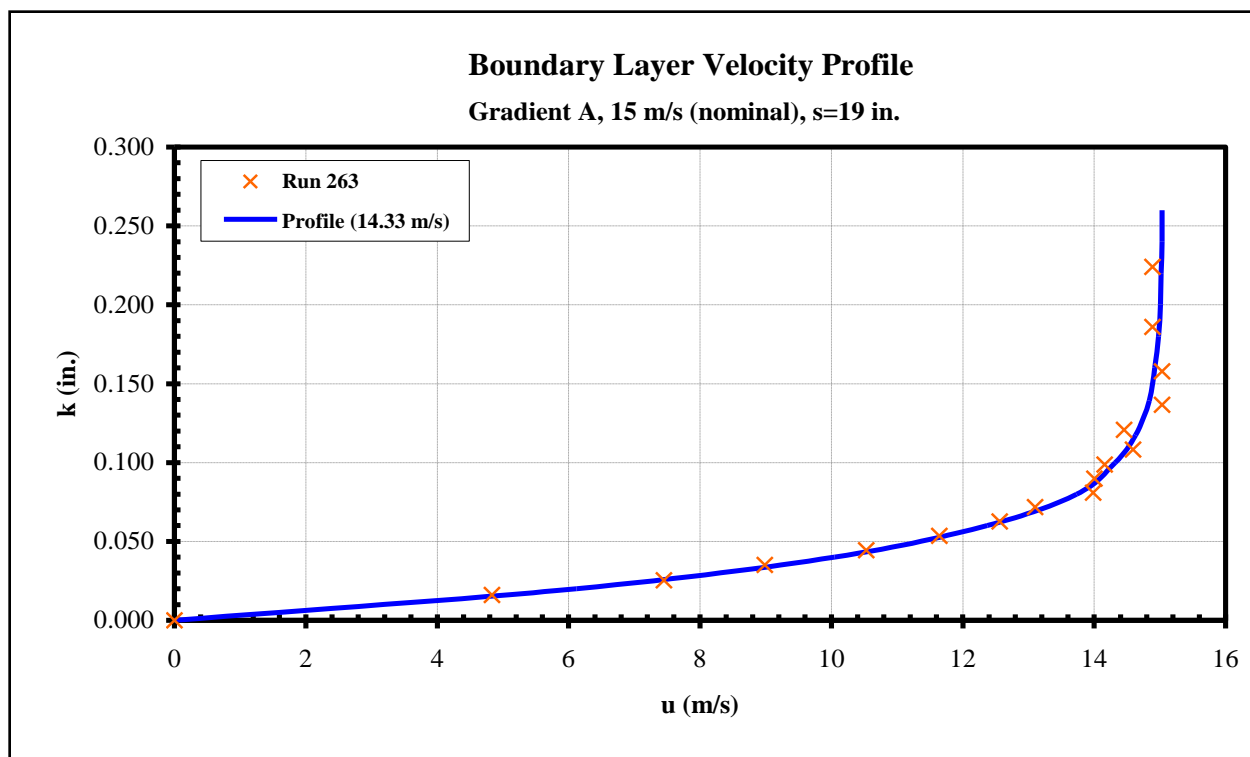


Figure 855: Gradient-A boundary layer velocity profile, U=15 m/s (nominal).

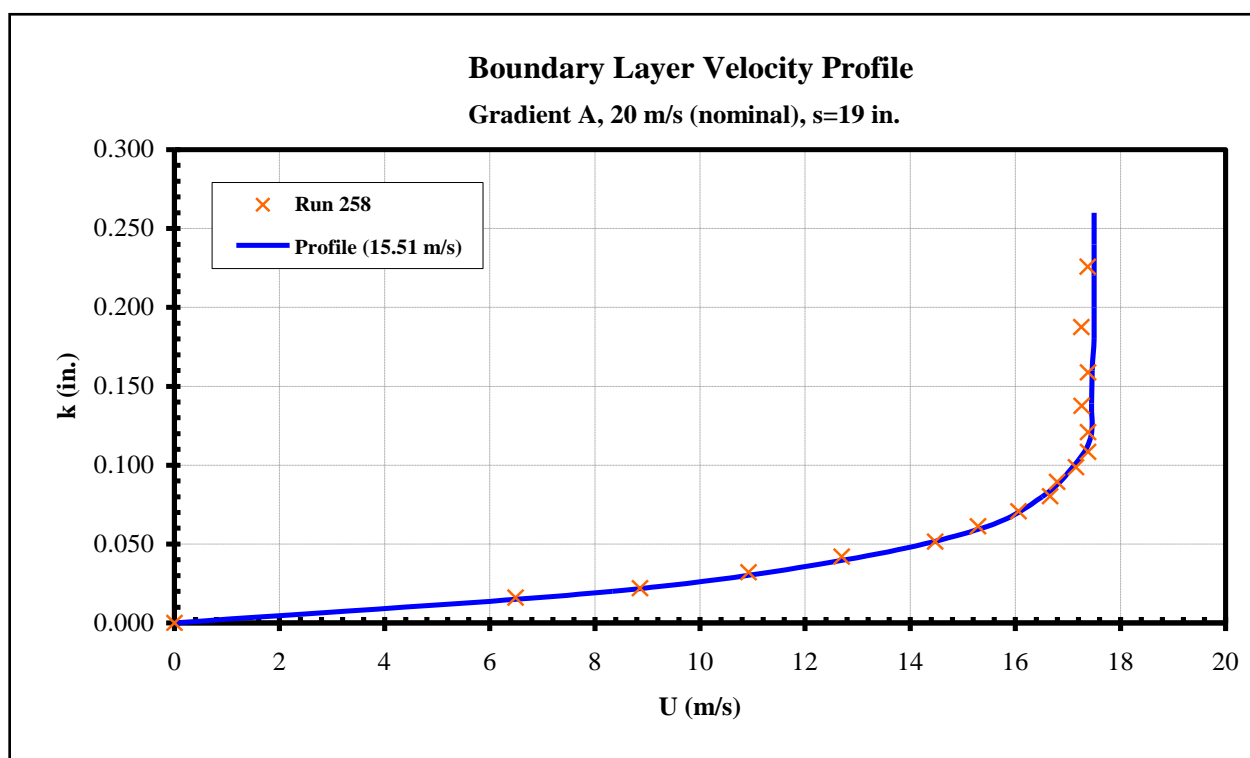


Figure 856: Gradient-A boundary layer velocity profile, U=20 m/s (nominal).

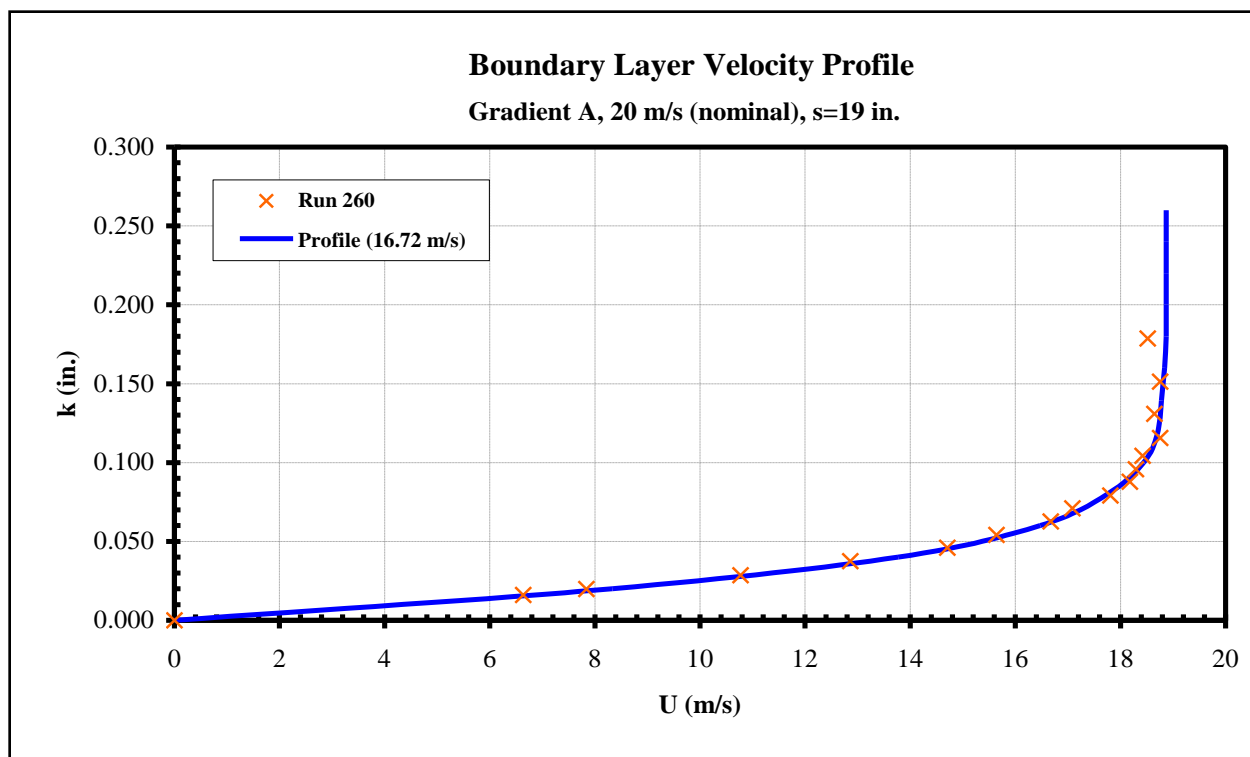


Figure 857: Gradient-A boundary layer velocity profile, U=20 m/s (nominal).

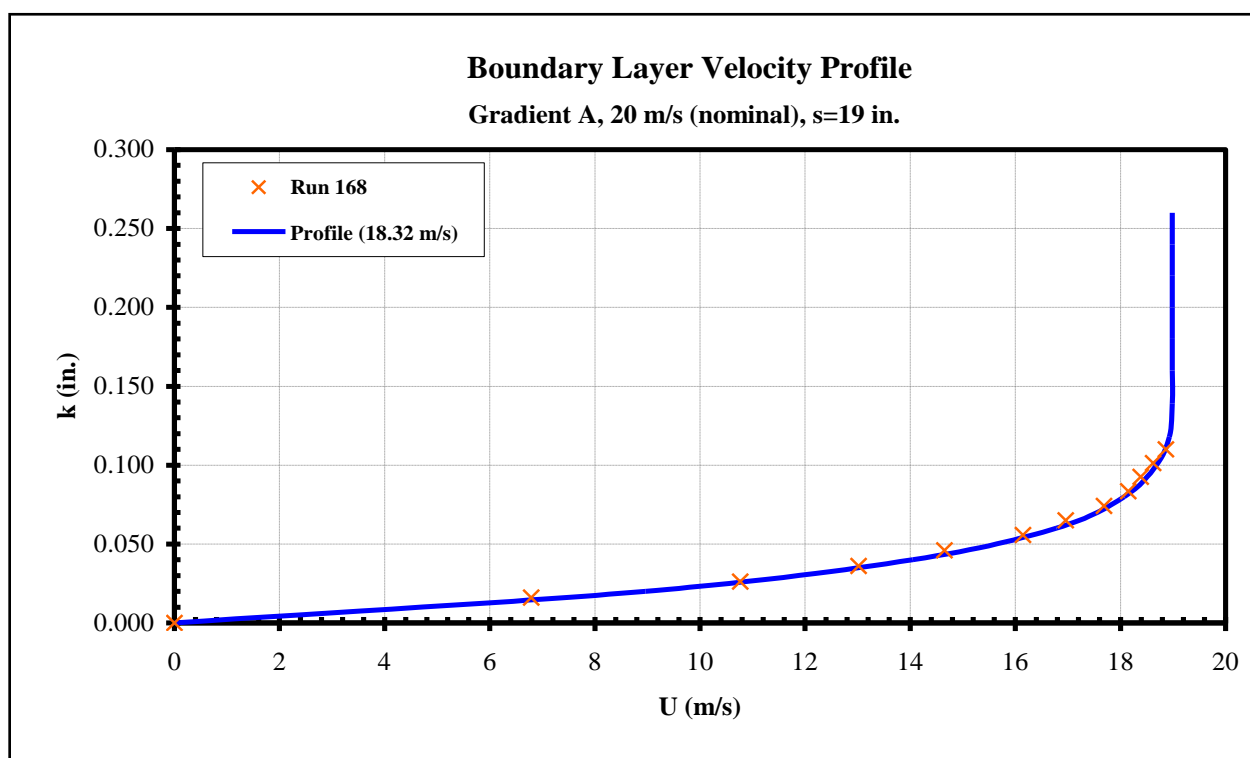


Figure 858: Gradient-A boundary layer velocity profile, U=20 m/s (nominal).

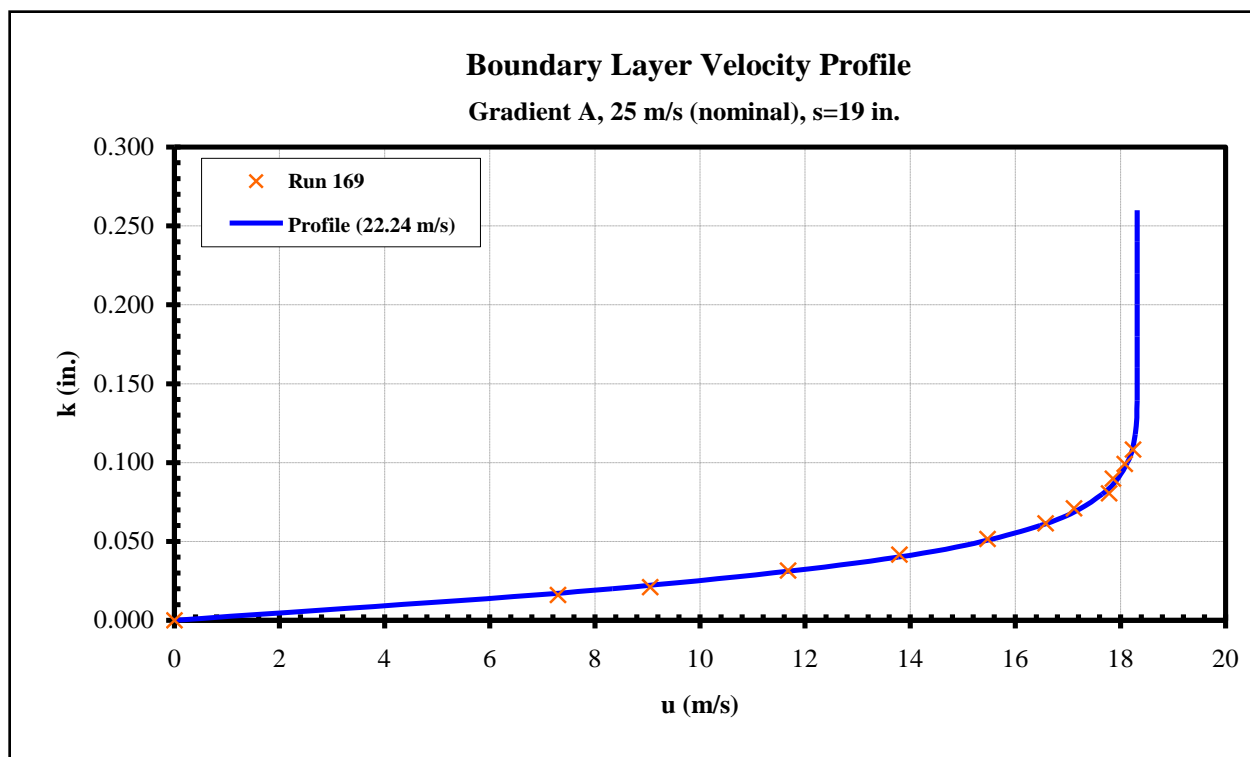


Figure 859: Gradient-A boundary layer velocity profile, U=25 m/s (nominal).

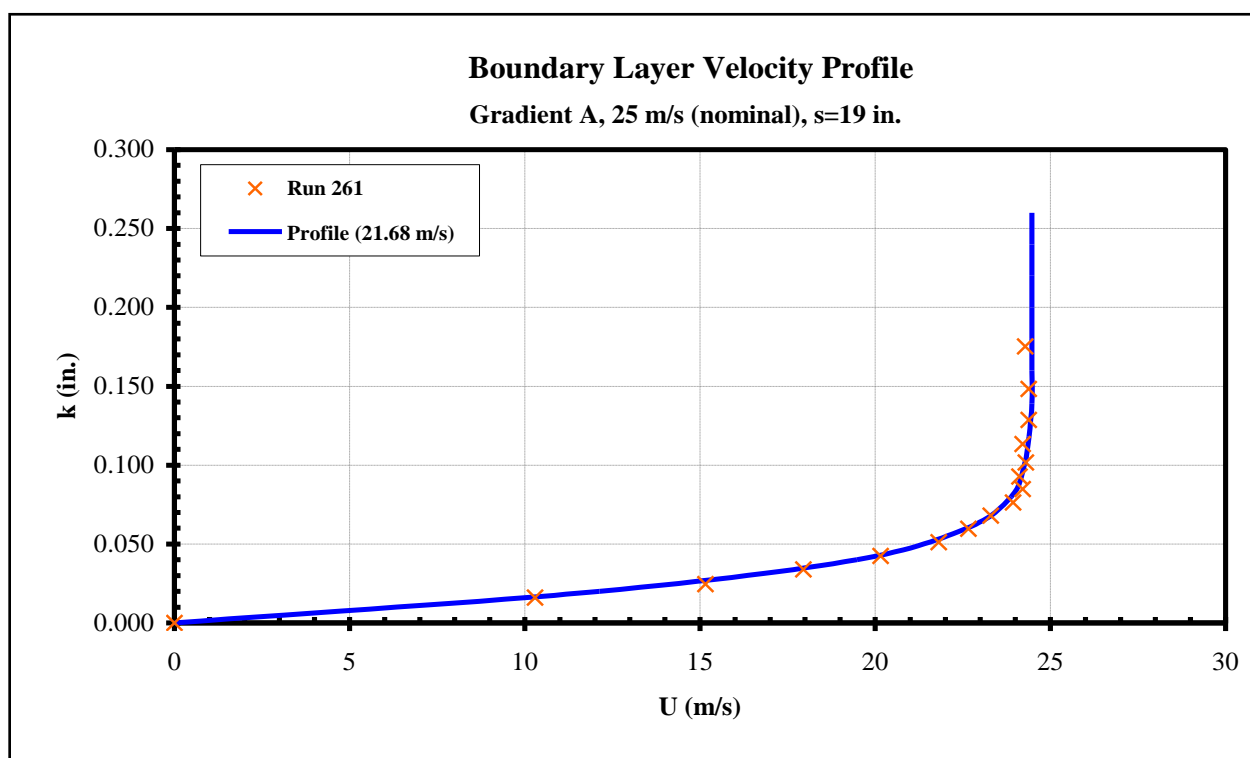


Figure 860: Gradient-A boundary layer velocity profile, U=25 m/s (nominal).

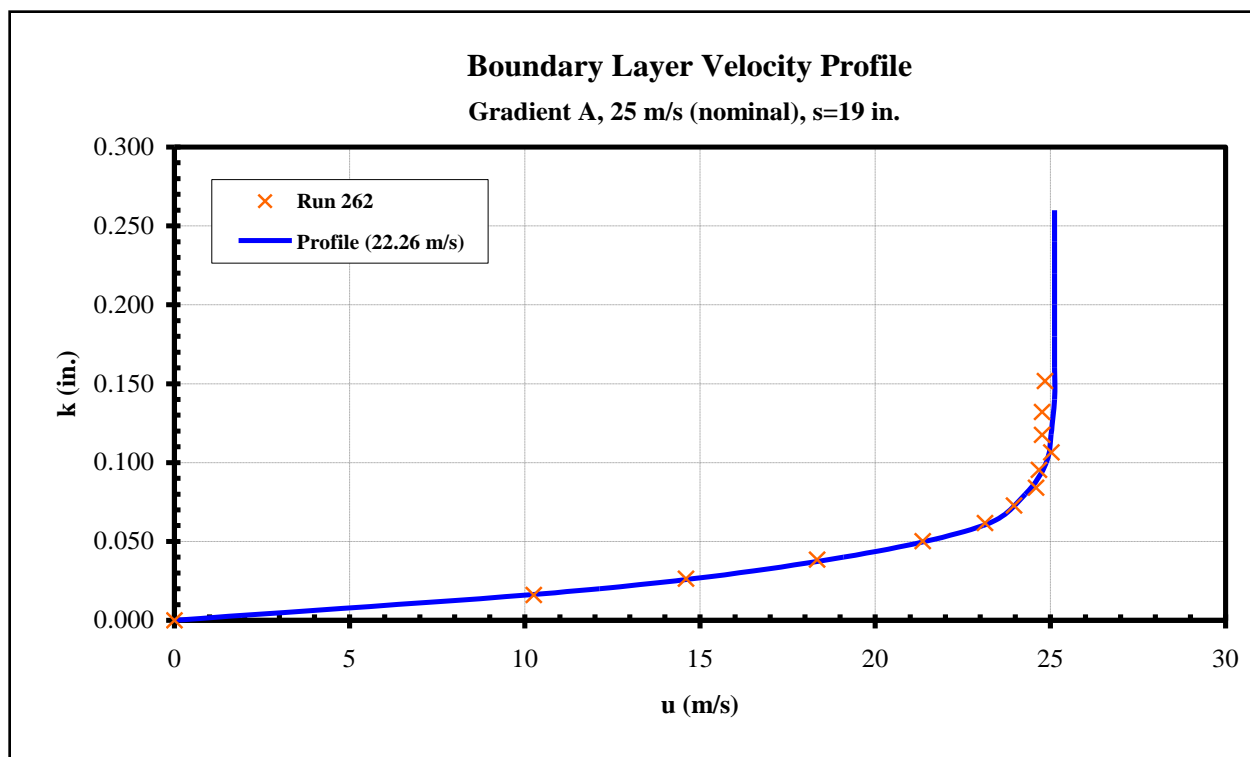


Figure 861: Gradient-A boundary layer velocity profile, U=25 m/s (nominal).

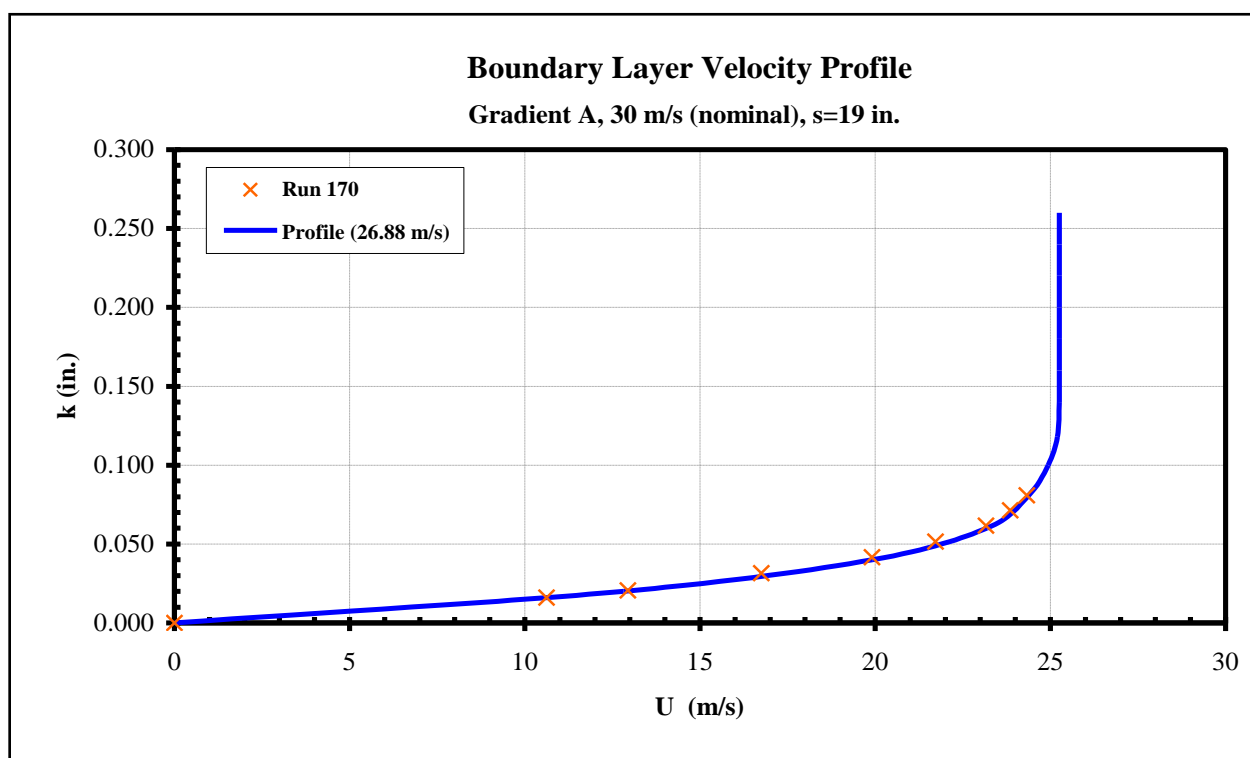


Figure 862: Gradient-A boundary layer velocity profile, U=30 m/s (nominal).

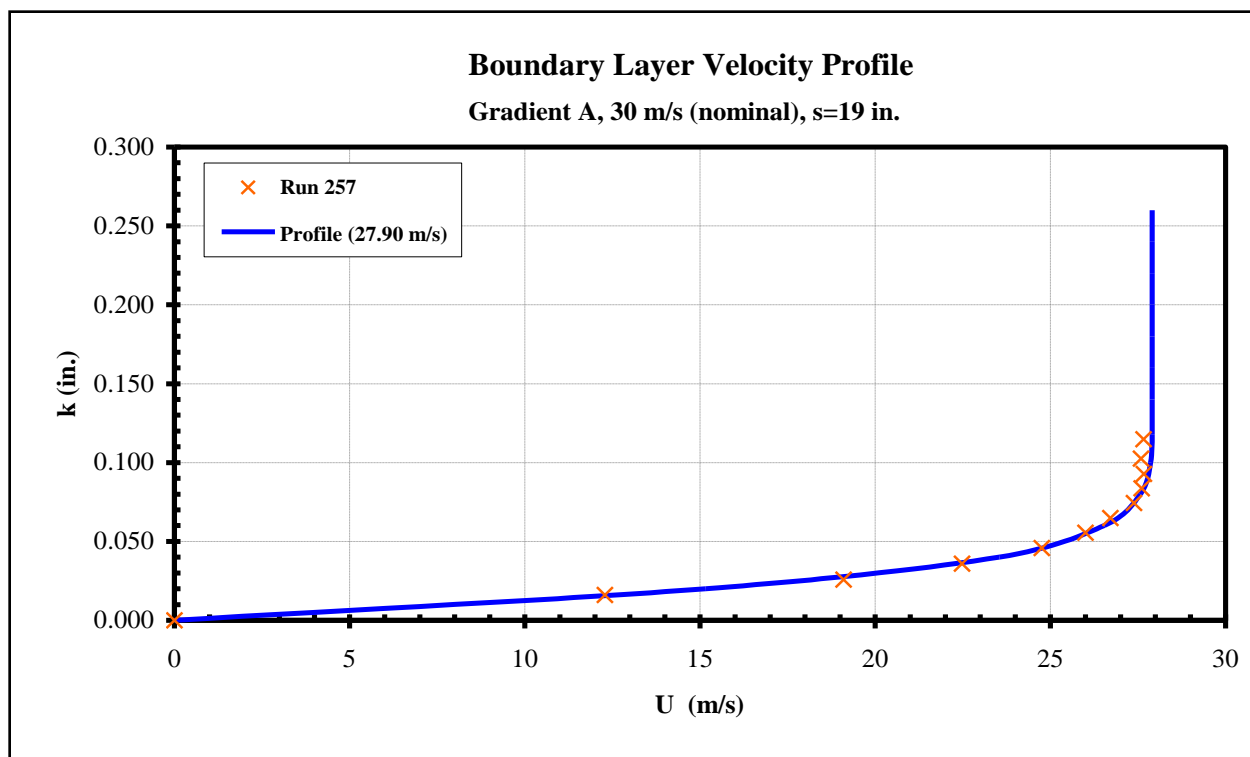


Figure 863: Gradient-A boundary layer velocity profile, U=30 m/s (nominal).

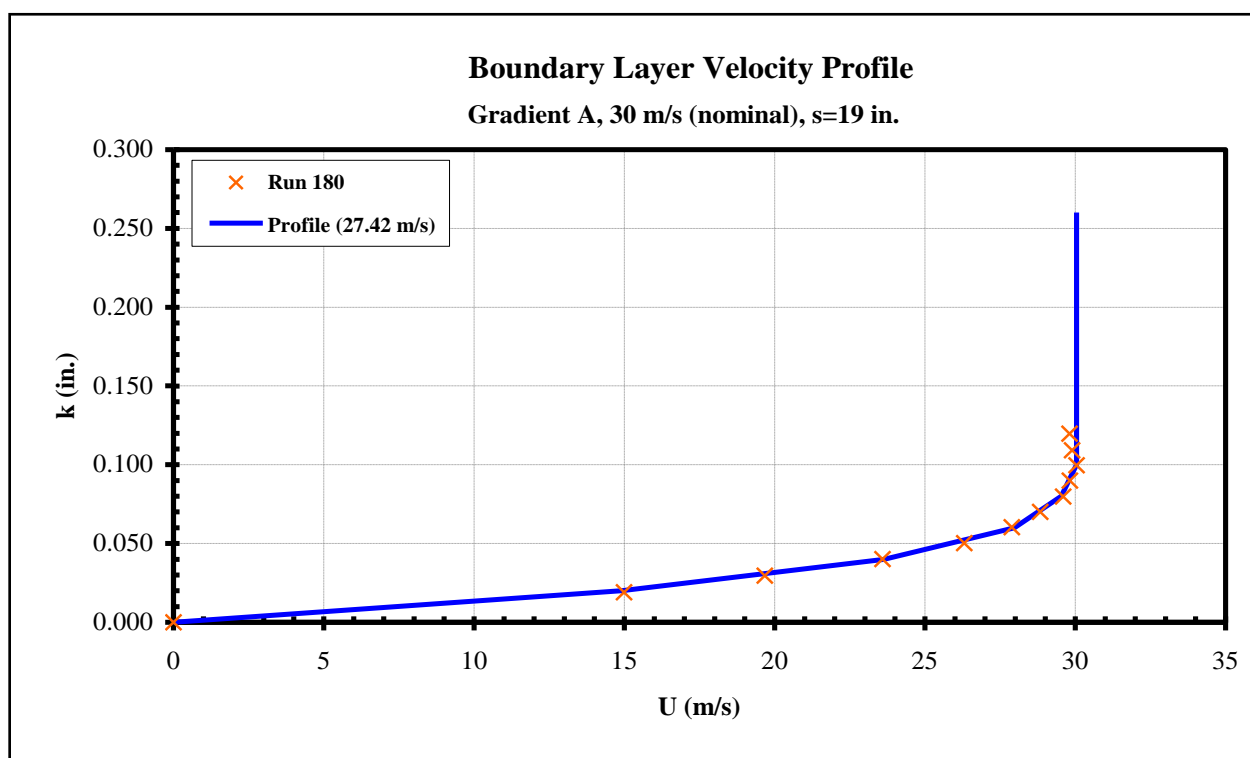


Figure 864: Gradient-A boundary layer velocity profile, U=30 m/s (nominal).

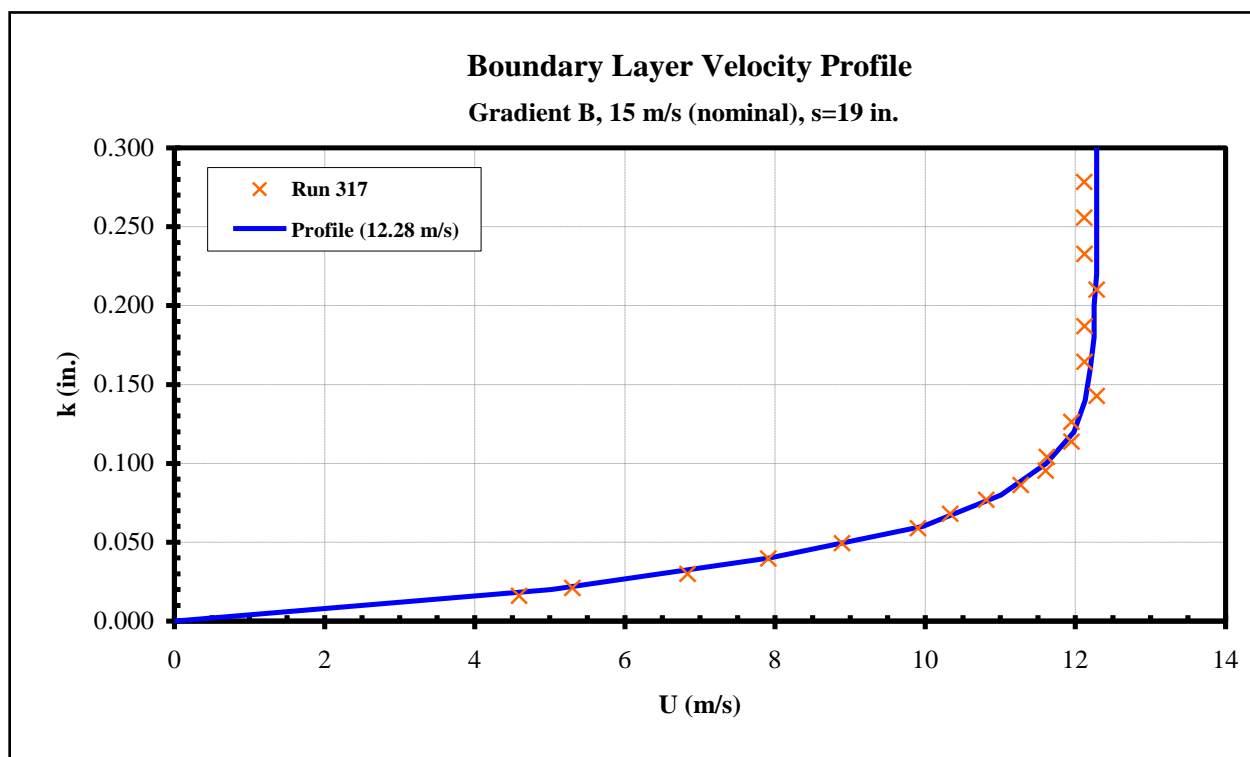


Figure 865: Gradient-B boundary layer velocity profile, U=15 m/s (nominal).

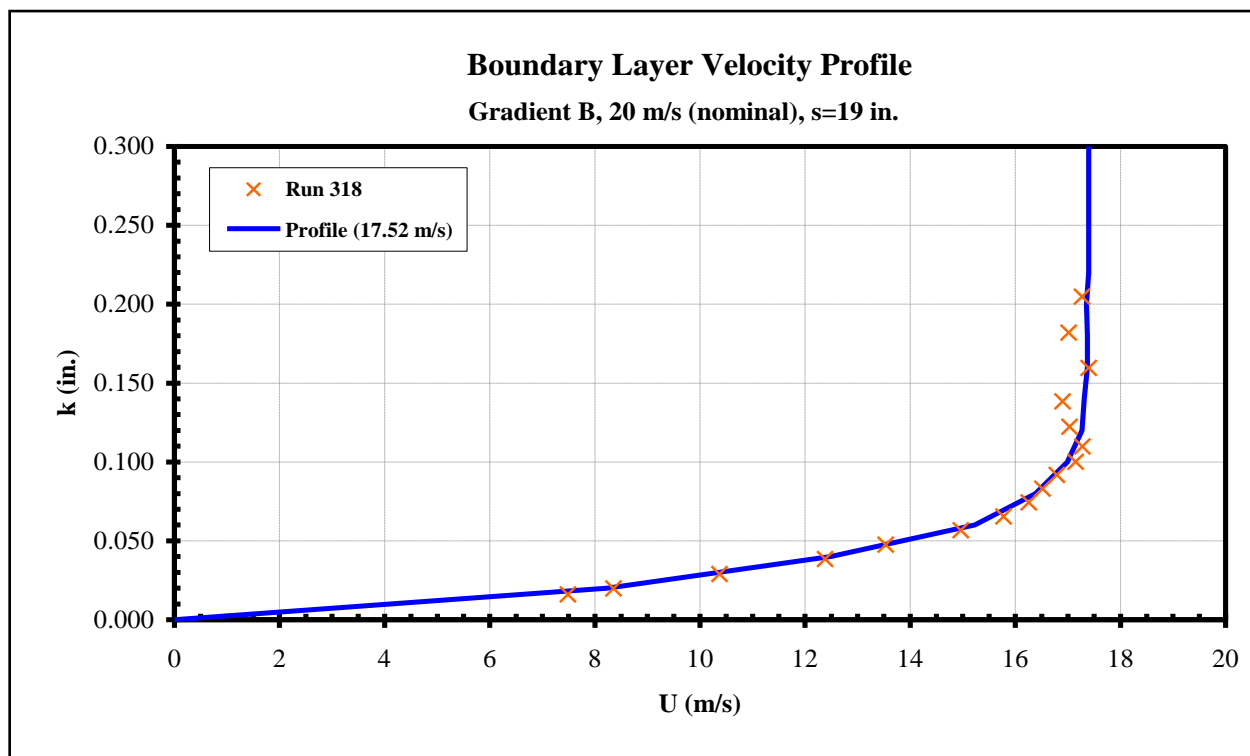


Figure 866: Gradient-B boundary layer velocity profile, U=20 m/s (nominal).

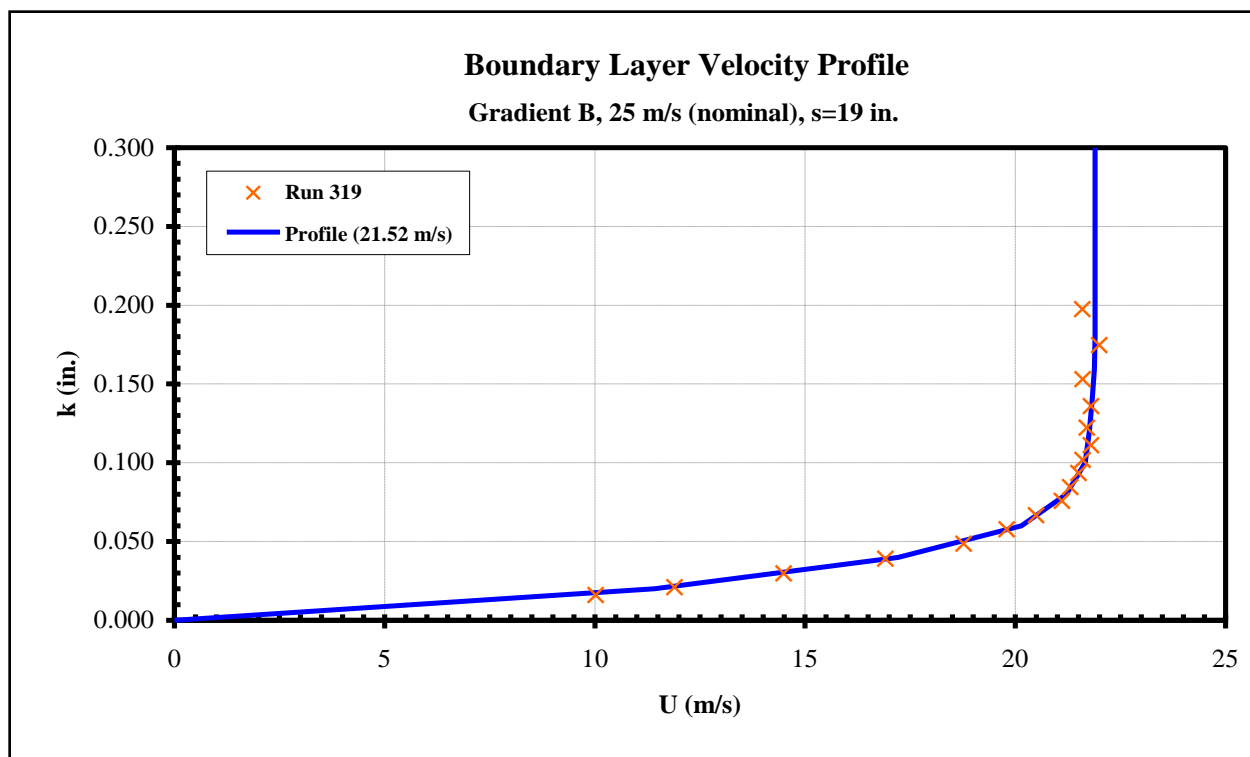


Figure 867: Gradient-B boundary layer velocity profile, U=25 m/s (nominal).

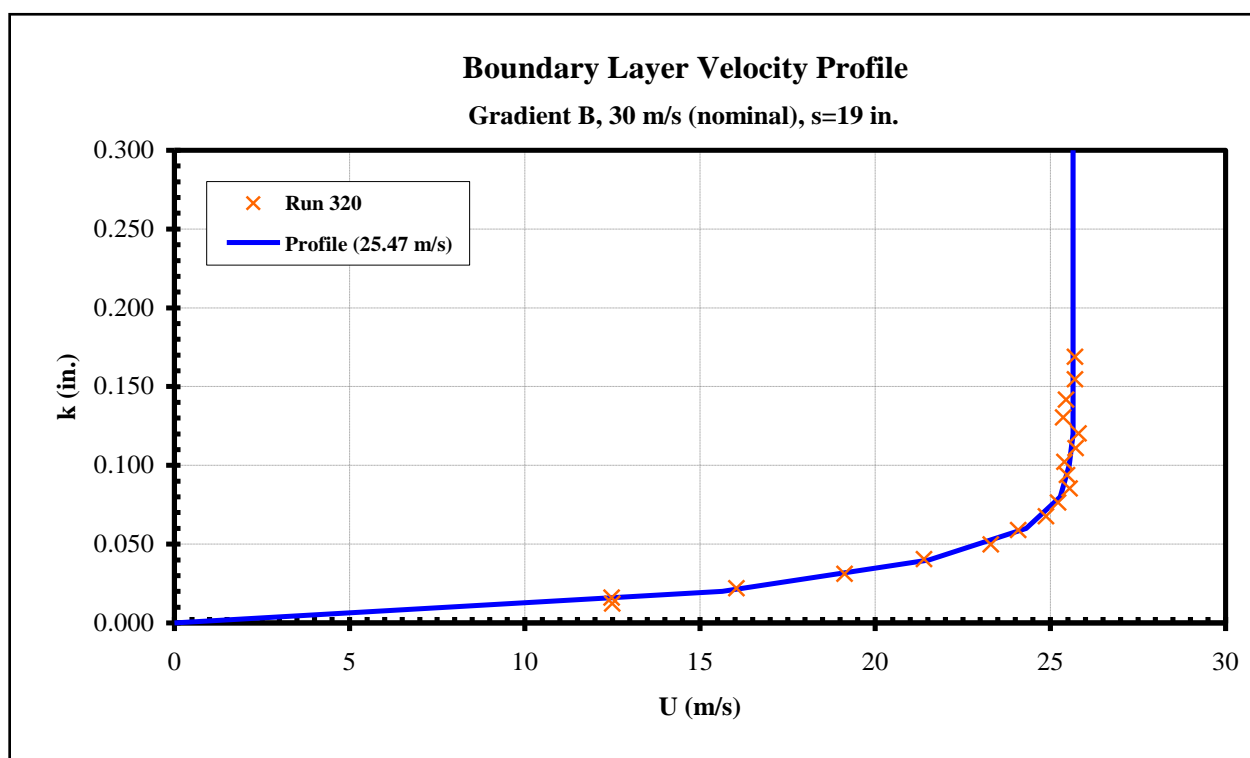


Figure 868: Gradient-B boundary layer velocity profile, U=30 m/s (nominal).

APPENDIX E

Hot Wire Calibration Procedure

1. Warm-up Anemometer, DAQ and Power supply for pressure transducer at least for 20min.
2. Connect hot-wire cables to the Anemometer inputs and amplifiers outputs according to numbering on their tags.
3. Connect hot-wire cables to DAQ (use cables which arrived with Anemometer):
hw1 to channel ai0,
hw2 to channel ai1,
hw3 to channel ai2,
hw4 to channel ai3.
4. Connect pressure transducer output cable to channel ai5.
5. Power pressure transducer with bipolar +15 and -15 Volts.
6. Pressure input tagged with letter "P" connect to Pitot tube.
7. Another pressure input attach with tape to the calibrator close to measurement location.
8. *Make sure there is no wind around the calibrator.*
9. Put into clamped holder located on top of the calibrator both Pitot tube and hot-wire holder (Pitot tube should be glued to the holder). Make sure they are as close to each other as possible, approximately in the center of the nozzle, and slightly below the edge of the nozzle.
10. Attach with tape the hot-wire cable to the calibrator for safety.
11. Set the anemometer channel's mode switch to "ADJUST".
12. Insert a short probe (follow a mark on the holder) into probe support (at this stage we wish to compensate for the resistances of support and cable). Refer to Anemometer Manual for more details on the next steps.
13. Set the decade digits to 0.00. Balance the cable/support resistances with the "NULL" trimpot by nulling the Test Module display bringing it to zero.
14. Insert the first hot-wire sensor (follow a mark on the holder). Dial the thumbwheel switch of the resistor decade until you balance the bridge. The resistance displayed on the decade is the resistance of the probe itself.
15. Multiply the sensor resistance by the overheat ratio you want to work with (we used 1.8) and get approximately between 7 to 9 Ω . Set the resistor decade to the new resistance. When the feedback circuit balances the bridge (after the "OPERATE" mode is selected), it will heat the probe until its resistance matches that indicated by the resistor decade.
16. Change the mode selector on the channel module to "N". Using the "DAMPING" trimpot, change the anemometer output voltage to about -9V to prevent undesirable oscillations during transition to "OPERATE" mode.
17. Switch the mode selector on the channel module to the "OPERATE" mode. Connect cable from "BRIDGE OUTPUT" of the channel of interest to oscilloscope. Use 1V/div and 50 μ sec/div on oscilloscope. Select "PULSE RESPONSE" on the test module. The channel's frequency response should appear on the screen of the oscilloscope. Trim the damping factor of the frequency response with the "DAMPING" trimpot and try to get 1-1.5 period of oscillations only. In principle this should be done first at zero flow velocity and then repeated at the highest flow velocity found in experiment.
18. Select "AMPLIFIER OUTPUT" on the test module. Play with the gain and DC offset for

the amplifier to adjust it in the range of velocities of interest: approximately +9V should correspond to 0m/s and -9V to 40m/s. Make sure also the Pitot tube tip and hot-wire sensor are at the same height and approximately 1-3mm lower the nozzle edge.

19. Open LabView program for calibration named: Calib_pressure_HW.vi
20. In Block Diagram configure DAQ Assistant for hw1:
Voltage Order: 0 Physical channel: Dev1/ai0
Voltage_0 Order: 1 Physical channel: Dev1/ai5
The first line is always stands for hw, and the second line (channel ai5) is always reserved for pressure transducer output. *Keep this order when calibrating next hot-wire!*
21. Double click on Write To Measurement File and change File Name to proper directory for saving
(Currently it reads: C:\Users\Sergiy\Caltech\data\112808\cal_hw1_1.lvm,
where: cal_hw1_1.lvm means hw number 1, calibration number 1).
Options should be marked already as:
Save to one file,
Append to file,
File format: Text,
No headers,
One column only,
Delimiter: Tab.
22. In Front Panel should be:
Number of blocks: 5,
Sample Frequency: 300,
Block size: 900,
Input Temperature: you choose.
23. Press Run to get data for zero offset (no air supplied at this moment to the calibrator).
24. When the Run in the previous step is finished, open a little bit the pressure regulator and supply air to the calibrator and press Run.
25. Increment air pressure by opening the pressure regulator to get about 10-15 points for calibration curve.
26. For visual control in the Front Panel:
Make sure not to exceed 1V for pressure transducer (Pitot Volts) for largest velocity which corresponds to about 40m/s in Pitot Velocity.
HW Mean should be in the limits +9 to -9V and HW RMS should not be larger than about 0.1V.
27. After calibration of the first hw1 is over the output file with the name *cal_hw1_1.lvm* (the first column in the file is information about blocks, second column is Pitot Volts, third column is HW Mean Volts).
28. Change the mode selector on the channel module to "N". Now very important step is removing the calibrated hot-wire from the calibrator holder: *do not take out the hot-wire probe from its holder and do not disconnect hot-wire cable, just unscrew the clamp and take carefully out the hot-wire probe together with the probe holder* (Pitot tube stays in place attached to the calibrator holder because it was glued to it before).
29. Put the calibrated hot-wire probe in safe place.
30. Repeat the calibration procedure for the next hot-wires. Do not forget to make changes for a new hot-wire in the program before calibration.

31. After calibration is over for all hot-wires, open Matlab file named: `calibrator.m`
32. Make changes in the header of the file:
 `hw1_switch=1` (if hw1 was calibrated, "0" if not). The same applied for all other hot-wire.
 `calibdir=` (choose directory where calibration files are located).
 `temper=` (measured temperature of air from the nozzle).
33. Run the Matlab file and get the output file similar to:
 `cal_hw1234_1.lvm`
 Each line in the file is the polynomial coefficients in order from highest to lowest power. Order of lines from top to bottom is for hw1, hw2, hw3, hw4 correspondingly. The typical calibration curve is shown in Figure 869.
34. Open LabView file named: `HW_aquization_calib.vi`
35. Open Block Diagram and put new calibration coefficients to the Expression Nodes (order of nodes from top to bottom is for hw1, hw2, hw3, hw4 correspondingly).

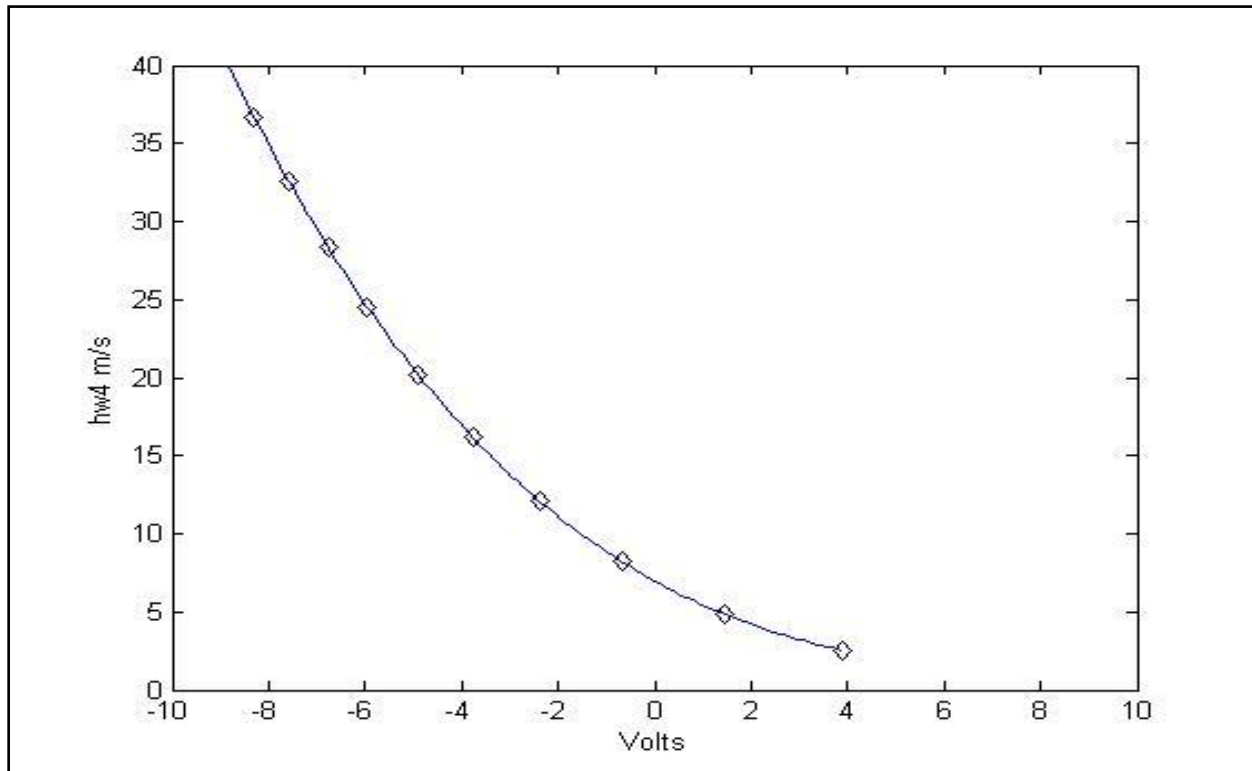


Figure 869: Typical calibration curve for hot-wire.

APPENDIX F

Hot-wire Repair Procedure

1. Insert broken hot-wire into vertical rotational translational stage. Manipulate with the stage, basement plate and microscope magnification to have the tops of the both prone tips in a field of view and well in focus.
2. Remove the old wire and/or leftovers of solder from the top of the prone tips with sandpaper of fine grit (1000-2000). Check under microscope if they are completely removed (tops of the prone tips should look flat and of uniform brightness).
3. Put on the tops of the prone tips small amount of solder paste (use water to remove excess amount as the paste is water soluble). Heat the solder iron to about 300 C and attach a small drop of tin from solder wire to the iron tip (use in advance a tip cleaner if the iron tip is dirty). *Gently* touch to the tops of the prone tips with solder iron and after doing this check under microscope if the tops of the prone tips have hemispheres of solder tin on them. If not, repeat steps 2-3.
4. Insert the wire cartridge into horizontal rotational stage above the prone and manipulate the rotational and translational stages to have a wire exactly on tops of the prone tips. Important: *Do not process a wire with solder paste as it found to destroy the golden thin layer of a wire.*
5. This step requires very high accuracy. Heat the iron to about 450 C. *Gently* touch for one second each tip of the prone from side with iron tip (make sure in advance that the surface of the iron tip is clean). After this check under microscope if the wire is “immersed” into the hemisphere of solder tin.
6. Cut with razor blade a wire out of the cartridge and then remove gently the wire overhangs from the prone tips (try not to deform the prone tips while doing this).
7. Anneal the hot-wire for several hours. (It assumes using hot-wire anemometer and running the hot-wire under working conditions. Check the Calibration Procedure (Appendix E) for details.)

APPENDIX G

Hot-wire Experimental Procedure

1. After the calibration procedure is completed and new calibration coefficients are filled into the Expression Nodes of the Block Diagram of HW_acquisition_calib.vi, the following changes have to be made in the Block Diagram:
in Write To Measurement File choose the path to save data and file name should be: *run number*;
in Write To Measurement File2 choose the path to save data and file name should be: *calib_run number*.
Do it only once and after the files will be incremented automatically for the next runs.
Check also in Front Panel:
Time delay: 0,
Sample frequency: 3000,
Block size: 3000,
Number of blocks: 300.
The output data file then will contain 10 columns: 1st column is data point count number, 2-5 columns are voltage/velocity from hot-wires, 6th column for temperature in Celsius, 7-9 columns for time stamps hour/min/sec, and last 10th column for date.
2. Put all equipment to a car; do not forget to disconnect pressure transducer. Connect temperature controller output to the channel ai4 of the DAQ.
3. Data acquisition to LogBook. (The reason why the priority was given to the data recorded with DAQ is that the velocity power spectra showed less noise and better performance and in the absence of the signal power spectrum obtained from DAQ was zero whereas the LogBook has its own nonzero spectra in the absence of the signal.)
4. Connect cables from Anemometer and accelerometers to LogBook: four Anemometer channels to CH0-CH3 of LogBook and two accelerometers to CH4 and CH6. Make necessary settings in LogBook acquisition parameters. For this first connect LogBook memory card to Laptop through CompactFlash PCMCIA Adapter. Open LogView software. Go to: Hardware Configuration - P1 – Analog IO – P1_CH00. Choose DBK8 Voltage Input Card. This card arrived with the LogBook (see DBK Manual for more details about the card). Go to: Analog Input Channel Configuration and mark physical channels 0-4 and 6 ON. All the rest should be OFF. Go to: Acquisition Configuration, set Pre-trigger to 0, Trigger to When Armed, Post trigger to expected acquisition duration. Check box Enable Time Stamp, choose Frequency, Base Rate A 3000 Hz. Make necessary settings in Preferences on downloading, uploading and general. Go to: Device, Select PC card destination. Then download the configuration to the memory card. Take the card out of the CompactFlash PCMCIA Adapter and insert to the LogBook. The LogBook is ready to work. The output data file then will contain 9 columns: 1-2 columns for time stamps, 3rd for date, 4-7 for hot-wires 8-9 for accelerometers. When experiment is finished for uploading data from the card to Laptop insert card to CompactFlash PCMCIA Adapter, open LogView software and press Upload button.
5. Put L-brackets on the model and attach hot-wire holders with probes. Start from hot-wire that is closest to leading edge (usually hw1) (Figure 870).
6. Install in advance Camera Control Pro 2 software (from installation disk), open this software, connect camera to Laptop through USB port, switch in the software to LIVE

mode, focus camera on the hot-wire sensor and get as sharp image as possible (Figure 872). Put a ruler close to hot-wire sensor to measure distance from wall. Try to adjust the same distances from wall for all hot-wire with the height adjuster (Figure 871) (we had about 0.02 in.).

7. When everything is ready and all hot-wires are installed (two typical hot-wire configurations are shown in Figure 873 and Figure 874), operate Anemometer channels and run HW_aquisition_calib.vi (sometimes channels of the Anemometer do not respond. Restarting of the Anemometer usually helps).

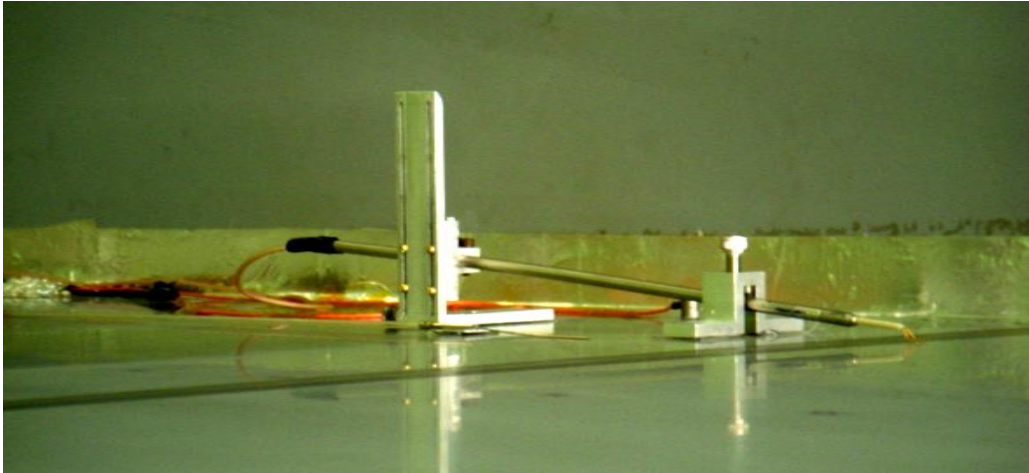


Figure 870: Hot-wire probe attached to a surface of the model with L-bracket. Height adjuster is used to adjust distance of hot-wire from surface.

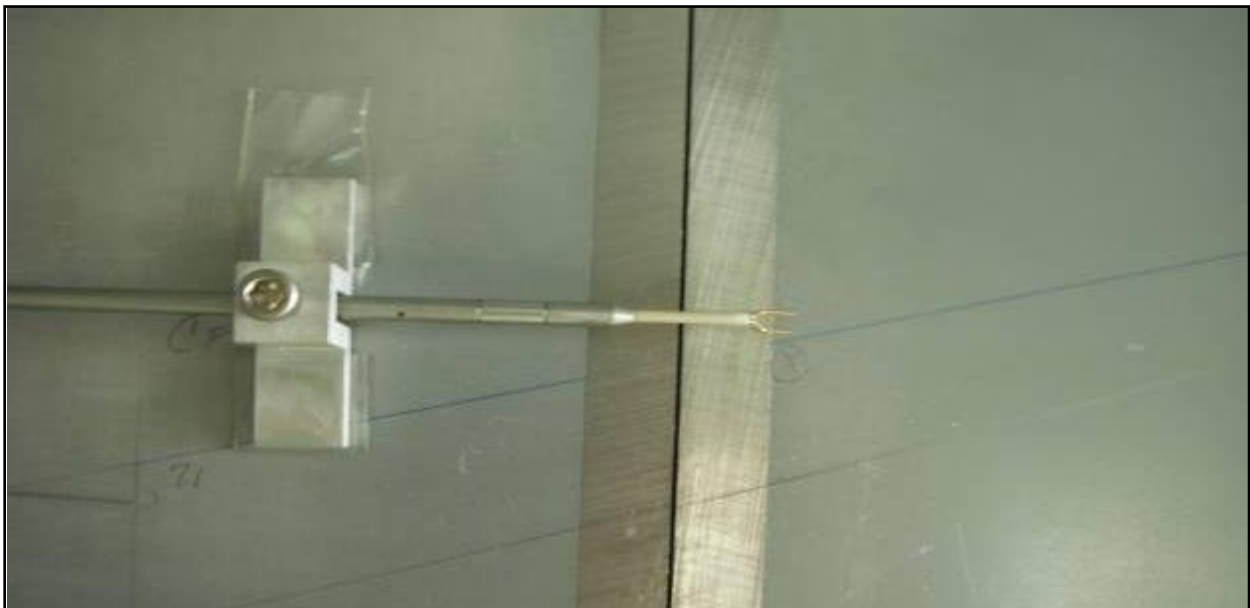


Figure 871: Hot-wire height adjuster.

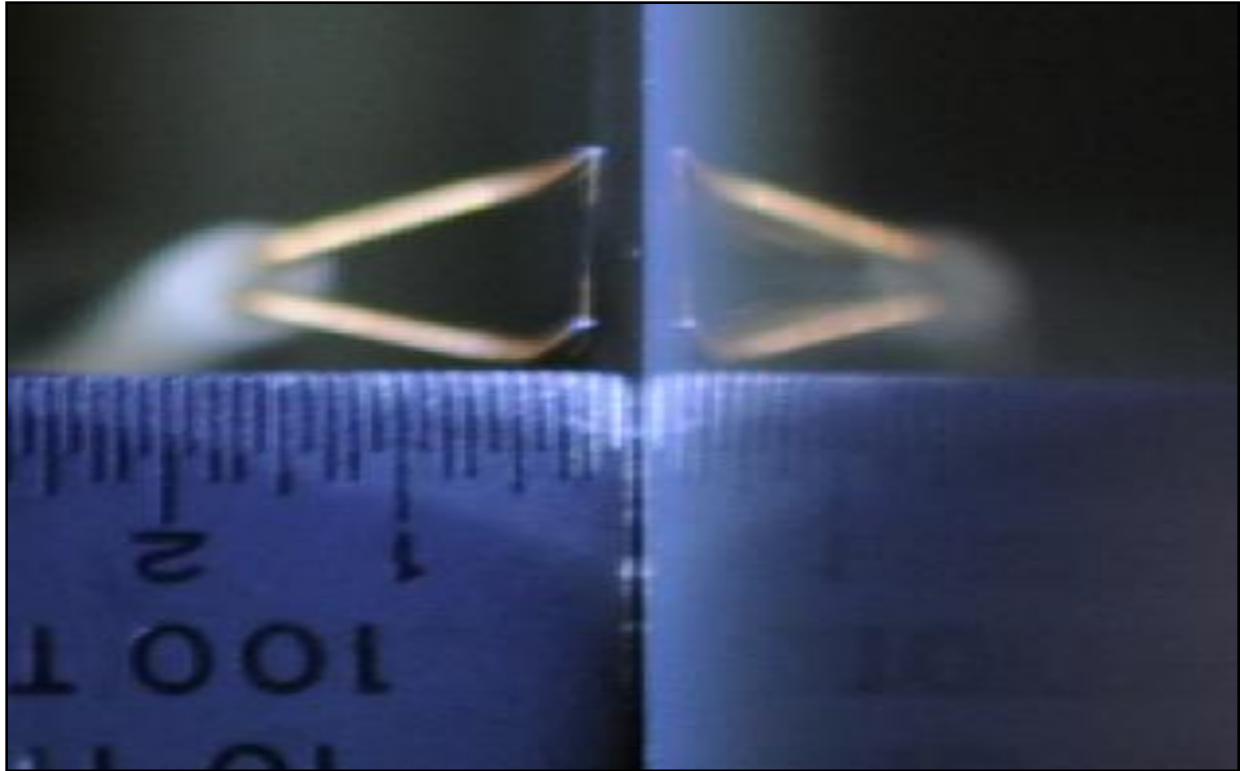


Figure 872: Distance measurement between a hot-wire probe and model surface.

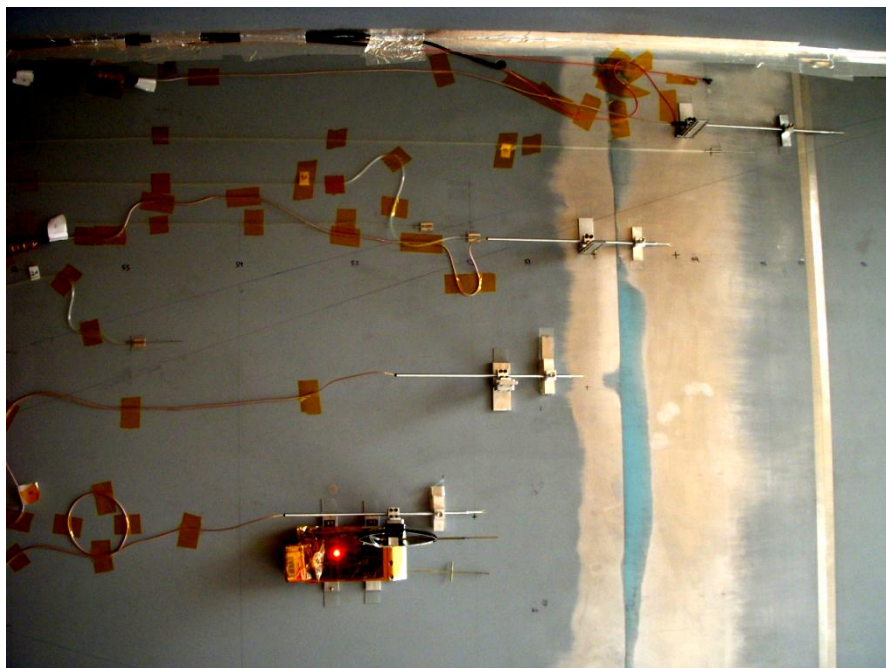


Figure 873: Hot-wire probe typical configuration on the model for stream wise flow measurements.



Figure 874: Hot-wire typical configuration on the model for span wise flow uniformity measurements.